CT-Meeting 2016

Proceedings

The 4th International Meeting on

Image Formation in

X-Ray Computed Tomography

July 18-22, 2016, Bamberg, Germany

Conference Chair:
Marc Kachelrieß (German Cancer Research Center, DKFZ)

ct-meeting.org

The 4th International Conference on Image Formation in X-Ray Computed Tomography is supported by:

Deutsche Forschungsgemeinschaft

GE Healthcare

Siemens Healthineers

Toshiba Medical Systems

Varian Medical Systems

Ziehm Imaging

We thank our sponsors for their important and valuable contributions!

We would like to thank the members of the scientific committee for their great work by taking the opportunity to mention them in alphabetical order:

Scientific Committee

Name	Institute
Adam Wunderlich	National Institute of Standards and Technology, USA
Alexander Zamyatin	Samsung, Korea
Bruno De Man	GE Global Research, USA
Carl Crawford	Csuptwo, USA
Frédéric Noo	University of Utah School of Medicine, USA
Ge Wang	Rensselaer Polytechnic Institute (RPI), USA
Guang-Hong Chen	University of Wisconsin-Madison, USA
Gunnar Brix	Federal Office for Radiation Protection, Germany
Günter Lauritsch	Siemens Healthineers, Germany
Harry Martz	Lawrence Livermore National Laboratory, USA
Hengyong Yu	University of Massachusetts Lowell, USA
Hiroyuki Kudo	University of Tsukuba, Japan
Jakob Sauer Jørgensen	Technical University of Denmark, Denmark
Jed Pack	GE Global Research, USA
Jeff Fessler	University of Michigan, USA
Jeff Siewerdsen	Johns Hopkins University School of Medicine, USA
Jing Wang	University of Texas Southwestern Medical Center, USA
Johan Nuyts	KU Leuven, Belgium
Joost Batenburg	Centrum Wiskunde & Informatica, Netherlands
Josh Star-Lack	Varian Medical Systems, USA
Karl Stierstorfer	Siemens Healthineers, Germany
Katsuyuki Taguchi	Johns Hopkins University School of Medicine, USA
Kirsten Boedeker	Toshiba Medical Research Institute, USA
Kyle Myers	U.S. Food and Drug Administration, USA
Lifeng Yu	Mayo Clinic, USA
Martin Fiebich	Technische Hochschule Mittelhessen, Germany
Michael Grass	Philips Research Hamburg, Germany

Michael McNitt-Gray	UCLA, USA
Michael Wucherer	Klinikum Nürnberg, Germany
Michel Defrise	Vrije Universiteit Brussel, Belgium
Norbert Pelc	Stanford University, USA
Patrick La Riviere	University of Chicago, USA
Rebecca Fahrig	Siemens Healthineers, Germany
Srinivasan Vedantham	UMass Medical School, USA
Stephen Glick	U.S. Food and Drug Administration, USA
Thilo Michel	University of Erlangen-Nürnberg, Germany
Thomas Flohr	Siemens Healthineers, Germany
Thomas Koehler	Philips Research Hamburg, Germany
Web Stayman	Johns Hopkins School of Medicine, USA
Wenly Wang	Toshiba Medical Research Institute, USA
Xiangyang Tang	Emory University, USA
Xiaochuan Pan	University of Chicago, USA
Yoram Bresler	University of Illinois at Urbana-Champaign, USA
Yuxiang Xing	Tsinghua University Beijing, China
Zhou Yu	Toshiba Medical Research Institute, USA

Organization Committee

Andrea Kachelrieß	Society of High Performance Computational Imaging (SHPCI)
Carsten Funck	German Cancer Research Center (DKFZ)
Carsten Leinweber	German Cancer Research Center (DKFZ)
İrem Özdemir	German Cancer Research Center (DKFZ)
Jan Kuntz	German Cancer Research Center (DKFZ)
Juliane Hahn	German Cancer Research Center (DKFZ)
Marc Kachelrieß	German Cancer Research Center (DKFZ)
Nadine Waltrich	German Cancer Research Center (DKFZ)
Sebastian Sauppe	German Cancer Research Center (DKFZ)
Sedat Aktaş	German Cancer Research Center (DKFZ)
Stefan Sawall	German Cancer Research Center (DKFZ)

Tuesday, July 19

Oral Session : General
Time : 07:55 – 09:40
Chairs : Günter Lauritsch and Katsuyuki Taguchi

Time	Author	Title	Page
07:55 – 08:00	Marc Kachelrieß	*Opening Remarks*	
08:00 – 08:20	Tao Sun, Jung-Ha Kim, Roger Fulton, Johan Nuyts	*Data-driven Correction for Head Motion In Helical X-ray CT*	17
08:20 – 08:40	Jiabei Zheng, Jeffrey A. Fessler, Heang-Ping Chan	*Digital Breast Tomosynthesis Reconstruction with Detector Blur and Correlated Noise*	21
08:40 – 09:00	Matthias Wieczorek, Christoph Jud, Florian Schaff, Franz Pfeiffer, and Tobias Lasser	*X-Ray Tensor Tomography – A Linear System Approach to Reconstruction*	25
09:00 – 09:20	Aswin John Mathews, Steven Tilley II, Grace Gang, Satomi Kawamoto, Wojciech Zbijewski, Jeffrey H. Siewerdsen, Reuven Levinson, J. Webster Stayman	*Design of Dual Multiple Aperture Devices for Dynamical Fluence Field Modulated CT*	29
09:20 – 09:40	P. Trueb, P. Zambon, and C. Broennimann	*Hybrid Photon Counting Detectors for Spectral X-ray Imaging*	33

Coffee Break

Oral Session : Spectral
Time : 10:00 – 11:40
Chairs : Bernhard Brendel and Norbert Pelc

10:00 – 10:20	Emil Y. Sidky, Taly Gilat-Schmidt, Rina Foygel Barber, Wooseok Ha, and Xiaochuan Pan	*Simultaneous spectral scaling and basis material map reconstruction for spectral CT with photon-counting detectors*	37
10:20 – 10:40	Bernhard Brendel, Frank Bergner, Kevin Brown, and Thomas Koehler	*Penalized Likelihood Decomposition for Dual Layer Spectral CT*	41
10:40 – 11:00	Martin Sjölin and Mats Danielsson	*Angular Oversampling and Built-In Anti-Aliasing Filtration in CT with ultra-fast ASIC on Photon Counting Detector*	45
11:00 – 11:20	Nicolas Ducros, Simon Rit, Bruno Sixou, and Françoise Peyrin	*Non-Linear Regularized Decomposition of Spectral X-ray Projection Images*	49
11:20 – 11:40	George S.K. Fung, Karl Stierstorfer, Matthew Fuld, Satomi Kawamoto, Elliot K. Fishman, Benjamin M.W. Tsui, and Katsuyuki Taguchi	*Spectrum Optimization in Split-Filter Dual-Energy CT for Iodine Quantification and Virtual-Non-Contrast Imaging*	53

Lunch Break

Poster Session : Poster Session 1
Time : 13:20 – 15:00
Chairs : Hengyong Yu and Larry Zeng

Coffee Break

Oral Session : Cardiac
Time : 15:20 – 17:00
Chairs : Zhye Yin and Zhou Yu

Wednesday, July 20

Oral Session: Image Reconstruction
Time : 08:00 – 09:40
Chairs : Jeffrey Fessler and Emil Sidky

Time	Author	Title	Page
08:00 – 08:2	Emil Sidky	***Basic short course:*** *Image Reconstruction*	
08:20 – 08:40	Emil Sidky	***Basic short course:*** *Image Reconstruction*	
08:40 – 09:00	Jens Gregor, Philip Bingham, and Lloyd F. Arrowood	*Total Variation Constrained Weighted Least Squares Using SIRT and Proximal Mappings*	197
09:00 – 09:20	Dimple Modgil, David S. Rigie, Michael D. Bindschadler, Adam M. Alessio, and Patrick J. La Rivière	*Image-Domain Denoising for Myocardial Blood Flow Estimation in Dynamic CT*	201
09:20 – 09:40	Thibault Notargiacomo, Dominique Houzet, Guillaume Bernard, and Vincent Fristot	*Sparse Regularization of CBCT Reconstruction Using 3D Dual-Tree Complex Wavelet Transform and Dictionary Learning Techniques*	205

Coffee Break

Oral Session: Security and NDT
Time : 10:00 – 11:40
Chairs : Michael Knaup and Harry Martz

10:00 – 10:20	Andre Mouton and Toby P. Breckon	*Object Classification in Baggage-CT Imagery using Randomised Clustering Forests*	209
10:20 – 10:40	Kyle Champley, Jerel Smith, Jeff Kallman, and Philip Top	*Automatic Threat Detection for a Dual-Energy Four-View X-ray Carryon Luggage Scanner*	213
10:40 – 11:00	Joscha Maier, Carsten Leinweber, Stefan Sawall, Henning Stoschus, Frederic Ballach, Tobias Müller, Michael Hammer, Ralf Christoph, and Marc Kachelrieß	*Simulation-Based Artifact Correction for Computed Tomography in Metrology*	217
11:00 – 11:20	Navnina Bhatia, David Tisseur, and Jean Michel Létang	*Scattering Correction for Industrial CBCT using Continuously Thickness-Adapted Kernels at MeV Energy Range*	221
11:20 – 11:40	Corinne B. Brunelle, Mathieu Des Roches, Louis-Frederic Daigle, Pierre Francus, Bernard Long, and Philippe Després	*Combining CT Scan and Particle Imaging Techniques: Applications in Geosciences*	225

Lunch Break

Poster Session : Poster Session 2
Time : 13:20 – 15:00
Chairs : Klaus Müller and Zhou Yu

Time	Author	Title	Page
13:20 – 13:40	Poster fast forward (all authors)		
13:40 – 15:00	Rui Liu, Lin Fu, Bruno De Man, and Hengyong Yu	*GPU Acceleration of Branchless Distance Driven Projection and Backprojection*	229
13:40 – 15:00	Manuel Viermetz, Lorenz Birnbacher, Marian Willner, Peter B. Noël, Franz Pfeiffer, and Julia Herzen	*High Resolution Laboratory Grating-Based X-Ray Phase-Contrast CT*	233
13:40 – 15:00	Wenying Wang, Liuyuan Zhou, Xucheng Zhu, and Yuxiang Xing	*Image Reconstruction for Few-View and Limited-Angle MECT Based on Group-Wise Low Rank Constraint*	237
13:40 – 15:00	Andreas Fieselmann and Ludwig Ritschl	*Isocenter Determination for Arbitrary Planar Cone-Beam CT Scan Trajectories*	241
13:40 – 15:00	Jiulong Liu and Hao Gao	*Material Reconstruction for Spectral Computed Tomography with Detector Response Function*	245
13:40 – 15:00	Shouping Zhu, Yu Fan, Lei Xiong, Zhipeng Guo, Gaoqi Lv, Xu Cao, and Jimin Liang	*Fast Scanning Imaging of Micro-CT for Small Animals*	249
13:40 – 15:00	Sarah E. Divel, W. Paul Segars, Soren Christensen, Max Wintermark, Maarten G. Lansberg, and Norbert J. Pelc	*Use of Synthetic CT to Reduce Simulation Time of Complex Phantoms and Systems*	253
13:40 – 15:00	Natalia Dadivanyan, Detlev J. Götz, and Detlef Beckers	*Applying Soft Radiation in Computed Tomography Experiments on a Multipurpose Diffractometer*	257
13:40 – 15:00	André Aichert, Katharina Breininger, Thomas Köhler, and Andreas Maier	*Efficient Epipolar Consistency*	259
13:40 – 15:00	Qiulin Tang, Satoru Nakanishi, Zhou Yu, and Wenli Wang	*Fully Iterative Reconstruction for Cardiac CT*	263
13:40 – 15:00	Gengsheng L. Zeng and Wenli Wang	*Noise Weighting with an Exponent for Transmission CT*	267
13:40 – 15:00	Hussein Banjak, Marius Costin, Caroline Vienne, Ronan Guillamet, and Valérie Kaftandjian	*Reconstruction Algorithms for Reverse Helical Super-Short-Scan Mode*	271
13:40 – 15:00	Richard Sampson, Madison G. McGaffin, Thomas F. Wenisch, and Jeffrey A. Fessler	*Investigating Multi-threaded SIMD for Helical CT Reconstruction on a CPU*	275
13:40 – 15:00	Jakob S. Jørgensen, Sophia B. Coban, William R. B. Lionheart, and Philip J. Withers	*Effect of Sparsity and Exposure on Total Variation Regularized X-ray Tomography from few Projections*	279

Coffee Break

Oral Session : Phase-Contrast
Time : 15:20 – 17:00
Chairs : Bruno De Man and Web Stayman

Thursday, July 21

Oral Session : Image Quality
Time : 08:00 – 09:40
Chairs : Michel Defrise and Yuxiang Xing

Time	Author	Title	Page
08:00 – 08:20	Frédéric Noo	***Basic short course:*** *Image Quality Assessment*	
08:20 – 08:40	Frédéric Noo	***Basic short course:*** *Image Quality Assessment*	
08:40 – 09:00	Harald Schöndube and Frédéric Noo	*Statistically-Efficient Estimation of Hotelling Observer Performance with Unknown Means*	379
09:00 – 09:20	Bastian Bier, Kerstin Müller, Martin Berger, Jang-Hwan Choi, Ludwig Ritschl, Marc Kachelrieß, Rebecca Fahrig, and Andreas Maier	*Scatter Correction for C-Arm CT Using Primary Modulation*	383
09:20 – 09:40	Scott S. Hsieh and Norbert J. Pelc	*Pixel Size Tradeoffs for CdTe Spectral Photon Counting Detectors*	387

Coffee Break

Oral Session : Iterative Reconstruction
Time : 10:00 – 11:40
Chairs : Alexander Katsevich and Johan Nuyts

10:00 – 10:20	Pengwei Wu, Tingyu Mao, Shutao Gong, Jing Wang, Ke Sheng, Yaoqin Xie, and Tianye Niu	*Shading Correction Assisted Iterative Conebeam CT Reconstruction*	391
10:20 – 10:40	Sathish Ramani, Xin Wang, Lin Fu, and Michael Lexa	*Denoising-Based Accelerated Statistical Iterative Reconstruction for X-ray CT*	395
10:40 – 11:00	Qiaoqiao Ding, Yong Long, Xiaoqun Zhang, and Jeffrey A. Fessler	*Modeling Mixed Poisson-Gaussian Noise in Statistical Image Reconstruction for X-Ray CT*	399
11:00 – 11:20	Meng Wu, Andreas Maier, Yan Xia, and Rebecca Fahrig	*Auto-tuned Path-based Iterative Reconstruction (aPBIR) for X-ray Computed Tomography*	403
11:20 – 11:40	Grace J. Gang, Jeffrey H. Siewerdsen, and J. Webster Stayman	*Task-Based Design of Fluence Field Modulation in CT for Model-Based Iterative Reconstruction*	407

Lunch Break

Poster Session : Poster Session 3
Time : 13:20 – 15:00
Chairs : Timo Berkus and Jing Wang

Coffee Break

Oral Session : CBCT
Time : 15:20 – 17:00
Chairs : Brian Nett and Frédéric Noo

Friday, July 22

Oral Session: Artifact Reduction
Time : 08:00 – 09:40
Chairs : Jakob Jørgensen and Nicole Maaß

Time	Author	Title	Page
08:00 – 08:20	Marc Kachelrieß	***Basic short course**: Artifact Reduction*	
08:20 – 08:40	Marc Kachelrieß	***Basic short course**: Artifact Reduction*	
08:40 – 09:00	Brian E. Nett, Jang Hwan Cho, and Jed D. Pack	*Motion Evoked Artifact Deconvolution*	565
09:00 – 09:20	Dan Xia, David A. Langan, Stephen B. Solomon, Hao Lai, Zheng Zhang, Buxin Chen, Emil Y. Sidky, and Xiaochuan Pan	*Truncation Artifact Reduction by Exploiting Data Derivative and Image-TV Constraints in C-arm CBCT*	569
09:20 – 09:40	Richard Bismark, Robert Frysch, and Georg Rose	*Reduction of Beam Hardening Artifacts on Real C-Arm CT Data using Statistical Polyenergetic Image Reconstruction*	573

Coffee Break

Oral Session: General
Time : 10:00 – 11:40
Chairs : Karl Stierstorfer and Srinivasan Vedantham

10:00 – 10:20	Ivan G. Kazantsev, Ulrik L. Olsen, Henning F. Poulsen, and Per C. Hansen	*A Spectral Geometrical Model for Compton Scatter Tomography Based on the SSS Approximation*	577
10:20 – 10:40	Vicki T. Taasti, Jørgen B. B. Petersen, Jesper Thygesen, Ludvig P. Muren, Cai Grau, and David C. Hansen	*A Robust Method for Calculation of Proton Stopping Power Ratio using Dual Energy CT*	581
10:40 – 11:00	Gloria Vilches-Freixas, Jean Michel Létang, Nicolas Ducros, and Simon Rit	*Dual-Energy CT Spectra Optimization for Proton Treatment Planning*	585
11:00 – 11:20	Jan Hoskovec, Fabien Momey, Rolf Clackdoyle, Laurent Desbat, and Simon Rit	*Fan-Beam Reconstruction under Motion and Data Truncation: Comparing Analytic and Iterative Approaches*	589
11:20 – 11:40	$X+Y$	***Preview:** Fully 3D 2017, CT-Meeting 2018*	

Data-driven Correction for Head Motion In Helical X-ray CT

Tao Sun, Jung-Ha Kim, Roger Fulton, Johan Nuyts

Abstract— **Although current CT systems can scan the head in a very short time, patient motion sometimes still induces artifacts. If motion occurs, one has to repeat the scan; to avoid motion, sedation or anesthesia is sometimes applied. We propose a data-driven method to iteratively correct this motion together with the reconstruction. In every iteration, we estimate the motion view-by-view, which then can be used to update the system matrix used during reconstruction. A multi-resolution scheme was used to speed up the convergence of the joint estimation of the motion and reconstruction. The method was evaluated on simulations and on real patient scans. The quality of the reconstructed images was improved substantially after the correction. The proposed method eliminated motion-induced artifacts in head CT scans.**

Index Terms—**Computer Tomography (CT), iterative reconstruction, rigid motion, data-driven, motion correction.**

I. INTRODUCTION

A slight movement of the patient will lead to a reduction of spatial resolution in CT, in severe cases resulting in corrupted images unsuitable for diagnosis or further processing. To reduce the likelihood of motion artifacts, CT manufacturers have made scanners faster by increasing the number of detector rows and the rate of rotation of the x-ray source and detector. Other ways to reduce the patient motion include general anesthesia, sedation and the use of restraining devices for head and neck imaging [1].

Despite of the effectiveness of minimizing the motion beforehand, assessment of the subject motion is of considerable general interest in tomography. A variety of methods for the estimation of motion in CT exist, including direct motion estimation using a camera system with visual markers [2] or without markers [3]. Indirect estimation methods have been proposed where motion is estimated through the minimization of errors in consistency conditions [4], or iteratively updating the motion together with the reconstruction process [5]. Once motion parameters have been estimated, the motion can be corrected for either in the measured raw data or during the reconstruction process.

While most of the retrospective methods in CT imaging addressed the problem for circular cone beam CT (CBCT), relatively few studies has been done for helical CT. Motion correction is arguably simpler in CBCT since the entire object will normally be in the field of view at all times. In contrast, in helical CT the object is always truncated in axial direction, which provides limited information to restore the consistency in projections.

In this study, we propose an approach to reduce or eliminate the motion artifacts in helical-CT reconstruction. The approach is based on our previous work [6]. The correction only needs the measured raw data, hence it is called data-driven approach. We performed simulations and a patient study to validate the proposed approach, comparing reconstructions with and without motion correction.

II. METHOD

A. Coordinate system

A clinical helical CT system usually has a curved detector. We define a coordinate system $c = (x, y, z) \in \mathbb{R}^3$ in Fig. 1, which is fixed with respect to the scanner, its z-axis coincides with the rotation axis of the scanner. Detector coordinate system $c' = (u, v, z') \in \mathbb{R}^3$ is fixed with respect to the rotating source-detector system: its origin is in the center of the detector, z' is parallel to z, u is tangent and v is orthogonal to the detector. For one projection view, we define the rigid motion transform in the coordinate system c :

$$S_{world} = (\phi_x, \phi_y, \phi_z, t_x, t_y, t_z)^{\mathrm{T}} \qquad (1)$$

where ϕ_x, ϕ_y, ϕ_z are the 3 rotations, t_x, t_y, t_z are the 3 translations in the world coordinate system. The transform can be mapped in the coordinate system c' :

$$S_{\mathrm{det}ector} = (\phi_u, \phi_v, \phi_z, t_u, t_v, t_z')^{\mathrm{T}} \qquad (2)$$

where ϕ_u, ϕ_v, ϕ_z are the rotations t_u, t_v, t_z', are the translations in the detector coordinate system. A small motion t_v in the direction perpendicular to the detector results in a very small magnification of the projection, which we assume

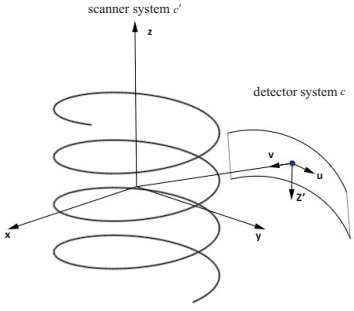

Manuscript received Mar. 31, 2016. This work was supported in part by the IWT MIRIAD SBO project and IMIR PF-project of KU Leuven.

T. Sun and J. Nuyts are with the Medical Imaging Research Center, Department of Nuclear Medicine, KU Leuven, Belgium.

J. Kim was with the Discipline of Medical Radiation Sciences, University of Sydney, Australia, and now is with the Faculty of Medicine, University of Sydney, Australia.

R. Fulton is with the Discipline of Medical Radiation Sciences, and School of Physics, University of Sydney, and the Department of Medical Physics, Westmead Hospital, Westmead, Australia.

Fig. 1 The scanner and detector coordinate systems on which motion correction is based.

to be negligible [7]. In every projection view, then, we set t_v as zero and only 5 parameters need to be estimated in our correction scheme ϕ_u, ϕ_v, ϕ_z, t_u and t_z':

$$S_{detector} = (\phi_u, \phi_v, \phi_z, t_u, t_z')^{\mathrm{T}} \tag{3}$$

The estimated motion in the detector coordinate system can later be transformed to the motion in the world coordinate system, as the reconstruction requires a transform in the world coordinate system:

$$\begin{aligned} S_{detector} &\rightarrow T_{detector} \\ T_{world} &= R \cdot T_{detector} \end{aligned} \tag{4}$$

where T is the 4×4 homogenous matrix representation of the transform, R is the 4×4 transformation matrix that maps the detector coordinate system to world coordinate system.

B. OSEM reconstruction

In the presence of object motion, the helical CT-orbit is distorted into an effective orbit with arbitrary shape. Since this is problematic for analytical reconstruction, an iterative reconstruction algorithm is needed. We used Ordered Subset Expectation Maximization (OSEM) as the reconstruction algorithm [8]. We used the OSEM-algorithm for convenience, but if the use of a better noise model would be required, it can be replaced with a dedicated iterative algorithm for transmission tomography.

C. General motion correction scheme

The following describes the basic idea of the data-driven motion correction: motion-corrected reconstruction and motion were alternately updated to increase the likelihood, the iterations were stopped when the motion estimate seemed to have converged (Fig. 2). The implementation involves: (1) a 2D-3D image registration to update the motion estimate for each view at the current iteration; (2) an image update with iterative reconstruction, incorporating the updated motion in the system matrix; (3) alternate updates of both image and motion with a multi-resolution scheme; (4) final reconstruction with a system matrix based on the last motion estimate. The following 4 paragraphs discuss the details about each part of the framework.

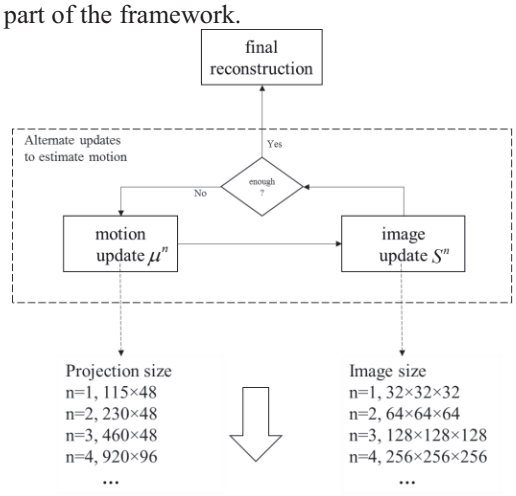

Fig. 2. General motion estimation scheme. μ is the update of the attenuation image, s is the update of the rigid transform, n is the iteration number. A multi-resolution scheme was applied to the motion estimation, increasing the sampling as the iteration number.

1) Motion update

From the measured raw data an initial image is reconstructed. This image can be reconstruction produced with the system software (postprocessed to convert Hounsfield units back to attenuation integrals), or a first iterative reconstruction (Eq. 5) from the measured data.

For one projection line i, we integrate along the projection line to define the forward projection of the current estimate μ:

$$f_i = \sum_j a_{ij} \mu_j \tag{5}$$

In helical CT, we organize the line integrals in views, where view θ contains all line integrals associated with a single source position:

$$f_\theta = \{ f_i \} \tag{6}$$

For each view, the 5 motion parameters are estimated one after the other. Suppose the general motion correction scheme (Fig. 2) is at the iteration n, hence the current motion update is s^n. Assuming that the motion represented by the (rotation or translation) parameter $\hat{s}$ is small, the derivative of projection f with respect to $\hat{s}$ can be approximated as a finite difference of the intensities:

$$\frac{\partial f_\theta}{\partial s} \approx \frac{f_\theta(\hat{s}) - f_\theta(s^n)}{\hat{s}} \tag{7}$$

where $f_\theta(s^n)$ is the calculated re-projection (using the current estimates for the image and motion) and $f_\theta(\hat{s})$ is the measured projection for view θ. To estimate $\hat{s}$ in Eq. 7, we need to know the derivative on the left hand side, hence we introduce another equation which is very similar to Eq. 7:

$$\frac{\partial f_\theta}{\partial s} \approx \frac{f_\theta(\Delta s) - f_\theta(s^n)}{\Delta s} \tag{8}$$

where Δs is known small increment of the parameter to be estimated. When Δs represents a translation, $f_\theta(\Delta s)$ can be approximated as simple translation of the current re-projection $f_\theta(s^n)$; for in-plane rotation, again $f_\theta(\Delta s)$ can be approximated as a simple rotation of the re-projection f_θ, as shown in Fig.3. For the two out-of-plane rotations, we calculate $f_\theta(\Delta s)$ with a forward projection using a system matrix adjusted with Δs.

Eq. 7 and 8 assume that a small increment of one degree-of-freedom rigid motion only results in a linear change of the intensities in the projection. All above lead to a least squares minimization problem for current view at current iteration :

$$s^n_{incre} = \arg\min_{\hat{s}} \left\| \begin{matrix} \Delta s \cdot \left[f_\theta(s^n + \hat{s}) - f_\theta(s^n) \right] - \\ \hat{s} \cdot \left[f_\theta(s^n + \Delta s) - f_\theta(s^n) \right] \end{matrix} \right\|^2 \tag{9}$$

To find s^n_{incre}, Eq. 9 was solved analytically. Defining

$$\begin{aligned} P_\theta &= f_\theta(s^n + \hat{s}) - f_\theta(s^n) \\ Q_\theta &= f_\theta(s^n + \Delta s) - f_\theta(s^n) \end{aligned} \tag{10}$$

and setting the derivative of the Eq. 9 with respect to $\hat{s}$ to zero, one obtains:

$$s_{incre}^{n} = \frac{\sum_{N} P_\theta \cdot \sum_{N} Q_\theta}{\left\| \sum_{N} Q_\theta^{2} \right\|} \cdot \Delta s \tag{11}$$

where N is total number of voxels in one projection view θ.

This procedure was applied to estimate all five parameters in Eq. 3. The sequence of the estimation is translation first, then rotation. The newly estimated parameter values were used immediately when estimating the value of next parameter. This sequential estimation of the five motion parameters for all projection views completes the update of the rigid motion in the current iteration. Then the rigid motion parameters for each projection view were transformed into a homogenous matrix in the detector coordinate system (Fig.1). Applying the Eq. 4, the matrix was mapped into world coordinate system. The transformation matrix obtained in the current iteration (n) was then used to update the previous motion estimate for every view, which will be used in the next iteration ($n+1$):

$$\begin{aligned} S_{incre}^{n} &\rightarrow \Delta T_\theta^{n} \\ T_\theta^{n+1} &= T_\theta^{n} \cdot \Delta T_\theta^{n} \end{aligned} \tag{12}$$

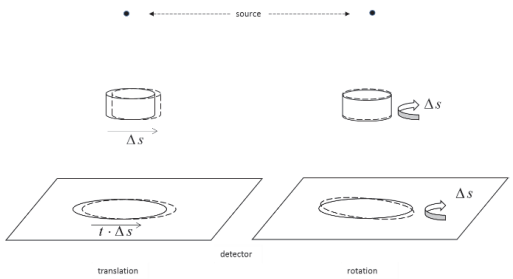

Fig. 3 Cartoon illustrating that the effect of object translation or rotation parallel to the detector can be well approximated as translation and rotation of the projection. For simplicity, the curvature of the detector was ignored. In the figure at left, t is the magnification factor from the object to detector.

2) Image update

After obtaining the motion, the image representing the attenuation coefficients can be updated with iterative reconstruction. We used OSEM as the reconstruction algorithm.

Instead of moving the reconstruction image, rigid motion correction was done by considering a coordinate system fixed to the object and incorporating the motion (now associated to the source-detector pair) into the system matrix. This corresponds to an arbitrary 3-dimensional (3D) motion of the virtual gantry around the object being scanned [2]. Motion correction was enabled by introducing a modified version of standard OSEM:

$$\begin{aligned} T_\theta^{n+1} &= invert(T_\theta^{n+1}) \\ \mu_j^{n+1} &= \frac{\mu_j^{n}}{\sum_i T_i^{n+1}(a_{ij})} \sum_i T_i^{n+1}(a_{ij}) \frac{m_i}{\sum_k T_i^{n+1}(a_{ij}) \mu_j^{n}} \end{aligned} \tag{13}$$

where i is the projection line index, j is the voxel index, a_{ij} is the effective intersection length of line i with voxel j, m is the log converted sinogram, S_b is one subset of projections of b subsets. T_i is a 4×4 rigid transformation matrix applied to the projection line i. If T_i is the identity matrix for all projection lines, then Eq. 13 is the same as original OSEM. In helical CT, T_i is constant for all projection lines in one projection view. Because of the high rotation speed and the large number of views, the motion within a single view is negligible.

Distance-driven projectors were used for interpolation during the (back) projection [9]. The new estimation of the attenuation from step 2 can then be used for next motion update step (step 1).

3) Multi-resolution alternate updates

By repeating steps 1 and 2 we can estimate the reconstruction (Eq. 13) and motion (Eq.14) alternately. Because the correction of the image and the correction of the transform parameters are jointly estimated from the measured data, the problem of error propagation is mitigated.

An approach to reduce the computation time is to apply a multi-resolution techniques. We utilize this technique by running the algorithm with a coarse to fine representation of the raw data and the image. As in Fig. 2, the image update is reconstructed at coarse resolution at early iterations, while the resolution increases as the iteration numbers increase. Similarly, the projections in Eq. 10 are computed with gradually increased resolution. An possible additional advantage of the multi-resolution scheme is that it may help to avoid convergence to an undesired local maximum. Since these computations are the most expensive ones in the multi-resolution scheme, we stopped the scheme at the one but finest resolution.

As proposed in [2], the motion estimates were smoothed (by filtering each component independently) to remove outliers. We chose the Savitzky-Golay filter [10] to do the smoothing right after every motion update. We found that selection of the 15-point and 201-point kernel can achieve satisfactory jitter suppression, in simulations and patient scans respectively.

It is not obvious to define good stopping criteria for the motion estimation, especially considering the ground truth image is missing for the clinical data. In the motion estimation scheme, a maximum number of iterations was chosen for each resolution level. In addition, the summation of projection errors between the re-projected and measured data over all the views was computed, and at each resolution level, the iterations were stopped earlier when the relative change of this error measure did not exceed 5% of the summed error between last re-projected and measured data.

4) Final reconstruction

When the motion estimate has converged, a final reconstruction of diagnostic quality must be produced. In simulation studies we start the final reconstruction with the last image update from the alternate updates. To achieve a similar speedup in the clinical study, we start the final reconstruction from an approximate helical Feldkamp-Davis-Kress reconstruction (motion correction was enabled in the backprojection step), provided the image is not affected much by the motion artifacts.

To further accelerate the final reconstructions, the forward and backward projection operations were implemented in OpenCL and run on a GPU (NIVIDIA Tesla C2075).

III. Experiments and Results

A. Simulation

In the simulation, a segment of measured motion from a volunteer was applied to a voxelized phantom to generate a simulated scan. Reconstructions from this scan were analyzed quantitatively to assess the performance of the motion correction algorithm. The phantom is a 3D voxelized phantom from the Visible Human Project [11]. The unit was converted from Hounsfield (HU) to attenuation coefficient (cm^{-1}) at peak kilovoltage of 70 kVp. The image size was 256×256×240, pixel size was 1×1×1 mm^3.

A helical scan was simulated as being scanned with a Siemens Definition AS CT scanner (Siemens Medical Solutions USA, Inc., Malvern, PA), with reduced angular sampling to reduce the computation times. The crucial parameters were: angles per rotation 250, pitch 1.0, collimation 32×1.2 mm. The motion was applied to the phantom for the simulated helical scan. To avoid the cone-beam artifacts, all simulated helical scans covered a bit more than the entire object.

OSEM was used for all reconstructions, with motion correction enabled (Eq. 13). During the joint estimation of the attenuation image and the motion, the attenuation image was updated using 1 OSEM iteration with 40 subsets. Reconstruction pixel size was 1×1×1 mm^3 at the finest resolution. Alternate updates of both image and motion were performed within a multi-resolution scheme to obtain the optimal motion. For the final reconstruction, 4 iterations and 60 subsets were applied. Fig. 4 and Fig. 5 show the estimated reconstruction and motion.

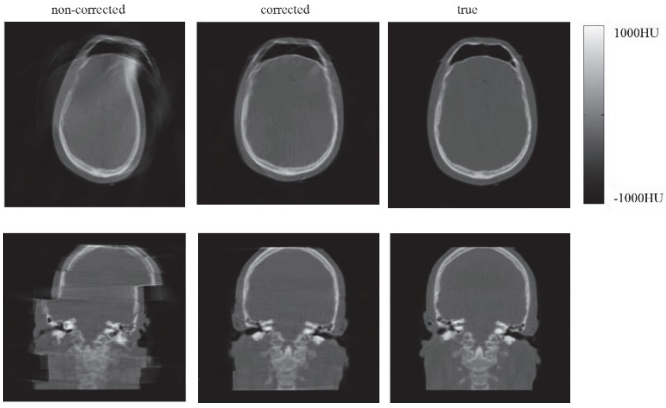

Fig. 4. Selected transaxial and coronal slices from reconstructions without and with motion correction, and also from the true image.

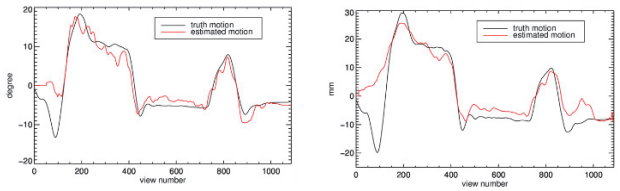

Fig. 5. The estimated motion values as a function of the view angle for the two most prominent motion parameters. Left: ϕ_x, right: t_x.

B. Real scan

The method has been applied to clinical studies in which motion artifacts had been observed. The outcome was evaluated by assessing the image visually.

The anonymized raw data of one patient who had previously undergone a head CT scan in the Department of Radiology at Westmead Hospital, Sydney, Australia, were collected with the approval of the Human Research Ethics Committee of the Western Sydney Local Health District. The scan was performed on a Siemens Force scanner (pitch 0.55, tube voltage 120 kVp, tube current 150 mAs, angles per rotation 1050, collimation 64×0.6 mm). Flying focus was turned on in both *z* and *phi* directions.

Because of the huge size of the raw data, we read and average every 8 projection of them for the motion estimation. This accelerated both the motion updates and the image updates. We used OSEM as the reconstruction algorithm. The motion correction was enabled for all reconstructions. Unlike in the simulation, 2 OSEM iterations with 40 subsets were done for the image updates. The final reconstruction pixel size was 0.40039×0.40039×0.75 mm^3, image size is 512×512×436. To accelerate the motion estimation, the multi-resolution scheme was applied as in II. C. Stopping criteria were also described in II. C. For the final reconstruction with motion correction, the starting image was set as the image from helical FDK reconstruction. Six OSEM iterations with 60 subsets were applied in combination with Nesterov's acceleration [12] on the GPU. Fig. 6 shows the original reconstructed image and motion-corrected reconstructed image.

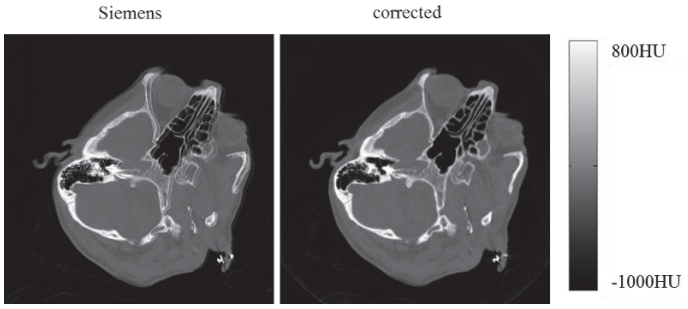

Fig. 6. Selected transaxial plane, without (left) and with correction (right) for motion artifacts in a clinical scan.

IV. Conclusion

In this paper, we proposed a motion estimation and correction approach for helical X-ray CT of the head, only based on the measured raw data. Since no additional measurements are needed, it can be applied retrospectively to standard helical CT data. Further testing of the method with clinical data is ongoing.

Acknowledgment

The authors want to thank Krystal Moore from the Department of Radiology at Westmead Hospital for collecting the datasets.

References

[1] J. F. Barrett et. al, *Radiographics*, vol. 24, 2004.
[2] J.-H. Kim et. al, *Phys. Med. Biol.*, vol. 60, 2015.
[3] A. Kyme et. al, *IEEE Trans. Med. Imaging*, vol. 33, 2014.
[4] H. Yu et. al, *IEEE Trans. Med. Imaging*, vol. 26, 2007.
[5] B. F. Hutton et. al, *IEEE Trans. Nucl. Sci.*, vol. 49, 2002.
[6] T. Sun et. al, *Proc. of the 13th Fully3D meeting*, 2015.
[7] G. T. Gullberg et. al, *Med. Phys.*, vol. 17, 1989.
[8] H. M. Hudson et. al, *IEEE Trans. Med. Imaging*, vol. 13, 1994.
[9] B. De Man et. al, *Phys. Med. Biol.*, vol. 49, 2004.
[10] A. Savitzky et. al, *Anal. Chem.*, vol. 36, 1964.
[11] M. J. Ackerman, *Proceedings of the IEEE*, vol. 86, 1998.
[12] Y. Nesterov, *Sov. Math. Dokl.*, vol. 27, 1983.

Digital Breast Tomosynthesis Reconstruction with Detector Blur and Correlated Noise

Jiabei Zheng*, Jeffrey A. Fessler*, Heang-Ping Chan†

***Abstract*—This paper describes a new reconstruction method for digital breast tomosynthesis (DBT). The new method incorporates detector blur into the forward model. The detector blur introduces correlation in the measurement noise. We formulate it as a regularized quadratic optimization problem with data-fit term that accounts for the non-diagonal noise covariance matrix. By making a few assumptions based on the breast imaging process, we can model the detector blur in the optimization problem and solve it with a separable quadratic surrogate (SQS) algorithm. This method was applied to DBT reconstruction of breast phantoms and human subjects. The contrast-to-noise ratio and sharpness of microcalcifications and the visual quality of mass margins were analyzed and compared to those by the simultaneous algebraic reconstruction technique (SART). The results demonstrated the potential of the new method in improving the image quality of the reconstructed DBT images. This work is our preliminary step towards a model-based iterative reconstruction (MBIR) for DBT.**

***Index Terms*—Digital breast tomosynthesis, detector blur, correlated noise, model-based iterative reconstruction**

I. Introduction

Digital breast tomosynthesis (DBT) has been developed to reduce the problem of overlapping tissue in conventional 2-D mammography. In DBT, commonly-used reconstruction methods include filtered back-projection, the maximum-likelihood expectation-maximization algorithm [1][2] and simultaneous algebraic reconstruction technique (SART) [3]. These methods do not account for noise correlation or other image degradation factors in the imaging process. In this paper, we introduce a new reconstruction method that includes a correlated noise model, as a first step towards model-based iterative reconstruction (MBIR) for DBT.

In an x-ray imaging system, the finite pixel size and light diffusion in the phosphor of an indirect detector contribute to blurring of the measured image. Neglecting detector blur introduces blurring to the reconstructed objects, especially for small objects such as microcalcification (MC) in DBT. We modeled the detector blur and the associated noise correlation into the cost function of the optimization problem. The optimization problem is simplified with a few assumptions and solved with a slightly modified separable quadratic surrogate (SQS) method [4].

In this paper, we first introduce our detector blur model and the assumptions used for its simplification. We describe the optimization problem and the cost function for regularized reconstruction. The usefulness of the method is demonstrated by comparing its reconstructed image quality with that by SART using DBT of both breast phantom and human subject.

* Jiabei Zheng and Jeffrey A. Fessler are with the Department of Electrical and Computer Engineering, University of Michigan, Ann Arbor, MI. (e-mail: {jiabei,fessler}@umich.edu)

† Heang-Ping Chan is with the Department of Radiology, University of Michigan, Ann Arbor, MI. (e-mail: chanhp@med.umich.edu)

II. Methods

A. Formulation of the Reconstruction Problem

Let $\mathbf{A}_i$ denote the projector and $\mathbf{f}$ denote the unknown array of attenuation coefficients in the imaged volume. Let $\mathbf{Y}_i$ denote the measured projection at the ith projection angle of all m projections ($i = 1, ..., m$). Considering the detector blur, the expected projection value $\bar{\mathbf{Y}}_i$ can be written as

$$\bar{\mathbf{Y}}_i = I_0 \mathbf{B}_i \exp(-\mathbf{A}_i \mathbf{f}) \tag{1}$$

where $\mathbf{B}_i$ denotes the blurring operation in matrix form and I_0 is the constant expected projection value if there is no object present in the imaged volume. $\mathbf{B}_i$ is assumed to be projection-angle-dependent but linear shift-invariant within a given projection.

To deal with the non-diagonal matrix $\mathbf{B}_i$ before the exponential, we assume that the image f consists of two parts: (1) a low-frequency background $\mathbf{f}_\mathrm{b}$ that is approximately uniform within the support of the blurring kernel; (2) small structures $\mathbf{f}_\mathrm{s}$ (such as MC in DBT) that only contributes very little to the projection value ($\mathbf{A}_i \mathbf{f}_\mathrm{s} \ll 1$). These assumptions are more reasonable in breast imaging than in CT of body parts that include bone or other high-attenuation objects. Under these assumptions, we can approximate (1) as:

$$\bar{\mathbf{Y}}_i \approx I_0 \exp(-\mathbf{B}_i \mathbf{A}_i \mathbf{f}) \tag{2}$$

Thus the expectation of the transformed projection $\mathbf{y}_i$ is:

$$\bar{\mathbf{y}}_i = \log\left(I_0 / \mathbf{Y}_i\right) \approx \mathbf{B}_i \mathbf{A}_i \mathbf{f} \tag{3}$$

We assume $\mathbf{y}_i$ has approximately a multivariate Gaussian distribution: $\mathbf{y}_i \sim \mathcal{N}(\bar{\mathbf{y}}_i, \mathbf{K}_i)$. $\mathbf{K}_i$ is the covariance matrix for the ith projection.

The quantum noise in the imaging process is affected by the detector blur but the detector electronic noise is not. A reasonable model for the noise covariance $\mathbf{K}_i$ is:

$$\mathbf{K}_i = \mathbf{B}_i \mathbf{K}_i^q \mathbf{B}_i' + \mathbf{K}_i^r \tag{4}$$

where $'$ denotes conjugate transpose (in case the kernel of $\mathbf{B}_i$ is asymmetric). $\mathbf{K}_i^q$ and $\mathbf{K}_i^r$ are diagonal matrices of the variances of quantum noise and readout noise at each detector element, respectively.

We then formulate the following reconstruction problem:

$$\begin{aligned} \hat{\mathbf{f}} &= \arg\min_{\mathbf{f}} \frac{1}{2} \sum_i \|\mathbf{y}_i - \mathbf{B}_i \mathbf{A}_i \mathbf{f}\|^2_{(\mathbf{B}\mathbf{K}_i^q \mathbf{B}' + \mathbf{K}_i^r)^{-1}} + R(\mathbf{f}) \\ &= \arg\min_{\mathbf{f}} \frac{1}{2} \sum_i \|\mathbf{P}_i \mathbf{y}_i - \mathbf{P}_i \mathbf{B}_i \mathbf{A}_i \mathbf{f}\|_2^2 + R(\mathbf{f}) \end{aligned} \tag{5}$$

where $R(\mathbf{f})$ is the regularization term and the inverse matrix square root of the noise covariance is

$$\mathbf{P}_i = (\mathbf{B}_i \mathbf{K}_i^q \mathbf{B}_i' + \mathbf{K}_i^r)^{-1/2} \tag{6}$$

B. Implementation of $\mathbf{P}_i$

Since $(\mathbf{B}_i\mathbf{K}_i^q\mathbf{B}_i' + \mathbf{K}_i^r)$ is non-diagonal, the implementation of $\mathbf{P}_i$ is very challenging. In CT application, one possible method is to solve another optimization problem with a set of conjugate gradient iterations [5]. In DBT, we can dramatically simplify the implementation by making some reasonable assumptions. Unlike body CT where there exist large bones and even perhaps metal objects of significant size that are strongly attenuating, the compressed breast has a fairly uniform thickness mainly composed of soft tissue. As a first-order approximation, we assume quantum noise to be constant for all detector elements in a given projection angle:

$$\mathbf{K}_i^q = \sigma_i^{q2}\mathbf{I} \tag{7}$$

In addition, we assume all detector elements have similar readout noise variance:

$$\mathbf{K}_i^r = \sigma_i^{r2}\mathbf{I} \tag{8}$$

Let $\mathbf{h}_i$ be the point spread function (PSF) of the detector, The blurring operation is given by $\mathbf{B}_i = \mathbf{Q}^{-1}\mathbf{H}_i\mathbf{Q}$, where $\mathbf{Q}$ is the discrete Fourier Transform (DFT) matrix and $\mathbf{H}_i = \mathrm{Diag}(\mathrm{DFT}\{\mathbf{h}_i\})$. Then the operation $\mathbf{P}_i$ by a vector can be easily implemented as a high-pass filter using FFT operations without needing any iterative method for matrix inversion:

$$\mathbf{P}_i = \mathbf{Q}^{-1}(\sigma_i^{q2}\mathbf{H}_i\mathbf{H}_i' + \sigma_i^{r2}\mathbf{I})^{-1/2}\mathbf{Q} \tag{9}$$

In our study, we used a Lucite slab with a similar thickness as the object to be reconstructed to estimate σ_i^q. σ_i^r was estimated from the dark current image of the detector.

C. Regularization

Since $\mathbf{P}_i$ is implemented as a high-pass filter, it would amplify noise in reconstruction if used without regularization. Regularization is very important for stable reconstruction. We use a Huber-like function $\eta(t)$ to define $R(\mathbf{f})$ in this work:

$$\eta(t) = \delta^2(\sqrt{1 + (t/\delta)^2} - 1) \tag{10}$$

Since the DBT reconstruction is non-isotropic, the regularization term is written separately in terms of the horizontal and vertical in-plane directions as

$$R(\mathbf{f}) = \beta_x \sum_j \eta([\mathbf{C}_x\mathbf{f}]_j) + \beta_y \sum_j \eta([\mathbf{C}_y\mathbf{f}]_j) \tag{11}$$

where $\mathbf{C}_x$ and $\mathbf{C}_y$ are operations to calculate difference between neighboring pixels along the x and y-direction, respectively, as defined in Fig. 1. Our DBT slice thickness is 10 times in-plane pixel size, making correlation between slices relatively weak and z-direction regularization unnecessary.

D. The Reconstruction Algorithm

Both the quadratic function of the data-fit term and $\eta(t)$ are convex and their second-order derivatives are less than or equal to 1. This allows us to use SQS with a small modification to account for the effective system matrix $\tilde{\mathbf{A}}$ and solve the optimization problem:

$$\begin{aligned}\mathbf{f}^{(n+1)} = \mathbf{f}^{(n)} - \big(&\beta_x\mathbf{C}_x'\dot{\eta}(\mathbf{C}_x\mathbf{f}^{(n)}) + \beta_y\mathbf{C}_y'\dot{\eta}(\mathbf{C}_y\mathbf{f}^{(n)}) \\ &+ \tilde{\mathbf{A}}'(\tilde{\mathbf{A}}\mathbf{f}^{(n)} - \tilde{\mathbf{y}})\big) \oslash \big(4\beta_x\mathbf{1} + 4\beta_y\mathbf{1} + |\tilde{\mathbf{A}}'\tilde{\mathbf{A}}|\mathbf{1}\big)\end{aligned} \tag{12}$$

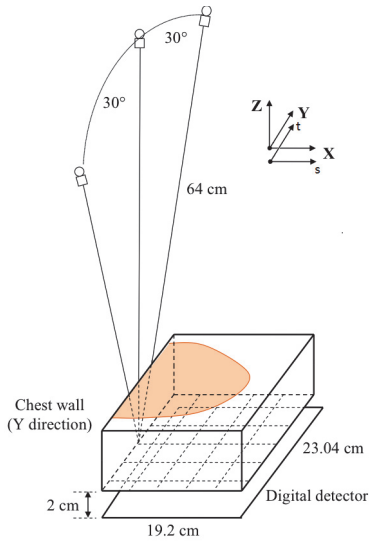

Fig. 1: Geometry of the DBT system used in this study.

where $\mathbf{1}$ is an all-one vector, $|\cdot|$ and $\oslash$ represent element-wise absolute value and division, and the effective system matrix is defined as

$$\tilde{\mathbf{A}} = \begin{pmatrix} \tilde{\mathbf{A}}_1 \\ \dots \\ \tilde{\mathbf{A}}_m \end{pmatrix} = \begin{pmatrix} \mathbf{P}_1\mathbf{B}_1\mathbf{A}_1 \\ \dots \\ \mathbf{P}_m\mathbf{B}_m\mathbf{A}_m \end{pmatrix} \tag{13}$$

$$\tilde{\mathbf{y}} = \begin{pmatrix} \tilde{\mathbf{y}}_1 \\ \dots \\ \tilde{\mathbf{y}}_m \end{pmatrix} = \begin{pmatrix} \mathbf{P}_1\mathbf{y}_1 \\ \dots \\ \mathbf{P}_m\mathbf{y}_m \end{pmatrix} \tag{14}$$

$\mathbf{P}_i$ is a high-pass filter with negative elements in its PSF. $\tilde{\mathbf{A}}$ has negative elements, making it challenging to implement $|\tilde{\mathbf{A}}'\tilde{\mathbf{A}}|\mathbf{1}$. The implementation of $|\tilde{\mathbf{A}}'\tilde{\mathbf{A}}|\mathbf{1}$ is still under investigation. We temporarily use $\tilde{\mathbf{A}}'\tilde{\mathbf{A}}\mathbf{1}$ as an approximation.

In DBT reconstruction, we usually use only one projection view at a time. Therefore, we assume that, for each i:

$$\nabla(\sum_{k=1}^{m} \|\tilde{\mathbf{y}}_k - \tilde{\mathbf{A}}_k\mathbf{f}\|_2^2) \approx m\nabla(\|\tilde{\mathbf{y}}_i - \tilde{\mathbf{A}}_i\mathbf{f}\|_2^2) \tag{15}$$

The ordered-subset (OS) reconstruction update is given by:

$$\mathbf{f}^{(n,i+1)} = \mathbf{f}^{(n,i)} - \nabla\Psi_i(\mathbf{f}^{(n,i)}) \oslash \big(4\beta_x\mathbf{1} + 4\beta_y\mathbf{1} + |\tilde{\mathbf{A}}'\tilde{\mathbf{A}}|\mathbf{1}\big) \tag{16}$$

$$\begin{aligned}\nabla\Psi_i(\mathbf{f}^{(n,i)}) = \beta_x\mathbf{C}_x'\dot{\eta}(\mathbf{C}_x\mathbf{f}^{(n,i)}) + \beta_y\mathbf{C}_y'\dot{\eta}(\mathbf{C}_y\mathbf{f}^{(n,i)}) + \\ m\tilde{\mathbf{A}}_i'(\tilde{\mathbf{A}}_i\mathbf{f}^{(n,i)} - \tilde{\mathbf{y}}_i)\end{aligned} \tag{17}$$

The iteration counter n is incremented by 1 after all measured projections have been used once.

III. Materials

A. DBT System

We used a GE GEN2 prototype DBT system for image acquisition. The imaging geometry is shown in Fig. 1. The system uses a CsI phosphor/a:Si active matrix flat panel detector with a pixel size of 0.1mm×0.1mm and an area of 1920×2304 pixels. The detector is enclosed inside the breast support and is stationary during image acquisition. The distance from the x-ray source to the fulcrum is 64cm. There is a 2cm gap between the imaged volume and the digital detector.

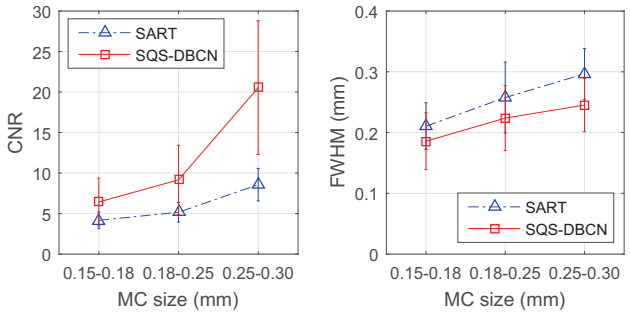

Fig. 3: Comparison of the mean CNR and mean FWHM averaged over all clusters in the phantom.

B. Breast Phantom and Human Subject DBT

MCs are small calcium deposits in the breast of sizes from about 0.1mm to 0.5mm. Clustered MCs are important signs of early breast cancer. One of the main challenges in DBT reconstruction is to reduce noise while enhancing MCs and preserving the margin features of masses. In this study, we used a breast phantom with embedded MCs for the evaluation of the effects of reconstruction methods and parameters on the image quality of MCs. It is difficult to build mass phantoms with realistic spiculated or ill-defined margins, which are strong indicators of breast cancer; we therefore used real breast DBT for visual evaluation of the image quality of masses.

The breast phantom consists of a stack of five 1-cm-thick slabs of breast tissue mimicking material [6]. Clusters of calcium carbonate specks of three nominal size ranges (0.15-0.18mm, 0.18-0.25mm, and 0.25-0.30mm) were sandwiched between the slabs to simulate MCs of different conspicuity levels. For the human subject DBT, we selected a case with a spiculated mass that was biopsy-proven to be an invasive ductal carcinoma. Both the phantom and human subject DBT were acquired with 60° scan angle, 3° increments and 21 projections. To simulate the DBT acquired with a GE commercial system, we used the 9 central projections for reconstruction, corresponding to DBT of 24° scan angle with 3° increments.

C. Figures of Merit (FOMs)

Quantitative comparison of reconstruction quality are based on two FOMs of MCs: contrast-to-noise ratio (CNR) and full-width at half maximum (FWHM). We applied a 2-D least-squares Gaussian fitting to each reconstructed MC. With the fitted standard deviation σ_{MC}, the FWHM is given by $2.355\sigma_{\mathrm{MC}}$. The noise level σ_{NP} is estimated from a noise patch near each cluster. The CNR is given as: $\mathrm{CNR} = A_{\mathrm{MC}}/\sigma_{\mathrm{NP}}$, where A_{MC} is the fitted amplitude of the MC.

IV. Results and Discussion

A. Reconstructed MC Clusters

We compared the new method (SQS with detector blur and correlated noise, or SQS-DBCN) with SART. We performed three complete iterations for SART since more iterations will amplify noise and reduce the CNR of MCs. Compared with SART, SQS-DBCN is regularized, allowing us to increase the number of iterations and enhance the contrast of MCs. We

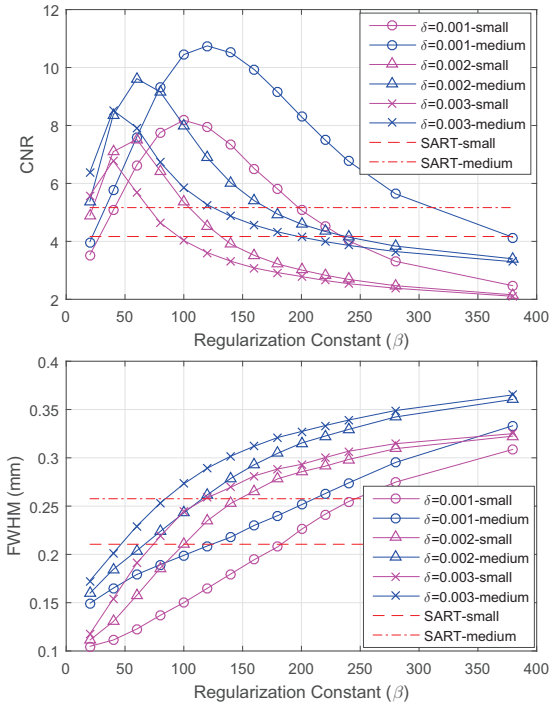

Fig. 4: Parameter selection: CNR and FWHM as a function of β for a range of δ. The red lines indicate the level of the SART.

experimentally chose 10 complete iterations for this study. To reduce the number of the parameters to be determined, we also set $\beta_x = \beta_y = \beta$. For the discussion in this section, the parameter combination is: $\beta = 80$, $\delta = 0.002/\mathrm{mm}$.

The reconstructed clusters are shown in Fig. 2. To make a more quantitative comparison, we used 49 of 0.15-0.18mm MCs, 66 of 0.18-0.25mm MCs and 64 of 0.25-0.30mm MCs from 5 clusters of each size. We calculated the mean CNR and FWHM of the MCs in each size range. The results are shown in Fig. 3. Compared with SART, SQS-DBCN generates more conspicuous and sharper MCs, as indicated by a higher CNR and smaller FWHM. For the smallest MCs (0.18-0.25mm), the mean CNR increases by 54.4% from 4.17 to 6.44 using the SQS-DBCN reconstruction. The mean CNRs increased by 77.3% and 139.7% for medium and large MCs. With SART, the FWHMs of the reconstructed MCs are larger than their nominal size. With the SQS-DBCN method, the FWHMs are closer to the nominal size, due to the 'shrink' effect of the deblurring by $\mathbf{P}_i$. The regularization suppressed background noise, making MCs more visible to the observer.

B. Regularization Parameter Selection

Performance of the method depends on parameter selection of the regularization term. We reconstructed the phantom DBT with different parameter combinations. Mean CNR and FWHM were calculated for each reconstruction and the trends are shown in Fig. 4. For MCs of different sizes, there exists a different 'optimal' parameter combination that yields maximum CNR. Over a large range of parameters, the new method outperforms the SART method in the sense of enhancing CNR.

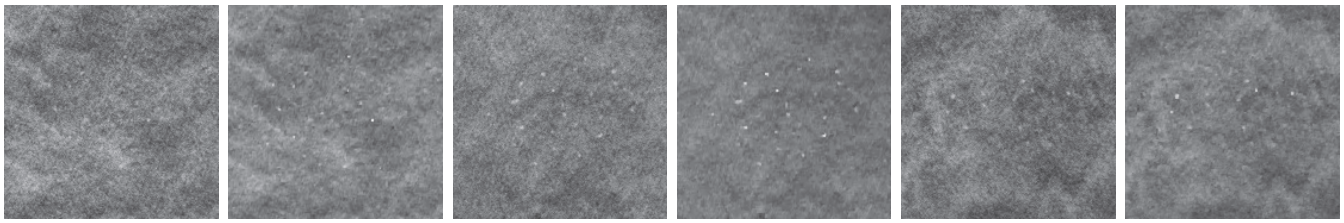

(A1) Cluster A: SART: mean CNR = 3.87, FWHM = 0.210mm

(A2) Cluster A: SQS: mean CNR = 6.86, FWHM = 0.172mm

(B1) Cluster B: SART: mean CNR = 5.56, FWHM = 0.235mm

(B2) Cluster B: SQS: mean CNR = 10.4, FWHM = 0.217mm

(C1) Cluster C: SART: mean CNR = 5.55, FWHM = 0.243mm

(C2) Cluster C: SQS: mean CNR = 8.37, FWHM = 0.222mm

Fig. 2: (A1)-(C2) shows the comparison of MC clusters. Mean CNR and FWHM of all MCs on the patch are given under each figure. (A1)(B1)(C1) used SART with 3 iterations, (A2)(B2)(C2) used SQS-DBCN with $\beta = 80$, $\delta = 0.002/mm$, 10 iterations. Size of MCs in Cluster A is 0.15-0.18mm, size of MCs in Cluster B and C is 0.18-0.25mm.

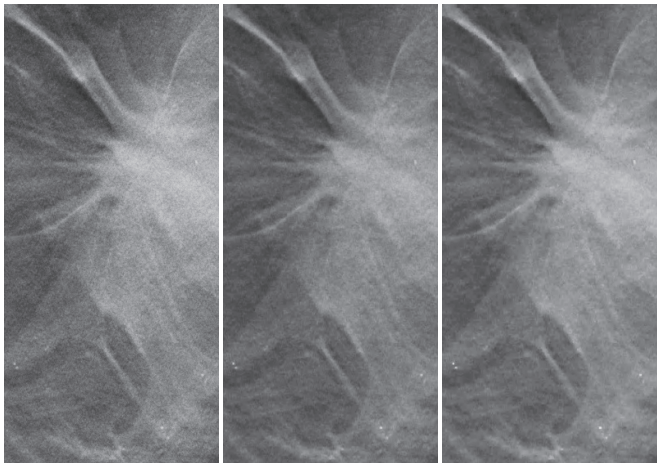

(a) SART, 3 iterations

(b) SQS-DBCN, 10 iterations, $\beta = 80$, $\delta = 0.002/\mathrm{mm}$

(c) SQS-DBCN, 10 iterations, $\beta = 120$, $\delta = 0.001/\mathrm{mm}$

Fig. 5: Comparison of reconstructed images for human subject DBT. The CNR of MCs increases from image (a) to (c). However, the spiculation and the tissue textures become more patchy and artificial in (c). The artifacts may not be readily visible in this reduced-size image.

The FWHM of all MCs increases as β increases due to the stronger smoothing effect from the regularization term.

The parameter combination used for reconstructing the examples in Fig. 2 was not the one with highest CNR shown in Fig. 4 to avoid the strong distortion of the background texture in the images (also see Fig. 5(c)).

C. Human Subject DBT

The FOMs used in this study only evaluated the CNR and FWHM of MCs. Currently there is no simple FOM that can describe the visual quality of the mass margin and tissue texture. Some reconstruction methods or parameter combinations can generate strong artifacts on the tissue texture, as observed in CT [7]. To evaluate the visual quality of the tissue texture, we applied SQS-DBCN to the human subject DBT. Fig. 5 shows a comparison of two parameter combinations to SART. It can be observed that the SQS-DBCN method enhanced MCs by the parameter combination ($\beta = 80$, $\delta = 0.002/mm$) (Fig. 5(b)), preserved tissue structure and did not generate noticeable artifact compared to the image by ($\beta = 120$, $\delta = 0.001/mm$) (Fig. 5(c)), in which the texture looks patchy and artificial. Therefore, the former is a better choice for human DBT although the latter provided higher CNR enhancement for MCs. We are investigating parameter selection strategies that can be more adaptive to different imaging conditions and for various breast lesions and parenchymal densities.

V. Conclusion

We proposed a DBT reconstruction method that incorporates detector blur and a correlated noise model as the first step towards developing a model-based iterative reconstruction method for DBT. We have shown quantitatively and visually that the new SQS-DBCN method can better enhance MCs compared with the SART while preserving the image quality of spiculations and tissue texture.

The SQS-DBCN method depends on several assumptions. The performance of the method depends on good parameter selection and accurate estimation of noise variance. Further study is underway to develop an adaptive method to select the parameters, better estimation of noise variance, and more general model to relax the assumptions.

Acknowledgment

This work is supported by National Institutes of Health grant number R01 CA151443.

References

[1] K. Lange and J. A. Fessler, *Globally Convergent Algorithms for Maximum a Posteriori Transmission Tomography*, IEEE Trans Image Processing, vol. 4, pp. 1430-1438, 1995.

[2] T. Wu, et al., *Tomographic Mammography Using a Limited Number of Low-dose Cone-beam Projection Images*, Medical Physics, vol. 30, pp. 365-380, 2003.

[3] Y. Zhang, H.-P. Chan, B. Sahiner, et al, *A Comparative Study of Limited-angle Cone-beam Reconstruction Methods for Breast Tomosynthesis*, Medical Physics, vol. 33, pp. 3781-3795, 2006.

[4] H. Erdogan and J. A. Fessler, *Ordered Subsets Algorithms for Transmission Tomography*, Physics in Medicine and Biology, vol. 44, pp. 2835-2851, 1999.

[5] J. W. Stayman, et al., *Generalized Least-Squares CT Reconstruction with Detector Blur and Correlated Noise Models*, Proc. SPIE, vol. 9033, 903335, 2014.

[6] H.-P. Chan, M. Goodsitt, et al., *Digital Breast Tomosynthesis: Observer Performance of Clustered Microcalcification Detection on Breast Phantom Images Acquired with an Experimental System Using Variable Scan Angles, Angular Increments, and Number of Projection Views*, Radiology 273, 675-685, 2014.

[7] F. E. Boas and D. Fleischmann, *CT Artifacts: Causes and Reduction Techniques*, Imaging in Medicine, vol. 4, pp. 229-240, 2012.

X-ray tensor tomography – a linear system approach to reconstruction

Matthias Wieczorek*, Christoph Jud†, Florian Schaff†, Franz Pfeiffer†‡ and Tobias Lasser*
*Computer Aided Medical Procedures (CAMP), Technische Universität München, Germany
Email: wieczore@cs.tum.edu
†Chair of Biomedical Physics & Institute of Medical Engineering, Technische Universität München, Germany
‡Department of Radiology, Klinikum rechts der Isar, Technische Universität München, Germany

***Abstract*—X-ray Tensor Tomography is a recently developed modality enabling the reconstruction of anisotropic scattering tensors using an X-ray grating interferometer. The reconstruction problem can be formulated as a large-scale linear system, which allows the application of regular reconstruction algorithms. As opposed to the block-based reconstruction approaches used so far, in this paper we suggest using a conventional reconstruction algorithm not based on blocks (the conjugate gradient method). We show first results applied to data acquired of a carbon fiber sample, demonstrating marked advantages in convergence speed while achieving comparable image quality.**

I. Introduction

Recent developments in grating-based X-ray imaging enable the additional extraction of X-ray phase-contrast [1] and dark-field [2] in a conventional X-ray setup. While phase-contrast provides a signal based on X-ray refraction, the dark-field signal is linked to scattering of the X-rays while traversing through an object. As opposed to absorption and phase-contrast, the dark-field signal provides an anisotropic signal, which is caused by the fact that scattering at a certain position within the measured object occurs strongest in directions orthogonal to microstructures at this position [3], [4].

Improved image contrast and resolution of micro-structures at sub-pixel level have been shown for several fields of application when using dark-field based radiography. Among others there have been studies regarding lung imaging [5], [6], breast imaging [7], [8], musculoskeletal imaging [9], [10], microbubbles as contrast agents[11] and material testing [12].

Due to the directional nature of the dark-field signal, tomographic reconstruction becomes more challenging than in the standard computed tomography (CT) case. Based on a superposition principle derived in [13], Malecki *et al.* [14] proposes the first tomographic reconstruction approach for X-ray dark-field tomography by incorporating the directional information. In this work Malecki *et al.* uses a rank-2 tensor to represent the anisotropic scattering, i.e. the mathematical formulation of an ellipsoid representing a gaussian scattering process, hence the name 'X-ray Tensor Tomography', or in short XTT. This approach has been further extended by Vogel *et al.* [15], who shows that the forward model and the corresponding inverse problem can be rewritten as a large-scale linear system. Both Malecki *et al.* and Vogel *et al.* use block-based algorithms to compute the tomographic reconstruction for each scattering direction in parallel.

In this work we will use the same problem formulation as a large-scale linear system, and directly apply an algorithm acting on the whole linear problem at once. This allows the use of regular reconstruction algorithms not based on blocks, in particular we will use the Conjugate Gradient method (CG).

II. Methods

In order to reconstruct the scattering tensors, Malecki *et al.* [14] derive a forward model for the anisotropic dark-field imaging based on superposition. Following this approach, let $\hat{\varepsilon}_k \in \mathbb{R}^3, k \in \{1, \dots, K\}$, denote a finite set of K normalized scattering directions. Assuming that scattering strictly occurs in these directions $\hat{\varepsilon}_k$, Malecki *et al.* provide a forward model similar to the standard forward model used for computed tomography,

$$m_j = \int_{L_j} \sum_{k=1}^{K} v_{kj} \cdot \eta_k(x) \; dx \tag{1}$$

Here, $m := (m_j)$, $j = 1, \dots, J$, denotes the negative logarithm of the dark-field measurements with L_j denoting the corresponding ray, v_{kj} denotes weights explained below, and η_k denotes the to-be-reconstructed scattering coefficients corresponding to the scattering direction $\hat{\varepsilon}_k$, $k = 1, \dots, K$.

Based on this forward model Vogel *et al.* [15] derives a reformulation of the reconstruction problem as a large-scale linear system. This reformulation is based on the fact that the above mentioned superposition model describes a weighted sum of standard CT X-ray transforms.

The corresponding weights v_{kj} are based on a model for the scattering probability and the detectability based on the normalized ray direction $\hat{I}_j$ and the orientation of the grating, represented by the orthogonal in-plane direction of the grating lines $\hat{t}_j$ (see [16], [13], [15]):

$$v_{kj} = (|\hat{I}_j \times \hat{\varepsilon}_k| \langle \hat{\varepsilon}_k, \hat{t}_j \rangle)^2 \tag{2}$$

According to [15], the problem of XTT reconstruction can now be represented as a large-scale linear system as follows: Let $P \in \mathbb{R}^{J \times I}$ denote the system matrix as used in standard CT, where J denotes the number of projections times the number of detector pixels, and where I denotes the number of voxels used to represent the reconstruction volume. Using diagonal weighting matrices $D_k = \text{diag}(v_{k1}, v_{k2}, \dots, v_{kJ})$, the XTT

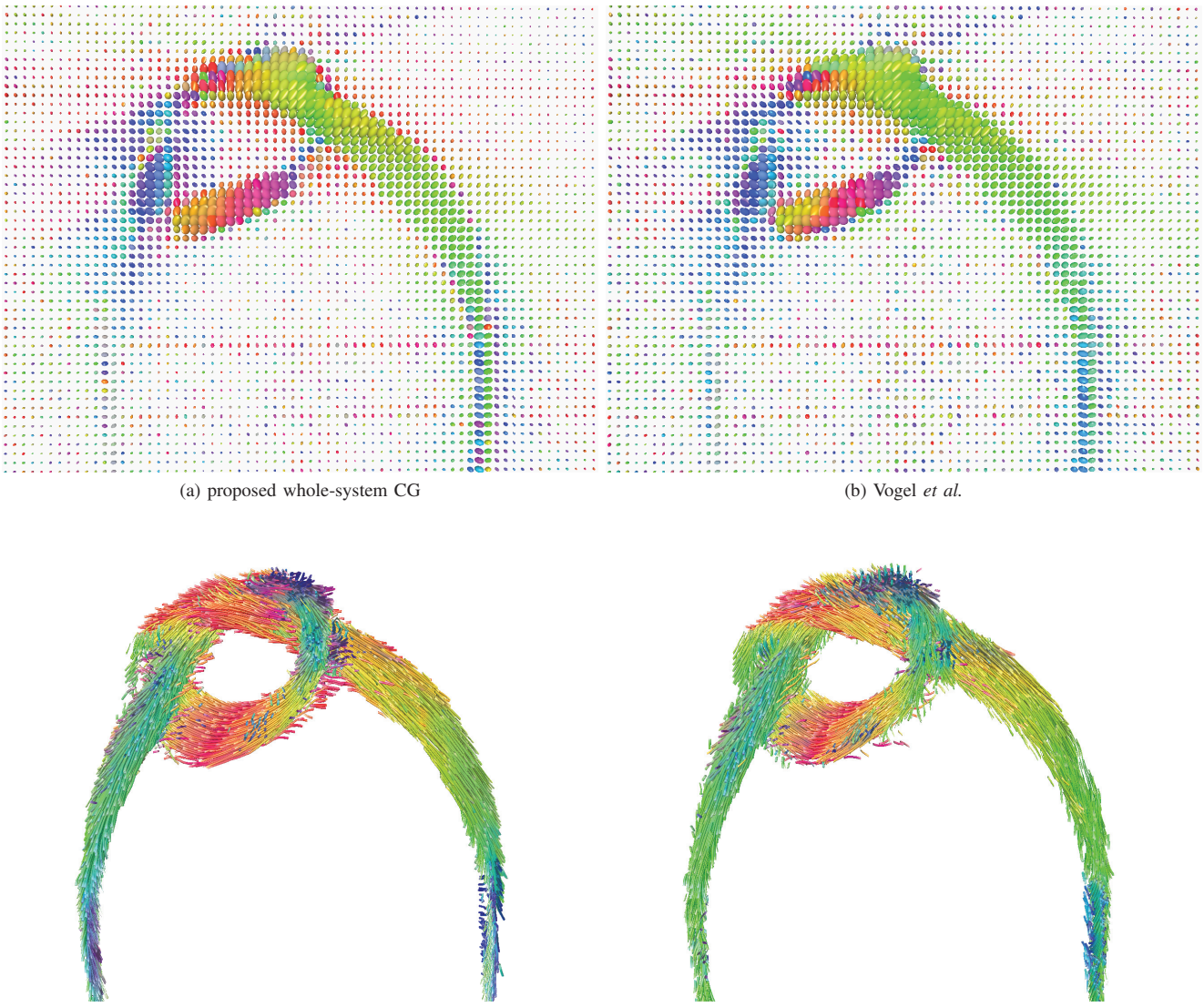

(a) proposed whole-system CG (b) Vogel *et al.*

(c) proposed whole-system CG (d) Vogel *et al.*

Fig. 1. Visualization of the reconstructed tensors for both our whole-system approach using CG (a,c) and the method of Vogel *et al.* (b,d). The ellipsoid tensor visualizations for slice 104 are shown in the upper row, while the bottom row shows the streamline visualization along the direction of the microstructures. In both cases, the results are color coded according to the orientation of the microstructure.

reconstruction problem to reconstruct the unknowns $\eta := (\eta_k)$ can be written as

$$m = \begin{pmatrix} D_1 P & D_2 P & \cdots & D_K P \end{pmatrix} \begin{pmatrix} \eta_1 \\ \eta_2 \\ \vdots \\ \eta_K \end{pmatrix} \tag{3}$$

Using $A := \begin{pmatrix} D_1 P & D_2 P & \cdots & D_K P \end{pmatrix} \in \mathbb{R}^{J \times IK}$, we can write the linear system in short

$$m = A\eta \tag{4}$$

In contrast to the previous works using block-based solvers, we now attack the whole problem (4) at once using the standard CG algorithm. Of course other, more elaborate algorithms could be used in place of CG here.

For implementation we use our software framework [17] for large-scale inverse problems, which allows to assemble the complete system matrix A in such a way that A is computed on-the-fly from on-the-fly versions of the $D_k P$ matrices. Thus the CG algorithm acts on this on-the-fly matrix A, allowing to solve the problem just as one would do if the matrix were stored in memory.

III. Experiments

For experimental evaluation of the whole-system approach we apply it to an experimental data set acquired using a grating interferometry setup as in [15].

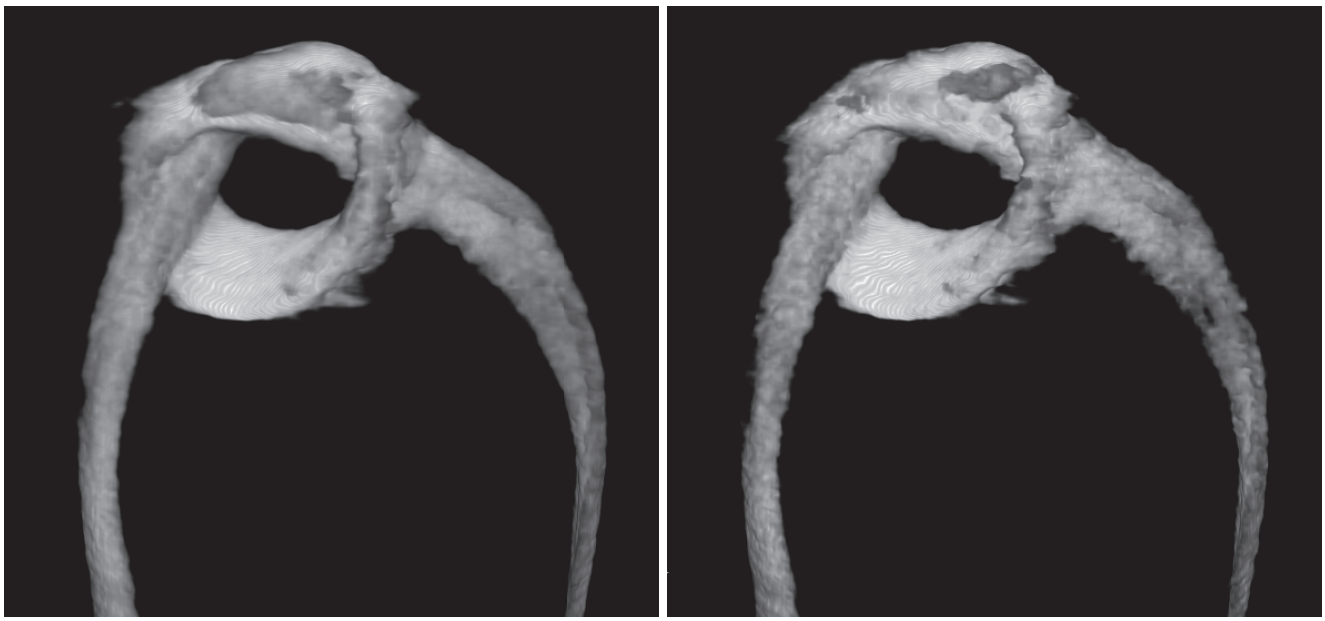

(a) proposed whole-system CG (b) Vogel *et al.*

Fig. 2. Volume rendering of the strongest scattering, i.e. the largest eigenvalue of the tensor at each location, for both methods.

The software implementation is done in our C++ framework [17]; to compute the system matrix P we used the projector developed by Fehringer *et al.* [18]. Further we compare our method to the one proposed by Vogel *et al.* [15], both executed on the same computer equipped with dual Intel Xeon E5-2687W processors and a Nvidia Tesla K20 GPU.

The experimental dataset is a knot made out of carbon fibers, for which 732 projections with 321x321 pixels each were recorded. The reconstruction volume consists of $201 \times 201 \times 201$ voxels.

In order to have comparable results to the method proposed by Vogel et al. [15], we stopped the iterations of our proposed CG approach as soon as the residual norm $\|A\eta - m\|_2$ dropped below the residual norm of the 100 iterations employed Vogel et al. in [15].

We provide two kinds of visualizations of the reconstructed results. The first one is a typical glyph visualization showing the whole information of the tensor as ellipsoids, the second one is a streamline visualization. For the latter, a Runge-Kutta (RK-4) was used to track fibers along the directions of least scattering, as this is supposed to be the direction of microstructures. In both cases we use color coding corresponding to the direction of the microstructures in order to improve the visual impression of the directional orientation of the tensors.

IV. Results

The results of the XTT reconstructions of the carbon knot sample using both our proposed method and the one from Vogel *et al.* [15] are shown in figures 1 and 2.

The reconstruction using the method from Vogel *et al.* using 100 iterations took approximately 2 hours on our machine. Using our proposed method, the residual norm criterion aborts the iteration already after 12 iterations, which cuts the reconstruction time down to approximately 12 minutes on the same machine. The computational effort per iteration of both methods is similar, so the gain in speed is only from requiring less iterations due to higher convergence speed of the reconstruction method.

Figure 1 shows different visualization of the reconstruction volumes of tensor using two different visualization paradigms. The upper row 1a,1b shows a visualization of the tensors in slice 104 of the reconstructed volumes in form of ellipsoids, i.e. the geometric equivalent of a rank-2 tensor. In order to improve the visual impression, we only display every third tensor. Furthermore the ellipsoid are color coded based on the direction of the microstructure (the direction of least scattering corresponding to the smallest half axis of the ellipsoid). While this visualization allows a complete representation of the tensors, it is not useful for 3D visualization.

In order to have meaningful 3D visualization, we extract the direction of the microstructure and compute a streamline visualization along those directions. The corresponding 3D visualizations are shown in Figures 1c, 1d.

Another 3D visualization is given in Figure 2, which shows a volume rendering of the strongest scattering direction, i.e. the largest eigenvalue of tensor at each location in the volume. While it does not give a visualization of the microstructures, it allows an impression of smoothness of the reconstruction.

V. Discussion and Conclusion

Comparing the results from both approaches in Figures 1 and 2, the results are qualitatively very similar. At a closer look we observe the whole-system CG reconstruction to be

slightly more regular, which might be caused by the implicit regularization due to stopping the iterations significantly earlier in this approach.

With respect to the amount of time needed to compute the reconstructions, we find a significant reduction when the whole-system approach is used due to faster convergence speed of the CG. While the method used by Vogel *et al.* also uses a single CG iteration in its block-parallel scheme, a single iteration of CG is equivalent to a single Landweber iteration, which explains the convergence speed advantage of our whole-system approach using multiple CG iterations.

In summary, we presented a whole-system approach for computing XTT reconstructions. Our first results show a significant reduction in the amount of time needed to compute the reconstruction compared to previous approaches, while yielding comparable reconstruction quality.

This work marks another step towards employing the well-founded theory of linear inverse problems to the novel XTT imaging modality, which in the future will also enable incorporation of regularization as a next step.

Acknowledgment

This work was partially funded by the DFG Cluster of Excellence MAP.

References

[1] F. Pfeiffer, T. Weitkamp, O. Bunk, and C. David, "Phase retrieval and differential phase-contrast imaging with low-brilliance X-ray sources," *Nat Phys*, vol. 2, no. 4, pp. 258–261, Mar. 2006.

[2] F. Pfeiffer, M. Bech, O. Bunk, P. Kraft, E. F. Eikenberry, C. Brönnimann, C. Grünzweig, and C. David, "Hard-X-ray dark-field imaging using a grating interferometer," *Nat Mater*, vol. 7, no. 2, pp. 134–137, Jan. 2008.

[3] T. H. Jensen, M. Bech, I. Zanette, T. Weitkamp, C. David, H. Deyhle, S. Rutishauser, E. Reznikova, J. Mohr, R. Feidenhans'l, and F. Pfeiffer, "Directional x-ray dark-field imaging of strongly ordered systems," *Phys. Rev. B*, vol. 82, no. 21, p. 214103, Dec. 2010.

[4] T. H. Jensen, M. Bech, O. Bunk, T. Donath, C. David, R. Feidenhans'l, and F. Pfeiffer, "Directional x-ray dark-field imaging," *Phys. Med. Biol.*, vol. 55, no. 12, pp. 3317–3323, May 2010.

[5] S. Schleede, F. G. Meinel, M. Bech, J. Herzen, K. Achterhold, G. Potdevin, A. Malecki, S. Adam-Neumair, S. F. Thieme, F. Bamberg, K. Nikolaou, A. Bohla, A. Ö. Yildirim, R. Loewen, M. Gifford, R. Ruth, O. Eickelberg, M. Reiser, and F. Pfeiffer, "Emphysema diagnosis using X-ray dark-field imaging at a laser-driven compact synchrotron light source." *PNAS*, vol. 109, no. 44, pp. 17 880–17 885, Oct. 2012.

[6] A. Yaroshenko, F. G. Meinel, M. Bech, A. Tapfer, A. Velroyen, S. Schleede, S. Auweter, A. Bohla, A. Ö. Yildirim, K. Nikolaou, F. Bamberg, O. Eickelberg, M. F. Reiser, and F. Pfeiffer, "Pulmonary Emphysema Diagnosis with a Preclinical Small-Animal X-ray Dark-Field Scatter-Contrast Scanner," *Radiology*, vol. 269, no. 2, pp. 427–433, Nov. 2013.

[7] S. Schleede, M. Bech, K. Achterhold, G. Potdevin, M. Gifford, R. Loewen, C. Limborg, R. Ruth, and F. Pfeiffer, "Multimodal hard X-ray imaging of a mammography phantom at a compact synchrotron light source," *J Synchrotron Radiat*, vol. 19, no. 4, pp. 525–529, May 2012.

[8] M. Stampanoni, Z. Wang, T. Thüring, C. David, E. Roessl, M. Trippel, R. A. Kubik-Huch, G. Singer, M. K. Hohl, and N. Hauser, "The first analysis and clinical evaluation of native breast tissue using differential phase-contrast mammography." *Investigative Radiology*, vol. 46, no. 12, pp. 801–806, Dec. 2011.

[9] G. Potdevin, A. Malecki, T. Biernath, M. Bech, T. H. Jensen, R. Feidenhans'l, I. Zanette, T. Weitkamp, J. Kenntner, J. Mohr, P. Roschger, M. Kerschnitzki, W. Wagermaier, K. Klaushofer, P. Fratzl, and F. Pfeiffer, "X-ray vector radiography for bone micro-architecture diagnostics," *Phys. Med. Biol.*, vol. 57, no. 11, pp. 3451–3461, Jun. 2012.

[10] F. Schaff, A. Malecki, G. Potdevin, E. Eggl, P. B. Noël, T. Baum, E. G. Garcia, J. S. Bauer, and F. Pfeiffer, "Correlation of X-Ray Vector Radiography to Bone Micro-Architecture," *Sci Rep*, vol. 4, Jan. 2014.

[11] A. Velroyen, M. Bech, A. Malecki, A. Tapfer, A. Yaroshenko, M. Ingrisch, C. C. Cyran, S. D. Auweter, K. Nikolaou, M. Reiser, and F. Pfeiffer, "Microbubbles as a scattering contrast agent for grating-based x-ray dark-field imaging," *Phys. Med. Biol.*, vol. 58, no. 4, pp. N37–N46, Feb. 2013.

[12] V. Revol, B. Plank, R. Kaufmann, J. Kastner, C. Kottler, and A. Neels, "Laminate fibre structure characterisation of carbon fibre-reinforced polymers by X-ray scatter dark field imaging with a grating interferometer," *NDT & E International*, vol. 58, pp. 64–71, Sep. 2013.

[13] A. Malecki, G. Potdevin, T. Biernath, E. Eggl, E. G. Garcia, T. Baum, P. B. Noël, J. S. Bauer, and F. Pfeiffer, "Coherent Superposition in Grating-Based Directional Dark-Field Imaging," *PLoS ONE*, vol. 8, no. 4, p. e61268, 2013.

[14] A. Malecki, G. Potdevin, T. Biernath, E. Eggl, K. Willer, T. Lasser, J. Maisenbacher, J. Gibmeier, A. Wanner, and F. Pfeiffer, "X-ray tensor tomography," *EPL (Europhysics Letters)*, vol. 105, no. 3, p. 38002, 2014.

[15] J. Vogel, F. Schaff, A. Fehringer, C. Jud, M. Wieczorek, F. Pfeiffer, and T. Lasser, "Constrained X-ray tensor tomography reconstruction," *Opt. Express*, vol. 23, no. 12, pp. 15 134–15 151, Jun. 2015.

[16] V. Revol, C. Kottler, R. Kaufmann, A. Neels, and A. Dommann, "Orientation-selective X-ray dark field imaging of ordered systems," *J. Appl. Phys.*, vol. 112, no. 11, p. 114903, 2012.

[17] M. Wieczorek, J. Vogel, and T. Lasser, "CampRecon," Tech. Rep. TUM-I1444, 2014.

[18] A. Fehringer, T. Lasser, I. Zanette, P. B. Noël, and F. Pfeiffer, "A versatile tomographic forward- and back-projection approach on multi-GPUs," in *SPIE Medical Imaging*, S. Ourselin and M. A. Styner, Eds. SPIE, Mar. 2014, p. 90344F.

Design of dual multiple aperture devices for dynamical fluence field modulated CT

Aswin John Mathews, Steven Tilley II, Grace Gang, Satomi Kawamoto,
Wojciech Zbijewski, Jeffrey H. Siewerdsen, Reuven Levinson, J. Webster Stayman

***Abstract*— A Multiple Aperture Device (MAD) is a novel x-ray beam modulator that uses binary filtration on a fine scale to spatially modulate an x-ray beam. Using two MADs in series enables a large variety of fluence profiles by shifting the MADS relative to each other. This work details the design and control of dual MADs for a specific class of desired fluence patterns. Specifically, models of MAD operation are integrated into a best fit objective followed by CMA-ES optimization. To illustrate this framework we demonstrate the design process for an abdominal phantom with the goal of uniform detected signal. Achievable fluence profiles show good agreement with target fluence profiles, and the ability to flatten projections when a phantom is scanned is demonstrated. Simulated data reconstruction using traditional tube current modulation (TCM) and MAD filtering with TCM are investigated with the dual MAD system demonstrating more uniformity in noise and illustrating the potential for dose reduction under a maximum noise level constraint.**

***Index Terms*—Fluence field modulation, Radiation dose reduction, Dynamic bow-tie filter, Region-of-interest CT, X-ray beam modulation, Patient-specific CT.**

I. Introduction

X-ray computed tomography has found widespread clinical utility; however, increasing concerns about the risks associated with ionizing radiation have driven the search for exposure reduction strategies. While many algorithmic strategies for producing better images at lower exposures have been developed, there has been relatively little research on innovative hardware-based dose reduction methods. Dose to an individual patient is naturally tied to the particular exposure settings of a CT scanner; however, finding minimum dose strategies is both complex due to the dependence on patient size, anatomical site, etc. and, currently, somewhat limited due to the relative inflexibility of modern CT scanners to control the distribution of x-rays used to image a patient.

Typical clinical scanners permit coarse control of the x-ray beam through exposure settings (tube current and voltage), and many systems have tube current modulation hardware that permits variation of exposure as a function of rotation angle and table position. Control of the spatial distribution of the x-ray beam is typically very limited and is achieved through the introduction of a bow-tie filter. Some systems allow selection from a small number (typically three or fewer) bow-tie filters based on patient size. Typical filters attenuate x-rays at large fan angles to achieve higher fluence levels in the center of the patient (where the attenuation is highest) and lower fluence at the edges (where attenuation is low). Unfortunately, such static beam shaping is limited and cannot account for variability in the width/size of the patient as a function of angle and table position. Similarly, static bow-tie filters can be sensitive to positioning since a well-centered patient is presumed.

Aswin John Mathews, Steven Tilley II, Grace Gang, Satomi Kawamoto, Wojciech Zbijewski, Jeffrey H. Siewerdsen and J. Webster Stayman are with the Department of Biomedical Engineering, Johns Hopkins University, Baltimore, MD 21212 USA. Reuven Levinson is with Philips, Haifa (corresponding author contact info: phone: 410-955-1314; e-mail: web.stayman@jhu.edu).

This work supported, in part, by NIH grant 5U01EB018758.

Fluence-field modulated (FFM) CT is an area of active research that seeks strategies for dynamic modulation of the spatial distribution of the x-ray beam. Successful implementation of FFM-CT increases acquisition flexibility permitting dose reduction objectives [1] as well as novel data collection strategies (e.g., region-of-interest scans). A number of different FFM strategies have been proposed including the use of heavy metal compounds on paper [2], digital beam attenuators [3], piece-wise linear dynamic bowties [4, 5], and fluid filled attenuators [6, 7].

Due to the severe operational requirements within a CT scanner (e.g. limited space, high rotation speeds, accelerations, etc.), the design of dynamic FFM-CT is a challenge. The authors of this paper have previously proposed a novel beam modulation strategy using Multiple Aperture Devices (MADs) which address some of the challenges associated with practical FFM-CT [8]. In this work, we present a strategy for MAD design to achieve specific desired dynamic fluence objectives.

II. Methods

A. The Multiple Aperture Device Concept

The conceptual operation of a MAD filter is illustrated in Figure 1. The device comprises thin bars of a highly attenuating material (e.g. tungsten) of varying widths and spacing. On a fine scale the MAD acts as a binary filter, either completely blocking or passing the X-ray beam using alternating bars and slots. In this fashion, one can concentrate the amount of x-rays spatially by varying the thickness of the blockers locally.

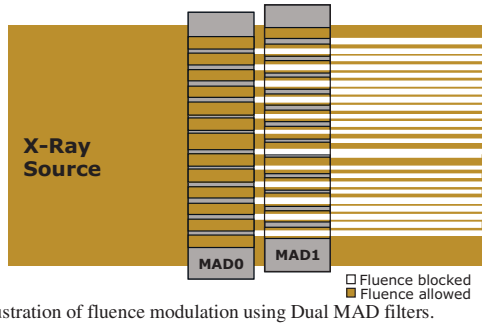

Fig. 1: Illustration of fluence modulation using Dual MAD filters.

As discussed in [8], the pitch (spacing between blockers) of the MAD device may be designed to minimize high-frequency patterns at the detector. For example, if the focal spot of the x-ray source is assumed to be a rectangle, the MAD pitch may be placed at the first null frequency associated with the focal spot blur MTF. In this fashion, the fine bar pattern of the MAD device is blurred out and is not visible at the detector. Desirable (lower frequency) spatial modulation associated with the variable bar width is still achievable.

A single fluence pattern can be obtained with a single MAD device. With multiple MADs in series, capable of moving with respect to each other, a range of fluence patterns can be obtained since it is the composition of two binary filters. Moreover, small relative displacement of the MADs with respect to each other can induce large changes in the fluence pattern. Because small actuations have a large effect on the x-ray distribution, speed and acceleration requirements can be reduced for device

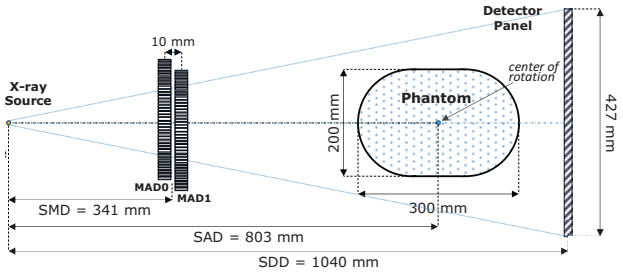

Fig. 2: Illustration of the simulated CT geometry and phantom.

construction. Similarly, because these filters do not rely on variable attenuation using a low atomic number material, the filters can be made very thin and compact. In the following sections, we discuss how to design dual MAD filters for specific fluence objectives.

B. Initial Phantom Study and System Geometry

For initial investigations, we have concentrated on fluence optimization for a single target object; however, the approach may be extended to classes of objects. Specifically, the known object in the simulation study was chosen to be an anthropomorphic phantom body of uniform material (acrylic), as illustrated in Fig. 2. This digital phantom emulates commercially available physical phantoms (QRM GmbH, Morehendorf, Germany) that will be used in subsequent studies.

The system geometry was chosen to emulate a CT scanner's source-to-detector distance and also geometry achievable in a flat-panel-based experimental test bench that is available for subsequent experiments. For our investigations, we considered 360 degree rotation, in steps of 0.5 degree. To create projection data for MAD design and analysis, we used a polyenergetic forward model and *Spektr* [9], a computational tool for x-ray spectral analysis, corresponding to a tube voltage of 100 kVp with additional filtration (2 mm of Al, 0.2 mm of Cu). The model also includes fluence adjustments to accommodate divergent beam effects.

C. Optimization Procedure

1) MAD parameterization

In order to design a set of MAD filters, the location and dimensions of many MAD attributes must be specified. The elements of a dual MAD design are identified in the illustration in Figure 3. Specifically, the free design parameters include: 1) $b_0(x)$, the thickness of each bar as a function of position in MAD0 that locally blocks X-rays; 2) $b_1(x)$, the analogous bar function for MAD1; 3) $\delta(x)$, a local offset function that specifies the position of individual bars in MAD1 relative to MAD0; and 4) the MAD pitch (e.g., the spacing interval between bars).

As mentioned in [8], the MAD pitch may be designed independently of other parameters based on the first null frequency of the focal spot, magnified to the MAD plane. For a rectangular focal spot size, f_s, the optimal MAD pitch is

$$m = f_s \times \left(1 - \frac{SMD}{SDD}\right)$$

We note that for nonrectangular focal spots, one can similarly find a null or minimal pass frequency to enforce smooth fluence profiles. Additionally, even though Fig. 3 shows MAD0 and MAD1 to be parallel with identical pitch, each of the flat MADs have a slightly different pitch and the bars/slots must be focused to the source due to the diverging x-ray beam.

The last parameter that is important for design is the control parameter Δ, which denotes the relative offset between MAD0 and MAD1. This is the one-dimensional actuation that controls the fluence profile enforced by the MAD filters. In general, this

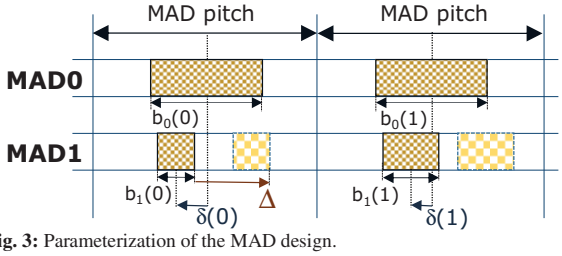

Fig. 3: Parameterization of the MAD design.

parameter must be part of the design process as well, and is a function of the CT rotation angle and/or table position, which we will denote as Δ(θ).

With MAD pitch specified, the remaining parameters: $b_0(x)$, $b_1(x)$, $\delta(x)$, and $\Delta(\theta)$ are sought. In [8], these values were determined analytically using an "endpoint" design to match two desired profiles by considering the minimum and maximum blocking conditions of a dual MAD system. While this approach is attractive due to its closed-form solution, it fails to provide best fit solutions for a wide range of desired fluence patterns. In this work, we seek that more optimal solution, which may be stated as a nonlinear, nonconvex optimization (discussed in the next section).

To facilitate optimization, we have chosen to further parameterize the dual MAD design using a low-dimensional set of basis functions. For example, rather than have a parameter for every bar width in MAD0, we presume neighboring bar widths vary smoothly as a function of position. Specifically, we chose to represent our parameters with a small set of Fourier coefficients, $c_p(\omega)$ such that

$$p(x) = {}^{m}/_{(1 + e^{-\hat{p}(x)})} \quad \hat{p}(x) = \mathcal{F}^{-1}\left[c_p(\omega)\right]$$

where $p(x)$ is one of $\{b_0(x), b_1(x), \delta(x), \text{or } \Delta(\theta)\}$. Thus, the optimization will focus on finding the optimal coefficients: $c_{b1}(\omega)$, $c_{b2}(\omega)$, $c_\delta(\omega)$, and $c_\Delta(\omega)$ which are functions of the spatial (or, for Δ, angular) frequencies selected for the basis set.

2) Objective function

To define our optimization objective, we construct a model of the fluence output which is a function of the design and actuation values and can be written in terms of the original parameters or vectors of low-dimensional Fourier coefficients:

$$M(b_0(x), b_1(x), \delta(x); \Delta(\theta)) \leftrightarrow M(x, \theta; c_{b1}, c_{b2}, c_\delta, c_\Delta)$$

Note that M is a function of spatial location (e.g., a fluence profile) as well as rotation angle.

Using this model, we pose the following optimization:

$$\begin{Bmatrix} \hat{c}_{b1}, \hat{c}_{b2}, \\ \hat{c}_\delta, \hat{c}_\Delta \end{Bmatrix} = \text{argmin} \sum_\theta \sum_{x \epsilon P} \left| \frac{t(\theta, x)}{t_0(\theta)} - \frac{M(x, \theta; c_{b1}, c_{b2}, c_\delta, c_\Delta)}{M_0(\theta)} \right|^2$$

where $t(\theta, x)$ denotes desired fluence patterns as a function of rotation angle. The objective is computed as the mean squared error between the desired and modeled fluence patterns over all projections that intersect the phantom (or patient). As such, X-rays passing outside the phantom (e.g. not contributing to dose) will be ignored in the optimization process.

Also note that both the modeled and desired fluence patterns are normalized by $M_0(\theta) = \sum_x M(x, \theta; .)$ and $t_0(\theta) = \sum_x t(\theta, x)$, respectively. This normalization concentrates the design process on achieving the proper fluence shape. The magnitude of the profile can be adjusted post-design through exposure settings and tube current modulation.While there are many potential desired fluence patterns that one might seek including those that enforce minimum peak variance [10], combined noise and dose objectives[1], or maximize task-based detectability[11], we will focus on fluence patterns that flatten the signal and homogenize noise in projection data.

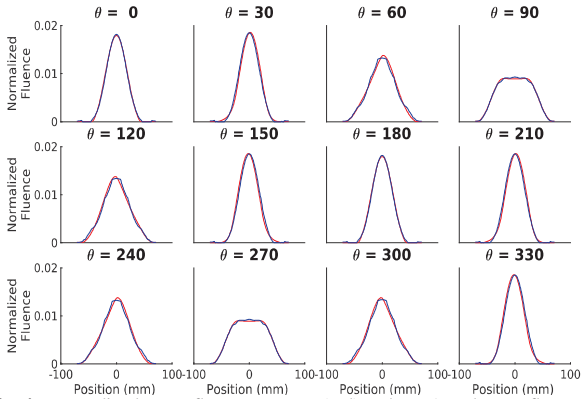

Fig. 4. Normalized target fluence patterns (red) at the MAD plane to flatten the fluence through the phantom at the detector plane, and achievable fluence patterns (blue) using the dual MAD setup. The fluence required is normalized such that the sum is unity.

3) Optimization framework

Covariance Matrix Adaptation Evolution Strategy (CMA-ES) was chosen for the optimization. CMA-ES requires no derivative computations and is well-suited to nonlinear nonconvex optimization since a population of solutions is employed to avoid local optima. We implemented the objective function and the profile modeling function in efficient C++ code including parallelized computation of objective function values (over the population) using OpenMP. The CMA-ES algorithm was initialized to the output of the end-point design process from [8]. A population size of 16 was selected and the stopping criteria for optimization was to stop if successive function evaluations differ less than 10^{-12} or 10,000 iterations was computed. All the MAD design parameters were constrained to lie between 0 and a single pitch, m, to avoid nonphysical and periodic solutions (e.g. beyond a single cycle of actuation).

III. Results/Discussion

A. Target and achieved fluence profiles

To generate desired fluence patterns, the phantom was rotated 360 degrees in steps of 0.5 degrees. The fluence is simulated at the detector plane, and the fluence profile at the MAD plane required to flatten this fluence is computed using the methodology of Section IIB. The MAD parameterization used 8 Fourier coefficients for each MAD feature (4 total), and only symmetric basis functions were employed to enforce symmetric MAD designs. A subset of these target fluence profiles are shown in Fig. 4. The fluence obtainable with the dual MADs using the CMA-ES optimization is also plotted.

The designed fluence profiles very closely match the desired fluence pattern suggesting that a dual MAD system can match a range of fluence profiles and, in this case, substantially flatten the fluence profiles at the detector for this phantom. For the fluence profiles with a flat top, the achievable CMA-ES profiles show fluctuation on the flat edge. The narrow fluence profiles show slight misalignment error, which is potentially correctable by shifting both MADs together. Such analysis is the topic of ongoing investigations and will likely be important for asymmetric beam profiles (e.g., for miscentered patients, off axis targets, etc.).

B. Estimated MAD design parameters

The optimized MAD design parameters are shown in Fig. 5. Note since the bar widths are directly proportional to the amount of local blockage and consequently inversely proportional to the local fluence, the effect of the MAD0 filter alone is not unlike a traditional bowtie (e.g. more fluence in the center of the field

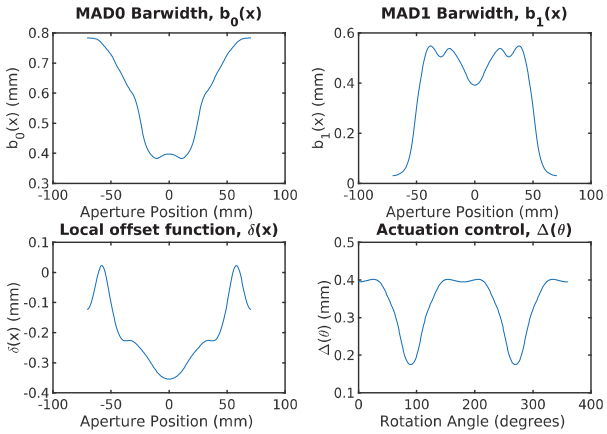

Fig. 5. Solutions to the dual MAD design optimization. A) Bar width function , $b_0(x)$ for MAD0; B) barwidth function $b_1(x)$ for MAD1; C) local offset function $\delta(x)$; and D) the actuation control, $\Delta(\theta)$, as a function of rotation angle.

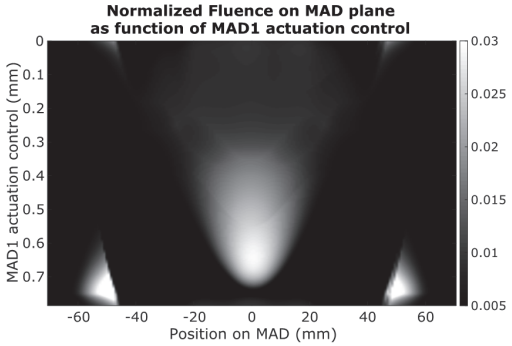

Fig. 6. Post-filtering fluence profiles at the MAD plane with a full range of control actuation (displacements of MAD1 with respect to MAD0).

and less at the edges). The MAD1 design is almost the opposite (when acting alone). The bar widths in both MADs span the range of approximately 50 µm to 800 µm. Such designs are largely within the constraints of modern tungsten sintering technology, though features <100 µm can present some challenges (such constraints can potentially be integrated into the design process). The local offset function, $\delta(x)$, is predominantly negative, meaning that the MAD1 bars are located to the left of the center position in each MAD period.

The actuation control shown in Figure 5D illustrates that MAD1 is displaced between 0.15 mm to 0.4 mm as the projection angle changes from 0 to 360 degrees. This minimal movement of the MADs causes the large change in the fluence patterns seen in Figure 4 and can be attributed to the relatively small MAD pitch. From an implementation standpoint, the potential mechanical advantage is the fast switching speed of the MAD fluence profiles as the CT gantry spins around the patient. The smooth profile of the displacement also reduces the acceleration requirements on the actuator. Though not done here, one could integrate specific acceleration limits as part of the optimization.

C. Achievable Fluence Patterns

It is interesting to note that the design of the previous sections only utilizes part of the actuation control range. Fig. 6 shows the full range of fluence patterns achievable as the second MAD is moved with respect to the first MAD within a single MAD pitch (e.g. one cycle). Recall, that for the selected phantom, only fluence profiles between MAD1 displacements of 0.1 to 0.4 were used.

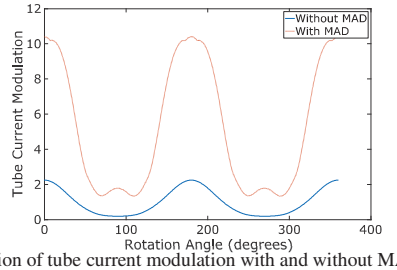

Fig. 7: Illustration of tube current modulation with and without MAD filters.

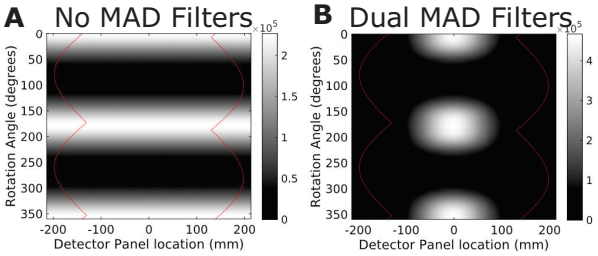

Fig. 8: Illustration of the fluence profiles received at the detector with no phantom in the scanner using A) no filters and AEC, and B) using optimally actuated and designed dual MAD filters and AEC. The space occupied by phantom is shown with a dotted red line. Unit are in photons.

However, from the fluence map, it is clear that much sharper fluence patterns can be obtained by changing the displacement to 0.7 mm. This potentially enables other applications such as region-of-interest fluence modulation and suggests additional design flexibility for larger classes of profiles (e.g. more complex objects, multiple classes, etc.).

D. Tube Current Modulation (TCM)

Although a variety of fluence patterns have been demonstrated, practical application and fitting to the desired fluence profiles requires proper scaling. This scaling can be achieved through tube current modulation (TCM). Typical Automatic Exposure Control (AEC) seeks to provide a constant fluence at the center of the detector. We have applied this strategy for the no filter scenario. For the MAD scenario, we applied the same strategy of providing constant fluence at the central detector pixel, through the Dual MAD and phantom. For comparison between the no filter and MAD filtered scenarios we have ensured that the total fluence (i.e., the number of simulated photons) incident on the phantom is constant for the two approaches. Specifically, TCM is scaled to enforce a total of 100,000 photons incident on the phantom.

Fig. 7 shows the TCM required to convert the fluence generated by the MADs to the required target fluence. Without the MAD filter, the TCM is largest when the path length of X-rays through the phantom is largest. The dual MAD filter has maximum attenuation when the fluence profile is narrow. Therefore, more photons are required at 0 and 180 degrees to flatten the fluence with MAD than at 90 or 270 degrees. The MAD requires higher scaling and modulation to generate the same number of photons incident on the phantom.

E. Simulated Projection Data

Figure 8 and 9 show the fluence profiles with and without the phantom in the field of view for the no filter and MAD filtered scenarios (TCM is used in both cases). In Fig. 8, we see that the no filter scenario can only modulate the per view number of photons through TCM while the dual MAD filter can customize both the shape and intensity of the beam. In Fig. 9, the post-object fluence is more uniform across object projections (the design goal) than the no filter, TCM-only scenario.

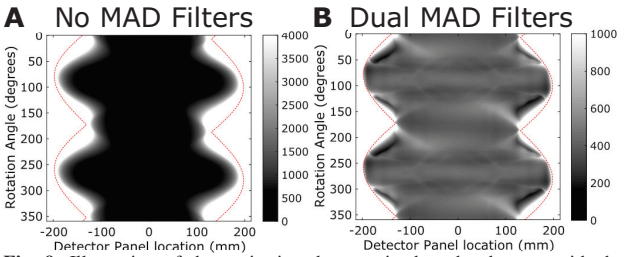

Fig. 9: Illustration of the projection data received at the detector with the phantom in the scanner using A) no filters and AEC, and B) using optimally actuated and designed dual MAD filters and AEC. The space occupied by phantom is shown with a dotted red line. Units are in photons.

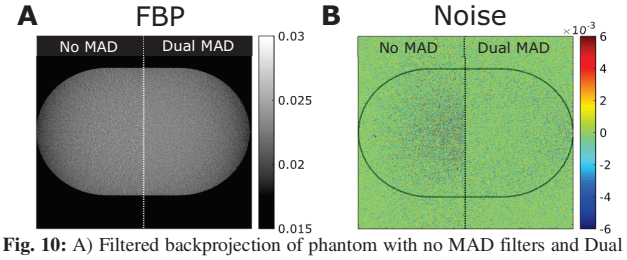

Fig. 10: A) Filtered backprojection of phantom with no MAD filters and Dual MAD filters. B) Noise image with no MAD filter and Dual MAD filter

F. Simulated Reconstructions

With Poisson noise added to the projection data in Fig. 9, filtered backprojection reconstructions were performed for both filtering scenarios. Results are shown in Figure 10. Both methods show approximately the same average noise level (as expected due to an equal number of incident photons). However, we see much greater noise uniformity in the MAD filtered image. This is significant if a minimum noise level is prescribed to obtain sufficient image quality. The TCM-only case will require more incident photons (hence larger dose) to obtain the same minimum noise level over the entire image.

G. Ongoing and Future Work

While these initial results suggest that dual MAD filters can successfully achieve a broad class of fluence patterns, we are seeking to extend this work to even larger classes of fluence patterns (e.g. different size patients). Similarly, parallel efforts are working to fabricate physical MAD devices and evaluate performance in an experimental CT system.

REFERENCES

[1] S. Bartolac, et al., "Fluence field optimization for noise and dose objectives in CT," Med. Phys., 38(2011), p. S2, 2011.
[2] B. H. Hasegawa, et al., "Selective Exposure Radiography using digitally-formed x-ray beam attenuators," Proc. SPIE, vol. 0419, pp. 282–288, 1983.
[3] T. P. Szczykutowicz and C. A. Mistretta, "Design of a digital beam attenuation system for computed tomography. Part II. Performance study and initial results." Med. Phys., 40(2013), p. 021906, 2013.
[4] S. S. Hsieh and N. J. Pelc, "The feasibility of a piecewise-linear dynamic bowtie filter." Med. Phys., 40(3), p. 031910, 2013.
[5] F. Liu, et al., "Dynamic bowtie filter for cone-beam/multi-slice CT," PLoS One, 9(7), pp. 1–10, 2014.
[6] P. Shunhavanich, S. S. Hsieh, and N. J. Pelc, "Fluid-filled dynamic bowtie filter: a feasibility study," in Proceedings of SPIE, 2015, vol. 9412, p. 94121L.
[7] T. P. Szczykutowicz and J. Hermus, "Fluid Dynamic Bowtie Attenuators," Proc. SPIE, vol. 9412, pp. 1–7, 2015.
[8] J. Webster Stayman, et al., "Fluence-Field Modulated X-ray CT using Multiple Aperture Devices," Proc. SPIE, 2016.
[9] J. H. Siewerdsen, et al., "Spektr: A computational tool for x-ray spectral analysis and imaging system optimization," Med. Phys., 31(11), p. 3057, 2004.
[10] S. S. Hsieh and N. J. Pelc, "Algorithms for optimizing CT fluence control," Proc. SPIE, vol. 9033, p. 90330M, 2014.
[11] G. J. Gang, et al., "Task-driven tube current modulation and regularization design in computed tomography with penalized-likelihood reconstruction," in SPIE Medical Imaging, 2016.

Hybrid Photon Counting Detectors for Spectral X-ray imaging

P. Trueb, P. Zambon and Ch. Broennimann

Abstract— **Hybrid Photon Counting (HPC) detectors revolutionized diffraction experiments at third generation synchrotrons. Allowing the simultaneous measurement of X-ray intensities in multiple energy bins, they have the potential to do the same in the field of medical imaging. In order to meet the requirements for human CT applications and other imaging modalities, high-Z sensor materials with high quantum efficiency for X-ray energies above 100 keV have to be used. Characterization results of suitable CdTe- and CZT-sensors are presented. The readout ASIC has to support accurate spectral measurements at very high photon fluxes. We observe stable operation of CZT detectors up to $3.7 \cdot 10^8$cts/mm^2/s. We use our measured data as input parameters for a Monte Carlo simulation, which is used to predict the spectral performance at high rates for various pixel sizes.**

Index Terms—**Photon Counting Detectors, Spectral Computed Tomography, Pixel Detectors, CdTe, CZT, Charge Summing**

I. Introduction

Hybrid Photon Counting (HPC) Detectors are believed to radically transform medical imaging from the year 2020 onward [1]. Due to the combination of direct X-ray detection in the structured high-Z semiconductor sensor and single photon counting electronics in each pixel of the ASIC, such detectors offer an unprecedented combination of high detection efficiency, high spatial resolution (below 100 μm), high count rate capability (up to $3 \cdot 10^8$ cts/mm^2/s), and good energy resolution (2-5 keV) in an energy range from 5 to above 100 keV. In the field of X-ray diffraction, HPC detectors proved to be a disruptive technology [2] both for scientific and industrial applications. In addition to the excellent performance of the detectors, the stable and maintenance-free operation of thousands of systems around the world is a key reason for the fast spread of the technology.

It is still questioned whether photon counting detectors can cope with very high photon fluxes. At typical operating conditions (120 kVp, 800 mA) of a clinical CT system, the flux can be as high as $1.6 \cdot 10^9$ ph/mm^2/s [3]. However, many groups have shown quite remarkable rate performance of their systems, see e.g. [4]. Due to the small capacitance of the pixelated sensor element (typically less than 100 fF) the input load of the pixel amplifier is very small. Modern CMOS processes allow the design of low noise and still very fast amplifiers. The minimum shaping time τ is around 20-30 ns, in order to collect the charge generated in the sensor. This allows for count rates well beyond 10^7 cts/pixel/s. However, all counting circuits suffer from pile-up effects due to the stochastic arrival of the X-rays. This leads to a limitation of the observed count rate. Most circuits are paralyzable counters, which reach a maximum observed count rate at an incoming count rate of τ^{-1} counts, and the detector paralyzes completely in the limit of very high incoming rates. The pixel size of different systems varies from 55 μm up to about 500 μm. Pixel sizes of >500 μm are not able to cope with the high incoming flux of CT systems.

Another very important aspect of HPC detectors is the improved spatial resolution. Due to the direct detection of the X-rays, the modulation transfer function (MTF) is very close to the theoretical value of a box function point spread function (PSF). The energy resolution of photon counting detectors is dependent on the capacitance of the sensor pixel, equivalent noise charge (ENC) of the preamplifier, shaper and comparator, on the leakage current from the sensor. Energy resolution is also limited by incoming rate per pixel due to pulse pile-up, i.e. for high rates, energy resolution is reduced. Thus it would make sense to make the pixels as small as possible. It is well known, that for small pixels more and more charge is shared by the adjacent pixels, and fluorescent photons have a higher probability of escaping the pixel, thus affecting the energy resolution as well. Another important point is the matching of a large ensemble of pixels, i.e. one has to look at the energy resolution of the sum of all pixels of a HPC detector.

The energy resolution is not the only parameter of interest, because material decomposition is not only dependent on the energy resolution but also on the fraction of charge sharing. We use a quantity called *Spectral Efficiency*, which is the photo-peak to background ratio. We compute the Spectral Efficiency as a function of pixel size and photon flux with a Monte-Carlo simulation, which includes all relevant contributions. The simulation has been validated by detailed measurements.

II. System Description

A. Sensor Materials

Thanks to their high atomic number, II-VI semiconductor Cadmium Telluride (Z=50) and Cadmium Zinc Telluride

Submitted on April 7th 2016.

P. Trueb, P. Zambon, C. Broennimann are with Dectris Ltd, 5405 Baden-Daettwil, Switzerland (e-mail: peter.trueb@dectris.com, pietro.zambon@dectris.com, christian.broennimann@dectris.com).

(Z≈49.1) offer the unique possibility to extend the detectable X-ray energy range up to levels unattainable with silicon sensors [5]. Though their wide spread has been formerly prevented by the poor material quality and in particular by the limited charge transport properties [6], in recent times they regained much interest due to the constant improvement of the growing techniques that made detector-grade material available [7]. In this context, DECTRIS investigated the feasibility of photon counting detectors featuring CdTe and CZT sensors and is finally able to successfully manufacture large area CdTe detectors with few or no defects, while CZT detectors are still in a prototyping phase and, though some further improvement are needed at the material level, show already promising results.

Typical CdTe and CZT sensor range from 1 mm to 2 mm thickness and thanks to their wide bandgap and extremely high resistivity (>10^9 Ω·cm) can be operated in ohmic mode already at room temperature – with beneficial results on the *polarization effect* [8][9]. Due to the higher μ·τ product of electrons with respect to holes, the detectors operate in electron collection mode and virtually all the charge is collected by the front-end electronics. The scaling of the pixel size brings further benefits in virtue of the *small pixel effect* [10]. The limit on the energy resolving capabilities is set by the electronic noise and a FWHM of 2 keV at 20 keV was measured with a PILATUS3-CdTe [13] detector.

In virtue of the direct photon conversion and despite the unavoidable *charge sharing effect* affecting the charge collection [11], the spatial resolution remains excellent. The impact of the charge sharing on the detector performances can be – under some assumptions – analytically described and accurate predictions can be drawn. For example, Table **1** reports the estimated percentage of pixel area subject to charge sharing (collected charge < 95%), for different pixel sizes and two sensor thicknesses, assuming a bias voltage of 500V.

Table 1: Estimated charge sharing area (collected charge <95%) expressed in percentage of the total pixel area for different pixel sizes and for two sensor thicknesses, under an assumed bias voltage of 500 V.

Pixel Size [μm]	Charge Sharing Area [%]	
	d=1000 μm	*d=1500 μm*
75	54.2	76.7
150	27.9	41.5
225	20.3	27.9
300	15.4	20.3
400	11.7	16.8
500	8.4	13
1000	3.9	6

It can be seen, that by doubling the pixel sixe from 75 to 150 μm the charge sharing is reduced by almost a factor of 2. In order to limit the charge sharing to about 15% for a 1 mm thick sensor a pixel size of at least 300 μm is required. Further reduction of charge sharing is only achieved by the implementation of charge sharing correction methods in the ASIC.

B. ASICs

The PILATUS ASIC, which is very widely used in X-ray diffraction systems [12] features a pixel size of 172 μm×172 μm and is compatible with both the hole-collection mode required by silicon and with the electron-collection mode required by high-Z sensors. High tolerance to radiation is achieved by design. Each pixel is equipped with a preamplifier, shaper and comparator with selectable threshold and a 20-bit counter, which provides an extra-large dynamic range. In order to cope with the incredible high local count-rates at 3rd generation synchrotron sources, the count-rate model in the pixel was improved. In the PILATUS 3 ASIC, the patented *instant retrigger technology* allows for a non-paralyzable counting mode, which achieves count rates above $3 \cdot 10^8$ cts/mm^2/s [13].

The EIGER ASIC [14] is used for applications, which require higher spatial resolution and higher frame rates. The pixel size has been shrunk to 75 μm×75 μm – with a total chip area of 19.3 mm×20m m – and thanks to the double-buffered counter the frame rate can be as high as 3 kHz..

C. Simulation

Numerical simulations play an important role in the design process of an HPC ASIC, since they allow rapid evaluation of new concepts and optimization of important detector specifications like the pixel size. While analytic models can be used to investigate some aspects of spectral photon counting detectors, Monte Carlo methods are an ideal tool to model stochastic effects like pulse pile-up in the ASIC or fluorescence in the sensor material.

A Monte-Carlo simulation framework, originally developed to study the effect of synchrotron bunch modes on pulse pile-up [15], was extended to incorporate fluorescence effects in high-Z sensors to study the spectral response of HPCs. For the purpose of the presented results, a continuous beam following Poisson statistics is used as a source of mono- or polychromatic X-rays. The photo-absorption in the sensor is followed by the creation and propagation of secondary fluorescence photons. Effects of Compton scattering are currently not implemented. The simulation of the charge cloud expansion during its drift to the readout electrodes uses a simple diffusion model. After splitting the charge over several pixels, each event generates a pulse with its height being proportional to the amount of collected charge. The pulse shape is taken from a transistor level simulation of the preamplifier and shaper response. Pulses overlapping in time are linearly summed up and finally compared to a predefined energy threshold. The results of the Monte-Carlo were crosschecked with analytical models and experimental data.

III. RESULTS

We conducted a comprehensive characterization campaign – carried out both in our in-house laboratory and at several synchrotron beamlines – in order to assess CdTe and CZT

sensor properties and their performances when coupled to the different ASICs .

A. Performance of CdTe and CZT systems

1) Modulation Transfer Function

The spatial resolution has been measured for a CdTe 0.75 mm-thick photon counting detector of 75 µm pixel size and compared to the one of a commercial flat-panel detector of same pixel size, where a scintillation layer provides the photon conversion. Fig. 1 shows the *Modulation Transfer Functions* (MTF) of the two detectors plus the ideal case under the same experimental conditions – direct X-ray tube beam at 60 kV_p filtered with 3 mm Al. At the Nyquist frequency (6.7 lp/mm) a MTF of >35% is achieved and at 10% MTF we get a resolution of 10 lp/mm.

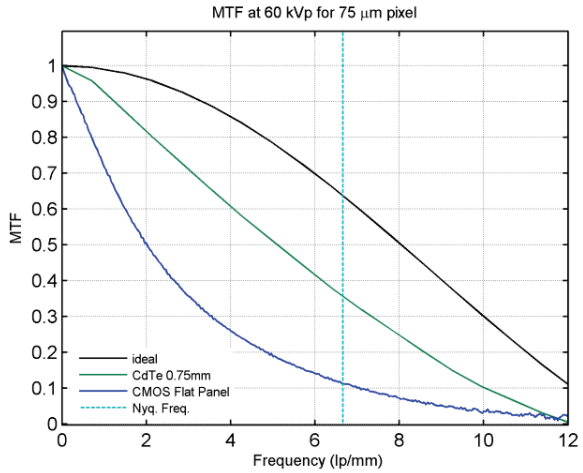

Figure 1: Measured MTF of a CdTe 0.75 mm-thickness photon counting detector and of a commercial flat-panel detector equipped with a scintillation layer. Both systems feature a pixel size of 75 µm and are irradiated with a direct X-ray tube beam at 60 kV_p (filtered with 3mm Al). The benefit of direct conversion over the indirect detection with a CMOS flat panel is clearly visible.

2) Retrigger and Count Rate Capability

PILATUS3-CdTe and -CZT count rate curves have been measured in the energy range 10-60 keV at the BAM beamline at BESSY-II synchrotron in collaboration with the PTB group. Figure 2 shows the measured and corrected count rate curves of CdTe 1 mm-thick, measured at 60 keV with the energy threshold at 50% and instant retrigger enabled (non-paralyzable counting mode). The rate-corrected curves saturate at ~$3.7 \cdot 10^8$cts/mm^2/s limited by the PILATUS ASIC.

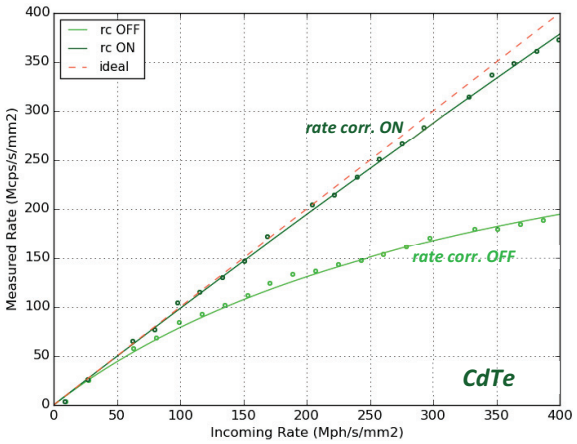

Figure 2: Measured and corrected count rate curves for 1 mm PILATUS3 CdTe detectors with an incoming photon energy 60 keV and a threshold at 50%. Instant retrigger is enabled, i.e. the detector is operated in non-paralyzable counting mode.

B. Simulation of different system configurations

The main factors affecting the spectral performance of HPC detectors are the finite sensor thickness, fluorescence effects in the sensor material, charge sharing between adjacent pixels, electronic noise and pulse pileup. Fig. 3 shows the influence of these factors on the spectrum of a W-tube operated at 120 kVp. The sensor thickness is 1 mm of CdTe. The pixel size is 300 µm, the equivalent noise charge 100 e^- and the flux $5 \cdot 10^7$ph/mm^2/s. The results are obtained with the Monte-Carlo simulation framework described above. Especially the fluorescence effects, the charge sharing between pixels and pule pileup degrade the spectral performance.

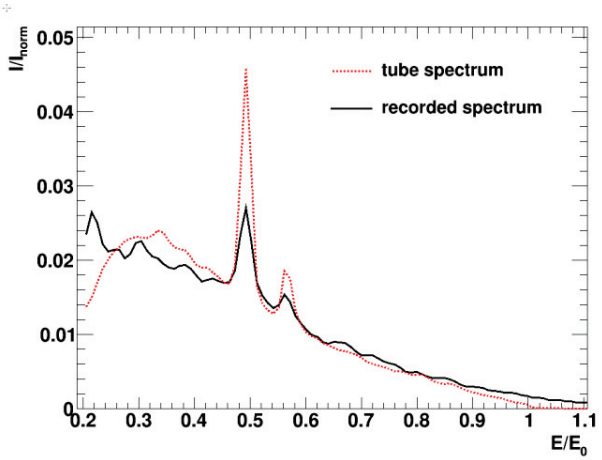

Figure 3: Simulation of the measurement of the spectrum from a W-tube operated at E_0=120 kVp by an HPC detector. The red dashed line shows the tube spectrum, the black solid line the spectrum as recorded by the detector. The peaks are smeared out corresponding to the energy resolution of the detector. The recorded low energy spectrum is increased due to fluorescence and charge sharing. The simulation parameters are given in the text.

The most import decision during detector design concerns the pixel size. While large pixels reduce the detrimental effect of charge sharing and fluorescence, smaller pixels are less

prone to pulse pile-up. Fig. 4 shows the simulated Spectral Efficiency for photons of 60 keV for a CdTe HPC detector as a function of pixel size and photon flux. The Spectral Efficiency (SE) is defined as the ratio of the photons counted in a given energy range to the total number of photons impinging on the sensor. The Spectral Efficiency *SE* in the energy interval (E_0, E_1) can be expressed as a function of the quantum efficiency *QE*: $SE(E_0 < E < E_1) = QE(E_t=E_0) - QE(E_t=E_1)$ with E_t the applied energy threshold. A constant pulse width of 44 ns and an equivalent noise charge of 100 e^- are assumed. For small pixel sizes the Spectral Efficiency decreases due to charge sharing and fluorescence, for large pixels due to pulse pileup. For a typical photon flux (after attenuation by an object) of $5 \cdot 10^7$ph/mm^2/s, the best performance is achieved with a pixel size in the range of 150 µm to 300 µm.

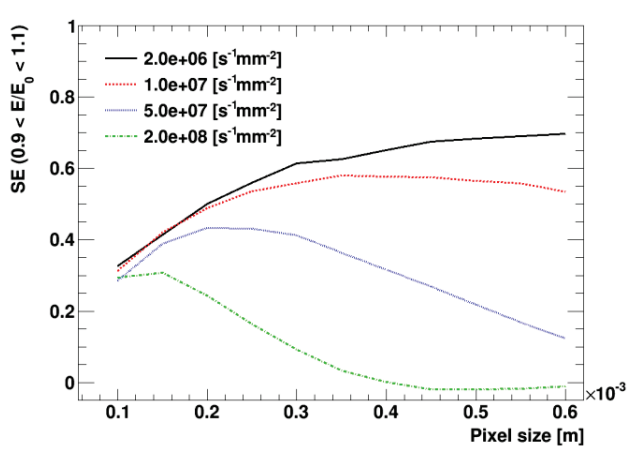

Figure 4: Simulated Spectral Efficiency (SE) in the energy range 54 keV < E < 66 keV for monochromatic X-rays with an energy of E_0=60 keV as a function of pixel size and incoming photon flux. For a typical photon flux of 5×10^7ph/mm^2/s, the optimal pixel size lies in the range between 150 µm and 300 µm.

C. Concept of a high rate high energy resolution system

Aside from the effects of charge sharing and fluorescence, small pixels offer many advantages for Spectral X-ray Imaging. Besides the higher spatial resolution, the small pixel effect allows for fast charge collection and the reduced count rates per pixel mitigate the distortion of the spectral information due to pulse pile-up. To compensate for the splitting of the deposited charge over multiple pixels, several charge-summing mechanisms have been proposed [4], but usually they lead either to a reduced rate capability or decreased quantum efficiency. A simpler and faster approach to perform the summing could improve the spectral performance compared to existing charge-summing mechanism. First simulations of a fast summing approach for small pixels below 150 µm size show encouraging results. Spectral Efficiencies of around fifty percent at $5 \cdot 10^7$ ph/mm^2/s seem to be within reach.

IV. Conclusion

Spectral X-ray imaging is a very demanding application for Hybrid Photon Counting detectors. To achieve high quantum efficiency, high-Z sensors materials like CdTe or CZT have to be used. Our extensive characterization of these materials in-house and at synchrotron beam lines shows that they provide high spatial resolution and that they are able to cope with high photon flux and are lag free.. Applying high bias voltages helps to mitigate polarization effects.

The most challenging task for HPC detectors is to provide accurate spectral information at the very high photon fluxes. Charge sharing, fluorescence effects and pulse pileup can significantly degrade the quality of the recorded spectrum. A promising approach to tackle this challenge is the implementation of a fast charge summing mechanism combined with pixels smaller than 150 µm. The Spectral Efficiency of a fast summing approach has been simulated and the results indicate improvements over existing solutions.

References

[1] K. Taguchi, J. S. Iwanczyik, "Vision 20/20: Single photon counting x-ray detectors in medical imaging," *Medical Physics*, vol. 40, no. 10, 2013.

[2] C. Broennimann, P. Trueb, "Hybrid Pixel Photon Counting X-ray Detectors for Synchrotron Radiation," in *Synchrotron Light Sources and Free-Electron Lasers,* E. Jaeschke et al., Ed. B e r l i n : Springer, 2015, Available: http://link.springer.com/referenceworkentry/10.1007/978-3-319-04507-8_36-1.

[3] Shikhaliev P. M., "Medical X-Ray and CT Imaging with Photon-Counting Detectors," in Radiation Detectors for Medical Imaging, S. J. Iwanczyik, Ed., pp. 47–80 , CRC Press 2015.

[4] Ballabriga R., et al., "Review of hybrid pixel detector readout ASICs for spectroscopic X-ray imaging", *Journal of Instrumentation*, vol. 11, P01007, 2016.

[5] C. Szeles, "CdZnTe and CdTe materials for x-ray and gamma ray radiation detector application," *Phys Stat. Sol.*,vol. 241, pp. 783–790, 2004.

[6] G. Ottaviani, et al., "Charge carrier transport properties of semiconductor materials suitable for nuclear radiation detectors," *IEEE Trans. Nuclear Science*, vol. NS-2, pp. 192–204, Feb. 1975.

[7] S. Del Sordo, et al., "Progress in the development of CdTe and CdZnTe semiconductor radiation detectors for astrophysical and medical applications," *Sensors*, vol. 9, pp. 3491–3526, 2009.

[8] A. Cola, et al., "The polarization mechanism in CdTe Schottky detectors," *Applied Physical Letters*, vol. 94, 2009.

[9] R. Grill, et al., "Polarization study of defect structures of CdTe radiation detectors," *IEEE Trans. Nuclear Science*, vol. 58, pp. 3172–3181, Dec. 2011.

[10] M. D. Wilson, et al., "Investigation of the small pixel effect in CdZnTe detectors," 2007 IEEE Nucl. Science Symp. Conference Records, N24-108, pp. 1255–1259, 2007.

[11] K. Mathieson, et al, "Charge sharing in silicon pixel detectors," *Nucl. Instrum. and Meth. A*, vol. 487, pp. 113-122, 2002.

[12] E. F. Eikenberry, et al, "PILATUS: a two-dimensional X-ray detector for macromolecular crystallography," *Nucl. Instr. and Meth. A*, vol. 501, pp. 260–266, 2003.

[13] T. Loeliger, et al., "The New PILATUS3 ASIC with Instant Retrigger Capability," *2012 Nucl. Science Symp. Conference Records*, N6-2, pp. 610–615 , 2012.

[14] R. Dinapoli, et al., "EIGER: Next generation single photon counting detector for X-ray applications," *Nucl. Istr. and Meth. A*, vol. 650, pp. 79–83, 2011.

[15] P. Trueb et al., "Bunch mode specific rate corrections for PILATUS3 detectors," *J. Synchrotron Rad.*, vol. 22, no. 3, pp. 701–707, May 2015.

Simultaneous spectral scaling and basis material map reconstruction for spectral CT with photon-counting detectors

Emil Y. Sidky[1], Taly Gilat-Schmidt[2], Rina Foygel Barber[3], Wooseok Ha[3], and Xiaochuan Pan[1]

***Abstract*—Photon-counting detectors are being investigated for use in spectral computed tomography (CT). The main advantage is that transmitted X-ray photon counts can be measured simultaneously in several energy windows. This capability is potentially useful for spectral CT when more than two basis images are desired as would be the case for the use of K-edge contrast agents [1,2]. An important practical issue for spectral CT with photon-counting detectors is accurately calibrating the spectral response of each of the detector pixels. Slight mis-calibrations result in prominent ring artifacts in the basis images. In this abstract we report on an image reconstruction algorithm for spectral CT that yields the basis maps while simultaneously solving for scaling factors for each of the detector pixel spectra. By including the spectral factors in the reconstruction process the pixel spectra receive small adjustments that reduce ring artifacts. The proposed algorithm is demonstrated on experimental spectral CT data.**

I. Introduction

We have recently developed a general algorithm for spectral CT image reconstruction that can perform image reconstruction of basis material maps from energy-windowed X-ray transmission data while incorporating convex constraints [3,4]. The algorithm is based on a large-scale first order solver for some forms of nonconvex optimization problems – the mirrored convex/concave (MOCCA) algorithm [3]. Use of the MOCCA algorithm on spectral CT allows for one-step inversion of the spectral CT data model going from photon count data directly to basis material maps. This approach differs from the more usual two-step processing, where the X-ray photon count data are pre-processed to material sinograms which are then fed into standard reconstruction algorithms [2]. For the purpose here, the one-step reconstruction is employed to exploit a bound on the material map total variation (TV) to constrain the inversion from count data to material maps for experimental spectral CT data.

In performing image reconstruction on spectral CT data with a photon-counting detector it is crucial to have accurate calibration of the spectral response of each detector pixel. Because the spectral response varies with each pixel, slight calibration errors can cause prominent ring artifacts. For this reason, we propose to allow for limited auto-calibration of the spectral response in the image reconstruction by including scaling factors for each energy window of each detector pixel. The spectrum scaling is seen to reduce the ring artifacts in the reconstructed material maps.

The data model including the spectrum scaling factors and the theory of the spectral CT image reconstruction is presented in Sec. II. Results for experimental spectral CT data are shown in Sec. III. A comparison of the reconstructed material maps with and without the use of spectrum auto-scaling is shown.

II. Methods

To model the spectral CT data, we allow for each detector pixel to have its own spectral response $S_{w,j}(E)$ for each energy window

$$I_{w,s,u} = \int dE\, S_{w,u}(E) \exp\left[-\int_{\ell(s,u)} dt\, \mu(E, \vec{r}(t))\right], \tag{1}$$

where $I_{w,s,u}$ is the transmitted X-ray photon fluence along ray $\ell(s,u)$ in energy window w for X-ray source and detector bin location s and u, respectively; t is a parameter indicating location on $\ell(s,u)$; $S_{w,u}(E)$ is the spectral response at the detector bin u in energy window w; and $\mu(E,\vec{r}(t))$ is the energy and spatial dependent linear X-ray attenuation coefficient. In the experiment $S_{w,u}(E)$ is not known *a priori*, and it is determined by measuring X-ray transmission through a phantom of known shape and composition [5]. As is standard, we employ a basis material decomposition to model the attenuation map

$$\mu(E, \vec{r}(t)) = \sum_m \left(\frac{\mu_m(E)}{\rho_m}\right) \rho_m f_m(\vec{r}[t]), \tag{2}$$

[1]The University of Chicago, Department of Radiology MC-2026, 5841 S. Maryland Avenue, Chicago IL, 60637.

[2]Marquette University, Department of Biomedical Engineering, PO Box 1881, Milwaukee WI, 53201.

[3]The University of Chicago, Department of Statistics, 5734 S. University Avenue, Chicago IL, 60637.

where ρ_m is the density of material m; $\mu_m(E)/\rho_m$ is the mass attenuation coefficient of material m; and $f_m(\vec{r})$ is the spatial map for material m.

To obtain the final data model, we combine Eq. (1) with Eq. (2), discretize all integrations, and include parameters $\alpha_{w,u}$ that allow for the fact that there is error in the experimentally determined spectra $S_{w,u}(E)$. The counts model becomes

$$I_{w,s,u} = \sum_i S_{w,u,i} \exp\left[-\alpha_{w,u} - \sum_{m,k} \mu_{m,i} X_{s,u,k} f_{m,k}\right], \tag{3}$$

where $S_{w,u,i} = S_{w,u}(E_i)$; $\mu_{m,i} = \mu_m(E_i)$; $X_{s,u,k}$ represents X-ray projection along the ray $\ell(s,u)$; and $f_{m,k}$ is the pixelized material map with k indexing pixel number. The unknowns in the model are the spectrum scaling coefficients $\alpha_{w,u}$ and the material maps $f_{m,k}$, and image reconstruction is comprised of determining these unknowns from measured values for $I_{w,s,u}$. Note that the scaling factors are put in the exponential. We formulate the scaling in this way because all the unknowns are combined linearly in the argument of the exponential and thus no change is required in the MOCCA algorithm for solving optimization problems involving this data model.

Constrained transmission Poisson likelihood maximization: Maximizing a Poisson likelihood model for the transmitted photon counts is equivalent to minimizing the following data fidelity function

$$D_{\text{TPL}}(I,c) = \sum_{w,s,u} \left[I_{w,s,u} - c_{w,s,u} - c_{w,s,u} \log \frac{I_{w,s,u}}{c_{w,s,u}}\right], \tag{4}$$

where $c_{w,s,u}$ are the measured counts in energy window w along ray $\ell(s,u)$. We employ TV constraints on the material maps to perform sparsity regularization in the material map gradient. We also constrain the magnitude of the spectrum scaling vector α. The complete optimization problem that we use for performing the image reconstruction is

$$f^\star, \alpha^\star = \arg\min_{f,\alpha} D_{\text{TPL}}\left((I(f,\alpha), c\right) \tag{5}$$

$$\text{subject to } \|\alpha\|_2 \le \delta; \tag{6}$$

$$\text{and } \|\nabla f_m\|_1 \le \gamma_m \text{ for } m = 1, \ldots, M,$$

where the constraint parameter δ bounds the spectrum scaling parameters α and γ_m is the TV constraint parameter for the material map m. The parameter M is the total number of material maps.

We favor use of TV constraints in formulation of this problem over TV penalties because changing the TV constraint parameter for one basis material map does not alter the TV of other material maps. Use of a penalization formulation may yield more complicated parameter dependences as changing the TV penalty parameter for one material map results in affecting the TV for all material maps.

The optimization problem of interest in Eq. (5) is nonconvex due to the nonconvexity of $D_{\text{TPL}}\left((I(f,\alpha),c\right)$ as a function of f and α. This nonconvexity results from the fact that the second derivative of the counts model in Eq. (3) with respect to components of f and α can be negative. Because the constraints are convex, this problem does fit within the MOCCA framework as applied by us previously to image reconstruction in spectral CT [4].

The simultaneous determination of the spectrum scaling vector α and material maps f_m depends on the choice of $M+1$ constraint parameters γ_m and δ. We aim to select these parameters in such a way that we accurately estimate the basis material coefficients in a quantitative sense. We hypothesize that the best values of γ_m and δ can be found through validation. For validation we randomly select 10% of the data – the testing data– to leave out during the reconstruction. The image reconstruction is performed on the remaining 90% of the data – the training data. Reconstruction is performed with the training data varying the parameters γ_m and δ and the data fidelity D_{TPL} is evaluated on the testing data and we select the constraint parameters by

$$\gamma_m, \delta = \arg\min_{\gamma_m,\delta} D_{\text{TPL}}\left(I^{(\text{testing})}(f^\star,\alpha^\star), c^{(\text{testing})}\right).$$

Performing the optimization over γ_m, δ can be too time-consuming for a basic grid search because evaluating each point in the search involves solving Eq. (5). For the work here we employ the simplex-based COBYLA algorithm, which is standard solver that does not require computation of numerical derivatives [6].

III. Results

Experimental spectral CT data were performed on a bench-top X-ray system with a photon-counting Cadmium-Zinc-Telluride (CZT) detector (NEXIS, Kromek) comprised of 192 detector pixels. Transmitted photon counts were acquired in three energy windows with a nominal setting of [25-50], [50-60], [70-100] keV. The actual spectral response for each energy-window and detector pixel was estimated from transmission measurements through 25 known combinations of Poly(methyl methacrylate) (PMMA) and Aluminum. For the spectral CT data set, 200 views were acquired of a 6.35cm-diameter PMMA cylinder that included empty (Air), Teflon, and low-density polyethylene (LDPE) inserts. The image reconstruction was performed as described above using two basis materials, Aluminum

and PMMA. Validation was used to select the constraint parameter values $\gamma_{\text{Al}}, \gamma_{\text{PMMA}}$, and δ_v. After obtaining these validated constraint parameters the reconstruction is performed with the full data set.

Shown in Fig. 1 are the reconstructed material maps from the three-window spectral CT data. The theoretical coefficients are shown in the top row of Fig. 1 for reference. The material maps obtained with the validated constraints values $\gamma_{\text{Al}}, \gamma_{\text{PMMA}}$, and δ_v show minimal ring artifacts, but there is error in the reconstructed material map coefficients. Most notable are the gray values corresponding the the PMMA rod and background cylinder; this material should appear only in the PMMA image. Overall the shifts in gray level from the theoretical values are likely due to missing physics in the imaging model. In an attempt to reduce the high spatial frequency artifacts, we show images for the material maps with tighter TV constraints: $\gamma_{\text{Al}}/2, \gamma_{\text{PMMA}}/2$, and δ_v. The high frequency artifacts are clearly reduced, but there is also an impact on the reconstructed gray levels. In particular the background PMMA cylinder appears noticeably darker (more negative) in the Aluminum map than the images obtained by the validation constraints. To see the impact of the use of the spectral scaling factors, images are shown for reconstruction without these factors while still employing the TV constraints with parameters γ_{Al}, and γ_{PMMA}. The TV constraints still have a regularizing effect in this case, but ring artifacts are visible.

In order to obtain a sense of the spectrum response calibration and the estimated spectrum scaling, we show results in Fig. 2 for a single view in the lowest energy window. In the top plot, where the raw photon counts are normalized to the incident average photon count, it is seen that there is substantial variation at the level of the integrated spectral response across the detector pixels. There is an equally large variation in the normalized spectra (not shown). The normalized count values are also shown after incorporating the calibrated spectral response for each detector pixel. It is seen that the rapid variations from pixel to pixel are substantially reduced. Finally, the spectrum scaling factors are shown that are estimated simultaneously with the basis material maps. The factors indicate corrections on the level of a couple percent.

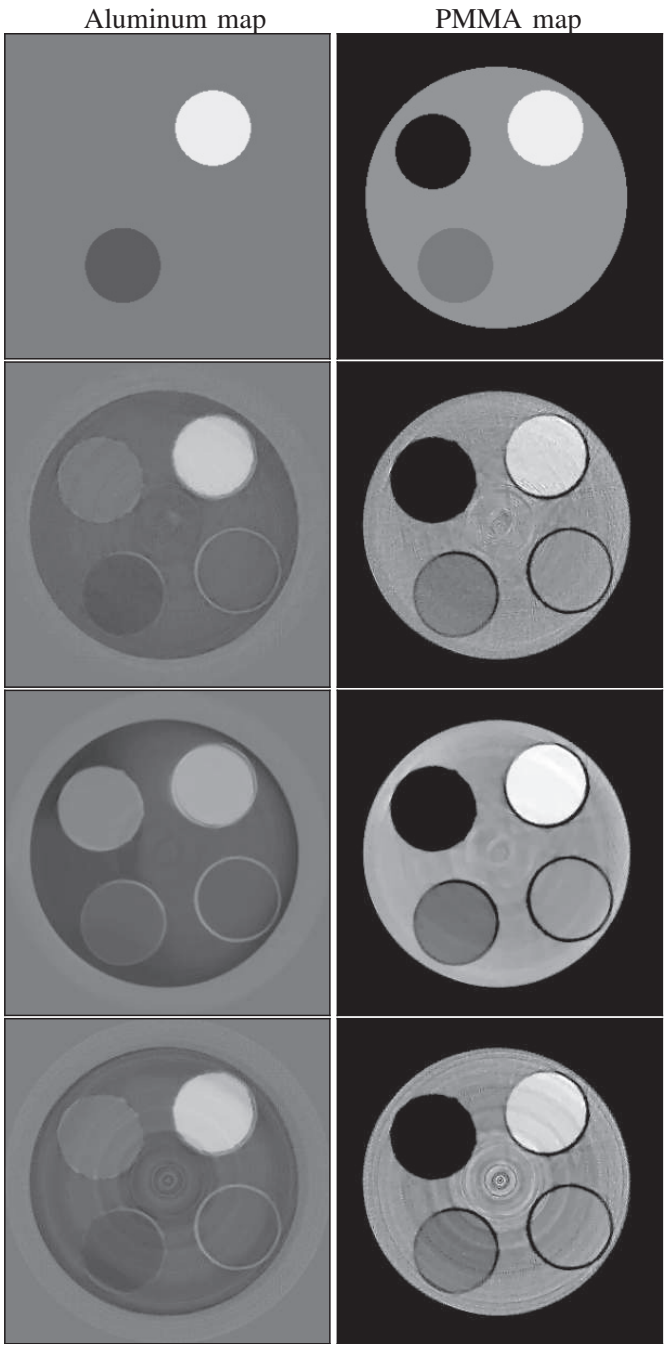

Fig. 1. Reconstructed material maps for the Aluminum (Left) and PMMA (Right) basis materials. The Aluminum map is shown in a gray scale window [-0.1,0.2] cm^{-1}, and the PMMA map is show in a gray scale window [0.5,1.5] cm^{-1}. The rod inserts are: Air (top left), Teflon (top right), PMMA (bottom right), and LDPE (bottom left). The background cylinder is PMMA. The top row indicates the coefficient values for the phantom. The second row shows the reconstructed material maps for the constraint values $\gamma_{\text{Al}}, \gamma_{\text{PMMA}}$, and δ_v obtained by validation. The third row shows the reconstructed material maps for tighter TV constraints: $\gamma_{\text{Al}}/2, \gamma_{\text{PMMA}}/2$, and δ_v. The fourth row shows the reconstructed material maps without allowing for spectrum scaling: $\gamma_{\text{Al}}, \gamma_{\text{PMMA}}$, and $\delta = 0$.

IV. Summary

We have applied the MOCCA algorithm to spectral CT image reconstruction with data acquired with a photon-counting detector using three energy windows. The spectral CT data model is calibrated by use of transmission measurements of a phantom of known composition and dimensions. The MOCCA reconstruction includes simultaneous determination of the basis material maps and spectrum scaling factors. Including the latter allows for reduction of ring artifacts in the images. Also of interest

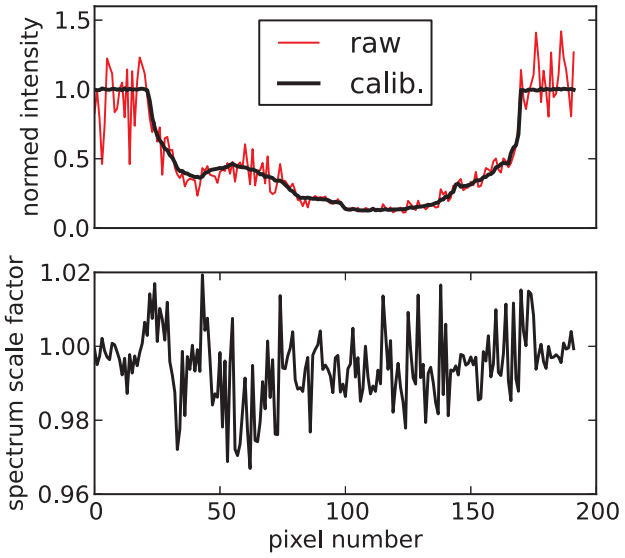

Fig. 2. Top graph shows the raw and calibrated X-ray photon counts in the lowest energy window for the first projection view; the photon counts are normalized to the incident counts. The bottom graph shows the estimated scaling factors obtained from the MOCCA reconstruction, plotted is $\exp(-\alpha_{w=1,u})$.

is the ability to perform quantitative measurements, which could potentially be useful for tissue identification in the tomographic images. We employ validation to obtain the constraint parameters, and we observe errors in the basis material gray levels on the order of 0.05 cm^{-1}.

The error seen in the experimental results can originate from physics outside of the model used for the image reconstruction. For example we have not included X-ray scatter nor a number of detector-physics issues [7] such as pulse pile-up and charge-sharing (although it is possible that some accounting of the detector physics is implicitly performed by estimating an effective spectral response). There is also the possibility of error within the spectral CT model used. That the phantom is decomposable into two basis materials is only approximately true. Also, the calibrated spectra can have error or the spectral response of the detector pixels can drift with time. The computation of spectrum scaling factors may only partially compensate for these errors, since they do not change the shape of the spectral responses.

At the meeting, in addition to showing image reconstruction from experimental spectral CT data, we will show simulation results that investigate error reduction within the spectral CT model. Namely, we will show results with more than two basis materials and higher order correction to experimentally determined spectral response. Furthermore, we will show simulation results testing the use of validation for obtaining constraint parameters that yield images with minimal bias.

V. Acknowledgment

This work was supported in part by NIH Grant Nos. R21-EB015094, R01-CA158446, R01-EB018102, and R01-CA182264. The contents of this article are solely the responsibility of the authors and do not necessarily represent the official views of the National Institutes of Health.

References

[1] S. Feuerlein, E. Roessl, R. Proksa, G. Martens, O. Klass, M. Jeltsch, V. Rasche, H.-J. Brambs, M. H. K. Hoffmann, and J.-P. Schlomka, "Multienergy photon-counting K-edge imaging: Potential for improved luminal depiction in vascular imaging 1," *Radiology*, vol. 249, no. 3, pp. 1010–1016, 2008.

[2] J. P. Schlomka, E. Roessl, R. Dorscheid, S. Dill, G. Martens, T. Istel, C. Bäumer, C. Herrmann, R. Steadman, G G. Zeitler, A. Livne, and R. Proksa, "Experimental feasibility of multi-energy photon-counting K-edge imaging in pre-clinical computed tomography," *Phys. Med. Biol.*, vol. 53, no. 15, pp. 4031–4048, 2008.

[3] R. F. Barber and E. Y. Sidky, "MOCCA: mirrored convex/concave optimization for nonconvex composite functions," 2015, http://arxiv.org/abs/1510.08842.

[4] R. F. Barber, E. Y. Sidky, T. Gilat-Schmidt, and X. Pan, "An algorithm for constrained one-step inversion of spectral CT data," 2015, http://arxiv.org/abs/1511.03384.

[5] E. Y. Sidky, L. Yu, X. Pan, Y. Zou, and M. Vannier, "A robust method of x-ray source spectrum estimation from transmission measurements: Demonstrated on computer simulated, scatter-free transmission data," *J. Applied Phys.*, vol. 97, no. 12, pp. 124701, 2005.

[6] M. J. D. Powell, "A view of algorithms for optimization without derivatives," 2007, Cambridge University Technical Report DAMTP: http://www.damtp.cam.ac.uk/user/na/NA_papers/NA2007_03.pdf.

[7] K. Taguchi and J. S. Iwanczyk, "Vision 20/20: Single photon counting x-ray detectors in medical imaging," *Med. Phys.*, vol. 40, pp. 100901, 2013.

Penalized Likelihood Decomposition for Dual Layer Spectral CT

Bernhard Brendel[1], Frank Bergner[1], Kevin Brown[2], Thomas Koehler[1]

***Abstract*—Dual layer CT systems are spectral CT systems, which acquire for each scan spatially and temporally synchronous spectral projection data. This has the advantage that spectral evaluations can be done retrospectively for every scan (even if the scan was initially not intended to deliver spectral results), and that material decomposition can be done directly in projection domain. The material decomposition in projection domain avoids inherently beam hardening artifacts, which is not the case for decomposition approaches in image domain [1]. Since material decomposition is an ill-posed nonlinear problem that amplifies noise of the native projection data and may generate bias, noise reduction in the projection domain is helpful to reduce noise streaks as well as bias in the reconstructed material images. An algorithm that combines material decomposition and noise reduction is introduced in this abstract. The algorithm, which is called Penalized Likelihood Decomposition (PL-Decomp), is derived in detail, and its performance and properties are illustrated.**

I. Introduction

CONVENTIONAL clinical CT has a number of drawbacks and limitations (e.g., beam hardening artifacts), which are due to the fact that the acquired projection data represents the attenuation properties of the object to be imaged for X-ray radiation of only one polychromatic spectrum. These drawbacks can be overcome if the acquired projections represent attenuation properties for at least two different X-ray spectra. This allows furthermore to derive additional attenuation properties of the object, including the derivation of quantitative attenuation values for different X-ray energies as well as discrimination and quantification of materials with different attenuation properties within the object.

Thus, techniques to acquire CT projection data representing different X-ray spectra have been developed in the last decades, embraced by the term "spectral CT". In recent years, CT systems using two different polychromatic spectra have been implemented, so called "dual energy" CT systems. The choice of two different spectra makes sense, since the attenuation of X-rays in the human body is mainly based on two physical processes, namely the photo-electric effect and Compton scattering. Examples for dual energy CT systems are "dual source" systems [2], "kVp-switching" systems [3], and "dual layer" systems. In the latter case, X-ray detectors are utilized that can differentiate different X-ray spectra on the detection side of the system [4], [5]. The usage of such energy resolving detectors has the advantage, that two projections under the same projection angle are acquired simultaneously representing spectrally different attenuation spectra of the object. Thus, for dual layer acquisitions the above mentioned decomposition into different materials (e.g., water, calcium, iodine, etc.) can be done directly on the projection data, since spatially and temporally matching acquisitions for both X-ray spectra are available.

For this, the attenuation line integral values derived from the two simultaneously acquired detector measurements of the two layers are transformed to material line integral values of two materials by a "material decomposition" [6], [7].

Basically, the energy dependent total x-ray attenuation $\mu(\vec{x}, E)$ in a volume is attributed to attenuation due to the photo-electric effect and due to Compton scattering:

$$\mu(\vec{x}, E) = a_p(\vec{x})\mu_p(E) + a_s(\vec{x})\mu_s(E)\,, \tag{1}$$

where the coefficients $a_p(\vec{x})$ and $a_s(\vec{x})$ describe the spatial distribution of the contribution of the photo-electric effect and Compton scatter to the total linear attenuation, and the attenuation spectra $\mu_p(E)$ and $\mu_s(E)$ represent the energy dependent attenuation of x-ray radiation for photo-electric effect and Compton scatter. The two images quantifying $a_p(\vec{x})$ and $a_s(\vec{x})$ are called the photo-electric effect image (or shorter the photo image) and the scatter image, respectively.

For any line L parametrized by a source position $\vec{s}$ and a normalized direction vector $\vec{n}$ pointing to a detector pixel, the expected measurement of the detector layer $k \in \{1, 2\}$ is

$$I_k = \int S_k(E) \exp\left(-m_p\mu_p(E) - m_s\mu_s(E)\right) \mathrm{d}E \tag{2}$$

with

$$m_p = \int_L a_p(\vec{s} + l\vec{n})\,\mathrm{d}l \qquad m_s = \int_L a_s(\vec{s} + l\vec{n})\,\mathrm{d}l \tag{3}$$

being the energy-independent line integrals of the photo image and the scatter image, respectively. In Eq. (2), the "effective tube spectra" $S_k(E)$ denotes the product of spectral x-ray photon fluence and the detector absorption efficiency of the two layers indexed by k.

The processing step of estimating the material line integrals $\hat{m}_p$ and $\hat{m}_s$ from noisy measurements I_1 and I_2 is called "material decomposition". Since two unknowns are estimated from two measurements, the decomposition represents a problem with a unique exact solution for a reasonable choice of materials. Different algorithms are thinkable to find these solutions. Here, a lookup-table based approach is used, called "conventional decomposition" in the following.

Since the energy dependencies $\mu_p(E)$ and $\mu_s(E)$ are similar in the x-ray energy range used for medical CT, and the

[1] Philips GmbH Innovative Technologies, Research Laboratories, Hamburg, Germany
[2] Philips Healthcare, Cleveland, OH

effective spectra $S_1(E)$ and $S_2(E)$ for the two detector layers overlap, the decomposition step is an ill-posed problem. Due to that, the estimated values m_p and m_s for the true line integrals $\hat{m}_p$ and $\hat{m}_s$ suffer from amplified and anti-correlated noise. Furthermore, since the material decomposition is a nonlinear function, the material line integrals are affected by a bias: While the noise affecting the measured intensities has a zero mean value, the noise affecting the decomposed line integrals has a non-zero mean value due to the non-linearity of the decomposition. This bias can lead to deviations of quantitative values in reconstructed material images. In the following, an algorithm is described that decomposes the measured line integrals to material line integrals, and at the same time reduces the noise and bias in the material line integrals.

II. Methods

The decomposition algorithm introduced here is a penalized likelihood method (called PL-Decomp in the following) based on a cost function comprising a data term and regularization terms. The decomposition is performed by minimizing the cost function. In the following spectral forward model, data term, regularization terms, and cost function, as well as a suited minimization algorithm are briefly described.

A. Cost Function

1) Spectral Forward Model: In the following, the spectral forward model as given in equation (2) is used:

$$I_{ki} = \int S_{ki}(E) \exp\left(-m_{pi}\mu_p(E) - m_{si}\mu_s(E)\right) \mathrm{d}E \quad (4)$$

where i indexes the measurements.

2) Data Term: In the data term the negative log-likelihood is utilized. For the noise model it is assumed that the noise in the measurements of different detector pixels/layers is not correlated [8]. Furthermore, a Gaussian noise distribution is assumed, leading to the following weighted least square data term for the negative log-likelihood:

$$D = \frac{1}{2} \sum_{i,k} \frac{N_{ki0}^2}{\sigma_{ki}^2} \left(\exp(-\hat{l}_{ki}) - \exp(-l_{ki}\left(m_{pi}, m_{si}\right))\right)^2 \quad (5)$$

$\hat{l}_{ki}$ are the measured line integral values of the two detector layers, and σ_{ki}^2 are the variances of the corresponding measured intensities. N_{ki0} represents the effective number of photons interacting with layer k for measurement i without object. Thus, $N_{ik0}\exp(-\hat{l}_{ki})$ converts the line integrals to intensities. $l_{ki}\left(m_{pi}, m_{si}\right)$ are the line integral values that can be derived from the intensities calculated with the forward model in equation (4):

$$l_{ki}\left(m_{pi}, m_{si}\right) = -\ln\left(\frac{I_{ki}}{\int_E S_{ki}(E)\,\mathrm{d}E}\right) \quad (6)$$

3) Regularization Terms: Two regularization terms are used here. One term penalizes differences between neighboring pixels:

$$R_G = \sum_i \left[\left(\sum_{l \in \mathcal{N}_i} w_{pil} \Psi\left(m_{pi} - m_{pl}\right) \right)^2 + \left(\sum_{l \in \mathcal{N}_i} w_{sil} \Psi\left(m_{si} - m_{sl}\right) \right)^2 \right]^{\frac{1}{2}} \quad (7)$$

$\mathcal{N}_i$ is a neighborhood of pixels around the pixel with the index i, w_{pil} and w_{sil} are weighting factors that define the influence of each neighbor, and Ψ is the Huber potential function [9], which is essentially a quadratically disturbed absolute value function, parameterized by a parameter δ.

The second term has the same form, but utilizes instead of the difference a 1D Laplace operator [-1 2 -1] for two symmetric neighbors l_1 and l_2 around the central pixel i:

$$R_L = \sum_i \left[\left(\sum_{l_1, l_2 \in \mathcal{N}_i} w_{pil} \Psi\left(2 \cdot m_{pi} - m_{pl_1} - m_{pl_2}\right) \right)^2 + \left(\sum_{l_1, l_2 \in \mathcal{N}_i} w_{sil} \Psi\left(2 \cdot m_{si} - m_{sl_1} - m_{sl_2}\right) \right)^2 \right]^{\frac{1}{2}} \quad (8)$$

The regularization term given in equation (7) is called Gradient-Huber regularization, and the regularization term given in equation (8) is called Laplace-Huber regularization in the following. The reason for using the additional Laplace-Huber regularization term is briefly discussed in the results section.

4) Cost Function: The cost function is the sum of the data term given in equation (5) and the regularization terms given in equations (7) and (8), with two additional weighting factors to adjust the influence of the two regularization terms:

$$L = D + \beta \cdot \left((1 - \alpha) \cdot R_G + \alpha \cdot R_L\right) \quad (9)$$

While β adjusts the overall regularization strength, α balances the influence of Gradient-Huber regularization and Laplace-Huber regularization.

B. Optimization

An optimization method based on the ICD (iterative coordinate descent) optimization [10] is utilized here. The ICD algorithm is an iterative method, where in each iteration the cost function is optimized for each unknown separately. The main disadvantage of ICD is that it is hard to parallelize, since a huge number of optimization problems have to be solved sequentially, if the cost function is not separable with respect to the unknowns. The main advantage of ICD is that it converges in many cases much faster than methods with simultaneous update. In the case considered here, the original ICD iteration is modified with respect to two aspects: Firstly, the original optimization problem is not split into 1D optimization problems, but into 2D optimization problems,

namely for each pair of unknowns m_{pi} and m_{si} of one measurement i. Thus, optimization is a bit more difficult. However, since m_{pi} and m_{si} are correlated in the data term, the 2D optimization is expected to converge much faster than two separate 1D optimizations for m_{pi} and m_{si}. Secondly, the optimization is parallelized nonetheless, since the cost function is separable with respect to the unknowns of each projection, if regularization is only done with neighbors within one projection. Furthermore, the cost function is separable for certain sets of detector pixels within one projection. These sets are constructed such that the neighborhoods of pixels used in the regularization do not overlap for any two pixels in the set. Since the optimization can be done for all separable unknowns simultaneously, it is done here with a considerable degree of parallelization.

The 2D search for each pair of unknowns m_{pi} and m_{si} is solved with a line method in multidimensions [11]. The most straight forward option for this is a gradient descent optimization, but this yields for the given cost function often slow convergence. Another method that is known to be faster in many cases is the Newton method [11], that utilizes apart from the gradient the Hessian to determine the search direction. However, the Newton method works only for convex regions of the function to optimize, and thus may fail to deliver a real descending direction for the non-convex cost function given here. Thus, a hybrid approach is applied: If the direction determined with the Newton method is a descending direction, it is used as search direction, otherwise the negative gradient is used. If the following criterion is fulfilled, the direction determined with the Newton method is a descending direction:

$$\nabla(L)^T H^{-1}(L) \nabla(L) > 0 \tag{10}$$

where $\nabla(L)$ is the gradient of the cost function L, and $H^{-1}(L)$ is the inverse Hessian. Once a search direction is determined, a golden section line search is performed (see [11] for details).

ICD is known to converge fast on high spatial frequencies and slow on low spatial frequencies. This is due to the fact that optimization is done for each detector pixel separately. In order to speed up the convergence for low spatial frequencies, another modification of the ICD method is implemented: After each full iteration of ICD the difference between the current output and the output of the last ICD iteration is used as search direction for a simultaneous optimization of all pixels in all views. The optimization is done with a 1D line search in multidimensions (see [11] for details).

C. Simulated Data

For evaluation purposes, a polychromatic simulation of a cylindrical water phantom with a number of calcium and iodine inhomogeneities (see Fig. 1) is done for the two detector layers. Subsequently, independent Poisson noise is realized to the signal for each detector layer. Details of phantom and simulations are described in [12]. Here the simulation for the "real detector" scenario detailed in [12] is applied.

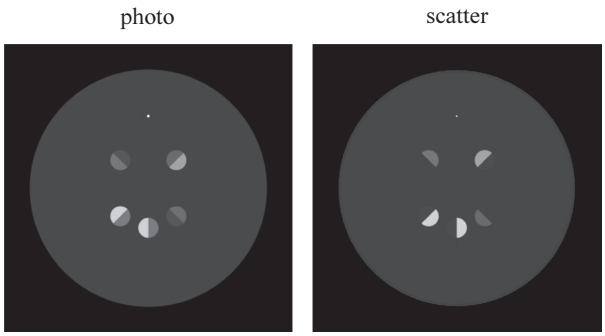

Fig. 1. Phantom for simulations: Photo image (left) and scatter image (right).

III. Results

A. Impact of Regularization Terms on PL-Decomp

In Fig. 2 the impact of the PL-Decomp processing on a photo projection is visualized. To the left the output of a conventional decomposition is shown. The result of PL-Decomp utilizing only the Gradient-Huber regularization is presented in the middle. The projection has a significantly lower noise level, but some noise-spikes are left, which would lead to streaks in reconstructed images. These noise peaks could be removed by increasing the strength of the Gradient-Huber regularization, but this would potentially lead to a loss of details in the reconstructed images. If additionally to the Gradient-Huber regularization the Laplace-Huber regularization is applied, the spikes are removed efficiently, as illustrated in Fig. 2 on the right.

B. Performance of PL-Decomp

In Fig. 3 reconstructed images for material line integrals generated with a conventional decomposition and with PL-Decomp are shown, together with illustrations of the biases in these images. The bias images are generated by taking the difference between the reconstructed images and the known phantom ground truth. For better visualization of the bias, these difference images are smoothed with a moving average filter within the slices. Clearly, the noise level in the images decomposed with PL-Decomp is significantly lower. Remaining noise can be removed in image domain, e.g. with methods described in [12]. Furthermore, the bias that occurs for the images reconstructed from a conventional decomposition is significantly reduced when PL-Decomp is applied.

IV. Conclusion

One of the central steps of spectral CT data processing is the material decomposition. For a dual layer CT system this can be done in projection domain, converting measured intensities to material line integrals. This decomposition is an ill-posed nonlinear problem, causing noise amplification and bias in the reconstructed material images. To address these two problems, a combined decomposition and denoising method called penalized likelihood decomposition (PL-Decomp) has been introduced. It has been shown that PL-Decomp efficiently reduces noise and bias compared to a conventional decomposition.

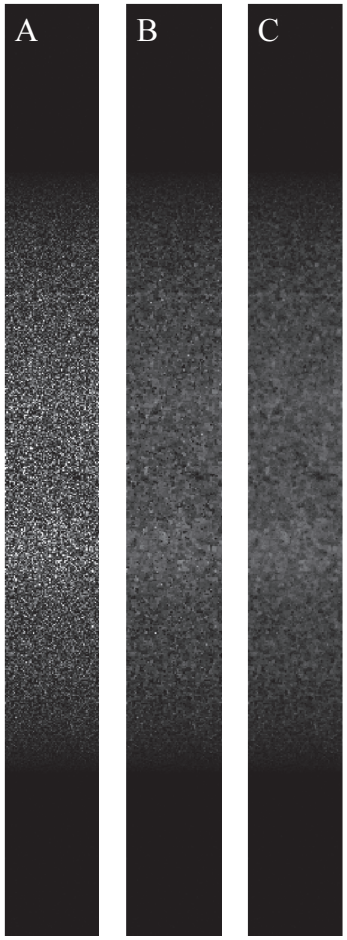

Fig. 2. Photo projection for different decomposition methods. A) Conventional decomposition B) PL-Decomp with Gradient-Huber regularization C) PL-Decomp with Gradient-Huber and Laplace-Huber regularization.

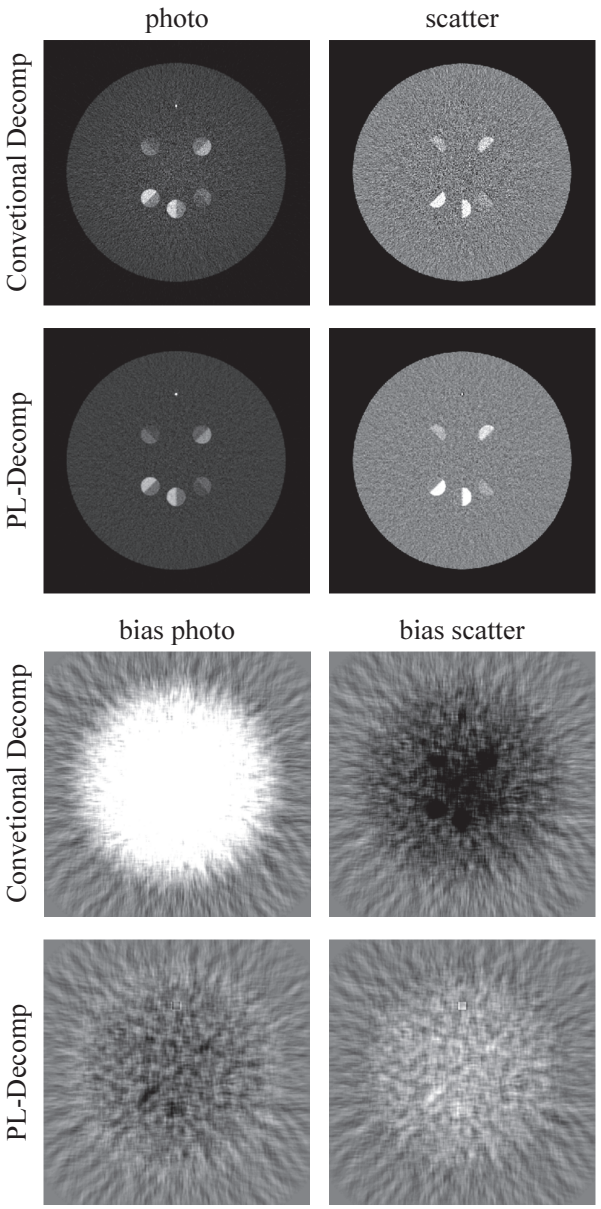

Fig. 3. Reconstruction results for different decomposition methods for simulated data. Upper four images: Photo images (left) and scatter images (right) for conventional decomposition (top) and PL-Decomp (bottom). Lower for images: Bias (smoothed difference of reconstructed images to ground truth) for photo images (left) and scatter images (right) for conventional decomposition (top) and PL-Decomp (bottom). Window width: 500 HU for photo and scatter images, 20 HU for bias images.

REFERENCES

[1] C. Maaß, M. Baer, and M. Kachelrieß, "Image-based dual energy CT using optimized precorrection functions: A practical new approach of material decomposition in image domain," *Med. Phys.*, vol. 36, no. 8, pp. 3818–3829, Aug 2009.

[2] M. Petersilka, H. Bruder, B. Krauss, K. Stierstorfer, and T. G. Flohr, "Technical principles of dual source CT," *European J. of Radiology*, vol. 68, pp. 362–8, Dec 2008.

[3] X. Wu, D. A. Langan, D. Xu, T. M. Benson, J. D. Pack, A. M. Schmitz, E. J. Tkaczyk, J. Leverentz, and P. Licato, "Monochromatic ct image representation via fast switching dual kvp," 2009, vol. 7258, p. 725845, SPIE.

[4] G. T. Barnes, R. A. Sones, M. M. Tesic, D. R. Morgan, and J. N. Sanders, "Detector for dual-energy digital radiography," vol. 156, no. 2, pp. 537–540, 1985.

[5] R. Carmi, G. Naveh, and A. Altman, "Material separation with dual-layer CT," in *Proceedings of the IEEE Medical Imaging Conference*, 2005, vol. 4, pp. 1876–1878.

[6] R. E. Alvarez and A. Macovski, "Energy-selective reconstructions in x-ray computerized tomography," *Phys. Med. Biol.*, vol. 21, no. 5, pp. 733–744, 1976.

[7] E. Roessl and R. Proksa, "K-edge imaging in x-ray computed tomography using multi-bin photon counting detectors," *Phys. Med. Biol.*, vol. 52, no. 15, pp. 4679–4696, Aug 2007.

[8] R. A. Sones and G. T. Barnes, "Noise correlations in images acquired simultaneously with a dual-energy sandwich detector," *Med. Phys.*, vol. 16, no. 6, pp. 858–861, 1989.

[9] J. A. Fessler, "Statistical image reconstruction methods for transmission tomography," in *Handbook of Medical Imaging, Vol. 2*, M. Sonka and J. M. Fitzpatrick, Eds., chapter 1, pp. 1–70. SPIE Press, Bellingham, WA, 2000.

[10] J.-B. Thibault, K. D. Sauer, C. A. Bouman, and J. Hsieh, "A three-dimensional statistical approach to improved image quality for multislice helical CT," *Med. Phys.*, vol. 34, no. 11, pp. 4526–4544, Nov 2007.

[11] W. Press, S. Teukolsky, W. Vetterling, and B. Flannery, *Numerical Recipes in C, Second edition*, Cambridge University Press, Cambridge, UK, 1992.

[12] K. Brown, S. Zabic, and G. Shechter, "Impact of spectral separation in dual-energy CT with anti-correlated statistical reconstruction," in *Proceedings of the 3D'2015 Conference*, NewPort, RI, 2015, pp. 493–496.

Angular oversampling and built-in anti-aliasing filtration in CT with ultra-fast ASIC on photon counting detector

Martin Sjölin and Mats Danielsson
Department of Physics, Section for Medical Imaging, Royal Institute of Technology
AlbaNova University Center, SE-106 91 Stockholm, Sweden,
Email: martin.sjolin@mi.physics.kth.se

***Abstract*—In this work, we suggest a method for obtaining angular oversampling and anti-aliasing filtration of the angular signal in continuous rotation CT by utilizing the overcapacity of the integrated circuit (ASIC) on a photon-counting detector. The ASIC on the detector can sample the photon counters at a higher rate than the read-out can handle. Previously, the sampling rate in the ASIC has been adapted to the read-out rate, but now we propose that the higher sampling rate in the ASIC is maintained and that a digital low-pass FIR filter is used for decimation to match the read-out capability. The method increases the modulation transfer function (MTF) of the angular (temporal) signal with up to 40% and reduces the risk of angular aliasing artifacts in the reconstructed image.**

***Index Terms*—computed tomography, oversampling, anti-aliasing, photon-counting**

I. Introduction

Insufficient angular sampling in CT leads to impaired spatial resolution and risk of aliasing artifacts and many techniques have been developed in order to handle data with sparse angular sampling[1], [2], [3].

In continuous rotation CT, the angular sampling rate is determined by the frame time and the rotation speed of the gantry via $\Delta\theta = \omega\Delta t$, where Δt is the frame time and ω is the angular velocity of the gantry. In order to increase the number of angular samples, it is necessary to either decrease the frame time, which leads to an increased amount of data per second, or to decrease the rotation speed, which leads to more motion artifacts and longer scan times. The angular sampling rate in today's CT systems is generally limited by the rate at which data can be read out from the detector. Meanwhile, procedures that require high rotation speed, such as cardiac and perfusion imaging, are becoming more common[4]. If the angular sampling rate is insufficient and aliasing occurs, the only way to remove the aliasing is by suppressing the signal at the aliased frequencies, which compromises the image quality.

Photon-counting detectors are an interesting alternative to today's energy integrating detectors used in CT. The potential benefits include: spectral imaging, better trade-off between noise and dose and improved spatial resolution[5], [6].

We are currently developing a spectral photon-counting silicon-strip detector for x-ray computed tomography[5], [7]. The detector (shown in Fig. 1) consists of a silicon wafer with read-out electrodes on a 2D grid. Each individual electrode is connected to a subsequent channel in an ultra-fast ASIC (application specific integrated circuit), mounted on the detector module [8]. Each ASIC channel comprises an analog channel, pulse-height comparators and a digital channel. When an x-ray interacts in the range of an electrode, the deposited energy is converted into an electric pulse. The pulse is processed by the analog part of the corresponding ASIC channel and the pulse-height comparators are used to determine the energy of the pulse. Finally, in the digital part, a counter corresponding to the highest triggered comparator is incremented. The digital part of the ASIC counts the number of detected pulses during the frame time and the counters are read out in parallel once per frame.

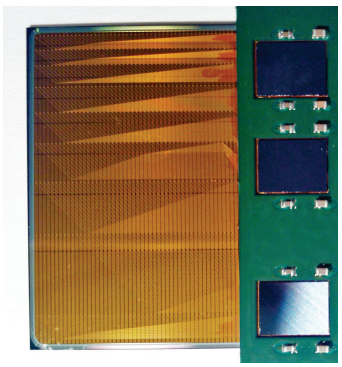

(a)

Figure 1: A photon counting silicon detector with three ASICs visible on the right side. Each ASIC has 150 channels connected to individual electrodes on the silicon wafer.

The AISC on the detector can sample the photon counters at a higher rate than the read-out can handle. Previously, the sample rate in the ASIC has been adapted to the capacity of the read-out. In this paper, we propose that the high sample rate in the ASIC is maintained and that the signal is preprocessed by a digital FIR filter in the ASIC before being downsampled and read out to the storage module. The method both reduces the risk of aliasing and increases the modulation transfer function (MTF) of the angular (temporal) sampling process. This paper contains a theoretical evaluation of the proposed method.

II. Methods

A digital FIR (finite impulse response) filter for decimation [9], [10] is implemented in the ASIC on the photon counting detector. The choice of a FIR filter, and not a IIR (infinite impulse response) filter for example, is based in that the filter has to be *linear phase*, such that the the relative phase of the input is conserved. The goal for the FIR filter is to suppress the frequency content above Nyquist frequency of the data read-out such that aliasing is mitigated [11]. The filtration is implemented by convolution, and the signal is downsampled by returning every second sample of the filtered signal.

A. The filter process

A first-in, first-out (FIFO) memory on the ASIC can be used to store the $2M+1$ latest samples. Lets call the elements in the memory $\hat{f}$, where the first element is the oldest. The convolution kernel can be stored in a static memory on the ASIC as the vector $\hat{g}$, which has finite support in the set $\{-M, -M+1, ..., M-1, M\}$. After the acquisition and storage of the sample $i+M$, the filtered value of the sample at i can be computed by the sum:

$$\hat{f}_{\text{filtered}}[i] = \hat{f}^T\hat{g} = \sum_{j=-M}^{M} \hat{f}[j]\hat{g}[i-j] \tag{1}$$

B. Filter design

Now assume that the data has to be N times decimated before being read out. The cut-off frequency, f_c, of the low-pass filter should then lie at $1/2N$ of the original sampling frequency in order to lie at the Nyquist frequency of the decimated signal.

The ASIC filter is required to have a high stop-band attenuation in order to remove the frequency content which otherwise would cause aliasing in the decimated signal. The attenuation in the pass-band is not as important since it can be reversed after the read-out by, for example, dividing the Fourier transform of the signal from the ASIC by the transfer function of the ASIC filter ($G(\xi)$):

$$\tilde{f}(t) = \mathscr{F}^{-1}\left(\frac{\mathscr{F}(\hat{f}_{\text{filtered}}(t))(\xi)}{G(\xi)}\right), \tag{2}$$

This is possible without blowing up the noise since both the noise and the signal are subject to the same filtration, i.e. the signal-to-noise ratio (SNR) per frequency is conserved in the filtration process. This allows using a non-ideal filter as long as the requirement on the stop-band attenuation is fulfilled, which is cheaper in terms of required memory and computation than a near-ideal filter. A suitable approach to filter design is that proposed by McClellan and Parks [12] in which the optimal FIR filter is found under a set of constraints on the desired pass-band and stop-band ripple.

In this preliminary study, we implement a windowed sinc kernel, which approaches an ideal low-pass filter for wide windows, in order to demonstrate the effect filtering without also implementing a post processing step such as that described by Eq. 2. The windowed sinc kernel is given by

$$g(i) = w(i)\,\text{sinc}(2\pi f_c i) = w(i)\frac{\sin(2\pi f_c i)}{2\pi f_c i},$$

where f_c is the cut-off frequency. Here we will use a Blackman window, given by

$$w(i) = 0.42 - 0.5\cos(\pi i/M) + 0.08\cos(2\pi i/M) \text{ for } i = 0, 1, 2, .., 2M$$

The length of the kernel ($2M+1$) determines the quality in terms of pass-band ripples and how fast the filter drops after the cut-off frequency. The implementation of a $2M+1$ long linear phase filter for decimation by a factor of 2 requires $M/2+1$ multiplications (every second filter coefficient is zero and the symmetry of linear phase filters can be used by first adding the values which are to be multiplied by the same factor) and M additions. Also, this requires storing $2M+1$ samples in a FIFO memory and storing the $M/2+1$ non-zero unique elements of the filter kernel in a static memory. With filter optimization, the filter length can be reduced and the number of operations minimized.

C. Simulation

The modulation transfer functions (MTF) of the sampling process with and without applying a FIR filter were simulated. In the simulation, an analytical input signal consisting of a windowed sinusoid was used and the sampling was emulated by integrating the analytical signal over the duration of a frame. An example of a simulated signal is shown in Fig. 2a. The output signal without preprocessing was created by simply summing every consecutive pair of samples, emulating a twice as long frame time. The simulated FIR filter was a windowed sinc kernel designed for decimation by a factor of 2. The length of the kernel was $2M+1$ with $M = 100$, which makes it a near-ideal low-pass filter. To simulate the MTF, the frequency of the input sinusoid was incremented and the modulation transfer was estimated by integrating the Fourier transform of the output signal over a small interval near the input frequency.

To prove the concept in a CT imaging case, a mathematical phantom, consisting of an off-center 2D Gaussian, is imaged. The angular signal with and without AISC filter were created in the same way as when simulating the MTF (described above). The image was simulated without noise in order to emphasize the artifacts. The FWHM of the Gaussian was gradually decreased until aliasing artifacts were visible in the reconstruction without ASIC filter. The images were reconstructed by filtered back-projection using the MATLAB (2012, The Mathworks Inc., Natick, MA) iradon function with a Ram-Lak filter and linear interpolation.

III. Results

The resulting MTFs, with and without applying the FIR filter, are shown in Fig. 2b. The FIR filter increases the MTF for all frequencies in the pass band, the largest increase being

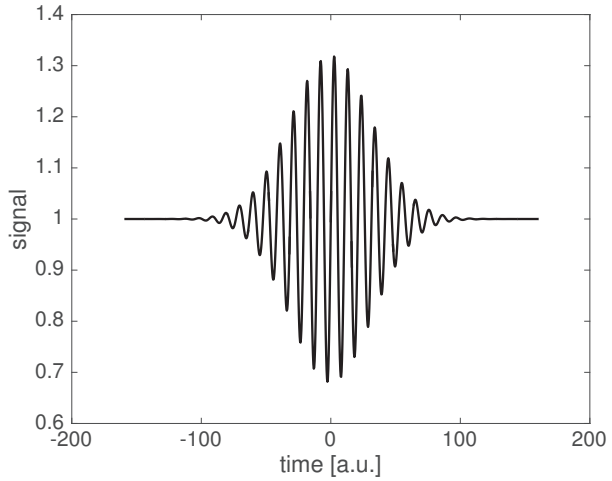

(a)

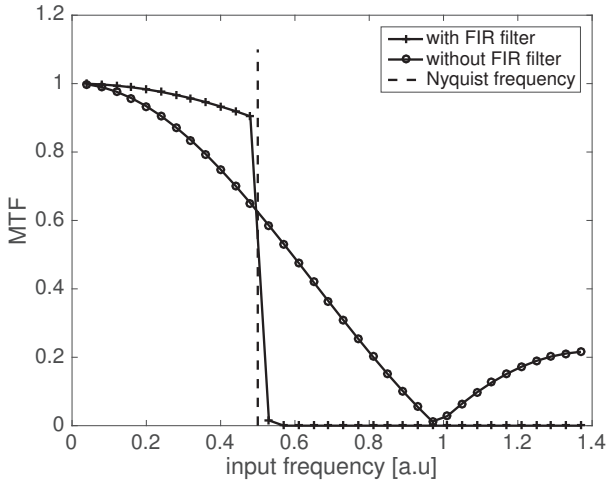

(b)

Figure 2: a) The simulated signal input (a windowed sinusoid) used to simulated the MTF. b) The simulated MTF of the sampling process with and without ASIC preprocessing. The frequency axis is scaled to the output data rate, i.e. the Nyquist frequency lies at 0.5.

for frequencies close the Nyquist frequency, for which the MTF is increased by approximately 40%. Also, the frequencies above the Nyquist frequency are effectively suppressed, mitigating aliasing in the downsampled signal. Without the FIR filter, any frequency content in the input signal above the Nyquist frequency will "alias" and appear at a different frequency, obscuring the signal.

A part of the reconstructed image of the 2D Gaussian without using the ASIC filter in which aliasing artifacts were present is shown in Fig. 3a. The 2D Fourier transform of the sinogram used to reconstruct Fig. 3a is shown in Fig. 3b. The Fourier transform shows frequency folding in the angular direction. The same part of the reconstructed image, but now with the ASIC filter, is shown in Fig. 4a. The Fourier transform of the sinogram (Fig. 4b) now shows that the frequency content above the cut-off frequency of the filter has been efficiently suppressed and there are no signs of frequency folding.

IV. Discussion

A. Noise and SNR

Due to the Poisson nature of the photon counting process, short frame times lead to higher relative standard deviation in each sample. Therefore it is not obvious that the SNR per frequency is increased by short frame times even though the MTF is increased. However, the low-pass filter removes the noise power above the cut-off frequency, which otherwise would have folded into the signal during the downsampling. This implies that the noise amplitude per frequency in the pass-band for the preprocessed signal is, for downsampling by a factor of two, equal to that of a signal with twice as long frame time. The SNR per frequency in the pass-band of the preprocessed signal is therefore higher than that of a signal with twice as long frame time, since they both have the same noise amplitude, but the preprocessed signal has a higher MTF.

B. Further investigations

Further investigations can include: design of the convolution kernel; technical implementation on the ASIC; more thorough investigations of the imaging performance; or post-processing steps.

References

[1] D. L. Donoho, "Compressed sensing," *Information Theory, IEEE Transactions on*, vol. 52, no. 4, pp. 1289–1306, 2006.

[2] T. P. Szczykutowicz and G.-H. Chen, "Dual energy ct using slow kvp switching acquisition and prior image constrained compressed sensing," *Physics in medicine and biology*, vol. 55, no. 21, p. 6411, 2010.

[3] W. Zbijewski and F. J. Beekman, "Characterization and suppression of edge and aliasing artefacts in iterative x-ray ct reconstruction," *Physics in medicine and biology*, vol. 49, no. 1, p. 145, 2004.

[4] J.-J. Sonke, L. Zijp, P. Remeijer, and M. van Herk, "Respiratory correlated cone beam ct," *Medical physics*, vol. 32, no. 4, pp. 1176–1186, 2005.

[5] H. Bornefalk and M. Danielsson, "Photon-counting spectral computed tomography using silicon strip detectors: a feasibility study," *Physics in medicine and biology*, vol. 55, no. 7, p. 1999, 2010.

[6] R. Carmi, G. Naveh, and A. Altman, "Material separation with dual-layer ct," in *Nuclear Science Symposium Conference Record, 2005 IEEE*, vol. 4. IEEE, 2005, pp. 3–pp.

[7] M. Persson, B. Huber, S. Karlsson, X. Liu, H. Chen, C. Xu, M. Yveborg, H. Bornefalk, and M. Danielsson, "Energy-resolved ct imaging with a photon-counting silicon-strip detector," *Physics in medicine and biology*, vol. 59, no. 22, p. 6709, 2014.

[8] C. Xu, M. Persson, H. Chen, S. Karlsson, M. Danielsson, C. Svensson, and H. Bornefalk, "Evaluation of a second-generation ultra-fast energy-resolved asic for photon-counting spectral ct," *Nuclear Science, IEEE Transactions on*, vol. 60, no. 1, pp. 437–445, 2013.

[9] R. E. Crochiere and L. R. Rabiner, "Optimum fir digital filter implementations for decimation, interpolation, and narrow-band filtering," *Acoustics, Speech and Signal Processing, IEEE Transactions on*, vol. 23, no. 5, pp. 444–456, 1975.

[10] E. Hogenauer, "An economical class of digital filters for decimation and interpolation," *Acoustics, Speech and Signal Processing, IEEE Transactions on*, vol. 29, no. 2, pp. 155–162, 1981.

[11] C. E. Shannon, "Communication in the presence of noise," *Proceedings of the IRE*, vol. 37, no. 1, pp. 10–21, 1949.

[12] J. H. McClellan, T. W. Parks, and L. R. Rabiner, "A computer program for designing optimum fir linear phase digital filters," *Audio and Electroacoustics, IEEE Transactions on*, vol. 21, no. 6, pp. 506–526, 1973.

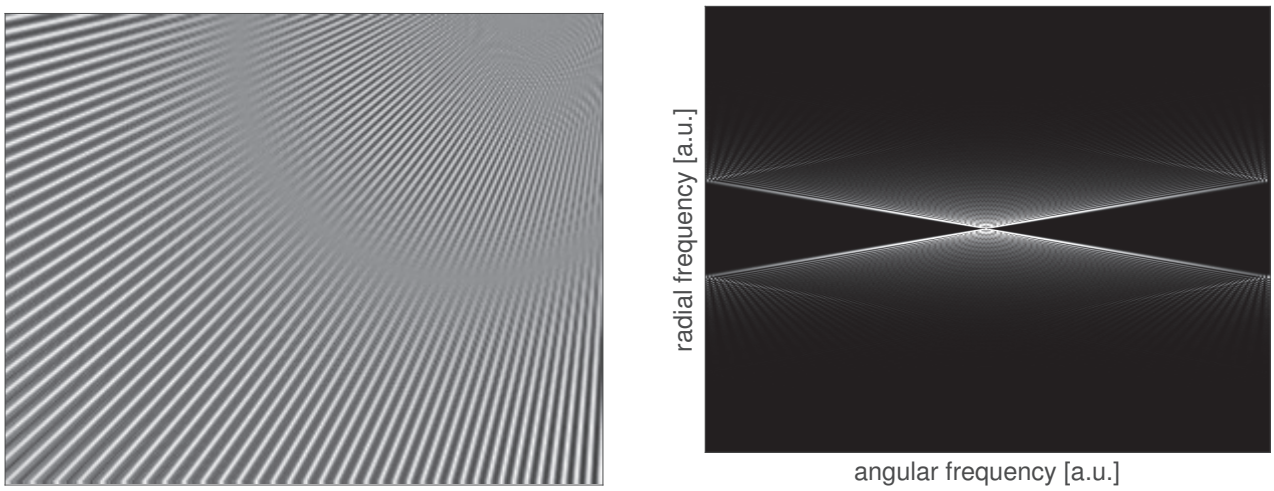

(a) (b)

Figure 3: a) A zoom-in on a part of a reconstructed image of a 2D Gaussian without the ASIC filter containing sever aliasing artifacts. b) The 2D Fourier transform of the sinogram used to reconstruct the image in a) shows frequency folding in the angular direction.

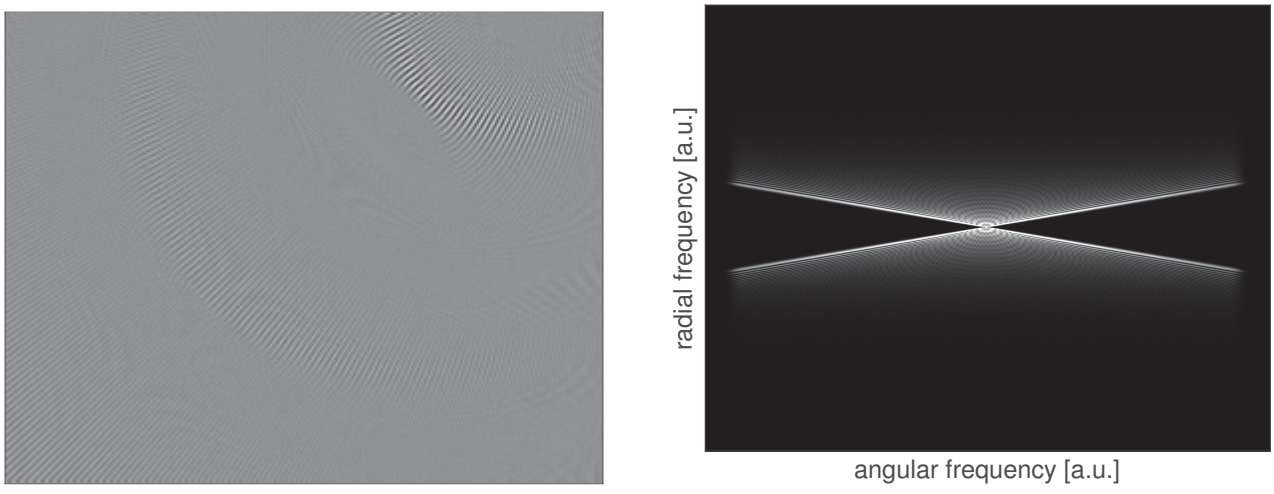

(a) (b)

Figure 4: a) The same part of the image as in Fig. 3a (with the same window), but now with an ASIC filter performing 2 times decimation before readout. b) The 2D Fourier transform of the sinogram used to reconstruct the image in a). The frequency content has been effectively suppressed above the Nyquist frequency and there are no signs of frequency folding.

Non-linear regularized decomposition of spectral x-ray projection images

Nicolas Ducros*, Simon Rit, Bruno Sixou and Françoise Peyrin

***Abstract*—Spectral computed tomography (CT) exploits measurements from x-rays with different energies to obtain the 3D description of the patient in a material basis. It requires to solve two subproblems, namely the material decomposition and the tomographic reconstruction problems, either sequentially or jointly. In this work, we address the material decomposition problem, which an ill-posed non-linear problem. Our main contribution is to introduce a material-dependent spatial regularization scheme. The problem is solved iteratively using the Gauss-Newton's method. The framework is validated on numerical experiments of a thorax phantom made of soft tissue, bone and gadolinium scanned with a 90 kV source and a 3-bin photon counting detector.**

I. Introduction

Spectral photon counting detectors [1] can be used to image high Z contrast agents by exploiting the K-edge discontinuity of their energy-dependent linear attenuation coefficient (LAC) [2], [3]. These new scanners open new clinical applications for x-ray imaging as a functional imaging tool, e.g., for the characterization of the atherosclerotic plaque [4].

Spectral CT image reconstruction can be split in two subproblems: (1) decomposition of the energy-resolved data and (2) tomographic reconstruction. The two subproblems can be solved sequentially (projection-based approach) or jointly (image-based approach). Both approaches face challenging difficulties. First, spectral CT is a non-linear problem. Although it can be linearized [5], taking into account the non-linearities of the forward model is more adequate [2]. Second, the sensitivity of spectral imaging is limited [6] and several groups have investigated statistical penalties and spatial priors in the image domain in order to improve the signal-to-noise ratio of the reconstruction [7]–[11].

In this work, we address the basis material decomposition (BMD) problem of the projection-based approach. The main contribution of this work is to introduce a material-specific spatial regularization scheme. Like in [2], our forward model is non-linear and takes into account the spectral response of the detector but we also regularize each material projection image. While the spatial regularization might not be optimal, working on a smaller problem, i.e., one projection at a time, has several advantages: the inverse problem is easier to optimize using explicit computation of sparse matrices, and each problem can be solved in parallel. We present preliminary simulations on synthetic data and the projection of a real thorax phantom.

All authors are with the University of Lyon, INSA-Lyon, Université Lyon 1, CNRS, Inserm, CREATIS UMR 5220 U1206, F-69621, Villeurbanne, France.

F. Peyrin is also with the Synchrotron Radiation Facility, 6 rue Jules Horowitz, F-38043 Grenoble Cedex, France

* nicolas.ducros@creatis.insa-lyon.fr

II. Theory

We consider a 3-dimensional (3-D) object in Ω that is imaged with a 2-D detector with a sensing surface $\mathcal{S}$.

A. Physical models

1) X-ray / matter interactions: Let $n(E, \mathbf{u})$ denotes the number of photons of energy E that reaches the detector at the pixel position $\mathbf{u} \in \mathcal{S}$. Neglecting scattering within the object, n follows the Beer-Lambert law. Mathematically,

$$n(E, \mathbf{u}) = n^0(E) \exp\left[-\int_{\mathcal{L}(\mathbf{u})} \mu(E, \mathbf{x}) \, \mathrm{d}\mathbf{x}\right] \tag{1}$$

where $n^0(E)$ is the source spectrum, $\mathcal{L}(\mathbf{u})$ is the acquisition line that depends on the source emission geometry (parallel, cone-beam, etc), and $\mu(E, \mathbf{x})$ is the local LAC of the object at energy E and point $\mathbf{x} \in \Omega$.

2) Detection model: The signal recorded by a photon counting detector may be modelled by

$$s(\mathcal{E}, \mathbf{u}) = \int_{\mathbb{R}} d(\mathcal{E}, E) \, n(E, \mathbf{u}) \, \mathrm{d}E \tag{2}$$

where $d(\mathcal{E}, E)$ accounts for the detector response function and is the probability density function for an x-ray photon hitting the detector with energy E to be detected at energy $\mathcal{E}$. The photons detected within the ith energy bin $[\mathcal{E}_i, \mathcal{E}_{i+1}]$ are accumulated electronically thanks to a counting circuit. The number of photons detected within the ith energy bin is given by

$$s_i(\mathbf{u}) = \int_{\mathbb{R}} d_i(E) \, n(E, \mathbf{u}) \, \mathrm{d}E \tag{3}$$

where

$$d_i(E) = \int_{\mathcal{E}_i}^{\mathcal{E}_{i+1}} d(\mathcal{E}, E) \, \mathrm{d}\mathcal{E} \tag{4}$$

is the response function of the ith bin of the detector. Note that the detection model assumes that the value measured at a given pixel is not correlated to the value measured at another pixel, i.e. charge sharing can be neglected or is corrected for. It is common to have charge sharing corrected for at the ASIC level.

B. Object decomposition

It is assumed that the LAC is the superposition of M basis functions that are separable in energy and space. We have

$$\mu(E, \mathbf{x}) = \sum_{m=1}^{M} \rho_m(\mathbf{x}) \tau_m(E), \quad \forall \mathbf{x} \in \Omega \tag{5}$$

where the τ_m are some well-chosen basis functions and the ρ_m are the corresponding weights in the decomposition. Following the work of [5], two approaches have emerged for the choice of the basis functions τ_m: i) physics-based where τ_m models the physical effects, e.g. photoelectric, Compton scattering, k-edge, and, ii) material-based where τ_m is the mass attenuation of the constituents of the objects (in $\text{cm}^2.g^{-1}$). Note that in the latter method, ρ_m is the density of material m (in g.cm^{-3}).

C. Forward problem

Substituting (1) and (5) into (3), the measured signal may be written

$$s_i(\mathbf{u}) = \int_{\mathbb{R}} d_i(E) n^0(E, \mathbf{u}) \exp\left[- \sum_{m=1}^{M} a_m(\mathbf{u}) \tau_m(E) \right] \mathrm{d}E \tag{6}$$

where

$$a_m(\mathbf{u}) = \int_{\mathcal{L}(\mathbf{u})} \rho_m(\mathbf{x}) \, \mathrm{d}\mathbf{x} \tag{7}$$

is the projection of the weights ρ_m along the line integral $\mathcal{L}(\mathbf{u})$. When a material-based decomposition is performed, a_m is the mass of the mth material projected onto the detector (in g.cm^{-2}). One main difficulty of the problem we address is the non linearity of the forward mapping expressed in (6).

D. Inverse problem

The detector is assumed to be an array of P pixels centred at $\mathbf{u}_p$, $p \in \{1, \dots, P\}$, and have I energy bins. Let $\mathbf{s} \in \mathbb{R}^{PI}$ be the measurement vector defined by

$$\mathbf{s} = \begin{bmatrix} s_{1,1} & \dots & s_{I,1} & \dots & \dots & s_{1,P} & \dots & s_{I,P} \end{bmatrix}^\top \tag{8}$$

and $\mathbf{a} \in \mathbb{R}^{PM}$ be the (unknown) vector containing the mass of each material in each pixel, which is defined by

$$\mathbf{a} = \begin{bmatrix} a_{1,1} \dots & a_{M,1} & \dots & \dots & a_{M,P} & \dots & a_{M,P} \end{bmatrix}^\top. \tag{9}$$

Our problem is to recover the mass vector $\mathbf{a}$ from the measured data $\mathbf{s}$. This is an ill-posed problem that requires prior knowledge about the solution to stabilize the inversion in the presence of noise.

III. Material and methods

A. Cost function

In this manuscript, we propose to recover the mass vector minimizing the cost function

$$\mathcal{C}(\mathbf{a}) = \|\mathbf{s} - \boldsymbol{\mathcal{F}}(\mathbf{a})\|_2^2 + \alpha \mathcal{R}(\mathbf{a}) \tag{10}$$

where $\boldsymbol{\mathcal{F}}(\mathbf{a})$ is the non-linear forward mapping defined by (6), $\mathcal{R}$ the regularization functional, and α is a global regularization parameter.

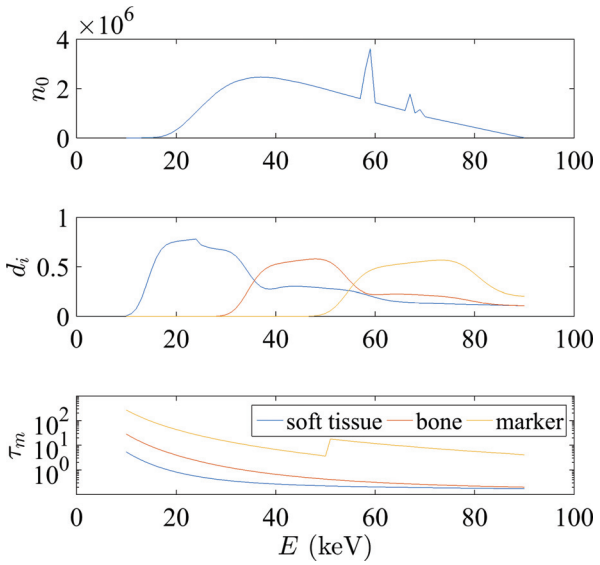

Fig. 1. Spectrum of the x-ray source (top), detector response per bin (middle) and LACs of the three constituents used in the numerical experiments.

B. Regularization functional

We adopt the following regularizing functional, which allows the prior of the different materials to be tuned independently:

$$\mathcal{R}(\mathbf{a}) = \sum_m \alpha_m \mathcal{R}_m(\mathbf{a}_m), \tag{11}$$

where $\mathcal{R}_m$ is the regularizing functional of the mth material weighted by the regularization parameter α_m and $\mathbf{a}_m = [a_{m,1} \dots a_{m,P}]^\top$ is a vector in $\mathbb{R}^P$ that accounts for the mass of the mth material.

C. Optimisation algorithm

We propose to minimize (10) using Gauss-Newton's method, which is a classical iterative tool for non-linear minimization. It starts with an initial guess $\mathbf{a}^{(0)}$ and builds new estimates

$$\mathbf{a}^{(k+1)} = \mathbf{a}^{(k)} + \Delta\mathbf{a}^{(k)} \tag{12}$$

with the so-called Gauss-Newton step $\Delta\mathbf{a}^{(k)}$

$$({\mathbf{J}^{(k)}}^\top \mathbf{J}^{(k)} + \mathbf{H}^{(k)}) \Delta\mathbf{a}^{(k)} = -\mathbf{g}^{(k)}, \tag{13}$$

where $\mathbf{J}^{(k)}$ is the Jacobian matrix of $\boldsymbol{\mathcal{F}}$ about $\mathbf{a}^{(k)}$, $\mathbf{H}^{(k)}$ is the Hessian matrix of $\alpha\mathcal{R}$ about $\mathbf{a}^{(k)}$, and $\mathbf{g}^{(k)}$ is the gradient of $\mathcal{C}$ about $\mathbf{a}^{(k)}$.

D. Numerical simulations

1) Acquisition parameters: We consider the source spectrum $n_0(E)$ that is depicted on the top row of figure 1. It was obtained with a tube voltage of 90 kV. Measurements were performed in $I = 3$ energy bins. The response function of each bin is plotted in the middle row of figure 1 and was taken from [2] (3 out of 8 bins). The measurements were corrupted by Poisson noise assuming 10^8 x-ray photons are launched onto the patient towards each each pixel of the detector. We

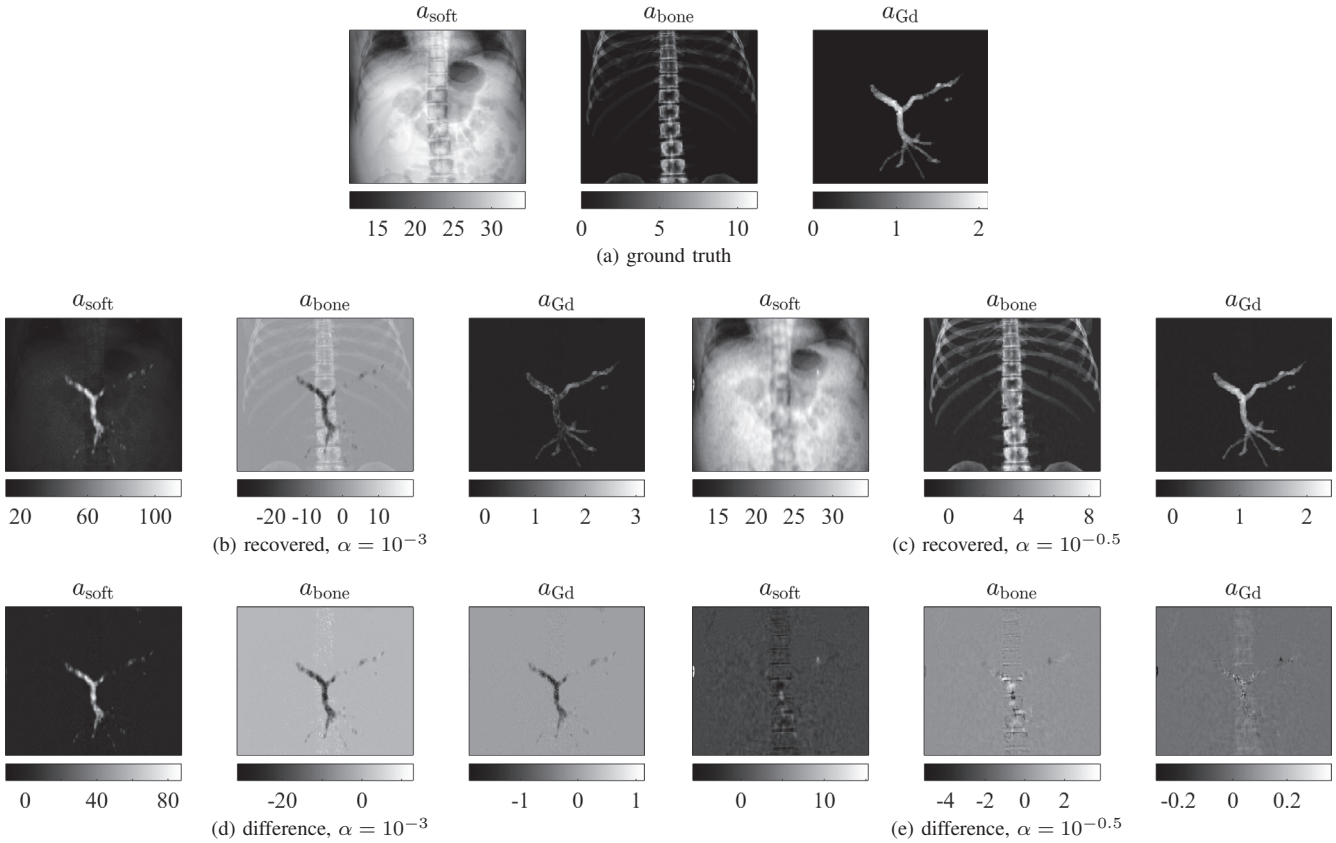

Fig. 2. Mass of the constituents of the phantom in units of g.cm^{-2}, namely soft tissue, bone, and gadolinium. a) ground truth images, b) recovered images for a small regularization parameter, c) recovered images for the best regularization parameter, d) difference between b) and a), and e) difference between c) and a).

approximated this Poisson noise to a Gaussian distribution and the square L_2 norm chosen in this work is effective as a data fidelity term.

2) Phantom: We considered the 3D thorax phantom that was segmented from a CT scan in [12]. Each voxel has been associated to either soft tissue or bone, according to the segment it belongs to. The material density in each voxel was estimated from the CT images. The portal vein was marked with gadolinium at a concentration of 1 g.cm^{-3}. The mass attenuations of soft tissue, bone, and gadolinium were taken from ICRU report 44 [13] and are depicted in figure 1 (bottom row). The projected masses for each material are finally computed according to (7), by integrating densities along parallel lines chosen perpendicular to the coronal plane. The resulting material images are displayed on the top row of figure 2.

3) Spatial regularization: For this 3-material phantom, we choose

$$\alpha\mathcal{R}(\mathbf{a}) = \alpha\left(\|\Delta\mathbf{a}_{\text{soft}}\|_2^2 + \|\nabla\mathbf{a}_{\text{bone}}\|_2^2 + \|\nabla\mathbf{a}_{\text{Gd}}\|_1\right) \quad (14)$$

where $\mathbf{a}_{\text{soft}}$, $\mathbf{a}_{\text{bone}}$, and $\mathbf{a}_{\text{Gd}}$ represents the projected masses of soft tissues, bone, and gadolinium, respectively, while ∇ and Δ are the first- and second-order differential operators, respectively. This functional promotes solutions for which i) the soft tissue and bone images are smooth, ii) the marker image is piecewise constant, and iii) the soft tissue image is smoother than the bone image. As a first approach, we set $\alpha_m = 1$ for each of the material images, keeping only the global regularization parameter as a free parameter. To compute $\mathbf{H}^{(k)}$ and $\mathbf{g}^{(k)}$, a smooth approximation of the ℓ_1-norm is considered, namely the pseudo-Huber loss function [14].

IV. Results

The cost function given by (10) was minimized iteratively by a Gauss-Newton algorithm according to (12) and (13). The algorithm is initialized with the uniform material images $\mathbf{a}_{\text{soft}}^{(0)}$ = 20 g.cm^{-2}, $\mathbf{a}_{\text{bone}}^{(0)}$ = 2 g.cm^{-2}, and $\mathbf{a}_{\text{Gd}}^{(0)}$ = 0 g.cm^{-2}. The algorithm is stopped when the cost function decrease is less than 0.1%. The minimization was performed for different regularization parameters α ranging from 10^{-2} and 10^{1}. For our 361×167 images, updating $\mathbf{a}^{(k)}$ took 2 s on a standard laptop (2.6 GHz i7 CPU and 16 GiB of RAM). Depending on the regularization parameter, from 15 to 30 iterations were necessary before convergence, which leads to a computation time of about 30 to 60 s to minimize (10).

The plot of the points $(\|\mathbf{s} - \boldsymbol{\mathcal{F}}(\mathbf{a})\|_2^2, \mathcal{R}(\mathbf{a}))$ for different values of the regularization parameter α, which is known as the L-curve, is provided in figure 3. The reconstruction error $\|\mathbf{a} - \mathbf{a}_{\text{true}}\|_2 / \|\mathbf{a}_{\text{true}}\|_2$ is displayed with respect to α in figure 4. The smallest reconstruction error was obtained for $\alpha = 10^{-0.5}$, which corresponds to the corner of the L-curve,

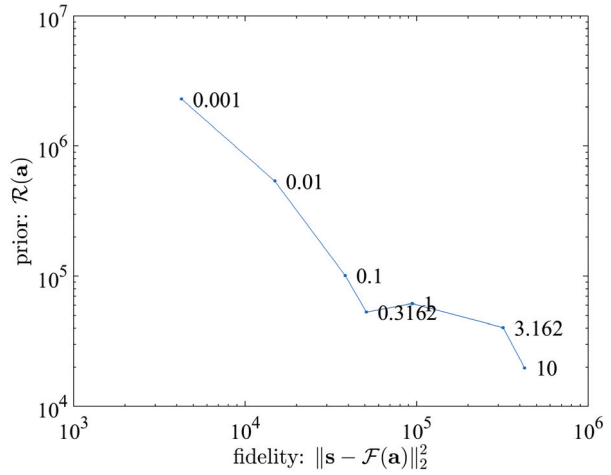

Fig. 3. L-curve for the proposed experient, i.e., $(\|\mathbf{s} - \boldsymbol{\mathcal{F}}(\mathbf{a})\|_2^2, \mathcal{R}(\mathbf{a}))$ for a regularization parameter α ranging from 10^{-2} to 10^{1}.

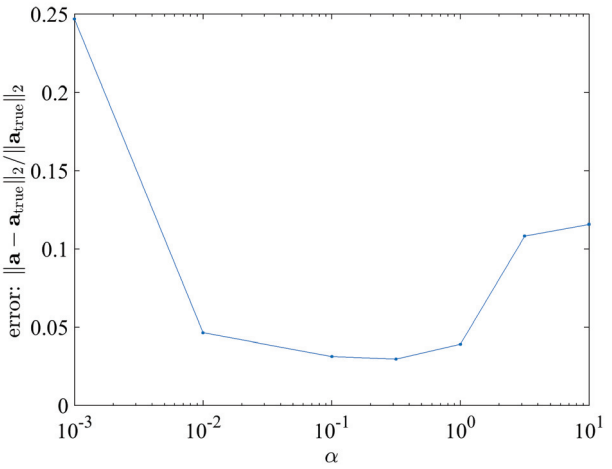

Fig. 4. Decomposition error with respect to regularization parameter.

indicating than the L-curve may be an appropriate tool for selecting the regularization parameter when the ground truth is unknown. The material images recovered by our method are given in the middle row of figure 2. Two regularization parameters were considered, one being very small (left) and the other being the best one according to the L-curve (right). When no regularisation scheme is used (see figures 2b and 2d), the different materials are poorly separated. However, the three material images are nicely recovered when an appropriate regularization scheme is considered.

V. Discussion and Conclusion

These preliminary results indicate that the decomposition of x-ray spectral projection images greatly benefits from the implementation of a regularization scheme. Similar results have been reported in the image domain but working in the projection domain is advantageous because the dimensionality is smaller and, therefore, more tractable. For example, we have been able to compute the L-curve in figure 3, which might not be tractable considering the image-based approach.

We have used a single regularization parameter in this work. Future works include the use of several regularization parameters. We will also investigate other statistical methods that better accounts for the statistical noise in the projection images and other regularizations, e.g., a non convex prior for the gadolinium favoring a small support. After a satisfying solution has been developed in the projection domain, a set of projection images can be decomposed and reconstructed using existing filtered-backprojection or iterative CT reconstruction algorithms.

Acknowledgment

This work was partly supported by the grant ANR-11-INBS-0006 and by the grant ANR-13-IS03-0002-01 (DEXTER project) of the French National Research Agency (ANR). It was also performed within the framework of the LABEX PRIMES (ANR-11-LABX-0063) of Université de Lyon, within the program ANR-11-IDEX-0007.

References

[1] K. Taguchi and J. S. Iwanczyk, "Vision 20/20: Single photon counting x-ray detectors in medical imaging," *Medical Physics*, vol. 40, no. 10, p. 100901, 2013.

[2] J. P. Schlomka, E. Roessl, R. Dorscheid, S. Dill, G. Martens, T. Istel, C. Bumer, C. Herrmann, R. Steadman, G. Zeitler, A. Livne, and R. Proksa, "Experimental feasibility of multi-energy photon-counting k-edge imaging in pre-clinical computed tomography," *Physics in Medicine and Biology*, vol. 53, no. 15, p. 4031, 2008.

[3] C. Schirra, B. Brendel, M. Anastasio, and E. Roessl, "Spectral CT: a technology primer for contrast agent development," *Contrast Media Mol Imaging*, vol. 9, no. 1, pp. 62–70, 2014.

[4] D. P. Cormode, E. Roessl, A. Thran, T. Skajaa, R. E. Gordon, J.-P. Schlomka, V. Fuster, E. A. Fisher, W. J. M. Mulder, R. Proksa, and Z. A. Fayad, "Atherosclerotic plaque composition: Analysis with multicolor ct and targeted gold nanoparticles1," *Radiology*, vol. 256, no. 3, pp. 774–782, 2010.

[5] R. E. Alvarez and A. Macovski, "Energy-selective reconstructions in x-ray computerised tomography," *Physics in Medicine and Biology*, vol. 21, no. 5, p. 733, 1976.

[6] E. Roessl, B. Brendel, K. Engel, J. P. Schlomka, A. Thran, and R. Proksa, "Sensitivity of photon-counting based k -edge imaging in x-ray computed tomography," *Medical Imaging, IEEE Transactions on*, vol. 30, no. 9, pp. 1678–1690, 2011.

[7] C. Schirra, E. Roessl, T. Koehler, B. Brendel, A. Thran, D. Pan, M. Anastasio, and R. Proksa, "Statistical reconstruction of material decomposed data in spectral ct," *Medical Imaging, IEEE Transactions on*, vol. 32, no. 7, pp. 1249–1257, 2013.

[8] Y. Long and J. Fessler, "Multi-material decomposition using statistical image reconstruction for spectral ct," pp. 1–1, 2014.

[9] A. Sawatzky, Q. Xu, C. Schirra, and M. Anastasio, "Proximal admm for multi-channel image reconstruction in spectral x-ray ct," pp. 1–1, 2014.

[10] Q. Xu, A. Sawatzky, M. A. Anastasio, and C. O. Schirra, "Sparsity-regularized image reconstruction of decomposed k-edge data in spectral ct," *Physics in Medicine and Biology*, vol. 59, no. 10, p. N65, 2014.

[11] R. Zhang, J.-B. Thibault, C. Bouman, K. Sauer, and J. Hsieh, "Model-based iterative reconstruction for dual-energy x-ray ct using a joint quadratic likelihood model," *Medical Imaging, IEEE Transactions on*, vol. 33, no. 1, pp. 117–134, Jan 2014.

[12] R. Kechichian, S. Valette, M. Desvignes, and R. Prost, "Shortest-path constraints for 3d multiobject semiautomatic segmentation via clustering and graph cut," *Image Processing, IEEE Transactions on*, vol. 22, no. 11, pp. 4224–4236, Nov 2013.

[13] ICRU, "Report 44 of the tissue substitutes in radiation dosimetry and measurement," International Commission on Radiation Units and Measurements (ICRU), Tech. Rep., 1989.

[14] P. Charbonnier, L. Blanc-Feraud, G. Aubert, and M. Barlaud, "Deterministic edge-preserving regularization in computed imaging," *IEEE Trans Image Process*, vol. 6, no. 2, pp. 298–311, 1997.

Spectrum Optimization in Split-Filter Dual-Energy CT for Iodine Quantification and Virtual-Non-Contrast Imaging

George S.K. Fung, Karl Stierstorfer, Matthew Fuld, Satomi Kawamoto,
Elliot K. Fishman, Benjamin M.W. Tsui, Katsuyuki Taguchi

Abstract **– The aim of this research is to develop a spectrum optimization method in split-filter dual-energy CT (DECT) for the iodine quantification and virtual-non-contrast (VNC) imaging through a realistic simulation study. In split-filter DECT system, low-energy (LE) and high-energy (HE) projection data are collected simultaneously by adding two different in-beam prefilters and by two detector channel or row ranges for the LE and HE beams. In the latest Siemens TwinBeam CT system, gold and tin prefilters are employed to split the cone beams into LE and HE beams for lower and upper halves of the detector rows, respectively. In this research, we have studied and optimized the LE spectrum by changing (1) the prefilter thickness, (2) the tube voltage, and (3) the prefilter material, for the applications of iodine quantification and VNC imaging. A water phantom with multiple iodine inserts and the 3D XCAT phantom with iodine enhanced lesion in liver were used in the simulation study. The analytical CT projection simulation program, DRASIM, was employed to generate the LE and HE projection data with the corresponding prefilter and tube settings. The Monte Carlo x-ray simulation program, MOCASSIM, was employed to calculate the total energy deposited in the phantom and was used as the dose index. Water beam hardening correction was applied before the image reconstructed by the filtered backprojection reconstruction algorithm. Image-based two-material decomposition method was applied to obtain the iodine and VNC images from the reconstructed DECT images. The figures-of-merit (FOMs) used for optimization are the normalized inverse of the noise-dose products in iodine and VNC images obtained using specific prefilters and tube settings. Our results show that the optimal thickness for gold prefilter is around 0.225 mm with over 80% improvement in combined FOM. Both tube voltage settings of 110kVp and 120kVp performed significantly better than other kVp settings. Among the 16 feasible candidate materials studied, tungsten, tantalum, and gold are the best LE prefilter materials, which achieve over 80% improvement at the thickness of around 0.225mm to 0.25mm. In conclusion, significant improvement of noise in material images and reduction in patient dose could be achieved by employing the optimal prefilter thickness, material and tube voltage.**

Manuscript received January 25, 2016. This work was partly supported by Siemens-JHU research grant.

G. Fung, S. Kawamoto, E. Fishman, B. Tsui, and K. Taguchi are with the Department of Radiology, Johns Hopkins University, Baltimore, MD 21287 USA (e-mail: gfung2@jhmi.edu).

K. Stierstorfer is with the Siemens Healthcare, Computed Tomography, Forchheim, Germany.

M. Fuld is with the Siemens Healthcare, Diagnostic Imaging, Siemens Medical Solutions, USA.

I. INTRODUCTION

The concept of dual-energy CT (DECT) is to acquire the spatial distribution of the energy-dependent attenuation coefficient of the patient or object-of-interest using low-energy (LE) and high-energy (HE) x-ray spectra. The major benefit of DECT technology is that it can provide additional information of the material composition. With the availability of clinical DECT systems, numerous new clinical applications have become available, such as iodine quantification and virtual non-contrast (VNC) imaging [1], kidney stones classification [2], and VNC of kidney multi-phasic scans [3]. Nowadays, several clinical CT vendors have achieved DECT acquisition using different approaches [1], including dual-source CT, kVp switching, sandwich detectors and the latest split-filter [4] methods.

In the present work, different from the previous study on HE prefilter [5], we focus on the LE prefilter in a split-filter DECT system. The idea of split-filter DECT system was first proposed in 1980 [6] with left-right split-filter, while the new Siemens TwinBeam DECT system employs upper-lower rows system design (Fig. 1). Since split-filter scanner cannot freely adjust the energy fluence independently between LE and HE beams, the thickness and the material of the prefilters and the tube voltage are means to shape the x-ray spectra. In this paper, we describe the development of a spectra optimization method in split-filter DECT for iodine quantification and VNC imaging through physics-based analytical and Monte Carlo CT simulation techniques. We aim to demonstrate significant improvement in image quality and reduction in patient dose could be achieved by using optimized LE x-ray spectra. The gains could be determined by performing highly realistic simulations of using a wide range of combinations of prefilter thickness and material, and tube voltage settings.

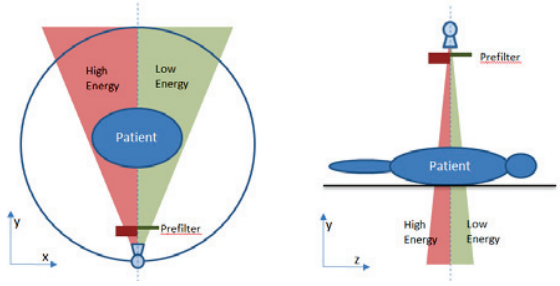

Fig. 1. Split-filter DECT designs: left-right (channel) vs upper-lower (row)

II. Methods

A. Digital Water and XCAT phantoms

Two surface-based digital phantoms were used in the simulation study. A cylindrical water phantom, based on mathematical primitive representation, with a diameter of 30cm and 6 inserts of different iodine concentrations, including 5, 10, 15, 20, 25 and 30mgI/cc, was defined. Also, the NURBS-based anthropomorphic XCAT phantom [7] (at abdominal region), representing an average-size male was used. A hyperdense hepatic lesion with the diameter of 8cm and 10mgI/cc was inserted.

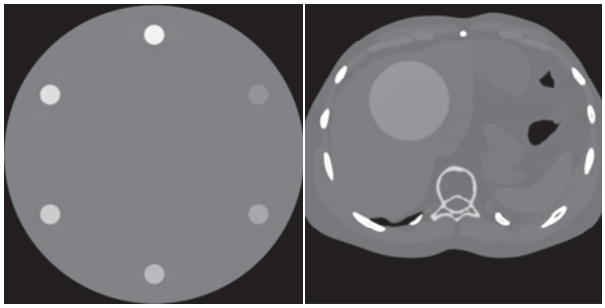

Fig. 2. Digital phantoms: water phantom with iodine inserts (5-30mgI/cc) and XCAT phantom with lesion (10mgI/cc)

B. CT Simulation and Material Decomposition

The system and data acquisition parameter settings of DRASIM (Siemens Healthcare) [8] were based on the Siemens clinical CT scanner. The cylindrical water phantom was defined by the geometric primitive representation supported by DRASIM, while the XCAT simulation was performed using the XCAT/DRASIM integration method reported in our previous work [9]. A set of sample CT simulation images of the water phantom is depicted in Fig. 3.

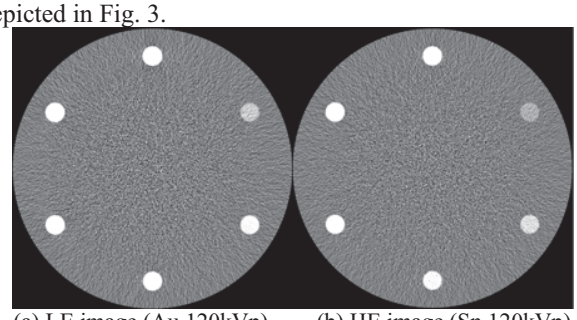

(a) LE image (Au 120kVp) (b) HE image (Sn 120kVp)

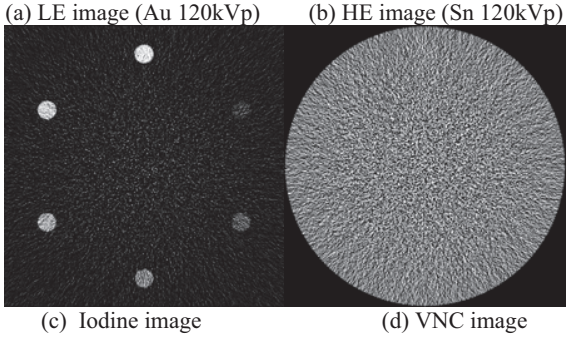

(c) Iodine image (d) VNC image

Fig. 3. Sample noisy simulated CT images of water phantom consisting of iodine inserts with gold and tin prefilter at 120kVp (C/W=0/400HU & C/W=15/30mgI/cc for iodine image)

The geometry settings, including source to isocenter distance, isocenter to detector distance, number of detector channels, number of views per rotation, fan-angle of the x-ray beam, prefilters used, and many others were specified accordingly. The x-ray spectrum settings [1], including prefilter consisting of 1mm aluminum and 0.9mm Ti, and GOS detector, were modeled in the simulation. The HE prefilter was fixed to a 0.6mm thick tin. No bowtie filter was used. Water beam hardening effect correction method was applied before reconstruction by filtered backprojection. In general, 2-material image-based material decomposition can be defined as the weighted-sum of LE and HE CT images:

$$g_{iodine}(x) = w_{i1} f_{LE}(x) + w_{i2} f_{HE}(x) \quad (1)$$

$$g_{VNC}(x) = w_{v1} f_{LE}(x) + w_{v2} f_{HE}(x) \quad (2)$$

The weighting values were determined by calibrating using noise-free DE CT images. Forty independent noise realizations were performed for each setting.

C. Spectrum Optimization

To determine the optimal LE spectrum, we performance a comprehensive simulations of wide range of settings for the following parameters: (1) the prefilter thickness (***t***) : 0mm to 0.5mm in step of 0.025mm; (2) the tube voltage (***kVp***): 100kVp to 150 kVp in step of 10 kVp; and (3) the prefilter material (***mat***): 16 feasible and stable metals (Ti, Zr, Nb, Mo, Ag, Cd, In, Sn, Ce, Sm, Gd, Ta, W, Au, Pb, and Bi). The x-ray spectra of different settings of prefilter thickness, kVp, and prefilter material are depicted in Fig 4, 5 and 6 respectively.

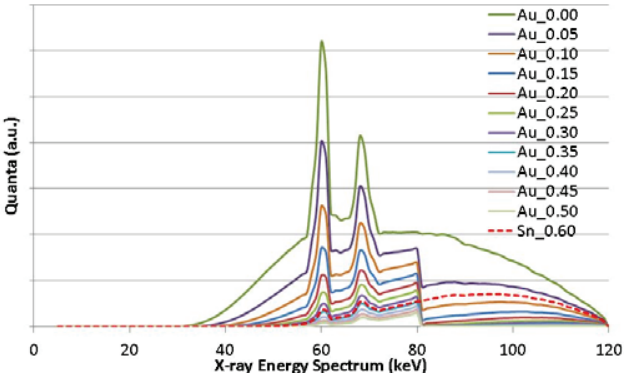

Fig. 4. X-ray spectra with different gold prefilter thicknesses.

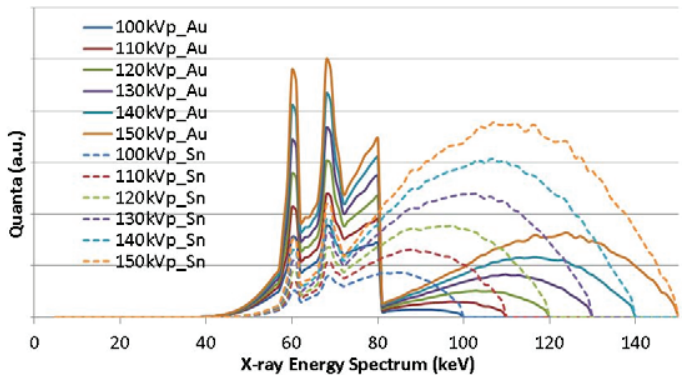

Fig. 5. X-ray spectra obtained with different tube voltage settings.

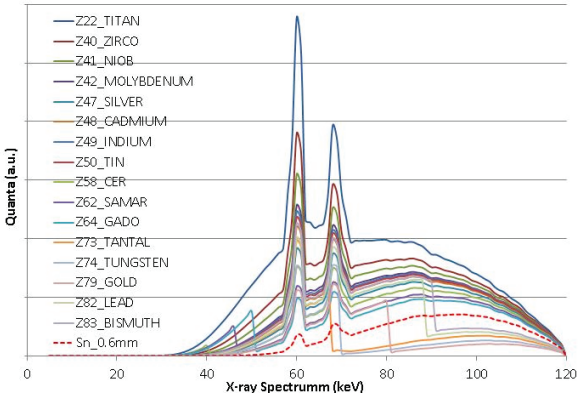

Fig. 6. X-ray spectra obtained using 16 different prefilter materials.

The goal of our study is to determine the optimal LE spectrum which minimizing noise in iodine quantification and VNC images while the patient radiation is minimized. The optimization figure-of-merit's (FOMs) were defined as:

$$FOM_{iodine}(t,kVp,mat) = \frac{noise_{iodine}(t,kVp,mat)^2 * dose(t,kVp,mat)}{noise_{iodine}(t=0,kVp)^2 * dose(t=0,kVp)}, \quad (3)$$

$$FOM_{VNC}(t,kVp,mat) = \frac{noise_{VNC}(t,kVp,mat)^2 * dose(t,kVp,mat)}{noise_{VNC}(t=0,kVp)^2 * dose(t=0,kVp)}. \quad (4)$$

Equations (3) and (4) are the normalized inverse of square-noise-dose products of the iodine and VNC images obtained using the specific setting. The Monte Carlo x-ray simulation program, MOCASSIM (Siemens Healthcare) [10], was employed to calculate the total energy deposited in the phantom and was used as the dose index.

III. Results and Discussions

As shown in Fig. 7, the normalized FOM_iodine, FOM_VNC, and FOM_combined increase from 1.0 to around 1.6, 2.3 and 1.8 at Au thickness of 0.20mm, 0.25mm and 0.225mm, respectively. As the thickness of the gold prefilter increases, the radiation dose to the patient decreases and the LE CT image suffers from higher noise level. When the gold prefilter is well below 0.2mm, the LE images are much less noisier than that of the HE images from using a 0.6mm Sn prefilter. However, when the gold prefilter reaches the 0.2mm to 0.25mm range, the noise levels of the LE and HE images are nearly the same. When the gold prefilter is over 0.25mm thick, the noise level of the LE CT images becomes higher than that of the HE images despite the benefit of dose reduction.

Results in Fig. 8 demonstrate that the performance rankings of different tube voltage settings from best to worst are: 110kVp, 120kVp, 100kVp, 130kVp, 140kVp, and 150kVp, for all three FOMs. Both tube voltage settings of 110kVp and 120kVp performed significantly better than other kVp settings. As shown in Fig. 5, the magnitude of the x-ray spectrum obtained from using a gold prefilter is greatly suppressed beyond the k-edge of Au (80.7keV). However, if the tube voltage is set too low (e.g., at 100kVp), a large portion of the HE spectrum is overlapping with the LE spectrum below k-edge. If the tube voltage is set too high (e.g., at 150kVp), a large portion of the LE spectrum is overlapping with the HE spectrum above k-edge. The voltage settings of 110kVp and 120kVp reach a good balance of avoiding large spectral overlap below and above the k-edge of Au.

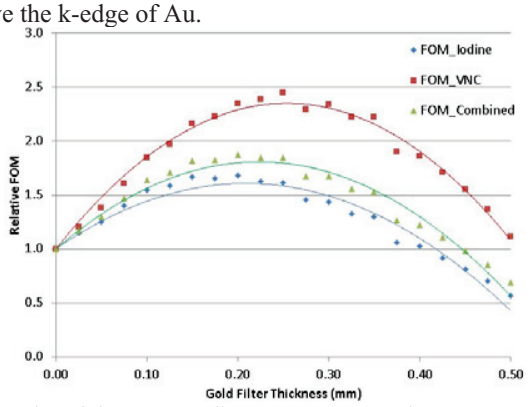

Fig. 7. Plot of the FOM_Iodine, FOM_VNC and FOM_Combined for Au filter thickness up to 0.5mm.

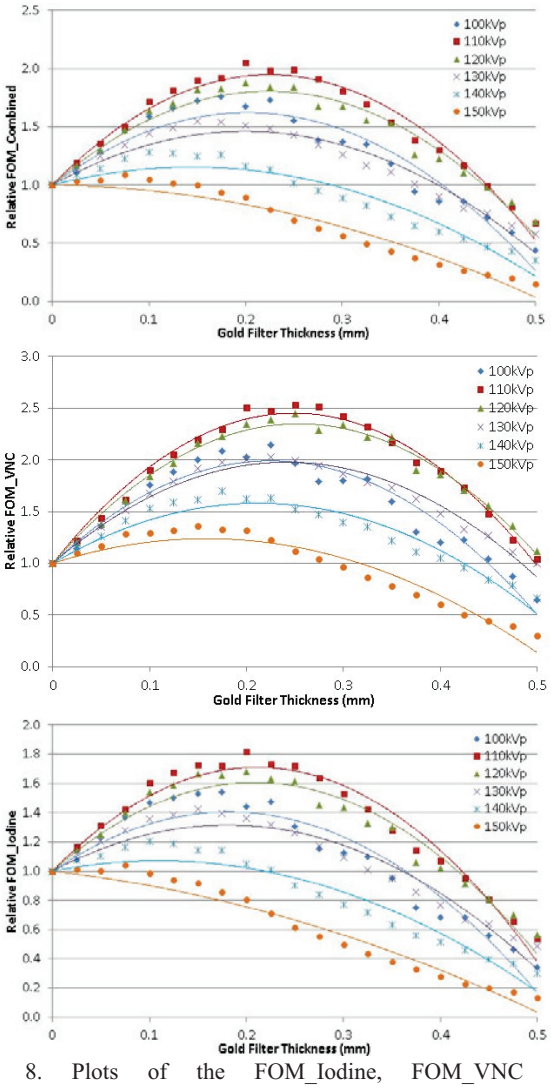

Fig. 8. Plots of the FOM_Iodine, FOM_VNC and FOM_Combined for tube voltage ranging from 100kVp to 150 kVp and Au filter thickness up to 0.5mm.

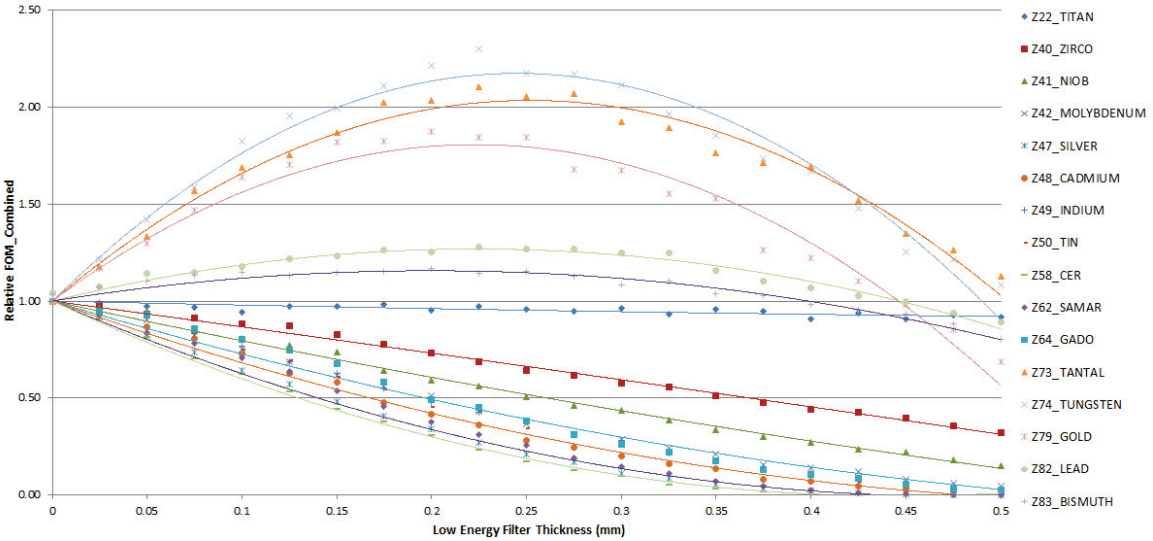

Fig. 9. Plots of the FOM_Combined for 16 prefilter materials

As shown in Fig. 9, the FOM_Combined of 16 different prefilter materials up to 0.5mm thickness is depicted. Tungsten, tantalum, and gold are the best LE prefilter materials, which achieve over 80% improvement at the prefilter thickness in the range of 0.225mm to 0.25mm. The atomic numbers of tungsten, tantalum and gold are 73, 74 and 79, and their k-edges are in the range of 70 to 80keV. The range of k-edge locations seems to provide a good suppression of the middle to high band of the x-ray spectrum. The rest of candidate prefilter materials could only provide insignificant improvement or deterioration in terms of FOM used. Further investigation of additional candidate materials is underway.

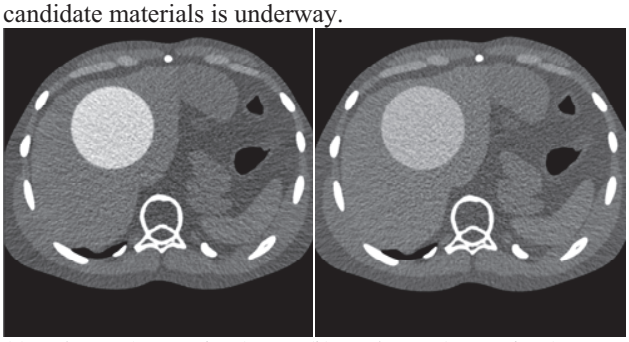

(a)LE image (Au 120kVp) (b) HE image (Sn 120kVp)

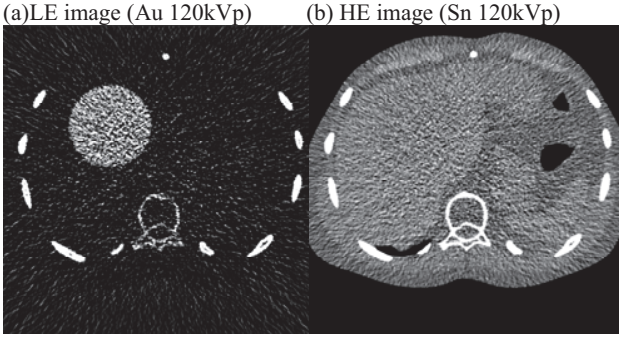

(c) Iodine image (d) VNC image

Fig.10. CT simulation with noise of water phantom with iodine inserts at Au 120kVp and Sn 120kVp (C/W=0/400HU & C/W=15/30mgI/cc for iodine image)

Our thorough simulation study using a water phantom provides essential insights and findings to identify the most promising search space. More clinical relevant simulations using the XCAT phantom (as in Fig. 10) are underway.

IV. Conclusion

In conclusion, we have performed a comprehensive study to determine the optimal x-ray tube setting, and prefilter material and thickness for the LE spectrum in split-filter DE-CT to provide the best iodine quantification and VNC imaging. We have demonstrated that significant improvement of resultant DECT image quality and reduction of radiation dose to the patient could be achieved by employing the optimal tube voltage and prefilter material and thickness.

References

[1] Faby, Sebastian, et al. "Performance of today's dual energy CT and future multi energy CT in virtual non-contrast imaging and in iodine quantification: A simulation study." *Medical physics* 42.7 (2015): 4349-4366.

[2] Fung, George SK, et al. "Differentiation of kidney stones using dual-energy CT with and without a tin filter." *American Journal of Roentgenology* 198.6 (2012): 1380-1386.

[3] Kawamoto, Satomi, et al. "Virtual noncontrast renal imaging using dual-energy CT: evaluation of CT numbers of renal parenchyma and renal masses." *Imaging in Medicine* 3.5 (2011): 501-511.

[4] Hofmann, Christian, et al. "Assessment of Dose Performance of a New Technique for Single Source Dual Energy Acquisition." Annual Meeting of RSNA, SSG14-04, 2015.

[5] Primak, A. N., et al. "Improved dual-energy material discrimination for dual-source CT by means of additional spectral filtration." *Medical physics* 36.4 (2009): 1359-1369.

[6] Rutt, Brian, and Aaron Fenster. "Split-filter computed tomography: a simple technique for dual energy scanning." *Journal of computer assisted tomography* 4.4 (1980): 501-509.

[7] Segars, W. P., Sturgeon, G., Mendonca, S., Grimes, J., and Tsui, B. M. W., "4D XCAT phantom for multimodality imaging research," Medical Physics, 37(9), 4902-4915 (2010).

[8] Stierstorfer, K., "Software Package for CT Data Simulation: CT_SIM and DRASIM," Internal Report, Siemens Healthcare, 2011.

[9] Fung G.S.K., Stierstorfer K., et al., "A realistic CT/Human-Model Simulation Package," Proc. 2nd Int. Conf. on Image Formation in X-ray CT, 66-69 (2012).

[10] Stierstorfer, K., "MOCASSIM: Monte Carlo Scatter Simulation," Internal Report, Siemens Healthcare, 2014.

5D respiratory motion model based image reconstruction algorithm for 4D cone-beam computed tomography

Jiulong Liu, Xue Zhang, Xiaoqun Zhang, Hongkai Zhao, Yu Gao, David Thomas, Daniel A Low, and Hao Gao

***Abstract*—A 5D model has been developed as an accurate model of respiratory motion. That is, given the measurements of breathing amplitude and its time derivative, the 5D model parametrizes the respiratory motion by three time-independent variables, i.e., one reference image and two vector fields. This work aims to develop a new 4DCBCT reconstruction method based on 5D model. Instead of reconstructing a temporal sequence of images after the projection binning, the new method reconstructs time-independent reference image and vector fields with no requirement of binning. The image reconstruction is formulated as a optimization problem with total-variation regularization on both reference image and vector fields, and the problem is solved by the proximal alternating minimization algorithm, during which the split Bregman method is used to reconstruct the reference image, and the Chambolle's duality-based algorithm is used to reconstruct the vector fields. Validated by the simulation studies, the new method has significantly improved image reconstruction accuracy due to no binning and reduced number of unknowns via the use of the 5D model.**

***Index Terms*—image reconstruction, 4D cone-beam computed tomography.**

I. Introduction

THE 5D model was established to model breathing motion [1] such that the position of a region of interest within the patient can be expressed as a linear function of a reference position vector field, breathing amplitude and its time derivative (rate). That is, given the measurements of breathing amplitude, 5D model parametrizes the respiratory motion by three time-independent variables, i.e., one reference image and two deformation vector fields (corresponding to breathing amplitude and rate).

The purpose of this work is to develop a new 4DCBCT reconstruction method based on the 5D model. Instead of reconstructing a temporal sequence of images after the projection binning, the new method reconstructs time-independent reference image and vector fields with no requirement of binning. Compared with the conventional approaches [2]–[15] that require data binning, the new method does not require binning, and therefore is free from binning artifacts caused by inaccurate or uneven binning in phase. Compared with the cine CBCT approach [16] with no data binning requirement, the proposed method utilizes the breathing measurement (breathing amplitude and rate), and therefore is expected to improve the image reconstruction quality. Compared with existing approaches with motion reconstruction [13]–[15], the method here reconstructs only three time-independent vector fields instead of time-dependent deformation vector fields, and therefore has a significantly reduced number of unknowns.

In terms of reconstruction algorithms, the image reconstruction will be formulated as a nonconvex optimization problem with simultaneous reconstruction of reference image and time-independent vector fields, both of which are regularized by the total variation [17]. Specifically the proximal alternating minimization [18], [19] will be developed to solve this nonconvex problem, during which the split Bregman method (or so-called alternating direction method of multipliers) is used to reconstruct the reference image [20], [21], and the Chambolle's duality-based algorithm is used to reconstruct the vector fields [22].

J. Liu and H. Gao are with Department of Mathematics and School of Biomedical Engineering, Shanghai Jiao Tong University, Shanghai 200240, CHINA (e-mail: hao.gao.2012@gmail.com)

X. Zhang is with Department of Mathematics, Shanghai Jiao Tong University, Shanghai 200240, CHINA

X. Zhang is with Department of Mathematics and Institute of Natural Sciences, Shanghai Jiao Tong University, Shanghai 200240, CHINA

H. Zhao is with Department of Mathematics, University of California, Irvine, CA 92697, USA

Y. Gao, D. Thomas, and D. A. Low are with Department of Radiation Oncology, University of California, Los Angeles, CA 90095, USA

II. 5D Model based 4DCBCT and Algorithm

A. Overview of 4DCBCT and 5D model

1) 4DCBCT: Let I_t be the image phases to be reconstructed with T phases of 2D N by N images, i.e., $\{I_t(x_i, y_j), 1 \leq i, j \leq N, 1 \leq t \leq T\}$. The conventional phase-by-phase 4DCBCT method can be formulated as the following iterative reconstruction method with the total variation (TV) regularization [17]

$$\min_{I_t} \|AI_t - y_t\|_2^2 + \mu|\nabla I_t|_1, 1 \leq t \leq T, \tag{1}$$

where A is the system matrix from the X-ray transform [23], y_t the binned projection data to the phase t, and λ the regularization parameter for the spatial TV term (for the purpose of denoising the image during the iterative reconstruction) defined by

$$|\nabla I_t|_1 = \sum_{i,j} \sqrt{(\partial_x I_t)^2 + (\partial_y I_t)^2}, \tag{2}$$

with $\partial_x I_t = I_t(x_{i+1}, y_j) - I_t(x_i, y_j)$ and $\partial_y I_t = I_t(x_i, y_{j+1}) - I_t(x_i, y_j)$.

In this work, we also compare with a state-of-art 4DCBCT method that utilizes a priori knowledge that the patient anatomy is correlated for the dynamic images to be reconstructed,

through the use of TV to promote the temporal similarity among image phases in addition to the spatial smoothness for each phase [6], i.e.,

$$\min_{\{I_t\}} \sum_t \|AI_t - y_t\|_2^2 + \mu \sum_t |\nabla I_t|_1 + \lambda |\nabla_t I_t|_1, \quad (3)$$

with the temporal TV term defined by

$$|\nabla_t I_t|_1 = \sum_{i,j,t} |\partial_t I_t| \quad (4)$$

with $\partial_t I_t = I_{t+1}(x_i, y_j) - I_t(x_i, y_j)$ and the regularization parameter λ_t.

For the above convex optimization problems (1) and (3), the solution algorithm can be conveniently developed based on the split Bregman method [20], [21] with the details given in our previous work [8], [9].

2) 5D Respiratory Motion Model: The 5D model [1] is developed to accurately model the respiratory motion. It parametrizes the dynamic position of a region of interest on the reference image based on reference position, breathing amplitude and rate, i.e.,

$$\vec{X}_t = \vec{X} + v_t \vec{M}_1 + f_t \vec{M}_2 \quad (5)$$

in which $\vec{X}_t$ and $\vec{X}$ are spatial coordinates in I_t and the reference image I_0 with the same image intensity value, v_t the breathing amplitude, f_t the breathing rate (v_t and f_t both measured data during free breathing), $\vec{M}_1$ and $\vec{M}_2$ the corresponding time-independent deformation vector fields. Correspondingly,

$$I_0(\vec{X}) = I_t(\vec{X}_t). \quad (6)$$

That is, the region of interest at $\vec{X}$ in the reference image I_0 deforms to a new location $\vec{X}_t$ in an arbitrary image phase I_t through the 5D model (5) parameterized by the reference image I_0 and its corresponding time-independent vector fields $\vec{M} = (\vec{M}_1, \vec{M}_2)$. Note that $\vec{M}$ is dependent on I_0 and therefore $\vec{M}$ has different values for a different I_0.

B. 5D Model based 4DCBCT

The innovation of this work is to consider the 4DCBCT image reconstruction based on 5D model (5) through

$$\min_{I_0, M} \sum_t \|AI_t(I_0, M) - y_t\|_2^2 + \mu |\nabla I_0|_1 + \lambda |\nabla M|_1 \quad (7)$$

where M denotes time-independent vector fields, e.g., $M = (M_{1x}, M_{1y}, M_{2x}, M_{2y})$ in 2D with $\vec{M}_1 = (M_{1x}, M_{1y})$, and $\vec{M}_2 = (M_{2x}, M_{2y})$ correspondingly in (5), and M is regularized in the TV norm component-wise for improved smoothness, i.e., $|\nabla M|_1 = \sum_{i\in\{1,2\}, j\in\{x,y\}} |\nabla M_{ij}|_1$. Note that (1) the regularization on M is essential to resolve the illposedness when solving M [24]; (2) no data binning on y_t is assumed here and therefore the number of image phases I_t to be reconstructed is the same as the number of projections y_t. For notation convenience, we shall eliminate $\sum_t$ from the data fidelity term in (7) from now on.

Next we adapt (7) to the linearized form based on which the proximal alternating linearized minimization algorithm can be conveniently developed. Recall that I_t is related to the reference image I_0 and vector fields M by (5) and (6), i.e.,

$$I_0(\vec{X}) = I_t(\vec{X} + L_t(M)). \quad (8)$$

with $L_t(M) = v_t \vec{M}_1 + f_t \vec{M}_2$. Then from the linearization

$$I_0(\vec{X}) \approx I_t(\vec{X}) + \nabla^T I_t \cdot L_t(M) \quad (9)$$

where $\nabla^T I_t \cdot L_t(M) = \partial_x I_t \cdot (v_t M_{1x} + f_t M_{2x}) + \partial_y I_t \cdot (v_t M_{1y} + f_t M_{2y})$, we have

$$I_t = I_0 - \nabla^T I_t \cdot L_t(M) \quad (10)$$

and correspondingly the linearized form of (7)

$$\min_{I_0, M} \|A(I_0 - \nabla^T I_t \cdot L_t(M)) - y_t\|_2^2 + \mu |\nabla I_0|_1 + \lambda |\nabla M|_1. \quad (11)$$

Note that since the vector field M is with respect to I_0, I_t can be computed based on the deformation from I_0, but not vice versa. Also, during the computation of I_t, since the deformed spatial coordinates $\vec{X} + L_t(M)$ from the Cartesian coordinate $\vec{X}$ of I_0 may not be on the Cartesian coordinate of I_t, the interpolation is necessary to derive the Cartesian values of I_t, which is through cubic interpolation here.

C. Alternating Reference-Image and Vector-Field Reconstruction

We apply the proximal alternating linearized minimization [18], [19] for (7), i.e.,

$$\begin{cases} I_0^{K+1} = \underset{I_0}{\operatorname{argmin}} & \|A(I_0 - \nabla^T I_t^K \cdot L_t(M^K)) - y_t\|_2^2 \\ & +\mu |\nabla I_0|_1 + \frac{1}{2\sigma} \|I_0 - I_0^K\|_2^2 \\ M^{K+1} = \underset{M}{\operatorname{argmin}} & \|A(I_0^{K+1} - \nabla^T I_t^{K+1} \cdot L_t(M)) - y_t\|_2^2 \\ & +\lambda |\nabla M|_1 + \frac{1}{2\eta} \|M - M^K\|_2^2. \end{cases} \quad (12)$$

Here K indexes the outer loop by the proximal alternating linearized minimization, and its inner loop (indexed by k) for solving I_0^{K+1} and M^{K+1} will be described next. Here we found the constant values for η and σ work well for our problem, although they could vary during iterations (12). Note that although the optimization problem (7) is nonconvex and nonsmooth, the proximal operator added to the subproblems guarantees the convergence of the outer loop [18], [19].

1) Reference-Image Reconstruction: In this section, we consider the I_0 subproblem of (12), i.e.,

$$I_0^{K+1} = \underset{I_0}{\operatorname{argmin}} \|AI_0 - y_t^K\|_2^2 + \mu |\nabla I_0|_1 + \frac{1}{2\sigma} \|I_0 - I_0^K\|_2^2 \quad (13)$$

where $y_t^K = A(\nabla^T I_t^K \cdot L_t(M^K)) + y_t$, and I_t^K is obtained through cubic interpolation on the deformed I_0^K.

Since (13) is a convex problem with sparsity regularization, we adopt the split Bregman method [20], [21] with the details given in our previous work [8], [9]. For algorithm completeness, we shall briefly describe it here. That is, introducing dummy variables $(d_x, d_y) = (\partial_x I_0, \partial_y I_0)$ and its auxiliary

variables (b_x, b_y) for isotropic TV norm (2), the convex problem (13) is reformulated as

$$(I_0, d_x, d_y) = \underset{I_0,d_x,d_y}{\operatorname{argmin}} \|AI_0 - y_t^K\|_2^2 + \mu|(d_x^k, d_y^k)|_1 + \frac{\rho}{2}\|(d_x - \partial_x I_0 - b_x, d_y - \partial_y I_0 - b_y)\|_2^2 + \frac{1}{2\sigma}\|I_0 - I_0^K\|_2^2. \quad (14)$$

Then we update I_0 and (d_x, d_y) alternately through

$$I_0^{k+1} = \underset{I_0}{\operatorname{argmin}} \|AI_0 - y_t^K\|_2^2 + \frac{1}{2\sigma}\|I_0 - I_0^K\|_2^2 + \frac{\rho}{2}\|(d_x^k - \partial_x I_0 - b_x^k, d_y^k - \partial_y I_0 - b_y^k)\|_2^2 \quad (15)$$

$$(d_x^{k+1}, d_y^{k+1}) = \underset{d_x,d_y}{\operatorname{argmin}} |(d_x, d_y)|_1 + \frac{\rho}{2}\|(d_x - \partial_x I_0^k - b_x^k, d_y - \partial_y I_0^k - b_y^k)\|_2^2 \quad (16)$$

with auxiliary variables (b_x, b_y) updated by

$$b_x^{k+1} = b_x^k + (\partial_x I_0^{k+1} - d_x^{k+1}) \quad (17)$$

$$b_y^{k+1} = b_y^k + (\partial_y I_0^{k+1} - d_y^{k+1}). \quad (18)$$

Here the linear system for L_2 subproblems in (15) is never explicitly formulated, since the problem (15) can be conveniently solved by conjugate gradient method as described in our previous work [8], [9] without explicitly forming the system matrix A, which can be computed on-the-fly through the parallel computation of X-ray transform and its adjoint [23]. And the (d_x, d_y) subproblem (16) has the explicit solution, i.e., the so-called isotropic shrinkage formula

$$(d_x^{k+1}, d_y^{k+1}) = \max(s^k - \frac{\mu}{\rho}, 0)\frac{(\partial_x I_0^k, \partial_y I_0^k) + (b_x^k, b_y^k)}{s^k} \quad (19)$$

where $s^k = \sqrt{(\partial_x I_0^k + b_x^k)^2 + (\partial_y I_0^k + b_y^k)^2}$.

2) Vector-Field Reconstruction: Next we consider the M subproblem of (12), i.e.,

$$M^{K+1} = \underset{M}{\operatorname{argmin}} \|A(I_0^{K+1} - \nabla^T I_t^K \cdot L_t(M)) - y_t\|_2^2 + \lambda|\nabla M|_1 + \frac{1}{2\eta}\|M - M^K\|_2^2 \quad (20)$$

via the Chambolle's duality-based algorithm.

First we introduce a convex relaxation of (20)

$$(M^{K+1}, U^{K+1}) = \underset{M,U}{\operatorname{argmin}} \lambda|\nabla U|_1 + \frac{1}{2\theta}\|U - M\|_2^2 + \frac{1}{2\eta}\|M - M^{(K)}\|_2^2 + \|A(I_0^{(K+1)} - \nabla^T I_t^K \cdot L_t(M)) - y_t\|_2^2 \quad (21)$$

where U is an auxiliary variable. Since (20) is convex, (21) is still convex. Thus, the following alternating scheme (22) is convergent.

$$\begin{cases} U^{k+1} &= \underset{U}{\operatorname{argmin}} \lambda|\nabla U|_1 + \frac{1}{2\theta}\|U - M^k\|_2^2 \\ M^{k+1} &= \underset{M}{\operatorname{argmin}} \|A(I_0^{K+1} - \nabla^T I_t^K \cdot L_t(M)) - y_t\|_2^2 \\ & \quad + \frac{1}{2\eta}\|M - M^K\|_2^2 + \frac{1}{2\theta}\|M - U^{k+1}\|_2^2 \end{cases} \quad (22)$$

Then from the Chambolle's duality-based algorithm [22], the problem (22) can be solved by

$$\begin{cases} U^{k+1} &= \underset{U}{\operatorname{argmin}} |\nabla U|_1 + \frac{1}{2\theta\lambda}\|U - M^k\|_2^2 \\ &= \underset{U}{\operatorname{argmin}} \max_{\|p\|_* \le 1} \langle p, \nabla U\rangle + \frac{1}{2\theta\lambda}\|U - M^k\|_2^2 \\ &= \underset{U}{\operatorname{argmin}} \max_{\|p\|_* \le 1} \langle \mathbf{div}p, U^k\rangle + \frac{1}{2\theta\lambda}\|U - M^k\|_2^2 \\ M^{k+1} &= \underset{M}{\operatorname{argmin}} \|A(I_0^{K+1} - \nabla^T I_t^K \cdot L_t(M)) - y_t\|_2^2 \\ & \quad + \frac{1}{2\theta}\|M - U^{k+1}\|_2^2 + \frac{1}{2\eta}\|M - M^K\|_2^2 \end{cases} \quad (23)$$

For the U subproblem, the solution can be analytically obtained by first computing the fixed point of the following iteration (24) over the dual variable p [22]

$$p^{k+1} = \frac{p^k + \tau/\theta\nabla(M^{k+1} + \theta\mathbf{div}(p^k))}{1 + \tau/\theta|\nabla(M^{k+1} + \theta\mathbf{div}(p^k))|} \quad (24)$$

and then

$$U^{k+1} = M^{k+1} + \theta\mathbf{div}(p^k). \quad (25)$$

Note that both (24) and (25) are with respect to each component of M, e.g., $U_{0x}^{k+1} = M_{0x}^{k+1} + \theta\mathbf{div}(p_{0x}^k)$ in (25) for M_{0x}. The solution M^{k+1} for the second L_2 subproblem in (23) can be obtained again by conjugate gradient method based on the following first-order optimality conditions. Again there is no need to explicitly form the system matrix A, which can be computed on-the-fly through the parallel computation of X-ray transform and its adjoint [23].

III. Numerical Results

The proposed method (abbreviated as "5D Method") (7) was validated based on experimental data of a lung patient in comparison with the conventional phase-by-phase reconstruction (abbreviated as "TV") (1) and a state-of-art method with spatiotemporal TV regularization (abbreviated as "TVt") (3). The reconstructed reference image and vector fields, measured breathing amplitude and rate were used to simulate a 4DCBCT in 2D. In our numerical simulation, there were 570 projections evenly distributed in one rotation with 500 detection pixels for each projection. The reconstructed images were 500×500, and the displayed images were 500×300 (central parts) for better visualization.

For "FBP", "TV" and "TVt", the 570 projections data were first binned into 10 phases. After image reconstruction, the 10 reconstructed image phases were re-mapped to 570 projections in the same order of projection binning. For the proposed "5D Method", no projection binning is necessary and dynamic images I_t were formed based on reconstructed (I_0, M) through the 5D model (5). The reconstruction results (Figures 1 and 2) were presented with optimized reconstruction parameters.

Next we consider the model error to evaluate the robustness of the proposed method, when there is a discrepancy between the ideal 5D model and the realistic model. For this purpose, the projection data is generated from the following perturbed 5D model with 10% relative difference in motion magnitude

$$\vec{X}_t = \vec{X}_0 + (v_t\vec{M}_1 + f_t\vec{M}_2)(1 + 0.1\sin(15\frac{2\pi}{T}t)). \quad (26)$$

Here T is the total number of frames/projections; 15 in (1) is the number of the breathing cycle, assuming 4 seconds

per breathing cycle and 60 seconds per scan rotation. Then the proposed method based on the ideal 5D model is used to reconstruct the CBCT images using perturbed projection data. The corresponding results are plotted in Figures 3 and 4. In addition, the quantitative errors in L_2 norm are summarized in Table I, which again suggest that the proposed "5D Method" improves the image quality.

TABLE I
RELATIVE ERRORS BETWEEN RECONSTRUCTED IMAGES AND GROUND TRUTH (UNIT IN %)

	FBP	TV	TVt	5D Method
Without model error	28.14	3.86	2.96	0.45
With model error	28.04	4.18	3.52	1.33

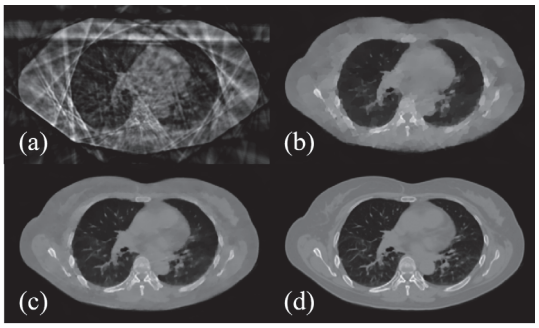

Fig. 1. Reconstruction results. (a) FBP; (b) TV; (c) TVt; (d) 5D Method.

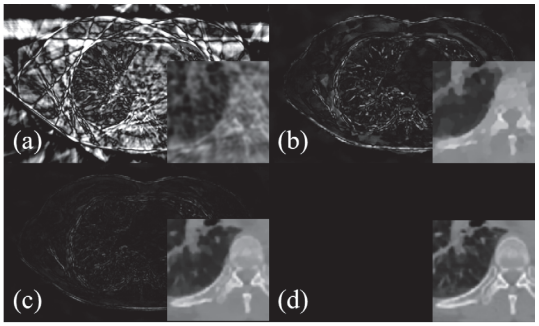

Fig. 2. Reconstruction errors and zoom-in details. (a) FBP; (b) TV; (c) TVt; (d) 5D Method.

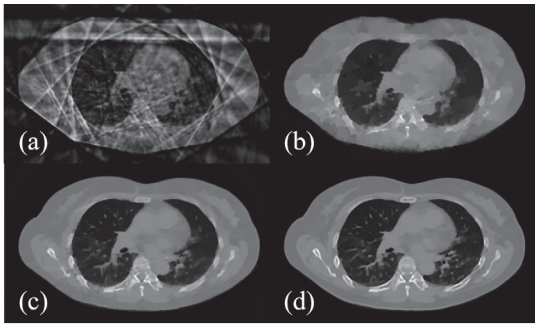

Fig. 3. Reconstruction results (with model error). (a) FBP; (b) TV; (c) TVt; (d) 5D Method.

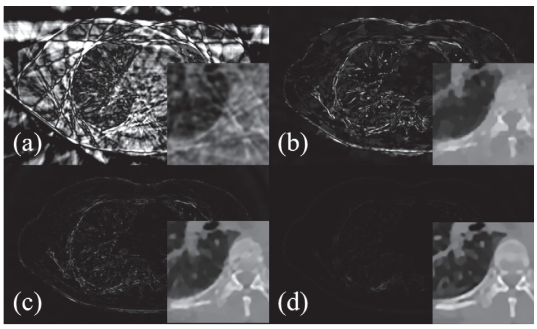

Fig. 4. Reconstruction errors and zoom-in details (with model error). (a) FBP; (b) TV; (c) TVt; (d) 5D Method.

IV. CONCLUSION

We have developed a new 4DCBCT image reconstruction method based on 5D respiratory motion model, with improved image reconstruction from standard and state-of-art methods. The new reconstruction algorithm is formulated as a nonconvex and nonsmooth optimization problem with the reconstruction of reference image and time-independent vector fields, which is solved by the proximal alternating minimization in this work.

REFERENCES

[1] D. A. Low et al, International Journal of Radiation Oncology Biology Physics, 63, 921-929, 2005.
[2] J-J. Sonke et al, Medical physics, 32, 1176-1186, 2005.
[3] S. Kriminski et al, Physics in Medicine and Biology, 50,5263-5280,2005.
[4] L. Dietrich et al, Physics in Medicine and Biology, 51, 2939-2952, 2006.
[5] T. Li et al, Medical Physics, 33, 3825-3833, 2006.
[6] G.-H. Chen et al, Medical physics, 35, 660-663, 2008.
[7] X. Jia et al, Medical Image Computing and Computer-Assisted Intervention-MICCAI 2010 Springer Berlin Heidelberg, 2010, 143-150, 2010.
[8] H. Gao et al, Physics in Medicine and Biology, 56, 3181-3198, 2011.
[9] H. Gao et al, Inverse Problems, 27, 115012, 2011.
[10] L. Ritschl et al, Physics in Medicine and Biology, 57, 1517-1525, 2012.
[11] H. Wu et al, International Society for Optics and Photonics, 2012, 83133J-7, 2012.
[12] H. Gao et al, Medical Physics, 39, 6943-6946, 2012.
[13] C. P. Christoffersen et al, Medical Imaging, IEEE Transactions on, 32, 2064-2077, 2013.
[14] H. Yan et al, Medical Physics, 41, 071903, 2014.
[15] J. Wang et al, Medical Physics, 40, 101912, 2013.
[16] J. Cai et al, IEEE transactions on medical Imaging, 33, 1581-1591, 2014.
[17] L. I. Rudin et al, Physica D: Nonlinear Phenomena, 60, 259-268, 1992.
[18] J. Bolte et al, Mathematical Programming, 146, 459-494, 2014.
[19] H. Attouch et al, Mathematics of Operations Research, 35, 438-457, 2010
[20] T. Goldstein et al, SIAM Journal on Imaging Sciences, 2, 323-343, 2009.
[21] S. Boyd et al, Foundations and Trends in Machine Learning, 3, 1-122, 2011.
[22] A. Chambolle, Journal of Mathematical imaging and vision, 20, 89-97, 2014.
[23] H. Gao, Medical physics, 39, 7110-7120, 2012.
[24] B. K. Horn et al, Technical Symposium East International Society for Optics and Photonics, 1981, 319-331, 1981.

Study on geometric efficiency for MDCT

Jingwen Zhuang, Junzheng Zheng and Mei Bai

Abstract—**The objective of this study was to investigate the dependence of geometric efficiency of a MDCT system on several exposure parameters such as tube voltage, collimation and pitch. Dose profiles in PMMA phantom for Siemens Definition Flash CT and GE Discovery CT750 HD were derived in helical mode using different tube voltages, collimations and pitches. Corresponding geometric efficiencies and weighted geometric efficiencies were calculated. Kruskal-Wallis test was performed to test the differences between weighted geometric efficiencies using different exposure parameters and the Spearman's correlation coefficient was calculated to determine correlation between different exposure parameters and weighted geometric efficiencies. The results shows with larger collimation the weighted geometric efficiency in head and body phantom can be improved by 10-30%, while combined with larger pitch the weighted geometric efficiency can be reached to about 60%. Weighted geometric efficiencies had positive correlation with beam collimation and pitch ($p<0.05$) for both CT scanners, while there was no significant difference between weighted geometric efficiencies with different tube potentials ($p>0.05$). The decrease of geometric efficiency leads to the increase of patient radiation dose. It is necessary to improve the geometric efficiency and reduce the burden of patients by optimal setting beam collimation and pitch for CT scans.**

Index Terms—**multidetector computed tomography; geometric efficiency; radiation dose.**

I. INTRODUCTION

GEOMETRIC efficiency (GE) has been defined as the ratio of the integral of the dose profile over the nominal active detector array width and the total integral of the dose profile by the International Electro technical Commission (IEC) [1]. It has been also considered as a value to measure the utilization of x-ray radiation along the z axis [2-3]. In CT imaging inhomogeneous penumbra always reduces the quality of images. In single detector CT system, the penumbra area was partly included in the active detector length, accordingly, geometric efficiency is generally high [4]. But nowadays with the fast development of CT technology, the number of CT detector rows is growing rapidly [5-8]. Manufactures increases the x-ray beam width in multi-detector CT system to make the penumbra fall outside the detector array and ensure all active detector elements along z axis receive the same amount of radiation when the system is operated free-in-air [9-10]. This improves the quality of images but increases the radiation burden of patients because a portion of x-ray beam does not make contribution to form images. A recent study showed that the decrease of geometric efficiency leads to the increase of patient radiation dose [4]. Therefore, it is necessary to improve the geometric efficiency of MDCT in CT examinations to decrease the patient dose burden. The objective of this study was to investigate the dependence of geometric efficiency of a MDCT system on several exposure parameters such as tube voltage, collimation and pitch.

This work is supported by the National Natural Sciences Foundation of China (NSFC) grant no.81372923.

Jingwen Zhuang is with the Xuanwu Hospital of Capital Medical University, Beijing, 100053 (e-mail: jswei65@163.com).

Junzheng Zheng is with the Xuanwu Hospital of Capital Medical University, Beijing, 100053 (e-mail: xwhosp@ sina.com).

Mei Bai is with the Xuanwu Hospital of Capital Medical University, Beijing, 100053 (e-mail: baimei@xwh.ccmu.edu.cn).

II. MATERIALS AND METHODS

Two CT scanners from different manufactures were used in the current study: a Siemens SOMATOM Definition Flash CT scanner (Siemens AG, Forchheim, Germany) and a GE Discovery CT750 HD scanner (GE Healthcare, Waukesha, USA). The Piranha x-ray multi-meter equipped with a CT-SD 16 radiation detector (RTI Electronics AB, Mölndal, Sweden) was used to obtain dose profiles. A standard cylindrical head PMMA phantom (16cm diameter) and a standard cylindrical body PMMA phantom (32 diameter) [11] were used. Each phantom contains five holes, one is located in the center (position A) and four are around the periphery at "12 o'clock", "3 o'clock", "6 o'clock", "9 o'clock"(Position B, C, D, E), separately. Dose profiles in PMMA phantom were derived in helical mode using different tube voltages, collimations and pitches. Corresponding geometric efficiencies and weighted geometric efficiencies were calculated.

The geometry efficiency at position A was determined by [4]:

$$GE=\frac{\int_{-w/2}^{+w/2} D(z)dz}{\int_{-\infty}^{+\infty} D(z)dz} \qquad (1)$$

Where D (z) is the dose profile along z axis, w is the length of the active detector array at position A the isocenter (i.e. the beam collimation). The geometric efficiency at the peripheral holes of the phantoms was determined by the same formula, but the length of the detector array was changed at the peripheral holes of the PMMA phantoms due to the distance from the peripheral holes to isocenter.

A weighted geometric efficiency was also calculated in the current study. It was determined by:

$$GE_w = \frac{1}{3}GE_c + \frac{2}{3}GE_p \quad (2)$$

Where GE_c and GE_p are the geometric efficiencies measured at the center and periphery of the PMMA phantoms.

Kruskal-Wallis test was performed to test the differences between weighted geometric efficiencies using different exposure parameters and the Spearman's correlation coefficient was calculated to determine correlation between different exposure parameters and weighted geometric efficiencies.

III. RESULTS

The dose profiles of isocenter (i.e. position A) determined using head phantom at 120kV tube voltage and 1.0 pitch for Siemens SOMATOM Definition Flash CT scanner were displayed in Fig. 1 for four different beam collimations.

The weighted geometric efficiency values of head and body phantom determined using different parameters was shown in Fig. 2 and Fig. 3, were found to range from 16% to 63%. As shown in Fig. 1 weighted geometric efficiency at 1.6×0.3mm beam collimation is lower than 20%, while weighted geometric efficiency at 32×1.2mm beam collimation is higher than 50%. With larger collimation the weighted geometric efficiency in head and body phantom can be improved by 30%. As shown in Fig. 3 weighted geometric efficiency at 0.5 pitch is lower than 50%, with larger pitch the weighted geometric efficiency can be reached to about 60%. The results shows weighted geometric efficiencies had positive correlation with beam collimation and pitch ($p<0.05$) for both CT scanners, while there was no significant difference between weighted geometric efficiencies with different tube potentials ($p>0.05$).

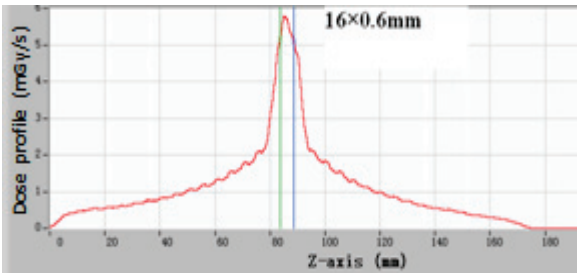

(a)

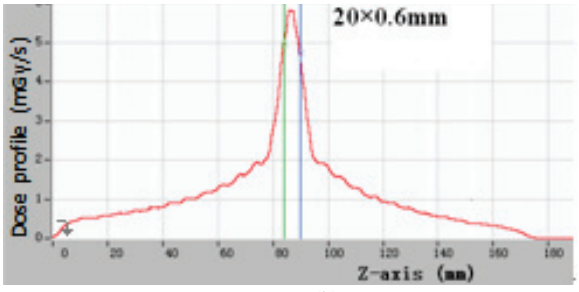

(b)

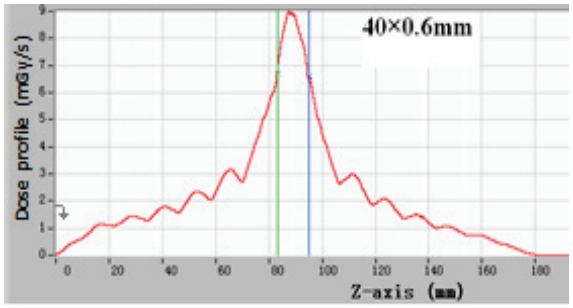

(c)

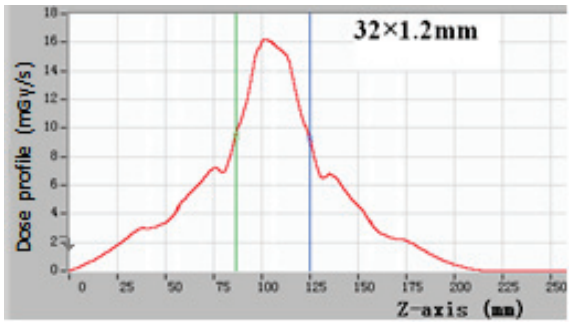

(d)

Figure 1 The dose profiles of position A determined using head phantom at 120kV tube voltage, 1.0 pitch and different collimations for Siemens SOMATOM Definition Flash CT scanner. The vertical lines indicate the beam width. (a) 16×0.6mm beam collimation, (b) 20×0.6mm beam collimation, (c) 40×0.6mm beam collimation, (d) 32×1.2mm beam collimation

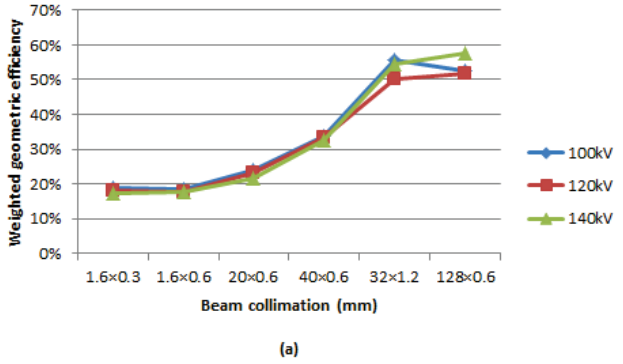

(a)

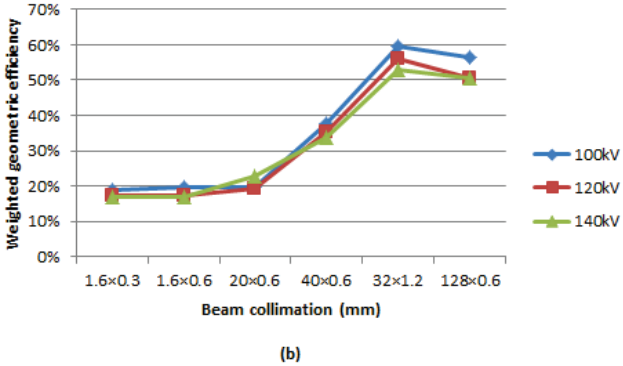

(b)

Figure 2 weighted geometric efficiency is growing with beam collimation increasing (pitch=1.0). (a) using head phantom, (b) using

body phantom

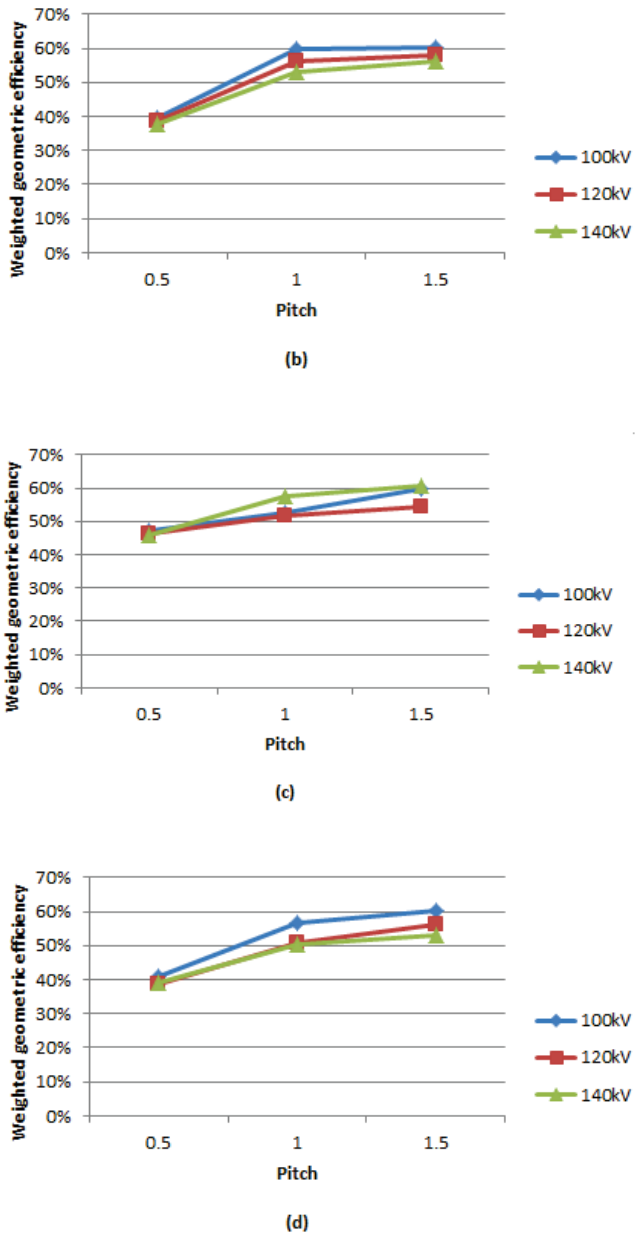

Figure 3 weighted geometric efficiency is growing with increased pitch. (a) using head phantom at 32×1.2mm beam collimation, (b) using body phantom at 32×1.2mm beam collimation, (c) using head phantom at 128×0.6mm beam collimation, (d) using body phantom at 128×0.6mm beam collimation

IV. Conclusion and Discussion

According to fig. 1, in a single scan, the ratio of the integral of dose profile falling within the active detector width and the integral of dose profile along its total length along the z axis was growing for increasing beam collimation, i.e. geometric efficiency was increasing for increasing beam collimation.

Compared to pitch, beam collimation was found to have a better positive correlation coefficient with geometric efficiency in most cases (i.e. r=0.836, p=0.000 vs r=0.463, p=0.004 and r=0.834, p=0.000 vs r=0.417, p=0.011 for Siemens SOMATOM Definition Flash CT scanner using head and body phantom, separately; r=0.739, p=0.000 vs r=0.684, p=0.002 for GE Discovery CT750 HD scanner using head phantom). Therefore, wider beam collimation could reduce the "wasted" x-ray which is beyond the active detector array.

The result of the Spearman's rank order correlation coefficient also indicated that tube voltage which affects beam quality of the produced x-ray was found to have an insignificant negative correlation with geometric efficiency (i.e. r=-0.016, p=0.924 and r=-0.249, p=0.143 for Siemens SOMATOM Definition Flash CT scanner using head and body phantom, separately; r=-0.039, p=0.877 and r=-0.079, p=0.756 for GE Discovery CT750 HD scanner using head and body phantom, separately).

With the ever growing utilization of CT in clinical activities [12-15], it is imperative to investigate the dosimetric aspects of CT. Geometric efficiency as an important exposure feature of CT scanners affecting radiation dose should be taken seriously.

Geometric efficiency was found to have positive correlation with collimation and pitch while tube voltage was found to have little influence on geometric efficiency. Examiners should raise beam collimation and pitch to improve the geometric efficiency and reduce the burden of patients.

Acknowledgments

This work was supported by the National Natural Sciences Foundation of China (NSFC) grant no.81372923.

References

[1] International Electrotechnical Commission. International Standard Amendment 1 to IEC 60601-2-44, edition 2: medical electrical equipment, part 2-44: particular requirements for the safety of x-ray equipment for computed tomography 1-7. Geneva, Switzerland: IEC; 2002.

[2] Kobayashi M, Koshida K, Suzuki S, et al, "Evaluation of geometric efficiency and radiation exposure in z-axis for volume scan," Radiat Prot Dosimetry, vol.143, no.1,pp. 63-68, 2011.

[3] Berris T, Perisinakis K, Papadakis AE, et al, "Comparison of methods for assessing geometric efficiency on multi-detetor CT scanners," Phys Med, vol.29, no.3, pp.:312-322, 2013.

[4] Perisinakis K, Papadakis AE, Damilakis J, "The effect of x-ray beam quality and geometry on radiation utilization efficiency in multidetector CT imaging," Med Phys, vol. 36, no.4, pp. 1258-1266, 2009.

[5] Vemema HW, den Heeten GJ, "Substraction helical CT angiography of intra- and extracranial vessels: technical considerations and preliminary experience: technical considerations and preliminary experience--rediscovery of matched mask bone elimination," AJNR Am J Neuroradiol, vol. 24, no.7, pp.1491-1492, 2003.

[6] Hsiao EM, Rybicki FJ, Steigner M, "CT coronary angiography: 256-slice and 320-detector row scanners." Curr Cardiol Rep, vol.12, no.1, pp:68-75, 2010.

[7] Choi SI, George RT, Schuleri KH, et al, "Recent developments in wide-detector cardiac computed tomography," Int J Cardiovasc Imaging, vol.25, Suppl. 1, pp. 23-29, 2009.

[8] Khan A, Khosa F, Nasir K, et al, "Comparison of radiation dose and image quality: 320-MDCT versus 64-MDCT coronary angiography," AJR Am J Roentgenol, vol.197, no. 1, pp.163-168, 2011.

[9] Toth TL, Bromberq NB, Pan TS, et al, "A dose reduction x-ray beam positioning system for high-speed multislice CT scanners,". Med Phys; vol.27, no.12, pp. 2659-2568, 2000.

[10] Lewis MA, “Multislice CT: opportunities and challenges,” Br J Radiol, vol.74, no.885, pp. 779-781, 2001.
[11] Goldman LW, “Principles of CT: radiation dose and image quality,” J Nucl Med Technol, vol.35, no.4, pp. 213-225, 2007.
[12] Hansen J, Jurik AG, “Analysis of current practice of CT examinations,” Acta Oncol, vol. 48, no.2, pp.295-301, 2009.
[13] Brenner DJ, Hall EJ, “Computed tomography – an increasing source of radiation exposure,” N Engl J Med, vol.357, no.22, pp. 2277-2284, 2007
[14] Smith-Bindman R, Lipson J, Marcus R, et al, “Radiation dose associated with common computed tomography examinations and the associated lifetime attributable risk of cancer,” Arch Intern Med, vol. 169, no.22, pp.2078-2086, 2009.
[15] Zhang YK, Li X, Segars WP, et al, “Organ doses, effective doses, and risk indices in adult CT: comparison of four types of reference phantoms across different examination protocols,” Med Phys, vol.39, no.6, pp. 3404-3423, 2012.

Statistical Image-Domain Multi-Material Decomposition for Dual-Energy CT

Meili Yang, Yong Long*, and Tianye Niu*

***Abstract*—Dual-energy CT (DECT) enhances tissue characterization because of its basis material decomposition capability. In addition to conventional two-material decomposition from DECT measurements, multi-material decomposition (MMD) is required in many clinical applications. To solve the ill-posed problem of reconstructing multiple-material images from dual-energy measurements, additional constraints are incorporated into the problem formulation, including volume and mass conservation and the assumptions that at most three materials in each pixel and various material types among pixels. One-step MMD methods which reconstruct multiple images directly from DECT measurements are computationally expensive due to repeated forward projecting multiple material images and backward projecting measurements at low and high energies. The image-domain direct MMD method proposed by Mendonça *et al*. decomposes pixels sequentially into multiple basis materials using direct inversion scheme and leads to magnified noise in the material images. In this paper, we propose a statistical image-domain MMD method for DECT to suppress noise. It applies penalized weighted least-square (PWLS) estimation with edge-preserving regularization. The statistical weight is the inverse of the estimated variance-covariance matrix of decomposed basis materials. The proposed method is evaluated using Catphan©600 phantom and pelvis patient data. Compared with the image-domain direct inversion method, the proposed method reduces noise standard deviation (STD) by 52%, 80%, 96% and 83% for bone, iodine, soft-tissue and air images for the pelvis patient data, respectively, and it substantially reduces noise with minimal effect on decomposition accuracy for the contrast rods slice of the Catphan©600 phantom. The proposed method is thus practical and promising for advanced clinical applications using DECT imaging.**

***Index Terms*—Dual-energy CT, Image-domain, Multi-material decomposition, Noise suppression, Optimization transfer, Penalized weighted least-square (PWLS).**

M. Yang and T. Niu were supported by the Zhejiang Provincial Natural Science Foundation of China (Grant No. LR16F010001), National High-tech R&D Program for Young Scientists by the Ministry of Science and Technology of China (863 Program, 2015AA020917). Y. Long was partially supported by NSFC (61501292), Shanghai Pujiang Talent Program (15PJ1403900), SJTU-UM Collaborative Research Program and Returned Overseas Chinese Scholars Program.

M. Yang and T. Niu are with Sir Run Run Shaw Hospital and Institute of Translational Medicine, Key Laboratory of Biomedical Engineering of Ministry of Education, Zhejiang University, Hangzhou, Zhejiang, 310009, China.

Y. Long is with University of Michigan–Shanghai Jiao Tong University Joint Institute, Shanghai Jiao Tong University, Shanghai, 200240, China.

*Correspondence should be sent to T. Niu via e-mail: tyniu@zju.edu.cn and Y. Long via e-mail: yong.long@sjtu.edu.cn.

I. Introduction

Spectral CT enhances tissue characterization because of its basis materials decomposition capability. In principle, two basis materials with various linear attenuation coefficients (e.g. bone and soft-tissue) can be accurately reconstructed using dual-energy CT (DECT) technique [1]. However, many clinical applications require three or more component images. For example, liver-fat quantification requires four constitute materials: liver tissue, blood, fat and contrast agent [2]. One method to achieve this is using expensive hardware, e.g., energy-sensitive photon-counting detectors, to acquire multi-energy projection data. In this paper, we design a multi-material decomposition (MMD) algorithm using conventional dual-energy measurements which are readily available from clinical DECT scanners.

DECT methods are classified into three categories: projection-domain, image-domain and direct reconstruction methods [3]. Projection-domain methods decompose DECT measurements into sinograms of basis materials, and generate material images using conventional reconstruction algorithms. Projection-domain methods avoid beam-hardening artifacts because the material specific projections are estimated prior to image reconstruction. One major challenge for projection-domain methods is the calibration of spectral transmission model which is nonlinear and computationally expensive. Image-domain methods apply standard reconstruction techniques to obtain low- and high-energy CT images, and decompose the resulting images into basis materials using linear approximation of decomposition process. Mendonça *et al*. [2] proposed an image-domain pixel-wise MMD method for DECT. In addition to mass and volume conservation, this method assumes that each pixel contains at most three basis materials and the material types vary among pixels. It suffers from significantly magnified noise in the decomposed basis images since direct inversion at each pixel is used to estimate volume fractions of basis materials. Long and Fessler [4] proposed a direct MMD method for DECT using penalized-likelihood (PL) reconstruction with edge-preserving regularizers for each material. This method has advantages of modeling the physics of spectral transmission exactly, incorporating similar constrains in [2] to its CT object model, and significantly decreasing noise and cross-artifacts in the decomposed material images. However, it is computationally expensive due to the repeated forward projecting multiple material images and backward projecting measurements at low and high energies and the modeling of poly-energetic spectra.

The decomposition procedure of DECT measurements is

highly sensitive to noise since X-ray spectra of low and high energies are overlapped. In this paper, assuming similar constraints in [2], [4], we investigate the noise suppression in image-domain MMD methods. As noise in multi-material images is correlated, we include the inverse of the estimated variance-covariance matrix of decomposed basis materials as the statistical weight in the least-square term for a better noise suppression performance, which has shown potential in image-domain noise suppression of dual-material decomposition [5]. The cost function of the proposed method is in the form of penalized weighted least-square (PWLS) estimation with edge-preserving regularization. We apply optimization transfer principles to develop a pixel-wise separable quadratic surrogate (PWSQS) at each iteration to monotonically decrease the cost function [4]. The separability in each pixel enables simultaneous update of all pixels.

II. Method

A. Object model for Multi-material decomposition (MMD)

Multi-material decomposition (MMD) from DECT measurements is an ill-posed problem since multiple sets of images are estimated from two sets of measurements associated with low and high energies. To solve this ill-posed problem, we apply the constraints of volume and mass conservation [2], [4], [6] and additional assumption that each pixel contains at most three materials where the triplet-material types vary among pixels [2], [4].

The spatially- and energy-dependent attenuation distribution $\vec{\mu}_E$ is

$$\vec{\mu}_E = \sum_{l=1}^{L_0} \mu_{lE}\, \vec{x}_l, \tag{1}$$

where $\vec{x}_l$ denotes the volume fraction image of the l-th material, L_0 is the total number of basis material types, and μ_{lE} is the linear attenuation coefficient (LAC) of the l-th material at energy level E. According to the constraints of volume and mass conservation, volume fraction $\vec{x}_l$ satisfies the sum-to-one and box constraint:

$$\begin{cases} \sum_{l=1}^{L_0} x_{lp} = 1, \forall p \\ a_l \le x_{lp} \le b_l, \forall l, p. \end{cases} \tag{2}$$

where p indexes the p-th pixel. We relax the lower limit a_l of the box constraint to be slightly smaller than 0, and the upper limit b_l to be slightly greater than 1. Under the assumptions that each pixel contains at most three materials and triplet-material types vary among pixels, volume fraction $\vec{x}_l$ also satisfies the following constraint,

$$\sum_{l=1}^{L_0} 1_{\{x_{lp}\neq 0\}} \le 3, \forall p. \tag{3}$$

Let Ω be a triplet library containing all triplets generated from pre-selected materials of interest [4]. The method in [2] directly decomposes each pixel into optimal triplet in the library Ω under constraints (2) and (3). This method is referred to as the direct inversion method hereafter in this paper. The direct inversion method can be implemented readily in a sequential pixel-by-pixel fashion, but leads to significantly magnified noise in the decomposed basis material images as addressed in our previous publication [4], [5].

B. Statistical image-domain MMD

To suppress noise in the decomposed material images, we extend our previous method in dual-material decomposition [5] to MMD. We include inverse of the estimated variance-covariance matrix of decomposed basis materials as the statistical weight in the weighted least-square term. The penalized weighted least-square (PWLS) cost function is:

$$\Phi(\vec{x}) = (A\vec{x} - \vec{\mu})^T V^{-1} (A\vec{x} - \vec{\mu}) + R(\vec{x}). \tag{4}$$

The $2N_p \times L_0N_p$ material composition matrix A is

$$A = \begin{pmatrix} \mu_{1H}I & \cdots & \mu_{L_0H}I \\ \mu_{1L}I & \cdots & \mu_{L_0L}I \end{pmatrix}, \tag{5}$$

where N_p is the total number of pixels and I is a $N_p \times N_p$ identity matrix. $\vec{\mu} = [\vec{\mu}_H^T\ \vec{\mu}_L^T\ ]^T$ is a $2N_p$ vector where $\vec{\mu}_H$ and $\vec{\mu}_L$ are the high- and low-energy CT images, respectively. T denotes the transpose operator. $\vec{x} = [\vec{x}_1^T, \ldots, \vec{x}_{L_0}^T\ ]^T$ is a L_0N_p vector composed of $\vec{x}_1, \ldots, \vec{x}_{L_0}$ basis material images.

V is a $2N_p \times 2N_p$ diagonal matrix whose diagonal elements are the noise variance of pixels in the high- and low-energy CT images [5], i.e.,

$$V = diag\left(var_{H1}, \ldots, var_{HN_P}, var_{L1}, \ldots, var_{LN_P}\right). \tag{6}$$

where var_{Hp} and var_{Lp} are the statistical noise variance of the p-th pixel in the high- and low-energy CT images, respectively, which ignores the noise correlation between DECT images obtained from two separate scans. To evaluate the noise variance, we first select a region of homogeneous material in the high/low CT image and evaluate the numerical variance as the noise variance of all pixels (i.e., assuming uniform noise distribution).

The edge-preserving regularization term $R(\vec{x})$ [4], [7] is

$$R(\vec{x}) = \sum_{l=1}^{L_0} \beta_l R_l(\vec{x}_l). \tag{7}$$

where the regularizer for the l-th material is

$$R_l(\vec{x}_l) = \sum_{p=1}^{N_P} \sum_{k\in N_{lp}} \psi_l\left(x_{lp} - x_{lk}\right). \tag{8}$$

where the potential function ψ_l is a hyperbola function

$$\psi_l(t) = \frac{\delta_l^2}{3}\left(\sqrt{1 + 3\left(\frac{t}{\delta_l}\right)^2} - 1\right). \tag{9}$$

and N_{lp} is a neighborhood of pixel x_{lp}. The regularization parameters β_l and δ_l can be chosen differently for various materials to achieve desired edge preservation and noise-resolution tradeoff for each material image.

C. Optimization Algorithm

The basis materials are estimated by minimizing the cost function $\Phi(\vec{x})$ in (4) under the constraints given in (2) and (3), i.e.,

$$\hat{\vec{x}} \triangleq \underset{\vec{x}\ subject\ to\ (2)\&(3)}{argmin} \Phi(\vec{x}). \tag{10}$$

Due to the constraints on each pixel, it is difficult to minimize the cost function directly. To monotonically decrease the cost function, we use optimization transfer principles to design a serial of pixel-wise separable quadratic surrogates (PWSQS) [4]. We loop over all the possible triplets in the triplet library Ω, minimize the surrogate functions for each material triple under the constraints in (2), and determine the optimal triplet for each pixel as the one minimizing the surrogate of that pixel.

D. Evaluation

The noise is quantitatively measured using standard

deviation (STD) of image pixels within a region of interest (ROI). We use the root-mean-square (RMS) of the average percent error $E(\%)$ of the electron densities of all rods as a metric to quantify the decomposition accuracy. The electron density distribution is calculated as follows,

$$\vec{\rho}_e = \sum_{l=1}^{L_0} \rho_l \vec{x}_l. \quad (11)$$

where $\vec{x}_l$ and ρ_l are volume fractions and electron density of the l-th basis material, respectively. For each rod, the average percent error $E(\%)$ of associated pixels inside the rod is calculated as

$$E(\%) = \left(\frac{\bar{\rho}_e - \bar{\rho}_{e0}}{\bar{\rho}_{e0}}\right) \times 100\%. \quad (12)$$

where $\bar{\rho}_e$ is the average value of estimated electron densities inside a rod and $\bar{\rho}_{e0}$ is the ground-truth value of the rod.

III. Results

To quantitatively evaluate performance of the proposed method, we tested it on the contrast rods slice Catphan©600 phantom and pelvis patient data. We initialized the proposed method using results of the direct inversion method [2], and compared their performance. Table I listed the regularization coefficient β_l, the edge-preserving parameter δ_l for each material and number of iterations for each study.

TABLE I
THE SELECTED REGULARIZER COEFFICIENT, EDGE-PRESERVING PARAMETER AND NUMBER OF ITERATIONS FOR EACH STUDY.

Data	Catphan©600 phantom	Pelvis patient
β_l (for Teflon/bone, iodine, soft-tissue and air image)	0.8, 0.2, 1, 10	1, 0.3, 1, 0.2
δ_l (for Teflon/bone, iodine, soft-tissue and air image)	0.005, 0.02, 0.012, 0.01	0.01, 0.005, 0.01, 0.1
Iterations	200	100

A. Catphan©600 phantom study

Fig. 1 shows the low- and high-energy CT images of Catphan©600 phantom on the contrast rods slice. The rods are marked with digits as shown in Fig. 1. In this study, we select Teflon (#1), the Iodine solution with a concentration of 10 mg/ml (#3), the inner soft-tissue and air as basis materials. The decomposed basis material images using the proposed method and direct inversion method [2] are shown in Fig. 2. Table II shows the means and STDs of pixel values inside the ROI indicated by blue solid rectangle shown in Fig. 2 (b3). Compared with the direct inversion method, noise STDs in Teflon, iodine, soft-tissue and air images reconstructed by the proposed method are reduced by 49%, 76%, 92% and 96%, respectively. The RMS of average percent errors are 14.91% and 14.98% for the direct inversion and the proposed methods, respectively, indicating that the proposed method can substantially reduce noise in decomposed images with minimal effect on decomposition accuracy.

B. Pelvis patient study

Fig. 3 shows the low- and high-energy CT images of the pelvis patient data. Fig. 4 shows the decomposed multi-material images by the direct inversion method [2] and the proposed method. The means and STDs are calculated inside the red solid rectangle as shown in Fig. 4(b3) and summarized in Table IV. The noise STDs of bone, iodine, soft-tissue and air images are reduced by 52%, 80%, 96% and 83%, respectively. The noise magnification is significantly suppressed while anatomical structure profiles are faithfully retained.

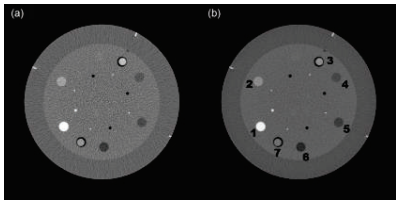

Fig. 1. CT images of the Catphan©600 phantom on the contrast rods slice: (a) 75kVp and (b) 125kVp. Display window is [0.01 0.04] mm^{-1}. The digits in (b) indicate the rods applied in this study: (1) Teflon, (2) Delrin, (3) Iodine solution of 10 mg/ml, (4) Polystyrene, (5) low density Polyethylene (LDPE), (6) Polymethylpentene (PMP), and (7) Iodine solution of 5 mg/ml.

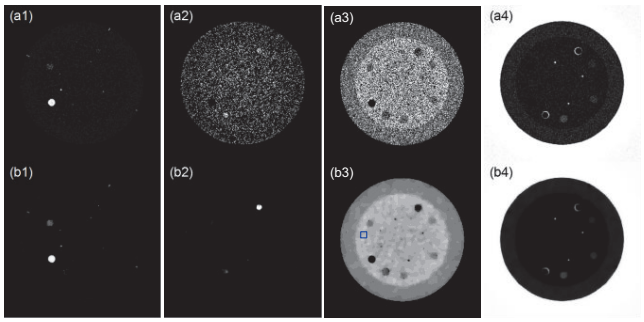

Fig. 2. The decomposed Teflon (first column), iodine (second column), soft-tissue (third column) and air (last column) images of the Catphan©600 phantom on the contrast rods slice. Row (a): direct inversion method; (b): proposed method. The blue solid rectangle in (b3) indicates the region where the means and STDs in Table IV are calculated. Display windows are: [0.22 1] for Teflon images, [0.4 0.7] for iodine images, [0.2 1] for soft-tissue images, and [0.2 1] for air images, respectively.

TABLE II
THE MEANS AND STDS OF PIXEL VALUES INSIDE THE ROI INDICATED BY THE BLUE SOLID RECTANGLE AS SHOWN IN FIG. 2(b3).

Method	Direct inversion	Proposed
Teflon image	0.054±0.113	0.021±0.058
Iodine image	0.22±0.261	0.167±0.063
Soft-tissue image	0.60±0.314	0.704±0.024
Air image	0.12±0.117	0.108±0.005

TABLE IV
THE MEANS AND STDS OF PIXEL VALUES INSIDE THE ROI INDICATED BY THE RED SOLID RECTANGLE AS SHOWN IN FIG. 4(b3).

Method	Direct inversion	Proposed
Bone image	0.002±0.0287	0 ±0.0137
Iodine image	0.264±0.1000	0.272±0.0205
Soft-tissue image	0.568±0.1194	0.561±0.0042
Air image	0.165±0.0406	0.166±0.0068

IV. Conclusions

We proposed a statistical image-domain MMD method for DECT. Taking the noise correlation of basis materials into consideration, we include the inverse of the estimated

TABLE III

ELECTRON DENSITIES INSIDE THE CATPHAN©600 CONTRAST RODS. THE NUMBERS OF THE RODS ARE MARKED IN FIG. 1(b). THE LAST COLUMN IS THE ROOT-MEAN-SQUARE (RMS) OF AVERAGE PERCENT ERRORS OF THE SEVEN RODS. THE GROUND-TRUTH ELECTRON DENSITY VALUES OF TEFLON, SOFT-TISSUE AND AIR ARE OBTAINED FROM CATPHAN©600 PHANTOM MANUAL. THE ELECTRON DENSITIES OF IODINE SOLUTIONS ARE CALCULATED BASED ON IODINE CONCENTRATIONS.

Rods	1 Teflon	2 Delrin	3 Iodine solution (10 mg/ml)	4 Polystyrene	5 LDPE	6 PMP	7 Iodine solution (5 mg/ml)	RMS of Average Percent Errors
Ground truth	6.240	4.525	3.368	3.400	3.155	2.851	3.356	
Direct inversion	6.127	3.928	3.812	2.702	2.512	2.305	3.356	
Average Percent Errors $E(\%)$	1.8%	13.2%	13.2%	20.5%	20.4%	19.2%	0%	14.91%
Proposed	6.132	4.824	3.779	2.654	2.490	2.255	3.231	
Average Percent Errors $E(\%)$	1.7%	6.6%	12.2%	21.9%	21.1%	20.9%	3.7%	14.98%

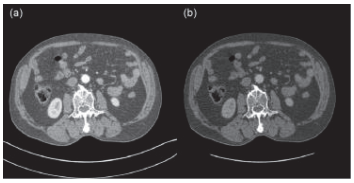

Fig. 3. The CT images of pelvis patient data. (a) The low-energy: 100kVp and (b) the high-energy: 140kVp. Display window is [0.012 0.022] mm^{-1}.

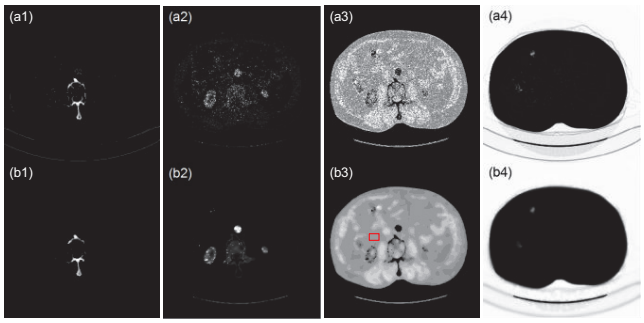

Fig. 4. The decomposed bone (first column), iodine (second column), soft-tissue (third column) and air (last column) images of the pelvis patient data. Row (a): direct inversion method; (b): proposed method. The red solid rectangle in (b3) indicates the region where the means and STDs in Table IV are calculated. Display windows are: [0.2 1] for bone images, [0.33 0.8] for iodine images, [0.3 0.8] for soft-tissue images, and [0.18 1] for air images, respectively.

variance-covariance matrix of decomposed basis materials as the statistical weight in the weighted least-square term for a better noise suppression performance. Under the mass and volume conservation constraints and the assumptions that each pixel contains at most three materials and material triplets vary among pixels, the proposed cost function is difficult to solve directly. We designed a series of pixel-wise separable quadratic surrogates (PWSQS) to monotonically decrease the cost function [4]. As the surrogates are pixel-wise separable, the proposed method can update all pixels simultaneously, which allows faster convergence. The proposed method is a practical image-domain method where CT images at low and high energies are modeled as linear combinations of linear attenuation coefficients of basis materials with weights of their volume fractions. The proposed method incorporates noise correlation into statistical weight in PWLS estimation, which effectively overcomes the issue of significantly magnified noise in the decomposed basis materials by the direct inversion method [2] and retains anatomical structure profiles faithfully.

The cost function of the proposed method has two tunable parameters (i.e., regularization coefficient and edge-preserving coefficient). In current implementation, for balancing noise suppression and spatial resolution maintenance preferably, we empirically selected the two parameters. In the future, we will further investigate optimal selection of these parameters using material-cross penalty. We assume uniform distribution of noise variance map in CT images, and measure the noise variance inside a manually selected region of homogeneous material. The performance of the proposed method can be further improved by substituting the uniform noise variance map with a pixel-dependent one. Several analytic algorithms are proposed in literature to calculate the variable noise variance map for CT images. In future work, we will combine noise variance estimation with the proposed decomposition method, and evaluate its performance on objects of clinical interests.

V. REFERENCES

[1] R. E. Alvarez and A. Macovski, "Energy-selective reconstructions in x-ray computerised tomography," *Phys. Med. Biol*., vol. 21, no. 5, pp. 733-44, Sep. 1976.

[2] P. R. S. Mendonca, P. Lamb, and D. Sahani, "A flexible method for multi-material decomposition of dual-energy CT images," *IEEE Trans. Med. Imag*., vol. 33, no. 1, pp. 99-116, Jan. 2014.

[3] R. F. Barber, E. Y. Sidky, T. G. Schmidt and X. Pan, "An algorithm for constrained one-step inversion of spectral CT data," *arXiv preprint arXiv*:1511.03384. 2015.

[4] Y. Long, and J. A. Fessler, "Multi-material decomposition using statistical image reconstruction for spectral CT," *IEEE Trans. Med. Imag*., vol. 33, no. 8, pp. 1614-26, Apr. 2014.

[5] T. Niu, X. Dong, M. Petrongolo, and L. Zhu, "Iterative image-domain decomposition for dual-energy CT," *Med. Phys*., vol. 41, no. 4, pp. 041901, Mar. 2014.

[6] X. Liu, L. Yu, A.N. Primak, and C. H. McCollough, "Quantitative imaging of element composition and mass fraction using dual-energy CT: three-material decomposition," *Med. Phys*., vol. 36, no. 5, pp. 1602-9, Apr. 2009.

[7] J. A. Fessler and W. L. Rogers, "Spatial resolution properties of penalized likelihood image reconstruction methods: Space-invariant tomographs," IEEE Trans. Im. Proc., vol. 5, no. 9, pp. 1346–58, Sep. 1996.

Fast Quantitative Evaluation of the Resolution of Compressed Sensing Tomographic Reconstructions

Jonas Dittmann*, Michael Trapp*, Kilian Dremel*
*Lehrstuhl für Röntgenmikroskopie, Universität Würzburg, Germany

***Abstract*—Compressed Sensing changes the relation between available data and achievable resolution in tomographic reconstructions. In contrast to classical Filtered Backprojection, the spatial resolution of Compressed Sensing reconstructions is primarily dependent on the structure of the imaged sample rather than solely on the amount of acquired projection images.**

While this on the one hand facilitates reconstruction from a reduced number of projections in many cases, it on the other hand complicates the quantification of the actually achieved spatial resolution that is now also dependent on the image to be reconstructed.

In order to quantify the reliability (i.e. the local resolution) of each pixel of a Compressed Sensing reconstruction, we parallelize the local point spread function (LPSF) approach and demonstrate first results showing the steady improvement of measured resolution with progression of an iterative Total Variation minimizing tomographic reconstruction algorithm.

Analyzing the reconstruction quality of spatially localized signals is particularly relevant to Compressed Sensing in computed tomography, as exact recoverability of such features is its fundamental assumption.

***Index Terms*—Compressed Sensing, Computed Tomography, Resolution**

I. Introduction

COMPRESSED Sensing (CS), i.e. the reconstruction of signals from incomplete data (under certain conditions), plays an important role in the field of Computed Tomography due to the prospect of reduced X-ray dose or acquisition time, depending on the particular application.

Although the exact reconstruction principle [1], [2] gives a well founded theory for successful complete signal recovery, not all assumptions are met precisely in practice. On the one hand, the linear imaging model is not strictly correct in the presence of beam hardening, scattering and noise, and on the other hand time constraints always impose limits on the practically achievable solution to the computationally costly optimization task definded by CS theory. The quality of the reconstruction result is in particular strongly dependent on the image to be reconstructed itself.

In order to utilize Compressed Sensing computed tomography as a reliable measurement instrument, the ability to quantify the precision of the obtained reconstructions is thus essential. Similar to classical Filtered Backprojection (FBP), the impulse response or point spread function will generally not be translation invariant over the spatial dimensions of the reconstructed images. In contrast to FBP though, a point spread function of a nonlinear operator as required for CS reconstrucion can only be defined locally in the space of all possible outputs of that operator, i.e. will besides spatial location also depend on the image to be reconstructed.

Contact: jonas.dittmann@physik.uni-wuerzburg.de

This approach of local point spread functions (LPSF) was presented by several authors [3]–[5] in the context of iterative maximum-likelihood reconstruction techniques and recently applied to CS reconstructions in magnetic resonance imaging by Wech et al. [6]. We will use it to evaluate the performance of an iterative CS reconstruction algorithm for X-ray computed tomography. In order to obtain fully spatially resolved resolution information for a particular reconstruction result, we extend the LPSF approach to simultaneous evaluation of many spatial locations in order to reduce the required computation time to a feasible amount.

II. Theory

Given a linear forward model of the measurement process $\mathbf{A}$, a nonlinear iterative reconstruction procedure $\mathbf{R}^{\mathrm{CS}}$, the measured data $\mathbf{g}$, the signal to be recovered $\mathbf{f}$, the perturbation $\mathbf{p}_j$ with j indicating the location of the nonzero in $\mathbf{p}_j$, the LPSF $\mathbf{l}_j(\mathbf{f})$ for pixel j is defined in the neighborhood of $\mathbf{f}$ as

$$\mathbf{l}_j(\mathbf{f}) = \mathbf{R}^{\mathrm{CS}}(\mathbf{g} + \mathbf{A}\mathbf{p}_j) - \mathbf{R}^{\mathrm{CS}}(\mathbf{g})\,.$$

In order for the LPSF to be independent of the actual amplitude of the perturbation $\mathbf{p}_j$, the latter has to be small enough such that

$$\lim_{\alpha\to 0}\frac{1}{\alpha}\left(\mathbf{R}^{\mathrm{CS}}(\mathbf{g}+\alpha\mathbf{A}\mathbf{p}_j)-\mathbf{R}^{\mathrm{CS}}(\mathbf{g})\right) \approx \mathbf{R}^{\mathrm{CS}}(\mathbf{g}+\mathbf{A}\mathbf{p}_j)-\mathbf{R}^{\mathrm{CS}}(\mathbf{g})$$

holds, i.e. such that a linear expansion of $\mathbf{R}^{\mathrm{CS}}$ around $\mathbf{g}$ is valid [4], [6].

As a measure of resolution, the standard deviation σ of a gaussian fit to its respective LPSF will be attributed to each image pixel j.

The LPSF has to be evaluated for each pixel (or voxel, in 3D) of the tomogram to get a full resolution map of the latter. This implies that the reconstruction has to be repeated for a perturbation at each pixel's location, i.e. 2×10^5 times even for a rather small tomographic slice of 500×500 pixels. At reconstruction times in the order of magnitude of minutes, this would take in the range of a year.

To greatly reduce the amount of necessary calls to the reconstruction algorithm $\mathbf{R}^{\mathrm{CS}}$ we thus parallelize the process of LPSF analysis by introducing many perturbations p_j simultaneously. This has two implications which need to be considered: First, the sparsity properties of the solution are changed which is relevant to the reconstruction algorithm

itself. By ensuring that the introduced signal components are few compared to the signal itself, this should be negligible. Secondly, the presence of multiple perturbations affects the interpretation of the LPSF as local expansion coefficient of $\mathbf{R}^{\mathrm{CS}}$, which we also neglect for the purpose of resolution estimation.

Expressed formally, we assume

$$\sum_{j \in S_k} \mathbf{l}_j \approx \mathbf{R}^{\mathrm{CS}}(\mathbf{g} + \sum_{j \in S_k} \mathbf{A}\mathbf{p}_j) - \mathbf{R}^{\mathrm{CS}}(\mathbf{g}),$$

where S_k describes a set of perturbed pixels.

Overlapping of the accumulated LPSFs is avoided by ensuring that the respective pixels j in the set S_k have a sufficient spatial distance from each other. By fitting multiple gaussians to the result, the resolution at each of the locations j in S_k can be determined simultaneously (i.e. with only one call to $\mathbf{R}^{\mathrm{CS}}$).

By regarding all possible disjoint sets S_k, a complete map of LPSF widths can be obtained. The required number of calls to the time consuming algorithm $\mathbf{R}^{\mathrm{CS}}$ is now the amount of necessary sets of perturbations or approximately the amount of regarded pixels divided by the average size of the sets.

The sets S_k are created by first defining a minimal distance between each perturbation and then randomly selecting indices that are in no previous set yet and respect the minimal distance to every other pixel index in the current set. If no further points can be found in a fixed number of attempts, further sets will be populated until no unregarded locations are left. The minimum required distance between pixels within each set S_k must be chosen such that the LPSFs do not overlap significantly in order to fit gauss curves to each LPSF individually.

III. Results

The described method is used to characterize the performance of a SART-based[1] iterative Total Variation (TV) minimizing tomographic reconstruction algorithm as described in [7]. The algorithm can be summarized as alternating SART sub-iterations with TV gradient descent steps using a custom stepsize heuristic. The test phantom (cf. Fig. 1) is specifically designed to challenge CS reconstruction techniques with respect to spatial resolution.

The simulated measurement consists of 105 fanbeam projections of the phantom (defined on a 512^2 grid) onto a 512 pixel wide detector array. The projection angles are equidistantly distributed over 360°, and the fanbeam opening angle is 15°. Classically, the required number of projections for complete reconstruction by Filtered Backprojection is about the $\frac{\pi}{2}$-fold of the amount of detector bins [9]. 105 projections as used in this example thus represent less than 15 percent of the classically required data.

A first impression of this test setup is given in Fig. 1 which shows a comparison of regular SART versus Compressed Sensing reconstruction. Visually, the resolution has clearly increased with respect to the regular reconstruction.

To quantify the actual resolution achieved, the described simultaneous LPSF characterization technique is applied. In this

[1] Simultaneous Algebraic Reconstruction Technique [8]

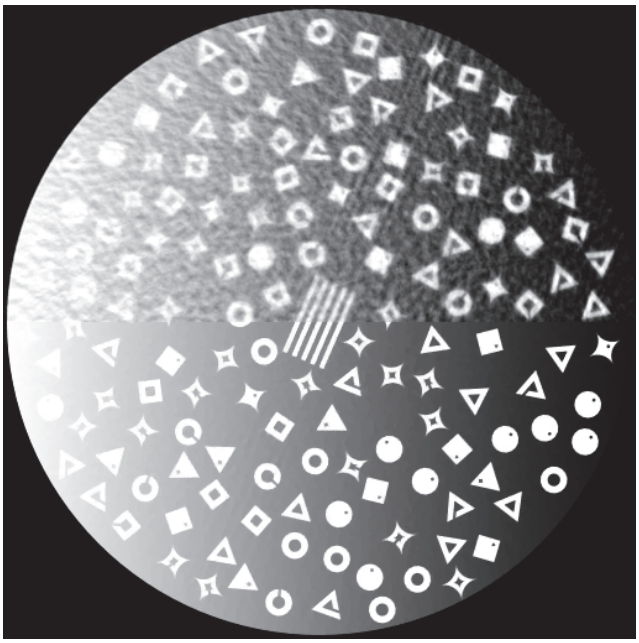

Fig. 1. Example of a reconstruction of an 512x512 tomographic slice from 105 projections of a test phantom. The upper half shows the result of a regular SART algorithm, while the bottom half shows the result of the Total Variation minimizing Compressed Sensing algorithm. Both used 200 iterations. The phantom was designed to have no specific symmetry, contain structures at different level of detail and contrast and cover most important geometric primitives [7].

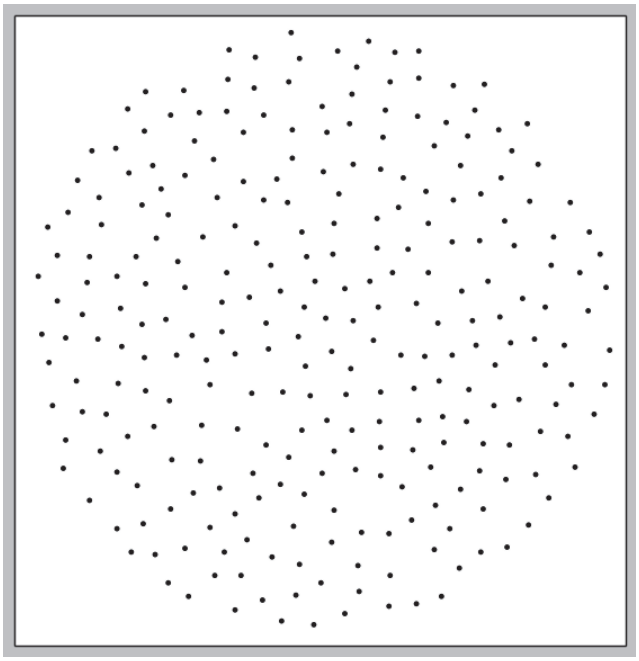

Fig. 2. Example of the distribution of perturbations within one set S_k. The minimal distance was chosen to be 20 pixels here and the total amount of simultaneous perturbations is 273 here. For the computation of the local PSF's, these perturbations will be forward projected and added to the measurements.

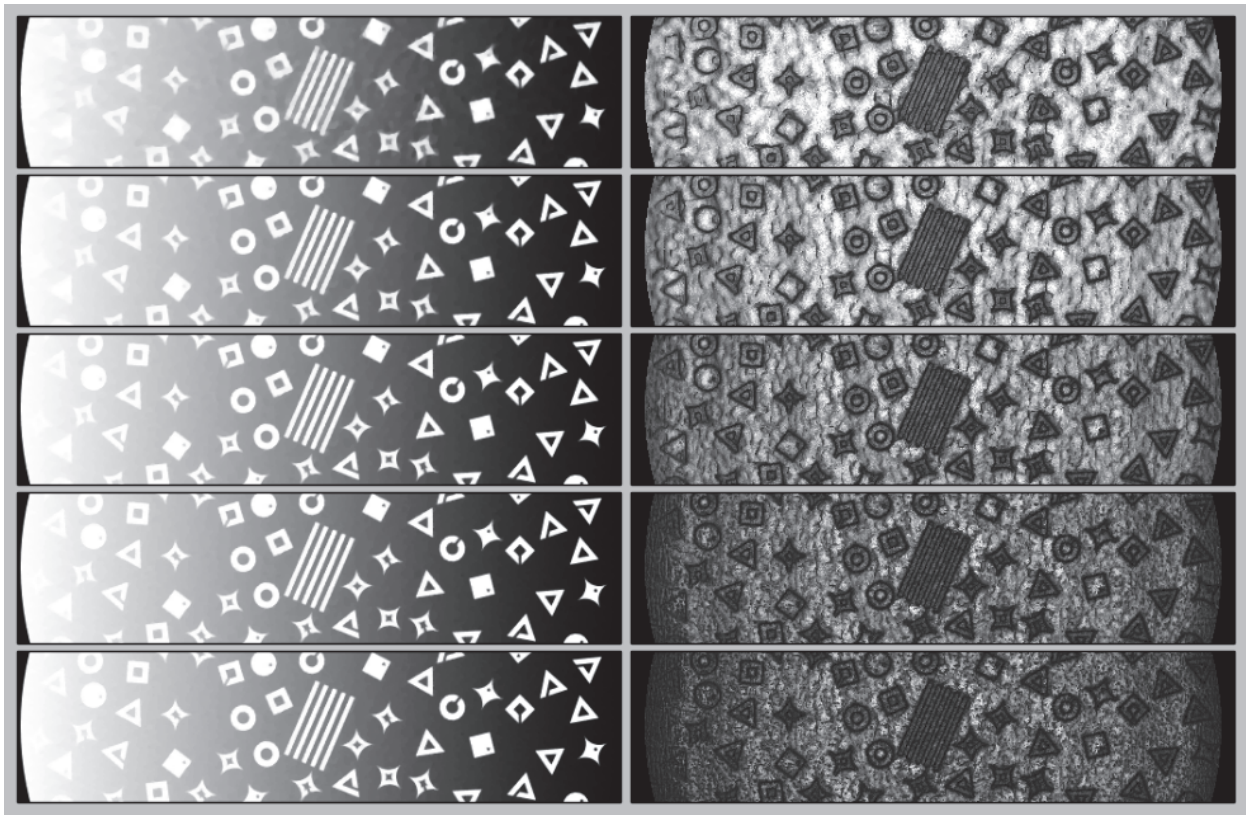

Fig. 3. The reconstruction results (left column) as well as the corresponding resolution maps (right column) are shown for different stages in the iterative reconstruction process. The reconstruction is based on 105 projections of the 512×512 phantom. From top to bottom the results at 20, 50, 100, 150 and 200 iterations are shown. The colourbar for the right column ranges from black for $\sigma = 0$ to white for $\sigma = 3$. $\sigma = 0.4$ implies perfect reconstruction of the perturbation, while larger sigmas indicate diminished resolution.

case, a minimal distance of 20 pixels between simultaneous perturbations is defined resulting in an average of 280 parallel LPSF measurements per reconstruction run. The perturbation amplitude was chosen to be 10 percent of the maximum value in the phantom, which was tested to comply with the linear expansion interpretation of the LPSF definition (data not shown). An exemplary perturbation pattern $\sum_{j \in S_k} \mathbf{p_j}$ is depicted in Figure 2. To complete the entire resolution map a total of 682 reconstruction runs with different perturbation patterns were evaluated.

Figure 3 shows the progress of the iterative reconstruction algorithm both in terms of the actual reconstruction result at increasing iteration counts (left column) as well as the corresponding LPSF sigma maps (right column). For demonstration purposes, only a representative middle section of each slice is shown. Most recognizable is the effect of steadily increasing resolution in the low contrast region at the very left of the phantom. The high contrast edges emerge quite fast, while the low contrast background only converges very slowly to better resolution values (indicated by smaller standard deviations σ, i.e. darker shades of grey in Fig. 3 (right), of the gauss fits to each LPSF).

IV. Discussion

We proposed a massive parallelization of the LPSF evaulation technique in order to facilitate fully spatially resolved resolution maps for a given reconstruction problem in a manageable amount of time. Whe used it to characterize the performance of a Compressed Sensing reconstruction procedure and demonstrate the (expected) increase in image quality throughout the iterative process. When concentrating on small and low contrast features of the reconstructed phantom, the results indicate a good correlation between measured and perceived image quality, while the apparent property of the employed reconstruction technique to generally perform ”worse” in areas of actually low variation will leave room for further investigations.

The LPSF ansatz is particularly interesting in the context of CS, as it allows to test the validity of the theoretic assumptions on a case by case basis, i.e. it can particularly give a straight forward answer to the question whether any given image feature will or will not be detectable by a given incomplete imaging matrix in combination with some practical (and possibly imperfect) implementation of the CS optimization task.

Regarding the application to engineering problems though, the perceived resolution of a CT scan not only depends on the ability of a reconstruction technique to reproduce impulse responses, yet also on the local contrast of that impulse response with respect to noise, which was not shown in the present article. In order to provide meaningful resolution measures to CT users, an extended definition beyond LPSF

width is necessary.

V. Conclusion and future work

By relaxing the strict interpretation of the local point spread function (LPSF) as a locally linear expansion of a nonlinear operator, we massively parallelize the process of LPSF evaluation and facilitate the evaluation of fully spatially resolved resolution maps also for computationally costly reconstruction operators. These maps foremost serve as an objective performance measure for reconstruction techniques and indicate for each part of an image whether small variations in the imaged sample adequatly translate to the reconstructed image.

As the latter is the fundamental assumption of CS theory, respective objective tests are an important tool both for algorithm development and image assessment.

The technique was demonstrated on an iterative Compressed Sensing tomographic reconstructions using about 15 percent of the classically required amount of measurements. The obtained resolution maps still leave some questions especially with respect to the correlation of strong contrasts in the data and low σ, i.e. high resolution the LPSF map.

In order to utilize the LPSF technique for image (in contrast to algorithm) quality assessment in practice, further study of the relation between measured impulse response and perceived quality in presence of noise will be necessary.

With respect to the testing of the individual validity of CS assumptions, testing the reproducibilty of differently shaped impulses will be a relevant question as well, given that CS strongly depends on the assumption of spatially localized signal features.

Acknowledgment

The authors would like to thank Tobias Wech for making us aware of the local PSF approach.

References

[1] E. J. Candès, J. Romberg, and T. Tao, "Robust uncertainty principles: Exact signal reconstruction from highly incomplete frequency information," *Information Theory, IEEE Transactions on*, vol. 52, no. 2, pp. 489–509, 2006.

[2] E. J. Candes and T. Tao, "Near-optimal signal recovery from random projections: Universal encoding strategies?" *Information Theory, IEEE Transactions on*, vol. 52, no. 12, pp. 5406–5425, 2006.

[3] J. A. Stamos, W. L. Rogers, N. H. Clinthorne, and K. F. Koral, "Object-dependent performance comparison of two iterative reconstruction algorithms," *IEEE Transactions on Nuclear Science*, vol. 35, no. 1, pp. 611–614, Feb 1988.

[4] D. Wilson and B. Tsui, "Spacial resolution properties of fb and ml-em reconstruction methods," in *Nuclear Science Symposium and Medical Imaging Conference, 1993., 1993 IEEE Conference Record.* IEEE, 1993, pp. 1189–1193.

[5] J. A. Fessler and W. L. Rogers, "Spatial resolution properties of penalized-likelihood image reconstruction: space-invariant tomographs," *Image Processing, IEEE Transactions on*, vol. 5, no. 9, pp. 1346–1358, 1996.

[6] T. Wech, D. Stäb, J. C. Budich, A. Fischer, J. Tran-Gia, D. Hahn, and H. Köstler, "Resolution evaluation of mr images reconstructed by iterative thresholding algorithms for compressed sensing," *Medical physics*, vol. 39, no. 7, pp. 4328–4338, 2012.

[7] J. Dittmann, "Tomographic reconstruction from few x-ray projections based on compressed sensing theory," Master's thesis, University of Wuerzburg, Germany, Jun 2013.

[8] A. H. Andersen and A. C. Kak, "Simultaneous algebraic reconstruction technique (sart): a superior implementation of the art algorithm," *Ultrasonic imaging*, vol. 6, no. 1, pp. 81–94, 1984.

[9] T. M. Buzug, *Einführung in die Computertomographie: mathematisch-physikalische Grundlagen der Bildrekonstruktion*. Springer-Verlag, 2011.

Selection of Monochromatic Energy-Pair for Hybrid Decomposition in Dual-Energy CT

Sathish Ramani and Bruno De Man
GE Global Research, Niskayuna, NY 12309, USA

***Abstract*—Dual-energy (DE) computed tomography (CT) provides the ability to decompose an object into two (or more) representative material components. The hybrid decomposition (HD) approach of Shen *et al.* for DECT combines the principles of existing sinogram- and image-based decomposition methods by first converting measured DE polychromatic data (poly-data) sets to a pair of *equivalent* monochromatic data (mono-data) sets at a given monochromatic energy-pair (MEP) in the sinogram-domain followed by material decomposition in the image-domain. However, similar to sinogram-based methods, HD can lead to correlated noise in the resulting mono-datasets depending upon the choice of MEP, which may not be desirable for further (non-linear) processing, e.g., model-based image reconstruction (MBIR), of the mono-datasets. In this work, we present two simple approaches for selecting MEP for HD so as to reduce the amount of noise-correlation between the pair of mono-datasets. This strategy *approximately* decouples the statistical-modeling of the mono-datasets allowing us to apply conventional MBIR techniques *individually* on each mono-dataset. We demonstrate the usefulness of the proposed strategy using simulations.**

Keywords*—Dual-energy, material decomposition, monochromatic data, model based image reconstruction.

I. Introduction

Dual-energy (DE) computed tomography (CT) offers many advantages over conventional CT including elimination of beam-hardening artifacts and decomposition of the scanned object into two or more physically meaningful basis functions [1], [2], [3], [4]. Existing material decomposition (MD) approaches can be broadly classified as either image-based [4] or sinogram-based [1], [2], [3]. Image-based methods [4] have the advantage that the DE-images can be reconstructed from the measured DECT datasets *independently* for each energy, so that the reconstruction and denoising algorithms can use noise statistics of the *original* DECT measurements. However, image-based methods need to rely on approximate methods to correct for beam-hardening in the reconstructed DE-images and therefore are not quantitatively accurate.

Sinogram-based MD has the advantage of accurately eliminating beam-hardening errors in the projection-domain before those errors propagate and spread all over the reconstructed image. However, they introduce (positive and negative) noise correlation between the decomposed material-sinograms requiring advanced (and complicated) MBIR techniques to suppress correlated noise.

This work is supported by Department of Homeland Security, Science and Technology Directorate, Explosives Division, BAA 13-05, Contract # HSHQDC-14-C-B0048. The authors thank Dr. Yannan Jin, GE Global Research, Niskayuna, NY, USA, for helpful suggestions.

Zhang *et al.* proposed a MBIR method [5] that accounts for noise correlation in decomposed material-sinograms in the statistical-modeling. Long *et al.* [6] proposed to incorporate MD as part of the MBIR reconstruction problem and jointly reconstruct all material-images from all measurements. While [6] considers a more wholesome reconstruction model than [5], both [5], [6] perform joint reconstruction of material-images and can thus be computationally expensive.

Our focus in this work is to develop a method that not only eliminates spectral artifacts accurately, but is also computationally simpler than joint reconstruction techniques. For this, we use the hybrid decomposition (HD) method of Shen *et al.* [7] that combines the principles underlying sinogram- and image-domain methods: first, the measured DE polychromatic projection data (poly-data) sets $(\boldsymbol{p}_{\mathsf{L}}, \boldsymbol{p}_{\mathsf{H}})$ (at low (L) and high (H) kVps) are converted in to *equivalent* monochromatic projection data (mono-data) sets $(\boldsymbol{p}_{\mathsf{E}_1}, \boldsymbol{p}_{\mathsf{E}_2})$ at a chosen monochromatic energy-pair (MEP) given by $(\mathsf{E}_1, \mathsf{E}_2)$, where we assume $\mathsf{E}_1 < \mathsf{E}_2$. Next, monochromatic images (mono-images) are reconstructed from the mono-datasets, which are used for image-domain material decomposition. Shen *et al.* [7] demonstrated the effectiveness of HD for eliminating spectral artifacts and estimation of material properties in a *noise-free* setting. Due to its similarity to sinogram-domain methods however, HD also leads to correlated noise in $(\boldsymbol{p}_{\mathsf{E}_1}, \boldsymbol{p}_{\mathsf{E}_2})$ when $(\boldsymbol{p}_{\mathsf{L}}, \boldsymbol{p}_{\mathsf{H}})$ are noisy.

Rather than tackling correlated noise by joint reconstruction techniques [5], [6], we propose to reduce noise correlation in $(\boldsymbol{p}_{\mathsf{E}_1}, \boldsymbol{p}_{\mathsf{E}_2})$ by selecting $(\mathsf{E}_1, \mathsf{E}_2)$ suitably. Specifically, we propose two approaches where we optimize $(\mathsf{E}_1, \mathsf{E}_2)$ (a) jointly so as to minimize the *cumulative magnitude* of noise covariance between $(\boldsymbol{p}_{\mathsf{E}_1}, \boldsymbol{p}_{\mathsf{E}_2})$—**Method-1**; (b) separately to minimize the *cumulative magnitude* of noise covariance between $(\boldsymbol{p}_{\mathsf{E}_1}, \boldsymbol{p}_{\mathsf{H}})$ and between $(\boldsymbol{p}_{\mathsf{E}_2}, \boldsymbol{p}_{\mathsf{L}})$, respectively—**Method-2**. While the reasoning behind **Method-1** is straightforward, **Method-2** amounts to reducing "flow" of noise from high-kVp poly-dataset to low-energy mono-dataset and vice versa, thus encouraging the noise in $\boldsymbol{p}_{\mathsf{E}_1}$ and $\boldsymbol{p}_{\mathsf{E}_2}$ to be more "similar" to that in $\boldsymbol{p}_{\mathsf{L}}$ and $\boldsymbol{p}_{\mathsf{H}}$, respectively. We observed in our experiments that both (a) and (b) led to similar choices for $(\mathsf{E}_1, \mathsf{E}_2)$. After optimizing $(\mathsf{E}_1, \mathsf{E}_2)$, we apply MBIR to $(\boldsymbol{p}_{\mathsf{E}_1}$ and $\boldsymbol{p}_{\mathsf{E}_2})$ independently and perform material decomposition on the resulting mono-images. We show using simulations that we obtain better quality material decompositions with optimized $(\mathsf{E}_1, \mathsf{E}_2)$ than without.

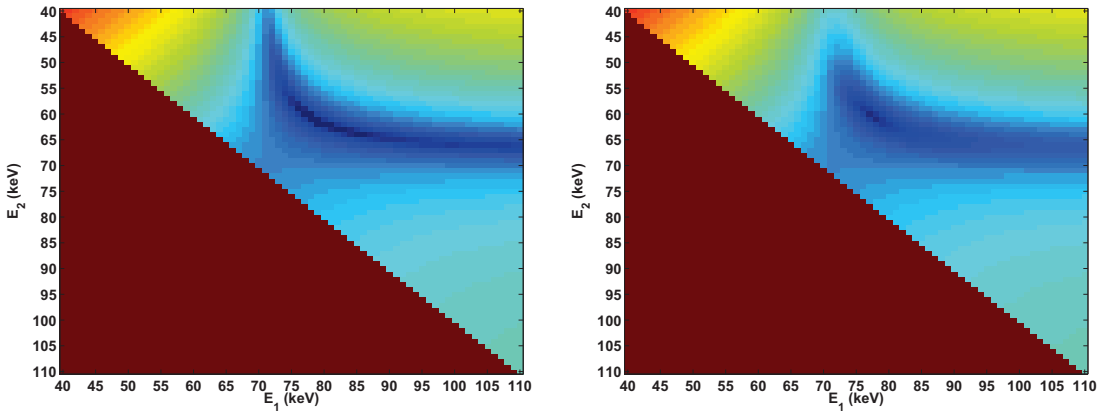

Fig. 1. Experiment 1. 2D-maps of covariance $\mathsf{C}_{\mathsf{E}_1,\mathsf{E}_2}$ in (7) for **Method-1**: Empirical (left); Estimated (right). These maps are symmetric about the identity line; only one side is shown. Both maps are shown on the same display window.

II. Measurement Model

We assume a simple Poisson-Gaussian noise model [5, Sec. A] for the DECT raw measurements $(\lambda_{i,\mathsf{L}}, \lambda_{i,\mathsf{H}})$, with respective raw air-scan measurements $(\lambda_{i,0,\mathsf{L}}, \lambda_{i,0,\mathsf{H}})$, $i = 1, \ldots, M$. We assume that the raw measurements are background-subtracted and that noise in $\lambda_{i,\mathsf{L}}$ and $\lambda_{i,\mathsf{H}}$ are *statistically independent* of each other. The projection-values $\boldsymbol{p}_{\mathsf{L}} = \{p_{i,\mathsf{L}}\}_{i=1}^{M}$ and $\boldsymbol{p}_{\mathsf{H}} = \{p_{i,\mathsf{H}}\}_{i=1}^{M}$ are then computed as

$$p_{i,\star} \quad = \quad -\log\left[\frac{\lambda_{i,\star}}{\lambda_{i,0,\star}}\right], i = 1, \ldots, M, \ \star = \{\mathsf{L}, \mathsf{H}\}. \quad (1)$$

Based on a first-order Taylor-approximation of (1), we can arrive at the following approximation [5, Sec. A] of the covariance of $p_{i,\mathsf{L}}$ and $p_{i,\mathsf{H}}$:

$$\mathsf{C}_{\mathsf{L},\mathsf{H}}^{(i)} \approx \mathsf{diag}\left\{\frac{\lambda_{i,\mathsf{L}} + \sigma_{\mathrm{e}}^2}{\lambda_{i,\mathsf{L}}^2}, \frac{\lambda_{i,\mathsf{H}} + \sigma_{\mathrm{e}}^2}{\lambda_{i,\mathsf{H}}^2}\right\}, \quad (2)$$

where σ_{e} is the standard deviation of electronic noise.

III. Polychromatic-to-Monochromatic Conversion & Covariance Estimation

While Shen *et al.* [7] used a polynomial-fitting approach for converting DE polychromatic raw measurements to monochromatic raw data, we use a similar approach in the projection domain to convert measured poly-datasets $(\boldsymbol{p}_{\mathsf{L}}, \boldsymbol{p}_{\mathsf{H}})$ to mono-datasets $(\boldsymbol{p}_{\mathsf{E}_1}, \boldsymbol{p}_{\mathsf{E}_2})$. Specifically, the ith mono-data sample p_{i,E_j}, for the two energies $\{\mathsf{E}_j,\ j = 1, 2\}$, is estimated using the following polynomial expansion

$$p_{i,\mathsf{E}_j} = f_{\mathsf{E}_j}(p_{i,\mathsf{L}}, p_{i,\mathsf{H}}) \stackrel{\mathrm{def}}{=} \sum_{\substack{k_1=0,\ldots,K \\ k_2=0,\ldots,K \\ 0<k_1+k_2\leq K}} a_{k_1,k_2}^{(\mathsf{E}_j)} [p_{i,\mathsf{L}}]^{k_1} [p_{i,\mathsf{H}}]^{k_2}, \quad (3)$$

with $K = 5$, for $i = 1, \ldots, M$. We obtain the set of coefficients $\{a_{k_1,k_2}^{(\mathsf{E}_j)}\}$ by least-squares fit of a known set of (noise free) mono-data samples $\{p_{n,\mathsf{E}_j}\}_{n=1}^{N}$ for a known set of (noise free) pair of poly-data samples $\{p_{n,\mathsf{L}}, p_{n,\mathsf{H}}\}_{n=1}^{N}$. To save compute time, we precompute and store $\{a_{k_1,k_2}^{(\mathsf{E}_j)}\}$ for a range of mono-energies (E_j) for a given low- and high-kVp DE protocol.

Based on (2) and a first-order Taylor-expansion of $f_{\mathsf{E}_1}(p_{i,\mathsf{L}}, p_{i,\mathsf{H}})$ in (3), we can then arrive at the following approximations for the covariance of $(p_{i,\mathsf{E}_1}, p_{i,\mathsf{E}_2})$:

$$\mathsf{C}_{\mathsf{E}_1,\mathsf{E}_2}^{(i)} \approx [\nabla f_{\mathsf{E}_1}(p_{i,\mathsf{L}}, p_{i,\mathsf{H}})]' \ \mathsf{C}_{\mathsf{L},\mathsf{H}}^{(i)} \ [\nabla f_{\mathsf{E}_2}(p_{i,\mathsf{L}}, p_{i,\mathsf{H}})], \quad (4)$$

the covariance of $(p_{i,\mathsf{E}_1}, p_{i,\mathsf{H}})$:

$$\mathsf{C}_{\mathsf{E}_1,\mathsf{H}}^{(i)} \approx \left(\frac{\lambda_{i,\mathsf{H}} + \sigma_{\mathrm{e}}^2}{\lambda_{i,\mathsf{H}}^2}\right)\left(\frac{\partial f_{\mathsf{E}_1}(p_{i,\mathsf{L}}, p_{i,\mathsf{H}})}{\partial p_{i,\mathsf{H}}}\right), \quad (5)$$

and the covariance of $(p_{i,\mathsf{E}_2}, p_{i,\mathsf{L}})$:

$$\mathsf{C}_{\mathsf{E}_2,\mathsf{L}}^{(i)} \approx \left(\frac{\lambda_{i,\mathsf{L}} + \sigma_{\mathrm{e}}^2}{\lambda_{i,\mathsf{L}}^2}\right)\left(\frac{\partial f_{\mathsf{E}_2}(p_{i,\mathsf{L}}, p_{i,\mathsf{H}})}{\partial p_{i,\mathsf{L}}}\right). \quad (6)$$

IV. Selection of $(\mathsf{E}_1, \mathsf{E}_2)$

Using the estimate, $\mathsf{C}_{\mathsf{E}_1,\mathsf{E}_2}^{(i)}$, of the covariance of $(p_{i,\mathsf{E}_1}, p_{i,\mathsf{H}})$, in **Method-1** we propose to select the MEP $(\mathsf{E}_1, \mathsf{E}_2)$ by jointly minimizing the *cumulative magnitude* of $\mathsf{C}_{\mathsf{E}_1,\mathsf{E}_2}^{(i)}$ over all data samples $i = 1, \ldots, M$, i.e.,

$$(\mathsf{E}_1^{\mathsf{opt}_1}, \mathsf{E}_2^{\mathsf{opt}_1}) \stackrel{\mathrm{def}}{=} \arg\min_{(\mathsf{E}_1,\mathsf{E}_2)} \left\{\mathsf{C}_{\mathsf{E}_1,\mathsf{E}_2} \stackrel{\mathrm{def}}{=} \sum_{i=1}^{M} \left|\mathsf{C}_{\mathsf{E}_1,\mathsf{E}_2}^{(i)}\right|\right\}. \quad (7)$$

We consider the *cumulative magnitude* in (7) so as to reduce both positive and negative correlation between $(p_{i,\mathsf{E}_1}, p_{i,\mathsf{E}_2})$ combined over all data samples. In **Method-2**, we obtain the desired MEP by individual minimization of the *cumulative magnitudes* of $\mathsf{C}_{\mathsf{E}_1,\mathsf{H}}^{(i)}$ and $\mathsf{C}_{\mathsf{E}_2,\mathsf{L}}^{(i)}$, i.e,

$$\mathsf{E}_1^{\mathsf{opt}_2} \stackrel{\mathrm{def}}{=} \arg\min_{\mathsf{E}_1}\left\{\mathsf{C}_{\mathsf{E}_1,\mathsf{H}} \stackrel{\mathrm{def}}{=} \sum_{i=1}^{M}\left|\mathsf{C}_{\mathsf{E}_1,\mathsf{H}}^{(i)}\right|\right\}, \quad (8)$$

$$\mathsf{E}_2^{\mathsf{opt}_2} \stackrel{\mathrm{def}}{=} \arg\min_{\mathsf{E}_2}\left\{\mathsf{C}_{\mathsf{E}_2,\mathsf{L}} \stackrel{\mathrm{def}}{=} \sum_{i=1}^{M}\left|\mathsf{C}_{\mathsf{E}_2,\mathsf{L}}^{(i)}\right|\right\}. \quad (9)$$

We perform the above minimizations by an explicit search over a range of mono-energies, while in practice, sophisticated numerical algorithms may be employed for this purpose.

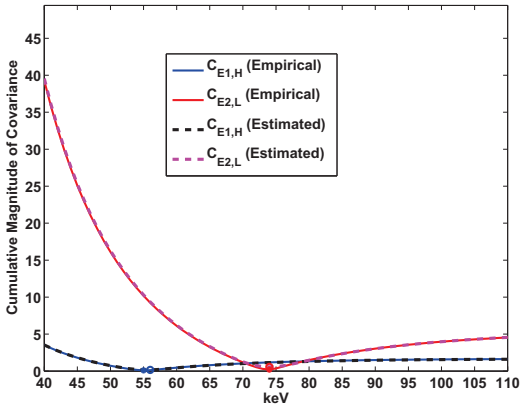

Fig. 2. Experiment 1. Plot of empirical and estimated covariances $\mathsf{C}_{\mathsf{E}_1,\mathsf{H}}$ and $\mathsf{C}_{\mathsf{E}_2,\mathsf{L}}$ in (8)-(9) for **Method-2** as a function of monochromatic energy.

TABLE I. EXPERIMENT 1: MONOCHROMATIC ENERGY-PAIRS SELECTED BY MINIMIZING COVARIANCES IN (7)-(9)

	[80, 140] kVp			
	Method-1 $(\mathsf{E}_1^{\mathsf{opt}_1}, \mathsf{E}_2^{\mathsf{opt}_1})$ (keV)		**Method-2** $(\mathsf{E}_1^{\mathsf{opt}_2}, \mathsf{E}_2^{\mathsf{opt}_2})$ (keV)	
mA	Empirical	Estimated	Empirical	Estimated
20	[62, 80]	[60, 77]	[55, 75]	[56, 74]
50	[61, 79]	[60, 77]	[55, 74]	[55, 73]
100	[61, 79]	[59, 76]	[55, 73]	[55, 73]
	[120, 180] kVp			
	Method-1 $(\mathsf{E}_1^{\mathsf{opt}_1}, \mathsf{E}_2^{\mathsf{opt}_1})$ (keV)		**Method-2** $(\mathsf{E}_1^{\mathsf{opt}_2}, \mathsf{E}_2^{\mathsf{opt}_2})$ (keV)	
mA	Empirical	Estimated	Empirical	Estimated
20	[71, 88]	[70, 86]	[68, 83]	[68, 83]
50	[71, 87]	[70, 85]	[68, 83]	[68, 83]
100	[71, 87]	[70, 85]	[68, 83]	[68, 82]

V. SIMULATION RESULTS

A. *Experiment 1*

We first verify the accuracy of the proposed covariance estimation and MEP selection procedures in Secs. III-IV. Using the CatSim simulation package [8], we generated noisy DE measurements (for a GE VCT-type system with energy-integrating detectors, 50 cm FOV, and no bowtie filter) for an analytical cylindrical water (density = 0.5 g/cm^3) phantom of 40 cm diameter enclosed in PVC cylinder of 5 mm thickness at $[80, 140]$ and $[120, 180]$ kVp-pairs of tube-voltages (888 channels $\times$ 1000 views for each kVp) with varying tube-currents (20 mA, 50 mA, 100 mA). Due to circular symmetry of the phantom, all views may be treated as independent noisy realizations of any one noise free view. For each mA and each kVp-pair, we computed *empirical* estimates of the covariances in the LHS of equations (4)-(6) by averaging over the 1000 views. We also computed the corresponding approximate estimates in the RHS of equations (4)-(6) from just one noisy view.

The empirical and estimated 2D-maps of $\mathsf{C}_{\mathsf{E}_1,\mathsf{E}_2}$ (7) in Fig. 1 agree in their trend. Similarly, the empirical and estimated values of $\mathsf{C}_{\mathsf{E}_1,\mathsf{H}}$ and $\mathsf{C}_{\mathsf{E}_2,\mathsf{L}}$ (8)-(9) as a function of mono-energy (in keV) in Fig. 2 closely agree with each other.

We list MEPs $(\mathsf{E}_1^{\mathsf{opt}_1}, \mathsf{E}_2^{\mathsf{opt}_1})$, and $(\mathsf{E}_1^{\mathsf{opt}_2}, \mathsf{E}_2^{\mathsf{opt}_2})$, that respectively minimized the empirical and estimated *cumulative magnitude* of covariances $\mathsf{C}_{\mathsf{E}_1,\mathsf{E}_2}$, and $\mathsf{C}_{\mathsf{E}_1,\mathsf{H}}$ and $\mathsf{C}_{\mathsf{E}_2,\mathsf{L}}$ (7)-(9) in Table IV. There is a good agreement between minimum-empirical-covariance and minimum-estimated-covariance MEPs for all considered kVp-pairs and tube-currents. There is a slight difference between $(\mathsf{E}_1^{\mathsf{opt}_1}, \mathsf{E}_2^{\mathsf{opt}_1})$ and $(\mathsf{E}_1^{\mathsf{opt}_2}, \mathsf{E}_2^{\mathsf{opt}_2})$ in Table IV, which is to be expected since $\mathsf{C}_{\mathsf{E}_1,\mathsf{E}_2}$ (7) is different from $\mathsf{C}_{\mathsf{E}_1,\mathsf{H}}$ and $\mathsf{C}_{\mathsf{E}_2,\mathsf{L}}$ (8)-(9). However, the values of $\mathsf{C}_{\mathsf{E}_1,\mathsf{E}_2}$ at $(\mathsf{E}_1^{\mathsf{opt}_1}, \mathsf{E}_2^{\mathsf{opt}_1})$ and $(\mathsf{E}_1^{\mathsf{opt}_2}, \mathsf{E}_2^{\mathsf{opt}_2})$ are close (as seen in Fig. 1), indicating that both $(\mathsf{E}_1^{\mathsf{opt}_1}, \mathsf{E}_2^{\mathsf{opt}_1})$ and $(\mathsf{E}_1^{\mathsf{opt}_2}, \mathsf{E}_2^{\mathsf{opt}_2})$ lead to a comparatively smaller covariance $\mathsf{C}_{\mathsf{E}_1,\mathsf{E}_2}$ in the converted mono-datasets.

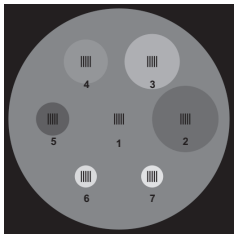

Fig. 3. Experiment 2. Cylindrical phantom with different materials: (1) Water, (2) Ethanol, (3) Graphite, (4) PVC, (5) PMMA, (6) Aluminium, (7) Salt (NaCl).

B. *Experiment 2*

We considered an analytical cylindrical water phantom of 20 cm diameter with material inserts illustrated in Fig. 3 and generated noisy DE datasets (for a GE VCT-type system with energy-integrating detectors, 20.8 cm FOV, and no bowtie filter) at $[80, 140]$ kVp-pair of tube-voltage (360 channels $\times$ 1000 views for each kVp) and 100 mA tube-current using CatSim [8]. We performed the minimizations in (7)-(9), obtained $(\mathsf{E}_1^{\mathsf{opt}_1}, \mathsf{E}_2^{\mathsf{opt}_1}) = [56, 74]$ keV and $(\mathsf{E}_1^{\mathsf{opt}_2}, \mathsf{E}_2^{\mathsf{opt}_2}) = [54, 72]$ keV, and computed the corresponding pairs of mono-datasets. For comparison, we also computed a pair of mono-datasets at a sub-optimal [compared to the optimalities in (7)-(9)] MEP $(\mathsf{E}_1^{\mathsf{sub}}, \mathsf{E}_2^{\mathsf{sub}}) = [48, 80]$ keV.

We ran an (accelerated) MBIR algorithm similar to that in [9, Table V] *independently* on each mono-dataset taking care to adjust the regularization-strength in each case to obtain similar resolution (horizontal-profile) across the bars in each material in Fig. 3. We then performed a two-component material decomposition on the resulting pairs of MBIR-reconstructed mono-images with *water* and *salt* (NaCl) as the basis materials. We also obtained the material decompositions for the noise free ground-truth using CatSim and computed root mean-squared difference (RMSD) of the noisy material decompositions (for each material) with respect to the ground-truth.

The water- and salt-images in Fig. 4 corresponding to $(\mathsf{E}_1^{\mathsf{opt}_1}, \mathsf{E}_2^{\mathsf{opt}_1})$ and $(\mathsf{E}_1^{\mathsf{opt}_2}, \mathsf{E}_2^{\mathsf{opt}_2})$ are comparable in quality, with $(\mathsf{E}_1^{\mathsf{opt}_1}, \mathsf{E}_2^{\mathsf{opt}_1})$ having the least noise. The sub-optimal choice $(\mathsf{E}_1^{\mathsf{sub}_1}, \mathsf{E}_2^{\mathsf{sub}_1})$ has more noise than either of the proposed choices. The RMSD of the densities of the water- and salt-components for each material is tabulated in Table V-B. Again, the RMSD-values for $(\mathsf{E}_1^{\mathsf{opt}_1}, \mathsf{E}_2^{\mathsf{opt}_1})$ and $(\mathsf{E}_1^{\mathsf{opt}_2}, \mathsf{E}_2^{\mathsf{opt}_2})$ are comparable with $(\mathsf{E}_1^{\mathsf{opt}_1}, \mathsf{E}_2^{\mathsf{opt}_1})$ yielding the lowest RMSD-values (in bold) and $(\mathsf{E}_1^{\mathsf{sub}_1}, \mathsf{E}_2^{\mathsf{sub}_1})$ yielding the highest RMSD-values for both water- and salt-components for all materials.

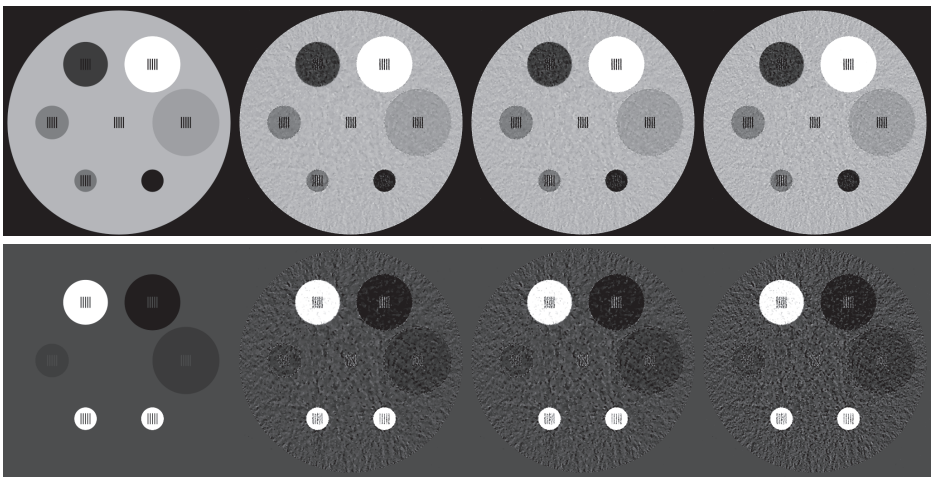

Fig. 4. Experiment 2. Water- (top) and Salt- (bottom) components of the phantom in Fig. 3 obtained from (left to right) noise free ground-truth, and pairs of mono-images corresponding to the choices of $(\mathsf{E}_1^{\mathsf{opt}_1}, \mathsf{E}_2^{\mathsf{opt}_1})$—**Method-1**, $(\mathsf{E}_1^{\mathsf{opt}_2}, \mathsf{E}_2^{\mathsf{opt}_2})$—**Method-2**, and $(\mathsf{E}_1^{\mathsf{sub}}, \mathsf{E}_2^{\mathsf{sub}})$—**Sub-optimal**, respectively. Display window is [0 1.5] g/cm^3 for Water-component (top) and [-0.1 0.5] g/cm^3 for Salt-component (bottom).

TABLE II. EXPERIMENT 2. RMSD OF ESTIMATED DENSITIES OF WATER AND SALT

Water component (g/cm^3) of the decomposition

Material	Ground-truth Density	RMSD for $(\mathsf{E}_1^{\mathsf{opt}_1}, \mathsf{E}_2^{\mathsf{opt}_1})$ **Method-1**	RMSD for $(\mathsf{E}_1^{\mathsf{opt}_2}, \mathsf{E}_2^{\mathsf{opt}_2})$ **Method-2**	RMSD for $(\mathsf{E}_1^{\mathsf{sub}}, \mathsf{E}_2^{\mathsf{sub}})$ **Sub-Optimal**
Water	1.0000	**0.0515**	0.0577	0.0718
Ethanol	0.8338	**0.0443**	0.0497	0.0656
Graphite	1.6868	**0.0462**	0.0537	0.0701
PVC	0.1560	**0.0705**	0.0789	0.0898
PMMA	0.5993	**0.0489**	0.0542	0.0693
Aluminium	0.5318	**0.0717**	0.0792	0.0906
Salt	0	**0.0863**	0.0943	0.1034

Salt component (g/cm^3) of the decomposition

Material	Ground-truth Density	RMSD for $(\mathsf{E}_1^{\mathsf{opt}_1}, \mathsf{E}_2^{\mathsf{opt}_1})$ **Method-1**	RMSD for $(\mathsf{E}_1^{\mathsf{opt}_2}, \mathsf{E}_2^{\mathsf{opt}_2})$ **Method-2**	RMSD for $(\mathsf{E}_1^{\mathsf{sub}}, \mathsf{E}_2^{\mathsf{sub}})$ **Sub-Optimal**
Water	0	**0.0336**	0.0377	0.0496
Ethanol	0.0379	**0.0282**	0.0320	0.0448
Graphite	0.0987	**0.0309**	0.0360	0.0496
PVC	0.5521	**0.0493**	0.0548	0.0646
PMMA	0.0250	**0.0316**	0.0354	0.0476
Aluminium	0.7547	**0.0520**	0.0560	0.0664
Salt	1.0800	**0.0594**	0.0645	0.0733

We obtained similar results (not shown) for another experiment using the phantom in Fig. 3 with tube-current set to 50 mA in CatSim.

VI. DISCUSSION

We proposed two methods for selecting monochromatic energy-pairs (MEPs) for conversion of measured DE poly-chromatic data (poly-data) sets to monochromatic data (mono-data) sets so as to minimize the amount of noise correlation in them. This strategy allows us to (approximately) decouple the statistical-modeling of noise in the mono-datasets and thus apply conventional MBIR individually on each mono-dataset. We demonstrated using simulations that the proposed selections of MEP yield better material decompositions (with an average reduction in RMSD of $1.4\times$ and $1.25\times$ respectively for **Method-1** and **Method-2**) than an arbitrary choice of MEP.

The proposed scheme only minimizes and does not eliminate noise covariance between the mono-datasets. We are currently implementing a joint reconstruction technique (similar to that in [5]) that accounts for (any residual) noise covariance in the mono-datasets in the joint-MBIR statistical-modeling. We plan to compare this joint reconstruction technique against the methods proposed in this paper and validate their practical usefulness as part of future work.

REFERENCES

[1] R. E. Alvarez and A. Macovski, "Energy-selective reconstruction in X-ray computerized tomography," *Phys. Med. Biol.*, vol. 21, no. 5, pp. 733–44, 1976.

[2] W. A. Kalender, W. H. Perman, J. R. Vetter, and E. Klotz, "Evaluation of a prototype dual-energy computed tomographic apparatus. I. Phantom studies," *Med. Phys.*, vol. 13, no. 3, pp. 334–9, 1986.

[3] X. Wu, D. A. Langan, D. Xu, T. M. Benson, J. D. Pack, A. M. Schmitz, J. E. Tkaczyk, J. Leverentz, and P. Licato, "Monochromatic CT image representation via fast switching dual kVp," *Proc. SPIE Med. Imag.: Phys. Med. Imag.*, p. 725845, 2009.

[4] T. Johnson, B. Krau, M. Sedlmair, M. Grasruck, H. Bruder, D. Morhard, C. Fink, S. Weckback, M. Lenhard, B. Schmidt, T. Flohr, M. F. Reiser, and C. R. Becker, "Material differentiation by dual energy CT: Initial experience," *Eur. J. Radiol.*, vol. 17, no. 6, pp. 1510–7, June 2007.

[5] R. Zhang, J. B. Thibault, C. A. Bouman, K. D. Sauer, and J. Hsieh, "Model-based iterative reconstruction for dual-energy x-ray CT using a joint quadratic likelihood model," *IEEE Trans. Med. Imag.*, vol. 33, no. 1, pp. 117–34, Jan. 2014.

[6] Y. Long and J. A. Fessler, "Multi-material decomposition using statistical image reconstruction for spectral CT," *IEEE Trans. Med. Imag.*, vol. 33, no. 8, pp. pp.1614–26, Aug. 2014.

[7] L. Shen, Y. Xing, L. Zhang, Q. Huang, and X. Jin, "Hybrid decomposition method for dual energy CT," *Proc. IEEE Conf. NSS and MIC*, 2014.

[8] B. De Man, S. Basu, N. Chandra, B. Dunham, P. Edic, M. Iatrou, S. McOlash, P. Sainath, C. Shaughnessy, B. Tower, and E. Williams, "CatSim: a new computer assisted tomography simulation environment," in *Proc. SPIE 6510, Medical Imaging 2007: Physics of Medical Imaging*, J. Hsieh and M. J. Flynn, Eds., Mar. 2007, p. 65102G.

[9] D. Kim, S. Ramani, and J. A. Fessler, "Combining ordered subsets and momentum for accelerated X-ray CT image reconstruction," *IEEE Trans. Med. Imag.*, vol. 34, no. 1, pp. 167–78, 2015.

Characterization CT unit using a dose efficiency index concept

Damien Racine[1], Pascal Monnin[1], François O. Bochud[1], Anaïs Viry[1], Alexander Schegerer[2], Sue Edyvean[3], Francis R. Verdun[1]

Abstract — **The aim of this study is to propose a methodology to benchmark clinical CT protocols using mathematical model observer metrics. Two model observers (NPWE and CHO) were used to assess the high and low contrast detectability on four CT units. One CT unit provides high image quality (at low and high contrast) in comparison to the three others. These results show that it is possible to compare units with several task-based image quality criteria. In the future this approach, will be used to compare 8 CT units using 6 clinical protocols.**

Index Terms— **Computed Tomography, Low contrast detectability, Model observer, Spatial Resolution**

I. Introduction

Computed tomography (CT) is an imaging technique in which interest has been quickly growing since it began to be used in the 1970s. Today, it has even become an extensively used modality because of its ability to produce accurate diagnostic images. However, even if a direct benefit to patient healthcare is attributed to CT, the dramatic increase in the number of CT examinations performed has raised concerns about the potential negative effects of ionizing radiation on the population. In order to ensure that the benefits-risk ratio still remains in favor of the patient, it is necessary to make sure that the delivered dose leads to the proper diagnosis without producing unnecessarily high-quality images; that is to optimize the way the unit is used on patients [1]. In this context many efforts have been made to better estimate the risk part of CT examinations by introducing standardized ways to quote patient exposure (CTDIvol, SSDE and DLP concepts) [2]. Then diagnostic reference levels (DRL) have been introduced to reduce the spread of the practice. However, the most important outcome of the examination, the clinical image quality, remains subjectively assessed. In such a context the optimization scheme between risk and benefit cannot be properly performed. One needs a way to objectively assess the performance of the CT unit together with one or several image quality criteria that check the detection/characterization of pathologies. This requirement is particularly critical with the introduction of iterative reconstruction in CT where very low dose images can be produced without the traditional image signs (artifacts, high noise level) that alert radiologists that a low contrast lesion could be missed. To adapt the image quality level to the diagnostic question to be answered, to benchmark protocols and units one should have access not only to a dose report but also to objective image quality criteria [3]. The goal of this contribution is to present a strategy to qualify clinical CT protocols using two concepts: one to assess the low contrast detectability and localization of homogeneous spheres placed in homogeneous background and the other to assess the performances concerning the high spatial resolution properties of the image using the CHO (Channelized Hotelling Observer) and the NWPE (Non pre-whitening match with eye filter) mathematical model observers.

1) Institute of Radiation Physics, Lausanne University Hospital, 1 Rue du Grand-Pre, 1007 Lausanne, Switzerland
2) Department for Radiation Protection and Health External and Internal Dosimetry, Biokinetics, Ingolstadter Landstr, 1, 85764 Neuherberg, Germany
3) Medical Dosimetry Group, Centre for Radiation Chemicals and Environmental Hazards, Public Health England, Didcot, UK(e-mail: author@nrim.go.jp).

II. Materials and methods

A. Description of phantoms and CT

Three phantoms were scanned on 4 CT units: GE Revolution and VCT (GE Healthcare, USA), Toshiba Aquilion Prime and Activion 16 (Toshiba Medical Systems, Japan). Each phantom was scanned following the parameters acquisitions described in table I and images were reconstructed with the algorithm available and usually used in clinical routine (FBP or iterative). For this comparison that involves multiple institutions and CT units, the acquisitions parameters were kept constant as much as possible between CT units and the tube currents (mA) were fixed to obtain comparable CTDIvol values.

First a low contrast head phantom (MITA CCT 191, The Phantom Laboratory, USA) with four rods of different sizes and contrast levels (3mm/5HU, 2mm/9HU, 4mm/4HU, 3mm/5HU) placed in a homogeneous background were used to assess the low contrast detectability for the head protocol.

Second a custom made phantom with three cylindrical inserts of diameter 10cm and of different materials was used to assess

TABLE I
Scanning parameters for different protocols

	Head Protocol	Thorax Protocol	Abdomen Protocol
CTDIvol (mGy)	55	15	5/10/15
Slice Thickness (mm)	2.5/3	2.5/3	2.5/3
kV	120	120	120
X-ray collimation	≈40	≈40	≈40
Pitch	≈1	≈1.4	≈1.4
FOV (mm)	220	250	320
Rotation time (s)	1	1	1
Filter	Standard Head	Lung	Standard Body
Phantom	MITA	TTF	QRM Abdomen

the spatial resolution; in Teflon mimics cortical bone, low-density Polyethylene mimics fatty tissue and Plexiglas mimics' cartilaginous tissue. The inserts are centered in the phantom and surrounded by 7.5 cm of water. At the end of the phantom a water region without insert was used to compute the NPS.

Third an abdominal anthropomorphic phantom, equivalent diameter 24 cm (QRM, Moehrendorf, Germany) was used to mimic the X-ray attenuation of a thin abdomen. Two modules were inserted inside, a homogeneous module and another module containing spheres of different diameters (8, 6, 5, 4 and 3 mm) of low contrasts (-20 and -10 HU at 120 kV). Only the spheres of 5 mm and 20HU, and 8mm at 10HU were analyzed in this study.

B. *Non Prewhitening With Eye filter*

The NPWE detectability index was evaluated based on the TTF and NPS calculated for each CT unit and protocol.

$$d' = \frac{\sqrt{2\pi\Delta HU \int_0^{f_{NY}} S^2(f)TTF^2(f)VTF(f)^2 f df}}{\sqrt{\int_0^{f_{NY}} S^2(f)TTF^2(f)NPS(f)VTF(f)^4 f df}}$$

Equation 1

The spatial resolution was evaluated using the Target Transfer Function (TTF) that takes into account the effect of contrast on the spatial resolution parameter. The methodology used is described in ref. [4]. The mean radial NPS was evaluated according to ICRU report 54 using 256 x 256 pixel area taken on 10 water slices[5]. (The reader interested in all the mathematical details of the process will find extensive details in Ott et al. [4]).

C. *Channelized Hotelling Observer*

A Channelized Hotelling Observer (CHO) was used to evaluate the low contrast detectability with the head and abdomen phantoms. The methodology used is described in ref. [6]. This model is used for localization and detection tasks and the detectability index calculated from the AUC obtained with a ROC or LROC analysis is used as a figure of merit [7][8]. For the localization task, the CHO scans all possible locations to generate a map with all decision variables calculated for every location investigated. The target position defined by the model corresponds to the position with the highest decision variable. If the difference between the calculated position and the actual target location is less than the radius of the target, the estimated position is considered correct. Finally, to compare the performance of the CHO, the AUC was converted into detectability index (d_A) using equation 2.

$$d_A = 2\,\Phi^{-1}(2AUC-1) \quad \text{Equation 2}$$

III. RESULTS

A. *Detection task (QRM abdomen phantom):*

As expected, the image quality metrics improve with the $CTDI_{vol}$ between 5 and 15 mGy. For category 5mm/20HU @ 15mGy, which corresponds to a relatively high dose level for this phantom, only the CT unit "B" is inferior to the others. For the unit "C" image quality remains relatively constant whatever the dose (Figure 1). Thus, this particular unit has an important potential for patient dose reduction.

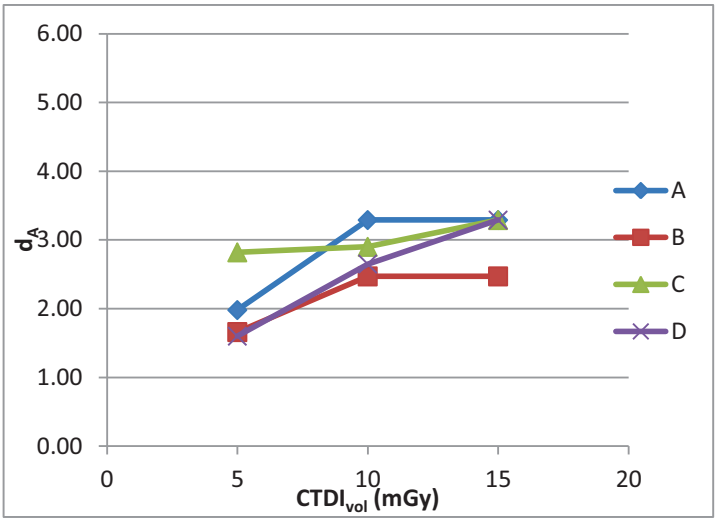

Fig. 1. Detectability as a function of dose for category 5mm/20HU (QRM phantom)

For category 8mm/10HU @ 15mGy, the CT unit "C" is superior to the others (Figure 2). It is interesting to notice that the detectability does not reach a plateau as opposed to the behaviour observed when dealing with category 5mm/20HU shown in Figure 1.

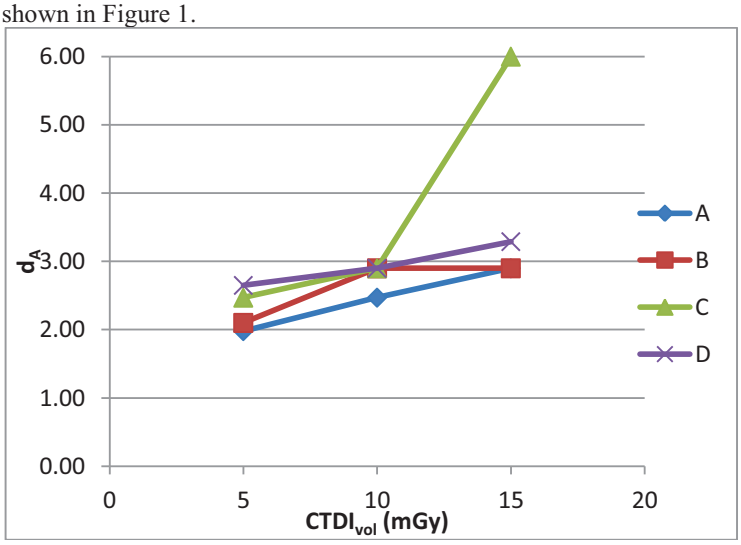

Fig. 2. Comparison between the 4 CT units as a function of dose for the ROC study at 8mm/10HU

B. *Localization task (MITA head phantom):*

Table II shows the LAUC and AUC obtained with the CHO. The difference between the 4 CT units is more important for the LAUC, showing that the introduction of the localization task increases the difficulty of the image quality assessment.

C. *Spatial resolution and image noise (TTF phantom):*

TABLE II
LROC AND ROC RESULTS FOR THE CATEGORY 5MM/3HU @ 55 MGY USING THE MITA PHANTOM

CT unit	d_{LAUC}	d_{AUC}
A	6	6
B	2.46 ± 0.2	6
C	6	6
D	1.52 ± 0.4	4.3

Examples of TTF and NPS used to estimate the detectability index d' with the NPWE model observer are shown in Figures 3 and 4, respectively. The NPS is determined in a volume region and were radially averaged over 1D for an easier comparison.

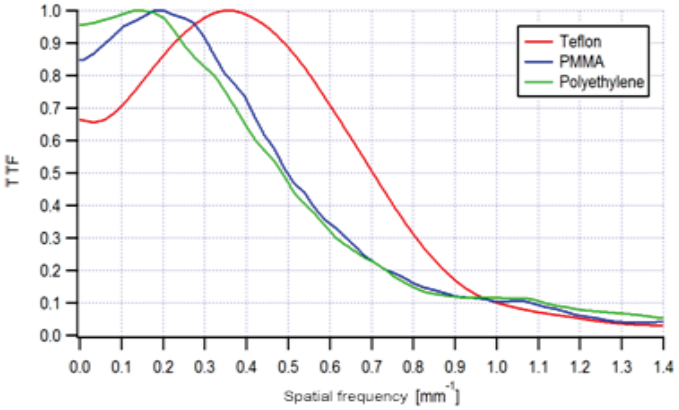

Fig. 3. TTF for three materials at 15mGy for CT unit "C"

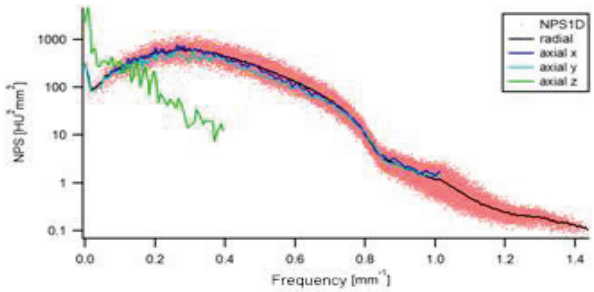

Fig. 4. NPS for CT unit "C" at 15mGy

Table III shows the d' obtained for a sphere of 0.5mm in diameter for three contrast values with Equation 1. As expected from the contrasts of the three materials considered, d' for PMMA in water is higher than for Polyethylene in water,and d' is the highest for Teflon in water. If, for a given contrast the units "A, B, D" provide comparable outcomes, the unit "C" gives higher d'. This difference is mainly explained by the shape and amplitude of a NPS about 150 times lower compared to the other systems. All units had comparable TTF outcomes.

TABLE III
SUMMARY OF d' FOR DIFFERENT CT AND DIFFERENT MATERIALS

CT unit	LAUC	AUC
A	4.23	0.52
B	5.75	0.63
C	43.3	3.84
D	3.94	0.5

TABLE III
SUMMARY OF d' FOR DIFFERENT CT AND DIFFERENT MATERIALS

CT unit	d' Teflon	d' PMMA	d' Polyethylene
A	4.23	0.52	0.34
B	5.75	0.63	0.46
C	43.3	3.84	2.29
D	3.94	0.5	0.33

IV. LIMITATIONS - CONCLUSION

In the framework of patient dose optimization it is essential to ensure that comparable image quality levels are obtained. The goal of this study was to use model observers to compare CT units using task-based image quality criteria. These results show that it is possible to compare units using several task-based paradigms, and thus ensure a comparable level of image quality for several types of CT units used in clinical routine. The proposed methodology allows also a task-based evaluation of the advantages of new CT technologies. Our approach has several limitations: first of all the tasks are very simple especially for the abdominal protocol, and our phantoms have homogeneous backgrounds. However, the level of complexity of model observer can be increased aiming at predicting the human performance when dealing with the detection/localization of target placed in more realistic backgrounds.

V. ACKNOWLEDGEMENTS

This work was supported by the German Radiation Protection Agency (BfS – UFO-Plan Vorhabens 3613S20007)

REFERENCES

[1] H. H. Barrett, K. J. Myers, C. Hoeschen, M. A. Kupinski, and M. P. Little, "Task-based measures of image quality and their relation to radiation dose and patient risk," *Phys. Med. Biol.*, vol. 60, no. 2, p. R1, Jan. 2015.

[2] "J. Boone, K. Strauss, D. Cody, C. McCollough, M. McNitt-Gray, and T. Toth, 'Size-specific dose estimates (SSDE) in pediatric and adult body CT exams,' Report of AAPM Task Group 204, 2011."

[3] J. Y. Vaishnav, W. C. Jung, L. M. Popescu, R. Zeng, and K. J. Myers, "Objective assessment of image quality and dose reduction in CT iterative reconstruction," *Med. Phys.*, vol. 41, no. 7, p. 071904, Jul. 2014.

[4] J. G. Ott, F. Becce, P. Monnin, S. Schmidt, F. O. Bochud, and F. R. Verdun, “Update on the non-prewhitening model observer in computed tomography for the assessment of the adaptive statistical and model-based iterative reconstruction algorithms,” *Phys. Med. Biol.*, vol. 59, no. 15, pp. 4047–4064, Aug. 2014.

[5] W. Vennart, “ICRU Report 54: Medical imaging—the assessment of image quality,” *Radiography*, vol. 3, no. 3, pp. 243–244, Apr. 1996.

[6] D. Racine, A. H. Ba, J. G. Ott, F. O. Bochud, and F. R. Verdun, “Objective assessment of low contrast detectability in computed tomography with Channelized Hotelling Observer,” *Phys. Medica Eur. J. Med. Phys.*, vol. 0, no. 0.

[7] International Commission on Radiation Units and Measurements, “Receiver Operating Characteristic Analysis in Medical Imaging,” in *ICRU Report n°79*, International Commission on Radiation Units and Measurements., vol. 79, Bethesda (MD), 2008.

[8] J. Beutel, H. Kundel, and R. Van Metter, “Handbook of medical imaging Volume I. Physics and Psychophysics,” SPIE Press, 2000, pp. 595–695.

TICMR: Total Image Constrained Material Reconstruction via nonlocal total variation regularization for spectral CT

Jiulong Liu, Huanjun Ding, Sabee Molloi, Xiaoqun Zhang, and Hao Gao

***Abstract*—The purpose of this work is to develop a material reconstruction method for spectral CT, namely Total Image Constrained Material Reconstruction (TICMR), to maximize the utility of projection data in terms of both spectral information and high signal-to-noise ratio (SNR). This is motivated by the following fact: when viewed as a spectrally-integrated measurement, the projection data can be used to reconstruct a total image without spectral information, which however has a relatively high SNR; when viewed as a spectrally-resolved measurement, the projection data can be utilized to reconstruct the material composition, which however has a relatively low SNR. That is, first we reconstruct a total image using spectrally-integrated measurement without spectral binning, and build the NLTV weights from this image that characterize nonlocal image features; then the NLTV weights are incorporated into a NLTV-based iterative material reconstruction scheme using spectrally-binned projection data, so that these weights serve as a high-SNR reference to regularize material reconstruction. In terms of solution algorithm, TICMR is formulated as an iterative reconstruction method with the NLTV regularization, in which the nonlocal divergence is utilized based on the adjoint relationship . The alternating direction method of multipliers (ADMM) is developed to solve this sparsity optimization problem. The proposed TICMR method was validated using both simulated and experimental data. In comparison with FBP and total-variation-based iterative method, TICMR had improved image quality, e.g., contrast-to-noise ratio (CNR) and spatial resolution.**

***Index Terms*—image reconstruction, spectral CT, nonlocal total variation.**

I. Introduction

Spectral CT aims to reconstruct the material compositions from the multi-energy projection data. It can be determined in a two-step procedure, i.e., image reconstruction for spectral images and then material decomposition from these spectral images to material compositions [1], [4]–[10], or alternatively material-specific sinogram decomposition and then material reconstruction [2], [11]–[13]. Various iterative reconstruction models have been developed, with energy-by-energy reconstruction [1], [2], [5], [7], [8], [11]–[13] and joint reconstruction [4], [6], [9], [10], such as total variation (TV) sparsity [10], tight frame sparsity [1], [7], bilateral filtration [8], patch-based low-rank model [9], rank-and-sparsity decomposition model [4] and its tensor version [6]. In order to fully utilize the image similarity in the spectral dimension, the joint reconstruction is a natural formulation [4], [6], [9], [10]. With local sparsity (such as TV), cautiousness is required to handle such an intensity difference for joint spectral reconstruction [10]. Nevertheless, with the aforementioned two-step procedure where image reconstruction is independent of material decomposition, there are two major limitations: (1) it may not fully utilize the prior that material compositions share common structures; (2) given that the number of energy bins is often more than the number of materials, reconstructing a larger number of spectral images, which are subsequently decomposed into a smaller number of materials, may be unstable and can possibly deteriorate the reconstruction quality. Therefore, the reconstruction of an overdetermined set of spectral images independent of material decomposition is unnecessary.

In this work, we propose a material reconstruction method for spectral CT that maximizes the utility of projection data in terms of both spectral information and high signal-to-noise ratio (SNR), i.e., Total Image Constrained Material Reconstruction (TICMR). The constraint via total image for improved SNR is achieved via nonlocal total variation (NLTV) regularization [14], [15]. As mentioned earlier, even if spectral images or material compositions share common structures, their intensity values may differ significantly. Therefore, the prior of spectral similarity may not be efficient to regularize locally. Instead, we use NLTV as a global sparsity method to extract image features from the total image and then use these high-SNR features to regularize the material reconstruction. That is, first we reconstruct a total image using spectrally-integrated measurement without spectral binning, and build the NLTV weights from this image that characterize nonlocal image features; then the NLTV weights are incorporated into a NLTV-based iterative material reconstruction scheme using spectrally-binned projection data, so that these weights serve as a high-SNR reference to regularize material reconstruction.

II. Method

A. Spectral Model

Consider a set of spectral measurement Y_{im}, $i = 1, \cdots, N$, $m = 1, \cdots, N_e$, where N_e is the number of spectral energies, N_v is the number of projection views, N_d the number of detectors, and $N = N_d \cdot N_v$. Let $M = N \cdot N_e$ be the total number of spectral data, $s(E)$ the incident spectrum, ΔE_m the length of the mth energy interval, and L_i the path of line integral for Y_{im}. Assuming the perfect detector response [16],

J. Liu and H. Gao are with Department of Mathematics and School of Biomedical Engineering, Shanghai Jiao Tong University, Shanghai 200240, CHINA (e-mail: hao.gao.2012@gmail.com).

H. Ding and S. Molloi are with Department of Radiological Sciences, University of California, Irvine, CA 92697, USA (e-mail: huanjund@uci.edu).

X. Zhang is with Department of Mathematics and Institute of Natural Sciences, Shanghai Jiao Tong University, Shanghai 200240, CHINA.

the expectation Y_{im}^* of spectral measurement Y_{im} is given by the following spectral model

$$Y_{im}^* = \int_{\Delta E_m} s(E) e^{-\int_{L_i} u(x,E)dx} dE \quad \text{for } i = 1, \cdots, N, m = 1, \cdots, N_e, \tag{1}$$

where multi-energy attenuation coefficient $u(x, E)$ linearly depends on the material composition Z [4], i.e.,

$$u(x, E) = \sum_{k=1}^{N_z} Z_k(x) B_k(E). \tag{2}$$

Here N_z is the number of basis materials, $Z_k(x)$ is the material composition of the kth basis material at the spatial location x, which is spectrally independent, and $B_k(E)$ is the attenuation coefficient of the kth basis material at the energy E, which is spatially independent.

We then consider a spatially discretized version of (1) with a piecewise-constant spatial grid x_j, $j = 1, \cdots, N_x$. Let A be the system matrix for discretized X-ray transform with the matrix element A_{ij}, e.g., the length of the ray L_i overlapping with the grid x_j. Then

$$Y_{im}^* = \int_{\Delta E_m} s(E) e^{-\sum_j A_{ij} (\sum_k Z_{jk} B_k(E))} dE, \tag{3}$$

where Z_{jk} is the kth material composition at the grid x_j.

Next we introduce the effective attenuation coefficient B_{km} of the kth basis material for the energy interval ΔE_m, i.e.,

$$Y_{im}^* = s_m e^{-\sum_j A_{ij} (\sum_k Z_{jk} B_{km})}, \tag{4}$$

where

$$s_m = \int_{\Delta E_m} s(E) dE. \tag{5}$$

Here (4) is justified by the mean value theorem for definite integrals, thanks to the continuity of $B(E)$ with respect to E.

In the matrix notation, (4) is

$$Y^* = S \cdot e^{-AZB}, \tag{6}$$

where $Y^* \in \mathbb{R}^M$ is a column vector of the spectral measurement, $S \in \mathbb{R}^M$ a column vector of the source spectrum distribution formed by replicating $\{s_m\}$ in spatial dimension, $A \in \mathbb{R}^{N \times N_x}$ the system matrix, $Z \in \mathbb{R}^{N_x \times N_z}$ the material composition, and $B \in \mathbb{R}^{N_z \times N_e}$ the material-attenuation matrix.

Last, assuming Poisson distribution for Y, our spectral model to reconstruct material composition Z from spectral measurement Y, i.e., the data fidelity term, can be formulated as the following quadratic functional [17]

$$L(Z) = \frac{1}{2}(AZB - P)^T W (AZB - P) = \frac{1}{2}\|AZB - P\|_W^2, \tag{7}$$

where $P = \mathbf{ln}(\frac{S}{Y}) \in \mathbb{R}^M$ and $W = \text{diag}(Y) \in \mathbb{R}^{M \times M}$.

B. Total Image Constrained Material Reconstruction

The proposed TICMR consists of two steps: (i) to reconstruct a total image using spectrally-integrated measurement without spectral binning, and build the NLTV weights from this image that characterize nonlocal image features; (ii) to incorporate these NLTV weights computed from high-SNR total image into material reconstruction using spectrally-resolved projection data.

Let Y_0 be the spectrally-integrated measurement, i.e., $Y_{0i} = \sum_m Y_{im}$, $i = 1, \cdots, N$. Then the total image $X^* \in \mathbb{R}^{N_x}$ is reconstructed by the following TV based iterative method

$$X^* = \arg\min_X \frac{1}{2}\|AX - P_0\|_{W_0}^2 + \lambda |\nabla X|_1 \tag{8}$$

where $P_0 = \mathbf{ln}(\frac{s_0}{Y_0}) \in \mathbb{R}^N$ with total source energy $s_0 = \sum_m s_m$, $W_0 = \text{diag}(Y_0) \in \mathbb{R}^{N \times N}$, and $|\nabla X|_1$ an isotropic TV norm with regularization parameter λ, e.g.,

$$|\nabla X|_1 = \sqrt{\partial_x^2 X + \partial_y^2 X}. \tag{9}$$

Then the material composition Z^* is reconstructed by the following NLTV based iterative method

$$Z^* = \arg\min_Z \frac{1}{2}\|AZB - P\|_W^2 + \lambda |\nabla_w Z|_1 \tag{10}$$

where $|\nabla_w Z|_1$ is the NLTV norm that will be given in the next section.

To summarize, TICMR is achieved in this work through TV and NLTV regularization, i.e., (8) and (10), during which the total image X^* reconstructed by (8) provides high-SNR NLTV weights for the material reconstruction of Z^* by (10).

In the result section, we compare TICMR with FBP and the following TV based material reconstruction

$$Z^* = \arg\min_Z \frac{1}{2}\|AZB - P\|_W^2 + \lambda |\nabla Z|_1. \tag{11}$$

The solution algorithm for sparsity-based reconstruction problems (8), (10), and (11) is based on alternating direction method of multipliers [19] or split Bregman method [20].

C. Nonlocal Total Variation

An essential component of NLTV is to characterize the patch-by-patch similarity [18] instead of pixel-by-pixel similarity (e.g., TV). That is, for a given image X, the following weights can be constructed between any two spatial node x and y,

$$w_X(x, y) = e^{-\frac{\int_{\Omega_1} G_\sigma(t)(X(y+t) - X(x+t))^2 dt}{\sigma^2}}, \tag{12}$$

where G is a Gaussian kernel with the standard deviation σ, and Ω_1 represents the spatial neighborhood to be compared around x and y.

Such a patch-by-patch similarity at the spatial grid x from a high-SNR image X can be used to regularize the low-SNR image u via the following nonlocal gradient at x [14], i.e.,

$$\nabla_w u(x, y) = (u(y) - u(x))\sqrt{w_X(x, y)}, \forall y \in \Omega_2. \tag{13}$$

Here Ω_2 is the spatial neighborhood around x where the nonlocal gradient $\nabla_w u(x, y)$ is computed by (13).

Then the NLTV norm of Z in (10) is given by

$$|\nabla_w Z|_1 = \sum_k |\nabla_w Z_k|_1, \tag{14}$$

where the nonlocal weights w are constructed based on the total image X^* reconstructed from (8).

On the other hand, we need to compute the adjoint of (13) during the reconstruction, for which we utilize the following adjoint relationship with a nonlocal divergence operator div_w

$$\langle \nabla_w u, v \rangle = \langle u, \text{div}_w v \rangle \tag{15}$$

with the nonlocal divergence operator [14] defined as

$$(\text{div}_w v)(x,y) = \int_{\Omega_2} (v(x,y) - v(y,x)) \sqrt{w_X(x,y)} dy \tag{16}$$

III. Results

A. Simulation Results

Simulations were performed at tube voltage of 65 kVp. The mean glandular dose was estimated to be approximately 2 mGy for a 10 cm breast with 40% density. A 10 cm PMMA phantom (Fig. 1) which contains both iodine and calcium of various concentrations (TABLE I) was used.

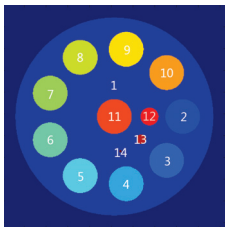

Fig. 1. The simulation phantom.

TABLE I
THE CONCENTRATION AND SIZE OF PHANTOM OBJECTS

Object	Material	Radius	Concentration
1	adipose	48mm	
2	iodine	8mm	16mg/ml
3,10	iodine	8mm	8mg/ml
4	iodine	8mm	4mg/ml
5,11	iodine	8mm	2mg/ml
6	calcium	8mm	400mg/ml
7,10	calcium	8mm	200mg/ml
8	calcium	8mm	100mg/ml
9,11	calcium	8mm	50mg/ml
12	calcium	4mm	400mg/ml
13	calcium	2mm	400mg/ml
14	calcium	0.6mm	400mg/ml

To compare with the proposed TICMR method (8) and (10), we applied the FBP method to reconstruct material compositions from the material-specific projection data $\hat{P}$, i.e.,$\hat{P} = PB^T(BB^T)^{-1}$. In addition, we compared with the TV method (11) to reconstruct material compositions directly from the projection data P.

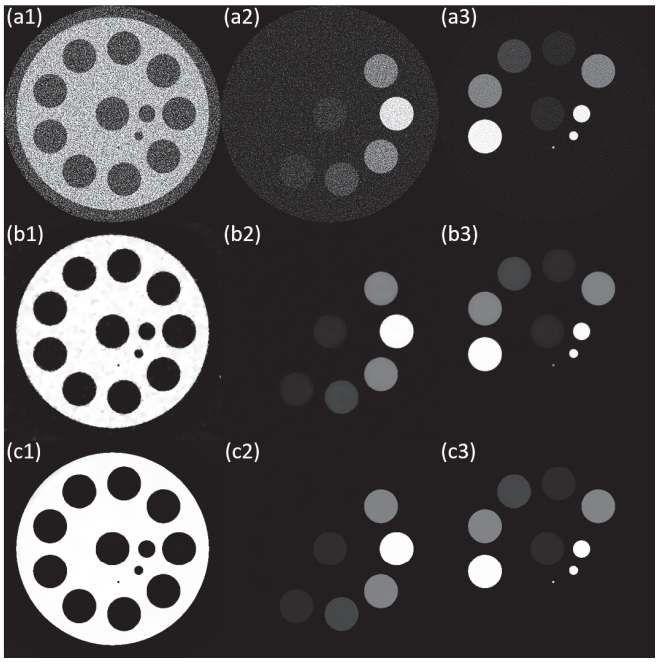

Fig. 2. Simulation results. (a) FBP; (b) TV; (c) TICMR. (1) adipose; (2) iodine; (3) calcium.

The reconstructed material composition images with simulated data are shown in Fig. 2. All three reconstruction methods were able to decompose the phantom into adipose, iodine and calcium basis with good accuracy. However, the noise characteristic of the images was significantly different for three methods. TICMR has improved image quality from FBP and TV. Note that the small objects of calcium can be clearly observed in the TICMR result, which suggests that the spatial resolution was well preserved.

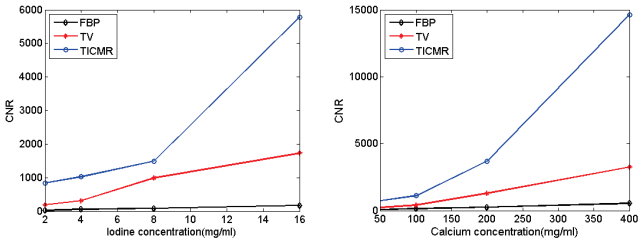

Fig. 3. Left: CNR of iodine (object 2-5); right: CNR of calcium (object 6-9).

For quantitative evaluation, the CNR of iodine and calcium are plotted in Fig. 3, which clearly shows TICMR had the best CNR among all three methods. Here the significant improvement of CNR of TICMR and TV from FBP was due to the piecewise-constant representation of simulation phantom.

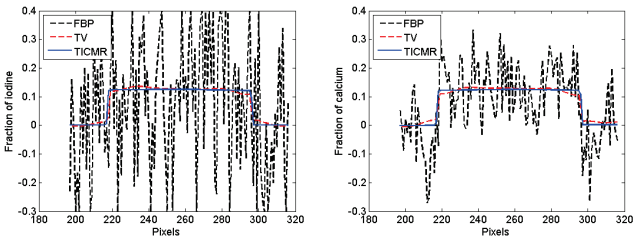

Fig. 4. Material composition curve along the horizontal and central line passing through Object 11. Left: iodine; right: calcium.

In order to evaluate the spatial resolution of reconstructed material compositions, two material composition curves were drawn along the horizontal and central line passing through Object 11 as shown in Fig. 6, which suggest that the TICMR had the best spatial resolution.

To summarize, the TICMR result had not only the highest SNR, but also the best spatial resolution. This is enabled by high-SNR total image constrained material reconstruction through the NLTV regularization.

B. Experimental Results

Experimental data was acquired from a postmortem breast with a spectral CT system based on a CZT photon-counting detector at a mean glandular dose of 1.2 mGy. All X-ray photons interacting with the CZT detector were sorted into five user-definable energy bins.

The reconstructed material compositions are shown in Fig. 5, which again show that TICMR had improved image quality from FBP and TV.

To quantitatively evaluate the reconstruction quality, we applied CNR(ROI_1, ROI_2) and CNR(ROI_2, ROI_1) to calculate CNR as summarized in TABLE II including adipose (Column 1 of Fig. 5) and glandular (Column 2 of Fig. 5).

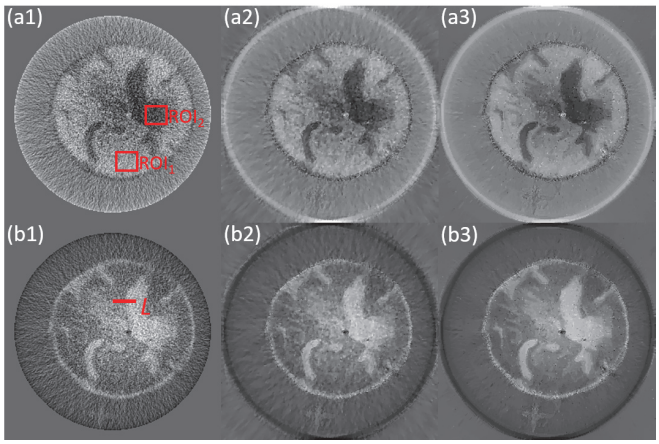

Fig. 5. Experimental results. (1) FBP; (2) TV; (3) TICMR. (a) adipose; (b) glandular.

TABLE II
THE CNR RESULTS WITH EXPERIMENTAL DATA

Material	FBP	TV	TICMR
adipose	24.64	43.03	58.51
glandular	26.26	45.20	62.34

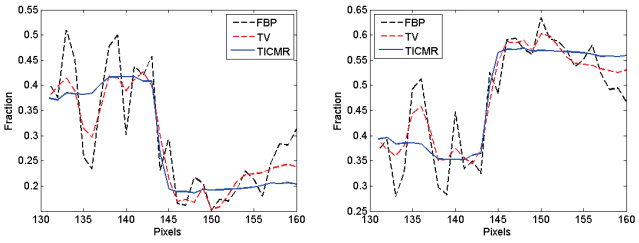

Fig. 6. Material composition profile along the line L in Fig. 5. Left: adipose; right: glandular.

IV. CONCLUSION

TICMR is proposed for spectral CT with improved image quality, i.e., both CNR and spatial resolution. Such an improvement is enabled by the total image constraint via the NLTV regularization. That is, a high-SNR total image is first reconstructed with energy-integrated projection data of relatively high SNR, and then built into the NLTV weights to regularize the material reconstruction with energy-resolved projection data of relatively low SNR via the NLTV regularization.

REFERENCES

[1] H. Ding et al, Physics in medicine and biology, 59, 6005, 2014.
[2] E. Roessl et al, Phys. Med. Biol, 52, 4679-4696, 2007.
[3] H. Bornefalk et al, Physics in Medicine and Biology, 55, 1999-2022, 2010.
[4] H. Gao et al, Inverse problems, 27, 115012, 2011.
[5] B. Zhao et al, Physics in medicine and biology,57, 8217, 2012
[6] L. Li, Z. Chen, G. Wang, J. Chu, and H. Gao, Journal of X-ray science and technology, 2, 147-163, 2013.
[7] B. Zhao et al, Medical physics, 40, 031905, 2013.
[8] D. P. Clark et al, Physics in medicine and biology, 59, 6445, 2014.
[9] K. Kim et al, Medical Imaging, IEEE Transactions on, 34, 748-760, 2015.
[10] L. Shen et al, Medical physics, 42, 282-296, 2015.
[11] R. E. Alvarez et al, Phys. Med. Biol., 21, 733-744, 1976.
[12] C. O. Schirra et al, Medical Imaging, IEEE Transactions on, 32, 1249-1257, 2013.
[13] Q. Xu et al, Physics in medicine and biology, 59, N65, 2014.
[14] G. Gilboa et al, Multiscale Modeling and Simulation, 7, 1005-1028, 2008.
[15] X. Zhang et al, SIAM Journal on Imaging Sciences , 3, 253-276, 2010.
[16] H. Ding et al, Medical physics, 41, 121902, 2014.
[17] K. Sauer et al, Signal Processing, IEEE Transactions on, 41, 534-548, 1993.
[18] A. Buades et al, Multiscale Modeling & Simulation, 4, 490-530, 2005.
[19] S. Boyd et al, Foundations and Trends in Machine Learning, 3,1-122, 2011.
[20] T. Goldstein et al, SIAM Journal on Imaging Sciences, 2, 323-343, 2009.

On Approximation of Compound Poisson by Poisson

Gengsheng L. Zeng and Wenli Wang

Abstract– **Purpose: This paper investigates whether a more accurate noise model can result in less noisy images in CT iterative reconstruction. Methods: X-ray photons detected by the CT detector are usually modeled as Poisson statistics. A more accurate noise model for the x-ray photons is based on the compound Poisson distribution. A variance formula for the compound Poisson noise is derived and presented. Computer simulations are conducted with 12 different noise weighting methods, and their results are compared. Results: Almost no differences are observed between the compound Poisson noise model and the regular Poisson noise model used in the maximum likelihood iterative reconstruction, when the projection data are generated with a compound noise model. Conclusions: A more accurate noise model does not necessarily produce a less noisy image. It seems that modeling the system's electronic noise does not help. A simpler noise model sometimes can outperform the complicated and accurate noise model**.

I. Introduction

IN In transmission tomography especially in x-ray computed tomography (CT), the iterative image reconstruction algorithms assume a simple Poisson model [1-5]. In this Poisson noise model, it is assumed that the number of photons I_0 emitted from the x-ray tube is a constant (not random) because this number is extremely large. After the x-ray photons travel through an attenuating/scattering object, the number of photons escaping from the object is significantly reduced and follows the Poisson noise model.

Based on the belief that a more accurate noise model used in an iterative image reconstruction algorithm may improve the signal-to-noise ratio in the reconstructed image, the assumption of the source photon count being a constant is dropped, and the number of photons emitted from the x-ray tube is characterized as the Poisson distribution. This more accurate noise model is justified in multi-energy x-ray CT imaging, where the x-ray energy spectrum is considered. The x-ray energy spectrum can be divided into many sub energy windows (or bins); the number of x-ray photons in each window is Poisson. The mean value of the photons in each energy window can be characterized by a spectrum function $\Phi(E)$. Since the source photon counts are random and Poisson, the detected (after object) x-ray photons are compound Poisson distributed [6,7].

The linear attenuation coefficient of a material is energy dependent and this fact is the cause of the infamous beam-hardening artifacts in CT. The purpose of this paper is to investigate whether the difference between the compound Poisson and regular Poisson can make any differences in the reconstructed images. The beam-hardening issues are not in the scope of this paper, and the linear attenuation coefficient is assumed to be energy *independent* in all of our computer simulations.

Gengsheng L. Zeng is with Department of Engineering, Weber State University, Ogden, UT 84408 USA (telephone: 801- 626-6864, e-mail: larryzeng@weber.edu) and also with Department of Radiology, University of Utah, Salt Lake City, UT 84108 USA (telephone: 801-581-3918, e-mail: larry@ucair.med.utah.edu).Wenli Wang is with Toshiba Medical Research Institute USA, Inc., Vernon Hills, IL 60061 USA.

II. Methods

This section first introduces the compound Poisson model, and then derives the pre-log and post-log formulas for the mean and variance. Descriptions of the setup of the computer simulations are also presented.

2.1 Compound-Poisson distribution

The Poisson distribution is well known in medical imaging. The most distinguishing feature of the Poisson distribution is that its mean and its variance are the same. Symbolically, a Poisson random variable q can be represented as

$$q = Poisson(\lambda) \ , \tag{1}$$

where λ is the mean value as well as the variance. A general compound-Poisson random variable p can be expressed by

$$p = a_1 Poisson\big(a_2 Poisson(\lambda)\big) \ , \tag{2}$$

where a_1 and a_2 are two non-random constants. The mean and variance of the compound-Poisson distribution can be derived from the law of total expectation and the law of total variance [10]. Thus

$$E_p(p) = E_q[E_{p|q}(p)] = E_q[a_1 a_2 q] = a_1 a_2 \lambda \ . \tag{3}$$

$$\begin{aligned} Var_p(p) &= E_q[Var_{p|q}(p)] + Var_q[E_{p|q}(p)] \\ &= E_q[a_1^2 a_2 q] + Var_q[a_1 a_2 q] = a_1^2 a_2 \lambda + (a_1 a_2)^2 \lambda \\ &= a_1^2 (a_2 + a_2^2)\lambda \ . \end{aligned} \tag{4}$$

2.2 Pre-log multi-energy noise

The number of photons I_0 emitted from an x-ray tube is Poisson distributed. Since I_0 is so large, it is justified to assume I_0 to be a non-random constant. Let the energy spectrum distribution function of the x-ray source be $\Phi(E)$ which is normalized to unity (similar to a probability density function).

The x-ray energy spectrum (before entering the object) can be divided into many sub energy windows (or bins); the number of x-ray photons in each window is Poisson distributed. The mean value of the number of x-ray photons in the kth energy window is $I_0 \Phi(E_k)$.

After the x-rays pass through the object, on the detector, each energy window produces a compound-Poisson x-ray measurement p_k, which can be modeled as [8,9]

$$p_k = Poisson\Big(e^{-\int \mu(x)dx} Poisson\big(I_0 \Phi(E_k)\big)\Big), \tag{5}$$

where μ is the linear attenuation coefficient and μ is *assumed* to be independent of the photon energy in this paper; the line integral $\int \mu(x)dx$ is along the associated projection ray.

The energy-integrating detection outputs a signal of $aE_k p_k$, where E_k is the photon energy of the energy window and a is the system gain. Using the definition (2) with $a_1 = aE_k$, $a_2 = \exp(-\int \mu(x)dx)$, and $\lambda = I_0\Phi(E_k)$, by (3) and (4), the mean and variance of the weighted compound-Poisson variable are given as:

$$\text{Mean of } aE_k p_k = aE_k I_0 \Phi(E_k) e^{-\int \mu(x)dx}; \quad (6)$$

Variance of $aE_k p_k$ =

$$(aE_k)^2 I_0 \Phi(E_k)(e^{-\int \mu(x)dx} + e^{-2\int \mu(x)dx}). \quad (7)$$

The total signal p received by the energy-integrating system along this ray should include the signals from all energy windows and the noise d generated in the electronic circuits:

$$p = \sum_k aE_k p_k + d. \quad (8)$$

where d can be assumed to be a zero-mean Gaussian random variable with a variance σ^2. Using (6) and (7), the mean and variance of the random variable p in (8) can be obtained as

$$\text{Mean of } p = \sum_k aE_k I_0 \Phi(E_k) e^{-\int \mu(x)dx} + 0$$
$$= aI_0 e^{-\int \mu(x)dx} \sum_k E_k \Phi(E_k)$$
$$= aI_0 e^{-\int \mu(x)dx} \overline{E} \quad (9)$$

with the first moment of the x-ray source distribution

$$\overline{E} = \sum_k E_k \Phi(E_k); \quad (10)$$

Variance of p

$$= \sum_k (aE_k)^2 I_0 \Phi(E_k)(e^{-\int \mu(x)dx} + e^{-2\int \mu(x)dx}) + \sigma^2$$
$$= a^2 I_0 (e^{-\int \mu(x)dx} + e^{-2\int \mu(x)dx}) \sum_k E_k^2 \Phi(E_k) + \sigma^2$$
$$= a^2 I_0 (e^{-\int \mu(x)dx} + e^{-2\int \mu(x)dx}) \overline{\overline{E}} + \sigma^2 \quad (11)$$

with the second moment

$$\overline{\overline{E}} = \sum_k E_k^2 \Phi(E_k). \quad (12)$$

2.3 Post-log multi-energy noise

The mean and variance formulas in Section 2.2 are for the pre-log data that is a weighted sum of compound-Poisson data and Gaussian electronic noise. Normally, the post-log data are used for analytical and iterative reconstruction. Let the post-log data be obtained as

$$y = \ln(\frac{a\overline{E}I_0}{p}). \quad (13)$$

The mean and variance of y can be obtained as

$$\text{Mean of } y = \bar{y} = \ln(\frac{a\overline{E}I_0}{aI_0 e^{-\int \mu(x)dx}\overline{E}}) = \int \mu(x)dx; \quad (14)$$

$$\text{Variance of } y = \sigma_y^2 = \left|\frac{dy}{dp}\right|^2_{p=\text{Mean of } p} \quad (\text{Variance of } p)$$
$$= \frac{1}{(aI_0 e^{-\int \mu(x)dx}\overline{E})^2}[a^2 I_0 (e^{-\int \mu(x)dx} + e^{-2\int \mu(x)dx})\overline{\overline{E}} + \sigma^2]$$
$$= \frac{1}{(aI_0 e^{-\bar{y}}\overline{E})^2}[a^2 I_0 (e^{-\bar{y}} + e^{-2\bar{y}})\overline{\overline{E}} + \sigma^2]. \quad (15)$$

Formula (15) should be used to calculate the weighting function in a post-log iterative reconstruction algorithm for the given projection ray:

Weighting for ray y

$$= \frac{1}{\sigma_y^2} = \frac{(aI_0 e^{-\bar{y}}\overline{E})^2}{a^2 I_0 (e^{-\bar{y}} + e^{-2\bar{y}})\overline{\overline{E}} + \sigma^2}. \quad (16)$$

However, in practice, the mean value $\bar{y}$ of the post-log data is not available. The one-time measurement y is used instead.

2.4 Computer simulations

A gradient descent algorithm will be used to minimize the noise-weighted post-log maximum likelihood objective function:

$$\text{Objective Function} = \sum_j w_j (\sum_i a_{ij}\mu_i - y_j)^2, \quad (17)$$

where μ_i is the image pixel whose value is the linear attenuation coefficient, y_j is the post-log measurement (i.e., the noisy Radon transform), a_{ij} is the contribution from the ith pixel μ_i to the jth measurement y_j, and w_j is the weighting factor which is chosen to be the reciprocal of the noise variance of y_j, as shown in (16). The gradient descent algorithm is expressed as

$$\mu_i^{(k+1)} = \mu_i^{(k)} - \alpha \frac{\sum_j a_{ij} w_j (\sum_n a_{nj}\mu_n^{(k)} - y_j)}{\sum_j a_{ij} w_j \sum_n a_{nj}}, \quad (18)$$

where $\mu_i^{(k)}$ is the estimation of μ_i at the k^{th} iteration and the step size α is a small positive constant to prevent the algorithm from divergence. The value of α is set to 0.2 in this paper. The purpose of the denominator $\sum_j a_{ij} w_j \sum_n a_{nj}$ is to normalize the weighting factors w_j so that the step size of the algorithm is almost the same for any chosen weighting factor $w_j > 0$. The summation over the index n is the projector and the summation over the index j is the backprojector.

This paper will use 12 methods of implementing the weighting factor w_j, which is the reciprocal of the noise variance sinogram. These 12 methods of calculating the noise weighting are listed below.

Method 1 (Theoretical truth): The weighting factor w_j is calculated using (16), with $a = 0.1$, $I_0 = 10^4$, $\sigma^2 = 6.3^2$, and $\bar{y}_j$ being the noiseless post-log projection. The x-ray tube energy distribution function $\Phi(E)$ is measured in a Toshiba CT scanner. The energy spectrum is subdivided into 120 energy windows from 0 to 120 keV. The first and second moments of the spectrum $\overline{E}$ and $\overline{\overline{E}}$ are calculated using (10) and (12);

their numerical values are 67.8776 keV and 5036.9 $(\text{keV})^2$, respectively.

Method 2 (Ignoring electronic noise): This method is the same as Method 1, except that the electronic noise is ignored during image reconstruction. In other words, $\sigma^2 = 6.3^2$ is used in data generation, but $\sigma^2 = 0$ is assumed in reconstruction.

Method 3 (Statistical approach): This method uses 1000 realizations of the noisy post-log data sets. The ensemble variance "sinogram" is then calculated from these 1000 realizations, and the weighting function is the reciprocal of the variance "sinogram."

Method 4 (Practical approach): Almost the same as Method 1, except that the mean value $\bar{y}_j$ is replaced by one-time (i.e., one noise-realization) post-log measurement y_j. Electronic noise is modeled by σ^2.

$$\text{Weighting for ray } y = \frac{1}{\sigma_y^2} = \frac{(aI_0 e^{-y}\bar{\bar{E}})^2}{a^2 I_0 (e^{-y} + e^{-2y})\bar{\bar{E}} + \sigma^2}. \quad (19)$$

Method 5 (Modified version of Method 1): We replace the variance by a power function of the variance.

$$\text{Weighting for ray } y = \frac{1}{\sigma_y^{2p}} = \left[\frac{(aI_0 e^{-\bar{y}}\bar{\bar{E}})^2}{a^2 I_0 (e^{-\bar{y}} + e^{-2\bar{y}})\bar{\bar{E}} + \sigma^2}\right]^p \quad (20)$$

Method 6 (Most vendors used model): This is a simplified version of (19). The expression is

$$\text{Weighting for ray } y = \frac{1}{\sigma_y^2} = \frac{(aI_0 e^{-y})^2}{a^2 I_0 e^{-y} + \sigma^2}. \quad (21)$$

Method 7 (Practical Poisson approximation): Instead of using the more accurate compound-Poisson model, this method uses the more popular (but less accurate) Poisson model and ignores electronic noise, which leads to the variance sinogram being $\exp(\bar{y}_j)$. To make it practical, the mean value $\bar{y}_j$ is replaced by one-time measurement value y_j.

$$\text{Weighting for ray } y = \frac{1}{\sigma_y^2} = e^{-y}. \quad (22)$$

Method 8 (Constant weights, i.e., No weights): The variance sinogram is set to a constant for all projection rays.

$$\text{Weighting for ray } y = 1. \quad (23)$$

Method 9 (Totally wrong): This will show what damages wrong weighting factors can do to the reconstruction. The totally wrong variance sinogram is chosen to be $\exp(-y_j)$.

$$\text{Weighting for ray } y = e^{y}. \quad (24)$$

Method 10 (Method 7 with the noiseless y): This is more accurate than Method 7, where $\bar{y}$ is the noiseless true value.

$$\text{Weighting for ray } y = \frac{1}{\sigma_y^2} = e^{-\bar{y}}. \quad (25)$$

Method 11 (Method 10, plus a power p): This method uses the same idea of Method 5, but uses the model in Method 10:

$$\text{Weighting for ray } y = \left(\frac{1}{\sigma_y^2}\right)^p = e^{-p\bar{y}}. \quad (26)$$

Method 12 (Method 11, 1 realization, 5-point average): Method 11 is not practical, because the noiseless measurement is never available. On the other hand, the one realization measurement is too noisy. This method replaces $\bar{y}$ in (24) by a 5-point running averaged (i.e., lowpass filtered) value of y in the detector channel direction. This method is practical.

III. Results

See Tables 1-2 and Figure 1.

IV. Conclusion

A more accurate noise model may or may not reduce the noise variance for a given spatial resolution (or image contrast). This paper investigates whether the more accurate compound-Poisson noise model in x-ray CT pre-log data can give better images than the less accurate Poisson noise model. This paper gives a negative answer. A more accurate noise model does not necessarily give a better image.

Based on the compound-Poisson noise model, this paper derived the expressions for the mean and variance for both pre-log data and post-log data. Those formulas were verified statistically by computer simulations.

The linear attenuation coefficient is x-ray energy dependent, and this fact causes beam-hardening artifacts, even when the data are noiseless. This paper focuses on noise model; the beam-hardening effects are not in the scope of this paper. Thus, the linear attenuation coefficients are assumed to be energy independent in this paper.

Computer simulations using Methods 1, 2, 3, 4, 6, 7, and 10 give similar results. This implies that it is reasonable to approximate the more accurate compound-Poisson noise model by the less accurate Poisson model. Mathematically speaking, this approximation is justified if $\exp(-2\int \mu(x)dx)$ is much smaller than $eep(-\int \mu(x)dx)$ and can be ignored. Another observation is that the use the one-time measurement to approximate the mean value of the measurement can introduce some noise to the output image. Therefore, one should smooth the projection measurements when they are used to form the weighting factors.

Methods 1, 2, 3, 4, 6, 7, and 10 can generate some low-frequency shadowing artifacts. If we modify the weighting function by a power function of the weighting function this low-frequency shadowing artifacts can be reduced without scarifying the image contrast, see Methods 5, 11, and 12. A thorough study of the weighting function with an exponent parameter is outside the scope of this paper, and will be conducted in a different paper.

References

[1] K. Lange and R. Carson, "EM reconstruction algorithms for emission and transmission tomography," *J. Comput. Assist. Tomogr.,* vol. 8, pp. 306–316,1984.

[2] K. Lange, M. Bahn, and R. Little, "A theoretical study of some maximum likelihood algorithms for emission and transmission

tomography," *IEEE Trans. Med. Imag*., vol. MI-6, pp. 106–114, 1987.
[3] J. A. Browne and T. J. Holmes, "Developments with maximum likelihood X-ray computed tomography," *IEEE Trans. Med. Imag*., vol. 11,pp**.** 40–52, 1992.
[4] J. A. Fessler, "Statistical image reconstruction methods for transmission tomography *Handbook of Medical Imaging, Medical Image Processing and Analysis*, M. Sonka and J. M. Fitzpatrick, Eds. (Bellingham, WA: SPIE), vol. 2, pp. 1-70, 2000.
[5] T. M. Buzug, *Computed Tomography: From Photon Statistics to Modern Cone-Beam CT* (Springer-Verlag Berlin Heidelberg), 2010.
[6] B. R. Whiting, P. Massoumzadeh, O. A. Earl, J. A. O'Sulivan, D. L. Donald, and J. F. Williamson, "Properties of preprocessed sonogram data in x-ray computed tomography," *Med. Phys*., vol. 22, p. 3290-3303, 2006.
[7] G. M. Lasio, B. R. Whiting, and J.F. Williamson, "Statistical reconstruction for x-ray computed tomography using energy-integrating detectors," *Phys. Med. Biol*., vol. 52, pp. 2247-2266, 2007.
[8] R. M. Adelson, "Compound Poisson distribution." *Operat. Res. Quart.,* vol. 17, pp. 73-75, 1966.
[9] P. W. Den Iseger, M.A. J. Smith, and R. Dekker, "Computing compound Poisson distributions faster," *Insurance Mathematics and Economics,* vol. 20, pp. 23-34, 1997.
[10] N.A. Weiss, *A Course in Probability* (Boston: Addison–Wesley), pp. 380–383, 2005.

Table 1.Evaluation of compound noise variance given by Eq. (15) by using 1000 noise realizations

$\int \mu dx$	Variance calculated by Eq. (15)	Variance computed by 1000 noise realizations
0.5	0.0003	0.0003
1	0.0004	0.0004
1.5	0.0006	0.0006
2	0.0009	0.0009
2.5	0.0014	0.0015
3	0.0023	0.0021
3.5	0.0037	0.0035
4	0.0061	0.0062
4.5	0.0100	0.0097
5	0.0165	0.0170
5.5	0.0274	0.0321
6	0.0456	0.0457
6.5	0.0716	0.0912
7	0.1304	0.1943
7.5	0.2259	0.3868
8	0.4025	0.9354
8.5	0.7455	1.2479
9	1.4516	1.4094
9.5	2.9982	1.3063
10	6.5876	1.1831

Table 2. Ranking of the methods in terms of ROI 2 normalized standard deviation

Rank	Method
1 (best)	Method 12 (Exponential, 1 noise realization, 5-point running average)
2	Method 7 (Exponential, 1 noise realization)
3	Method 11 (Exponential, with a power *p*, noiseless weight)
4	Method 5 (Theoretical true weight with a power *p*)
5	Method 10 (Exponential, noiseless weight)
6	Method 1 (Theoretical true weight)
7	Method 2 (Theoretical true weight, ignoring electronic noise)
8	Method 3 (Theoretical true weight, 1000 noise realization)
9	Method 8 (Constant weight)
10	Method 6 (Most vendors used model)
11	Method 4 (Theoretical true weight, 1 noise realization)
12 (worst)	Method 9 (Totally wrong)

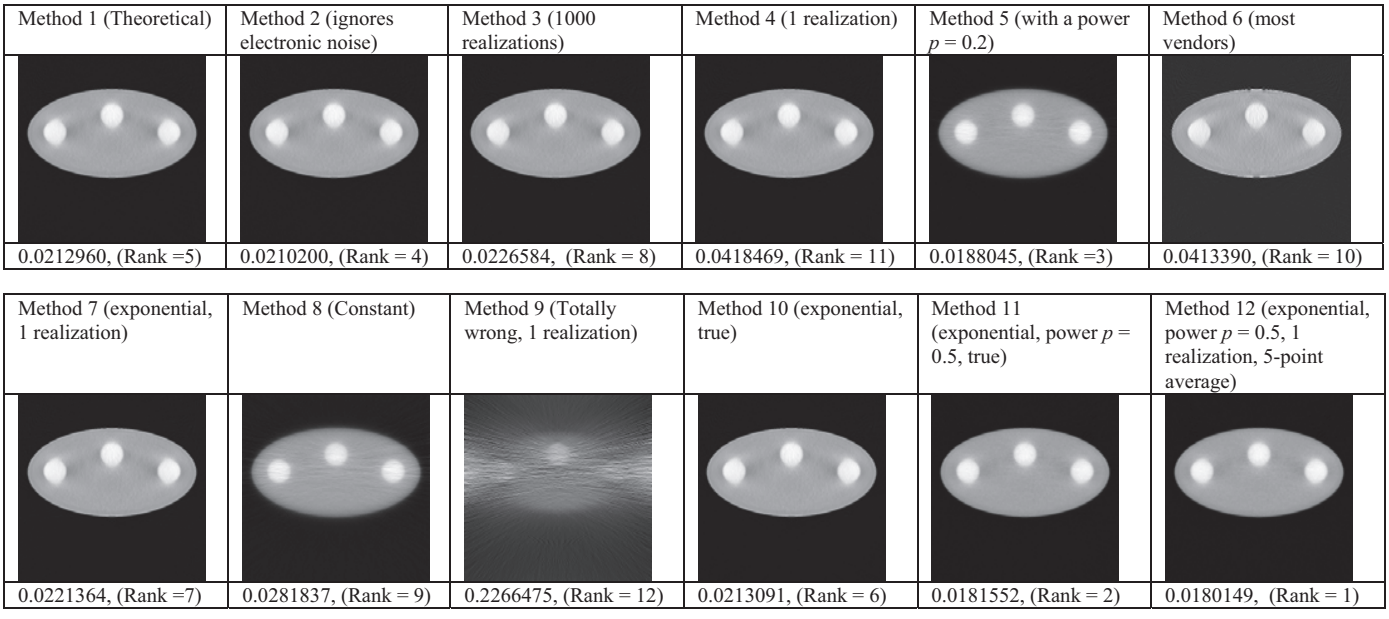

Figure 1. Reconstructed images with Methods 1~12, using a stopping rule that a pre-specified image contrast of 0.55 is reached. The last row lists the normalized standard deviation in a constant region inside the object.

Virtual Single-frame Subtraction Imaging

Mathias Unberath*†, André Aichert*, Stephan Achenbach‡, and Andreas Maier*†
*Pattern Recognition Laboratory, FAU Erlangen-Nuremberg, Germany
†Graduate School in Advanced Optical Technologies, Erlangen, Germany
‡University Hospital: Cardiology and Angiology, FAU Erlangen-Nuremberg, Germany
Email: mathias.unberath@fau.de

***Abstract*—We outline a generic framework for single-frame, detector-domain material decomposition. The method involves a segmentation and a background estimation step yielding a virtual mask image that can be used for subtraction. In many cases, material decomposition yields non-truncated difference images enabling the use of novel motion estimation methods that exploit epipolar consistency conditions.**
In this work, a pipeline for virtual digital subtraction coronary angiography is presented and evaluated on a phantom data set. The pipeline consists of Hessian-based vessel segmentation followed by background estimation in Fourier domain. Center of mass tracking and a metric based on epipolar consistency conditions is then used to estimate vertical detector translations that serve as a surrogate for respiratory and cardiac motion. When assessing the heart phase, we achieved a correlation of 0.91 between the ground truth ECG and the image-based surrogates. The results encourage further experiments on real data as well as the application for intra-scan motion compensation.

I. Introduction

Robust methods for intra-scan patient motion estimation, such as center-of-mass (CoM) tracking or use of epipolar consistency conditions (ECC), require non-truncated data [1]. Unfortunately, this requirement is hardly ever satisfied for scans of thoracic or abdominal regions. However, the object of interest, such as the coronary arteries, may lie completely in the field of view. In order to increase visibility and enable above-mentioned motion estimation techniques, it would be beneficial to separate the object from the background.
A widely used technique for decomposition is digital subtraction imaging, allowing separation of structures that can be enhanced using some sort of contrast-agent. The most widely known representative of these techniques is digital subtraction angiography (DSA) [2]. Traditionally, the method requires two acquisitions with and without contrast enhancement, that are being referred to as the fill and mask scan, respectively. Requiring two asynchronous scans makes the method susceptible to intra- and inter-scan patient motion [3]. Single-frame material decomposition, however, does not rely on asynchronous imaging of the same scene and allows for lower patient dose. So far, it has been described in the context of energy-resolving X-ray detectors that are not yet part of clinical routine [4]. Nonetheless, single-frame material decomposition may be possible for conventional acquisitions exploiting segmentation and interpolation strategies. Similar methods have been applied in the context of high-intensity object masking [5] and background estimation [6] where they are used for artifact reduction in reconstructions.
We outline a generic framework for virtual single-frame subtraction imaging of spatially sparse structures, such as contrasted vessels or metal implants, to enable the application of algorithms that are restricted to non-truncated data. We present preliminary results of coronary artery motion estimation using CoM-tracking and ECC on phantom data [7], and show that the motion patterns can be used for image-based gating.

II. Material and Methods

The schematic of the generic procedure is shown in Fig. 1. A projection image in which the object of interest is well visible serves as input to the method. The method involves the following steps:

i. Segmentation of the structure yielding a binary mask
ii. Background estimation in the masked regions
iii. Digital subtraction of input and virtual background

Success of the method relies on the two key components segmentation and background estimation, which we will refer to as inpainting. Both elements can be exchanged arbitrarily in the sense that their function is fixed while the specific method can be chosen to best handle the underlying problem.
We describe an exemplary pipeline designed for rotational C-arm CT coronary angiography, elaborating on the methods used for segmentation and inpainting of coronary arteries.

A. Preprocessing and segmentation

The segmentation algorithm described here makes use of derivatives that act like a high-pass filter. To suppress the influence of noise while preserving edges, a bilateral filter is applied to the input images $I'_a,\ a = 1, ..., N$ [8]. The filtered image I_a at position $\mathbf{u} \in \mathbb{R}^2$ is given as

$$I_a(\mathbf{u}) \propto \sum_{\mathbf{u}_i \in \Omega} I'_a(\mathbf{u}_i) \cdot f_{\sigma_r}(\|I'_a(\mathbf{u}_i) - I'_a(\mathbf{u})\|) \cdot f_{\sigma_d}(\|\mathbf{u}_i - \mathbf{u}\|)\,,$$

where Ω is a local neighborhood, and $f_\sigma(x) \propto \exp(-x^2/2\sigma^2)$ is a Gaussian function defining neighborhood weights in spatial and intensity domain. In the above equation, we omitted the normalization factor $\mathcal{N}(\mathbf{u})$ for more compact notation.
Subsequently, the projection images are segmented using a combination of morphological and Hessian-based filters [9]. Coronary arteries manifest as bright, small tubular structures on a darker, slowly varying background. A circular top-hat filter yields high responses for bright structures smaller than its radius R and can, therefore, be used to remove all structures larger than the structuring element [10]. Generally, in the

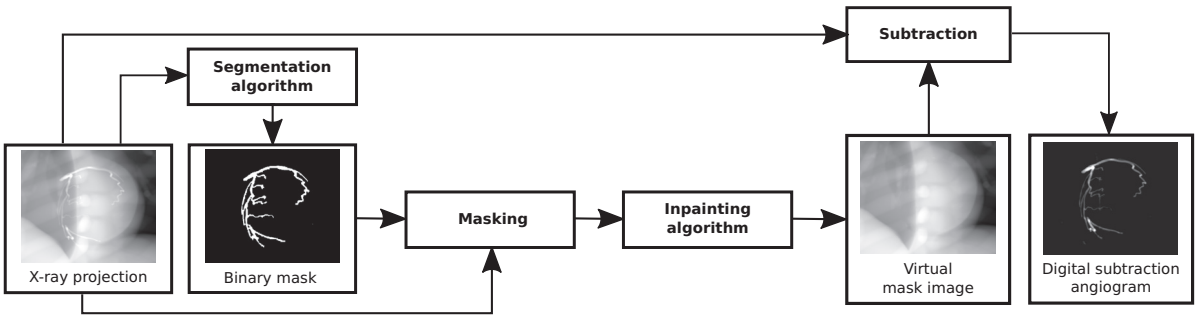

Fig. 1. Schematic of the proposed method. Having obtained a binary segmentation of the object of interest, the background is estimated using an inpainting method. The virtual mask image can then be subtracted from the original projection yielding the difference image.

top-hat filtered image I_a^{TH} responses from non-tubular structures are not sufficiently suppressed. Therefore, we include a vesselness-filtered version of the image I_a^{V}. The filter uses the Eigenvalues of the Hessian $\lambda_{1,2} = \lambda_{1,2}(\mathbf{u}, s)$ at position $\mathbf{u}$ and scale s such that $|\lambda_1| \geq |\lambda_2|$. They enable the definition of physically meaningful measures, the blobness $R_b = {}^{\lambda_2}/_{\lambda_1}$, and the structureness $\mathcal{S} = \sqrt{\lambda_1^2 + \lambda_2^2}$. Then if $\lambda_1 > 0$, the vesselness reads

$$V(\mathbf{u}) = \max_s \ \exp(-\alpha R_b) * (1 - \exp(-\beta \mathcal{S}))\,, \qquad (1)$$

where α, and β are constants [11]. The enhanced images I_a^{E} are then obtained by combination of vesselness and top-hat filtered images I_a^{V} and I_a^{TH}, respectively, yielding

$$I_a^{\mathrm{E}}(\mathbf{u}) = \begin{cases} I_a^{\mathrm{V}}(\mathbf{u}) & \text{if } I_a^{\mathrm{V}}(\mathbf{u}) > t_{\mathrm{V}} \ \wedge \ I_a^{\mathrm{TH}}(\mathbf{u}) > 0 \\ 0 & \text{else} \end{cases}, \qquad (2)$$

where t_{V} is an empirically determined threshold. A binary segmentation mask $\mathcal{W}_a$ is then calculated from the enhanced image I_a^{E} using hysteresis thresholding. The mask will be used as a binary defect window. Therefore, $\mathcal{W}_a(\mathbf{u}) = 1$ if $\mathbf{u}$ belongs to the background and 0 otherwise.

B. Background estimation: Spectral inpainting

Masking the object of interest can be expressed as a multiplication of the projection with the defect window in spatial domain, yielding a defective image $G_a(\mathbf{u}) = I_a(\mathbf{u}) \cdot \mathcal{W}_a(\mathbf{u})$. Inpainting of the defective image is equivalent to estimating the measurement of defect detector pixels, where spatially extensive regions do not carry information. Many estimation techniques in spatial domain, such as Thin-Plate-Spline interpolations, exist [5]. However, due to their locality they only perform well for sufficiently small defects and change the noise characteristic, which may lead to an unnatural appearance of the image [12].

Frequency domain methods, such as spectral interpolation, have been shown to work well for large defect areas and noisy structures [5][12]. We seek to estimate the undistorted background $\mathcal{B}_a$ from the observation $G_a(\mathbf{u}) = \mathcal{B}_a(\mathbf{u}) \cdot \mathcal{W}_a(\mathbf{u})$. In frequency domain the relation is expressed in terms of convolution $g_a = b_a \star w_a$, where lowercase letters denote the Fourier transform of its uppercase equivalent. The method tries to iteratively deconvolve the unknown background spectrum b_a and the window spectrum w_a, utilizing the symmetry property of the Fourier transform of real valued signals [12].

To preserve the locality of image appearance, spectral interpolation is performed consecutively on patches rather than on the whole projection at once. Patch-based processing, however, implies weighting with a rectangular window that decreases the dynamic range and sensitivity due to spectral leakage [13]. To mitigate such effects, an apodization window is applied to the patches before converting to Fourier domain.

Finally, the estimated background image is then subtracted from the projection, yielding the virtual digital subtraction angiogram $D_a(\mathbf{u}) = I_a(\mathbf{u}) - \mathcal{B}_a(\mathbf{u})$.

C. Intra-scan motion and its implications

The subtraction images D_a are, in contrast to the original projections I_a not truncated and can, therefore, serve as an input to CoM- and ECC-based motion estimation algorithms. The CoM $\mathbf{c}_a$ in frame a is calculated from the pixel intensities:

$$\mathbf{c}_a = \frac{1}{\sum_{\mathbf{u} \in D_a} D_a(\mathbf{u})} \sum_{\mathbf{u} \in D_a} D_a(\mathbf{u}) \cdot \mathbf{u}. \qquad (3)$$

The method yields 2D shifts, corresponding to motion in the plane orthogonal to the viewing direction.

Use of ECC relies on the epipolar geometry between views a_1 and a_2 with projection matrices P_{a_1} and P_{a_2}, respectively. Assuming a parallel acquisition geometry, integration over corresponding epipolar lines $\mathbf{l}_{a_1}(\kappa)$ and $\mathbf{l}_{a_2}(\kappa)$ gives two redundant ways of calculating the integral over the epipolar plane $\mathbf{E}(\kappa)$ through the object, where κ defines the angle of the epipolar plane [1]. There exists a pencil of such planes around the baseline each with a different angle κ, allowing for the definition of consistency conditions. For cone-beam geometry the relationship outlined above has to be modified using Grangeat's theorem, yielding

$$\frac{\mathrm{d}}{\mathrm{d}t} \rho_{a_1}(\mathbf{l}_{a_1}) - \frac{\mathrm{d}}{\mathrm{d}t} \rho_{a_2}(\mathbf{l}_{a_2}) \approx 0, \qquad (4)$$

where $\frac{\mathrm{d}}{\mathrm{d}t} \rho_a(\mathbf{l})$ is the derivative of the integral over line $\mathbf{l}_a$ in image I_a, and t is the distance of the line to the image origin. Requiring mutual consistency among all images $I_a,\ a = 1, ..., N$ at multiple lines $\mathbf{l}$ allows the definition of a

metric that can be optimized to estimate motion parameters responsible for the inconsistencies [1].

D. Surrogate signal extraction

Respiratory and cardiac motion both are assumed to manifest in a global translation in head-foot direction with low and high frequency, respectively [14]. Therefore, we will restrict the motion model to 1D translations in vertical detector coordinate direction, that we will refer to as v-shifts. The shifts $\mathbf{v} = (v_1, ..., v_N)$ are transformed to Fourier domain applying a Hann window for apodization [13]. Subsequently, the signal is separated into two components $\mathbf{v}_{\text{resp}}$ and $\mathbf{v}_{\text{card}}$ containing frequencies below and above a certain threshold f_{sep}, respectively. Then, the heart rate f_{ecg} is extracted as the dominant frequency in the power spectral density of $\mathbf{v}_{\text{card}}$. Using f_{ecg} as the heart rate, a normalized cardiac time is calculated for each image a as $t_{a,\text{card}} = \frac{aTf_{\text{card}}}{N} \pmod 1$, where T is the scan duration.

E. Data and Experiments

The proposed methods were evaluated on Cavarev, an XCAT-based phantom data set exhibiting respiratory and cardiac motion [7], [15]. The data set consists of 133 projections acquired over 5 s. The radius for top-hat filtering was 4 pixels, the vesselness threshold $t_{\text{V}} = 0.5$. The segmentation accuracy was assessed using the Dice score. The patch size used for spectral interpolation was 160×160, 100 iterations were used. A Blackman window was applied to each patch. We calculated v-shifts using CoM- and ECC-based methods. As no mask scan is included in the Cavarev data set, the inpainting and subtraction algorithm could only be evaluated implicitly using the results of both motion estimation techniques. The threshold for respiratory and cardiac signal separation was chosen as $f_{\text{sep}} = 1\,\text{Hz}$. We demonstrate the correlation of the respiratory signal $\mathbf{v}_{\text{resp}}$ with the ground-truth qualitatively, but present quantitative results for the normalized cardiac time, i.e. Pearson's R.

III. Results and Discussion

Representative results of the virtual single-frame subtraction pipeline are shown in Fig. 2. The segmentation algorithm described in Sec. II-A yielded a Dice score of 0.98 ± 0.14 with respect to a manual segmentation. Nevertheless, segmentation errors were present (see Fig. 2b) indicating that a more complex segmentation algorithm may be necessary to handle real data. The virtual mask and difference image are shown in Fig. 2c and 2d, respectively. While quantitative evaluation of the background estimation is not possible with Cavarev, the visual results suggest that spectral interpolation is able to satisfactorily estimate the background for narrow structures such as the coronary arteries. Larger scale structures, however, may require different inpainting algorithms up to a point where reliable background estimation becomes impossible as too much information is omitted from the image. Segmentation errors are not as prominent in the resulting difference image or not visible at all, indicating that background estimation may hamper artifact propagation if the erroneously masked region is well explained by the remaining image. This observation is encouraging, as the subsequent motion estimation step then has to deal with fewer artifacts which may lead to a more robust estimation.

The v-shifts $\mathbf{v}$ obtained from CoM- and ECC-based methods are shown in Fig. 3a. Both shifts have a similar range on the detector of $37.64\,\text{mm}$ and $39.24\,\text{mm}$ for CoM and ECC, respectively. The offset, both in Fig. 3a and 3b, was adjusted for better visualization. Shifts obtained using the ECC-based method appear smoother than the ones extracted using CoM tracking. An explanation for this behavior could be that CoM calculation is more susceptible to remaining artifacts as it directly uses image intensities of every image independently. The ECC-based method on the other hand requires integration over epipolar lines and bundle optimization [1], potentially allowing more robust estimations. In the same figure it can be observed that the extracted low frequency signal $\mathbf{v}_{\text{resp}}$ is in good agreement with the ground truth respiratory phase. An attempt to directly assess the breathing frequency using the power spectral density did not yield meaningful results. We believe this shortcoming to be related to the low amount of observed breathing cycles (fewer than 1.5).

The high frequency signal $\mathbf{v}_{\text{card}}$, resulting normalized time $\mathbf{t}_{\text{card}}$, and the ground truth cardiac time are shown in Fig. 3b. The periodic signals $\mathbf{v}_{\text{card}}$ visually correlate well with the ground truth and support the assumption of global head-foot motion during contraction at least for this phantom study. Albeit different in spatial and frequency domain, both signals exhibit the same dominant frequency of $1.41\,\text{Hz}$ yielding the same normalized times $\mathbf{t}_{\text{card}}$ and, therefore, Pearson R of 0.91. Hence, the shifts could be used as surrogate for the heart phase allowing image-based gating. This may be beneficial for gated reconstructions as the surrogate is derived from the actual motion state rather than the electrophysiological excitation.

Separation of low and high frequency components of $\mathbf{v}$ by thresholding in Fourier domain worked well overall. However, the separation does not seem optimal everywhere. For the signals obtained using the CoM and the ECC the effect can be observed at small and large projection numbers, respectively. Although the effect was subtle and did not affect the heart rate estimation in Fourier domain, it may become bothersome when using the shifts for motion compensated reconstructions. In such cases, however, the signal decomposition could be performed in a reversed order if an ECG was acquired simultaneously. Then frequencies related to the heart beat could easily be omitted allowing for accurate respiratory motion estimation.

IV. Conclusion

We discussed a generic pipeline for virtual single-frame subtraction imaging enabling detector domain material decomposition. We introduced a representative pipeline targeted

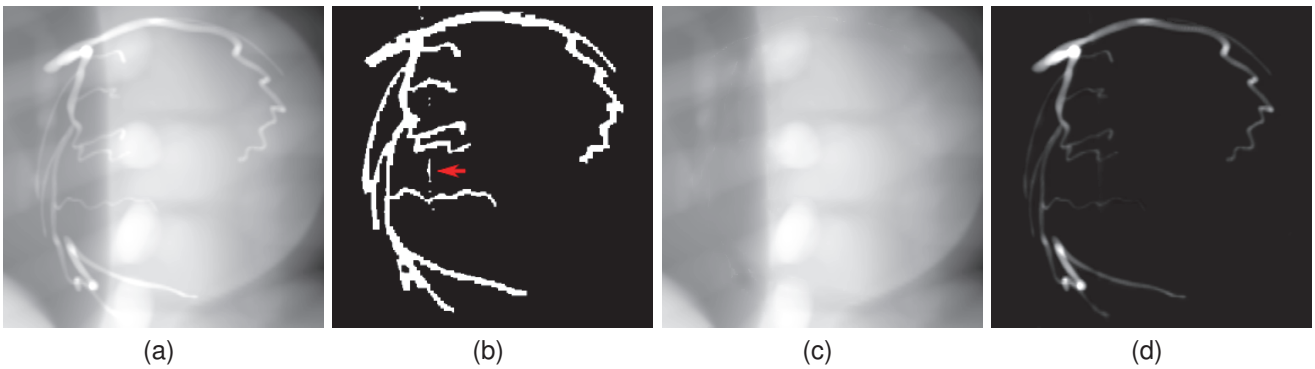

Fig. 2. Crop of the original projections (not shown here) to the region of interest. The original projection, the segmentation mask, the inpainted image, and the DSA image are shown in Fig. 2a, 2b, 2c, and 2d, respectively.

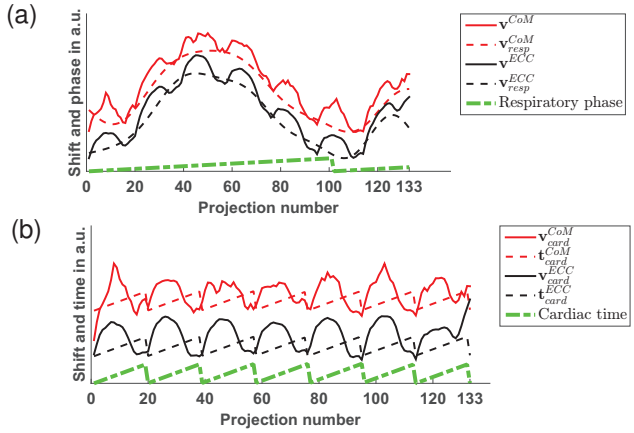

Fig. 3. 1D motion estimation of CoM- and ECC-based methods (solid lines) and the low frequency respiratory signal (dashed lines) are shown in Fig. 3a together with the ground-truth respiratory phase. Fig. 3b shows the high frequency signal, the corresponding normalized time, and the ground-truth.

at coronary arteries and demonstrated its capabilities and limitations in a phantom study. We argued that material decomposition may void truncation for the object of interest allowing for motion estimation techniques based on the CoM or ECC. We demonstrated the applicability of such methods and showed that v-shifts correlate well with both, the respiratory and the cardiac phase. In future work we will evaluate the method on real patient data including but not limited to interventional coronary angiography. We see applications in metal artifact reduction but most importantly in image-based motion compensation. A natural next step would be the extension of the motion model. Estimating 3D translations may allow for respiratory motion compensation, which is hardly feasible using vertical detector coordinate shifts only.

Acknowledgment

The authors gratefully acknowledge funding of DFG MA 4898/3-1 and the Erlangen Graduate School in Advanced Optical Technologies (SAOT) by the German Research Foundation (DFG) in the framework of the German excellence initiative.

References

[1] A. Aichert, M. Berger, J. Wang, N. Maass, A. Doerfler, J. Hornegger, and A. Maier, "Epipolar Consistency in Transmission Imaging," *Medical Imaging, IEEE Transactions on*, vol. 34, no. 10, pp. 1–15, 2015.

[2] W. R. Brody, "Digital subtraction angiography," *Nuclear Science, IEEE Transactions on*, vol. 29, no. 3, pp. 1176–1180, 1982.

[3] M. Nejati and H. Pourghassem, "Multiresolution image registration in digital X-Ray angiography with intensity variation modeling," *Journal of Medical Systems*, vol. 38, no. 2, pp. 1–10, 2014.

[4] X. Wang, D. Meier, K. Taguchi, D. J. Wagenaar, B. E. Patt, and E. C. Frey, "Material separation in X-ray CT with energy resolved photon-counting detectors," *Medical Physics*, vol. 38, no. 3, pp. 1534–1546, 2011.

[5] M. Berger, C. Forman, C. Schwemmer, J. H. Choi, K. Müller, A. Maier, J. Hornegger, and R. Fahrig, "Automatic Removal of Externally Attached Fiducial Markers in Cone Beam C-arm CT," in *Bildverarbeitung für die Medizin 2014*, 2014, pp. 168–173.

[6] C. Blondel, R. Vaillant, G. Malandain, and N. Ayache, "3D tomographic reconstruction of coronary arteries using a precomputed 4D motion field," *Physics in Medicine and Biology*, vol. 49, no. 11, p. 2197, 2004.

[7] C. Rohkohl, G. Lauritsch, A. Keil, and J. Hornegger, "CAVAREV - An Open Platform for Evaluating 3D and 4D Cardiac Vasculature Reconstruction," *Physics in Medicine and Biology*, vol. 55, no. 10, pp. 2905–2915, 2010.

[8] C. Tomasi and R. Manduchi, "Bilateral filtering for gray and color images," in *Computer Vision. Sixth International Conference on*. IEEE, 1998, pp. 839–846.

[9] M. Unberath, S. Achenbach, R. Fahrig, and A. Maier, "Exhaustive Graph Cut-based Vasculature Reconstruction," in *Biomedical Imaging, 2016 IEEE 13th International Symposium on*. IEEE, 2016, to appear.

[10] C. Schwemmer, C. Rohkohl, G. Lauritsch, K. Müller, and J. Hornegger, "Residual motion compensation in ECG-gated interventional cardiac vasculature reconstruction." *Physics in Medicine and Biology*, vol. 58, no. 11, pp. 3717–37, 2013.

[11] A. F. Frangi, W. J. Niessen, K. L. Vincken, and M. A. Viergever, "Multiscale vessel enhancement filtering," in *MICCAI 1998: 1st International Conference, Proceedings of the*. Springer, 1998, pp. 130—-137.

[12] A. Aach and V. Metzler, "Defect interpolation in digital radiography - how object-oriented transform coding helps," in *SPIE Medical Imaging*, 2001, pp. 824–835.

[13] F. J. Harris, "On the use of windows for harmonic analysis with the discrete Fourier transform," *Proceedings of the IEEE*, vol. 66, no. 1, pp. 51–83, 1978.

[14] C. Blondel, G. Malandain, R. Vaillant, and N. Ayache, "Reconstruction of Coronary Arteries from a Single rotational X-ray projection sequence." *IEEE Transactions on Medical Imaging*, vol. 25, no. 5, pp. 653–63, 2006.

[15] A. Maier, H. Hofmann, C. Schwemmer, J. Hornegger, A. Keil, and R. Fahrig, "Fast Simulation of X-ray Projections of Spline-based Surfaces using an Append Buffer," *Physics in Medicine and Biology*, vol. 57, no. 19, pp. 6193–6210, 2012.

Adaptive Multi Band Frequency Filter (aMBF) for Noise Reduction in Dynamic CT Perfusion Dataset

Francesco Pisana, Thomas Henzler, Stefan Schönberg, Bernhard Schmidt, Ernst Klotz, and Marc Kachelrieß

***Abstract*—Dynamic CT Perfusion (CTP) provides voxel-related functional information which has proven to be very useful in clinical decision in many fields such as neuroradiology and oncology. Radiation exposure is significantly higher than conventional CT while the signal that has to be detected can be sometimes much lower, making this technique very challenging. Many approaches to reduce noise in CTP have been and are still investigated. In this study we propose an improved version of the Multi Band Frequency filter (MBF), which aims at discriminating noise contribute from anatomical information in each voxel, and adapting the filter's temporal width accordingly. We named our filter Adaptive Multi Band Frequency filter (aMBF). The aMBF was compared to conventional MBF both on an in-house developed digital phantom, and on different clinical datasets. Results show that the aMBF is able to better preserve true arterial input function (AIF), while improving the contrast to noise ratio and keeping the same spatial resolution in comparison to the MBF.**

***Index Terms*—Dynamic CT Perfusion, Noise Reduction, Multi Band Frequency Filter.**

I. Introduction

DYNAMIC CT Perfusion (CTP) consists of repeatedly scanning the same body section, during a compact and short injection of contrast media. The goal is to measure the changes of enhancement of each voxel due to contrast media dynamics. All sources of CT value changes over time which are not caused by contrast media dynamics, like motion or other artifacts, have to be corrected or minimized [1] [2]. CTP is nowadays a well-accepted and established technique which provides useful functional information for each voxel at the expenses of higher radiation dose. Some of the most commonly derived functional parameters are blood flow (BF), blood volume (BV) and mean transit time (MTT), which give important information related to tissue hemodynamics. CTP has proven to be very useful in application such as neuroradiology [3] [4] and oncology [5] [6].

While the same parameters can be obtained also with dynamic MRI, CTP remains attractive for the higher spatial resolution, faster acquisition times and higher availability. The only drawback stays in the higher radiation dose compared to conventional CT [7]. Dose reduction methods can only be applied up to certain limits, since functional parameters are normally obtained via deconvolution (or related) algorithms [8], which might fail when signal-to-noise ratio (SNR) becomes low. Moreover, depending on clinical application, the enhancement to be detected can be sometimes very low.

The dynamic nature of CTP gives one additional degree of freedom to be exploited (namely the temporal dimension) and different methods have been and are still investigated to be able to improve SNR specifically for dynamic CTP, ranging from iterative reconstructions [9], high dimensional image filters [10], wavelet transforms [11] and so on. Recently, some interesting approaches have been developed which share a common principle: low spatial frequency components of each image in time $f_{\mathrm{L}}(\boldsymbol{r}, t)$ contain the signal that needs to be detected, while high frequency components $f_{\mathrm{H}}(\boldsymbol{r}, t)$ contain noise as well as small anatomical structures and edges. Under the assumption of negligible motion between the images acquired in different time steps, averaging over time only the high frequency components would result in a reduction of noise, while preserving anatomical information. To restore an improved image, averaged high spatial frequencies are added back to the original low spatial frequencies.

This approach might be carried out in slightly different ways, of which the multiband frequency filter (MBF) is probably the most straightforward [12]. In this study we decided to start from the original implementation of the MBF, and to improve some of its features, in particular investigating the contribution of noise and anatomy for each voxel in the high spatial frequency images, and adapting the width of the temporal average process as a consequence. We name our filter the adaptive MBF (aMBF).

The present article is structured in the following way: in the methods section we start with a theoretical explanation of the MBF in II-A. In II-B we explain more in detail the algorithm of our proposed improved version and justify its robustness with some practical considerations. In II-C we discuss the digital brain perfusion phantom implementation, the clinical datasets specifications and the metrics according to which we evaluated our results. Finally, in the results section we show the improvements of the aMBF compared to the MBF both qualitatively and quantitatively.

II. Methods

A. MBF

In this subsection we will explain the theoretical background of the MBF approach [12]. The high dimensionality of CTP datasets offer some data redundancy, which can be exploited for noise reduction. Particularly, it can be assumed that noise is uncorrelated in temporal direction, and hence could be

Francesco Pisana and Prof. Dr. Marc Kachelrieß work in Medical Physics Department in German Cancer Research Center (DKFZ) in Heidelberg, Germany. Contact author: francesco.pisana@dkfz.de

PD. Dr. Thomas Henzler and Prof. Dr. Stefan Schönberg work in Radiology Department in Mannheim University Clinic, Mannheim, Germany.

Dr. Bernhard Schmidt and Ernst Klotz work in Siemens Healthcare GmbH, Forchheim, Germany.

reduced simply by an average in this domain. To have a representation of noise, a high-pass filter might be employed, since the noise spectrum is shifted towards higher frequencies compared to the signal. This assumption is in general more robust in spatial domain rather than in temporal domain. In fact some voxels' temporal signal (time-attenuation curve, TAC) has higher frequency components compared to noise, for example vessels and tumors might have a very quick and high enhancement. A low-pass filter in time direction would smooth out vessels TAC, which would seriously bias the resulting functional parameters. Low-pass filtering in spatial direction would be safer: low spatial frequency components $f_{\mathrm{L}}(\boldsymbol{r},t)$ would contain the noiseless tissue which might or might not enhance over time and which will thus not be averaged over time, while high spatial frequency components $f_{\mathrm{H}}(\boldsymbol{r},t)$ would mainly contain noise but also the edges of the images and possibly small anatomical structures (like arteries in the brain). Assuming that motion is absent or compensated, the edges would not be affected by an average over time, since they would not change their position nor their enhancement. In principle, noise could be reduced by a factor equal to the root mean square of the number of time points averaged together. In practice, also small vessels will be included in $f_{\mathrm{H}}(\boldsymbol{r},t)$, which should not be averaged over time. Decreasing the cutoff frequency would make more anatomy fall into $f_{\mathrm{H}}(\boldsymbol{r},t)$, while increasing it would make less noise fall into $f_{\mathrm{H}}(\boldsymbol{r},t)$. The formula of the MBF is the following:

$$f^{*}(\boldsymbol{r},t) = f_{\mathrm{L}}(\boldsymbol{r},t) + \bar{f}_{\mathrm{H}}(\boldsymbol{r},t). \tag{1}$$

Where:

$$\bar{f}_{\mathrm{H}}(\boldsymbol{r},t) = \frac{1}{2N+1}\sum_{\delta=-N}^{N} f_{\mathrm{H}}(\boldsymbol{r},t+\delta).$$

and $f^{*}(\boldsymbol{r},t)$ is the filtered image, $\boldsymbol{r}$ is a three dimensional vector identifying a voxel position, t is the temporal index, δ is the temporal shift and $2N+1$ is the total number of time points averaged together for the high frequency components. To reduce the inevitable smoothing of small vasculature, the $\bar{f}_{\mathrm{H}}(\boldsymbol{r},t)$ is obtained from a running average process, instead of a full average over time. In our implementation of MBF, $N = 2$. Simulated and clinical cases we used have total number of acquired time points T ranging from 26 to 30.

B. aMBF

We propose an improved version of the MBF, where the number of adjacent time points used for the running average of the high spatial frequencies is not constant, but it is instead a function of the voxel position $N(\boldsymbol{r})$. We mentioned at the beginning that $f_{\mathrm{H}}(\boldsymbol{r},t)$ contains both noise and anatomical structures like edges and small vessels. We decided to use the temporal autocorrelation function of $f_{\mathrm{H}}(\boldsymbol{r},t)$ to gain information whether one voxel contains mainly noise or partially contains edges or vessels. If a voxel mainly contains noise, than a full temporal average might also be employed, resulting in a stronger noise reduction compared to a fixed running average. On the other hand, if a voxel partially contains anatomical information, then we could shrink or potentially avoid the temporal averaging process. The temporal autocorrelation function of $f_{\mathrm{H}}(\boldsymbol{r},t)$ has the following form:

$$\mathrm{AC}_{\mathrm{H}}(\boldsymbol{r},\delta) = \frac{1}{T}\sum_{t=1}^{T}\frac{\left(f_{\mathrm{H}}(\boldsymbol{r},t)-\bar{f}_{\mathrm{H}}(\boldsymbol{r})\right)\left(f_{\mathrm{H}}(\boldsymbol{r},t+\delta)-\bar{f}_{\mathrm{H}}(\boldsymbol{r})\right)}{\sigma^{2}_{\mathrm{H}}(\boldsymbol{r})}.$$

where $\sigma^{2}_{\mathrm{H}}(\boldsymbol{r})$ is the variance image of $f_{\mathrm{H}}(\boldsymbol{r},t)$. As a second step we created a guide $g(\boldsymbol{r}) = \left|\sum_{\delta=1}^{D}\mathrm{AC}_{\mathrm{H}}(\boldsymbol{r},\delta)\right|$ where D was chosen to be 10. $g(\boldsymbol{r})$ is basically the sum of the autocorrelation coefficients of each voxel's TAC of the high spatial frequency components. Since white noise has autocorrelation coefficients centered around 0, $g(\boldsymbol{r})$ was thresholded at 1.5, and forced to be 0 for values lower than that. If a certain voxel of $f_{\mathrm{H}}(\boldsymbol{r},t)$ contains some non-stochastic change over time, like the hemodynamics of a small vessel or steps associated to motion, its temporal signal will contain some autocorrelation and $g(\boldsymbol{r})$ will drift away from 0. On the other hand, if a voxel in $f_{\mathrm{H}}(\boldsymbol{r},t)$ contains an edge, and its temporal autocorrelation coefficients are centered around 0, it means that there is no significant change over time in that voxel, meaning that there is no motion and it is relatively safe to average that edge over a wider temporal window to reduce noise. This theoretical derivation was confirmed in our study as we will show in the results and discussion.

The last step was to define a relationship between the guide $g(\boldsymbol{r})$ and the number of adjacent time points along which to perform the running average. We first defined a maximum and a minimum number of time points for the average, where the maximum was defined as the total number of acquired time points and the minimum was defined as 3 (meaning only 1 time point before and 1 after the considered one). We defined two corresponding Gaussian curves with a $\sigma_{\max}$ and a $\sigma_{\min}$ respectively. Finally we decided to implement a decreasing exponential function to shrink the $\sigma(\boldsymbol{r})$ of the Gaussian function starting from the $\sigma_{\max}$:

$$\sigma(\boldsymbol{r}) = \max(\sigma_{\min}, e^{-g(\boldsymbol{r})}\,\sigma_{\max}) \tag{2}$$

After that, the aMBF formula was defined exactly like (1), but with:

$$\bar{f}_{\mathrm{H}}(\boldsymbol{r},t) = \frac{1}{2N(\boldsymbol{r})+1}\sum_{\delta=-N(\boldsymbol{r})}^{N(\boldsymbol{r})}\frac{1}{\sigma(\boldsymbol{r})\sqrt{2\pi}}\,f_{\mathrm{H}}(\boldsymbol{r},t+\delta)e^{-\delta_{*}^{2}/\sigma(\boldsymbol{r}^{2})}.$$

where with δ_{*} we indicate that for the averaging process the real measured delay was used and not the integer temporal shift δ. In this way the temporal average become effectively a weighted average, where closely acquired time points receive higher weights compared to distant ones. The number of adjacent time points to be used for the average $N(\boldsymbol{r})$ was directly derived from $\sigma(\boldsymbol{r})$ truncating the Gaussian function at a value of 0.05. In future works, another function might be used instead of the exponential to calculate $\sigma(\boldsymbol{r})$. Moreover, a time-dependent $\sigma(\boldsymbol{r})$ might be considered [13].

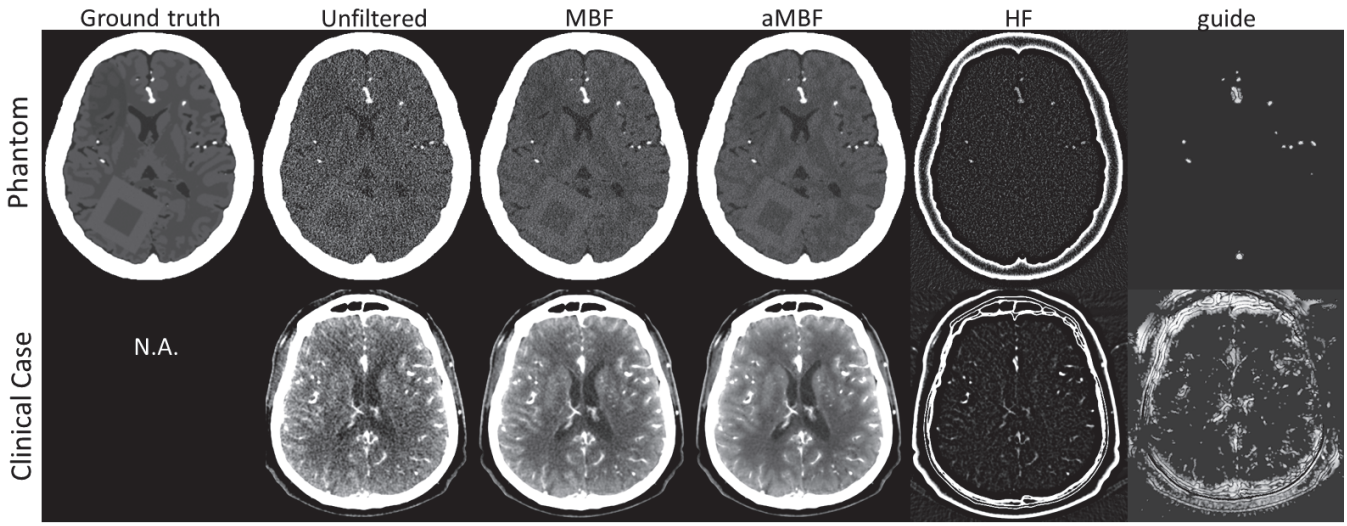

Fig. 1. Unfiltered, MBF filtered, aMBF filtered, high frequency component and guide for phantom (upper row) and one clinical case (bottom row).

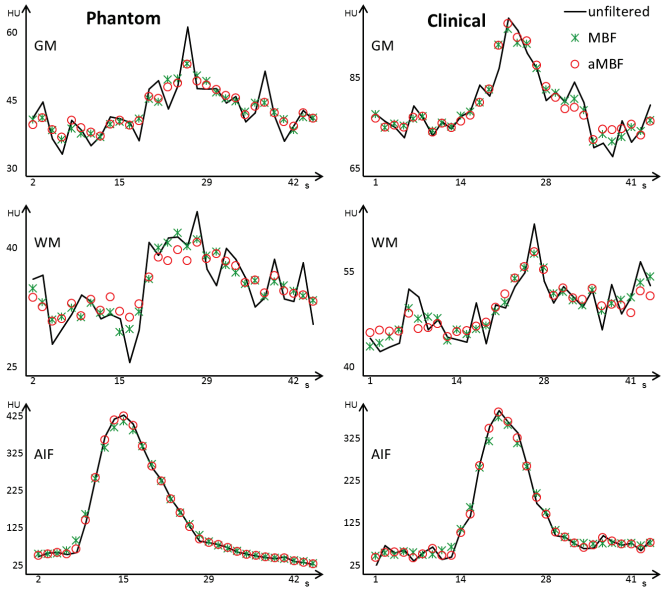

Fig. 2. Right column: phantom grey matter (GM), white matter (WM) and arterial (AIF) TACS. Left column: similar TACs for one clinical case. aMBF shows smoother and sharper TACs compared to MBF.

C. Phantom creation, clinical data and measurements

A digital phantom was developed starting from a brain atlas [14]. Grey and white matter, cerebral spinal fluid and vessels were defined. The signal in temporal dimension was obtained defining a tissue-specific impulse response function (IRF) and convolving it by an arterial input function (AIF) defined as:

$$\mathrm{AIF}(t) = \begin{cases} 0 & \text{if } t < \mathrm{TTS} \\ a\left(\frac{t-\mathrm{TTS}}{\mathrm{TTP}}\right)^b e^{b\left(1-\frac{t-\mathrm{TTS}}{\mathrm{TTP}}\right)} & \text{if } t \geq \mathrm{TTS} \end{cases}$$

Where TTS and TTP stand for time to start and time to peak respectively. The IRFs were defined according to Bredno definition [15]. Poisson-distributed quantum noise was added in the projection domain after forward projection and the noisy images were obtained via filtered back-projection. Forward and back-projection were performed assuming a monochromatic beam with a pencil beam geometry. Two concentric squares of grey and white matter were introduced into the phantom to be able to evaluate eventual loss in spatial resolution via line spread function (LSF). No motion artifacts were simulated. We evaluated our approach also on 10 different clinical cases retrospectively. All cases were acquired with a Somatom Force dual source spiral cone-beam CT (Siemens Healthcare GmbH, Forchheim, Germany). Images were reconstructed with an effective slice thickness od 1.5 mm to have higher noise.

For both MBF and aMBF, high spatial frequencies were obtained convolving the original images with a Gaussian kernel with $\sigma_s = 2.5$ mm and subtracting the low-passed images from the original. The kernel was stopped at the voxels with a weight equal to 0.05. This means that the kernel size was actually a function of the voxel size, as expected to be. Voxels size ranged from 0.4 mm to 0.7 mm. For MBF, the high frequencies were averaged with a box car of a fixed width, covering 5 adjacent time points (two before and two after the central one). Contrast-to-noise ratio improvements were evaluated for the clinical cases using MBF and aMBF. For the phantom, also root-mean-square errors of TACs in different tissues ROI compared to the ground truth were evaluated. Results and further considerations are shown in the next session.

III. Results and Discussion

In Fig. 1 the original images, the filtered images, the high frequency components and the guides $g(\boldsymbol{r})$ are shown both for the phantom and for one clinical case. It can be seen how the guide $g(\boldsymbol{r})$ is able to identify, in the high frequencies, only the voxels which contain some sort of signal over time, being it contrast enhancement (like for the vessels) or motion (like for the anatomical edges). Since in the phantom no motion was simulated, the guide has a 0 value for the edges, meaning

TABLE I
CNR IMPROVEMENTS FOR MBF AND AMBF BOTH SEPARATELY AND COMPARED TO EACH OTHER.

	MBF	aMBF	aMBF/MBF
average	1.61	2.44	1.41
max	3.02	6.58	2.17
min	1.04	1.03	0.98

TABLE II
ROOT MEAN SQUARE ERRORS FOR DIFFERENT TISSUES AND FILTERS. RMSE DESCRIBES THE DEVIATION OF FILTERED TACS FOR DIFFERENT TISSUES (GREY MATTER GM, WHITE MATTER WM, ARTERIAL INPUT FUNCTION AIF AND CEREBRAL SPINAL FLUID CSF) FROM THE GROUND TRUTH DEFINED IN THE PHANTOM CREATION.

	Unfiltered	MBF	aMBF
GM	3.95	1.64	1.5
WM	3.2	1.67	1.19
AIF	8	13.33	7.79
CSF	1.63	1.12	0.93

that a higher noise reduction can be achieved extending the temporal average window. In clinical cases the guide gives higher values to generally more voxels due to the presence of motion artifacts.

In Table I the average improvements in the CNR for the MBF and the aMBF are reported. In the last column it can be seen that, on an average, the aMBF results in a CNR of about 41% higher than the MBF. We noted that CNR improvements are particularly higher in brain cases. In body cases improvements of the aMBF over the MBF are less significant; we think one reason for this might be the higher presence of motion, which reasonably limits the $\sigma(\boldsymbol{r})$ of the aMBF for more voxels.

On the other hand, spatial resolution remains unchanged. This result was expected since both the MBF and the aMBF reduce noise only in temporal direction and do not involve any spatial convolution. The FWHM of the LSF of the non filtered phantom was 2.04 mm. For MBF and aMBF a value of 2.02 mm and 2.08 mm was measured.

Fig. 2 shows the better preservation of AIF for the aMBF compared to the MBF. Moreover, parenchyma TACs are smoother, but peak is preserved. In Table II, also the RMSE of different tissues TACs are reported (only for the phantom study). The major benefit is, as expected, in the AIF fidelity, which is of crucial importance for perfusion parameters calculation.

IV. CONCLUSIONS

The aMBF filter is an improved version of the conventional MBF. When compared to MBF, aMBF average CNR improvement was 40% higher. Moreover, aMBF is able to better preserve the original arterial input function and it is more robust with respect to motion artifacts compared to MBF. Spatial resolution is maintained and performance times are comparable.

ACKNOWLEDGMENT

This study was partially founded by Siemens Healthcare GmbH, Forchheim, Germany. Parts of the reconstruction software were provided by RayConStruct®GmbH, Nürnberg, Germany.

REFERENCES

[1] P. Stenner, B. Schmidt, T. Allmendinger, T. Flohr, and M. Kachelrieß, "Dynamic iterative beam hardening correction (DIBHC) in myocardial perfusion imaging using contrast-enhanced computed tomography." *Invest Radiol*, vol. 45, no. 6, pp. 314–323, Jun 2010.

[2] P. Stenner, B. Schmidt, H. Bruder, T. Allmendinger, U. Haberland, T. Flohr, and M. Kachelrieß, "Partial scan artifact reduction (PSAR) for the assessment of cardiac perfusion in dynamic phase-correlated CT." *Med Phys*, vol. 36, no. 12, pp. 5683–5694, Dec 2009.

[3] B. F. Tomandl, E. Klotz, R. Handschu, B. Stemper, F. Reinhardt, W. J. Huk, K. E. Eberhardt, and S. Fateh-Moghadam, "Comprehensive imaging of ischemic stroke with multisection CT." *Radiographics*, vol. 23, no. 3, pp. 565–592, 2003.

[4] K. M. Thierfelder, W. H. Sommer, A. B. Baumann, E. Klotz, F. G. Meinel, F. F. Strobl, K. Nikolaou, M. F. Reiser, and L. von Baumgarten, "Whole-brain CT perfusion: reliability and reproducibility of volumetric perfusion deficit assessment in patients with acute ischemic stroke." *Neuroradiology*, vol. 55, no. 7, pp. 827–835, Jul 2013.

[5] J. Shi *et al.*, "Dynamic volume perfusion CT in patients with lung cancer: baseline perfusion characteristics of different histological subtypes." *Eur J Radiol*, vol. 82, no. 12, pp. e894–e900, Dec 2013.

[6] C. S. Reiner, M. Roessle, T. Thiesler, D. Eberli, E. Klotz, T. Frauenfelder, T. Sulser, H. Moch, and H. Alkadhi, "Computed tomography perfusion imaging of renal cell carcinoma: systematic comparison with histopathological angiogenic and prognostic markers." *Invest Radiol*, vol. 48, no. 4, pp. 183–191, Apr 2013.

[7] E. Klotz, U. Haberland, G. Glatting, S. O. Schoenberg, C. Fink, U. Attenberger, and T. Henzler, "Technical prerequisites and imaging protocols for CT perfusion imaging in oncology." *Eur J Radiol*, vol. 84, no. 12, pp. 2359–2367, Dec 2015.

[8] A. Fieselmann, M. Kowarschik, A. Ganguly, J. Hornegger, and R. Fahrig, "Deconvolution-based CT and MR brain perfusion measurement: Theoretical model revisited and practical implementation details." *Int J Biomed Imaging*, vol. 2011, p. 467563, 2011.

[9] R. Fang, S. Zhang, T. Chen, and P. Sanelli, "Robust low-dose CT perfusion deconvolution via tensor total-variation regularization." *IEEE Trans Med Imaging*, Feb 2015.

[10] A. M. Mendrik, E.-j. Vonken, B. van Ginneken, H. W. de Jong, A. Riordan, T. van Seeters, E. J. Smit, M. A. Viergever, and M. Prokop, "TIPS bilateral noise reduction in 4D CT perfusion scans produces high-quality cerebral blood flow maps." *Phys Med Biol*, vol. 56, no. 13, pp. 3857–3872, Jul 2011.

[11] L. Havla, K. M. Thierfelder, S. E. Beyer, W. H. Sommer, and O. Dietrich, "Wavelet-based calculation of cerebral angiographic data from time-resolved CT perfusion acquisitions." *Eur Radiol*, vol. 25, no. 8, pp. 2354–2361, Aug 2015.

[12] R. Raupach, E. Klotz, H. Bruder, B. Schmidt, and T. Flohr, "A new multiband spatiotemporal filter for dose reduction in 4D-CT," in *Program of the 96th Scientific Assembly and Annual Meeting of the RSNA*, November 2009, pp. SSJ22–05.

[13] F. Pisana, T. Henzler, S. Schönberg, H. Schlemmer, and M. Kachelrieß, "Dose or noise reduction for dynamic CT perfusion: 4D adaptive time-intensity profile similarity bilateral filters (aTIPS-BF)," in *Program of the 101st Scientific Assembly and Annual Meeting of the RSNA*, November 2015, pp. SSJ22–04.

[14] C. Cocosco, V. Kollokian, R. Kwan, and A. Evans, "Brainweb: Online interface to a 3D MRI simulated brain database," *NeuroImage*, vol. 5, no. 4, 1997.

[15] J. Bredno, M. E. Olszewski, and M. Wintermark, "Simulation model for contrast agent dynamics in brain perfusion scans." *Magn Reson Med*, vol. 64, no. 1, pp. 280–290, Jul 2010.

A Highly Adaptable X-ray Imaging System Simulator

Serge A. Soloviev

***Abstract*— RayTracer is an X-ray imaging system simulator developed by the author at Reveal Imaging. It is designed to assist development of X-ray imaging systems at various design stages, as well as for image processing and reconstruction algorithms. Its usefulness has been demonstrated during development of several different security imaging computed tomography (CT) and non-rotational X-ray scanners, resulting in engineering validation and image quality improvements. RayTracer provides raw data for scanners prior to their actual manufacture, allowing study of how various hardware changes affect final image quality and permitting inexpensive development and testing of the image processing and reconstruction algorithms. This paper describes several potential applications of RayTracer and compares simulated data to raw data obtained using metrics based on existing image quality standards for actual security imaging systems.**

***Index Terms*— X-ray imaging system simulator, product design, image processing algorithms, image quality, security imaging systems.**

I. Introduction

RayTracer is an adaptable set of software tools that can be used to model various X-ray systems. General X-ray systems that are compatible with RayTracer include: fixed source and detection elements with objects moving in straight lines, rotating source and detection elements with fixed objects, rotating source and detection elements with objects moving in straight lines orthogonal to the plane of rotation of the source, rotating source and detection elements moving in the direction orthogonal to the plane of rotation of the source with fixed objects.

To simulate an X-ray system using RayTracer, a user defines the parameters of the system using several input files describing: the geometric layout of detection elements of the system; the source X-ray spectrum; parameters (geometric and physical) of objects to be simulated; motion vectors describing the motion of the X-ray source and the objects; and other parameters related to system filters and channels.

Comparing RayTracer's simulation results with actual data obtained using real scanners showed good agreement between the simulated and actual data (less than 5% absolute error for most measures per ANSI N42.25 standard [16]). The high simulation accuracy made it possible to add a number of novel applications. Before an X-ray scanner is manufactured, RayTracer can be used to predict system performance and to test changes and improvements to the system design, image processing and algorithms. After the scanner is manufactured, RayTracer can be used to generate quality assurance (QA) test data to validate system and/or image processing algorithm performance, or to generate useful synthetic data not yet available in the real database which might be beneficial to algorithm development and improvement.

Manuscript submitted on January 25, 2016.

S. A. Soloviev is with the Reveal Imaging division of Leidos, 900 Technology Park Drive, Billerica, MA 01821 USA (phone: 978-313-5078; fax: 978-667-3870; e-mail: serge.soloviev@leidos.com).

II. Simulation Process, Input and Output

This section contains a general description of the simulation process, from input source spectra to A/D counts.

A. Basic Processing Steps

Basic processing steps could be described in the following pseudo-code:

```
for (temporal step = 1:end)
   for (array element = 1:end)
      for (ray per element = 1:end)
         attenuation <- 0;
         for (object = 1:end)
            find
               intersection of ray & object: thickness
            use
               thickness to calculate x-ray attenuation
            sum
               attenuation across objects, rays
         end
      end
      process
         attenuated x-ray intensity through
         element channel parameters to get A/D counts
   end
end
```

B. X-ray Source Model

An X-ray system's source spectrum can be directly measured and then supplied to RayTracer in an input text file, or it can be computed using any X-ray source modeling tool such as SpekCalc, a program for calculating the X-ray emission spectra from tungsten anodes [1], or XSPECW2 [2]. For modeling heel effect in multi-row CT systems, several anode angle-dependent source spectra should be used.

Focal Spot Size

X-ray source focal spot size is modeled in RayTracer by defining the extent of the best-fit rectangle in the projected view of the anode surface looking back from the exit port where the X-ray emission from the anode surface falls to about 20% of the average emission.

System Inherent Filtration

The X-ray source may include several materials of various thicknesses placed between the tungsten target within the tube and the source's exit port. These materials attenuate (i.e., filter) the X-ray intensity spectrum as generated by the X-ray tube at the tungsten target surface. The total filtration resulting from all these layers is defined as the source inherent filtration.

C. Object Model

Each object is modeled by precisely defining its material, geometric shape, three-dimensional (3D) location and orientation. To model the attenuation properties of various materials and compounds, RayTracer uses the National Institute of Standards and Technology (NIST) database of mass attenuation coefficients for 92 elements and 48 various materials [3]. Mixtures and compounds that are not in the database can be modeled if their densities and precise chemical compositions are known, as follows [3]:

$$\boldsymbol{\mu/\rho} = \sum_{i=1}^{N} \boldsymbol{w_i}(\boldsymbol{\mu/\rho})_i \qquad (1)$$

where w_i is the fraction by weight of the *i*-th atomic constituent, and $(\mu/\rho)_i$ values are from NIST database.

If a polychromatic beam is used, object attenuation can be described using well-known formulas such as [4]:

$$\boldsymbol{I(x)} = \int \boldsymbol{I_0(E)} e^{-\mu(E)x} \boldsymbol{dE} \qquad (2)$$

where $x = \rho L$ is mass *thickness*, $I_0(E)$ is incident spectrum, $I(x)$ is the output transmission spectrum, and $\mu(E)$ is the linear attenuation coefficient of the material.

Modeling Complex Shapes

Basic shapes supported by RayTracer include 3D shapes that have a precise mathematical description, such as ellipsoids, cylinders, and parallelepipeds. To model objects that have more complex shapes, such as holes or objects within objects, a combined description in terms of basic shapes is created and supplied to RayTracer in an XML file. The combined effect on the spectra can be described by the following equation [4]:

$$\boldsymbol{I(x)} = \int \boldsymbol{I_0(E)}\, e^{-\sum_i \mu^i(E)x} \boldsymbol{dE} \qquad (3)$$

Determining Thickness

RayTracer provides an analytical solution for determining thickness by computing the intersection of each ray with each shape. As an example of computing an intersection of a ray with an ellipsoid, the ray can be defined by an initial point (x_1, y_1, z_1), while the direction vector (dx, dy, dz) can be defined using well-known coordinate geometry textbook formulas [5]:

$$\begin{aligned} x &= x_1 + u(x_2 - x_1) \\ \boldsymbol{y} &= \boldsymbol{y_1} + \boldsymbol{u(y_2 - y_1)} \\ z &= z_1 + u(z_2 - z_1) \end{aligned} \qquad (4)$$

Consider the coordinate transformation $p' = Rp + T$ (where R and T are rotation and translation matrixes) into a coordinate system in which an ellipsoid is axis-aligned and given by [5]:

$$\left(\frac{x - x_3}{r_x}\right)^2 + \left(\frac{y - y_3}{r_y}\right)^2 + \left(\frac{z - z_3}{r_z}\right)^2 = \mathbf{1} \qquad (5)$$

To find an intersection of a ray with an ellipsoid, equations (4) can be substituted into equation (5). A quadratic equation is thus obtained, which can be further solved for the case of two intersections ($D > 0$), or one intersection ($D = 0$):

$$au^2 + bu + c = 0$$

where

$$a = \frac{(x_2 - x_1)^2}{r_x^2} + \frac{(y_2 - y_1)^2}{r_y^2} + \frac{(z_2 - z_1)^2}{r_z^2}$$

$$b = 2\left(\frac{(x_1 - x_3)(x_2 - x_1)}{r_x^2} + \frac{(y_1 - y_3)(y_2 - y_1)}{r_y^2} + \frac{(z_1 - z_3)(z_2 - z_1)}{r_z^2}\right)$$

$$c = \frac{(x_1 - x_3)^2}{r_x^2} + \frac{(y_1 - y_3)^2}{r_y^2} + \frac{(z_1 - z_3)^2}{r_z^2}$$

$$D = b^2 - 4ac$$

Finally, the resulting intersection points are transformed back to the original coordinate system, solving the problem.

Derivation of the intersections of a ray with other 3D shapes follows the same method described for finding an intersection of a ray with an ellipsoid described above.

Computing Multiple Rays

The transmitted and absorbed spectra through each object are computed for each simulated X-ray. RayTracer models several rays between the X-ray source and each detection element to account for blurring due to the finite size of the focal spot and each detection element. Each ray is given a weight corresponding to the measured distribution of the radiation intensity within the system's focal spot. There is a trade-off between the number of rays needed to account for hardware limitations on the system resolution (due to the system geometry) and the computational speed. An example of a model using five rays to account for the hardware limitations mentioned above is shown in Fig. 1.

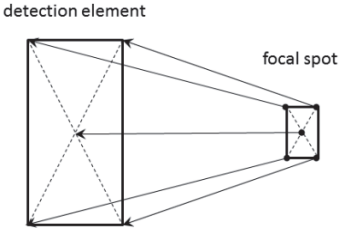

Fig. 1. A model using several rays from the focal spot to the detector element to account for hardware limitations.

The following assumptions are used in computing the rays in Fig. 1. The central ray location is defined between the focal spot center and each detection element center. The four other rays are located between four opposite corners of the X-ray spot and the corresponding corners of the detector element, assuming that detector element surface is orthogonal to the central X-ray.

Modeling Motion of X-ray Source and Detection Elements

Because the input parameters only define the initial location of X-ray source and each detection element, the location of each ray change with time. A description of the "motion vectors" in the system is supplied to RayTracer in a text file. The motion of the X-ray source and detector array is further computed; for example, for a rotational CT system, the dependence of source and detector array location on time is derived in a number of publications [6, 7].

D. Scintillation, Amplifier and A/D counts

Each channel can be characterized by its overall gain from X-ray photons to A/D counts. The overall gain is a product of a sequence of gains. For example, scintillator gain is defined as the ratio of the number of "green" photons to the unit energy input. The amplifier gain is defined as the analog voltage at the output to the integrated charge on the feedback capacitor, as shown in Fig. 2.

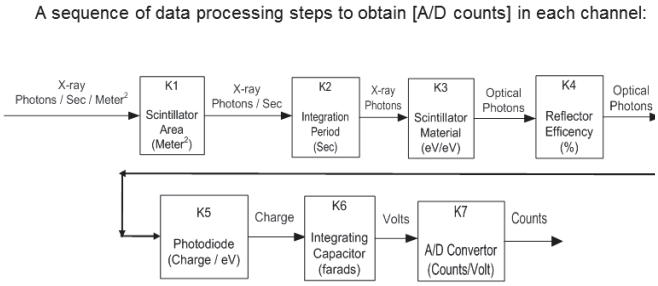

Fig. 2. Sequence of data processing steps required to obtain A/D counts in each channel.

Noise Model

RayTracer's noise model contains quantization noise to represent A/D counts or the number of photons as unsigned integers. Uniform noise is used for modeling the amplifier noise, while Gaussian noise is used for modeling the photon statistics noise.

III. Simulation Results

Before an X-ray scanner is manufactured, RayTracer can be used to confirm analytical calculations on image quality [8]; to predict system performance; and to test changes and improvements to system design, image processing and algorithms. After the scanner is manufactured, RayTracer can be used to generate quality assurance (QA) test data to validate system and/or image processing algorithm performance.

System Design

RayTracer has been used successfully to simulate various aspects of X-ray scanner system designs prior to their manufacture. In particular, RayTracer has proved beneficial in studying the effect of changes in system geometry and/or inherent filtration on the resulting image quality and/or system performance. There are many reasons for testing various possible hardware configurations: reducing cost, avoiding radiation damage to electronics, improving image quality, etc. Simulations performed using RayTracer allowed the right choices to be made in system design long before resources are allocated to manufacture unnecessary prototypes. In the example shown in Fig. 3-Fig. 4, two hardware configurations were simulated using RayTracer: one with extra filtration added to the detector array and one with no extra filtration. The RayTracer simulation results yielded crucial reference points that illustrate the extent to which extra filtration improves the image quality of metal artifacts in the reconstructed slices while simultaneously reducing discrimination capabilities in the system.

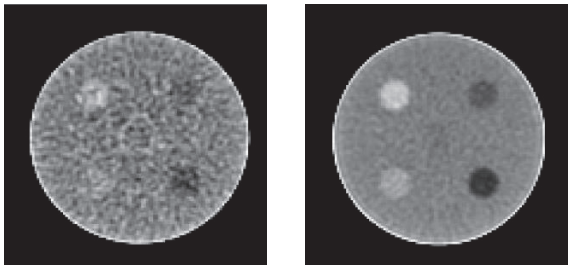

Fig. 3. RayTracer simulation of four different materials inserted into a uniform medium with physical properties very similar to that of the medium. Comparison of reconstructed slices using two possible system designs: Extra filtration added to the detector array (left); No extra filtration (right).

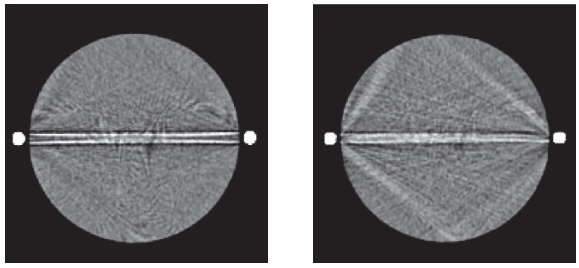

Fig. 4. RayTracer simulation of artifacts in a uniform object located between two metal rods. Comparison of reconstructed slices using two possible system designs: Extra filtration added to the detector array (left); No extra filtration (right).

Reconstruction Algorithm Performance

RayTracer can also be used to test the performance of various image processing (e.g., reconstruction) algorithms. Many different methods of evaluating image quality are described in the literature [9-15]. Two standard image quality phantoms are used to evaluate image artifacts and image quality in X-ray screening systems. Both phantoms were simulated in RayTracer, and an image quality analysis in compliance with American National Standards Institute (ANSI) N42.25 [16] was performed to evaluate the image quality obtained using four different reconstruction algorithms, as shown in Fig. 5.

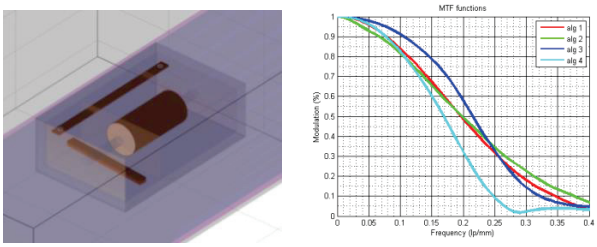

Fig. 5. Testing the reconstruction algorithm performance: Visualization of the simulated Image Quality Type-B phantom in RayTracer (left); Comparison of MTFs obtained using four different reconstruction algorithms (right).

Simulations vs. Real Data

Comparing RayTracer's simulation results with actual data obtained using real scanners, image quality analysis performed using over a dozen measures defined in the ANSI N42.25 standard [16] showed good agreement between the simulated and actual data (less than 5% absolute error for most measures), as shown in Fig. 6.

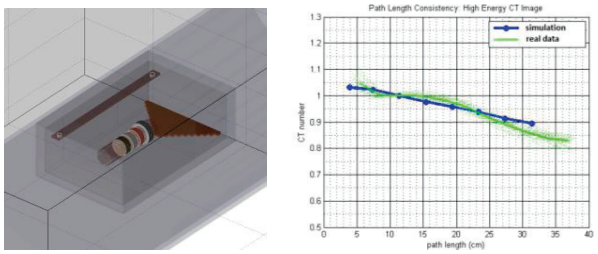

Fig. 6. Comparison to real data: Visualization of the simulated Image Quality Type-A phantom in RayTracer (left); Path length CT value test results [16], simulation (in blue) vs. real data (in green) (right).

Limitations on System Resolution

To improve image quality in X-ray imaging systems, it is important to understand where the limitations of performance arise and which hardware components or software algorithms must be improved to achieve better overall image quality. RayTracer simulations were used to selectively switch on and off certain physical effects to test and better understand various limitations on system resolution: heel effect, focal spot size, photon and amplifier noise, polychromatic beam, sampling rate, distance from the iso-center, reconstructed pixel size, etc. The effect of these variations is shown in Fig. 7.

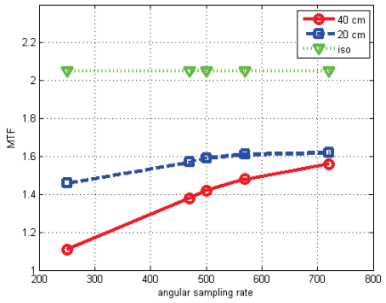

Fig. 7. Study of limitations on imaging system resolution: dependence of the system MTF on the angular data sampling rate at different distances from the system iso-center.

ACKNOWLEDGMENT

The author wishes to thank Michael Litchfield, Robert Shuchatowitz and the Reveal research and development team for helping to validate RayTracer's capabilities in real-life applications.

REFERENCES

[1] G Poludniowski *et al.,* "*SpekCalc*: a program to calculate photon spectra from tungsten anode x-ray tubes," *Phys. Med. Biol.,* 2009, vol. 54, no. 433.

[2] E. de Paula, "XSPEC," *Center for Instrumentation, Dosimetry and Radiation Protection (CIDRA)*, 1984.

[3] J.H. Hubbel and S.M. Seltzer, "Tables of x-ray mass attenuation coefficients and mass energy-absorption coefficients from 1 keV to 20 MeV for elements $Z = 1$ to 92 and 48 additional substances of dosimetric interest," *National Institute of Standards and Technology,* 1995, Report NISTIR 5632, Gaithersburg, MD.

[4] A. C. Kak and M. Slaney, "Principles of computerized tomographic imaging," *IEEE Press*, 1988.

[5] D. V. Wood, "The elements of coordinate geometry: in three parts: 1. Cartesian geometry," Willey Publication, 1879.

[6] M. Kachelrieß, S. Schaller, and W.A. Kalender, "Advanced single-slice rebinning in cone-beam spiral CT," *Medical Physics,* 2000, vol. 27, no. 4, pp. 754-772.

[7] A. J. Wunderlich, "The Katsevich inversion formula for cone-beam computed tomography," *Oregon State University, Department of Mathematics,* MS Thesis, 2006.

[8] G. D. Boreman, "Modulation transfer function in optical and electro-optical systems," *SPIE Press,* 2001.

[9] E. Samei, "Performance of digital radiographic detectors: quantification and assessment methods," *In: Advances in digital radiography,* RSNA, 2003, pp. 37-47.

[10] E. Samei, N. T. Ranger, J. T. Dobbins III, and Y. Chen, "Intercomparison of methods for image quality characterization. I. Modulation transfer function," *Medical Physics,* 2006, vol. 33, no. 5, pp. 1454-65.

[11] J. T. Dobbins III, E. Samei, N. T.Ranger, and Y. Chen," Intercomparison of methods for image quality characterization. II. Noise power spectrum," *Medical Physics*, 2006, vol. 33, no. 5, pp. 1466-75.

[12] K. M. Hanson, "Detectability in computed tomographic images," *Medical Physics*, 1979, vol. 6, no. 5, pp. 441-51.

[13] K. M. Hanson, "A simplified method of estimating noise power spectra," *Proc. SPIE,* 1998, vol. 3336, pp. 243-250.

[14] R. Grimmer, J. Krause, M. Karloczak, R. Lapp, and M. Kachelrieß, "Assessment of spatial resolution in CT," *Nuclear Science Symposium Conference Record*, 2008, pp. 5562-66.

[15] M. F. Kijewski and P. F. Judy, "The noise power spectrum of CT images," *Phys. Med. Biol.,* 1987, vol. 32, no. 5, pp. 565-575.

[16] "American national standard for evaluation the image quality of x-ray computed tomography (CT) security-screening systems," *ANSI N42.45-2011*, 2011, pp.1-58.

Serge Soloviev received the M.S. degree in Applied Mathematics and Physics from MIPT, Moscow, Russia in 1991, and the M.S. degree in Computer Science from the Weizmann Institute, Rehovot, Israel in 1997 for his work on Modeling of the Shift Invariant Recognition. Currently, as a Principal Scientist in Reveal Imaging, a division of Leidos, he is responsible for image quality analysis, design of new image processing algorithms and simulations of x-ray security systems. He is an author of a number of publications in Computational Mathematics, Modeling, and in Biomedical Engineering.

The 4th International Conference on Image Formation in X-Ray Computed Tomography

Algorithm-Enabled Half-Rotation Data Reconstruction in Spectral CT

Buxin Chen, *Member, IEEE,* Yan Liu, Zheng Zhang, Zhou Yu, Richard Thompson, Emil Sidky, *Member, IEEE,* and Xiaochuan Pan, *Fellow, IEEE,*

***Abstract*—In this work, we apply a previously developed one-step spectral CT reconstruction method to scanned data from a physical phantom with iodine and calcium contrast inserts. A flexible scanning configuration using only half-rotation data from both low and high kVp scans, enabled by the one-step method with its associated algorithm, are studied. Such configuration is of practical interest for realizing spectral CT scanning with reduced dose and time on conventional CT scanners. The results, consisting of visual and quantitative assessment and a classification task, suggest that the performance of the reconstructed images from the half rotation data is close to that from the full rotation data.**

I. Introduction

Spectral CT exploits the underlying spectral properties of materials, with multispectral data sets. It is investigated mainly in the interest of enhancing material contrast and reducing beam-hardening (BH) effect. Basis material decomposition model [1]–[3] has been used as the main method for spectral CT reconstruction. However, most studies in spectral CT separate the decomposition step with the reconstruction, bringing limitation to the data acquisition schemes [2], [4]. As an example, in commercially available dual energy CT scanners, it is required that two scans with different kVp settings should each cover a full 2π angular range. On the other hand, one-step reconstruction for spectral CT [5] is flexible in scan configuration and allows direct constraints in the image domain. We have been developing an optimization-based method that integrates the decomposition into the reconstruction [6], [7]. Such method allows basis material maps to be reconstructed directly from the measured data, enabling flexible designs of the scanning configuration for spectral CT. In this work, we apply the developed reconstruction method and its associated algorithm to real scan data at 80 and 135 kVp of a physical phantom with contrast inserts. A flexible scanning configuration is simulated by using only half-rotation data from each of the two kVp scans, for reducing the imaging time and radiation dose. Such scan configuration, enabled by the algorithm, can be employed by conventional diagnostic CT scanners without any special hardware upgrade.

B. Chen, Z. Zhang, and E. Sidky are with the Department of Radiology, The University of Chicago, Chicago, IL 60637, USA

Y. Liu, Z. Yu, and R. Thompson are with the Toshiba Medical Research Institute USA, Inc., Vernon Hills, IL 60061, USA

X. Pan is with the Departments of Radiology & Radiation and Cellular Oncology, The University of Chicago, Chicago, IL 60637, USA

II. Materials and methods

A. Data Acquisition

The dual energy phantom from GAMMEX™ (model 472) was scanned. It has 16 insert chambers allowing for 7 rods of iodine with concentrations ranging from 2.0 to 20.0 mg/ml, 7 rods of calcium with concentrations from 50 to 600 mg/ml, and 2 rods of solid water. In this study, the rods were arranged such that the inner circle holds 7 iodine rods with 1 solid water and the outer circle holds 7 calcium ones with 1 solid water. More detail about the phantom can be found on the website [8].

The Aquilion™ (Toshiba Medical Systems Corporation, Tokyo, Japan) 16-slice CT scanner was used to scan the phantom in circular mode. Two full-rotation scans over 2π range were performed at 80 and 135 kVp, with 360 and 100 mA respectively. From the two full-rotation scans, half-rotation data within each kVp scan were extracted, as the 0-to-π-rotation data from the 80 kVp and the π-to-2π-rotation data from the 135 kVp are joined together. The ensemble of data from the two full-rotation scans at two kVps is referred to as the full-rotation spectral scan or full-rotation data, while the ensemble of data from the two half-rotation scans, extracted in the way described above, is referred to as the half-rotation spectral scan or half-rotation data. Both full-rotation and half-rotation data are used for basis image reconstruction, and the results are compared with each other.

In addition, the phantom was scanned at a higher mA level for multiple times at both kVps to acquire very-low-noise data as the benchmark. The full-rotation data from the very-low-noise scan, after average, are reconstructed into basis images as the reference in the quantitative evaluation.

B. Optimization-Based Reconstruction

1) Linearized Data Model: The material decomposition model is combined into the polychromatic attenuation model to form the forward model as

$$g_m = -\ln\int S(E)\exp\left[-\int_L \sum_{t=1}^{2} c_t(\vec{r})\mu_t(E)\mathrm{d}l\right]\mathrm{d}E, \quad (1)$$

which can be rewritten, after linearization, as

$$g = g_m - g_{BH} = \sum_{t=1}^{2}\bar{\mu}_t\int_L c_t(\vec{r})\mathrm{d}l, \quad (2)$$

where g_{BH} is the non-linear beam-hardening (BH) term defined as

$$g_{BH} \equiv -\ln\int S(E)\exp\left[-\sum_{t=1}^{2}\Delta\mu_t(E)\int_L c_t(\vec{r})\mathrm{d}l\right]\mathrm{d}E, \tag{3}$$

and

$$\Delta\mu_t(E) = \mu_t(E) - \bar{\mu}_t \quad \& \quad \bar{\mu}_t \equiv \int S(E)\mu_t(E)\mathrm{d}E. \tag{4}$$

As a result, a linearized data model is formed as

$$g = \mathcal{H}c, \tag{5}$$

where $g^\intercal = (g^{L\intercal}, g^{H\intercal}) = ((g_m^L - g_{BH}^L)^\intercal, (g_m^H - g_{BH}^H)^\intercal)$, $c^\intercal = (c_1^\intercal, c_2^\intercal)$ ($\intercal$ indicates matrix or vector transpose), and

$$\mathcal{H} = \begin{pmatrix} \bar{\mu}_1^L A^L & \bar{\mu}_2^L A^L \\ \bar{\mu}_1^H A^H & \bar{\mu}_2^H A^H \end{pmatrix}. \tag{6}$$

Here, A^L and A^H describe two discrete X-ray transforms that correspond to the 0-to-π rotation scan with the low-kVp (80) and the π-to-2π rotation scan with the high-kVp (135). g^L and g^H are the corresponding data vectors, as defined in Eq. (2), from the low and high kVp scans. c_1 and c_2 are basis image vectors representing two bases materials used in the study, water and bone. Each basis image vector is of size 512×512 to denote the discrete image in a concatenated form. All vectors are column vectors unless otherwise indicated.

2) Reconstruction Program and Algorithm: A constrained total variation (TV)-minimization program is formulated as

$$\begin{aligned}(c_1^\intercal, c_2^\intercal) = \ & \arg\min(\|c_1\|_{TV} + \|c_2\|_{TV}) \\ & \text{s.t. } D(g_m - g_{BH}, c) \le \epsilon \text{ and } c_1, c_2 \succeq 0,\end{aligned} \tag{7}$$

where

$$\begin{aligned}D(g_m - g_{BH}, c) &= \|\mathcal{H}c - (g_m - g_{BH})\|^2 \\ &= \sum_{s=L}^{H}\left\|A^s \cdot \sum_{t=1}^{2}\bar{\mu}_t^s\vec{c}_t - (g_m^s - g_{BH}^s)\right\|_2^2\end{aligned}$$

is the l_2-norm of data vector difference between the model data $\mathcal{H}c$ and the BH-corrected measured data $(g_m - g_{BH})$. ϵ is a positive parameter accounting for the inconsistencies, including noise and residual BH effect that are not corrected for by the estimation of g_{BH}.

It is observed that $D(g_m - g_{BH}, c)$ becomes non-convex in the presence of g_{BH}, which is a function of c, as defined in Eq. (3). For the lack of mathematically converging algorithm, we use an strategy previously developed [6], [7] to solve the reconstruction program numerically. The approach, in addition to the ASD-POCS algorithm [9], includes notably estimating g_{BH} from c in the current iteration using Eq. (3), and subtracting it from the measured data to correct for the BH effect feeding into the POCS step. In other words, the constraint $D(g_m - g_{BH}, c) \le \epsilon$ is updated by iteration and rendered into a convex form after each update.

C. Evaluation

1) Visualization: Water and bone basis images reconstructed from both the full- and half-rotation data are compared visually. Monoenergetic imagee at 40 and 120 KeV are composed from the basis images and converted to HU values. In addition, a separate reconstruction program is employed using Eq. (7) with $D(g_m, c)$ replacing $D(g_m - g_{BH}, c)$, in combination with the ASD-POCS algorithm sans the BH correction step. The monoenergetic images from the half-rotation data reconstructed in this way are presented to contrast those reconstructed using the proposed method with BH correction, demonstrating the effectiveness of the BH correction step in the proposed reconstruction.

2) Quantification: A series of monoenergetic images are composed from basis images from three reconstructions, including the full-rotation data, the half-rotation data, and the half-rotation data without BH correction in the reconstruction. ROIs of the same size are drawn to cover the background and each of the rods. Within each ROI, mean pixel value (MPV) and standard deviation (STD) are calculated. Next, biases of the MPV are calculated with respect to the image reconstructed from the very-low-noise benchmark data. The bias and STD are plotted against energies ranging from 40 to 140 KeV.

3) Classification: The inserted rods in the phantom include two materials, iodine and calcium, that are usually not well differentiated using single HU value. However, using spectral information, for example, HU values from two different monoenergetic images, the two material may potentially be distinguished. Such classification task is illustrated by mapping the MPV from 80 and 140 KeV monoenergetic images for each ROI [10], [11]. The results from both the full-rotation and half-rotation data are presented and compared.

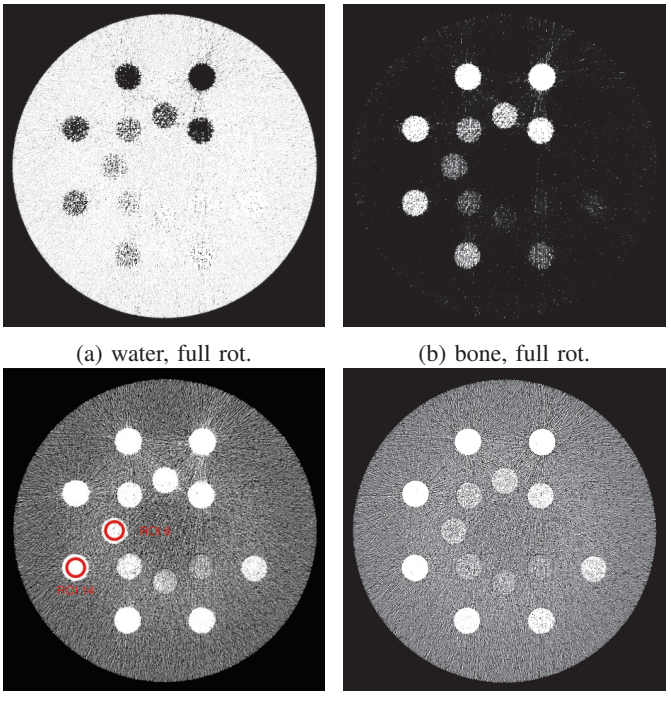

(a) water, full rot. (b) bone, full rot.

(c) 40 KeV, full rot. (d) 120 KeV, full rot.

Fig. 1: Basis images (first row (a) and (b)) and monoenergetic images (second row (c) and (d)) reconstructed from the full-rotation data. The display windows are [0,1] for basis images and [-200,200]HU for monoenergetic images.

III. Results

A. Visualization

The reconstructed images from the full-rotation data are presented in Fig. 1. Most of the rods are separated from the water background as they appear bright in the bone basis image (Fig. 1b). The rods with low concentrations, iodine or calcium, display low contrast in the bone image in the [0,1] display window, while distinct contrast in both the monoenergetic images are observed. Some streak artifacts can be observed around the high concentration rods in the 40 keV image (Fig. 1c), that are likely from remaining uncorrected BH effect or the partial volume effect.

The reconstructed images from the half-rotation data are presented in Fig. 2. There is no significant visual difference observed as compared to their counterparts in Fig. 1. The images are slightly noisier, due to the reduction of data to half, but the impact is alleviated by the control of TV strength in the reconstruction. Fig. 3 shows monoenergetic images composed from basis images that are reconstructed without the BH correction step. The images are visibly darker, under the same display window, as compared to (c) and (d) in Figs. 1 and 2. There is also a decrease of contrast in the images, especially for the inner circle rods in the 120 KeV image on the right (Fig. 3b).

It shall also be marked that, in all monoenergetic images in Figs. 1- 3, the iodine rods in the inner circle and the calcium rods in the outer circle have an overlap of HU values that makes them difficult to be differentiated using the HU value from a single kVp image.

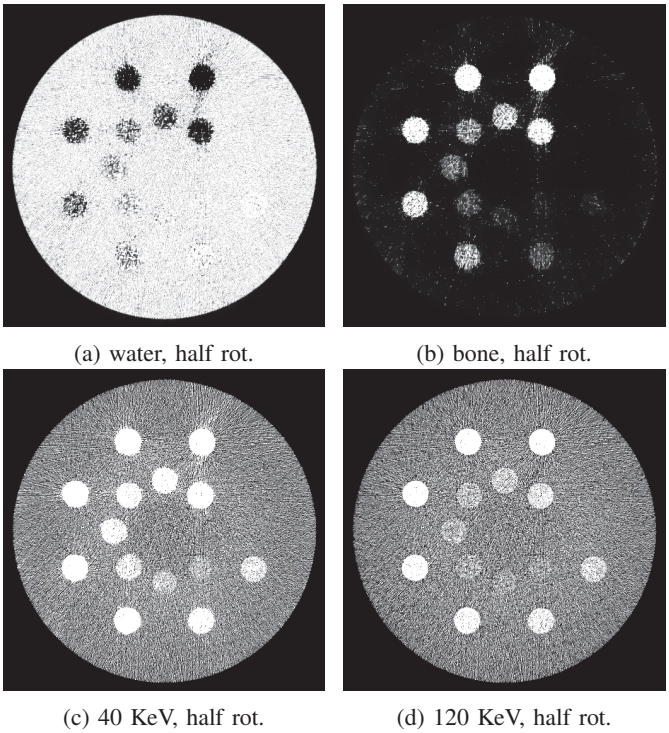

(a) water, half rot. (b) bone, half rot.

(c) 40 KeV, half rot. (d) 120 KeV, half rot.

Fig. 2: Basis images (first row (a) and (b)) and monoenergetic images (second row (c) and (d)) reconstructed from the half-rotation data. Same display windows are used as in Fig. 1. No significant difference is observed as compared to the counterparts in Fig. 1.

B. Quantification

The bias and STD results from two of the ROIs, iodine rod (no. 6) and calcium rod (no. 14) as indicated in Fig. 1c, are presented in Fig. 4. Both bias plots indicate that monoenergetic images are quantitatively more accurate with increasing energy level, when the STD plots show a decrease of noise level. The bias results also show that images from the half-rotation data are as unbiased as those from the full-rotation data within the selected ROI, when the STD results demonstrate that the images are indeed noisier. It is also observed that the images reconstructed without the BH correction step display bigger bias than the other two reconstruction results, largely due to the DC shift from the BH effect. It shall be noted that the plots from the two ROIs selected to be shown here are representative of those from all other ROIs.

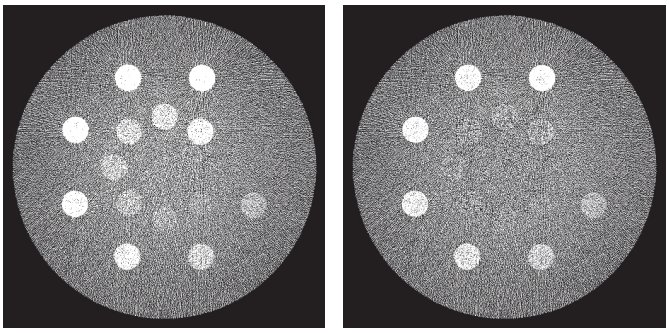

(a) 40 KeV, half rot. w/o BHc (b) 120 KeV, half rot. w/o BHc

Fig. 3: Monoenergetic images from the half-rotation data without the BH correction step in the reconstruction. The images are visibly darker as compared to (c) and (d) in Figs. 1 and 2. There is also a decrease of contrast for the inner circle rods in the 120 KeV image.

C. Classification

HU pairs from 80 and 140 KeV monoenergetic images for each iodine and calcium ROIs are mapped in Fig. 5, with the results from the full-rotation data on the left (Fig. 5a) and the half-rotation data on the right (Fig. 5b). Different labeling are used to differentiate the iodine and calcium groups. It is clear that the two groups of data points lie on two lines, making it possible to differentiate them. The results from half-rotation data are almost identical to those from the full-rotation date.

IV. Conclusions

In this work, we have applied a recently developed reconstruction algorithm for spectral CT to a dual energy phantom scan data and simulated a flexible scanning configuration with half-rotation data, for reducing the imaging time and radiation dose. The half-plus-half rotation scan with low and high kVps can be used by conventional diagnostic CT scanners without any special hardware upgrade. The reconstructed images display no significant visual difference with those from the full-

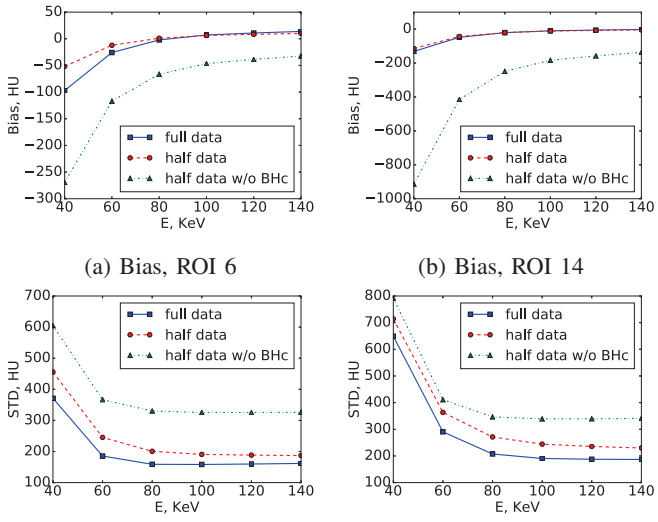

(a) Bias, ROI 6 (b) Bias, ROI 14

(c) STD, ROI 6 (d) STD, ROI 14

Fig. 4: Biases (first row (a) and (b)) and STD (second (c) and (d)) results from a water background ROI no. 0 (left column) and a iodine rod ROI no. 6 (right column). The bias results indicate that images from the half-rotation data are quantitatively very close to those from the full-rotation data, when the STD results demonstrate that the images are noisier. It also shows that the images reconstructed without the BH correction step have larger biases.

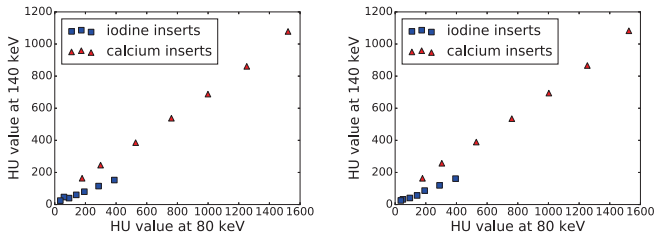

(a) full rot. data (b) half rot. data

Fig. 5: Distribution of iodine and calcium rod ROIs' HU value pairs from the full-rotation data (left (a)) and the half-rotation data (right (b)). It is clear that the two group of material data points, with different labeling, lie on two separate lines in the plots. The two plots show almost identical results.

rotation data, except for slightly elevated noisy level. These are confirmed by the quantitative analysis of bias and STD over inserted rods. The reconstruction results are further assessed with a classification task, where the half-rotation data perform almost identically to the full-rotation data, with the iodine and calcium materials separated on two lines in a mapping with their HU value pairs from monoenergetic images at two different energy levels.

ACKONWLEDGMENT

This work was supported in part by NIH R01 Grant Nos. CA158446, CA182264, and EB018102. The contents of this article are solely the responsibility of the authors and do not necessarily represent the official views of the National Institutes of Health.

REFERENCES

[1] R. E. Alvarez and A. Macovski, "Energy-selective reconstructions in x-ray computerised tomography," *Phys. Med. Biol.*, vol. 21, no. 5, p. 733, 1976.

[2] Y. Zou and M. D. Silver, "Analysis of fast kv-switching in dual energy ct using a pre-reconstruction decomposition technique," in *Medical Imaging*. International Society for Optics and Photonics, 2008, pp. 691 313–691 313.

[3] P. R. Mendonça, P. Lamb, and D. V. Sahani, "A flexible method for multi-material decomposition of dual-energy ct images," *Medical Imaging, IEEE Transactions on*, vol. 33, no. 1, pp. 99–116, 2014.

[4] C. Maaß, M. Baer, and M. Kachelrieß, "Image-based dual energy ct using optimized precorrection functions: A practical new approach of material decomposition in image domain," *Med. Phys.*, vol. 36, no. 8, pp. 3818–3829, 2009.

[5] Y. Long, J. Fessler *et al.*, "Multi-material decomposition using statistical image reconstruction for spectral ct," *Medical Imaging, IEEE Transactions on*, vol. 33, no. 8, pp. 1614–1626, 2014.

[6] X. Pan, B. Chen, Z. Zhang, E. Pearson, E. Sidky, and X. Han, "Optimization-based reconstruction exploiting spectral information in ct," in *The Third International Conference on Image Formation in X-Ray Computed Tomography*, 2014, pp. 228–232.

[7] B. Chen, Z. Zhang, E. Pearson, E. Sidky, and X. Pan, "An investigation of regularization for basis image reconstruction in spectral ct," in *IEEE Nucl. Sci. Sym. & Med. Imaging Conf.*, 2014.

[8] *GAMMEX Dual Energy CT Phantom*, 2016 (accessed Jan. 10, 2016). [Online]. Available: http://www.sunnuclear.com/snc_site/solutions/diagnostic/subcat/ct_solutions/ct_dual_energy_phantom

[9] E. Y. Sidky and X. Pan, "Image reconstruction in circular cone-beam computed tomography by constrained, total-variation minimization," *Phys. Med. Biol.*, vol. 53, pp. 4777–4807, 2008.

[10] T. Johnson, C. Fink, S. O. Schnberg, and M. F. Reiser, Eds., *Dual Energy CT in Clinical Practice*, ser. Medical Radiology. Berlin, Heidelberg: Springer Berlin Heidelberg, 2011. [Online]. Available: http://link.springer.com/10.1007/978-3-642-01740-7

[11] K. M. Brown, S. Zabic, and G. Shechter, "Impact of spectral separation in dual-energy ct with anti-correlated statistical reconstruction," in *The 13th International Meeting on Fully Three-Dimensional Image Reconstruction in Radiology and Nuclear Medicine*, 2015.

First *in-vivo* Experiments with a Large field-of-view Flat Panel Photon-Counting Detector

Moiz Ahmad, Rebecca Fahrig, Martin Spahn, Jang-Hwan Choi,
Niko Köster, Silke Reitz, Waldo Hinshaw, Leland Pung, Teri Moore, Andreas Maier, and Kerstin Müller

***Abstract*—In the recent years, dual-energy CT becomes of more and more interest in clinical practice. The ability to distinguish different materials and tissue provides additional information to the clinician to make treatment decisions. Material decomposition for example allows to separate iodinated contrast agent from soft tissue due to its stronger enhancement at low photon energies compared to other materials that do not show this behavior. In conventional CT imaging several techniques are investigated for dual-energy imaging, whereas dual-energy imaging has not found its way into interventional C-arm CT imaging, yet. In the angiographic suite, discrimination of iodine from soft tissue would for example allow the generation of digital subtraction images without any motion artifacts. In this work, the first images generated with a large field-of-view photon-counting detector integrated into a clinical C-arm system have been investigated. The acquired 2D and 3D images of an *in-vivo* pig study look promising and open up the way for dual-energy imaging in the angiographic suite.**

I. Introduction

A. Purpose of this Work

One major goal in medical CT research today investigates the decomposition of the scanned object into its different materials. Dual-energy imaging allows to exploit the different absorption behavior of distinct materials and tissue under varying X-ray photon energies. For example, the attenuation of iodine, which is broadly used as intravascular contrast agent, decreases less than the attenuation of soft tissue with increasing photon energy. Possible clinical applications that benefit from this are, e.g. improved detection of a hyperenhancing malignancies in abdominal imaging [1], detection of endoleaks after endovascular aneurysm repair [2], distinguishing tumor bleed from pure hemorrhage [3] or coronary atherosclerotic plaque characterization [4]. In order to acquire images with different photon energies, multiple techniques can be applied: (i) acquisition of two consecutive scans with two different tube voltages, (ii) acquisition of a single scan using one X-ray tube with fast voltage switching, (iii) using a dual-or multilayer detector, (iv) acquisition with two (or more) X-ray tubes simultaneously with different voltage settings, and (v) using a photon-counting energy-discriminating detector with two or more energy thresholds [5]. In conventional CT, most of the previously mentioned approaches are integrated into clinical CT scanners from different vendors. However, photon-counting detectors are still on-going research in dual-energy CT and not clinical applicable, yet [6], [7].

In this work, the first setup of a customized manufactured large filed-of-view photon-counting detector mounted on a research clinical angiographic C-arm CT system is presented. The setup allows to acquire 2D energy discriminating images during 2D static and 3D rotational scans.

M. Ahmad, W. Hinshaw, and K. Müller are with the Radiological Sciences Lab, Department of Radiology, Stanford University, Stanford, CA, USA. E-mail: moiz@stanford.edu. R. Fahrig and J.-H. Choi were with the Radiological Sciences Lab, Department of Radiology, Stanford University, Stanford, CA, USA. R. Fahrig is now with Siemens Healthcare GmbH, Forchheim, Germany. M. Spahn, N. Köster, S. Reitz are with Siemens Healthcare GmbH, Forchheim, Germany. L. Pung and T. Moore are with Siemens Medical Solutions Inc, Malvern, USA. A. Maier is with the Pattern Recognition Lab, Department of Computer Science, Friedrich-Alexander-Universität Erlangen-Nürnberg, Germany.

B. State of the Art

Photon-counting detectors (PCDs) divide the transmitted X-ray spectrum into a number of different energy bins. The number of bins is highly dependent on the design and application of the distinctive detector. This principle varies completely from the conventional energy integrating detector that does not allow for energy differentiation. PCDs can help to overcome certain limitations of the current available detector technology, e.g. tissue-specific images to distinguish blood from contrast agent and/or to improve the signal-to-noise ratio by exploiting energy dependent image properties. The two most used materials to convert the absorbed photon energy of the emitted X-ray spectrum into an electrical signal are cadmium telluride (CdTe) and cadmium zinc telluride. The magnitude of the electrical signal is proportional to the incident photon's energy. In order to build a clinical applicable PCD for X-ray and CT imaging, some hardware design challenges need to be addressed. One major challenge is the pulse pileup due to the high peak X-ray flux in CT imaging. This means that pulses generated by coincident photons might be piled up and observed as one. This leads to a wrong detected energy, and a loss in the number of overall counts. There are many more challenges and a more detailed description can be found in [5], [7].

II. Methods and Materials

A. Photon-Counting Detector

In this paper, we investigated a large field-of-view dual-energy photon-counting detector for its application in interventional radiology. The detector is a customized OEM product manufactured by XCounter AB (Danderyd, Sweden), hereafter referred to as "XCD" (Fig. 1a). In this detector, 1 mm cadmium telluride (CdTe) is used as conversion material from the X-ray energy to an electrical signal. The detector covers an active area of 30×5 cm^2 made up of several individual modules, each having a size of 1.25×2.5 cm^2. Overall the 2D image matrix is 3072×512 pixel with an isotropic resolution of 100 μm. The exposure integration range is from 100 μs-5 s. The XCD features two energy bins per pixel with adjustable thresholds with each counter on the pixel has a counter depth of 12 bit. Therefore, synchronous acquisition of a total energy

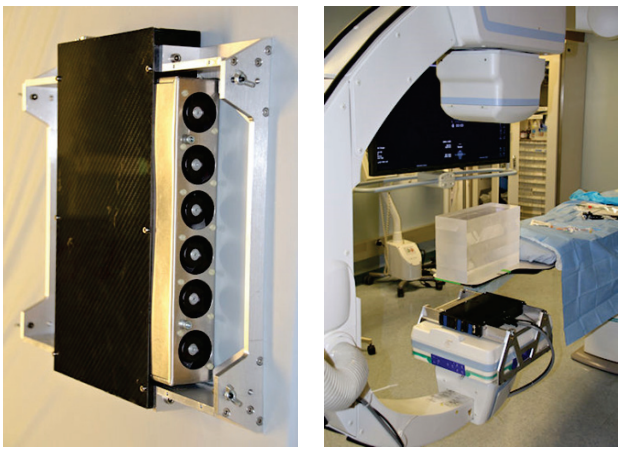

(a) (b)

Figure 1: (a) Large field-of-view photon-counting detector (XCD) and (b) mounted to an Artis zeego system (Siemens Healthcare GmbH, Forchheim, Germany).

(TE) and a high energy (HE) image can be performed. The detector also features a charge sharing correction feature to restore the energy that may spread over several neighboring pixel due to fluorescence or charge dispersion and to count the event only once. The detector design is similar to the small PCD presented in Ullberg et al. [8]. The readout is performed over a gigabit ethernet connection and the generated 2D images are visualized and stored on an external workstation.

In order to perform 2D and 3D clinical imaging, the XCD was "piggy-back" mounted to the flat panel detector (FD) of an Artis zeego system (Siemens Healthcare GmbH, Forchheim, Germany) (Fig. 1b). The clinical system's X-ray tube (MEGALIX CAT Plus) was used. A software application enables manual control of the tube current (mA), pulse width (ms), and voltage (kV).

B. 2D Image Processing

The XCD provides the ability to acquire either 2D images from one static view or 2D images during a rotational scan. Both image stacks need to be processed to correct for gain variations, defect pixels, geometric deviations between individual detector modules, and count rate linearization. A rough overview of the image processing pipeline is given in Fig. 2. The first step is to correct for pixel wise variations in efficiency. For conventional FDs a flat-field correction can be applied, where multiplicative coefficients characterizing the relative efficiency of each pixel to the mean pixel efficiency can be found. However, the efficiency of each pixel is energy dependent, and this dependence is unique for each of them [9]. Hence, the detection efficiency depends individually on the local attenuation properties of the imaged sample, and consequently, a simple flat-field correction is not sufficient. Here, the signal-to-equivalent thickness calibration (STC) method presented by Vavrik et al. is applied to correct for variations in pixel efficiency [10]. The method also works for slightly different calibration and sample materials [9]. As a

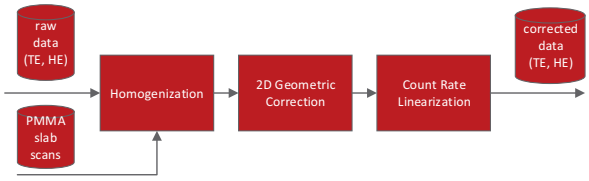

Figure 2: Overview of the image processing pipeline.

"calibrator" different thicknesses of polymethyl methacrylate (PMMA) slabs (1.18 g/cm^2) were used and imaged with specific exposure parameters equivalent to the later acquisitions. Additionally, a defect pixel correction step is applied. As a next step, minor gaps at the module edges are removed and the modules might be shifted in whole pixel steps to fit to the adjacent modules. Additionally, the butting zones around each module show high signal variations. These are homogenized by detection of the modules and whole butting pixel from neighboring pixels are introduced to approximate the gaps. Afterwards, a specifically designed count rate linearization algorithm is performed. Overall, this results in corrected TE and HE image stacks. The low energy (LE) image stack is generated by simple subtraction LE = TE-HE.

C. 3D Image Reconstruction

The XCD mounted on the C-arm CT system provides the ability to acquire simultaneous photon-counting 2D images or image series from static projections or to reconstruct volumetric data from a cone-beam CT run. Since the mounting of the XCD onto the FD changes the pre-calibrated system trajectory, new 3D projection matrices need to be computed [11]. Due to the different extent of the XCD and the FD, a customized PDS-3 phantom was manufactured with slightly varying phantom diameter, height and adapted helical slope of the bead inserts (Fig. 3).

For 3D imaging a scan protocol with a duration of 10 s and 30 fps was used to acquire 248 (TE and HE) imaging stacks, distributed over 200° with an angular distance of 0.8°. The XCD projection images have a size of 3072×512 pixel with an isotropic pixel size of 100 μm. The source-to-detector distance measured 120 cm. For a preliminary image comparison, the same image protocol has been performed without the XCD mounted to the FD. The 2D FD projection images have a size of 1240×960 with an isotropic pixel size of 0.308 mm.

For 3D XCD image generation using the TE stack, the Feldkamp-Davis and Kress (FDK) algorithm with a shepp-logan ramp filter with a cut-off frequency of 0, quadratic cut-off strength, and a slope cut-off of 4.0, available in the CONRAD software package was used[12]. The FD images were sent to the external workstation from the clinical system and reconstructed with a matrix size of 512^3 and a voxel size of 0.425 mm. One XCD reconstruction was performed using 1×1 native detector pixel size on a 512^2×140 matrix with an isotropic voxel size of 0.2125 mm. Another XCD reconstruction mimics the acquired FD data, with a 3×3 binning on the XCD and a reconstruction of a 512^2×70 volume with a voxel size of 0.425 mm.

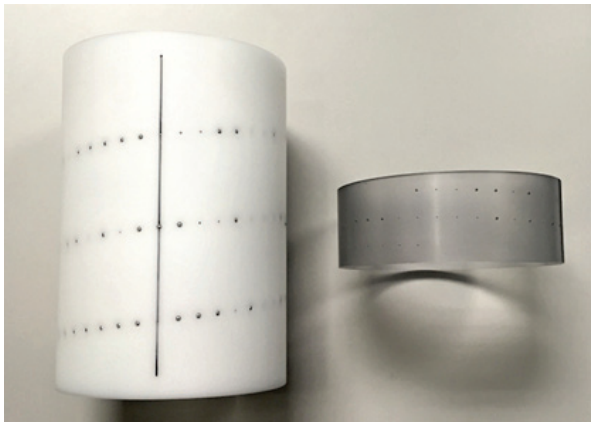

(a)

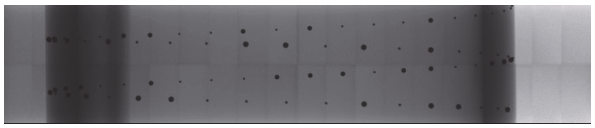

(b)

Figure 3: (a) PDS-2 and customized PDS-3 phantom. (b) TE image of PDS-3 phantom.

III. Results

Stanford University's Administrative Panel on Laboratory Animal Care approved the protocol for this *in-vivo* animal study. One Yorkshire pig (approximately 50 kg) was used for this study. A self-expanding nickel–titanium, single-wire braid LVIS Jr stent (Microvention/Terumo, Tustin, California, US) was placed into the transverse facial artery. The LVIS Jr outer wire diameter is 0.0024" (≈0.06 mm). The 3D acquisition was performed with requesting 81 kV, 12.5 ms and 150 mA from the X-ray tube and the thresholds of the XCD were set to 8 keV for the lower and 39 keV for the higher energy threshold. An example of one *in-vivo* corrected 2D image (TE, HE, and LE) from a rotational run is illustrated in Fig. 4. It can be seen that the image noise increases with a lower photon count rate. The butting zones are slightly visible in the HE and LE images. In Fig. 5 the 3D reconstructions of the *in-vivo* pig acquisitions are presented. The XCD data set shows the superior spatial resolution of the stent. But it also shows the impact of the visible butting zones transitions.

IV. Conclusion

In this paper, the first setup of a large field-of-view photon-counting detector with an angiographic C-arm CT system has been presented. The acquired *in-vivo* pig images look promising and are a major step towards dual-energy imaging within the angiographic suite.

Disclaimer: The concepts and information presented in this paper are based on research and are not commercially available.

Acknowledgment

The authors gratefully acknowledge funding support from the NIH Shared Instrument Grant S10 RR026714 supporting the zeego@StanfordLab, and Siemens Healthcare GmbH Advanced Therapy. Special thanks also goes to Jeremy Heit, MD, PhD and Yamil Saenz for their help with the in-vivo pig experiment and to Microvention/Terumo, Tustin, California, US to provide the intracranial stent.

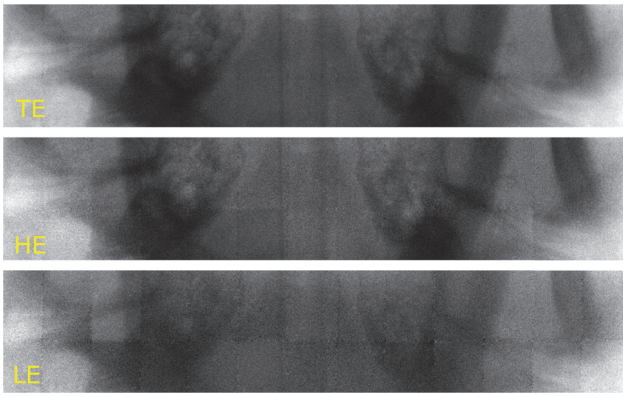

Figure 4: 2D anterior-posterior images of the *in-vivo* pig dataset from a 3D rotational scan after pre-processing.

References

[1] M. Anzidei, M. Di Martino, B. Sacconi, L. Saba, F. Boni, F. Zaccagna, D. Geiger, M. Kirchin, A. Napoli, M. Bezzi, and C. Catalano, "Evaluation of image quality, radiation dose and diagnostic performance of dual-energy CT datasets in patients with hepatocellular carcinoma," *Clinical Radiology*, vol. 70, no. 9, pp. 1–8, 2015.

[2] V. Buffa, A. Solazzo, V. D'Auria, A. Del Prete, A. Vallone, M. Luzietti, M. Madau, R. Grassi, and V. Miele, "Dual-source dual-energy CT: dose reduction after endovascular abdominal aortic aneurysm repair," *La radiologia medica*, vol. 119, no. 12, pp. 934–941, 2014.

[3] S. J. Kim, H. K. Lim, H. Y. Lee, C. G. Choi, D. H. Lee, D. C. Suh, S. M. Kim, J. K. Kim, and B. Krauss, "Dual-energy CT in the evaluation of intracerebral hemorrhage of unknown origin: Differentiation between tumor bleeding and pure hemorrhage," *American Journal of Neuroradiology*, vol. 33, no. 5, pp. 865–872, 2012.

[4] I. Danad, Z. A. Fayad, M. J. Willemink, and J. K. Min, "New Applications of Cardiac Computed Tomography," *JACC: Cardiovascular Imaging*, vol. 8, no. 6, pp. 710–723, 2015.

[5] C. H. McCollough, S. Leng, L. Yu, and J. G. Fletcher, "Dual- and Multi-Energy CT: Principles, Technical Approaches, and Clinical Applications.," *Radiology*, vol. 276, no. 3, pp. 637–653, 2015.

[6] Z. Yu, S. Leng, S. Jorgensen, Z. Li, R. Gutjahr, B. Chen, X. Duan, A. Halaweish, L. Yu, E. Ritman, and C. McCollough, "Initial results from a prototype whole-body photon-counting computed tomography system," in *Proceedings of SPIE Medical Imaging*, 2015.

[7] K. Taguchi and J. S. Iwanczyk, "Vision 20/20: Single photon counting x-ray detectors in medical imaging.," *Medical Physics*, vol. 40, no. 10, p. 100901, 2013.

[8] C. Ullberg, M. Urech, N. Weber, A. Engman, A. Redz, and F. Henckel, "Measurements of a Dual-Energy Fast Photon Counting CdTe Detector with Integrated Charge Sharing Correction," *Proceedings of SPIE Medical Imaging*, vol. 8668, pp. 86680P–86680P–8, 2013.

[9] J. Jakubek, "Data processing and image reconstruction methods for pixel detectors," in *Proceedings of the 8th International Workshop on Radiation Imaging Detectors*, vol. 576, pp. 223–234, 2007.

[10] D. Vavrik, J. Dammer, T. Holy, J. Jakubek, S. Pospisil, and Z. Vykyda, "Direct thickness calibration: way to radiographic study of soft tissues," in *Proceedings of the 9th ICATPP Conference on Astroparticle, Particle, Space Physics, Detectors and Medical Physics Applications*, pp. 773–778, 2005.

[11] N. K. Strobel, B. Heigl, T. M. Brunner, O. Schütz, M. M. Mitschke, K. Wiesent, and T. Mertelmeier, "Improving 3D Image Quality of X-ray C-Arm Imaging Systems by Using Properly Designed Pose Determination Systems for Calibrating the Projection Geometry," in *Proceedings of SPIE Medical Imaging*, vol. 5030, pp. 943–954, 2003.

[12] A. Maier, H. G. Hofmann, M. Berger, P. Fischer, C. Schwemmer, H. Wu, K. Müller, J. Hornegger, J.-H. Choi, C. Riess, A. Keil, and R. Fahrig, "CONRAD – a software framework for cone-beam imaging in radiology.," *Medical Physics*, vol. 40, no. 11, p. 111914, 2013.

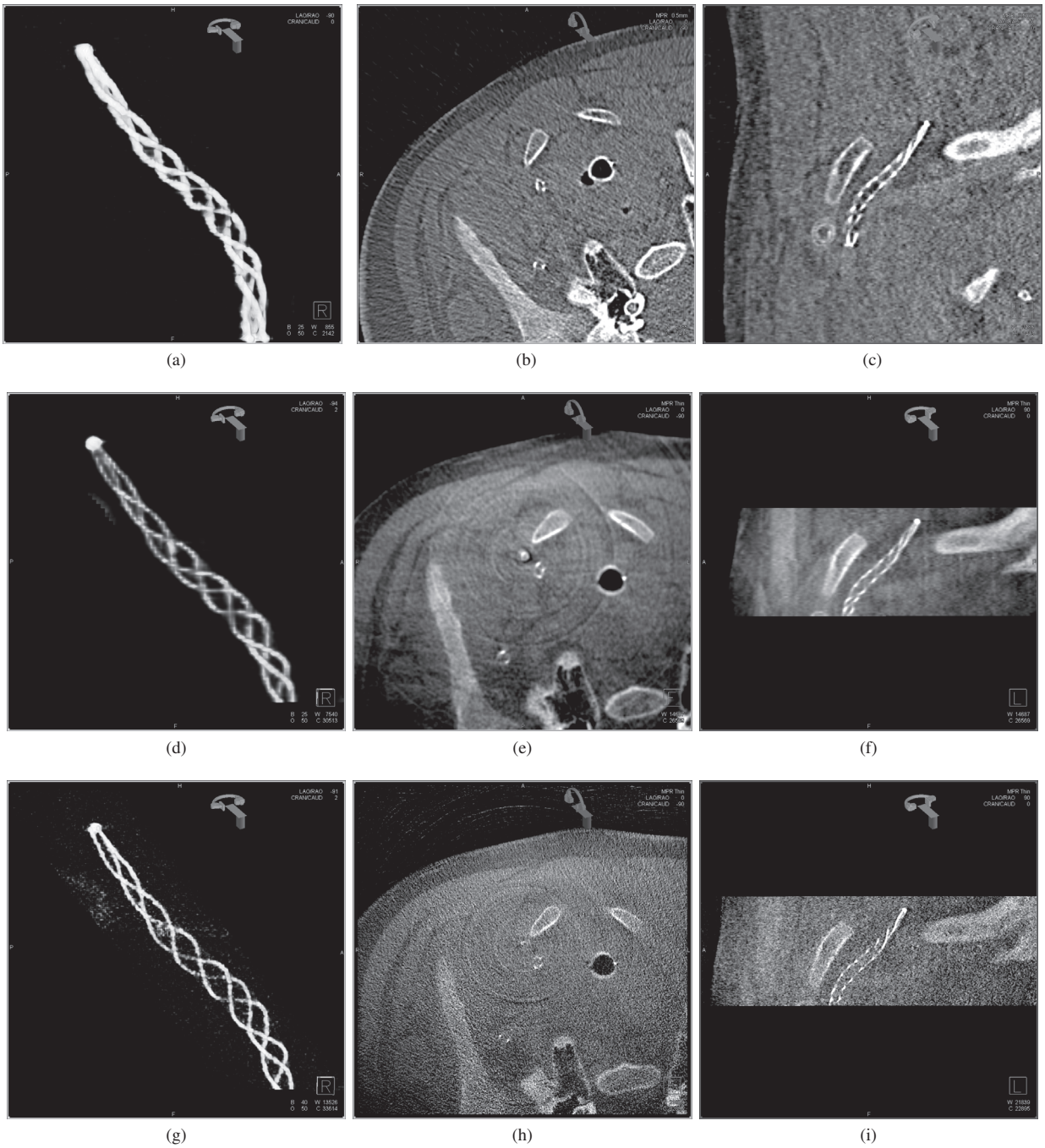

(a) (b) (c)

(d) (e) (f)

(g) (h) (i)

Figure 5: 3D reconstructions of the *in-vivo* pig dataset. From left to right, volume rendered image, axial slice, and sagittal view. The first row shows the FD, the second row the 3×3 binned FD-mimicked, and the third row the 1×1 XCD reconstruction.

Noise Reduction in Low-dose CT by Non-local Means on Local Principle Components

Yuanke Zhang, Hongbing Lu*, Jing Meng, Junliang Shang, Junying Zhang and Pinghong Ren

***Abstract*—In this paper, we develop an efficient noise reduction scheme for low-dose CT by using nonlocal means (NLM) on local principle components (PC-NLM). In the PC-NLM denoising scheme, PCA on local neighbor patches is utilized to derive a locally adaptive basis set and to decorrelate data signal correlation among a patch, and then the NLM-mechanism is employed to average the corresponding principle components of local neighbor patches based on the similarity of the target patch and its neighbor patches. Through extracting redundancy information from corresponding principle components of neighbor patches with such a NLM operation, each principle component of the target patch can be properly regularized so that the inherent noise can be efficiently mitigated after inverse transformation. In addition, the principle neighborhood dictionary (PND) technique is introduced to the PC-NLM scheme to increase the accuracy of similarity calculation between patches, as well as to reduce the computational load. The effectiveness of the proposed method is validated by the experimental studies.**

***Index Terms*—low-dose CT, noise, artifact suppression, principle component analysis (PCA), nonlocal means (NLM).**

I. Introduction

LOW-DOSE CT technique can efficiently reduce the x-ray radiation exposure to patients. However, this approach is highly detrimental to image quality, resulting in images with significant noise and streak artifacts [1]. Up to now, many noise reduction strategies have been proposed to address this problem, including statistic-based iterative reconstruction (SIR) approaches [2-3], pre-processing methods [4-5] and post-processing algorithms [6-7]. In the present work, we focus on the third strategy, post-processing approaches, which mitigate noise and artifacts of the FBP reconstructed CT image directly. Post-processing methods can utilize priori structural information of objects with less computational demands. Another advantage of post-processing methods is that they have a wide applicability considering that only reconstructed images are available in most equipped CT scanners.

Yuanke Zhang, Jing Meng, Junliang Shang and Pinghong Ren are with the School of Information Science and Engineering, Qufu Normal University, Rizhao, Shandong 276826, China (e-mail: yuankezhang@163.com; qfmj@163.com; shangjunliang110@163.com; renpinghong@163.com).

Hongbing Lu is with the Department of Biomedical Engineering, Fourth Military Medical University, Xi'an, Shaanxi 710032, China (e-mail: luhb@fmmu.edu.cn).

Junying Zhang is with the School of Computer Science and Technology, Xidian University, Xi'an, Shaanxi 710071, China (e-mail: jyzhang@mail.xidian.edu.cn).

Principle components analysis (PCA) is a classical decorrelation technique in statistical signal processing which provides the best locally adaptive transformation basis set. PCA on local image patches has previously been used for image denoising. Muresan et al. [8] proposed a PCA-based scheme for image denoising, which computed the locally fitted basis to transform the image and preserved only the several most significant principal components to remove the noise. Zhang et al. [9] improved Muresan's method and presented a two-stage LPG-PCA denoising strategy. Their result shows state-of-the-art denoising performance for the Gaussian noise corrupted image where the noise variance is known or can be well estimated. However, for the FBP reconstructed low-dose CT image, the noise are non-stationary and do not obey to any specific statistics model. Hence, it is necessary to investigate superior PCA-based noise and artifacts mitigation methods for low-dose CT image. In this work, we propose a low-dose CT noise reduction scheme by using nonlocal means (NLM) [10] on local principle components (PC).

II. Methods

The proposed PC-NLM denoising method adapts the NLM mechanism to extract the redundant information from corresponding PCs of local neighboring patches. The PC-NLM method contains three major steps: (a) Sorting and selecting patches similar to the central one in the local search window as the training samples; (b) Decompose sample patches into uncorrelated PCs by locally fitted PCA basis set computed from training samples; (c) NLM weighted averaging of corresponding PCs of local neighboring patches to estimate the central patch. In the following subsections, we describe each step in detail.

A. Training Patches Grouping

For a target pixel to be denoised, we set a $K\times K$ square neighborhood centered on it, *called a patch* and denoted by $\mathbf{x}_0 = [x_1^0, x_2^0, \cdots, x_M^0]^T$, $M = K^2$. Also, we define an $L\times L$ ($L>K$) *search window* centered on the target pixel. By sliding inside the window pixel by pixel, we can extract $(L\text{-}K+1)^2$ overlapped patches from the search window, denoted by $\tilde{\mathbf{x}}_i, i = 0,1,\cdots,(L-K+1)^2-1$. Then we compute the distance between the central patch and the other patches for patch similarity measurement, which can be expressed as:

$$\tilde{\rho}_i = \left\|\tilde{\mathbf{x}}_i - \mathbf{x}_0\right\|_{2,a}^2, \qquad i = 0,1,2,\cdots,(L-K+1)^2-1 \tag{1}$$

where the notation $\|\cdot\|_{2,a}$ denotes a Gaussian weighted Euclidean distance between two patch vectors with a being the standard deviation of the Gaussian kernel. Finally, we sort the distance in ascending order and select the most similar N patches (including the central patch $\mathbf{x}_0$) as the training samples to compute the PCA transformation matrix. We denote these training patches as $\mathbf{x}_0$, $\mathbf{x}_1$, ⋯, $\mathbf{x}_{N-1}$, with ρ_i being the corresponding distance between $\mathbf{x}_0$ and $\mathbf{x}_i$, which will be used in the following NLM weights calculation in Subsection II.*C*. Then the training patch set for $\mathbf{x}_0$ is formed by

$$\mathbf{X}=[\,\mathbf{x}_0, \mathbf{x}_1, \cdots, \mathbf{x}_{N-1}\,] \tag{2}$$

where $\mathbf{x}_i=[x_1^i, x_2^i, \cdots, x_M^i]^T, i=0,1,\cdots,N-1$.

Here, we take the number of training patches $N=C\cdot M$ with constant C=8~10 as in [8], which can guarantee the robust estimation of the local statistics.

B. PCA Transformation of Local Patches

Given the training patch set $\mathbf{X}$, the PCA transformation is to seek a basis set that minimizes the sum of the square errors between the first M bases and the training patches. Denote the ith row of training matrix $\mathbf{X}$ as

$$X_i=\left[x_i^0, x_i^1, \cdots, x_i^{N-1}\right], i=1,2,\cdots,M \tag{3}$$

We compute the mean value of X_i as

$$\upsilon_i=\frac{1}{N}\sum_{j=0}^{N-1}x_i^j \ , \tag{4}$$

and then centralize X_i as

$$\overline{X}_i=X_i-\upsilon_i \tag{5}$$

Accordingly, the centralized matrix of $\mathbf{X}$ is

$$\overline{\mathbf{X}}=[\overline{X}_0^T, \overline{X}_1^T, \cdots, \overline{X}_{N-1}^T]^T==\left[\overline{\mathbf{x}}_0, \overline{\mathbf{x}}_1, \cdots, \overline{\mathbf{x}}_{N-1}\right] \tag{6}$$

where $\overline{\mathbf{x}}_j$ is the centralized result of $\mathbf{x}_j$. Next we compute the covariance matrix of the centralized dataset as

$$\mathbf{\Omega}=\frac{1}{N}\overline{\mathbf{X}}\overline{\mathbf{X}}^T \ , \tag{7}$$

and decompose $\mathbf{\Omega}$ as

$$\mathbf{\Omega}=\mathbf{\Phi}\mathbf{\Lambda}\mathbf{\Phi}^T \tag{8}$$

where $\mathbf{\Lambda}=diag\{\lambda_1, \lambda_2, \cdots, \lambda_M\}$ and $\mathbf{\Phi}=[\,\varphi_1, \varphi_2, \cdots, \varphi_M]$. The terms $\lambda_1, \lambda_2, \cdots, \lambda_M$ are the eigenvalues of $\mathbf{\Omega}$ with $\lambda_1\geq\lambda_2\geq\cdots\geq\lambda_M$ and the terms $\varphi_1, \varphi_2, \cdots, \varphi_M$ are the eigenvectors of $\mathbf{\Omega}$ that are exactly the desired basis set for transformation.

We decompose the centralized patches through applying $\mathbf{\Phi}^T$ to $\overline{\mathbf{X}}$ and have

$$\mathbf{Y}=\mathbf{\Phi}^T\overline{\mathbf{X}} \tag{9}$$

where $\mathbf{Y}=[\mathbf{y}_0, \mathbf{y}_1, \cdots, \mathbf{y}_{N-1}]$ represents ordered principle components of $\overline{\mathbf{X}}$.

Without loss of generality, the noise in the local search window with a small window size can be assumed to follow approximately an independent and identically distribution. Though the covariance matrix $\mathbf{\Omega}$ is calculated from the noisy training patches, the eigenvectors of $\mathbf{\Omega}$ would not change in any noticeable way, based on the fact that principal directions of a multivariate probability distribution function are not altered by addition of independent and identically distributed noise [11].

C. NLM Weighted Average of Principle Components

The NLM concept was first proposed by Buades et al. [10] which can extract the redundancy information from neighborhood through a weighted average scheme. In the PC-NLM scheme, the NLM mechanism is employed to regularize the target patch in the PCA domain through weighted averaging the corresponding principle components of local neighbor patches based on the similarity of the target patch and the other local patches.

Denoted the ith row of decomposition matrix $\mathbf{Y}$ by $Y_i=\left[y_i^0, y_i^1, \cdots, y_i^{N-1}\right]$, where y_i^l is the ith principle component of the local patch $\overline{\mathbf{x}}_l, l=0,1,\cdots,N-1$. The ith principle component of the centralized target patch can be regularized as

$$\hat{y}_i^0=\sum_{l=0}^{N-1}w(\mathbf{x}_0,\mathbf{x}_l)y_i^l \ , i=1,2,\cdots M \tag{10}$$

where $w(\mathbf{x}_0,\mathbf{x}_l)$ is the weight assigned to y_i^l. The weight $w(\mathbf{x}_0, \mathbf{x}_l)$, l=1, 2, ⋯, N-1 depends on the similarity between patch $\mathbf{x}_0$ and $\mathbf{x}_l$, and satisfies the conditions of $0\leq w(\mathbf{x}_0, \mathbf{x}_l)\leq 1$ and $\sum_{j=0}^{N-1}w(\mathbf{x}_0,\mathbf{x}_l)=1$. It can be computed as

$$\begin{aligned} w(\mathbf{x}_0,\mathbf{x}_l)&=\frac{1}{Z(\mathbf{x}_0)}\exp\left(-\frac{\left\|\mathbf{x}_0-\mathbf{x}_l\right\|_{2,a}^2}{h^2}\right)\\ &=\frac{1}{Z(\mathbf{x}_0)}\exp\left(-\frac{\rho_l}{h^2}\right)\end{aligned} \tag{11}$$

Here, ρ_l is the Gaussian weighted Euclidean distance between the patches $\mathbf{x}_0$ and $\mathbf{x}_l$, as calculated by (1) in the Subsection II.A. The term $Z(\mathbf{x}_0)=\sum_{l=0}^{N-1}\exp\left(-\rho_l/h^2\right)$ is a normalizing factor. In (11), the exponential function converts the distances to weights, determined by the *filtering parameter h* which controls the overall smoothness of the filtering.

Accordingly, all the principle components of the centralized target patch can be regularized as

$$\hat{\mathbf{y}}_0=\sum_{l=0}^{N-1}w(\mathbf{x}_0,\mathbf{x}_l)\mathbf{y}_l \tag{12}$$

By transforming $\hat{\mathbf{y}}_0$ back to the time domain, we obtain the denoising result of the centralized target patch $\overline{\mathbf{x}}_0$ as

$$\hat{\overline{\mathbf{x}}}_0=\mathbf{\Phi}\hat{\mathbf{y}}_0 \tag{13}$$

Denoted by $\mathbf{\upsilon}=[\upsilon_1,\upsilon_2,\cdots,\upsilon_M]^T$ the mean vector of the training matrix $\mathbf{X}$, then the denoising result of the target patch $\mathbf{x}_0$ can be obtained by adding the mean vector $\mathbf{\upsilon}$ back to $\hat{\overline{\mathbf{x}}}_0$ as

$$\hat{\mathbf{x}}_0=\hat{\overline{\mathbf{x}}}_0+\mathbf{\upsilon} \tag{14}$$

Applying such procedures to each pixel and finally averaging the corresponding values in the overlapped patches at a given location, the whole image can be denoised. The PC-NLM procedure should be iterated two times for complete removal of the noise artifacts.

D. *Fast and Efficient Realization*

A straightforward implementation of the PC-NLM method is highly computationally demanding. Most of the computational cost spends on the computation of similarities between patches in the local search window. Here, we adapt the principle neighborhood dictionary (PND) method proposed by Tasdizen [11] to reduce the computational load of similarity calculation between patches. In the PND method, all patches are first projected onto a lower dimensional subspace using PCA. Then patches similarities are computed using distances in this subspace rather than the full space, resulting in significant computational savings. More importantly, Tasdizen has shown that this approach results in increased accuracy over using the full-dimensional ambient space [11]. Let $\mathbf{f}_{d,i}$ be the d-dimensional projection vector of the patch $\tilde{\mathbf{x}}_i$. Then instead of using (1), distances between the central patch and the other patches are computed by

$$\rho_{d,i} = \left\| \mathbf{f}_{d,i} - \mathbf{f}_{d,0} \right\|_{2,a}^2, \quad i = 0,1,2,\cdots,(L-K+1)^2 - 1 \qquad (15)$$

In [11], Tasdizen experimentally showed that about the first 40% principle components can be chosen as the significant components. In this paper, we take the number of significant components $d = \lfloor 0.4M \rfloor$, where M is the size of the full-dimensional space.

E. *Parameter Selection*

In implementation, we experimentally found that by setting K=3 and L=15 for images with relatively low level of noise and artifacts, and by setting K=5 and L=21 for images with relatively high level of noise and artifacts can lead to satisfying denoising result in both structures preservation and noise/artifacts suppression.

In the NLM mechanism, the *filtering parameter h* controls the overall smoothness of the filtering. Typically, h depends on the standard deviation of the image noise. In practice, the *filtering parameter h* can also be empirically selected, as in [7]. Here, we set h empirically. There are still many noise and artifacts residuals in the processing result after one round of the PC-NLM procedure described above. Therefore, the PC-NLM procedure should be iterated once more for complete removal of the noise and artifacts. Since the noise and artifacts have been much mitigated in the first round of PC-NLM, the value of the *filtering parameter h* used in the following iterations should be reduced to adapt for the new noise level of the result. Denote by $h^{(i)}$ the filtering parameter used in the ith iteration. We experimentally found that setting $h^{(2)} = 0.17h^{(1)}$ can lead to satisfying denoising results for low-dose CT images.

III. Experiment Results

A. *Data Acquisition*

The effectiveness of the proposed PC-NLM method was validated with a low-dose scan acquired by a GE Hi-Speed multislice CT scanner at 120 kVp, 10 mAs protocol from a GE QA phantom. The time per gantry rotation was 1s. The slice thickness was 1.25mm. A standard reconstruction kernel and tradition FBP method was employed to reconstruct the images. Besides, a scan acquired with 120 kVp and 190 mAs was used to serve as the reference image.

B. *Visual Evaluation*

The FBP algorithm, the NLM algorithm [10] and the LPG-PCA [9] algorithm were adopted for comparison. Fig.1 shows the processing results. Fig.1(a)-(b) show the reference phantom and the FBP reconstruction of the low-dose sinogram, respectively. Severe noise/artifacts can be seen in Fig.1(b). Fig.1(c)-(d) give the results of Fig.1(b) filtered by the NLM algorithm and the LPG-PCA algorithm, respectively. Fig.1(e) shows the processing result by the proposed PC-NLM algorithm with patch size of 5×5. As shown in Fig.1(c)-(d), the NLM and LPG-PCA methods are not only ineffective in suppressing streak artifacts, but also lead to obvious structure obscurity. Instead, the proposed PC-NLM algorithm performs much better in both suppressing noise and artifacts (please see the green arrow in the Fig.1(e)) and preserving subtle structures (please see the blue arrows in Fig.1(e)).

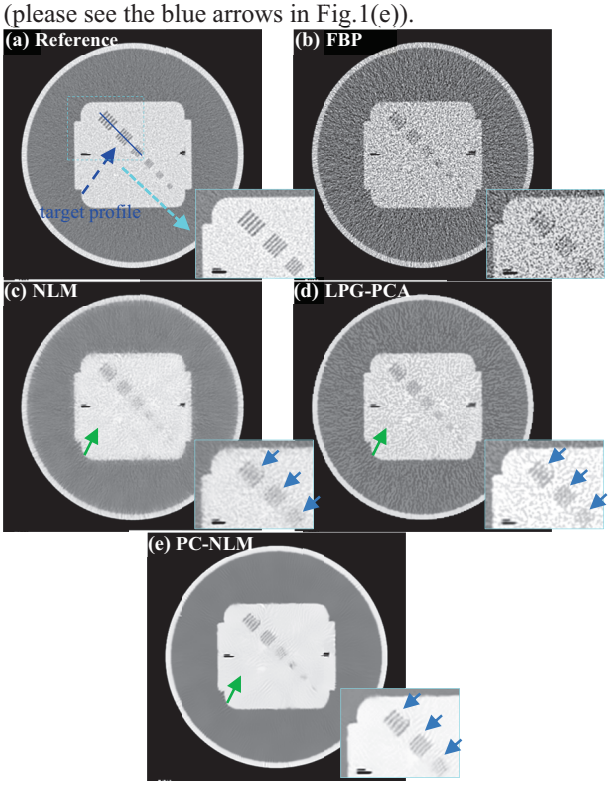

Fig.1. Processing results of the QA phantom. The display window is [0,600] HU.

Fig.2 shows the intensity profiles along the blue line in Fig.1(a) by the aforementioned algorithms as compared to that of the reference phantom. Here too, the intensity values of the proposed PC-NLM algorithm match better to that of the reference image (please see the blue arrows in Fig.2).

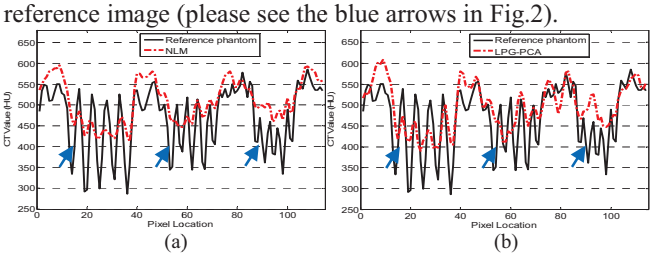

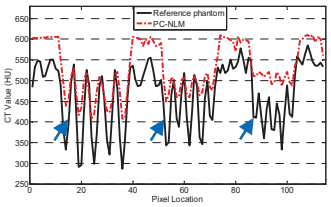

(c)

Fig.2. Intensity profiles along the vertical blue line labeled in Fig.1(a).

C. Quantitative Evaluation

The performance of aforementioned algorithms was quantitatively evaluated using the correlation coefficient (CC) and the structural similarity index comparisons (SSIM) metrics [13]. These metrics are defined as

$$\mathrm{CC}=\sum_{i=1}^{I}(x_i-\bar{x})(r_i-\bar{r})\Big/\sqrt{\sum_{i=1}^{I}(x_i-\bar{x})^2\sum_{i=1}^{I}(r_i-\bar{r})^2} \tag{16}$$

$$\mathrm{SSIM}=\frac{(2\bar{x}\cdot\bar{r}+c_1)(2\sigma_{xr}+c_2)}{(\bar{x}^2+\bar{r}^2+c_1)(\sigma_x^2+\sigma_r^2+c_2)} \tag{17}$$

where, r and x denote the reference phantom and the processing result, respectively, $\bar{r}$ and $\bar{x}$ are the mean intensities, σ_r and σ_x are the standard deviations, and σ_{xr} is the covariance between the phantom and the processed image. I represents the number of pixels. c_1 and c_2 are small constants with $c_1=(K_1L_s)^2$ and $c_2=(K_2L_s)^2$, where L_s is the dynamic range of the image (was set as 610 for the range from 0 HU to 610 HU in our phantom study), and K_1 and K_2 were set to 0.01 and 0.03 based on [13]. The quantitative results were list in Table I. Quantitatively, the PC-NLM methods outperformed NLM and LPG-PCA methods.

TABLE I
NUMERICAL COMPARISON OF THE RESULTS OBTAINED FOR THE QA PHANTOM VIA VARIOUS METRICS

Metric	FBP	NLM	LPG-PCA	PC-NLM
CC	0.686	0.822	0.808	**0.899**
SSIM	0.302	0.589	0.536	**0.793**

D. Computation Costs

Table II shows the run times (in seconds) of the PC-NLM algorithm to process one 512×512 slice with/without using the PND technique. Table I also shows the average run times of the PC-NLM algorithm with different sizes of the local patch and the local search window. The algorithm was coded in Matlab on 3.6G Intel Core i7 CPU. It shows that the run times of the PC-NLM method can be greatly reduced by using the PND technique.

TABLE II
THE AVERAGE RUN TIME (IN SECOND) FOR PC-NLM ALGORITHM WITH/WITHOUT PND TECHNIQUE

	PC-NLM without PND	PC-NLM with PND
Average run time for one **512×512** slice, with ***K*=3** and ***L*=15**.	44.31	34.72
Average run time for one **512×512** slice, with ***K*=5** and ***L*=21**.	103.53	84.91

IV. CONCLUSION

This paper presents a noise reduction scheme for low-dose CT by using nonlocal means on local principle components. In this scheme, the PCA technique on local neighbor patches was employed to derive a locally adaptive basis set and to decompose the strong data signal correlation among a patch. Thus the NLM operation can be utilized to extract redundancy information from corresponding principle components of neighbor patches. To speed up the implementation of the proposed PC-NLM method, we further employ the principle neighborhood dictionary (PND) technique to reduce the computational load in patches similarity calculation.

V. ACKNOWLEDGEMENTS

This work was supported by the National Natural Science Foundation of China under Grant Nos. 61572283, 81230035 and 61502272, the Award Foundation Project of Excellent Young scientists in Shandong Province under Grant Nos. BS2014DX005 and BS2014DX004, the Project of Shandong Province Higher Educational Science and Technology Program under Grant Nos. J13LN31, the Scientific Research Foundation of Qufu Normal University under Grant No. XJ201226, and the Doctoral Scientific Research Foundation of Qufu Normal University under Grant Nos. BSQD20110124.

REFERENCES

[1] J. Hsieh, “Adaptive streak artifact reduction in computed tomography resulting from excessive X-ray photon noise,” *Med. Phys.*, vol. 25, no. 3, pp. 2139–2147, 1998.

[2] Q. Xu，X. Mou，G. Wang，J. Sieren，EA. Hoffman，H. Yu, “Low-dose X-ray CT Reconstruction via Dictionary Learning,” *IEEE Trans. Med. Imag.*, vol. 31, no. 9, pp. 1682-1697, 2012.

[3] H. Zhang, H. Han, J. Wang, J. Ma, Y. Liu, W. M, and Z. Liang, “Deriving Adaptive MRF Coefficients from Previous Normal-dose CT Scan for Low-dose Image Reconstruction via Penalized Weighted Least-squares Minimization,” *Med. Phys.*, vol. 41, no. 4, pp. 1916-1931, 2014.

[4] P. J. La Rivière, J. Bian, and P. A. Vargas, “Penalized-likelihood Sinogram Restoration for Computed Tomography,” *IEEE Trans. Med. Imag.*, vol. 25, no. 8, pp. 1022-1036, 2006.

[5] J. Wang, T. Li, H. Lu, and Z. Liang, “Penalized weighted least-squares approach to sinogram noise reduction and image reconstruction for low-dose X-ray computed tomography,” *IEEE Trans. Med. Imag.*, vol. 26, no. 10, pp. 1272-1283, 2006.

[6] H. Yu, S. Zhao, E. A. Hoffman, and G.Wang, “Ultra-low dose lung CT perfusion regularized by a previous scan,” Acad. Radiol., vol. 16, no. 3, pp. 363-373, 2009.

[7] J. Ma, J. Huang, Q. Feng, H. Zhang, H. Lu, Z. Liang, and W. Chen, “Low-dose computed tomography image restoration using previous normal-dose scan,” *Med. Phys.*, vol. 38, no. 10, pp. 5713-5731, 2011.

[8] D.D. Muresan, T.W. Parks, “Adaptive principal components and image denoising,” in: Proceedings of the 2003 International Conference on Image Processing, 14–17 September, 2003, vol. 1, pp. I101–I104.

[9] L. Zhang, W. Dong, D. Zhang, and G. Shi, “Two-stage image denoising by principal component analysis with local pixel grouping,” *Pattern. Recognit.*, vol. 43, pp. 1531-1549, 2010.

[10] A. Buades, B. Coll, and J. M. Morel, “A review of image denoising algorithms, with a new one,” *Multiscale Model. Sim.*, vol. 4, no. 2, pp. 490-530, 2005.

[11] T. Tasdizen, “Principal neighborhood dictionaries for nonlocal means image denoising,” *IEEE Trans. Image. Process.*, vol. 18, no. 12, pp. 2649-2660, 2009.

[12] R. Everson and S. Roberts, “Infering the eigenvalues of covariance matrices from limited, noisy data,” *IEEE Trans. Signal. Process.*, vol. 48, no. 7, pp. 2083-2091, 2000.

[13] Z. Wang, A. C. Bovik, H. R. Sheikh and E. P. Simoncelli, “Image quality assessment: from error visibility to structural similarity,” *IEEE Trans. Image. Process.*, vol. 13, no. 4, pp. 600-612, 2004.

Characterization of the previous normal-dose CT scan induced nonlocal means regularization method for low-dose CT image reconstruction

Hao Zhang, Jianhua Ma, William Moore, and Zhengrong Liang*

Abstract—**Repeated computed tomography (CT) scans are required in some clinical applications such as image-guided radiotherapy and follow-up observations over a time period. To optimize the radiation dose utility, a normal-dose (or full-dose) CT scan is often first performed to set up reference, followed by a series of low-dose scans. Using the previous normal-dose scan to improve follow-up low-dose scans reconstruction has drawn great interests recently, such as the previous normal-dose induced nonlocal means (ndiNLM) regularization method. However, one major concern with this method is that whether it would introduce false structures or miss true structures when the previous normal-dose image and current low-dose image have different structures (e.g., a tumor could be present, grow, shrink or absent in either image). This study aims to investigate the performance of the ndiNLM regularization method in the above mentioned situations. A patient with lung nodule for biopsy was recruited to this study. A normal-dose scan was acquired to set up biopsy operation, followed by a few low-dose scans during needle intervention toward the nodule. We used different slices to mimic different possible cases wherein the previous normal-dose image and current low-dose image have different structures. The experimental results characterize performance of our ndiNLM regularization method.**

I. Introduction

X-ray computed tomography (CT) has been widely exploited in clinic for different applications. Recent discoveries regarding the potential harmful effects of X-ray radiation including genetic and cancerous diseases have raised growing concerns to patients and medical physics community [1]. Repeated CT scans are required in some clinical applications such as image-guided radiotherapy and follow-up observations over a time period, and the accumulated radiation dose could be significant. To optimize radiation dose utility, a normal-dose scan is often first performed to set up reference, followed by a series of low-dose scans. In these applications, the previous normal-dose scan can be exploited as prior information due to the similarity among the reconstructed image series of the scans. While somewhat misalignment and/or deformation may occur among the image series, they can be mitigated through registration of the image series. Using the reconstruction from previous normal-dose scan to improve the follow-up low-dose scans reconstruction has become a research interest recently, some of which exploited the previous normal-dose image as a penalty for regularized iterative image reconstructions. For instance, Nett et al. [2] incorporated a registered normal-dose image into their prior image constrained compressed sensing (PICCS) framework for iterative reconstruction of subsequent low-dose CT images. Stayman et al. [3, 4] presented a PICCS-type penalty term, but the high-quality normal-dose image was formulated into a joint estimation framework for both image registration and image reconstruction in order to better capturing the anatomical motion among different scans. Zhang et al. [5, 6] predicted MRF coefficients from previous normal-dose CT image and exploited this prior information to improve the follow-up statistical Bayesian low-dose image reconstruction. Moreover, Ma et al. [7, 8] proposed previous normal-dose image induced nonlocal means (ndiNLM) penalty terms to improve the following low-dose CT image reconstruction for perfusion and interventional imaging, wherein the previous normal-dose scan was also pre-registered with the low-dose scans. Because of the patch-based search mechanism, this approach does not heavily depend on the accuracy of registration, and a rough registration would be adequate in practice [7, 8]. However, one major concern with the ndiNLM regularization method is that whether it would introduce false structures or miss true structures when the previous normal-dose image and current low-dose image have different structures (e.g., a tumor could be present, grow, shrink or absent in either the previous or current image). This study investigates the different scenarios wherein the previous normal-dose image and current low-dose image have different structures, and characterizes the performance of the ndiNLM regularization method in these situations.

Manuscript received January 18, 2016. This work was supported in part by NIH/NCI under grants #CA143111 and #CA082402. *indicates the corresponding author.

H. Zhang is with the Departments of Radiology and Biomedical Engineering, State University of New York at Stony Brook, NY 11794, USA.

J. Ma is with the School of Biomedical Engineering, Southern Medical University, Guangdong 510515, China.

W. Moore is with the Department of Radiology, State University of New York at Stony Brook, NY 11794, USA.

*Z. Liang is with the Departments of Radiology and Biomedical Engineering, State University of New York at Stony Brook, NY 11794, USA (jerome.liang@sunysb.edu).

II. Methods

A. Statistical model

The noise property of the calibrated line integrals has been investigated by analyzing experimental data of a physical phantom from repeated scans. The statistical analysis showed that the calibrated line integrals can be fitted approximately by a Gaussian distribution with a nonlinear signal-dependent variance [9, 10]:

$$y_i \sim Gaussian(\bar{y}_i, \sigma_{y_i}^2) \quad (1)$$

With the 'Poisson+Gaussian' noise model for the transmitted photons, it has been shown in that the variance of the line integral y_i can be given by [11, 12]:

$$\sigma_{y_i}^2 = \frac{\bar{N}_i + \sigma_e^2}{\bar{N}_i^2} = \frac{1}{\bar{N}_{0i}} \exp(\bar{y}_i) \left(1 + \frac{\sigma_e^2}{\bar{N}_{0i}} \exp(\bar{y}_i) \right) \quad (2)$$

where $\bar{N}_{0i}$ represents the mean number of X-ray photons just before entering the patient and going toward the detector bin *i*, and σ_e^2 denotes the variance of the electronic noise.

B. PWLS image reconstruction

The penalized weighted least-squares (PWLS) cost function in the image domain can be written as:

$$\Phi(\boldsymbol{\mu}) = (\mathbf{y} - \mathbf{A}\boldsymbol{\mu})^T \boldsymbol{\Sigma}^{-1} (\mathbf{y} - \mathbf{A}\boldsymbol{\mu}) + \beta R(\boldsymbol{\mu}) \quad (3)$$

where $\mathbf{y} = (y_1, ..., y_I)^T$ is the vector of measured line integrals, and I is the number of projection measurements; $\boldsymbol{\mu} = (\mu_1, ..., \mu_J)^T$ is the vector of attenuation coefficients of the object to be reconstructed, and J is the number of image pixels; $\mathbf{A}$ is the projection matrix with the size $I \times J$, and its element A_{ij} is typically calculated as the intersection length of projection ray i with pixel j. In our implementation, the system matrix is pre-calculated by a fast ray-tracing technique and stored as a file to serve as a lookup table during iterations. $\boldsymbol{\Sigma}$ is the covariance matrix, and since the measurement among different detector bins are assumed to be independent, the matrix is diagonal and $\boldsymbol{\Sigma} = \mathrm{diag}\{\sigma_{y_i}^2\}$. The symbols T and -1 herein are transpose and inverse operators, respectively. $R(\boldsymbol{\mu})$ denotes the penalty term and β is a smoothing parameter which plays a role of controlling the tradeoff between the data fidelity term and the penalty term. Eq. (3) is the well-known PWLS criterion in the image domain.

The goal for CT image reconstruction is to estimate the attenuation coefficients $\boldsymbol{\mu}$ from the noisy measurement $\mathbf{y}$:

$$\hat{\boldsymbol{\mu}} = \arg\min_{\mu \geq 0} \Phi(\boldsymbol{\mu}) \quad (4)$$

Minimization of Eq. (4) could also be efficiently achieved with the Gauss-Seidel update strategy, and the details can be found in a previous paper [8].

C. ndiNLM regularization

The ndiNLM penalty in the image domain can be described as [7]:

$$R(\boldsymbol{\mu}) = \sum_j (\mu_j - \sum_{k \in SW_j} w_{jk} \mu_k^{ND})^2 \quad (5)$$

where $\boldsymbol{\mu}^{ND} = (\mu_1^{ND}, ..., \mu_J^{ND})^T$ denotes the vector of attenuation coefficients for the previous normal-dose image (ND is short for normal-dose), SW denotes a search-window, and the NLM-based weighting coefficients w_{jk} are given as:

$$w_{jk} = \frac{\exp\left(-\left\| PW(\mu_j) - PW(\mu_k^{ND}) \right\|_{2,a}^2 / h^2 \right)}{\sum_{k \in SW_j} \left[\exp\left(-\left\| PW(\mu_j) - PW(\mu_k^{ND}) \right\|_{2,a}^2 / h^2 \right) \right]} \quad (6)$$

where PW denotes a patch-window, and h is the filtering parameter.

III. Results

A. Data acquisition

To evaluate the ndiNLM regularization method in a more realistic situation, a patient with lung nodule for biopsy at Stony Brook University Hospital was recruited to this study under informed consent after approval by the Institutional Review Board. The patient was scanned using a Siemens CT scanner. The X-ray tube voltage was set to be 120 kV, and the tube current was set to be 100 mAs. The raw data was calibrated by the CT system and outputted as sinogram data or line integrals. We regarded this acquisition as the previous normal-dose scan, and simulated the corresponding low-dose sinogram data by adding noise to the normal-dose sinogram data using the simulation method in [13]. The noisy measurement N_i at detector bin i was generated according to the statistical model:

$$N_i \sim \mathrm{Poisson}(\bar{N}_{0i} \exp(-\bar{y}_i)) + \mathrm{Gaussian}(0, \sigma_e^2) \quad (7)$$

Then the corresponding noisy line integral $\{y_i\}$ is calculated by the logarithm transform.

B. Scenario 1: low-dose CT image having nodule

Fig. 1 illustrates one transverse image of the patient from the simulated low-dose sinogram data, reconstructed by the FBP method. The red arrow indicates a lung nodule. Fig. 2 (P1)-(P3) illustrates three transverse images of the patient from the acquired normal-dose sinogram data, reconstructed by the FBP method. They serve as the previous normal-dose image for the PWLS-ndiNLM method, to mimic the different cases wherein the previous normal-dose image and current low-dose image may have different structures. Fig. 2 (R1)-(R3) show the corresponding reconstructed images from the simulated low-dose sinogram data, by the PWLS-ndiNLM method. It should be noted that the $\beta = 1 \times 10^5$, SW=34×34, PW=5×5, and h=0.005 for all of our implementations. We can see that Fig. 2 (R2) and (R3) still retain the lung nodule even though the corresponding previous normal-dose image has shrinking nodule (P2) or no nodule (P3).

FIG. 1. One transverse image of the patient with a lung nodule, reconstructed by the FBP method from simulated low-dose sinogram data.

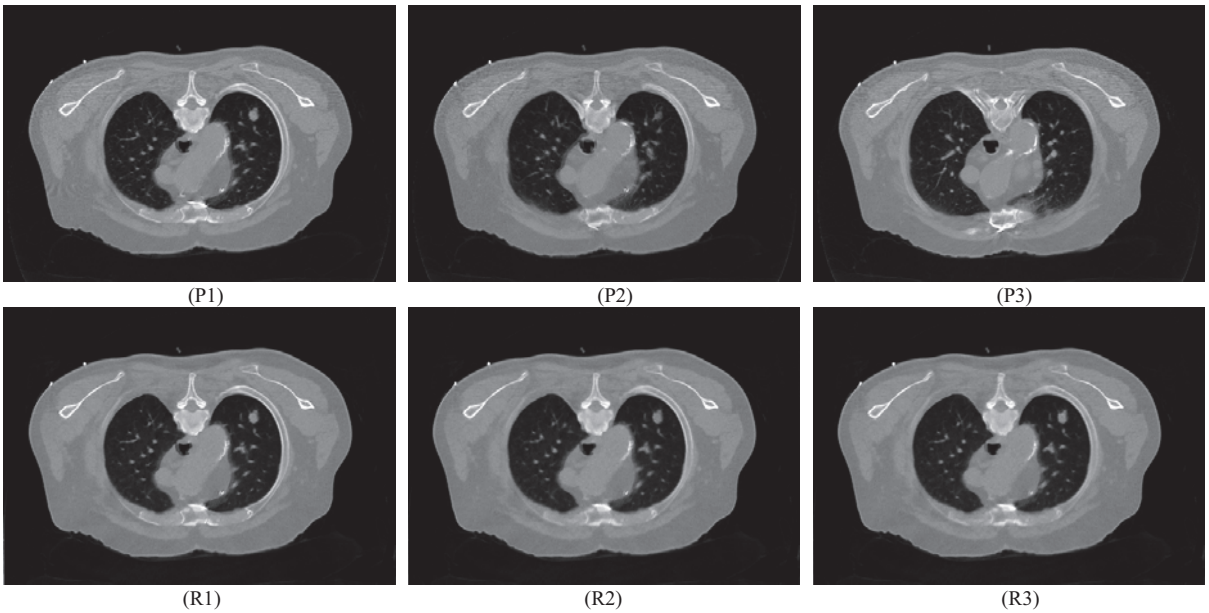

FIG.2. Transverse images of the patient. (P1)-(P3) -- three transverse images of the patient from the normal-dose sinogram data, reconstructed by the FBP method; (R1)-(R3) -- one transverse image of the patient reconstructed by the PWLS-ndiNLM method, from the simulated low-dose sinogram. All the images are displayed with the same window.

C. Scenario 2: low-dose CT image having no nodule

Fig. 3 illustrates another transverse image of the patient from the simulated low-dose sinogram data, reconstructed by the FBP method. It can be observed that this image has no lung nodule. Again, Fig. 4 (P1)-(P3) illustrate three transverse images of the patient from the acquired normal-dose sinogram data, reconstructed by the FBP method. They serve as the previous normal-dose image for the PWLS-ndiNLM method, to mimic the different cases wherein the previous normal-dose image and current low-dose image may have different structures. Fig. 4 (R1)-(R3) shows the corresponding reconstructed images from the simulated low-dose sinogram data, by the PWLS-ndiNLM method. We can observe that Fig. 4 (R1) and (R2) does not introduce false lung nodule when the corresponding previous normal-dose image has lung nodule.

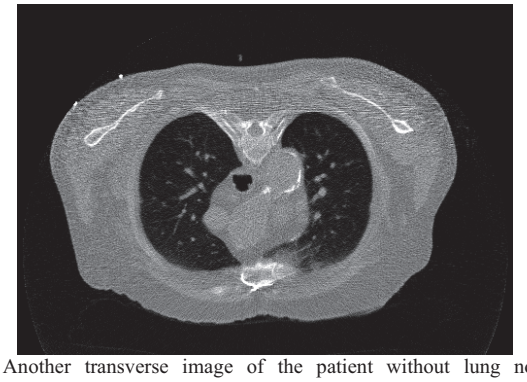

FIG. 3. Another transverse image of the patient without lung nodule, reconstructed by the FBP method from simulated low-dose sinogram data.

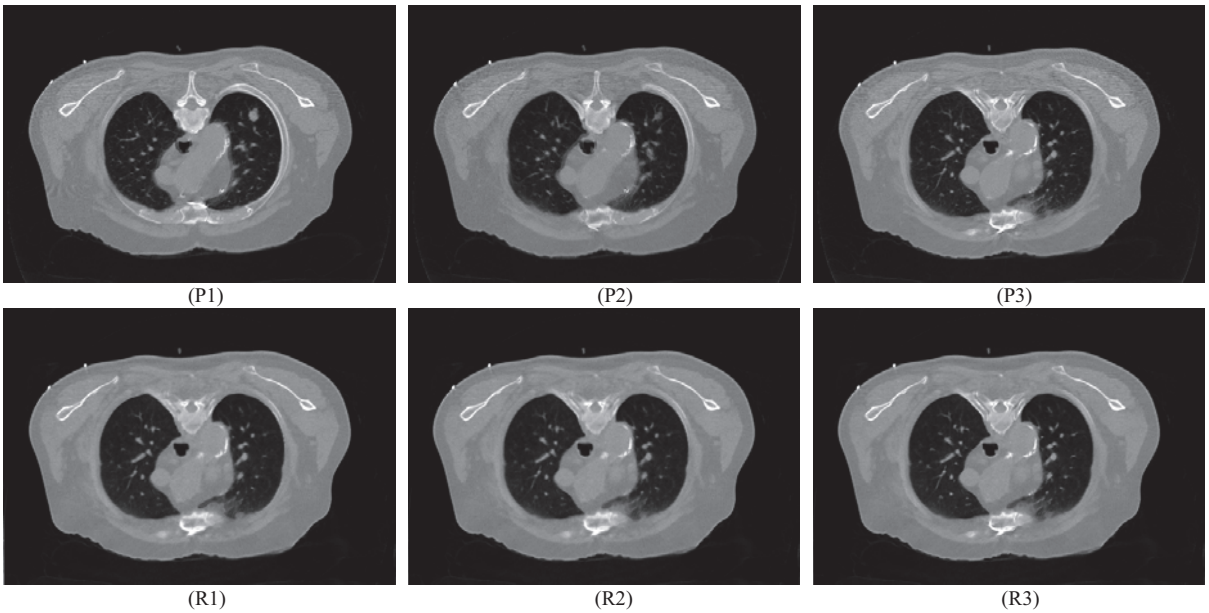

FIG.4. Transverse images of the patient. (P1)-(P3) -- three transverse images of the patient from the normal-dose sinogram data, reconstructed by the FBP method; (R1)-(R3) -- another transverse image of the patient reconstructed by the PWLS-ndiNLM method, from the simulated low-dose sinogram. All the images are displayed with the same window.

IV. Discussions and Conclusions

In this work, we investigated the performance of the ndiNLM regularization when the previous normal-dose image and current low-dose image have different structures, for example, the normal-dose image has lung nodule but the low-dose image has no nodule, or *vice versa*. This preliminary study relieves the concern of introducing false information when the previous scan has or does not have small abnormalities into the current scan by demonstrating that the ndiNLM regularization does not introduce false nodule or miss true nodule. This is an important characteristic for the ndiNLM regularization. However, further quantitative evaluations may be needed to illustrate the reconstruction quality of whole image and lung nodule, and is currently under progress.

Compared with the generic NLM regularization [14, 15] which only utilizes current low-dose image, the ndiNLM regularization may need a larger search-window to take into account the structure difference between the previous normal-dose image and current low-dose image. Therefore, a 17×17 search-window was used in [14, 15] for the generic NLM regularization, but a 34×34 search-window was used in this study for the ndiNLM regularization. Otherwise, the ndiNLM regularization may have an inferior performance and generate undesirable results. This is another finding for this study.

References

[1] D. Brenner, E. Hall, "Computed tomography-an increasing source of radiation exposure," The New England Journal of Medicine, 357, 2277-2284 (2007).

[2] B. Nett, J. Tang, B. Aagaard-Kienitz, H. Rowley, and G. Chen, "Low radiation dose C-arm cone-beam CT based on prior image constrained compressed sensing (PICCS): Including compensation for image volume mismatch between multiple data acquisitions," Proc. SPIE Medical Imaging, 7258: 725–803 (2009).

[3] J. Stayman, H. Dang, Y. Ding, and J. Siewerdsen, "PIRPLE: A penalized-likelihood framework for incorporation of prior images in CT reconstruction," Physics in Medicine and Biology, 58(21): 7563–7582 (2013).

[4] H. Dang, A. Wang, M. Sussman, J. Siewerdsen, and J. Stayman, "dPIRPLE: A joint estimation framework for deformable registration and penalized likelihood CT image reconstruction using prior images," Physics in Medicine and Biology, 59: 4799–4826 (2014).

[5] H. Zhang, H. Han, J. Wang, J. Ma, Y. Liu, W. Moore and Z. Liang, "Deriving adaptive MRF coefficients from previous normal-dose CT scan for low-dose image reconstruction via penalized weighted least-squares minimization," Medical Physics, 41(4): 041916 (2014).

[6] H. Zhang, H. Han, Z. Liang, Hu Y, Y. Liu, W. Moore, J. Ma, and Lu H, "Extracting information from previous full-dose CT scan for knowledge-based Bayesian reconstruction of current low-dose CT images." IEEE Transactions on Medical Imaging (DOI 10.1109/TMI.2015.2498148).

[7] J. Ma, H. Zhang, Y. Gao, J. Huang, Z. Liang, Q. Feng, W. Chen, "Iterative image reconstruction for cerebral perfusion CT using a pre-contrast scan induced edge-preserving prior," Physics in Medicine and Biology, 57, 7519-7542 (2012).

[8] H. Zhang, J. Huang, J. Ma, Z. Bian, Q. Feng, H. Lu, Z. Liang, W. Chen, "Iterative reconstruction for X-ray CT using prior-image induced nonlocal regularization," IEEE Transactions on Biomedical Engineering, 61(9): 2367–2378 (2014).

[9] H. Lu, X. Li, and Z. Liang, "Analytical noise treatment for low-dose CT projection data by penalized weighted least-square smoothing in the K-L domain", Proc. SPIE Medical Imaging, vol. 4682 (2002).

[10] T. Li, X. Li, J. Wang, J. Wen, H. Lu, J. Hsieh, and Z. Liang, "Nonlinear sinogram smoothing for low-dose X-ray CT", IEEE Transactions on Nuclear Science, 51, 2505-2513 (2004).

[11] J. B. Thibault, C. Bouman, K. Sauer, and J. Hsieh, "A recursive filter for noise reduction in statistical iterative tomographic imaging," Proc. of the SPIE/IS&T Symposium on Electronic Imaging Science and Technology—Computational Imaging, 6065, 15–19 (2006).

[12] J. Ma, Z. Liang, Y. Fan, Y. Liu, J. Huang, W. Chen and H. Lu, "Variance analysis of x-ray CT sinograms in the presence of electronic noise background," Medical Physics, 39, 4051–4065 (2012).

[13] P.J. La Rivière and D. M. Billmire. "Reduction of noise-induced streak artifacts in X-ray computed tomography through spline-based penalized-likelihood sinogram smoothing," IEEE Transactions on Medical Imaging, 24(1), 105-11 (2005).

[14] H. Zhang, J. Ma, J. Wang, Y. Liu, H. Lu, and Z. Liang, "Statistical image reconstruction for low-dose CT using nonlocal means-based regularization." Computerized Medical Imaging and Graphics 38(6): 423-435 (2014).

[15] H. Zhang, J. Ma, J. Wang, Y. Liu, H. Han, H. Lu, W. Moore and Z. Liang, "Statistical image reconstruction for low-dose CT using nonlocal means-based regularization. Part II: An adaptive approach." Computerized Medical Imaging and Graphics 43: 26-35 (2015).

Monte Carlo Simulation for Polychromatic X-ray Fluorescence Computed Tomography with Sheet-Beam Geometry

Shanghai JIANG, Biao WEI, Peng FENG*, Peng HE

***Abstract*—X-ray fluorescence computed tomography based on sheet-beam can save a huge amount of time to obtain a whole set of projections using synchrotron. However, it is clearly unpractical for most biomedical research laboratories. In this paper, a benchtop x-ray fluorescence computed tomography system with polychromatic source with sheet-beam geometry is implemented, the feasibility of this kind of setup is tested by Monte Carlo method. Acquired data is reconstructed by Fliter Backprojection (FBP) and maximum likelihood expectation maximization (MLEM), and contrast-to-noise ratio (CNR) is used to evaluate image quality. Our results may provide necessary justification and impetus for future development of a benchtop XFCT for *in vivo* imaging.**

***Index Terms*—Monte Carlo, polychromatic fluorescence x-ray, computed tomography, CNR**

I. Introduction

X-ray fluorescence computed tomography (XFCT), which combines x-ray fluorescence measurements and tomographic reconstruction algorithms, can obtain the distribution of trace elements within samples in a nondestructive and noninvasive manner [1-3]. Synchrotron x-ray sources are ideal for XFCT because their tunable energy can easily maximize the fluorescence-to-background ratio for interrogated material[4]. However, it is clearly unpractical for most biomedical research laboratories.

With the recent emergence of various biomedical applications using gold nanoparticles (GNPs), it has been suggested that a benchtop XFCT system can be developed. In recent years, simulation and experimental demonstration of benchtop x-ray XFCT and based on cone beam geometry were implemented to reduce dose and scan time[4-6]. Although XFCT based on sheet beam geometry using synchrotron x-ray source were also developed, fewer researches were done using polychromatic x-ray source.

This work is partially supported by the National Natural Science Foundation of China (61201346, 61401049). the Fundamental Research Funds for the Central Universities (CDJZR14125501).

Shanghai JIANG, Biao WEI, Peng FENG*, Peng HE are with the Key Lab of Optoelectronic Technology and Systems, Ministry of Education, Chongqing University, Chongqing, 400044, China (e-mail for the corresponding author: coe-fp@cqu.edu.cn)

In this paper, we developed a Monte Carlo model of benchtop polychromatic sheet-beam XFCT using the Monte Carlo N-particle (MCNP). Two phantoms contained several GNP-loaded regions were used in this current model. Acquired data was reconstructed using FBP and MLEM algorithm, then, contrast-to-noise ratio (CNR) was used to evaluate image quality. Our results may provide necessary justification and impetus for future development of a benchtop XFCT for in vivo imaging.

II. Principle and Method

A. Imaging system

The schematic diagram of Sheet-Beam CT system is shown in figure 1. The system consists of polychromatic sheet beam x-ray source, collimator and array detectors.

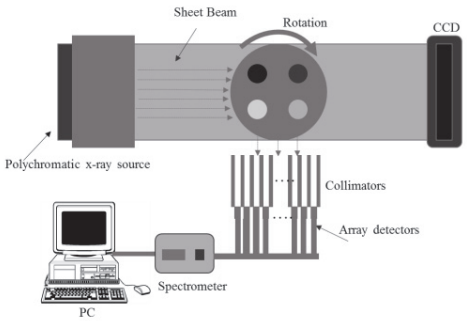

Fig.1. Schematic diagram of XFCT imaging system using sheet-beam and linear detector arrays

Incident polychromatic sheet beam generated from x-ray tube then paralleled using collimator impinges on the object to cover the cross-section. GNPs are thus excited and isotropically emit x-ray fluorescence photos on de-excitation. Linear array photon-counting detectors with energy resolution are positioned perpendicular to the beam propagation direction for x-ray fluorescent spectra[7].

B. Monte Carlo model

In order to improve simulation efficiency, X-ray source in the system above was replaced by a virtual source, whose spectrum was calculated by SpekCalc program. SpekCalc is a software tool used to calculate, display and store the X-ray source spectrum, which simulates X-ray spectra emitted from

thick-target tungsten anode X-ray tubes [8]. In current model, X-ray spectrum obtained by SpekCalc was shown in figure 2. Tungsten excited by 120keV electron beam generated X-rays and then filtered by 1mm Sn.

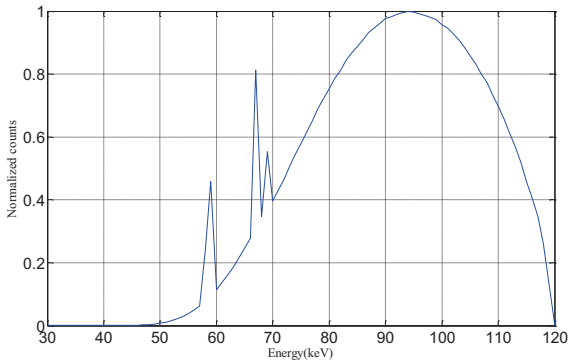

Fig.2. Spectrum of incident polychromatic X-ray source

Two GNP-loaded PMMA phantoms are shown in figure 3. The PMMA phantom is 6.4*cm* in both height and diameter. The phantom on the left side contained several GNP-loaded regions, which has the same size (10*mm*) in height and diameter but different gold concentration ranging from 0.3% to 1.8%. The GNP-loaded regions in right phantom has the same concentration (1.5%) but different diameter ranging from 1*mm* to 9*mm*.

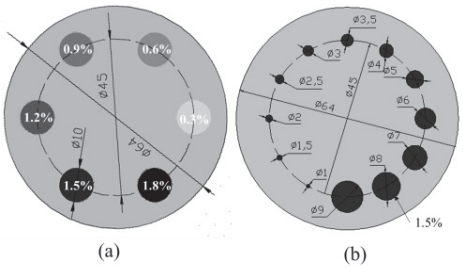

Fig.3. Phantoms contained GNP-loaded regions. (a) GNP-loaded regions with same size in height and diameter but different Au weight concentration; (b) GNP-loaded regions with same Au weight concentration but different diameter

MC data were acquired by a series of energy-sensitive tallies are shown in Fig.1. They were positioned 1mm behind lead collimator with a series of pinhole openings of diameter 0.6mm. In order to simulate the entire XFCT scanning procedure, an independent simulation was performed for each projection angle. The deterministic point detector tally (F5) and E card were used to simulate energy sensitive detectors (64 detectors and each detector with same sensitive area) and acquired x-ray fluorescent spectrum. The uncertainty in each simulation was less than 5% for relevant photon energies (50-75keV) using 10M histories.

C. Data acquisition and imaging reconstruction

The spectrum of photons arriving at the detectors mainly stem from both Compton scatter and characteristic x-ray fluorescence. Considering fluorescent field and the attenuation of low-energy photon in the phantom, the gold K_α lines (67.0 and 68.8keV) are the best candidates in our system setup. In order to extract the fluorescence peak height from the Compton background, a third degree polynomial was fit to the points on either side of the gold fluorescence peaks. The fluorescence signal counts at that detector for that projection angle was then given by the difference of the measured signal and the polynomial fit[9, 10]. A sinogram of the gold fluorescence signal counts was reconstructed using the extracted gold fluorescence signal intensity from each detector at each projection.

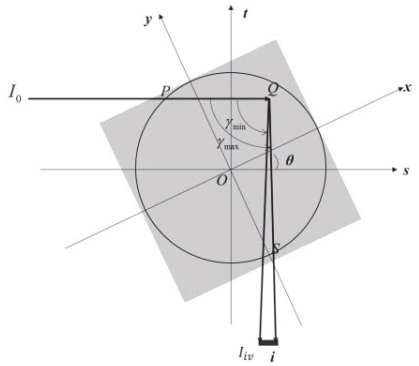

Fig.4. Schematic diagram of XFCT imaging geometry using sheet-beam

The physics and imaging model of sheet-beam XFCT were well known[7] and its geometry is presented in Fig.4. While the *xy*-coordinate system is attached to an object, the *st*-coordinate system is spun with the data acquisition system, and can be at any instant obtained by rotating the *xy*-coordinate system by an angle θ counterclockwise. That is, the relationship between the two coordinate systems can be expressed as follows:

$$\begin{pmatrix} s \\ t \end{pmatrix} = \begin{pmatrix} \cos\theta & \sin\theta \\ -\sin\theta & \cos\theta \end{pmatrix} \begin{pmatrix} x \\ y \end{pmatrix} \tag{1}$$

According to the results of previous research[7, 11-13], the total photons of fluorescent x-ray reaching the *i*th detector is represented as follows:

$$I_{iv}(\theta,s) = \int_{-\infty}^{+\infty} f(\alpha,s,t) \bullet g(\alpha,s,t) \bullet \Omega(s,t)\, d(x,y)dt \tag{2}$$

Where

$$f(\theta,s,t) = I_0 \exp[-\int_{-\infty}^{t} \mu^I(x,y)dt] \tag{3}$$

$$g(\theta,s,t) = \mu_{ph}\omega \int_{\gamma_{\min}}^{\gamma_{\max}} \exp[-\int_0^{\infty} \mu^F(x,y)db]d\gamma \tag{4}$$

ω and Ω are the yield of the fluorescent x-ray and the solid angle at which the point, Q, is viewed by the by the *i*th detector, respectively. μ_{ph} is the photoelectric linear attenuation coefficient of Au. The $d(x,y)$, $\mu^I(s,t)$, $\mu^F(s,t)$ are the distribution of Au weight concentration, linear attenuation coefficient of incident x-ray energy and linear coefficient of fluorescent x-ray. Here, in order to simplify reconstruction, the equation (4) can be expressed approximately as follows:

$$I_{iv}(\theta,s) \approx \mu_{ph}\omega I_0 \Omega \int_{-\infty}^{+\infty} d(x,y)dt \tag{5}$$

Thus, the measurement process by the XFCT based on sheet beam geometry can be viewed approximately as Radon transform. XFCT images (64×64) were reconstructed using FBP and MLEM respectively.

III. RESULT AND DISCUSSION

Reconstruction images are shown in fig.5. Images on the left column are obtained by FBP and the right column images obtained using MLEM. Obviously, grey values of GNP-loaded regions decrease with reduction of Au weight concentration shown in first row of Fig .5.

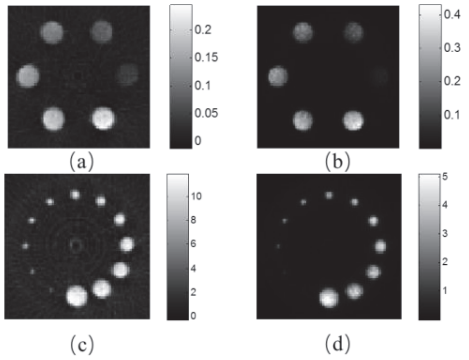

Fig.5. Reconstruction images by FBP and MLEM of phantoms with loaded-GNPs. (a) and (c) acquired using FBP. (b) and (d) acquired using MELM

The reconstructed XFCT images are evaluated as CNR by calculating the ratio of difference between the mean value of each GNP-loaded region and background (PMMA) and square root of sum of variance of GNP-loaded region and background. CNR is defined as follows[14]:

$$CNR = \frac{\bar{\Psi}_{Region} - \bar{\Psi}_{BK}}{\sqrt{\Phi^2_{ROI} + \Phi^2_{BK}}} \quad (6)$$

Where $\bar{\Psi}_{Region}$ and $\bar{\Psi}_{BK}$ are mean reconstructed values of GNP-loaded region and background, Φ^2_{ROI} and Φ^2_{BK} are corresponding variances of GNP-loaded region and background. The CNR of XFCT images are shown in Fig.6 and Fig.7. Both of bar charts show us that most values of CNR in our setup has lower than 4, which means that the setup needed be modified including length and diameter of collimators, spectrum of x-ray source, distance from x-ray source to the center of phantom, and so on[15]. Reconstruction algorithm may influence CNR as shown in Fig.6 and Fig.7. For each GNP-loaded region, different algorithm may result different CNR.

The reconstructed relative fluorescent counts (left phantom) calculated from the mean value of each GNP-loaded region as a function of true contrast concentration in Fig.8. The figure shows that relative fluorescent counts of GNP-loaded region is linear proportional to Au weight concentration.

In Fig.9, the reconstructed relative fluorescent counts (right phantom) calculated from the mean value of each GNP-loaded region as a function of their size. The reconstructed counts acquired by FBP are distributed near the linear fitting curve while the counts acquired by MLEM fluctuate largely, which may mean that MLEM algorithm is required to optimized to improve image quality. However, the reconstructed counts by both algorithms are stable when the size of GNP-loaded region is ranging from 4mm to 9mm. The phenomenon illustrates that size of GNP-loaded region can influence counts acquired when incident x-ray width is invariant.

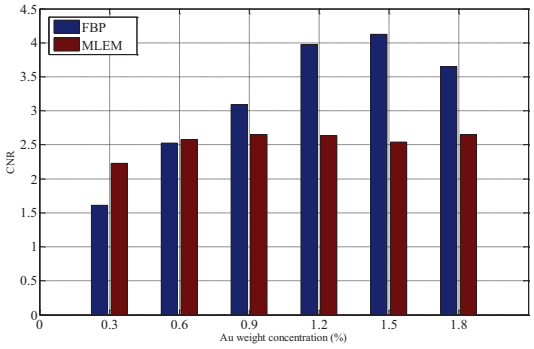

Fig.6. CNR for reconstructed XFCT image using FBP and MLEM as a function of Au weight concentration.

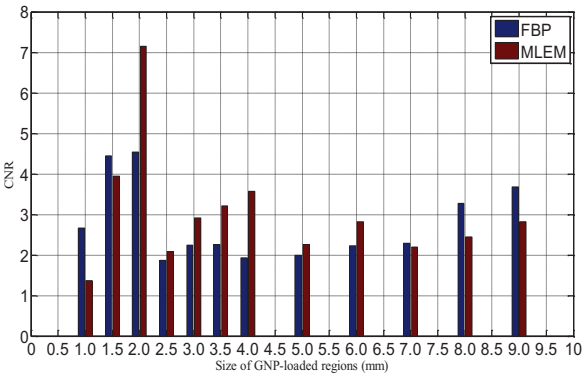

Fig.7. CNR for reconstructed XFCT image using FBP and MLEM as a function of GNP-loaded region size

The feasibility of a polychromatic sheet-beam XFCT device described in this MC study may not be fully established without a successful demonstration by an experimental study. However, the simulation results may provide valuable method for reducing overall scanning time, compared to the pencil-beam XFCT[9].

Although the current Monte Carlo results may provide an encouraging outlook for a drastic reduction of scanning time, improvement of detection limit and CNR will be a technical challenge in our design[9]. They may be improved further by additional modifications to the current setup such as quasi-monochromatization of incident x-ray spectrum, further optimization of detector collimation and further optimization of reconstruction algorithm. The loss of sensitivity in the detector collimator seems severe, but more sensitive detectors may be used to improve it.

IV. CONCLUSION

In this investigation, the feasibility of polychromatic sheet-beam XFCT setup was test by Monte Carlo method. Two phantoms contained several GNP-loaded regions were imaged using MCNP. Accurate images were reconstructed by FBP and

MLEM respectively. Relative fluorescent count of GNP-loaded region is linear proportional to Au weight concentration. Our results may provide necessary justification and impetus for future development of a benchtop XFCT for in vivo imaging.

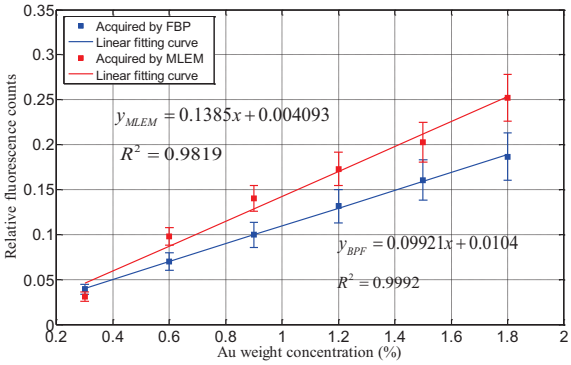

Fig.8. The reconstructed relative fluorescent counts using FBP and MELEM calculated from the mean value of each GNP-loaded region as a function of Au weight concentration

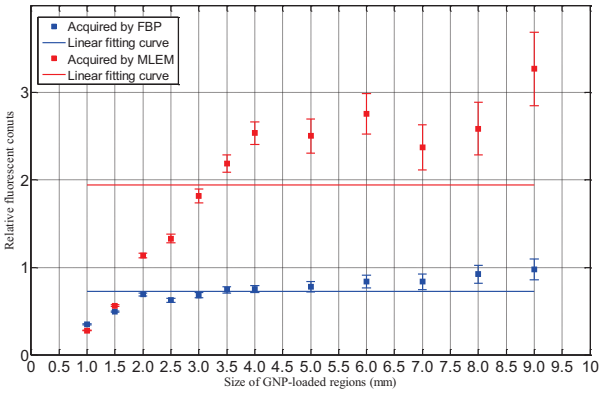

Fig.9. The reconstructed relative fluorescent counts using FBP and MELEM calculated from the mean value of each GNP-loaded region as a function of their size.

REFERENCES

[1] G. R. Pereira, R. T. Lopes, M. J. Anjos, H. S. Rocha, and C. A. Pérez, "X-ray fluorescence microtomography analyzing reference samples," *Nucl Instr Meth Phy Res,* vol. 579, pp. 322-325, 2007.

[2] D. H. Mcnear, P. Edward, E. Jeff, R. L. Chaney, S. Steve, N. Matt*, et al.*, "Application of quantitative fluorescence and absorption-edge computed microtomography to image metal compartmentalization in Alyssum murale," *Environ Sci Technol,* vol. 39, pp. 2210-2218, 2005.

[3] T. Takeda, Q. Yu, T. Yashiro, T. Zeniya, J. Wu, Y. Hasegawa*, et al.*, "Iodine imaging in thyroid by fluorescent X-ray CT with 0.05 mm spatial resolution," *Nucl Instr Meth Phy Res,* vol. 467–468, pp. 1318–1321, 2001.

[4] B. L. Jones, N. Manohar, F. Reynoso, A. Karellas, and S. H. Cho, "Experimental demonstration of benchtop x-ray fluorescence computed tomography (XFCT) of gold nanoparticle-loaded objects using lead- and tin-filtered polychromatic cone-beams," *Phys Med Biol,* vol. 57, pp. N457-67, Dec 7 2012.

[5] C. Yoon and W. Lee, "Fluorescence X-ray computed tomography (FXCT) using a position-sensitive CdTe detector," *J Korean Phys Soc,* vol. 64, pp. 122-128, 2014.

[6] H. M. Hertz, J. C. Larsson, U. Lundström, D. H. Larsson, and C. Vogt, "Laboratory x-ray fluorescence tomography for high-resolution nanoparticle bio-imaging," *Opt Lett,* vol. 39, pp. 2790-2793, 2014.

[7] S. Nakamura, Q. Huo, and T. Yuasa, "Reconstruction technique of fluorescent x-ray computed tomography using sheet beam," in *Signal Processing Conference (EUSIPCO), 2014 Proceedings of the 22nd European*, 2014, pp. 1975 - 1979.

[8] G. Poludniowski, G. Landry, F. DeBlois, P. M. Evans, and F. Verhaegen, "SpekCalc: a program to calculate photon spectra from tungsten anode x-ray tubes," *Phys Med Biol,* vol. 54, pp. N433-8, Oct 7 2009.

[9] B. L. Jones and S. H. Cho, "The feasibility of polychromatic cone-beam x-ray fluorescence computed tomography (XFCT) imaging of gold nanoparticle-loaded objects: a Monte Carlo study," *Phys Med Biol,* vol. 56, pp. 3719-30, Jun 21 2011.

[10] S. K. Cheong, B. L. Jones, A. K. Siddiqi, F. Liu, N. Manohar, and S. H. Cho, "X-ray fluorescence computed tomography (XFCT) imaging of gold nanoparticle-loaded objects using 110 kVp x-rays," *Phys Med Biol,* vol. 55, pp. 647-62, Feb 7 2010.

[11] Q. Yang, B. Deng, W. Lv, F. Shen, R. Chen, Y. Wang*, et al.*, "Fast and accurate X-ray fluorescence computed tomography imaging with the ordered-subsets expectation maximization algorithm," *J Synchrotron Radiat,* vol. 19, pp. 210-5, Mar 2012.

[12] P. J. Riviere, "Accelerating X-ray fluorescence computed tomography," *Conf Proc IEEE Eng Med Biol Soc,* vol. 2009, pp. 1000 - 1003, 2009.

[13] Q. Huo, H. Sato, T. Yuasa, T. Akatsuka, J. Wu, T.-T. Lwin*, et al.*, "First experimental result with fluorescent X-ray CT based on sheet-beam geometry," *X-Ray Spectrom,* vol. 38, pp. 439-445, 2009.

[14] P. Feng, W. Cong, B. Wei, and G. Wang, "Analytic Comparison between X-ray Fluorescence CT and K-edge CT," *Biomedical Engineering, IEEE Transactions on,* vol. 61, pp. 975-985, 2014.

[15] M. Bazalova, Y. Kuang, G. Pratx, and L. Xing, "Investigation of x-ray fluorescence computed tomography (XFCT) and K-edge imaging," *Medical Imaging, IEEE Transactions on,* vol. 31, pp. 1620-1627, 2012.

An Adaptive Reconstruction Algorithm for Spectral CT Regularized by a Reference Image

Miaoshi Wang[1,2], Yanbo Zhang[2], Rui Liu[2], Shuxu Guo[1], and Hengyong Yu[2,*]

[1]College of Electronic Science and Engineering, Jilin University, Changchun 130012, China
[2]Department of Electrical and Computer Engineering, University of Massachusetts, Lowell, MA 01854, USA
*Corresponding author, Email: hengyong-yu@ieee.org

***Abstract*—To reconstruct high quality spectral images from low-dose projections, an adaptive image reconstruction algorithm is proposed assuming a known reference image (RI). It is implemented by minimizing the patch-wise correlation between the object image and the RI. Extensive numerical simulations demonstrate the feasibility and merits of the proposed algorithm. It also performs well for truncated local projections, and the surrounding region of the region-of-interest can almost be accurately reconstructed. Furthermore, a method is introduced in the implementation for adaptive step length, making the algorithm more feasible and easier for applications.**

***Index Terms*—Spectral CT, image reconstruction, anti-noising, reference image, adaptive step length**

I. Introduction

Since Godfrey Hounsfield invented the first prototype in 1971, the x-ray computed tomography (CT) has been extensively employed in many fields. Among all the available nondestructive medical imaging modalities, x-ray CT possesses the highest spatial resolution and temporal resolution. However, there are also some drawbacks, such as low contrast resolution and beam hardening artifact [1], *etc*. To overcome the aforementioned drawbacks, the dual-energy (DE) CT was proposed [2-6]. Because most of the DECT also employ the energy-integrating detectors, there also exists a significant spectral overlap between two x-ray sources. This implies that the DECT hasn't fully exploited the spectrum information and there are lots of rooms for improvements.

To make full use of the spectrum information, the concept of spectral CT was proposed by extending the idea of DECT along the energy dimension. Till now, the state-of-the-art spectral CT system is based on a photon counting detector which can divide the whole x-ray spectrum into several channels [7]. The photon counting detector is characterized by high signal-noise-ratio (SNR) because the thresholds corresponding to each channel can block low-energy noise. Furthermore, it has been demonstrated that the spectral CT system has higher dose efficiency than the conventional one [8]. These merits make the spectral CT a hot field in recent years and inspire many research topics on different aspects of the spectral CT and its applications. Although the spectral CT techniques have made a big progress in recent years, there still exist many technical problems that need to be conquered. If we assume the same amount of total photons as that for a corresponding energy-integrating detector, the smaller amount of photons in each channel implies higher noise in the projections of each channel and the reconstructed image quality will be degraded. However, increased photon numbers will result in excessive radiation dose.

For practical clinical applications, the aforementioned weakness of spectral CT can be partially overcame by the interior reconstruction technique, because we are always interested in smaller internal regions-of-interests (ROIs) for diagnosis. This motivates us to develop a new spectral CT reconstruction algorithm to improve the image quality in each individual channel, and apply it for spectral interior reconstruction.

By comparing the reconstructed images from different channels for the same object, we notice some common features among them especially for the relative locations between different materials, that is, the reconstructed images from different channels are highly correlated. If a high quality image of the object is known, it can be used to serve as a RI to improve the low-dose reconstruction of each individual channel by incorporating the aforementioned correlation relationship. The steepest descent method (SDM) and adaptive step length (ASL) [9] are introduced to optimize the results. In this paper, we will also demonstrate that the proposed algorithm performs well for spectral CT, especially for the interior problem.

The rest of this paper is organized as follow. In Section II, the proposed algorithm and implementation details will be presented. In Section III, both numerical simulation and preclinical experiments will be performed to evaluate the proposed algorithm. Finally, some related issues will be discussed and conclusions will be made in Section IV.

II. Method

As aforementioned, although the reconstructed images from each channel are different in spectral CT, they are highly correlated. Thus, if a high quality image is available, it can be treated as the RI to help to reconstruct the relevant images in different channel from low-dose projections or truncated projections. Here, the RI can be reconstructed from a set of pre-existing normal dose projections. If there are no pre-existing projections, we can always combine all the photons in

different channels to synthesize a set of projections of energy-integrating detector and reconstruct a high-quality RI.

A. Imaging Model

Usually, one CT system is consist of three main components, which are image, projection and system matrix. A 2D digital image can be rearranged into a vector $\vec{f} = [f_1, \cdots, f_n, \cdots f_N]^T \in \mathbb{R}^N$, where N is the number of image pixels. The projection dataset can be presented as $\vec{g} = [g_1, \cdots, g_m, \cdots, g_M]^T \in \mathbb{R}^M$, where M represents the total amount of ray integration that equals to the product of the number of projections and the number of detector elements, and g_m denotes a measured line integration along the m^{th} x-ray path. In the projection procedure, the contribution of n^{th} pixel f_n to the m^{th} ray path can be denoted as $a_{m,n}$. As a result, we have a system matrix $A = (a_{m,n}) \in \mathbb{R}^M \times \mathbb{R}^N$, and the CT system can be modelled as the following linear matrix equation:

$$\vec{g} = A\vec{f} + \vec{e}, \tag{1}$$

where $\vec{e} \in \mathbb{R}^M$ is measured noise. To recover the original image vector $\vec{f}$, one can make full use of the system matrix A and the measured projection dataset $\vec{g}$ based on (1). Generally speaking, we can employ an iterative approach to solve this problem. In this work, one method called ordered-subset simultaneous algebraic reconstruction techniques (OS-SART) is selected [10].

B. Regularization Function

To solve the illposed problems uniquely, especially for spectral CT, an additional constraint $\Phi(\vec{f})$ should be introduced. For the spectral CT reconstruction problem, the reconstructed images from projections of different channels are highly correlated. For a given high-quality RI $\vec{u}$, we can define a regularization function for one target image (TI) $\vec{f}$ in any individual channel,

$$\widetilde{\Phi}(\vec{f}) = -\cos(\theta) = -\frac{\vec{f}^T\vec{u}}{\|\vec{f}\|\|\vec{u}\|}. \tag{2}$$

Because both TI and RI are treated as vectors in high-dimensional space, (2) can be interpreted as the minus cosine of the space angle (SA) θ between the two vectors. To improve the sensitivity, we further modify (2) as

$$\Phi(\vec{f}) = -\frac{(\vec{f}-\bar{f})^T(\vec{u}-\bar{u})}{\|\vec{f}-\bar{f}\|\|\vec{u}-\bar{u}\|}, \tag{3}$$

where $\bar{f}$ and $\bar{u}$ are the means of $\vec{f}$ and $\vec{u}$, respectively. Because the main common features hidden in different channels come from the alternating current components, (3) should be an excellent regularization function for the correlation.

C. Reconstruction Algorithm

To minimize the regularization term, we choose the SDM. During the inner iteration process, the updating of the TI can be described by

$$\vec{f}^{k,l+1} = \vec{f}^{k,l} + \alpha_{k,l}\vec{p}^{k,l}, \tag{4}$$

where l denotes the iteration index, k is a constant parameter indicating the outer loop number, $\alpha_{k,l}$ and $\vec{p}^{k,l}$ represent the step length and a normalized direction vector to update the estimated image in l^{th} iteration. The direction vector can be obtained by calculating the gradient of $\Phi(\vec{f})$.

In this work, the step length in (4) plays an important role to control the convergence of the inner iteration. To improve the computing efficiency, we propose to employ one adaptive step length method. For that purpose, the strong Wolfe conditions based method is chosen [9]. It is a typical inexact line search condition described as follow

$$\Phi(\vec{f}^{k,l} + \alpha_{k,l}\vec{p}^{k,l}) \le \Phi(\vec{f}^{k,l}) + c_1\alpha_{k,l}\nabla\Phi_{k,l}^T\vec{p}^{k,l}, \tag{5}$$

$$\left|\nabla\Phi(\vec{f}^{k,l} + \alpha_{k,l}\vec{p}^{k,l})^T\vec{p}^{k,l}\right| \le c_2\left|\nabla\Phi_{k,l}^T\vec{p}^{k,l}\right|, \tag{6}$$

where c_1 and c_2 are constants satisfying $0 < c_1 < c_2 < 1$, and $\nabla\Phi_{k,l}$ is short for $\nabla\Phi(\vec{f}^{k,l})$. To implement the strong Wolfe conditions, we first need to set an initial step length $\alpha_{k,0}$ for each inner iterating. Actually, this initial step length is always the same for all the outer iterations. The implementation step can be found in [9].

To keep the image details and suppress the effect of direct current component, a patch processing method is adopted. We first set the patch size (PS) as $D = d \times d$. A pair of patches would be treated as RI and TI and processed by the aforementioned strategy if they are extracted from the original RI and TI exactly at the same position. To distinguish different patches, a new index i is introduced to represent the i^{th} patch. One patch works like a window, which keeps moving in images. In practice, we can traverse the image pixel by pixel to extract patches. In this way, each tiny structure in the RI could be used to guide the update of the reconstructed image. After one patch has been corrected with a certain step length, the resulting patch is normalized to ensure the same module value as the original one, and the DC component is added

TABLE I
PSEUDO-CODES FOR THE PROPOSED ALGORITHM

Initialization
  Setting $\alpha_{k,i,1}, \alpha_{max}, c_1, c_2, l_{max}, D, k_{max}$;
  Initializing $\vec{f}^0$, $k = 0$;
  Obtaining an RI $\vec{u}$;
Reconstruction procedure (for any channel)
  while $k < k_{max}$
    $k++$;
    Updating $\vec{f}^k$ to $\vec{f}^k_{OS-SART}$ using the OS-SART method;
    Initializing the patch index i;
    Repeat (until patch window move over all the image)
      Subtracting the DC component to get $\tilde{f}^{k,i,0}_{OS-SART}$ and $\tilde{u}^i$;
      Determining the update direction $\vec{p}^{k,i}$ with $\tilde{f}^{k,i,0}_{OS-SART}$ and $\tilde{u}^i$;
      Determining the step length $\alpha_{k,i,*}$ using $\tilde{f}^{k,i,0}_{OS-SART}$, $\tilde{u}^i$ and $\vec{p}^{k,i}$ according to conditions (5) and (6);
      Updating i^{th} patch using equation (4);
      Normalizing the patch and adding back the DC component to get $\tilde{f}^{k,i,*}_{OS-SART}$;
      $i++$;
    end (Repeat)
    Averaging different values for the same pixel to get the image estimate $\vec{f}^{k+1}$;
    Accelerating the result by using FISTA;
  end (while)
Output: $\vec{f}^{k_{max}}$

back. Because the patches have overlaps, each pixel may have multiple values in different patches. For the same pixel, all the values are uniformly weighted to generate the mean as the final result of the regularization term. The aforementioned procedure is referred to as adaptive space angle (AdSA) method.

In this paper, a simple maximum iteration number k_{max} is selected as the stopping criterion. By combining the OS-SART based CT reconstruction and the AdSA based regularization, we obtain a new reconstruction algorithm as summarized in Table 1.

III. Results

The proposed algorithm is implemented according to the pseudo-codes summarized in Tables 1. To demonstrate the feasibility and evaluate the proposed algorithm for spectral CT, extensive numerical simulations are performed. In the numerical simulation studies, the classical filtered backprojection (FBP) is first used to reconstruct images from noise-free projections as benchmarks, which are compared

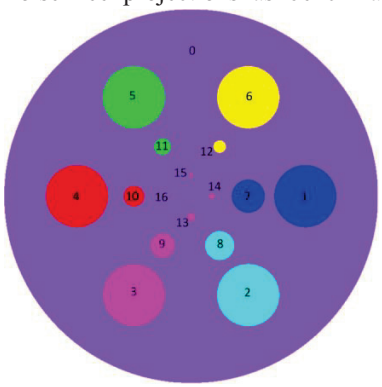

Fig. 1. Sketch map of the 2D phantom, in which different colors represent different materials.

TABLE II
Parameters for 17 disks of the 2D phantom

Obj.	Center(cm)	Radius (cm)	Material
0	(0.000,0.000)	0.9	Soft Tissue
1	(0.550,0.000)	0.15	12.4%Ca + 87.6%Water
2	(0.275,-0.4763)	0.15	6.2%Ca + 93.8%Water
3	(-0.275,-0.4763)	0.15	1.2%Iodine + 98.8%Water
4	(-0.550,0.000)	0.15	1.4%Barium + 98.6%Water
5	(-0.275,0.4763)	0.15	1.5%Gadolinium + 98.5%Water
6	(0.275,0.4763)	0.15	1.6%Gold + 98.4%Water
7	(0.275,0.000)	0.08	12.4%Ca + 87.6%Water
8	(0.1375,-0.23815)	0.07	6.2%Ca + 93.8%Water
9	(-0.1375,-0.23815)	0.06	1.2%Iodine + 98.8%Water
10	(-0.275,0.000)	0.05	1.4%Barium + 98.6%Water
11	(-0.1375,0.23815)	0.04	1.5%Gadolinium + 98.5%Water
12	(0.1375,0.23815)	0.03	1.6%Gold + 98.4%Water
13	(0.000,-0.100)	0.02	1.2%Iodine + 98.8%Water
14	(0.100,0.000)	0.015	1.2%Iodine + 98.8%Water
15	(0.000,0.100)	0.01	1.2%Iodine + 98.8%Water
16	(-0.100,0.000)	0.005	1.2%Iodine + 98.8%Water

with the results reconstructed by the proposed method for both global and truncated projections.

A 2D analytic phantom (see Fig.1.) containing 17 disks is constructed, whose parameters are listed in Table 2. To analytically generate projections of the 2D numerical phantom, we assume fan-beam geometry with an equidistant detector, and the detector element size is 0.08 mm. 512 and 256 detector elements are assumed to simulate a long and a short detector to collect global and truncated projections, respectively. The distance between the x-ray source focal spot and the origin (the center of the phantom) is assumed to be 5cm. We also assume that the detector is perpendicularly to and symmetric with the line passing the origin and the x-ray focal spot, and the distance between the focal spot and the detector is 10cm. 720 projections are uniformly acquired over a range of full scan. To simulate a polychromatic x-ray source, an x-ray tube produced by GE is selected. According to the attenuation curves of different materials, four k-edges among the material attenuation coefficients around 33, 37.4, 50.2 and 80.7KeV for Iodine, Barium, Gadolinium and Gold can be found, respectively. To optimize the channels for the best image quality, it is better to make the total photons in each channel as equal as possible and the difference between different channels as great as possible. According to the aforementioned principles, eight spectral channels are set: 25~32KeV, 32~37KeV, 37~43KeV, 43~50KeV, 50~58KeV, 58~65KeV, 65~80KeV, 80~120KeV. After the projections at all energy levels are collected, exponential, weighted summation and logarithmic operations are performed to produce linearized projections for the polychromatic x-ray spectrum. To further evaluate the performance of the proposed algorithm, different photon numbers are assumed. Here we mainly use 2×10^4 and 10^5 incident photons to simulate two different dose levels.

A. Global Reconstruction

Because there are few features in the phantom, the reconstructed images are set as 256×256 matrix to cover a 2.0×2.0 cm^2 region which is sufficient to cover the biggest

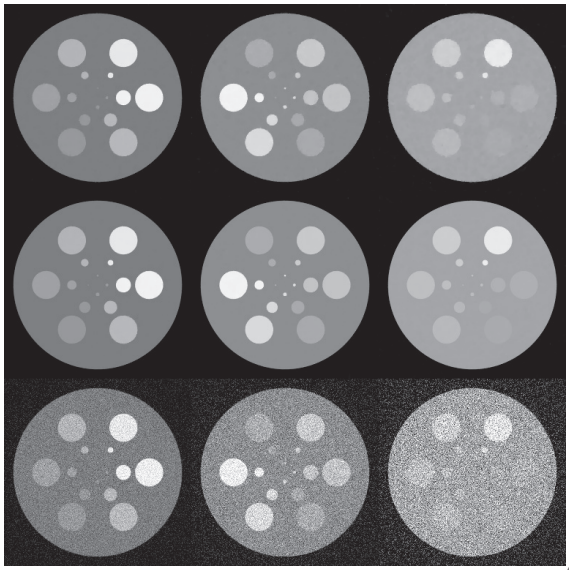

Fig. 2. Spectral reconstruction results from projections with 10^5 incident photons. From top to bottom rows, the images are reconstructed by the StTV, AdSAand FBP, respectively. From left to right columns, the images are respectively for the 1st, 4th and 8th channels, and the display windows are respectively [0 1], [0 0.5] and [0 0.3] cm^{-1}.

disk of the phantom. The AdSA method is terminated after 100 iterations. The coefficients c_1 and c_2 are respectively set as 0.0001 and 0.01, and the PS is set as 8×8. In this work, the filtered FBP method is adopted to reconstruct an image from the noise-free projections as the RI. For comparison, a soft-threshold filtering based TV (StTV) minimization [11] method is also implemented, which is stopped after 200 iterations.

Figure 2 shows the reconstructed images of representative channels. It can be seen that the FBP images have heavy noise. While the major information is retained in the low photon energy channel (1st channel), only some outlines could be recognized in the high energy (8th channel). With the increase of the photon energy, the StTV images also become seriously blurred. However, the AdSA reconstructs almost all the details, and even the smallest spot in the images can be recognized.

B. Interior Reconstruction

In interior reconstruction experiments, only the central 256 detector elements are used to collect projections. The reconstructed image size and the corresponding region are the same as the global reconstruction. For the AdSA, the main loop is terminated after 200 iterations and the RIs are the corresponding global images reconstructed by the StTV method. The StTV is also implemented with compact support information and it is terminated after 300 iterations. The rest of other parameters concerning with the AdSA and StTV are the same as the previous subsection for global reconstruction.

TABLE III
QUANTITATIVE EVALUATION RESULTS OF INTERIOR RECONSTRUCTION IN TERM OF RMSE (UNIT: CM^{-1})

	Noise-free		10^5 photons		2×10^4 photons	
Channel	**StTV**	**AdSA**	**StTV**	**AdSA**	**StTV**	**AdSA**
1st	0.007	0.006	0.015	0.007	0.026	0.011
2nd	0.005	0.004	0.014	0.005	0.023	0.008
3rd	0.005	0.003	0.012	0.005	0.021	0.007
4th	0.003	0.002	0.011	0.003	0.019	0.005
5th	0.003	0.002	0.010	0.003	0.017	0.004
6th	0.002	0.001	0.009	0.002	0.016	0.003
7th	0.001	0.001	0.009	0.001	0.015	0.002
8th	0.001	0.001	0.009	0.001	0.015	0.002

The RMSE (see Table 3) and SSIM (see Table 4) are used to quantitatively evaluate the AdSA and StTV for interior reconstruction. Because only the ROI can be theoretically exact reconstructed from truncated projections, we calculate the indices only using the pixels inside the ROI. From Table 3, one can see that the AdSA outperforms the StTV, especially for the heavy noise condition. This is because although a compact support can be given, the strong noise makes an obvious attenuation coefficients shift that the StTV cannot suppress. The SSIM values in Table 4 further verify that the AdSA performs well for interior problem. When the photon energy increases, the corresponding SSIM values increase to close 1. Furthermore, the SSIM indices for the AdSA are not sensitive to noise. On the other hand, the performance of the StTV is worse and worse, no matter when the photon energy is increased or the incident photon number is reduced.

TABLE IV
QUANTITATIVE EVALUATION RESULTS OF INTERIOR RECONSTRUCTION IN TERM OF SSIM

	Noise-free		10^5 photons		2×10^4 photons	
Channel	**StTV**	**AdSA**	**StTV**	**AdSA**	**StTV**	**AdSA**
1st	0.997	0.997	0.989	0.996	0.973	0.989
2nd	0.996	0.997	0.985	0.995	0.960	0.985
3rd	0.997	0.997	0.988	0.995	0.962	0.985
4th	0.997	0.998	0.985	0.996	0.941	0.987
5th	0.998	0.998	0.984	0.996	0.942	0.989
6th	0.998	0.998	0.981	0.997	0.930	0.990
7th	0.998	0.999	0.972	0.997	0.914	0.991
8th	0.999	0.999	0.964	0.997	0.893	0.992

IV. DISCUSSION AND CONCLUSION

In conclusion, an algorithm is proposed for spectral image reconstruction by incorporating the information of a RI. Both the extensive numerical simulations demonstrate that the proposed algorithm has a strong capability for anti-noising. It is also robust and stable for interior reconstruction. This can help to advance the spectral CT to improve the accuracy of material decomposition from low-dose projections. Furthermore, the strategy to adjust the SL makes the proposed algorithm more competitive.

REFERENCES

[1] R. A. Brooks and G. Di Chiro, "Beam hardening in x-ray reconstructive tomography," *Physics in medicine and biology,* vol. 21, p. 390, 1976.

[2] R. E. Alvarez and A. Macovski, "Energy-selective reconstructions in x-ray computerised tomography," *Physics in medicine and biology,* vol. 21, p. 733, 1976.

[3] A. Macovski, R. Alvarez, J.-H. Chan, J. Stonestrom, and L. Zatz, "Energy dependent reconstruction in X-ray computerized tomography," *Computers in biology and medicine,* vol. 6, pp. 325-336, 1976.

[4] R. E. Alvarez and A. Macovski, "X-ray spectral decomposition imaging system," ed: Google Patents, 1977.

[5] W. H. Marshall Jr, R. E. Alvarez, and A. Macovski, "Initial results with prereconstruction dual-energy computed tomography (PREDECT)," *Radiology,* vol. 140, pp. 421-430, 1981.

[6] J. P. Stonestrom, R. E. Alvarez, and A. Macovski, "A framework for spectral artifact corrections in X-ray CT," *IEEE Transactions on Biomedical Engineering,* vol. 2, pp. 128-141, 1981.

[7] J. Jakůbek, "Semiconductor pixel detectors and their applications in life sciences," *Journal of Instrumentation,* vol. 4, p. P03013, 2009.

[8] M. J. Tapiovaara and R. Wagner, "SNR and DQE analysis of broad spectrum x-ray imaging," *Physics in Medicine and Biology,* vol. 30, p. 519, 1985.

[9] S. J. Wright and J. Nocedal, *Numerical optimization* vol. 2: Springer New York, 1999.

[10] G. Wang and M. Jiang, "Ordered-subset simultaneous algebraic reconstruction techniques (OS-SART)," *Journal of X-ray Science and Technology,* vol. 12, pp. 169-178, 2004.

[11] H. Yu and G. Wang, "A soft-threshold filtering approach for reconstruction from a limited number of projections," *Physics in medicine and biology,* vol. 55, p. 3905, 2010.

Metal artifact reduction algorithm based on the data-adapted moving least squares using minimum estimated sinogram

Haewon Nam
Yonsei Institute of Convergence Technology
Yonsei University
Incheon, Republic of Korea 406-804
Email: haewonn@yonsei.ac.kr

Jongduk Baek
School of Integrated Technology,
Yonsei Institute of Convergence Technology
Yonsei University
Incheon, Republic of Korea 406-804
Email: jongdukbaek@yonsei.ac.kr

***Abstract*—We propose a novel metal artifact reduction algorithm that completes corrupted data of the metal trace, which generates a severe deteriorated image. When metal implants are located inside of the field of view, metal traced sinogram is corrupted due to high attenuation of the metal. In this work, we propose a novel metal artifact reduction algorithm which completes corrupted data by metal implants. The proposed algorithm utilizes the idea of sinogram decomposition, where we consider sinogram curves corresponding to image points near metal implants. We introduce to estimate the metal traced sinogram based on the minimum value along the sinogram curve. It ensures efficient reduction of metal artifacts at high image quality with enhanced preservation of details close to metal implants. The proposed algorithm is based on the sinogram completion algorithm by using minimum estimated sinogram as a structure of the whole sinogram. We propose to estimate the corrupted data by minimum estimation. Both 2D numerical and 3D experimental phantoms are simulated to show the superiority of the proposed algorithm. Both quantitative and visual evaluations are presented.**

I. Introduction

Metal artifact is one of the most common problems in computed tomography. Various metal implants are inserted in the human body such as dental filling, orthopedic implants, hip prostheses, implanted marker bins, and branchy-therapy seeds. High attenuation of metal generates dark and bright streaks which degrades CT image quality and mislead to inaccurate diagnosis. Most of the clinical CT scanners use the filtered backprojection with monochromatic X-ray assumption. The streaking artifacts appear along tangent lines of the boundary of metallic objects [1]. Over several decades, metal artifact reduction (MAR) algorithms have been developed but none of them has been treated as a gold standard. The metal artifact reduction algorithms can be classified into two groups: the projection completion methods and the statistically iterative methods. The former case is intuitive such that the projections through a metal region are treated as missing data. The incomplete data are filled using the neighboring measured data. Linear [2], higher order [3], [4], [5], or wavelet [6] interpolation methods were used. But simple interpolation may generate new artifacts. To overcome, projection completion with filtering technique [7], [8], [9] has been proposed. The second categorized algorithms attempt to reduce the mismatch via iterative reconstruction algorithm, dealing with the image domain to reduce the artifact in the iterative reconstruction algorithm [10], [11], [12], [13]. Excluding metal trace in the sinogram, iterative algorithms reconstruct image with incomplete projections using model based regularization term. Compared to the first categorized algorithms, the iterative technique utilizes prior knowledge of the image to solve an ill-posed problem. Besides expensive computational cost, the second categorized algorithms are sensitive to the system configurations, parameters, and noise. In addition, wrong prior information or any problem of parameter setting may not guarantee the good performance of the algorithm.

Recently, majority of the first categorized algorithms complete the metal trace using forward projection of a prior image [14], [15], [16], [17], [18], [19], [20], [21]. Generally, a prior image is obtained by a simple thresholded CT image. It is very obvious that better prior image will generate the better performance. On the other hand, wrong prior will generate the worse performance with a new artifact. Comparing with the second categorized algorithms, metal artifact reduction algorithm with a prior image is computationally simple. Moreover, pixel values do not vary substantially within materials, facilitating segmentation in these kinds of images.

The proposed metal artifact reduction algorithm is designed to satisfy 1)stability, 2)robustness, and 3) can be applied to the sinogram before reconstruction. It can be used with any reconstruction method, and thus, does not depend on the reconstruction algorithm. Inspired by the sinogram decomposition algorithm [22], [23], the proposed MAR algorithm combines a priori information for projection completion without a prior image. Zamyatin and Nakanishi [22] proposed a truncation correction algorithm using minimum value along the sinogram curve. Corresponding to a single voxel in the image space, a sinogram curve is a function of radon transform with the variable of rotation angle. Similar to the work in [22], we estimated unmeasured data using the information of minimum

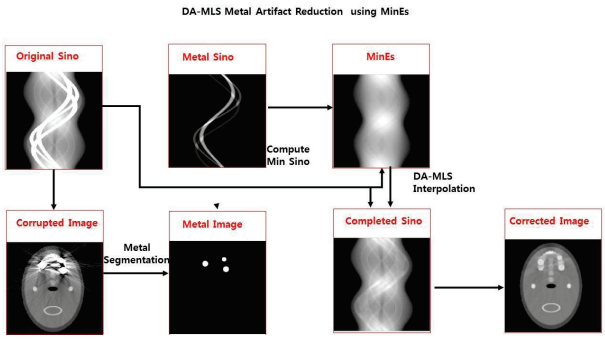

Fig. 1. Flowchart of the proposed algorithm: The original raw data are obtained. Metal segmentation is done by thresholding the corrupted image and forward projected metal sinogram is computed. By using the original sino with metal sinogram, compute the min sinogram. DA-MLS interpolation is done based on the shape information of MinEs.

estimate. In the proposed algorithm, we estimate the metal corrupted sinogram by taking the minimum of the uncorrupted data over the sinusoidal curve. Unlike to the work of [22], [23], we only use the structural shape of minimum estimated sinogram. The proposed algorithm approximate the missing data using data-adapted moving least squares [24].

II. Methods

The main idea of our approach is to complete sinogram without creating prior image. It is not always possible to create good prior with metal implants. If the image is a piecewise constant phantom, good prior can be made by simple thresholding. Unfortunately, human body is more complicated than the piecewise constant phantom data. Furthermore, bad prior may generate unwanted artifact. To avoid error from wrong prior, we use Minimum Estimate Sinogram (MinES) based on the original sinogram of the uncorrupted part.

A. Minimum Estimated Sinogram (MinES)

The original sinogram is decomposed to estimate the metal corrupted part of the sinogram. To approximate the corrupted sinogram on the metal part, we adapt the minimum value estimate motivated by [22], [23]. Let $x \in X$ be a point in FOV and X be the subset of the FOV which has nonzero CT number. The function γ be the radon transform over the ray defined by a fan angle θ and a view angle ϕ. Define a single curve $s(x)$ as a set of the projection $\gamma(\theta,\phi)$ corresponding to an image point x. The original sinogram is the summation of the $s(x)$ for all $x \in X$. If the x is in the metal, the whole sinusoidal curve $s(x)$ is corrupted. If the x is in non-metal part but the curve $s(x)$ intersects with the metal trace, some portion of the curve $s(x)$ is corrupted. This corrupted portion needs to be completed. To estimate the corrupted portion, we take the minimum value of the $s(x)$ in the un-corrupted part as

$$\gamma_{\min}(\theta,\phi) = \min_{(\tilde{\theta},\tilde{\phi})\in s(x)} \gamma(\tilde{\theta},\tilde{\phi})$$

To obtain $\gamma_{\min}(\theta,\phi)$, we search the minimum value in the $s(x)$. The advantage of this approach is that it doesn't need to find the proper prior image, and only computed with uncorrupted part of the sinogram and the system geometry. Since the obtained minimum estimate $\gamma_{\min}(\theta,\phi)$ is measured by the line integral along the line of least attenuation, the minimin estimated sinogram needs to be normalized by the ray path and integrate over all rays.

B. Data-adaptive moving least squares (DA-MLS) approximation using MinES

Moving least squares (MLS) is one of the most efficient methods of data approximation algorithms. DA-MLS [24] adaptively gathers the neighboring points to estimate unknown data. Using the structural shape by the gradient of the image, we compute data adapted penalty function and estimate the corrupted data. The data-adapted penalty function is given by

$$\theta(x,x_i) := \exp((x-x_i)^T \mathbf{H}(x-x_i)) - 1,$$

where $\mathbf{H}$ is a 3×3 matrix so that $x^T\mathbf{H}x = 1$ is an ellipsoid defined by

$$\frac{\langle x,v_3\rangle^2}{a^2} + \frac{\langle x,v_2\rangle^2}{b^2} + \frac{\langle x,v_1\rangle^2}{c^2} = 1,$$

where the vector v_1 indicates the gradient direction of the image, and forms the minor axis of the ellipsoid. The vectors v_2 and v_3 indicate the median and the major axes of the ellipsoid, respectively. If $a = b = c = 1$ and the vectors $v_1 = (0,0,1)^T$, $v_2 = (0,1,0)^T$, and $v_3 = (1,0,0)^T$, then DA-MLS is identical to the classical MLS method. The size of the ellipsoid depends on the local data feature. Since our application is to the sinogram data, we fixed $a = 2$, $b = 0.5$, and $c = 0.5$, which produce elongated shape along the main direction, which the data is relatively homogeneous.

The classical DA-MLS approximation algorithm estimates the gradient of the image data and uses to estimate the shape structure. Since the sinogram is a complicated image, it is hard to estimate the shape structure by moving least squares estimation. Moreover, metal trace is in the form of thick curved band with width related to the size of the metal. Simple approximation may mislead to generate a new artifact due to the lack of the neighboring data in the middle of the metal trace. Instead, we used MinES in subsection II-A and its gradient. With using the sinogram shape in the metal trace part in MinES, we use DA-MLS to approximate missing data with neighboring data.

Flow chart of the whole process is illustrated in the figure 1. The brief steps are described as below.

1) For a given original sinogram p, a metal artifact image is reconstructed.
2) Metal image is segmented by simple thresholding and the metal sinogram is computed by forward projection.

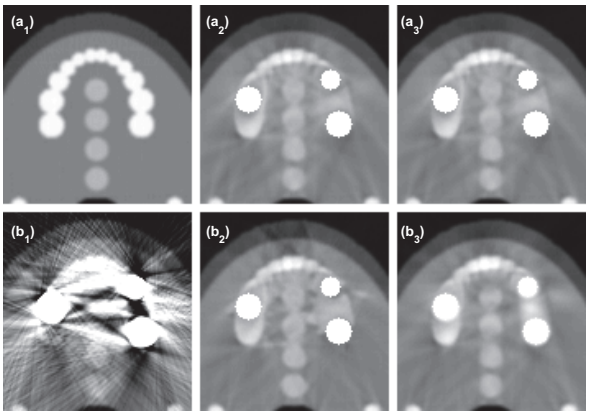

Fig. 2. Result of the MAR algorithms of the 2D tooth phantom. First column: (a_1) Original image, and (b_1) Metal artifacted image. Other four images are metal artifact corrected by (a_2): LIN, (a_3) CUB, (b_2) NMAR, and (b_3) DA-MLS

3) Minimum estimated sinogram $p^{\min}$ is computed by taking minimum over the sinusoidal curve of the un-corrupted sinogram.

4) DA-MLS approximation is done on the metal corrupted part of the sinogram. Gradient of the MinES is used for the gradient of the sinogram.

5) Reconstruct corrected image by FBP.

III. Experiments and Results

To evaluate the performance of the proposed algorithm, the numerical simulations were performed with a fan beam CT geometry with a monochromatic spectrum using two dimensional CT phantom images; abdomen, and tooth images. FBP algorithm is used for all image reconstruction. We compared the proposed algorithm DA-MLS with linear interpolation (LIN), cubic polynomial interpolation (CUB), and classical normalized metal artifact reduction (NMAR).

A. Numerical Phantom Simulation

Two numerical simulations were done using 2D CT phantom images; abdomen and tooth phantom. In our numerical simulations, tooth phantom have 256×256 pixels with size $1.9mm^2$, and abdomen has 300×300 with $1.67mm^2$. We computed 360 forward projections. Figure 2 show the result of 4 different MAR algorithms of the 2d numerical tooth phantom. In the first column, (a_1) original image without metal, (b_1) FBP reconstruction result with the presence of metals. The images (a_2) and (a_3) are those corrected by LIN and CUB, (b_2) and (b_3) are those corrected by NMAR and DA-MLS, respectively. The corresponding corrected sinograms are shown in figure 3. The proposed algorithm outperforms other algorithms in both imaging space and the sinogram space. Corrected sinogram by NMAR seems similar to the result of the proposed algorithm. But unexpected trace is presented, which generate artifact

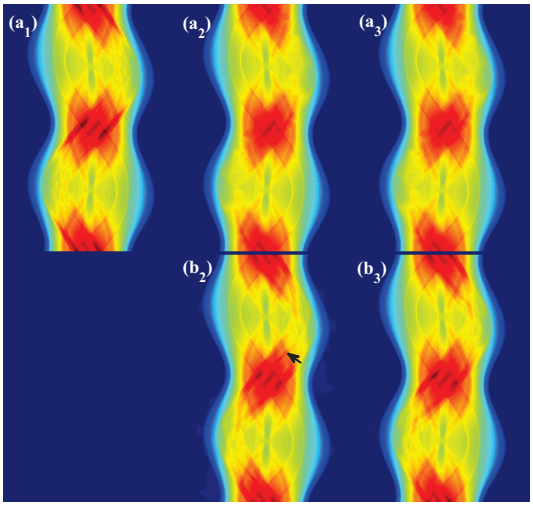

Fig. 3. Result of the MAR algorithms of the 2D tooth sinogram related to figure 2. First column: (a_1) Original sinogram. Other four sinograms are metal artifact corrected by (a_2): LIN, (a_3) CUB, (b_2) NMAR, and (b_3) DA-MLS

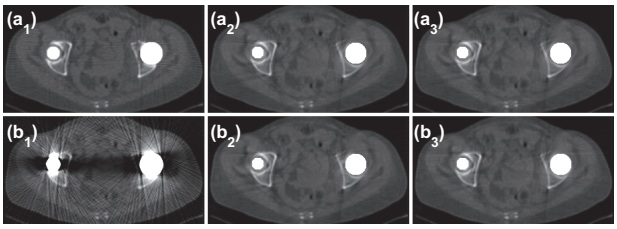

Fig. 4. Result of the MAR algorithms of the 2D abdomen image. First column: (a_1) Original image, and (b_1) Metal artifacted image. Other four images are metal artifact corrected by (a_2): LIN, (a_3) CUB, (b_2) NMAR, and (b_3) DA-MLS

in the image. Abdomen phantom (figure 4) has the similar result. As shown in the figure 4, in the presence of two metals. All other results except the proposed algorithm has a streak after MAR applied. For the quantitative evaluation, we computed mean squared errors for 2D numerical phantoms in both image and sinogram spaces. Error is computed on the non-metal image for the imaging space. Let X_0 be the FBP reconstruction without metal, which is the ground truth, and p_0 be the sinogram without metal implants. Mean square error is computed as

$$E_{Img} = \|X_0 - X\|, \; E_{Sino} = \|p_0 - p\|.$$

Table I shows the result of the mean squared errors. The proposed algorithm achieves the lowest error among other algorithms in both image and sinogram spaces.

IV. Conclusions and Discussion

We introduced a new metal artifact reduction (MAR) algorithm using minimium estimated sinogram and data-adapted MLS interpolation and successfully applied to 2D phantoms. The proposed algorithm combines DA-MLS interpolation with

		LIN	CUB	NMAR	DA-MLS using MinES
Tooth	E_{Img}	5.0224	4.906	4.7724	3.3630
	E_{Sino}	51.8489	51.5621	51.4093	28.9054
Abdomen	E_{Img}	4.6052	4.6200	4.6038	3.5545
	E_{Sino}	117.9404	117.4622	117.0720	116.5964

TABLE I
MEAN SQUARED ERROR OF NUMERICAL PHANTOMS. BOTH IMAGE AND SINOGRAM MEAN SQUARES ERRORS ARE COMPUTED.

minimum estimated sinogram (MinES). To overcome the limitation of the simple interpolation strategy, we estimated the shape of the sinogram in the corrupted part by MinES. A quantitative evaluation was performed using two experimental examples of 2D phantoms. For metal-free images as ground truth were compared to images corrected with MAR methods. By computing the normalized mean square error on the non-metal area, we showed the DA-MLS outperformed other MAR algorithms. We compared mean squared errors both on the image and sinogram space. On both spaces, the proposed algorithm outperformed other MAR methods. In conclusion, we showed that MinES can be used as a sinogram structure for the corrupted part of the sinogram, that is, it allows to obtain accurate outline of the sinogram.

ACKNOWLEDGMENTS

This work was supported by the MSIP (Ministry of Science, ICT and Future Planning), Korea, under the IT Consilience Creative Program (IITP-2015-R0346-15-1008) supervised by the IITP (Institute for Information & Communications Technology Promotion).

REFERENCES

[1] H. S. Park, J. K. Choi, and J. K. Seo, "Characterization of metal artifacts in X-ray computed tomography," Technical Report, Yonsei University (2014).

[2] W. A. Kalender, R. Hebel, and J. Ebersberger, "Reduction of CT artifacts cuased by metalic implants," Radiology, **164**, 576–577 (1987).

[3] G. H. Glover and N. J. Pelc, "An algorithm for the reduction of metal clip artifacts in CT reconstructions," Med. Phys., **8**(6), 799-807 (1981).

[4] A. H. Mahnken et al., "A new algorithm for metal artifact reduction in computed tomography: In vitro and in vivo evaluation after total hip replacement," Invest. Radiol., **38**(12), 769-775 (2003).

[5] M. Yazdia, L. Gingras, and L. Beaulieu, "An adaptive approach to metal artifact reduction in helical computed tomography for radiation therapy treatment planning: Experimental and clinical studies," Int. J. Radiation Oncol. Biol. Phys., **62**(4), 1224-1231 (2005).

[6] S. Y. Zhao, D. D. Roberston, G. Wang, B. Whiting and K.T. Bae, 2000 X-ray CT metal artifact reduction using wavelets: arm application for imaging total hip prostheses IEEE Trans. Med. Imag. 19 123847

[7] O. Watzke and W. A. Kalender, "A pragmatic approach to metal artifact eduction in CT: Merging of metal artifact reduced images," Eur. Radiol., **14**, 849-856 (2004).

[8] J. Wei et al., "X-ray CT high-density artefact suppression in the presence of bones," Phys. Med. Biol., **49**, 5407-5418, (2004).

[9] M. Bal and L. Spies, "Metal artifact reduction in CT using tissue-class modeling and adaptive prefiltering," Med. Phys., **33**(8), 2852-2859 (2006).

[10] G. Wang et al., Iterative deblurring for CT metal artifact reduction, *IEEE Trans. Med. Imaging 15*, 657664 (1996).

[11] D. D. Robertson et al., Total hip prosthesis metal-artifact suppression using iterative deblurring reconstruction, *J. Comput. Assist. Tomogr. 21*, 293298 (1997).

[12] J. Nuyts, B. De Man, and P. Dupont, Iterative reconstruction for helical CT: A simulation study, *Phys. Med. Biol. 43*, 729737 (1998).

[13] X. Zhang, J. Wang, and L. Xing,"Metal artifact reduction in x-ray computed tomography (CT) by constrained optimization," Med. Phys. **38**, 701–711 (2011).

[14] W. J. H. Veldkamp, R. M. S. Joemai, A. J. van der Molen, and J. Geleijns, "Development and validation of segmentation and interpolation techniques in sinograms for metal artifact suppression in CT, " Med. Phys., **37**(2), 620–628 (2010)

[15] A. H. Mahnken et al., "A new algorithm for metal artifact reduction in computed tomographyIn vitro and in vivo evaluation after total hip replacement," Invest. Radiol. **38**, 769-775 (2003).

[16] M. Yazdia, L. Gingras, and L. Beaulieu, "An adaptive approach to metal artifact reduction in helical computed tomography for radiation therapy treatment planning: Experimental and clinical studies," Int. J. Radiat. Oncol., Biol., Phys. **62**, 1224-1231 (2005).

[17] H. Y. Yu et al., "A segmentation-based method for metal artifact reduction," Acad. Radiol. **14**, 495-504 (2007).

[18] Y. Zhang et al., "Reducing metal artifacts in cone-beam CT by tracking and eliminating metal shadows in raw projection data," Med. Phys. **33**, 2288–2288 (2006).

[19] Y. B. Zhang et al., "Reducing metal artifacts in cone-beam CT images by preprocessing projection data," Int. J. Radiat. Oncol., Biol., Phys. **67**, 924-932 (2007).

[20] E. Meyer, R. Raupach, M. Lell, B. Schmidt, M. Kachelrieβ, "Normalized metal artifact reduction (NMAR) in computed tomography", Med. Phys. **37**, 5482–5493 (2010).

[21] E. Meyer, R. Raupach, M. Lell, B. Schmidt, M. Kachelrieβ, "Frequency split metal artifact reduction (FSMAR) in computed tomography", Med. Phys. **39**, 1904–1916 (2012).

[22] A. A. Zamyatin and S. Nakanishi "Extension of the reconstruction field of view and truncation correction using sinogram decomposition," *Med. Phys., vol. 34, 2007* pp. 1593-1604.

[23] R. N. Chityala, K. R. Hoffmann, S. Rudin, and D. R. Bednarek, "Artifact reduction in truncated CT using sinogram completion," *Proc. SPIE, vol. 5747, 2005* pp. 2110-2117.

[24] H. Nam, Y. Lee, B. Jeong, H. Park and J. Yoon "Motion correction of magnetic resonance imaging data by using adaptive moving least squares method" *Magnetic Resonance Imaging, in press, 2015*

Ultra-fast cone-beam SIR on 2k-cubed data

Andreas Fehringer, Korbinian Mechlem, Michael Epple,
Sebastian Allner, Lorenz Hehn, Franz Pfeiffer, and Peter B. Noël

***Abstract*—We demonstrate an integral concept to make statistical iterative reconstruction (SIR) feasible for large datasets. The maximum volume size investigated is 2048 (2k) cubed with corresponding projection data to fulfill the Nyquist criterion. We investigate how to exploit a heterogeneous computing system consisting of multiple GPUs and CPUs to perform the task within a fraction of the total data acquisition time of a micro CT. We employ and extend several data splitting techniques that enable GPU-accelerated forward- and backprojections for large cone-beam datasets. Furthermore, we split the data and regularization term of the SIR cost function in a way to make state-of-the-art solvers, in our case the OS-mom, perfectly suited for heterogeneous computing. In a test study, SIR was used to recover the details of a 2k-cubed micro-CT dataset for a reduced exposure time of one sixth. The total reconstruction time for that study could be pushed down to two hours involving 32 subiterations in total.**

I. Introduction

X-ray micro CT is a powerful tool in non-destructive testing. It can deliver detailed information about the interior of a sample without the need for disassembling or destroying it. Hence it is used on a daily basis for many industrial applications. The downside of the high-quality measurements are however very long acquisition times. One single CT scan can take up to several days.

Statistical iterative reconstruction (SIR) is capable of modeling physical properties and noise statistics for solving tomographic problems. [1] Its vast image improvements especially for drastically reduced x-ray dose make it more and more common in medical CT. [2] Likewise it could be a great asset for micro CT in order to reduce the acquisition time.

For medial applications, the high computational effort of SIR can be compensated with parallel high-performance computing. Suitable hardware found its way into compact and affordable computing systems in form of GPU devices. [3], [4] However, when it comes to high-resolution x-ray CT, the limited memory and bandwidth of these devices is soon stretched to the limit.

We demonstrate a heterogeneous multi-GPU and -CPU framework for SIR including a very fast forward- (FP) and backprojection (BP) implementation capable of handling large amounts of data in decent time. We show furthermore how to efficiently use one of the currently fastest specialized solver for tomographic problems, the OS-mom, within a heterogeneous computing environment.

A. Fehringer, K. Mechlem, M. Epple, S. Allner, L. Hehn and F. Pfeiffer are with the Chair of Biomedical Physics, Technische Universität München, Munich, Germany.

P. B. Noël is with the Department of Radiology, Technische Universität München, Munich, Germany.

Table I
Data sizes of the different components in the cost function for a 2k-cubed dataset.

variable	dimensions	size
$\boldsymbol{x}$: reconstruction guess	2048^3	32 GB
$\boldsymbol{p}$: measurement (same for the weights $\boldsymbol{w}$)	3217×2048^2	50 GB
A: system matrix	$[\boldsymbol{x}] \times [\boldsymbol{p}]$	402 EB

All sizes are computed for values in single floating-point precision.

II. Methods

SIR is based on a cost function including a statistical model for the measured data and a regularization term pushing the result into a realistic noise realization. Within this work, a Gaussian noise model was assumed. It holds well for the photon statistics in our kind of measurements and is furthermore easy to compute. Our regularization is the Huber penalty [5]. It favors a smooth solution with sharp edges by evaluating the difference of each voxel to each of its 26 neighbors in the 3D environment. The problem can be stated minimizing the cost function

$$L = \boldsymbol{w}\left[A\boldsymbol{x} - \boldsymbol{p}\right]^2 + \lambda \mathrm{R}_\gamma\left(\boldsymbol{x}\right)$$

where $\boldsymbol{x}$ is the vector containing all voxel values in the current guess of the reconstruction, A is the system matrix containing the forward model, $\boldsymbol{p}$ the vector of all measured projection pixels in all views and $\boldsymbol{w}$ the vector of their corresponding statistical weights. The square brackets indicate that the squaring operation is applied element-wise. The parameter λ determines the strength of the regularization and $\mathrm{R}_\gamma\left(\boldsymbol{x}\right)$ is the Huber regularization penalty. The Huber parameter defining the transition between noise and signal is indicated with the subscript γ. The first addend of the cost function will be referred to as data term in the following, the second as regularization term.

The data sizes of the different components for a 2k cubed dataset can be found in table I. The sparse system matrix obviously has to be computed on the fly. For maximum speed we use a simple GPU-accelerated voxel-driven back projector (BP) and a ray-driven forward projector (FP) with bilinear hardware interpolation. [6]

We chose the ordered-subset separable quadratic surrogates solver (OS-SQS) with momentum acceleration (OS-mom) [7]. It is currently one of the fastest in convergence. Convergence is however not the only advantage over the usual OS-SQS. OS-mom also favors larger numbers of views per subset. This asset becomes especially visible for smaller datasets, where the data throughput of the GPU-based FP and BP is significantly higher if more views can be processed at once [6].

A. SIR on heterogeneous multi-GPU and -CPU hardware

A heterogeneous system consists of several computing devices which differ in architecture and thus capabilities. The idea of heterogeneous computing is to split up a task into several parts and distribute them over the different devices in order to maximize performance.

The key concept for best exploiting our multi-GPU and -CPU system is splitting up the cost function into data term and regularization. For computing an update, the solver requires the gradient of the cost function for the current guess and its curvature. Both can be split up in the same way as the cost function itself.

Although the curvature for the data term can be precomputed once for all updates [8], the FP and BP required for the gradient make the data term still much more expensive than the regularization. This is why we use the GPU devices for that task. As stated above their highly superior computing power can be exploited very well for the required operations. However, large datasets require sophisticated splitting techniques in order to deal with the limited memory resources. For cone-beam datasets this can be quite challenging as the next section shows.

Our choice of hardware for the data term leaves two options for the gradient and curvature of the regularization. One is to compute them subsequently also on the GPUs. The mathematically simple and spatially local operations required would go very well with the capabilities of a GPU. We decided however for the other option, namely using the CPUs for the regularization. Although the execution time is most likely a little longer, it can be hidden behind computing the data term. Apart from joining the two results of gradient and curvature respectively in the end, this approach delivers the regularization for free. The only premise is that computing the regularization on the CPUs does not take significantly longer than computing the data term on the GPUs. The results presented below show that this premise is fulfilled very well.

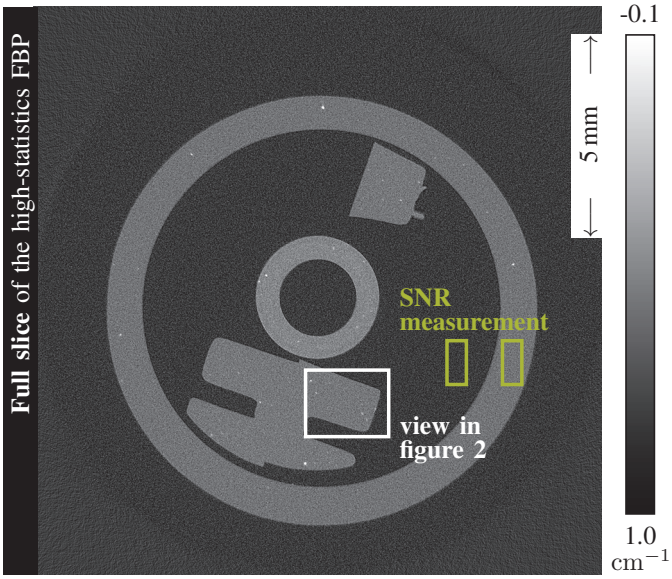

Figure 1. **A full slice of the FBP-reconstructed high-statistics scan.** The sample investigated is a plastic ball pen. The slice shows the plastic housing, the refill in the middle and parts of the mechanical system. On a closer look the plastic includes several small impurities in all parts. The white rectangle marks the region shown in figure 2. The green rectangles highlight the two areas taken for the SNR measurement.

B. Data splitting for GPU projectors

Splitting the huge data volume into pieces of manageable size for the GPU memory is a crucial part for operating the presented framework successfully. Therefore we combined two already known concepts [6] with an additional third one.

The splitting into slice chunks and angular wedges works with both, FP and BP. Slice chunks split up the output volume into equidistant parts perpendicular to the axis of rotation, i. e. the set of projection views for the FP and the image volume for the BP. The sections of the input volume corresponding to each slice chunk is then calculated according to the cone-beam geometry. The main advantage of this way of splitting are completely distinct subtasks that can also be distributed over several GPU devices without any computational overhead.

Angular wedges is a splitting technique working independently of the cone-beam geometry. It reduces the data size per device by subsequently processing subsets of the projection views while keeping the image volume chunk constantly in GPU memory.

We found however that for the FP the two techniques were not yet sufficient for 2k cubed data. That is why we added a third splitting approach called ray chunks. It splits up the image volume chunk into additional equidistant chunks along the main ray direction and loads them subsequently.

All three concepts are designed in a way that they produce no additional computational overhead. Together they guarantee that the GPU devices do not run out of memory and that, apart from negligible transfers at the very beginning and end, all data transfers between host memory and device are hidden behind computations.

C. Benchmark conditions

Before being able to prove the feasibility of SIR for large datasets and the resulting benefits in acquisition time, we first have to define a realistic reconstruction task to be solved. Therefore we carried out two high-resolution micro CT measurement providing each the data for a 2k cubed reconstruction volume as given in table I. The first measurement uses an exposure time of $30\,\mathrm{s}$ per view in order to receive a filtered backprojection (FBP) reconstruction of good quality. It will be referred to as the high-statistics, or reference scan in the following. Subsequently a second, low-statistics measurement was taken by reducing the exposure time by a factor of six, i. e. to $5\,\mathrm{s}$ per view. The task we defined for our benchmark is now a SIR that reaches the same level of detail at a comparable or lower noise level in the reconstruction for the low-statistics scan than FBP does for the high-statistics one.

The investigated sample is a plastic ball pen. The micro CT was operated with a cone-beam opening angle of $19.4\,\mathrm{deg}$ and a voxel size $6.83\,\mu\mathrm{m}$. The system has a flat detector. Figure 1

shows a slice of the high-statistics measurement reconstructed with FBP.

The compute system used for reconstruction is equipped with

- four *NVIDIA Titan X* GPU devices providing 12 GB of memory and 3072 threads each,
- two *Intel Xeon E5-2667 v3* CPUs at 3.20 GHz providing 32 threads in total (including hyperthreading), and
- 512 GB of DDR4 RAM operating at 2133 MHz.

The regularization parameters λ and γ were tuned by hand on the subvolume of the 32 innermost slices and rescaled accordingly to apply them on the whole dataset. For simplicity all weights $\boldsymbol{w}$ were set to one. The initial guess was a low-pass filtered FBP. The splitting parameters for FP and BP were chosen as suggested previously [6]. We chose a random set of views for each subiteration. The OS-mom required four full iterations involving eight subsets each until the desired level of detail is reached. The quality measures applied were visual inspection of the small impurities and the signal-to-noise ratio (SNR) as shown in figure 2.

III. Results

The results of the benchmark for the suggested SIR algorithm applied to the 2k dataset introduced in the previous section can be seen in figure 3. They show that it is possible to carry out the whole reconstruction within 2:07 h. This is less than half the total exposure time of $3217 \times 5\,\mathrm{s} = 4{:}28\,\mathrm{h}$ and only about one third of the total acquisition time. The profiling plot clearly makes visible the 4×8 subsets resulting in 32 total subiterations. Each consists of a multi-GPU FP and BP for computing the gradient of the data term. Concurrently the gradient and curvature of the Huber regularization is computed on the CPUs. The curvature of the data term is precomputed only once for all subiterations. The only idle times for the GPUs are required for three short tasks marked as *other CPU tasks*. The first is adding the gradient and curvature of data term and regularization, respectively, the second is computing the momentum and updating the volume, and the third is choosing the views for the next subset. All three take approximately equally long.

The memory consumption is high but still manageable for a single computer. Surely there is room for improvements in the future. The main contributions are the measured data (50 GB as shown in table I), the reconstructed volume or momentum, respectively (32 GB), and the arrays to store the gradient and curvature of data term and regularization (4×32 GB).

We also tried the presented methods on smaller datasets to test their scalability. The result can be seen in figure 4. There is no obvious reason why the suggested techniques should perform better on powers of two but it seemed to be a natural choice for our test. The number of corresponding projection views fulfills the sampling criterion, namely $\pi/2$ times the number of voxels on each side of the volume. [9] For a fair comparison, the number of full iterations is constantly kept at four and the number of subsets at eight. In practice it might however be more advantageous to adapt the latter individually for each volume size.

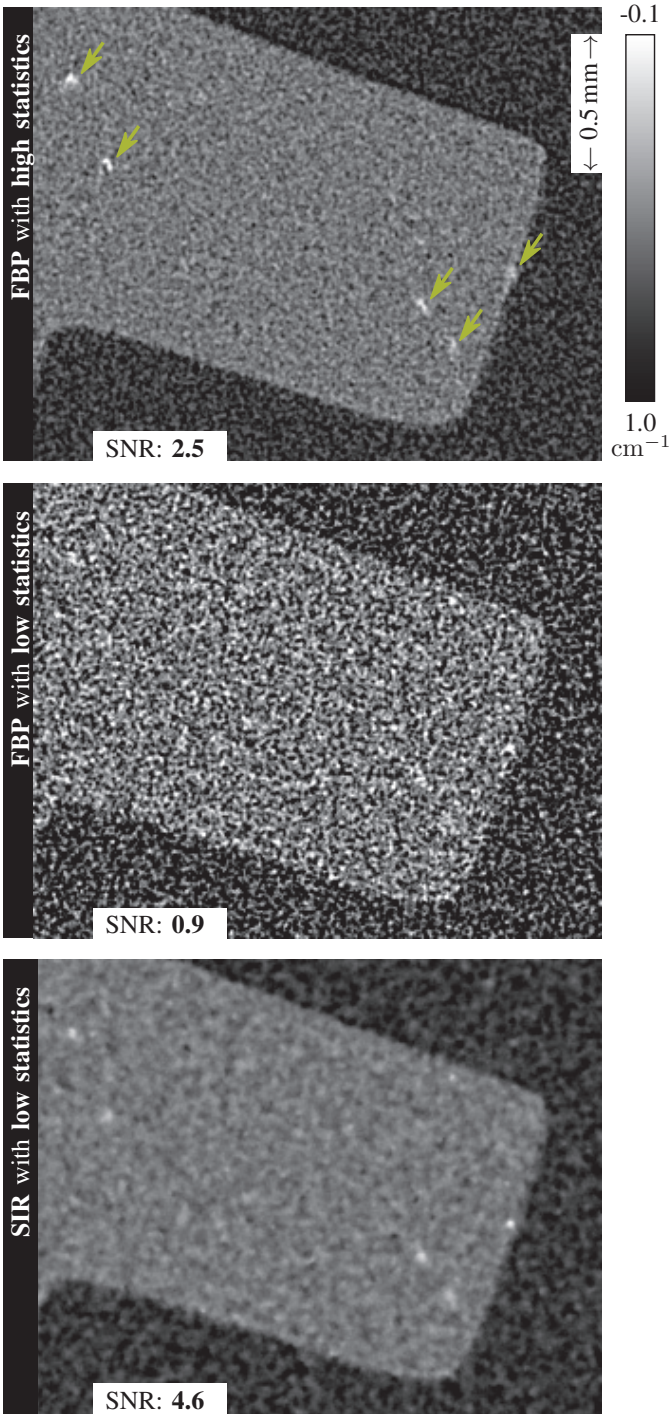

Figure 2. **Quality evaluation of the benchmarked SIR.**
The three figures in row show the result of the FBP for the high-statistics measurement as well as FBP and SIR applied to the low-statistics data. The purpose of this comparison is to show that the benchmarked SIR reaches the same level of detail despite the sixfold reduced exposure time.
Therefore we look exemplarily at five impurities marked with the green arrows in the top image. They are well visible in the high-statistics reference, get mostly lost in the noise of the low-statistics FBP and can be recovered by the suggested SIR as shown at the bottom.
Although the patchy structure of the noise pattern in the SIR result gives an equally rough visual impression as the noise in the reference, the signal-to-noise ratio is strongly improved.

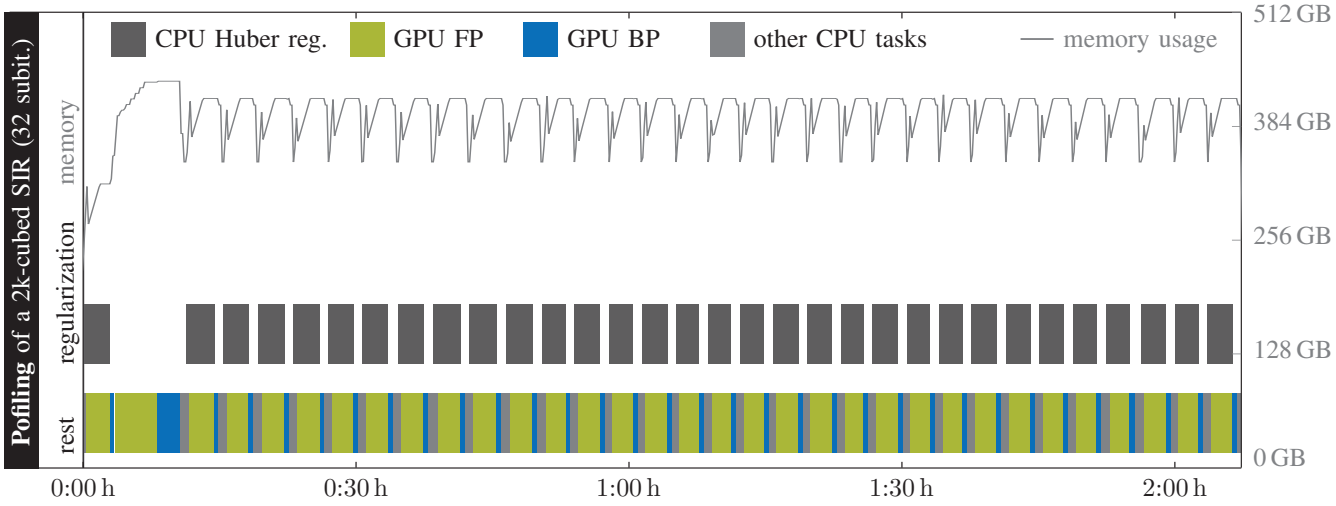

Figure 3. **The profiling of suggested SIR approach**.
The combined plot shows on the same timeline the memory usage as lineplot in the upper part and a profiling of the computational tasks displayed as bars in the lower part. The units for the memory can be found on the right axis. The benchmarked algorithm is the suggested SIR applied on the 2k-cubed dataset described in the methods part. The time measurement starts with the first iteration and does not include loading the dataset, saving the result or computing the initial guess. The total reconstruction time is 2:07 h.
The recurrent equal chunks of the profiling mark the 4×8 subiterations executed. The single longer pair of FP and BP after the first subset is for computing the constant curvature of the data term. The profiling shows that the regularization comes almost for free as its computation is completely hidden behind processing the data term. The only offset is a very short operation for adding the two results which is about one third of the *other CPU tasks*. The memory bar shows an expectedly high but relatively constant memory consumption over the whole process.

IV. Conclusion

We demonstrated a way to make statistical iterative reconstruction possible for 2k-cubed cone-beam datasets on current heterogeneous hardware. Therefore we showed how to use one of the fastest solvers for CT, the OS-mom, within a multi-GPU and -CPU environment by combining several data splitting technologies for GPU-driven forward- and backprojection with a clever way to hide virtually the whole compute time of the regularization.

We found that our approach makes SIR not only feasible within a current workflow at micro-CT systems but still when exploiting its great power to drastically reduce the total acquisition time. As an example we reconstructed a 2k-cubed dataset with a total acquisition time of about six hours within about two hours. The example shows that there is even still quite some room left for weaker hardware or more complex algorithms in the future. The details visible in a reference measurement with six-fold longer exposure time could be recovered successfully by SIR. We also showed that our concept works well for smaller datasets.

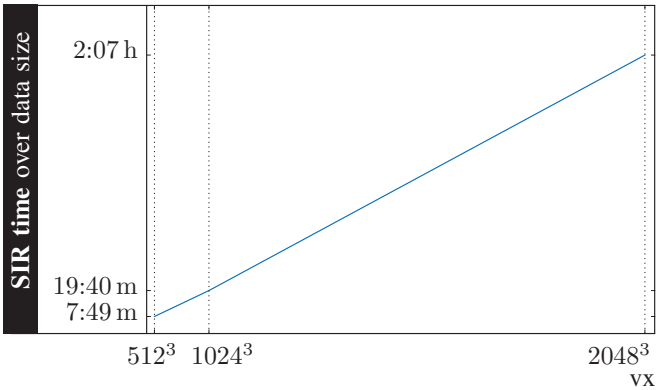

Figure 4. **Benchmarks for different volume sizes**
The curve shows the total reconstruction time of the suggested SIR for different volume sizes. The numbers given on the horizontal axis are the total numbers of voxels within the cubic reconstruction volume.
The runtimes for the three different sizes lie on the same line which means that our approach scales linearly with the number of total voxels. The measured times indicate that it does not only perform well for very large data sizes but also for conventional sizes.

References

[1] Jeffrey A. Fessler. Statistical image reconstruction methods for transmission tomography. In Milan Sonka and J. Michael Fitzpatrick, editors, *Handbook of Medical Imaging, Volume 2: Medical Image Processing and Analysis*, pages 1–70. SPIE, Bellingham, 2000.

[2] Peter B. Noël, Bernhard Renger, Martin Fiebich, Daniela Münzel, Alexander A. Fingerle, Ernst J. Rummeny, and Martin Dobritz. Does iterative reconstruction lower ct radiation dose: Evaluation of 15,000 examinations. *PLoS ONE*, 8(11):e81141, 11 2013.

[3] Fang Xu and Klaus Mueller. Real-time 3d computed tomographic reconstruction using commodity graphics hardware. *Physics in Medicine and Biology*, 52(12):3405, 2007.

[4] Marcel Beister, Daniel Kolditz, and Willi A. Kalender. Iterative reconstruction methods in x-ray CT. *Physica Medica*, 28(2):94 – 108, 2012.

[5] Peter J. Huber. *Robust Statistics*. New York: Wiley, 1981.

[6] Andreas Fehringer, Tobias Lasser, Irene Zanette, Peter B. Noël, and Franz Pfeiffer. A versatile tomographic forward- and back-projection approach on multi-gpus. *Proceedings of SPIE*, 9034:90344F–90344F–7, 2014.

[7] Donghwan Kim, Sathish Ramani, and Jeffrey A. Fessler. Combining ordered subsets and momentum for accelerated x-ray CT image reconstruction. *Medical Imaging, IEEE Transactions on*, 34(1):167–178, Jan 2015.

[8] Hakan Erdogan. *Statistical Image Reconstruction Algorithms Using Paraboloidal Surrogates for PET Transmission Scans*. PhD thesis, The University of Michigan, 1996.

[9] Avinash C. Kak and Malcolm Slaney. *Principles of computerized tomographic imaging*. Classics in applied mathematics. IEEE Press, 1988.

Bone-Enhanced Small-Animal Microtomography with Single-Shot Dual-Energy Sandwich Detectors

Seung Ho Kim, Daecheon Kim, Hanbean Youn, Seungryong Cho, and Ho Kyung Kim

***Abstract*—Single-shot dual-energy x-ray sandwich detector can produce sharp images because of its inherent unsharp masking effect on the subtracted images. Inspired by this observation, the authors have developed a microtomography system with the sandwich detector in pursuit of high-resolution bone-enhanced small-animal imaging. The preliminary results show that the bone-enhanced images reconstructed with the subtracted projection data are better in visibility of bone details than the conventionally reconstructed images. In addition, the bone-enhanced images obtained from the sandwich detector are relatively immune to the artifacts caused by photon starvation. The microtomography with the single-shot dual-energy sandwich detector will be useful for the high-resolution bone imaging without use of elaborate equipment such micro-focus x-ray source and high-resolution x-ray imaging detectors.**

***Index Terms*—Computed tomography, microtomography, micro-CT, sandwich detector, dual-energy imaging, single-shot dual-energy imaging, mouse imaging**

I. Introduction

SINCE the physical characteristics of bone are affected by numerous factors, such as age, hormones, arthritis, and exercise [1], a preclinical study with small animals with respect to those various factors would be helpful for theoretical and computational models of bone [2]. Moreover, longitudinal, histological studies without sacrificing animals are essential [3], [4]. In this regard, the x-ray microtomography (or micro-CT) has been popular for small-animal bone studies [5], [6], [7], [8].

In previous studies [9], [10], the authors described the multilayer ("sandwich") detector by stacking two flat-panel detectors (FPDs) and demonstrated its prospect for "motion-artifact-free" single-shot dual-energy imaging (DEI) by obtaining bone and soft-tissue images of a postmortem mouse. In addition, it was observed that the single-shot method showed better visibility at higher spatial frequencies (e.g. edge regions and bone details) than the conventional double-shot method (e.g. switching the applied tube voltages). The reason can be explained by the inherent "unsharp masking" effect of the sandwich detector [10]; the rear FPD with a thicker scintillator provides a blurrier image than the front FPD, hence subtraction of the two images enhances edges in the resultant image. Inspired by this observation, the authors have applied the sandwich-detector concept to the micro-CT for small-animal "bone" imaging.

This work was supported by the National Research Foundation (NRF) grants funded by the Korea government (MSIP) (No. 2013M2A2A9046313 and No. 2014R1A2A2A01004416). *H. K. Kim is the corresponding author for this article.

S. H. Kim and D. Kim are with the School of Mechanical Engineering, Pusan National University, Busan 46241, South Korea.

H. Youn is with the Department of Radiation Oncology, Pusan National University Yangsan Hospital, Gyeongsangnam-do 50612, South Korea.

S. Cho is with the Department of Nuclear and Quantum Engineering, Korea Advanced Institute of Science and Technology, Daejeon 34141, South Korea.

*H. K. Kim is with the School of Mechanical Engineering and the Center for Advanced Medical Engineering Research, Pusan National University, Busan 46241, South Korea (e-mail: hokyung@pusan.ac.kr).

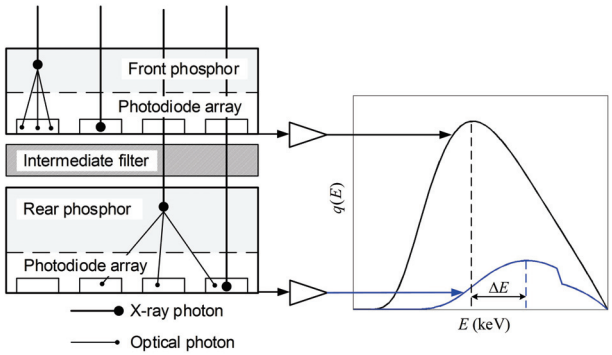

Fig. 1. Conceptual illustration of the sandwich detector operation.

II. Background

While the front FPD measures relatively low energy, as shown in Fig. 1, the rear one measures relatively high energy because of x-ray beam hardening through the front FPD. Onto the same photodiode platform, thus, a thicker scintillator in the rear FPD is preferred to that in the front FPD to achieve high quantum efficiency for the relatively higher-energy x-ray spectrum. It is noted that an intermediate filter layer, as described in Fig. 1, can be used to further increase spectral separation between the two FPD measurements, which may provides a better contrast-to-noise performance in the subtracted images.

From weighted subtraction, a bone-enhanced projection can be obtained

$$p_{bone} = wp_F - p_R, \tag{1}$$

where p_j denotes the projection obtained from the jth FPD layer (i.e. front or rear). The optimal w can be determined by minimizing contrast between the soft tissue to be subtracted and background [10].

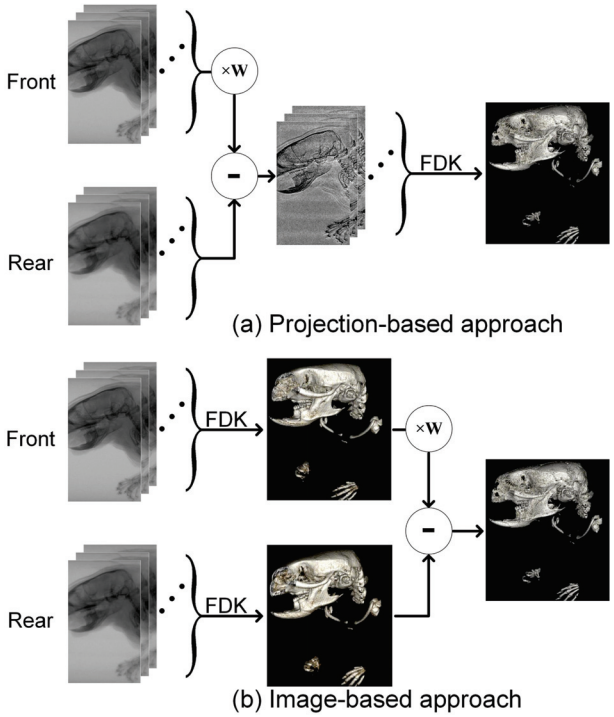

Fig. 2. Schematic views describing two different approaches for bone-enhancing image recontruction: (a) projection-based and (b) image-based subtraction methods.

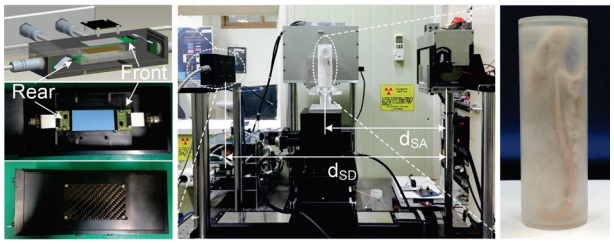

Fig. 3. Picture describing the micro-CT system with the sandwich detector. The enlarged views show the sandwich detector and a postmortem mouse phantom.

In a similar way, bone-enhanced tomographic images may be obtained by reconstructing bone-enhanced projection data

$$f_{proj}(\mathbf{r}) = \mathcal{FDK}\left\{\mathbf{W}\mathbf{P}_F - \mathbf{P}_R\right\}, \tag{2}$$

where $\mathbf{P}_j$ denotes the projection data in a matrix form obtained from the jth FPD layer and $\mathbf{W}$ is a diagonal matrix consisting of weighting factors determined at each projection angle $w(\theta)$. The operator $\mathcal{FDK}\{\cdots\}$ implies the approximate filtered backprojection operation [11] with the Hann filter. If the weighting factor is independent upon the rotation angle, $\mathbf{W}$ becomes a scalar w. The procedure is schematically described in Fig. 2(a).

III. Materials and Methods

As shown in Fig. 3, a bench-top micro-CT system has been developed using the sandwich detector. During continuous x-ray irradiation, the object rotated on its axis by an amount of prescribed step angle and then the rotation stayed until the sandwich detector produced two projection images. These motion and image readout were computer-controlled and lasted till a single rotation completed. The distances from the x-ray focal spot to the detector (d_{SD}) and to the axis of rotation (d_{SA}) were computer-controlled variables. The traveling ranges of the object jig were 600, 300, and 75 mm along the x, y, and z directions, respectively.

The x-ray source (Series 5000 XTF5011, Oxford Instruments, Inc., US) employed a tungsten (W) anode and could operate up to the maximum power of 50 Watts. The W x-ray spectra were further tailored by an additional 1-mm thick aluminum (Al) filter. According to the manufacturer, the nominal focal-spot size was 0.035 mm.

Each FPD layer constituting the sandwich detector employed a combination of a Gd_2O_2S:Tb phosphor screen for conversion of x-ray into optical quanta and a photodiode array for detection of them. The thicknesses of the front and rear phosphors were $\sim$ 34 and $\sim$ 67 mg cm^{-2}, respectively. The same photodiode arrays (RadEye1$^{\text{TM}}$, Teledyne Radicon Imaging Corp., Sunnyvale, US) were used for the front and rear FPDs. The pixel pitch of the photodiode array was 0.048 mm, and the magnification of the pixel pitch of the rear detector was negligible. The active area of the sandwich detector was $\sim 25 \times 50$ mm^2.

For a small-animal imaging, a postmortem mouse phantom ($\sim$ 40 g) was prepared, as shown in Fig. 3, by replacing blood by paraformaldehyde. Head part of the mouse phantom was scanned using two different designs of sandwich detector; one design used no intermediate filter and the other used a copper (Cu) filter with a thickness of 0.3 mm. Irradiation x-ray spectrum was from a W target at 50 kVp/1 mm Al filter. 360 projection views were obtained for a single circular scan and they were used for reconstruction. All the reconstructed images were calibrated into the Hounsfield units (HU) using separate scans of water phantom.

IV. Results

Figure 4 compares projection images obtained from the each FPD layer of the two designs of sandwich detectors (i.e., one design included a 0.3 mm-thick Cu filter and the other did not) and their resultant DE images for the postmortem mouse phantom. The images were displayed with the level of their mean value (μ) and a window of two times their standard deviation (σ) (other images below were displayed with the same level and window). It was observed that the projections from the front FPD were sharper than those from the rear FPD as the font FPD employed a thinner phosphor than the rear FPD. Comparing Figs. 4(b) with (e), use of the intermediate filter resulted in higher noise in the rear FPD image, and the reason could be explained by the reduction in the number of x-ray photons reaching the rear FPD due to the additional attenuation through the filter layer. Weighted logarithmic subtraction successfully provided bone-enhanced images as shown in Figs. 4(c) and (f).

Figure 5(a) shows a response function (or edge-spread function, ESF) extracted from the subtracted image for an edge-knife phantom. The subtraction operation resulted in a characteristic of a processed impulse response. The corresponding modulation-transfer function (MTF) result is shown

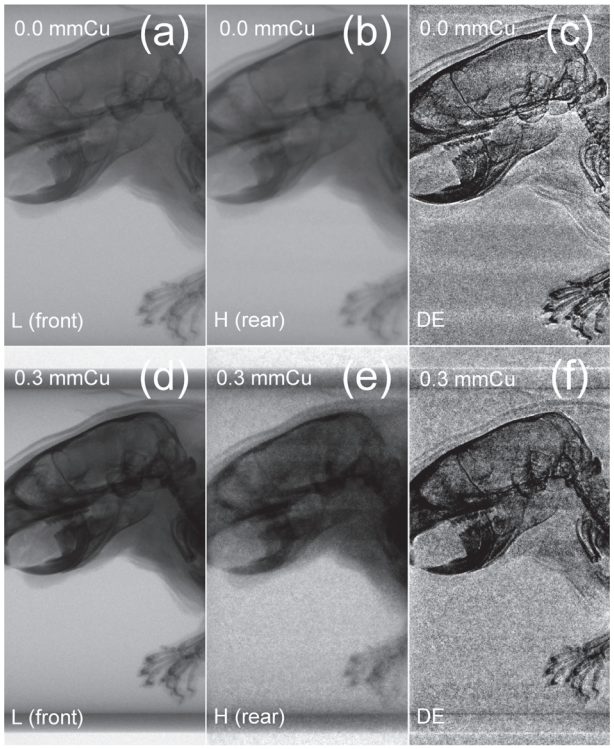

Fig. 4. Projection images obtained from the each FPD layer of the sandwich detectors without and with a Cu filter layer and their resultant DE images for the postmortem mouse phantom. (L/W = $\mu/\pm 2\sigma$).

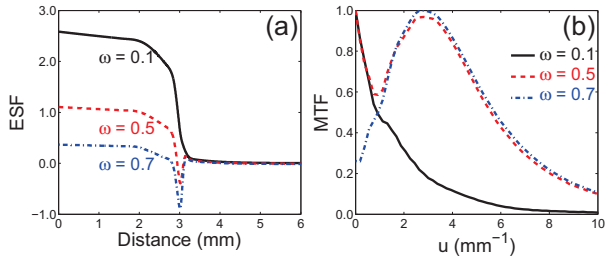

Fig. 5. Impulse response functions of the sandwich detector for an edge-knife phantom: (a) edge-spread function and (b) modulation-transfer functions.

in Fig. 5(b). Unlike the low-pass characteristic of the conventional MTF curve, a band-pass characteristic was observed. While the contrast performance for low-frequency object content was decreased with increasing weighting factor, the contrast performance for specific spectral information (e.g., $\sim$ 3 mm^{-1} in this example) was enhanced. These MTF characteristics can support the analysis of subtracted images as shown in Figs. 4(c) and (f).

Tomographic images reconstructed using each projection dataset, as exemplarily shown in Fig. 4, are summarized in Fig. 6. The characteristics observed from the projection data were well reflected into the tomographic images. Comparing Figs. 6(c) with (f), use of the intermediate filter gave rise to a more reduction of soft tissues. It was also observed that the DE tomographic images showed less streak artifacts due to photon starvation compared to the images obtained using the front FPD.

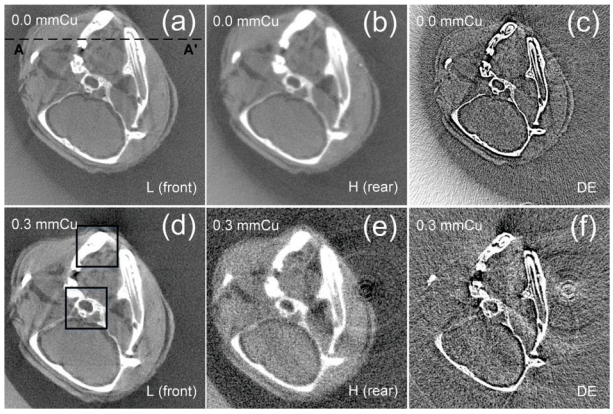

Fig. 6. Comparison of tomographic images reconstructed from the corresponding projection dataset.

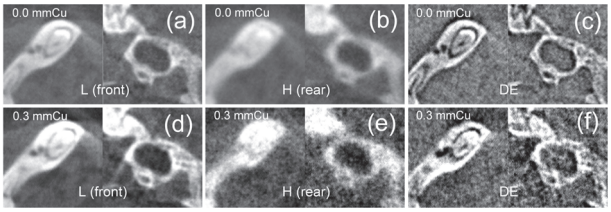

Fig. 7. Enlarged images indicated by the boxes Fig. 6(d) for more detailed displays of tomographic images.

As shown in Fig. 7, the regions indicated as boxes in Fig. 6(d) have been investigated in detail. The rear FPD with a thick phosphor provided a blur image as shown in Fig. 7(b), and it became noisier, as shown in Fig. 7(e), when the Cu filter was additionally used. The DE tomographic image obtained form the sandwich detector without any filter layers showed the best visual performance for bone details.

Figure 8 compares profiles extracted along the line $A - A'$ (as possible as the authors can), as designated in Fig. 6(a), for each reconstruction image. Bone signal in the reconstructed image with projections from the front FPD was the largest, the rear FPD the second, and then the DE results. Although the DE tomographic image signals were noisy, they consisted mostly of only bone signals. As observed from Figs. 4(e) and 6(e), the images obtained from the rear FPD of the sandwich detector with the Cu filter were noisy.

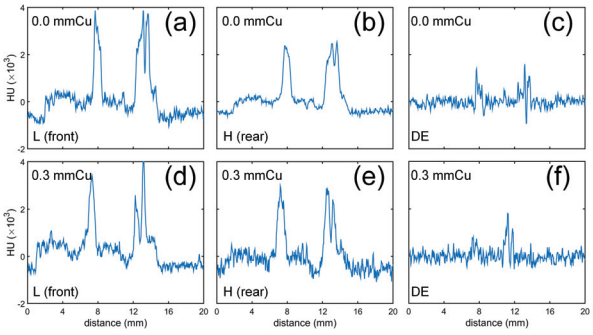

Fig. 8. Profiles extracted along the line $A - A'$, as designated in Fig. 6(a), for each corresponding reconstruction image.

V. Summary and Future Work

Bone-enhanced tomographic images have been obtained using dual-energy sandwich detectors for a postmortem mouse phantom, and they outperformed the tomographic images obtained from the conventional detectors (i.e., the front and rear flat-panel detectors constituting the sandwich detectors) for bone details. Although use of an intermediate filter, which was placed between the front and rear flat-panel detectors, resulted in less residual soft tissues in the reconstructed bone-enhanced images, it degraded the visual image quality of bone details because of increased noise. Optimal filter design in terms of material and thickness is required for a more tissue separability and less noise performance in images. This study shows a great potential of microtomography with a sandwich detector for high-resolution bone-enhanced small-animal imaging without use of elaborate equipment such as micro-focus x-ray source and high-resolution x-ray imaging detectors.

In the present work, the bone-enhanced tomographic image was obtained by reconstructing weighted-subtraction sinogram. Alternatively, the bone-enhanced images may also be obtained by subtraction of two tomographic images reconstructed with projections separately obtained from the front and rear FPDs, as shown in Fig. 2(b),

$$f_{bone}(\mathbf{r}) = w\mathcal{FDK}\left\{\mathbf{P}_F\right\} - \mathcal{FDK}\left\{\mathbf{P}_R\right\}. \qquad (3)$$

This approach is under progress and comparison with the present method will be made. Furthermore, the bone-enhanced DE tomographic images may be combined with the images reconstructed with projections obtained from the front FPD as the conventional unsharp masking digital image processing. The authors anticipate the resultant images will be similar to conventional tomographic images for low spatial-spectral contents but better for high spatial-spectral contents. These further studies will be a future study.

References

[1] J.-T. Hsu, Y.-J. Chen, J.-T. Ho, H.-L. Huang, S.-P. Wang, F.-C. Cheng, J. Wu, and M.-T. Tsai, "A comparison of micro-CT and dental CT in assessing cortical bone morphology and trabecular bone microarchitecture," *PLoS ONE*, vol. 9, no. 9, p. e107545, 09 2014.

[2] N. A. Hanson and C. M. Bagi, "Alternative approach to assessment of bone quality using micro-computed tomography," *Bone*, vol. 35, no. 1, pp. 326–333, 2004.

[3] E. L. Ritman, "Molecular imaging in small animals - Roles for micro-CT," *J. Cell. Biochem.*, vol. 87, no. S39, pp. 116–124, 2002.

[4] S. C. Lee, H. K. Kim, I. K. Chun, M. H. Cho, S. Y. Lee, and M. H. Cho, "A flat-panel detector based micro-CT system: Performance evaluation for small-animal imaging," *Phy. Med. Biol.*, vol. 48, no. 24, pp. 4173–4185, 2003.

[5] M. J. Paulus, S. S. Gleason, S. J. Kennel, P. R. Hunsicker, and D. K. Johnson, "High resolution x-ray computed tomography: An emerging tool for small animal cancer research," *Neoplasia*, vol. 2, no. 1-2, pp. 62–70, 2000.

[6] D. W. Holdsworth and M. M. Thornton, "Micro-CT in small animal and specimen imaging," *Trends Biotechnol.*, vol. 20, no. 8, pp. S34–S39, 2002.

[7] E. L. Ritman, "Micro-computed tomography - Current status and developments," *Annu. Rev. Biomed. Eng.*, vol. 6, no. 1, pp. 185–208, 2004.

[8] D. Clark and C. Badea, "Micro-CT of rodents: State-of-the-art and future perspectives," *Phys. Medica*, vol. 30, no. 6, pp. 619–634, 2014.

[9] S. Yun, J. C. Han, D. W. Kim, H. Youn, H. K. Kim, J. Tanguay, and I. A. Cunningham, "Feasibility of active sandwich detectors for single-shot dual-energy imaging," vol. 9033, 2014, pp. 90 335T–90 335T–8.

[10] J. C. Han, H. K. Kim, D. W. Kim, S. Yun, H. Youn, S. Kam, J. Tanguay, and I. A. Cunningham, "Single-shot dual-energy x-ray imaging with a flat-panel sandwich detector for preclinical imaging," *Cur. Appl. Phys.*, vol. 14, no. 12, pp. 1734–1742, 2014.

[11] L. A. Feldkamp, L. C. Davis, and J. W. Kress, "Practical cone-beam algorithm," *J. Opt. Soc. Am. A*, vol. 1, no. 6, pp. 612–619, Jun 1984.

CT Alignment Correction in Iterative Reconstruction Methods

Kilian Dremel [1], Daniel Althoff [2], and Simon Zabler[2]

[1]X-ray Microscopy (LRM), Physics and Astronomy, University Würzburg, Josef-Martin-Weg 63, Würzburg, Germany
[2]Fraunhofer Institute for Integrated Circuits IIS, Development Center for X-ray Technology (EZRT), Josef-Martin-Weg 63, Würzburg, Germany

***Abstract*—Computed tomography at micrometer scale often suffers from unknown misalignments of the axes resulting in a loss of image quality. In iterative reconstruction methods the cost functions need a forward projection for every view. These projections can be used to calculate the cross-correlation between the measured and forward-projected data to get improved geometrical data for the next iteration step. We present simulations and measurements reconstructed with in a maximum-likelihood framework including the proposed alignment-correction step.**

***Index Terms*—computed tomography, reconstruction, alignment correction**

I. Introduction

UNKNOWN misalignments or wobbling of the rotational axis, focal spot movements and variable detector shifts lower the resolution in CT systems. While detector shifts usually produce double edges in the reconstructed volume and can - as long as they are non-varying over the projections - easily be compensated, wobbling of the axes or focal spot movements are not easy to be seen. Moreover sample movements like thermal drifts lower the resolution of CT scans at high magnifications. Mayo et al. [1] used an iterative Feldkamp algorithm ([2]) to improve the geometrical information by the cross-correlation of forward projected and measured data. Since they used a X-ray microscope scanning at voxel sizes below one micron, their main goal was to correct the temperature-drift of their manipulation system. Other methods to compensate alignment problems are the evaluation of the image sharpness (as in Kingston et al. [3]) or the search for sinogram symmetries (see [4]).
In iterative CT reconstruction forward projections are calculated at every iteration to perform an update equation on the volume. A cross-correlational comparison of the computed and the measured projections can be included between the update steps at low computational cost. This results not only in improved sharpness of the reconstruction but also gives the chance to detect misalignments in the manipulation system.
The unknown geometrical information can be evaluated for one of the three components of the CT systems: source, rotational axis or detector.

II. Method

As iterative reconstruction algorithm we use a total-variation regularized maximum-likelihood method. The forward projection $\bar{y}$ is computed as detector intensity and gets compared to the measured intensities y by cross-correlation. The cross-correlation $y_i^\dagger$ of two discrete signals with index i is given by

$$y_i^\dagger = \mathcal{F}_{2D}^{-1}(\mathcal{F}_{2D}(y_i)^* \mathcal{F}_{2D}(\bar{y}_i)) \tag{1}$$

where $\mathcal{F}_{2D}$ denotes the two-dimensional Fourier transform. The position of the maximum of $y^\dagger$ defines the deviation ($\Delta\vec{x}$) of the computed projection from the measurement. To find the maximum a bilinear interpolation is used to get sub-pixel accuracy. Although the correlation is fast compared to the iterative steps of the reconstruction in most instances it is possible to use only a small part of the projection matrix for the correlation. In cases of low contrast, before correlating the signals an optional edge filter (for example a simple image gradient) can be applied to both projection and measurement. The update of the geometrical information can be performed for the detector, the rotational axis or the source coordinates, but at each view only in the corresponding detector plane. The detector($\vec{D}$)- source($\vec{S}$)- and rotational axis($\vec{R}$)-coordinates are updated by:

$$\vec{D} = \vec{D} + \lambda\Delta\vec{x}\Delta d \tag{2}$$

$$\vec{R} = \vec{R} + \lambda\frac{\Delta\vec{x}\Delta d}{m} \tag{3}$$

$$\vec{S} = \vec{S} + \lambda\Delta\vec{x}\Delta d\frac{1}{m-1} \tag{4}$$

with the detector pixel-size Δd and the magnification m in a cone-beam setup. To avoid divergence in the case of strongly uncorrelated projections the coefficient λ can be set to values < 1. If correction of an uniform offset is required only, a mean deviation can be calculated before applying them to the geometrical setup. If the projections are processed independently, the following steps are performed at each iteration:

1) Forward projection
2) (Edge filter on both projection and measurement)
3) Cross-Correlation of the signals
4) Search for the maximum of $y_i^\dagger$
5) Computation of the deviation with sub-pixel accuracy
6) Back projection
7) Update of the geometrical information

III. Phantoms and setup

Both simulations and measurements have been performed to test the algorithm. The simulations show one slice of a hole plate used as calibration phantom in NDT applications

Contact: kdremel@physik.uni-wuerzburg.de

(see [5], [6]). It consists of a solid aluminium block (5 cm x 5 cm x 0.8 cm) with 28 drill holes. To show the operational capability and to evaluate the influence of poisson noise on the projections, we used a virtual mono energetic source at 225 kV in the simulations. The magnification m was set to 3.6. The poisson noise was calculated for 1000 photons per pixel. The reconstruction started after the third iteration with the correlation to make sure the iterative reconstruction converged enough to get higher frequencies in the forward projection. The reconstruction was performed with 200 subsets in the case of noiseless projections and 50 subsets in the case of projections including noise, so the convergence speed of the datasets can differ.

The simulated deviations were incorporated by shifting the projection image by a random floating point value of pixels in horizontal and vertical direction. The random value was allowed to be positive or negative limited by a maximum value of 4, 8 or 16 pixels. The projections were interpolated in the shift.

For the measurements we used a calibration phantom from PTB (Physikalisch-Technische Bundesanstalt) consisting of four spheres of ruby building a triangular pyramid (see [7]). The spheres have a diameter of $500\,\mu m$. The measurements were performed with a high magnification of $m = 99.2$ with a Comet micro focus tube at a voltage of $80\,kV$. Although detector and source were well aligned, the rotational axis operated imprecise at the measurements. Therefore the coordinates of the rotational axis were chosen to be corrected during the reconstruction. The reconstructions have a voxel size of $2.1\,\mu m$ and a size of 512^3 voxels. Each iteration, containing the update of 800 projections, was divided into 40 subsets. The correction process started at iteration 5 with a coefficient $\lambda = 1.0$.

IV. Results

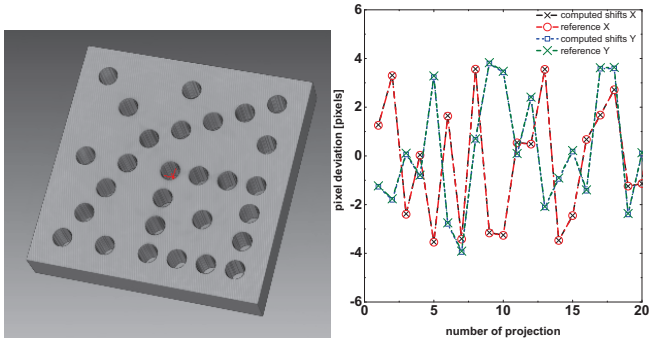

Fig. 1. On the left: Phantom used for the simulations. On the right: Geometrical aberrations of the first 20 iterations for a maximum shift of 4 pixels on the detector.

Fig. 1 shows the simulated and computed shifts after 50 iterations for the first 20 projections. The iterative evaluated shifts correspond with the simulated shifts. The middle slices of the reconstructed volumes are shown in Fig. 3 for the Filtered-Back-Projection (FBP) and the alignment corrected maximum-likelihood method. The uncorrected reconstructions show a worse signal-to-noise-ratio (SNR) inside the material than the corrected slices. Although a few visible discrepancies remain in the reconstructions the image quality is improved. Fig. 2 shows the mean deviation of the simulated and computed detector positions. With larger maximum aberrations the remaining offset increases, because the incomplete correction of a few projections gains more influence. The mean deviation after 50 iterations is lower than the pixelsize in all cases. The mean-squared-error (MSE) of the difference between the reconstructions and the reference reconstruction without shift or noise is shown in Fig 4. For the reconstructions without noise as well as for the noisy data the dataset with a maximum shift of 4 pixels in each direction converges to a better solution than the other datasets, but the improvement from iteration 3 to 4 clearly shows the corrections starting in iteration 3. The difference between the noisy and noiseless datasets exists due to the reference data which was build from noiseless projections. The non-monotonic behaviour of some datasets MSE shows the iterative changes of the geometry information.

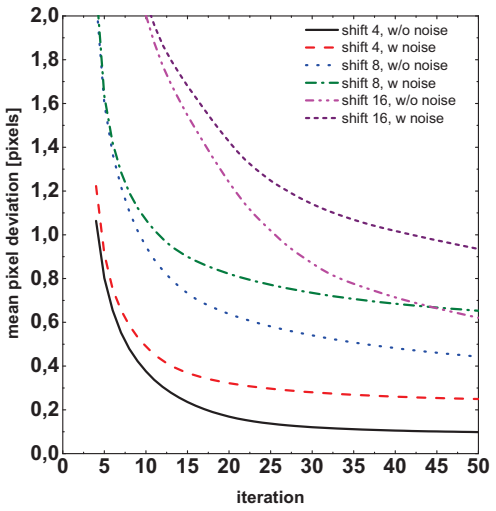

Fig. 2. Mean deviation of the detector position. The plots start at iteration 3 when the correction was started. The larger the maximum alignment offset gets, the bigger is the remaining offset after 50 iterations, because the contribution of a single projection rises.

The measurements were reconstructed with and without activated alignment correction with 50 iterations. For all reconstructions the iterative maximum-likelihood method with a slight total-variation regularization was used. The uncorrected slices (see Fig. 6) show double edges only in particular directions. While symmetric double edges could result from a constant detector shift, this asymmetry indicates aberrations in the assumed geometry-setup.

In Fig. 5 the three parts of the correction are shown: The forward projected image, the measurement and the cross-correlated image. The use of an edge filter before executing the correlation was not necessary in this case, because the projections showed high contrast.

Fig. 6 also shows the results of the 50th iteration with alignment correction. With the alignment correction not only the double edges disappear but also the SNR inside the ruby

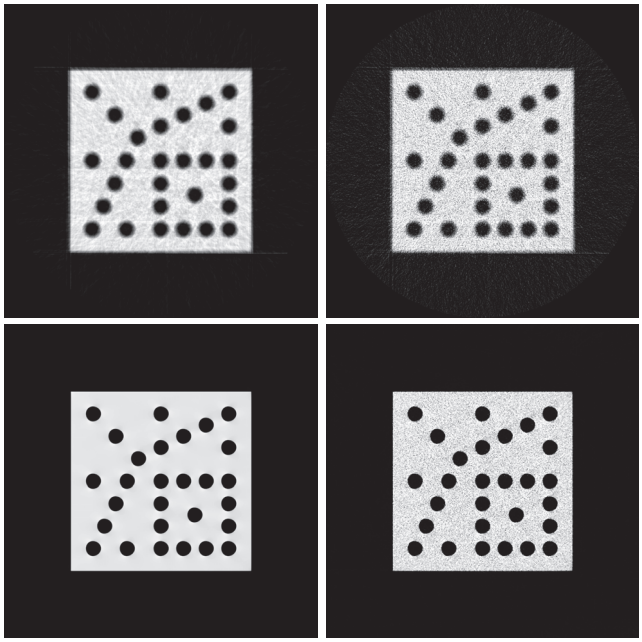

Fig. 3. Middle slice of the reconstructed volume with maximum shift of 8 pixels. First row: FBP with Shepp-Logan filter without corrections. Second row: Iterative reconstruction with corrections. Left: without noise. Right: with noise. Same range of grey values for all images.

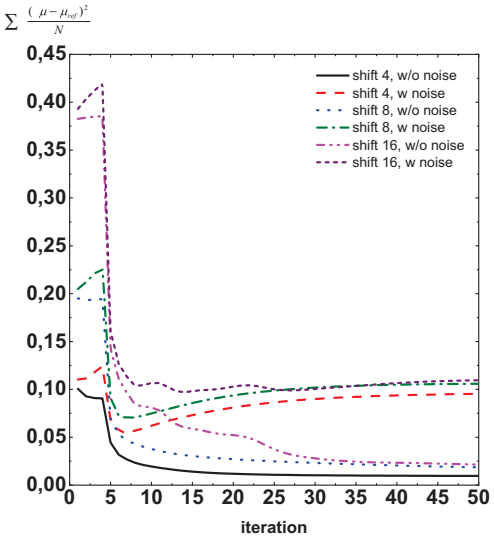

Fig. 4. Mean-squared-error of the reference reconstruction and the reconstructed data of the simulations. The trend to lower values for larger maximum deviations shows the influence of non-sufficiently corrected projections. The rising values of noisy data at higher iterations is caused by the sharpening of the noise in the reconstruction.

spheres rises because the projections become more consistent to each other. The computed deviation of the rotational axis is shown in Fig. 7. While the movement in the XY plane (orthogonal to the rotation) shows jitter movement, the ascending trend of the Z direction - the direction of the rotational axis - can be interpreted as thermal drift.

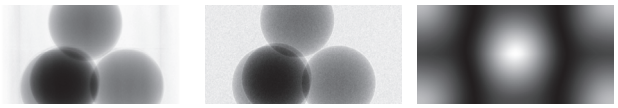

Fig. 5. The three parts of the correction after the beginning of the correction process at iteration 5. In the first row the correlation is processed on the forward projected image. Left: Forward projected image, middle: measured projection, right: cross-correlation.

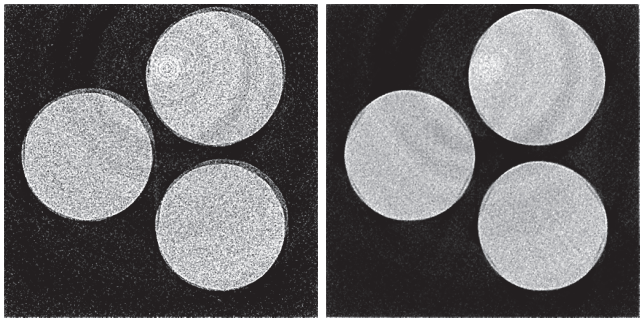

(a) Reconstructed volumes after 50 iterations - XY slice. Left side: without correction, right side: with correction.

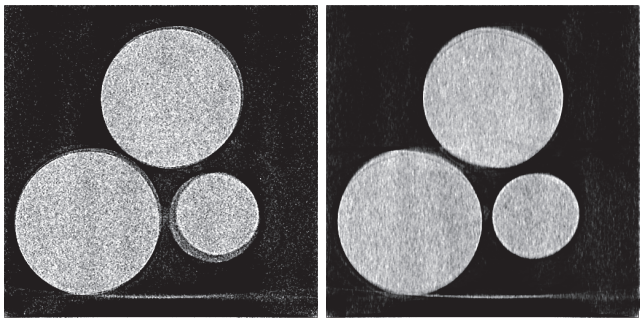

(b) Reconstructed volumes after 50 iterations - XZ slice. Left side: without correction, right side: with correction.

Fig. 6. Reconstructed volumes of the measured datasets.

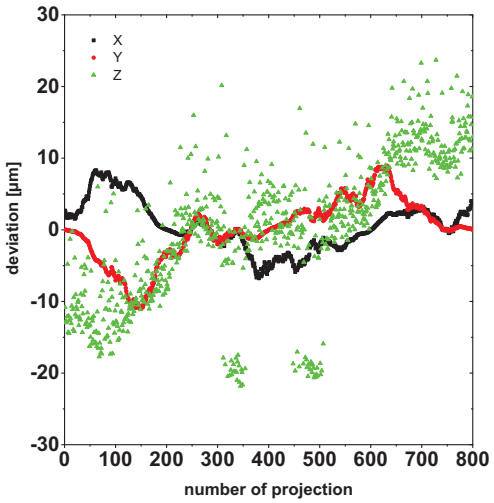

Fig. 7. Deviation of the rotational axis in μm from the originally assumed geometry.

V. Conclusion and future work

The alignment correction using cross-correlation on the projections is a simple and easy-to-use method to correct geometry misalignments in computed tomography. If iterative reconstruction methods are used, this requires nearly no additional computational effort. In the case of projection-dependent alignment problems not only the sharpness of the reconstruction is improved but also the correction data can be used to adjust the setup. Since problems with region-of-interest (ROI) scans appear using the cross-correlation in an iterative approach with FBP, an iterative reconstruction method also gives the chance to improve the convergence of the alignment correction. This behaviour and a quantitative analysis of the resolution-loss will be evaluated in future research.

References

[1] S. Mayo, P. Miller, D. Gao, and J. Sheffield-Parker, "Software image alignment for x-ray microtomography with submicrometre resolution using a sem-based x-ray microscope," *Journal of microscopy*, vol. 228, no. 3, pp. 257–263, 2007.

[2] L. Feldkamp, L. Davis, and J. Kress, "Practical cone-beam algorithm," *JOSA A*, vol. 1, no. 6, pp. 612–619, 1984.

[3] A. Kingston, A. Sakellariou, T. Varslot, G. Myers, and A. Sheppard, "Reliable automatic alignment of tomographic projection data by passive auto-focus," *Medical physics*, vol. 38, no. 9, pp. 4934–4945, 2011.

[4] M. Berger, A. Maier, Y. Xia, J. Hornegger, and R. Fahrig, "Motion compensated fan-beam ct by enforcing fourier properties of the sinogram," in *Proceedings of the Third International Conference on Image Forma-tion in X-Ray Computed Tomography*, 2014.

[5] M. Bartscher, O. Sato, F. Härtig, and U. Neuschaefer-Rube, "Current state of standardization in the field of dimensional computed tomography," *Measurement Science and Technology*, vol. 25, no. 6, p. 064013, 2014.

[6] S. Kasperl, R. Schielein, F. Sukowski, P. Hornberger, and A. Gruber, "Ct simulation study to demonstrate material impact using hole plates," in *11th European Conference on Non-Destructive Testing (ECNDT 2014)*, 2014.

[7] K. Ehrig, M. Bartscher, J. Goebbels, S. Matthias, and A. Staude, "Dimensionelles messen unter phasenkontrast mit synchrotron computertomographie," in *DGZfP-Jahrestagung*, 2010.

Feasibility study on many-view under-sampling(MVUS) using spiral beam filter

Sunhee Wi, Hoyeon Lee, and Seungryong Cho *

***Abstract*—This study was conducted to demonstrate the feasibility of using a new type beam filter for low-dose CT in the many-view under-sampling (MVUS) framework. We have earlier proposed a rotating disk type filter that has open spokes and demonstrated its feasibility of dual-energy imaging at low-dose. In this work, we propose a new rotating disk that has a spiral shaped opening. The spiral MVUS filter is supposed to provide advantages over the spoke-type one in that the x-ray beam divergence angle can be kept constant during the scanning and that the image processing dealing with the penumbra effects would be easier to implement. We have shown in this study that using such a spiral MVUS filter can produce sparsely sampled data for image reconstruction in the compressed sensing theory inspired approach. Sampling density was investigated to optimize the design of the spiral MVUS filter. We also performed a comparative study considering various tube currents and opening rates of the spiral MVUS.**

***Index Terms*—Sparse sampling, many-view under-sampling, MVUS, Low dose CT reconstruction, Spiral beam filter**

I. Introduction

Low-dose imaging capability of a CT system is now becoming a must rather than an option. Lowering x-ray tube current as well as optimizing tube voltage is considered the primary approach to such low-dose CT in the community. Although not actively incorporated in commercialized CT systems yet, sparse sampling approach would also be possibly contributing to the advancement of low-dose technology alone or in combination with the low-tube current method. Sparse view sampling is a straightforward way of sparse sampling and it has shown its potentials in various tasks. However, to our best knowledge, sparse view sampling has not been realized in a fast gantry-based diagnostic CT perhaps due to challenges of preserving stable x-ray output for quite a short pulse duration time. We have earlier proposed a moving beam-blocker-based sparse sampling approach which we named many-view under-sampling (MVUS)[1], and demonstrated its feasibility in cone-beam CT[2, 5] and in diagnostic CT system as well[4]. We have particularly used a rotating disk filter for MVUS which consists of apertures of spokes shape. Through the spoke-type apertures, the x-ray beam is irradiated with its full intensity; the beams are blocked elsewhere. During a gantry motion, the MVUS filter is rotating and creates sparsely sampled x-ray projection data. One critical caveat of the MVUS approach is the sacrifice of the data due to penumbra. A finite focal spot size of the x-ray, a finite thickness of the MVUS filter, and a geometric magnification would lead to an unsharp edge images of the MVUS filter. This penumbra would limit the full use of the data in the entire projection space. Instead, one has to select penumbra-free regions only for image reconstruction. It is desirable if the data in the penumbra regions can be actively utilized, or if it can be minimized unless avoidable. In this work, we propose a new MVUS filter that has a spiral aperture. In order to minimize the effects of penumbra, we propose to place the MVUS filter in front of the x-ray tube such that the fan-beam covers the central portion of the rotating disk. By doing so, one can keep the penumbra shape consistent in the entire field-of-view and can make the projection data processing easier and more efficient. To demonstrate its feasibility for low-dose CT imaging, we have performed a numerical study that includes various combinations of rotation speed and number of apertures in the MVUS filter. Additionally, a hybrid approach to low-dose CT that combines with the low tube current method has been investigated.

Sunhee Wi, Hoyeon Lee and Seungryong Cho are with Department of Nuclear and Quantum engineering, KAIST, Dae-jeon, Korea.
(Telephone: +82 42-350-3868, e-mail: wi5425@kaist.ac.kr, scho@kaist.ac.kr)

II. Methods

A. Spiral filter for many-view under-sampling(MVUS)

A schematic of spiral MVUS filter is shown in Fig 1. On the mid-horizontal line, one pair of opening and blocking regions is called one slit in this work. The ratio of the aperture length to the blocked part is defined by the opening rate of the proposed filter. X-ray fan-beam of a diagnostic CT penetrates through the central horizontal part of the spiral MVUS filter. Sinogram acquired by use of the rotating spiral MVUS filter would show constantly changing blocked region in a straight line fashion with respect to the scan angle as shown in Fig 2. For comparing performances, we have varied the number of slits and also the rotation speed of the MVUS filter per gantry rotation. Table 1 summarizes the parameters in the numerical study. The opening rate was fixed by 20%, which implies about 80% of dose reduction. We have not considered penumbra in the numerical study and it would impair the reduction of dose by a certain factor. Even though the proposed MVUS filter is largely motivated by minimizing the penumbra, we have assumed that such fabrication is feasible and the penumbra effects would thus be minimized.

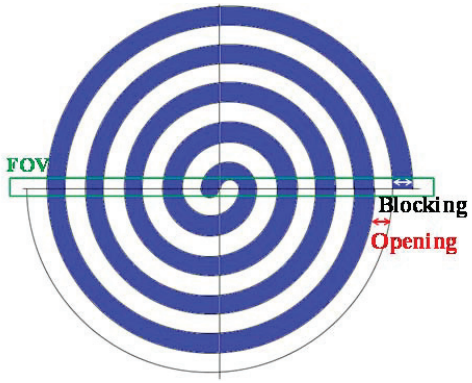

Fig. 1. Spiral beam filter for MVUS technique.

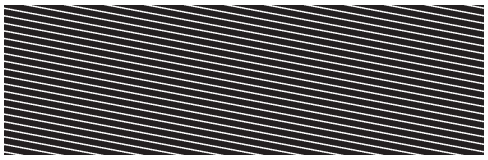

Fig. 2. Sinogram of mid-plane from spiral MVUS.
(# of slits : 12, opening rate : 20)

B. *Sampling density*

Sampling density was calculated to explain the reconstructed image quality from the sampling point of view. It is one of the assessment tools for validating a scanning scheme and represents the sum of weighted intersection lengths of the rays for a given pixel. This metric has been discussed in more detail in Ref. 2.

MVUS technique provides various scanning schemes with different shapes of beam filters and other control parameters. Therefore, sampling density must be considered when deriving an optimal condition. For a linear type MVUS, Abbas *et al* carried out a comparative study between static and moving beam filter[2]. They employed sampling density and data incoherence to analyze the image quality in terms of filter designs.

In this study, sampling density was employed to optimize the spiral MVUS filter.

C. *Numerical simulation*

A low contrast phantom was used for numerical phantom in the simulation study as shown in Fig. 3. For image reconstruction from sparsely sampled data, we employed a projection-onto-convex-sets constrained total variation minimization algorithm(POCS-TV)[3]. Poisson noise and electronic noise(Gaussian noise) were considered to simulate low current projection data. In the first simulation study, we varied the number of slits and rotation speed of spiral MVUS filter while the opening rate was fixed by 20%. After optimizing of the spiral MVUS filter, we considered the quality of reconstructed image from a combination of different x-ray tube current and opening rate of the spiral MVUS filter in the second simulation study. The distance between the source and the object was set to be equal to that between the source and the detector in the simulation study.

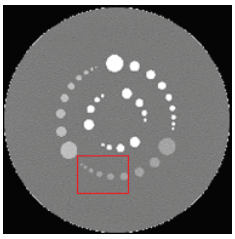

Fig. 3. Selected ROI on numerical low contrast phantom.

TABLE I. CONDITIONS OF DATA ACQUISITION

# of slits	8, 12, 16
Rotation speed	10, 20, 30, 40 rotation/scan
# of projection	720
Source to object [mm]	500
Source to detector [mm]	500
Detector size [mm]	320×1.56

III. RESULTS

A. *Optimization of spiral MVUS*

Spiral MVUS filter produced various 2D sampling density patterns in the image domain depending on the filter parameters as shown in Table 2. Higher rotation speed of the spiral MVUS filter is necessary for higher number of slits. From the results of sampling density calculation, a combination of 8 slits and 30 rotation/scan appears to be the optimal condition for spiral MVUS. One thing to note is that a higher rotation speed is not always preferred as shown in the 8 slits and 40 rotation/scan case.

TABLE Ⅱ. 2D SAMPLING DENSITY DISTRIBUTION DEPENDING ON # OF SLITS AND ROTATION SPEED OF SPIRAL MVUS

Rotation / 1scan	8silts	12silts	16slits
10			
20			
30			
40			

>25.0<32.0

In table 3, reconstructed images show the results corresponding to previous sampling density results. When using 10 rotation speed, we failed to gain any structural information from all kinds of number of slits. For the cases of 12 and 16 slits, higher rotation speed of spiral MVUS provides clearer reconstructed images in the ROI. Higher rotation speed gives more uniform sampling density is thought to lead to a better image quality. Visual inspection and also the image similarity index study (though its results are not shown in this manuscript) confirmed that the combination of 8 slits and 30 rotation speed is optimal.

TABLE Ⅲ.
RECONSTRUCTED IMAGES DEPENDING ON
OF SLITS AND ROTATION SPEED OF SPIRAL MVUS

Rotation / 1scan	8silts	12silts	16slits
10			
20	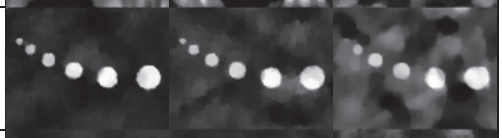		
30			
40	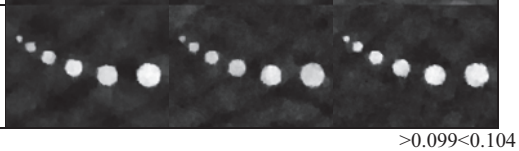		

>0.099<0.104

B. Reconstructed images: mAs-opening rate

A comparative study was also conducted that includes both mAs and opening rate of spiral MVUS. All simulation study employed the optimal conditions of the spiral MVUS filter acquired from the previous study. Reconstructed images in different mAs level and opening rates are summarized in Table 4, 5. Table 5 shows the ROIs of the reconstructed images to better visualize the low-contrast objects.

From the right top to the left bottom, diagonally displayed images are reconstructed under the same dose reduction ratio. 180mAs-20%, 90mAs-40% and 45mAs-60% represent 80% dose reduction ratio of the standard scan that assumes 180mAs-100%. Among the three reconstructed images, the one from 180mAs-20% appears to show highest contrast between white circles and background in the ROI. And smallest white circle is less distorted compared to the ones from other conditions.

For 90% dose reduction ratio, there are four conditions such as 180mAs-10%, 90mAs-20%, 45mAs-40%, and 22.55mAs-60%. In cases of 180mAs-10% and 90mAs-20%, contrasts of the objects seem to be higher than the other two with less image noise. However, the images are relatively more distorted particularly for the smaller ones.

For 95% dose reduction ratio, there are also four conditions available such as 90mAs-10%, 45mAs-20%, 22.5mAs-40%, 11.25mAs-60%. It appears that the condition of 11.25mAs-60% is the best condition overall considering image distortion. For higher dose reduction ratio than 95%, it is hard to decide which condition is better because image distortion is too severe for all the reconstructed images.

In conclusion, we would like to claim that higher mAs and smaller opening rate is preferred for low or intermediate dose reduction and lower mAs and larger opening rate for high dose reduction.

IV. CONCLUSION

We proposed a new type filter for many-view under-sampling technique. Spiral MVUS filter is easy to implement in a diagnostic CT gantry and provides useful data in the sparse sampling context. Our feasibility study examined optimal parameters of the spiral MVUS filter. In addition, from a comparative study, a combination of low tube current and sparse sampling has been investigated in the TV minimization image reconstruction framework.

REFERENCES

[1] S. Cho, T. Lee, J. Min, and H. Chung, "Feasibility study on many-view under-sampling technique for low-dose computed tomography," *Opt. Eng.*, 51(8), p. 080501, 2012.

[2] S. Abbas, T. Lee, S. Shin, R. Lee, and S. Cho, "Effects of sparse sampling schemes on image quality in low-dose CT," *Med. Phys.*, vol. 40, p. 111915, 2012.

[3] E. Y. Sidky, and X. Pan, "Image reconstruction in circular cone-beam computed tomography by constrained, total-variation minimization," *Phys. Med. Biol.*, 53, pp. 4777-4907, 2008.

[4] S. Cho, T. Lee, J. Lee, K. Lee, and D. Kim, "Many-view under-sampling dual-energy low-dose diagnostic CT scan," *Proceedings of Fully 3D conference*, 2015.

[5] T. Lee, S. Abbas, B. Cho, I. Kim, B. Han and S. Cho, "Many-view under-sampling(MVUS) technique for low-dose CT," *Proceedings of IEEE NSS/MIC.*, pp. 3617-3619, 2013

Opening \ mAs	11.25	22.5	45	90	180
10%	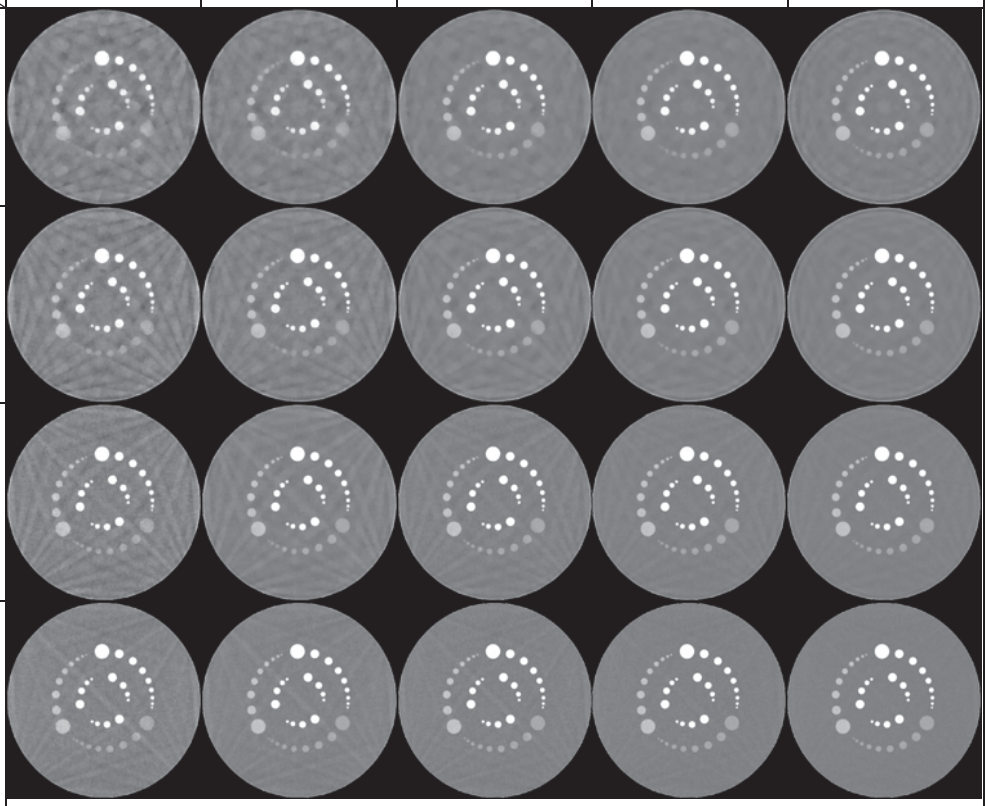				
20%					
40%					
60%					

TABLE Ⅳ. RECONSTRUCTED IMAGES DEPENDING ON MAS AND OPENING RATE >0.09<0.11

Opening \ mAs	11.25	22.5	45	90	180
10%	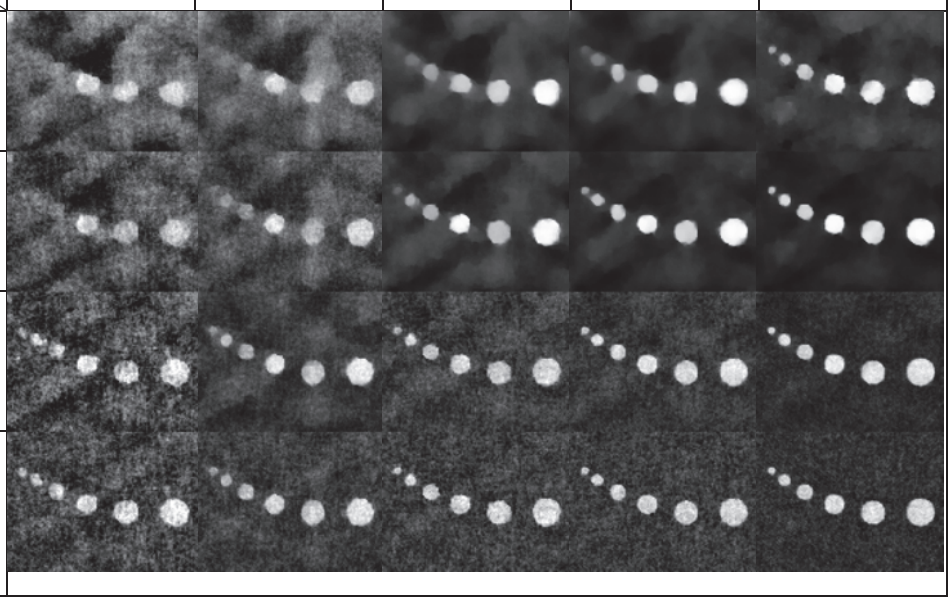				
20%					
40%					
60%					

TABLE Ⅴ. ROIS OF RECONSTRUCTED IMAGES DEPENDING ON MAS AND OPENING RATE >0.099<0.104

Augmented Likelihood Image Reconstruction with Non-local Prior Image Regularization

Maik Stille and Thorsten M. Buzug

***Abstract*—The presence of high-density objects remains an open problem in medical CT imaging. The recently published Augmented Likelihood Image Reconstruction (ALIR) algorithm has shown to outperform current methods for phantom data and real clinical cases of patients with different kinds of metal implants. A variation of the algorithm with an additional non-local prior image based regularization term is proposed. The prior image should hold anatomical information that are similar to the target image. In every iteration of the ALIR algorithm, a new image is calculated based on the given prior image and a registration step. The resulting image is then used to penalize intensity variations. Reconstruction results show that the regularization step improved the reduction of streaking artifacts.**

I. Introduction

Computed tomography (CT) remains one of the key imaging methods in clinical practice. Image quality of reconstructed CT images can be reduced by the occurrence of different artifacts, which are caused by physical phenomena such as scattering, beam hardening, noise, or total absorption. These phenomena can be amplified due to high-density objects such as metal implants or surgical instruments. The resulting streaking artifacts obstruct the assessment of the anatomy of the patient and can reduce the diagnostic value of the images drastically.

In order to reduce metal artifacts a variety of approaches have been proposed in the last decades [1]–[3]. The recently published Augmented Likelihood Image Reconstruction (ALIR) algorithm has shown to outperform current methods for phantom data and real clinical cases of patients with different kinds of metal implants including hip implants, knee implants and amalgam fillings [4]. Due to its iterative reconstruction scheme and the augmented Lagrangian based optimization the algorithm enables a high degree of flexibility. We present an ALIR variation with a prior image based non-local regularization term, which was recently published in [5]. The regularization term penalizes intensity variations between the image to be reconstructed and a prior image. While the prior image holds information from an image that looks similar to the image that is to be reconstructed, the regularization term forces the reconstruction to keep anatomical information of the original image while reducing streaking artifacts.

II. Methods

Given a set of intensity measurements $\{n_i\}_{i=1}^{M}$, the negative log-likelihood function for transmission tomography for statistical image reconstruction is defined as

$$l(f) = \sum_{i=1}^{M} \left(-n_i \ln(n_0) + n_i \sum_{j=1}^{N} a_{ij} f_j + \ln(n_i!) + n_0 \exp(-\sum_{j=1}^{N} a_{ij} f_j) \right) \tag{1}$$

where $f \in \mathbb{R}^N$ is a vector that consists of the expected attenuation coefficients [3]. The number of photons that are detected in the absence of absorption is denoted by n_0, the total number of projections is denoted by M, and the number of pixels in the image is denoted by N.

In order to reconstruct an image without the usage of x-rays that run through a metal object, the set of projections indices $\mathcal{M} = \{1, \ldots, M\}$ can be divided into a set of indices for projections that are not affected by metal, $\mathcal{M}_1$, and a set for projections that are affected by metal, $\mathcal{M}_2$. In ALIR the constant terms in (1) are omitted and only projection indices of x-rays that are not affected by metal are used, which results in

$$\hat{l}_\Lambda(f) = \frac{1}{|\mathcal{M}_1|} \sum_{i \in \mathcal{M}_1} \left(n_i \sum_{j=1}^{N} a_{ij} f_j + n_0 \exp(-\sum_{j=1}^{N} a_{ij} f_j) \right). \tag{2}$$

Furthermore, the ALIR algorithm works with the assumption that prior knowledge in form of shape and known attenuation coefficients of the metal object is available. This knowledge can be gained by an exact computer-aided design (CAD) description of these objects, which can be potentially provided by manufacturers [6]. However, if an exact model of the metal object is not available, the proposed algorithm is able to operate with an approximation of the shape, gained from a segmentation step, combined with arbitrary attenuation coefficients. Let $b \in \mathbb{R}^N$ be a vector that contains attenuation coefficients of the implant and $Q \in [0,1]^{N \times N}$ a diagonal matrix with $q_{ij} = 0$ if $i \neq j$ that represents a mask.

In the ALIR algorithm, the prior knowledge of the metal object is used to introduce the equality constraint

$$c_\Lambda(f) = \frac{\mu}{2} \sum_{j=1}^{N} \left(\frac{q_{jj}(f_j - b_j)}{N} \right)^2 - \sum_{j=1}^{N} \lambda_j \frac{(q_{jj}(f_j - b_j))}{N}, \tag{3}$$

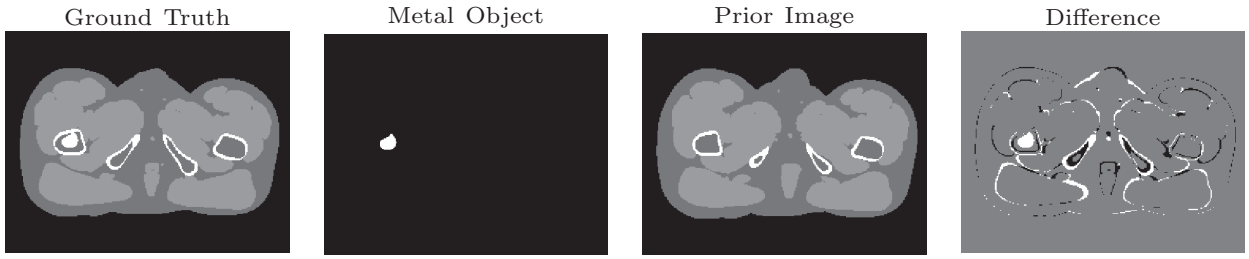

Figure 1. The used XCAT phantom. From left to right: the ground truth image of the image that is be reconstructed, the artificial metal object, the prior image, which is located approx. 2 cm proximal to the first image, and the difference between the prior image and the image that is to be reconstructed.

with the multipliers $\lambda \in \mathbb{R}^n$ and $\mu \in \mathbb{R}$, which is applied in order to assign the given attenuation coefficients to the correct position in the reconstructed image. The objective is formulated as an augmented Lagrangian, which incorporates (3) directly in

$$\Lambda_\zeta(f;\lambda,\mu) = \hat{l}_\Lambda(f) + \zeta c_\Lambda(f) + \gamma R, \tag{4}$$

where γ is a regularization parameter, R is a regularization term and the weighting factor $\zeta > 0$ is introduced in order to control the influence of the constraints in relation to the log-likelihood function [4].

In the course of the algorithm, projection values

$$p_i = \sum_{j=1}^{N} a_{ij} f_j, \qquad i \in \mathcal{M}_2 \tag{5}$$

are replaced by a forward projection of a bilateral filtered version of interim results and the set of all indices $\mathcal{M}$ is used in (2) instead of the set $\mathcal{M}_1$ [4], [7].

For the regularization R the previously proposed non-local prior image regularization is used [5]. The term penalizes intensity variations to a prior image $g \in \mathbb{R}^N$ that should include similar anatomical information as the image f and is defined as

$$R(f,\Gamma(g,\gamma)) = \sqrt{\sum_{x=0}^{N} \delta_x \left(f_x - \frac{1}{\omega_x} \Psi_x(f,\Gamma(g,\gamma)) \right)^2}, \tag{6}$$

with

$$\Psi_x(f,\Gamma(g,\gamma)) = \sum_{y \in \mathcal{N}_x} \Gamma(g_x,\gamma) \exp\left(\frac{-||f_{\eta_x} - \Gamma(g,\gamma)_{\eta_y}||_p}{h^2} \right) \tag{7}$$

where $\Gamma(g,\gamma)$ is the transformed prior image g with the transformation parameter γ [5]. Without loss of generality, an affine transformation is used. The parameters of the transformation result from the optimization problem

$$\mathcal{D}(f^{(k)}, \Gamma(g,\gamma)) \stackrel{!}{=} \min \tag{8}$$

where $\mathcal{D} : \mathbb{R}^{2N} \to \mathbb{R}$ denotes a distance measure. Problem (8) is solved in every iteration of the reconstruction algorithm using the l-BFGS-b algorithm [5], [8]. Within (7) η_x denotes a patch window around pixel x, $\mathcal{N}_x$ denotes a search window around pixel x, and $||\cdot||_p$ denotes the Minkowski distance of order p. Furthermore, $\lambda \in \{0,1\}^N$ is a mask with

$$\delta_x = \begin{cases} 0 & \text{if } g_x = 0 \\ 1 & \text{if } g_x \neq 0 \end{cases}, \tag{9}$$

which forces the regularization to ignore all pixels where the prior image holds no information.

III. Results

In order to investigate the performance of the proposed ALIR algorithm with non-local prior image regularization, a software phantom was generated using the XCAT software [9]. Two different slices were used that are located around the pectoral girdle. In the first slice an artificial metal object was manually added within the left humerus. This slice is used as the target image f. The second slice is located approximately 2 cm proximal to the first slice and is used as the prior image g. Most importantly, the image g shows anatomical differences compared to the image f and contains no metal artifacts nor metal objects as can be seen in figure 1.

For the initialization of the ALIR algorithm a forward-projection of the ground truth image is calculated and all projection values that are affected by the artificial metal object are removed. The description of the metal object in the form of b and Q is gained from a segmentation of the metal object in the ground truth image. Furthermore, the prior image that is seen in figure 1 is used for the regularization, which is given in (6).

After 19 iterations the ALIR algorithm reached convergence. In figure 2 selected interim results are shown together with the calculated prior images $\Psi_x(f,\Gamma(g,\gamma))$. In the course of the reconstruction the each time recalculated prior imaged shows more and more similarity to the image f. After approx. 13 iterations no changes in the new prior image can be observed. However, the regularization ignores pixels that do not hold any information. Therefore, holes in the recalculated prior image are not inherited into the image f.

In figure 3 the final reconstruction results are given for the ALIR algorithm, the ALIR algorithm with non-local prior image regularization and the linear interpolation approach [1]. The amount and severity of streaking artifacts is highest in the reconstruction result of the linear interpolation approach. The ALIR algorithm is able to reduce most of the artifacts and results in a substantially enhanced image. However, the

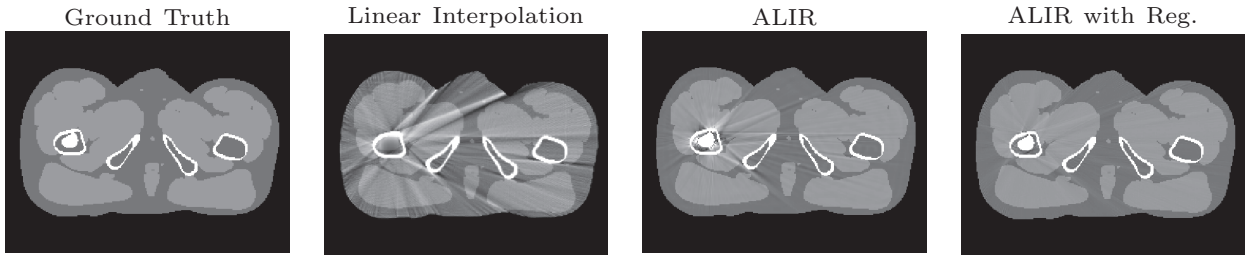

Figure 3. Reconstruction results. From left to right: the ground truth image, the linear interpolation approach, ALIR and ALIR with additional non-local prior image regularization.

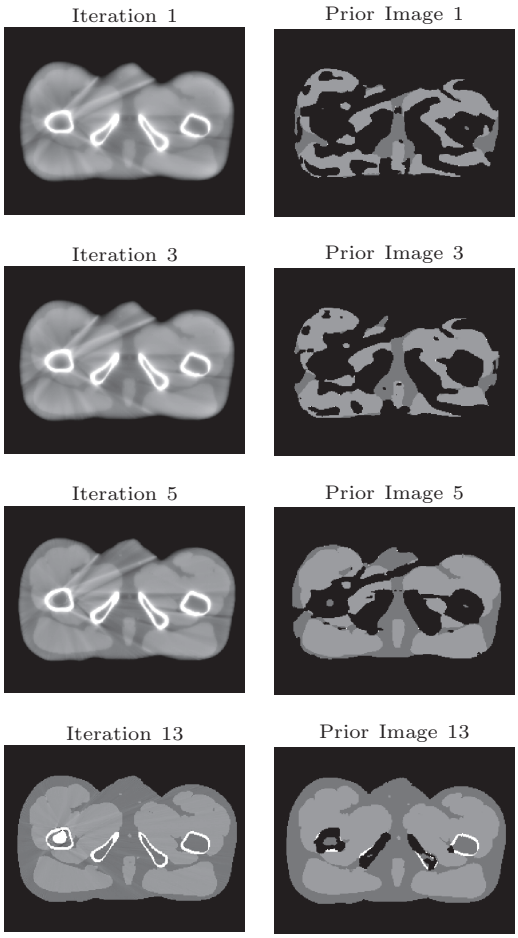

Figure 2. Interim results and the corresponding prior image of the ALIR reconstruction with non-local prior image regularization.

regularization step based on a prior-image is further beneficial for the metal artifact reduction.

In order to confirm the visual impression quantitatively, the sum of squared differences between the ground truth and the result of each reconstruction method is calculated. Table I shows an unambiguous result that the linear interpolation shows clearly the highest error with 1195.9 HU. The ALIR algorithm already shows a much better performance with 134.4 HU. However, an additional non-local prior image regularization reduces the error further to a minimal error of 32.7 HU.

MAR Method	SSD [HU]
linear interpolation	1195.9
ALIR	134.4
ALIR with regularization	32.7

Table I
SUM OF SQUARED DIFFERENCES (SSD) OF DIFFERENT MAR METHODS COMPARED TO GROUND TRUTH. SEE FIGURE 3 FOR THE CORRESPONDING IMAGES.

IV. CONCLUSION

A variation of the Augmented Likelihood Image Reconstruction algorithm with a non-local prior image based regularization is proposed. In every iteration a transformation between intermediate results of the ALIR algorithm and the prior image is found. Based on a non-local approach a new prior image is calculated that is used to penalize intensity variations between the recalculated prior and the image that is to be reconstructed. Reconstruction results show an enhanced artifact reduction compared to ALIR without regularization and the linear interpolation approach. While incorporating information based on a prior image that holds similar anatomical structures, the correct detailed anatomical information of the target image could be reconstructed.

REFERENCES

[1] W. Kalender, R. Hebel, and J. Ebersberger, "Reduction of CT artifacts caused by metallic implants," *Radiology*, vol. 164, no. 2, pp. 576–577, 1987.
[2] B. Kratz, I. Weyers, and T. M. Buzug, "A fully 3D approach for metal artifact reduction in computed tomography," *Medical Physics*, vol. 39, no. 11, p. 7042, 11 2012.
[3] M. Oehler and T. M. Buzug, "Statistical image reconstruction for inconsistent CT projection data," *Methods of Information in Medicine*, vol. 46, no. 3, pp. 261–269, 1 2007.
[4] M. Stille, M. Kleine, J. Haegele, J. Barkhausen, and T. M. Buzug, "Augmented Likelihood Image Reconstruction," *IEEE Transactions on Medical Imaging*, vol. 35, no. 1, pp. 158–173, 7 2015.
[5] M. Stille and M. Thorsten Buzug, "Metal artifact reduction by projection replacements and non-local prior image integration," *Current Directions in Biomedical Engineering*, vol. 1, no. 1, pp. 100–103, 1 2015.
[6] J. W. Stayman, Y. Otake, J. L. Prince, a. J. Khanna, and J. H. Siewerdsen, "Model-based tomographic reconstruction of objects containing known components," *IEEE Transactions on Medical Imaging*, vol. 31, no. 10, pp. 1837–1848, 10 2012.
[7] C. Tomasi and R. Manduchi, "Bilateral filtering for gray and color images," *Sixth International Conference on Computer Vision (IEEE Cat. No.98CH36271)*, pp. 839–846, 1998.

[8] C. Zhu, R. H. Byrd, P. Lu, and J. Nocedal, "Algorithm 778: L-BFGS-B: Fortran subroutines for large-scale bound-constrained optimization," *ACM Transactions on Mathematical Software*, vol. 23, no. 4, pp. 550–560, 1997.

[9] W. P. Segars, M. Mahesh, T. J. Beck, E. C. Frey, and B. M. W. Tsui, "Realistic CT simulation using the 4D XCAT phantom," *Medical physics*, vol. 35, no. 8, pp. 3800–3808, 2008.

A New Scale Space Total Variation Algorithm for Limited Angle Tomography

Yixing Huang*, Oliver Taubmann*‡, Xiaolin Huang*, Viktor Haase§, Guenter Lauritsch† and Andreas Maier*‡
*Pattern Recognition Lab, Friedrich-Alexander-University Erlangen-Nuremberg, Erlangen, Germany
†Siemens Healthcare GmbH, Forchheim, Germany
‡Erlangen Graduate School in Advanced Optical Technologies (SAOT), Erlangen, Germany
§Institute for Signal Processing, University of Luebeck, Luebeck, Germany

Email: yixing.yh.huang@fau.de

***Abstract*—This paper proposes a scale space total variation (ssTV) algorithm to reduce large scale streaks in limited angle tomography. The weighted total variation (wTV) algorithm is able to remove most small scale streaks. However, it fails to reduce larger streaks since total variation (TV) regularization is scale-dependent and may regard them as homogeneous areas. Derived from the wTV algorithm, the proposed ssTV algorithm applies wTV regularization on the image at different scales using down-sampling and up-sampling operations and thus can reduce streaks more effectively. Advantages of the ssTV algorithm are demonstrated on both 2-D numerical data and a 3-D clinical dataset.**

I. Introduction

Limited angle tomography is an essential but challenging task in practical applications of computed tomography (CT). The limited angle problem arises when the gantry rotation is restricted by other system parts or scanning time. Due to data incompleteness, the reconstructed images have severe streak artifacts and obtaining high quality images is difficult.

Researchers have put a lot of effort into suppressing streak artifacts in limited angle reconstruction. One approach is to recover the missing sinogram data in the projection domain based on data consistency conditions like Ludwig-Helgason consistency [1]. In addition, iterative reconstruction with total variation (TV) regularization algorithms [2]–[4] was demonstrated to be effective in limited angle tomography since compressed sensing technologies can use relatively few data to achieve good image quality with the prior assumption that medical images are sparse in the gradient domain.

In the case of limited angle tomography, the shape and orientation of streak artifacts are closely related to the angles missing in the acquisition. With this additional prior information, Chen et al. [5] developed the anisotropic TV (aTV) by assigning different weighting factors to different directions, which shows better performance on edge recovery and streak artifact reduction than the isotropic TV algorithm. However, some structures in the clinical reconstructed image may be blurred due to the staircasing effect [6].

The weighted TV (wTV) algorithm proposed by Candès et al. [7] can help avoid this effect. In our previous work [8], we demonstrated that wTV can reduce noise well while preserving image resolution and contrast in the case of complete data.

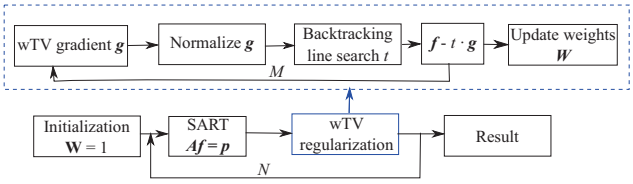

Fig. 1. The wTV algorithm iterates SART and wTV regularization steps alternatively N times in the outer loop. The wTV regularization step repeats the gradient descent process M times as the inner loop.

In the limited angle case, wTV can reduce small streaks well yet is unable to remove large streaks. Due to the scale-dependent property of TV regularization [9], large streaks may be regarded as homogeneous areas and real edges. To enhance homogeneity particularly along the streaks' normal direction, we proposed the weighted anisotropic TV (waTV) algorithm [8] by using four neighboring pixels instead of two to calculate the gradient along that direction. The waTV algorithm showed promising potential in streak reduction. However, it may produce new "zebra crossing"-like artifacts. Besides, it is cumbersome to incorporate anisotropy analytically since new formulas need to be derived for different scales. With the aims of enabling convenient implementation and avoiding zebra crossing artifacts while reducing streaks of various sizes, the scale space TV (ssTV) algorithm is proposed in this paper.

II. Methods

The reconstruction model of the wTV algorithm can be

$$\min_{\boldsymbol{f}} ||\boldsymbol{f}||_{\text{wTV}} \quad \text{subject to} \quad \boldsymbol{A}\boldsymbol{f} = \boldsymbol{p}, \tag{1}$$

where $\boldsymbol{f}$ is the image, $\boldsymbol{A}$ is the system matrix and $\boldsymbol{p}$ is the acquired projection data. Based on Candès et al. [7], $||\boldsymbol{f}||_{\text{wTV}}$ is defined as

$$\begin{aligned} ||\boldsymbol{f}||_{\text{wTV}} &= \sum_{x,y,z} \boldsymbol{W}_{x,y,z} || \left(\mathcal{D}\boldsymbol{f}\right)_{x,y,z} ||, \\ \boldsymbol{W}_{x,y,z} &= \frac{1}{||(\mathcal{D}\boldsymbol{f})_{x,y,z}|| + \epsilon}, \end{aligned} \tag{2}$$

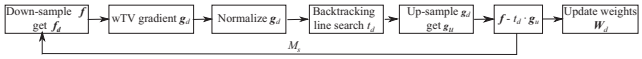

Fig. 2. The ssTV minimization substep down-samples the image $\boldsymbol{f}$ to calculate the down-sampled wTV gradient $\mathbf{g}_d$ and step size t_d, then it uses t_d and the up-sampled $\mathbf{g}_u$ to update the original image $\boldsymbol{f}$.

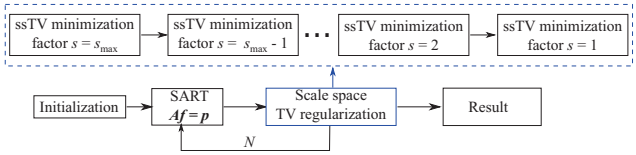

Fig. 3. The ssTV algorithm uses multiple scales during wTV regularization. See Fig. 2 for an overview of the ssTV minimization step.

where $\boldsymbol{W}$ is the weight matrix, $\mathcal{D}\boldsymbol{f}$ is the gradient of $\boldsymbol{f}$, x, y and z are pixel indices and ϵ is a parameter influencing the reconstructed image resolution. The flow chart of the whole algorithm is shown in Fig. 1. The main loop iterates at most N times and each iteration consists of a simultaneous algebraic reconstruction technique (SART) [10] step to increase data fidelity as well as a wTV regularization step. In each wTV regularization step, we regard the weight matrix $\boldsymbol{W}$ as constant for computing the gradient of $||\boldsymbol{f}||_{\text{wTV}}$ with respect to the image to retain a convex problem [7],

$$\boldsymbol{g}_{x,y,z} = \frac{\partial ||\boldsymbol{f}||_{\text{wTV}}}{\partial \boldsymbol{f}_{x,y,z}}, \tag{3}$$

and repeat the gradient descent process M times using backtracking line search algorithm [11]. After that, $\boldsymbol{W}$ is updated.

The effects of conventional TV regularization are often quite local [9]. It mostly reduces small streaks well while larger streaks remain essentially intact. We assume that if we apply TV regularization at various resolutions using a scale-space approach, larger streaks may also be reduced well. This is the main idea of our proposed ssTV algorithm.

Fig. 2 is an ssTV minimization substep. It first down-samples the image $\boldsymbol{f}$ with a certain scaling factor s to calculate the down-sampled wTV gradient $\mathbf{g}_d$ and find a suitable step size t_d to make sure that the TV value of $\boldsymbol{f}_d - t_d \cdot \mathbf{g}_d$ is decreased. With the down-sampling operation, the scale of the streaks is decreased relative to the spatial gradient computation used in TV. Then $\mathbf{g}_d$ is up-sampled with the same scaling factor s to get $\mathbf{g}_u$, which means that the scale of TV regularization effects are increased. Finally, with t_d and $\mathbf{g}_u$ the original scale image $\boldsymbol{f}$ can be updated as $\boldsymbol{f} - t_d \cdot \mathbf{g}_u$. The above process is repeated M_s times, then the corresponding weight matrix $\boldsymbol{W}_d$ is updated.

In limited angle tomography, orientations of streaks can be aligned with a coordinate axis, e.g. the X-axis, if we choose a proper corresponding scan angle range 10° - 170° (Fig. 4) such that anisotropic scaling along Y direction can be performed.

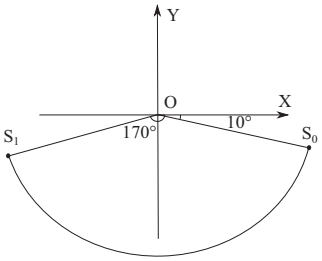

Fig. 4. Scan trajectory.

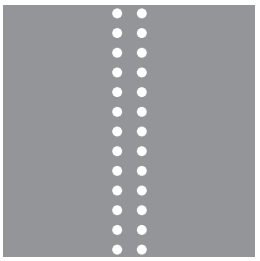

Fig. 5. Numerical phantom, window: [-240 240] HU.

The down-sampling and up-sampling operations with a scaling factor $s > 1$ are defined as

$$\begin{aligned}
\boldsymbol{f'}_{x,y,z} &= \sum_{j=-L}^{j=L} \boldsymbol{h}_{j+L} \boldsymbol{f}_{x,y+j,z}, \\
(\boldsymbol{f}_d)_{x,y,z} &= \left(\sum_{j=0}^{j=s-1} \boldsymbol{f'}_{x,s\cdot y+j,z} \right) / s, \\
\boldsymbol{f}_{x,s\cdot y+j,z} &= \left((\boldsymbol{f}_d)_{x,y,z} \cdot (s-j) + (\boldsymbol{f}_d)_{x,y+1,z} \cdot j \right) / s, \\
& \quad j = 0, 1, ..., s-1,
\end{aligned} \tag{4}$$

where $\boldsymbol{h}$ is a 1-D Gaussian filter kernel with length $2L+1$ and standard deviation $\sigma = s/2$ to avoid aliasing and $\boldsymbol{f'}$ is the filtered image.

As regularization on a single scale is most sensitive to artifacts of a specific spatial extent, we perform it in scale space, i.e. on several scales, $s = s_{\max}, s_{\max} - 1, ..., 2, 1$ with increasing resolution (Fig. 3), where $s_{\max}$ is the maximum scaling factor. In this way, both noise and streaks of various sizes can be reduced. Note that ssTV minimization with $s = 1$ is the regular wTV minimization.

III. EXPERIMENTS

A. Numerical Phantom

In order to validate the advantage of our proposed ssTV algorithm in reducing large streaks, a 2-D numerical phantom is designed (Fig. 5). It contains two columns of circular areas (radius = 10 mm). The attenuation coefficient for the circular areas is 1200 HU while the background is 0 HU. The phantom size is 512×512 pixels and the pixel size is 1 mm. Regarding the acquisition parameters, the scan angle from 10° to 170° is chosen such that most streaks are almost in the horizontal direction. The detector size is 768 pixels and the pixel size is 1 mm. The source to detector distance is $d = 2175$ mm, the fan angle is $\gamma_{\max} = 20^\circ$ and the angular increment is 1°. The whole experimental setup, including generation of the phantoms, is implemented in CONRAD [12].

The ssTV algorithm and the regular wTV algorithm are employed to reconstruct this phantom from limited angle data. For wTV, we choose $M = 10$ heuristically. Consequently, for ssTV, the same number of TV minimization steps should be applied, i.e. $\sum_{s=1}^{\infty} M_s = M = 10$. With this constraint, combinations of different scaling factors are investigated as

follows: $[M_1, M_2, M_3, M_4, M_5]$ = [2, 8, 0, 0, 0], [2, 4, 4, 0, 0], [2, 2, 2, 4, 0] and [2, 2, 2, 2, 2]. Besides, ssTV with $s = 2$ only, i.e. $[M_1, M_2, M_3, M_4, M_5]$ = [0, 10, 0, 0, 0], is also investigated as a control.

All images, including clinical data described below, are reconstructed with $\epsilon = 0.001$ in Eqn. 2. The reconstruction algorithms stop when they reach the termination criteria $\sigma < 8.0 \cdot 10^{-3}$ HU or $n = 400$, where σ is the root-mean-square difference of two consecutive iteration results and n is the iteration number.

B. Clinical Data

The algorithms are also compared in a 3-D clinical head dataset acquired with a Siemens Artis zee angiographic C-arm system (Siemens Healthcare GmbH, Forchheim, Germany). The detector size is 1240×960 and the detector pixel size is 0.308 mm. The complete data contains 496 projections obtained in a 200° short scan. We simulate a limited angle acquisition with a scan angle from 10° to 170° where only the projections 25 through 422 are used. The reconstruction image grid size is $512 \times 512 \times 256$, and the pixel sizes are 0.4 mm, 0.4 mm and 0.8 mm in X, Y and Z direction, respectively.

We first use the wTV algorithm to reconstruct the complete data as an image quality reference. Then, wTV and ssTV are applied to the limited angle data. In [8], we determined that it is beneficial to apply 30 iterations of SART first as initialization, then 50 additional iterations of wTV or ssTV are applied.

IV. Results And Discussion

The reconstruction results of the numerical phantom and their root-mean-square errors (RMSE) are shown in Fig. 6. Large streaks still exist in the wTV reconstruction result (Fig. 6(a)) while they are reduced by ssTV with $s = 2$ (Fig. 6(b)). However, ssTV with scaling factor 2 only is unable to reduce high frequency noise. In contrast, ssTV with $s_{\max} = 2$ (Fig. 6(c)) and $s_{\max} = 3$ (Fig. 6(d)) can reduce both large streaks and high frequency noise effectively. Fig. 7 also demonstrates that combinations of multiple scaling factors (curves C, D, E and F) converge faster than wTV (curve A) while using scale 2 only (curve B) is insufficient.

The reference images reconstructed from the complete clinical dataset with wTV are shown in Fig. 8. Image results of SART, wTV and ssTV for limited angle tomography are shown in Fig. 9. Compared to SART (Figs. 9(a) and 9(b)), wTV shows its advantage in reducing small streaks and high frequency noise since the bony structures and the brain textures are preserved much better. However, severe large streaks still remain in the wTV results (Figs. 9(c) and 9(d)). The proposed ssTV algorithm with $s = 2$ only can reduce large streaks better than wTV. However, Fig. 9(f) shows that it suffers from severe high frequency noise like the SART result and thus the brain texture is obscured. This confirms that combining various scaling factors is beneficial for reducing noise and streaks of various sizes. Figs. 9(g) - (j) illustrate that ssTV with $s_{\max} \geq 2$ can reduce large streaks more effectively while high frequency noise is also removed.

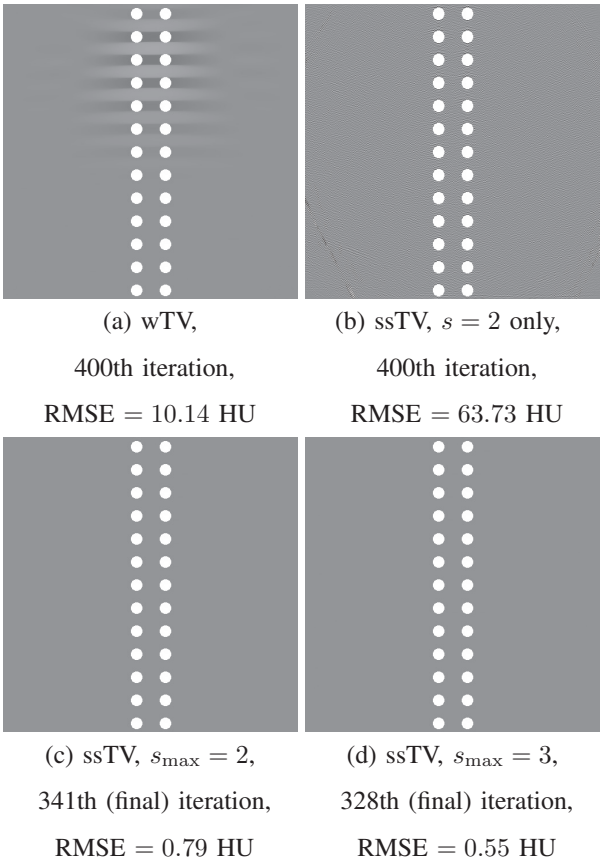

(a) wTV, 400th iteration, RMSE = 10.14 HU

(b) ssTV, $s = 2$ only, 400th iteration, RMSE = 63.73 HU

(c) ssTV, $s_{\max} = 2$, 341th (final) iteration, RMSE = 0.79 HU

(d) ssTV, $s_{\max} = 3$, 328th (final) iteration, RMSE = 0.55 HU

Fig. 6. Comparison of wTV, ssTV with $s = 2$ only, $s_{\max} = 2$ and $s_{\max} = 3$, windowing: [-240 240] HU, (a) $M = 10$, (b) $[M_1, M_2] = [0, 10]$, (c) $[M_1, M2] = [2, 8]$, (d) $[M_1, M_2, M_3] = [2, 4, 4]$.

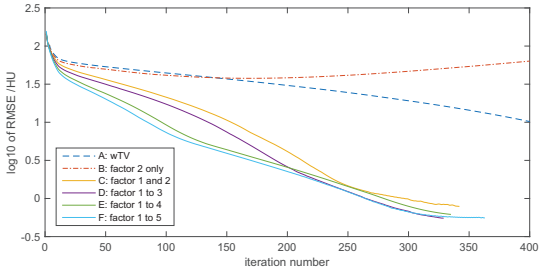

Fig. 7. Comparison of different scaling factor combinations, $M = 10$ for A, $[M_1, M_2, M_3, M_4, M_5]$ =[0, 10, 0, 0, 0], [2, 8, 0, 0, 0], [2, 4, 4, 0, 0], [2, 2, 2, 4, 0] and [2, 2, 2, 2, 2] for B, C, D, E and F, respectively.

V. Conclusion

In this paper, we proposed the ssTV algorithm for streak reduction in limited angle tomography. From the experiments above, we conclude that the ssTV algorithm with various scaling factors converges faster and reduces large streaks better than wTV. It is convenient to implement based on an existing

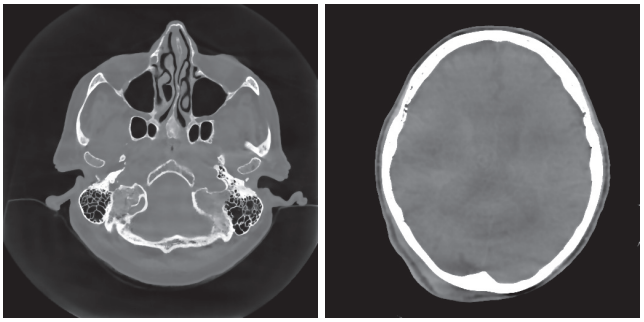

(a) wTV, 65th slice (b) wTV, 140th slice

Fig. 8. Reference images reconstructed from the complete clinical dataset with the wTV algorithm. Windowing: [-1000 1730] HU for (a) and [-220 365] HU for (b).

wTV implementation as it only introduces additional down-sampling and up-sampling operations.

Disclaimer: The concepts and information presented in this paper are based on research and are not commercially available.

REFERENCES

[1] J. L. Prince and A. S. Willsky, "Constrained sinogram restoration for limited-angle tomography," *Optical Engineering*, vol. 29, no. 5, pp. 535–544, 1990.

[2] M. T. Manhart, M. Kowarschik, A. Fieselmann, Y. Deuerling-Zheng, K. Royalty, A. K. Maier, and J. Hornegger, "Dynamic iterative reconstruction for interventional 4-D C-arm CT perfusion imaging," *Medical Imaging, IEEE Transactions on*, vol. 32, no. 7, pp. 1336–1348, 2013.

[3] H. Wu, A. Maier, R. Fahrig, and J. Hornegger, "Spatial-temporal total variation regularization (STTVR) for 4D-CT reconstruction," in *Proc of SPIE*, vol. 8313, 2012.

[4] E. Sidky, C. Kao, and X. Pan, "Accurate image reconstruction from few-views and limited-angle data in divergent-beam CT," *Journal of X-ray science and technology*, vol. 14, pp. 119–139, 2006.

[5] Z. Chen, X. Jin, L. Li, and G. Wang, "A limited-angle CT reconstruction method based on anisotropic TV minimization," *Physics in medicine and biology*, vol. 58, no. 7, pp. 2119–2141, 2013.

[6] V. Y. Panin, G. L. Zeng, and G. T. Gullberg, "Total variation regulated EM algorithm," *Nuclear Science, IEEE Transactions on*, vol. 46, pp. 2202 – 2210, 1999.

[7] E. Candès, M. Wakin, and S. Boyd, "Enhancing sparsity by reweighted l_1 minimization," *The journal of fourier analysis and applications*, vol. 14, pp. 877–905, 2008.

[8] Y. Huang, O. Taubmann, X. Huang, V. Haase, G. Lauritsch, and A. Maier, "A new weighted anisotropic total variation algorithm for limited angle tomography," in *International Symposium on Biomedical Imaging*. IEEE, 2016, to appear.

[9] D. Strong and T. Chan, "Edge-preserving and scale-dependent properties of total variation regularization," *Inverse Problems*, vol. 19, no. 6, p. S165, 2003.

[10] L. Ritschl, F. Bergner, C. Fleischmann, and M. Kachelriess, "Improved total variation-based CT image reconstruction applied to clinical data," *Physics in medicine and biology*, vol. 56, no. 6, pp. 1545–1561, 2011.

[11] S. Boyd and L. Vandenberghe, *Convex Optimization*. Cambridge University Press, 2004.

[12] A. Maier, H. Hofmann, M. Berger, P. Fischer, C. Schwemmer, H. Wu, K. Müller, J. Hornegger, J. Choi, C. Riess, A. Keil, and R. Fahrig, "CONRAD - a software framework for cone-beam imaging in radiology," *Medical physics*, vol. 40, no. 11, p. 111914, 2013.

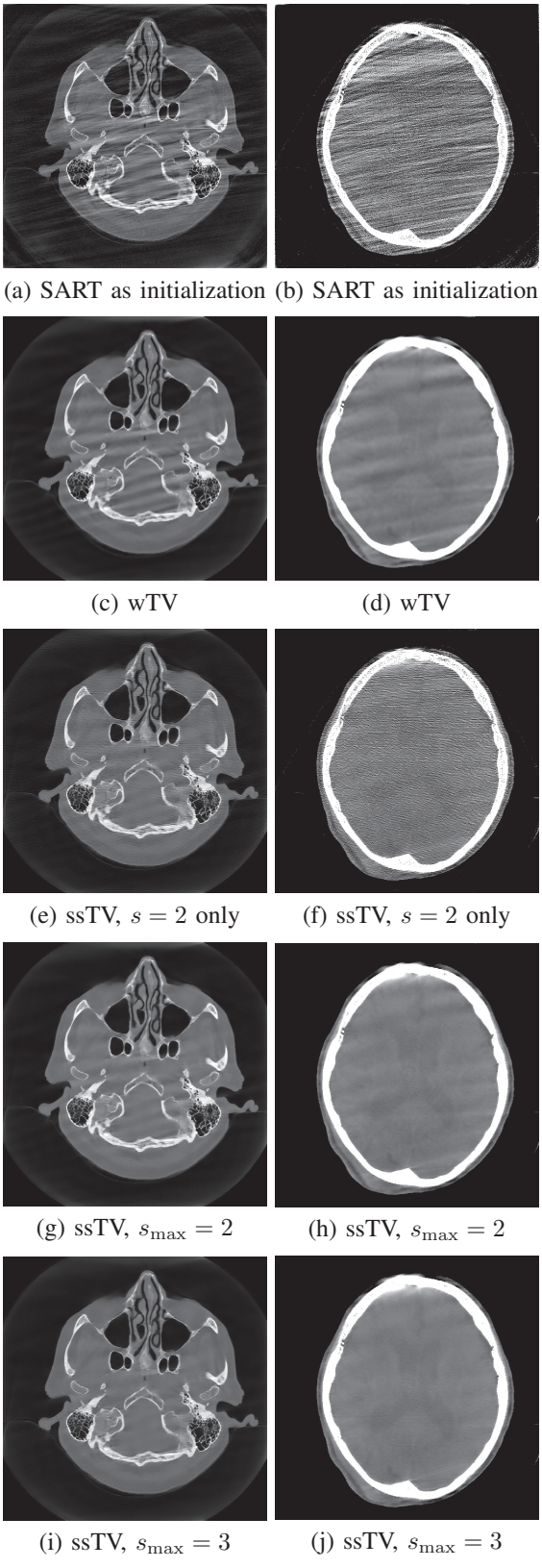

(a) SART as initialization (b) SART as initialization

(c) wTV (d) wTV

(e) ssTV, $s = 2$ only (f) ssTV, $s = 2$ only

(g) ssTV, $s_{\max} = 2$ (h) ssTV, $s_{\max} = 2$

(i) ssTV, $s_{\max} = 3$ (j) ssTV, $s_{\max} = 3$

Fig. 9. Comparison of SART, wTV, ssTV with $s = 2$ only and $s_{\max} = 2, 3$ in limited angle tomography, $M = 10$ for wTV, $[M_1, M_2, M3] = [0, 10, 0]$, $[2, 8, 0]$ and $[2, 4, 4]$ for ssTV with $s = 2$ only, $s_{\max} = 2$ and $s_{\max} = 3$, respectively. Windowing: [-1000 1730] HU for the left images, [-220 365] HU for the right images.

CNR improvement in a sparse-view cone-beam computed tomography using an anti-scatter grid

Sanghoon Cho, and Seungryong Cho

***Abstract*—Anti-scatter grids are known to suppress the scatter significantly thus improving contrast of image in radiography. However, its use in cone-beam CT for the purpose of improving contrast-to-noise ratio (CNR) has not been successful mainly due to increased noise related to Poisson statistics of photons. This paper proposes a sparse view cone-beam CT with the use of an anti-scatter grid to improve CNR. Compared to the conventional method, the proposed method reduces the number of projections and increases exposure in one projection to enhance image quality in terms of CNR without an additional cost of radiation dose. For image reconstruction from sparse-view data, a total-variation minimization algorithm was adopted. We conducted both simulation study and experiment to compare the resulting images by the conventional and the proposed methods quantitatively. The results showed that contrast and CNR by the proposed method have increased compared to the conventional method at the same total radiation dose condition and that the cupping artifact has been reduced as well. The proposed method can provide high quality image by using an anti-scatter grid with no additional radiation dose to the patient.**

***Index Terms*—Anti-scatter grid, contrast, CNR, cupping artifacts**

I. Introduction

In x-ray cone-beam CT (CBCT) imaging, scatter is a physical process which constitutes a critical factor for degrading image contrast. It has been under our research interest that clinicians' demand for image quality particularly including contrast in such as prostate imaging or brain imaging is high compared to the ones that are available in commercial CBCT systems. There have been a host of correction approaches in CBCT with varying degrees of success. Using an anti-scatter grid is one of the methods that directly suppresses scatter recorded in the detector thus improving contrast in radiography. Anti-scatter grids are usually composed of Pb strips at regular intervals that are filled with interspacer. However, its use in CBCT has not been successful in increasing the contrast-to-noise ratio (CNR) mainly because the noise related to the Poisson statistics of photons is increased while contrast is improved as well.

The influence of an anti-scatter grid in CBCT on image quality has been systematically studied and turns out to be rather ineffective in improving CNR in the filtered-backprojection (FBP) algorithm framework for image reconstruction. Siewerdsen et al. (2004) reported that the motivation of using grids in CBCT is not so strong in that regards [1]. When using high resolution detectors, Singh and Jain (2014) reported that, even in radiography, there is little improvement of CNR because of nonnegligible physical dimension of the grids [2]. The study on the case of C-arm CBCT showed similar results. Schafer and Stayman (2012) found that using an anti-scatter grid in C-arm CBCT would need a dose increment to reinstate a CNR level gained in a gridless case [3]. It appears that an additional radiation dose is inevitable in CBCT with a grid system to increase image CNR. However, it should be also noted that such discussions have been based on the FBP image reconstruction framework.

The purpose of the study was to demonstrate a CNR improvement is feasible when an anti-scatter grid is used in CBCR by reducing the number of projections and increasing the exposure in each projection to suppress noise, thereby retaining the total dose, in the iterative image reconstruction framework that is inspired by compressed sensing theory. A total-variation minimization algorithm was employed for image reconstruction from sparse-view data [4-6]. Although a further evaluation study comparing with existing scatter correction approaches is necessary, the proposed method showed a promising solution to the CBCT applications that require high quality images of low-contrast anatomy.

II. Methods and Materials

A. Simulation study

We carried out a simulation study to test a feasibility of the proposed method. Projections of the XCAT phantom were taken at 720- and 120- views, the formers of which incorporate larger amount of scatter and more noise compared to the latters that simulate the use of an anti-scatter grid. The full-view data (720-views) have been fed into the FBP algorithm for image reconstruction, and the sparse-view data (120-views) into the TV algorithm. CNR analysis has been performed on both images.

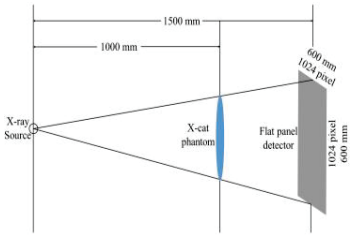

Figure 1. Simulation geometry.

Sanghoon Cho and Seungryong Cho are with the Nuclear and Quantum Engineering Department, Korea Advanced Institute of Science and Technology, Daejeon, South Korea (e-mail: shcho26@kaist.ac.kr, scho@kaist.ac.kr).

Table 1. Simulation condition.

Conventional method	Proposed method
- Full view (720)	- Sparse view (120)
- Poisson noise	- Poisson noise
- Scatter contaminated	- Scatter reduced
- FBP reconstruction algorithm	- Total-Variation minimization reconstruction algorithm

B. Experiment

We conducted experiments using a prototype CBCT system as shown in Fig. 2, and the specifications of an anti-scatter grid used for experiments are summarized in Table 2. The grid is composed of lead strips in 200 lines per inch.

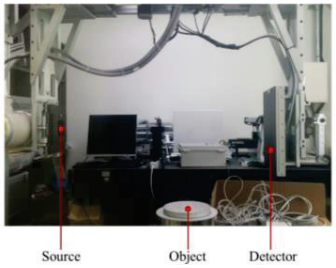

Figure 2. Experiment system.

Table 2. Specification of anti-scatter grid for experiment.

Spec of anti-scatter grid
- Type: converging to source (2D grid)
- Size: 337 × 328 mm
- Lines/Inch: 200
- Ratio: 10:1
- Material Absorber (strip): Pb Interspacer: Al

First, we conducted an experiment using a multi-slit blocker made of lead to see whether the anti-scatter grid we used is functioning as much as we expect. By using a multi-slit beam-blocker in between the x-ray source and the imaged object, one can create scatter signals only in the shadow regions of the beam-blocker in the detector. If the anti-scatter grid suppresses those scattered signals, one would expect to see practically null signals down to the dark current levels in the shadow. We compared the signals of the shadows in a grid case and a gridless case as shown in Fig. 3 to assess the performance of the anti-scatter grid used.

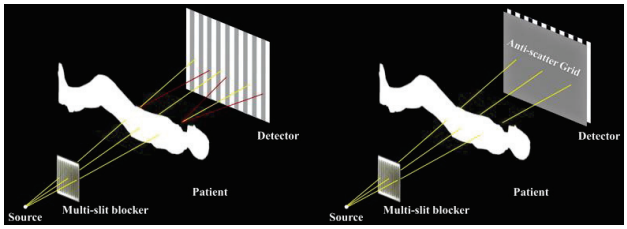

Figure 3. Grid assessment using beam blocker.

Head phantom as shown in Fig. 4 was used for the experiment. For the gridless case, the tube voltage of 100kVp and the tube current of 10mA were used; and for the grid case, 100kVp and 20mA were employed. Then, the two resulting projection images were quantitatively analyzed.

Figure 4. Head phantom and multi-slit blocker.

Second, the water equivalent CATPhan phantom was used for the experiment to see the cupping artifact reduction by using the proposed method. As shown in Table 3, in the conventional method, 600 projections without an anti-scatter grid were taken for 360° scan with the X-ray source of 105 kVp with 10 mA, and FBP algorithm was used for image reconstruction [7]. Whereas, in the proposed method, 300 projections with an anti-scatter grid were taken for 360° scan with the X-ray source of 105 kVp with 20 mA, and TV algorithm was used for image reconstruction [4]. Then, cupping artifact degree was analyzed quantitatively.

Figure 5. Water equivalent CATPhan phantom.

Table 3. Experiment condition.

Conventional method	Proposed method
- Without a grid	- With a grid
- 600 view (360° scan)	- 300 view (360° scan)
- 105 kVp, 10 mA	- 105 kVp, 20 mA

- Feldkamp, Davis, and Kress (FDK) reconstruction algorithm	- Total-Variation minimization reconstruction algorithm

Third, as shown in Fig. 6, the contrast resolution CATPhan phantom was used for comparing the resultant images of conventional method and proposed method. The experiment conditions were the same with those summarized in Table 3. After image reconstruction, Contrast, CNR, and magnitude of cupping artifact were analyzed quantitatively.

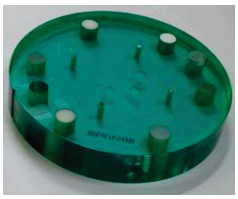

Figure 6. Resolution CATPhan phantom.

C. Contrast, CNR, and $t_{cup}(\%)$

Metrics of *Contrast*, *CNR*, and $t_{cup}(\%)$ were used for image analysis. Eq. (1) represents a contrast where n_1 and n_2 represent a signal and background, respectively.

$$contrast = \frac{mean(n1) - mean(n2)}{mean(n2)} \tag{1}$$

Similarly, Eq. (2) represents *CNR* where n_1 and n_2 represent two different signals, and *standard deviation(n)* represents a standard deviation of *n2*.

$$CNR = \frac{mean(n1) - mean(n2)}{standard\ deviation(n2)} \tag{2}$$

Lastly, as is defined in Eq. (3), $t_{cup}(\%)$ represents the magnitude of the cupping artifact, where $\bar{\mu}$ represents average value of the attenuation coefficients on edge and center region.

$$t_{cup}(\%) = 100 \times \frac{\bar{\mu}_{edge} - \bar{\mu}_{center}}{\bar{\mu}_{edge}} \tag{3}$$

III. Results

A. Simulation study

Fig. 7 represents tomographic images using (a) a conventional method, and (b) a proposed method. Fig. 8 shows the midline profiles of image (a) in Fig. 6 as a black straight line, and image (b) in Fig. 6 as a blue dot line. As seen in the figures, cupping artifacts has been enhanced and contrast has increased evidently. Quantitatively, contrast has been increased by a factor of 1.50.

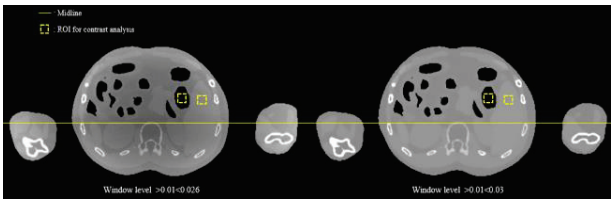

Figure 7. Reconstruction images of (a) conventional method, and (b) proposed method.

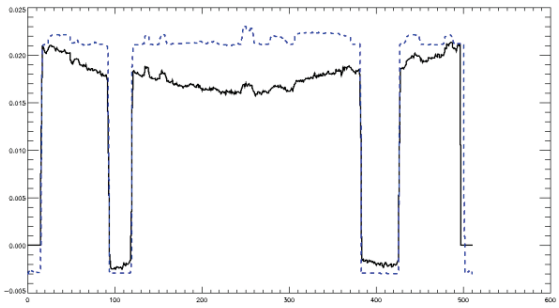

Figure 8. Midline profiles of reconstruction images using (a) conventional method (black straight line), and (b) proposed method (blue dot line).

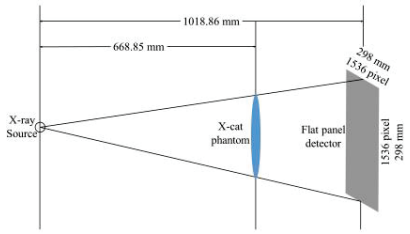

Figure 9. Experiment geometry

B. Experiment

All experiments were conducted under the condition in Fig. 9. Fig. 10 represents images (a) without a grid, and (b) with a grid. As shown in the figures, black and white pattern appears more clearly when using a grid. Midline profiles of the images are shown in Fig. 11. Quantitatively, contrast has been increased by a factor of 1.87.

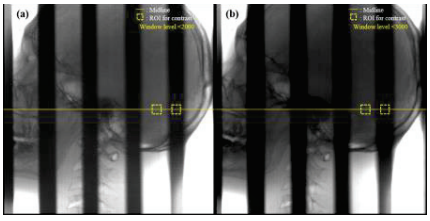

Figure 10. Projection images with (a) without a grid, and (b) with a grid.

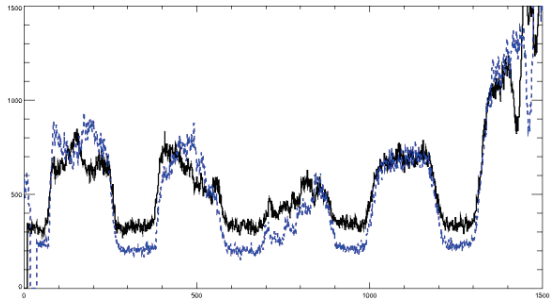

Figure 11. Midline profiles of projection images (a) without a grid (black straight line), and (b) with a grid (blue dot line).

Fig. 12 represents tomographic images of water equivalent catphan phantom using (a) a conventional method, and (b) a proposed method. Fig. 13 shows midline profiles of image (a) in Fig. 12 as a black straight line, and image (b) in Fig. 12 as a blue dot line. As seen in the figures, cupping artifacts has been enhanced evidently. Quantitatively, image (a) in Fig. 12 has higher t_{cup}(%) value than (b) by a factor of 2.12.

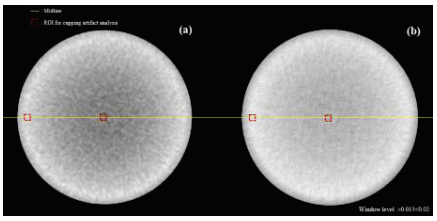

Figure 12. Reconstruction images of (a) conventional method, and (b) proposed method.

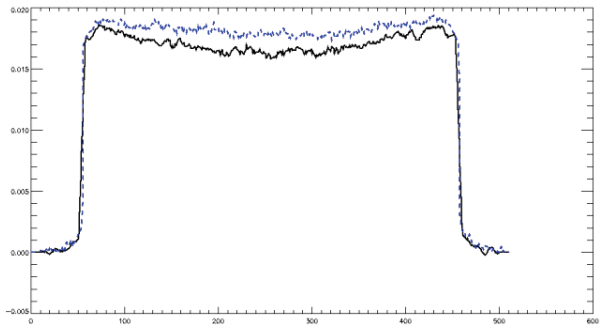

Figure 13. Midline profiles of reconstruction images using (a) conventional method (black straight line), and (b) proposed method (blue dot line).

Fig. 14 represents tomographic images of resolution catphan phantom using (a) a conventional method, and (b) a proposed method. Fig. 15 shows midline profiles of image (a) in Fig. 14 as a black straight line, and image (b) in Fig. 14 as a blue dot line. Quantitatively, contrast has been increased by a factor of 1.28, and CNR has been increased by a factor of 1.13. Also, image (a) in Fig. 14 has higher t_{cup}(%) value than (b) by a factor of 1.46.

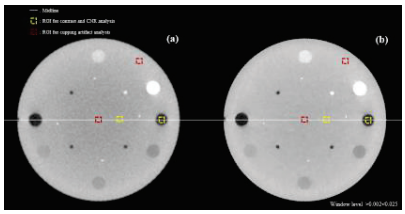

Figure 14. Reconstruction images of (a) conventional method, and (b) proposed method.

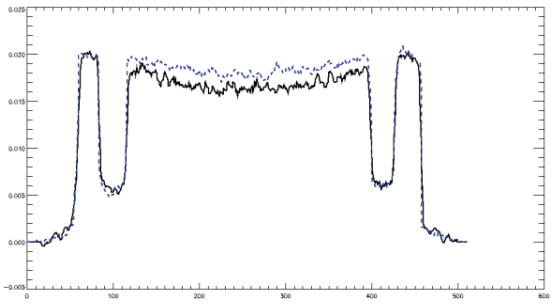

Figure 15. Midline profiles of reconstruction images using (a) conventional method (black straight line), and (b) proposed method (blue dot line).

IV. Conclusion

We proposed the method of sparse view cone-beam CT with the use of an anti-scatter grid to improve CNR without additional radiation dose to the patient. The results from simulation study and experiments have shown that by using proposed method, contrast and CNR have increased and the magnitude of cupping artifacts decreased compared to the conventional method.

V. References

[1] J. H. Siewerdsen, "The influence of antiscatter grids on soft-tissue detectability in con-beam computed tomography with flat panel detectors", Med.Phys., 2004, pp. 3506-3520.

[2] V. Singh (2014 March 19), "Limitations of anti-scatter grids when used with high resolution image detectors", SPIE, p. 903362-.

[3] S. Schafer, "Antiscatter grids in mobile C-arm cone-beam CT: Effect on image quality and dose", Med.Phys., 2012, pp. 153-159.

[4] Emil Y Sidky, "Image reconstruction in circular cone-beam computed tomography by constrained, total-variation minimization", Phys.Med.Biol., 2008, pp. 4777-4807.

[5] Sajid Abbas, "Super-sparsely view-sampled cone-beam CT by incorporating prior data", Journal of X-Ray Science and Technolohy, 2013, pp. 71-83.

[6] Sajid Abbas, "Effects of sparse sampling schemes on image quality in low-dose CT", Med.Phy., 2013, 111915.

[7] Avinash C. Kak, "Principles of Computerized Tomographic Imaging", NY: IEEE Press, 198

Model-Based Dose Reconstruction for CT Dose Estimation

Mingye Wu, Bruno De Man, Zhye Yin

***Abstract*—We present an improved real-time, patient-specific dose reconstruction algorithm for CT based on improved physics modeling. The new algorithm more accurately models the variation of materials in the human body, especially for higher attenuation materials such as bone. We performed validation experiments with analytic phantoms and a polychromatic X-ray spectrum. We used Monte Carlo simulation (GEANT4) as the ground truth. The results show that the proposed method has improved accuracy in both soft tissue region and bone region: less than 6% voxel-wise errors and less than 3.2% ROI-based errors. Since the computational cost is on the order of a low-resolution filtered backprojection reconstruction, the proposed algorithm could potentially be used for real-time applications such as patient and organ specific scan planning and organ dose reporting.**

***Index Terms*—Computed Tomography, radiation dose estimation**

I. Introduction

Computed tomography (CT) has become one of the most widely used diagnostic tools in medicine. At the same time, CT radiation dose has become an important concern and an area of intense research and development. Some recent dose reduction methods target patient-specific, organ-based dose optimization and hence fast, accurate and volumetric dose estimation is in demand.

Dose estimation using Monte Carlo simulation can be very accurate [1] but it is inherently computationally expensive. Analytic, model-based methods often have larger errors since they don't fully incorporate the complexity of the human anatomy and the X-ray spectrum. We previously proposed a fast dose reconstruction algorithm based on a backprojection framework and we demonstrated good accuracy in soft tissue region (error < 10%) but larger error in bone regions (sometimes exceeding 50%) [2].

In this paper, we propose an improved dose reconstruction method, more accurately modeling the variation of materials in the human body, especially for higher attenuation materials such as bone. The proposed method has three steps:

1) Compute the first order interaction energy using a ray tracing method
2) Separate the interaction energy into the absorbed and scattered energy
3) Distribute the scattered energy by convolution with a tuned scatter kernel and multiplying by an absorption map.

Section II gives a detailed description of the methods. Section III contains the results and discussion of the validation experiments.

Mingye Wu is with X-ray and CT Laboratory, GE Global Research, Shanghai, 201203, China (e-mail: Mingye.Wu@ge.com).

Bruno De Man and Zhye Yin are with Image Reconstruction Laboratory, GE Global Research, Niskayuna, NY 12309, USA.

II. Methods

A. Interaction energy

The basic physics of the first order interaction options between the incident X-ray and a slab is shown in Figure 1. X-rays can interact through absorption and scattering. X-rays that do not interact are transmitted through the object.

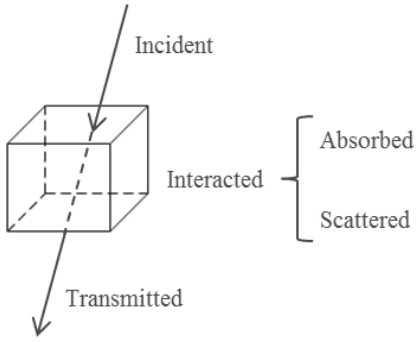

Figure 1: Basic interactions between an incident X-ray beam and an object

The interaction energy is calculated as

$$E_{int} = E_{inci} \cdot (1 - \exp(-\mu \cdot l)), \quad (1)$$

where E_{inci} is the total energy of the incident X-ray beam, μ is the attenuation coefficient of the incident X-ray (dependent on the photon energy) and l is the path length through the object.

To obtain the interaction energy of incident X-rays at a given energy, we need to determine the attenuation at that energy, which typically means that we need to take a reconstructed image and apply material decomposition. With a conventional single energy acquisition, only approximate material decomposition is feasible. We assume that the body is made of two materials with variable densities: water and bone, and we apply thresholding to each voxel to determine its material fractions. We also assume that beam hardening correction is applied. With these assumptions, the total attenuation coefficient at a given energy can be calculated as:

$$\mu = \mu_0 \cdot \frac{\mu_E}{\mu_{cal}}, \quad (2)$$

where μ_0 is the reconstructed linear attenuation coefficient, and the second factor scales this attenuation to different energies, where μ_{cal} and μ_E are the material attenuation coefficients at the reconstructed energy and at the desired energy respectively.

B. Separation into absorbed and scattered energy

Three processes govern the X-ray interactions in the diagnostic energy range:

Photoelectric: The primary X-rays are completely absorbed and the tissue emits photo-electrons and characteristic X-rays. The photo-electrons cannot travel far (compared to the voxel size of the CT image), thus would be re-absorbed in the same voxel; the characteristic X-rays cannot travel far either due to their low energy, e.g., the K-alpha line of Calcium is 3.69 keV. Thus 100% of the primary photon energy is absorbed within the voxel.

Compton scattering: The primary X-ray loses some energy and keeps moving in a different direction. The energy loss depends on the scattering angle. A scattered electron is created, which cannot travel far and is re-absorbed within the same voxel. Thus some of the energy is absorbed by the voxel, the fraction depending on the scattering angle.

Rayleigh scattering: The primary X-ray changes its direction without energy loss. No energy is absorbed in the voxel.

For a single event, it's not certain which interaction mechanism will play. However, for statistically large number of X-ray interactions, we can determine the average occurrence of the three processes as well as the average energy absorption in Compton scattering, so that we can compute the average absorbed energy and scattered energy for all interactions.

The average energy deposition of Compton scattering can be calculated with the Klein-Nishina formula [3] or numerically. We used Monte Carlo simulation toolkit GEANT4 [4] to obtain it in the energy range from 10 keV to 160 keV, shown in Figure 2.

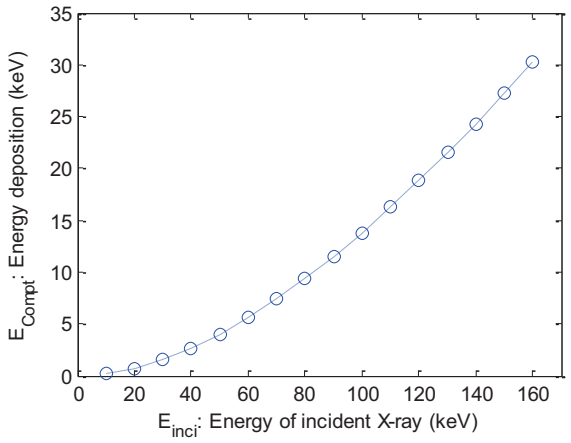

Figure 2: Average energy deposition of Compton scattering E_{Compt}, for incident energy E_{inci} from 10 keV to 160 keV

The average energy deposition E_{abs} (absorbed energy) and the scattered energy E_{sc} of the first order interaction are calculated as:

$$E_{abs} = \left(\frac{E_{Compt}}{E_{inci}} \cdot \frac{\sigma_{Compt}}{\sigma} + \frac{\sigma_{PE}}{\sigma} \right) \cdot E_{int}, \quad (3)$$

$$E_{sc} = E_{int} - E_{abs}, \quad (4)$$

where E_{int} is the average interaction energy, E_{Compt} is the average energy loss for Compton scattering of the incident X-ray with energy E_{inci}; σ_{Compt} and σ_{PE} are the cross sections of Compton scattering and photoelectric and σ is the total cross section of all three processes.

C. Convolution model and the final absorbed energy

We developed a model based on 3D convolution to simulate the transportation of scattered X-ray. The convolution kernel is tuned per energy bin, from 10 keV to 160 keV, so that their linear combination is able to cover any polychromatic X-ray source spectrum below 160 kVp.

After this convolution, the absorption of the scattered energy is calculated by multiplying with the absorption factor k, defined as

$$k = 1 - \exp(-\mu_{sc} \cdot d), \quad (5)$$

where μ_{sc} is the total attenuation coefficient of the scattered X-ray, d is the voxel size. Even though the incident X-ray used to define each convolution kernel is monochromatic, the scattered X-rays are polychromatic, and therefore μ_{sc} is defined as the *effective* attenuation coefficient weighted by the scatter spectrum. The scatter spectrum is obtained using Monte Carlo simulation, shown in Figure 3.

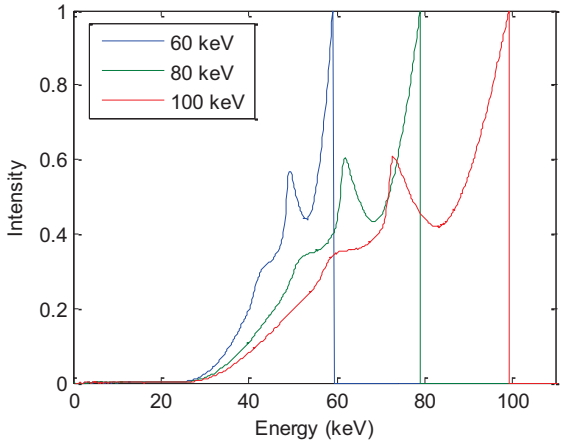

Figure 3: The scattered X-ray energy distribution for 60 keV, 80 keV and 100 keV incident X-rays, obtained by Monte Carlo simulation

The final absorbed energy for a monochromatic incident X-ray beam is calculated as:

$$E_{mono} = E_{abs} + conv(E_{sc}, Kernel) \cdot k, \quad (6)$$

Furthermore, the absorbed energy for polychromatic X-ray is the weighted sum of mono energies:

$$E_{poly} = \sum_i I_i \cdot \left(E_{abs,i} + conv(E_{sc,i}, Kernel_i) \cdot k_i \right), \quad (7)$$

where i is the incident energy index and I_i is the intensity of the X-ray source spectrum as a function of energy bin i.

D. Simulation studies

We used an elliptical water cylinder (40 cm × 20 cm and 120 cm in length) to validate the performance of the proposed method at monochromatic X-ray, and we defined a thorax phantom for polychromatic evaluation. The thorax phantom is

shown in Figure 4. It includes 4 regions-of-interest (ROIs) used for evaluating the absorbed dose. Simulations were performed using 541 mm source-to-iso distance, a fan angle of 52°, a longitudinal beam collimation of 40 mm or 64 slices, 10^9 incident X-rays per monochromatic case and 1.2×10^{10} per polychromatic case.

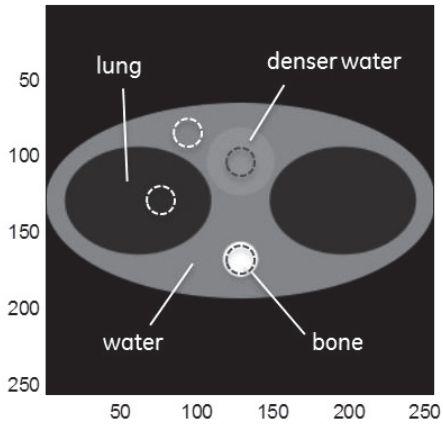

Figure 4: Thorax phantom used for polychromatic validation experiments. The dashed ROIs are used for average dose calculation.

III. Results and Discussion

Figure 5 shows the results of the water phantom computations at various monochromatic energies. The differences between the proposed approach and Monte Carlo simulation are in the range of [-12; 12] and the relative error in all voxels remains less than 6% of the absolute values in the Monte Carlo results. The results also indicate that the dose near the surface of the phantom is slightly over-estimated and the dose inside the phantom is slightly underestimated. In the case of bone, this behavior is inverted (not shown).

Figure 6 shows the results for the thorax phantom with 120 kVp and 140 kVp polychromatic spectra. Images from the Monte Carlo simulation and the proposed approach are shown in Figure 7(a, d) and Figure 7(b, e) respectively. The absolute difference between the two approaches is in the range of [-350; 350] and remains below 6% for all voxels, shown in Figure 7(c, f). The average dose in the 4 ROIs are shown in Table 1 and Table 2. The relative error for the 4 sample regions is in the range of -1.5% – 3.2%.

IV. Summary

We introduced improved physics-based models in a fast CT dose reconstruction approach. The improved approach demonstrated quantitatively good correspondence to a Monte Carlo gold standard in both soft tissue and bone regions in a chest phantom with a realistic polychromatic spectrum. Given its real-time computing efficiency, the proposed approach could be used in applications such as patient specific scan protocol optimization, organ-weighted dose optimization and dose prediction [5] [6].

Table 1: Average dose and the error, 120 kVp

ROI	MC dose (MeV)	Recon dose (MeV)	% error
Spine	7534	7774	3.2
Lung	645	643	-0.36
Water	2350	2350	0.0011
Denser water	1313	1294	-1.5

Table 2: Average dose and the error, 140 kVp

ROI	MC dose (MeV)	Recon dose (MeV)	% error
Spine	8928	9174	2.8
Lung	799	797	-0.30
Water	2900	2901	0.055
Denser water	1684	1663	-1.3

References

[1] W. Chen, D. Kolditz, M. Beister, R. Bohle, and W. A. Kalender, “Fast on-site Monte Carlo tool for dose calculations in CT applications,” Medical Physics, vol. 39. p. 2985, 2012.

[2] Bruno De Man, Mingye Wu, Paul FitzGerald, Mannudeep Kalra and Zhye Yin, “Dose reconstruction for real-time patient-specific dose estimation in CT,” Med. Phys. 42, 2740 (2015)

[3] Klein, O; Nishina, Y, "Über die Streuung von Strahlung durch freie Elektronen nach der neuen relativistischen Quantendynamik von Dirac". Z. Phys. 52 (11-12): 853 and 869 (1929)

[4] S. Agostinelli, J. Allison, K. Amako, et al., “Geant4—a simulation toolkit,” Nucl. Instruments Methods Phys. Res. Sect. A Accel. Spectrometers, Detect. Assoc. Equip., vol. 506, no. 3, pp. 250–303, Jul. 2003.

[5] Hui Wang, Zhye Yin, Yangyang Yao, Mingye Wu, Yannan Jin, Kun Tao, Mannudeep K. Kalra and Bruno De Man, “CT Dose Minimization using Personalized Protocol Optimization and Aggressive Bowtie,” SPIE Medical Imaging 2016

[6] Yannan Jin, Zhye Yin, Yangyang Yao, Hui Wang, Mingye Wu, Mannudeep Kalra, Bruno De Man, “Patient Specific Tube Current Modulation for CT Dose Reduction,” SPIE Medical Imaging 2015

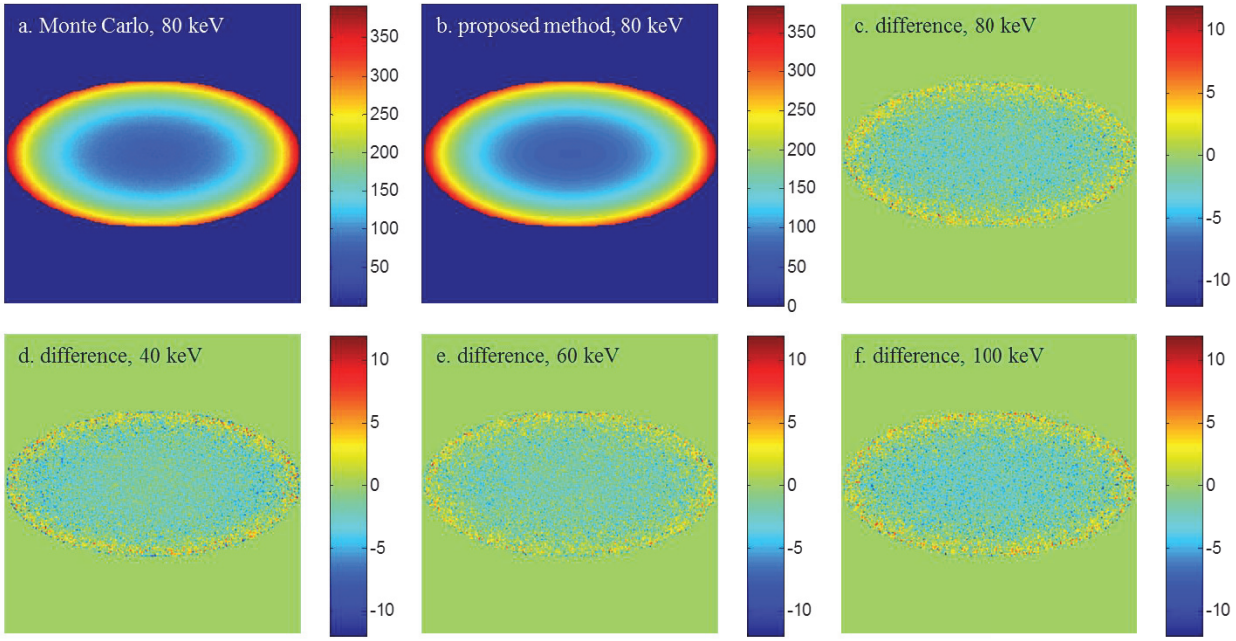

Figure 5: Dose estimation for water phantom and monochromatic spectrum: (a) Monte Carlo at 80keV, (b) proposed method at 80keV, (c-f) difference images at 40keV, 60keV, 80keV and 100keV.

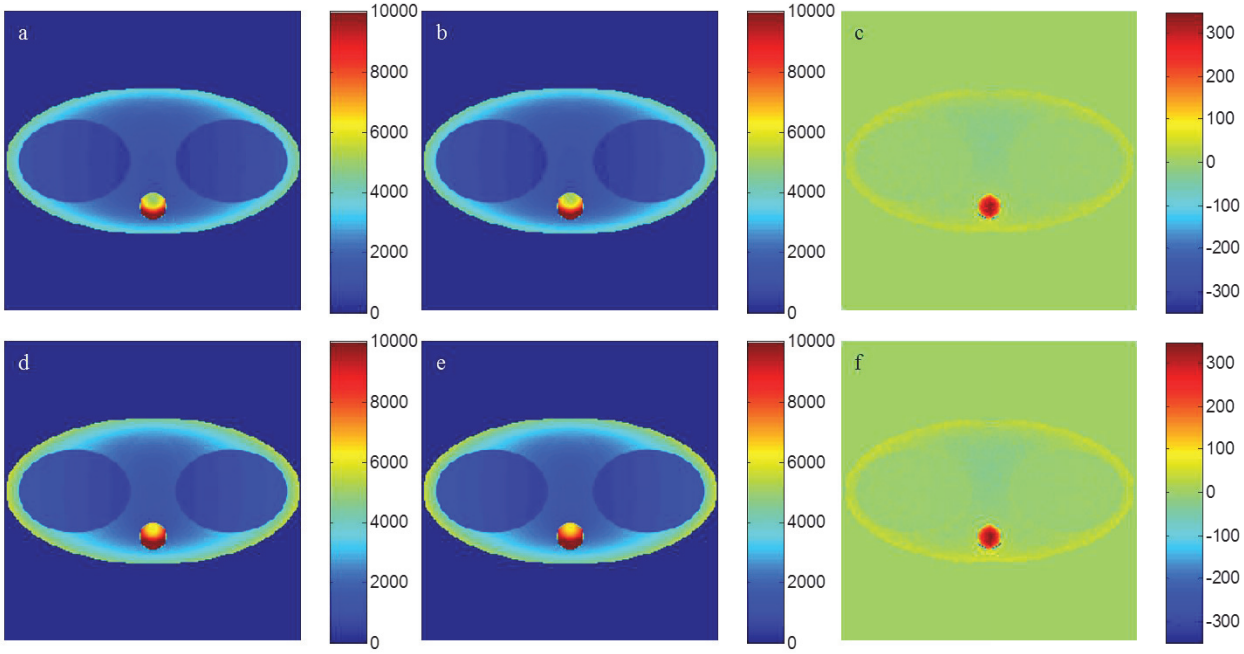

Figure 6: Comparison between proposed method and Monte Carlo simulation; a) Monte Carlo simulation at 120kVp, b) proposed dose reconstruction at 120kVp, c) difference image at 120kVp, d) Monte Carlo simulation at 140kVp, e) proposed dose reconstruction at 140kVp, f) difference image at 140kVp.

Automatic geometric calibration of chest tomosynthesis using data consistency conditions

Jeroen Cant, Gert Behiels, Jan Sijbers

***Abstract*—In medical imaging, Chest Tomosynthesis (TS) is a form of limited angle tomography that allows to compute section images of a patient, in planes parallel to a flat panel detector placed behind the patient. Projection images are acquired using an X-ray tube that moves on a linear path with respect to the stationary detector.**

An important cause of artifacts in TS images are errors in the assumed geometrical setup of the system, especially the orientation of the X-ray tube path with respect to the detector. In this paper, we present a method for correcting errors in the acquisition geometry without the need for a calibration phantom. The method is evaluated on simulation data and experimental acquisitions and proves to substantially reduce reconstruction artifacts caused by geometry mismatches.

I. Introduction

Chest Tomosynthesis is a form of limited angle X-ray tomography with which 3D images of a patient can be computed. Cone beam projection images are acquired using a fixed flat panel detector which is placed behind the patient, and a motorized X-ray tube, typically moving on a straight line, to create projection images from a limited angle. Subsequently, a reconstruction algorithm is used to reconstruct section planes parallel to the detector. Chest TS can be performed using standard X-ray modalities with a motorized X-ray tube and a dynamic flat panel detector. The technique offers a high in-plane resolution but suffers from a low depth resolution, due to the limited acquisition angle of the projection images [1], [2]. Nevertheless, chest TS is capable of separating overlapping anatomy into subsequent section planes, making the detection of certain pathologies easier compared to standard X-ray images [3].

In order to reconstruct high quality TS images, accurate knowledge of the relative positions of the X-ray source and detector is crucial. Inaccuracies in the assumed acquisition geometry lead to reconstruction artifacts such as striping and blurring. For chest tomosynthesis, an important geometric parameter is the orientation of the detector relative to the linear motion path of the X-ray tube. Even inaccuracies smaller than 0.5° on the detector orientation may lead to significant image reconstruction artifacts. If acquisitions are acquired with a rectangular detector in a table, these inaccuracies are frequently present as the detector can often be rotated 90° by the operator, resulting in inaccurate orientation due to mechanical limitations. In tomosynthesis systems with a flat panel fixed to a wall stand, the X-ray source moves on a motorized column attached to the ceiling of the room, which also complicates exact control of the tube motion path relative to the detector.

Therefore, methods are needed to accurately calibrate the acquisition geometry. The acquisition geometry can be measured offline, using a calibration phantom [4], and online using the projection images. For online calibration, radiopaque markers can be used to derive the acquisition geometry [5]. Another way is to exploit data consistency conditions, which describe redundancies between projection images. From these conditions, a cost function can be formulated that, after minimization, leads to the optimal geometric parameters such as detector orientation and position. Such a technique was developed for estimating and correcting the geometric parameters in a cone beam computed tomography setup, based on epipolar consistency conditions (ECC) [6].

However, improvements are necessary for tomosynthesis, as the ECC are not robust enough to deal with truncated projections. In recent work, a heuristic weighting function was introduced to weigh the gray values in the projection images, depending on the fraction of the ray passing the part of the object that is visible on all projections and an estimation of the maximal object thickness [7].

In this work, modifications to the original ECC based estimation of geometrical parameters are presented, specifically designed for chest tomosynthesis. We present a weighting function that does not depend on the patient thickness, and additional modifications to increase robustness against geometrical parameter outliers.

The proposed method is described in Section II. Experiments with simulations and experimental acquisitions are presented in Section III. Discussion and conclusion are in Section IV and V.

II. Method

In this section, the original method of Debbeler [6] is summarized for reference. Subsequently, a modification is presented to improve its robustness against truncation. Finally, a modified cost function is presented specifically designed for estimating the detector orientation in chest tomosynthesis.

A. Plane-based raw data redundancy criterion

A schematic representation of chest tomosynthesis is illustrated in Fig. 1. Projections are acquired of a patient f with a stationary detector Θ. The N subsequent positions of the X-ray source are indicated as $s(\lambda_i)$. Note that in our setup, the X-ray source moves on a linear path S. In other tomosynthesis

JC and JS are with the iMinds-Vision Lab, University of Antwerp, Belgium. JC and GB are with Agfa HealthCare NV, Belgium. Corresponding author: jeroen.cant@agfa.com

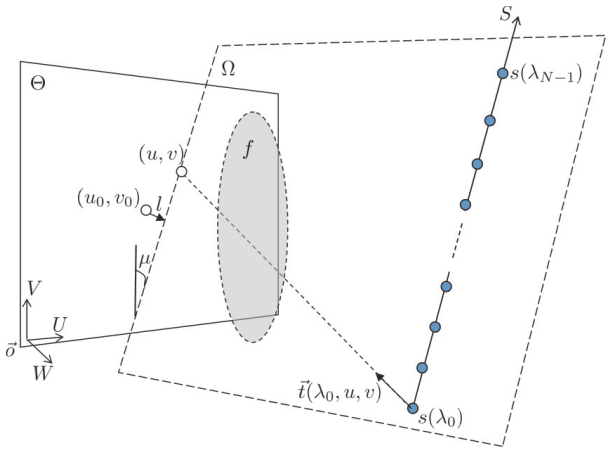

Fig. 1. Illustration of a chest tomosynthesis acquisition. N X-ray images are acquired on a stationary flat panel detector Θ with an X-ray tube that moves on a straight line S. The angle μ represents the orientation of the detector, relative to the X-ray tube path. Most chest tomosynthesis systems are designed such that $\mu = 0$.

setups the source might move on a circular path over a limited angle, which is not considered in this work. The coordinate frame attached to the detector has axes (U, V, W).

The epipolar redundancy criterion describes the following relationship between two projection images. For two source points $s(\lambda_n)$ and $s(\lambda_{\hat{n}})$, multiple planes Ω can be drawn that intersect both points and the detector along an intersection which can be parameterized by an angle μ and a distance l from the detector center (u_0, v_0). For noiseless acquisitions and without truncation, it can be proven [6] that

$$g_3(\lambda_n, \mu, l) = g_3(\lambda_{\hat{n}}, \mu, l) \tag{1}$$

with g_3 defined as:

$$g_3(\lambda_n, \mu, l) = \frac{\partial}{\partial l} g_2(\lambda_n, \mu, l) \tag{2}$$

where

$$g_2(\lambda_n, \mu, l) = \int_{-\infty}^{\infty} g_1(\lambda_n, l\cos\mu - t\sin\mu, l\sin\mu + t\cos\mu)dt \tag{3}$$

and

$$g_1(\lambda_n, u, v) = \frac{1}{|\mathbf{w} \cdot \mathbf{t}(\lambda_n, u, v)|} p(\lambda_n, u, v) \tag{4}$$

with p the projection data, $\mathbf{w}$ the normal of the detector and $\mathbf{t}(n, u, v)$ the direction of the ray arriving in detector pixel (u, v) of the n^{th} projection. Based on Eq. (1), a redundant planes cost function c_{RP} can be derived which reaches a minimum if the geometric parameters (and hence μ and l) are correctly estimated:

$$c_{RP} = \sqrt{\sum_{n=0}^{N-1} \sum_{\mu=-\pi/2}^{\pi/2} \sum_{l=-L_{\max}}^{L_{\max}} (g_3(\lambda_n, \mu, l) - g_3(\lambda_{\hat{n}}, \mu, l))^2} \tag{5}$$

In this work, we will focus on the estimation of the detector orientation μ, relative to the linear motion path of the X-ray tube.

B. Truncation weighting

In the presence of noise and moderate truncation in the acquisitions, minimizing the cost function c_{RP} in Eq. (5) has been reported to still provide a good indication for estimating parameters of the acquisition geometry in Cone Beam CT [6]. However, in chest TS, substantial truncation of the object is present in the projections both in the horizontal and vertical direction. If the X-ray source moves on a linear path with a very small angle μ relative to the detector, the largest inconsistencies between the projections can intuitively be expected to be at the top and bottom regions of the projections as certain parts of the patient will not be imaged, depending on the acquisition angle of the tube. Intuitively, the horizontal truncation would cause less inconsistencies. In previous work, a weighting function was therefore derived to reduce the weight in the cost function c_{RP} of pixels that were suspected to contain information that was not present in all projections [7].

However, Eq. (3) is very sensitive for pixels near the upright (horizontal) image edges, even if an object would have been imaged that fitted perfectly on the detector without horizontal truncation. A small deviation from 0 in μ would cause a large part of the image pixels in the image border to fall off the intersection with the plane Ω, causing a large discontinuity in g_3 and thus making the entire cost function c_{RP} unstable.

Therefore, we propose to use a truncation filter which gradually reduces the weight of the pixels near the horizontal image borders (Fig. 2), with w the relative width of the left and right regions of the image where the weight is reduced using a Gaussian function. The same filter is also proposed to compensate vertical truncation.

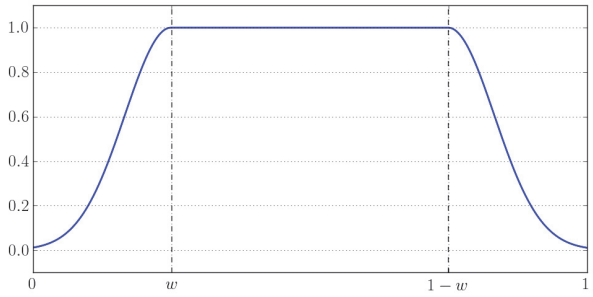

Fig. 2. To reduce the impact of pixels near the edge of the projections on the cost function, a weighting functions is applied. In the regions of relative width w, weights are increased from 0 to 1 according to a Gaussian distribution with $3\sigma = w$.

C. Robust cost function for linear tube motion

In case of linear source motion along a path S, the plane Ω intersects all source positions $s(\lambda_i)$ simultaneously, with $i \in [0..N-1]$. Moreover, the detector remains fixed throughout the entire acquisition in tomosynthesis. The epipolar redundancy of Eq. (1) can thus be generalized to

$$g_3(\lambda_i, \mu, l) = g_3(\lambda_j, \mu, l) \tag{6}$$

with $0 \leq i < j < N$. The cost function c_{RPL} for linear source motion can be written as

$$c_{RPL}(\mu) = \sum_{l} \sum_{i=0}^{N} \left(g_3(\lambda_i, \mu, l) - \bar{g_3}(\mu, l) \right)^2 \qquad (7)$$

with $\bar{g_3}(\mu, l) \equiv \frac{1}{N} \sum_n g_3(\lambda_n, \mu, l)$.

III. Experiments

In a first series of experiments, the presented method was evaluated on the XCAT phantom [8]. Subsequently, experimental projections were acquired of an anthropomorphic phantom (Humanoid Systems, Carson, USA) with a tomosynthesis modality.

A. XCAT simulations

A chest tomosynthesis exam was simulated using the XCAT [8] phantom. The ASTRA [9] toolbox was used to compute 11 projections of the XCAT phantom with a source image distance of 120 cm and a linear X-ray tube motion path of 20 cm. The first and last projection image are displayed in Fig. 3. Detector size was set to 360×420 pixels of 1 mm size. Moderate Poisson noise was added to the projections, corresponding to an unattenuated photon count $I_0 = 10^5$. The detector was placed at a relative rotation of $10°$ with the motion path of the X-ray tube. Experiments were performed to estimate this simulated detector rotation.

The error ϵ on the estimation of the detector orientation angle μ can be written as

$$\epsilon = 10° - \arg\min_{\mu} c_{RPL}(\mu)$$

The maximum achievable accuracy of the estimation is related to the detector size. In Eq. (3), line integrals are computed of the projection images along rays with orientation μ. The maximum accuracy Δ is defined as the angle increment for which a rays passes through a neighboring pixel at the edge of the image: $\Delta = \tan^{-1}(1/210) = 0.27°$.

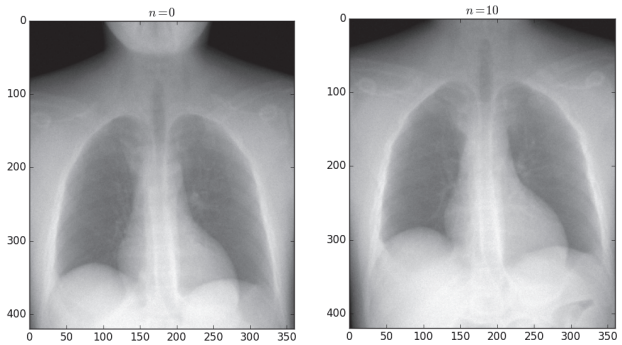

(a) $n = 0$ (b) $n = 10$

Fig. 3. First (a) and last (b) simulated XCAT projection.

In a first experiment, the effect of the truncation filtering as described in section II-B was studied. Without truncation filtering, c_{RPL} reached a minimal value for $\mu = 12.7°$ which is well above the true rotation angle of the detector (Fig. 4(a)). Subsequently, the use of the proposed truncation filtering was studied. Gaussian truncation filters were used with varying values w.

Despite vertical truncation causing the largest data inconsistencies between the projections, c_{RPL} does not reach a minimal value around $10°$ if only vertical filtering is applied (Fig. 4(b)). However, horizontal filtering causes the minimum of c_{RPL} to move towards $10°$ for filter widths $w > 0.10$ (Fig. 4(c)). Combining both horizontal and vertical filters more or less produces the same results, confirming the need for horizontal filtering despite the mainly vertical truncation inconsistencies (Fig. 4(d)).

The estimation errors are displayed in Fig. 5. Truncation filters along horizontal and both directions produce a stable estimated angle within the maximal accuracy of the experiment, for filter widths $w > 0.10$. Vertical filtering only does not result in a correct estimation of the rotation angle μ.

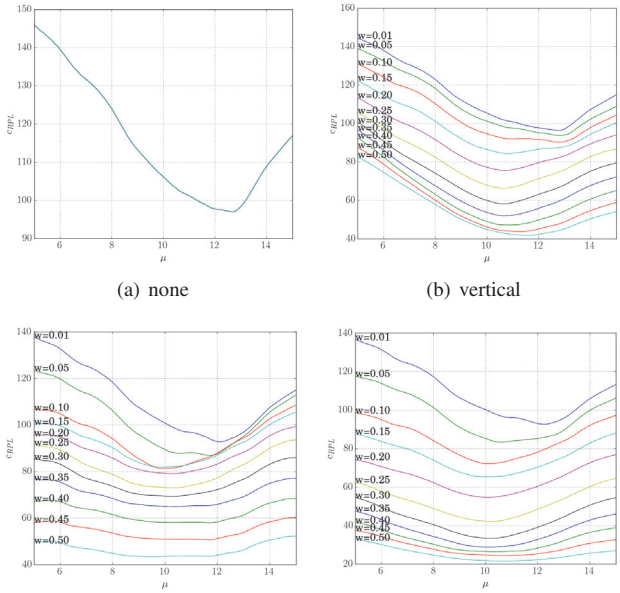

(a) none (b) vertical

(c) horizontal (d) both

Fig. 4. Cost function c_{RPL} for estimated detector angle μ (true orientation = $10°$). (a) c_{RPL} without truncation filtering (b) c_{RPL} with vertical truncation filtering, for different filter widths w (c) c_{RPL} with horizontal truncation filtering (d) c_{RPL} using both horizontal and vertical truncation filtering.

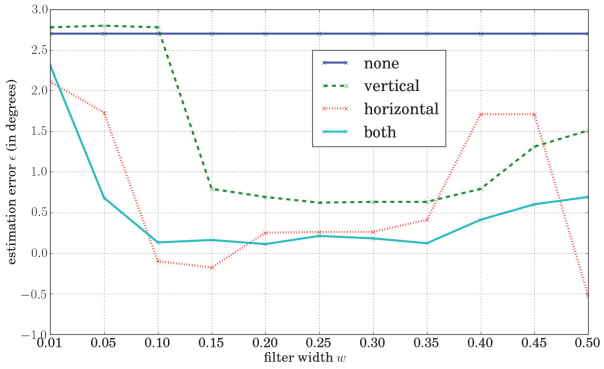

Fig. 5. Error on estimated detector orientation angle (in degrees) for different truncation filter directions and filter widths w.

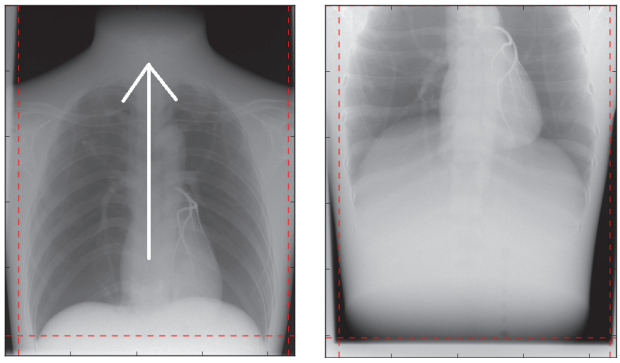

(a) $n = 0$ (b) $n = 65$

Fig. 6. First (a) and last (b) image of the tomosynthesis acquisition of the anthropomorphic phantom. The red dashed lines indicate border regions with incomplete radiation due to X-ray beam collimation. The white arrow indicates the path of the X-ray tube.

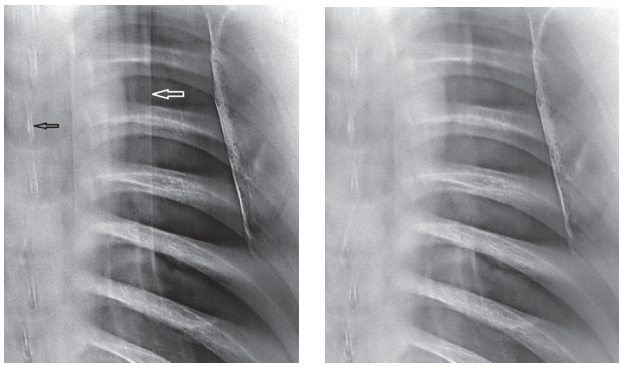

(a) $\mu = 0$ (b) $\mu = 0.57$

Fig. 7. (a) cropped region of a slice of the tomosynthesis reconstruction of the anthropomorphic phantom, without correction of the acquisition geometry. The white arrow shows a large stripe artifact. The black arrow shows a distorted representation of the vertebrae. (b) The same slice, corrected for a detector rotation $\mu = 0.57°$. Note the absence of the stripes and geometrical distortions.

B. Experimental data

To evaluate the effect of the correction of the relative detector orientation, experimental tomosynthesis projections were acquired of an anthropomorphic phantom. Corrected and uncorrected reconstructions were computed with 45 iterations of the Simultaneous Algebraic Reconstruction Technique (SIRT) and compared visually. A motorized X-ray modality was used to acquire 66 projection images using a flat panel detector of 2208×2668 pixels of $160\mu m$ width. The first and last image of the acquisition are displayed in Fig. 6. The X-ray tube moved on an arc above the detector center with a radius of 148cm along the longitudinal axis, as illustrated by the white arrow. Due to X-ray beam collimation, regions near the left, right and bottom edges of the projections contained unexposed pixels and were therefore cropped as illustrated by the red dashed lines. Projection angles were distributed equiangularly from $-20°$ to $21°$. The cost function c_{RPL} reached a minimum for $\mu = 0.57°$. The striping artifacts and geometrical distortions in the uncorrected reconstruction (Fig. 7(a) are not present anymore in the corrected reconstruction (Fig.7(b)).

IV. Discussion

The experiments show that the optimal width of the truncation filter is primarily depending on the orientation angle of the detector and the range around which the function g_2 is computed.

With filter widths $w > 0.35$, the cost function becomes unstable. A possible explanation could be that more than 70% of the projections has been weighted down, leaving too little useful information in the projections to compute a cost function robustly.

In the experimental setup, the X-ray tube moved on an arc in stead of a linear path, as assumed in the robust cost function c_{RPL} of Section II-C. No plane Ω could therefore be fitted exactly through all the tube positions, for all intersection lines with the detector. Nevertheless, the cost function c_{RPL} still showed a clear minimum around $0.57°$, which improved reconstruction quality substantially.

V. Conclusion

In this work, truncation filtering was presented to increase the performance of the epipolar consistency conditions (ECC) for estimating the relative detector orientation in chest tomosynthesis. Corrected reconstructions showed substantial increase in reconstruction quality and reduction of striping artifacts and geometrical distortions.

VI. Acknowledgement

This work was supported by Agfa HealthCare and the Agency for Innovation by Science and Technology in Flanders (IWT).

References

[1] J. T. Dobbins, H. P. McAdams, D. J. Godfrey, and C. M. Li, "Digital tomosynthesis of the chest," *Journal of Thoracic Imaging*, vol. 23, no. 2, pp. 86–92, 2008.

[2] S. Chou, G. Kicska, S. Pipavath, and G. Reddy, "Digital Tomosynthesis of the Chest: Current and Emerging Applications," *RadioGraphics*, pp. 359–373, 2014.

[3] N. Molk and E. Seeram, "Digital tomosynthesis of the chest: A literature review," *Radiography*, vol. 21, no. 2, pp. 197–202, 2015.

[4] H. Miao, X. Wu, H. Zhao, and H. Liu, "A phantom-based calibration method for digital x-ray tomosynthesis." *J. Xray. Sci. Technol.*, vol. 20, no. 1, pp. 17–29, jan 2012.

[5] R. Han, L. Wang, Z. Liu, F. Sun, and F. Zhang, "A novel fully automatic scheme for fiducial marker-based alignment in electron tomography." *J. Struct. Biol.*, vol. 192, no. 3, pp. 403–17, dec 2015.

[6] C. Debbeler, N. Maass, M. Elter, F. Dennerlein, and T. M. Buzug, "A New CT Rawdata Redundancy Measure applied to Automated Misalignment Correction," *Proc. Fully Three-dimensional Image Reconstr. Radiol. Nucl. Med.*, pp. 264–267, 2013.

[7] A. Grulich, Tobias and Holub, Wolfgang and Hassler, Ulf and Aichert, André and Maier, "Geometric Adjustment of X-ray Tomosynthesis," in *Fully Three-Dimensional Image Reconstr. Radiol. Nucl. Med.*, Newport, 2015, pp. 468–471.

[8] W. P. Segars, M. Mahesh, T. J. Beck, E. C. Frey, and B. M. W. Tsui, "Realistic CT simulation using the 4D XCAT phantom," *Med. Phys.*, vol. 35, no. 8, pp. 3800–3808, 2008.

[9] W. van Aarle, W. J. Palenstijn, J. De Beenhouwer, T. Altantzis, S. Bals, K. J. Batenburg, and J. Sijbers, "The ASTRA Toolbox: A platform for advanced algorithm development in electron tomography." *Ultramicroscopy*, vol. 157, pp. 35–47, may 2015.

A unified x-ray computed tomographic reconstruction framework

Ti Bai, Xuanqin Mou, Hao Yan, Hengyong Yu and Ge Wang

***Abstract*—Despite the recent advances in low-dose x-ray computed tomography, image noise and artifacts remain major issues in clinical and preclinical applications, which come mainly from data noise, beam hardening, and scattering. While extensive efforts were devoted to address individual causes for image quality degradation, little attention has been paid to minimize the adverse effects in a unified fashion. In this paper, we combine image reconstruction and artifact reduction in a physics-based synergistic framework with a high computational efficiency. Experimental results show that we can achieve 44% and 35% image noise reduction along with significant HU number accuracy improvement in the cases of prostate and head-neck cancer patients, as compared to a standard statistical reconstruction method. Moreover, the overall reconstruction process can be finished within 2 minutes.**

***Index Terms*—Image reconstruction, cone beam CT, noise, beam hardening, scattering**

I. Introduction

THE great demands of accurate non-destructive imaging of structures inside an object have driven a rapid development of x-ray computed tomography (CT) technologies over the past decades. Now, CT has been widely applied in an array of scenarios, such as industrial non-destructive detection, medical diagnostic imaging, image guided radiation therapy/surgery, and preclinical small animal studies. Despite the significant progress made in hardware and algorithm, there still exist substantial flaws impairing the image reconstruction performance stemmed from various sources of data degradation including data noise, beam hardening, scattering, and so on.

Given the inherent stochastic nature of the photon emission and photon-material interaction, quantum noise in projection data is inevitable which will be propagated to reconstructed images, resulting in streak artifacts and reducing low-contrast resolution. Major efforts were devoted to noise reduction, which can be divided into two categories: pre/post-processing methods and model-based iterative algorithms. The strategy of pre/post-processing is to apply a sophisticated linear or nonlinear filter directly on projection data or reconstructed images for noise suppression[1]. On the other hand, a model-based iterative algorithm formulates the reconstruction task into an optimization problem by taking into account the statistical property of data noise and prior knowledge in a specific application[2]. Either a Poisson distribution of raw data before log or a Gaussian distribution of line integral data after log are often adopted[1], [2]. As far as prior knowledge is concerned, sparsity and low-rank promotion regularizers, such as total variation (TV) minimization[3] and dictionary learning (DL) based representation[4] are very popular, thanks to compressive sensing techniques..

Beam hardening is due to the polychromaticity of the x-ray spectrum, and leads to cupping and streak artifacts without any correction. An ensemble of studies were carried out to alleviate this problem. For example, the classical method that combines water correction[5] and bone correction[6] in the commercial systems. Also, a statistical polyenergetic reconstruction framework was proposed and showed a promising outcome[2].

Scattering becomes pronounced when a large area detector array is used for cone-beam CT. As a result, cupping artifacts and loss can be problematic[7].A variety of methods were designed to avoid or compensate for scattering. The hardware-based methods include air-gap, anti-scatter grid, beam stop, and primary modulation[8] and so on. The software-based methods often estimates the scatter in either the projection or image domain under the assumption that the attenuation coefficients of the human tissues are known[9], and then performs a correction accordingly. The scatter can be estimated with the Monte Carlo (MC) technique[10] or the analytic formula[11].

Various techniques were proposed to address data noise, beam hardening, and scattering respectively. However, to our best knowledge, little attention has been paid to construct a unified reconstruction framework with respect to all these degradation factors. In this paper, we attempt to initiate such a unified reconstruction framework in which the scatter components are iteratively separated while updating a reconstructed image according to a polychromatic x-ray source spectrum. In the next section, we describe a unified formulation characterized by an augmented objective function. In the third section, we report the experimental results. In the last section, we will discuss relevant issues and conclude the paper.

II. Methods and Materials

A. Formulation

Let us first introduce notations. Based on the noise statistics, a broad x-ray source spectrum and an assumed smooth scatter background, we define an overall objective function as follows:

$$\Phi(\rho, s) = \min \sum_i (\bar{Y}_i - Y_i \log(\bar{Y}_i)) + \lambda ||\nabla s||_p + \beta R(\rho) \quad (1)$$

where ρ is the unknown density map, i indexes the detector element, $\bar{Y}_i = \sum_e I_i(e) \exp(-\sum_k \sum_j m_{kj}(e) \rho_j l_{ij}) + s_i$ and Y_i denote the expected value and the real measurement,

This work was supported by National Natural Science Foundation of China (NSFC) (No. 61571359).

Ti Bai and Xuanqin Mou are with the Institute of Image processing and Pattern recognition, Xi'an Jiaotong University, Xi'an, Shaanxi 710049, China. (e-mail: tibaiw@163.com, xqmou@mail.xjtu.edu.cn)

Hao Yan is with Cyber Medical Corporation, Shannxi 710049, China. (e-mail: hao.yan@cybermedical.com)

Hengyong Yu is with Department of Electrical and Computer Engineering, University of Massachusetts Lowell, Lowell, MA, 91854 (e-mail: hengyongyu@ieee.org)

Ge Wang is with Biomedical Imaging Center/Cluster, CBIS, Dept. of BME, Rensselaer Polytechnic Institute, Troy, NY, 12180 (email: wangg6@rpi.edu)

respectively. $I_i(e)$ and s_i represent the fluence of photon energy e and the detected scatter signal. l_{ij} is an element in the system matrix, giving the intersection between the i_{th} ray and the j_{th} voxel of the image volume. It is supposed in this study that the reconstructed volume could be classified into K types of materials. $m_{kj}(e)$ is the mass attenuation coefficient of the j_{th} voxel in the energy bin e if the voxel is of the k_{th} material type. Regarding the scatter component s, which is known to be dominated by low frequency components, a sparsity promotion penalty $||\nabla s||_p$ is used with $p = 1$ and a weight parameter λ. $R(\rho)$ is a regularization term quantifying the roughness/smoothness of the restored density map ρ whose strength is controlled by β.

With Eq. (1), we can simultaneously estimate the scatter components and reconstruct an image in the spectrally-informed fashion. When the source spectrum is unknown, an effective monoenergetic source spectrum model is commonly utilized for the reconstruction process, which must be followed by a beam hardening correction step to minimize the cupping and streaking artifacts. In that case, the expected value of Y_i can be expressed as $\bar{Y}_i = I_i(\epsilon)\exp(-\sum_k \sum_j m_{kj}(\epsilon)\rho_j l_{ij})$, where ϵ is the effective x-ray energy. When the scatter component s is omitted in Eq. (1), the proposed framework will be reduced to the classical polyenergetic reconstruction model.

B. Algorithm

Since the iterative reconstruction algorithms were extensively studied based on the statistical model of data noise or the polychromaticity of the x-ray source spectrum, here we concentrate on the estimation of the scatter component by employing an effective monochromatic source spectrum and utilizing a square error based fidelity term between the expected values and the measurements. This preliminary study can be generalized to be a fully unified reconstruction framework, i.e., Eq. (1), which is our final goal to be achieved based on this work-in-progress.

Supposed that $x_j(\epsilon) = \sum_k m_{kj}(\epsilon)\rho_j$ is the linear attenuation coefficient of voxel j, and for simplicity, the symbol ϵ will be omitted in the rest of the paper. Considering a dictionary learning based ℓ_0-norm sparse regularizer, the simplified unified reconstruction framework could be expressed as:

$$\min_{x,s,\alpha} \sum_i ||I_i\exp(-\sum_j x_j l_{ij}) + s_i - Y_i||_2^2 + \lambda||\nabla s||_1 + \beta \sum_t (||E_{\mathrm{t}}x - D\alpha_t||_2^2 + \nu||\alpha_t||_0), \quad (2)$$

where E_{t} denotes the extraction of the t_{th} patch. α is the sparse coefficient with respect to the dictionary D, ν is the parameter balancing the sparse coding tolerance and the sparsity level described by $||\alpha_t||_0$.

It is worth emphasizing that with this simplified framework based on an effective energy source model, the cupping artifacts from the beam hardening effect can be significantly reduced by attributing the cupping artifacts to scattering, although the streaking artifacts due to the beam hardening effect may still exist, as will be demonstrated in S ec. (III).

The optimization of Eq. (2) can be alternatively pursued by splitting it into the following three sub-problems:

$$\min_x \sum_i ||I_i\exp(-\sum_j x_j l_{ij}) + s_i - Y_i||_2^2 + \beta \sum_t ||E_{\mathrm{t}}x - D\alpha_t||_2^2, \quad (3)$$

$$\min_s \sum_i ||I_i\exp(-\sum_j x_j l_{ij}) + s_i - Y_i||_2^2 + \lambda||\nabla s||_1, \quad (4)$$

$$\min_\alpha \sum_t (||E_{\mathrm{t}}x - D\alpha_t||_2^2 + \nu||\alpha_t||_0). \quad (5)$$

The well-known separable paraboloidal surrogate(SPS) algorithm can be employed to minimize Sub-problem (3) with the variables s and α being fixed. The classical split Bregman algorithm is tailored as the solver of Sub-problem (4), which is a typical problem to perform total variation minimization based image restoration. Sub-problem (5) is to find the sparse representation which can be achieved with the orthogonal matching pursuit algorithm. These are well-known and will not presented due to the limited space.

C. Initialization

To facilitate the whole reconstruction process, a suitable initialization is needed to rapidly converge to a satisfactory solution. Specifically, the reconstructed volume x can be initialized with the FDK reconstruction[12], based on which the sparse coefficients α are initialized with the solution of Sub-problem (5). Moreover, a method is specifically developed for the initialization of the scatter s.

It is reasonable to assume that the attenuation coefficients of the human soft tissues are quite stable and fairly uniform within each tissue type. However, the FDK result is significantly contaminated due to a variety of degradations including data noise, beam hardening, scattering, etc. Given the attenuation coefficient range for soft tissue from μ_1 to μ_2, we can simply map attenuation coefficients for soft tissues to μ_{water}, while keeping the rest structures including the air and bone parts unchanged. Then, a "water-bone-mixture" surrogate object can be digitally designed as described in [9], [11]. Substituting the above object into Sub-problem (5), the solution can be used for the initialization of the scatter component s.

Note that the map $Y_i - I_i\exp(-\sum_j x_j l_{ij})$ contains both the high frequency components including approximation errors between the designed object an the ideal volume, and the low frequency components from the smooth scatter background. Therefore, a large λ should be chosen so as to extract the low frequency components, i.e., scatter s.

D. Experiments

Two real datasets from patients were collected, which are a head-neck case and a prostate case respectively, with the on-board imager integrated in a Varian TrueBeam medical accelerator (Varian Medical System, Palo Alto, CA). All the projection data were rebinned in a 4×4 mode into 512×384 pixels with a resolution of $0.776 \times 0.776\mathrm{mm}^2$. In each case, 364 and 656 views were respectively collected in the full-fan mode with a 200 degrees circular arc and the half-fan mode

TABLE I
ROI STATISTICS OF THE PROSTATE PATIENT CASE. THE NUMBERS INSIDE THE PARENTHESES ARE THE STANDARD DEVIATIONS.(UNIT: HU)

Mean HU(STD)	FDK	Pre-correction	TF-iterative	DL-iterative
Red ROI	-223(33)	-20(50)	-48(17)	-42(20)
Green ROI	-49(30)	17(46)	45(14)	42(17)
Blue ROI	-176(36)	15(54)	33(16)	36(18)

TABLE II
ROI STATISTICS OF THE HEAD-NECK PATIENT CASE. THE NUMBERS INSIDE THE PARENTHESES ARE THE STANDARD DEVIATIONS(UNIT: HU)

Mean HU(STD)	FDK	Pre-correction	TF-Iterative	DL-Iterative
Red ROI	-133(49)	-20(48)	-94(24)	-83(32)
Green ROI	-24(40)	12(37)	31(23)	21(23)
Blue ROI	-139(45)	-23(53)	-72(26)	-65(32)

TABLE III
TIME CONSUMPTION PER STEP OF THE PELVIS PATIENT CASE.

operation time	forward projection 4s	backward projection 4s	TF 0.5s	DL 15s

with a 16cm lateral detector shift and a complete scanning circle. The reconstructed volumes are of $512 \times 512 \times 200$ with a voxel size of 0.57mm^3 and 1.0137mm^3 in the two cases respectively.

After the FDK reconstruction, x, s and were initialized as stated in Sec. (II-C). Since the effective monoenergy ϵ is unknown in this study, the commonly used 70keV was employed to facilitate the computation, and μ_1, μ_2 and μ_{water} were set to 0.1cm^{-1}, 0.25cm^{-1} and 0.2cm^{-1} respectively for image segmentation. We also tested the performance fluctuation with different selections of ϵ by varying μ_{water}. To demonstrate the necessity of the iteration, the FDK algorithm was also applied to pre-corrected data, i.e., subtracted the initialized scatter component directly from the measured raw data. To compare with the 3D dictionary learning based regularizer,, the tight frame (TF) based sparse representation[13] was also tried in the proposed framework. For performance quantification, the averaged standard deviation (STD) of noise and the error in HU were calculated in selected regions of interest (ROIs).

III. RESULTS

Figure (1) demonstrates the experimental results in the prostate patient case. Sever scatter artifacts, such as the ring artifact resulted from the bow-tie filter and the black-hole artifact resulted from the half-fan detector geometry [14], are evident in the conventional FDK reconstruction. After the pre-correction, the overall accuracy in HU was remarkably improved at the expense of noise aggravation, as shown in Fig. (1)b. As indicated by the arrows, the artifacts were induced by the mismatch between the real object and the "water-bone-mixture" surrogate object, based on which the scatter was initialized. On the other hand, it can be seen in Fig. (1)c and (1)d that after the proposed unified reconstruction substantial scatter artifacts were suppressed while the noise level was also effectively reduced, underlying the merits of the proposed algorithm. As expected, the subtle structures in the dictionary learning based reconstruction were more faithfully retained, as compared to that based on tight frame based reconstruction, as indicated by the magnified ROIs in the second row.

To corroborate the above qualitative results, quantitative assessment was performed in terms of the mean HU number and the standard deviation in three ROIs as indicated in Fig. (1). The key results are summarized in Table I in the prostate patient case. Comparison of the dictionary learning based unified reconstruction with the conventional FDK reconstruction without any correction shows that the average standard deviation is reduced by dictionary learning up to 44%, while the HU number accuracy is also improved substantially by the same method.

The results associated with the head-neck patient are in Fig. (2). The scatter artifacts generated biases in HU numbers, which were more pronounced in the peripheral regions. Similar conclusions could be made in the prostate patient case. Specially, the reconstruction with the pre-correction could not distinguish the muscle and adipose tissues well, as indicated by the red solid and the green dot rectangles.

Quantitative results in the head-neck patient case are in Table II. Using the dictionary learning method, a 35% noise reduction performance was achieved accompanied with a significantly improved HU number accuracy.

Finally, we repeated the experiments by setting μ_{water} to 0.18, 0.19, 0.21, and 0.22, respectively. No significant difference could be observed in terms of the HU accuracy, demonstrating that the proposed algorithm is robust with respect to the selection of μ_{water}.

IV. DISCUSSION AND CONCLUSION

In this study, promising reconstructions were achieved with the proposed unified reconstruction framework, despite that only an effective monochromatic x-ray source spectrum model was incorporated. It is expected to be more powerful if a polychromatic x-ray source spectrum is available, which will be reported in our next paper. Also, we will investigate for more effective means to control noise amplification after scatter correction.

One barrier preventing iterative reconstruction from being practically used is the high computational burden. This issue is more serious with the incorporation of correction algorithms, such as MC-based scatter correction. The proposed unified reconstruction framework promises added-on values to the practically relevant situations at a moderate cost, which is only an extra forward projection per iteration relative to the conventional iterative reconstruction. Additionally, the ordered subset based SPS algorithm accompanied with the Nesterov's momentum acceleration technique is very efficient as the optimization solver. Since both of them are highly parallelizable, the computational speed can be enhanced with graphic processing units (GPUs). In this project, a single NVIDIA GTX 980 video card was used. The overall reconstruction process can be finished in 4 loops within less than 2 minutes for the dictionary learning based reconstruction. Table III lists the times needed per step in the pelvis patient case.

In this study, the scatter component was initialized based on a "water-bone-mixture" surrogate object from the FDK reconstruction. In clinical applications, however, sometimes a better but "free" prior image could employed for the calculation, such as a registered CT volume for image guided radiation surgery/therapy (IGRT).

As there were only two datasets from IGRT examined in this feasibility study, a more systematic comparion would

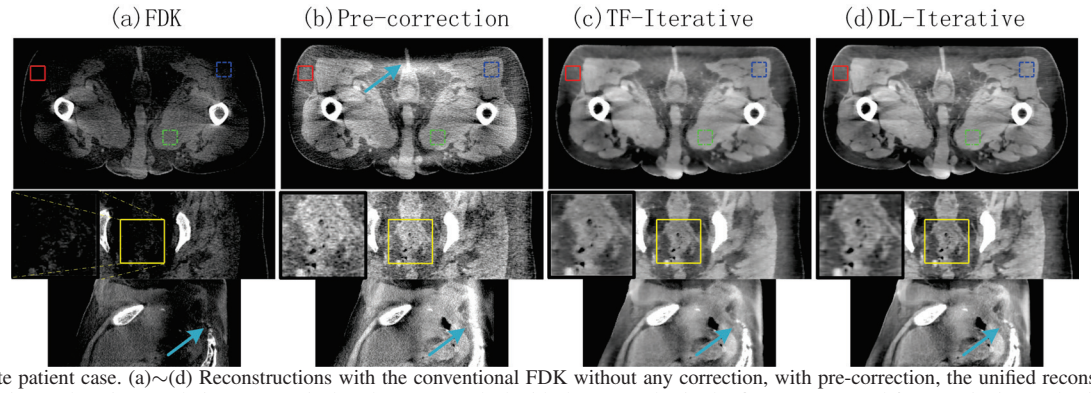

Fig. 1. Prostate patient case. (a)∼(d) Reconstructions with the conventional FDK without any correction, with pre-correction, the unified reconstructions with the TF and dictionary learning regularizers respectively. The ROIs marked with the rectangles in the first row are used for quantitative evaluation. The insets in the second row are the magnified ROIs marked in the yellow rectangles. Display window: [-250 250].

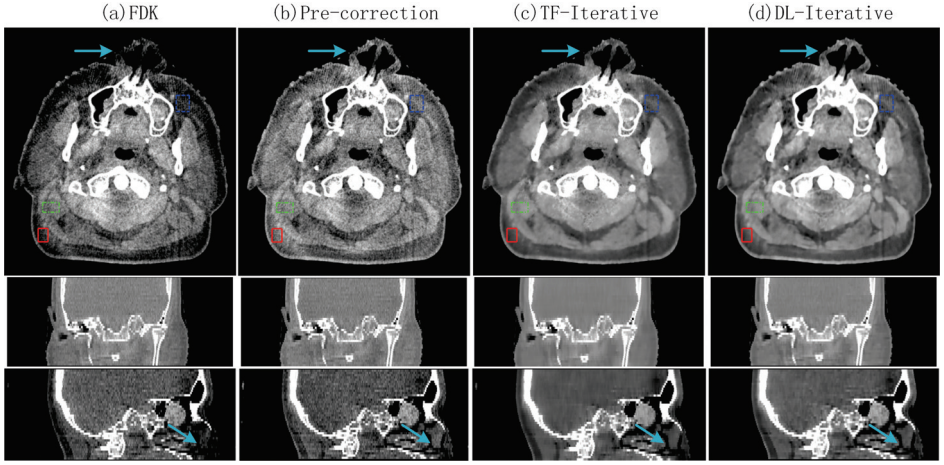

Fig. 2. Head-neck patient case. The sub-figures are arranged in the same way as for those in Fig. (1). The display windows from the top row to the bottom row are [-250 250], [-750 750] and [-250 500] in HU, respectively.

be desirable to establish the extent to which the proposed unified reconstruction framework can be applied, especially in different scenarios such as small animal imaging, dental CBCT imaging, and etc.

In conclusion, a unified reconstruction framework has been proposed that considers various degradations simultaneously with a high computational efficiency. Substantial image quality gains have been achieved with the proposed framework in terms of significantly reduced noise level reduction and improved HU number accuracy, as evaluated in the cases of prostate and head-neck patients respectively, relative to the conventional FDK reconstruction. Incorporation of the polyenergetic source spectrum model is expected to improve the imaging performance further, which is currently under way.

REFERENCES

[1] J. Wang, T. Li, H. Lu, and Z. Liang, "Penalized weighted least-squares approach to sinogram noise reduction and image reconstruction for low-dose x-ray computed tomography," *Medical Imaging, IEEE Transactions on*, vol. 25, no. 10, pp. 1272–1283, 2006.

[2] I. A. Elbakri and J. A. Fessler, "Statistical image reconstruction for polyenergetic x-ray computed tomography," *Medical Imaging IEEE Transactions on*, vol. 21, no. 2, pp. 89 – 99, 2002.

[3] E. Sidky and X. Pan, "Image reconstruction in circular cone-beam computed tomography by constrained, total-variation minimization," *Physics in medicine and biology*, vol. 53, no. 17, p. 4777, 2008.

[4] Q. Xu, H. Yu, X. Mou, L. Zhang, J. Hsieh, and G. Wang, "Low-dose x-ray ct reconstruction via dictionary learning," *Medical Imaging, IEEE Transactions on*, vol. 31, no. 9, pp. 1682–1697, 2012.

[5] W. D. Mcdavid, R. G. Waggener, W. H. Payne, and M. J. Dennis, "Correction for spectral artifacts in cross-sectional reconstruction from x rays." *Medical Physics*, vol. 4, no. 1, pp. 54–57, 1977.

[6] P. M. Joseph and R. D. Spital, "A method for correcting bone induced artifacts in computed tomography scanners." *Journal of Computer Assisted Tomography*, vol. 2, no. 2, pp. 100–8, 1978.

[7] J. H. Siewerdsen and D. A. Jaffray, "Cone-beam computed tomography with a flat-panel imager: Magnitude and effects of x-ray scatter," *Medical Physics*, vol. 28, no. 2, pp. 220–231, 2001.

[8] L. Zhu, N. R. Bennett, and R. Fahrig, "Scatter correction method for x-ray ct using primary modulation: Theory and preliminary results," *Medical Imaging, IEEE Transactions on*, vol. 25, no. 12, pp. 1573–1587, 2006.

[9] P. Wu, X. Sun, H. Hu, T. Mao, W. Zhao, K. Sheng, A. A. Cheung, and T. Niu, "Iterative ct shading correction with no prior information," *Physics in Medicine and Biology*, vol. 60, no. 21, p. 8437, 2015.

[10] Y. Xu, T. Bai, H. Yan, L. Ouyang, A. Pompos, J. Wang, L. Zhou, S. B. Jiang, and X. Jia, "A practical cone-beam ct scatter correction method with optimized monte carlo simulations for image-guided radiation therapy," *Physics in Medicine & Biology*, vol. 60, no. 9, pp. 3567–3587, 2015.

[11] W. Zhao, S. Brunner, K. Niu, S. Schafer, K. Royalty, and G. H. Chen, "Patient-specific scatter correction for flat-panel detector-based cone-beam ct imaging," *Physics in Medicine & Biology*, vol. 60, no. 3, pp. 1339–1365(27), 2015.

[12] L. Feldkamp, L. Davis, and J. Kress, "Practical cone-beam algorithm," *JOSA A*, vol. 1, no. 6, pp. 612–619, 1984.

[13] X. Jia, B. Dong, Y. Lou, and S. B. Jiang, "Gpu-based iterative cone-beam ct reconstruction using tight frame regularization," *Physics in medicine and biology*, vol. 56, no. 13, p. 3787, 2011.

[14] M. Sun, T. Nagy, G. Virshup, L. Partain, M. Oelhafen, and J. Star-Lack, "Correction for patient table-induced scattered radiation in cone-beam computed tomography (cbct)a)," *Medical Physics*, vol. 38, no. 4, pp. 2058–2073, 2011.

Adaptation of the OSC-TV Reconstruction Algorithm for 4D Cone Beam Computed Tomography

Julia Mascolo-Fortin, Dmitri Matenine and Philippe Després

***Abstract*—Four-dimensional cone beam computed tomography (4D-CBCT) allows for temporally resolved imaging with useful applications in radiotherapy. However, it is also subject to clinically prohibitive reconstruction artifacts when performed with standard reconstruction algorithms. A GPU-accelerated ordered subsets convex algorithm (OSC), combined with the total variation minimization (TV) regularization technique, is particularly adapted for this problematic: the TV technique improves image quality despite the use of a limited number of projections, while the use of ordered subsets and the GPU implementation reduce the computation time. Two methods were studied to adapt the OSC-TV algorithm to 4D reconstruction. In the first method, the reconstruction of each phase was initialized with a 3D OSC-TV reconstruction, while in the second one, a blank image was used. Reconstruction algorithms were tested on a dynamic numerical phantom after a classification in phases based on the respiratory signal detected by the Amsterdam Shroud algorithm. Both methods allowed for an adequate visualization of the respiratory movement, while the 4D reconstruction initialized from a prior 3D reconstruction led to better overall image quality. Reconstructions were performed on a single GPU and the total execution times for 8 phases were of about 35 minutes for 672 projections of 512×384 pixels and a reconstruction grid of 384×384×188 voxels.**

I. Introduction

External beam radiotherapy in the thoracic region presents the particular problematic of a substantial target displacement during the treatment due to respiratory motion [1]. To reduce the irradiation of healthy tissues, image-guided radiation therapy (IGRT) should consider this temporal displacement by using a 4D representation of the patient's body. Being acquired over a relatively long period, cone beam computed tomography (CBCT) projections contain information about this displacement. A 4D reconstruction algorithm aims to recover this information and use it to improve the general quality of the reconstructed image and, eventually, the accuracy of IGRT.

The low number of projections from each phase and their uneven spacing are the major problem in 4D CBCT, leading to major artifacts [2]. Total variation regularization (TV) [3] has been frequently used to partially correct this problem [4] [5], but has not been used in combination with the ordered subsets convex (OSC) [6] algorithm in the context of 4D imaging. The advantage of this expectation-maximization algorithm is to offer clinically acceptable reconstruction times using an optimized GPU implementation [7].

Considering that many image regions remain static during respiratory movement, the use of information from all projections to reconstruct each phase can improve image quality. To this end, different strategies had already been explored, such as optical flow based registration [8] or auto-adaptive phase correlation algorithm [9]. The use of a prior 3D reconstruction had already been considered to constrain the convergence of an iterative reconstruction algorithm [10], [11] or to serve as a base to which add a correction image for each phase [12]. The present work studies a novel approach to optimize the 4D OSC-TV algorithm by the initialization of each phase by a prior 3D reconstruction. Using reconstructions of a numerical phantom, this alternative initialization scheme is compared to a standard initialization by a blank image. Consequently, two objectives are pursued in this study: the adaptation of the OSC-TV algorithm to 4D CBCT and the comparison of the aforementioned initialization schemes.

II. Materials and methods

A. OSC-TV algorithm

The selected reconstruction algorithm, OSC-TV [7], combines a modified ordered subsets convex algorithm and a total variation minimization regularization technique. The OSC step optimizes a Poisson log-likelihood objective function via expectation-maximization. The TV step is applied alternately with the OSC step, and minimizes the 3D total variation of the image estimate. This algorithm seems particularly suitable for 4D reconstruction due to the ability of the TV regularization to reduce noise and undersampling artifacts and the acceleration of computation supplied by the modified OSC algorithm. All of the computational tasks above are implemented on GPU using the CUDA architecture (NVIDIA, Santa Clara, CA). The distance elements for the re-projection and backprojection are obtained via the Siddon's method [13] and are computed on the same GPU for one projection angle at a time.

B. Adaptation to 4D reconstruction

The Amsterdam Shroud algorithm [14], as implemented in the Reconstruction Toolkit library (RTK) [15], was used to characterize the respiratory movement from a full cone beam CT acquisition. This signal allowed for the identification of

Julia Mascolo-Fortin (email: julia.mascolo-fortin.1@ulaval.ca) and Dmitri Matenine (email: dmitri.matenine.1@ulaval.ca) are with Département de physique, de génie physique et d'optique, Université Laval, Québec (QC), Canada

Philippe Després (email: philippe.despres@phy.ulaval.ca) is with Département de physique, de génie physique et d'optique, Université Laval, Québec (QC), Canada, and Département de radio-oncologie, CHU de Québec, Québec (QC), Canada

respiratory cycles and then the separation of the projections set into 8 respiratory phases.

Two methods had been developed to adapt the OSC-TV algorithm to 4D reconstruction, each method having a different way of initializing the reconstructed image. In the first method (4D OSC-TV), a standard initialization of the reconstructed image is performed with a blank image. Each respiratory subset is therefore reconstructed completely separately from the other ones. In the second method (p3D+4D OSC-TV), the 4D reconstruction image is initialized from a prior 3D OSC-TV reconstruction. This prior reconstruction enables the use of information from the whole projections set, which could potentially reduce streaking artifacts in the final image. However, motion artifacts present in the initial 3D reconstruction could affect the final 4D image. We conjecture that those artifacts will be reduced by limiting the number of 3D iterations: while being blurrier, the initialization image is expected to be less prone to streaking artifacts after fewer iterations.

C. Projection data and GPU hardware

The proposed algorithm was evaluated on the XCAT anthropomorphic numerical phantom [16]. The use of a numerical phantom was justified by the desire of a fully controllable acquisition, while the choice of this particular phantom was motivated by its accurate representation of human anatomy and respiratory movement. A total of 56 3D phantoms were generated to sample the respiratory movement, which had a period of 5 seconds (3 seconds of inspiration and 2 seconds of expiration), an amplitude of 1.2 cm in the anterior-posterior axis and of 2 cm in the vertical axis. A sphere of soft tissue of 1 cm diameter was also added in the right lung to simulate a lung tumor. Cardiac motion and noise were not simulated.

The projections were obtained using the XCAT projector with parameters inspired from those of a Varian OBI (Palo Alto, CA) low-dose thorax scan. Attenuation of 70 keV photons was simulated for a half-fan detector of 397×298 mm^2, to obtain 672 projections on a fine grid of 1024×768 pixels. In order to reduce reconstruction time, the simulated projections were brought to 512×384 pixels via averaging of 2×2 pixel groups. The reconstruction grid consisted of $384\times384\times188$ voxels of $1.2\times1.2\times1.5$ mm^3.

The reconstructions were performed on a Titan (NVIDIA, Santa-Clara, CA) GPU, fitted with 2688 computing cores and a global random access memory (RAM) size of 6 GiB for the GPU.

III. Results and Discussion

The error of each reconstruction algorithm was estimated by the normalized root-mean-square deviation (NRMSD), defined as follows:

$$\text{NRMSD} \equiv \left(\frac{1}{\mu_{p,\max}-\mu_{p,\min}}\right)\sqrt{\frac{\sum_j\left(\mu_{j,p}-\mu_{j,r}\right)^2}{j_{\max}}}, \quad (1)$$

where μ_p denotes phantom voxel values and μ_r reconstructed voxel values. The normalization is performed with respect to the phantom voxel values extrema. The progression of NRMSD as a function of the number of iterations performed (in 4D for 4D algorithms or in 3D for the standard 3D algorithm) is shown in Fig.1. Phase 1 and 4 were selected to show the accuracy of reconstruction methods for both an end phase (phase 1, end-expiration) and a central phase (phase 4). Fig.1 shows that approximately 2 iterations are necessary to obtain the best 3D image estimate. For both studied phases, NRMSD did not significantly decrease after 2 iterations for the 3D OSC-TV reconstruction. Based on this result, 2 iterations were performed for the 3D part of the p3D+4D OSC-TV method. For the 4D part of the p3D+4D approach, it was decided from results of Fig.1 to complete 10 iterations, the NRSMD decreasing insignificantly starting at this point (average decrease of 0.4%).

As seen in Fig.2, projections of the moving phantom were first reconstructed by two 3D algorithms, the OSC-TV iterative algorithm and the conventional filtered backprojection method, namely Feldkamp-Davis-Kress (FDK) [17]. For all reconstructed images (Fig.2 and Fig.3), the same slice is shown with a μ range of [0, 0.3] cm^{-1}. In Fig.2, both images display significant motion blurring and artifacts, which would compromise clinical use; these reconstructions are rather shown for comparison and reaffirm the usefulness of a phase-correlated algorithm.

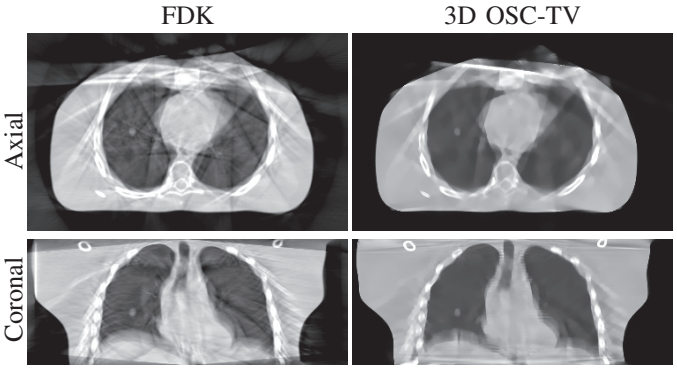

Fig. 2. 3D reconstruction of the XCAT phantom in movement using the FDK algorithm and the OSC-TV algorithm. Both reconstructions display significant motion blurring and artifacts. μ range of [0, 0.3] cm^{-1} shown.

Fig.3 shows, for phases 1 and 4, the results obtained by the 4D methods (p3D+4D OSC-TV and 4D OSC-TV), as well as the phantom representing the central position of the studied phases. It can be observed that the use of a prior 3D reconstruction for initialization of the 4D reconstruction significantly increases image quality for an end phase such as phase 1, while, for a central phase such as phase 4, both reconstruction approaches (p3D+4D and 4D) provide similar results. This is due to the fact that projections identified as belonging to extremal movement phases, such as fully inhaled and fully exhaled, are bundled in one position of the respiratory cycle, while projections belonging to the middle movement phases appeared at two positions of the cycle, leading to a better angular coverage for middle phases. Qualitatively, p3D+4D OSC-TV reconstruction better reproduces motionless regions (back and the exterior of the chest cavity) than the simple 4D OSC-TV version, but some motion artifacts present in the 3D reconstruction are still visible, mostly in the sternum region,

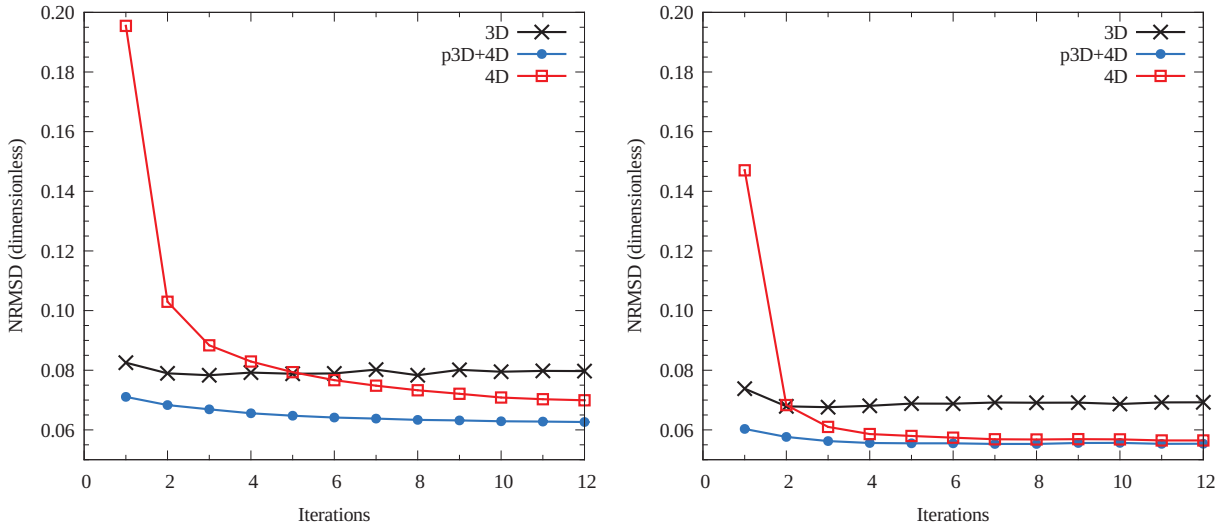

(a) Phase 1 (b) Phase 4

Fig. 1. NRMSD as a function of completed iterations for different OSC-TV reconstructions (standard 3D, p3D+4D and 4D) for (a) phase 1 and (b) phase 4. Both 4D algorithms yield a lower estimation error than standard 3D, while p3D+4D yields a lower NRMSD than simple 4D for phase 1 reconstruction.

as seen in Fig.3.

The correct detection of the tumor position was also evaluated. Both 4D OSC-TV and p3D+4D OSC-TV could predict the position of the tumor for phases 1 and 4 with an error within the uncertainty due to pixel size (1.2 mm in vertical and lateral directions and 1.5 mm in longitudinal direction). This precision, combined with a low tumor edge blurring, suppose an adequate temporal resolution. However, for the 4D OSC-TV method, detection of some of the real tumors could be complexified by their eventual proximity to artifacts. Since the p3D+4D method allows for a better image quality for end movement phases, detection of small objects' motion could be facilitated by its use. From a more general perspective, it is understood that in this work, the simplicity of the studied movement i.e., a respiratory movement of constant frequency and amplitude and no cardiac movement, as well as the absence of noise, have simplified the problem. Nevertheless, these conditions were already somewhat challenging and demonstrated the impact of the initialization image on convergence.

To evaluate the execution time, 10 repetitions of each reconstruction were performed to obtain a mean execution time and the corresponding standard deviation. Each iteration completed with the full data set (3D iterations) took 167.7±0.8 seconds, while an iteration for the reconstruction of a single phase, using only 1/8th of the projections, took about 21.81±0.07 seconds. Considering that the p3D+4D approach required 2 3D iterations and 10 4D iterations, while the 4D approach required 12 4D iterations, the total reconstruction time for the p3D+4D method was of 34.7±0.1 minutes and of 34.9±0.1 minutes for the 4D method. However, it is to be noted that each phase's reconstruction could easily be executed in parallel on several GPUs, reducing the computation time of the 4D part of both methods by a factor of 8, if 8 GPUs were available for the task. The 3D reconstruction could also be performed via the FDK algorithm to reduce computation time.

IV. Conclusion

In the present study, the ability of the OSC-TV algorithm to perform 4D reconstructions on cone-beam CT projection datasets obtained via the Amsterdam Shroud algorithm has been examined. It was shown that the initialization of each phase's reconstruction by a prior 3D reconstruction improved overall image quality. The p3D+4D approach was more robust, being able to reconstruct end movement phases with less artifacts in motionless regions, but showed slightly more streaking artifacts than the simple 4D approach. Reconstructions were performed on a single GPU and the total execution times for 8 phases were of about 35 minutes. To continue the validation of a four-dimensional version of the OSC-TV algorithm, it is envisioned to compare it with other 4D CBCT reconstruction algorithms and study reconstructions of clinical CBCT acquisitions.

Acknowledgements

The authors acknowledge partial support by the CREATE Medical Physics Research Training Network grant of the Natural Sciences and Engineering Research Council of Canada (Grant number: 432290).

References

[1] J. M. Balter, R. K. T. Haken, T. S. Lawrence, K. L. Lam, and J. M. Robertson, "Uncertainties in CT-based radiation therapy treatment planning associated with patient breathing," *International Journal of Radiation Oncology*Biology*Physics*, vol. 36, no. 1, pp. 167 – 174, 1996.

[2] S. Leng, J. Zambelli, R. Tolakanahalli, B. Nett, P. Munro, J. Star-Lack, B. Paliwal, and G. . Chen, "Streaking artifacts reduction in four-dimensional cone-beam computed tomography," *Medical physics*, vol. 35, no. 10, pp. 4649–4659, 2008.

[3] E. Y. Sidky, C.-M. Kao, and X. Pan, "Accurate image reconstruction from few-views and limited-angle data in divergent-beam CT," *X-ray Sci. Tech.*, vol. 14, no. 2, pp. 119–139, 2006.

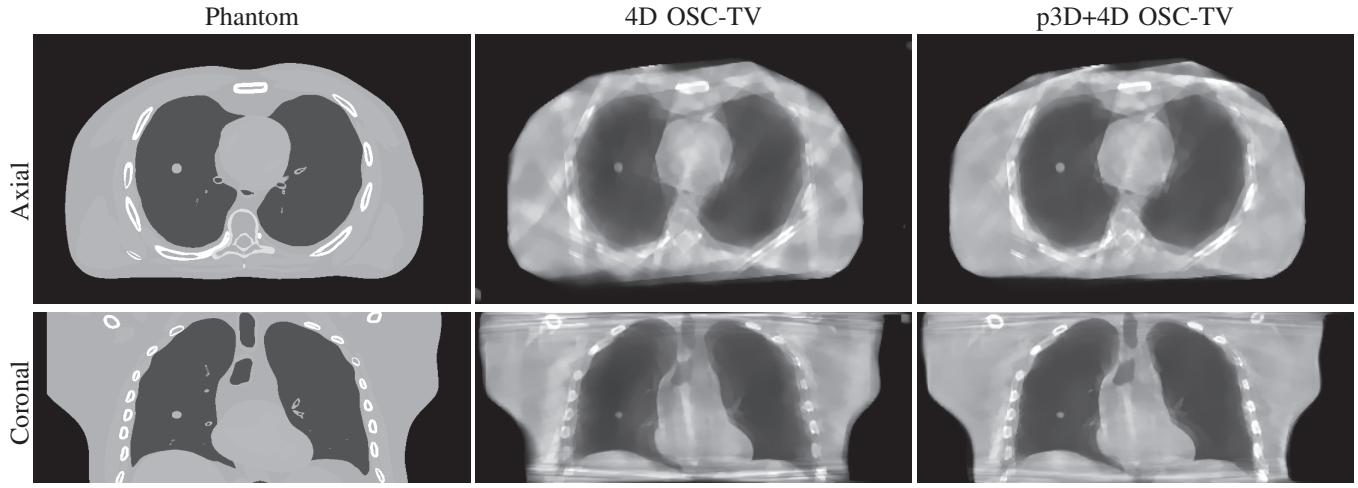

(a) Phase 1

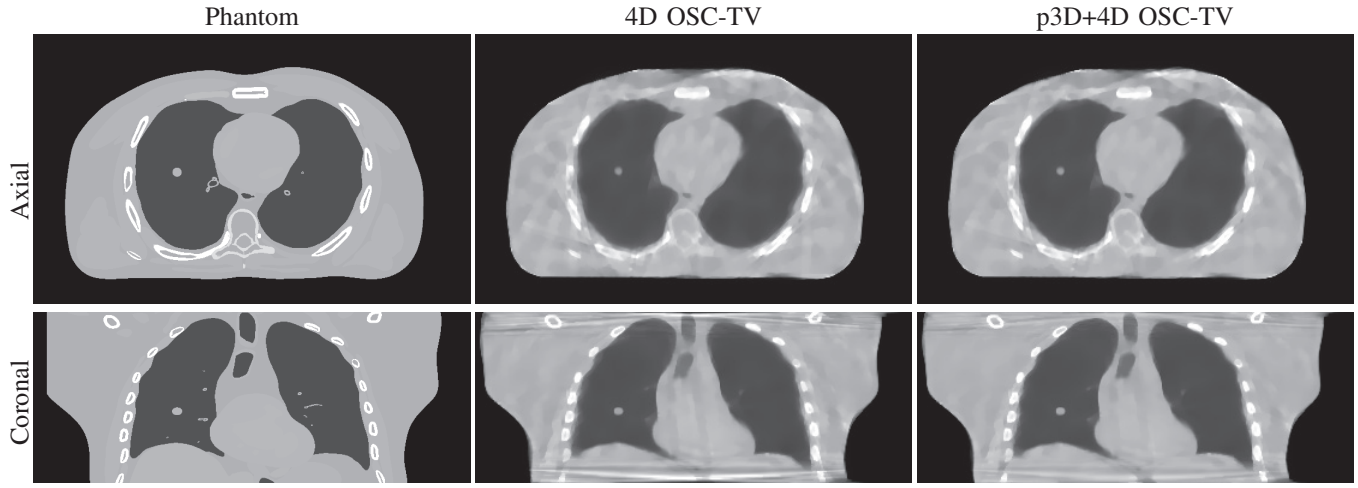

(b) Phase 4

Fig. 3. XCAT phantom and its 4D reconstructions for (a) respiratory phase 1 (end-expiration) and (b) respiratory phase 4 (central respiration phase). For phase 1, the use of a prior image initialization significantly increased image quality, while, for phase 4, both versions of the reconstruction algorithm provided comparable results. μ range of [0, 0.3] cm^{-1} shown.

[4] L. Ritschl, S. Sawall, M. Knaup, A. Hess, and M. Kachelriess, "Iterative 4D cardiac micro-CT image reconstruction using an adaptive spatio-temporal sparsity prior," *Physics in Medicine and Biology*, vol. 57, no. 6, p. 1517, 2012.

[5] M. L. Schmidt, P. R. Poulsen, J. Toftegaard, L. Hoffmann, D. C. Hansen, and T. S. Sorensen, "Clinical use of iterative 4D-cone beam computed tomography reconstructions to investigate respiratory tumor motion in lung cancer patients," *Acta Oncologica*, vol. 53, no. 8, pp. 1107–1113, 2014.

[6] C. Kamphuis and F. J. Beekman, "Accelerated iterative transmission CT reconstruction using an ordered subsets convex algorithm," *IEEE Transactions on Medical Imaging*, vol. 17, no. 6, pp. 1101–1105, 1998.

[7] D. Matenine, Y. Goussard, and P. Després, "GPU-accelerated regularized iterative reconstruction for few-view cone beam CT," *Medical Physics*, vol. 42, no. 4, pp. 1505–1517, 13 March 2015.

[8] C. P. V. Christoffersen, D. Hansen, P. Poulsen, and T. S. Sorensen, "Registration-based reconstruction of four-dimensional cone beam computed tomography," *IEEE Transactions on Medical Imaging*, vol. 32, no. 11, pp. 2064–2077, November 2013.

[9] F. Bergner, T. Berkus, M. Oelhafen, P. Kunz, T. Pan, and M. Kachelriess, "Autoadaptive phase-correlated (AAPC) reconstruction for 4D CBCT," *Medical Physics*, vol. 36, no. 12, pp. 5695–5706, December 2009, iSSN 0094-2405.

[10] G.-H. Chen, J. Tang, and S. Leng, "Prior image constrained compressed sensing (PICCS): A method to accurately reconstruct dynamic CT images from highly undersampled projection data sets," *Medical physics*, vol. 35, no. 2, pp. 660–663, 2008.

[11] S. Leng, J. Tang, J. Zambelli, B. Nett, R. Tolakanahalli, and G.-H. Chen, "High temporal resolution and streak-free four-dimensional cone-beam computed tomography," *Physics in Medicine and Biology*, vol. 53, no. 20, pp. 5653–5673, 2008.

[12] G. C. McKinnon and R. H. T. Bates, "Towards imaging the beating heart usefully with a conventional CT scanner," *IEEE Transactions on Biomedical Engineering*, vol. 28, no. 2, pp. 123–127, 1981.

[13] R. L. Siddon, "Fast calculation of the exact radiological path for a three-dimensional CT array," *Medical Physics*, vol. 12, no. 2, pp. 252–255, 1985.

[14] L. Zijp, J. J. Sonke, and M. Herk, "Extraction of the respiratory signal from sequential thorax cone-beam x-ray images," *Proceedings of ICCR, Seoul, Korea*, pp. 507–509, 2004.

[15] S. Rit, M. V. Oliva, S. Brousmiche, R. Labarbe, D. Sarrut, and G. C. Sharp, "The reconstruction toolkit (RTK), an open-source cone-beam CT reconstruction toolkit based on the insight toolkit (ITK)," *Journal of Physics: Conference Series*, vol. 489, no. 1, p. 012079, 2014.

[16] W. P. Segars, M. Mahesh, T. J. Beck, E. C. Frey, and B. M. W. Tsui, "Realistic CT simulation using the 4D XCAT phantom," *Medical Physics*, vol. 35, no. 8, 2008.

[17] L. A. Feldkamp, L. C. Davis, and J. W. Kress, "Practical cone-beam algorithm," *J. Opt. Soc. Amer. A*, vol. 1, pp. 612–619, June 1984.

Helical CT Reconstruction with Real-time Focal-Spot-Shift Correction

Pei Han, Xin Jin, Yuxiang Xing

***Abstract*—X-ray focal-spot shift (FSS) can cause artifacts in CT reconstruction. In industrial and security applications, FSS needs to be corrected real-timely as it changes during the CT scan. In this work, we propose a practical real-time correction method. Based on cone-parallel reconstruction, only one time of rebinning and filtering is needed to estimate the amplitude of FSS in our method. It greatly reduces the time cost compared with the correction method in flying focal-spot systems, which makes real-time correction possible. Results of simulation show that the image after correction using this method is close enough to the real one.**

***Index Terms*—CT reconstruction, focal spot shift, reconstruction algorithm**

I. Introduction

In industrial CT applications, X-ray ***F***ocal-***S***pot ***S***hift (FSS) is one of the most important problems that degrade image quality. FSS is mainly caused by variations of the tube temperature and imperfect mechanical accuracy of the rotating gantry. As both factors make FSS change all the time during usage, the problem cannot be solved just by pre-correction before usage. Although improving the hardware precision may help to reduce the negative effect of FSS, the total cost of the whole CT device will be increased greatly. In this work, we propose a *practical* real-time correction method for this problem. Since the amplitude of FSS is unknown, we firstly build a method to estimate the FSS. Then, according to the estimation, an analytic CT reconstruction algorithm with FSS correction is executed. In our method, the FSS correction is performed only during the back-projection process to save computation so that we are able to implement it for real-time CT applications which are usually required in security inspections.

Focal-spot offset compensation methods have been an interesting topic in this field [1] [2] [3] [4]. Most of them are used in flying focal-spot systems. In those cases, the regular movement of focal spot is controllable and useful to improve the spatial resolution. In this work, the variation of focal spot is unknown and needs to be corrected in real time to avoid any delay in real-time applications. To our best knowledge, few publications are involved in the research of such unpredicted FSS.

This paper is organized as follows. In Section II, we describe the whole process of our method, including the reconstruction algorithm parameterized with FSS and the indicator function defined upon an object (referred as *indicator*) in reconstructed images that can reflect the scale of FSS. In Section III, we display our initial experimental results. In Section IV, we give conclusion and some discussions.

II. Method

The proposed method can be separated into two parts. Firstly, given an FSS, a CT reconstruction algorithm accommodating FSS correction can be performed. Secondly, the degree of FSS can be measured by reconstructed images from a given indicator. In this work, we figure out an overall method to solve these two aspects.

Given a machine calibrated before usage ($\mathrm{FSS} = 0$ at the beginning), the real-time correction method includes following steps:

1) Enumerate a list of possible FSSs around the current FSS (e.g. $\mathrm{FSS} \in \{\mathrm{FSS}_{\mathrm{current}} \pm k \cdot 0.1\mathrm{mm},\ k = 1, 2, \cdots, 10\}$).

2) For each possible FSS estimation, reconstruct a small region with the indicator inside (namely *local reconstruction*).

3) Calculate a quantity that reflects the degree of FSS (namely *indicator function*) for each one.

4) Reconstruct the whole image using FSS estimation with the smallest value of indicator function, and set this FSS as the current FSS.

A. Analytical CT Reconstruction Algorithm with FSS Correction

Theoretically speaking, reconstruction method of flying focal spot [1] [2] can be used to solve the FSS problem. In those methods, focal-spot shift is corrected within the *rebinning* process, then filtering and back-projection process is done on such rebinned data. However, once the FSS value is changed, a different rebinning and filtering process should be done, which involves the whole acquisition data. This means that a great amount of calculation caused by rebinning and filtering are required, which obviously cannot meet the acquirement of real-time reconstruction. Therefore, our method corrects the FSS in the process of *backprojection*. Once the rebinning and

This work was partially supported by the grant from China Postdoctoral Science Foundation (2014M560092 and 2015T80109) and National Natural Science Foundation of China (No. 11275104).

Pei Han and Yuxiang Xing are with the Department of Engineering Physics, Tsinghua University and Key Laboratory of Particle & Radiation Imaging (Tsinghua University), Ministry of Education, Beijing 100084, China. Email: p-han13@mails.tsinghua.edu.cn, xingyx@mail.tsinghua.edu.cn.

Xin Jin is with the Security CT Center, Nuctech Company Limited, Beijing 100084, China. E-mail: jinxin@nuctech.com.

filtering have been done, only a small region containing the indicator (to be introduced in Section II.B) needs to be reconstructed several times for FSS estimation, which can avoid massive calculation.

Our reconstruction method is extended from a standard CB-FBP algorithm with cone-parallel geometry [5]. According to [5], a 3D map of linear attenuation coefficient is computed based on a cone-parallel geometry.

For convenience, we illustrate cross-section view of the cone-parallel geometry, i.e. project all rays on *Oxy* plane, as shown in figure 1. Here, the focal spot is denoted by *S*. The ray passing an object point (x, y, z) has its projection P on a circular virtual detector. Angle β is used to index view angles on the *Oxy* plane and t indices detector bins. The central ray of view β is denoted by S_0P_0. Rotation axis (Z) of a helical scan is perpendicular to this plane and cone angle α is out of the plane.

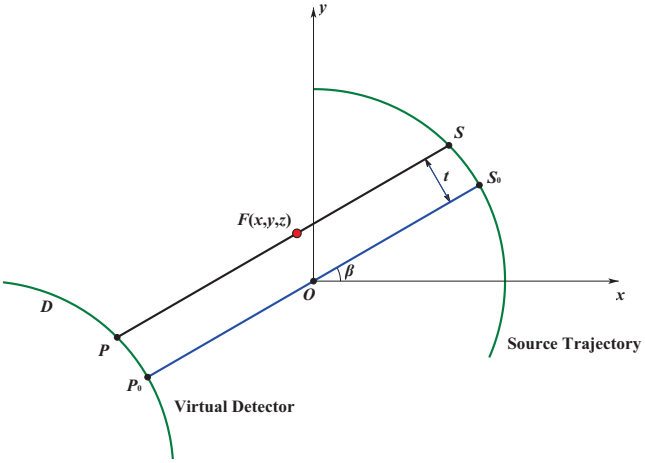

Fig. 1. Cross-section view of cone-parallel back-projection geometry.

With a standard helical CT geometry, reconstructions can be obtained by:

$$\tilde{f}(x,y,z) = \frac{\pi}{\beta_{\max} - \beta_{\min}} \cdot \int_{\beta_{\min}}^{\beta_{\max}} \frac{R}{\sqrt{R^2 + Z^2}} w_{3d}(\alpha,\beta,t)\tilde{g}(\alpha,\beta,t)\mathrm{d}\beta \quad (1)$$

$$\tilde{g}(\alpha,\beta,t) = g(\alpha,\beta,t) * g(t) \quad (2)$$

where $g(\alpha,\beta,t)$ is the projection, $g(t)$ represents the 1D ramp filtering kernel, R is the radius of the trajectory, Z is the projected z-coordinate of point (x, y, z) onto the virtual detector, and $w_{3d}(\alpha,\beta,t)$ is the 3D view weighting function.

Now, we consider a non-standard case with FSS. In theory, FSS could be in all directions. Since slice thickness in helical CT reconstruction is relatively larger than in-place resolution, the degradation from FSS along Z is less important to us. Also, reconstruction is not sensitive to radius FSS. Therefore, we just focus on tangential FSS. As shown in figure 2, we denote S' to be the actual location of the focal spot, which deviates from S within the helical source trajectory. In this way, the amount of shift can be defined as the arc-length $\widehat{SS'}$ (or the chord-length $\overline{SS'}$, because $\widehat{SS'}$ is small), and count-clockwise direction is noted as position direction.

Assume that FSS remains almost the same during the short time over a few circles of scan. The central line of view angle β also deviates from S_0P_0 to $S_0'P_0$, where $\widehat{S_0S_0'} = \widehat{SS'}$. Since $\widehat{SS'}$ (within in several mm) is much smaller than the distance between the source and detector (about 1.2 ~ 1.5 m), and S is not so far from S_0, we can assume that $\angle SPS' \approx \angle S_0P_0S_0'$, i.e. $PS' \parallel P_0S_0'$.

In this way, the real ray projecting at P is emanated from S', rather than S. Directly replacing $g(\alpha,\beta,t)$ with this projection will obviously cause artifacts. In fact, the real ray passing through P within this view angle β is the red dot line in figure 2, which projects at P'' and is parallel to ray S_0P_0 (or $S'P$).

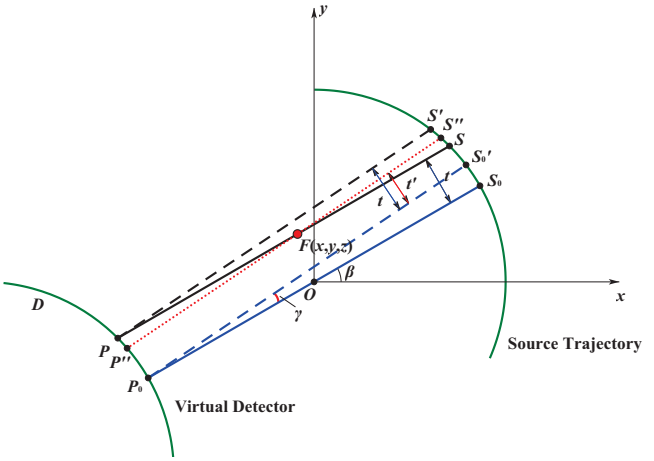

Fig. 2. Cross-section view of cone-parallel back-projection geometry with FSS.

In order to use the CB-FBP method with cone-parallel geometry, we need to find the true orthogonal iso-distance t', which refers to the distance between $S_0'P_0$ and $S''P''$. Based on the geometric relations shown in figure 2, we have

$$\triangle FPP'' \sim \triangle PSS' \quad (3)$$

Therefore

$$t' = t - \overline{PP''}\cos\gamma = t - \frac{\overline{FP}}{\overline{SP}}\overline{SS'}\cos\gamma = t - \frac{d}{L}\cos\gamma \cdot \overline{SS'} \quad (4)$$

where γ is the angle between the central rays with and without FSS (the blue dash line and blue solid line in figure 2), L is the distance between source and virtual detector D, and d is the distance between virtual detector D and the object point.

Consequently, the reconstruction method parameterized with FSS can be rewritten as

$$\tilde{f}(x,y,z) = \frac{\pi}{\beta_{\max} - \beta_{\min}} \cdot \int_{\beta_{\min}}^{\beta_{\max}} \frac{R}{\sqrt{R^2 + Z^2}} w_{3d}(\alpha,\beta,t')\tilde{g}(\alpha,\beta,t')\mathrm{d}\beta \quad (5)$$

$$t' = t - \frac{d}{L}\cos\gamma \cdot \overline{SS'} \quad (6)$$

where $\overline{SS'}$ is the shift value, L is the distance between source S and virtual detector D, d is the distance between virtual detector D and the object point (x, y, z), and γ is the angle between the central rays with and without FSS. We can see that the only

difference between (5) and (1) is back-projection geometry.

B. Indicator function to measure FSS

In order to estimate and correct the offset, we need to find an object in the reconstructed images to be an indicator. We expect the image of our indicator demonstrate some features monotonically related to FSS. An object *uniform* in z-direction can be considered as a good choice because it appears as the same in every slice, but the tangential FSS can cause periodic deviation of its location in slices.

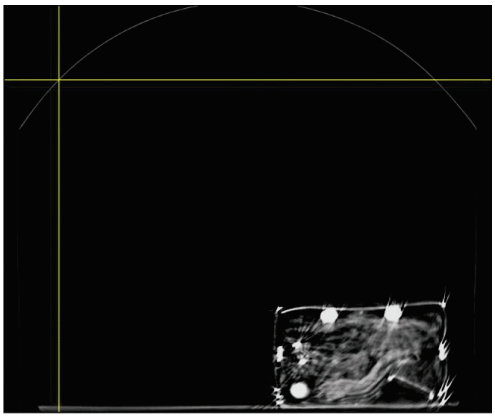

Fig. 3. A slice image of a real security check CT system, in which the tunnel wall appears as the narrow bright boundary around.

1 Choice of Indicator

The indicator employed in this article is *the tunnel wall* of the security CT machine. It often appears as a narrow bright line in each slice of reconstructed images, as shown in Figure 3. Obviously, it not only satisfies the 'z-uniformity' requirement, but also has the following additional advantages:

1) It is perfectly stable. External changes (e.g. temperature variations and wind disturbances) will not destroy its uniformity in z-direction.

2) While reconstructing different luggage, the tunnel is always in the same location. This guarantees a stable and reliable indicator calculation of the proposed method.

3) It introduces no extra cost. Placing a standard object in the machine is operable but not necessary here.

2 Definition of Indicator Function

The goal of the indicator function is to evaluate the uniformity of the tunnel area in reconstructed image. In this work a simple but efficient indicator function is used.

First, let us denote $f_{i,j,k} \in \mathbb{R}^{N_x \times N_y \times N_z}$ as the discrete version of the reconstructed image $f(x,y,z)$ here. We choose a pixel (i_0, j_0, k_0) on the tunnel wall in one of the slices. Two rectangular regions (referred as M_{yz} and M_{xz} respectively) on x_0yz and y_0xz planes are defined with (i_0, j_0, k_0) at their center, described as

$$\begin{aligned} M_{yz}: &\quad i = i_0, j \in [j_0 - m, j_0 + m] \\ M_{xz}: &\quad i \in [i_0 - m, i_0 + m], j = j_0 \end{aligned} \tag{7}$$

For each k, we can calculate 1D centroid of M_{yz} and M_{xz} along x and y direction, respectively:

$$\begin{aligned} x_C(k) &= \sum_{i=i_0-m}^{i_0+m} i f_{i,j_0,k} \Big/ \sum_{i=i_0-m}^{i_0+m} f_{i,j_0,k} \\ y_C(k) &= \sum_{j=j_0-m}^{j_0+m} j f_{i_0,j,k} \Big/ \sum_{j=j_0-m}^{j_0+m} f_{i_0,j,k} \end{aligned} \tag{8}$$

The images of (7) and (8) are shown as figure 4(a) and 4(b) respectively.

Then, the variance of $x_C(k)$ and $y_C(k)$ can be evaluated by σ_x^2 and σ_y^2:

$$\begin{aligned} \sigma_x^2 &= \frac{\sum_k \left(x_C(k) - \overline{x_C} \right)^2}{K} \\ \sigma_y^2 &= \frac{\sum_k \left(y_C(k) - \overline{y_C} \right)^2}{K} \end{aligned} \tag{9}$$

where $\overline{x_C} = \sum_k x_C(k) \Big/ K$ and $\overline{y_C} = \sum_k y_C(k) \Big/ K$, K is the number of slices to be chosen.

Finally, the indicator function noted as φ_I can be expressed as

$$\varphi_I = \sqrt{\sigma_x^2 + \sigma_y^2} \tag{10}$$

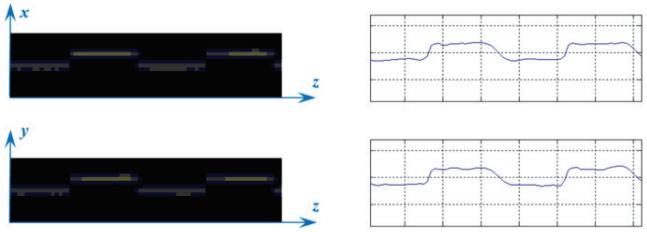

Fig. 4. Examples of (a) images within regions M_{yz} and M_{xz}; (b) Centroid along x and y direction of M_{yz} and M_{xz}, respectively.

3 Computational Complexity

For a whole backprojection, $(N_x \cdot N_y \cdot N_z)$ pixels should be reconstructed. Assume that enumeration of indicator function values at 20 FSSs are needed in our correction method. In each calculation of indicator function, only $2(2m+1)K$ pixels will be involved based on (7) and (9). Thus, $40(2m+1)K$ pixels should be calculated totally during the FSS correction process in our method. Since K is about the same as N_z, and an m smaller than 10 is generally enough, we have the following proportion given that N_x and N_y are around 10^3:

$$40 \times (2m+1) \times K \sim 80m \times N_z \sim 10^{-3} N_x \times N_y \times N_z \tag{11}$$

This means that the correction step only takes 0.1% time cost of a regular backprojection, which makes real-time correction possible.

III. Experiments and Results

A. Correlation between Indicator Function and FSS

Using the algorithm in II.B, we can simulate the reconstructed images with different FSSs. The 3D effect of our simulating model and the reconstructed image (without FSS) of its cross-section are shown in Figure 5.

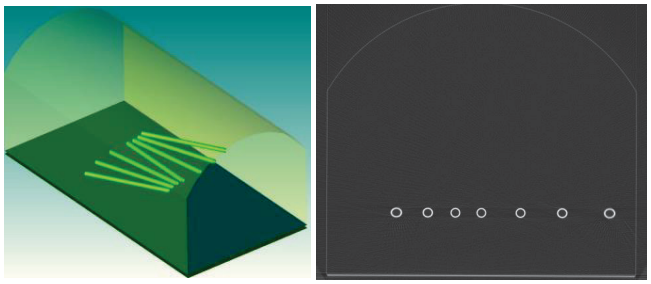

Fig. 5. (a) 3D illustration of the phantom for simulation; (b) A reconstruction of transverse-plane from the 0-FSS data ($z = 108$).

In this model, the reconstructed images are 768×640 for each slice, with 216 slices in total, i.e. $N_x = 768$, $N_y = 640$, $N_z = 216$. Choose the slices in which the tunnel wall can be easily discerned, i.e. $97 \le z \le 216$ so that $K = 120$ in (9).

The correlation of φ_I~FSS is shown as Figure 6. We can see that φ_I is a monotone increasing function of |FSS| as we needed.

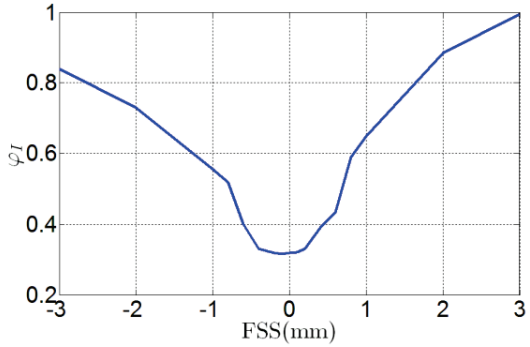

Fig. 6. Correlation between φ_I and FSS from simulated data shown in fig. 5.

B. *Evaluation of Reconstructed Image*

We use simulated data of FSS = 0 and FSS = 2mm for comparison. The reconstructed results of the **2mm FSS data** without correction are shown in Figure 7. The FSS effect can be clearly observed in Figure 7(b), where the tunnel wall looks discrete in the *YZ* view.

Using the method at the beginning of Section II with the precision of 0.1mm, we finally estimate FSS as 1.6mm for the 2mm FSS data, and then reconstruct the whole image. We use a chosen line in the same position of the same slice to show the results, which is marked red in figure 7(a).

Profiles of the chosen line are shown in Figure 8. In figure 8(a), we show the profiles of the ground truth (0-FSS data) and the one without correction (2mm-FSS data). In figure 8(b), we show the profiles of the ground truth and the one after correction. We can see that the profile of the 2mm FSS data is close to the 0-FSS data after correction (almost coinciding with each other in the two peaks), which is much better than the one before correction.

However, this estimation is not accurate enough. A main reason is the lack of image resolution for 'local reconstruction' (see the beginning of Section II), in which the size of one pixel is as large as 1.4mm, which restricts the accuracy of FSS estimation.

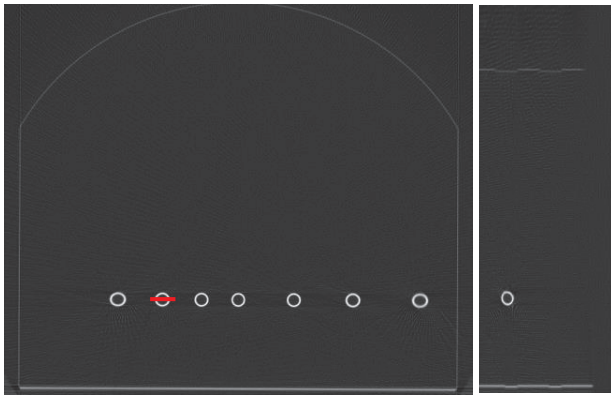

Fig. 7. (a) A reconstructed transverse-plane of the 2mm-FSS data ($z = 108$); (b) A reconstructed x_0yz plane of the 2mm-FSS data ($x = 666$). Both (a) and (b) are reconstructed without FSS correction.

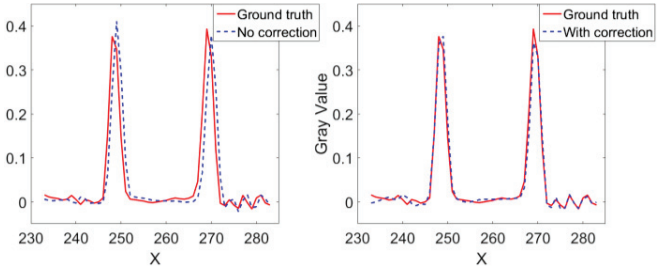

Fig. 8. Profiles of the same line: (a) in the reconstructed images of 0 FSS (ground truth) and 2mm FSS without correction; (b) in the reconstructed images of 0 FSS (ground truth) and 2mm FSS with correction.

IV. Conclusion and Discussion

In this paper, we give a novel method that can correct FSS real-timely. Theoretically, the FSS correction method introduced here has larger error than the accurate flying focal-spot method. However, it avoids massive calculation caused by repetition of rebinning, and experimental results have shown that such approximation is acceptable.

Our future work will include improving the accuracy of FSS estimation, performing experiments on actual data, and the real-time monitoring of the focal-spot location using the indicator.

References

[1] Kachelrieß M, Knaup M, Penßel C, et al. Flying focal spot (FFS) in cone-beam CT[J]. Nuclear Science, IEEE Transactions on, 2006, 53(3): 1238-1247.

[2] Tang X, Narayanan S, Hsieh J, et al. Enhancement of in-plane spatial resolution in volumetric Computed Tomography with focal spot wobbling-overcoming the constraint on number of projection views per gantry rotation[J]. Journal of X-ray science and technology, 2009, 18(3): 251-265.

[3] Flohr T G, Stierstorfer K, Ulzheimer S, et al. Image reconstruction and image quality evaluation for a 64-slice CT scanner with z-flying focal spot[J]. Medical physics, 2005, 32(8): 2536-2547.

[4] A.H. Lonn, Computed tomography system with translatable focal spot, Patent, US. 5,173,852, 1992.

[5] Tang X, Hsieh J, Nilsen R A, et al. A three-dimensional-weighted cone beam filtered backprojection (CB-FBP) algorithm for image reconstruction in volumetric CT—helical scanning[J]. Physics in Medicine and Biology, 2006, 51(4): 855.

Investigation towards simulation-based determination of measurement uncertainties for X-ray computed tomography

Michael Reiter and Johann Kastner

***Abstract*— X-ray Computed tomography (XCT) is a common tool for the industrial purposes non-destructive testing and metrology. For latter the knowledge of measurement uncertainty is of great importance. This paper gives an overview of methods to determine the expanded measurement uncertainty for a measurand based on experiments and simulations. Furthermore, we present a simulation-based case study that demonstrates the influence of several effects on the expanded measurement uncertainty for three measurement features on a selected specimen.**

***Index Terms*—XCT, metrology, dimensional measurement, measurement uncertainty, simulation**

I. Introduction

Metrology is besides non-destructive testing the most important application of XCT. Contrary to metrology technologies like tactile and optical measuring systems (CMSs), X-ray Computed tomography (XCT) is capable of scanning a complete workpiece at once. Furthermore, XCT can provide measurement values of inner and inaccessible measurement features.

However, the complete process chain from an XCT scan of a specimen to a final measurand (e.g., radius, roundness, distance) plus uncertainty value is rather complex, since there are numerous factors that influence the uncertainty.

The expanded measurement uncertainty is a quality indicator of a measurement and especially important, when a decision is necessary, if a manufactured part is within the tolerance. This article presents a simulation-platform and a case study that gives more insight into the relevance of selected influencing factors.

II. Measurement process with XCT

At first, the metrologist has to plan the XCT measurement and make choices on several free parameters, before performing the XCT scan. The scan is followed by evaluation procedures to determine the required measurand. The following list summarizes this workflow for measurements with XCT and states degrees of freedom:

1) *Choose an orientation of the specimen in the X-ray beam*
   This should ensure the minimization of artefacts and systematic measurement errors due to X-ray related effects or inexact reconstructions.
2) *Select device, CT and reconstruction parameter*
   The chosen parameters of X-ray source (e.g. acceleration voltage, current, filter plates) and detector (e.g. integration time, averaging, gain) have to ensure sufficient transmission of X-rays through the specimen, reduce beam-hardening by a sufficient amount, and lead to a sufficient signal-to-noise and contrast-to-noise ratio. Besides that, the number of projections and reconstruction parameters have to be chosen.
3) *Perform the XCT scan of the specimen*
   Projection images are acquired from different views of the specimen and are reconstructed to a 3D image that consists of voxels, which represents the spatial X-ray attenuation of the specimen. Optionally, artefact corrections are applied before or after the reconstruction.
4) *Perform dimensional measurements*
   Various tools of XCT and software manufacturer are available to extract the surface points (point clouds) from voxel data and can perform measurements on surface points. Actual/nominal comparison is a geometrical comparison in 3D, where the alignment of reference and specimen is of importance to determine differences. Similarly, measurements and tolerance verifications of geometrical features (e.g. size, form, position, …) are influenced by user choices on the positions and number of extracted surface points (measurement strategy).

A lot of effort is put into the establishment of automated procedures that support the user during the scanning and measurement workflow described above. Nevertheless, device operators induce uncertainty to the measurement. Other factors that contribute to the uncertainty of a measurand Y are: (i) device stability and knowledge of the actual geometry, (ii) correction, reconstruction and evaluation procedures, (iii) the measurement environment (e.g., Temperature, Humidity, Vibrations), (iv) properties of the specimen. The interested reader can refer to [1,2]. The determination of measurement uncertainty is described in chapter III.

Submission date is the 25th of January 2016. This work was supported by the "K-Project for non-destructive testing and tomography plus" financed by FFG and the governments of Upper Austria and Styria.

Michael Reiter and Johann Kastner are with the University of Applied Sciences Upper Austria, Campus Wels, Stelzhamerstrasse 23, 4600 Wels, Austria (e-mail: michael.reiter@fh-wels.at, johann.kastner@fh-ooe.at).

III. Methods to Determine the Measurement Uncertainty

The Guide to the Expression of Uncertainty in Measurement (GUM) [3] provides basic methods for the determination of measurement uncertainty, also applicable to XCT. The most common approach for XCT is the experimental method, which needs reference measurements. The second approach is based on simulations using the Monte-Carlo method. Describing the propagation of measurement errors by a model function is currently not realizable for XCT.

A. Experimental method using calibrated workpieces

The experimental approach described in ISO 15530-3 [4] for CMSs can be adapted to XCT [5,6], but is not yet covered by a dedicated standard. This approach is based on setting up an uncertainty budget to describe the expanded measurement uncertainty U of a measurand y without investigating error sources of XCT measurements separately. There are two definitions of U. In the uncorrected case, the systematic deviations b (Equation 1) between the XCT and reference value is treated as random error and added to the expanded measurement uncertainty (Equation 2). On the other hand, the corrected case, which is suggested by [3], considers only the uncertainty of the bias correction as additional standard uncertainty u_b. The complete and corrected measurement result Y is then given by Equation 3. Descriptions of factors contributing to these formalisms are given in Table 1. To perform this statistical assessment at least 20 repeated XCT measurements are required [4], as well as repeated measurements performed with a reference method. Typically, tactile or optical CMSs are used to calibrate workpieces. For further details, we refer to [4,6].

Overall, this is a time-consuming and costly procedure, which is only applicable if the workpiece has features that are accessible by the reference method [5]. Simulation-based estimation of measurement uncertainties could partially overcome these drawbacks.

$$b = \bar{y} - y_{\mathrm{cal}} \tag{1}$$

$$Y = y \pm U, \qquad U = k \cdot \sqrt{u_{\mathrm{cal}}^2 + u_{\mathrm{p}}^2 + u_{\mathrm{w}}^2 + b^2} \tag{2}$$

$$Y = y - b \pm U, \qquad U = k \cdot \sqrt{u_{\mathrm{cal}}^2 + u_{\mathrm{p}}^2 + u_{\mathrm{w}}^2 + u_{\mathrm{b}}^2} \tag{3}$$

B. Simulation-based approach using the Monte-Carlo method

Investigating the uncertainty in metrology on the basis of the Monte Carlo method (MCM) by numerical simulation is a well-established procedure. It is applicable to any kind of measurement technology and is published in the supplement 1 to the GUM [7]. The virtual coordinate measuring machine (VCMM) is based on the MCM and is already used in metrology laboratories for uncertainty assessments [8].

Hiller et al. [1] adapted and applied the MCM more recently to XCT. The complete measurement process is simulated multiple times, as realistic as possible, with varying input parameters X_i to gain measurand Y from dimensional measurements on the virtual XCT images (Fig 1).

TABLE 1
Details to the Uncertainty Budget

y	Uncorrected measurand
y_{cal}	Calibrated measurand determined by the reference method
b	Systematic deviation between reference and XCT
$\bar{y}$	Mean of the uncorrected measurand values (XCT)
U	Expanded measurement uncertainty of the XCT measurement
k	Expansion coefficient (k=2 represents a confidence level of 95% for the assumption for a normal distribution)
u_{cal}	Standard uncertainty of the calibration measurements
u_{p}	Standard uncertainty of the XCT measurements
u_{w}	Standard uncertainty from material and manufacturing variations of the workpiece (variation of expansion coefficients, form errors, roughness, elasticity, etc.)
u_{b}	Standard uncertainty of the correction of systematic errors b

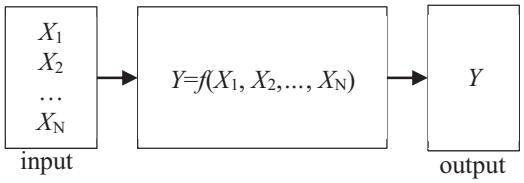

Fig. 1. Process chain of the Monte Carlo method for uncertainty estimation. X are input quantities and Y is the measurand. f represents a simulation platform that generates realistic XCT data.

The input parameters X_i are assumed to be random variables that follow a defined probability density function (PDF) (e.g. uniform or normal distribution) and are stochastically selected by pseudo-random generators for every simulation run. This leads to a standard uncertainty u_{sim} of Y (Equation 4). According to [9], total uncertainty values can be obtained by additional including uncertainty contribution from other sources (hybrid approach).

$$Y = y \pm U, \qquad U = k \cdot \sqrt{u_{\mathrm{sim}}^2 + u_{\mathrm{other}}^2} \tag{4}$$

Preferably, the distribution functions of X_i are determined by experiments or given by manufacturer specifications. If experiments are not available, their characteristics have to be estimated.

IV. Simulation Platform for the Estimation of Measurement Uncertainties

This work uses SimCT [11] a simulation tool for X-ray imaging and XCT. The tool considers all relevant effects from the generation of X-rays, to the interaction of X-rays with the virtual specimen and finally to the detection of X-ray. Surface models (triangle meshes and constructive solid geometries) and corresponding materials define virtual specimens. SimCT is capable of considering static, time and angle dependent misalignments during XCT scans with circular acquisition trajectories. Within this work, only static detector misalignments are considered by the MCM, whereby all other effects are considered as realistic as possible.

Projection images are reconstructed using the filtered back-projection algorithm published by Feldkamp et al. [12].

V. CASE STUDY

This paper presents a case study performed on an aluminum workpiece (alloy EN-AW7075) shown in Figure 2, where the measurement features diameter d_1, d_2 and d_3 are of interest.

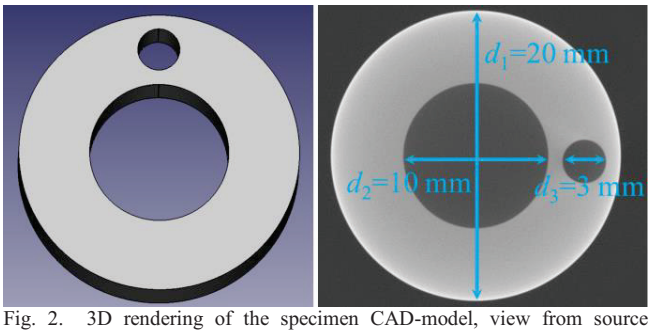

Fig. 2. 3D rendering of the specimen CAD-model, view from source towards detector in the first CT projection (left). Simulated slice image of the disk-like workpiece (thickness 4 mm) with three measurement features (right). The three diameter values are nominal values.

Several uncertainty estimations, based on the MCM, were done to analyze the relevance of five different uncertainty sources i listed in Table 2, where one uncertainty source contains at least one input parameter. Simulation series and uncertainty assessments (Equation 5) have been done for these five sources separately and all enabled at-once. Additionally, the separately determined uncertainties have been combined by Gaussian error propagation (Equation 6) to determine the expanded measurement uncertainty per measurand d_1, d_2 and d_3. Equations 5 and 6 do not contain the standard uncertainties u_b and u_{cal} due to the simulation-based determination.

$$U_{i,\mathrm{corr}} = k \cdot \sqrt{u_i^2} \tag{5}$$

$$U_{\mathrm{combined,corr}} = k \cdot \sqrt{\sum u_i^2} = k \cdot \sqrt{u_\mathrm{t}^2 + u_\mathrm{s}^2 + u_\mathrm{r}^2 + u_\mathrm{d}^2 + u_\mathrm{n}^2} \tag{6}$$

Realistic XCT simulations are done for scans on a micro-focus XCT device Rayscan 250E. This device uses an Viscom micro-focus tube XT9225-D 225 kV and a Perkin Elmer flat panel detector XRD 1620 AN14 (2048x2048 pixels, pixel size 200 µm). Table 2 shows the investigated, realistically chosen and bias-free uncertainty sources with x being the magnification axis. The label i will reflect the cause for a standard uncertainties u_i. Note that u_n is the uncertainty caused by enabling image noise in the simulation. Further constant scan parameters are: source-detector-distance 1500 mm, exposure time 266 ms, detector gain 16, binning 2x2, 600 projections, voxel size 40 µm, no additional filter plate to harden the spectrum. Simulations are done with four virtual rays per pixel, which is a trade-off between calculation time and sufficiently modeling partial volume effects. For the assessment of the measurement uncertainty per input parameter selection, 100 XCT simulations were done. The calculation time for 100 simulations was approximately 30 hours on an Intel Core i7 975 (3.33GHz) with an Nvidia GTX 285.

TABLE 2
INVESTIGATED UNCERTAINTY SOURCES

i	Input parameter	Unit	Distribution function
t	**X-ray tube**		
	Voltage	kV	uniform, a=178.0, b=182.0
	Current	µA	uniform, a=147.0, b=153.0
s	**Specimen**		
	translation in x	mm	uniform, a=-2.00, b=2.00
	translation in y	mm	uniform, a=-2.00, b=2.00
	translation in z	mm	uniform, a=-2.00, b=2.00
	rotation around x	°	uniform, a=68.0, b=72.0
	rotation around y	°	uniform, a=-1.00, b=1.00
	rotation around z	°	uniform, a=-1.00, b=1.00
r	**Rotary table**		
	x-position	mm	normal, μ=150, σ=0.01
d	**Detector**		
	y-position	mm	uniform, a=-0.20, b=0.20
	z-position	mm	uniform, a=-0.20, b=0.20
	rotation around x	°	uniform, a=-0.25, b=0.25
	rotation around y	°	uniform, a=-0.25, b=0.25
	rotation around z		uniform, a=-0.25, b=0.25
n	**Noise**		

Dimensional measurements on the virtual data were done using Volume Graphics Studio MAX 2.2.6. Surface points are determined by a local adaptive threshold [13] and have been geometrically registered to a CAD model of the workpiece. After that, cylinder geometries were fitted to approximately 1000 surface points per cylinder by the Gaussian best-fit method to determine the diameters d_1, d_2 and d_3.

VI. RESULTS

Initially, a simulation was performed as realistic as possible without any random input parameter. Results showed that systematic errors to the CAD values are significant with b_1=15.38 µm, b_2=-16.47 µm and b_3=-10.54 µm at a voxel size of 40 µm. The measurand's mean values of this simulation were used as reference value for all five uncertainty sources i. Additional, ideal simulations with monochromatic radiation without scatter confirmed, that these systematic deviations are caused by beam-hardening and scattered radiation. Consequently, reducing those effects by selecting an appropriate spectrum can lead to higher accuracies. Further, Figure 3 shows $U_{i,\mathrm{corr}}$ of diameters determined for the five different input parameter selections i given by Table 2. Their relevance depends on the measurement feature. For the presented investigation, the most relevant errors are caused by detector misalignments that remain uncorrected. All five effects had bias free PDFs and therefore induced only negligible additional systematic errors (<0.25 µm). Figure 4 shows the uncorrected measurands d_1 and d_2 of simulations were all five uncertainty sources were stochastically selected at-once "t,s,r,d,n". The corresponding uncertainty is shown in Figure 3. Expanded measurement uncertainties of this simulations and combined uncertainties of separate simulations (Equation 6) are only comparable for d_2 and d_3., This means Equation 6 might not be a suitable approximation to estimate measurement uncertainties for any kind of measurement feature, even though the uncertainty sources are bias free. Causes for this behavior will be investigated in future work. Note that all corrected expanded measurement uncertainties were beyond 5 µm (equivalent to 1/8 of the used voxel size) for realistic uncertainty sources.

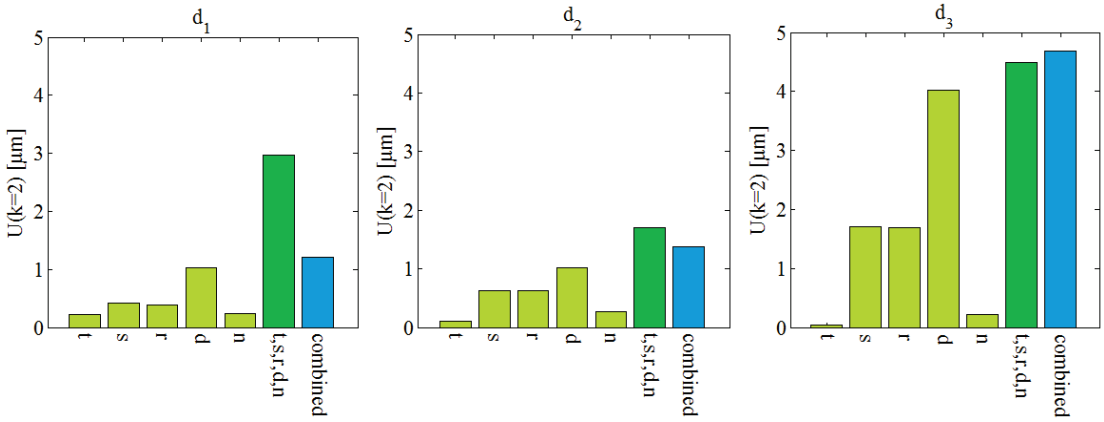

Fig. 3. Corrected expanded measurement uncertainty of diameter d_1 (left), d_2 (mid) and d_3 (right). Corrected bias b_1=15.38 µm, b_2=-16.47 µm and b_3=-10.54 µm. Bright green, the uncertainties resulting from separated simulations per input parameter combination i. In dark green the result of simulations that consider all uncertainty sources at-once (Equation 6) and in blue the combined uncertainty calculated by Equation 5.

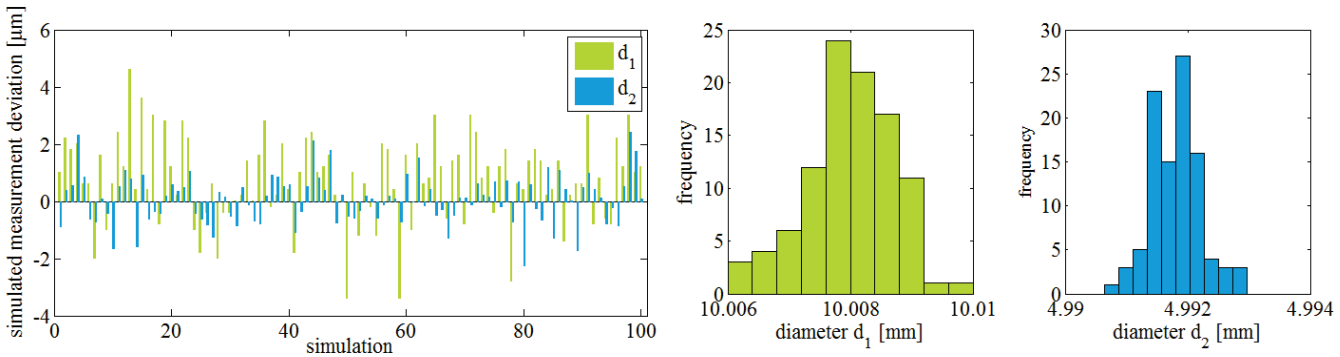

Fig. 4. Measurement deviation of d_1 and d_2 for the 100 simulations with all uncertainties sources enabled at at-once "t,s,r,d,n" (left) and the corresponding histogram of the uncorrected measurement values (right).

VII. CONCLUSIONS

We have applied the MCM to dimensional XCT by using an established simulation platform (SimCT), investigated several uncertainty sources and estimated measurement uncertainties. For the shown investigation, the most relevant random measurement errors were caused by bias-free detector misalignments. Beam-hardening and scattered radiation are significant sources for systematic measurement errors. Consequently, we see simulation-based approaches as useful tool to estimate measurement uncertainties, investigate the relevance of uncertainty sources and to verify any kind of correction method.

REFERENCES

[1] J. Hiller, L. M. Reindl, A computer simulation platform for the estimation of measurement uncertainties in dimensional X-ray computed tomography, Measurement, Volume 45, Issue 8, October 2012, Pages 2166-2182, ISSN 0263-2241

[2] J.P. Kruth, M. Bartscher, S. Carmignato, R. Schmitt, L. De Chiffre, A. Weckenmann, Computed tomography for dimensional metrology, CIRP Annals, Manufacturing Technology 60 (2) (2011) 821–842.

[3] Guide to the Expression of Uncertainty in Measurement - JCGM, 100:2008, BIPM, 2008.

[4] ISO 15530-3, Geometrical product specifications (GPS) - Coordinate measuring machines (CMM): Technique for determining the uncertainty of measurement - Part 3: Use of calibrated work pieces or measurement standards. International Organization for Standardization, 2011.

[5] Bartscher M, Neukamm M, Koch M, Neuschaefer-Rube U, Staude A, Goebbels J, et al. Performance assessment of geometry measurements with micro-CT using a dismountable work-piece-near reference standard. European Conference on Non-destructive testing (ECNDT), 6/2010.

[6] VDI/VDE Gesellschaft Mess- und Automatisierungstechnik. VDI/VDE 2630 Part 2.1: Computertomographie in der dimensionellen Messtechnik; Bestimmung der Messunsicherheit und der Prüfprozesseignung von Koordinatenmessgeräten mit CT-Sensoren. Berlin: Beuth Verlag GmbH, 06/2015.

[7] Evaluation of measurement data - Supplement 1 to the "Guide to the expression of uncertainty in measurement" - Propagation of distributions using a Monte Carlo method – JCGM, 100:2008, BIPM, 2008.

[8] M. Hernla, M. Franke, K. Wendt, Aufgabenspezifische Messunsicherheit von Koordinatenmessungen (Task Specific Uncertainty of Coordinate Measurements), tm Technisches Messen, 2010.

[9] VDI/VDE 2617-7: Accuracy of Coordinate Measuring Machines – Parameters and their Checking – Estimation of Measurement Uncertainty of Coordinate Measuring Machines by Means of Simulation, Beuth, Berlin, 09/2008.

[10] ISO 10360-2, Geometrical product specifications (GPS) – Acceptance and reverification tests for coordinate measuring machines (CMM) – Part 2: CMMs used for measuring linear dimensions. International Organization for Standardization, 2011.

[11] M. Reiter, M. Erler, C. Kuhn, C. Gusenbauer, J. Kastner, SimCT: a simulations tool for X-ray imaging, Proceedings of Conference on Industrial Computed Tomography (iCT2016), Austria, Wels, 02/2016.

[12] L. A. Feldkamp, L. C. Davis und J. Kress, „Practical cone-beam algorithm," J.Opt.Soc.Am. A, Vol. 1, No. 6, p. 1984.

[13] C. Reinhart, Industrial computer tomography – a universal inspection tool, in: Proceedings of the 17th World Conference on Nondestructive Testing (WCNDT), Shanghai, 10/2014.

Micro-CT resolution promotion based on coupled dictionary training in sinogram

Shouping Zhu, Zhipeng Guo, Cuiping Bao, Jianxun Wang, Gaoqi Lv, Xu Cao, Jimin Liang, and Jie Tian

***Abstract*—The purpose of this manuscript is to promote the reconstruction resolution in micro-CT. We approach this problem by super-resolution via coupled dictionary training in sinogram. The coupled dictionaries are firstly trained from the sinogram images of 100 different random phantoms. Then super-resolution sinogram data are estimated based on the low resolution sinogram data with the help of coupled dictionaries. Finally the filtered back-projection method is utilized for reconstruction using the low resolution and the estimated high resolution sinogram data. Simulation and real data experiments show that super-resolution via coupled dictionary training in sinogram can promote the resolution of reconstructed result of micro-CT to a certain degree.**

***Index Terms*—promote resolution, super-resolution, coupled dictionary training, sinogram, micro-CT**

I. INTRODUCTION

MICRO-computed tomography (micro-CT) is widely used in small animal and materials research as its high resolution. Although the resolution of the micro-CT can reach several microns, the pace to get clearer CT image never stop. There are two ways to promote the resolution of CT image: hardware and software. Resolution can be promoted straightforward with the hardware upgrade, but it will accompany the increase of the whole system cost or the decrease of the field of view (FOV). On the other hand, some advanced or improved reconstruction algorithms can promote the resolution indirectly [1][2]. It will promote the resolution to a certain degree at a cost of calculating time and the algorithm complexity increase.

Super-resolution (SR) is an image restoration method which can restore the high resolution image from the low resolution image. SR algorithms have been widely developed and play an important role in image processing [3]. In recent decades, SR algorithms have spread to medical image process. In 2002, Hayit et al. used an iterative super-resolution algorithm to give improved resolution and better edge definition in the slice-select direction in magnetic resonance imaging (MRI) [4]. In 2006, John et al. demonstrated a super-resolution method for improving the resolution in clinical positron emission tomography (PET) scanners [5]. They obtain super-resolution images by combining four data sets with spatial shifts between consecutive acquisitions and applying an iterative algorithm. In 2014, Wim et al. introduced a discrete tomography super-resolution reconstruction approach, and applied to increase the reconstruction resolution [6]. In 2015, Yan et al. put forward a general framework of super-resolution in computed tomography system [7]. Dictionary training methods have been widely studied for image super resolution[8][9][10]. In this manuscript, we will use coupled dictionary training method for sinogram super resolution to promote the CT resolution.

The manuscript is organized as follows. Section II introduces the super-resolution algorithm via coupled dictionary training and the implement in sinogram data. In section III, simulation and real data experiments are carried out to evaluate the resolution promotion effect of the proposed method. Finally, a conclusion is given in Section IV.

This work was supported in part by the Natural Science Foundation of China under Grant Nos.81227901, 61471279, and the Fundamental Research Funds for the Central Universities.

Shouping Zhu, Zhipeng Guo, Cuiping Bao, Jianxun Wang, Gaoqi Lv, Xu Cao, Jimin Liang, and Jie Tian are with the Engineering Research Center of Molecular and Neuro Imaging of Ministry of Education, and the School of Life Science and Technology, Xidian University, Xi'an, Shaanxi 710071, China. Jie Tian is also with Key Laboratory of Molecular Imaging, Institute of Automation, Chinese Academy of Sciences, Beijing 100190, China. (Email: spzhu@xidian.edu.cn, tian@ieee.org)

II. METHODS

There are many kinds of super-resolution methods have been developed, interpolation-based, regularization based, training-based, and so on. Since the training-based super-resolution method put forward by Yang et al. in 2012 [8] performanced well in reality, we applied it into sinogram image super-resolution and it can be described as follows.

A. Coupled dictionary training for sparse recovery

For two coupled sparse feature spaces the latent space $X \subseteq \mathbb{R}^{d_1}$ and the observation space $Y \subseteq \mathbb{R}^{d_2}$, the existing mapping function $F : X \to Y$ can be represented from recovered signal x in X to observed signal y in Y as that $y = F(x)$. Assuming that the mapping function is nearly injective, we should find a coupled dictionary pair D_x and D_y in space X and Y, which should satisfy a condition that for any signal $y \in Y$, we can use its sparse representation in terms of D_y to recover the corresponding latent signal $x \in X$ in terms of D_x. Thus the coupled dictionary should satisfy the following equations for each signal pair $\{y_i, x_i\}$:

$$z_i = \underset{\alpha_i}{\operatorname{argmin}} \|y_i - D_y\alpha_i\|_2^2 + \lambda \|\alpha_i\|_1, \forall i = 1, ..., N \quad (1)$$

$$z_i = \underset{\alpha_i}{\operatorname{argmin}} \|x_i - D_x\alpha_i\|_2^2, \forall i = 1, ..., N \quad (2)$$

where $\{x_i\}_{i=1}^N$ and $\{y_i\}_{i=1}^N$ are the training samples from X and Y, α_i is the sparse code of x_i, λ is a parameter controlling the sparsity penalty and representation fidelity, and $\{z_i\}_{i=1}^N$ are the sparse representations.

The recovery of x from y can be divide into two part, find the sparse z representation of y in terms of D_y and estimate the latent signal as $x = D_x z$. The following squared loss term is defined to minimize the recovery error of x in dictionary training.

$$L(D_x, D_y, x, y) = \frac{1}{2} \|D_x z - x\| \tag{3}$$

Find the optimal dictionary pair $\{D_x^*, D_y^*\}$ by minimizing the empirical expectation of the squared loss term over the training signal pairs

$$\min_{D_x, D_y} \frac{1}{N} \sum_{i=1}^{N} L(D_x, D_y, x, y)$$

$$s.t. z_i = \underset{\alpha_i}{\operatorname{argmin}} \|y_i - D_y \alpha_i\|_2^2 + \lambda \|\alpha_i\|_1, i = 1, ..., N$$

$$\|D_x(:,k)\|_2 \leqslant 1, \|D_y(:,k)\|_2 \leqslant 1, k = 1, ..., N \tag{4}$$

where $\|D_x(:,k)\|_2$ is the kth column of Dx, $\|D_y(:,k)\|_2$ is the kth column of Dy.

As empirical loss in (4) does not guarantee that y can be well represented by D_y, a new loss function is defined.

$$L = \frac{1}{2}(\gamma \|D_x z_i - x_i\|_2^2 + (1-\gamma) \|D_y z_i - y_i\|_2^2) \tag{5}$$

here $\gamma (0 < \gamma \leqslant 1)$ used to balances the two reconstruction errors. When D_y is fixed, the sparse representation z_j can be determined for each y_i with D_y, and the problem of (5) can be reduces to

$$\min_{D_x} \sum_{i=1}^{N} \frac{1}{2} \|D_x z_i - x_i\|_2^2$$

$$s.t. z_i = \underset{\alpha}{\operatorname{argmin}} \|y_i - D_y \alpha_i\|_2^2 + \lambda \|\alpha\|_1, i = 1, ..., N$$

$$\|D_x(:,k)\|_2 \leqslant 1, k = 1, ..., N. \tag{6}$$

Since D_y is a highly nonconvex bilevel programming problem [11], descent method is applied to solve this problem.

$$\frac{\partial L}{\partial D_y} = \frac{1}{2}\{\sum_{j \in \Omega} \frac{\partial(\gamma R_x + (1-\gamma) R_y)}{\partial z_j} \frac{dz_j}{dD_y} + (1-\gamma) \frac{\partial R_y}{\partial D_y}\} \tag{7}$$

Here, $R_x = \|D_x z - x\|_2^2$ and $R_y = \|D_y z - y\|_2^2$, z_j is the jth element of z, and Ω denotes the index set for j.

In practice, a projected stochastic gradient descent procedure is employed to optimize D_y, many techniques are developed in the calculation optimization either. Thus the coupled dictionaries D_x and D_y can be obtained after training.

B. Coupled dictionary training in sinogram

In order to find the coupled dictionaries D_x and D_y in sinogram, we should first select a training data set. The data set consists of a series of high resolution (HR) images $\{X_i\}_{i=1}^N$. The low resolution (LR) images $\{Y_i\}_{i=1}^N$ are obtained by bicubic interpolation with the down sampled HR images. Since the super-resolution in angle space will bring many artifacts, the super-resolution is only carried out in detector bins. Then a large number of training HR/LR image patch pairs are obtained in HR images. The selected training data $\{x_i, y_i\}_{i=1}^N$ is N pairs of HR/LR patches of size $p \times p$ sample in $\{X_i, Y_i\}_{i=1}^n$. Then coupled dictionaries D_x and D_y in sinogram can be found as said in the preceding subsection.

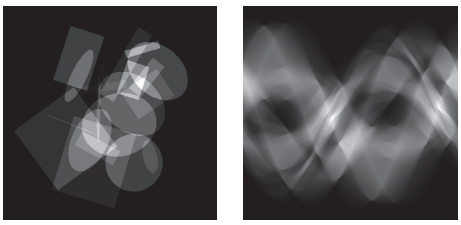

(a) Phantom (b) Sinogram

Fig. 1: Random phantom and sinogram. Each phantom consists of 10 ellipses and 10 rectangles, sinogram was obtained in 360 center degrees with 1024 detector pixels.

C. Patch wise sparse recovery

Since the coupled dictionaries D_x and D_y is found, HR image X can be restored from the LR image Y using the patch wise sparse recovery. It can be described as follow:

Step 1. Input low resolution image Y.

Step 2. Set HR image $X = 0$; upscale Y to Y' by bicubic interpolation.

Step 3. Select a $p \times p$ patch y_p in Y', $m = mean(y_p)$, $r = \|y_p - m\|_2$.

Step 4. Extract normalized gradient feature y for y_p.

Step 5. Calculated $z = argmin_a 1/2 \|D_y \alpha - y\|_2^2$.

Step 6. Recover HR patch feature: $x = D_x z / \|D_x\|$.

Step 7. Recover HR image patch $x_p = (c \times r) \bullet x + m$. Here c is a constant depending on the magnification scale.

Step 8. Add x_p to the corresponding pixels in X.

Step 9. Repeat Steps 3 to 8 until every divided patch is calculated.

III. EXPERIMENTS AND RESULTS

A. Super-resolution in sinogram

For coupled dictionary training, 100 random phantoms with the size 512×512 are created. Each phantom consists of 10 ellipses and 10 rectangles. The side length of the rectangles and the axis length of the ellipses are generated randomly, and the positions of the rectangles and the ellipses are also generated randomly. Projection data of these phantoms is acquired by distance-driven projection method [12]. 360 projections were generated cover 360°. The detector is modeled as a line array of 1024 bins. Therefore the size of each projection is 1024×360. Fig. 1 shows an example of the phantom and its corresponding sinogram. These sinograms are regarded as HR images, and the LR images are generated by binning the detector with a factor of 2. Therefore the size of low resolution projection is 512×360.

These sinogram images are applied for couple dictionaries training. 1,000,000 patches are selected and each patch contains 5×5 pixels. The magnification is set to 2×1, which

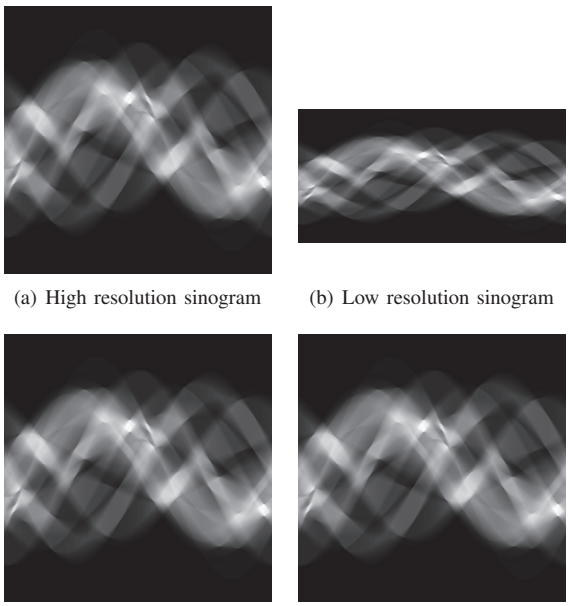

(a) High resolution sinogram (b) Low resolution sinogram

(c) Bicubic interpolation of (b) (d) Super-resolution of (b)

Fig. 2: Super-resolution for sinogram data. (a) is the original high resolution sinogram with the size 1024×360; (b) is correspond low resolution sinogram with the size 512×360; (c) is the bicubic interpolation result and (d)) is the result of super-resolution by direction training. Comparing with (a), the peak signal noise ratio (PSNR) of (c) is 65.63, and (d) is 66.96.

means that we only implemented super-resolution in detector bin direction. The training process is performed on a PC with Intel i7-3770 3.4 GHz CPU and Matlab 2012b is used. 234 seconds were taken after all the patches training completed. The super-resolution process of siongram data from low-resolution to high-resolution cost 216 seconds. The super-resolution results of sinogram are shown in Fig. 2. We chose the peak signal noise ratio (PSNR) as the image evaluation criteria, the lager the PSNR, the closer the compared two images. Comparing with (a), the PSNR of (c) is 65.63, and (d) is 66.96.

B. Simulation data experiment

In order to verify the promotion effect of the resolution in reconstruction, we create a phantom and perform simulation experiments. The phantom consists of some quartet grids in different width with 256×256 pixels. The projection is acquired in 360 degrees by 800 detector pixels, twice to enlarged with super-resolution in sinogram after double binning, and reconstruct with filtered back projection (FBP) method. The reconstruct results are shown in Fig. 3 and Fig. 4.

In Fig. 3(b), from left to right, top to bottom, the PSNR are 21.3868, 13.7068, 14.0551, and 15.4425 refer to the ideal image. Fig. 4 gives the corresponding profile of Fig. 3. We can see that the super-resolution reconstruction results are better than the bicubic interpolation and low resolution reconstruction result.

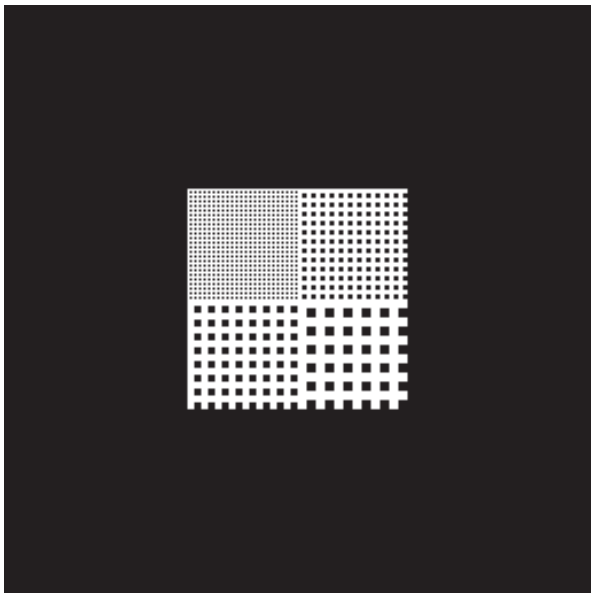

(a) Testing phantom

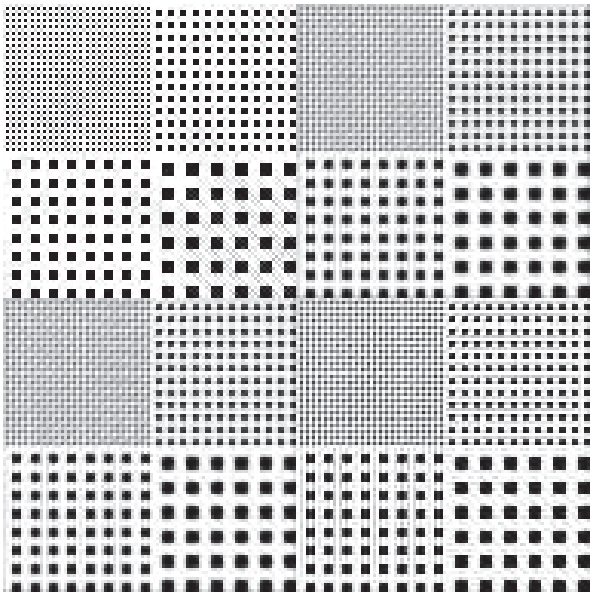

(b) Super-resolution of test phantom

Fig. 3: Simulation experiment effect in reconstruction. (a) is the ideal image. In (b), from left to right, top to bottom are the center region of reconstruction result with high resolution sinogram, low resolution sinogram, bicubic interpolation and super-resolution of low resolution sinogram. Referenced to the ideal image, the PSNR are 21.3868, 13.7068, 14.0551, and 15.4425.

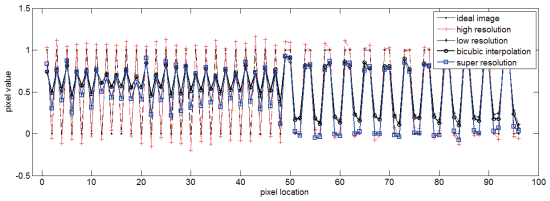

Fig. 4: Profile of the reconstruction result.

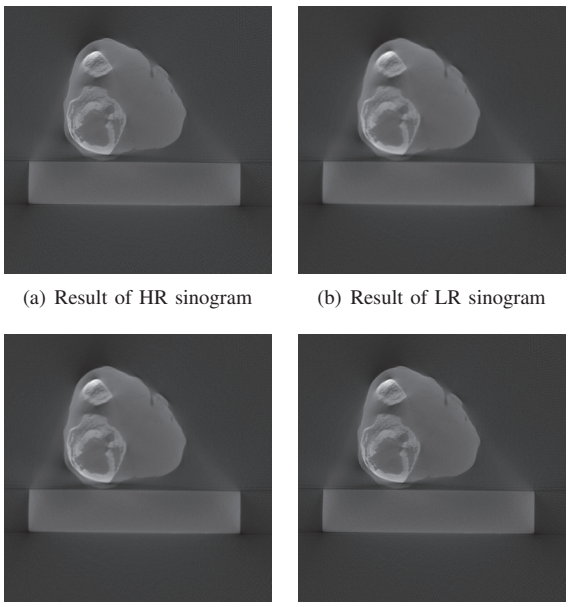

(a) Result of HR sinogram (b) Result of LR sinogram

(c) Result of BI sinogram (d) Result of SR sinogram

Fig. 5: Reconstruction result of high resolution (HR) sinogram, low resolution (LR) sinogram, bicubic interpolation (BI) sinogram and super resolution (SR) sinogram.

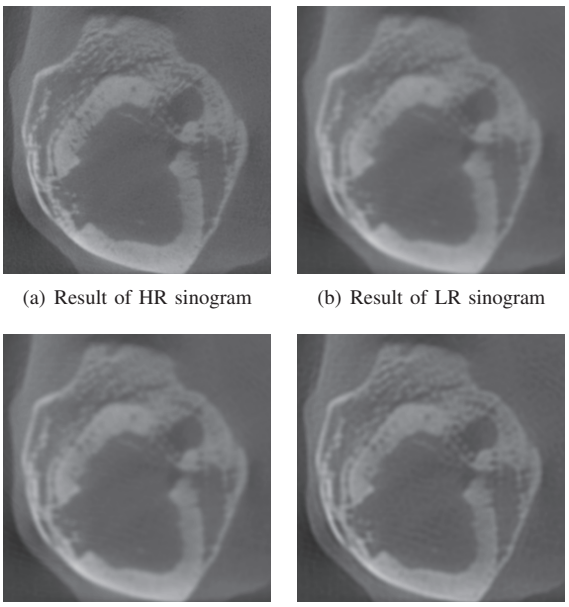

(a) Result of HR sinogram (b) Result of LR sinogram

(c) Result of BI sinogram (d) Result of SR sinogram

Fig. 6: Enlarged views of Fig. 5. Referenced to (a), the PSNR of (b), (c), (d) are 33.7142, 35.4099, and 36.1565.

C. Real data experiment

To investigate the effectiveness of the proposed method in real data, a rabbit leg is scanning by the prototype micro-CT system built in our lab. The system consists of a flat detector (Dexela1512, Dexela, UK) and a micro focus X-ray tube (L9181-02, Hamamatsu, Japan). 360 projections are collected around the subject over 360°. During scanning, the detector is set to 2×2 binning, and the center row of each projection is extracted to form a fan beam sinogram. Therefore the size of the sinogram is 972×360, with the pixel size 150μm. It is regarded as the high resolution data. The low resolution data is generated by binning the projection with the factor of 2×1. The super resolution sinogram is generated by the coupled dictionary training from the low resolution data. we also generate the corresponding bicubic interpolation(BI) super resolution sinogram for comparison in our experiment. The reconstruction of the sinogram is performed by the FBP method with the image size 1024×1024. The results are shown in Fig. 5, and the corresponding enlarged results are shown in Fig. 6. We can see the PSNR of (b), (c), (d) are 33.7142, 35.4099, and 36.1565 referenced to (a) in Fig. 6.

IV. CONCLUSION

In this paper, we have applied the super-resolution algorithm via coupled dictionary training to CT reconstruction to promote the reconstruction resolution. Simulation experiment shows that the resolution of reconstruction result after super-resolution in sinogram is significantly improved. In real data experiment, we can see more details in super-resolution group compared to the bicubic interpolation group. In conclusion, both simulation and real experiments show that super-resolution via coupled dictionary training in sinogram can promote the resolution of reconstructed result of micro-CT to a certain degree.

REFERENCES

[1] Pan X, Yu L, Kao C M, et al. “Spatial-resolution enhancement in micro-CT.”, *Nuclear Science Symposium Conference Record, 2003 IEEE*, vol. 5, pp. 3244-3247, 2003 .

[2] Toma A, Sixou B, Denis L, et al. “Higher order total variation super-resolution from a single trabecular bone image.”, *Biomedical Imaging (ISBI), 2014 IEEE 11th International Symposium on*, pp. 1152-1155, 2014.

[3] Park S C, Park M K, Kang M G. “Super-resolution image reconstruction: a technical overview.”, *Signal Processing Magazine*,vol. 20, no. 3, pp. 21-36, 2003.

[4] Greenspan H, Oz G, Kiryati N, et al. “Super-resolution in MRI.”, *Biomedical Imaging, 2002. Proceedings. 2002 IEEE International Symposium on IEEE*, pp. 943-946, 2002.

[5] Kennedy J A, Ora I, Alex F, et al. “Super-resolution in PET imaging.”, *IEEE Transactions on Medical Imaging*, vol. 25, no. 2, pp. 137-147, 2006.

[6] Van Aarle W, Batenburg K J, Van Gompel G, et al. “Super-resolution for computed tomography based on discrete tomography.”, *Image Processing, IEEE Transactions on*, vol. 23, no. 3, pp. 1181-1193,2014

[7] Yan Z, Li J, Yao L, et al. “Super resolution in CT.”, *International Journal of Imaging Systems and Technology*, vol. 25, no. 1, pp. 92-101, 2015.

[8] Jianchao Y, Zhaowen W, Zhe L, et al. “Coupled Dictionary Training for Image Super-Resolution.”, *IEEE Transactions on Image Processing A Publication of the IEEE Signal Processing Society*, vol. 21, no. 8, pp. 3467-3478, 2012.

[9] Gao J, Guo Y, Yin M., “Restricted Boltzmann machine approach to couple dictionary training for image super-resolution”, *Image Processing (ICIP), 2013 20th IEEE International Conference on*, pp. 499-503, 2013.

[10] Xiang S, Meng G, Wang Y, et al., “Image deblurring with coupled dictionary learning”, *International Journal of Computer Vision*, pp. 1-24, 2014.

[11] Colson B, Marcotte P, Savard G, “An overview of bilevel optimization.”, *Annals of Operations Research*, vol. 153, no. 1, pp. 235-256, 2007.

[12] De Man B, Basu S., “Distance-driven projection and backprojection in three dimensions.”, *Physics in medicine and biology*, vol. 49, no. 11, pp. 1477-1480, 2004.

Cardiac Motion Compensation from Short Scan CT Data: A Comparison of Three Algorithms

Juliane Hahn, Herbert Bruder, Thomas Allmendinger, Karl Stierstorfer, Thomas Flohr, and Marc Kachelrieß

***Abstract*—Aside from dose minimization, improving the temporal resolution is a main issue in cardiac computed tomography, when trying to provide images with diagnostic value. We compare three algorithms improving the temporal resolution of a single cardiac phase without taking information from any other phase: an iterative reconstruction technique, working on only a subset of the acquired data, and two motion vector field estimating algorithms, which are based on the optimization of an image artifact measuring cost function. The methods are compared with the help of a phantom measurement and are applied to patient cases.**

I. Introduction

THE location-dependent temporal resolution t_{res} of a standard short scan reconstruction is limited by the gantry rotation time t_{rot} and can be approximated by $t_{\text{res}} \approx t_{\text{rot}}/2$ close to the isocenter in case of single source systems as illustrated in reference [1].

Measurements of coronary artery velocities have demonstrated that the right coronary artery moves with an average speed between $35\,\text{mm/s}$ and $70\,\text{mm/s}$ for patients with heart rates between 45 bpm and 100 bpm [2]–[5]. Such velocities can lead to large displacements of the vessels during data acquisition which introduces strong motion artifacts in the reconstructions.

As a consequence, quite a few algorithmic solutions have been proposed in cardiac CT to further increase the temporal resolution and thus the image quality. They can be divided into two major groups: iterative reconstruction techniques utilizing a smaller data range than needed for a conventional reconstruction via filtered back projection (FBP) [6]–[8], and motion compensation (MoCo) algorithms estimating space- and time-resolved motion vector fields (MVFs) compensating for the motion during data acquisition [9]–[14].

The iterative reconstruction algorithms aim at increasing the temporal resolution by using only little more than half of the short scan data for reconstruction ($\approx 120°$). In such approaches, an additional regularization must be introduced to prevent limited angle artifacts, which occur due to missing data. In order to restrict the influence of the limited view, prior knowledge has to be introduced during iterative reconstruction which is realized by a regularization.

The Temporal Resolution Improvement Using Prior Image Constraint Compressed Sensing (TRI-PICCS) - algorithm [6] uses a low-temporal resolution short scan reconstruction as prior image and performs an iterative PICCS [15] reconstruction over only a subset of the measured data. The PICCS algorithm employs a regularization via total variation to limit the influence of the limited view associated with the data used for reconstruction and the motion incorporated in the prior image. However, in reference [1] it has been emphasized that the apparent improvement in temporal resolution is only comparable to an improvement in temporal resolution from direct fan-beam reconstruction with Parker weights to a parallel-rebinned FBP reconstruction.

Another option to prevent limited angle artifacts in an iterative reconstruction from less than the short scan data has been introduced with the Temporal Resolution Improvement Method (TRIM) [7], [8]. A constraint based on a prior image histogram is introduced, pushing small gray values towards higher values, thereby reducing limited angle artifacts as explained in more detail in section II-A.

Completely differing from the first group, most of the algorithms of the second category employ a 3D registration routine working on the reconstructions of multiple cardiac phases to obtain motion compensation. For those algorithms much more data than needed for a single short scan reconstruction have to be acquired and in general a reference phase of quite good image quality must exist. Though, especially in cases of patients with high or irregular heart rates, such a "good" reference phase, which is often the mid-diastole, might not exist [2].

For this reason and with regard to dose minimization we are going to focus on algorithms of this group increasing the temporal resolution by utilizing only the data needed for the reconstruction of a single cardiac phase, which is the short scan data range. The first MoCo method, which is dubbed after Motion Artifact Metric optimization (MAM) [13], derives the MVFs analytically by optimizing a cost function, which measures the amount of motion artifacts in the image, and applies them to the rawdata. This leads to an image with reduced motion artifacts after FBP reconstruction (see section II-B1). The second MoCo algorithm [14] is based on the reconstruction of a series of partial angle images or volumes that are used to estimate the motion and then are shifted and added to obtain a motion artifact–free volume (see section II-B2). We herein entitle this method PAMoCo (Partial Angle reconstruction-based Motion Compensation).

We compare the iterative reconstruction technique TRIM and the two MoCo methods. In a previous comparison between the TRIM and the TRI-PICCS algorithm (reference [1]) the TRIM algorithm has already proven superior visualization.

J. Hahn and Prof. Dr. M. Kachelrieß: German Cancer Research Center (DKFZ), Im Neuenheimer Feld 280, Heidelberg, Germany.

Dr. H. Bruder, Dr. T. Allmendinger, Dr. K. Stierstorfer, and Prof. Dr. T. Flohr are with Siemens Healthcare GmbH, Siemensstraße 1, Forchheim, Germany.

Corresponding author: Juliane Hahn (juliane.hahn@dkfz.de)

Therefore, we choose the TRIM method for comparison. Furthermore, this way we are able to compare algorithms of the different groups starting from the same rawdata for reconstruction. We here focus on single source CT systems that inherently suffer from a lower temporal resolution than dual source CT systems, although some of the presented algorithms can be straight forward applied to dual source systems.

II. Materials and Methods

A. Iterative Reconstruction TRIM

In order to prevent limited angle artifacts, when utilizing less than the short scan data, a conventional simultaneous algebraic reconstruction technique (SART), which optimizes the raw data fidelity $C_1(f) = |\mathsf{X}f - p'|^2$ has been extended by a regularization term $C_2(f)$ to

$$C(f) = C_1(f) + \beta C_2(f). \tag{1}$$

Herein f is the reconstructed image to be determined, p' the raw data subset containing approximately 120° of the original short scan projection data and X the forward projection operator. The parameter β controls the strength of the regularization, which has been chosen to be a histogram constraint

$$C_2(f) = -\sum_i \log(\omega(f(x_i))). \tag{2}$$

The probability density ω to find a gray value $f(x_i)$ is approximated by local histograms which are derived in small parts of the image f, e.g. of the regions close to the coronary arteries. The optimization is divided into a SART-step and an adaption-step considering the regularization term, in which unnatural gray values introduced by limited angle artifacts are pushed towards local maxima of the histogram. Initializing the optimization with the original low-temporal resolution FBP image f_{FBP}, the FBP image guarantees that the SART finds a solution close to it and acts as prior information when providing the histograms. However, since f_{FBP} is a low-temporal resolution image, a dependence of the histogram to motion artifacts might have an influence on the final reconstruction.

Interestingly, exactly this fact is used in the following two methods, where the images entropy E, which is computed using histograms of the images, is employed as a measure for the artifact amount in the reconstruction.

B. Motion Compensation Algorithms

The concept of motion estimation is to estimate MVFs $\boldsymbol{s}(\boldsymbol{r}, t)$ which are sub-sampled in time and space in order to compensate for the unknown motion during data acquisition. Usually, the two major steps - motion estimation - and motion-compensated reconstruction - are performed in an alternating manner during a cost-function optimization to obtain a final, image artifact-free reconstruction. The two methods which we are going to investigate focus on those regions of the heart where motion artifacts are typically occurring and which are of relevance for diagnosis: the coronary arteries and their surrounding regions. Their visualization is highly relevant for the diagnosis of cardiovascular diseases, for stent evaluation or for plaque detection and quantification.

For this reason, and in order to reduce the computational costs, as a first step a segmentation is performed reducing the volume relevant for MoCo to the region of interest (ROI) Ω_{seg}. The MoCo operates only on the voxels of this ROI.

The two methods differ in the way how motion is modelled as well as how the MVFs are applied.

1) MAM Algorithm: Due to the limitation to the usage of short scan data, motion estimation in this case is not based on a registration of images. Instead, the MAM algorithm is based on the assumption that the amount of motion artifacts can be measured and compressed to a single number. As suggested in reference [13], the image entropy

$$E = \sum_v h(v) \ln h(v) \tag{3}$$

is used. It is known from information theory and it has been shown to be a viable measure for the occurrence of motion artifacts. In equation (3) v is the CT value and $h(v)$ is the image's histogram. Motion is modeled by a vector field

$$M(t, \boldsymbol{r}, \boldsymbol{s}) = \boldsymbol{r} + \boldsymbol{s}(t, \boldsymbol{r}), \tag{4}$$

composed of in time and space sub-sampled motion vectors $\boldsymbol{s} \in \mathbb{R}^N$, which are placed along in time and space equally spaced control points at voxel positions $\boldsymbol{r} \in \mathbb{R}^3$. In between the control points the vectors are simply obtained by linear interpolation. A motion-compensated reconstruction is done by warping the voxel space according to equation (4) and performing a back-projection in an FBP-like manner as proposed by Schäfer et al. [16]. For fast and efficient motion estimation a gradient descent algorithm with adaptive step size has been chosen for the motion estimation, which is possible when approximating the entropy by Parzen-windowing with Gaussian kernels enabling to calculate derivatives of the cost function.

2) PAMoCo Algorithm: The algorithm proposed in references [14], [17] is based on the reconstruction of a series of partial angle images, from small double-overlapping segments of the original short scan data. Since the projection angle ϑ can be interpreted as time coordinate, the temporal resolution of the partial angle reconstructions (PARs) is increased by a factor of $(2K+1)/2$, depending on the number $S = 2K+1$ of partial angle reconstructions. The PARs are shifted using the estimated MVFs. Finally, the motion-compensated reconstruction is obtained by adding shifted PARs

$$f_{\text{MoCo}}(\boldsymbol{r}) = \sum_k f_k(\boldsymbol{r} + \boldsymbol{s}(\boldsymbol{r}, t_k)), \tag{5}$$

where $-K \leq k \leq K$ counts the PARs $f_k(\boldsymbol{r})$ centered around the angles $\vartheta_k = \vartheta_0 + k\Delta\vartheta$ and angular span $\Delta\vartheta = \pi/(2K+1)$ defining the temporal resolution of the reconstruction. In order to reduce the computational amount and to regularize the MVF, the temporal dependence of the motion model is approximated by a low degree polynomial

$$\boldsymbol{s}(\boldsymbol{r}, t) = \sum_{p=1}^{P} \boldsymbol{a}_p(\boldsymbol{r})(t - t_0)^p, \tag{6}$$

where P denotes the highest power of the polynomial. The unknown coefficients $\boldsymbol{a}_p(\boldsymbol{r})$ are determined by optimizing

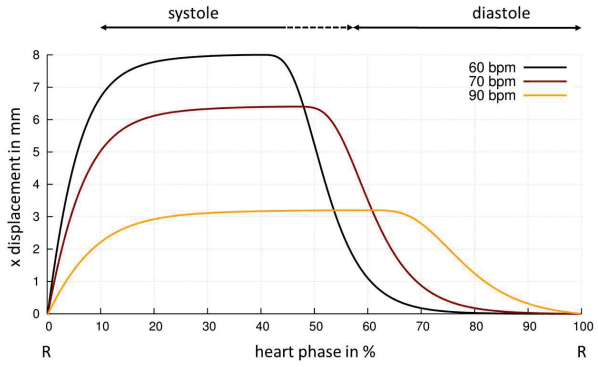

Figure 1. x-motion in mm in dependence of the heart phase applied by the motion robot at three different heart rates: 60, 70 and 90 bpm. With increasing heart rate, a lowering of the amplitude and shortening of the diastolic phase, as indicated by the dashed line, has been taken into account.

an image metric, e.g. the entropy, as proposed in reference [13]. Because of the non-convexity of the cost function, the optimization is re-initialized multiple times. For the actual optimization, Powell's algorithm is used, which is a derivative-free optimization routine, where non-linear constraints to the parameters can be included.

C. Evaluation

We compare the algorithms presented above with the help of a phantom measurement. A motion robot triggered by an ECG-like signal is connected to a synthetic vessel phantom. Each vessel phantom consists of a cylinder of diameter d imitating the attenuation properties of a vessel in the absence of contrast media with an attenuation leading to a CT value of $50\,\mathrm{HU}$ at $120\,\mathrm{kV}$ in the absence of motion. The vessel is placed inside a water tank, which is surrounded by a body phantom. The simulated motion depends on the heart rate, also simulating the non-proportional shortening of diastole and systole at higher heart rates as described in reference [2]. The effect of the shortening in case of the x-component of the simulated motion at different heart rates is illustrated in figure 1. The data were acquired with a Siemens SOMATOM Force system in a low pitch spiral acquisition mode enabling the reconstruction of multiple cardiac phases.

We measured three vessel phantoms with $d = 1.5\,\mathrm{mm}, 2.5\,\mathrm{mm}$ and $3\,\mathrm{mm}$ diameter and equipped each cylinder with a suitable stent, each of different type, showing different characteristics in the reconstruction. Due to the rotation time of $t_{\mathrm{rot}} = 250\,\mathrm{ms}$ of the CT system, the temporal resolution can be approximated by $t_{\mathrm{res}} \approx 125\,\mathrm{ms}$ at the location of the vessel which was positioned approximately in the center of the field of view (FOV) when using only data acquired by detector A for the reconstruction. In a first step, we measured the stents without applying motion. Each measurement was then repeated three times with heart rates $60\,\mathrm{bpm}, 70\,\mathrm{bpm}$ and $90\,\mathrm{bpm}$ and motion. With this setup we are able to simulate the translation of a rigid object and scan it under realistic conditions. Since we are interested in increasing the temporal resolution in case of single source systems, we used only the data acquired by detector A for motion estimation and motion-compensated reconstruction. We scanned at a voltage of $90\,\mathrm{kV}$ with an effective dose of $640\,\mathrm{mAs}$ per rotation.

We further compare the algorithms with five coronary CT angiography patient cases with heart rates between 50 bpm and 70 bpm acquired with a Siemens SOMATOM Definition AS system, with a rotation time of $t_{\mathrm{rot}} = 285\,\mathrm{ms}$ and perform several reconstructions at phases slightly shifted from the best phase for reconstruction.

Since the MAM and TRIM algorithm are designed to improve the image quality of a reconstruction close to a best phase, we are going to compare the three algorithms only in this region.

We proceeded in a similar manner in case of the phantom measurement, where we determined the heart rate dependent best phase by introducing a quality measure Q. Q assesses the amount of motion taking place during data acquisition by summing over the absolute displacement in the respective heart phase:

$$Q(c) = \int_{c}^{c+\Delta c} |\dot{\boldsymbol{p}}(c')| dc', \tag{7}$$

where $\boldsymbol{p}(c')$ is the position of the vessel phantom, c the start heart phase of the reconstruction and Δc the half scan range in units of the heart phases. Q as a function of c for a heart rate of 70 bpm is shown in figure 2, where we evaluate only phases between 20% and 80% of the cardiac cycle, since the other would not be considered for reconstruction anyways due to the strong displacement close to the R-peak. At this heart rate we detect the best phase at $c = 70\%$ and choose to slightly shift the phase of interest in 5%-steps to 65% and 60% for the evaluation of the algorithms.

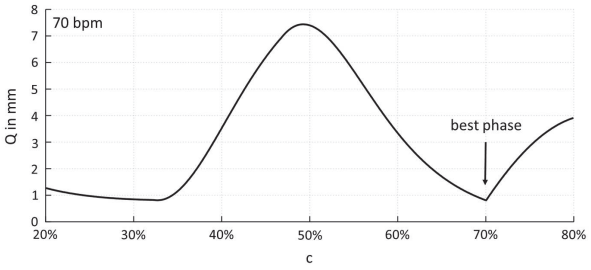

Figure 2. Motion measure Q in dependence of the reconstruction phase c in % of the heart beat at 70 bpm.

III. Results

As explained in section II-C in case of the phantom measurement and the clinical cases we reconstructed at cardiac phases slightly shifted from the best phase in order to compare the three algorithms.

The reconstructions at a simulated heart rate of 70 bpm with a vessel phantom of $d = 2.5\,\mathrm{mm}$ at $c = 60\%$ and $c = 65\%$ are shown in figures 3 and 4. From left to right the standard short scan reconstruction, TRIM, MAM and PAMoCo results are presented. In the first row an axial view of the middle image

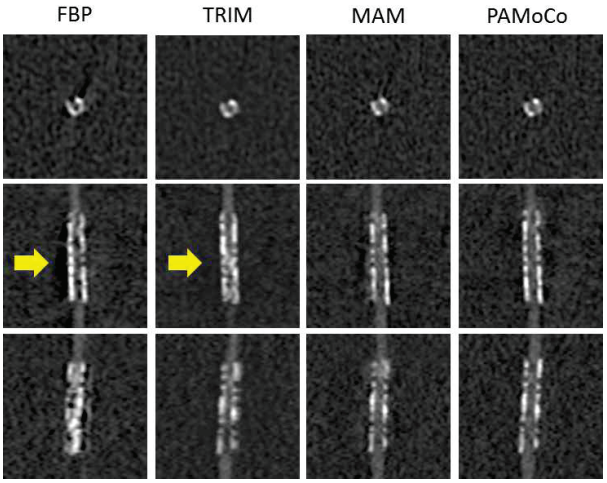

Figure 3. FBP, TRIM, MAM and PAMoCo reconstructions (from left to right) at 65% of the simulated cardiac cycle with C = 400 HU, W = 1500 HU. From the first to the last row axial, coronal and sagittal planes of the respective reconstructions are displayed. A stent with a diameter of $d = 2.5\,\mathrm{mm}$ and a simulated heart rate of 70 bpm has been used for this measurement.

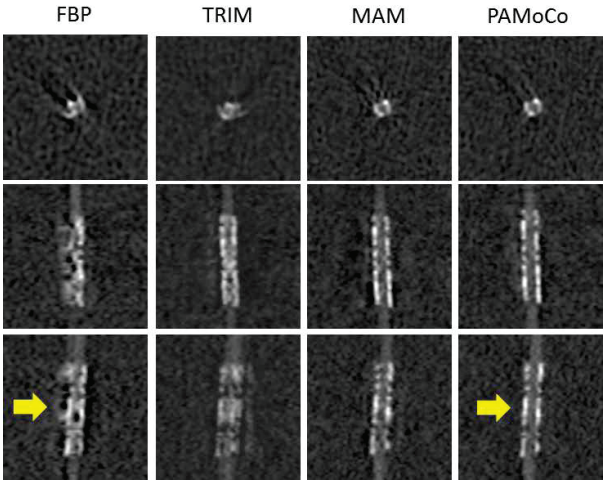

Figure 4. FBP, TRIM, MAM and PAMoCo reconstructions (from left to right) at 60% of the simulated cardiac cycle with C = 400 HU, W = 1500 HU. From the first to the last row axial, coronal and sagittal planes of the respective reconstructions are displayed. A stent with a diameter of $d = 2.5\,\mathrm{mm}$ and a simulated heart rate of 70 bpm has been used for this measurement.

plane is depicted. For a better three-dimensional visualization we further show coronal and sagittal planes in the second and third row. The intersection point of the planes has been chosen such that the best visualization could be achieved for each reconstruction.

At the heart phase of $c = 65\%$ (see figure 3) a strong shading artifact appears in the standard reconstruction due to motion, which is best visible in the second image of the first column. Due to an increased temporal resolution in the other reconstructions, the shading disappears and an image of increased sharpness is the result in case of all three algorithms under investigation. Note that in case of TRIM it looks as if image sharpness has increased more strongly, since the stent can be differentiated better from the background than in the MoCo cases. This is due to the fact that negative entries evoked by noise are pushed towards higher values during the iterative reconstruction as well. Hence, the noise seems to be smoothed in the region the TRIM algorithm operates.

However, in the reconstructions at $c = 60\%$ (see figure 4) more severe blurring artifacts induced by motion are visible as indicated by the yellow arrow in the third row of the first column. In the phantom study, at higher heart rates and at phases featuring stronger motion, we observe a slight advantage of the MoCo algorithms, since depending on the number of temporal control points, which we chose to be 6 for the MAM algorithm and 31 for the PAMoCo, a higher temporal resolution when compared to TRIM, can potentially be reached.

Similar results were obtained in the patient study, where we have to note that no patient with a really high or irregular heart rate was included. Reconstructions of the patient cases with curved MPRs will be shown at the meeting due to a limited amount of space in this abstract. in the revised abstract.

IV. Conclusion

All algorithms have proven their capability of improving the image quality in the region of the coronary arteries when slight motion artifacts are present in case of the phantom study and patient data. However, the PAMoCo algorithm might have the ability to compensate for motion even in cardiac phases showing very severe motion artifacts. For this reason, the PAMoCo algorithm should be compared to some registration-based algorithms as described in section I, which have been shown to have the biggest impact in case strong motion is apparent.

References

[1] H. Schöndube *et al.*, *Med. Phys.*, vol. 40, pp. 31 112–31 122, 2013.
[2] L. Husmann *et al.*, *Radiology*, vol. 245, no. 2, pp. 567–576, November 2007.
[3] S. Achenbach *et al.*, *Radiology*, vol. 216, p. 457463, 2000.
[4] M. Vembar *et al.*, *Med. Phys.*, vol. 30, pp. 1683 – 1693, July 2003.
[5] G. Shechter *et al.*, *IEEE Transactions on Medical Imaging*, vol. 25, no. 3, pp. 369 – 375, March 2006.
[6] G.-H. Chen *et al.*, *Med. Phys.*, vol. 36, pp. 2130 – 2135, June 2009.
[7] H. Schöndube *et al.*, *SPIE Medical Imaging Conference program*, pp. 7961 – 7968, February 2011.
[8] ——, *Conference Program of the 1st International Conference on Image Formation in X-Ray Computed Tomography*, pp. 189–193, 2010.
[9] S. Kim *et al.*, *Med. Phys.*, vol. 42, pp. 2560 – 2571, May 2015.
[10] R. Bhagalia *et al.*, *Med- Phys.*, vol. 39, pp. 4245 – 4254, July 2012.
[11] Q. Tang *et al.*, *Med- Phys.*, vol. 39, pp. 4291 – 4305, July 2012.
[12] A. Isola *et al.*, *Med. Phys.*, vol. 37, pp. 1093 – 1109, March 2010.
[13] C. Rohkohl *et al.*, *Med. Phys.*, vol. 40, pp. 31 901 – 31 916, March 2013.
[14] J. Hahn *et al.*, *Program of the 101st Scientific Assembly and Annual Meeting of the RSNA*, p. 152, November 2015.
[15] G.-H. Chen *et al.*, *Med. Phys.*, vol. 35, pp. 660 – 663, May 2008.
[16] D. Schäfer *et al.*, *IEEE Transactions on Medical Imaging*, vol. 25, pp. 898 – 906, 2006.
[17] J. Hahn *et al.*, *SPIE Medical Imaging Conference Program*, 2016, accepted for an oral presentation at the SPIE Medical Imaging conference 2016.

Motion estimation for cardiac functional analysis using low dose x-ray computed tomography

George S. K. Fung, Luisa Ciuffo, Hiroshi Ashikaga, and Katsuyuki Taguchi*

Johns Hopkins University School of Medicine
(*ktaguchi@jhmi.edu, 601 N. Caroline St., JHOC 4263, Baltimore, MD 21287 U.S.A.)

***Abstract*—This work concerns an image-based cardiac motion estimation method (iME) for computed tomography (CT)-based cardiac functional analysis (CFA) with a reduced radiation dose. As CT-CFA requires images over the entire heart beat, the scans are often performed at 10-20% of the tube current settings that are typically used for coronary CT angiography. A large image noise then degrades the accuracy of motion estimation. In this study, we propose to use two CT scan data, one for CT angiography at a quiescent phase at a standard (full) dose and the other for CFA over the entire heart beat at the low dose. We modified the iME we have previously developed for a full-dose retrospectively-gated coronary CT angiography for the 2-scan protocol and assessed the accuracy of the estimated motion vector field. The study confirmed that the modified iME was robust against the mismatch of noise levels, contrast enhancement levels, and shapes of the chambers.**

***Index Terms*—CT, motion estimation, cardiac function analysis**

I. Purposes

Cardiavascular diseases remain the leading cause of death in the western world, placing an ever-increasing burden on both private and public health services. Electrocardiogram (ECG)-gated coronary computed tomography (CT) angiography imaging is an established non-invasive technique for detecting coronary stenosis caused by calcium deposits and fatty soft atherosclerosis. CT angiography's negative predictive value (NPV) for coronary artery diseases is high enough (>90%) to be integrated into the diagnostic workflow patients with chest pain and a risk of heart failure. It has been discussed, however, that in order to better predict the future heart events, it is highly desirable to obtain the functional information on the cardiac motion such as asynchrony in addition to the anatomical information on coronary arteries and the heart. Cardiac functional analysis (CFA) provides a different class of information, which is critical to heart failure, is currently obtained by echocardiography (ultrasound), tagged magnetic resonance imaging (MRI), or nuclear medicine. Neither of them is perfect with limitations in the number of view angles and strong operator-dependency in echo, a cost and availability of the system in MRI, and the spatial resolution and signal-to-noise ratio of images in nuclear medicine.

When a heart is scanned for one heart beat by CT, it provides 4-D cardiac images for 10-20 cardiac phases with a good spatial resolution [$(0.5\ \text{mm})^3$ per voxel] and tissue contrast. Regional motion and the correlation to coronary plaques can be analyzed reliably without a problem with mis-registrations, which would have been an issue if two separate exams were performed, one for CT angiography and the other for CFA. Thus, CT-based CFA can be a valuable option in practice.

One of the major issues with CT exams is a radiation dose to patients, thus, in order to minimize the dose, there are two possible scenarios in clinical routines: (a) First, a CT angiography scan is performed at a standard (full) dose. When an onsite review is not normal, a CT-CFA is then performed at a low dose level. The CT angiogram will target at one cardiac phase (typically a mid-diastole) for 1-3 mSv, while the CFA scan will provide 10-20% dose for the entire cardiac cycle for 0.4-2.4 mSv. (b) A joint CT angiography-CFA is performed with a single scan. A prospectively-gated tube current modulation is used to provide a full dose for one cardiac phase and 10-20% dose for the other phases. In this study, we tackle the scenario (a), as it was approved by our institutional review board.

The problem of the low-dose CFA scan is that images are very noisy, which may degrade the accuracy of CFA severely. A method which estimates the motion between adjacent consecutive frames sequentially as many video encoders (Fig. 1a), may not be suitable as it may try to match an image noise in one frame to an image noise in the next frame. A method that uses a local-matching technique such as the demon algorithm may not perform well due to the large image noise.

We have developed an image-based motion estimation method (iME) which uses one cardiac phase as an anchor and estimates motion to the other phases (Fig. 1b) [1]. iME estimates a non-rigid deformation of the heart using an intensity-based optimization method by minimizing a sum of squared weighted differences with spatial and temporal roughness penalty terms. iME has been evaluated with images at the full dose over the heart beat with clinical data [1,2] and swine data [3]. In this study, we modified iME to adapt to scenario (a) and assessed the performance using clinical data.

II. Methods

We briefly describe the original iME in Sec. II.A and outline how it is adapted to handle scenario (a) in Sec. II.B, and evaluation methods in Sec. II.C.

A. The original iME

The following three major components of the algorithm are described: the deformation model, the cost function, and the optimization algorithm.

Deformation model: An image at a quiescent motion phase, $f(\vec{x}, t_0)$, was chose as a reference phase and a point $\vec{x}$ at t_0 moves to a point

$$\vec{x}' = \vec{x} + \vec{u}(\vec{x}, t_0, t) \quad (1)$$

at phase t, where a motion vector $\vec{u}$ is uniquely defined by $\vec{x}$, t_0 and t. An image at phase t can then be calculated from the reference image as

$$f_c(\vec{x}', t) = f(\vec{x}, t_0). \quad (2)$$

The motion vector $\vec{u}$ is modeled by a finite number of knots

using cubic B-splines as

$$\vec{u}(\vec{x},t_0,t)=\sum_{\tau=1}^{N_\tau}\sum_{\vec{i}}\ \theta_{\vec{i},\tau}b\left(\frac{t}{\Delta t}-\tau\right)\beta\left(\frac{\vec{x}}{|\Delta\vec{x}|}-\vec{i}\right), \qquad (3)$$

where $|\Delta\vec{x}|$ and Δt are the knots spacing in the spatial and temporal domain, respectively, $\vec{i}$ and τ are the corresponding discrete sampling indices, $\theta_{\vec{i},\tau}$ are the cubic B-spline coefficients, N_τ is the number of knots in time, b is the 1-D cubic B-spline, and β is a 3-D tensor product of cubic B-splines.

Cost function: The warping parameters $\theta_{\vec{i},\tau}$ are estimated by minimizing a regularized weighted least-squared difference between the warped reference image and the target images

$$\hat{\theta}_{\vec{i},\tau}=argmin_{\theta_{\vec{i},\tau}}\ L_w\left(\theta_{\vec{i},\tau}\right)+R\left(\theta_{\vec{i},\tau}\right), \qquad (4)$$

where $L_w\left(\theta_{\vec{i},\tau}\right)$ is a similarity metric

$$L_w\left(\theta_{\vec{i},\tau}\right)=\sum_{m=1\ldots N_m}\left\|w(\vec{x},t_m)\left[f\left(\vec{x}',t\right)-f_c\left(\vec{x}',t\right)\right]\right\|^2, \qquad (5)$$

where N_m is the number of discrete phases in one heart beat, $w($) is a weighting function, and $R\left(\theta_{\vec{i},\tau}\right)$ denotes weighted two quadratic penalty terms, one in space and the other in time.

Optimization: We use an iterative coordinate descent-type method with the conjugate gradient (CG) algorithm to minimize the cost function Eq. (4). The cost function is minimized with respect to one cardiac phase m at a time using CG sweeping through phases, then repeat the process for the next iteration. This local optimization method allows for making the size of the Hessian matrix manageable. Further, to save computation time, the Hessian matrix was updated once in every five iterations. The detail of the algorithm can be found in [1].

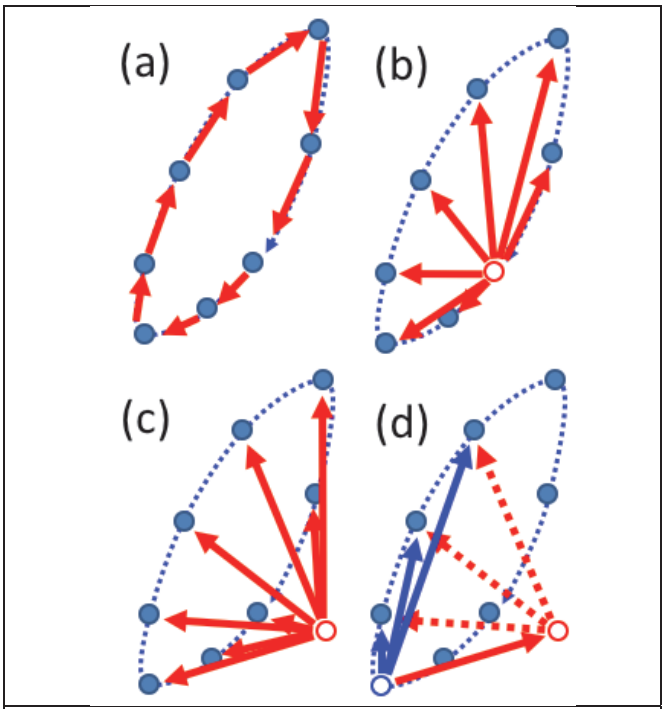

Figure 1. Diagrams to outline various strategies for motion estimation. Blue dashed curve, the the true motion path; blue solid circles, locations at discrete phases. (a) The motion paths between the adjacent phases (red arrows) are estimated sequentially. (b) One of the phases is used as an anchor phase (red open circle) and the motion from the anchor to other phases are estimated. The original iME uses this strategy. (c) The anchor is obtained from a different scan and the motion from the anchor to all of the phases are estimated. The proposed, modified iME uses this strategy. (d) A new anchor phase is decided (open blue circle) and the motion from the new anchor to other phases (blue solid arrows) are obtained by concatenating the inversed motion path (red solid arrow) to the old anchor (red open circle) and the estimated motion to other phases (red dashed arrows).

B. *Modifications for low-dose 2-scan CT-CFA*

We have made two modifications to the original iME: (1) the reference image $f(\vec{x},t_0)$ is obtained from a separate CT angiography image; and (2) a 3-D median filter is applied to the noisy CFA scan images, $f_s(\vec{x}',t)=median\left(f(\vec{x}',t)\right)$, and the smooth images $f_s(\vec{x}',t)$ are used in the place of $f(\vec{x}',t)$ in Eq. (5).

Problems with image noise: Since the reference image is obtained from a standard (full) dose scan, the reference image is much less noisy, thus, it allows us to avoid matching noise to noise discussed in Introduction. In addition, applying a median filter decreases the noise in target images, while maintaining the anatomical edges reasonably well.

Problems with two scans: The use of the reference image from a different scan, however, poses a challenges in terms of mis-registration due to different breath-holding levels different heart motion, and different contrast enhancement levels.

C. *Evaluation methods*

Patients: The study was approved by the institutional review board. Patients who agreed to participate in the study were undergone two CT scans using a 320-detector row CT (Aquilion One, Toshiba, Otawara, Japan). The first scan was a prospectively-gated CT angiography scan at the end-systole at a full dose and the second scan was a retrospectively-gated CT-CFA scan for the entire cardiac phases at a low dose, typically 20% of the full dose.

Image reconstruction: An image volume at the end-systole (typically at 40% of R-R interval) was reconstructed from the full-dose CTA scan which was used as the reference image, and 20 images with a 5% R-R increment were reconstructed from the low-dose CT-CFA scan, which was used as the target images after a 3×3×3 median filter was applied. Images which covered a volume of 200 mm × 200 mm × 160 mm by 512×512×160 or 320 voxels centering the heart, were reconstructed by the system's default cardiac algorithm with a body kernel.

iME and motion vector fields (MVFs): The proposed iME was performed using NVIDIA's graphic processing unit C2070 with C and CUDA programming platform (NVIDIA, Santa Clara, CA). The number of knots was 16×16×11-15 knots in the x, y, z (longitudinal) axes, which corresponded to Δ_x=14.6 mm, Δ_y=14.6 mm, and Δ_z=12.0-16.0 mm, and 20 knots in the temporal axis.

Once the cardiac motion vector field (MVF) from the reference image to the target images at 20 cardiac phases of the CT-CFA scan was estimated, a cardiac motion from the end-diastole to the end-systole of the CT-CFA scan was calculated by inverting the estimated MVF using a method proposed by Ref. 2 and concatenate it with 20 different phases, respectively (Fig. 1d)

$$\hat{\vec{u}}(\vec{x}',t_{ED},t)=\hat{\vec{u}}^{-1}(\vec{x},t_0,t_{ED})+\hat{\vec{u}}(\vec{x},t_0,t). \qquad (3)$$

Assessment: The accuracy of the estimated MVFs was evaluated by an attending cardiologist with 20 years of experience (H.A.) comparing with the physiological knowledge and actual images.

III. Results

A total of 30 patients were included in the study and in a majority of cases the locations of surrounding structures such as chest wall, aorta, spines looked consistent with two scans, while the noise levels and pulmonary vessels looked different from each other in terms of the locations and shapes. The following 3 cases have been assessed in more detail.

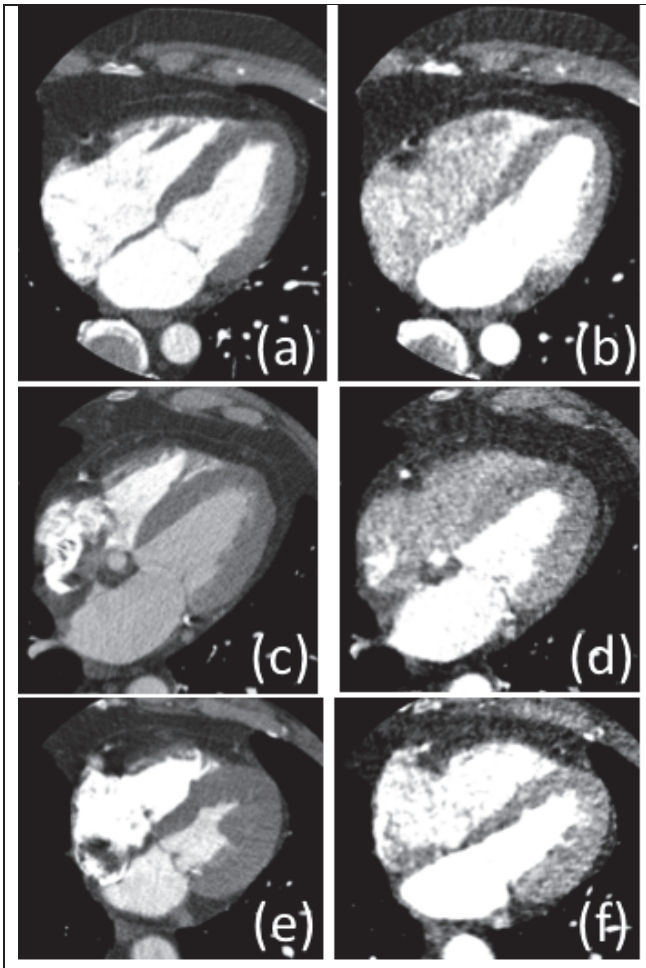

Figure 2. Cardiac CT images obtained by coronary CT angiography scans at full (100%) dose levels (a,c,e) and by CT-CFA scans at 10-20% dose levels (b,d,f): (a,b) Case A, (c,d) case B, and (e,f) case C. Window width/level are 600 H.U./50 H.U.

Case A was a case with a reasonably good match between the two scans in terms of the contrast of chambers and the thicknesses of left ventricle myocardium (Figs. 2a-2b), although the noise levels were significantly different from each other as expected. The estimated MVFs from the end-diastole and end-systole in the standard case (Figs. 3a-3c) seem to capture the following features very well, which are typical in the systolic motion: a large contraction motion at the lateral wall of the left ventricle in all three images, a quick expanding motion of the left atrium near the lateral wall in sagittal and axial images (arrows), and a motion oblique but somewhat parallel to the inter-atrial septa of the left atrium (circle). These motions were delineated as well as the previous studies which uses retrospectively-gated scans with the full dose.

Case B was a case with a mismatch in contrast enhancement levels in the two scans (Figs. 2c-2d). The right ventricle and right atrium were barely enhanced in the CT-CFA scan probably because the scan timing was several seconds later than the coronary CT angiography scan. Despite that, the MVFs seemed reasonable (Figs. 3d-3f): the lateral walls of both left ventricle and right ventricle were contracting inward (arrows) while the inter-ventricular septa did not move significantly (circle). And the left atrium was expanded iso-tropically. We initially thought before the study that it might be necessary to pre-process images or change the similarity metric to normalize the difference in pixel values of blood chambers; however, it seems that the modified iME was able to absorb the difference.

Case C was a case with a mismatch in shape of the myocardium (Figs. 2e-2f). The myocardium of the left ventricle was much thicker and both the left atrium and the right ventricle were significantly smaller in the coronary CT angiography scans while the myocardium was thinner and the left atrium were larger in the CT-CFA scan. The estimated motion vectors (Figs. 3g-3i) looked very large at the lateral/anterior-base of the left ventricle (arrow) as well as the lateral wall of the right ventricle (circle), possibly due to the effect of different shapes. The MVF on the sagittal image (Fig. 3i), however, looked very reasonable.

By the time of the conference, the assessment will include all of the 30 cases and a semi-quantitative assessment will be performed. The observer will grade MVFs with a 4-point scale: 'Excellent' (the MVFs were spatially and temporally smooth and agreed with wall motion subjectively at a level similar to previous studies [1-3], 'Good' (the smoothness and the agreement with the wall motion were good but worse than 'excellent'), 'Fair' (the smoothness and the agreement with the wall motion were even worse but the CFA may provide qualitatively sufficient information), and 'Unacceptable' (the MVFs looked weird and the CFA information was not trust worthy). We will perform the rating with the original iME and the proposed/modified iME and the difference between their ratings will be assessed with a $P<0.05$ being significant.

IV. Conclusions

We have modified an image-based motion estimation method (iME) for a low-dose CT-CFA scan with a full-dose coronary CT angiography scan. The modified iME performed well despite the various mis-matches between the two scans and a large image noise in CT-CFA images. One of the three cases seemed to present suboptimal motion vector field, possibly indicating a need to improve the modified iME further. A systematic semi-quantitative assessment will be performed with 30 cases by the time of the conference.

Acknowledgement—This work was supported by NIH research grant No. R56 HL 125680. We thank Elliot K. Fishman, M.D., Okkyun Lee, Ph.D., Yoshito Otake, Ph.D. for discussion throughout the course of the study.

REFERENCES

[1] Q. Tang, J. Cammin, S. Srivastava, and K. Taguchi, "A fully four-dimensional, iterative motion estimation and compensation method for cardiac CT," Medical Physics, vol. 39, pp. 4291-4305, 2012.

[2] H. Ashikaga, J. Cammin, Q. Tang, K. Knudsen, Y. Inoue, E. K. Fishman, et al., "Quantitative Assessment of Atrial Regional Function Using Motion Estimation Computed Tomography," Journal of Computer Assisted Tomography vol. 38, pp. 773-778, 2014.

[3] A. Al-Issa, Y. Inoue, J. Cammin, Q. Tang, S. Nazarian, H. Calkins, et al., "Regional function analysis of left atrial appendage using motion estimation CT and risk of stroke in patients with atrial fibrillation," European Heart Journal Cardiovascular Imaging, vol. September 4, p. jev207, 2015.

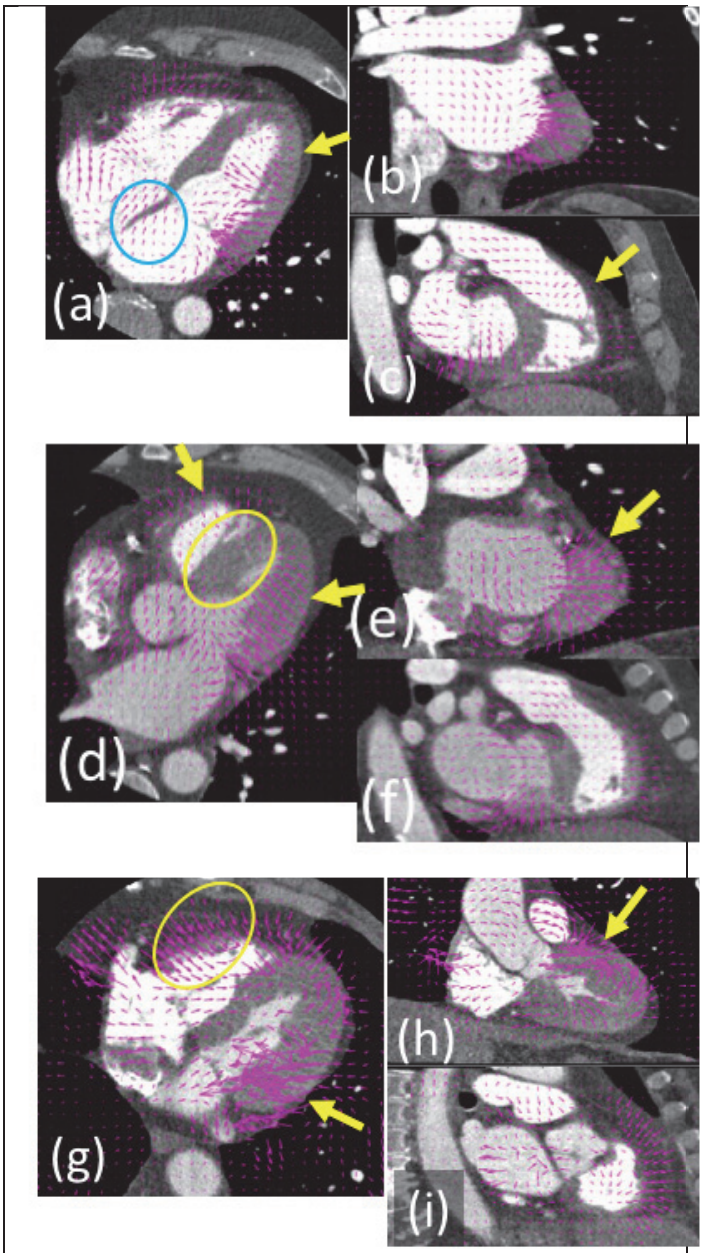

Figure 3. The estimated MVFs superimposed on axial (a,d,g), coronal (b,e,h), and sagittal (c,f,i) cardiac CT images obtained by coronary CT angiography scans at full (100%) dose levels: (a-c) Case A, (d-f) case B, and (g-i) case C. Window width/level are 600 H.U./50 H.U.

Hybrid Local Tomography Image Reconstruction Algorithm and Its Diagnostic Accuracy for Evaluating Coronary Arteries with Calcified Plaque and Stents

Alexander Katsevich, Michael Frenkel, Marcus Chen, Michael Bungo, and Alan Cohen

***Abstract*—In this paper, we propose a novel reconstruction algorithm, which combines a conventional reconstruction with local tomography (LT) reconstruction. An advantage of this combination is that it provides edge enhancement, while keeping the overall appearance of the reconstructed image the same and reconstructing HU values accurately. We test the algorithm on a synthetic example and show that the HU values are indeed reconstructed fairly accurately. Then, using cardiac clinical data collected by the National Institutes of Health (NIH), we show that the algorithm helps to reduce blooming artifacts from calcified plaque and stents in the coronary arteries.**

***Index Terms*—local tomography, iterative reconstruction, cardiac imaging, reduction of blooming artifacts.**

I. Introduction

Blooming artifacts from calcified plaques and stents can compromise reader confidence and diagnostic accuracy of coronary computed tomography angiography (CCTA). Hybrid Local Tomography (HLT) image reconstruction algorithm is a novel reconstruction technique that combines a conventional reconstruction (e.g., iterative- or FBP-based) with high spatial resolution Local Tomography (LT)-based edge-enhanced reconstruction, potentially reducing artifacts from calcified or stented regions.

The purpose of this paper is to describe the HLT algorithm, the workflow for practical applications of HLT, and evaluate using a set of clinical cases collected by the National Institutes of Health (NIH) with the Toshiba Aquilion ONE 320-detector row CT scanner whether HLT reconstruction improves diagnostic accuracy and reader confidence.

Submitted on January 22, 2016.

A.K. is with the University of Central Florida, Orlando, FL 32816 USA and with iTomography Corporation (e-mail: alexander@itomography.com).

M.F. is with iTomography Corporation, Houston, TX 77021, USA (e-mail: michael@itomography.com).

II. Hybrid Local Tomography (HLT) Algorithm

Local Tomography (LT) is an established technique for reconstructing sharp spatial features, e.g. edges, in an object (see below and [1–4]). Besides its ability to resolve regions with sharp changes of density better than conventional image reconstruction algorithms, LT has a number of other advantages over conventional reconstructions, such as computational simplicity and ability to deal with truncated data. One of its disadvantages is that LT images look different from conventional reconstructions because LT does not reconstruct the attenuation coefficient in Hounsfield units (HU). Hence, it is sometimes difficult to differentiate between tissue types and even to see the presence of the X-ray contrast agent in the blood using an LT-based reconstruction.

In this paper, we propose a Hybrid Local Tomography (HLT) algorithm, which provides edge-enhanced reconstruction, while also providing fairly accurate HU values. The main idea of the HLT algorithm is to efficiently combine a conventional (e.g., iterative or any other exact/approximate image reconstructions) and LT-based reconstructions to improve quality of image produced by a conventional reconstruction algorithm [5].

Let $f_c(x)$ denote an image reconstructed by a conventional (i.e., exact or quasi-exact) algorithm. Such an algorithm can be, for example, iterative or of the FBP type. Let $f_1(x)$ denote the reconstructed LT image. As follows from the LT theory [1–4], f_1 preserves and enhances all the edges (or features with high spatial frequency content) visible from the data in the object being scanned. On the other hand, low-frequency features contained in f_1 carry little useful information regarding edges

M.C. is with National Institutes of Health, Bethesda, MD 20892, USA.

M.B. and A.C. are with the University of Texas Health Science Center at Houston, TX 77030, USA and with iTomography Corporation (e-mails: mbungo@iTomography.com and alan@iTomography.com).

or sharp changes of the attenuation coefficient μ and may even create artifacts in LT-based images. Hence, we propose to remove low frequency content from f_1. As such, let $\overline{f}_1$ be the result of applying a high-pass filter to f_1 in the image domain: $\overline{f}_1 = f_1 * \omega$. Here ω is a high-pass filter, and the star denotes convolution in the image domain. The hybrid reconstruction formula we propose is $f_{hlt} = f_c + c\overline{f}_1$, where c is some constant. In order to provide the best image quality using the proposed algorithm, one needs to balance the frequency contents of f_c and $\overline{f}_1$. The optimal value of c can be determined using, for example, synthetic simulations and/or multiple case studies. In our study described below, an expert opinion was used to determine the optimal value of c.

From the above description, it is clear that the proposed HLT algorithm belongs to the general family of the so-called frequency-split approaches [6-7], where different frequency contents of an image are reconstructed using different methods, and then the two sub-images are combined. However, there is one important difference between previously suggested frequency-split approaches and the HLT approach.

Normally, the goal of any frequency-split approach is to reconstruct the original image as accurately as possible. In our approach, the high-frequency sub-image is not intended to represent the high-frequency content of the original image, but rather an edge-enhanced version of it.

III. Numerical Experiments

A. Synthetic Testing of HLT Algorithm

In the first experiment, we simulated a circular source trajectory, and the phantom consisted of various ellipsoids of different densities; the data were contaminated by the Poisson noise, and the HLT image reconstruction workflow consisted of the following steps:

(1) raw data denoising (e.g., using bilateral filtration),
(2) iterative reconstruction to compute f_c,
(3) computation of the LT function f_1,
(4) high-pass filtering f_1 to produce $\overline{f}_1$,
(5) combining $f_{hlt} = f_c + c\overline{f}_1$, and
(6) performing denoising in image domain (e.g., using a total variation-based (TV) regularizer).

Steps (2) – (5) of the presented above workflow are the core steps of the HLT algorithm workflow. Steps (1) and (6) are optional and can be applied only if the reconstructed images are too noisy for performing clinical analysis by a radiologist.

Some intermediate and the final results for a synthetic test are illustrated in Fig. 1. In this test, to reconstruct the conventional image f_c, we used our iterative algorithm (IR) similar to one presented in [8]. We used 10 subsets and the IR algorithm was run for 12 full iterations. The LT image was computed by backprojecting the second order derivative of the data along detector rows.

To compute the filtered LT image $\overline{f}_1$, the high-pass filter ω was chosen to be the identity minus a moving average over a cube of size 7x7x7 voxels. To calculate the HLT image, f_{hlt}, the predetermined optimal value of constant $c = 2100$ was used.

As the last step (6), fairly minor image enhancement using TV-based denoising was also applied to f_{hlt}. An analysis of the results show that HU values in the HLT reconstructed volume are close to the true ones.

In Fig. 1, panels (a) and (b) show the same slices through the volumes f_c (IR) and f_1 (LT), respectively. In Fig. 1, panels (c) and (d) show the slices through the original f_{hlt} and its denoised version, respectively. As can be seen from Fig. 1(c) and 1(d), image denoising applied at step (6) was pretty minor.

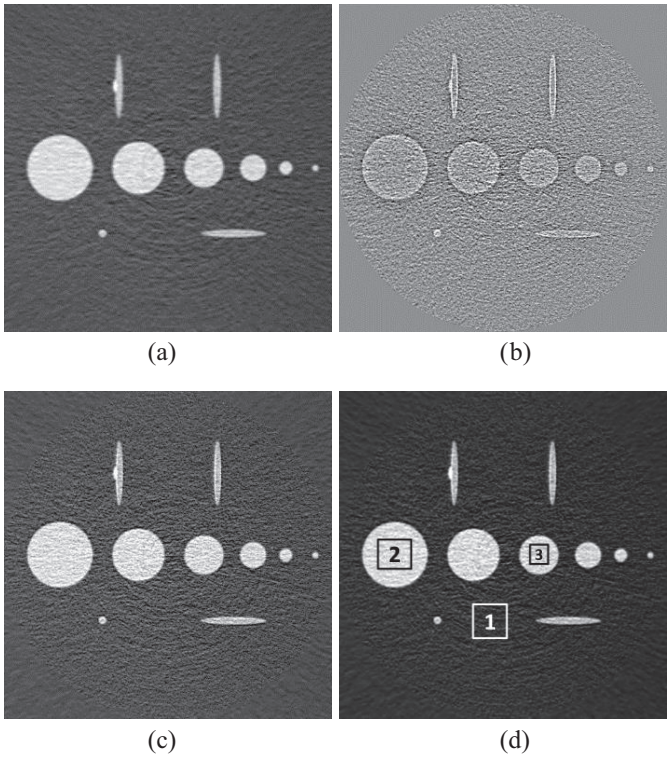

(a) (b)

(c) (d)

Fig. 1. A slice through the reconstructed volume of a synthetic phantom. (a) f_c, (b) f_1, (c) f_{hlt}, and (d) results of TV-based image denoising applied to f_{hlt}. Three rectangles in (d) were used for computing average values of the attenuation coefficient in different parts of the phantom.

The three rectangles shown in Fig. 1(d) were used for computing average values of the attenuation coefficient in different parts of the phantom, including its background part (rectangle #1) and two embedded objects (rectangles #2 and #3). The computed HU values are 23, 329, and 319 in squares #1, 2, and 3, respectively. The correct HU values are 0, 300, and 300, respectively. Thus, we see that the HU values provided by the HLT algorithm are rather close to the exact values.

B. Evaluation of HLT Algorithm Using NIH Clinical Data

CT data collected at the National Heart, Lung, and Blood Institute (NHLBI) of the National Institutes of Health (NIH) during evaluation of 33 patients who underwent invasive coronary angiography and CCTA using the Toshiba Aquilion ONE 320-detector row CT scanner was used in this study.

Two datasets were reconstructed: a conventional CCTA (STD) from the Aquilion ONE scanner console and Hybrid Local Tomography CCTA (HLT) from a standalone (offline) workstation. For the HLT algorithm, we used the same parameters as in the synthetic test described in section III.A.

Two blinded readers independently assessed coronary segments from each reconstruction in separate sessions. Epicardial coronary arteries greater than 2 mm were included in the analysis. Reader confidence was assessed with a 4-point Likert score. Coronary angiograms from each patient (Fig. 3) were used to perform Quantitative Coronary Angiography (QCA) by a reader blinded to CCTA data. QCA stenosis >50% was considered significant coronary artery disease.

TABLE I

DIAGNOSTIC ACCURACY OF STD vs. HLT RECONSTRUCTION UTILIZING QUANTITATIVE CORONARY ANGIOGRAPHY AS THE REFERENCE STANDARD

OVERALL	**STD (95% C.I.)**	**HLT (95% C.I.)**
Area Under Receiver Operating Curve (p=0.03)	0.87 (0.833-0.904)	0.93 (0.902-0.956)
Sensitivity	0.78 (0.660- 0.875)	0.89 (0.688-0.955)
Specificity	0.96 (0.934-0.98)	0.97 (0.950-0.989)
Positive Predictive Value	0.81 (0.686-0.896)	0.88 (0.772-0.945)
Negative Predictive Value	0.96 (0.926-0.975)	0.98 (0.954-0.991)
CALCIFIED SEGMENTS	**STD (95% C.I.)**	**HLT (95% C.I.)**
Area Under Receiver Operating Curve (p=0.03)	0.85 (0.793-0.899)	0.93 (0.881-0.960)
Sensitivity	0.78 (0.644-0.879)	0.91 (0.797-0.969)
Specificity	0.93 (0.867-0.964)	0.95(0.895-0.979)
Positive Predictive Value	0.81 (0.675-0.904)	0.88 (0.759-0.948)
Negative Predictive Value	0.91 (0.851-0.954)	0.96 (0.914-0.987)

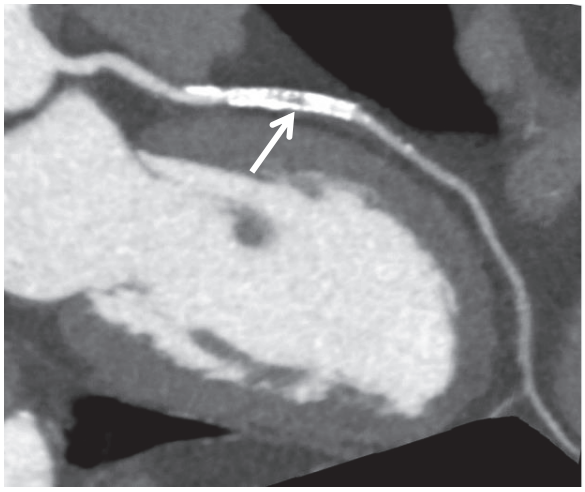

(a)

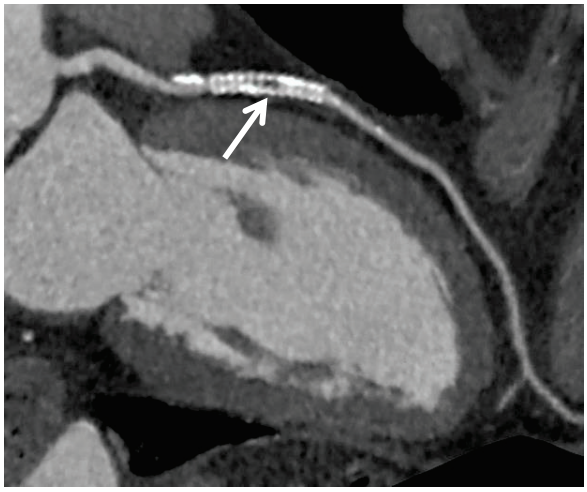

(b)

Fig. 2. Image reconstruction results for one NIH clinical case with cardiac coronary artery stent. Standard (STD) reconstruction ("a") versus HLT reconstruction ("b") showing in-stent stenosis within a stent located in the Left Anterior Descending Coronary Artery (LAD). The white arrows point to the stent locations.

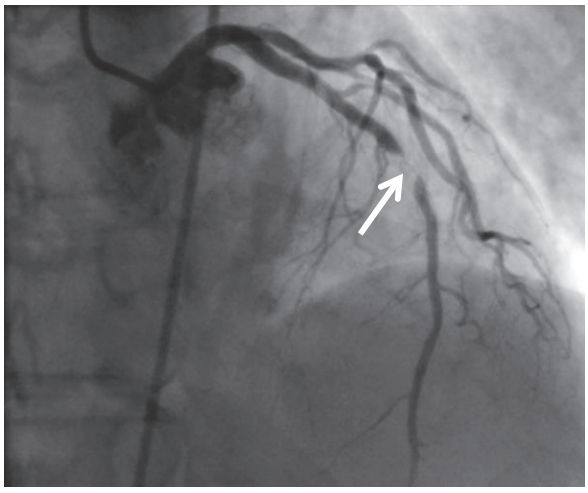

Fig. 3. Coronary angiogram with severe in-stent stenosis for the NIH case shown in Fig. 2. The white arrow points to the stent location.

CT data was compared to the "gold standard" QCA results to determine sensitivity (fraction of people with the disease that the test correctly identified as positive), specificity (fraction of people without the disease that the test correctly identified as negative), positive predictive value (probability that subjects with a positive test have the disease), and negative predictive value (probability that subjects with a negative test don't have the disease).

A total of 442 target segments were identified; 209 segments contained calcified plaque and 11 segments had stents. Mean confidence scores improved between the STD and HLT reconstructions (3.3 vs. 3.5, $p<0.0001$, particularly in stented segments (2.1 vs. 3.4, $p<0.0001$) and calcified segments (2.9 vs. 3.2, $p<0.0001$).

A p value ≤ 0.05 was considered significant. The results of clinical evaluation are summarized in Table I, which indicates that there was improved diagnostic accuracy of HLT over STD.

C. Clinical Case with Cardiac Coronary Artery Stent

To illustrate the results of this study, we present images for one selected clinical case with cardiac coronary artery stent. The images of Fig. 2 show examples of STD ("a") and HLT ("b") reconstructions, respectively, for the selected case. The white arrows point to the region of interest - a metal stent in the Left Anterior Descending Coronary Artery (LAD). Due to metal stent blooming artifact, the STD image (Fig. 2a) might lower confidence in assessing the severity of the in-stent stenosis (narrowing of the blood vessel indicated by a dark area within the stent). Conversely, the HLT image (Fig. 2b) clearly indicates a severe in-stent stenosis. This conclusion is independently confirmed by an image of the coronary angiogram presented in Fig. 3 showing near total occlusion of the artery at the level of the stent.

IV. Conclusions

- We presented a new HLT image reconstruction algorithm and the workflow for its practical applications. HLT allows to efficiently combine a conventional (e.g., iterative or any other exact/approximate image reconstructions) and LT-based reconstructions to improve quality of image produced by a conventional reconstruction algorithm.
- We also presented the results of assessment of HLT diagnostic accuracy for evaluating coronary arteries with calcified plaque and stents. The clinical assessment of the HLT algorithm was performed by the NIH readers blinded and independent of the reconstructions.
- The NIH readers found that there was significant overall improvement in diagnostic accuracy with the HLT reconstruction technique, including in regions with calcified plaque. There was also increased reader confidence, particularly in calcified vessels and stented segments.
- The novel HLT imaging technology may enhance detection of significant coronary artery disease particularly in challenging coronary segments.

V. Discussion

We think that the HLT algorithm will work well and can be beneficial in other clinical applications where the presence of calcium or metal results in the blooming artifact that can mask parts of the region of interest. HLT can also be applicable for a variety of industrial CT applications, including non-destructive testing. These applications will be the subject of additional studies.

Acknowledgments

Authors would like to thank A. Rao, MD; K. Parikh, MD; J. Yu, MD; S. Shanbhag, MD; and S. Rollison, RT(R)(CT), NIH, for their help in performing the clinical analysis of diagnostic accuracy of the HLT algorithm. We would also like to thank Toshiba Medical Research USA (TMRU) for technical support and, in particular, J. Schuzer, RT(R)(CT), TMRU, for collecting clinical data sets at NIH and additional information needed for performing HLT reconstructions.

References

[1] A. G. Ramm and A. Katsevich, *The Radon Transform and Local Tomography*. CRC Press, 1996.

[2] A. Katsevich, "Improved cone beam local tomography" *Inverse Problems*, vol. 22, pp. 627–643, 2006.

[3] A. Faridani, K. Buglione, P. Huabsomboon et al., "Introduction to local tomography" in *Radon transforms and tomography*. Contemp. Math., vol. 278, Amer. Math. Soc., pp. 29–47, 2001.

[4] V. Krishnan and E. T. Quinto, "Microlocal analysis in tomography" in *Handbook of Mathematical Methods in Imaging* (O. Scherzer, ed.), Springer, New York, pp. 847–902, 2015.

[5] A. Katsevich and M. Frenkel, "System and method for hybrid local tomography image reconstruction," U.S. Patent 9 042 626, May 5, 2015.

[6] G. Shechter, T. Köhler, A. Altman, and R. Proksa "*The frequency split method for helical cone-beam reconstruction*" Medical Physics, vol. 31, pp. 2230-2236, 2004.

[7] L. Fu, J. D. Pack, and B. D. Man, "Frequency-Split Iterative Tomographic Reconstruction in Targeted Region-of-Interest" in *Proceedings of The 13th International Meeting on Fully Three-Dimensional Image Reconstruction in Radiology and Nuclear Medicine*, pp. 224 – 227, 2015.

[8] D. Kim, S. Ramani, and J. A. Fessler, "Accelerating X-ray CT ordered subsets image reconstruction with Nesterov's first-order methods" in *Proceedings of The 12th International Meeting on Fully Three-Dimensional Image Reconstruction in Radiology and Nuclear Medicine*, pp. 22 – 25, 2013.

Total Variation Constrained Weighted Least Squares Using SIRT and Proximal Mappings

Jens Gregor, Philip Bingham and Lloyd F. Arrowood

***Abstract*—Tomographic image reconstruction can be formulated as a weighted least squares problem. Regularization is often added to ensure uniqueness and/or smoothness of the solution. For low dose applications, be they few-view and/or low-count oriented, total variation has become a popular option. Rose et al recently proposed a framework based on ART-like reconstruction and proximal mappings. In this paper, we show that reconstruction can be achieved by an appropriately modified version of SIRT. The result is an algorithm that more readily facilitates parallel implementation. Experimental results are provided for phantom data.**

I. Introduction

Limiting X-ray exposure is important for imaging of living organisms as well as certain man-made objects. Typically, this means acquiring data using fewer views and/or reducing the dose associated with each view. This makes the task of reconstructing a tomographic image substantially more challenging.

X-ray CT imaging can be cast as a weighted least squares (WLS) problem for which regularization is used to ensure uniqueness and/or smoothness of the solution. For example, Sauer and Bouman [1] showed that a second-order Taylor-series expansion of a Poisson log-likelihood leads to a WLS problem. Fessler et al showed that separable quadratic surrogate (SQS) methods for optimizing Poisson log-likelihoods also lead to WLS inner minimization problems [2], [3]. In both formulations, weighting has statistical meaning related to the modeled variance of the projection data.

Mathematically, let $\boldsymbol{A}=[a_{ij}]$ denote a non-negative system matrix, and let $\boldsymbol{x}=[x_j]$ and $\boldsymbol{y}=[y_i]$ denote vectors representing the unknown image and log-normalized projection data, respectively. Furthermore, let $\boldsymbol{W}=\mathrm{diag}\{w_i\}$ be a diagonal statistical weighting matrix with positive diagonal entries, and let $\boldsymbol{Q}$ be a Tikhonov regularization matrix chosen to emphasize structural characteristics of $\boldsymbol{x}$ that are undesirable. Quadratically regularized WLS image reconstruction can then be stated as

$$\boldsymbol{x}^* = \underset{0\leq\boldsymbol{x}}{\arg\min}\, \tfrac{1}{2}\|\boldsymbol{A}\boldsymbol{x}-\boldsymbol{y}\|^2_{\boldsymbol{W}} + \beta\tfrac{1}{2}\|\boldsymbol{Q}\boldsymbol{x}\|^2_2. \qquad (1)$$

Common examples of $\boldsymbol{Q}$ include the identity matrix, which yields a minimum norm solution, and a finite-differences encoding matrix, which penalizes roughness thereby encouraging smoothness. When $\boldsymbol{A}$ and $\boldsymbol{Q}$ have disjoint null spaces, the cost function in (1) has a unique minimizer as it is strictly convex.

We have shown that SIRT can be made to solve a statistically weighted reconstruction problem like (1) instead of the geometrically weighted one solved by the classical version of the algorithm [4]. As part of that work, we also showed that SIRT is indistinguishable from SQS when applied to such problems in spite of the two algorithms being derived from entirely different premises.

Building on their seminal work on image reconstruction centered around total variation (TV) minimization [5], Rose et al recently proposed a framework for low dose X-ray CT based on TV constrained WLS reconstruction [6], namely,

$$\boldsymbol{x}^* = \underset{0\leq\boldsymbol{x}}{\arg\min}\, \tfrac{1}{2}\|\boldsymbol{A}\boldsymbol{x}-\boldsymbol{y}\|^2_{\boldsymbol{W}} \text{ s.t. } \mathrm{TV}(\boldsymbol{x}) \leq \epsilon \qquad (2)$$

where $\mathrm{TV}(\boldsymbol{x}) = \sum_i \|\nabla_i \boldsymbol{x}\|$. By sparsifying the gradient magnitude image, a solution can be obtained that exhibits smooth regions with well-defined edges. They solve the convex optimization problem using a relaxed, incremental proximal gradient scheme which consists of a two-step iteration. First, the WLS term is minimized using an ART-like algorithm. Regularization in the form of a proximal mapping keeps the image somewhat close to the one produced in the previous iteration. Second, the TV constraint is satisfied by mapping the image to the closest point on the surface of an L1-ball. This mapping is carried out using the Chambolle-Pock algorithm [7], [8] combined with a method by Duchi et al [9].

In this paper, we show that the WLS minimization can be achieved by an appropriately modified version of SIRT implemented using ordered subsets. The result is an algorithm that more readily facilitates parallel implementation and thus supports contemporary multi-core CPU and many-core GPU computer architectures. Emphasis is on algorithmic feasibility. Experimental results are provided for phantom data.

II. Algorithmic Details

A. WLS Minimization

In order to support use of SIRT, we replace the incremental WLS formulation of the original WLS-TV algorithm by the following minimization problem:

$$\boldsymbol{x}^* = \underset{0\leq\boldsymbol{x}}{\arg\min}\, \tfrac{1}{2}\|\boldsymbol{A}\boldsymbol{x}-\boldsymbol{y}\|^2_{\boldsymbol{W}} + \beta\tfrac{1}{2}\|\boldsymbol{x}-\bar{\boldsymbol{x}}\|^2_2. \qquad (3)$$

Initially, $\bar{\boldsymbol{x}} = 0$ which leads to a minimum norm solution. Once the TV constraint satisfaction step discussed below has been executed, $\bar{\boldsymbol{x}}$ is set equal to the solution thereof. Thereby the next iteration of the WLS minimization becomes subjected

J. Gregor is with the Dept. of Electrical Engr. & Computer Science, Univ. of Tennessee, Knoxville, TN 37996. Email: jgregor@utk.edu. P. Bingham is with Oak Ridge National Laboratory, Oak Ridge, TN 37931. Email: binghampr@ornl.gov. L.F. Arrowood is with Consolidated Nuclear Security, LLC. Oak Ridge, TN 37830. Email: lloyd.arrowoodIII@cns.doe.gov.

to a proximal mapping that discourages deviation from the TV solution. As the computation progresses, the value of β is gradually increased to further enforce this behavior. That is,

$$\beta = \beta_0 \left(\lfloor \tfrac{k}{20} \rfloor + 1 \right) \tag{4}$$

where β_0 is a user-defined initial value. We used $\beta_0 = 10/\left\|y\right\|$ for the experimental work reported below.

We now derive a SIRT-like algorithm for solving (3). Let the diagonal matrices corresponding to the inverse row and column sums of $\boldsymbol{A}$ be given by $\boldsymbol{R} = \operatorname{diag}\{1/r_i\}$ and $\boldsymbol{C} = \operatorname{diag}\{1/c_j\}$ where $r_i \triangleq \sum_j a_{ij}$ and $c_j \triangleq \sum_i a_{ij}$. The classical SIRT iteration can then be expressed as [10]:

$$\boldsymbol{x}^{(k+1)} = \boldsymbol{x}^{(k)} + \alpha\, \boldsymbol{C}\boldsymbol{A}'\boldsymbol{R}(\boldsymbol{y} - \boldsymbol{A}\boldsymbol{x}^{(k)}). \tag{5}$$

This is a gradient descent with diagonal preconditioner $\boldsymbol{C}$ of the cost function $\frac{1}{2}\|\boldsymbol{A}\boldsymbol{x} - \boldsymbol{y}\|^2_{\boldsymbol{R}}$. Weighting by $\boldsymbol{R}$ means that minimization of the residual errors is per unit length.

We are interested in weighting by $\boldsymbol{W}$ to account for the statistical nature of the underlying data. With reference to [4], this can be achieved by applying SIRT to a slightly modified but related problem. Let $\tilde{\boldsymbol{A}} = [\tilde{a}_{ij}]$ and $\tilde{\boldsymbol{y}} = [\tilde{y}_i]$ where $\tilde{a}_{ij} \triangleq w_i r_i a_{ij}$ and $\tilde{y}_i \triangleq w_i r_i y_i$. Furthermore, let $\tilde{\boldsymbol{R}} = \operatorname{diag}\{1/\tilde{r}_i\}$ and $\tilde{\boldsymbol{C}} = \operatorname{diag}\{1/\tilde{c}_j\}$ where $\tilde{r}_i \triangleq \sum_j \tilde{a}_{ij} = w_i r_i^2$ and $\tilde{c}_j \triangleq \sum_i \tilde{a}_{ij}$. By applying the identities $\tilde{\boldsymbol{A}}'\tilde{\boldsymbol{R}}\tilde{\boldsymbol{A}} = \boldsymbol{A}'\boldsymbol{W}\boldsymbol{A}$ and $\tilde{\boldsymbol{A}}'\tilde{\boldsymbol{R}}\tilde{\boldsymbol{y}} = \boldsymbol{A}'\boldsymbol{W}\boldsymbol{y}$ to the SIRT iteration for minimizing the cost function $\frac{1}{2}\|\tilde{\boldsymbol{A}}\boldsymbol{x} - \tilde{\boldsymbol{y}}\|^2_{\tilde{\boldsymbol{R}}}$, we obtain a gradient descent with diagonal preconditioner $\tilde{\boldsymbol{C}}$ of the WLS cost function $\frac{1}{2}\|\boldsymbol{A}\boldsymbol{x} - \boldsymbol{y}\|^2_{\boldsymbol{W}}$. Adding the gradient of the $\bar{\boldsymbol{x}}$-based proximal mapping leads to the desired SIRT-like algorithm, namely,

$$\boldsymbol{x}^{(k+1)} = \boldsymbol{x}^{(k)} + \alpha\, \tilde{\boldsymbol{C}}(\boldsymbol{A}'\boldsymbol{W}\,(\boldsymbol{y} - \boldsymbol{A}\boldsymbol{x}^{(k)}) + \beta(\bar{\boldsymbol{x}} - \boldsymbol{x}^{(k)})). \tag{6}$$

This is a Richardson Iteration. Since the eigenvalues of matrix $\tilde{\boldsymbol{C}}(\boldsymbol{A}'\boldsymbol{W}\boldsymbol{A} + \beta\boldsymbol{I})$ are strictly positive, i.e., $0 < \lambda_{\min} \le \lambda_{\max}$, it follows that convergence is guaranteed for an arbitrary initial choice $\boldsymbol{x}^{(0)}$ if $0 < \alpha < 2/\lambda_{\max}$ with the fastest rate of convergence obtained for $\alpha^* = 2/(\lambda_{\max} + \lambda_{\min})$ [11]. We note that said matrix is identical to the one for minimum norm regularization for which the following near-optimal value has been derived [4]:

$$\alpha^* \approx \frac{2}{1 + \beta\left(\frac{1}{\min_j \tilde{c}_j} + \frac{1}{\max_j \tilde{c}_j}\right)}. \tag{7}$$

Relative to $\alpha = 1$, use of α^* may double the convergence rate.

SIRT establishes the low-frequency components of an image faster than the high-frequency components. Ordered subsets are commonly used to accelerate convergence. We follow the approach taken for SQS which has each full iteration use the gradients of M partial cost functions representing a partitioning of the data. Preconditioner $\tilde{\boldsymbol{C}}$ remains as defined above. Each subset is assumed to have a view of all voxels.

B. TV Constraint Satisfaction

Should the WLS minimization violate the TV constraint, the image is mapped to the closest point on the surface of an L1-ball of radius ϵ. This is achieved by solving

$$\bar{\boldsymbol{x}} = \arg\min_{\boldsymbol{x}} \tfrac{1}{2}\|\boldsymbol{x} - \boldsymbol{x}^*\|_2^2 \text{ s.t. } \mathrm{TV}(\boldsymbol{x}) \le \epsilon \tag{8}$$

using the Chambolle-Pock algorithm [7], [8] which applies to problems of the form

$$\boldsymbol{s}^* = \arg\min_{\boldsymbol{s}} G(\boldsymbol{s}) + F(D\boldsymbol{s}) \tag{9}$$

where G and F are convex functions, and D is a linear transform. For the present problem, G is the proximal mapping based on $\boldsymbol{x}^*$, F is an indicator function representing the TV constraint, viz.,

$$\delta_\epsilon(\boldsymbol{x}) = \begin{cases} 0 & \text{if } \mathrm{TV}(\boldsymbol{x}) \le \epsilon \\ \infty & \text{otherwise} \end{cases}, \tag{10}$$

and D is the discrete gradient operator. The solution to (9) is found by iterating over two proximal mappings, namely,

$$\boldsymbol{u}^{(k+1)} = \operatorname{prox}_\sigma[F^*](\boldsymbol{u}^{(k)} + \sigma D\bar{\boldsymbol{v}}^{(k)}) \tag{11a}$$

$$\boldsymbol{v}^{(k+1)} = \operatorname{prox}_\tau[G](\boldsymbol{v}^{(k)} - \tau D^T\boldsymbol{u}^{(k+1)}) \tag{11b}$$

$$\bar{\boldsymbol{v}}^{(k+1)} = 2\boldsymbol{v}^{(k+1)} - \boldsymbol{v}^{(k)} \tag{11c}$$

where

$$\operatorname{prox}_\rho[H](\boldsymbol{s}) = \arg\min_{\boldsymbol{s}'} H(\boldsymbol{s}') + \tfrac{1}{2\rho}\|\boldsymbol{s} - \boldsymbol{s}'\|_2^2. \tag{12}$$

Next, we summarize the computation when applied to (8). See the note by Rose and Sidky [12] for more details.

The proximal mapping of F^*, which denotes the convex conjugate of F, involves the mentioned projection onto the L1-ball. The sequence of operations can be written as

$$\boldsymbol{u} = \boldsymbol{u}^{(k)} + \sigma\nabla\bar{\boldsymbol{v}}^{(k)} \tag{13a}$$

$$\boldsymbol{h} = [\ \|\boldsymbol{u}_j\|_2\ ] \tag{13b}$$

$$\boldsymbol{s} = \mathcal{P}(\boldsymbol{h}/\sigma;\ \text{L1-ball}(\epsilon)) \tag{13c}$$

$$\boldsymbol{H} = \operatorname{diag}\{s_i/h_i\} \tag{13d}$$

$$\boldsymbol{u}^{(k+1)} = \boldsymbol{u} - \sigma\boldsymbol{H}\boldsymbol{u} \tag{13e}$$

where $\boldsymbol{u}$ should be interpreted as a multi-column matrix that represents 2D or 3D operations as appropriate with the jth row vector given by $\boldsymbol{u}_j = [u_{j1}\ u_{j2}\ \cdots]$, $\boldsymbol{h}$ is a vector whose elements represent the row vector norms of $\boldsymbol{u}$, diagonal scaling matrix $\boldsymbol{H}$ is defined to have zero entries for elements of $\boldsymbol{h}$ that are zero, and projection operation $\mathcal{P}$ is carried out using a method by Duchi et al [9].

The proximal mapping of G can straightforwardly be expressed as

$$\boldsymbol{v} = \boldsymbol{v}^{(k)} - \tau\nabla'\boldsymbol{u}^{(k+1)} \tag{14a}$$

$$\boldsymbol{v}^{(k+1)} = \frac{\boldsymbol{v}/\tau + \boldsymbol{x}^{(k+1)}}{1 + 1/\tau} \tag{14b}$$

To ensure convergence, σ and τ must satisfy $L^2\sigma\tau < 1$ where $L = \|\nabla\|_2$; for 2D, $L = \sqrt{8}$ while for 3D, $L = \sqrt{12}$. However, $\sigma = \tau = 1/L$ seems to work in practice [6].

C. WLS-TV Algorithm

The proposed WLS-TV algorithm implements the above computations as follows. Variables $\boldsymbol{x}^{(0)}$, $\bar{\boldsymbol{x}}$, $\boldsymbol{u}^{(0)}$, $\boldsymbol{v}^{(0)}$, and $\bar{\boldsymbol{v}}^{(0)}$ are initialized to zero. Then an outer loop is entered that first produces an approximate solution to (3) in the form of $\boldsymbol{x}^{(k+1)}$ which is the result of running a single, full iteration of

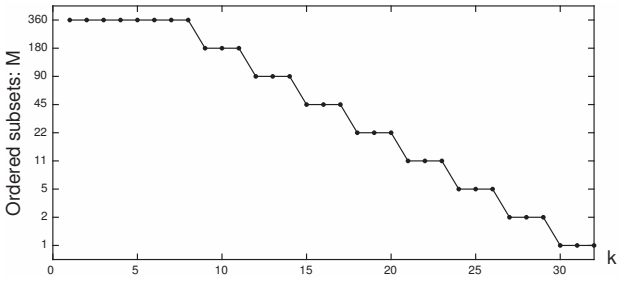

Fig. 1. The number of ordered subsets is decreased during the computation.

the SIRT-like algorithm given by (6) using M ordered subsets. At this point, the TV constraint has typically been violated. This causes an inner loop to execute the updates given by (13) and (14) either until $\mathrm{TV}(\boldsymbol{v}^{(k+1)})$ has come close enough to the value of the TV constraint or for a small, fixed number of iterations. Eventually, $\boldsymbol{x}^{(k+1)}$ and $\bar{\boldsymbol{x}}$ are set equal to $\boldsymbol{v}^{(k+1)}$. Depending on the iteration, β is also updated to tighten the proximal mapping for the WLS minimization. Then execution of the outer loop continues.

The early iterations of the WLS-TV algorithm serve to produce an approximate solution which subsequent iterations refine. This suggests initially advancing the WLS minimization as fast as possible in order to quickly violate the TV constraint and thus activate the associated correction. From then on, the WLS minimization should advance in a more controlled manner so that it doesn't move too far away from the TV solution. We use the following heuristic scheme to achieve this behavior. Initially, M is set equal to the number of projections thereby making each projection its own subset. This accelerates the rate of convergence. We then systematically decrease M till we have just a single subset that contains all the projections. This slows the rate of convergence. With reference to Fig. 1, the subset decrease is based on repeatedly reducing M by a factor of two and making each configuration run for the same number of iterations as all the other configurations to the extent possible. Once created, the subsets are randomly perturbed to subsequently allow sequential processing without regard to the actual order.

III. Parallel Implementation

The ART-like WLS-TV algorithm by Rose et al [6] is difficult to parallelize since the incremental WLS update is based on a single ray and the small number of voxels intersected thereby. This limits the number of cores that can contribute effectively to the computation.

The SIRT-like algorithm proposed here, on the other hand, uses many rays to update all voxels during every sub-iteration and is thus quite amenable to parallelization. Forward projection can be carried out simultaneously for all rays considered and can thus be executed in parallel using equally many cores. Backprojection must ensure unique access to the voxels. Our present implementation does that by partitioning the image into subvolumes which can be updated independently of one another. When a core becomes responsible for a subvolume, it computes and applies the system matrix elements for all rays that intersect it (using interpolation). Backprojection can thus be done in parallel using a number of cores that equals the number of subvolumes.

IV. Experimental Results

We report preliminary results for a 2D Shepp-Logan phantom. We generated 360 projections spaced 1° apart and added Poisson noise corresponding to a count rate of 1,000 photons per ray. We conducted a WLS reconstruction using 32 iterations of the modified SIRT algorithm without applying the TV constraint but with the minimum norm regularization in effect. We also conducted WLS-TV reconstructions using TV constraints of $\epsilon = 1.20 \times \mathrm{TV}(\boldsymbol{x})$ and $\epsilon = 1.02 \times \mathrm{TV}(\boldsymbol{x})$, respectively, where $\boldsymbol{x}$ denotes the original, noise free phantom. The reconstructions were recomputed using 180 projections spaced 2° apart to illustrate the effect of using fewer views.

As shown in Fig. 2, TV constrained reconstruction is seen to produce smother images with more uniform regions than unconstrained reconstruction. Tables I and II provide mean and standard deviation values for the dark gray background ellipse (ROI 1: ground truth value 0.20) and the three larger black and gray organ ellipses (ROI 2–4: ground truth values 0.00, 0.00, and 0.30). Figure 3 plots improvement of image quality in terms of the relative error $\left\|\boldsymbol{x}^{(k)} - \boldsymbol{x}\right\| / \|\boldsymbol{x}\|$ as a function of iteration. TV constrained reconstruction is seen to produce images that are substantially closer to ground truth than does unconstrained reconstruction.

TABLE I
ROI $\mu \pm \sigma$ Statistics: 360 Projections

ROI	Unconstrained	$\epsilon = 1.20 \times \mathrm{TV}(\boldsymbol{x})$	$\epsilon = 1.02 \times \mathrm{TV}(\boldsymbol{x})$
1	0.20 ± 0.031	0.20 ± 0.011	0.20 ± 0.006
2	0.00 ± 0.003	0.00 ± 0.003	0.00 ± 0.004
3	0.00 ± 0.004	0.00 ± 0.004	0.00 ± 0.004
4	0.30 ± 0.033	0.30 ± 0.011	0.30 ± 0.005

TABLE II
ROI $\mu \pm \sigma$ Statistics: 180 Projections

ROI	Unconstrained	$\epsilon = 1.20 \times \mathrm{TV}(\boldsymbol{x})$	$\epsilon = 1.02 \times \mathrm{TV}(\boldsymbol{x})$
1	0.20 ± 0.035	0.20 ± 0.016	0.20 ± 0.012
2	0.00 ± 0.006	0.00 ± 0.005	0.00 ± 0.006
3	0.00 ± 0.008	0.00 ± 0.006	0.00 ± 0.007
4	0.30 ± 0.035	0.30 ± 0.013	0.30 ± 0.007

Acknowledgments

Sean Rose and Emil Sidky provided invaluable insights and help without which the present paper would not have been possible. Jens Gregor was funded in part by the Plant-Directed Research Development and Demonstration Program at the Y-12 National Security Complex, which is managed by Consolidated Nuclear Services, LLC for the U.S. Department of Energy.

References

[1] K. Sauer and C. Bouman, "A local update strategy for iterative reconstruction from projections," *IEEE Trans. Signal Proc.*, vol. 41: 534–548, 1993.

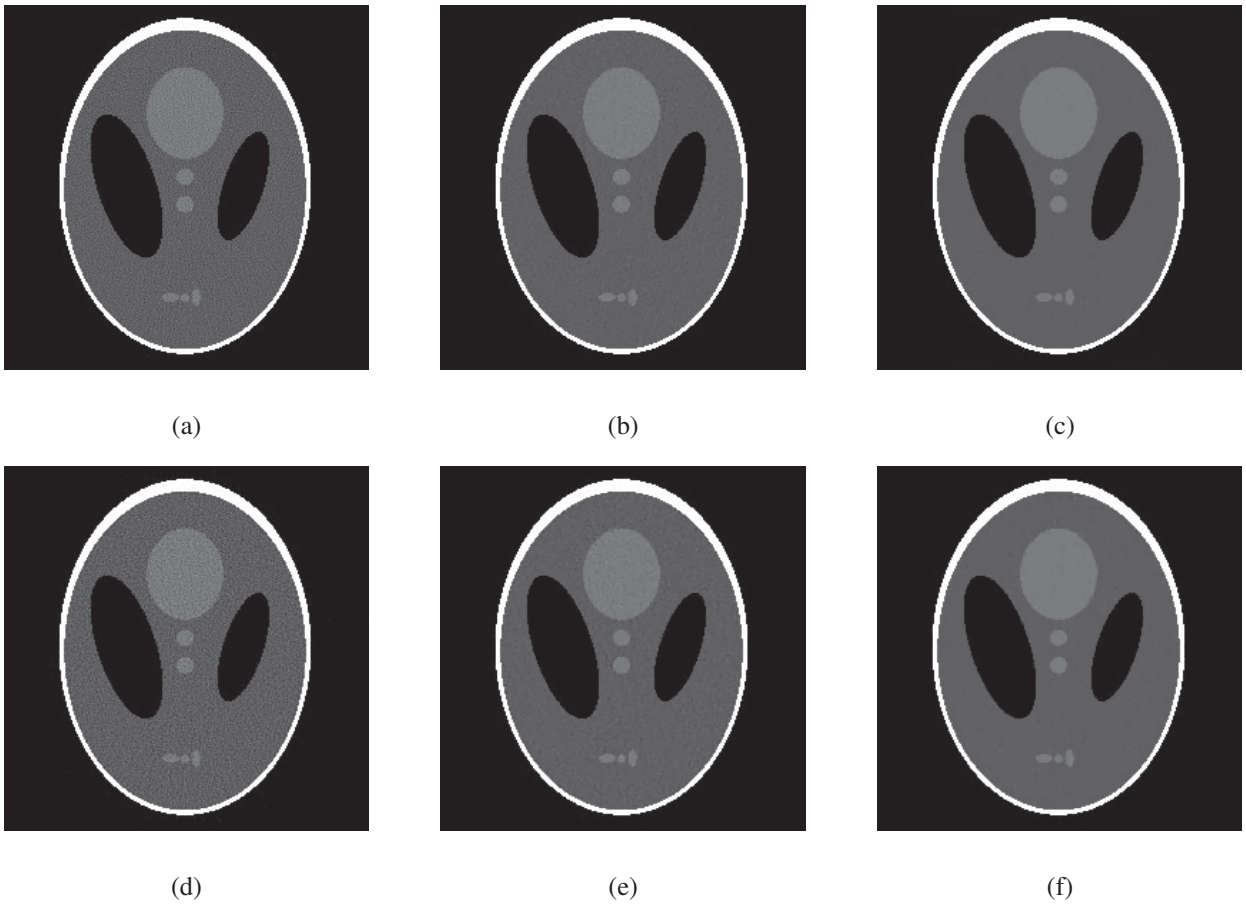

Fig. 2. Reconstructions: (a-c) 360 projections, (d-f) 180 projections; (a,d) WLS; (b,e) and (c,f) WLS-TV using ϵ based on $\times 1.20$ and $\times 1.02$, respectively. Noise free phantom TV value: 1468. Reconstructed TV values for noisy data: (a-c) 3050, 1763, and 1498; (d-e) 3041, 1760, and 1496. TV constrained solutions are thus obtained as desired. Graylevels windowed to [0-0.8].

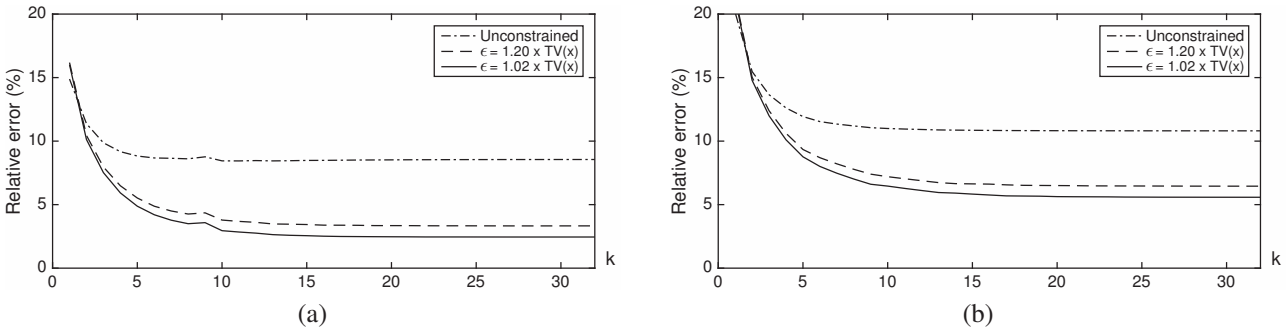

Fig. 3. Relative error plots: (a) 360 projections; and (b) 180 projections. All reconstructions reach their near-final relative error after about 15 iterations.

[2] H. Erdogan and J. Fessler, "Ordered subsets algorithms for transmission tomography," *Physics in Medicine and Biology*, vol. 44: 2835-2851, 1999.

[3] I.A. Elbakri J. Fessler, "Statistical image reconstruction for polyenergetic x-ray computed tomography," *IEEE Trans. Medical Imaging*, vol. 21: 89–99, 2002.

[4] J. Gregor and J. Fessler, "Comparison of SIRT and SQS for regularized weighted least squares image reconstruction," *IEEE Trans. Computational Imaging*, vol. 1: 44–55, 2015.

[5] E. Sidky and X. Pan, "Image reconstruction in circular cone-beam computed tomography by constrained, total-variation minimization," *Phys. Med. Biol.*, vol. 53: pp. 4777-4807, 2008.

[6] S. Rose, M. Andersen, E. Sidky, and X. Pan "Noise properties of CT images reconstructed by use of constrained total-variation, data-discrepancy minimization," *Medical Phys.*, vol. 42: 2690–2698, 2015.

[7] A. Chambolle and T. Pock, "A first-order primal dual algorithm for convex problems with application to imaging," *J. Math. Imaging Vis.*, vol. 40: 120–145, 2011.

[8] E. Sidky, J. Jørgensen, and X. Pan, "Convex optimization problem prototyping for image reconstruction in computed tomography with the Chambolle-Pock algorithm," *Phys. Med. Biol.*, vol. 57: pp. 3065-3091, 2012.

[9] J. Duchi, S. Shalev-Shwartz, Y. Singer and T. Chandra, "Efficient projections onto the L1-ball for learning in high dimensions," *Proc. 25th Intl. Conf. Machine Learning*, Helsinki, Finland, pp. 272–279, 2008.

[10] J. Gregor and T. Benson, "Computational analysis and improvement of SIRT," *IEEE Trans. Medical Imaging*, vol. 27: 918–924, 2008.

[11] Y. Saad, *Iterative Methods for Sparse Linear Systems*, PWS Publishing Co. (Boston), 1996.

[12] S. Rose and E. Sidky, "Incremental algorithms for TV constrained optimization: Notes," *University of Chicago*, June 18, 2015.

Image-domain denoising for myocardial blood flow estimation in dynamic CT

Dimple Modgil, David S. Rigie, Michael D. Bindschadler*, Adam M. Alessio* and Patrick J. La Rivière

I. Introduction

Clinical evaluation of coronary artery disease (CAD) can benefit from the quantification of myocardial blood flow (MBF). Currently, there are several techniques that can be used to detect and evaluate atherosclerosis including invasive catheter-based angiography, non-invasive computed tomography angiography (CTA) or magnetic resonance angiography (MRA) [1]. It has been shown that the addition of MBF information leads to better outcomes and reduced costs in the diagnosis and treatment of CAD [2]. There is great interest in using CT to assess myocardial perfusion, especially since CTA is already being used in the emergency room setting to assess chest pain. Dynamic CT holds the promise of achieving true quantitative MBF imaging [3]. This entails acquiring a series of CT images of the myocardium during uptake and washout of iodinated contrast agent. The resulting pixel-based or regional time-attenuation curves (TACs) can be analyzed using physiological models of iodine exchange to estimate MBF in absolute units (ml/g/min).

The principal drawback of dynamic CT for MBF estimation is the potential for a large radiation dose imparted to the patient during this multi-frame exam. Acquiring each frame at very low dose leads to very noisy images and TACs. Some groups have sought to exploit frame-to-frame temporal correlations to reduce noise. They have used techniques such as bilateral filtering as well as iterative reconstruction methods [4], [6], [5], [7], [8]. Previously, we have explored techniques to smooth the noisy data in the sinogram domain using sinogram restoration in 4D [9] and the KL transform in the temporal domain [11].

In this work, we compare several image-domain smoothing techniques, including a novel technique for noise reduction using vectorial total variation (VTV) that was previously introduced by our group for spectral CT [10] and dynamic CT [12]. This method is a generalization of the total-variation method to multiple time frames of dynamic CT data. In our previous work, we applied VTV only to 2D dynamic CT slices. In this work, we apply VTV to 3D volumes using simulated and patient data. We compare the two variants of VTV technique to scalar, frame-by-frame TV smoothing as well as with bilateral filtering in the spatial and temporal domains for the task of MBF estimation [13].

*Adam Alessio and Michael Bindschadler are with the Departments of Bioengineering and Radiology at the University of Washington. The other authors are with the Department of Radiology, The University of Chicago.

II. Methods

A. Iterative Denoising using total variation (TV) penalty

We perform iterative image-domain denoising by solving the following data-constrained optimization problem:

$$\mathbf{u}^* = argmin_{\mathbf{u}} \{TV_X(\boldsymbol{u})\} \; s.t. \; \|\boldsymbol{u} - \boldsymbol{u}_{\text{noisy}}\|_2 \leq \varepsilon, \qquad (1)$$

where $\boldsymbol{u}$ represents dynamic image series (N pixels x M frames), TV_X refers to a set of modified total variation penalties (to be described below) and ε is a free parameter that controls the strength of the regularization. We used the data-constrained optimization because this allows for a direct comparison between various types of penalty terms. To solve this constrained optimization problem iteratively, we use the primal-dual algorithm proposed by Chambolle and Pock [15].

Total variation regularized CT reconstruction algorithms have been studied extensively due to the approximate gradient sparsity of CT images [14]. Several works have demonstrated that such schemes may yield accurate reconstructions from noisy data in CT [16], [17]. The total variation penalty term, TV_X, can be defined for a multi-frame image series in a variety of ways.

1) Scalar total variation or frame-by-frame TV: The most straightforward way to extend TV to multiple frames in dynamic CT is to sum over the total variation in each frame. This approach does not impose any coupling between the frames. We denote this by TV_S,

$$TV_S(\mathbf{u}) = \sum_{m=1}^{M} TV(u_m), \qquad (2)$$

where,

$$TV(u_m) = \sum_{j=1}^{N} ||\nabla u_m||_2. \qquad (3)$$

2) Vectorial total variation: Another way to extend TV to multiple frames is to use a novel edge-preserving penalty that can be viewed as a variant of the total variation. After approximate registration, we expect that all frames should have essentially the same edge structure, so it is advantageous to process them simultaneously and encourage this type of coupling. To accomplish this, we use the "vectorial" TV (VTV) penalty recently proposed for multi-energy CT reconstruction[10]. The VTV penalty is given by the following equation.

$$TV_N(\boldsymbol{u}) = \sum_{j=1}^{N} \|[D\boldsymbol{u}]_j\|_* = \sum_{j=1}^{N} \|\sigma([D\boldsymbol{u}])_j||_1 \qquad (4)$$

In this formulation, we view our image series $\boldsymbol{u}$ as a vector function, where each spatial coordinate maps to a vector of image values. The quantity, $[D\boldsymbol{u}]_j$ is the discrete approximation to the Jacobian matrix corresponding to the j^{th} pixel, and $\|.\|_\star$ is the nuclear norm, which is given by the sum of singular values, σ. In particular the matrix $[D\boldsymbol{u}]_j$ in 2D will have the following structure,

$$[D\boldsymbol{u}]_j = \begin{bmatrix} \left(\frac{\partial u_1}{\partial x}\right)_j & \left(\frac{\partial u_1}{\partial y}\right)_j \\ \vdots & \vdots \\ \left(\frac{\partial u_M}{\partial x}\right)_j & \left(\frac{\partial u_M}{\partial y}\right)_j \end{bmatrix}_{M\times 2} \tag{5}$$

where each row corresponds to the gradient of one image frame at pixel j in 2D and M is the number of frames. By minimizing the nuclear norm of this matrix, we are encouraging it to be low rank, which will encourage images that are approximately piece-wise constant and have gradient vectors pointing in the same direction.

We applied VTV to one slice at a time (2D VTV) as well as using three slices to smooth a slice (3D VTV). It has been shown analytically that the amount of smoothing in TV is directly proportional to the smoothing parameter ε and inversely proportional to the size of the object [18]. This results in reducing the contrast level in the smoothed image while reducing noise. The use of three slices for smoothing in VTV increases each objects's size and thus helps preserve the contrast in the smoothed images.

B. Simulations

We generated dynamic material phantoms to mimic the exchange of iodine in the myocardium. Simulated projection data were generated using our polychromatic projector [11] and the dynamic material phantom data [13]. Noise matching was done on the simulator to model the photon fluence with various tube currents. Noisy projection data were generated for 30 acquisitions of the dynamic phantom spaced at 1 second intervals, with tube current set at 25, 70, or 140 mAs. We looked at four different myocardial blood flow rates in order to simulate different disease states: 0.5, 1.0, 2.0, 3.0 ml/g/min. The projection data were corrected for water-based beam hardening (BH). The five processing/reconstruction methods considered were:

1) Filtered backprojection (FBP) on noisy sinogram data and the reconstructed images beam hardening corrected (BHC) for iodine and bone [19].
2) Scalar TV applied to BHC noisy images as reconstructed above referred to as '2D STV'.
3) VTV applied to, single slice at a time, BHC noisy images as reconstructed above referred to as '2D VTV'.
4) VTV applied to, 3 slices at a time, BHC noisy images as reconstructed above referred to as '3D VTV'.
5) Spatio-temporal bilateral filtering applied to BHC noisy images referred to as 'BF'.

Four different ROIs (5x5 pixels) were chosen in the left ventricular myocardium in the reconstructed images for the the task of estimating MBF. The average CT number was computed for these ROIs and plotted as a function of time to obtain the time-attenuation curves (TACs). We used the two-component model (as described in [13]) to estimate the myocardial blood flow. Our estimation performance metric is the root mean square percentage error (%RMSE) in the MBF estimates, averaged over 4 ROIs, 10 noise realizations, and 4 flow rates.

C. Patient Data

Dynamic CT perfusion study was performed on patients stressed with regadenoson. 50 mL of iodinated contrast was administered to the patient at 5 mL/s. CT data were acquired for one axial bed position at end diastole for 12 frames at 140 kVp, 18 mAs. The total effective dose to the patient was about 2 mSv. The images were reconstructed with vendor FBP. The noisy images were smoothed using the three versions of TV as well as bilateral filtering.

III. Results

The smoothing parameters for the various TV methods as well as for the BF method were chosen so as to minimize the %RMSE in flow estimates. Figure 1 shows the %RMSE in MBF estimates for 25 mAs tube current and for 1s, 2s and 3s sampling.

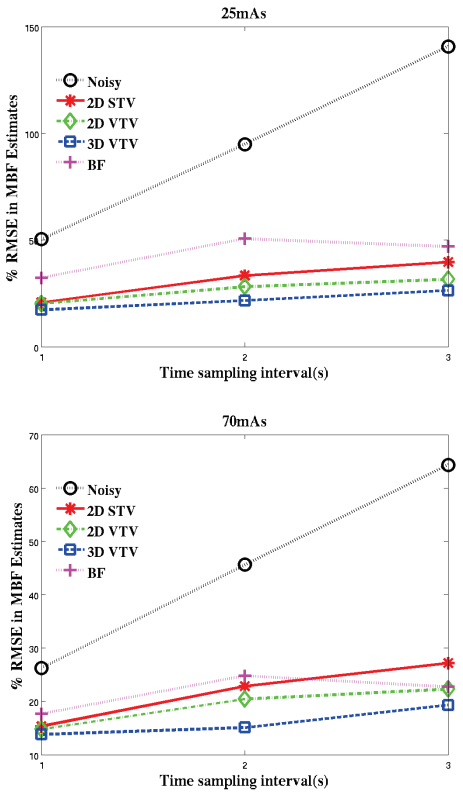

Figure 1. Variation of %RMSE in MBF estimates for 25 and 70 mAs

For unsmoothed data, the %RMSE in MBF estimates increases sharply with sampling interval, while the % RMSE

for the TV and BF methods grows much more slowly on increasing the sampling interval. This can result in potential dose savings since we can get almost equally accurate MBF estimates by reducing the dose by a factor of three. We observe that the two VTV methods give the most accurate MBF estimates at lower tube currents. Figure 2 shows the zoomed-in view of the cardiac region in the reconstructed images and the TACs extracted from images reconstructed using the various methods and 25mAs tube current.

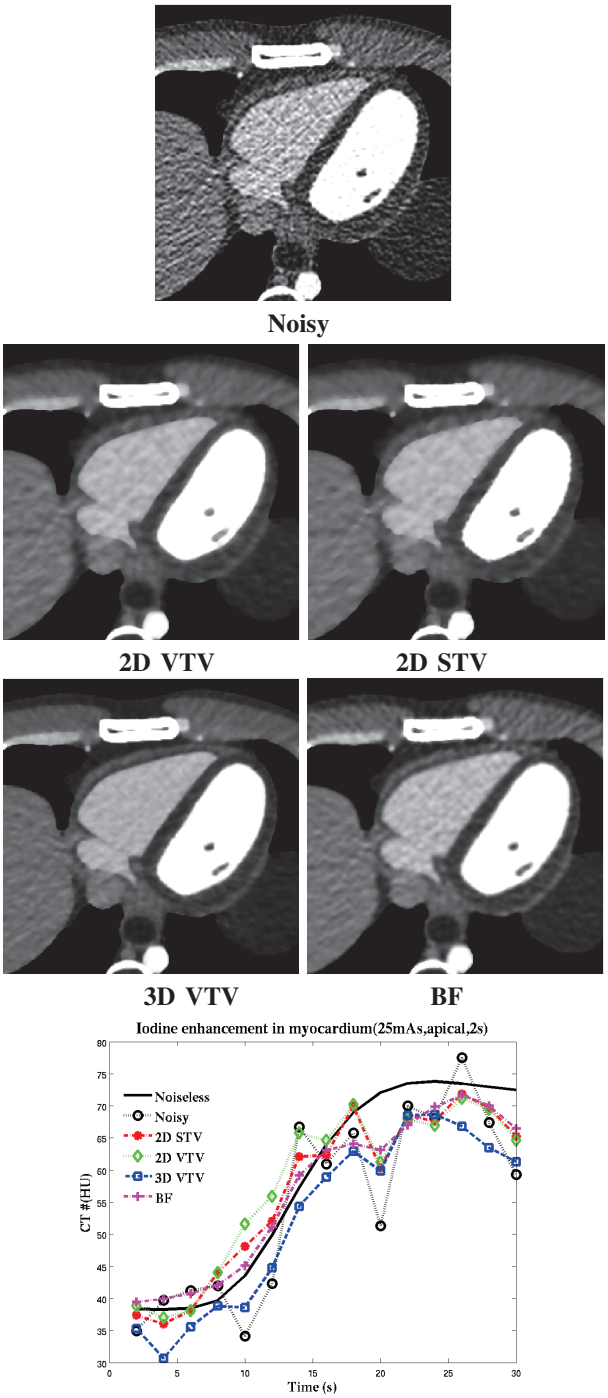

Figure 2. Cardiac region in the images reconstructed using various methods for simulated data at 25 mAs and TACs in the apical region with 2s sampling

Figure 3 shows sample TACs and reconstructed images for a patient data using various methods.

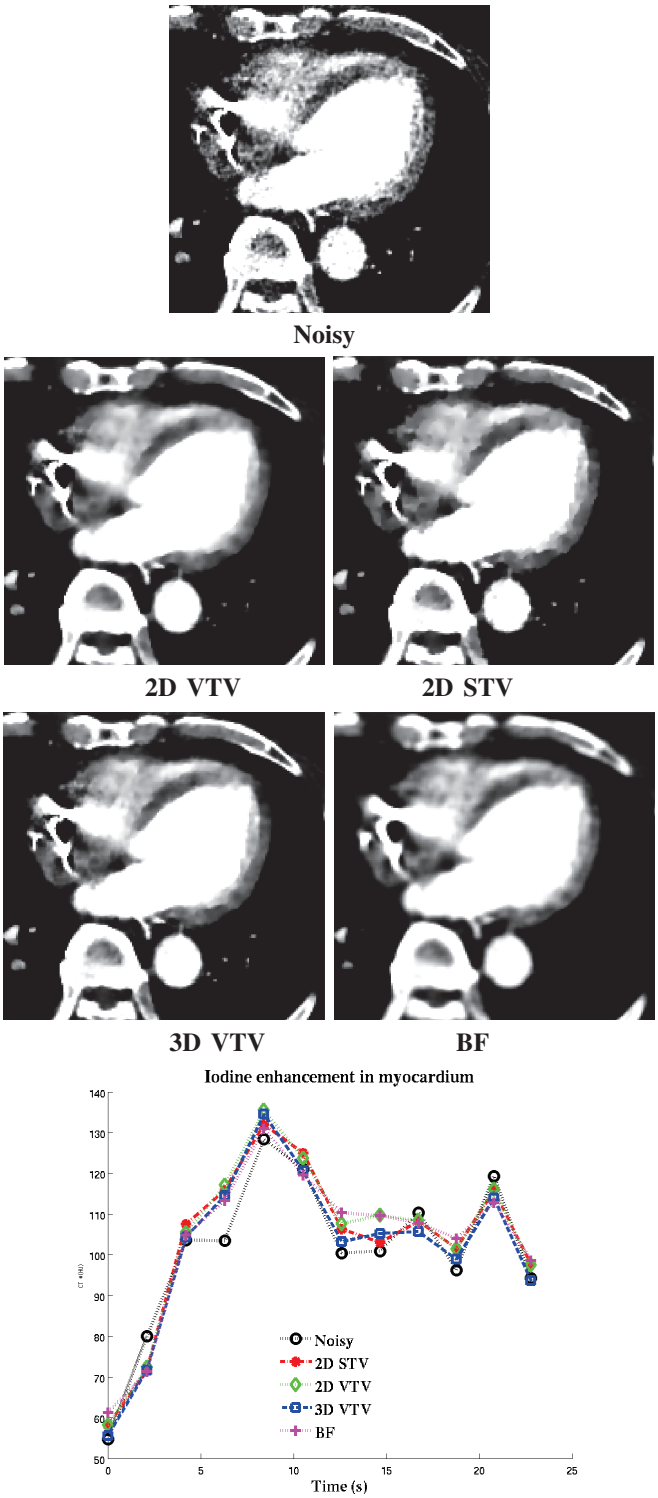

Figure 3. Reconstructed images and TACs for myocardial segment 14 for a patient

3D VTV method gives us the sharpest image amongst all these methods while bilateral filtering results in more blurring. We observe that smoothing images also makes the TACs

Method	RMSE of Fit (HU)
Noisy	18.28
2D STV	15.29
2D VTV	14.66
3D VTV	14.08
BF	14.09

Table I
AVERAGE RMSE OF FIT OF TACS TO THE MBF MODEL ACROSS 17 MYOCARDIAL SEGMENTS FOR A PATIENT

smoother. The smoothing parameters used for the various methods were such that the resulting smoothed images were noise-matched in a static ROI. The TACs (averaged over 25 voxels) were used to obtain the MBF estimates using the two-compartment model. We find that the average RMSE of fit to the two-compartment model [13] of a given TAC decreases with smoothing as shown in table I. A better fit to the model TAC may lead to a better MBF estimate. So smoothing could help with more accurate MBF estimates with dose savings in dynamic CT. However, the true MBF for the patient is not known. Both the 3D VTV method and bilateral filtering gave the best fit of the resulting TACs to the MBF model. Ultimately, the choice of smoothing parameter and method will involve a tradeoff between bias and variance in MBF estimates .

IV. CONCLUSIONS

In this paper, we compared several image-domain denoising methods applied to a sequence of dynamic cardiac CT images. We found that our proposed 3D VTV method achieves best MBF estimator performance at low tube currents and sparse temporal sampling using simulated data. The performance of other smoothing methods including bilateral filtering becomes comparable to the 3D VTV method at higher tube currents. We applied our smoothing methods to a patient study. All of the smoothing methods reduce the noise in the TACs and provide a better fit of the TACs to the MBF estimation model. The proposed 3D VTV method leads to TACs with a good fit to the MBF model (reduced RMSE of fit by ~23% compared to original images). In the future, we will apply these methods to more patient studies in a trial comparing quantitative CT to quantitative PET to determine the optimal smoothing approach.

REFERENCES

[1] Hendel, R.C., Patel, M.R. and Kramer, C.M., "Appropriateness Criteria for Cardiac Computed Tomography and Cardiac Magnetic Resonance Imaging: A Report of the American College of Cardiology Foundation Quality Strategic Directions Committee Appropriateness Criteria Working Group", American College of Radiology, Society of Cardiovascular Computed Tomography, Society for Cardiovascular Magnetic Resonance, American Society of Nuclear Cardiology, North American Society for Cardiac Imaging, Society for Cardiovascular Angiography and Interventions, and Society of Interventional Radiology, J. Am. Coll. Cardiol. 48(7), 1475-1497, (2006).

[2] Tonino, P.A., De Bruyne, B., Pijls, N.H., "Fractional flow reserve versus angiography for guiding percutaneous coronary intervention", N. Engl. J. Med. 360, 213-224(2009).

[3] George, R.T., Jerosch-Herold, M. and Silva, C., "Quantification of myocardial perfusion using dynamic 64: detector computed tomography," Invest. Rad. 42, 815-822 (2007).

[4] Sawall, S., Bergner, F., Lapp, R., Mronz, M., Karolczak, M., Hess, A. and Kachelriess, M., "Low-dose cardio-respiratory phase-correlated cone-beam micro-CT of small animals," Med. Phys. 38(3), 1416-1424(2011).

[5] Sawall, S., Kuntz J., Socher, M., Knaup, M., Hess, A., Bartling, S. and Kachelriess, M., "Imaging of cardiac perfusion of free-breathing small animals using dynamic phase-correlated micro-CT", Med. Phys. 39(12), 7499-7506 (2012).

[6] Ritschl, L., Sawall, S., Knaup, M., Hess, A. and Kachelriess, M., "Iterative 4D cardiac micro-CT reconstruction using an adaptive spatio-temporal sparsity prior," Phys. Med. Biol. 57, 1517-1525 (2012).

[7] Chen, G-H. , Teirault-Lauzier, P., Tang, J., Nett, B., Leng, S.,Zambelli, J., Qi, Z., Bevines, N., Raval, A., Reeder, S. and Rowley, H., "Time-resolved interventional cardiac C-arm cone-beam CT: an application of the PICCS algorithm," IEEE Trans. Med. Img. 31(4), 907-923 (2012).

[8] Tao, Yinghua and Chen, Guang-Hong and Hacker, Timothy A. and Raval, Amish N. and Van Lysel, Michael S. and Speidel, Michael A., "Low dose dynamic CT myocardial perfusion imaging using a statistical iterative reconstruction method," Med. Phys. 41, 071914 (2014), DOI:http://dx.doi.org/10.1118/1.4884023.

[9] D. Modgil, A.M. Alessio, M.D. Bindschadler, K.J.Little, D. Rigie, P.A. Vargas and P.J. La Rivière, "Multi-dimensional sinogram restoration for myocardial blood flow estimation from dose-reduced dynamic CT," Proc. Fully 3D meeting, 2013.

[10] D.S. Rigie and P.J. La Rivière, "Joint reconstruction of multi-channel, spectral CT data via constrained total nuclear variation minimization," Phys Med Biol. 2015 Mar 7;60(5):1741-62, 2015, doi: 10.1088/0031-9155/60/5/1741.

[11] D. Modgil, A.M. Alessio, M.D. Bindschadler and P.J. La Rivière, "Adaptive temporal smoothing of sinogram data using Karhunen-Loeve (KL) transform for myocardial blood flow estimation from dose-reduced dynamic CT," Proc. SPIE 9034, Medical Imaging 2014: Image Processing, 903422, 2014.

[12] D. Modgil, D.S. Rigie, M.D. Bindschadler, A.M. Alessio and P.J. La Rivière, "Vectorial total variation denoising for myocardial blood flow estimation in dynamic CT,", NSS MIC Conf. 2014.

[13] M. Bindschadler, D. Modgil, K. Branch, P.J. La Rivière, and A.Alessio, "Comparison of Blood Flow Models and Acquisitions for Quantitative Myocardial Perfusion Estimation from Dynamic CT," Phys. Med. Bio., 59(7), 2014.

[14] L.I. Rudin, S. Osher and E. Fatemi, "Nonlinear total variation based noise removal algorithms." Physica D: Nonlinear Phenomena 60.1, pp. 259-268, 1992.

[15] A. Chambolle, and T. Pock. "A first-order primal-dual algorithm for convex problems with applications to imaging." Journal of Mathematical Imaging and Vision 40.1 (2011): 120-145.

[16] L. Ritschl, F. Bergner, C. Fleischmann, M. Kachelriess, "Improved total variation-based CT image reconstruction applied to clinical data,", Phys Med Biol. Mar 21;56(6):1545-61, 2011. doi: 10.1088/0031-9155/56/6/003.

[17] Sidky E Y, Jørgensen J H and Pan X Convex optimization problem prototyping for image reconstruction in computed tomography with the Chambolle-Pock algorithm Phys. Med. Biol. 57 3065–91, 2012.

[18] D. Strong and T.Chan, "Edge-preserving and scale-dependent properties of total variation regularization," Inverse Problems 19 (2003) S165–S187, 2003.

[19] P. Stenner, B. Schmidt, T. Allmendinger, T. Flohr and M. Kachelriess, "Dynamic iterative beam hardening correction in myocardial perfusion imaging using contrast-enhanced CT," Invest. Rad., 45(6), pp. 314-323, June, 2010.

Sparse Regularization of CBCT Reconstruction Using 3D Dual-Tree Complex Wavelet Transform and Dictionary Learning Techniques

Thibault Notargiacomo*, Dominique Houzet†, Guillaume Bernard‡ and Vincent Fristot§
*Univ. Grenoble Alpes, CNRS GIPSA-Lab, 38000 Grenoble, France Email: gnthibault@gmail.com
†Univ. Grenoble Alpes, CNRS GIPSA-Lab, Email: dominique.houzet@gipsa-lab.grenoble-inp.fr
‡Thales TED, 38430, Moirans, France Email: guillaume.bernard@thalesgroup.com
§Univ. Grenoble Alpes, CNRS GIPSA-Lab, Email: vincent.fristot@gipsa-lab.grenoble-inp.fr

***Abstract*—Cone Beam tomography, being potentially less expensive than helical CT, may allow a generalization of 3D imaging to annual screening of disease like osteoporosis or osteoarthritis. Frequent assessment of anatomical metrics over bones and joints motivates the design of reconstruction algorithms capable of accurate retrieval of bone microstructure from low dose acquisitions. In this paper, we assess the behaviour of two 3D overcomplete transform for real CT image representation and their performance for sparse regularization of CBCT reconstructions over a human knee dataset featuring complex microstructure.**

I. Introduction

Sparse priors have been extensively used, for the past few decades as a regularizing tool for common inverse problems in imaging. The literature about design of efficient sparsifying transform and sparsity promoting algorithm is huge, and it would be difficult to establish an exhaustive list of all approaches that have been applied to the problem of CT reconstruction. Instead we will focus on two specific tools, one arising from the field of harmonic analysis, known as dual-tree complex wavelet transform (DT$\mathbb{C}$WT) and the other from the statistics community: dictionary learning.

Our aim here, is to try to overcome some limitations of well-known sparsifying transform, like the loss of texture informations often attributed to the total variation model or the lack of directionality of some wavelet with high order vanishing moments like Daubechies'. A previous study with a similar approach has been conducted in [1], shearlet transform yielded better results that TV, but only in a 2D setting. Although extensions of ridgelet, curvelets, shearlets, ... to 3D have been studied, and seem to provide optimal sparsity properties for some class of functions, we first tried to address DT$\mathbb{C}$WT as a numerically efficient 3D separable and semi orthogonal transform. It should be noticed that, in the framework of 3D imaging, lack of directionality of common real wavelets and computational cost of non separable wavelets become increasingly challenging obstacle to practical use of many interesting wavelet basis.

Work financially supported by France CIFRE convention No. 2013/0971 and Thales Electron Devices Moirans.

We will show that properties featured by the DT$\mathbb{C}$WT like directionality and shift invariance although being related to an important redundancy, are manageable on today's hardware when using moderate image size like 512^3 voxels.

Dictionary learning techniques received an important attention in various field of inverse problems, its use in the field of medical imaging, have shown promising results [2], and many approaches even include an adaptive dictionary learning as a part of the reconstruction algorithm [3], [4].

However, to our knowledge, statistical learning of atoms remained mostly restricted to 2D images, as a consequence, extension of dictionaries of 2D data to 3D, although computationally demanding, seems to be an interesting lead.

II. Background

A. Dual-Tree Complex Wavelets transform in CT

The rational behind the design of dual-tree complex wavelet transform has been exposed in [5], we may retain that DT$\mathbb{C}$WT possess the following desirable properties: *shift invariance*, reduced *aliasing* in the analysis operator, high *directionality* and efficient separable filterbank based transform with small support filters. Previous work in 2D [6] suggested, that, also theoretically less efficient for providing a best k-approximation to the class of smooth objects with discontinuities along C^2 curves, some specific application were able to reconstruct signals with less artifacts using thresholded DT$\mathbb{C}$WT coefficients than curvelets. Practical use of 3D DT$\mathbb{C}$WT for video denoising has also ben studied in [7], and outperformed classical separable wavelet although it appeared that 2D directionality was more relevant for modeling 2D signal than its extension to 3D for 2D+time signals. Successfull use of 2D DT$\mathbb{C}$WT has also been reported in fingerprint reconstruction tasks [8], whose visual appearance resemble microstructure observed inside human bones along various orientations.

B. Dictionary Learning Techniques

Many wavelets design rely on statistical properties shared by most of the natural signals to a certain extent: regularity,

stationarity, polynomial behaviour, ...that have been studied in analytical framework and exploited on purpose. However, dictionary learning methods, generate directly atoms from a predefined class of signals, without prior, seeking for a possibly overcomplete dictionary able to provide a sparse approximation, this consideration gave birth to many formulations of sparse dictionary learning.
Here, we restricted our attention to a constrained version of the l_1 convex relaxation version of sparse recovery, related to the LASSO problem :

$$\underset{D\in C}{min}\ \frac{1}{n}\sum_{i=1}^{n}\|\alpha_i\|_1 \text{ s.t } \|x_i - D\alpha_i\|_2^2 \leq \lambda \tag{1}$$

Mairal in [9] studied this problem, as well as various other sparsity inducing learning techniques, including non convex ones in the more general framework of sparse coding and matrix factorization, and showed how to practically address them in high dimensional settings.

III. Material and methods

A. Sparsity Terminology

In [10] the author recall that compressible signals can be caracterized by their appartenance to a weak l_p ball, and derives another caracteization using the l_2 norm of the difference between a signal x and its best k-term approximation using k coefficients (denoted x_k) in the basis Φ which decays as :

$$\|x - x_k\| \leq C.R.k^{\frac{1}{2}-\frac{1}{p}} \tag{2}$$

As the later definition is used in many applications of approximation theory and compressive sensing, we will use it in order to compare our two over complete basis. Best k-approximation being provided by hard thresholding in the case of DT$\mathbb{C}$WT, and by LASSO regression for the dictionary basis.

B. Implementation of the DT$\mathbb{C}$WT

Implementing separable complex wavelet transform requires first a basic understanding of the relation between multiresolution analysis and filterbanks. The specific case of filterbank design for complex wavelets has been tackled in [5], especially the method to obtain nearly analytic wavelets (without negative frequencies), which is the key feature for high directionality.
We used the Q-shift filter based solution to generate the half sample delay as a hilbert transform. This methods mimics the 90° phase shift applied in single sideband modulation, and has the nice property of perfect reconstruction, short support (6tap) and orthogonality. In the framework of convex optimization, fully orthogonal wavelet trees at every stage are desirable, even in the case of redundant transformations, in order to construct tight frames and match the requirements of easy proximity operator computation in both analysis and synthesis formulation, see [11]. In practice we used the (9,7) bi-orthogonal Antonini filter at the first stage only, without significant convergence problem. It should be noticed that directionality given by the nearly analytic behaviour of $\mathbb{C}$WT comes with a redundancy ratio of greater importance with the growth of the number of spatial dimension D as 2^D, which gives the 3D DT$\mathbb{C}$WT a redundancy factor of 8. In order to take advantage of recent advances in high performance computing, we implemented our own GPU version of the n-D DT$\mathbb{C}$WT using Cuda.

C. Dictionary learning for 3D CT images

To conduct our study on reference dataset, we used a CT version of the Human Visible Project [12], eventually concatenated, cropped and scaled to form 9 cubes of data. Among the various formalizations that have been used to set up dictionary learning methods, we choose eq. 1. We did so because the optimization problem it casts can be parametrized using only one information that can be, under some assumption, easily interepreted as the variance of a stationary additive centered noise inside a learning patch.
Before learning, every patch is centered, reduced and scaled to a unitary vector, we did not used whitening in order to keep local correlation informations (low frequencies) and ensure optimal performances for reconstructions. The value $\lambda = 0.01$ equivalent to 1% of the patch norm for our pre-processing settings gave us satisfying results when challenged using compressibility assessment exposed in the next section. A constant patch of norm 1 was added to the dictionary resulting from solving the above problem. In practice, we used the software SPAMS [13], to solve this optimization problem, using trainDL method in mode 1 with 1000 iterations

D. Dictionary operator in CT reconstruction

A dictionary, in finite length, discrete time signal processing, can be defined as a $p \times n$ matrix D, potentially featuring an overcompleteness ratio of n/p, whose columns are discrete atoms ψ_i of size p:

$$D = \begin{pmatrix} \psi_{00} & \cdots & \psi_{n-10} \\ \psi_{01} & \cdots & \psi_{n-11} \\ \vdots & \vdots & \vdots \\ \psi_{0p-1} & \cdots & \psi_{n-1p-1} \end{pmatrix} \tag{3}$$

Once dictionary is learned, it is easy to define $D_{fullimage}$, a matrix that is simply the block-diagonal reproduction of the dictionary D, where each row corresponds to one specific voxel to be reconstructed. The synthesis operator is still a simple matrix-vector multiplication. In practice although we use this definition in order to compute image/patch correlations through $D^{\intercal}_{fullimage}$, it is interesting to add more overcompleteness to the full dictionary by overlapping patches during the reconstruction.
This method allows to smooth the signal at patch boundaries, avoiding macroblocking artifacts similar to those arising when using block DCT for jpeg compression.
Unfortunately, in order to setup this method, we had to define a new operator $D_{overlap}$ that is not an equivalent of $D_{fullimage}$ but a slightly different version that exhibits non zero terms at patches from neighbouring spatial locations (columns) for a given voxel (row). The overlapping rows sees

their contribution weighted by a factor equal to the inverse of the number of different patch involved in the overlap.
Here is an example of such $D_{overlap}$ matrix that reconstruct a $1D$ signal of size $2p-1$ made of two patches of size p overlapping at one spatial site.

$$D_{overlap} = \begin{pmatrix} \psi_{00} & \dots & \psi_{n-10} & 0 & \dots & 0 & \\ \psi_{01} & \dots & \psi_{n-11} & 0 & \dots & 0 & \\ \vdots & \vdots & \vdots & \vdots & \vdots & \vdots & \\ \psi_{0p-2} & \dots & \psi_{n-1p-2} & 0 & \dots & 0 & \\ \frac{1}{2}\psi_{0p-1} & \dots & \frac{1}{2}\psi_{n-1p-1} & \frac{1}{2}\psi_{00} & \dots & \frac{1}{2}\psi_{n0} & \\ 0 & \dots & 0 & \psi_{01} & \dots & \psi_{n-11} & \\ \vdots & \vdots & \vdots & \vdots & \vdots & \vdots & \vdots \\ 0 & \dots & 0 & \psi_{0p-1} & \dots & \psi_{n-1p-1} & \end{pmatrix} \tag{4}$$

Then the reconstruction of the signal from its coordinates in the dictionary D can be expressed as:

$$D_{overlap} \begin{pmatrix} \alpha_0 \\ \alpha_1 \\ \vdots \\ \alpha_{n-1} \\ \beta_0 \\ \beta_1 \\ \vdots \\ \beta_{n-1} \end{pmatrix} = \begin{pmatrix} x_0 \\ x_1 \\ \vdots \\ x_{p-1} \\ \vdots \\ x_{2p-2} \end{pmatrix} \tag{5}$$

This method was also implemented using Cuda for our 3D patch setting.

E. Sparse Reconstruction algorithm

There is an abundant literature about optimization methods for solving sparsity related problems, many of them are related to convex relaxation of l_0 norm like the l_1 or l_p with $0 < p < 1$. In the current study, we restricted ourselves to one of the most simple algorithm, derived from the forward backward splitting algorithm, thats uses a nesterov accelerated first order method called Fista [14] in order to solve the following problem:

$$\min_{x \in \mathbb{R}^n} \frac{1}{2}\|ADx - y\|_2^2 + \lambda |x|_1 \tag{6}$$

where A is our cone beam tomographic projection operator, D is our dictionary, and x is the unknown expression of the 3D volume in the dictionary basis, whether this dictionary is our semi orthogonal DT$\mathbb{C}$WT transform, or our overcomplete dictionary learned from a pre-existing dataset. Our practical implementation includes a GPU ray casting projector with 3D linear interpolation and a GPU voxel based back projector with 2D linear interpolation.

IV. Numerical experiments

A. Validity of signals model for generic CT images

In order to assess the validity of the 3D Dual Tree Complex Wavelets tight frame and the 3D dictionary, we decided to study the decay profile of the l_2 error presented in 2 over a man head CT image of size 256^3. For DT$\mathbb{C}$WT, we challenged the number of decomposition levels, and for the dictionary, we challenged the overcompleteness of our dictionary for a given learning dataset made of 8 other images of size 256^3 with a reconstruction overlap of 1 voxel in every direction for patches of size $6 \times 6 \times 6$. This methodology first helped us to tune learning parameters like the size of the training set, and the λ in eq. 1. In figure 1 we can see that, above 4 levels of decomposition, best k-term error decay in the 3D DT$\mathbb{C}$WT tight frame seems to follow a power law (linearized using a log/log scale) suggesting that CT images lies in a weak l_p ball where p is close to 1.7. However, due to the absence of multiscale structure, the dictionary approach exhibits a more complex pattern, the LASSO sparse coding method is unable to provide a global approximation with less than $10^{3.5}$ coefficients. Then two decay profiles appears sequentially, the first similar to DT$\mathbb{C}$WT between $10^{3.5}$ and $10^{4.5}$ but still inferior in quadratic error and the second part in the sparsity range over $10^{4.5}$ where sparse coding over the dictionary basis outclasses the DT$\mathbb{C}$WT. We can notice that, beyond 10^7, DT$\mathbb{C}$WT seems to be the only method capable of providing a nearly perfect reconstruction, however, as summing small errors over a large number of terms may generate numerical instability, we prefere avoiding interpretation here.

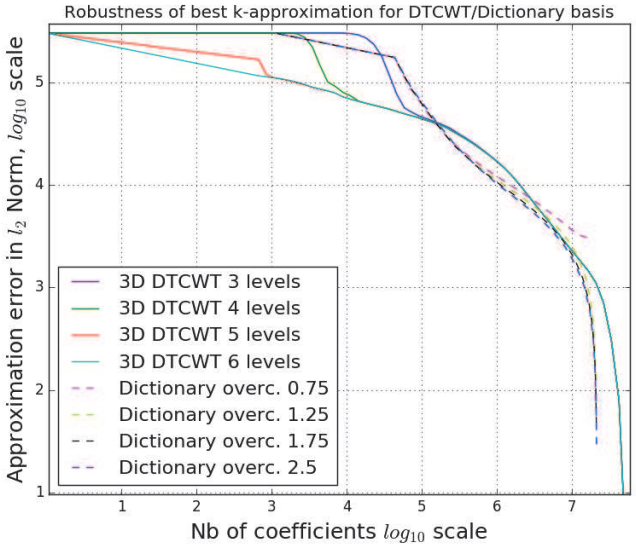

Fig. 1: Robustness of the best k-term approximation error.

B. Sparse reconstruction of human knee specimen

Our experiment was conducted on a homemade rotating platform using a Thales 2630S flat panel detector and a IAE RTC 600 HS 0.6/1.2 X-Ray source. 600 images, binned in 780×720 ($368\mu m$ equivalent pixels) were acquired at 70 kVp and 8mA over a 300° angular range, no denoising filter was applied nor beam hardening correction. Attenuation maps were obtained using a constant I_0 estimation. Reconstruction

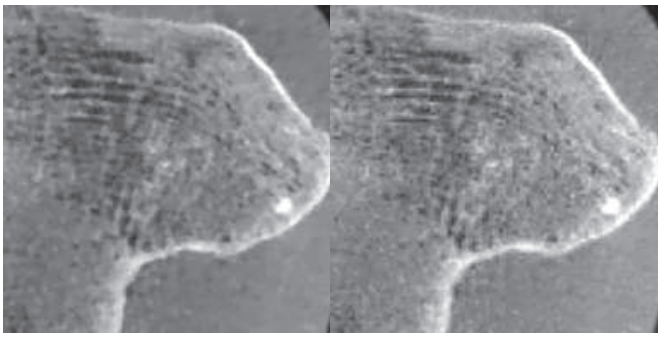

(a) ADMM-TV (b) ADMM-Daubechies

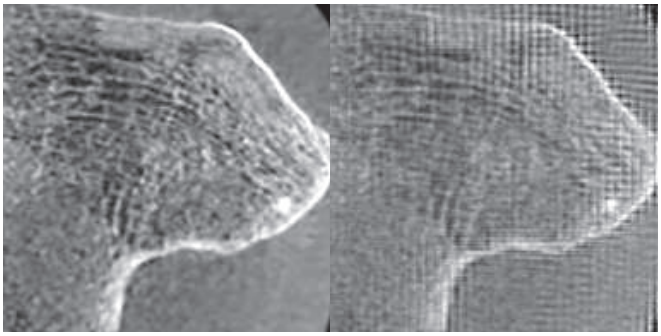

(c) Fista-DT$\mathbb{C}$WT (d) Fista-Dictionary

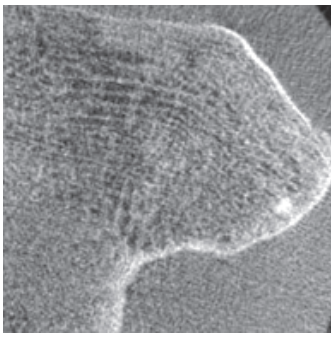

(e) Short-Scan FDK

Fig. 2: Visual overview of an axial slice with 5 different reconstruction methods

of 512^3 voxels of size $244 \times 244 \times 488 \mu m$, was performed using a single NVidia GTX Titan X, with 100 Fista iterations and a regularisation parameter λ equal to 0.05 for the DT$\mathbb{C}$WT and 0.01 for the dictionary, with a 1.66 redundancy ratio and minimal overlap. Run time was approximately 18 minutes and 28 minutes respectively for DT$\mathbb{C}$WT and dictionary sparsifying transform. Other methods used here comes from RTK [15].

V. Conclusion

The results of the present study shows practical feasibility of sparse regularization of CBCT reconstruction using highly redundant dictionaries on a single high end personal computer. In our specific use case, exploiting sparsity prior in the DT$\mathbb{C}$WT domain yielded visually better results than 3D dictionary learning, total variation and Daubechies wavelet models. However, probably due to the inhomogeneity of the learning dataset, our reconstruction yielded severe macroblocking artifacts near thick bones, better results may be obtained by carefully selecting the learning dataset and reconstruction parameters.

Acknowledgment

The authors would like to thank Thibaut Tezenas du Montcel, for his work on the cuda acceleration of the 2D DT$\mathbb{C}$WT and Christine Chappard from Bioingenierie et Bioimagerie Osteo-Articulaire (B2OA) laboratory for providing the plastinated human knee specimen.

References

[1] B. Vandeghinste, B. Goossens, R. Van Holen, C. Vanhove, A. Pizurica, S. Vandenberghe, and S. Staelens, "Iterative ct reconstruction using shearlet-based regularization," *Nuclear Science, IEEE Transactions on*, vol. 60, no. 5, pp. 3305–3317, 2013.

[2] Y. Zhang, H. Yu, X. Mou, and G. Wang, "Dictionary learning and low rank based multi-energy ct reconstruction," in *International Conference on Image Formation in X-Ray Computed Tomography*, 2014, pp. 95–98.

[3] Q. Xu, H. Yu, X. Mou, L. Zhang, J. Hsieh, and G. Wang, "Low-dose x-ray ct reconstruction via dictionary learning," *Medical Imaging, IEEE Transactions on*, vol. 31, no. 9, pp. 1682–1697, 2012.

[4] L. Pfister and Y. Bresler, "Adaptive sparsifying transforms for iterative tomographic reconstruction," in *International Conference on Image Formation in X-Ray Computed Tomography*, 2014, pp. 107–110.

[5] I. W. Selesnick, R. G. Baraniuk, and N. G. Kingsbury, "The dual-tree complex wavelet transform," *Signal Processing Magazine, IEEE*, vol. 22, no. 6, pp. 123–151, 2005.

[6] C. Amiot, "Débruitage de séquences par approche multi-échelles: application à l'imagerie par rayons x," Ph.D. dissertation, Grenoble, 2014.

[7] I. W. Selesnick and K. Y. Li, "Video denoising using 2d and 3d dual-tree complex wavelet transforms," in *Optical Science and Technology, SPIE's 48th Annual Meeting*. International Society for Optics and Photonics, 2003, pp. 607–618.

[8] K. RameshKumar and M. U. Latha, "Efficient fingerprint image reconstruction by 2d dtcwt," *International Journal of Advanced Computing*, vol. 35, no. 10, pp. 415–422, 2012.

[9] J. Mairal, F. Bach, J. Ponce, and G. Sapiro, "Online learning for matrix factorization and sparse coding," *The Journal of Machine Learning Research*, vol. 11, pp. 19–60, 2010.

[10] E. J. Candès *et al.*, "Compressive sampling," in *Proceedings of the international congress of mathematicians*, vol. 3. Madrid, Spain, 2006, pp. 1433–1452.

[11] I. W. Selesnick and M. A. Figueiredo, "Signal restoration with overcomplete wavelet transforms: comparison of analysis and synthesis priors," in *SPIE Optical Engineering+ Applications*. International Society for Optics and Photonics, 2009, pp. 74 460D–74 460D.

[12] NIH and U. of Iowa Magnetic Resonance Research Facility. (2001) Visible human project ct datasets. [Online]. Available: https://mri.radiology.uiowa.edu/visible_human_datasets.html

[13] J. Mairal, F. Bach, J. Ponce, and G. Sapiro. (2010) Sparse modeling software. [Online]. Available: http://spams-devel.gforge.inria.fr/

[14] A. Beck and M. Teboulle, "A fast iterative shrinkage-thresholding algorithm for linear inverse problems," *SIAM journal on imaging sciences*, vol. 2, no. 1, pp. 183–202, 2009.

[15] S. Rit, M. V. Oliva, S. Brousmiche, R. Labarbe, D. Sarrut, and G. C. Sharp, "The reconstruction toolkit (rtk), an open-source cone-beam ct reconstruction toolkit based on the insight toolkit (itk)," in *Journal of Physics: Conference Series*, vol. 489, no. 1. IOP Publishing, 2014, p. 012079.

OBJECT CLASSIFICATION IN BAGGAGE-CT IMAGERY USING RANDOMISED CLUSTERING FORESTS

Andre Mouton, Toby P. Breckon

am2742

ABSTRACT

We present a random forest-based Bag of Visual Words (codebook) approach for threat classification in noisy 3D baggage-CT imagery. Features are extracted from a dense sampling grid and encoded using extremely randomised clustering forests [1]. An SVM classifier using these feature encodings is shown to outperform a state-of-the-art visual cortex model [2] in two classification tasks. In addition to improved classification accuracy, we also demonstrate a reduction of several orders of magnitude in processing time over the cortex model. Crucially, these results are achieved without applying any noise or artefact reduction, which brings into question the relevance of the widely-held assumption that computationally expensive artefact reduction techniques are a necessity in automated image-understanding tasks for low-quality baggage-CT imagery.

Index Terms— Classification, Bag-of-Words, Random forests, baggage CT

1. INTRODUCTION

The key role of baggage screening in the transport security domain has lead to an increased interest in the development of automated threat detection strategies. Traditionally, X-ray based 2D imaging technologies have been used for this purpose [3]. Due to variations in object orientation, clutter and density confusion, contraband objects are often challenging to detect in 2D X-ray images. Recently, the use of 3D Computed Tomography (CT) based screening systems have become more widespread as a means of addressing these limitations. Typically, Dual-Energy Computed Tomography (DECT) scanners are used to allow for material-based detection of explosives [4]. This primary, non-object-recognition based objective of typical baggage-CT scanners, coupled with the demand for high throughput, means baggage-CT imagery is typically of a much poorer quality than that encountered in the medical domain and presents with substantial noise, metal streaking artefacts and poor voxel resolution [5] (Figure 1).

A. Mouton is with the Deptartment of Computer Science, University of Bath, UK (email: am2742@bath.ac.uk; andremouton.email@gmail.com).
T.P. Breckon is with the School of Engineering and Computer Sciences, Durham University, UK.
This work was funded under the Innovative Research Call in Explosives and Weapons Detection (2010), sponsored by HOSDB, DfT, CPNI and MPS.

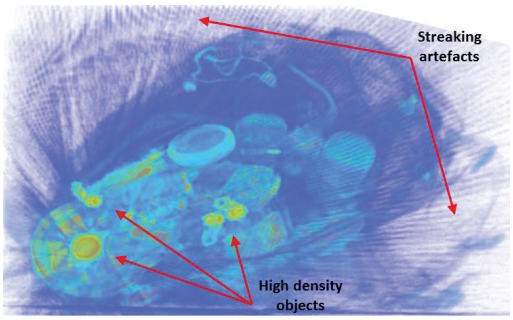

Fig. 1: Cluttered baggage-CT scan with streaking artefacts.

Prior work related to the automated classification of objects within complex non-medical 3D volumetric imagery is limited. Chen *et al.* [6] address the classification of pistols in DECT imagery. The problem is, however, simplified to an examination of the characteristic cross sections and no experimental results are presented. Megherbi *et al.* [7] propose the use of a classifier-based approach using volumetric shape characteristics for the recognition of pre-segmented bottles in complex 3D CT imagery. While the study demonstrates reasonable results, only a very limited dataset is considered. Flitton *et al.* [2] have presented what may perhaps be considered the current state-of-the-art in automated object recognition in such complex 3D imagery. Particularly, a novel 3D extension to the hierarchical visual cortex model for object recognition is used for the automated detection of threats in pre-segmented 3D CT baggage imagery. The approach is shown to outperform a traditional BoW approach with correct detection rates in excess of 95% and low false-positive rates. In addition to incurring a large computation overhead (in the construction of the cortex model), performance is shown to decline in the presence image noise and artefacts.

The Bag of (Visual) Words (BoW), or codebook, model [8] has enjoyed success in various object recognition and image classification tasks . BoW approaches require a clustering of the feature space to generate visual codebooks. Traditional clustering techniques (e.g. k-means clustering [9]) are computationally expensive when the feature space is large. Moosmann *et al.* [1] demonstrate state-of-the-art classification performance at a significant reduction in computational cost by constructing visual codebooks using Extremely Randomised Clustering (ERC) forests. Similar forest-based clustering approaches have enjoyed success in a variety of image classifi-

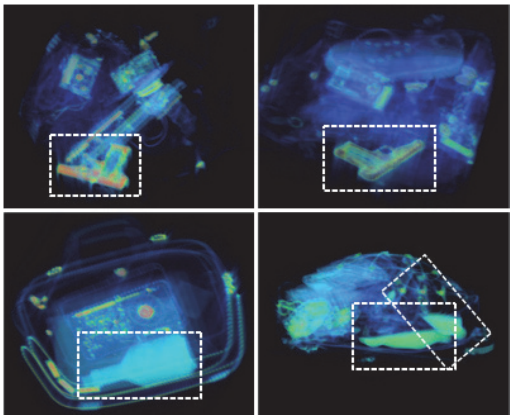

Fig. 2: Example scans containing handguns (top) and bottles (bottom) in cluttered surroundings representative of common airport luggage. Rendering colours chosen to highlight target objects (delineated in white).

cation, registration and segmentation tasks [10, 11].

We extend the use of ERC forests to the previously unconsidered domain of threat classification in noisy volumetric baggage-CT imagery and demonstrate that state-of-the-art performance is obtainable without considering the computationally expensive noise and artefact reduction techniques, traditionally considered a necessity.

2. METHODS

We adopt the following traditional BoW classification framework [12]: 1) feature detection and description; 2) visual codebook generation and vector quantisation and 3) classification. The methods presented here represent the optimal choices based on extensive empirical studies [13, 14].

Feature detection and description: We adopt a dense feature point sampling strategy (as per [15]), whereby keypoints are sampled uniformly and randomly. An invariance to uniform changes in image scale is obtained by sampling interest points from three image scales. At each of the scales a limit of $\tau_N = 0.006N$ on the number of randomly sampled points is enforced (where N is the number of voxels in the Gaussian scale-space image and τ_N is determined empirically). For the data used in this study ($N \sim 3 \times 10^5$), the proposed sampling strategy typically leads to an increase of two orders of magnitude in the number of sampled points compared to the original 3D SIFT keypoint detection approach of Flitton *et al.* [16] (making conventional k-means unsuitable).

Flitton *et al.* [17] have shown that simple density statistics-based descriptors outperform more complex 3D descriptors (SIFT [16] and RIFT [18]) in object detection within low resolution, complex volumetric-CT imagery. In accordance with these findings, the Density Histogram (DH) descriptor [17] is used here. The descriptor characterises the local density variation at a given interest point as an N-bin histogram defined over a continuous density range. The optimal descriptor parameters are selected in accordance with [14] and result in a 60-dimensional feature vector.

Visual codebook generation: Extremely Randomised Clustering (ERC) forests assign separate codewords to every leaf node in a given forest (i.e. a forest containing N leaf nodes, yields a codebook of size N). The BoW representation for a given image is obtained by accumulating the codeword counts after applying the forest to all the descriptors in the image. The resulting histogram of codewords is then used in subsequent classification in the same way as any standard BoW model. In contrast to k-means clustering, ERC forests are supervised. Trees are trained in a top-down recursive fashion [19] using a set of labelled training descriptors, where the labels are obtained from global image annotations (i.e. all descriptors from a given image share the same label). A simple thresholding function is used as the node split function for all internal nodes of the forest:

$$f(v_i, \theta_j) = \begin{cases} 0 & v_i < \theta_j \\ 1 & \text{otherwise} \end{cases} \quad (1)$$

where $v_i, i = 1, \ldots, D$ is a single feature attribute selected from a D-dimensional descriptor vector $\mathbf{v} \in \mathbb{R}^D$ and θ_j is a scalar valued threshold ($D = 60$). The optimality criterion used for node splitting is the classical Information Gain (IG) [20]. Randomness is injected into the trees by considering a fixed-size random subset of the available node split function parameter values at each node.

Classification is performed using a Support Vector Machine (SVM) classifier with a Radial Basis Function (RBF) kernel.

3. RESULTS

We considered the classification of two target objects (handguns and bottles). The performance of the proposed ERC codebook-based model was evaluated against the baseline visual cortex-based approach of [2].

The data used in the study was captured on a CT80-DR dual-energy baggage-CT scanner (Reveal Imaging Inc.), at anisotropic voxel resolutions of $1.56 \times 1.61 \times 5.00$mm. A fan-beam geometry was adopted with a focus-to-isocentre distance of 550mm, a focus-to-detector distance of 1008.4mm and nominal tube voltages of 160kVp and 80kVp. Two distinct datasets were constructed for each of the target classes (handguns and bottles). Each dataset was composed of the given target object scanned in random poses (to obtain rotational invariance) and surrounded by various 'clutter' items (e.g. clothing, books, mobile phones etc.) to provide bags representative of those encountered at airport security checkpoints (Fig. 2). The target objects were subsequently isolated prior to feature extraction, using a 3D sliding-window operator. The two object classes were considered independently of one another. The handgun and bottle datasets consisted of 1255 samples (284 target; 971 clutter) and 1704 samples (534 target; 1170 clutter) respectively. Ten-fold cross-validation testing was performed using the identical data and data-splits

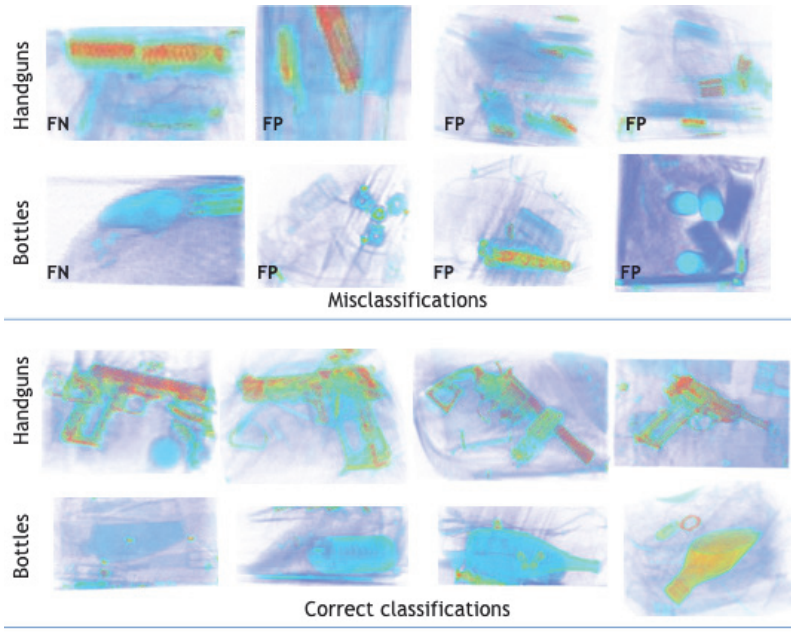

Fig. 3: Examples of correct and incorrect (False-Positive (FP) and False-Negative (FN)) results or the proposed codebook classification model.

Method	Class	TPR (%)	FPR (%)	Precision	Time (s)
ERC Codebook	Handgun	99.71 ± 0.51	0.28 ± 0.21	0.990 ± 0.013	186.89
	Bottle	98.88 ± 0.68	0.60 ± 0.25	0.987 ± 0.021	
Cortex [2]	Handgun	96.81 ± 2.64	1.10 ± 0.93	0.962 ± 0.029	$> 3.6 \times 10^3$
	Bottle	96.62 ± 3.23	1.01 ± 1.63	0.977 ± 0.034	

Table 1: Comparison of the proposed ERC codebook to the visual cortex model [2]

.

used in [2], allowing for a direct performance comparison between the ERC Codebook and the visual cortex-based approach of [2].

The cost C and the kernel width γ of the RBF kernel used in the SVM classifier were optimised using a standard grid-search cross-validation procedure [21]. Internal nodes in the ERC forests were optimised by performing 30 tests at each node - this value was fixed for all nodes. Trees were grown to a maximum depth of $D_T = 10$, with a lower bound of $IG_{min} = 10^{-4}$ on the information gain. The settings resulted in trees with approximately 1000 leaf nodes each. For a forest containing $T = 25$ trees, codebooks therefore typically contained approximately 25000 codewords.

Experiments were performed on an Intel Core i5 machine running a 2.30GHz processor with 6GB of RAM. The random forest methods were implemented in C++ using the Sherwood decision forest library [22]. The processing times, measured over the entire 10-fold cross-validation procedure and averaged over the two experiments (bottles and handguns), are recorded in the final column of Table 1.

Table 1 shows the quantitative results of the aforementioned experiments averaged over the 10 folds. The proposed codebook approach (dense feature sampling, ERC forest encoding and SVM classifier) produced state-of-the-art classification results for both the handgun (TPR = 99.71%; FPR = 0.28%) and bottle (TPR = 98.88%; FPR = 0.60%) datasets, which correspond to significant improvements over the baseline cortex model [2] (Handguns: TPR = 96.81%; FPR = 1.10% and Bottles: TPR = 96.62%; FPR = 1.01%).

Figure 3 illustrates several examples of correct and incorrect classifications produced by our proposed codebook models. The presence of high-density objects (coloured red/orange), were the predominant factor contributing to False-Positive (FP) handgun classifications, while handguns containing low-density handles relative to the barrels led to False-Negative (FN) classifications.

The two major factors contributing to false-positive bottle classifications were: 1) the presence of items with circular cross sections similar to that of a full bottle and 2) the presence of image regions similar in density to the liquids used in the training set. It is worth noting that these observations are in accordance with those made in the previous works of Flitton *et al.* [2, 14].

Finally, we emphasise again that noise and metal arte-

fact reduction [5, 23, 24] have not been considered in this work. While this demonstrates the robustness of the dense feature sampling to background noise and artefacts, it more importantly brings into question the widely-held assumption that such techniques are a necessity in automated image-understanding tasks for low-quality baggage-CT imagery. A more extensive evaluation of this observation is being conducted in an ongoing study.

4. CONCLUSIONS

We have presented a random forest-based codebook approach for the classification of threats in low-resolution, cluttered volumetric baggage-CT imagery and demonstrated improvements over the state-of-the-art [2] of $> 3\%$ and $> 2\%$ in the TPR for handgun and bottle classification respectively and reductions of 70% and 40% in the corresponding FPR. These improvements, together with a reduction of several orders of magnitude in processing time, were achieved without performing any noise or artefact removal, representing an important finding in a domain where these computationally expensive pre-filtering techniques have traditionally been considered mandatory. Future work will consider an extension to multiple target classes and present a more extensive investigation into the relevance of denoising and artefact reduction in this domain.

5. REFERENCES

[1] F. Moosmann, B. Triggs, and F. Jurie, "Fast discriminative visual codebooks using randomized clustering forests," *Advances in Neural Information Processing Systems 19*, pp. 985–992, 2007.

[2] G. Flitton, T. Breckon, and N. Megherbi, "A 3D Extension to Cortex Like Mechanisms for 3D Object Class Recognition," in *Proceedings of the IEEE International Conference on Computer Vision and Pattern Recognition*, June 2012, pp. 3634–3641.

[3] B. R. Abidi, Y. Zheng, A. V. Gribok, and M. A. Abidi, "Improving weapon detection in single energy X-ray images through pseudocoloring," *IEEE Transactions on Systems, Man, and Cybernetics*, vol. 36, no. 6, pp. 784–796, 2006.

[4] S. Singh, "Explosives detection systems (EDS) for aviation security," *Signal Processing*, vol. 83, no. 1, pp. 31–55, 2003.

[5] A. Mouton, N. Megherbi, G. Flitton, and T. Breckon, "An evaluation of CT image denoising techniques applied to baggage imagery screening," in *Proceedings IEEE International Conference on Industrial Technology*, 2013, pp. 1063–1068.

[6] W. Bi, Z. Chen, L. Zhang, and Y. Xing, "A volumetric object detection framework with dual-energy CT," in *Proceedings of the IEEE Nuclear Science Symposium Conference Record*, 2008, pp. 1289–1291.

[7] N. Megherbi, G. T. Flitton, and T. P. Breckon, "A classifier based approach for the detection of potential threats in CT based baggage screening," in *Proceedings of the IEEE International Conference on Image Processing*, 2010, pp. 1833–1836.

[8] J. Sivic and A. Zisserman, "Video Google: A text retrieval approach to object matching in videos," in *Proceedings of the IEEE International Conference on Computer Vision*, 2003, pp. 1470–1477.

[9] F. Jurie and B. Triggs, "Creating efficient codebooks for visual recognition," in *Proceedings of the IEEE International Conference on Computer Vision*, 2005, vol. 1, pp. 604–610.

[10] J. Gall and V. Lempitsky, "Class-specific Hough forests for object detection," in *Decision Forests for Computer Vision and Medical Image Analysis*, pp. 143–157. Springer, 2013.

[11] D. Zikic, B. Glocker, and A. Criminisi, "ATLAS encoding by randomized forests for efficient label propagation," in *Medical Image Computing and Computer-Assisted Intervention*, pp. 66–73. Springer, 2013.

[12] E. Nowak, F. Jurie, and B. Triggs, "Sampling strategies for bag-of-features image classification," in *Proceedings European Conference on Computer Vision*, 2006, pp. 490–503.

[13] A. Mouton, T. Breckon, and G. Flitton, "3D object classification in complex volumes using randomised clustering forests," in *IEEE International Conference on Image Processing*, 2014 - to appear.

[14] G. Flitton, A. Mouton, N. Megherbi, and T. P. Breckon, "A codebook approach to object detection in 3D computed tomography baggage imagery (submitted to pattern recognition - under review)," 2013.

[15] E. Nowak, F. Jurie, and B. Triggs, "Sampling strategies for bag-of-features image classification," in *European Conference on Computer Vision*, 2006, pp. 490–503.

[16] G. Flitton, T. Breckon, and N. Megherbi, "Object recognition using 3D SIFT in complex CT volumes," in *Proceedings British Machine Vision Conference*, 2010, pp. 11.1–11.12.

[17] G. Flitton, T. P. Breckon, and N. Megherbi, "A comparison of 3D interest point descriptors with application to airport baggage object detection in complex CT imagery," *Pattern Recognition*, 2013.

[18] S. Lazebnik, C. Schmid, and J. Ponce, "A sparse texture representation using affine-invariant regions," in *Proceedings of the IEEE International Conference on Computer Vision and Pattern Recognition*, 2003, vol. 2, pp. II–319 – II–324.

[19] L. Breiman, "Random forests," *Machine Learning*, vol. 45, no. 1, pp. 5–32, 2001.

[20] A. Criminisi, "Decision forests: A unified framework for classification, regression, density estimation, manifold learning and semi-supervised learning," *Foundations and Trends in Computer Graphics and Vision*, vol. 7, no. 2-3, pp. 81–227, 2011.

[21] A. Ben-Hur and J. Weston, "A user's guide to support vector machines," *Methods in Molecular Biology*, vol. 609, pp. 223–239, 2010.

[22] A. Criminisi and J. Shotton, *Decision Forests for Computer Vision and Medical Image Analysis*, Springer Publishing Company, Incorporated, 2013.

[23] A. Mouton, N. Megherbi, T. Breckon, K. Van Slambrouck, and J. Nuyts, "A distance driven method for metal artefact reduction in computed tomography," in *Proceedings IEEE International Conference on Image Processing*, 2013, pp. 2334–2338.

[24] A. Mouton, N. Megherbi, K. van Slambrouk, J. Nuyts, and T. Breckon, "An experimental survey of metal artefact reduction in computed tomography," *Journal of X-Ray Science and Technology*, vol. 21, no. 2, pp. 193–226, 2013.

Automatic Threat Detection for a Dual-Energy Four-View X-ray Carryon Luggage Scanner

Kyle Champley, Jerel Smith, Jeff Kallman, and Philip Top

***Abstract*— All passengers and their carryon luggage are inspected for explosives prior to boarding an aircraft. The primary screening technology for inspecting carryon luggage is X-ray radiography systems. There is great interest in the development of automatic threat detection algorithms for these systems because of their cost-saving potential. In this paper we describe the development and testing of a chain of processing algorithms for classification of threats from 3D image reconstruction volumes of data from a four-projection, dual energy X-ray scanner developed by ScanTech Identification Beam Systems.**

***Index Terms*—computed tomography, image reconstruction, automatic threat detection, airport security**

I. Introduction

ALL passengers and their carryon luggage are inspected for explosives prior to boarding an aircraft. To save on screening costs, a number of automated systems are deployed. The primary screening technology for inspecting carryon luggage is X-ray radiography systems. The classification of objects as threats or non-threats is made by analyzing the measured distribution of one or more X-ray energy spectra over a few views (angles). From this information one attempts to determine the effective atomic number and density of all materials in the field of view of the scanner. Accurately determining these quantities for all objects in a piece of luggage is extremely difficult due to the limited number of views and high level of clutter in luggage.

Recent years have seen significant advances in few-view Computed Tomography (CT) image reconstruction algorithms. In this project we leverage these advancements in CT imaging to reconstruct volumetric images from the SENTINEL® III, a four-view, dual-energy X-ray carryon luggage scanner developed by ScanTech Identification Beam Systems. Since this scanner collects dual energy data, we are able to reconstruct volumetric images of the effective atomic number and electron density (electrons·mol/cm^3). These images are then segmented and features are extracted from each segment. Segments are classified as threats or non-threats based on the distribution of their features based on a machine learning classification algorithm.

The authors are with Lawrence Livermore National Laboratory, Livermore, CA 94550. Corresponding author: Kyle Champley (champley1@llnl.gov).

II. SENTINEL® III Scanner

The ScanTech SENTINEL® III scanner employs four dual energy X-ray projections. The four X-ray projections are composed of a collection of linear detector arrays placed around the rectangular system gantry. A sketch of this four view geometry is shown in Figure 1. Note that the projections lie in three different planes while the projections of conventional X-ray CT system are essentially co-planar. Dual energy spectra are measured with so-called sandwich detectors. These detectors are composed of a high-energy detector placed behind a low-energy detector with a copper filter between the two detectors.

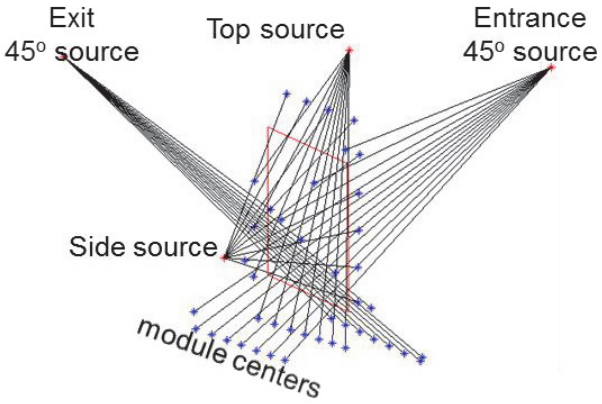

Figure 1. ScanTech SENTINEL® III X-ray projection geometry. The red box shows a slice parallel to the tunnel entrance plane of the field of view of the scanner.

III. Description of Algorithms

We take an X-ray CT approach to imaging in order to achieve the best image quality and highest accuracy possible. First the radiographs are converted to attenuation data and outliers are identified and corrected. Second, we apply a dual energy decomposition algorithm to remove beam hardening artifacts. Here the polychromatic attenuation values are converted into essentially monochromatic attenuation values at the mean system spectral response energies. Then few-view CT image reconstruction algorithms are applied independently to the low and high-energy data. We employed a segmentation-feedback loop to this reconstruction process to improve image quality. The low and high attenuation coefficient images are converted to volumes of the effective atomic number and electron density distributions. The high-energy 3D image volume is segmented. Features from each of

these 3D segments are extracted from the low attenuation, high attenuation, effective atomic number, and electron density volumes and fed into a classification algorithm.

Narrow slit collimators in front of the source and detector modules relax the need for scatter correction algorithms. The loss of image quality and image accuracy due to the lack of employing a scatter correction algorithm are overshadowed by poor image quality achieved from reconstructing with four views. Thus we did not apply any scatter correction algorithms to the data.

A. *Dual Energy Decomposition*

Dual energy decomposition [1] is employed to remove beam hardening artifacts from the measured data. We use the energy basis functions of the total Klein-Nishina cross section and the reciprocal of the energy cubed. This is commonly referred to as the Compton/ Photoelectric basis [1] because these functions approximate the Compton and photoelectric cross section components. After the decomposition takes place we transform the components back to attenuation coefficients at the mean system spectral responses of the spectra pair [2]. This decomposition procedure requires accurate models of the spectral response pair. The determination of this spectral response pair is outlined in section IV.

B. *Few-View CT Image Reconstruction*

Mathematically speaking, the problem of few-view CT reconstruction is solving an underdetermined system of linear equations in the presence of noisy measurements. Modern approaches to this problem use constrained optimization techniques to reconstruct the voxelized 3D image. These constraints shrink the solution space and thus shrink the null space of the forward operator. Shrinking the null space helps to reduce image artifacts such as streaking. Common image constraints include non-negativity, image sparsity, and image gradient sparsity. Many few-view CT image reconstruction algorithms work by clever combination of Simultaneous Algebraic Reconstruction Technique (SART) and Total Variation (TV) regularization.

We make use of the Adaptive Steepest Descent- Projection onto Convex Sets [3] (ASD-POCS) reconstruction algorithm. We have found much success with this algorithm. The use of this algorithm alone did not provide sufficient reduction of artifacts and quantitative accuracy, so we employed an image reconstruction- segmentation feedback loop to improve image quality. This segmentation-reconstruction feedback loop encourages increased smoothing between voxels in the same segment. Figure 2 shows some representative slices from a reconstructed data set of a collection of glass bottles filled with different aqueous solutions packed in a box of clothing.

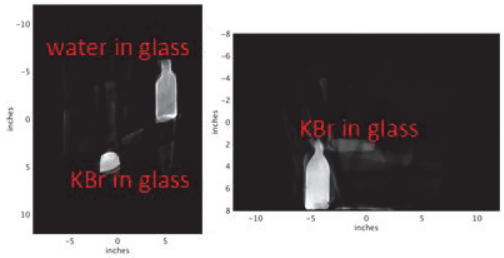

Figure 2. Reconstructed slices of data from the ScanTech SENTINEL® III scanner. (left) Slice parallel to floor. (right) Slice parallel to tunnel entrance plane.

C. *Conversion to Effective Atomic Number and Electron Density*

The CT image reconstruction algorithm provides us with estimates of the distributions of the attenuation coefficients of the object being imaged at two different energies. Let $\sigma(\gamma, Z)$ be the electron cross section (cm^2 / (electrons · mol)) of the element with atomic number Z at the energy, γ, measured in keV. These cross sections may be extended to non-integer Z by linear interpolation. Let ρ_e denote the electron density (electrons · mol / cm^3) of an object. Then the attenuation coefficient of an object can be expressed as $\rho_e\sigma(\gamma, Z)$. Let γ_L and γ_H denote the mean system spectral responses of the two measured spectra. Note that in the dual energy decomposition step, we decomposed our polychromatic attenuation pair into a monochromatic attenuation pair at these energies. Then our reconstruction algorithm produced estimates of the attenuation coefficient maps at these two energies. Denote these maps by f_L and f_H. Then we may determine ρ_e and Z_e, the effective atomic number, by solving the following system of two equations $f_L = \rho_e\sigma(\gamma_L, Z_e)$ and $f_H = \rho_e\sigma(\gamma_H, Z_e)$.

D. *Volume Segmentation*

The volume is segmented into objects by first separating it into slices. Those slices are broken into superpixels (using the SLIC superpixelization algoritm [4]) and a graph is created to represent the adjacencies and statistics of those superpixels (mean and standard deviation of the contained pixels). All the superpixels with mean values below a user chosen threshold are merged, and then the graph is aggregated until a predetermined merging cost is reached. The graphs, representing objects in each slice, are aggregated across slices to complete the segmentation of the volume.

In any slice, the number of superpixels is chosen such that each superpixel represents approximately 400 raw pixels. The cost for merging graph nodes is given by

$$C_{ij} = \frac{N_i N_j}{N_i + N_j} \frac{(\mu_i + \mu_j)^2}{\sigma_i + \sigma_j} \qquad (1)$$

where C_{ij} is the cost of merging nodes i and j, N_i and N_j are the number of pixels in nodes i and j, μ_i and μ_j are the mean values of the pixels in nodes i and j, and σ_i and σ_j are the standard deviations of the pixels in nodes i and j. There is no cost for merging nodes with mean values below the user

chosen threshold, and a severe cost to merging nodes with values on either side of the threshold (the cost in equation 1 is multiplied by 100).

E. Classification Algorithms

Following the Volume Segmentation algorithm described in the previous section; we apply a post processing algorithm to detect a multi-model distribution in individual segments. If these modes are spatially separable we split the segments by properties and use a 3D median filter to reduce noise.

For each segment we extract a number of features, these included the mean, median, mode, standard deviation, and skew of the 4 images (ρ_e, Z_e, f_H, f_L), the voxel count, and the total estimated density of the entire image. Of these features, eight were used in the final classifier. The features used included: the voxel count, ρ_e median, Z_e mean, Z_e skew, f_H mean, f_L mean, f_L skew, and total Z_e. Of these features, voxel count, Z_e mean, and f_L skew were the most significant in terms of the final classifier. These eight features for each segment were fed into a random forest classifier [5]. The random forest classifier used included 225 classifier trees and a minimum leaf size of 3.

IV. Spectral Modeling and Calibration

Material property (defined as the combined effective atomic number, Z_e, and electron density, ρ_e) is derived from measuring the attenuation of the two polychromatic spectra defined by the x-ray source, detectors, and filtration by any materials lying between. Accurate knowledge of those spectra is essential for accurate decomposition. For the SENTINEL® system the details are complex.

The source spectra are determined by the energy of the electrons striking the anode/target of the source, the target material (tungsten) and the azimuthal angle of each detector element relative to the target surface. The spectral response of the detector is governed by the energy-absorption properties of the low- and high-energy scintillators and by filtration due to internal components of the detector "sandwich." Additionally, internal absorption in the path of each source-detector ray is uniquely determined by the thickness and orientation of all materials (windows, tunnel-walls and filters, conveyor belt) traversed by that ray. The angularly-dependent spectra were calculated using a model by Finkelshtein and Pavlova [6]. X-ray transport and absorption is based on LLNL's EPDL data base [7].

While it is important to use the best spectral information available, there is inevitably some degree of uncertainty in the composition of some the objects between source and detector. For this purpose, two linear arrays of 1-cm wide metal strips (1-mm aluminum and ¼ mm copper) were laid across the entrance windows to the tunnel. Final adjustments to the spectral models were then made as addition or subtraction of small amounts of aluminum in the path, such that the "as-measured" and "as-modeled" attenuations closely matched.

V. Methods

The test plan was designed to primarily support the research and development goals of developing and evaluating algorithms to identify and characterize objects, not to emulate actual luggage. The goals were to provide samples with a broad range of material properties, deployed with in a range of container environments and imaging challenges, in a range of locations and orientations within their packages, with the constraint that the identity, location and orientation of every object be recorded and indexed so that results could be evaluated against the actual configuration.

The test samples comprised water, graphite, magnesium, Teflon, Delrin, silicon, and two aqueous solutions of alkali-halide salts. For conciseness, the polymer trade-names "Teflon®" and "Delrin®" are used loosely here to refer to generic samples of polytetrafluoroethylene (PTFE) and a polyoxymethylene co-polymer (POM). One of the alkali-halide solutions was mixed using LiCl, the other a combination of KBr and RbBr. All specimens were approximately 5-cm diameter, and 15 cm long. All liquids were provided in containers of polyethylene, aluminum, and glass to evaluate the effects of container attenuation.

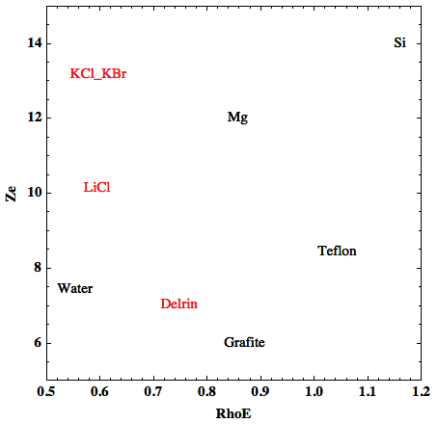

Figure 3. Plot of the Ze vs. RhoE properties for characterized materials used in the Tests.

The range of material properties deployed in the experiments is shown in Figure 3. The effective atomic number, Z_e, is defined such that the material's x-ray transmission through a sample thickness of 2.5 g/cm^2 optimally matches (in a least-square sense) a mixture of two neighboring elements in the periodic chart [8] by linear interpolation of their cross sections.

The test objects were deployed at three clutter densities. Low-clutter configurations were deployed in 1-ft x 1-ft x 4-ft boxes, objects deployed parallel to the horizontal, vertical and axial directions (x, y, z), such that objects did not overlap in the views. Medium- and high-clutter configurations were in 1-ft cubical boxes, with one object in the center of the box, and three additional objects placed near the sides. High clutter boxes have the additional objects on all of the six sides. In some cases the side objects were chosen to severely block one side (1-inch stack of magazines or ¼-inch iron plate). All

configurations were deployed once each with a low-density (polystyrene foam) of medium-density (flannel) fill. All configurations were also deployed with and without a 15-gauge aluminum casing to simulate attenuation by hard-sided luggage. Medium- and hi-clutter boxes were scanned in six different orientations with respect to the belt motion. The full data set comprised 616 distinct scans, exclusive of scans included to monitor system performance and stability. The tests provided data to evaluate the effects of clutter, enclosure, container, location, orientation, blocking and packing on reconstruction, segmentation, classification and property measurements. Photographs of a test object with and without aluminum shielding are shown in Figure 4.

Figure 4. Photographs of a test data box with flannel fill, with and without the aluminum casing.

Our classification tests evaluated the ability of our algorithms to identify the presence of either Delrin, LiCl solution, or KBr solution.

VI. Results

A scatter plot of the estimated median Z_e and ρ_e values for water, LiCl solution, and magnesium is shown in Figure 5. One can visually see the discrimination ability using only these two features.

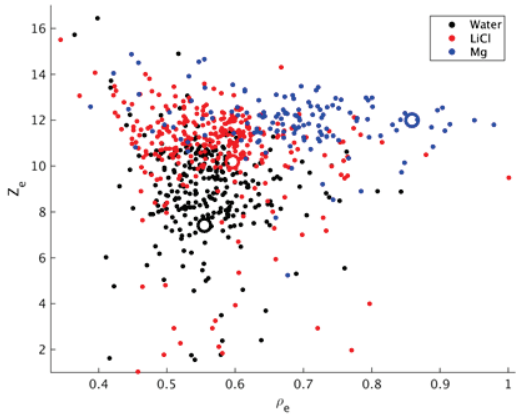

Figure 5. Scatter plot of the median of the Ze and rhoe values. Open circles mark the theoretical values.

Plots of the probability of false alarm versus probability of detection are show in Figure 6 for the three targets: Delrin, LiCl solution, and KBr solution.

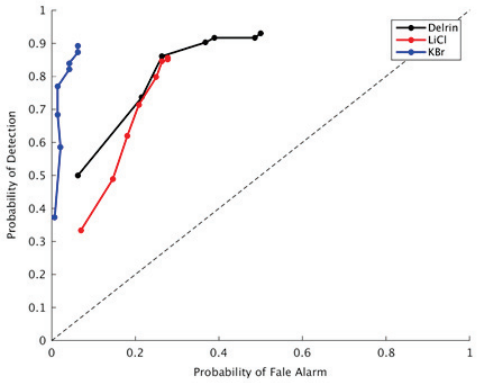

Figure 6. Probability of false alarm versus probability of detection.

VII. Conclusion

In this paper we have described a collection of algorithms for the classification of objects with dual energy, few-view radiography systems. The approach is centered on the goal of reconstructing quantitatively accurate volumes of the effective atomic number and electron density distributions of the object in the field of view of the scanner.

Results show the feasibility and effectiveness of this approach.

Acknowledgment

This work is supported by Department of Homeland Security, Science and Technology Directorate, Explosives Division and UK Home Office, Contract #HSHQDC-14-X-B0001. This work performed under the auspices of the U.S. Department of Energy by Lawrence Livermore National Laboratory under Contract DE-AC52-07NA27344, document release number LLNL-ABS-681605.

References

[1] R. E. Alvarez and A. Macovski, "Energy Selective Reconstructions in X-ray Computerized Tomography," *Physics in Medicine and Biology*, vol. 21, no. 5, pp. 733-744, 1976.

[2] Kyle Champley and Timo Bremer, "Efficient and Accurate Correction of Beam Hardening Artifacts," *3rd International Congress on Image Formation in X-ray CT*, 2013.

[3] Emil Sidky and Xiaochuan Pan, "Image reconstruction in circular cone-beam computed tomography by constrained, total-variation minimization," *Phys. Med. Biol.*, 53:4777-4807, 2008.

[4] Radhakrishna Achanta, Appu Shaji, Aurelien Lucchi, Pascual Fua, Sabine Susstrunk, "SLIC Superpixels Compared to State-of-theArt Superpixel Methods," *IEEE Trans. Pattern Analysis and Machine Intelligence*, 34:2274-2281, 2012.

[5] L. Breiman, "Random Forests," *Machine Learning*, 45(1): 5-32, 2001.

[6] A. L. Finkelshtein and T. O. Pavlova, "Calculation of X-Ray Tube Spectral Distributions," *X-Ray Spectrum*. 28, (1999).

[7] D. E. Cullen, J.H. Hubbell, L. Kissel, EPDL97: "The Evaluated Photon Data Library '97 Version," *UCRL-LR-50400,* vol. 6, Rev. 5., Sep. 1997.

[8] S. Azevedo, H. Martz, M. Aufderheide, W. Brown, K. Champley, J. Kallman, G. Roberson, D. Schneberk, I. Seetho, Jerel. Smith, "System-Independent Characterization of Materials using Dual-energy Computed Tomography, *IEEE Trans. Nucl. Sci.*, slated publication Feb. 2016.

Simulation-Based Artifact Correction for Computed Tomography in Metrology

Joscha Maier, Carsten Leinweber, Stefan Sawall, Henning Stoschus, Frederic Ballach, Tobias Müller, Michael Hammer, Ralf Christoph and Marc Kachelrieß

***Abstract*—Computed tomography (CT) is a valuable tool for three-dimensional measurement of industrial components. However, CT reconstructions are often corrupted by CT artifacts caused by beam hardening, x-ray scatter, off-focal radiation, partial volume effects or the cone-beam reconstruction itself. Especially, if highly attenuating objects are investigated, these artifacts lead to a severe degradation of image quality and may prevent an accurate metrological assessment of the object. In order to correct for these artifacts, our approach uses computer simulations of the CT measurement process to calculate an estimate of the contribution of artifacts to the measured projection data. Based on an appropriate model of the object, e.g. an initial reconstruction or a CAD model, two simulations are carried out. One simulation considers all physical effects that cause artifacts using dedicated analytic methods as well as Monte Carlo-based models. The other one represents an "ideal" CT measurement without any artifacts i.e. a measurement in parallel beam geometry with a monochromatic, point-like x-ray source and no x-ray scattering. The difference gives an estimate of the contribution of artifacts and is used to correct the measured data. The performance of the proposed method is evaluated for measurements of single- and multi-material objects conducted on a commercial industrial CT system. The correction results are compared to tactile reference measurements as well as to reference artifact reduction algorithms. Our approach allows for the reconstruction of volumes that are nearly free of artifacts and thus clearly outperforms the other artifact reduction algorithms.**

***Keywords*—Artifact correction, cone-beam CT, industrial computed tomography, metrology**

I. Introduction

In recent years CT has been increasingly used in metrology since it provides high measurement point density, requires comparably short measurement times, and allows the non-destructive assessment of internal features [1]. Coordinate measuring machines with CT sensor are available to meet very stringent requirements for resolution, measurement uncertainty, or for measuring large objects. However, the investigation of metallic or highly attenuating components is still challenging as the reconstructed volumes are often corrupted by severe CT artifacts [2]. These CT artifacts are a result of inappropriate modeling of the x-ray physics within the reconstruction process. Widely used analytic reconstruction algorithms, for instance, assume the acquired projection data to be the monochromatic x-ray transform of the measured object. However, this assumption neglects several physical effects of the CT data acquisition such as beam hardening, x-ray scatter, off-focal radiation or partial volume effects. As a consequence artifacts associated with these effects are introduced to the reconstructed volumes.

First of all, artifact correction was achieved using a reference measurement of a master part with high precision tactile, optical, or tactile-optical sensors on a multisensor coordinate measuring machine with CT. This method is still applied if traceability and absolute precision are required. Considering software-based artifact correction, there are basically two strategies: The consideration of the x-ray physics within the reconstruction process or the correction of the acquired projection data prior to the reconstruction. The first type of approach is usually implemented as an iterative reconstruction scheme that incorporates dedicated models of the interaction between x-rays and matter within its forward model. Several models that allow for the consideration of CT artifacts have been proposed [3]. However, since the reconstruction problem has to be solved iteratively, these algorithms have the drawback of high computational cost. Therefore, the second type of approach applies correction terms prior to an analytic reconstruction. In case of multi-material components containing metal so called metal artifact reduction (MAR) algorithms are commonly applied. MAR algorithms identify the metal trace within the acquired projection data by a forward projection and replace it using different interpolation schemes [4, 5, 6, 7, 8]. However, interpolation errors may introduce new artifacts. More general precorrection approaches are based on physical considerations. A correction curve which maps the measured intensities to monochromatic intensities can be calculated or derived from a reference measurement [9] [2]. Scattered x-rays and off-focal radiation can be estimated and corrected by convolution approaches [10] [11]. CT artifacts such as cone-beam artifacts or non-linear partial volume artifacts cannot be corrected by precorrection approaches. Thus, we propose an alternative method that uses an a priori model of the object to derive a correction term in image space. Based on this model two simulations are performed. One of them considers all effects that cause artifacts while the other one represents an ideal CT measurement. Since the correction is applied to an analytic reconstruction the approach is comparably fast and can be applied to any CT artifact that is included in the simulation.

Joscha Maier and Carsten Leinweber: German Cancer Research Center (DKFZ), Im Neuenheimer Feld 280, Heidelberg, Germany and Werth Messtechnik GmbH, Siemensstraße 19, 35394 Gießen, Germany.

Dr. Stefan Sawall and Prof. Dr. Marc Kachelrieß: German Cancer Research Center (DKFZ), Im Neuenheimer Feld 280, Heidelberg, Germany.

Dr. Henning Stoschus, Frederic Ballach, Tobias Müller, Michael Hammer and Dr. Ralf Christoph: Werth Messtechnik GmbH, Siemensstraße 19, 35394 Gießen, Germany.

Corresponding author: Joscha Maier (joscha.maier@dkfz.de)

II. Material and Methods

A. Simulation-Based Artifact Correction

Analytic reconstruction algorithms only lead to reconstruction results without artifacts in case of ideal projection data p, i.e. data that are the x-ray transform of the measured component:

$$p = X\,f. \tag{1}$$

Here f represents distribution of the object's attenuation coefficient and X is the x-ray transform operator which corresponds to a monochromatic forward projection of the object. Subsequently, the unknown function f can be recovered from a CT measurement by applying the inverse x-ray transform X^{-1}. However, conventional CT systems acquire projection data q which deviate from ideal data due to beam hardening, off-focal radiation, the contribution of scattered x-rays and partial volume effects. Thus, the projection data measured by the detector element (u, v) are given by:

$$q_{u,v} = -\ln\Big[\, I_{s,u,v} + \int dk\; G(k) \int dE\; E\; w(E)\; e^{-\int d\lambda(k) f(\boldsymbol{s}+\lambda\boldsymbol{\theta})}\Big], \tag{2}$$

in which I_s describes the scatter contribution, $G(k)$ the intensity distribution of the focal spot, $w(E)$ the detected x-ray spectrum, and $\int d\lambda(k) f(\boldsymbol{s}+\lambda\boldsymbol{\theta})$ the line integral over the attenuation coefficient from the focal spot position k to the detector. Since $q \neq p$, the application of the inverse x-ray transform X^{-1}does not yield f but a function g that is corrupted by artifacts:

$$\begin{aligned} g = X^{-1}q &= X^{-1}p + X^{-1}(q-p) \\ &= f \quad + X^{-1}(q-p) \\ &= f \quad + a \end{aligned} \tag{3}$$

According to equation (3) the function f can be recovered from g by subtraction of the artifact term $a = X^{-1}(q-p)$. Therefore, the proposed approach aims at deriving an estimate of the artifact term $\tilde{a} \approx a$ which is subsequently used to get an estimate of the ideal reconstruction $\tilde{f} \approx f$:

$$\tilde{f} = g - \tilde{a} = g - X^{-1}(\tilde{q} - \tilde{p}). \tag{4}$$

Here $\tilde{p}$ and $\tilde{q}$ represent estimates of the ideal data p and the measured data q, respectively. In order to calculate $\tilde{p}$ and $\tilde{q}$, we perform CT simulations using an a priori model f_{prior} of the measured object. That model is derived from the initial reconstruction g by segmentation:

$$f_{\mathrm{prior}} = T\,g. \tag{5}$$

Here T represents the segmentation operator which is, for our purpose, a marching cubes algorithm. In case of multi-material components, the segmentation is only applied to the meatal component. The ideal data $\tilde{p}$ is generated by a monochromatic forward projection of reference energy E_0:

$$\tilde{p} = \int d\lambda\, f_{\mathrm{prior}}(\boldsymbol{s}+\lambda\boldsymbol{\theta}) \tag{6}$$

In order to generate the real data $\tilde{q}$, all physical effects of the CT measurement are modeled in the simulation process. Beam hardening is simulated by a polychromatic forward projection based on a modification of the semi-empirical tube spectrum $\widetilde{w}(E)$ of Tucker et al. [12], and on tabulated values of the attenuation coefficient of the object μ_{o}, the prefilter μ_{p}, and the x-ray detector μ_{d}, as well as the corresponding intersection length L. The contribution of off-focal radiation is approximated by convolving the simulated polychromatic intensities with an off-focal kernel $\tilde{G}$ that is determined by a calibration measurement. Nonlinear partial volume artifacts are reproduced by an appropriate subsampling of the simulated intensities. The contribution of scattered x-rays $\widetilde{I_{\mathrm{s}}}$ is calculated using a hybrid approach that uses a Monte-Carlo scatter simulation with a reduced number of photons to determine the free parameters of an analytic scatter convolution algorithm [13]. Using the detected spectrum $\widetilde{w}_D$,

$$\widetilde{w}_D(E) = \widetilde{w}(E)\; e^{-\mu_{\mathrm{p}}(E) L_{\mathrm{p}}}\; (1 - e^{-\mu_{\mathrm{d}}(E) L_{\mathrm{d}}}), \tag{7}$$

the simulated projection data are calculated as follows:

$$\tilde{q} = -\ln[\widetilde{I_{\mathrm{s}}} + \tilde{G} * \int dE\; E\; \widetilde{w}_D(E)\; e^{-\int d\lambda\, f_{\mathrm{prior}}(\boldsymbol{s}+\lambda\boldsymbol{\theta})}] \tag{8}$$

Finally, the difference between $\tilde{p}$ and $\tilde{q}$ is reconstructed to derive the correction term. However, if the measurement as well as the simulations is performed in cone-beam geometry, cone-beam artifacts may remain in the corrected volume. In order to correct also for cone-beam artifacts, the simulation as well as the reconstruction of the ideal data $\tilde{p}$ has to be performed in parallel beam geometry. In that case the inverse x-ray transform operator X^{-1} of equation (4) is not the same for $\tilde{p}$ and $\tilde{q}$ and the difference has to be calculated in image domain which requires one additional reconstruction.

B. Data Acquisition

The proposed approach was evaluated for measured data of single-material components (ruby sphere, die-cast zinc hinge) and a multi-material component (multi-material plug). The measurements were conducted on a Werth TomoScope® 200 that is equipped with a commercial micro-focus x-ray tube and an energy integrating flat detector. The acquisition parameters for each measurement are given in table 1.

TABLE I: Acquisition Parameters of the CT measurements

Component	Tube voltage	Tube current	Prefilter	Projections per 360°	Pixel size at isocenter
Ruby sphere	150 kV	150 µA	0.5 mm Al	400	10 µm
Die-cast zinc hinge	215 kV	180 µA	1 mm Sn	800	43 µm
Multi-material plug	225 kV	170 µA	1.2 mm Sn	1200	25 µm

C. Evaluation of Correction Results for Single-Material Components

The metrological assessment of single-material components is commonly performed by evaluating a surface mesh that is calculated from the CT reconstruction. The presence of

artifacts within the CT reconstruction leads to deviations of that surface representation from the real surface. In order to demonstrate the potential of the proposed approach to increase to accuracy of the surface representation, the triangle mesh of the initial and of the corrected reconstruction is compared to a tactile reference measurement. The reference measurement was performed using a Werth Touch Probe TP 200 that uses a tactile sensor to derive a highly accurate point cloud of the components surface with deviations of less than two micrometer.

D. Evaluation of Correction Results for Multi-Material Components

For the measurement of the multi-material component there is no tactile reference measurement available. Therefore, the correction result of the proposed approach was compared to commonly used artifact reduction algorithms namely normalized metal artifact reduction (NMAR) [5] and iterative reconstruction with total variation regularization [14].

III. Results

A. Single-Material Components

Figure 1 shows the CT reconstructions of the die-cast zinc hinge measurement. While the CT reconstruction without correction shows strong CT artifacts, the application of the simulation-based artifact correction leads to images that are nearly free of artifacts. The reduced amount of artifacts also leads to a higher accuracy of surface meshes that are calculated from the CT reconstruction. Figure 2 shows the deviation of the surface mesh from a tactile reference measurement. When no correction is applied, there are large deviations. The simulation-based artifact correction leads to a surface mesh that deviates almost fits the reference measurement.

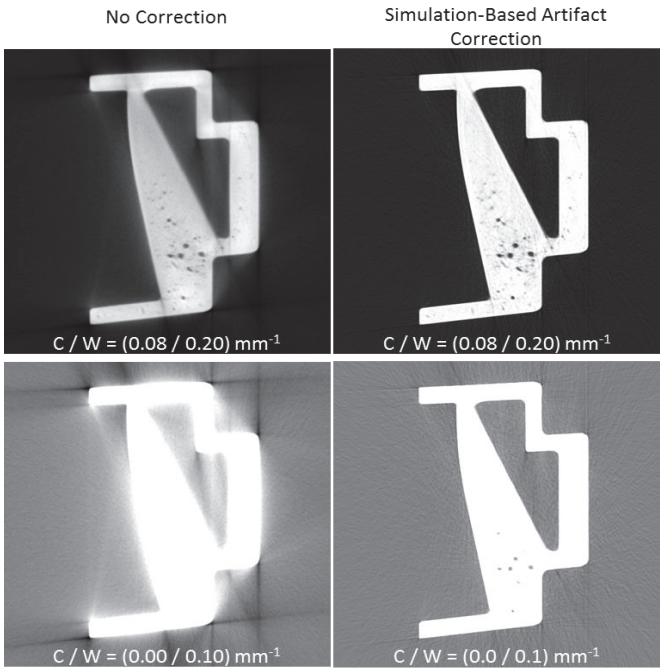

Fig.1. Reconstructions of the die-cast zinc hinge displayed at different window levels. The left column shows the reconstruction without correction. The right column shows the results of the simulation-based artifact correction.

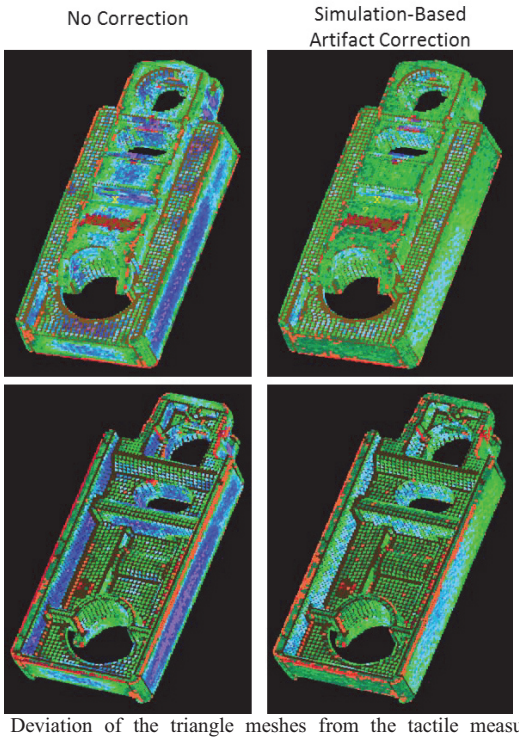

Fig. 2. Deviation of the triangle meshes from the tactile measurement. Results displayed in the left column are calculated from the reconstruction of the die-cast zinc hinge without correction. Results displayed in the right column are calculated from the simulation-based artifact correction of the die-cast zinc hinge.

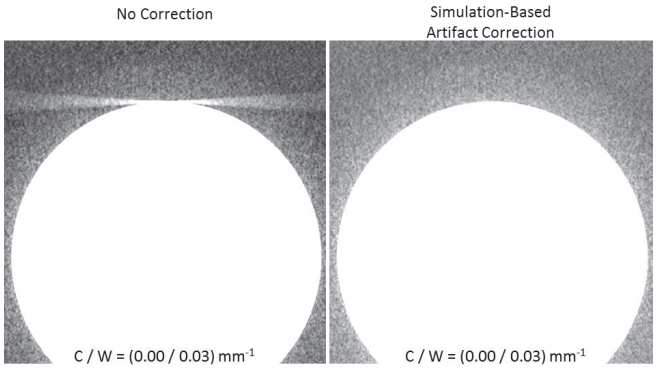

Fig. 3. Reconstructions of the ruby sphere. The left column shows the reconstruction without correction. The right column shows the results of the simulation-based artifact correction.

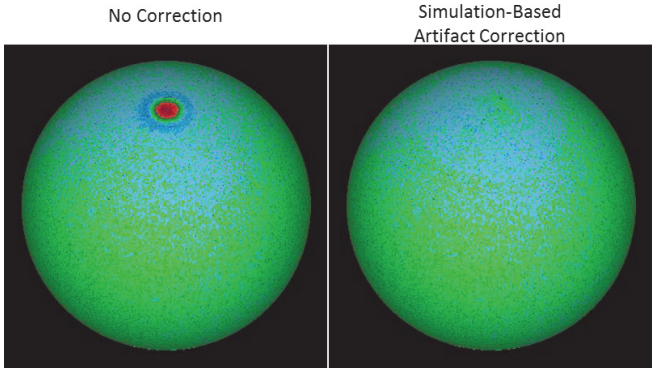

Fig. 4. Deviation of the triangle meshes from the tactile measurement. Results displayed in the left column are calculated from the reconstruction of the ruby sphere without correction. Results displayed in the right column are calculated from the simulation-based artifact correction of the ruby sphere.

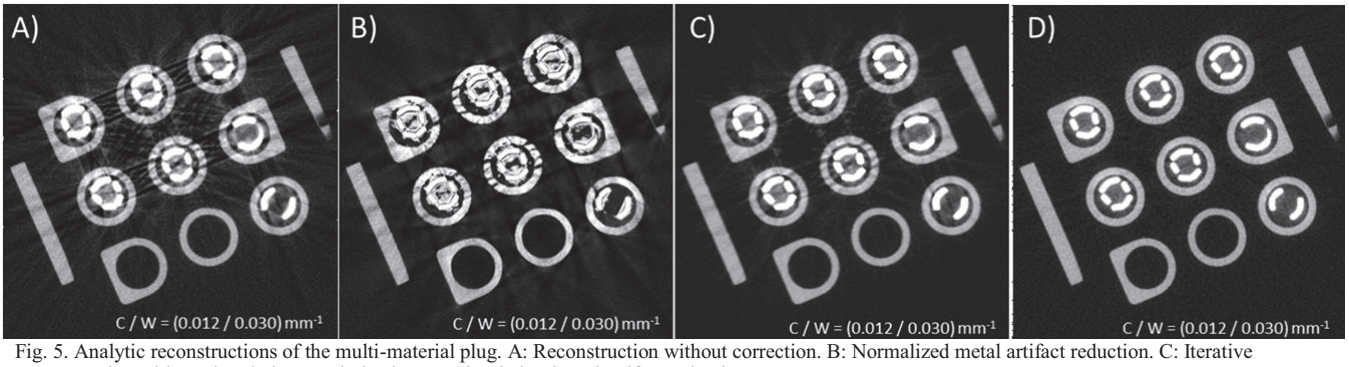

Fig. 5. Analytic reconstructions of the multi-material plug. A: Reconstruction without correction. B: Normalized metal artifact reduction. C: Iterative reconstruction with total variation regularization. D: Simulation-based artifact reduction.

Figure 3 demonstrates the application of the simulation-based artifact correction to reconstructions that are mainly corrupted by cone-beam artifacts. Therefore, a calibration sphere was measured with a very high cone angle. The cone-beam artifacts that appear as bright streaks at the pole of the sphere in the standard reconstruction can be totally removed by the simulation-based artifact correction. Figure 4 shows a similar result for the deviation to the tactile measurement.

B. Multi-Material Components

Figure 5 shows the CT reconstructions of the multi-material plug using an analytic reconstruction, normalized metal artifact reduction, iterative reconstruction with total variation regularization as well as the simulation-based artifact correction. The analytic reconstruction suffers from severe CT artifacts that appear as dark streaks within the reconstructed volume. While the normalized metal artifact reduction and the iterative reconstruction are not able to remove the streak artifacts, the proposed simulation-based artifact correction leads to images that are nearly free of artifacts.

IV. Conclusion

We presented a new method that uses CT simulations to correct for CT artifacts. It was successfully applied to CT measurements of single- and multi-material components and provides volumes that are almost free of artifacts. Furthermore we demonstrated that the simulation-based artifact correction can increase the accuracy of surface meshes that are calculated from the CT reconstructions. In case of multi-material components, this approach is clearly superior to inpainting-based metal artifact reduction techniques (when the object contains a high proportion of metal) and iterative reconstruction algorithms that do not incorporate sophisticated models of the interaction between x-rays and matter within the reconstruction process.

Acknowledgements

This work was supported by the AiF under grant KF2301004UW1. Parts of the reconstruction software were provided by RayConStruct® GmbH, Nürnberg, Germany.

References

[1] I. Schmidt, „Vollständig und zerstörungsfrei - Zehn Jahre Computertomografie in der Koordinatenmesstechnik," *QE - Quality Engineering,* pp. 22-25, März 2015.

[2] I. Schmidt, "Flexibel und genau messen - Artefaktkorrektur in der Computertomografie," *QZ - Qualität und Zuverlässigkeit,* pp. 68-69, November 2014.

[3] J. Nuyts, B. D. Man, J. A. Fessler, W. Zbijewski and F. J. Beekman, "Modelling the physics in the iterative reconstruction for transmission computed tomography," *Physics in Medicine and Biology,* vol. 58, no. 12, pp. R63-R96, 2013.

[4] W. Kalender, R. Hebel and J. Ebersberger, "Reduction of CT artifacts caused by metallic implants," *Radiology,* vol. 164, no. 2, pp. 576-7, 1987.

[5] E. Meyer, R. Raupach, M. Lell, B. Schmidt and M. Kachelrieß, "Normalized metal artifact reduction (NMAR) in computed tomography," *Medical Physics,* vol. 37, no. 10, pp. 5482-5493, 2010.

[6] E. Meyer, R. Raupach, M. Lell, B. Schmidt and M. Kachelrieß, "Frequency split metal artifact reduction (FSMAR) in computed tomography," *Medical Physics,* vol. 39, no. 4, pp. 1904-1916, 2012.

[7] J. Wang, S. Wang, Y. Chen, J. Wu, J. Coatrieux and L. Luo, "Metal artifact reduction in CT using fusion based prior image," *Medical Physics,* vol. 40, pp. 081903 1-8, 2013.

[8] A. H. Mahnken, R. Raupach, J. E. Wildberger, B. Jung, N. Heussen, T. G. Flohr, R. W. Günther and S. Schaller, "A new algorithm for metal artifact reduction in computed tomography: in vitro and in vivo evaluation after total hip replacement," *Investigative Radiology,* vol. 38, no. 12, pp. 769-775, 2003.

[9] G. T. Herman, "Correction for beam hardening in computed tomography," *Physics in Medicine and Biology,* vol. 24, no. 1, pp. 81-106, 1979.

[10] T. F. K. K.-R. B. Ohnesorge, "Efficient object scatter correction algorithm for third and fourth generation CT scanners," *European Radiology,* vol. 9, no. 3, pp. 563-569, 1999.

[11] H. Sun, S. Qiu, S. Lou, C. Li, J.Liu, S. Li and G. Jiang, "An Improved Correction Method for Reducing Off-Focal Artifacts in CT Imaging," in *Engineering in Medicine and Biology*, Shanghai, 2005.

[12] D. M. Tucker, G. T. Barnes and P. Chakraborty, "Semiempirical model for generating tungsten target x-ray spectra," *Medical Physics,* vol. 18, no. 2, pp. 211-218, 1991.

[13] M. Baer and M. Kachelrieß, "Hybrid scatter correction for CT imaging," *Physics in Medicine and Biology,* vol. 57, no. 21, pp. 6849-6867, 2012.

[14] E. Y. Sidky and X. Pan, "Image reconstruction in circular cone-beam computed tomography by constrained, totalvariation minimization," *Physics in Medicine and Biology,* vol. 53, no. 17, pp. 4777-4807, 2008.

Scattering correction for industrial CBCT using continuously thickness-adapted kernels at MeV energy range

Navnina Bhatia
CEA-LIST
F-91191 Gif-sur-Yvette France
Email: navnina.bhatia@cea.fr

David Tisseur
CEA-LIST
F-91191 Gif-sur-Yvette France
Email: david.tisseur@cea.fr

Jean Michel Létang
Université de Lyon,
CREATIS ; CNRS UMR5220 ; INSERM U1044 ;
Université Claude Lyon 1 ;
Centre Léon Bérard, France
Email: jean-michel.letang@creatis.insa-lyon.fr

***Abstract*—One of the principal disadvantages of Cone Beam Computed Tomography (CBCT) is the contribution of secondary radiation originating from scattering of photons in the object and detector. The presence of these scattered photons causes streaks and cupping artifacts in reconstruction images. The effect is more dominant and challenging in the case of MeV energy due to higher scatter to primary ratio (SPR). Additionally, the incident high energy photons which are scattered are more forward directed and hence more likely to reach the detector. Moreover, for MeV energies, the contribution of photons produced by annihilation and bremsstrahlung process also becomes important. We propose validation of projection wise scatter correction method using continuously-thickness adapted kernels method on MeV range data. Scatter correction is performed for a homogeneous gear made of iron in a robust iterative manner suitable for high SPR, using pencil beam kernels. The simulated kernels are analytically parameterised to obtain a continuous map of kernels with respect to the thickness of the object. The result obtained show effectively improved reconstruction values after scatter correction proving the efficiency of the method for MeV data.**

I. Introduction

One of the main artifact causing factor in CBCT is scattering of photons inside the object and the detector. Scattered photons are altered from their original path after interaction with matter. This additional share of scattered X-rays results in increased measured intensities, since the scattered intensities simply add to the primary intensity. This effect is seen in back projection reconstruction algorithms as overestimated intensities thus corresponding to an underestimation of absorption. This results in artifacts like cupping, shading, streaks etc on the reconstruction images.

The effect of scattering becomes more prominent when the input X-ray energy is high. Specially in case of MeV energy a number of aspects are needed to be taken into account. First of all, there is an appreciable increase in the forward Compton scattering of the photons and hence they are more likely to reach the detector. Also, these scattered photons are more energetic and therefore more likely to escape from the scattering object. By increasing the incident energy, the energy of charged particles released (recoil electrons and positrons) in the scattering object also increases, resulting in a marked increase in the number of photons generated through the bremsstrahlung process. At photon energies in excess of 1.022 MeV, positrons are generated through pair production, which, upon annihilation, produce photons that can contribute to the scatter fluence.

There are some existing scatter correction methods for MeV source. For example, Maltz et al. [1] employ a method of scatter correction in MeV range using beam stop arrays. They derive an expression that allows to estimate the scatter in an image taken without the array present, given image values in a second image with the array in place. Such methods face problems like increased X-ray exposure due to more than one scans per projection and prolonged scanning time. Steven et al. [2] use scatter kernel superposition (SKS) method for correction cupping artifacts for low dose MeV CBCT images of arbitrary objects. However, the scatter signal is modeled as the sum of the scatter contributions from a group of pencil beams passing through the object. They approximate the scatter distribution, as the convolution of primary signal with scatter kernels. However, pencil beam kernels are thickness dependent kernels and there is an appreciable change in the amplitude and shape of these kernels with respect to small variation in the thickness of the object. The classical convolution based scatter correction methods [3] [4], are based on a discrete set of thickness-dependent kernels and for a range of thickness only one kernel is used. These methods give satisfactory results in many applications. However, when a high range is considered, the SPR is expected to be very large and the different steps of the SKS correction algorithm have to be reconsidered. In particular a better sampling of the kernels with respect to the thickness of the object is required to get an accurate model of variability in shape and in amplitude of the scatter kernels over the whole thickness range.In this article, we focus on scatter correction by continuously thickness adapted Scatter Kernel Superposition (SKS) method [5]. Continously thickness adapted method tackles this issue by generating a continuous kernel map with respect to thickness. The method description in detail can be found in [5]. A case study of the set up with

iron gear as the object with a 6 MeV source is described below. We do not take into account the contribution of electrons and photons produced after bremsstrahlung in this paper.

II. Method and Materials

A. Scatter Correction Using Pencil Beam Kernels

In the SKS scatter correction approach [5], the scatter signal can be modeled as the sum of the scatter contributions from a group of pencil beams passing through the object and the detector. For each pencil beam input, a resulting kernel which has the weight of the scatter to primary ratio is determined. The total scatter signal $S(m,n)$ with m and n as the pixel position on the detector, can then be modeled as:

$$S(m,n) = \sum_k \sum_l P(k,l) h_{T(k,l)}(m-k, n-l) \qquad (1)$$

where,

h_T is the thickness (T) dependent kernel, with amplitude equal to the ratio of the scattered signal at the current pixel to the primary signal, at the pencil beam centered pixel. P is the primary signal contributed by the photons passing directly without any attenuation, O is the full beam intensity; The thickness is calculated with the Beer Lambert law

$$T(k,l) \approx \frac{1}{\mu} \ln \frac{O(k,l)}{P(k,l)} \qquad (2)$$

with μ being the attenuation constant of the object under consideration at the mean energy of the spectrum used. The pencil beam kernel h_T can be fitted into the equation formed by four circularly symmetric Gaussian functions describing the shape of the kernel:

$$\begin{aligned} h_T(m-k, n-l) = A \exp\left(-\frac{(m-k)^2 + (n-l)^2}{2\sigma_1^2}\right) \\ + B \exp\left(-\frac{(m-k)^2 + (n-l)^2}{2\sigma_2^2}\right) \\ + C \exp\left(-\frac{(m-k)^2 + (n-l)^2}{2\sigma_3^2}\right) \\ + D \exp\left(-\frac{(m-k)^2 + (n-l)^2}{2\sigma_4^2}\right) \end{aligned} \qquad (3)$$

Where parameters $A, B, C, D, \sigma_1, \sigma_2, \sigma_3, \sigma_4$ are function of thickness T.

The four Gaussian are necessary to fit the shape of the kernels at the energy range used. The first two Gaussian represent the contribution of the object and the last two that of the detector. The four Gaussian model is absolutely necessary in order to clearly separate the low frequency contribution of the object and high frequency contribution of the detector. The low frequency contribution of the detector scatter generates a strong peak in the center pixel of the detector where the pencil beam is impinged. This shape calls for the necessity of four Gaussian model to ensure a good fitting of the kernels.

B. Generation and fitting of kernels

For the generation of kernels, Monte Carlo (MC) simulations were performed in the CT module of CIVA software [6]. Developed by CEA LIST, CT module of CIVA combines deterministic and MC approach for the generation of primary and secondary radiation in tomography [7].

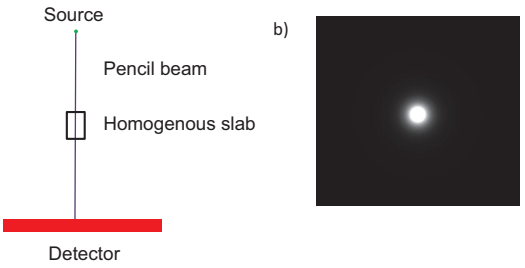

Fig. 1: a) Schematic of the kernel simulation using pencil beam b) generated 2D kernel

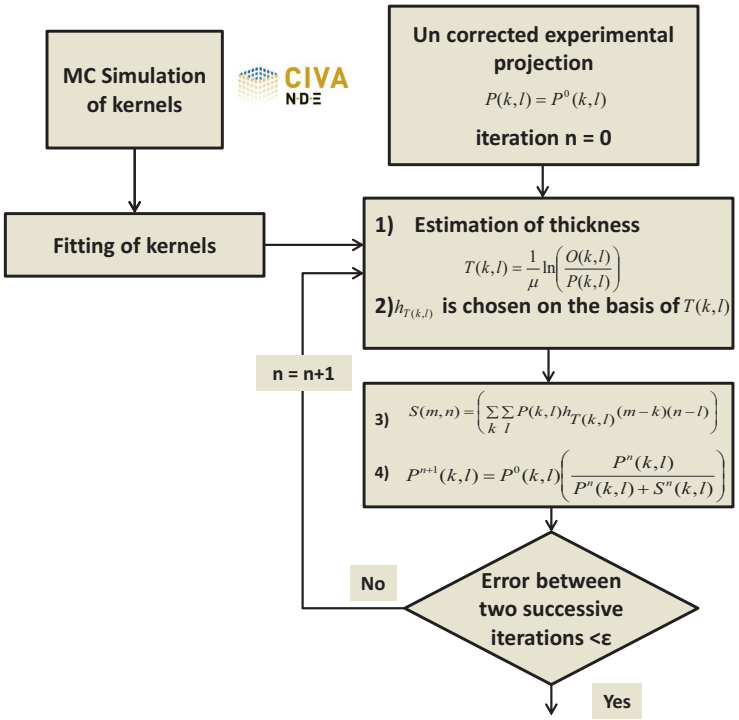

Fig. 2: Schematic representation of the projection wise scatter correction process

Imaging geometry corresponding to the acquisition set up was modeled in CIVA for the simulation of kernels. Pencil beam source was impinged on slabs of same material as the object under study and discrete set of point spread 2D kernels were obtained on the flat panel detector. Equation 3

was fit on these kernels using non-linear least square fitting and the values for parameters $A, B, C, D, \sigma_1, \sigma_2, \sigma_3, \sigma_4$ were calculated for these discrete sets of kernels.

To obtain the continuous kernel map, we analytically calculated the expression for the parameters $A, B, C, D, \sigma_1, \sigma_2, \sigma_3, \sigma_4$ in terms of the thickness of the object [5]. To obtain these expressions, the values of the parameters obtained for discrete set of kernels were fitted with respect to the thickness using non linear least square curve fitting technique. The low frequency contribution of the object are given by σ_1, σ_2 which are expected to increase with the thickness of the object due to high order scattering. The high frequency contribution of the detector given by σ_3, σ_4 are expected to remain constant with the thickness of the object.

C. Iterative Scatter Correction

The iterative scatter correction scheme described in Figure 2 consists of the following steps:

1) The measured projection is taken as the first estimate of the primary.
2) Equivalent thickness is calculated for each pixel by using equation (2).
3) Pixel wise convolution is performed by choosing the suitable kernel for the respective thicknesses.
4) Scatter is estimated using equation 1.
5) The primary estimate is updated using a multiplicative approach to ensure positive primary estimate at each iteration step

$$P^{n+1}(m,n) = P^0(m,n) \times \frac{P^n(m,n)}{P^n(m,n) + S^n(m,n)} \quad (4)$$

Steps 1 to 5 are repeated until convergence is achieved.

D. Acquisition set up with iron gear

The acquisitions are performed on a linear accelerator 6.0 MV source. The source to detector distance was 3.18 m and the source to object distance was 2.45 m. The acquisitions were performed on gear made of iron as shown in Figure 3 with a maximum diameter of 7.5 cm. The detector used was a flat panel detector of pixel size of 200 µm, consisting of a 10 mm copper window.

Fig. 3: Photo of iron gear sample

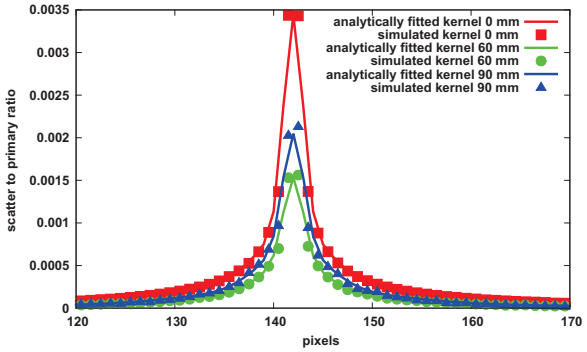

Fig. 4: Simulated kernels for variation in thickness of iron slabs

III. Results

Figure 4 shows the simulated kernels obtained using MC simulations for different iron slab thickness. The acquisition set up and geometry is kept same as the experimental set up for the acquisitions of the iron slab. Figure 5 displays an example of the fitting of parameters to obtain a continuous map of kernels, in this case σ_1 with respect to thickness. It increases with respect to the thickness of the object due to the increase in contribution of the higher order scattering from the object.

Reconstruction was performed on the uncorrected and corrected projections using FDK algorithm in CIVA software. Figure 6 a) displays the reconstruction slice obtained with uncorrected projections. The scatter correction on the projections was applied using continuously thickness adapted kernels. The result obtained is shown in Figure 6 b). Figure 7 displays the cropped view of the reconstructions. We can notice horizontal artifacts on the reconstruction images (see Figure 6 a) due to the jamming of the rotational axis during the acquisition and not due to scatter.

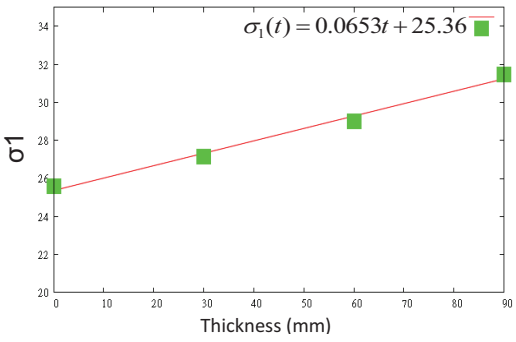

Fig. 5: Fitting of parameter σ_1 in terms of thickness(t)

Figure 8 shows the plot profile of the uncorrected and corrected reconstruction images. Table 1 summarizes the mean and standard deviation of the reconstructed values for corrected and uncorrected data in air and iron region calculated using binary masks. It can be clearly seen that scatter correction improves the contrast of the reconstruction image.

Uncorrected value of 0.172 cm^{-1} for the linear attenuation coefficient of iron is estimated. After the scatter correction, we obtain a value of 0.41 cm^{-1} for the linear attenuation coefficient of iron. In the considered energy range, the value of linear attenuation constant per cm for mean energy 1100 keV is 0.44 cm^{-1}. The relative absolute error is reduced from to 29.8% to 6.8%.

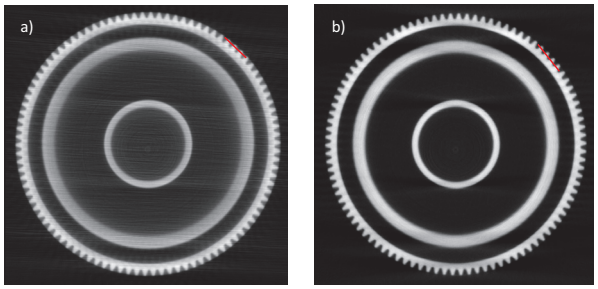

Fig. 6: Reconstruction slice with a) Uncorrected projections b) Corrected projections

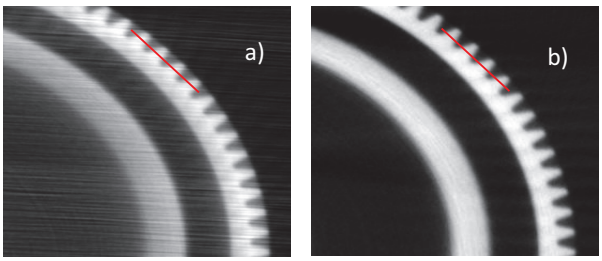

Fig. 7: Cropped reconstruction slice with a) Uncorrected projections b) Corrected projections

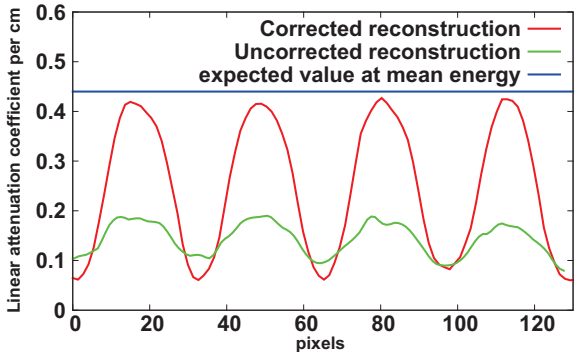

Fig. 8: Plot profile of uncorrected and corrected projections

Further scope of improvement in the reconstruction value can be implemented here after considering the contribution of the photons produced with bremsstrahlung process.

		mean (cm^{-1})	std. dev.
Uncorrected	iron	0.172	$\pm$ 0.095
	air	0.085	$\pm$ 0.0044
Corrected	iron	0.414	$\pm$ 0.032
	air	0.038	$\pm$ 0.0026
Mean spectrum value	iron	0.44	
	air	0.0001	

TABLE I: Mean and standard deviation values for aluminum and air region for uncorrected and corrected reconstruction slices

IV. Conclusion

Significant improvement in the quantitative reconstruction values for the homogeneous object like the iron gear is obtained. The relative absolute error between the obtained reconstruction value and the true value at the spectrum of the linear attenuation coefficient is reduced from to 29.8% to 6.8% validating the efficiency of the method for MeV energy range. A scope of further improvement is possible by including the contribution of the electrons and photons by bremsstrahlung process.

References

[1] J S Maltz, B Gangadharan, M Vidal, A Paidi, S Bose, B A Faddego, M Aubi, O Morin, J Pouliot, Z Zheng, M M Svatos, and A R Bani-Hashemi. Focused beam-stop array for the measurement of scatter in megavoltage portal and cone beam CT imaging. *Med Phys*, 35(6):2452–2462, 2008.

[2] S F Petit, W J C Elmpt, S M J J G Nijsten, A L A J Dekker, and P Lambin. Correction of cupping artifacts in megavoltage cone beam computed tomography. *Department of Radiation Oncology (MAASTRO), Masters thesis*.

[3] M Sun and J M Star-Lack. Improved scatter correction using adaptive scatter kernel superposition. *Phys Med. Biol*, 55(22):6675 – 6720, 2010.

[4] V N Hansen, W Swindell, and P M Evans. Extraction of primary signal from EPIDs using only forward convolution. *Med. Phys.*, 24(49):1477–1484, 1997.

[5] N Bhatia, D Tisseur, F Buyens, and J M Letang. Scattering correction using continuously thickness-adapted kernels. *NDT & E*, 78:52–60, 2016.

[6] http://www-civa.cea.fr/.

[7] J Tabary, R Guillemaud, F Mathy, A Gliere, and P Hugonnard. Combination of high resolution analytically computed uncollided flux images with low resolution Monte Carlo computed scattered flux images. IEEE, 51(1):212–217, 2004.

Combining CT scan and particle imaging techniques: applications in geosciences

Corinne B. Brunelle, Mathieu Des Roches, Louis-Frederic Daigle, Pierre Francus, Bernard Long, Philippe Després

***Abstract*—A small scale physical model of a river and its bed was built to study sediment transport. This model was installed through a CT scanner in order to validate a data acquisition system coupling a CT scan and a particle image velocimetry (PIV) system. The PIV structure is fixed to the scanner, which moves along 2.6 meters rails. This combined system provides high spatial and temporal resolution measurements of bed density and fluid velocity. The data acquisition is time-synchronized and co-located greatly improving our understanding of the dynamics inside the scanned object. The bed topography and porosity as well as the fluid velocity profiles near the bed were successfully derived. These parameters are essential to link hydrodynamic processes over the bed and sediment transport. The methodology holds promising advancements in experimental sedimentology, and could also find interesting applications in other non-medical fields.**

***Index Terms*— CT scan, particle image velocimetry (PIV), physical model, particle-fluid dynamics**

I. Introduction

X-RAY computed tomography (CT) technology has useful applications in geosciences providing density and porosity of non-homogenous materials (Ketcham and Carlson, 2001; Ketcham and Iturrino, 2005; Otani and Obara, 2004). The medical CT scanner is interesting because of its large opening (i.e., 80 cm), allowing a field of view (FOV) up to 65 cm for the reconstructed image. Dynamic systems could also be studied with the CT scan by doing temporally resolved measurements. This paper reports on the use optical imaging techniques to characterize the effect of different flow types on sediment transport. The method consists of coupling a medical CT scanner and a particle image velocimetry (PIV) system. The two datasets are combined to provide an image with density values as well as velocity vectors.

The modeling of sediment transport is one application that would benefit from the proposed methodology since parameterization of shear velocity and sediment density at the boundary layer is essential but otherwise difficult to determine (Sternberg, 1971; Grant and Madsen, 1979). The combined image is interpreted with current knowledge of the sediment dynamics. The specific objectives of this work are to 1) add a high-resolution grid of velocity vectors to the CT scan image and 2) optimize the acquisition parameters to get the best resolution and image quality. Spatial and temporal acquisitions were tested. For spatial measurements, steady flows were used. For temporal measurements, water waves were used considering that the vector field changes rapidly with time. This new perspective would greatly improve the quantification of hydrodynamic properties and sediment transport using experimental work.

C. B. Brunelle, M. Des Roches, L.-F. Daigle, P. Francus and B. Long are with the Multidisciplinary Laboratory of CT Scan for Non-Medical Use, Institut national de la recherche scientifique (INRS), G1K 9A9, Québec, Canada, (corresponding author e-mail: corinne.bourgault-brunelle@ete.inrs.ca). P. Després is with the Université Laval, G1V 0A6, Québec, Canada, (e-mail: philippe.despres@phy.ulaval.ca).

II. Materials and Methods

A movable sand-bed model was built in the Multidisciplinary Laboratory of CT Scan for Non-Medical Use at the Institut National de la Recherche Scientifique (Québec, Canada). A rectangular flume (0.30 m x 0.30 m x 7.0 m) made with 0.025 m thick transparent acrylic material was inserted into a medical X-ray CT scanner (*Siemens*, Somatom Definition AS+ 128) as conducted by Yamada et al. (2013) and Montreuil (2014). The CT scanner moves on 2.6 meters rails along the flume. The water depth in the flume is 0.14 m. The sand bed is composed of quartz (SiO_2), Ottawa sand, with grain median diameter (d_{50}) of 217 μm and uniform density. The bed height is 0.05 m. In addition, as the examination table is static and the gantry moves along the object, the use of large fixed physical models is possible. First, a steady flow is created using a water pump joining the two water tanks placed at each extremity of the flume. A honeycomb diffuser reduces the turbulence at the water inlet. Second, a wavemaker is installed at one extremity to generate waves. A wave absorber made of angular pebbles is placed at the other extremity. The wave period is 1.5 seconds.

A. CT scan measurements

The CT scanner measures attenuation coefficients which are scaled in Hounsfield unit (*HU*). The *HU* values vary from -1024 to +3071 *HU* providing 4096 levels of grey, where air and water values are -1000 and 0, respectively. Images were obtained with a tube current of 600 mAs at a tube voltage of 140 kV. Perfusion mode is used. In this mode, the scan does not move allowing PIV co-located measurements. The collimation is 64 x 0.6 mm providing a set of 64 images every 0.15 seconds (i.e., 6.6 Hz) of the cross-section. In the longitudinal axis, the image is 0.038 m long. The image is reconstructed by a dedicated computer and reconstruction parameters are defined in the *Syngo* software. The convolution

kernel used for the image reconstruction is the B30f which is a relatively soft smoothing filter. The field of view used in the cross-section for the reconstruction is 0.30 m. The isotropic voxel edge length is 0.6 mm. An analogue signal from the CT scan is sent to the PIV for acquisition synchronization.

B. Particle image velocimetry

A LaVision planar particle image velocimetry (PIV) measurement system is mounted on the CT scanner allowing time-synchronized and co-located measurements. To avoid astigmatism effect, a mirror is placed upstream of the scan to reflect the image in the scan zone to the PIV camera located downstream (Fig. 1). The camera is protected from the X-ray by a lead sheet. Image distortion due to optical path or oblique viewing is corrected automatically using a calibration plate. The calibration is a length scale conversion for orthogonal camera viewing. The PIV is set to acquire 2D images of the flow velocity in the longitudinal axis of the flume (sagittal plane). A pulsed laser beam is formed into a light sheet and is fired twice with a short time delay (*dt*). Both illuminations are recorded by one double-frame high resolution CCD camera. The recorded pair of images is divided into small interrogation windows of 32 x 32 pixels. The resulting vector field grid resolution is 1 mm and the field of view is 0.35 m x 0.29 m. The *dt* is adjusted according to the measured velocities to make sure that the movement of a particle is smaller than a quarter of the interrogation window size. The *dt* value is 6 ms for steady flow and 11 ms for waves. Increasing the *dt* increase the detection of high velocity but neglect the slow movements. It appeared that the *dt* was unnecessarily short for steady flow and was increased for waves, for which the *dt* was fast enough. During the time interval *dt*, between the laser shots, the particles of each interrogation window have moved by a displacement *ds*. The velocity is then simply given by the ratio *ds*/*dt*. The calculation of the particle displacement *ds* is done by fast FFT-based cross-correlation of two corresponding interrogation windows. Only vectors calculated with a great correlation are conserved. The interrogation window overlap is 75 %, which has the effect of smoothing the velocity vector field. The PIV system samples at 6.66 Hz during 3 seconds and starts at the same time as the CT scan measurements. This way, there is one PIV grid of vector for each CT scan image. There is approximately one velocity vector for two CT scan pixels.

C. Data post-treatment

The *HU* values can directly be interpreted as a function of density in this study because the sand used is 99.5% pure silica (i.e., uniform) and a voxel can only contain water and sand. Otherwise, the regression used to convert *HU* values into density would vary as a function of the atomic numbers (Boespflug et al. 1994). The artefacts in the water column mostly affect the side of the image in the cross-section. Thus, only pixels in the center of the flume are interpreted. In the longitudinal axis, this area corresponds to the PIV plane of the flume. However, *HU* values in the ripple region itself need to be interpreted with care because streaks can appear near the bed. The interface of water and sand is first determined by thresholding. The sand density (ρ_s) is determined by equation (1), where the measured *HU* value (HU_m) is compared to *HU* value of water (HU_w) and of pure quartz (HU_q) using the density of pure quartz (ρ_q).

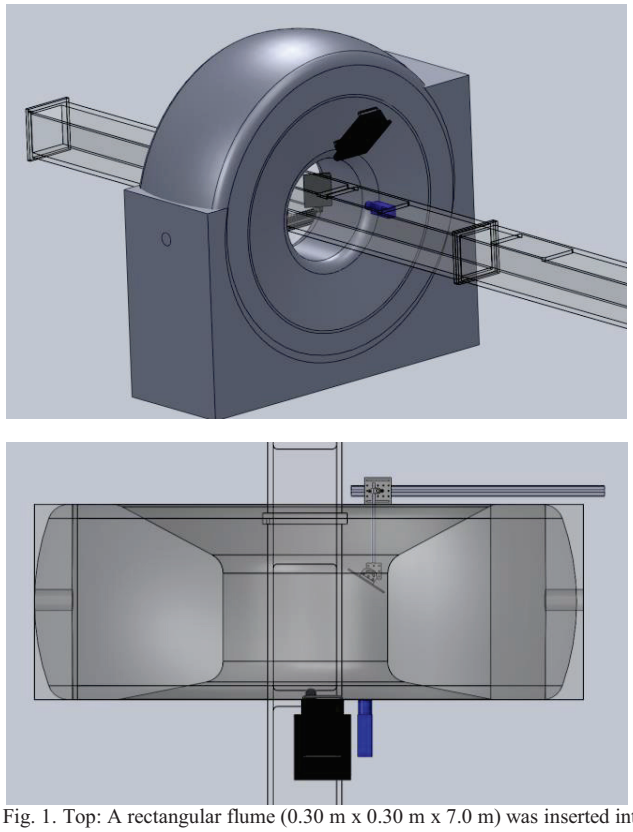

Fig. 1. Top: A rectangular flume (0.30 m x 0.30 m x 7.0 m) was inserted into a medical X-ray CT scanner (Siemens, Somatom Definition AS+ 128). The PIV system is fixed to the CT scanner. Bottom: The laser (black) of the PIV system shoots in the CT scan measurement zone, the light is reflected to the mirror (on the support) and back projected to the camera (blue).

$$\rho_s = \left(\frac{HU_m - HU_{H2O}}{HU_q - HU_{H2O}}\right)\rho_q \quad (1)$$

The porosity (n) is defined as:

$$\rho_s = (1 - \mathrm{n})\rho_q \quad (2)$$

The porosity of well-sorted sand is approximately 0.4, meaning that 0.6 (i.e., 1-0.4) multiplied by the pure quartz density (2.64 g/cm^3) is equal to the sand bed density (1.6 g/cm^3). The images of the CT scanner and the PIV are superposed using a reference point with a known position in the two coordinate systems, which is located on a PIV calibration plate. This plate is also scanned with the CT scanner. Only instantaneous measurements are shown in the results section (i.e., snapshots).

III. Results and Discussion

Co-located and time synchronized images of fluid motion are taken over a ripple. The experimental setup is used to test two types of acquisition sequences. First, the PIV and the CT scanner, which are fixed together, move at different locations in a short period of time to describe the hydrodynamics of a steady flow in space (section A). Second, the PIV system and the CT scanner are located at a fixed point making fast temporal measurements of wave motion (section B).

A. Spatial analysis of a steady flow

The PIV and the CT scan measure the flow properties in front of a ripple (Fig. 2a). Then, the scanner is moved after 30 seconds on the top of the ripple for another 3 seconds of measurements (Fig. 2b). The scan is moved again after 30 seconds behind the ripple (Fig. 2c). The ripple moves in the current direction. The results show that the hydrodynamics of a steady flow over a ripple are observed with high spatial resolution. The velocity profiles near the bed determine the bottom shear stress (τ_b). This parameter is important because it is related to the force per unit area acting on the sand bed. The sediment transport is a function of that parameter as well as the grain size and the porosity of the bed (Van Rijn, 1984). The reference bed porosity value 0.4 gives a sand bed density (ρ_s) of 1.6 g/cm^3, which is similar to measurements. The sand-water interface (dashed black line) is delimitated by using a threshold *HU* value (i.e., 1400). This way, it is possible to calculate the ripple displacement by doing repetitive scans. Consequently, the bedload transport of sediments can be calculated. The front face of the ripple (i.e., the stoss face) is the divergence zone resulting in erosion. The so-called lee face is the convergence zone on the trailing edge of the ripple, where accretion results in ripple migration.

B. Temporal periodicity of wave motion

The PIV and the CT scan do not move and they measure only in the ripple trough (Fig. 3). The images show the hydrodynamic features of a wave passage in that area. The ripple trough is a zone of interest for sediment transport because sand re-suspension by eddies are expected there. The vector orientation and length are coherent with typical wave induced movements (i.e., orbital). The current is oriented in the wave propagation direction under the wave crest (Fig. 3a). Then, the current is oriented downward during the wave trough approach (Fig. 3b) and finally totally reverses, little oriented upward, before the passage of the second wave (Fig. 3c).

It would be expected to find higher sediment concentration just after the wave passage. Further analyses of CT artefacts are needed to better quantify the suspended matter concentration in that region. The problem is the change in geometry of the experimental setup (e.g., the wave passage or ripple formation) which changes the absolute *HU* values within the image. However, the technique shows the potential to characterize rapid flow variations and bed deformation with time.

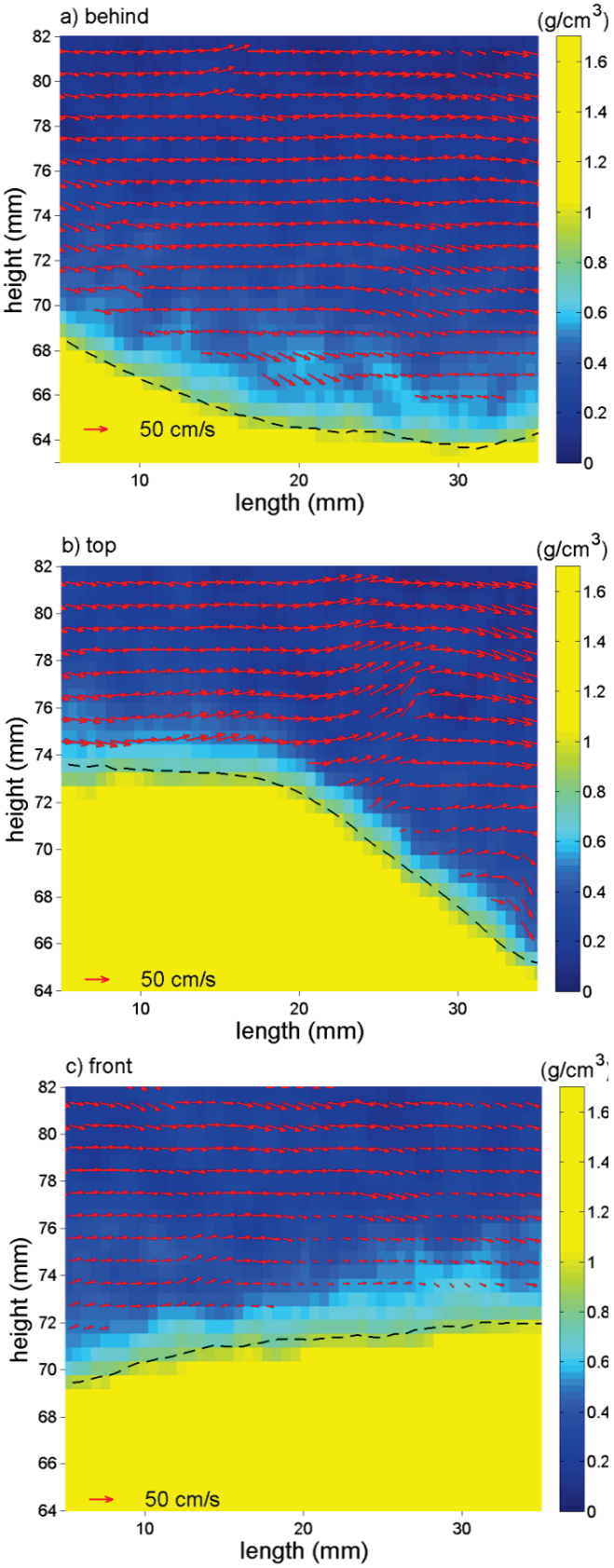

Fig. 2. Sand ripple and steady flow: instantaneous sediment density is measured with the CT scanner (colored background) combined with fluid velocity vectors measured using the PIV (red vectors). The hydrodynamics of a steady flow is illustrated a) behind, b) on the top and c) in the front of the ripple (yellow). The time lap between two images is approximately 30 seconds.

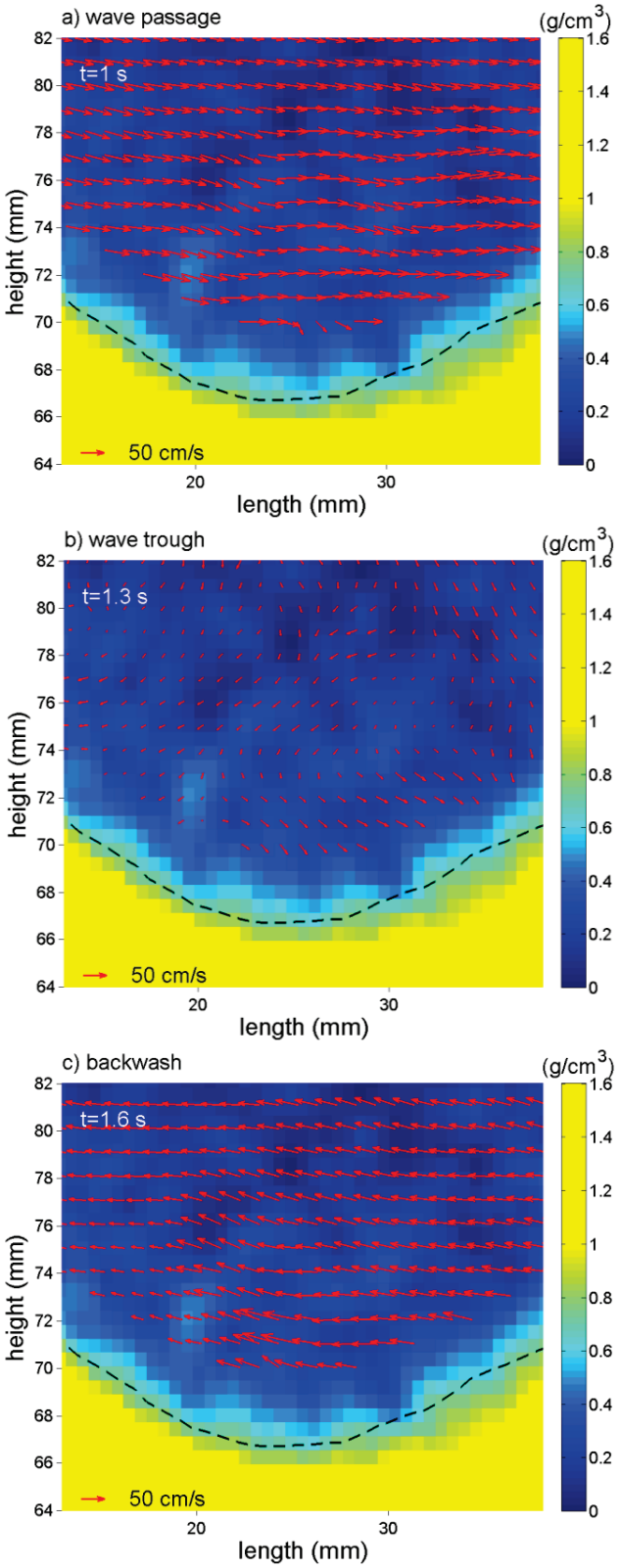

Fig. 3. Ripple trough and wave current: instantaneous sediment density measured with the CT scanner (colored background) combined with fluid velocity vectors measured using the PIV (red vectors). The hydrodynamics induced by waves in the ripple trough (yellow) is illustrated for a) the wave passage, b) the wave trough and c) the backwash occurring before the wave passage (i.e., approaching wave). The time lap between two images is approximately 0.3 s and the wave period is 1.5 s.

IV. Conclusion

The PIV system was successfully synchronized with the CT scanner. This adds velocity vectors to the image of density that could ultimately give the transport rate of sediments. This is fundamental information to understand the physics of particle-fluid dynamics and improve the modeling of the underlying processes, and was never achieved before. Still, we made several observations to be taken into account to improve further experiments. The stability of the experimental setup is fundamental and the image appears to be really sensitive to that factor. The acquisition restriction mostly comes from tube thermal loading. The noise in the water pixels greatly affects the accuracy of suspended particle concentration detection. By optimizing the tube voltage and current as well as the beam collimation, the pause between the scans and the noise in the image could be reduced. For the X-ray image artefacts, further work will be conducted to better described the effects of the geometry setup on the reconstructed image as well as test different reconstruction algorithms. The beam hardening artifacts are also a challenge that needs to be addressed considering that no correction is applied for sand. Overall, the experiment showed interesting results that could have many applications in different non-medical research field providing a fast temporal acquisition and high spatial resolution data.

Acknowledgment

The authors want to thank the Canada Foundation for Innovation for their financial contribution, *Siemens* for their support and the Government of Québec (Ministère des Transports & Ministère de la Sécurité publique) for the student scholarships.

References

Boespflug, X., N. Ross, B. Long, and J. F. Dumais. 1994. “Tomodensitométrie Axiale: Relation Entre L’intensité Tomographique et La Densité de La Matière.” Canadian Journal of Earth Sciences 31 (2): 426–34.

Grant, William D., and Ole Secher Madsen. 1979. “Combined Wave and Current Interaction with a Rough Bottom.” Journal of Geophysical Research: Oceans (1978–2012) 84 (C4): 1797–1808.

Ketcham, Richard A., and William D. Carlson. 2001. “Acquisition, Optimization and Interpretation of X-Ray Computed Tomographic Imagery: Applications to the Geosciences.” Computers & Geosciences 27 (4): 381–400.

Ketcham, Richard A., and Gerardo J. Iturrino. 2005. “Nondestructive High-Resolution Visualization and Measurement of Anisotropic Effective Porosity in Complex Lithologies Using High-Resolution X-Ray Computed Tomography.” Journal of Hydrology 302 (1): 92–106.

Otani, Jun, and Yuzo Obara. 2004. Xray CT for Geomaterials: Soils, Concrete, Rocks International Workshop on Xray CT for Geomaterials, Kumamoto, Japan. CRC Press.

Montreuil, S. 2014. “Définition des paramètres sédimentologiques mesurés au scanographe densitométrique et estimation de la contrainte de cisaillement sur une ride sableuse. ” Thèse. Québec, Université du Québec, Institut national de la recherche scientifique, Doctorat en sciences de la terre, 340 p.

Sternberg, Richard W. 1971. “Measurements of Incipient Motion of Sediment Particles in the Marine Environment.” Marine Geology 10 (2): 113–19.

Van Rijn, L. C. 1984. “Sediment Transport, Part I: Bed Load Transport. ” Journal of Hydraulic Engineering 110 (10): 1431–56.

Yamada, Fumihiko, Ryuta Tateyama, Gozo Tsujimoto, Seiya Suenaga, Bernard Long, and Constant Pilote. 2013. “Dynamic Monitoring of Physical Models Beach Morphodynamics and Sediment Transport Using X-Ray CT Scanning Technique.” Journal of Coastal Resarch, 1617–22.

GPU Acceleration of Branchless Distance Driven Projection and Backprojection

Rui Liu[1], Lin Fu[2], Bruno De Man[2], and Hengyong Yu[1]

[1]Department of Electrical and Computer Engineering, University of Massachusetts, Lowell, MA 01854
[2]Image Reconstruction Lab, GE Global Research, Niskayuna NY 12309

Abstract—**Projection and backprojection operations usually are the computational bottlenecks in a variety of tomographic imaging algorithms. The distance-driven (DD) algorithms offer a highly sequential memory access pattern and low arithmetic cost on CPU platforms. However, the original DD algorithm has an inner loop that adjusts the calculation depending on the relative position between voxel and detector cell boundaries. The irregularity of the branch behavior makes it difficult to implement the DD on massively parallel vector computing devices (such as Graphics Processing Units). In this work, we implement a branchless DD algorithm that is highly parallelizable and amenable to vectorization on GPUs. We demonstrate that the proposed implementation obtains the same results as the original DD algorithm to a reasonable precision, while significant speedup is achieved compared with a state-of-the-art 32-core CPU implementation.**

Index Terms—**GPU, branchless distance driven, projection, back projection, computed tomography**

I. Introduction

A variety of computed tomography (CT) algorithms are based on a linear system model $\mathbf{Ax} = \boldsymbol{y}$, where $\mathbf{A}$ is the system matrix, $\mathbf{x}$ is an object being scanned, and $\boldsymbol{y}$ is the measured data. The projection and backprojection (P/BP) operators, namely $\mathbf{A}$ and $\mathbf{A}^T$, frequently arise in CT image reconstruction algorithms (both analytical and iterative), as well as in many physical modeling and artifacts correction algorithms. The entries of $\mathbf{A}$ are commonly computed on-the-fly to allow flexible selection of acquisition parameters and reconstruction voxel sizes. With the huge size of data from the state-of-the-art scanners and the ever increasing complexity of CT algorithms, there is a strong demand for efficient algorithms for P/BP operations.

Various CT P/BP models differ in their trade-off characteristics between computational speed and modelling accuracy. Ray tracing (line-integral) models ignore the finite size of detector cells and treat the x-ray paths as ideal pencil-beams[1], [2]. Area- or volume-integral models take into account of the finite sizes of both the image voxels and the detector cells, although calculating the exact intersection area or volume is difficult [3]–[5]. Distance-driven (DD) algorithms [6] instead compute the overlap lengths or areas between the voxel and the detector cell after mapping their boundaries to a common axis. The original DD algorithm [6] offers a highly sequential memory access pattern and low arithmetic cost. It simultaneously avoids high-frequency artifacts in some other methods and ensures that the P/BP operations are adjoint of each other.

Acknowledgements: The authors would like to thank Evgeny Drapkin, Ryan Thome, and Debashish Pal at GE Healthcare for helpful discussion, and Masako Yamada and Kang Zhang in the Advanced Computing Lab at GE Global Research for providing computing resources and helpful discussion.

One drawback of the original DD algorithm is that its inner loop adjusts the calculation with an if-else branch depending on the relative position between voxel and detector cell boundaries. For fan beam or cone-beam tomography, the pattern of voxel and detector cell boundaries is non-uniform when it is mapped to a common axis, resulting in irregularity and poor predictability of the branch behavior and making it difficult to implement on many-core vector computing devices such as Graphics Processing Units (GPUs). Divergence of parallel execution paths is detrimental to GPU performance.

GPUs and other multi-core devices have been shown to drastically accelerate the calculation of certain CT P/BP models[7]–[12]. However, GPU implementations of DD algorithms have not been reported to our knowledge. For example, Muller et al. accelerated CT reconstruction with a graphics-based P/BP on GPU by using the RGBA channels and 2D texture operation [11] or shading language in FDK algorithms [13], [12]. Compute Unified Device Architecture (CUDA) based GPU acceleration for CT FDK reconstruction with a 3×4 camera matrix-based P/BP was reported in [14].

To overcome the irregular branch behavior of the original DD algorithm, Basu and De Man presented a branchless DD model [15] by factorizing the DD operation as three branchless steps: integration, linear interpolation, and differentiation. All three steps are highly parallelizable and pipelinable. In this study, we implement the branchless DD P/BP algorithm on GPU. We apply the GPU-accelerated branchless DD to iterative tomographic reconstruction and evaluate its accuracy and computational speed.

II. Method

2.1. Original DD Algorithm

In one-dimension (1D), an object is modeled as a piecewise constant function $f(x)$. Its values are f_i and f_{i+1} over intervals $[x_i, x_{i+1})$ and $[x_{i+1}, x_{i+2})$, respectively. For a detector cell at location $[y_j, y_{j+1})$, the detector measurement is the integral

$$p_j = \frac{1}{y_{j+1} - y_j} \int_{y_j}^{y_{j+1}} f(x)dx. \quad (1)$$

Because the source signal $f(x)$ is piecewise constant, the DD model carries out this integration by calculating the extent of overlap

$$d_j = \frac{x_{i+1} - y_j}{y_{j+1} - y_j} f_i + \frac{y_{j+1} - x_{i+1}}{y_{j+1} - y_j} f_{i+1}, \quad (2)$$

assuming $y_j \in [x_i, x_{i+1})$ and $y_{j+1} \in [x_{i+1}, x_{i+2})$.

In a two-dimensional (2D) fan-beam geometry, the voxel and detector cell boundaries are mapped to a common X or Y axis. Then the coefficients of the system matrix are given by the overlap length weighted by voxel size, ray slope, and normalized by detector size.

In a three-dimensional (3D) cone-beam geometry, detector cell and voxel boundaries are mapped to a common plane. The overlap areas are calculated as the product of overlap lengths. The coefficient of the system matrix is the overlap area weighted by voxel size, the ray slope, and normalized by the detector area.

One drawback of the original DD algorithm (2) is that with curved detectors, detector cell boundary positions become non-uniform when mapped to the common axis or plane. The original DD algorithms has an inner loop that goes through all detector cell/voxel boundaries, and the calculation has to be adjusted depending on whether the next boundary is a voxel or detector cell boundary, hence an if-else branch is needed. Such branch behavior is detrimental to computational efficiency on GPUs because of the divergence of parallel execution paths.

2.2. Branchless DD Algorithm

A branchless DD algorithm [15] was previously proposed as a variant of implementation for the DD model in which the inner loop is essentially branchless, making it highly parallelizable and amenable to efficient implementation on GPUs. In branchless DD, the integral in equation (1) is re-formulated as the difference of antiderivatives

$$p_j = \frac{1}{y_{j+1} - y_j}\left(F\left(y_{i+1}\right) - F\left(y_i\right)\right), \tag{3}$$

where

$$F(t) = \int_{-\infty}^{t} f(x)dx + C, \tag{4}$$

and C is an arbitrary constant. C has no effect on the final result but it is proposed in [15] to subtract the DC component to reduce the dynamic range of $F(x)$. The advantage of this formulation is that since $f(x)$ is piecewise constant, $F(x)$ is piecewise linear, hence $F(x_k)$, $x_i \le x_k < x_{i+1}$ can be very efficiently evaluated from $F(x_i)$ and $F(x_{i+1})$ by dedicated texture interpolation hardware on GPUs.

In a 3D cone-beam geometry, equation (3) becomes

$$p_{mn} = \frac{F(x_{j+1}, y_{j+1}) + F(x_j, y_j) - F(x_j, y_{j+1}) - F(x_{j+1}, y_j)}{(u_{m+1} - u_m)(v_{n+1} - v_n)}, \tag{5}$$

where $\boldsymbol{u}, \boldsymbol{v}$ are coordinates of detector cell boundaries mapped to the common plane, $F(x,y) \triangleq \int_{-\infty}^{y}\int_{-\infty}^{x} f(x',y')\mathrm{d}x'\mathrm{d}y' + C$ is an integral image. $F(x,y)$ can be easily evaluated on the voxel grid by summation $F(x_i, y_i) = \sum_{x' \le x_i, y' \le y_j} f(x', y')$ Once the integral image is generated, evaluating equation (5) can be achieved in a constant time with texture interpolation hardware (Fig. 1).

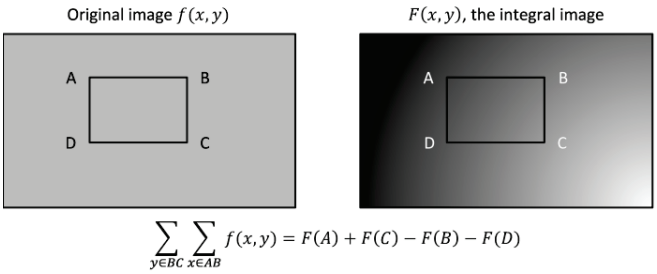

Fig. 1. Illustration of evaluation of equation (5). (a) is the image $f(x_i, y_j)$ and (b) is the corresponding integral image $F(x_i, y_j)$.

2.3. CUDA Implementation of Forward Projection

The branchless DD projection can be performed by the following steps.

(1) Integration. Two sets of integral image volumes, $F_x^{(i)}, i \in \{1,...,N_x\}$ and $F_y^{(j)}, j \in \{1,...,N_y\}$, are generated. $F_x^{(i)}$ are for each x-z slice i; . F_y^j are for each y-z slice j. Which set of integral images is used depends on the orientation of the common plane. The integral images are stored in the texture memory on GPU for utilization of the texture cache and interpolation hardware.

(2) Linear interpolation. As shown in Fig. 2(a), four vectors $\vec{e}_L, \vec{e}_R, \vec{e}_U, \vec{e}_D$ are defined by connecting the x-ray source and four middle points of the detector cell boundaries. With four intersection points (marked by red dots in Fig. 2 (b)) on the integral image, a rectangular area can be defined. The texels marked by blue dots in Fig. 2(b) are fetched with linear interpolation.

(3) Differentiation. The 2D overlap is calculated by taking the difference between the fetched texture values according to equation (5). The projection value is calculated by accumulating the overlap values (i.e.: the products of overlap areas and voxel values) through all image slices and then reweighting the sum by the x-ray path slope and the voxel size.

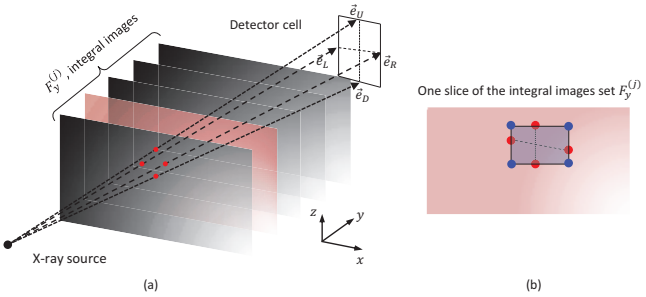

Fig. 2. Illustration of branchless DD projection. (a) demonstrates the branchless DD projection and (b) shows the calculation of the 2D DD kernel on one integral image.

In CUDA implementation, one thread calculates one detector cell value for one view angle. To achieve the benefit of texture cache and hardware based interpolation, the integral image volumes are bound to texture objects. A typical configuration of a CUDA thread block is (64, 8, 1), where the three dimensions correspond to the row index of the detector, the column index of the detector, and the view angle index, respectively. The first dimension of the thread block will be

adjusted according to the number of rows on the detector. At the same time, we keep the product of the first two dimensions a multiple of 32. The third dimension is kept to one to guarantee no branch divergence.

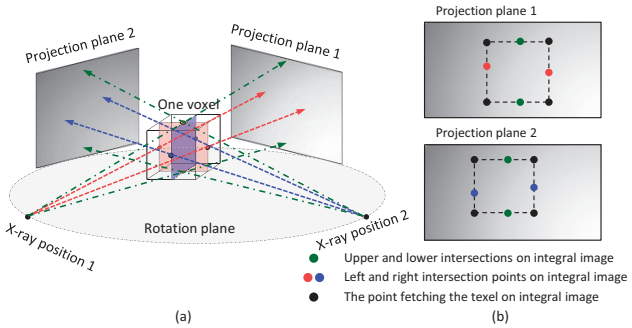

Fig. 3. Illustration of branchless DD backprojection. (a) demonstrates the selections of different center planes according to the current projection view angle, (b) are the corresponding projection plane 1 and plane 2 with respect to different center planes. The texels are fetched at the black dots on the integral images.

2.4. CUDA Implementation of Backprojection

To calculate the backprojection using the branchless DD model, the integral volumes are generated for every projection view. For each voxel, one of the two possible common planes for backprojection is selected according to the view angle, as shown by the red or blue planes in Fig. 3(a). After the common plane is determined, four middle points on the voxel boundaries are projected to the detector surface. They have four intersections on the detector as shown in Fig. 3(a). A rectangular overlap value is determined as illustrated in Fig. 3(b). The texels are fetched and the 2D overlap area is calculated by (5). The backprojection at the voxel is the accumulation over all projection views of 2D overlap values (i.e.: the products of overlap areas and detector values) weighted by ray slope and voxel size.

In our CUDA implementation, one thread calculates the backprojection value for a single voxel. The integral images of the projection data are also bound to the texture objects in clamping addressing mode. A thread block for backprojection is configured to address the Z, X and Y index of the image volume, respectively. We keep the total number of threads in the thread block a multiple of 32. Different from the projection procedure, the if-else instruction appears in the for-loop inside the kernel to decide which middle plane will be used. However, because all the voxels are backprojected from the same projection view set, the branch divergence will not happen inside the kernel.

III. Results

3.1. Experimental configuration

The GPU used in our experiments is the NVIDIA GeForce Titan X. Two Intel Xeon 16-core CPUs with core clock of 3.1GHz are used. The SART algorithm is employed to demonstrate cone-beam CT reconstruction [16]. The GPU-based branchless DD implementation is compared with a CPU-based 32-thread original DD implementation in terms of computing speed and numerical accuracy.

3.2. Forward and Back-projection

The CT geometry is described in Table 1. The projection data is collected evenly over 360°. We fix the image volume and detector size but increase the number of projections from 100 to 4400 in 100-view steps.

TABLE I
THE CONFIGURATION OF CT GEOMETRY

Parameters	Value
Source-to-iso-center distance	541mm
Source-to-detector distance	949mm
In-plane detector cell size	1.0239mm
Cross-plane detector cell size	1.0963mm
Number of detector columns	888
Number of detector rows	64
Reconstruction FOV	250mm
Detector offset	(-1.28,0)mm

The P/BP time and speedup with respect to number of views are shown in Fig. 4. We can see that the time for projection and backprojection increases almost linearly with the number of views. The speedup ratio is low when the number of views is small. This is presumably because of the overhead for data transfer between CPU and GPU. With more views, the speedup gradually increases and reaches a plateau. It indicates that when the number of views increase, the relative overhead of data transfer becomes less when compared to the computation time on GPU, and the benefit of GPU acceleration dominates. The speedup factor can be up to 10X for projection and 11X for backprojection. We further analyzed the kernel functions of projection and backprojection by the CUDA Visual Profiler version 7.5. The duration of projection and back projection kernels is 1.016 s and 0.807 s, respectively. The Streaming Multiprocessors in both projection and backprojection are fully utilized. Generating the integral images approximately occupies 0.13 s and 0.15 s.

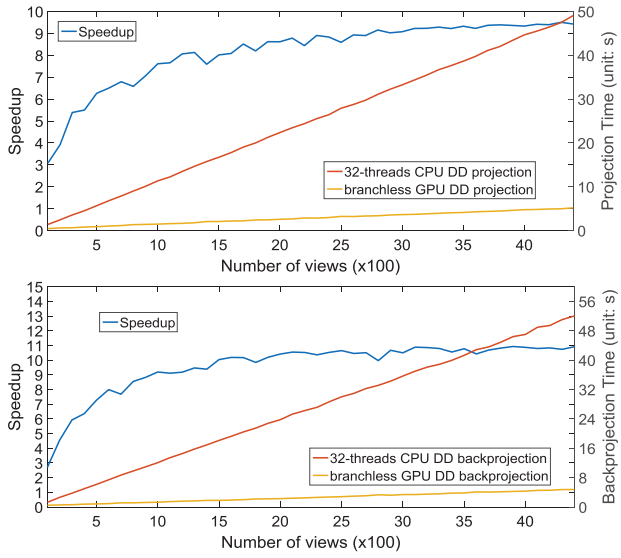

Fig. 4. CPU v.s. GPU P/BP compute time (and speedup) with respect to number of views.

3.3. Iterative OS-SART Reconstruction

Numerical simulations were conducted to investigate the effectiveness of the GPU based branchless DD for iterative

reconstruction algorithms. 2200 views of noiseless monochromatic CT data were evenly acquired over 360^{o}. The $512 \times 512 \times 64$ image volume is the center interception of a FORBILD head phantom [17]. The dynamic range of the phantom is [0,1.8]. It is projected on to a 3552×256 detector and then resized to the 888x64 detector by averaging 4x4 detector area into one detector cell. The linear attenuation coefficient of the phantom was reconstructed by the OS-SART algorithm, using 145 iterations. The number of OS is 10.

The reconstructed image volumes from GPU and CPU implementations along transverse, sagittal and coronal planes are shown in Fig. 5(a) and Fig. 5(b), respectively. The differences between CPU and GPU are shown in Fig. 5(c). The Root-Mean-Square-Errors (RMSEs) [18] with respect to the ground truth in CPU and GPU implementations are both 0.0282, while the RMSE between CPU and GPU results is 0.0017. The RMSE is still decreasing after 145 iterations. The high frequency artifacts in sagittal and coronal planes in both GPU and CPU results are caused by the high contrast array of small dots in the phantom. The relative structural similarities (SSIMs) [18] of the GPU results along transverse, sagittal and coronal slices of the image volume with respect to the CPU results are all larger than 0.999. Overall, the GPU and CPU reconstruction results are very consistent.

IV. Discussions and Conclusions

In this paper, we implemented GPU-based branchless DD projection and backprojection algorithms. The speedup factor is up to 10X and 11X for forward and backprojection, respectively, when compared with a state-of-the-art 32-thread CPU implementation. The high performance of the GPU implementation is achieved not only by the branchless execution but also by the texture cache mechanism and the dedicated interpolation hardware in GPU. There is about 0.5 s overhead for the data transfer between CPU and GPU and the calculation of integral images. To further improve speed, more advanced GPU algorithms can be used to calculate the integral images [19] and the data transfer latency can be concealed by asynchronous mechanisms.

In our GPU implementation, calculation of the integral image causes some precision loss. On the one hand, the precision is limited by the single-precision floating point arithmetic [19] which can be partially solved by subtracting the DC components of the image volume. On the other hand, some precision loss is due to the texture interpolation hardware on GPUs, because texture coordinates are represented by 9-bits fixed point values on GPUs.

References

[1] R. L. Siddon, "Fast calculation of the exact radiological path for a three-dimensional CT array," *Medical physics*, vol. 12, no. 2, pp. 252–255, 1985.

[2] P. M. Joseph, "An improved algorithm for reprojecting rays through pixel images," *Medical Imaging, IEEE Transactions on*, vol. 1, no. 3, pp. 192–196, 1982.

[3] H. Yu and G. Wang, "Finite detector based projection model for high spatial resolution," *J Xray Sci Technol*, vol. 20, no. 2, pp. 229–238, 2012.

[4] I. E. Sutherland and G. W. Hodgman, "Reentrant polygon clipping," *Communications of the ACM*, vol. 17, no. 1, pp. 32–42, Jan. 1974.

[5] D. Triangulation, D. T. Lee, and B. J. Schachter, "*Two Algorithms for Constructing a Delaunay Triangulation*" in International Journal of Computer & Information Sciences, vol. 9, issue 3, pp. 219-242, 1980.

[6] B. D. Man and S. Basu, "Distance-driven projection and backprojection in three dimensions," *Physics in Medicine and Biology*, vol. 49, no. 11, pp. 2463–2475, Jun. 2004.

[7] B. Cabral, N. Cam, and J. Foran, "Accelerated volume rendering and tomographic reconstruction using texture mapping hardware," in *Proceedings of the 1994 symposium on volume visualization*, New York, NY, USA, 1994, pp. 91–98.

[8] Y. Okitsu, F. Ino, and K. Hagihara, "High-performance cone beam reconstruction using CUDA compatible GPUs," *Parallel Computing*, vol. 36, no. 2, pp. 129–141, 2010.

[9] M. Kachelriess, M. Knaup, and O. Bockenbach, "Hyperfast parallel-beam and cone-beam backprojection using the cell general purpose hardware," *Med Phys*, vol. 34, no. 4, pp. 1474–1486, Apr. 2007.

[10] K. Mueller and R. Yagel, "Rapid 3D cone-beam reconstruction with the Algebraic Reconstruction Technique (ART) by utilizing texture mapping graphics hardware," presented at the IEEE Nuclear Science Symposium. Conference Record, 1998, pp. 1552 –1559 vol.3.

[11] F. Xu and K. Mueller, "Accelerating popular tomographic reconstruction algorithms on commodity PC graphics hardware," *IEEE Transactions on Nuclear Science*, vol. 52, no. 3, pp. 654 – 663, Jun. 2005.

[12] F. Xu and K. Mueller, "Real-time 3D computed tomographic reconstruction using commodity graphics hardware," *Physics in Medicine and Biology*, vol. 52, no. 12, p. 3405, 2007.

[13] K. Mueller, F. Xu, and N. Neophytou, "Why do commodity graphics hardware boards (GPUs) work so well for acceleration of computed tomography?," in *SPIE Electronic Imaging*, 2007, vol. 6498, p. 64980N.

[14] H. Scherl, B. Keck, M. Kowarschik, and J. Hornegger, "Fast GPU-Based CT Reconstruction using the Common Unified Device Architecture (CUDA)," in *IEEE Nuclear Science Symposium Conference Record, 2007. NSS '07*, 2007, vol. 6, pp. 4464 –4466.

[15] S. Basu and B. De Man, "Branchless distance driven projection and backprojection", Proc. SPIE 6065, Computational Imaging IV, 60650Y

[16] G. Wang and M. Jiang, "Ordered-subset simultaneous algebraic reconstruction techniques (OS-SART)," *J. X-Ray Sci. Technol.*, vol. 12, no. 3, pp. 169–177, 2004.

[17] "http://www.imp.uni-erlangen.de/phantoms."

[18] Z. Wang, A. C. Bovik, H. R. Sheikh, and E. P. Simoncelli, "Image quality assessment: from error visibility to structural similarity," *IEEE Transactions on Image Processing*, vol. 13, no. 4, pp. 600–612, Apr. 2004.

[19] J. Hensley, T. Scheuermann, G. Coombe, M. Singh, and A. Lastra, "Fast Summed-Area Table Generation and its Applications," *Computer Graphics Forum*, vol. 24, no. 3, pp. 547–555, 2005.

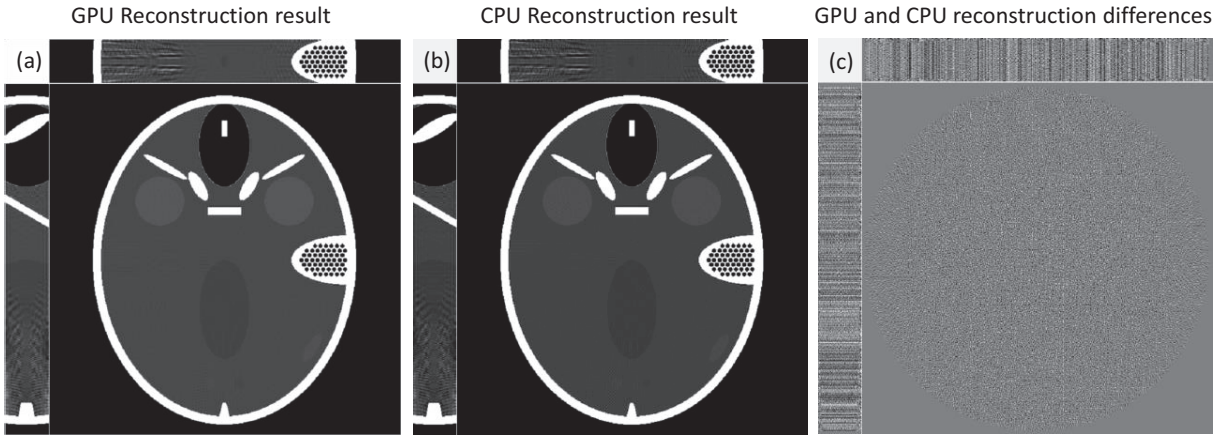

Fig. 5. The 512x512x64 FORBILD head phantom reconstruction with OS-SART. (a) and (b) are the transverse, sagittal and coronal planes of the reconstructed image volume from GPU based branchless DD model and CPU based DD model respectively in a display window [1.0, 1.2]. (c) the errors between CPU and GPU result along transverse, sagittal and coronal planes in a display window[-0.005, 0.005].

High Resolution Laboratory Grating-Based X-Ray Phase-Contrast CT

Manuel Viermetz, Lorenz Birnbacher, Marian Willner, Peter B. Noël, Franz Pfeiffer, and Julia Herzen

***Abstract*—The conventional form of computed tomography using X-ray attenuation without any contrast agents is of limited use for the characterisation of soft tissue in many fields of medical and biological studies. Grating-based phase-contrast computed tomography (gbPC-CT) is a promising alternative imaging method solving the problems of soft tissue contrast without the need of any contrast agent. The combination of high resolution and high sensitivity already showed convincing results at the synchrotron [1]. While high sensitivity measurements are possible using a conventional x-ray sources the spatial resolution does often not fulfil the requirements for specific imaging tasks, such as visualisation of pathologies. The focus of this study is the increase in spatial resolution without loss in sensitivity. To overcome this limitation and further improve the effective pixel size a super-resolution reconstruction based on sub-pixel shifts involving a deconvolution of the image data during each iteration is applied. In our study we could achieve an effective pixel sizes of $28\,\mu$m. The results show the increase in resolution without any drawback in terms of sensitivity or the ability to measure quantitative data. The combination of sparse sampling and statistical iterative reconstruction allowed to maintain the total measurement time to be equal to the standard measuring procedure using filtered back projection. In conclusion, we present high quality and high resolution tomographic images of biological samples to demonstrate the experimental feasibility of super-resolution reconstruction.**

I. High Resolution at grating-based Phase-Contrast-CT Setups

To overcome the limited soft tissue contrast in conventional absorption-based imaging, several new X-ray phase-contrast imaging methods have been developed [2]. While most of these techniques are restricted to highly brilliant X-ray sources like synchrotron radiation sources, grating-based phase-contrast imaging [3] has been successfully adapted to work with conventional X-ray sources [4] and has become a promising candidate for medical diagnostics and industrial testing [5]–[9].

In terms of contrast the differential phase x-ray imaging method allows better differentiation of sample materials than conventional absorption imaging. However, not only contrast is important for an imaging system, but also sufficient spatial resolution is necessary for optimal results.

In this study we achieve higher spatial resolution without significant loss in overall performance with a grating-based phase-contrast CT setup.

Manuel Viermetz, Lorenz Birnbacher, Marian Willner, Franz Pfeiffer and Julia Herzen are with the Department of Physics, Technische Universität München, Germany. E-mail: manuel.viermetz@tum.de

Peter B. Noël is with the Department of Radiology, Klinikum rechts der Isar, München, Germany

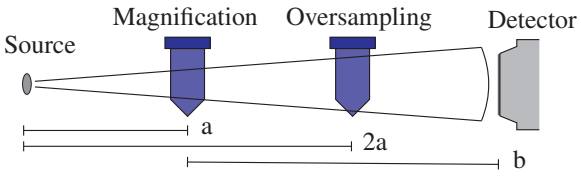

Fig. 1. Illustration of the two setup geometries evaluated to increase the resolution. At the *magnification sample position*, only geometric magnification is used. An oversampling approach is applied with the sample located at the other position further away from the source. The effective pixel size and the influence of source magnification resulting in source blurring are the major differences between the two configurations.

II. Path line to high resolution

One straight forward approach to increase the spatial resolution is to use a *higher resolving detector* with reduced physical pixel size. This approach is very limited, as smaller pixels are less sensitive to radiation, which is crucial when using low-flux laboratory sources.

The most common method to achieve high resolution is to exploit the *geometric magnification* effect. By placing the sample closer to the source the effective pixel size gets reduced resulting in an increased spatial resolution, as illustrated in Figure 1. One drawback in this application is the significantly smaller field of view. Another problem is the source magnification effect. If the sample is positioned closer to the source, the source magnification factor $M_s = b/a$ increases, which means that the projection is blurred by a magnified version of the original source intensity profile.

A more sophisticated method to increase the spatial resolution by taking multiple sub-pixel shifted images of the same scene is the *super-resolution* approach. Advanced algorithms to reconstruct the high resolution image from the low resolution images are needed [10], but problems such as source blurring can be avoided since a sample position with less geometric magnification and thus further away from the source can be chosen.

III. Experimental Setup

At the presented setup a high-flux rotating anode with a molybdenum target operating at 40 kVp and a single-photon counting Eiger 1M (Dectris Ltd.) detector are used for imaging at a highly-sensitive Talbot-Lau interferometer [11], [12]. The gold gratings have a period of $5.4\,\mu$m and are produced by the Karlsruhe Institute of Technology (KIT) [13]. The gratings are positioned in a symmetric geometry with distances of $50\,$cm optimised for high spectral acceptance leading to a visibility of approximately $36\,\%$ [14].

The distance between source and detector is constant for all experiments but the sample position is varied, as illustrated in Figure 1. The number of tomographic angles is 800 in all depicted data. The distances a and $2a$ for both configurations lead to the same effective pixel size after processing of the data. This allows the direct comparison of the results.

IV. Geometric Magnification based results

At the *magnification sample position*, as depicted in Figure 1, the geometry of the system is utilised to allow imaging with a small effective pixel size. The measured tomographic dataset of a liver cirrhosis sample was processed and reconstructed using filtered back-projection. In Figure 2, an exemplary axial slice of the reconstructed volume is presented. It can be seen that the features are strongly blurred and therefore the increased resolution is nullified. This demonstrates that geometric magnification of this extend cannot deliver sufficient resolution improvement.

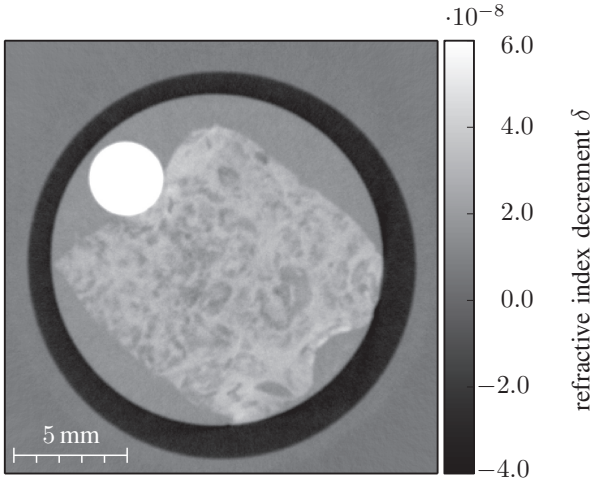

Fig. 2. Axial slice of a filtered backprojection of a liver cirrhosis sample at *magnification sample position* with 29 µm effective pixel size. Due to the geometry of the used setup strong blurring occurs nullifying the increase in resolution.

V. Super-Resolution based results

An alternative setup configuration is the *oversampling sample position*, which is located further away from the source and is therefore less influenced by source blurring but with doubled effective pixel size. To achieve high spatial resolution super-resolution reconstruction is used. In the demonstrated results 2x2 oversampling is applied, which means that four low resolution images are acquired during the measurement as illustrated in Figure 3.

After processing of all low resolution (LR) stepping scans belonging to one projection angle a reconstruction algorithm is applied to calculate the high resolution (HR) image. The presented implementation follows a super-resolution reconstruction method called *iterative backprojection (IBP)* [15]. The principle has similarity to back-projection used in tomography. In this approach, the HR image is estimated by back-projecting the error (difference) between simulated LR images and the

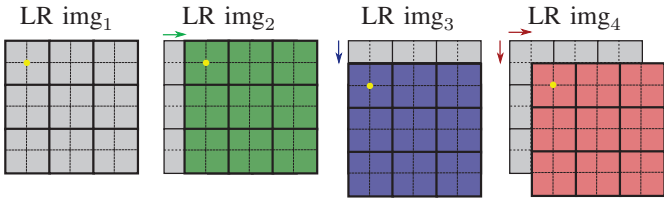

Fig. 3. Illustration of the data acquisition procedure for 2x2 oversampling. In total four low resolution (LR) images are taken, the upper left pixel is marked with a yellow spot for each measurement. It can be seen that the sub-pixel shifts lead to an overlap between the different images. This overlap can be used to reconstruct the HR image.

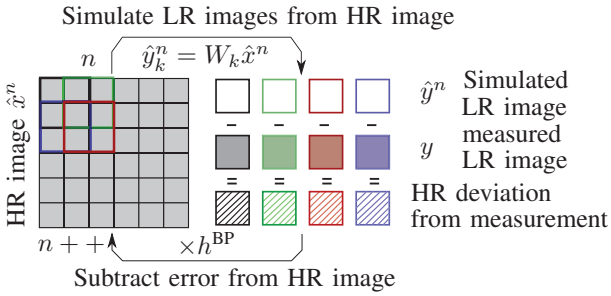

Fig. 4. Super-resolution reconstruction using an iterable workflow to minimize the error of the high resolution image. From the high resolution image the low resolution images are simulated. These simulated images are compared to the originally measured ones. The deviation is then subtracted from the high resolution image during the backprojection step.

measured LR images. This process is repeated iteratively to minimise the error [10].

The IBP algorithm can be expressed by

$$\hat{x}^{n+1} \quad = \quad \hat{x}^n + \sum_k (y_k - \hat{x}_k^n) \times h^{\mathrm{BP}} \,, \qquad (1)$$

where $\hat{x}^n$ represents the generated high resolution image after iteration n, $\hat{y}_k^n = W_k\,\hat{x}^n$ the simulated low resolution image at oversampling position k and y_k is the corresponding measured LR image. Here, W_k is the physical model for the

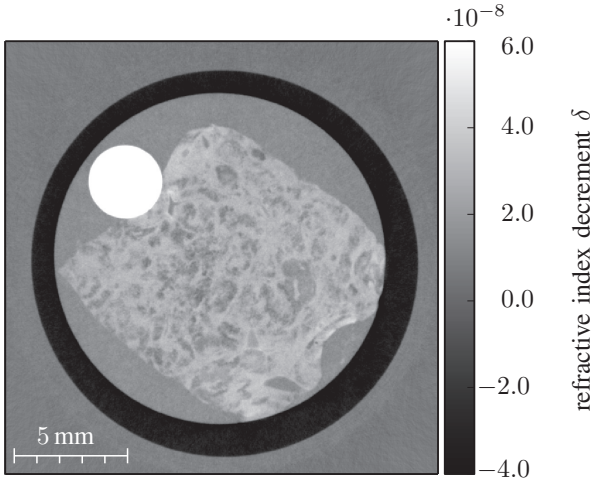

Fig. 5. Exemplary axial slice of a filtered backprojection of a liver cirrhosis sample at the *oversampling sample position*. By using IBP super-resolution reconstruction the effective pixel size is 28 µm and a high quality representation of the sample is obtained.

forward projection. System properties such as the PSF can be implemented into this model for a better simulation result. The errors $y_k - \hat{y}_k^n$ are back-projected using the kernel h^{BP}.

In Figure 4, the principle of the iterative process is illustrated. The number of iterations and the resulting quality is highly dependent on the noise in the measured LR image data.

An exemplary axial slice of a liver cirrhosis dataset measured with oversampling and IBP super-resolution reconstruction is shown in Figure 5. The volume is sharply reconstructed without any blurring or artefacts. Apart from the qualitative improvement of the image the data remains also quantitative. A calibration based on the electron density of a PMMA tube (white) and the measured signal is used [16]. This is important for the compatibility between datasets with and without oversampling and IBP.

VI. Comparison of High Resolution results

Both presented setup configurations achieve an effective pixel size of 28 to 29 µm and the exposure times for both measurements as well as the number of angles are the same.

By the influence of the extended PSF of the system due to the high source magnification factor the geometric magnification approach cannot deliver the spatial resolution which can be obtained by super-resolution reconstruction.

The increase in quality is therefore based on the chosen sample position and the used oversampling reconstruction method. For the *oversampling sample position* the source magnification factor is 0.34, which means that the PSF for this setup geometry is about five times smaller than at the *magnification sample position*. This sharpened PSF leads to almost no blurring of the low resolution images.

Further measurements confirm qualitatively that also the sensitivity of the setup is not affected by application of the super-resolution reconstruction. In Figure 6, an exemplary phase-contrast tomographic scan of a rat brain sample allows to differentiate structures in the brain such as the cerebellum and cancerous tissue. High sensitivity of the interferometer by optimised geometry and gratings are crucial parameters as well as the reliable stability of the setup.

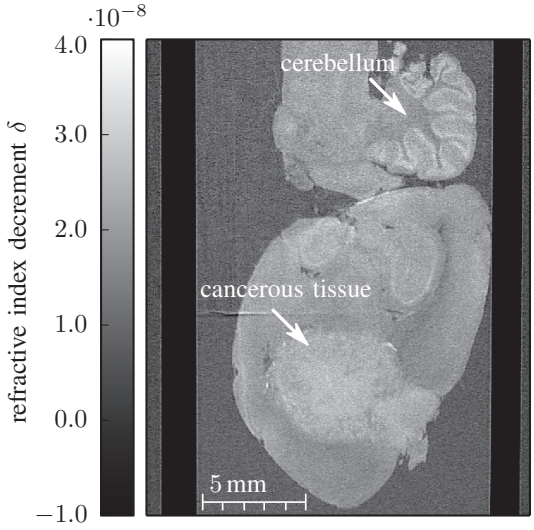

Fig. 6. Exemplary tomographic slice of a rat brain sample with a tumor. The effective pixel size is 28 µm after the IBP super-resolution reconstruction of the oversampled data. The sample is represented sharply and tissue structures are visible. In the lower part the tumor is clearly apparent and in the upper right the cerebellum is shown.

VII. Measurement Time Optimization

Applying the described oversampling approach gbPC-CT with strongly increased spatial resolution can be performed at the presented setup but the increase in measurement time needs to be considered. A standard tomographic measurement at this setup usually takes about 19 hours using the Eiger 1M detector. For the oversampling measurement this duration is about four times longer resulting in a total data acquisition time of 76 hours. As this duration is not practical, further improvements are necessary.

One straight forward time improvement can be reached by increase of the X-ray flux. This has been done by reducing the sample size to a diameter of about 1 cm and the water tank in which the sample is inserted to correct for beam hardening is only 15 mm thick.

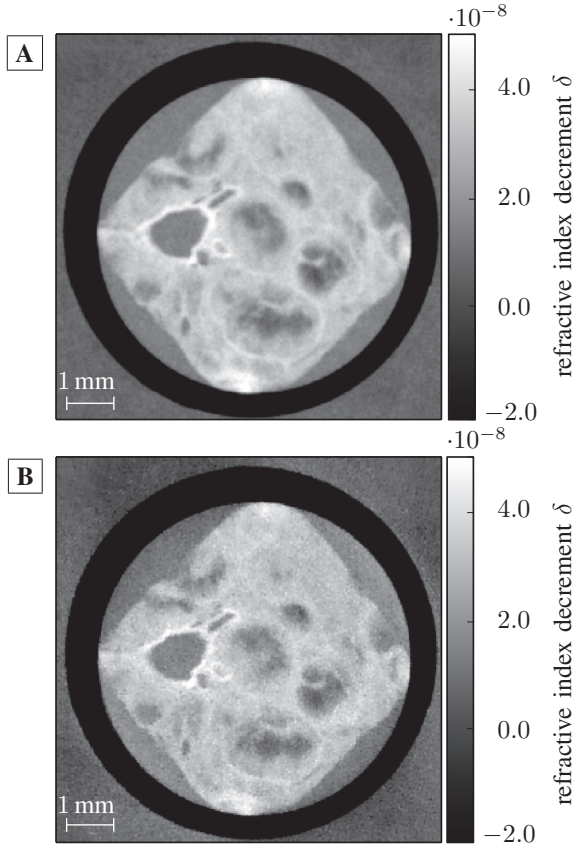

Fig. 7. Axial slice of a tomographic scan of a liver cirrhosis sample at *oversampling sample position* with 28 µm effective pixel size. In **A**, the filtered backprojection is used for the reconstruction based on the full dataset measured within a total data acquisition time of about 44 hours. In contrast to this, in subfigure **B** the statistical iterative reconstruction with only 50% of the available projection angles is shown. Exploiting this reconstruction method the measurement time can be reduced to approximately 22 hours.

Another approach to reduce the data acquisition time is to reduce the number of measured tomographic angles. To obtain sufficient volume reconstruction quality a statistical iterative reconstruction (SIR) instead of a filtered back projection (FBP) is used. SIR can provide sharper and less noisy reconstruction results if the regularisation parameters are chosen well. Another advantage of this method is that for comparable output quality less projection angels are necessary than for a FBP and thus SIR can be used to reduce the measurement time.

In Figure 7 **A**, the reconstruction with filtered back projection (FBP) of the differential phase contrast is shown. The quality is comparable to the measurement of the larger sample in the same setup configuration (see Figure 5), however the total measurement time has been reduced to $55\,\%$ by the thinner water tank and smaller sample.

In Figure 7 **B**, the same dataset of the small liver cirrhosis sample is reconstructed with only $50\,\%$ of the available projection angles using SIR. It is obvious that by doing so the image quality is reduced in comparison to the slice reconstructed via FBP from all available data. However, no under-sampling or other artefacts are visible. Only a slight increase of noise can be observed.

Furthermore, it has to be mentioned that the geometry and the gratings have been optimised for the spectral performance of the used detector. However, the quantum efficiency of the detector is the limiting factor. Development of detectors with higher quantum efficiency can significantly reduce the measurement time.

VIII. Conclusion

The measurements verify that super-resolution reconstruction methods such as IBP can be directly applied on differential phase-contrast measurements. By optimisation of the measurement concerning the geometry and the PSF higher spatial resolution than with conventional geometric magnification can be obtained. The demonstrated results show that combining the high sensitivity of the setup with the high resolution approach can allow measurements at a laboratory X-ray source comparable to synchrotron measurements. However, the usually lower flux of the X-ray tube and the high number of overlapping stepping curves lead to much longer measurement duration, which is the major drawback at laboratory setups. It has been shown that by the application of SIR the data acquisition time can be significantly reduced to an extend which is practicable for use in biological, medical, and material science studies.

Acknowledgment

The authors would like to thank the Karlsruhe Institute of Technology (KIT), Dectris Ltd. for the fruitful collaboration and the support through the DFG Cluster of Excellence 'Munich - Centre for Advanced Photonics'.

References

[1] F. Pfeiffer, O. Bunk, C. David, M. Bech, G. L. Duc, A. Bravin, and P. Cloetens, "High-resolution brain tumor visualization using three-dimensional x-ray phase contrast tomography," *Physics in Medicine and Biology*, vol. 52, no. 23, p. 6923, 2007. [Online]. Available: http://stacks.iop.org/0031-9155/52/i=23/a=010

[2] A. Momose, "Phase-sensitive imaging and phase tomography using x-ray interferometers," *Opt. Express*, vol. 11, no. 19, pp. 2303–2314, Sep 2003. [Online]. Available: http://www.opticsexpress.org/abstract.cfm?URI=oe-11-19-2303

[3] T. Weitkamp, A. Diaz, C. David, F. Pfeiffer, M. Stampanoni, P. Cloetens, and E. Ziegler, "X-ray phase imaging with a grating interferometer," *Optics Express*, vol. 13, no. 16, pp. 6296–6304, 2005.

[4] F. Pfeiffer, T. Weitkamp, O. Bunk, and C. David, "Phase retrieval and differential phase-contrast imaging with low-brilliance x-ray sources," *Nature Physics*, vol. 2, no. 4, pp. 258–261, 2006.

[5] F. Pfeiffer, J. Herzen, M. Willner, M. Chabior, S. Auweter, M. Reiser, and F. Bamberg, "Grating-based x-ray phase contrast for biomedical imaging applications," *Zeitschrift für medizinische Physik*, vol. 23, no. 3, pp. 176–185, 2013.

[6] A. A. Fingerle, M. Willner, J. Herzen, D. Münzel, D. Hahn, E. J. Rummeny, P. B. Noël, and F. Pfeiffer, "Simulated cystic renal lesions: Quantitative x-ray phase-contrast ct: An in vitro phantom study," *Radiology*, vol. 272, no. 3, pp. 739–748, 2014.

[7] M. Willner, J. Herzen, S. Grandl, S. Auweter, D. Mayr, A. Hipp, M. Chabior, A. Sarapata, K. Achterhold, I. Zanette *et al.*, "Quantitative breast tissue characterization using grating-based x-ray phase-contrast imaging," *Physics in medicine and biology*, vol. 59, no. 7, p. 1557, 2014.

[8] H. Hetterich, M. Willner, S. Fill, J. Herzen, F. Bamberg, A. Hipp, U. Schuller, S. Adam-Neumair, S. Wirth, M. Reiser, F. Pfeiffer, and T. Saam, "Phase-contrast ct: qualitative and quantitative evaluation of atherosclerotic carotid artery plaque." *Radiology*, vol. 271, no. 3, pp. 870–878, Jun 2014.

[9] J. Herzen, T. Donath, F. Beckmann, M. Ogurreck, C. David, J. Mohr, F. Pfeiffer, and A. Schreyer, "X-ray grating interferometer for materials-science imaging at a low-coherent wiggler source," *Review of Scientific Instruments*, vol. 82, no. 11, 2011. [Online]. Available: http://scitation.aip.org/content/aip/journal/rsi/82/11/10.1063/1.3662411

[10] S. C. Park, M. K. Park, and M. G. Kang, "Super-resolution image reconstruction: a technical overview," *Signal Processing Magazine, IEEE*, vol. 20, no. 3, pp. 21–36, May 2003.

[11] A. Hipp, M. Willner, J. Herzen, S. Auweter, M. Chabior, J. Meiser, K. Achterhold, J. Mohr, and F. Pfeiffer, "Energy-resolved visibility analysis of grating interferometers operated at polychromatic x-ray sources," *Opt. Express*, vol. 22, no. 25, pp. 30 394–30 409, Dec 2014. [Online]. Available: http://www.opticsexpress.org/abstract.cfm?URI=oe-22-25-30394

[12] L. Birnbacher, M. Willner, A. Velroyen, M. Marschner, A. Hipp, J. Meiser, F. Koch, T. Schröter, D. Kunka, J. Mohr, F. Pfeiffer, and J. Herzen, "Experimental realisation of high-sensitivity laboratory x-ray grating-based phase-contrast computed tomography," *(submitted)*, 2015.

[13] F. J. Koch, T. J. Schröter, D. Kunka, P. Meyer, J. Meiser, A. Faisal, M. I. Khalil, L. Birnbacher, M. Viermetz, M. Walter, J. Schulz, F. Pfeiffer, and J. Mohr, "Note: Gratings on low absorbing substrates for x-ray phase contrast imaging," *Review of Scientific Instruments*, vol. 86, no. 12, 2015. [Online]. Available: http://scitation.aip.org/content/aip/journal/rsi/86/12/10.1063/1.4939055

[14] T. Thuering and M. Stampanoni, "Performance and optimization of x-ray grating interferometry." *Philos Trans A Math Phys Eng Sci*, vol. 372, no. 2010, p. 20130027, Mar 2014.

[15] M. Irani and S. Peleg, "Improving resolution by image registration," *CVGIP: Graphical Models and Image Processing*, vol. 53, no. 3, pp. 231 – 239, 1991. [Online]. Available: http://www.sciencedirect.com/science/article/pii/104996529190045L

[16] J. Herzen, T. Donath, F. Pfeiffer, O. Bunk, C. Padeste, F. Beckmann, A. Schreyer, and C. David, "Quantitative phase-contrast tomography of a liquid phantom using a conventional x-ray tube source," *Opt. Express*, vol. 17, no. 12, pp. 10 010–10 018, Jun 2009. [Online]. Available: http://www.opticsexpress.org/abstract.cfm?URI=oe-17-12-10010

Image reconstruction for few-view and limited-angle MECT based on group-wise low rank constraint

Wenying Wang[1], Liuyuan Zhou[1], Xucheng Zhu[3], Yuxiang Xing[1,2*]
[1]Department of Engineering Physics, Tsinghua University, Bejing, China
[2]Key Laboratory of Particle & Radiation Imaging (Tsinghua University), Ministry of Education, China
[3]UC Berkeley-UCSF Graduate Program in Bioengineering, CA, USA
*Email of corresponding author: xingyx@mail.tsinghua.edu.cn

***Abstract*—In Multi-energy X-ray computed tomography (MECT), relation between photon energy and reaction cross section suggests information of material compositions. Using different energy spectra independently, traditional MECT requires multiple scan periods and causes extra exposure dose. To alleviate the total dose concern, we propose a new algorithm to reconstruct from under-sampling data, either limited-angle or few-view MECT data. A new group-wise low-rank penalty is designed to constrain spectral attenuation images, searching relationship among attenuation coefficients under different energies. Our method gives accurate reconstructions of attenuation map with under-sampled projection data, identifying its great potential in new MECT system design and reconstruction strategy, which could benefit in the aspects of lower dose and efficient implementation.**

I. Introduction

The past decades have seen X-ray computed tomography(CT) technology improved in both instrumentation and reconstruction algorithms areas. The advanced X-ray emitter and photon-counting detector array boost MECT from paper talk to practice. In common X-ray emitter, accelerated electrons hit on the target made of heavy material like Pd. Bremsstrahlung effects of electrons emit X-ray distributed in consecutive energy spectrum. X-ray photon carrying different energy has different cross-section when reacting with material, which cause problems (such as beam hardening) in conventional CT. However, if we utilize this features, we can benefit from information contained in energy domain. In 1976, Alvarez et al firstly obtained energy spectral information in CT reconstruction. [1] Later on, concepts like MECT, spectral CT joined the most popular topics. [2] [3]

Meanwhile, prosperity in computer science build up calculation capability, which benefits iterative reconstruction algorithms. Gorden published a tutorial on algebraic reconstruction techniques (ART) in 1974, ART [4] laid the foundation for future iterative reconstruction algorithms design. Methods such as Model-based Iterative Reconstruction (MBIR) [5] [6], total-variance (TV) [7] constraint improved image quality. Generally, iterative methods outperform traditional analytical algorithms, especially in low-dose or under-sampled data acquisition, in which case the reconstruction problem is of severe illness .

Nuclear norm or low-rank penalty are strong constraints efficient in figuring out linear relations between frames. It has been a well acknowledged tool in temporal CT and spectral CT. In time-resolved CT, Chen used nuclear norm to regularize the reconstruction of temporal frame series, exploiting structural information of the object. [8]

The purpose of this paper is to present an accurate image reconstruction method for under-sampling MECT like few-view and limited-angle. Utilizing conjugation pairs of rays, we firstly use other energy information as supplement to get prior images. Then, a group-wise low rank constrain (GLC) is applied to images to eliminate artifacts caused by data deficiency or inconsistency.

II. Method

A. MECT System Model

In this work, we denote MECT projections as $\mathbf{p}_k \in \mathbf{R}^{N_p} (k = 1, 2, ..., K)$ under K different X-ray energy spectra with N_P being the dimension of $\mathbf{p}_k$, i.e., # of projection views $\times$ # of detector bins per view. Let $\mathbf{x}_k \in \mathbf{R}_+^{N_x}$ be the map of linear attenuation coefficients at k^{th} X-ray spectrum with N_x being the number of discrete pixels in images. With polychromatic model, projections from such a multi-energy CT can be described as following,

$$\mathbf{p}_k = -\ln \int S_k(E) \exp\left(-\mathbf{A}_k \mathbf{x}(E)\right) dE, \quad k = 1, ..., K \quad (1)$$

where $\mathbf{A}_k \in \mathbf{R}^{N_p \times N_x}$ is the system matrix characterizing the geometrical configuration of data acquisition, and $S_k(E)$ is the normalized effective spectrum ($\int S_k(E)dE = 1$) combining the effect of source spectrum and detector response which can be wide (e.g. dual source systems) or narrow (e.g. energy selective systems). According generally used single-energy CT, the data fidelity term is commonly measured by a linear relationship [4] :

$$\mathbf{A}_k \mathbf{x}_k = \mathbf{p}_k \quad (2)$$

or, in noisy case with Gaussian, by a weighted least-square term $\Phi(\mathbf{X}) = \sum_{k=1}^{K} \left(\mathbf{A}_k \mathbf{x}_k - \mathbf{p}_k\right)^{\mathrm{T}} \mathbf{W}_k \left(\mathbf{A}_k \mathbf{x}_k - \mathbf{p}_k\right)$ where $^{\mathrm{T}}$ denotes matrix transposition. Obviously, $\mathbf{x}_k$ is a comprehensive description of $\mathbf{x}_k(E)$ under the spectrum $S_k(E)$.

As shown in Fig. 1, the angular coverage for different energy (by changing tube potential or energy threshold) can be either interlaced distribution (few-view) or segmented distribution (limited angle). For such an MECT reconstruction problem,

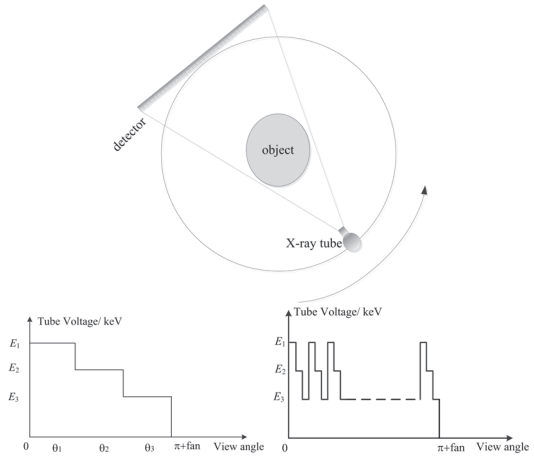

Fig. 1: Different configuration of MECT. Top: CT system geometry; Bottom: Segmental & Interlaced distribution of multi-energy data

we intend to reconstruct $N_x \times K$ unknowns from $N_p \times K$ data. In a regular MECT system, one would expect $N_p \sim N_x$. With our MECT configuration, $N_p \times K \sim N_x$, i.e., we reduce the size of data by a factor of $1/K$ compared with a regular MECT scan, which could mean reducing dose and scan time by $1/K$. Therefore, under such conditions, the data size for each energy is $N_p \ll N_x$ so that the reconstruction is severely ill-posed and severe artifacts will degrade image quality of reconstructions if reconstruct $\mathbf{x}_k$ from $\mathbf{p}_k$ with general reconstruction methods. In this work, we propose a level-grouped low-rank penalty to incorporate the common information between $\mathbf{p}_k$'s .

B. Group-wise Low-rank Penalty

Low-rank penalty is especially suitable for spectral CT reconstruction as the attenuation coefficient maps under different energy spectrum share same structural information of imaging objects. For a certain range of materials, their energy-dependent attenuation coefficients variations obey similar $\mu - E$ curves. The success of basis material and Compton-photoelectric decomposition methods told us the strong correlation between the $\mu - E$ curves of different materials. In typical medical imaging problems, the most important materials can be separated into groups according to attenuation level, e.g. osseous tissue with higher attenuation capacity and soft tissue with lower attenuation capacity. In this work, we propose a new low-rank penalty to constraint pixels within groups based on their attenuation level.

For the convenience of this discussion, let us denote a spatial-spectral matrix $\mathbf{X} \in \mathbf{R}^{N_x \times K}$ for final images:

$$\mathbf{X} = \begin{bmatrix} \mathbf{x}_1 & \mathbf{x}_2 & \dots & \mathbf{x}_K \end{bmatrix} \tag{3}$$

Assuming pixels in an object can be categorized into M groups, we define a characteristic vector χ with its elements being:

$$\chi_i^m = \begin{cases} 1 & \text{if pixel } \ i \in \text{Group}(m) \\ 0 & \text{(else)} \end{cases} \tag{4}$$

(We describe the pixel grouping in more detail in Section II-C.) Then we can form M spatial-spectral matrices of from images $\mathbf{x}_k$:

$$\mathbf{X}_m = \text{Diag}(\chi^m)\mathbf{X} \tag{5}$$

Within each group, a strong low rank penalty can be applied by:

$$\text{minimize} \quad \Psi(\mathbf{X}) = \sum_{m=1}^{M} \text{Rank}(\mathbf{X}_m) \tag{6}$$

With singular value decomposition (SVD), we can get the nuclear norm of each matrix,

$$\mathbf{X}_m = \mathbf{U}_m \mathbf{\Sigma}_m \mathbf{V}_m^{\mathrm{T}} \tag{7}$$

where $\mathbf{U}_m$ and $\mathbf{V}_m$ are orthogonal matrices consisting of singular vectors of spatial-spectral image matrix $\mathbf{X}_m$, and $\mathbf{\Sigma}_m$ is a diagonal matrix with its diagonal elements showing singular value of corresponding singular vector:

$$\Sigma_m = \begin{bmatrix} \sigma_{1,m} & 0 & \cdots & 0 \\ 0 & \sigma_{2,m} & \cdots & 0 \\ \vdots & \vdots & \ddots & \vdots \\ 0 & 0 & \cdots & \sigma_{K,m} \end{bmatrix} \tag{8}$$

In this way, Eq. (6) can be also expressed as:

$$\text{minimize} \quad \Psi(\mathbf{X}) = \sum_{m=1}^{M} \sum_{k=1}^{K} \sigma_{k,m}^l \tag{9}$$

Here, we use l order nuclear norm for generality. When l is set to 0, the nuclear-norm constraint degenerates to low-rank penalty. If attenuation coefficients for different tissues within a group are linearly dependent, the principle components will represent most information of the image, while secondary components will have relatively small contribution or even ignorable.

C. Pixel grouping

Pixel grouping is intended to limit the type of matters within a group. There will be many ways to do it, such as segmentation and clustering. Here, we present a straightforward and easy-to-implement way to do it.

In many applications, we are quite clear the material composition of objects being imaged. It is convenient to group pixels according to their attenuation capacity, i.e. level-based grouping. In this case, grouping is simplified to choosing thresholds and the indicator vector is define by:

$$\chi_i^m = \begin{cases} 1 & \text{if } \ T_m^{\text{Low}} < x_{k,i} \leq T_m^{\text{High}} \\ 0 & \text{(else)} \end{cases} \tag{10}$$

Here, $x_{k,i}$ is an element of $\mathbf{x}_k$, and the thresholds $T_m^{\text{Low}}$and T_m^{High} for m^{th} group vary according to the energy spectrum of k^{th} projection data $S_k(E)$. Setting $T_m^{\text{High}} = T_{m+1}^{\text{Low}}$ is a natural choice, but not necessary. Notice that $\mathbf{x}_{k,m}, \mathbf{x}_{k,m} \quad \in \mathbf{R}^{N_x}$. As we mentioned in Section II-A, $\mathbf{x}_k$ is an comprehensive measure of attenuation under kth spectrum. Assume we have

two typical matters (A_m and A_{m+1}) of interest in group m and $m+1$, we can calculate the threshold T_m^{High} with effective attenuation coefficient of $\tilde{\mu}_{A,k}$ under spectrum $S_k(E)$.

$$T_m^{\text{High}} = a\tilde{\mu}_{A_m,k} + b\tilde{\mu}_{A_{m+1},k},\ a+b=1 \tag{11}$$

In spectral CT imaging, we can pre-measure $\tilde{\mu}_{A,k}$ experimentally. Parameters a and b can be manually or automatically adjusted. If MECT running in a stable condition with no frequent tube potential or energy threshold adjustment, Eq. (11) can be pre-calculated and optimized.

D. Method Implementation

Combining the data-fidelity term and the nuclear-norm constraint term using Eqs. (2) and (9), we can express the overall optimization problem with an objective function as follow:

$$\Phi(\mathbf{X}) = \arg\min_{\mathbf{X}>0}\left(\sum_{k=1}^{K}\left\|\mathbf{A}_k\mathbf{x}_k - \mathbf{p}_k\right\|_2^2 + \lambda\sum_{m,k}\sigma_{k,m}^l\right) \tag{12}$$

For simplicity, $l1$-norm for the nuclear term is chosen in our implementation. For the data-fidelity term, image $\mathbf{x}_k$ is only related to projection data $\mathbf{p}_k$ and system matrix $\mathbf{A}_k$, so corresponding updating under different energy spectrum are unrelated. So it is convenient to apply ART separately to each image,

$$\mathbf{x}_k^{(i)} = \mathbf{x}_k^{(i-1)} + \alpha\mathbf{A}_k^{\mathrm{T}}\left[\ \mathbf{p}_k - \mathbf{A}_k\mathbf{x}_k^{(i-1)}\right] \tag{13}$$

For the nuclear-norm term, we use Chen's singular value thresholding (SVT) function [8]. The function is defined by,

$$\mathrm{SVT}_\lambda(\mathbf{X}) = \mathbf{U}(\mathbf{\Sigma} - \lambda\mathbf{I})_+\mathbf{V}^{\mathrm{T}} \tag{14}$$

$$(\mathbf{\Sigma} - \lambda\mathbf{I})_+ = \begin{cases}\sigma_i - \lambda, & \sigma_i \geq \lambda \\ 0, & \sigma_i < \lambda\end{cases} \tag{15}$$

In order to implement a simple but effective reconstruction method for limited-angle MECT data, we propose the iterative algorithm as pseudocode Algorithm 1.

Algorithm 1 Group-wise Low-rank Constraint (GLC)

Input:
Projection data: $\mathbf{p}_k, k = 1, 2, ..., K$
Heuristic images: $\mathbf{X}^0 = (\mathbf{x}_1^0, ..., \mathbf{x}_K^0)$
Thresholds: $T_m, m = 0, 1, ..., M$
Output: $\mathbf{X}^I$

repeat
  for $k = 1$ to K **do**
    $\mathbf{x}_k^{(i)} \leftarrow \mathbf{x}_k^{(i-1)} + \alpha\mathbf{A}_k^{\mathrm{T}}\left[\ \mathbf{p}_k - \mathbf{A}_k\mathbf{x}_k^{(i-1)}\right]$
  end for
  $\tilde{\mathbf{X}}^{(i)} \leftarrow (\mathbf{x}_1^0, ..., \mathbf{x}_K^0)$
  for $m = 1$ to M **do**
    $\tilde{\mathbf{X}}_m^{(i)} \leftarrow \mathrm{Diag}(\chi^m)\tilde{\mathbf{X}}^{(i)}$
    $\mathbf{X}_m^{(i)} \leftarrow \mathrm{SVT}_\lambda\left[\tilde{\mathbf{X}}_m^{(i)}\right]$
  end for
  $\mathbf{X}^{(i)} = \sum_{m=1}^{M}\mathbf{X}_m^{(i)}$
until $\left\|\mathbf{X}^{(i)} - \mathbf{X}^{(i-1)}\right\|_2 < \epsilon\left\|\mathbf{X}^{(i-1)}\right\|_2$

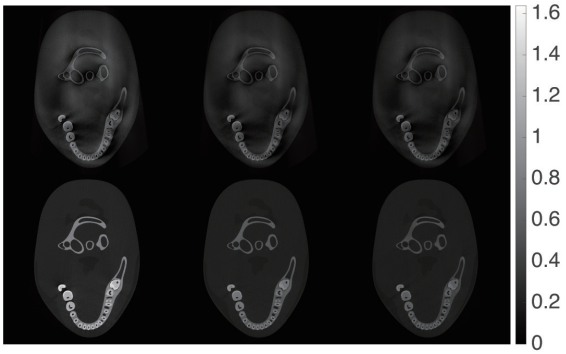

Fig. 2: upper: ART-reconstructed prior images from filled-up projection data. bottom: Attenuation map reconstructions of SegMECT with GLC. Energy from left to right: 60kVp, 90kVp, 120kVp.

III. Experimental Results

To examine our algorithm, a dental phantom and projection data as in [9] ars used so to ease result comparison. All images are of 512^2 pixels, and the detector array has 960 bins.

A. SegMECT reconstruction

In SegMECT, 360 views are uniformly distributed in a round. Sequentially 120 views with step of 1° for each energy are acquired separately at 60kVp, 90kVp and 120kVp, denoted as $\mathbf{p}_1$, $\mathbf{p}_2$ and $\mathbf{p}_3$. To obtain a prior images for k^{th} energy, we use weighted projection from other energy (k'^{th}) to form a complete (non-consistent) data set. The weight is calculated by the congregate ratio of conjugate rays in two energy: $w_{k,k'} = \frac{\sum_j p_j}{\sum_{j'} p_{j'}}$ with j and j' forming groups of conjugate rays. In this way we can get a filled-up full-angle projection data for each energy. With the supplemented data, we can reconstruct three prior images. As shown in the upper row of Fig. 2, we can see some structure like teeth and jawbone. In the meantime, prior images are suffused with severe artifact introduced by inconsistency in filled-up data. We apply our method using these priors of low quality. The accurate projection data in different energy are utilized mutually by GLC. It recovers attenuation information and eliminate artifacts. The image quality is improved with clearer structure, fewer artifact and higher accuracy.

We decompose the reconstructions into two basis materials (bone and soft tissue) according tri-energy attenuation coefficient maps. Compared with other reconstruction algorithms like FBP, Q-TV, PICCS, ART-TV in Fig. 3, our algorithm obviously provides best result. Quantitative comparison is shown in Table I.

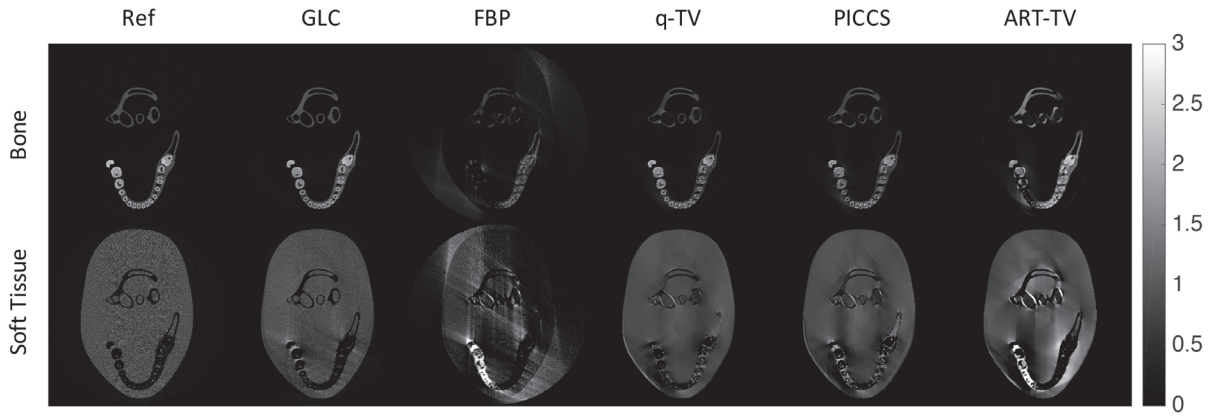

Fig. 3: Decomposition of the basis materials.
The first column shows full data FBP reconstruction result for reference.

TABLE I: MSE and PSNR: quantitative comparison between different reconstruction results.

	GLC	FBP	Q-TV	PICCS	ART-TV
MSE	0.0240	0.1628	0.0329	0.0417	0.1017
PSNR	25.05	16.74	23.68	22.66	18.78

B. MECT with interlaced energy distribution

For further evaluate the performance of our method, we test on MECT data with interlaced distribution of energy, we acquire views $(1 + 15k)^\circ$ at 60kVp, views $(6 + 15k)^\circ$ at 90kVp, views $(11 + 15k)^\circ$ at 120kVp ($k = 1, ..., 24$). As the streak artifacts in each energy map are different, part of these artifacts will be suppressed by GLC penalty. TV-constraint [7]can help reducing residue streaks, while GLC maintains most of the structural information. The heuristic prior images and the reconstruction results are shown in Fig. 4. Obviously, the algorithm helps to delineate the details of teeth and soft tissue in the center of the FOV, while streaking artifacts are suppressed to a lower level. Additional smoothing prior might help reduce residual streaks.

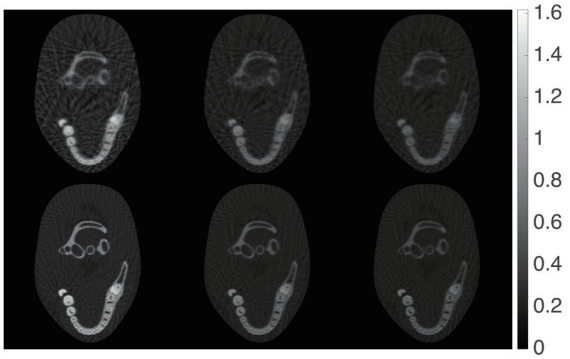

Fig. 4: upper: ART-reconstructed prior images
bottom: Attenuation map reconstructions with GLC
tube voltage from left to right: 60kVp, 90kVp, 120kVp.

IV. Conclusion

In this work, we introduce a group-wise low rank constraint (GLC) to propose an accurate spectral CT imaging for multi-energy CT with under-sampled data. Different from low rank penalty on full image space or patches, our GLC can model the relationship of $\mu - E$ among similar matters within a group in a more concise way. An easy-to-implement level-based grouping strategy is presented. The proposed method is tested with simulation studies on SegMECT [9] (limited-angle) and few view cases. Results are of better quality compared with algorithms like FBP, Q-TV, PICCS, ART+TV.

Acknowledgment

This work is supported by grants from the National Natural Science Foundation of China (No. 11275104 and No. 11435007).

References

[1] Alvarez R E. *Extraction of energy dependent information in radiography*[D]. Dept. of Electrical Engineering, Stanford University., 1976.
[2] Willson P D. *Apparatus and method for automatic recognition of concealed objects using multiple energy computed tomography: U.S. Patent 6,018,562*[P]. 2000-1-25.
[3] Schlomka J P, Roessl E, Dorscheid R, et al. *Experimental feasibility of multi-energy photon-counting K-edge imaging in pre-clinical computed tomography*[J]. Physics in medicine and biology, 2008, 53(15): 4031.
[4] Gordon R. *A tutorial on ART (algebraic reconstruction techniques)*[J]. Nuclear Science, IEEE Transactions on, 1974, 21(3): 78-93.
[5] Yu Z, Thibault J B, Bouman C, et al. *Fast model-based X-ray CT reconstruction using spatially nonhomogeneous ICD optimization*[J]. Image Processing, IEEE Transactions on, 2011, 20(1): 161-175.
[6] Zhang R, Thibault J B, Bouman C A, et al. *A model-based iterative algorithm for dual-energy X-ray CT reconstruction*[C]//Proc. Int. Conf. Image Form. in X-ray CT. 2012: 439-443.
[7] Sidky E Y, Pan X. *Image reconstruction in circular cone-beam computed tomography by constrained, total-variation minimization*[J]. Physics in medicine and biology, 2008, 53(17): 4777.
[8] Chen G H, Li Y. *Synchronized multiartifact reduction with tomographic reconstruction (SMART-RECON): A statistical model based iterative image reconstruction method to eliminate limited-view artifacts and to mitigate the temporal-average artifacts in time-resolved CT*[J]. Medical physics, 2015, 42(8): 4698-4707.
[9] Shen L, Xing Y. Multienergy CT acquisition and reconstruction with a stepped tube potential scan[J]. Medical physics, 2015, 42(1): 282-296.

Isocenter Determination for Arbitrary Planar Cone-Beam CT Scan Trajectories

Andreas Fieselmann and Ludwig Ritschl
Siemens Healthcare GmbH, Erlangen, Germany
email: andreas.fieselmann@siemens.com, ludwig.ritschl@siemens.com

***Abstract*—Novel cone-beam CT system designs allow acquiring projection data using non-circular scan trajectories. For example, twin robotic X-ray systems can acquire data on scan paths composed of linear, circular, ellipsoidal or rectangular segments and combinations thereof. The ideal isocenter is the point of intersection of all central rays from the tube to the detector center. The isocenter usually acts as a reference point to determine the center of the reconstruction volume. With increasing flexibility and complexity of scan trajectories it becomes more difficult to determine a practical isocenter. In this work, we present a novel and generic method to determine the isocenter of an arbitrary planar scan trajectory. It iteratively finds an isocenter which minimizes the distances to all central rays excluding rays which were not designed to pass near an isocenter. Our method shows high accuracy (distance of computed isocenter to reference location <5.4 mm) and robustness (influence of additional central rays not near the isocenter on computed isocenter <0.2 mm). This method can support clinical use of more complex scan trajectories with robotic X-ray systems.**

I. Introduction

Cone-beam computed tomography (CBCT) is an established modality in medical imaging which is used in a wide field of applications. Since the intended use covers different fields from diagnostic imaging to interventional imaging in the angio suite and operating room there exist several dedicated systems.

Two examples for such CBCT systems are the Artis zeego (Siemens Healthcare) and Multitom Rax (Siemens Healthcare) shown in Fig. 1 where X-ray tube and detector are kinematically uncoupled [1].

Many systems can also acquire CBCT data also using non-circular planar trajectories. The reasons therefore are manifold: Often the patient and table configuration setup do not allow for circular paths because of collision issues. Another reason might be a limited rotation range due to mechanical system properties. It was shown in [2] that the combination of rotational and translational scan segments can lead to the same volume coverage like a standard short scan (180° + fan angle, [3]). In these cases the field of measurement (FOM) which is defined by completely sampled voxels (>180°) can differ strongly from the circular shape in the case of a circular scan.

All trajectories require a geometric calibration which is typically performed offline using a dedicated calibration phantom [4]. The calibration information can be stored in form of perspective 3×4 matrices or source and detector coordinates. These geometric information will serve as input for image reconstruction. To guarantee that the volume which is typically a cube and the FOM are matching an additional registration procedure must be performed. This can be included into the calibration step before storing the geometry data or in the reconstruction pipeline before backprojection. To avoid an additional backprojection step it is desirable that this registration can be performed only using the geometric data of the scan trajectory.

For a perfectly circular scan, a circular fit can be applied where the center of the circle is the so-called isocenter.

A practical approach for fitting a circle to a scan trajectory has been described by Navab et al. [5]. First the axes of rotations between consecutive frames are determined. From this set of axes a mean axis of rotation is computed. Then a cylinder is fitted parallel to the mean axis of rotation to all X-ray source positions. Additionally a plane is fitted orthogonal to the axis of rotation to all X-ray source positions. The intersection of the plane with the cylinder is defined as the effective isocenter. An alternative approach for fitting a circle to the scan trajectory has been described by Jia et al. [6].

However, for non-circular and even non-symmetric trajectories an approach based on a circular fit will fail. In this paper we describe a method that can handle the isocenter computation of any arbitrary planar trajectory. Intended detector offsets or shifts will also be considered.

II. Material and Methods

A. Isocenter Determination

The complete scan consists of N_v views. For each view the corresponding focus position $\mathbf{a}_i = (a_{1,i}, a_{2,i}, a_{3,i})^\mathrm{T}$ ($i = 1, \ldots, N_\mathrm{a}$) and central ray unit vector $\mathbf{n}_i = (n_{1,i}, n_{2,i}, n_{3,i})^\mathrm{T}$ are known. These two parameters can be determined from the corresponding 3×4 projection matrices. We define the isocenter $\mathbf{p} = (p_1, p_2, p_3)^\mathrm{T}$ as the point that minimizes the sum of squared distances to all central rays. It is given by the expression [7], [8]

$$\begin{bmatrix} \sum_i (1-n_{1,i}^2) & -\sum_i n_{1,i}n_{2,i} & -\sum_i n_{1,i}n_{3,i} \\ \sum_i -n_{1,i}n_{2,i} & \sum_i (1-n_{2,i}^2) & -\sum_i n_{2,i}n_{3,i} \\ \sum_i -n_{1,i}n_{3,i} & -\sum_i n_{2,i}n_{3,i} & \sum_i (1-n_{3,i}^2) \end{bmatrix} \begin{bmatrix} p_1 \\ p_2 \\ p_3 \end{bmatrix} = \begin{bmatrix} \sum_i (1-n_{1,i}^2)a_{1,i} - n_{1,i}n_{2,i}a_{2,i} - n_{1,i}n_{3,i}a_{3,i} \\ \sum_i -n_{1,i}n_{2,i}a_{1,i} + (1-n_{2,i}^2)a_{2,i} - n_{2,i}n_{3,i}a_{3,i} \\ \sum_i -n_{1,i}n_{3,i}a_{1,i} - n_{2,i}n_{3,i}a_{2,i} + (1-n_{3,i}^2)a_{3,i} \end{bmatrix}. \quad (1)$$

This expression can be written as a linear system of equations

$$\mathbf{A}\mathbf{p} = \mathbf{b} \quad (2)$$

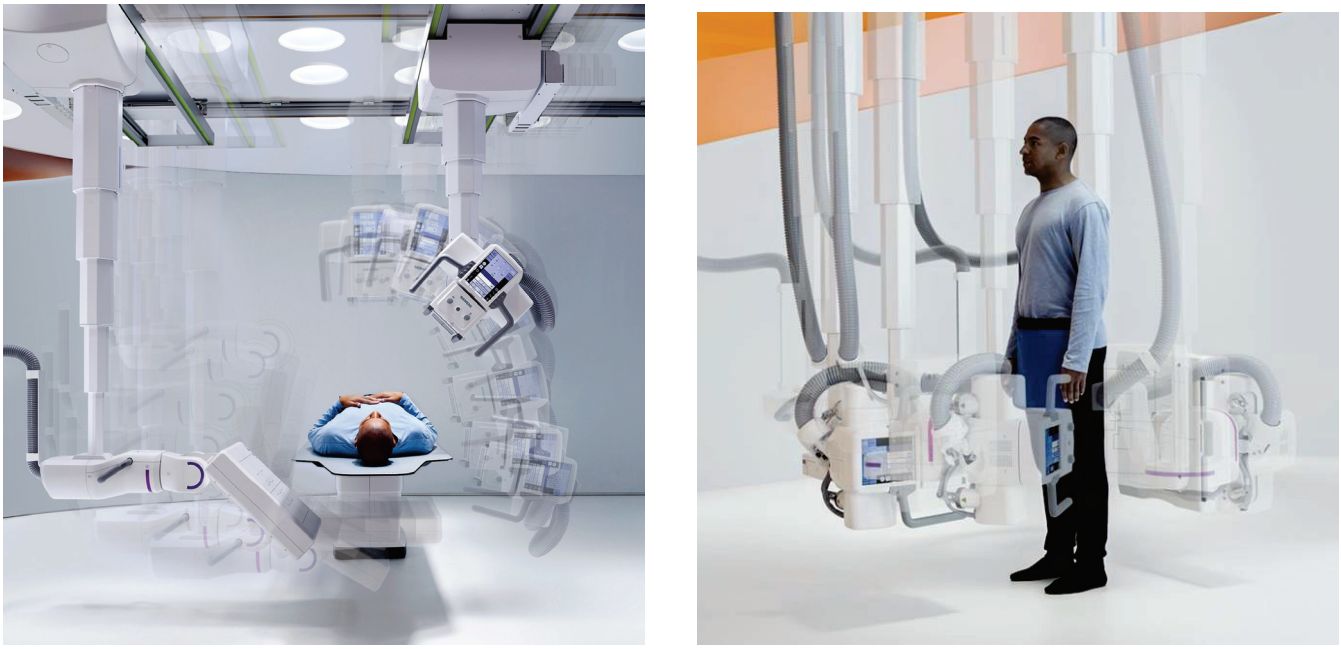

(a) scan around table (b) standing patient scan

Figure 1. Twin robotic X-ray system (Multitom Rax, Siemens Healthcare)

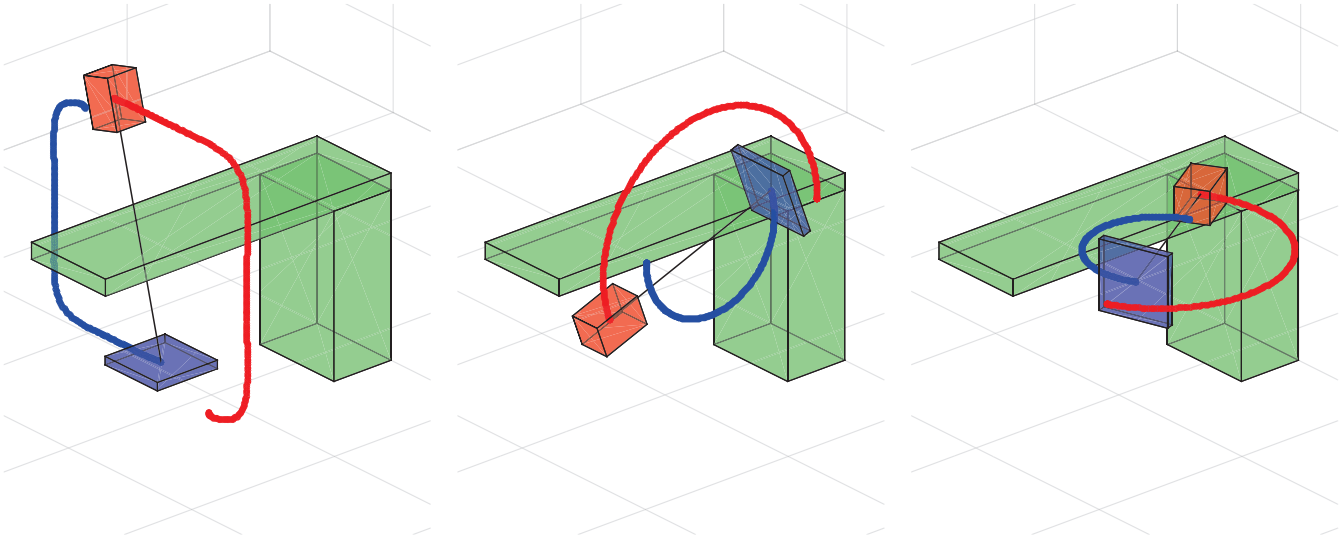

(a) scan around table (b) scan besides table (e.g. of hand) (c) standing patient scan

Figure 2. Examples of tube and detector scanning trajectories for Multitom Rax and their respective end positions.

which can be uniquely solved for $\mathbf{p}$ if not all central rays are parallel or anti-parallel. In (1) all central rays contribute equally to determine $\mathbf{p}$. However, there can be conditions when certain central rays should not be considered when determining the isocenter. E.g., a linear scan segment where detector and tube are moved on parallel paths can be added to a rectangular scan to increase coverage of the Radon space (Fig. 3). In this case the central rays of the linear segment intentionally do not pass near a common isocenter.

To account for central rays not passing through an isocenter a weighting factor w_i^j $(j = 1, 2, \ldots)$ is included in all sums in (1) such that

$$\sum_i (\ldots) \quad \Rightarrow \quad \sum_i w_i^j (\ldots) \quad . \tag{3}$$

Here w_i^j defines the weight of the ith central ray in the jth iteration step. The iterative approach can be written in pseudo code as:

initialize $w_i^1 = 0 \; \forall i$
repeat
S1: compute $\mathbf{p}^j$ by (1) and (3)
S2: compute distance d_i^j of each central ray to $\mathbf{p}^j$
S3: set w_i^{j+1} depending on d_i^j
until w_i^{j+1} is equal to w_i^j

In the step S1 the isocenter $\mathbf{p}^j$ is computed based on (1) and (3). In step S2 the Euclidean distance d_i^j of each central rays to $\mathbf{p}^j$ is computed as

$$d_i^j = ||(\mathbf{f}_i - \mathbf{p}^j)((\mathbf{f}_i - \mathbf{p}^j)^T \mathbf{n}_i)\mathbf{n}_i||_2 \quad (4)$$

In step S3 the weights w_i^{j+1} are computed as

$$w_i^{j+1} = f(d_{\max} - d_i^j) \quad (5)$$

where the function f can be a step function, a sigmoidal function or another type of (non-linear) function which has output values in the range $[0, 1]$. $d_{\max}$ indicates the maximal acceptable distance from the isocenter such that the projection view is still considered for determination of the isocenter. If it is a step function then the weights are set to zero if the distance exceeds $d_{\max}$.

B. Evaluation Approach

The evaluation is divided into two parts. In the first part of the evaluation we investigated the *accuracy* of the method. We computed the isocenter from the set of projection matrices of different types of trajectories (planar circular, planar ellipsoidal, planar rectangular; see Fig. 2). For each trajectory we performed an image reconstruction with the reconstruction center placed in this isocenter. We then determined the center of a bounding box around all voxels from the reconstruction which are seen in all projection views. This is considered to be the reference reconstruction center. We computed the distance of the isocenter to the center of the bounding box.

In the second part of the evaluation we investigated the *robustness* of the method. We created a scan trajectory consisting of a planar rectangular scan and an additional linear scan with central rays intentionally not passing through a common isocenter to increase coverage of Radon space (Fig. 3). We compared the isocenter computed from the extended trajectory and the non-extended trajectory. Our method is considered robust if the additional linear scan does not significantly affect the computation of the isocenter.

III. Results

The distances of the computed isocenter (using our novel method) and the measured isocenter (using the bounding box around the voxels in the reconstructed volume) are: 2.99 mm (planar circular), 1.44 mm (planar ellipsoidal), and 5.35 mm (planar rectangular).

Fig. 4 shows the position of the computed isocenter after the first and last iteration step (8^{th} step) when a rectangular scan with additional linear segment is used. The distance to the isocenter computed from the same trajectory without linear scan was 30.59 mm (first iteration step) and 0.17 mm (last iteration step).

IV. Discussion and Conclusion

For all trajectories investigated the distance of the computed isocenter to the reference point was small (<5.4 mm). Thus, it has been shown that the method can determine a practical isocenter to define the center of the reconstruction volume. Only a very small influence on the computed isocenter (0.17 mm distance) has been observed when an additional linear scan was added. It shows that the method is robust and works if (intentionally) certain central rays do not pass near an isocenter.

The approach has been evaluated for planar trajectories but may be extended to non-planar trajectories as well such as trajectories that cover a larger volume along the patient axis [9], [10].

To conclude, we have presented a novel and generic method to determine the isocenter from arbitrary planar CBCT scan trajetories. This method can support clinical application of more complex scan trajectories using robotic X-ray systems.

Discalaimer

The concepts and information presented in this paper are based on research and are not commercially available.

References

[1] A. Fieselmann, J. Steinbrener, A. K. Jerebko, J. M. Voigt, R. Scholz, L. Ritschl, and T. Mertelmeier, "Twin robotic x-ray system for 2D radiographic and 3D cone-beam CT imaging," in *Proc. SPIE Medical Imaging 2016: Physics of Medical Imaging*, vol. 9783, 2016, p. 97830G.

[2] L. Ritschl, J. Kuntz, and M. Kachelrieß, "The rotate-plus-shift C-arm trajectory: complete CT data with limited angular rotation," in *Proc. SPIE Medical Imaging 2015: Physics of Medical Imaging*, vol. 9412, 2015, p. 941221.

[3] D. L. Parker, "Optimal short scan convolution reconstruction for fan-beam CT," *Medical Physics*, vol. 9, no. 2, pp. 254–257, 1982.

[4] N. K. Strobel, B. Heigl, T. M. Brunner, O. Schuetz, M. M. Mitschke, K. Wiesent, and T. Mertelmeier, "Improving 3D image quality of x-ray C-arm imaging systems by using properly designed pose determination systems for calibrating the projection geometry," in *Proc. SPIE Medical Imaging 2003: Physics of Medical Imaging*, vol. 5030, 2003, pp. 943–954.

[5] N. Navab, A. Bani-Hashemi, M. S. Nadar, K. Wiesent, P. Durlak, T. M. Brunner, K. Barth, and R. Graumann, "3D reconstruction from projection matrices in a C-arm based 3D-angiography system," in *Proc. Medical Image Computing and Computer-Assisted Interventation (MICCAI)*, vol. 1496, 1998, pp. 119–129.

[6] F. Jia, Y. Li, H. Xu, X. Zhang, and Q. Hu, "A simple method to calibrate projection matrix of C-arm cone-beam CT," in *Proc. IEEE International Conference on Biomedical Engineering and Biotechnology*, 2012, pp. 682–685.

[7] G. Slabaugh, R. Schafer, and M. Livingston, "Optimal ray intersection for computing 3D points from N-view correspondences," Tech. Rep., October 2 2001.

[8] R. I. Hartley and A. Zisserman, *Multiple View Geometry in Computer Vision*, 2nd ed. Cambridge University Press, 2004.

[9] Z. Yu, A. Maier, G. Lauritsch, F. Vogt, M. Schönborn, C. Köhler, J. Hornegger, and F. Noo, "Axially extended-volume C-arm CT using a reverse helical trajectory in the interventional room," *IEEE Transactions on Medical Imaging*, vol. 34, no. 1, pp. 203–215, 2015.

[10] Z. Yu, G. Lauritsch, F. Dennerlein, Y. Mao, J. Hornegger, and F. Noo, "Extended ellipse-line-ellipse trajectory for long-object cone-beam imaging with a mounted carm system," *Physics in Medicine and Biology*, vol. 61, no. 4, pp. 1829–1851, 2016.

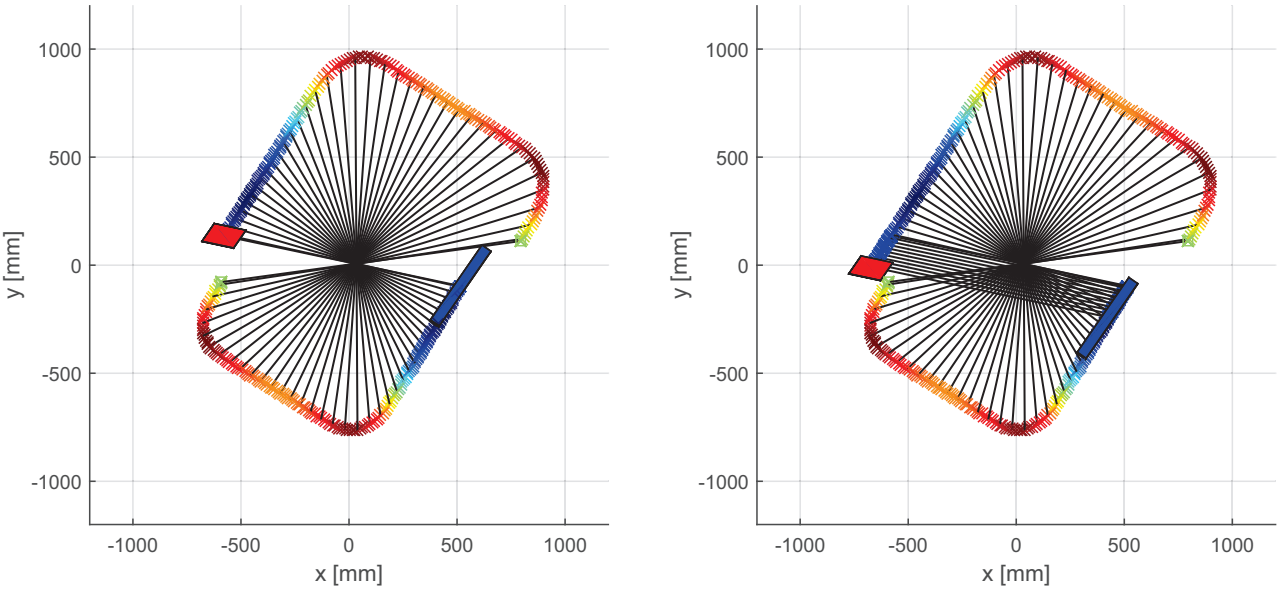

(a) (b)

Figure 3. Plot of rectangular scan trajectory (a) with and (b) without additional linear scan. Source-to-image distance is encoded by colors. Every 5th central ray is plotted.

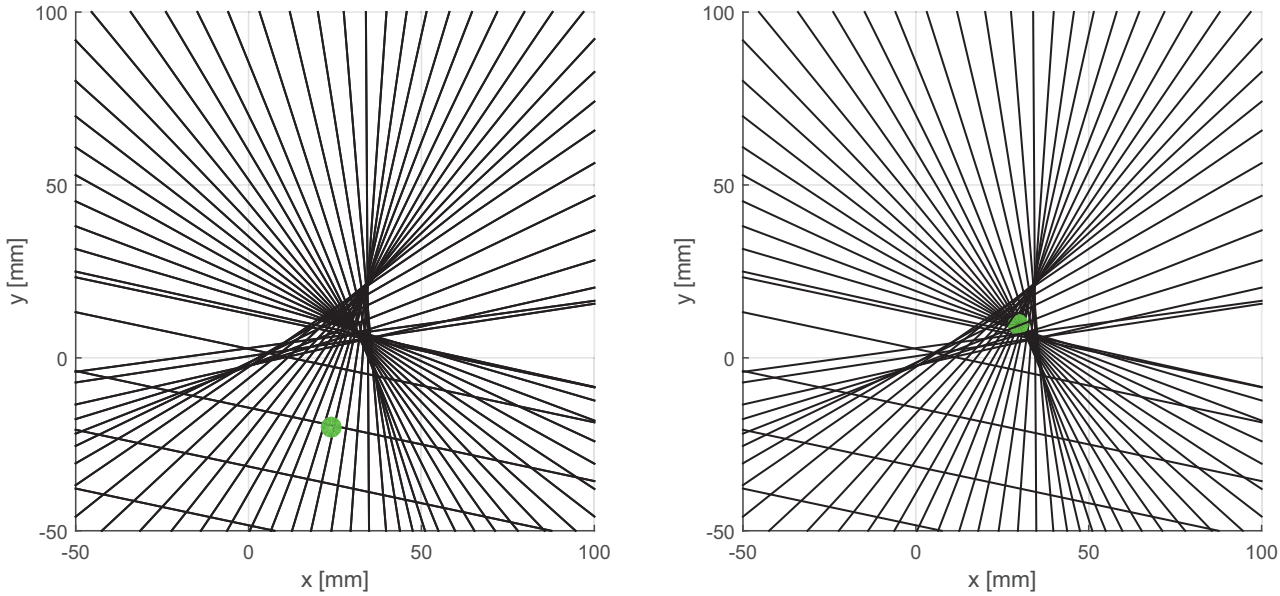

(a) after first iteration (b) after last iteration

Figure 4. Position of computed isocenter (green point) after first and last iteration step.

Material reconstruction for spectral computed tomography with detector response function

Jiulong Liu, and Hao Gao

***Abstract*—Different from the conventional computed tomography (CT), spectral CT based on energy-resolved photon-counting detectors is able to provide the unprecedented material compositions. However, an important missing piece for accurate spectral CT is to incorporate the detector response function (DRF), which is distorted by factors such as pulse pileup and charge-sharing. In this work, we propose material reconstruction methods for spectral CT with DRF. The simulation results suggest that the proposed methods provided more accurate material compositions than the standard method without DRF. Moreover, the proposed method with linear data fidelity had improved reconstruction quality from the proposed method with nonlinear data fidelity.**

***Index Terms*—image reconstruction, spectral CT, detector response function.**

I. Introduction

The X-ray photon transport is essentially polyenergetic rather than monoenergetic. That is both X-ray photons and attenuation coefficients have the spectral dependence. Thus the ideal forward model should be also polyenergetic. However, since the conventional CT detectors are charge-integrating with no spectral resolution, the CT inverse problem is often based on the monoenergetic forward model and equivalently reconstructs a spectrally-averaged attenuation image. As a result, the imaging quality can be significantly deteriorated, the so-called beam hardening artifact, when the imaging subject contains the material for which the modeling error using monoenergetic forward model is significant, such as the metal implant or the bony structure of a patient [1]. This can be addressed by the recent development in energy-resolved photon-counting detectors. Equipped with photon-counting detectors, spectral CT provides the unprecedented possibility to simultaneously reconstruct a series of spectral images [2]–[9].

Spectral CT allows the use of polyenergetic forward model and therefore its image reconstruction should be more accurate than the conventional CT. More importantly, it potentially meets the clinical and industrial needs of energy-resolved CT images or particularly material compositions, such as spectral breast CT [17]–[19] and K-edge imaging [12], [20]. In terms of reconstruction algorithm for spectral CT, the material compositions can be reconstructed with two different methodologies: a two-step procedure with first the reconstruction of spectral images and then material decomposition from these spectral images to material compositions [6], [10], [19], [21]–[26] or alternatively first material-specific sinogram decomposition and then material reconstruction [12], [27]–[29]; a one-step procedure that directly reconstructs the material compositions by incorporating the material-image model into the reconstruction [6], [30]. Ideally the latter is preferred for two reasons: first the direct material reconstruction can fully utilize the structural similarity among materials; second it avoids to reconstruct an overdetermined system of images for material decomposition since the number of energy bins, correspondingly the number of spectral images, is often more than the number of materials to be reconstructed. Various sparsity-based reconstruction methods have been developed with the energy-by-energy reconstruction such as dictionary learning [10], tight frame [19], [23] and bilateral filtration [24], and the joint reconstruction to utilize the structural similarity in the spectral dimension such as total variation (TV) [26], nonlocal TV [11], patch-based low-rank model [25], rank-and-sparsity decomposition model [6] and tensor rank-and-sparsity decomposition model [22].

However, an important missing piece for accurate spectral CT is to incorporate the detector response function (DRF) into the reconstruction, which has not been considered so far to the best of our knowledge. The DRF refers to the recorded spectral distribution for a monoenergetic incident beam at the detector [12]. Ideally the DRF should be a Gaussian distribution centered at the incident energy with a small standard deviation. Practically the DRF is distorted by factors such as pulse pileup and charge-sharing, and thus needs to be experimentally calibrated [12]–[14]. Without considering DRF, the reconstruction quality of spectral CT can be significantly reduced, particularly for the photon-counting detectors with high count rate and high spatial resolution [15], [16]. In this work, we consider the inverse problem for spectral CT based on the forward model with DRF.

II. Method

A. Detector Response Function

For the purpose of accurate spectral CT, we consider the DRF to account for the detector response distortion due to factors such as pulse pileup and charge-sharing. In particular, we adopt the following DRF calibrated using X-ray fluores-

J. Liu and H. Gao are with Department of Mathematics and School of Biomedical Engineering, Shanghai Jiao Tong University, Shanghai 200240, CHINA (e-mail: hao.gao.2012@gmail.com).

cence [14]

$$D(E',E) = \begin{cases} c_1(E), \text{ for } E/2 < E' < E - 3\sigma; \\ \frac{c_2(E)}{\sqrt{2\pi}\sigma(E)} \exp(-\frac{(E'-E)^2}{2\sigma(E)^2}) \\ + \frac{2c_3(E)}{\sqrt{2\pi}\sigma(E)} \int_{E'}^{\infty} \exp(-\frac{(E'-E)^2}{2\sigma(E)^2}) dE', \text{ for } E' > E - 3\sigma. \end{cases} \tag{1}$$

In (1), E denotes the incident photon energy at the detector, while E' is the received photon energy by the detector. Here the DRF is determined by four parameters that are experimentally calibrated for a particular detector: the standard deviation of the primary Gaussian peak $\sigma(E)$; three fitting parameters $c_1(E)$, $c_2(E)$ and $c_3(E)$ that are related to the fitted charge-sharing fractions [14].

B. Forward Model

In this section, we give the polyenergetic X-ray forward model with DRF. For the discretization purpose, let us consider an incident spectrum $s(E)$ that consists of N_e intervals, i.e., $\{\Delta E_n, n = 1, \cdots, N_e\}$ with ΔE_n as the length of the nth energy interval, and a set of polyenergetic measurement $\{Y_{im}, i = 1, \cdots, N_d, m = 1, \cdots, M_e\}$, where M_e is the number of energies at the detector, N_v the number of projection views, N_{d0} the number of detectors per view, and $N_d = N_{d0} \cdot N_v$. Let $M = N_d \cdot M_e$ be the total number of spectral data available for image reconstruction, $\Delta E'_m$ the length of the mth energy response interval at the detector, and L_i the path of line integral for Y_{im}. Here we assume the spectral measurement Y_{im} follows Poisson statistics with the expectation Y^*_{im}. With the above DRF (1) taken into account, the expectation Y^*_{im} obeys the following forward model

$$Y^*_{im} = \int_{\Delta E'_m} dE' \sum_n \int_{\Delta E_n} D(E',E)S(E)e^{-\int_{L_i} u(x,E)dx} dE. \tag{2}$$

Clearly many energy intervals (i.e., $\{\Delta E_n, n = 1, \cdots, N_e\}$) are in need for accurate discretization of the forward model (2), which implies the necessity of reconstructing a fair amount of $u(x, E)$, i.e., N_e spectral images. However, the goal of spectral CT is to reconstruct the material compositions. To avoid such a redundant step of reconstructing an overdetermined system of $u(x, E)$, we utilize the linear dependence of $u(x, E)$ on material compositions Z to directly reconstruct Z, i.e.,

$$u(x,E) = \sum_{k=1}^{N_z} Z_k(x)B_k(E). \tag{3}$$

Here N_z is the number of basis materials, $Z_k(x)$ is the material composition of the kth basis material at the spatial location x, and $B_k(E)$ is the attenuation coefficient of the kth basis material at the energy E. Note that $Z_k(x)$ is spectrally independent, while $B_k(E)$ is spatially independent.

Then let us consider the spatial discretization of (2) on a piecewise-constant spatial grid $\{x_j, j = 1, \cdots, N_x\}$. Let A be the system matrix for discretized X-ray transform with the matrix element A_{ij}, e.g., the length of the ray L_i overlapping with the grid x_j. Then our forward model with DRF for the direct reconstruction of material compositions is

$$Y^*_{im} = \int_{\Delta E'_m} dE' \sum_n \int_{\Delta E_n} D(E',E)S(E)e^{-\sum_j A_{ij}(\sum_k Z_{jk}B_k(E))} dE, \tag{4}$$

where Z_{jk} is the kth material composition at the grid x_j.

Next we introduce the effective attenuation coefficient B_{kn} of the kth basis material for the energy interval ΔE_n with respect to the incident spectrum, i.e.,

$$Y^*_{im} = \sum_n e^{-\sum\limits_j A_{ij}(\sum\limits_k Z_{jk}B_{kn})} R_{nm}, \tag{5}$$

with

$$R_{nm} = \int_{\Delta E'_m} dE' \int_{\Delta E_n} D(E',E)S(E)dE. \tag{6}$$

Here (5) is justified by the mean value theorem for definite integrals, thanks to the continuity of $B(E)$ with respect to E.

In the matrix notation, (5) is

$$Y^* = e^{-AZB}R. \tag{7}$$

In (7), $A \in \mathbb{R}^{N_d \times N_x}$ is the system matrix, $Z \in \mathbb{R}^{N_x \times N_z}$ the material composition, $B \in \mathbb{R}^{N_z \times N_e}$ the material-attenuation matrix, $R \in \mathbb{R}^{N_e \times M_e}$ the energy response matrix, and $Y^* \in \mathbb{R}^{N_d \times M_e}$ the spectral measurement. Note that we unfold Y and Z to column vectors as needed in the following.

Finally, our polyenergetic X-ray forward model with DRF for given spectral CT data Y obeying the Poisson distribution is based on the following maximum likelihood function

$$p(Y|Z) = \prod_{i,m} \frac{(Y^*_{im})^{Y_{im}}}{Y_{im}!} e^{-Y^*_{im}}, \tag{8}$$

and particularly its logarithmic version

$$\begin{aligned} L(Z) = & -\mathbf{ln}(p(Y|Z)) \\ = & -\sum_{i,m} (Y_{im}\mathbf{ln}([e^{-AZB}R]_{im}) - [e^{-AZB}R]_{im}), \end{aligned} \tag{9}$$

where $[\cdot]_{im}$ denotes the matrix element and $\mathbf{ln}(Y_{im}!)$ is ignored since it does not affect the optimization.

C. Material Reconstruction with Nonlinear Data Fidelity

We first consider the material reconstruction with nonlinear data fidelity (9), i.e.,

$$Z = \arg\min_Z L(Z) + \lambda|\nabla Z|_1, \tag{10}$$

where we use the isotropic TV term [31] for image regularization with a nonnegative regularization parameter λ, e.g., 2D isotropic TV term

$$|\nabla Z|_1 = \sqrt{(\partial_x Z)^2 + (\partial_y Z)^2}. \tag{11}$$

Note that the minimization problem is convex since both $|\nabla Z|_1$ and nonlinear data fidelity term are convex.

D. Material Reconstruction with Linear Data Fidelity

Despite the convexity of nonlinear data fidelity based material reconstruction (10), its reconstruction quality may suffer from the nonlinearity. Alternatively we consider the following linear data fidelity based material reconstruction. Here the essential idea is to collaboratively resample incident energy intervals and detected energy intervals so that $R \in \mathbb{R}^{N_e \times M_e}$ is invertible with optimized condition number. Thus $N_e = M_e$.

A heuristically robust method is to first group the incident energy intervals ΔE_n using $S(E)$ to achieve the equal weighting, i.e.,

$$\int_{\Delta E_n} s(E)dE = \frac{1}{M_e}\sum_n \int_{\Delta E_n} s(E)dE. \tag{12}$$

and then group the detected energy intervals $\Delta E'_m$ using $D(E', E)S(E)$ to also achieve the equal weighting, i.e.,

$$\begin{aligned} &\textstyle\int_{\Delta E'_m} dE' \sum_n \int_{\Delta E_n} D(E', E)s(E)dE \\ &= \textstyle\frac{1}{M_e}\sum_m \int_{\Delta E'_m} dE' \sum_n \int_{\Delta E_n} D(E', E)s(E)dE. \end{aligned} \tag{13}$$

In this work, we adopt the heuristic method (12) and (13) and it works well with the aforementioned DRF (1).

Then we reformulate the following linear data fidelity based material reconstruction from (7)

$$Z^* = \arg\min_Z \|AZB - P\|_F^2 + \lambda|\nabla Z|_1, \tag{14}$$

where $P = -\mathbf{ln}(YR^{-1}) \in \mathbb{R}^{N_d \times M_e}$ and $\|\cdot\|_F$ is matrix Frobenius norm.

The solution algorithm for sparsity-based reconstruction problems (10) and (14) can be based on alternating direction method of multipliers [32] or split Bregman method [33].

E. Material-Attenuation Matrix

Here we consider how to determine the material-attenuation matrix B_{kn} in (5).

Assuming Z is known for the calibration purpose, we can compute B by solving the following overdetermined nonlinear system (15)

$$e^{-AZB}R = Y. \tag{15}$$

Moreover, when using the linearized data fidelity model (14), we can simply solve the following overdetermined linear system (16)

$$AZB = P. \tag{16}$$

Alternatively, without assuming Z is known, we rewrite (5) as

$$\begin{aligned} &\textstyle\int_{\Delta E'_m} dE' \sum_n \int_{\Delta E_n} D(E', E)S(E)e^{-\sum_j A_{ij}(\sum_k Z_{jk}B_k(E))}dE \\ &= \textstyle\sum_n e^{-\sum_j A_{ij}(\sum_k Z_{jk}B_{kn})} \int_{\Delta E'_m} dE' \int_{\Delta E_n} D(E', E)S(E)dE. \end{aligned} \tag{17}$$

Now considering a unit circular/spherical domain of the kth material only, (17) is reduced to the following overdetermined nonlinear system

$$\begin{aligned} &\textstyle\int_{\Delta E'_m} dE' \sum_n \int_{\Delta E_n} D(E', E)S(E)e^{-B_k(E)}dE \\ &= \textstyle\sum_n e^{-B_{kn}} \int_{\Delta E'_m} dE' \int_{\Delta E_n} D(E', E)S(E)dE. \end{aligned} \tag{18}$$

Similarly, when using the linearized data fidelity model (14), we can simply solve the following full-rank linear system (16)

$$B_{kn} = -[\mathbf{ln}(Y^k R^{-1})]_n. \tag{19}$$

where $Y^k \in \mathbb{R}^{M_e}$ with $[Y^k]_m = \int_{\Delta E'_m} dE' \sum_n \int_{\Delta E_n} D(E', E)S(E)e^{-B_k(E)}dE$.

In this work, given the material-attenuation function $B(E)$, the material-attenuation matrix B is computed by (18) or (19).

III. Results

Simulations were performed at tube voltage of 65 kVp. The mean glandular dose was estimated to be approximately 2 mGy for a 10 cm breast with 40% density. A 10 cm PMMA phantom (Fig. 1) which contains both iodine and calcium of various concentrations (TABLE I) was used.

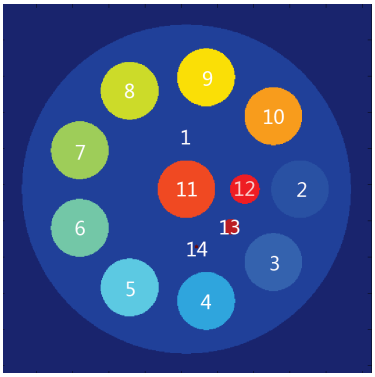

Fig. 1. The simulation phantom.

TABLE I
THE CONCENTRATION AND SIZE OF PHANTOM OBJECTS

Object	Material	Radius	Concentration
1	adipose	48mm	
2	iodine	8mm	16mg/ml
3,10	iodine	8mm	8mg/ml
4	iodine	8mm	4mg/ml
5,11	iodine	8mm	2mg/ml
6	calcium	8mm	400mg/ml
7,10	calcium	8mm	200mg/ml
8	calcium	8mm	100mg/ml
9,11	calcium	8mm	50mg/ml
12	calcium	4mm	400mg/ml
13	calcium	2mm	400mg/ml
14	calcium	0.6mm	400mg/ml

To mimic the generation of projection data in practice, we obtained 66 measurements linearly with respect to the energy with 1keV gap, i.e.,

$$Y^*_{m'} = \sum_{n=1}^{65} e^{-AZB_n}R(n, m'), \text{for} \quad m' = 1, \cdots, 65, \tag{20}$$

where AZB was computed by the parallel computation of X-ray transform [34] with 600 views and 768 detectors per view and with total exposure of 1200mR for each energy scan.

Then, we divided the energy $1 \le \tilde{E} \le 65$ into fifteen energy groups, and added the Poisson noise to the measurements.

TABLE II
ENERGY BINS($\Delta E_m = (E_{m-1}, E_m), \Delta E'_m = (E'_{m-1}, E'_m)$)

m	0	1	2	3	4	5	6	7
E_m	1	22	25	27	29	31	33	35
E'_m	1	20	23	25	27	29	31	33
m	8	9	10	11	12	13	14	15
E_m	37	39	42	45	47	51	55	65
E'_m	35	37	39	42	44	39	48	52

To compare with the proposed material reconstruction methods with DRF (10) and (14), we considered standard material reconstruction method without DRF [11].

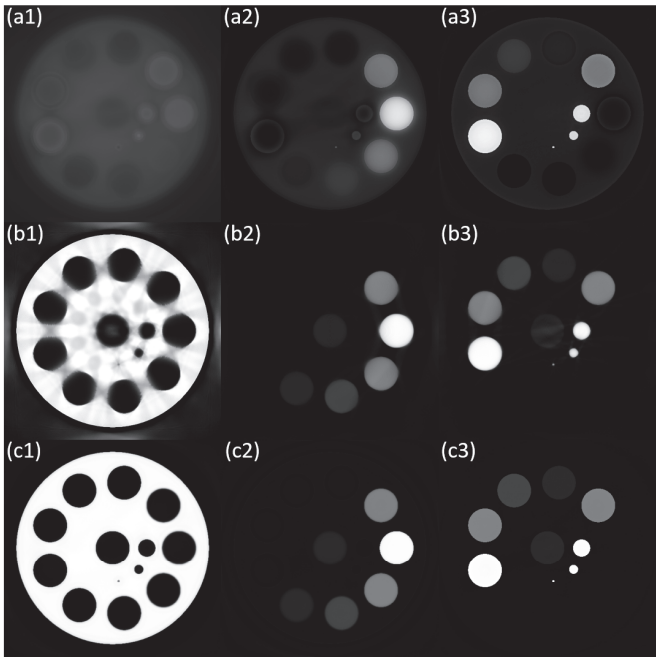

Fig. 2. Simulation results. (a) standard material reconstruction method without DRF; (b) the proposed method with DRF and nonlinear data fidelity; (c) the proposed method with DRF and linear data fidelity. (1) adipose; (2) iodine; (3) calcium.

The reconstructed material composition images with simulated data are shown in Fig. 2. Our proposed material reconstruction methods with DRF (10) and (14) were able to accurately reconstruct the phantom material compositions into adipose, iodine and calcium basis while the standard method failed to do so. Moreover, the reconstruction quality with nonlinear data fidelity (10) is better than that with linear data fidelity (14).

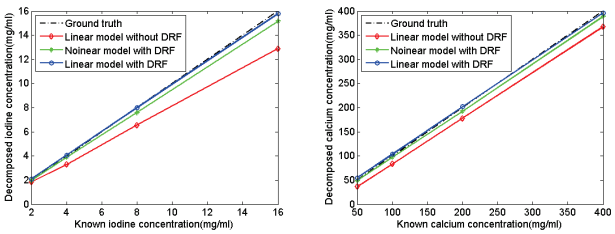

Fig. 3. Left: material concentration of iodine (object 2-5); right: material concentration of calcium (object 6-9).

The mean material concentration is plotted in Fig. 3, which again shows that the proposed methods with DRF provided accurate material compositions.

IV. CONCLUSION

We have proposed material reconstruction methods for spectral CT with DRF, which provided more accurate material compositions than the standard methods without DRF. Moreover, the proposed method with linear data fidelity had improved reconstruction quality from the proposed method with nonlinear data fidelity.

REFERENCES

[1] T. M. Buzug , Springer Science and Business Media.
[2] P. M. Fralicciardi , Nuclear Instruments and Methods in Physics Research Section A: Accelerators, Spectrometers, Detectors and Associated Equipment 607, 221-222,2009.
[3] K. Taguchi et al, In Nuclear Science Symposium Conference Record (NSS/MIC) 2009 3581-3585, 2009.
[4] H. Bornefalk et al, Physics in Medicine and Biology, 55, 1999-2022, 2010.
[5] D. P. Cormode et al, Radiology, 2010.
[6] H. Gao et al, Inverse problems, 27, 115012, 2011.
[7] P. M. Shikhaliev et al, Physics in medicine and biology, 56, 1905, 2011.
[8] X. Wang et al, Physics in medicine and biology, 2011, 56, 2791.
[9] H. Ding , Medical physics, 39, 1289-1297, 2012.
[10] B. Zhao et al, Physics in medicine and biology, 57, 8217,2012.
[11] Liu J, Medical physics, 42, 3570-3570, 2015.
[12] E. Roessl et al, Phys. Med. Biol, 52, 4679-4696, 2007.
[13] C. Xu et al, Nuclear Instruments and Methods in Physics Research Section A: Accelerators, Spectrometers, Detectors and Associated Equipment, 715, 11-17, 2013.
[14] H. Ding et al, Medical physics, 41, 121902, 2014.
[15] A. S. Wang et al, Medical physics, 38, 4265-4275, 2011.
[16] H. Ding et al, Medical physics, 39, 1864-1876, 2012.
[17] W. A. Kalender et al, Eur. Radiol. 22, 1-8, 2012.
[18] H. Ding et al, Radiology, 272, 731-738, 2014.
[19] H. Ding et al, Physics in medicine and biology, 59, 6005, 2014.
[20] H. Bornefalk et al, Physics in Medicine and Biology, 55, 1999-2022, 2010.
[21] B. Zhao et al, Physics in medicine and biology,57, 8217, 2012
[22] L. Li, Z. Chen, G. Wang, J. Chu, and H. Gao, Journal of X-ray science and technology, 2, 147-163, 2013.
[23] B. Zhao et al, Medical physics, 40, 031905, 2013.
[24] D. P. Clark et al, Physics in medicine and biology, 59, 6445, 2014.
[25] K. Kim et al, Medical Imaging, IEEE Transactions on, 34, 748-760, 2015.
[26] L. Shen et al, Medical physics, 42, 282-296, 2015.
[27] R. E. Alvarez et al, Phys. Med. Biol., 21, 733-744, 1976.
[28] SC. O. Schirra et al, Medical Imaging, IEEE Transactions on, 32, 1249-1257, 2013.
[29] Q. Xu et al, Physics in medicine and biology, 59, N65, 2014.
[30] Y. Long et al, Medical Imaging, IEEE Transactions on, 33, 1614-1626, 2014.
[31] L. I. Rudin et al, Physica D: Nonlinear Phenomena, 60, 259-268, 1992.
[32] S. Boyd et al, Foundations and Trends in Machine Learning, 3,1-122, 2011.
[33] T. Goldstein et al, SIAM Journal on Imaging Sciences, 2, 323-343, 2009.
[34] H. Gao, Medical physics, 39, 7110-7120, 2012.

Fast scanning imaging of micro-CT for small animals

Shouping Zhu, Yu Fan, Lei Xiong, Zhipeng Guo, Gaoqi Lv, Xu Cao, and Jimin Liang

***Abstract*—A fast scanning method was introduced to reduce the dose of micro-CT imaging for longitudinal studies of in vivo small animals. The feasibility of the method was analyzed briefly, and the design of the whole collection process was described in detail. The scanning time was reduced to 33 seconds for the fast scanning, which was nearly $1/10$ to $1/20$ of a classical traditional scanning. Phantom and mouse experiments were carried out to verify the performance of the fast scanning method. The results showed that there was less difference between the fast scanning mode and the traditional scanning mode, except for a larger noise in the fast scanning mode due to the shorter integral time of projection. In order to solve this issue, we utilized the non local means (NLM) filter to reduce the noise. There are three data domain for the NLM filtering: the projection domain, sinogram domain and the reconstructed volume domain. We compared the filtering results of the NLM method in these three domain by mouse imaging, and the results showed that filtering in the reconstructed volume domain performed better than in the other two domains.**

***Index Terms*—micro-CT imaging, fast scanning, non-local means (NLM)**

I. Introduction

MICRO-CT system has played a critical role in the field of non-invasive small animal imaging, as it can obtain high resolution anatomic information with relatively low cost and convenient operation [1]. One of the most issue of $in\ vivo$ micro-CT imaging is the radiation dose received by the subject. The typical radiation dose for a 3D micro-CT scan ranges from a 0.017 Gy to 0.78 Gy [2]. The LD50/30 for mice (the dose at which would kill 50% of the exposed animals within 30 days) is roughly between 5 - 7.6 Gy, which means a single micro-CT scan can represent as much as 10% of the LD50/30 [1][2]. For the longitudinal study, the animals will be scanned for several time over a period of days. In this case, the cumulative dose will become extremely high.

Roughly speaking, there are two categories applications of the micro-CT system: the first requires very high resolution ($\sim$10-20 microns), such as bone of the mouse, the second one requires relatively low resolution ($\sim$100 microns), such as quantification of adiposity, cardiac imaging, respiratory imaging, and imaging fusion with other modalities. For the latter, the lower resolution means lower dose, which invoke us to study new scanning mode. Most of the micro-CT systems work in a rotation-and-stop mode. Compared with the clinical CT, the scanning time for the micro-CT is relatively long, typically 5-10 minutes. Obviously, shorten the scanning time will reduce the X-ray dose effectively. One of the main limitations of the scanning time is the low frame rate of X-ray detector. With the development of the integrated circuit technique, X-ray detector with a fast frame rate (30-40 frames/s) is available, which makes the fast scanning of the micro-CT possible.

In this manuscript, we will introduce a fast scanning mode for micro-CT. During the fast scanning, the noise of the reconstructed image inevitably becomes larger due to the shorter integral time of projection. There are several strategies for CT denoising[3][4][5]. In recent years, lots of researchers pay attention to the non-local means method for denoising for its outstanding performance[6][7]. In this manuscript, we will utilize the non local means (NLM) method to reduce the noise in the fast scanning mode. There are three data domain for the NLM filtering: the projection domain, sinogram domain and the reconstructed volume domain. We will compare the denoising performance in these three domain.

The rest of the manuscript is organized as follows. The next section presents our fast scanning mode and the NLM based denoising method. In Section III, the experiments and results are shown to demonstrate the feasibility of the fast scanning mode, and the effect of the non local means filtering. Finally, we conclude the paper in Section IV.

II. Methods

A. Fast scanning Mode

In order to avoid the artifacts caused by the subject rotation during the scanning, the traditional micro-CT usually works in the ”rotation-and-stop” mode, as is shown in Fig. 1. To begin with, one must first set up the tube voltage and current of the X-ray source, then turn on the X-ray source. As most of the X-ray tubes in the micro-CT system work in the continue mode, the X-ray source will emit X-rays continuously until the total acquiring process is finished. When the X-ray output is stable and the motor is in the stop mode, the X-ray detector begins to acquire an image and send it to the control computer. After that, the motor will rotate a certain angle, and then stop to wait for the detector acquiring a new projection. This process will be repeated until the scanning is finished. The whole process will last for 5-10 minutes typically.

To reduce the time and the dose during the image acquiring, we introduce to use a fast scanning mode as shown in Fig. 2.

This work was supported in part by the Natural Science Foundation of China under Grant Nos.81227901, 61471279, and the Fundamental Research Funds for the Central Universities.

Asterisk indicates corresponding author.

Shouping Zhu, Yu Fan, Lei Xiong, Zhipeng Guo, Gaoqi Lv, Xu Cao, and Jimin Liang are with the Engineering Research Center of Molecular and Neuro Imaging of Ministry of Education, and the School of Life Science and Technology, Xidian University, Xi’an, Shaanxi 710071, China. (E-mail:spzhu@xidian.edu.cn)

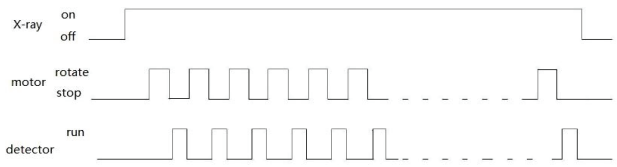

Fig. 1. Sequence diagram of the traditional rotation-and-stop mode.

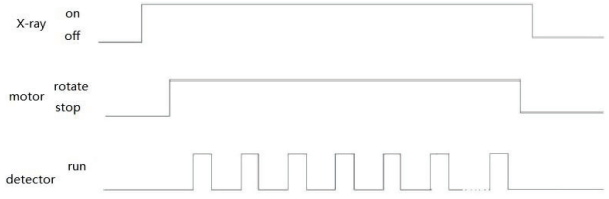

Fig. 2. Sequence diagram of the fast scanning mode.

At the beginning, the X-ray source is turned on as above. Then we start the motor to rotate continuously at a stable speed. When the X-ray output and the rotation speed of the motor are stable, we trigger the X-ray detector to acquire the images with a fixed period until the whole scanning is finished.

It is obvious that the subject is rotating during acquiring the projection. As a rule of thumb, the rotation amount should be less than or approximate equal to the voxel size to avoid obvious artifacts caused by the rotation. Let the angular velocity be ϖ, the integration time be ΔT, the distance between the outer edge and the rotation center be R, then the maximum rotation amount during the integration time is

$$\Delta = \varpi R \Delta T. \tag{1}$$

The value Δ should be as small as possible. However, there are some limitations and conflicts for this purpose. R represents the size of the subject. Assume that the subject is a mouse, the value of R is roughly 20 mm. In order to implement fast scanning, ϖ should be large, which is lead to a large rotation amount Δ. In this case, we have to reduce the value of the ΔT. The minimum ΔT is limited by the detector frame rate, and a smaller ΔT will cause a larger noise of the image. Therefore, there should be some balance for the parameters setting.

In the scanning mode, large amount of data will transfer to the control computer from the detector in a very short time. As the write speed of the hard disk is relatively low, we storage the projection data to the memory of the computer temporarily during the scanning. After the whole scanning is finished, all of the data are written to the hard disk for long-term storage.

B. Non local means filtering for denoising

The noise of the reconstructed image is very large due to the low dose in the fast scanning. In order to solve this issue, we utilize the non local means (NLM) method to reduce the noise. There are three data domain for the NLM filtering: the projection domain, the sinogram domain and the reconstructed volume domain. In the first two domain, we implement the NLM method in 2D data, while in the third domain, we perform the NLM algorithm in 3D. The basic idea of the algorithm in 2D and 3D are similar. In the follow we will introduce it briefly in the case of 3D.

In the non-local means method, the restored values can be calculated as the weighted average of the values in the search volume V_s as follows[6]

$$f^{NL}(i) = \sum_{j \in V_s} w(i,j) f(j), \tag{2}$$

where $f^{NL}(i)$ is the restored value at voxel i. The $f(j)$ is the value of data to be denoising at voxel j. The weights $w(i,j)$ represents the similarity between the neighborhoods of the voxel i and j.

$$w(i,j) = \frac{1}{Z(i)} exp\{-\frac{\|f(N_i) - f(N_j)\|_a^2}{h^2}\}. \tag{3}$$

where $Z(i) = \sum_j w(i,j)$, and h is the smoothing parameter of the weights. $f(N_i)$ is the vector of neighborhood voxels of i, $f(N_i) := \{f(j)\}, j \in N_i$, , where N_i expresses the neighborhood of i.

The smoothing parameter h depends on the standard deviation of the noise $\hat{\sigma}$, and it also needs to take into account N_i. According to [7], The equation was defined as

$$w(i,j) = \frac{1}{Z(i)} exp\{-\frac{\|f(N_i) - f(N_j)\|_2^2}{2\beta\hat{\sigma}^2\|N_i\|}\}. \tag{4}$$

where the Gaussian-weighted Euclidean distance is replace by the the classical Euclidean distance to simplify the complexity of the problem, and to reduce the computational time. The standard deviation of the noise $\hat{\sigma}$ can be estimated via pseudo-residuals[7]. The parameter β needs to be tuned manually.

III. Experiments and Results

A. Phantom experiment for fast scanning test

To test the performance of the fast scanning method, we carried out the following phantom experiment. The phantom was made of a foamed plastic with 13 pencil cores put on it at an interval of 5mm, and the diameter of the pencil core is about 0.5mm, as is shown in Fig. 3.

The phantom was scanning by normal rotation-and-stop mode and fast scanning mode respectively by our prototype micro-CT system, which consisted of a flat detector (Dexela1512, Dexela, UK) and a micro-focus X-ray tube (L9181-02, Hamamatsu, Japan). During the normal scanning mode, the tube voltage was set to 50kVp, and the tube was set to 300μA. 360 views were acquired around the subject with the detector integration time 500ms. It took about 5 min for the whole scanning. In the fast scanning mode, the tube voltage was set to 70kVp, and the tube was set to 300μA. The system rotated at the speed of 33 seconds per rotation and 360 views were acquired during the scanning with the detector integration time 30ms.

The 3D reconstruction was performed by FDK method[8]. The size of reconstructed volume data is $512 \times 512 \times 512$ with the voxel size $150\mu\text{m}^3$. The reconstructed phantom cross section of the two scanning mode were shown in Fig. 4(a) and

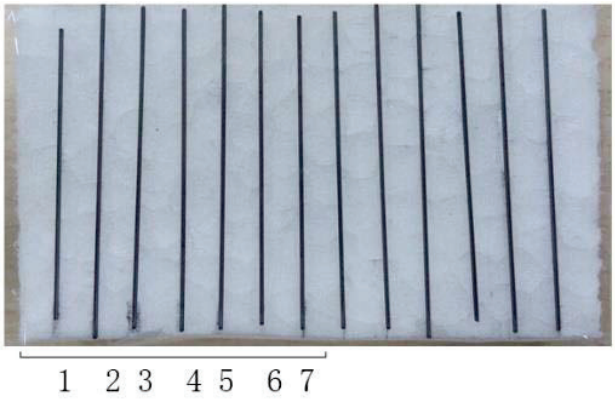

Fig. 3. Photograph of the phantom for fast scanning test.

(b) respectively. Fig. 5 showed the profile of the first point and the seventh point in the Fig. 4. The results showed that there was less difference between the normal scanning and the fast scanning, which verified feasibility of the fast scanning mode.

B. Mouse experiments for fast scanning and Non-local means filtering

In order to further verify the fast scanning mode and test the performance non-local means filtering in different data domain, we carried out the mouse experiments by our prototype micro-CT system. The normal rotation-and-stop mode scanning and the fast scanning were performed in the same the mouse, with the same scanning parameters as the above phantom experiments.

For the fast scanning data, the non-local means filtering were performed in the projection data (2D), the sinogram data (2D), and the reconstructed volume data (3D), respectively. For the 2D filtering, the size of the local neighborhood N_i was set to $|N_i| = 3 \times 3$, and the searching range was set to $|V_i| = 5 \times 5$. In the 3D filtering, $|N_i| = 3 \times 3 \times 3$ and $|V_i| = 5 \times 5 \times 5$. The value of the parameter β was set manually for the best performance. The results were shown in Fig. 6. The first and the second row were the different slice of the reconstructed results. The third row was the corresponding enlarged region marked by the red rectangle in the second row. The first column was the reconstructed results of the normal scanning mode. The second column was the results of the fast scanning mode without any filtering. From the third to the fifth column were the filtering results of the fast scanning data in the projection domain, in the sinogram domain, and in the reconstructed volume domain. The results demonstrates that there is no other obvious difference between the fast scanning mode and the normal scanning mode, except for the large image noise. The noise was decreased by the non-local means filtering in these three domain. The volume domain filter gave a better performance in denoising. However, there are some detail missing after filtering, which needs to research further.

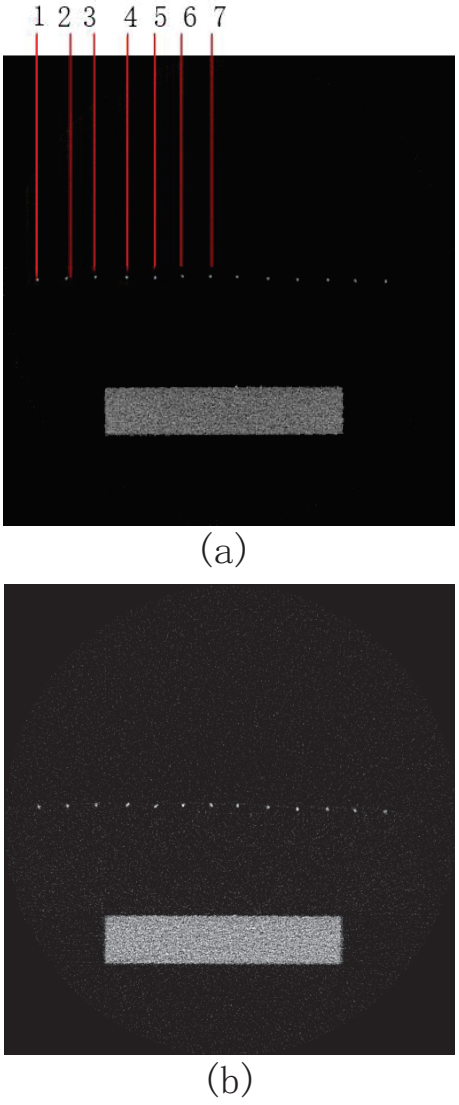

Fig. 4. Phantom results. (a) is corresponding to the normal rotation-and-stop mode, and (b) is corresponding to the fast scanning mode.

IV. Conclusion and Discussion

The rotation-and-stop scanning mode was adopted in most of the micro-CT systems, which would need a long scanning time and the X-ray dose was relatively large. In this manuscript, we performed the fast scanning mode for micro-CT imaging, and the non-local means method was utilized to reduce the noise. The scanning time of the fast scanning mode was reduce to 33 seconds, which was nearly $1/10$ to $1/20$ of a normal rotation-and-stop scanning mode. We compared the filtering results of the NLM method in three domain by mouse imaging, and the results showed that filtering in the reconstructed volume domain performed better than in the other two domains.

References

[1] S. R. Cherry, "In vivo molecular and genomic imaging: new challenges for imaging physics," *Phys. Med. Biol.*, vol. 49, pp. R13-R48, 2004.

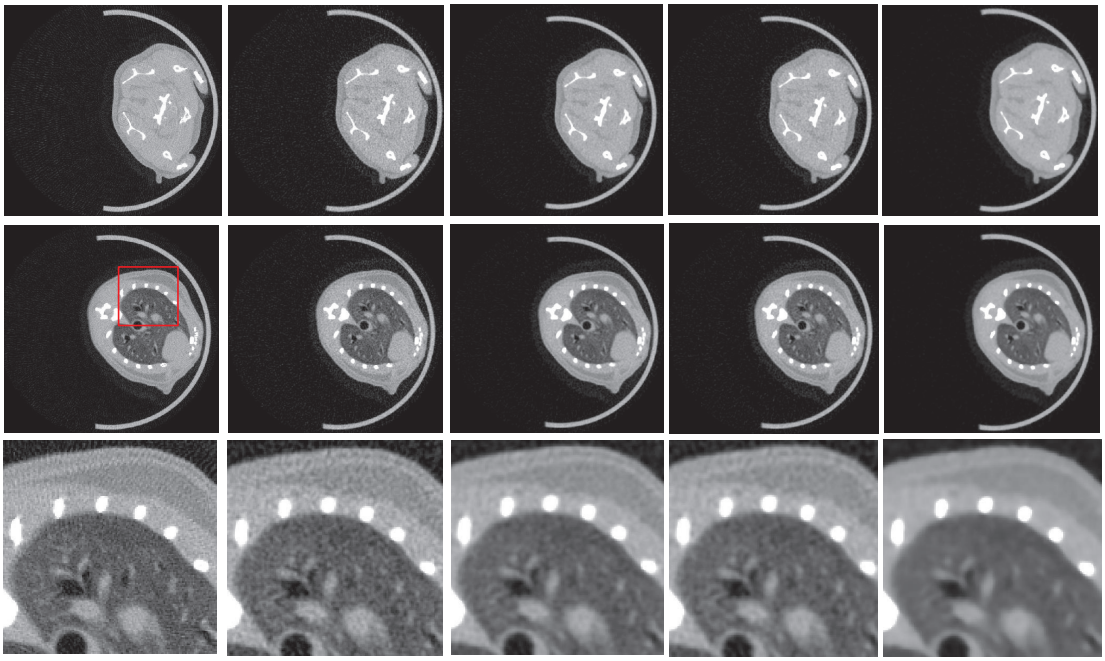

Fig. 6. Mouse experiments results. The first and the second row were the different slice of the reconstructed results. The third row was the corresponding enlarged region marked by the red rectangle in the second row. The first column was the reconstructed results of the normal scanning mode. The second column was the results of the fast scanning mode without any filtering. From the third to the fifth column were correspond to the filtering results of the fast scanning data in the projection domain, in the sinogram domain, and in the reconstructed volume domain. Display window [0 0.05].

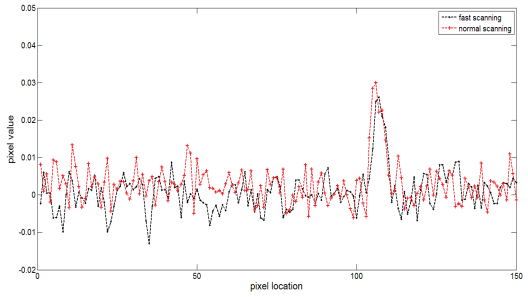

(a)

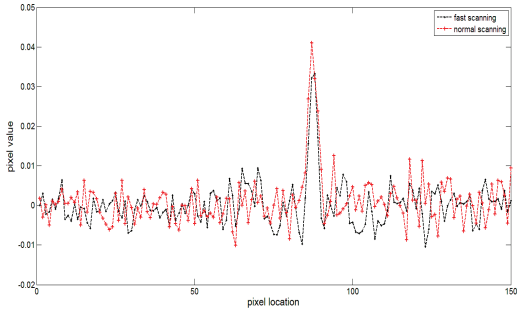

(b)

Fig. 5. Profile of the first point (a) and the seventh point (b) in Fig. 4.

[2] Badea C, Drangova M D, Johnson G, "In vivo small-animal imaging using micro-CT and digital subtraction angiography," *Phys. Med. Biol.*, vol. 53, no. 19, pp. R319-R350, 2008.

[3] J. Wang, H. Lu, J. Wen, and Z. Liang, "Multiscale Penalized Weighted Least-Squares Sinogram Restoration for Low-Dose X-Ray Computed Tomography," *IEEE trans. on Biomed. Engineering*, vol. 55, no. 3, pp.1022-1031, 2008.

[4] Z. Bian, J. Ma, J. Huang, H. Zhang, S.u Niu, Q. Feng, Z. Liang, and W. Chen, "SR-NLM: A sinogram restoration induced non-local means image filtering for low-dose computed tomography," *Computerized Medical Imaging and Graphics*, vol. 37, pp. 293-303, 2013.

[5] Y. Chen, L. Shi, Q. Feng, J. Yang, H. Shu, L. Luo, J.-L. Coatrieux, and W. Chen, "Artifact Suppressed Dictionary Learning for Low-Dose CT Image Processing," *IEEE trans. on Med. Imag.*, vol. 33, no.12, pp. 2271-2292, 2014.

[6] M. Mahmoudi and G. Sapiro, "Fast image and video denoising via nonlocal means of similar neighborhoods," *IEEE Signal Process. Lett.*, vol. 12, no. 12, 2005, pp.839-842.

[7] Coupe P, Yger P, Prima S, et al, "An Optimized Blockwise Nonlocal Means Denoising Filter for 3-D Magnetic Resonance Images," *IEEE trans. on Med. Imag.*, vol. 27, no. 4, pp. 425-441, 2008.

[8] L. A. Feldkamp, L. C. Davis, and J. W. Kress, "Practical cone-beam algorithm," *Journal of the Optical Society of America*, vol. 1, pp. 612-619, 1984.

Use of Synthetic CT to reduce simulation time of complex phantoms and systems

Sarah E. Divel, W. Paul Segars, Soren Christensen, Max Wintermark, Maarten G. Lansberg, and Norbert J. Pelc

***Abstract*—Simulation-based approaches to validate CT scanning methods, in which the exact anatomy and physiology of the phantom and the physical attributes of the system are known, provides a ground truth for quantitatively evaluating different techniques. However, long simulation times of complicated phantoms, especially when modeling many physical aspects (e.g., spectrum, finite detector and source size), hinder the ability to realistically and efficiently evaluate and optimize protocol performance. This work investigated the feasibility of reducing the simulation time of these complex cases by employing the principles of Synthetic CT. Noiseless simulations are performed at two monoenergetic energies and the projections are decomposed into basis materials. These can be used to quickly generate projections at any spectrum and dose level. After determining the optimum energy levels for the initial noiseless monoenergetic scans, the performance of the synthetic simulations was evaluated by comparing the reconstructed Hounsfield Unit (HU) values, reconstructed noise standard deviation, and time required to those of traditional simulations. The HU values of synthetic simulations matched traditional simulations within 2.9 HU (5.4%) in the brain tissue, within 27.6 HU (3.1%) in the iodine-enhanced blood vessels, and within 20.2 HU (1.5%) in the skull. The standard deviation of the synthetic simulation was within 2 to l0 HU. The synthetic processing reduced the execution time by 97.93% for each additional protocol run on the same anatomy.**

I. Introduction

Simulation of CT data provides tremendous insight by providing settings in which the ground truth is known to which techniques can be evaluated. These benefits include the validation and optimization of CT protocols, evaluation of new imaging techniques and reconstruction methods, and assessment and correction of artifacts. Simulation of CT perfusion (CTP) used for stroke assessment proves especially attractive because scanning exposes patients to radiation and iodinated contrast and the pathophysiology cannot be easily measured with alternative techniques.

Recent efforts have led to the development of a realistic, dynamic digital brain phantom for the validation and optimization of CTP protocols for stroke assessment [1]. However, due to the complex and realistic nature of both the phantom (having hundreds of geometric primitives) and simulation software that models the scanning geometry with many subsamples for each ray, simulation of a single 0.625 mm slice requires an execution time of several minutes with the acquisition an entire perfusion data set of the brain taking 1-2 days. The result of such long simulation times makes the goal of testing hundreds of scan protocols with many independent noise realizations unfeasible, and it is therefore desirable to reduce the simulation time. We investigated whether the principles of Synthetic CT can be applied to simulate arbitrary protocols from a single noiseless dual energy protocol [2].

S. E. Divel is with the Department of Electrical Engineering, Stanford University, Stanford, CA 94305 (e-mail: sdivel@stanford.edu)

W. P. Segars is with the Carl E. Ravin Advanced Imaging Laboratories, Department of Radiology, Duke University Medical Center, Durham, North Carolina 27705

S. Christensen and M. G. Lansberg are with the Stanford Stroke Center, Stanford University, Stanford, CA 94305

M. Wintermark is with the Department of Radiology, Stanford University, Stanford, CA 94305

N. J. Pelc is with the Department of Bioengineering and Department of Radiology, Stanford University, Stanford, CA 94305

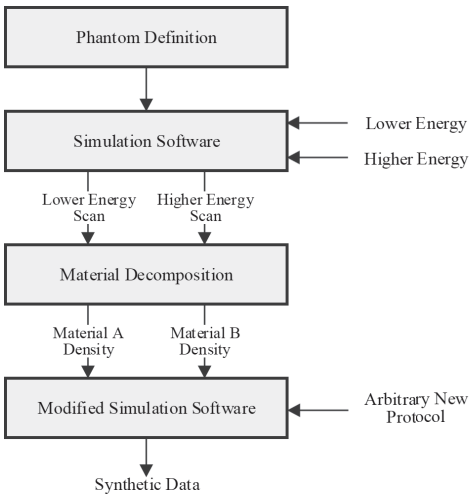

Fig. 1. Flow chart of simulation methods

II. Methods

Figure 1 displays a flow chart of the simulation method. We rely on basis material decomposition. Figure 1 is for the case when two basis materials suffice, but it can be generalized for cases when materials have K-edges within the spectrum of interest. Since the objects are defined by their true chemical composition, we use simulated transmission with monochromatic X-rays to yield data from which basis decomposition is computed. Because calculating the line integrals through a complex phantom results in a long simulation time, the synthetic simulation is far more efficient when the goal is to repeat various protocols for a particular anatomy because the many line integrals are probed by only a few (in our case two) monoenergetic beams. The conversion of these into polychromatic projections with arbitrary spectra

and the addition of noise is incredibly fast once the initial monoenergetic line integrals have been acquired. The main potential issue is the accuracy of the synthetic CT process due to (1) basis material decomposition and (2) the combination of monoenergetic rather than polyenergetic line integrals to simulate the beam aperture.

The phantoms used to develop and assess the performance of the synthetic simulation included a simple water cylinder object with iodine and bone inserts defined using primitive 3D shapes and the complex, realistic modified 4D extended cardiac-torso (XCAT) phantom defined using 3D nonuniform rational B-spline (NURBS) surfaces in which users can add time-varying contrast enhancement to the vessels, grey matter, and white matter by specifying time attenuation curves for each region [1], [3].

Two noiseless, monoenergetic simulations, one at a low energy and one at a high energy, were generated using CatSim, a physically realistic CT simulation software [4]. We tested 40, 50, and 60 keV for the low energy scan and used 100 keV for the high energy scan. Rather than collecting The two monoenergetic data sets individually, a polyenergetic simulation was performed using a spectrum consisting of two delta functions at the desired low and high energies. The two sinograms were subsequently separated and used to decompose the projections into two basis materials by solving the simple system of linear equations for the path lengths of the two materials represented by $\boldsymbol{\eta}_A$ and $\boldsymbol{\eta}_B$

$$\begin{aligned} \mathbf{S}\Big(E_{\text{low}}\Big) &= \boldsymbol{\eta}_A \mu_A\Big(E_{low}\Big) + \boldsymbol{\eta}_B \mu_B\Big(E_{low}\Big) \\ \mathbf{S}\Big(E_{\text{high}}\Big) &= \boldsymbol{\eta}_A \mu_A\Big(E_{high}\Big) + \boldsymbol{\eta}_B \mu_B\Big(E_{high}\Big) \end{aligned} \tag{1}$$

where $\mathbf{S}\big(E_{\text{low}}\big)$ and $\mathbf{S}\big(E_{\text{high}}\big)$ are the m bin by n view sinograms acquired at the low and high energies, respectively. This decomposition along with the user defined protocol (kVp, mAs) were then input into a modified version of CatSim, making use of the existing subroutines while bypassing the line integral calculations.

The decomposition allows for the calculation of the energy dependent line integrals for each view for any spectrum and noise model without needing to compute the line integrals through the phantom anew using

$$\begin{bmatrix} \mu_A(E_1) \\ \mu_A(E_2) \\ \vdots \\ \mu_A(E_p) \end{bmatrix} \begin{bmatrix} \eta_A(j,1) & \eta_A(j,2) & \cdots & \eta_A(j,n) \end{bmatrix} + \begin{bmatrix} \mu_B(E_1) \\ \mu_B(E_2) \\ \vdots \\ \mu_B(E_p) \end{bmatrix} \begin{bmatrix} \eta_B(j,1) & \eta_B(j,2) & \cdots & \eta_B(j,n) \end{bmatrix} \tag{2}$$

where $\mu_A(E)$ and $\mu_B(E)$ are the attenuation coefficients of the two basis materials at each energy level (specified by a user selected spectrum file generated using XSPECT [5]) and $\eta_A(i,j)$ and $\eta_B(i,j)$ are the path lengths of each material for a particular position of the sinogram with view number, j, and detector index, i. This data was then run through the remaining CatSim subroutines, including scatter addition, detection, log conversion, beam hardening correction, and reconstruction routines.

III. Results

Table I compares the mean error in Hounsefield Units (HU) within the three materials of the cylinder at various polychromatic kVp when either 40, 50, or 60 keV is used for the lower energy of the monoenergetic simulations, with 100 keV as the high energy. The lowest error for each case is highlighted in bold. Because using 50 keV as the lower energy for the initial monoenergetic simulations has the lowest error in all but three of the cases, the 50, 100 keV combination for the initial monoenergetic scans was determined to produce the best results. In the cases when this combination did not result in the lowest error (80 kVp water, 80 kVp iodine, 100 kVp iodine), the error was less than 0.03 HU different than the lowest error.

TABLE I
Comparison of the mean error in HU within the three materials of the synthetic simulated cylinder at 80, 100, 120, and 140 kVp

Lower keV	Water	Iodine	Bone
40	**0.1576**	**0.1763**	66.836
50	0.1641	0.2024	**17.901**
60	0.2661	0.3050	67.619

(a) 80 kVp

Lower keV	Water	Iodine	Bone
40	0.1413	**0.1551**	67.488
50	**0.1350**	0.1811	**7.866**
60	0.1959	0.2437	27.174

(b) 100 kVp

Lower keV	Water	Iodine	Bone
40	0.1379	0.1460	53.739
50	**0.1203**	**0.1456**	**11.138**
60	0.1474	0.1951	13.949

(c) 120 kVp

Lower keV	Water	Iodine	Bone
40	0.1377	0.1461	39.492
50	**0.1202**	**0.1280**	**8.506**
60	0.1223	0.1608	9.779

(d) 140 kVp

Figure 2 shows (a) a noiseless traditional simulation of the test cylinder at 80 kVp, (b) a noiseless synthetic simulation of the test cylinder at 80 kVp using the 50, 100 keV combination for the initial monoenergetic scans, and (c) the absolute value of the difference between the two. Due to the choice of iodine and water as the basis materials, the error in the bone insert is the largest, as seen in the difference image.

Figure 3 compares the reconstructed images of the complex brain phantom at 80 kVp and 150 mAs when iodine contrast has been added to the vessels. The synthetic image was generated using the 50, 100 keV combination for the initial monoenergetic scans. The two images appear nearly identical to the naked eye and present similar noise characteristics.

Figure 4 compares the mean and standard deviation of the HU values in four regions of interest (ROIs) within these images. Figure 3c shows the locations of the ROIs. ROI 1 and ROI 2 were placed in the brain tissue, ROI 3 was placed in the skull, and ROI 4 was placed in the superior sagittal sinus. The mean matched within 2.9 HU (5.4%) in the brain tissue, within 27.6 HU (3.1%) in the iodine-enhanced blood vessels, and within 20.2 HU (1.5%) in the skull. The standard deviation matched within 2 to 10 HU.

(a) Traditional simulated 80 kVp image

(b) Synthetic 80 kVp image using monoenergetic data at 50 and 100 keV

(c) Difference Image (HU)

Fig. 2. A comparison of reconstructed images of the water cylinder at 80 kVp using traditional simulation (2a) and synthetic simulation (2b). The center insert contains iodine with a density of .02465 $\mathrm{g/cm^3}$.The bottom insert contains bone with a density of 1.92 $\mathrm{g/cm^3}$. The display windows are $[-1000, 2500]$ HU for (2a) and (2b) and $[0, 40]$ for (2c).

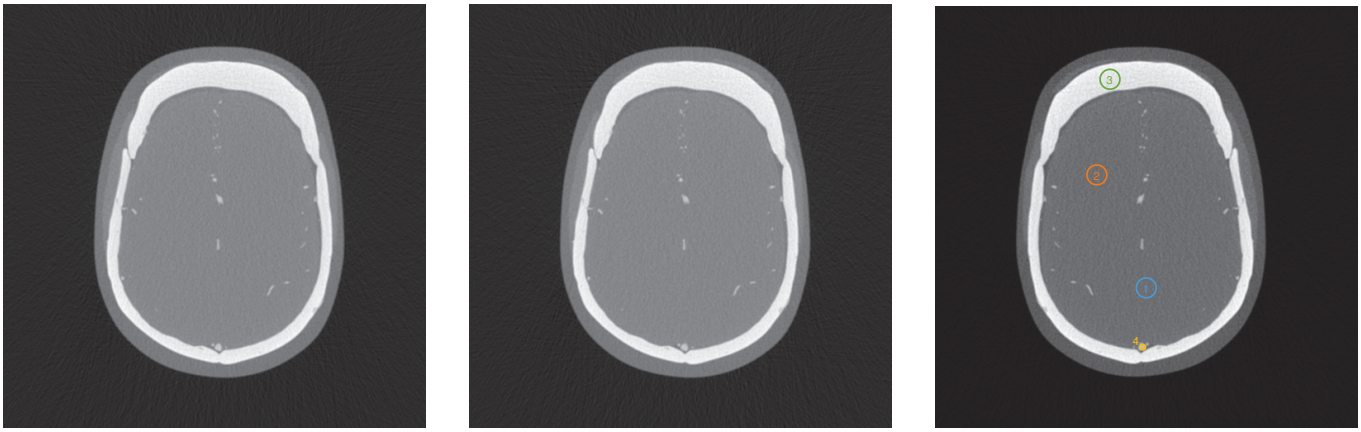

(a) Traditional simulated 80 kVp, 150 mAs image

(b) Synthetic 80 kVp, 150 mAs image generated using monoenergetic data at 50 and 100 keV

(c) ROI Locations

Fig. 3. A comparison of reconstructed images of the brain phantom at 80 kVp, 150 mAs using traditional simulation (3a) and synthetic simulation (3b). The display windows are $[-1150, 1600]$ HU.

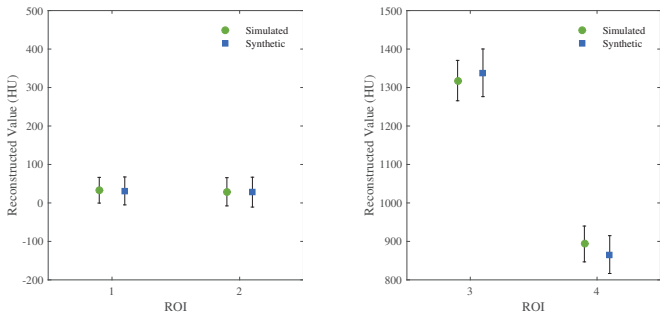

Fig. 4. A comparison of reconstructed values (HU) in regions of interest within the brain from a traditional simulation and a synthetic simulation generated using 50, 100 keV for the initial monoenergetic data. The reconstructed 0.625 mm slice is an effective 80 kVp, 150 mAs scan. The error bars represent one standard deviation.

TABLE II
SUMMARY OF AVERAGE SIMULATION TIMING

	0.625 mm Slice	**5 mm Slice**
Traditional Simulation (including reconstruction time)	6.409 minutes	48.516 minutes
First Synthetic Simulation Protocol (projection time + processing time + reconstruction time)	6.712 minutes	44.297 minutes
Additional Synthetic Simulation Protocol (Projection time + processing time + reconstruction time)	7.960 seconds	52.322 seconds

Table II provides a summary of the time required for the traditional and synthetic simulations. Running the first arbitrary protocol to generate a 0.625 mm synthetic slice takes 6.712 minutes on average. Each additional protocol of the same anatomy takes only 7.960 seconds on average, reducing the timing by 97.93% for each additional protocol run on the same anatomy. A similar timing improvement is seen for 5 mm slices.

IV. Discussion and Conclusion

The goal of this work was to develop a faster way to conduct repeated simulations and to quantify the agreement between the reconstructed images using the full simulation protocol versus those using the synthetic protocol. The results show excellent agreement. They demonstrate that using the 50, 100 keV combination for the initial monoenergetic scans produces the best results, with the synthetic reconstructed HU values in the brain matching the traditional simulation values within 2.9 HU (5.4%) in the brain tissue, within 27.6 HU (3.1%) in the iodine-enhanced blood vessels, and within 20.2 HU (1.5%) in the skull. Additional simulations of CTP cases will clarify if the accuracy obtained is sufficient. By selecting water and iodine as the basis materials, most of the error occurs in the bone. However, because the skull is not a primary structure of interest for CTP studies, we only require that bone has realistic HU values. In fact, most, if not all, perfusion post-processing software segment out the bone. This further reduces the impact of bone error in our results.

Because one of the primary goals in simulating perfusion scans of the brain phantom is to optimize protocols, many simulations of one pathology are required. The synthetic simulation framework makes this optimization simple and efficient, reducing the simulation from approximately six minutes per 0.625 mm slice to under 10 seconds when testing additional protocols on the same pathology.

Additionally, it is feasible to separate the line integrals of structures being perfused (gray matter, white matter, arteries, and veins) from the remaining structures in the brain. We can then modify each one to insert temporal dynamics and recombine in the projection domain. This could even further reduce the simulation of a full perfusion scan.

Acknowledgment

This work was supported by the Training in Biomedical Imaging Instrumentation Program (T32-EB009653) at Stanford University and GE Healthcare.

References

[1] S. E. Divel, W. P. Segars, S. Christensen, M. Wintermark, M. G. Lansberg, and N. J. Pelc, "Development of a realistic, dynamic digital brain phantom for CT perfusion validation," in *Proc. SPIE, Medical Imaging 2016: Physics of Medical Imaging*, Mar. 2016, p. 97830Y.

[2] A. S. Wang and N. J. Pelc, "Synthetic CT: simulating arbitrary low dose single and dual energy protocols," in *Proc. SPIE, Medical Imaging 2011: Physics of Medical Imaging*, vol. 7961, Mar. 2011, p. 79611R. [Online]. Available: http://dx.doi.org/10.1117/12.878771

[3] W. Segars, G. Sturgeon, S. Mendonca, J. Grimes, and B. M. Tsui, "4d XCAT phantom for multimodality imaging research," *Medical physics*, vol. 37, no. 9, pp. 4902–4915, 2010.

[4] B. De Man, S. Basu, N. Chandra, B. Dunham, P. Edic, M. Iatrou, S. McOlash, P. Sainath, C. Shaughnessy, B. Tower *et al.*, "Catsim: a new computer assisted tomography simulation environment," in *Medical Imaging*. International Society for Optics and Photonics, 2007, pp. 65 102G–65 102G.

[5] Henry Ford Health Systems, "XSpect Simulation Toolkit," Detroit, MI.

Applying Soft Radiation in Computed Tomography Experiments on a Multipurpose Diffractometer

Natalia Dadivanyan, Detlev J. Götz and Detlef Beckers

***Abstract*—Application of soft radiation (Cu and Co X-ray tubes) in computed tomography experiments on a laboratory X-ray diffractometer is presented. Using low energy (7-8 keV) X-ray sources provides the possibility to investigate objects made of light (organic) materials in more detail compared to the high energy case. A thorough qualitative as well as quantitative analysis of porous materials and samples with oriented components is demonstrated.**

***Index Terms*—computed tomography, soft radiation, x-ray diffraction.**

I. Introduction

COMPUTED tomography (CT) has been a well-established technology in medical diagnostics for decades. In the past few years, industrial CT has become a very powerful nondestructive analytical method. It can provide detailed information about the object of interest, *e.g.* its structure, materials it is made of, defect/pore sizes and their distribution. In this contribution we present CT measurements performed on the Empyrean platform - the only powder X-ray diffraction (XRD) instrument that allows combination of conventional XRD applications (Powder XRD, Stress & Texture, µ-XRD etc.) with a CT experiment on one multipurpose platform. Due to PANalytical's high-performance area detectors, the CT capability can be extended from metal or heavy element containing objects (typical for industrial CT) to light materials (pharmaceutical products, polymer composites *etc.*). Such challenging samples normally exhibit very little absorption and as consequence a low contrast towards the X-ray beam. A better contrast can be achieved by exchanging the high energy X-ray tubes (W, Ag, Mo) to the softer radiations like Cu [1] and Co X-ray sources.

II. Experimental

CT experiments were performed on a PANalytical multipurpose Empyrean diffractometer equipped with Cu (8.05 keV) and Co (6.93 keV) X-ray tubes. The size of the analyzed samples varied depending on the dimensions of the used area detector: PIXcel^{3D}, 14x14 mm or 28x28 mm, silicon chip technology. The measurement time varied between 7.5 and 15 minutes per sample. 3D reconstruction as well as the analysis of the reconstructed objects was performed using VGStudio MAX 2.2.6 software [2].

Natalia Dadivanyan, Detlev J. Götz and Detlef Beckers are with the PANalytical B.V., Lelyweg 1, 7602 EA, Almelo, The Netherlands (e-mail: natalia.dadivanyan@panalytical.com, detlev.gotz@panalytical.com and detlef.beckers@panalytical.com).

III. Results and Discussion

To demonstrate the capabilities of CT experiments with soft radiation few objects consisting of organic materials were chosen. Each measurement resulted in nine hundred 2D images, which were used to create a 3D reconstruction of the measured sample. This reconstructed object was used to perform various types of analysis. In the following examples we describe in more detail what kind of analysis can be done and which information can be obtained.

A. Multicomponent Samples

When dealing with multicomponent samples it is relevant to investigate their homogeneity. In Fig. 1 a pharmaceutical sample is presented. It consists of granules and a capsule around them. Wall thickness analysis was performed on this sample. The results are visualized both in 2D cross-sections (Fig. 1, on the left and top right) and in the 3D view (Fig. 1, bottom right). From the cross-sections one can observe, that the capsule consists of two pieces with slightly varying thickness and high number of spherical granules. The thickness of the capsule is changing from 0.1 mm to 0.3 mm when moving along the object (color gradient).

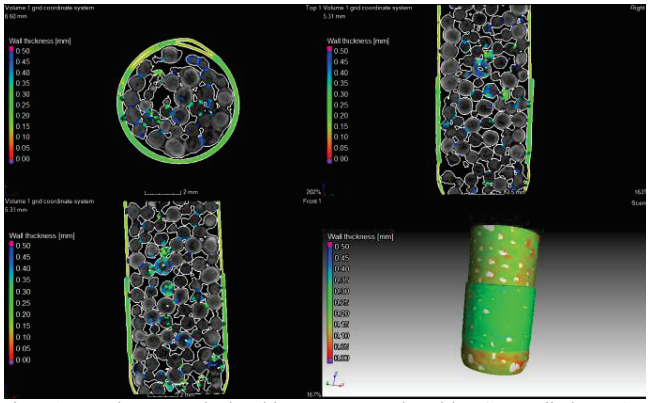

Fig. 1. Pharmaceutical object, measured with Cu radiation. 3D reconstruction as well as the wall thickness calculation and visualization were performed in VGStudio MAX 2.2 software.

B. *Composite Materials*

A composite material is usually made of two or more materials with significantly different physical and/or chemical properties. The individual components remain separate and distinct within the finished structure. A composite material, consisting of a polymer matrix and oriented glass fibers was measured with Cu radiation.

In Fig. 2 the orientation determination of the glass fibers inside the polymer matrix is presented using the *x*-axis as reference. Fibers parallel to the *x*-axis of the object are shown

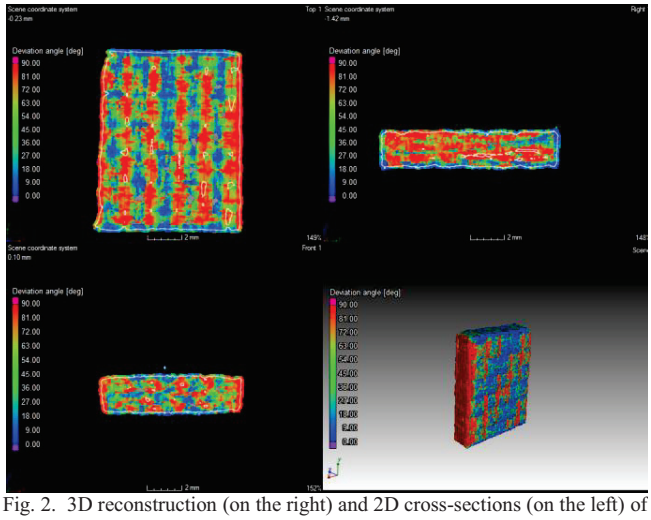

Fig. 2. 3D reconstruction (on the right) and 2D cross-sections (on the left) of a composite material (measured with Cu radiation) with the orientation distribution of the fiber component, presented in colors.

in blue color, whereas fibers oriented perpendicular to the *x*-axis of the object are shown in red. The colors between blue and red represent the fibers, which have a tilt in their orientation (tilt angle α, where $0\ ° < \alpha < 90\ °$). It is clearly seen in the Fig. 2 (left top side) that the fiber distribution is of basketwork type. From the orientation distribution calculation the partial fraction of the individual fiber direction can be extracted.

C. *Porous Materials*

A very important characteristic of many manufactured materials is their porosity. Knowledge of this parameter can help predicting the performance, endurance, *etc.* of the objects. A highly porous aerogel (see Fig. 3) has been measured using Co radiation. The volume fractions of the material itself and the containing air were determined. The ratio between the two resulted in the porosity value of 42 %. The direct visualization of the pore distribution within the object by using a color scheme is demonstrated in Fig. 3 (on the right).

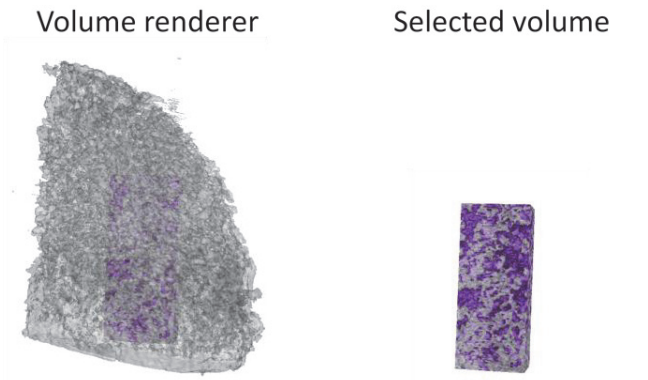

Fig. 3. A highly porous foam material, measured with Co radiation: 3D reconstruction and pore visualization (in purple).

IV. Conclusion

CT experiments of good quality can be performed on organic samples of various types when soft radiation, like Cu and Co, is applied. Once the 3D reconstruction is done, different parameters relevant for the samples can be extracted, such as porosity, orientation of certain components, distribution of the materials, size of inclusions, wall thickness or other features of the measured objects. The sensitivity of a CT experiment in case of samples made of light materials can be tremendously improved in this way.

References

[1] D. Götz, "Computed Tomography on a Standard Laboratory X-Ray Diffractometer", presented at the 3rd Int. Conf. Cellular Materials, Dresden, Germany, Oct. 22-24, 2014.

[2] Volume Graphics. (2014-08-13). *VGStudio MAX 2.2.6*. http://www.volumegraphics.com/en/products

Efficient Epipolar Consistency

André Aichert, Katharina Breininger, Thomas Köhler and Andreas Maier

Pattern Recognition Lab, Friedrich-Alexander Universität Erlangen-Nürnberg, Germany

***Abstract*—Epipolar consistency has been shown to be a powerful tool in calibration and motion correction for both flat panel detector CT (FD-CT) and other X-ray based applications. The epipolar consistency Conditions apply to projection data directly and can be used to correct for 3D parameters without 3D reconstruction. The computation of an epipolar consistency metric is real-time capable for small sets of images and can be parallelized for large sets of images. It has been shown to correct for motion in FD-CT scans in under one minute. This work presents a straight-forward and efficient implementation of the epipolar consistency metric. It shows that most of the algorithm is linear and can, in fact, be reduced to two 3×2 matrix-vector products by analytic simplification. This paper presents a full algorithm along with a brief validation of a GPU implementation. Said implementation is available as MATLAB source code to facilitate the application of Epipolar consistency to a variety of problems by other groups.**

I. Introduction

Consistency conditions in CT have been studied for decades. Yet, their practical application remains limited by hard assumptions on the imaging geometry (e.g. fan-beam only) and trajectory (e.g. full circle). Debbeler et al. [1] presented a raw data redundancy metric in 2013, which was later reformulated by Aichert et al. [2] to the epipolar consistency Conditions (ECC). Earlier work exists, which derives a similar set of consistency conditions from John's equation [3]. Not only is this consistency metric efficient to compute, it was also shown to be applicable to any set of X-ray projections, no matter the type and shape of trajectory (circular, saddle, circle and line to name a few), as long as the images showed the same part of the same object. Recent work by Maass et al. [4] and Frysch et al. [5] shows that ECC have practical applications for calibration and motion correction in flat detector CT and is fast enough to support clinical applications. It has also been suggested to apply ECC to other X-ray based modalities including fluoroscopy [6] and tomosynthesis [7].

This paper reviews the ECC algorithm presented in [6] to compute the epipolar consistency metric and further simplifies it, presenting an efficient and easily repeatable implementation. The paper presents both pseudo-code and a MATLAB implementation to estimate the relative geometry between two X-ray projections. Its extension to FD-CT is then merely an application of the presented algorithm to all pairs of projections of the scan. We hope that this paper allows other groups to apply the ECC to their problems and possibly find new applications.

II. Review of Epipolar Consistency Algorithm

A. Overview

This section provides mathematical tools and summarizes an algorithm to compute a metric of epipolar consistency. We consider two transmission-only projections I_0 and I_1, where each image point contains an integral over absorption coefficients along a ray through space. We denote the respective projection matrices as $\mathbf{P}_0$ and $\mathbf{P}_1 \in \mathbb{R}^{3\times4}$ with corresponding finite source positions $\mathbf{C}_0 \cong (C_0^0, C_0^1, C_0^2, 1)^\top \propto \text{null}(\mathbf{P}) \in \mathbb{P}^3$ and $\mathbf{C}_1$ accordingly, in homogeneous coordinates of oriented projective three-space, where $\cong$ denotes an equivalence relation up to positive scalar multiples.

The gist of epipolar consistency is that the baseline $\mathbf{B}$ connecting the two source positions $\mathbf{C}_0$ and $\mathbf{C}_1$ defines a pencil of planes. By intersection with the detectors, each plane defines two lines $\mathbf{l}_0$ and $\mathbf{l}_1 \in \mathbb{P}^2$ in the projection images I_0 and I_1. These lines are well known from Computer Vision as epipolar lines. In case of transmission-based modalities such as X-ray imaging, both lines go back to the absorption of the same plane through the object and therefore "contain" the same total absorption. In parallel geometries, i.e. if the source positions $\mathbf{C}_0$ and $\mathbf{C}_1$ are at infinity, an integral over the line $\mathbf{l}_0$ should be identical to an integral over the line $\mathbf{l}_1$, provided there is no truncation of the object. We can use Grangeat's theorem to generalize for arbitrary projections, which introduces a derivative in orthogonal direction to the lines [8]. Note that our work consistently and successfully ignores certain cosine weights, which are, however, addressed in [1], [4].

The ECC algorithm consists of the following major steps. 1) Pre-processing: First, the derivative orthogonal

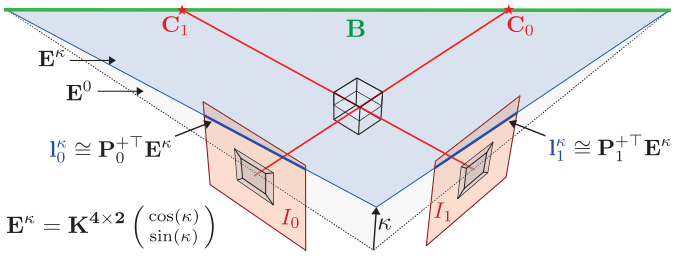

Figure 1. Epipolar geometry of two cone-beam projection images with projection matrices $\mathbf{P}_0, \mathbf{P}_1 \in \mathbb{R}^{3\times4}$. The source positions $\mathbf{C}_0, \mathbf{C}_1 \in \mathbb{P}^3$, along with the principal rays orthogonal to the detectors I_0 and I_1 are shown in red. The epipolar plane $\mathbf{E}^\kappa$ (light blue) intersects the reference plane $\mathbf{E}^0$ (light gray) in the baseline (green) at an angle κ. The corresponding epipolar lines $\mathbf{l}_0^\kappa, \mathbf{l}_1^\kappa \in \mathbb{P}^2$ are the points of intersection on the detectors with the plane $\mathbf{E}^\kappa$.

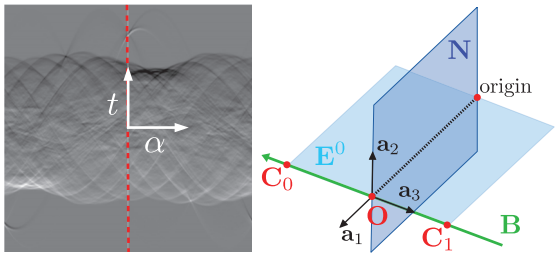

Figure 2. Left: Derivative $\frac{\partial}{\partial t}\rho_I(\alpha,t)$ of the Radon transform of an image I. Note the symmetry w.r.t. a change in angle by 180° $\frac{\partial}{\partial t}\rho_I(\alpha,t) = -\frac{\partial}{\partial t}\rho_I(\alpha+\pi,-t)$. Right: The three vectors $\mathbf{a}_1$, $\mathbf{a}_2$ and $\mathbf{a}_3$ form an orthogonal basis, where the vectors $\mathbf{a}_1$ and $\mathbf{a}_2$ span the plane $\mathbf{N}$, which contains the origin and is orthogonal to baseline $\mathbf{B}$ connecting the source positions $\mathbf{C}_0$ and $\mathbf{C}_1$.

to the lines of the Radon transform of all projection images is computed, compare Section II-B. 2) Geometry: Second, the geometric part of the algorithm finds a mapping from an angle κ that parametrizes the bundle of planes around the baseline to two lines, with redundant information, compare Section II-C. 3) Sampling: Third, the two epipolar lines are converted to angle α to the x-axis and signed distance to the origin t. The pre-computed Radon derivatives are then sampled at corresponding locations (α, t) , compare Section II-D. The last steps are repeated for all angles κ with some spacing $d\kappa$ and the sum of squared differences of the redundant values is computed and returned. This paper addresses only the computation of a consistency metric. Calibration and motion correction can be done numerically optimizing said metric over parameters of the projection geometry.

B. Algorithm: Derivative of the Radon Transform

The ECC compare the integrals of corresponding lines in projection images. Debbeler et al. [1] suggests pre-computing the integrals of all lines $\mathbf{l} \cong (-\sin(\alpha), \cos(\alpha), -t)^\top$ using the Radon transform $\rho_I(\alpha,t)$ of a projection image I. This is the most important optimization in the ECC algorithm, because we need to compare thousands of line-integrals. Once the Radon transform is computed, we can sample it, instead of repeatedly computing similar line integrals. The Radon transform is well-known in the CT community as the parallel-beam forward projector in two dimensions. In this case, however, it is computed from a cone-beam projection image. Care should be taken for the Radon transform to have sufficient bins, so as to avoid under-sampling. As a rule of thumb, the Radon transform should have at least as many bins as the input image has pixels. The 1st derivative $\frac{\partial}{\partial t}\rho_I(\alpha,t)$ in orthogonal direction to the lines t, can be done, for example, using a Sobel filter, see Figure 2, left. The rest of the ECC algorithm is to iterate over an angle κ that parametrizes the pencil of epipolar planes and sample the Radon derivatives in the appropriate places to measure their difference.

C. Algorithm: Parametrizing Epipolar Lines

The epipolar geometry of two images is closely related to the mathematics of the fundamental matrix. Our algorithm, however, uses the underlying concept of Plücker matrices directly [9]. This section summarizes how to find a matrix

$$\mathbf{K} \cong [\tilde{\mathbf{B}}]_\times \mathbf{A} = [\tilde{\mathbf{B}}]_\times \begin{pmatrix} \mathbf{a}'_1 & \mathbf{a}'_2 & \mathbf{O} \\ 0 & 0 & \end{pmatrix}, \tag{1}$$

which maps a vector $\mathbf{x}^\kappa = (\cos(\kappa), \sin(\kappa), 1)^\top$ to an epipolar plane $\mathbf{E}^\kappa = \mathbf{K} \cdot \mathbf{x}^\kappa \in \mathbb{P}^3$ which intersects the reference plane $\mathbf{E}^0 \in \mathbb{P}^3$ in the baseline at an angle κ, according to Algorithm 1 in [8].

The Plücker coordinates of the baseline $\mathbf{B}$ through the source positions $\mathbf{C}_0$ and $\mathbf{C}_1$ are

$$\mathbf{B} \cong (B_{01}, B_{02}, B_{03}, B_{12}, B_{13}, B_{23})^\top, \tag{2}$$

with $B_{01}B_{23} - B_{02}B_{13} + B_{03}B_{12} = 0$, where

$$\mathbf{B}_{ij} = C_0^i C_1^j - C_1^i C_0^j. \tag{3}$$

The Plücker Matrix $[\mathbf{B}]_\times$ and its dual $[\tilde{\mathbf{B}}]_\times$ are related via $[\tilde{\mathbf{B}}]_\times [\mathbf{B}]_\times = \mathbf{0}$. The direction $\mathbf{a}_3$ of the baseline $\mathbf{B}$ can be computed by multiplication with the plane at infinity $\pi^\infty = (0,0,0,1)^\top$

$$[\mathbf{B}]_\times \pi^\infty = \begin{pmatrix} -B_{03} \\ -B_{13} \\ -B_{23} \\ 0 \end{pmatrix} = \begin{pmatrix} \mathbf{a}_3 \\ 0 \end{pmatrix}. \tag{4}$$

The vector $\mathbf{a}_3$ points in the direction from the point $\mathbf{C}_0$ to the point $\mathbf{C}_1$. The infinite point $\mathbf{N} \cong [\tilde{\mathbf{B}}]_\times \pi^\infty = (\mathbf{a}_3, 0)^\top$ can also be interpreted as a plane through the origin. The common plane

$$\mathbf{E}^0 \cong [\tilde{\mathbf{B}}]_\times \mathbf{X}^0 \tag{5}$$

of the baseline $\mathbf{B}$ and some reference point $\mathbf{X}^0$ in the object defines where the plane with $\kappa = 0$ shall lie. Let $\mathbf{a}_2$ denote the first three components of $\mathbf{E}^0$, i.e. its orthogonal. Let $\mathbf{O}$ denote the intersection of the plane $\mathbf{N}$ with the baseline $\mathbf{B}$. Then, $\mathbf{O}$ is the orthogonal projection of the origin to the baseline and thus its closest point to the origin

$$\mathbf{O} \cong [\mathbf{B}]_\times \mathbf{N} \cong [\mathbf{B}]_\times [\mathbf{B}]_\times \pi^\infty. \tag{6}$$

We finally have $\mathbf{a}'_2 = \frac{\mathbf{a}_2}{\|\mathbf{a}_2\|}$, $\mathbf{a}'_3 = \frac{\mathbf{a}_3}{\|\mathbf{a}_3\|}$ and $\mathbf{a}'_1 = \mathbf{a}'_3 \times \mathbf{a}'_2$.[1] See Figure 2, right, for the geometry of the baseline and the vectors $\mathbf{a}_1$, $\mathbf{a}_2$, $\mathbf{a}_3$.

D. Algorithm: Sampling the Radon Transforms

Given an epipolar plane $\mathbf{E} \in \mathbb{P}^3$ we can find the two epipolar lines

$$\mathbf{l}_0 = \mathbf{P}_0^{+\top}\mathbf{E} \text{ and } \mathbf{l}_1 = \mathbf{P}_1^{+\top}\mathbf{E}, \tag{7}$$

where $\circ^{+\top}$ denotes the pseudo-inverse transpose of a projection matrix. The Radon transform is commonly parametrized by the signed distance to the image center, while the projection images typically have the coordinate origin in one of the corners. We account for this with

[1] Sign of $\mathbf{a}'_1$ determines direction of rotation, which is arbitrary.

Algorithm 1 Epipolar geometry in 12 lines of CUDA, see Section II-C and II-D. `sgemm` is the BLAS matrix multiply.

```
// Plücker coordinates of baseline (vectors a2 and a3):
float B01 = C0[0]*C1[1] - C0[1]*C1[0]; //  a2[2]
float B02 = C0[0]*C1[2] - C0[2]*C1[0]; // -a2[1]
float B03 = C0[0]*C1[3] - C0[3]*C1[0]; //  a3[0]
float B12 = C0[1]*C1[2] - C0[2]*C1[1]; //  a2[0]
float B13 = C0[1]*C1[3] - C0[3]*C1[1]; //  a3[1]
float B23 = C0[2]*C1[3] - C0[3]*C1[2]; //  a3[2]
// s3 = norm(a3)
float s3 = sqrt( B03*B03 + B13*B13 + B23*B23 );
// K is a 4x2 matrix (column major)
float K[] = {
      + B12*s3, - B02*s3, + B01*s3, 0, // a2*norm(a3)
      - B01*B13 - B02*B23,             // a1[0]
      + B01*B03 - B12*B23,             // a1[1]
      + B02*B03 + B12*B13,             // a1[2]
      -B12*B12 - B02*B02 - B01*B01     // -norm(a2)^2
};
// left-multiplication with pseudo-inverse transpose
sgemm<3,4,2>(P0invT,K,K0);
sgemm<3,4,2>(P1invT,K,K1);
```

a homography $\mathbf{H}$, which moves the coordinate origin by $(-\frac{1}{2}n_x, -\frac{1}{2}n_y)^\top$ to the image center. Lines transform contra-variant by its inverse transpose

$$\mathbf{H}^{-\top} = \begin{pmatrix} 1 & & \\ & 1 & \\ \frac{1}{2}n_x & \frac{1}{2}n_y & 1 \end{pmatrix}. \tag{8}$$

We can thus define two matrices

$$\mathbf{K}_0 = \mathbf{H}^{-\top}\mathbf{P}_0^{+\top}\mathbf{K} \text{ and } \mathbf{K}_1 = \mathbf{H}^{-\top}\mathbf{P}_1^{+\top}\mathbf{K}, \tag{9}$$

which map $\mathbf{x}^\kappa = (\cos(\kappa),\ \sin(\kappa),\ 1)^\top$ directly to the two corresponding epipolar lines relative to the image center

$$\mathbf{l}_0^\kappa = \mathbf{K}_0\mathbf{x}^\kappa \text{ and } \mathbf{l}_1^\kappa = \mathbf{K}_1\mathbf{x}^\kappa. \tag{10}$$

Finally, angles and signed distances have to be computed from the lines' coordinates.

III. Simplification for GPU implementation

A. World Origin as Reference Point

Without loss of generality, this paper considers the case, where the reference plane $\mathbf{E}^0$ shall pass through the origin. We can thus write down $\mathbf{a}_2$ explicitly

$$\mathbf{E}^0 \cong [\tilde{\mathbf{B}}]_\times \begin{pmatrix} 0 \\ 0 \\ 0 \\ 1 \end{pmatrix} = \begin{pmatrix} B_{12} \\ -B_{02} \\ B_{01} \\ 0 \end{pmatrix} = \begin{pmatrix} \mathbf{a}_2 \\ 0 \end{pmatrix}. \tag{11}$$

B. Last Column of $\mathbf{A}$ is Zero

Equation 6 defines $\mathbf{O}$ as a point on the baseline $\mathbf{B}$ with

$$[\tilde{\mathbf{B}}]_\times \mathbf{O} = \underbrace{[\tilde{\mathbf{B}}]_\times [\mathbf{B}]_\times}_{=\mathbf{0}} [\mathbf{B}]_\times \pi^\infty = \mathbf{0}. \tag{12}$$

We can simplify Equation 1, $\forall \mathbf{x} = (x_0, x_1, x_2) \in \mathbb{R}^3$:

$$\begin{aligned} \mathbf{K}\mathbf{x} &= [\tilde{\mathbf{B}}]_\times \mathbf{A}\mathbf{x} \\ &= [\tilde{\mathbf{B}}]_\times \begin{pmatrix} \mathbf{a}_1 & \mathbf{a}_2 \\ 0 & 0 \end{pmatrix} \begin{pmatrix} x_0 \\ x_1 \end{pmatrix} + \underbrace{[\tilde{\mathbf{B}}]_\times \mathbf{O}}_{=0} \cdot x_2. \end{aligned} \tag{13}$$

Hence the last column $\mathbf{O}$ of the matrix $\mathbf{A}$ can be dropped completely and we only need to find $\mathbf{a}_1$ and $\mathbf{a}_2$. In consequence, we can also drop the last columns of $\mathbf{K}_0$ and $\mathbf{K}_1$ and encode the whole geometry in two 3×2 matrices. By multiplication with $(\cos(\kappa), \sin(\kappa))^\top$ for some angle κ we directly obtain two corresponding epipolar lines.

C. Re-writing the Dual Plücker Matrix

Using a 3×3 Plücker matrix $[\mathbf{a}_3]_\times \mathbf{x} = \mathbf{a}_3 \times \mathbf{x}$ we have

$$[\tilde{\mathbf{B}}]_\times = \begin{pmatrix} [\mathbf{a}_3]_\times & \mathbf{a}_2 \\ -\mathbf{a}_2^\top & 0 \end{pmatrix}, \text{ with } [\mathbf{a}_3]_\times = \begin{pmatrix} 0 & -B_{23} & B_{13} \\ B_{23} & 0 & -B_{03} \\ -B_{13} & B_{03} & 0 \end{pmatrix}. \tag{14}$$

Equation 1 becomes

$$\begin{aligned} \mathbf{K}^{\mathbf{2\times4}} &\cong [\tilde{\mathbf{B}}]_\times \begin{pmatrix} \mathbf{a}_1 & \mathbf{a}_2\|\mathbf{a}_3\| \\ 0 & 0 \end{pmatrix} \\ &= \begin{pmatrix} [\mathbf{a}_3]_\times & \mathbf{a}_2 \\ -\mathbf{a}_2^\top & 0 \end{pmatrix} \begin{pmatrix} \mathbf{a}_1 & \mathbf{a}_2\|\mathbf{a}_3\| \\ 0 & 0 \end{pmatrix} \\ &\cong \begin{pmatrix} \mathbf{a}_2\|\mathbf{a}_3\| & \mathbf{a}_1 \\ 0 & \|\mathbf{a}_2\|^2 \end{pmatrix} \end{aligned} \tag{15}$$

The whole geometry of epipolar consistency is now encoded in the following matrix multiplication

$$\mathbf{E}^\kappa \cong \begin{pmatrix} +B_{12}\|\mathbf{a}_3\| & -B_{13}B_{01}-B_{02}B_{23} \\ -B_{02}\|\mathbf{a}_3\| & +B_{03}B_{01}-B_{12}B_{23} \\ +B_{01}\|\mathbf{a}_3\| & +B_{03}B_{02}+B_{12}B_{13} \\ 0 & -B_{12}^2-B_{02}^2-B_{01}^2 \end{pmatrix} \begin{pmatrix} \cos(\kappa) \\ \sin(\kappa) \end{pmatrix}, \tag{16}$$

with $\|\mathbf{a}_3\| = \sqrt{B_{03}^2 + B_{13}^2 + B_{23}^2}$. This is the main result of this paper and can be converted directly into source code. We obtain Algorithm 1.

D. Singularities

Note that the distance of the baseline to the origin can be written as $\frac{\|\mathbf{a}_3\|}{\|\mathbf{a}_2\|}$. This means that the presented optimization has singularities when the baseline $\mathbf{B}$ contains the origin. Nevertheless, this case is easily avoided by a global translation which brings any preferred reference point to the origin. The algorithm above also requires at least one of the source positions to be finite. However, the geometry of the parallel case is simpler and allows for the direct comparison of line integrals[10].

E. Interpretation

The result of Section III is surprisingly compact. We can even interpret the columns of the matrix $\mathbf{K}^{4\times2}$ as planes. The plane $\mathbf{E}^0 \cong [\tilde{\mathbf{B}}]_\times \pi^\infty$ is the reference plane, while the epipolar plane

$$\mathbf{E}^{\frac{\pi}{2}} \cong \left(\frac{\mathbf{a}_1}{\|\mathbf{a}_1\|}, \frac{\|\mathbf{a}_3\|}{\|\mathbf{a}_2\|} \right)^\top \cong [\mathbf{B}]_\times [\mathbf{B}]_\times \pi^\infty, \tag{17}$$

is parallel to the $\mathbf{a}_2$-$\mathbf{a}_3$ plane. It is exactly the plane for $\kappa = 90°$. Using the same argument, we can see that the columns of the matrices $\mathbf{K}_0^{3\times2} = \mathbf{P}_0^{+\top}\mathbf{K}^{4\times2}$ and $\mathbf{K}_1^{3\times2} = \mathbf{P}_1^{+\top}\mathbf{K}^{4\times2}$ contain the epipolar lines $\mathbf{l}_0^0$, $\mathbf{l}_0^{\frac{\pi}{2}}$ and $\mathbf{l}_1^0$, $\mathbf{l}_1^{\frac{\pi}{2}}$, respectively.

Although the epipolar lines depend linearly on the angle κ, their angle in the image is not linear in κ, because the upper 2×2 parts of $\mathbf{K}_0^{3\times2}$ and $\mathbf{K}_1^{3\times2}$ are generally not orthogonal, or of equal norm.

Algorithm 2 Sampling redundant value $\frac{\partial}{\partial t}\rho_{I_0}$ at $\mathbf{l}_0^\kappa$, see Section II-D. The function `tex2D` samples a texture `dtr0` in normalized coordinates using linear interpolation.

```
// Find epipolar line on I0 at angle kappa
float x_k = {cos(kappa), sin(kappa)};
sgemm<3,2,1>(K0,x_k,l0);
// Length of normal
float length0=sqrt(l0[0]*l0[0]+l0[1]*l0[1]);
// Angle between line and x-axis (from 0 to 2)
float dtr0_x=atan2(l0[1],l0[0])/Pi+1.0f;
// Signed distance to center (scaled to Radon bins)
float dtr0_y=(l0[2]/length0)/radon_range_t+0.5f;
// Sample Radon derivative textures (dtr)
if (dtr0_x<1.0f)
   sample0=+tex2D<float>(dtr0, 1.f-dtr0_x, 1.f-dtr0_y);
else // account for symmetry: rho(a,t)=-rho(a+Pi,-t)
   sample0=-tex2D<float>(dtr0, 2.f-dtr0_x, dtr0_y);
```

IV. Experiments and Results

We provide an open-source reference implementation of the epipolar consistency metric, in Octave (MATLAB) [2]. In addition, we evaluated and timed our GPU implementation on a mobile computer with NVIDIA GTX 860M, on an FD-CT short scan with $n = 133$ projections.

1) Pre-processing: We do not discuss the 2D Radon transform. CPU Computation of pseudo-inverse and null-space of $n = 133$ projection matrices and takes < 1ms.

2) Geometry: In a CT scan with n projections, there are $N = n \cdot \frac{n-1}{2}$ pairs (e.g. $N = 8,778$ for $n = 133$ and $N = 122,760$ for $n = 496$). We must compute $\mathbf{K}_0$ and $\mathbf{K}_1$ for each such pair, see Algorithm 1 and Equation 9. Our CUDA kernel uses 28 registers and takes 1.3 ms for $n = 496$, which is not much faster than the CPU.

3) Sampling: Most time is spent iterating over all pairs of projection images and over all angles κ to sample redundant values in the Radon derivatives from texture memory. This step benefits the most from palatalization. There are several ways of distributing the problem. The straightforward implementation computes the consistency for a pair of views in each thread. Using a reasonably dense sampling, the kernel takes about 160 ms for $n = 133$ projections at a achieved occupancy of 60% limited by 39 registers. On the CPU it would take > 1 second. This can be improved by handing a single value of κ in each thread and computing the consistency of a pair of views in each block. With the same settings, the improved kernel achieves an occupancy of 91% using 30 registers and takes 44ms to compute. We require only 26 registers when loading the matrices $\mathbf{K}_0$ and $\mathbf{K}_1$ into shared memory but are not faster. Algorithm 2 shows the sampling of the Radon derivative $\frac{\partial}{\partial t}\rho_{I_0}$ at $\mathbf{l}_0^\kappa$ in the inner-most loop. Algorithm 1 only shows the first half of the function body, because the same steps would be repeated with $\mathbf{l}_1^\kappa$ to obtain `sample1`. Note that this paper does not describe how to modulate the angle $d\kappa$ between individual epipolar planes so as to achieve an even sampling.

[2] https://www5.cs.fau.de/research/software/epipolar-consistency

V. Conclusion

This paper addresses the epipolar Consietency Conditions (ECC) of any two X-ray projections, which can be used for motion and calibration correction in FD-CT. We review an algorithm to measure the epipolar consistency and then simplify the geometric part of the algorithm analytically. We present a compact form, consisting of two 3×2 matrices, which can be computed from two source position in 12 lines of C-code. Accordingly, the computationally expensive part is reduced to multiplication by said matrices, conversion of the epipolar lines to angle and distance and two texture reads in the inner-most loop. Timing results of our GPU implementation provide a baseline for further optimizations. Future work might parametrize the Radon transform so as to avoid two `atan2` operations. As supplementary material, we provide an open-source example of the ECC algorithm. We hope that this work allows other groups interested in epipolar consistency to quickly adapt an efficient solution.

Acknowledgments: We are supported by the German Research Foundation; DFG MA 4898/3-1 "Consistency Conditions for Artifact Reduction in Cone-beam CT".

References

[1] C. Debbeler, N. Maass, M. Elter, F. Dennerlein, and T. M. Buzug, "A new ct rawdata redundancy measure applied to automated misalignment correction," in *Proceedings of the Fully 3D*, 2013, p. 264.

[2] A. Aichert, N. Maass, Y. Deuerling-Zheng, M. Berger, M. Manhart, J. Hornegger, A. K. Maier, and A. Doerfler, "Redundancies in X-ray images due to the epipolar geometry for transmission imaging," in *Proceedings of the third CT-meeting*, F. Noo, Ed., 2014, pp. 333–337.

[3] M. S. Levine, E. Y. Sidky, and X. Pan, "Consistency conditions for cone-beam ct data acquired with a straight-line source trajectory," *Tsinghua Sci Technol.*, vol. 15, no. 1, Feb 2010.

[4] N. Maass, F. Dennerlein, A. Aichert, and A. Maier, "Geometrical Jitter Correction in Computed Tomography," in *Proceedings of the third CT-meeting*, F. Noo, Ed., 2014, pp. 338–342.

[5] R. Frysch and G. Rose, "Rigid motion compensation in interventional c-arm ct using consistency measure on projection data," in *Proceedings of the MICCAI 2015*, ser. Lecture Notes in Computer Science, N. Navab, J. Hornegger, W. M. Wells, and A. F. Frangi, Eds., vol. 9349. Springer International Publishing, 2015, pp. 298–306.

[6] A. Aichert, J. Wang, R. Schaffert, A. Dörfler, J. Hornegger, and A. Maier, "Epipolar consistency in fluoroscopy for image-based tracking," in *Proceedings of the British Machine Vision Conference (BMVC)*, M. W. J. Xianghua Xie and G. K. L. Tam, Eds. BMVA Press, September 2015, pp. 82.1–82.10.

[7] T. Grulich, W. Holub, U. Ha ler, A. Aichert, and A. Maier, "Geometric Adjustment of X-ray Tomosynthesis," in *Proceedings of The 13th Fully 3D*, M. King, Ed., 2015, pp. 468–470.

[8] A. Aichert, M. Berger, J. Wang, N. Maass, A. Doerfler, J. Hornegger, and A. Maier, "Epipolar consistency in transmission imaging," *Medical Imaging, IEEE Transactions on*, vol. 34, no. 11, pp. 2205–2219, Nov 2015.

[9] J. F. Blinn, "A homogeneous formulation for lines in 3 space," *ACM SIGGRAPH Computer Graphics*, vol. 11, no. 2, pp. 237–241, Aug 1977.

[10] S. S. Brandt, K. Hommelhoff Jensen, and F. Lauze, "Bayesian epipolar geometry estimation from tomographic projections," in *Computer Vision - ACCV 2012*, K. M. Lee, Y. Matsushita, J. M. Rehg, and Z. Hu, Eds. Springer Berlin Heidelberg, 2012, pp. 231–242.

Fully iterative reconstruction for cardiac CT

Qiulin Tang, Satoru Nakanishi, Zhou Yu, Wenli Wang

***Abstract*– Fully iterative reconstruction has been developed and widely used in institute and industry because of its merits compared with classical filter backprojection (FBP) reconstruction, such as noise control and flexibility of adapting physical models. One of the major applications of fully iterative reconstruction in clinic is cardiac CT. To obtain an image with less motion artifacts, ECG gating and half reconstruction or even segment reconstruction are often desired. These increase the complexity of reconstruction. In the work, a fully iterative reconstruction scheme is proposed for cardiac volumetric CT, and evaluation is performed to verify its feasibility of achieving the same temporal resolution as classical FBP method, but still hold the general merits of IR.**

I. INTRODUCTION

Volumetric CT imaging is the major non-invasive modality for diagnosis of cardiac disease because it has both high spatial resolution and high temporal resolution. Currently, Electrocardiogram (ECG)-gating is routinely applied in cardiac CT imaging to choose reconstruction at quiet cardiac phase [1-3]. The temporal resolution can be further improved by segment reconstruction, especially in high heart rate case [4-6]. In segment reconstruction, data acquisition time is a couple of heart beats. From each heart beats, a part of data, which is no more than half scan range, were selected to gather together to build a minimum data range which are sufficient for a reconstruction.

The major concern of cardiac CT is the dose. Because of gating, many acquired data were not used in reconstruction. Segment reconstruction gives even higher radiation dose to patient [5], since X-ray is on for more than one single heart beat, which is sufficient for a half scan reconstruction. Dose reduction is then one of the major goals for cardiac CT imaging. Radiation dose can be reduced directly by lowering the X-ray tube current, but it leads to nosier image. Many researchers have contributed to suppressing image noise [5, 7]. Another type of approaches optimize the redundancy weighting scheme to reduce the image noise [5, 7].

Recently, fully iterative reconstruction algorithms (IR) have been used in CT reconstruction [8-11], and it shows that IR has better noise reduction and flexibility of modelling physics than analytical reconstruction. Moreover, cone beam artifacts in circular scan can be mitigated by IR [12, 13]. Also, IR can suppress low frequency cone-beam artifacts, which appears in analytical circular half reconstruction due to the non-uniformity of data redundancy [14].

In this work, a fully IR scheme is proposed for cardiac CT, which can handle the cardiac half and segment weights to achieve the same temporal resolution as analytical reconstruction, and in the meantime it also achieves the common benefits of IR.

II. ALGORITHMS

The major IR framework was reported in [13]. For the convenience of the reader, this approach was described briefly again. This approach is a penalized weighted least square (PWLS) approach [15] and its cost function $C(f)$ has a data fidelity term and regularization term.

$$C(f) = (A f - g)^T W (A f - g) + \beta U(f) \quad (1)$$

In Eqn. (1),

A: the forward projection operator;

f: the image to be reconstructed;

g: the measured projection data;

W: typically a diagonal weighting matrix;

$U(f)$: the penalty function (regularizer);

β: the regularization smoothing parameter.

Qiulin Tang, Zhou Yu, Satoru Nakanishi and Wenli Wang are with Toshiba Medical Research Institute, USA. 706 N. Deerpath Dr., Vernon Hills, IL, 60061, USA. (e-mail: qtang@tmriusa.com, snakanishi@tmriusa.com, zyu@tmriusa.com, wwang@tmriusa.com).

Image$f$ can be optimized by minimizing the cost function, $C(\cdot)$.

$$f = arg\min(C(f)) \quad (2)$$

Many approached have been developed to solve Eqn. (2), here, we use gradient descent algorithm for optimization, and use following basic framework to reconstruct image.

Step 1: Give an initial guess of image $f^{(0)}$;

Step 2: Update the guess of image as

for iter = 1 , …, N_{iter}

$f^{(n)} = f^{(n-1)} + \Delta f^{(n)}$;

Step 3: Stop iteration when reaching convergence criteria.

In the gradient descent algorithm, the quantity $\Delta f^{(n)}$ in Step 2 is some function of the negative gradient of the cost function in Eqn. (1).

In this work, half and segment scans weights were applied to this framework to achieve same temporal resolution as analytical cardiac reconstructions do. That is,

$$W = W * W_r, \quad (3)$$

Where, W_r is cardiac half and segment weight, and the data range selection for segment reconstruction is shown in figure 1. Red patches are the data used for reconstruction.

The weights W_r is selected as what our group developed for analytical cardiac reconstruction [6, 7, 16], and it was proved to have good performance, in term of suppression of artifacts and noise.

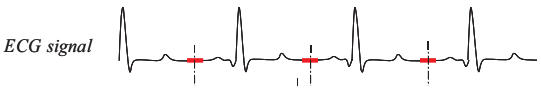

Fig. 1. Data range for segment reconstruction selected by ECG signal. Red patches are been selected.

III. Experiment and Results

In this study, motion simulation was performed, and it simulates the beating heart wall, high attenuation bone, non-attenuation air, water type of tissue and water. This simulation is noise-free, it then isolates motion artifacts (temporal resolution issue) from noise and noise related artifacts, such as streak artifacts.

Three clinical data were acquired by a single source, 320-row CT scanner (Aquilion ONE™, Toshiba, Otawara, Japan) with gantry rotation speeds of 275 ms/rot. And heart rates are about 60 beats per minute (bpm). The performance of the proposed IR was evaluated in three aspects: temporal resolution noise, streak artifacts. For comparison, classical FBP reconstruction was performed.

Figure 2 shows the comparison between FBP images and IR images with simulated motion phantom, where the center slice is shown. The heart rate is 90 bpm and image of systole phase was reconstructed. Top row are from classical FBP reconstruction and bottom row are from the proposed IR. From left to right columns from full scan reconstruction, half scan reconstruction and segment reconstruction with 3 heart beats data, respectively. Window width and level are 600 and 50 HU, respectively. It shows that half scan reconstruction has better temporal resolution than full scan reconstruction and segment reconstruction has better temporal resolution than half scan reconstruction. Also it is obvious that the proposed IR achieves the same temporal resolution as its corresponding analytical one.

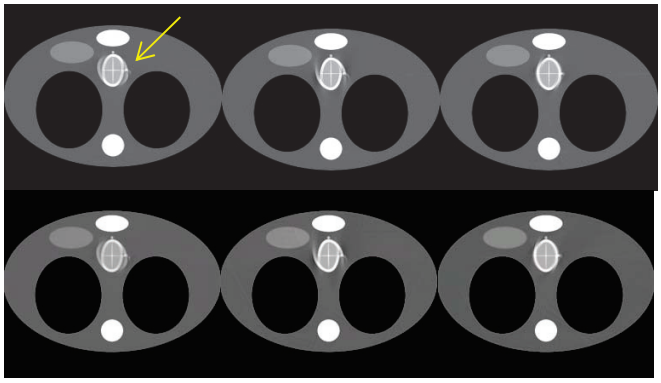

Fig. 2. Axial images: top row is from classical FBP reconstruction and bottom is from the proposed IR. From left to right columns are full scan reconstruction, half scan reconstruction and segment reconstruction, respectively. Window width and level are 600 and 50 HU, respectively. Arrow indicates the motion region.

Figure 3 shows the axial images of middle diastole from center slice of patient 1 with heart rate of 68.2 bpm. It is shown that half scan reconstruction has better temporal resolution and the proposed IR achieves the same temporal resolution as the analytical one. And the proposed

IR suppresses the noise and streak artifacts, which are the common merits of IR.

Figure 4 shows the coronary view images of middle diastole from center slice of patient 1. It also shows similar conclusion as in axial view image in figure 3.

For patient 2 and 3 we just show results of half reconstruction. These two patients are with heart rate of 62 and 67 bpm, respectively.

Figure 5 shows the result of patient 2. It shows similar conclusion as from results of patient 1. That is, same temporal resolution, but better noise and streak artifacts suppression can be achieved by the proposed IR.

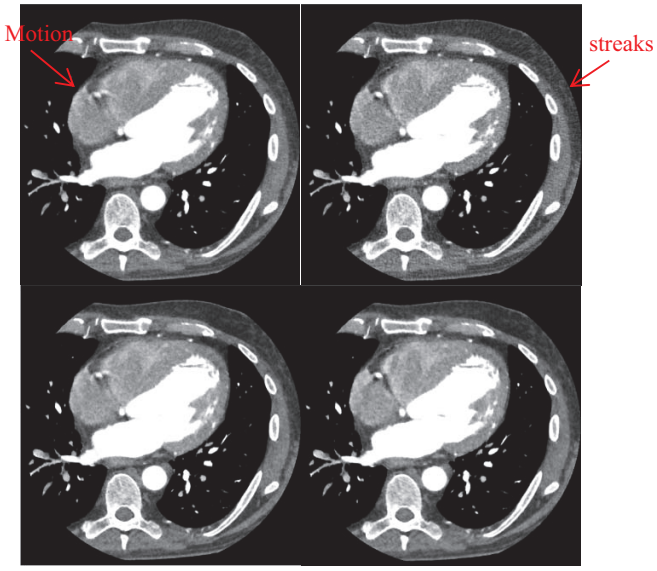

Fig. 3. Axial image of patient 1 with heart rate of 68.2 bpm. Top row are from classical FBP reconstruction; bottom row are from the proposed IR. Left column is from full scan reconstruction, and right column is from half scan reconstruction. Window width and level are 600 and 50 HU, respectively.

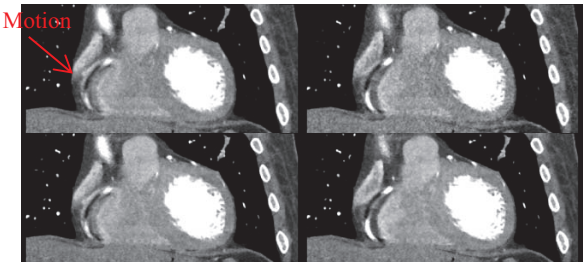

Fig. 4. Coronary image of patient 1. The four panels are the same as in fig. 3.

Figure 6 shows the result of patient 3. Same observations were obtained as results of patient 1 and 2. Moreover, it also shows that the proposed IR has better contrast detection (see the regions shown by arrows).

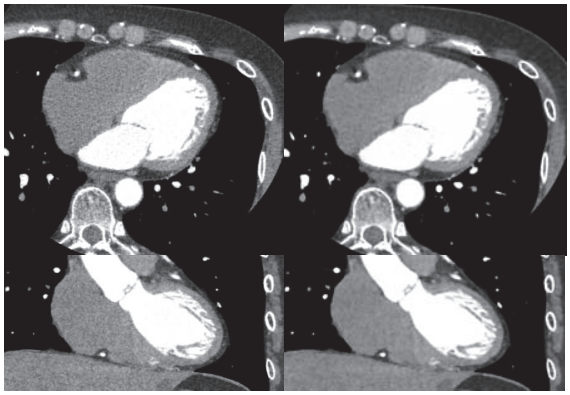

Fig. 5. Half scan reconstruction of patient 2 at middle diastole. Top row are from axial view; bottom row are coronary view. Left column is classical FBP reconstruction, and right column is the proposed IR. Window width and level are 600 and 50 HU, respectively.

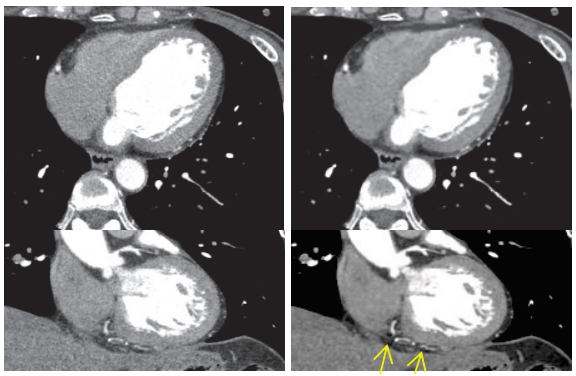

Fig. 6. Half scan reconstruction of patient 2 at middle diastole. The four panels are the same as in fig. 5.

IV. Conclusions

Our newly developed IR adapted the data redundancy weight for cardiac half and segment reconstruction. Simulation and clinical study were performed. It verified that the proposed IR can achieve the same temporal resolution as classical FBP method, as well as keep the common merits of fully IR, such as the flexibility of noise control, suppression of streak artifacts. Moreover, better

contrast detection was observed for the proposed IR.

REFERENCES

[1] B. Ohnesorge *et al.*, "Cardiac imaging by means of electrocardiographically gated multisection spiral CT: Initial experience," Radiology **217**, pp. 564–571, 2000.

[2] T. Flohr and B. Ohnesorge, "Heart rate optimization of spatial and temporal resolution for ECG gated multislice spiral CT of the heart," J. Comput. Assist. Tomogr. **25**, pp. 907–923 2001.

[3] J. Hsieh *et al.*, "Step-and-shoot data acquisition and reconstruction for cardiac x-ray computed tomography," Med. Phys. **33**, pp. 4236–4248, 2006.

[4] H. Bruder, S. Schaller, and T. Flohr, "High temporal volume heart imaging with multirow computed tomography," Proc. SPIE **3661**, pp. 420–432, 1999.

[5] M. Kachelrieß, M. Knaup, and W. A. Kalender, "Extended parallel backprojection for standard three-dimensional and phase-correlated four dimensional axial and spiral cone-beam CT with arbitrary pitch, arbitrary cone-angle, and 100% dose usage," Med. Phys. **31**, pp. 1623–1641, 2004.

[6] K. Taguchi, B. S. Chiang, and I. A. Hein, "Direct cone-beam cardiac reconstruction algorithm with cardiac banding artifacts correction," Med. Phys. **33**, pp. 521–539, 2006.

[7] K. Taguchi, B. S. Chiang, and M. D. Silver, "A new weighting scheme for cone-beam helical CT to reduce the image noise," Phys. Med. Biol. **49**, pp. 2351–2364, 2004.

[8] J. Nuyts, et al, "Iterative reconstruction for helical CT: a simulation study," Phys. Med. Biol. **43**, pp. 729–737, 1998.

[9] I. A. Elbakri and J. A. Fessler, "Statistical Image Reconstruction for Polyenergetic X-Ray Computed Tomography," IEEE Trans. Med. Imag., 21(2), 2002.

[10] J. Thibault, et al, "A three-dimensional statistical approach to improved image quality for multislice helical CT," Med. Phys. 34, pp 4526-4544, 2007.

[11] Z. Yu, et al, "Accelerated line search for coordinate descent optimization," *Proceedings of the IEEE Nuclear Science Symposium and Medical Imaging Conference*, 6498, pp. 2841–2844, 2006.

[12] F. Dennerlein, *et al*., "Constriction of cone-beam artifacts by the z-smart reconstruction method," IEEE *Nuclear Science Symposium Conference Record*, pp. 4090-4096, 2007.

[13] D. Shi, "Successful Suppression of Cone Beam Artifacts Using Iterative Reconstruction Algorithm," Submitted to IEEE MIC2014.

[14] Q. Tang, Z. Yu, and S. Nakanishi, "Low frequency cone-beam artifacts reduction using iterative reconstruction algorithm," Proceeding of IEEE NSS/MIC, 2014.

[15] J. Nuyts et al., "Modelling the physics in the iterative reconstruction for transmission computed tomography," *Phys. Med. Biol.* **58** R63, 2013.

[16] K. Taguchi, "VOLUMETRIC COMPUTED TOMOGRAPHY SYSTEM FOR IMAGING" US Patent 2006/0198491 A1

Noise Weighting with an Exponent for Transmission CT

Gengsheng L. Zeng and Wenli Wang

***Abstract*–It is widely believed that the correct weighting function is the reciprocal of the noise variance of the associated measurement. Many researchers are making great efforts to find the accurate variance for the measurements for imaging systems so that they can hopefully achieve an optimal reconstruction. This paper makes some interesting observations: There is no such thing as a correct noise weighting. There is no universal optimal weighting function. The noise weighting function can introduce artifacts. The optimal noise weighting varies with the object to be reconstructed and targeted image contrast in an iterative image reconstruction algorithm and in a filtered backprojection (FBP) algorithm that incorporates the projection noise. It is suggested that an exponent be used in the weighting function so that the artifacts caused by the weighting function can be reduced.**

I. Introduction

ONE of the advantages of using iterative algorithms to reconstruct a tomographic image is the ability to model and suppress the measurement noise [1-4]. Recently we have shown that the filtered backprojection (FBP) can be extended to model and suppress the measurement noise too [5,6]. In all these algorithms, the noise-control weighting function is normally set up as the reciprocal of the noise variance associated with the measurement [7]. This weighting function assignment is supported by the general maximum likelihood theory.

This paper will study the iterative algorithm that stops before convergence, and investigate how the weighting function influences the early solutions. The result of this paper will apply to the extend FBP algorithm that models and suppresses the noise.

II. Methods

2.1 The gradient descent iterative algorithm

The gradient descent iterative algorithm considered in this paper has the following form [8]

$$X_i^{(k+1)} = X_i^{(k)} - \alpha \frac{\sum_j A_{ji} w_j (\sum_n A_{jn} X_n^{(k)} - P_j)}{\sum_j A_{ji} w_j \sum_n A_{jn}}, \qquad (1)$$

where $X_i^{(k)}$ is the i^{th} image pixel at the k^{th} iteration, P_j is the j^{th} line-integral (ray-sum) measurement value, A_{ji} is the contribution of the i^{th} image pixel to the j^{th} measurement, w_j is the weighting factor for the j^{th} measurement, and α is a constant to prevent the algorithm from divergence. The purpose of the denominator $\sum_j A_{ji} w_j \sum_n A_{jn}$ is to normalize the step size so that the step size is independent from the system matrix A and the weighting function w_j. Thus the value of α is always 1 in [8]. However, this scaled step size does not always work and the algorithm may diverge for many situations. We set α to 0.1 in this paper. The summation over the index n is the projector and the summation over the index j is the backprojector.

2.2 The noise-weighted FBP algorithm

A noise-weighted FBP algorithm was recently developed to model and suppress noise [5,6]. This algorithm emulates the gradient descent algorithm and contains a control index k, which is similar to the iteration number in an iterative algorithm. This noise-weighted FBP algorithm is almost the same as the conventional FBP algorithm, except for the ramp filter. In a conventional FBP algorithm, the ramp filter is $|\omega|$, where ω is the frequency. In the noise-weighted FBP algorithm, the ramp filter is modified by a window function and is expressed as

$$H(\omega) = [1 - (1 - \frac{\alpha w_j}{|\omega|})^k] |\omega|, \text{ with } \omega \neq 0, \text{ and } H(0) = 0, \quad (2)$$

where α is a positive constant to prevent the algorithm from divergence. In this paper, α is set to 0.5.

The implementation of (2) is in the Fourier domain of the sinogram. The weighting factors w_j in (2) for all projection bins are quantized into 11 discrete values, and each of these 11 quantized weighting factors produces a filtered sinogram. A combined sinogram from these filtered sinograms is formed point-by-point according to the variance of the original sinogram. The details of the implementation can be found in [5].

2.3 Data generation and noise model

The computer simulations in this paper are based on a scaled-down x-ray CT fan-beam imaging geometry with a curved detector. The image array was 256 x 256, the pixel size was 1.52 mm x 1.52 mm, the number of views was 400 over 360°, the number of detection channels was 400, and the focal length was 240 mm. The x-ray source flux had $I_0 = 10^4$ counts, which corresponds to a low-dose imaging setup. The phantom is 355 mm x 187 mm ellipse with water background (μ=0.02/mm), 3 high contrast regions (μ=0.032/mm) with diameter 48 mm, 2 low-contrast regions (μ=0.0194mm) with diameter 36 mm, surrounded by outer layers of fat (μ=0.019/mm) and skin (μ=0.021/mm) , in which ROI 1 (high contrast object) and ROI 2 (water background) are used to evaluate the image quality. The projection data were generated in the pre-log format with the Poisson noise model and

Gengsheng L. Zeng is with Department of Engineering, Weber State University, Ogden, UT 84408 USA (telephone: 801- 626-6864, e-mail: larryzeng@weber.edu) and also with Department of Radiology, University of Utah, Salt Lake City, UT 84108 USA (telephone: 801-581-3918, e-mail: larry@ucair.med.utah.edu).Wenli Wang is with Toshiba Medical Research Institute USA, Inc., Vernon Hills, IL 60061 USA.

Gaussian electronic noise. No beam-hardening effects are simulated. The pre-log data were then converted into the post-log data for image reconstruction. If a pre-log data is less than one, it is changed to one before taking logarithm to avoid negative post-log sinogram values. The iterative algorithm was implemented according to (1), and the iterative algorithm stops when a pre-specified image contrast is reached. This value is set up as: $(ROI1 - ROI2)/ROI2 \geq 0.53$ (where the true contrast is 0.6). The reconstructed images are compared with the normalized standard deviation value in ROI 2. The normalized standard deviation value is the standard deviation value divided by the mean value.

A popular approach to assigning the weighting factor is to let w_j be the reciprocal of the noise variance of the ray-sum measurement. This approach is justified by using the likelihood function as the objective function for an optimization problem [9]. The philosophy is that we should trust the less noisy measurements more than noisier measurements.

In x-ray CT imaging, the noise in measured transmission data can be approximately described by a Poisson distribution, i.e., $\mathrm{var}(I) \approx I$, where I denotes an x-ray intensity transmission measurement [10]. If the additive electronic noise σ^2 is also considered for the detection system, the total variance of the pre-log transmission measurement is then $\mathrm{var}(I) \approx I + \sigma^2$. Here $\sigma^2 = 6.3^2$ was chosen in our simulated low-count x-ray CT data generation.

After log conversion the noise variance is described by $\mathrm{var}(I)/I^2 \approx (I + \sigma^2)/I^2$. If the x-ray source flux I_0 is stable and consistent, measurement intensity I can be written as $I = I_0 \exp(-p)$ according to Beer's law, where p is the ray-sum or the total attenuation along the ray. The variance of post-log measurement p can thus be expressed as

$$\mathrm{var}(p) \approx \frac{I + \sigma^2}{I^2} = \frac{I_0 \exp(-p) + \sigma^2}{I_0^2 \exp(-2p)}. \quad (4)$$

Our experiments indicated that modeling the electronic noise in an iterative algorithm does not reduce the image noise. Even though $\sigma^2 = 6.3^2$ in data generation, we assume $\sigma^2 = 6.3^2$ during image reconstruction. The conventional weighing factor is inversely proportional to the noise variance. Thus, the conventional weighing factor can be assigned as

$$w = \exp(-p). \quad (5)$$

This paper introduces a new parameter γ to the weighting function:

$$w = \exp(-\gamma p). \quad (6)$$

In our implementation of the weighting function (6) the post-log data p is first smoothed by a 5-point running average low-pass filter in the detector channel direction, in order to reduce the noise propagation from the weighting function to the reconstruction. However, the post-log projections used in (1) are not pre-filtered. The image quality is evaluated by the normalized standard deviation in ROI 2. The normalized standard deviation is defined as the ratio of the standard deviation and the mean value.

III. Results

3.1 Iterative reconstructions

The effects of the exponent γ are illustrated with the following variations.

(A) The default phantom as shown in Fig. 1 is used, and $I_0 = 10^4$. The target contrast is 0.53.
(B) The phantom is changed to an obese version.
(C) The phantom is changed to a slightly thinner version.
(D) The phantom is changed to a very thin version.
(E) Same as (A), but the target contrast is changed to 0.57.
(F) Same as (A), but I_0 is increased to 1.5×10^4.

The computer simulation results are summarized in Figs. 1-4. In all these figures, one can make the following observations. When γ is small, there are severe noise induced streaking artifacts. As the value of γ increases, the streaking artifacts are gradually suppressed. After passing the optimal value of γ, a larger value of γ causes more severe low-frequency shadowing artifacts. Sometimes these low-frequency shadowing artifacts may be mistaken as the beam-hardening artifacts. The cause of the shadowing artifacts is the extremely small values of the weighting factors w_j, due to the large p values. The shadowing artifacts are caused by the improper weighting factors, and is not causes by discarding negative sinogram values. The shadowing artifacts can appear with ideally generated, i.e., noise-less (i.e., $I_0 \to \infty$), line-integral sinogram when improper weighting factors are used during image reconstruction. When the weighting factors w_j are too small, some important tomographic information is neglected, resulting in limited data artifacts (similar to metal artifacts).

The optimal parameter γ depends on the object shape and image contrast (maybe less on dose I_0). The main idea of using a new exponent parameter γ is to reduce those large p values to some extend so that the over-suppressed tomographic information can be available for image reconstruction.

3.2 FBP reconstructions

Image reconstruction results using the noise-weighted FBP algorithm with a modified ramp filter (2) are listed in Fig.7. The FBP results have the same trend as that in the iterative reconstruction results. For a small parameter γ, we see streaking artifacts. The streaking artifacts are suppressed with a larger γ. However, when the parameter γ is too large, the low-frequency shadowing artifacts appear. An optimal parameter γ should be used. Thus only 3 representative images are shown. Similar to the iterative algorithm's iteration number, the parameter k is selected when the pre-specified image contrast is reached. We must point out that the parameter k in the FBP algorithm and the number of iteration k in the iterative algorithm, in general, are not the same; they are closely related. Similarly, the γ values in both algorithms are not the same, but have the same trend.

All images are displayed with the same linear gray scale.

IV. Conclusion

This paper uses an exact known noise model to investigate the effects of the weighting function. This paper suggests that a weighting function that is a power function of the reciprocal of the noise variance, $w = 1/\text{variance}^{\gamma}$, should be used. When $\gamma = 0$, the weighting function is a constant without any variation. A larger γ gives a larger variation of the weighting function. When $\gamma = 1$, the weighting function is the so-called "correct" weighting which is widely used among researchers.

Both an iterative gradient descent algorithm and an analytic noise-weighted FBP algorithm are used for the investigation. In order for the weighting function to be effective, the iteration number k in the iterative algorithm or the noise control parameter k in the FBP algorithm must be small enough so that the algorithm is not converged yet. Our computer simulations show that the optimal weighting scheme depends on the object and the pre-specified image contrast. Therefore, there is no universal optimal weighting function. The so-called "correct" weighting function is sub-optimal.

For a given object, the optimal weighting function is image contrast dependent, which in turn will be determined by the noise. The power function weighting function suggested in this paper is only one of many options that can help to achieve a desired image quality.

References

[1] D. E. Kuhl and R.Q. Edwards, "Image separation radioisotope scanning," *Radiology*, vol. 80, pp. 653–662, 1963.

[2] L. A. Shepp and Y. Vardi, "Maximum likelihood reconstruction for emission tomography," *IEEE Trans. Med. Imag.*, vol. 1, pp. 113–122, 1982.

[3] K. Langer and R. Carson, "EM reconstruction algorithms for emission and transmission tomography," *J. Comp. Ass. Tomogr.*, vol. 8, pp. 302-316, 1984.

[4] J. A. Fessler, "Penalized weighted least-squares image reconstruction for positron emission tomography," *IEEE Trans. Med. Imag.*, vol. 13(2), pp. 290-300, 1994.

[5] G. L. Zeng and A. Zamyatin, "A filtered backprojection algorithm with ray-by-ray noise weighting," *Med. Phys.*, vol. 40, 031113; http://dx.doi.org/10.1118/1.4790696 (7 pages), 2013.

[6] G. L. Zeng, "Model-based filtered backprojection algorithm: A tutorial," *Biomedical Engineering Letters*, (http://link.springer.com/article/10.1007/s13534-014-0121-7), vol. 4(1), pp. 3-18,2014.

[7] S. Geman and D. E. McClure, "Statistical methods for tomographic image reconstruction," *Bull. Int. Statist. Inst.,*vol. LII-4, pp. 5-21, 1987.

[8] A. Elbakri and J. A. Fessler, "Statistical image reconstruction for polyenergetic x-ray computed tomography," *IEEE Trans. Med. Imag.*, vol. 21, pp. 89-99, 2002.

[9] A. C. Aitken, "On least squares and linear combinations of observations," *Proceedings of the Royal Society of Edinburgh*, vol. 55, pp. 42–48, 1935.

[10] J. Hsieh, "Adaptive streak artifact reduction in computed tomography resulting from excessive x-ray photon noise," *Med. Phys.*, vol. 25, pp. 2139-2147, 1998.

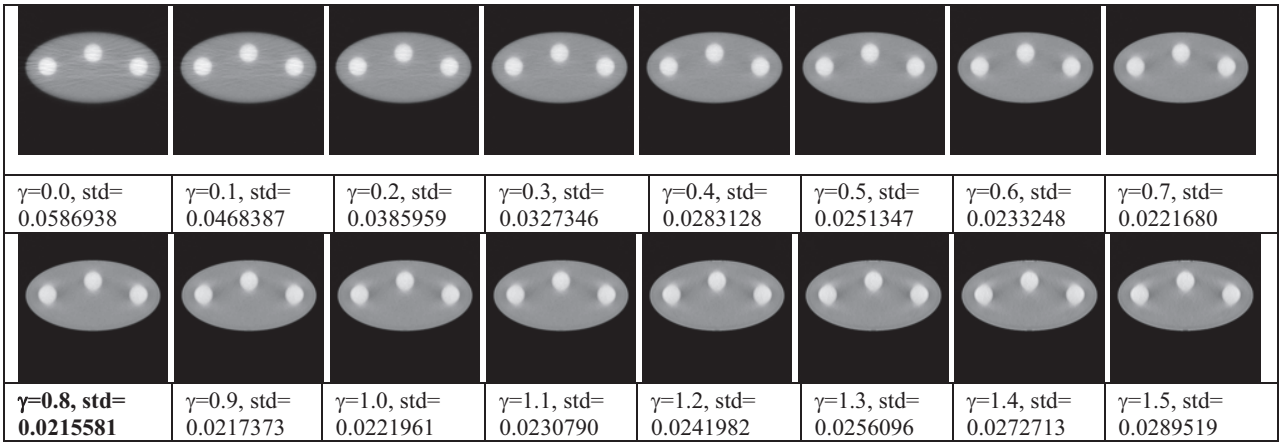

Fig. 1. Iterative reconstructions with various parameter γ and the normalized standard deviation in ROI 2 for Case (A): The default phantom as shown in Fig. 1 is used, and $I_0 = 10^4$. The target contrast is 0.53.

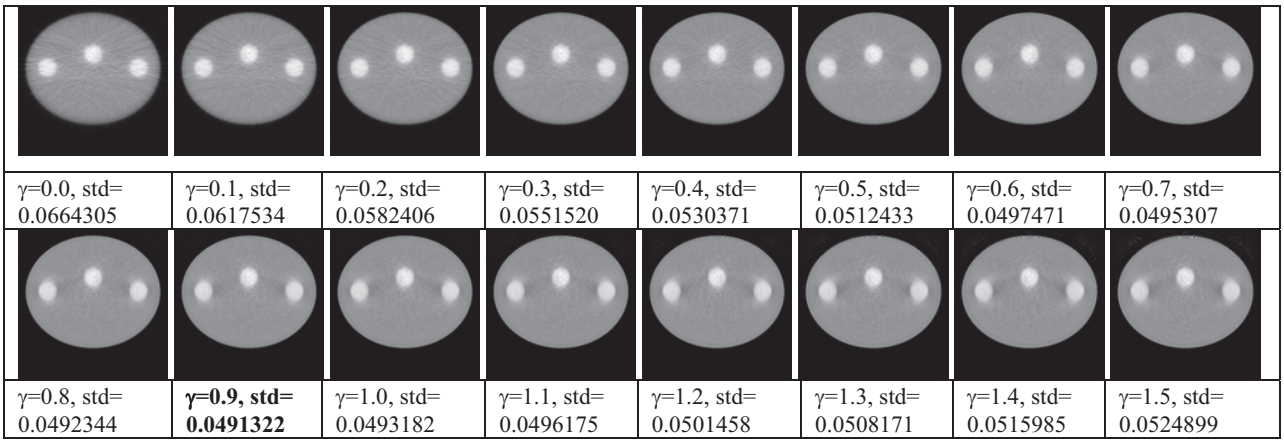

γ=0.0, std= 0.0664305	γ=0.1, std= 0.0617534	γ=0.2, std= 0.0582406	γ=0.3, std= 0.0551520	γ=0.4, std= 0.0530371	γ=0.5, std= 0.0512433	γ=0.6, std= 0.0497471	γ=0.7, std= 0.0495307
γ=0.8, std= 0.0492344	**γ=0.9, std= 0.0491322**	γ=1.0, std= 0.0493182	γ=1.1, std= 0.0496175	γ=1.2, std= 0.0501458	γ=1.3, std= 0.0508171	γ=1.4, std= 0.0515985	γ=1.5, std= 0.0524899

Fig. 2. Iterative reconstructions with various parameter γ and the normalized standard deviation in ROI 2 for Case (B): The phantom is changed to an obese version, and $I_0 = 10^4$. The target contrast is 0.53.

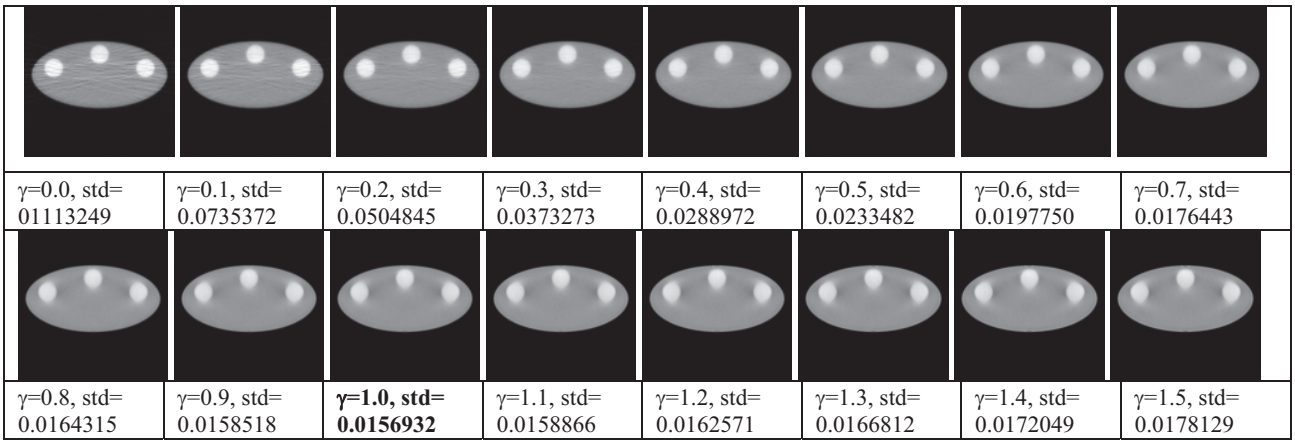

γ=0.0, std= 01113249	γ=0.1, std= 0.0735372	γ=0.2, std= 0.0504845	γ=0.3, std= 0.0373273	γ=0.4, std= 0.0288972	γ=0.5, std= 0.0233482	γ=0.6, std= 0.0197750	γ=0.7, std= 0.0176443
γ=0.8, std= 0.0164315	γ=0.9, std= 0.0158518	**γ=1.0, std= 0.0156932**	γ=1.1, std= 0.0158866	γ=1.2, std= 0.0162571	γ=1.3, std= 0.0166812	γ=1.4, std= 0.0172049	γ=1.5, std= 0.0178129

Fig. 3. Iterative reconstructions with various parameter γ and the normalized standard deviation in ROI 2 for Case (C): The phantom is changed to a slightly thinner version, and $I_0 = 10^4$. The target contrast is 0.53.

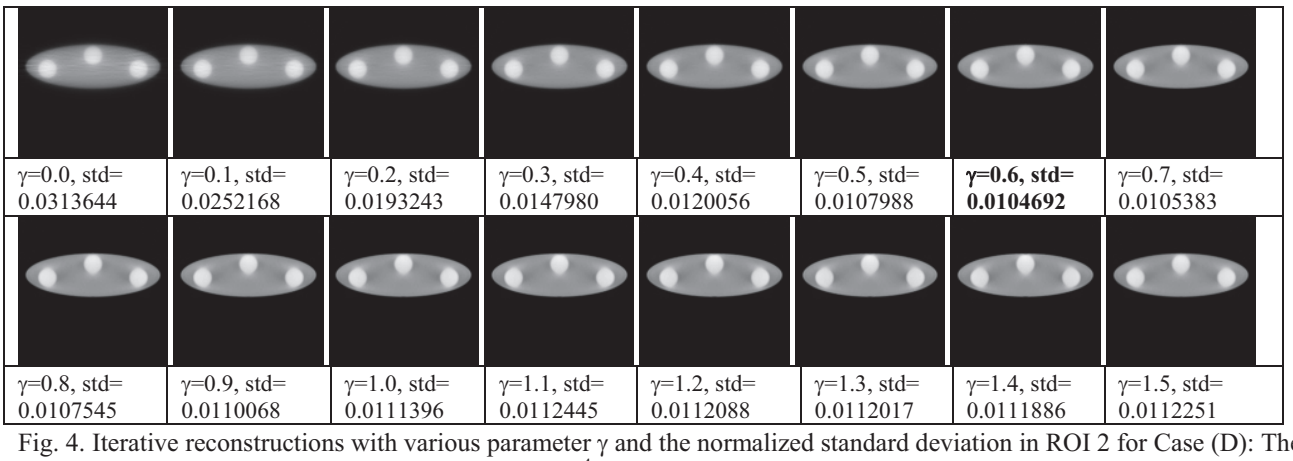

γ=0.0, std= 0.0313644	γ=0.1, std= 0.0252168	γ=0.2, std= 0.0193243	γ=0.3, std= 0.0147980	γ=0.4, std= 0.0120056	γ=0.5, std= 0.0107988	**γ=0.6, std= 0.0104692**	γ=0.7, std= 0.0105383
γ=0.8, std= 0.0107545	γ=0.9, std= 0.0110068	γ=1.0, std= 0.0111396	γ=1.1, std= 0.0112445	γ=1.2, std= 0.0112088	γ=1.3, std= 0.0112017	γ=1.4, std= 0.0111886	γ=1.5, std= 0.0112251

Fig. 4. Iterative reconstructions with various parameter γ and the normalized standard deviation in ROI 2 for Case (D): The phantom is changed to a very thin version, and $I_0 = 10^4$. The target contrast is 0.53.

Reconstruction Algorithms for Reverse Helical Super-Short-Scan Mode

Hussein Banjak*, Marius Costin*, Caroline Vienne*, Ronan Guillamet* and Valérie Kaftandjian †
* CEA, Department of Imaging and Simulation for Non-Destructive Testing
Gif-sur-Yvette, France
Email: firstname.secondname@cea.fr
†Laboratory of Vibrations and Acoustics, INSA-Lyon
Villeurbanne, France.
Email: valerie.kaftandjian@insa-lyon.fr

***Abstract*—In the context of the installation of a robotic platform, we are interested in a tomographic reconstruction on a reverse helical trajectory limited to $150°$. Two types of algorithms will be used to accomplish reconstruction on the defined trajectory: iterative and analytic. While the first one is directly adapted to such non-standard trajectory, we should handle data redundancy for the second one. As a primary step to test this platform, we are going to validate our algorithms using realistic data simulated by CIVA software. For performance evaluation, we illustrate a numerical comparison of these two reconstruction algorithms using both noiseless and noisy data. We also show reconstructions from a few number of projections.**

I. Introduction

An advanced robotic X-ray non-destructive testing platform is being developed at CEA LIST. This inspection platform (see Fig. 1) consists of two robotic arms carrying the X-ray source and the detector and which allows a large variety of acquisitions on non-standard trajectories. However, important constraints control the mechanical motion of the platform where the scan range around an object is limited to $150°$. We are planning to perform tomographic reconstruction with this robotic platform from both analytic and iterative algorithms.

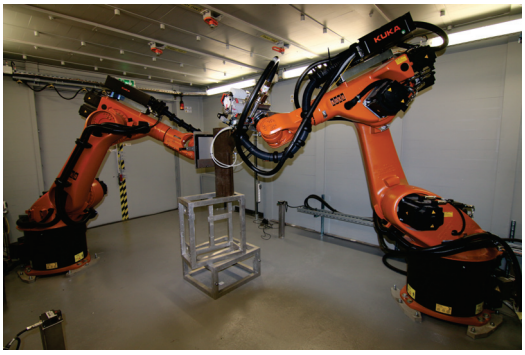

Fig. 1: Robotic X-ray inspection platform developed at CEA.

Analytic reconstruction is based on an idealized mathematical model and an inverse transform is employed. It is very efficient in case of complete and noiseless data with a sufficient data sampling. However, in practical situations, the projections are affected by noise, the X-ray source is poly-chromatic and not point-like as assumed by the model. Moreover, in many cases the object is not accessible for full measurements because of some geometrical constraints. Here, analytic reconstruction fails because it treats all X-rays equally and it is severely affected by incomplete or sparse data [1]. In this situation, iterative reconstruction methods perform much better. Within this type of reconstruction, it is possible to model some physical phenomena such as scatter and to deal with incomplete or sparse data. In addition, iterative algorithms can handle much more noisy data and allow more flexibility in the scanning geometry. The only drawbacks of iterative algorithms are their model complexity and high computational cost. However, this latter is becoming more acceptable with the high technological development in computer performance and the introduction of parallel implementation using graphics processing unit (GPU).

As reconstruction algorithms, we have chosen the Simultaneous Algebraic Reconstruction Technique (SART) [2] for the iterative case and a Feldkamp-Davis-Kress (FDK) [3], [4] type algorithm for the analytic case. In this paper, we start by describing the scanning geometry, then we show the structure of the two reconstruction algorithms and finally we demonstrate our numerical comparison and evaluation.

II. Scanning geometry and notations

In this section, we show the reverse helical trajectory in super-short-scan mode and we introduce the different notations used throughout the reconstruction inversion formulas. Consider a 3D object of attenuation function $f(\overrightarrow{r})$ where $\overrightarrow{r}$ is the position vector of a point M located in the object. The coordinates of M in the fixed coordinate system of the object $(\overrightarrow{e}_x, \overrightarrow{e}_y, \overrightarrow{e}_z)$ are given by (x, y, z). The actual support of the object is confined within a cylinder of radius r and central axis along the z-direction. Thus, we have

$$f(\overrightarrow{r}) = 0 \qquad \text{for} \qquad x^2 + y^2 > r^2. \tag{1}$$

As illustrated in Fig. 2, the X-ray source S moves on a reverse helical trajectory of radius R and angular range $150°$ (rotation

reversal every 150°). The coordinates of S in the system $(\overrightarrow{e}_x, \overrightarrow{e}_y, \overrightarrow{e}_z)$ are denoted by

$$\overrightarrow{y}(\lambda) = (R\cos\lambda, R\sin\lambda, h\lambda), \tag{2}$$

where $2\pi h$ is the helical pitch (axial translation distance of the source per 360°).

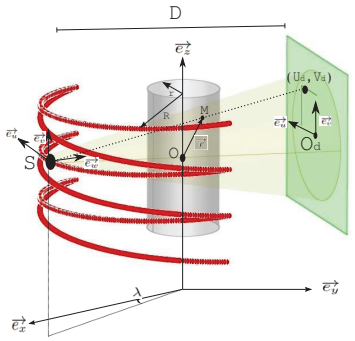

Fig. 2: Reverse helical cone-beam scanning geometry and associated notations.

A flat-panel detector is placed at a fixed distance D from the source with its axes defined by the unit vectors $\overrightarrow{e}_u$ and $\overrightarrow{e}_v$. O_d is the origin of the detector and corresponds to the orthogonal projection of S onto the detector. The unit vector joining O_d and S is given by $\overrightarrow{e}_w$. The expressions of the three unit vectors $\overrightarrow{e_u}(\lambda)$, $\overrightarrow{e_v}(\lambda)$ and $\overrightarrow{e_w}(\lambda)$ in the coordinate system $(\overrightarrow{e_x}, \overrightarrow{e_y}, \overrightarrow{e_z})$ are defined by:

$$\begin{cases} \overrightarrow{e_u}(\lambda) = (-\sin\lambda)\overrightarrow{e_x} + (\cos\lambda)\overrightarrow{e_y} \\ \overrightarrow{e_v}(\lambda) = \overrightarrow{e_z} \\ \overrightarrow{e_w}(\lambda) = (\cos\lambda)\overrightarrow{e_x} + (\sin\lambda)\overrightarrow{e_y}. \end{cases} \tag{3}$$

Each 3D point $M(x, y, z)$ is projected onto the detector on the pixel of coordinates (u_d, v_d) expressed as:

$$\begin{cases} u_d = D\left(\frac{x\sin\lambda - y\cos\lambda}{x\cos\lambda + y\sin\lambda - R}\right) \\ v_d = -D\left(\frac{z - h\lambda}{x\cos\lambda + y\sin\lambda - R}\right). \end{cases} \tag{4}$$

The measured cone-beam (CB) projection data are given by

$$g(u_d, v_d, \lambda) = \int_{l=0}^{+\infty} f(\overrightarrow{y}(\lambda) + \overrightarrow{\theta}(u_d, v_d, \lambda)l)dl, \tag{5}$$

where $\overrightarrow{\theta}(u_d, v_d, \lambda)$ is the unit vector of the X-ray emitted from the source point S of rotation angle λ and crossing the detector at the point of coordinates (u_d, v_d).

III. Reconstruction Algorithms

We explain in this section the steps performed in the FDK-type algorithm for reconstruction on a reverse helical trajectory in super-short-scan mode. Then, the steps performed in SART are illustrated also.

A. FDK-type algorithm

Most commercial CT scanners use the FDK algorithm [3], [4] due to its simplicity and high efficiency. Recently, three FDK-type reconstruction algorithms adapted to the reverse helical trajectory were proposed by Yu et al. [5]. In 2003, Kudo et al. [6] developed fan-beam and CB reconstruction algorithms for super-short scan on a circular trajectory. In this paper, we have extended one of the algorithms proposed by Kudo et al. [6] for reconstruction on a reverse helical trajectory using the same idea proposed in [5]. The structure of this algorithm consists of the following steps:

(a) Cosine weighting :

$$g'(u_d, v_d, \lambda) = \frac{D}{\sqrt{D^2 + u_d^2 + v_d^2}} g(u_d, v_d, \lambda).$$

(b) Hilbert-row-wise filtering:

$$g_H(u_d, v_d, \lambda) = \mathcal{H} g'(u_d, v_d, \lambda).$$

(c) Weighting for data redundancy:

$$g_W(u_d, v_d, \lambda) = W(u_d, v_d, \lambda) g_H(u_d, v_d, \lambda).$$

(d) Differentiation along the horizontal direction:

$$g_F(u_d, v_d, \lambda) = \frac{\partial}{\partial u_d} g_W(u_d, v_d, \lambda).$$

(e) Back-projection:

$$f^+(\overrightarrow{r}) = \frac{1}{\pi}\int_0^{\lambda_m} \frac{RD}{|R - \overrightarrow{r}\cdot\overrightarrow{e_w}(\lambda)|^2} g_F(u_d, v_d, \lambda)\, d\lambda,$$

$$f^-(\overrightarrow{r}) = \frac{1}{\pi}\int_{-\lambda_m}^0 \frac{RD}{|R - \overrightarrow{r}\cdot\overrightarrow{e_w}(\lambda)|^2} g_F(u_d, v_d, \lambda)\, d\lambda.$$

(f) Fusion:

$$f(\overrightarrow{r}) = f^+(\overrightarrow{r})F^+(z) + f^-(\overrightarrow{r})F^-(z).$$

In these equations, $\mathcal{H}$ refers to the Hilbert operator along u_d and $W(u_d, v_d, \lambda)$ is a weighting function used to handle redundant data (see [6]). To explain the fusion process, we

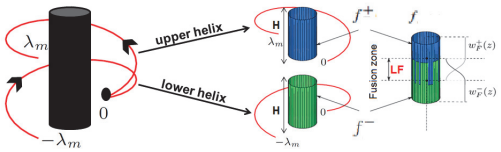

Fig. 3: Illustration of the fusion process in the FDK-type algorithm. Figure reproduced from [5].

take two helical turns defined by the endpoints $-\lambda_m$ and λ_m as illustrated in Fig. 3. Using data from these lower and upper helices, respectively, we can reconstruct two functions $f^-(\overrightarrow{r})$ and $f^+(\overrightarrow{r})$ and merge them to obtain $f(\overrightarrow{r})$. The two fusion weighting functions $F^-(z)$ and $F^+(z)$ are defined by:

$$F^-(z) = \begin{cases} 1 & -H \le z \le -0.5L_F \\ cos^2\left(\frac{\pi(z+0.5L_F)}{2L_F}\right) & -0.5L_F < z \le 0.5L_F \\ 0 & \text{otherwise,} \end{cases}$$

$$F^{+}(z) = \begin{cases} 1 & 0.5L_F \leq z \leq H \\ sin^2\left(\frac{\pi(z+0.5L_F)}{2L_F}\right) & -0.5L_F \leq z < 0.5L_F \\ 0 & \text{otherwise,} \end{cases}$$

where L_F is the length of the zone within which fusion is performed. Further explanations for the case of more than two helical turns can be found in [7].

B. SART algorithm

Unlike analytic methods which perform reconstruction within a single step using a specific inversion formula, iterative methods perform reconstruction within multiple iterations. Each iteration consists of the following three main steps:

(a) Forward projection of the current image.
(b) Estimation of the difference between the computed projections and the experimentally acquired projections.
(c) Back-projection of the weighted difference to update the 3D volume.

The iteration process is ended when a fixed number of iterations is reached or when there is a good agreement between the projections computed during the current iteration and the projections measured during acquisition. The global iterative process is illustrated in Fig. 4.

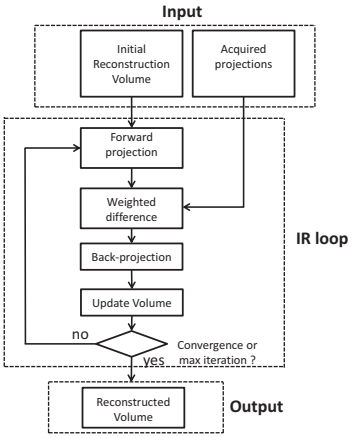

Fig. 4: Basic schema of iterative reconstruction process.

SART [2] is an algebraic method which represents the reconstruction problem as a linear system of equations P = A.f where P represents the projection data, A refers to the projection system model and f defines the voxel values in the object. It is a pure iterative algorithm without any modeling and which was introduced as an improvement of ART [8], the first algorithm to be used in CT. The reconstruction process of this algorithm is defined by:

$$f_j^{(k+1)} = f_j^k + \lambda \cdot \frac{\sum_{p_i \in P_\theta} \frac{p_i - \sum_{n=1}^{N} a_{in} f_n^k}{\sum_{n=1}^{N} a_{in}} \cdot a_{ij}}{\sum_{p_i \in P_\theta} a_{ij}}. \quad (6)$$

Here, a_{ij} represents an element in the matrix A with i is the index of a pixel in the projection matrix P and j is the index of a voxel in the image function f. For each iteration number k, the update of the voxel values in f are based on a whole 2D projection matrix computed at a specific angle of view θ. λ is a relaxation parameter between 0 and 2. In this work, a regularization technique [9] based on total variation (TV) minimization is applied to account for unrealistic variations between neighboring. Non-negativity constraint is considered as well. In this implementation, a gradient descent method is used to minimize $\|\mathbf{f}\|_{TV}$ which is the l_1-norm of the image gradient magnitude. In addition, we incorporate a fast iterative shrinkage-thresholding (FIST) algorithm [10] to accelerate the convergence speed of the SART-TV algorithm. In what follows, we refer the algorithm to as SART-FIST.

IV. Numerical results and evaluation

We present in this section a numerical comparison of the two described algorithms from data generated by CIVA [11]. Our simulated object is a computer-aided-design (CAD) model phantom which is similar to the Defrise multi-disk phantom with additional rectangular and circular holes of different sizes. The height of this phantom is 18.5 mm and consists of five circular disks with thickness 2.5 mm stacked along the z-direction and separated by 1.5 mm. In fact, Noo et al. [12] mentioned that for an exact ROI reconstruction from fan-beam projections on less than a short scan, each line passing through the ROI must intersect the source trajectory. Knowing that the FDK-type algorithm was based on a fan-beam reconstruction algorithm for super-short-scan, we show in Fig. 5 a horizontal slice of the phantom and we illustrate the ROI (region below the dashed-line) that we can reconstruct with this FDK-type algorithm. The FDK-type algorithm was implemented on a single-core CPU whereas the projection (pixel-driven) and backprojection (ray-driven) steps of SART-FIST were implemented on a Graphics Processing Unit (GPU) using C-CUDA

TABLE I: Numerical simulation parameters.

Object radius (r)	7.5 mm
Helix radius (R)	20 mm
Source-detector distance (D)	40 mm
Total number of turns	12
Number of projections per turn	30
Scanning range for each turn	150°
Detector pixel size	0.14×0.14 mm^2
Detector sampling	256×256 pixels
Reconstruction matrix	$256 \times 256 \times 256$ voxels

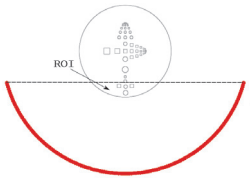

Fig. 5: ROI in a horizontal slice of the phantom.

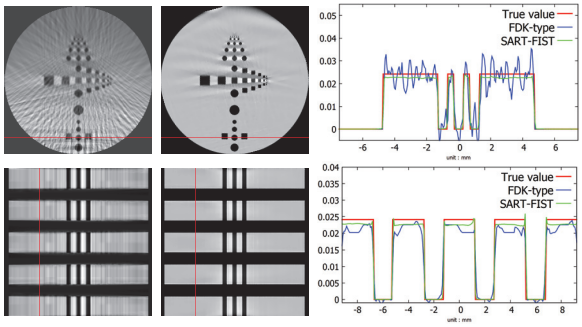

(a) FDK-type (b) SART-FIST (c) 1D profile

Fig. 6: Reconstruction from noiseless data.

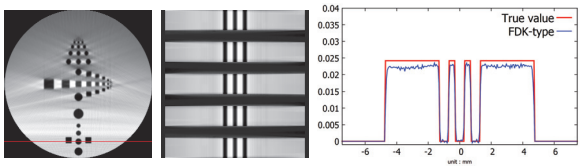

(a) horizontal (b) vertical (c) 1D profile

Fig. 7: FDK reconstruction with a large number of projections.

on nVidia TITAN card. Fig. 6 shows the reconstruction results from noiseless data with the data acquisition configuration specified in table I. We show a horizontal and a vertical slice in the reconstructed images with a 1D numerical comparison along the red lines. We can see that streak artifacts severely affect the image quality of the FDK reconstruction due to the small number of projections. The reconstruction time is 32 seconds for the FDK-type algorithm and 39 minutes for SART-FIST with a total number of iterations equal to 5. However, if

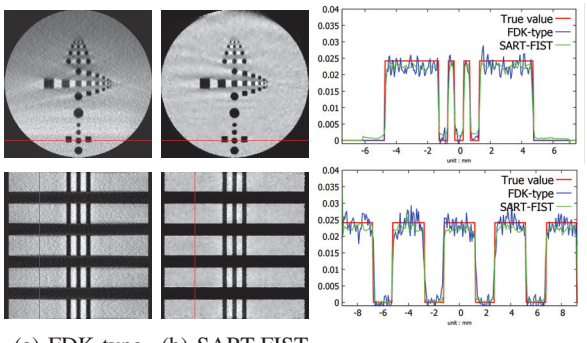

(a) FDK-type (b) SART-FIST (c) 1D profile

Fig. 8: Reconstruction from noisy data with a large number of projections for FDK.

we increase the number of projections to 150 projections per helical turn, the image quality of the FDK reconstruction is improved as illustrated in Fig. 7. Finally, we aim to compare the performance of these two algorithms in case of noisy data. We show in Fig. 8 reconstruction from noisy data. Gaussian noise with a standard deviation of 0.5% of the maximum value in the noise-free data was added prior to reconstruction. These results demonstrate that SART-FIST is more robust to noisy data than the described FDK-type algorithm where the integrated TV regularization step can suppress noise with affecting the spatial resolution.

V. Conclusion

The primary purpose of the performed simulations was to demonstrate numerically the pros and cons of each algorithm. As a conclusion, SART-FIST is more time consuming, but it is more robust to noisy data and it performs better than the FDK-type algorithm in case of reconstruction from few view projections. We can say that the FDK-type algorithm is computationally more efficient whereas SART-FIST can improve the image quality. Now, we are working on the calibration of the CT system and on integrating a correction method to deal with the position errors during the robotic experimental acquisitions. In the near future, we will show reconstruction results using this robotic inspection platform with the described algorithms.

References

[1] M. Beister, D. Kolditz, and W. A. Kalender, "Iterative reconstruction methods in x-ray ct," *Physica medica*, vol. 28, no. 2, pp. 94–108, 2012.

[2] A. H. A. A. C. Kak, "Simultaneous algebraic reconstruction technique (sart): A superior implementation of the art algorithm," *Ultrasonic Imaging*, 1984.

[3] L. Feldkamp, L. Davis, and J. Kress, "Practical cone-beam algorithm," *JOSA A*, vol. 1, no. 6, pp. 612–619, 1984.

[4] G. Wang, T.-H. Lin, P.-C. Cheng, and D. M. Shinozaki, "A general cone-beam reconstruction algorithm," *Medical Imaging, IEEE Transactions on*, vol. 12, no. 3, pp. 486–496, 1993.

[5] Z. Yu, F. Noo, F. Dennerlein, G. Lauritsch, and J. Hornegger, "Fdk-type reconstruction algorithms for the reverse helical trajectory," in *Nuclear Science Symposium and Medical Imaging Conference (NSS/MIC), 2011 IEEE*. IEEE, 2011, pp. 3980–3985.

[6] H. Kudo, F. Noo, M. Defrise, and R. Clackdoyle, "New super-short-scan algorithms for fan-beam and cone-beam reconstruction," in *Nuclear Science Symposium Conference Record, 2002 IEEE*, vol. 2. IEEE, 2002, pp. 902–906.

[7] Z. Yu, A. Maier, G. Lauritsch, F. Vogt, M. Schonborn, C. Kohler, J. Hornegger, and F. Noo, "Axially extended-volume c-arm ct using a reverse helical trajectory in the interventional room," *Medical Imaging, IEEE Transactions on*, vol. 34, no. 1, pp. 203–215, 2015.

[8] R. Gordon, R. Bender, and G. T. Herman, "Algebraic reconstruction techniques (art) for three-dimensional electron microscopy and x-ray photography," *Journal of theoretical Biology*, vol. 29, no. 3, pp. 471–481, 1970.

[9] E. Y. Sidky, C.-M. Kao, and X. Pan, "Accurate image reconstruction from few-views and limited-angle data in divergent-beam ct," *Journal of X-ray Science and Technology*, vol. 14, no. 2, pp. 119–139, 2006.

[10] A. Beck and M. Teboulle, "A fast iterative shrinkage-thresholding algorithm for linear inverse problems," *SIAM journal on imaging sciences*, vol. 2, no. 1, pp. 183–202, 2009.

[11] R. Fernandez, M. Costin, D. Tisseur, A. Leveque, and S. Legoupil, "Civa computed tomography modeling," *at WCNDT*, 2012.

[12] F. Noo, M. Defrise, R. Clackdoyle, and H. Kudo, "Image reconstruction from fan-beam projections on less than a short scan," *Physics in Medicine and Biology*, vol. 47, no. 14, p. 2525, 2002.

Investigating Multi-threaded SIMD for Helical CT Reconstruction on a CPU

Richard Sampson, Madison G. McGaffin, Thomas F. Wenisch, Jeffrey A. Fessler
Department of EECS, University of Michigan

***Abstract*—Iterative reconstruction for X-ray CT is computationally expensive, so it is desirable to examine acceleration methods such as algorithm design, software implementation, and computing hardware. This paper explores using single-instruction, multiple data (SIMD) operations on modern CPUs to accelerate projection and back-projection using the separable footprint (SF) method. Slightly modifying the axial footprint calculation facilitates SIMD implementation, providing up to 5× acceleration using 8-wide SIMD with Intel AVX2 instructions over multi-threading (MT) alone. Due to memory bandwidth constraints, overall speedup saturates at ≈55× faster than a single-thread, non-SIMD version (still 2× faster over MT with 72 threads). Despite the bandwidth limits, the MT+SIMD runtimes are competitive with corresponding GPU versions.**

I. Introduction

Model-based iterative reconstruction (MBIR) for X-ray CT has improved image quality and reduced X-ray dose compared to filtered back-projection [1]. However, MBIR's high computational requirements have led researchers to explore acceleration techniques to make it more practical for routine clinical use. Efforts to reduce computational requirements and speed convergence have shown great progress; nevertheless, the computation requirement still remains undesirably high.

One method for mitigating the high complexity is exploiting parallel computation. Previous work has achieved significant acceleration by using parallelism both in distributed systems in the cloud [2, 3] as well as locally on GPUs [4, 5]. However, these techniques are tuned to specific hardware platforms and can be difficult to adapt to new platforms. There has been less study of the enhanced capabilities of modern CPUs that support both higher thread counts and SIMD programming, allowing for even more parallelism on a single chip [6, 7]. SIMD instruction set extensions (e.g., Intel's AVX2) allow a single instruction to perform element-wise operations (e.g., 8 single-precision floating-point values) concurrently. The main challenge in exploiting SIMD lies in orchestrating memory layout, as the instructions are efficient only when accessing contiguous memory locations.

This work investigates using modern CPUs in MBIR for X-ray CT, focusing on the increased parallel performance enabled by the latest SIMD extensions. We describe reconstruction algorithm modifications that facilitate SIMD programming and examine the bandwidth limitations of combining SIMD with multi-threading. We also explore the performance of high parallelism on modern CPUs with and without SIMD in comparison to GPU-based reconstruction.

Supported in part by NIH grant U01 EB018753 and Intel equipment donations. {rsamp | mcgaffin | fessler | twenisch} @umich.edu

II. Methods

Consider the following MBIR problem for X-ray CT [1]:

$$\widehat{\mathbf{x}} = \arg\min_{\mathbf{x}\geq\mathbf{0}} \Psi(\mathbf{x}), \qquad \Psi(\mathbf{x}) = \frac{1}{2}\,||\mathbf{A}\mathbf{x}-\mathbf{y}||_{\mathbf{W}}^2 + \mathsf{R}(\mathbf{x}), \quad (1)$$

with X-ray CT system matrix $\mathbf{A} \in \mathbb{R}^{M\times N}$, noisy data $\mathbf{y}$, diagonal matrix of statistical weights $\mathbf{W}$ and convex edge-preserving regularizer R. The large dimension of $\mathbf{x}$, the often nonquadratic regularizer, the nonnegativity constraint, and the space-varying nature of the Hessian of Ψ make (1) challenging.

This paper accelerates primal gradient-based methods, *e.g.* [8, 9]. These methods perform an update of the form:

$$\mathbf{x}^{(n+1)} = \left[\mathbf{x}^{(n)} - \left[\mathbf{D}^{(n)}\right]^{-1}\mathbf{g}^{(n)}\right]_+; \quad (2)$$

where $\mathbf{D}^{(n)}$ is a diagonal majorizer [8]; $\mathbf{g}^{(n)}$ approximates the gradient of Ψ in (1) at the current iterate, $\mathbf{x}^{(n)}$; and $[\cdot]_+$ enforces the nonnegativity constraint. Iterative algorithms like (2) that update all the voxels of $\mathbf{x}$ simultaneously can exploit the increasing parallelism in modern computing hardware.

The gradient-approximating term $\mathbf{g}^{(n)}$ is often computed with an ordered-subsets (OS) approximation:

$$\begin{aligned}\mathbf{g}^{(n)} &= \nabla\mathsf{R}\left(\mathbf{x}^{(n)}\right) + \frac{N_{\text{view}}}{|\mathscr{S}_n|}\sum_{v\in\mathscr{S}_n}\mathbf{A}_v^\intercal\mathbf{W}_v\left(\mathbf{A}_v\mathbf{x}^{(n)}-\mathbf{y}_v\right)\\ &\approx \nabla\mathsf{R}\left(\mathbf{x}^{(n)}\right) + \mathbf{A}^\intercal\mathbf{W}\left(\mathbf{A}\mathbf{x}^{(n)}-\mathbf{y}\right) = \nabla\Psi(\mathbf{x}_n), \quad (3)\end{aligned}$$

where $\mathscr{S}_n$ is a subset of the views in the CT system matrix [8].

The most time-consuming step in the image update (2) is computing the data-fit part of the approximate gradient $\mathbf{g}^{(n)}$ (3). For example, for an 8-turn helical scan with 7,872 views and 12 subsets, each $\mathbf{g}^{(n)}$ requires 656 single-view projections and back-projections. These computations dominate the relatively inexpensive regularizer gradient computation. Thus, we focus on accelerating the projection and back-projection in (3).

A. Separable footprints CT system model

We consider the separable footprints (SF) CT system model [10]. The SF model is a "splatting" approach that implements the product $\mathbf{A}\mathbf{x}$ by superimposing the "footprints" of each voxel: $\mathbf{A}\mathbf{x} = \sum_{j=1}^{N}\mathbf{a}_j x_j$. Each 2D footprint is (ap-

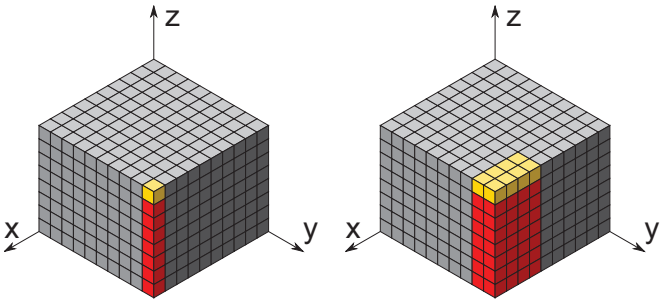

(a) Multi-threaded (b) SIMD

Fig. 1: Data Structure Layout: Data varies fastest along vertical (z) axis. Yellow blocks are data accessed in a single memory operation, and red blocks are future accesses in the entire iteration of forward or back projection loop. (a) Data layout and access of original multi-threaded code. (b) SIMD layout and access. Data needed per access spans across multiple columns, which would require expensive gather operations. We eliminated strided accesses by adjusting the mapping of image coordinates to memory addresses to densely pack each cluster of values together in memory, resulting in sequential accesses.

proximated by) a separable product of two functions, and the elements of $\mathbf{a}_j$ use 2D integrals of this function:

$$a_{ij} = r_i v_j \left(\int_{s \in S_i} g_{ij}(s)\ ds \right) \left(\int_{t \in T_i} h_{ij}(t)\ dt \right), \qquad (4)$$

where r_i and v_j are ray and voxel weights, respectively. We use a trapezoidal function g_{ij} in the channel (transaxial) direction and a rectangular function h_{ij} in the row (axial) direction; this corresponds to the "SF-TR" approximation detailed in [10].

Our implementation of the SF system model for projecting into a single view v is represented mathematically as:

$$\mathbf{A}_v = \mathbf{R}_v \mathbf{S}_v \mathbf{T}_v \mathbf{V}_v, \qquad (5)$$

where $\mathbf{R}_v$ and $\mathbf{V}_v$ are diagonal matrices that apply weights to each ray and voxel, respectively. The most computationally expensive operations are the multiplications with the separable matrices $\mathbf{S}_v$ and $\mathbf{T}_v$ that implement the s and t integrals of (4), respectively. Conceptually, $\mathbf{T}_v \in \mathbb{R}^{N_t N_x N_y \times N}$ and $\mathbf{S}_v \in \mathbb{R}^{N_s N_t \times N_t N_x N_y}$, although our implementation does not store the intermediate $N_t N_x N_y$-element vector. Our single-view back-projection implementation follows the transpose of (5): $\mathbf{A}_v^\mathsf{T} = \mathbf{V}_v \mathbf{T}_v^\mathsf{T} \mathbf{S}_v^\mathsf{T} \mathbf{R}_v$.

The ray and voxel scaling operations $\mathbf{R}_v$ and $\mathbf{V}_v$ are trivial to parallelize with SIMD, so we focus on the more difficult channel and row operators. The next few sections describe accelerating the projector; the back-projector is similar.

B. Existing implementation

We modify an existing projector that implements $\mathbf{A}_v \mathbf{x}$ as:

$$\mathbf{A}_v \mathbf{x} = \mathbf{R}_v \sum_{xy} \mathbf{S}_{v,xy} \mathbf{T}_{v,xy} \mathbf{V}_{v,xy} \mathbf{x}_{xy}. \qquad (6)$$

This is, the algorithm loops over each axial xy-column and applies the volume weights for that column ($\mathbf{V}_{v,xy}$), applies the footprints along the axial t/z direction ($\mathbf{T}_{v,xy}$), applies the footprints along the transaxial s direction ($\mathbf{S}_{v,xy}$), accumulating into a buffer where it applies the ray weights $\mathbf{R}_v$. Fig. 1(a) illustrates this behavior: the algorithm serially processes each red-colored xy-column of $\mathbf{x}$. We obtain parallelism across CPU cores by processing different views on each core.

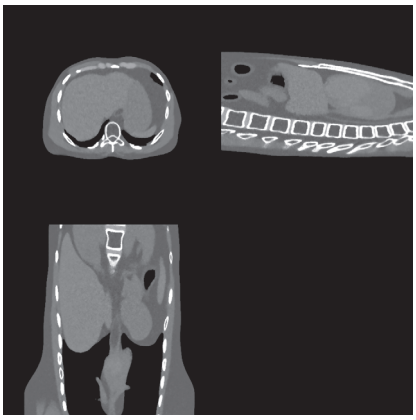

Fig. 2: Central slices of the reconstructed XCAT phantom with the conventional separable footprints system model. Images displayed on a $[800, 1200]$ modified Hounsfeld unit scale where air is 0 HU.

Fig. 3: Difference along central slices between the two reconstructed images, displayed on a [-20, 20] modified Hounsfeld unit window.

C. Modifying SF to suit SIMD

SIMD instructions require that an identical sequence of element-wise operations be performed on the vector operands of each instruction. A naive SIMD approach might process multiple elements of $\mathbf{x}_{xy}$ simultaneously. However, the axial footprint operation $\mathbf{T}_{v,xy}$ is heterogeneous within each xy-column, because the axial footprint of each successive voxel intersects a varying number of detector cells in a cone-beam CT geometry. Hence, a small loop with a trip count varying in z is needed to calculate the contribution of each voxel to each cell, thwarting SIMD efficiency.

To improve SIMD efficiency, we perform SIMD operations over a rectangular region of eight adjacent columns (as in Fig. 1(b)), projecting an xy-patch of 8 voxels with identical z. Our intuition is that the axial footprints of neighboring voxels in a small xy patch are all very similar, enabling an efficient SIMD loop. Whereas the original SF method approximates the axial footprint using the centers of the top and bottom faces of each *voxel*, for our SIMD investigation we approximate the axial footprint using the centers of the top and bottom faces of each *patch*. Section III reports the impact of this approximation.

Although this SIMD approach eliminates control flow divergence, it creates a new challenge. The conventional image volume memory layout for SF has z varying fastest, for which each SIMD instruction would require voxel values that are scattered in memory. Although supported by many SIMD instruction sets, gather-type memory operations that can load non-sequentially located data are highly inefficient. Instead, we transform the memory layout to interleave the eight voxels in each patch (shown in yellow in Fig. 1(b)) consecutively in memory before advancing to the next z coordinate, allowing a regular SIMD load operation to retrieve all eight values.

By applying our SIMD optimization to both forward and back-projection, we change the coordinate-to-memory address mapping throughout the CT code (i.e., there is no need to reorganize image layout during execution). Regularization requires gathers from disparate memory locations regardless of the data layout; we simply adjust the memory address calculations for the modified layout.

III. Results

A. Effect of footprint approximation

We performed an XCAT [11] simulation to validate that the axial footprint approximation that we introduced to facilitate SIMD-friendly control flow does not cause the reconstructed images to deviate significantly from those reconstructed using the original SF system model (which itself is also based on an approximation). Recall that for SIMD we approximate the axial footprint of neighboring voxels in a 2-by-4 patch with the axial footprint corresponding to the patch center. We compared results from the SIMD reconstruction to reconstruction using the original SF algorithm.

We reconstructed a 512^3 simulated scan of an XCAT phantom [11] using a detector with 888 channels, 64 rows and 8 helix turns of 984 views each. The edge-preserving regularizer R penalized the differences between each pixel and its 26 3D neighbors using the Fair potential function,

$$\psi(d) = \delta^2 \left(\left| \frac{d}{\delta} \right| - \log\left(1 + \left| \frac{d}{\delta} \right| \right) \right), \qquad (7)$$

with $\delta = 10$ HU. Fig. 2 shows orthogonal slices from a converged solution to the MBIR problem (1).

Fig. 3 shows the difference maps between the two reconstruction methods. The reconstructed images differ slightly with 1.5 HU root mean squared difference. We believe this difference is comparable to other approximation errors incurred by the SF system model and does not significantly degrade the quality of the reconstruction.

B. SIMD acceleration

We evaluated the acceleration provided by both multi-threading (MT) and by SIMD over a single-thread, non-SIMD implementation on a dual-socket Xeon 2699 system with a total of 72 logical CPU cores (36 physical). Our results compare average runtimes of computing forward and back projections for 572 views with a $528 \times 496 \times 768$-voxel volume with the same detector geometry. We averaged 25 runs each, varying the CPU thread count from 1 to 72. For SIMD we used 8-element AVX2 floating point operations as described in Section II.

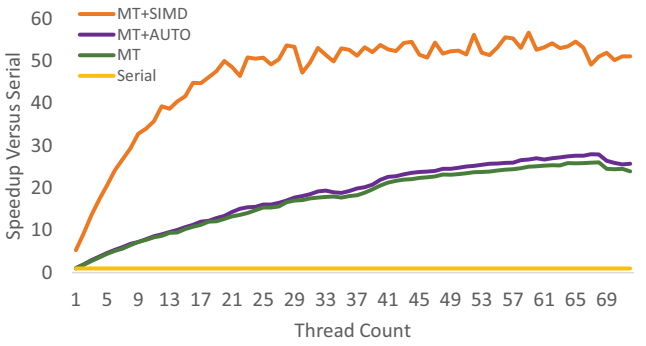

Fig. 4: Average speedup over single-thread, non-SIMD: Speedup of data-fit gradient computation for our multi-threaded SIMD (MT+SIMD) version, an auto-vectorized multi-threaded (MT+AUTO) version, and conventional non-SIMD multi-threaded (MT) version, versus a single-threaded, non-SIMD version (Serial). Times averaged over 25 runs.

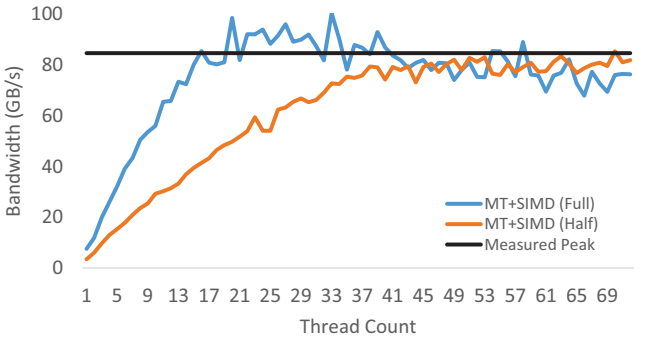

Fig. 5: Average Memory Bandwidth Consumption: Calculated bandwidth consumption for the $\mathbf{T}_v^{\mathsf{T}}$ operation in back-projection with multithreaded SIMD for 1-72 threads, each averaged over 25 runs, compared with measured peak bandwidth of the system. "Full" denotes 32-bit single-precision data, and "Half" is emulated 16-bit precision by reading/writing half of the data. Peak bandwidth measured using STREAM triad benchmark[12] with 72 threads.

Fig. 4 shows that our SIMD implementation (MT+SIMD) provides significant additional speedup over the multi-threaded baseline (MT), achieving over 5× speedup for lower thread counts. We also include the speedup achieved by automatic SIMD vectorization of the MT baseline using Intel's icc compiler (MT+AUTO), which provides minimal gains as it cannot perform the proposed algorithmic modifications and layout transformations. However, the results also show that the MT+SIMD performance saturates at roughly 25 threads, limiting any further speedup beyond 50-55x over the non-parallelized reconstruction. Nevertheless, MT+SIMD provides at least 2x speedup over the MT baseline for all thread counts.

C. Memory Bandwidth

The MT+SIMD performance saturates around 25 threads because it exhausts the available memory bandwidth in the Xeon 2699. Various phases of the CT reconstruction algorithm are memory intensive, and the concurrent accesses from many threads overwhelm the capability of the memory subsystem.

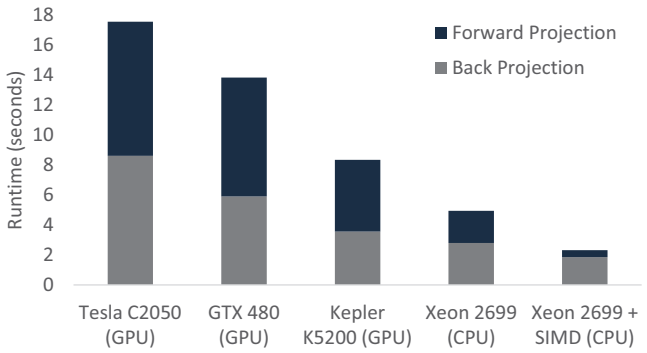

Fig. 6: Subset Gradient Runtime Comparison: Comparison of forward and back-projection runtimes (572 views) on various GPU generations and on the dual-socket Xeon 2699. Xeon MT and MT+SIMD reconstructions use all 72 logical cores. SIMD implementation uses 8-wide floating-point AVX2 instructions.

In particular, we found that the $\mathbf{T}_v^\intercal$ step of the back-projection, which performs an N-voxel read-modify-write operation, saturates available memory bandwidth with roughly 20 threads.

Fig. 5 illustrates average memory bandwidth consumption versus thread count. We estimated average memory bandwidth by precisely measuring the runtime of the $\mathbf{T}_v^\intercal$ step in each thread individually across 25 runs, then averaging across threads and runs. We then divide the total data read and written in each phase by the average runtime. The black line (Measured Peak) indicates the hardware's peak sustainable memory bandwidth, measured with the STREAM triad benchmark [12]. The average bandwidth consumption of our approach (MT+SIMD Full) matches the measured peak around 20 threads, and more threads do not improve performance.

Our bandwidth measurements imply that our multi-threaded SIMD aglorithm allows compute performance to greatly outstrip memory system performance on the Xeon 2699. Higher speedups could be obtained by using hardware with more memory bandwidth (*e.g.*, more DD4 memory channels or higher-bandwidth GDDR5 memory), or the same performance could be achieved at lower cost with a Xeon server with fewer cores. Alternatively, memory bandwidth can be reduced by storing the image more compactly in a half-precision format, still yielding acceptable reconstruction quality [13]. Fig. 5 (MT+SIMD Half) illustrates memory bandwidth scaling when we emulate half-precision format. Bandwidth of the $\mathbf{T}_v^\intercal$ step again saturates at the measured bandwidth peak, but with 40 threads instead of 20.

D. CPU vs GPU Comparison

Finally, we compare our MT+SIMD performance to prior SF results achieved with GPUs [5, 14]. Fig. 6 contrasts SF forward and back-projection on three GPU generations and our 72-thread MT and MT+SIMD performance on the Xeon 2699. The Xeon's high thread count allows the MT and MT+SIMD implementations to be faster than even the high-end K5200 GPU. The comparison also reveals the disparity in forward and back-projection runtimes for MT+SIMD that arise because back-projection incurs more memory traffic and saturates available bandwidth at a lower thread count. Future research should focus on memory bandwidth reduction (*e.g.*, via half-precision formats) to fully realize the remaining untapped speedup potential of SIMD.

IV. Summary and Conclusions

While iterative X-ray CT reconstruction provides excellent image quality, it still remains computationally expensive. Most prior work has focused on GPU and distributed computing to overcome this cost. This work examined the high thread count and SIMD support of modern CPUs. Our results show that with slight changes to the data mapping and a small approximation of the axial footprint, multi-threaded SIMD provides up to 55× speedup over a non-parallel implementation. We also showed that SIMD can provide up to 5× improvement over multi-threading alone, especially for lower thread counts; however, this improvement becomes limited by the memory bandwidth due to such high parallelism. Despite the bandwidth restrictions, multi-threaded SIMD performance was as good or better than a high-end GPU solution, so future work on overcoming the bandwidth limitations could provide even further improvement.

References

[1] J-B. Thibault, K. Sauer, C. Bouman, and J. Hsieh. A three-dimensional statistical approach to improved image quality for multi-slice helical CT. *Med. Phys.*, 34(11):4526–44, November 2007.

[2] J. M. Rosen, J. Wu, T. F. Wenisch, and J. A. Fessler. Iterative helical CT reconstruction in the cloud for ten dollars in five minutes. In *Proc. Intl. Mtg. on Fully 3D Image Recon. in Rad. and Nuc. Med*, pages 241–4, 2013.

[3] D. Kim and J. A. Fessler. Distributed block-separable ordered subsets for helical X-ray CT image reconstruction. In *Proc. Intl. Mtg. on Fully 3D Image Recon. in Rad. and Nuc. Med*, pages 138–41, 2015.

[4] M. Kachelrieß, M. Knaup, and O. Bockenbach. Hyperfast parallel-beam and cone-beam backprojection using the cell general purpose hardware. *Med. Phys.*, 34(4):1474–86, April 2007.

[5] M. McGaffin and J. A. Fessler. Alternating dual updates algorithm for X-ray CT reconstruction on the GPU. *IEEE Trans. Computational Imaging*, 1(3):186–99, September 2015.

[6] H. Scherl, M. Kowarschik, H. G. Hofmann, B. Keck, and J. Hornegger. Evaluation of state-of-the-art hardware architectures for fast cone-beam CT reconstruction. *Parallel Computing*, 38(3):111–24, March 2012.

[7] J. Treibig, G. Hager, H. G. Hofmann, J. Hornegger, and G. Wellein. Pushing the limits for medical image reconstruction on recent standard multicore processors. *Int. J. High Perf. Comp. Appl.*, 27(2):162–77, May 2013.

[8] H. Erdoğan and J. A. Fessler. Ordered subsets algorithms for transmission tomography. *Phys. Med. Biol.*, 44(11):2835–51, November 1999.

[9] D. Kim, S. Ramani, and J. A. Fessler. Combining ordered subsets and momentum for accelerated X-ray CT image reconstruction. *IEEE Trans. Med. Imag.*, 34(1):167–78, January 2015.

[10] Y. Long, J. A. Fessler, and J. M. Balter. 3D forward and back-projection for X-ray CT using separable footprints. *IEEE Trans. Med. Imag.*, 29(11):1839–50, November 2010.

[11] W. P. Segars, M. Mahesh, T. J. Beck, E. C. Frey, and B. M. W. Tsui. Realistic CT simulation using the 4D XCAT phantom. *Med. Phys.*, 35(8):3800–8, August 2008.

[12] J. D. McCalpin. Memory bandwidth and machine balance in current high performance computers. *IEEE Comp. Soc. Tech. Comm. on Comp. Arch. (TCCA) Newsletter*, pages 19–25, December 1995.

[13] C. Maaß, M. Baer, and M. Kachelrieß. CT image reconstruction with half precision floating-point values. *Med. Phys.*, 38(s1):S95–105, 2011.

[14] M. Wu and J. A. Fessler. GPU acceleration of 3D forward and backward projection using separable footprints for X-ray CT image reconstruction. In *Proc. Intl. Mtg. on Fully 3D Image Recon. in Rad. and Nuc. Med*, pages 56–9, 2011.

Effect of sparsity and exposure on total variation regularized X-ray tomography from few projections

Jakob S. Jørgensen*, Sophia B. Coban†, William R.B. Lionheart† and Philip J. Withers†

***Abstract*—We address effects of exposure and image gradient sparsity for total variation-regularized reconstruction: is it better to collect many low-quality or few high-quality projections, and can gradient sparsity predict how many projections are necessary? Preliminary results suggest collecting many low-quality projections is favorable, and that a link may exist between gradient sparsity level and successful reconstruction.**

I. Introduction

Sparsity regularization for X-ray computed tomography (CT) image reconstruction, for example total variation (TV) regularization [1] for gradient-sparse images, has been seen to allow drastically reduced numbers of projections compared to conventional analytical methods, see, e.g. [2]. In medical imaging and non-destructive testing this may allow reduced X-ray exposure or data acquisition time. In today's literature, there is little quantitative guidance on how much TV-regularization allows us to reduce the number of projections. In order for TV and other forms of sparsity regularization to become appropriately used this lack of knowledge must be filled. Our recent work [3] has indicated in simulations inspired by compressed sensing [4] that sparsity of the image gradient can predict how few projections will suffice for accurate TV-regularized reconstruction. A main goal of the present work is to investigate, for the first time, if the same argument holds using real X-ray CT data.

In the present study we consider exposure as the measurement cost, and – given a fixed total exposure – look at the trade off between more information obtained at lower quality (more projections at low exposure) and less information at higher quality (fewer projections at high exposure). The sparsity-regularization literature often takes number of projections as the primary variable, however the total exposure of a CT scan depends both on the number of projections and the exposure-per-projection. [2], [4]. So one could also reduce the total exposure by keeping the usual high number of projections but decreasing the exposure time of each. It is not immediately clear in which scenario TV-regularized reconstruction will perform better. Addressing this issue is the other main goal of this work.

In the present work we systematically study TV-regularized reconstruction quality at reduced numbers of projections as a function of both exposure time and gradient sparsity using real CT data. Specifically we address:

- Q1: Does TV-regularized reconstruction compensate better for reduced information from few high-exposure or many low-exposure projections?
- Q2: Is there a connection between gradient sparsity and how few projections provide enough information that TV-regularized reconstruction succeeds?

While Q1 considers a fixed total exposure with exposure-per-projection inversely proportional to the number of projections, Q2 considers a constant exposure-per-projection and a total exposure proportional to the number of projections.

We will use the recently published SophiaBeads data set, which has been designed specifically for systematic studies of advanced reconstruction algorithms. In addition to using this data set to address the stated questions, we apply the present work to examine how appropriately the SophiaBeads data set can serve the purpose of testing sparsity-regularized reconstruction methods.

An important note needs to be made here about our definition of an 'adequate reconstruction'. In our earlier work [3], we used a relative 2-norm measure to assess if reconstructions *perfectly* recovered the ground truth. This was appropriate for the idealized scenario and to stay consistent, we also report 2-norm errors in this work. However with real data, we wish to assess how well important features can be quantified; in this case known to be disk-shaped and we employ an aspect-ratio quality measure as explained in §IV-B.

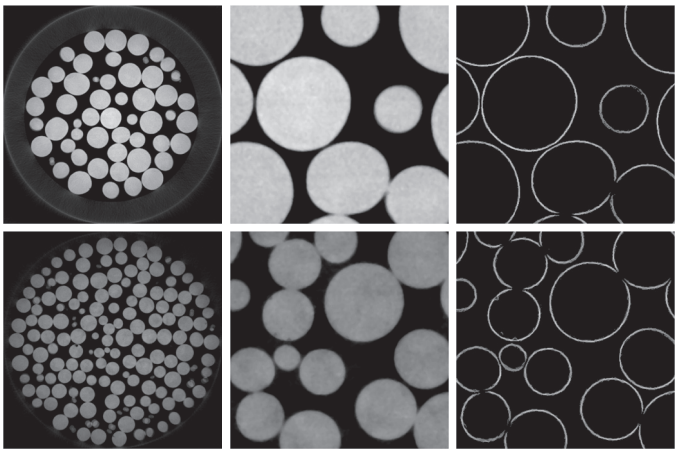

Fig. 1. Ground truths for SophiaBeads data sets S1 (top row) and S2 (bottom row) obtained by 30 CGLS iterations from pooled projections, followed by median filtering. Full 1564×1564 images (left), 350×350 region of interest around the centre (centre), and sparse thresholded gradient magnitude region of interests (right).

*Technical University of Denmark, 2800 Kgs. Lyngby, Denmark.
†The University of Manchester, Manchester, M13 9PL, United Kingdom.
Corresponding author contact: jakj@dtu.dk.

II. Test data

A. The SophiaBeads test data set

The SophiaBeads Dataset Project [5] is a collection of cone-beam X-ray CT data sets where the number of projections are varied while the total photon count (or the total exposure time) is kept constant, i.e. the exposure-per-projection is inversely proportional to the number of projections, as in Q1. This enables a wide range of algorithm comparisons and information content optimizations to be examined. For more detailed information on this experimental framework and the examples of such scenarios, we refer the reader to [6].

The SophiaBeads data set were collected using the *320/225 kV Nikon XTEK Bay* at the Manchester X-ray Imaging Facility (MXIF), the University of Manchester. The apparatus consists of a cone-beam microfocus X-ray source that projects polychromatic X-rays onto a 2000×2000 pixel-length and width, 16-bit flat detector panel. The optimal window size for the SophiaBeads reconstructions is 1564×1564, see [7].

There are two samples (henceforth referred to as S1 and S2) that were scanned using the framework described in [6], and both samples comprised a plastic tube with a diameter of 25mm, filled with uniform Soda-Lime Glass (SiO_2-Na_2O) beads of diameters 2.5mm (S1) and 1.0mm (S2). S1 is publicly available; S2 on request. Here, we use S1 and S2 to represent different sparsity levels: the smaller beads of S2 have relatively more boundary pixels, which equates to more non-zero pixels in the gradient, and hence is less sparse than S1.

The present study uses a single central row of the 3D cone-beam data, and a 2D fan-beam geometry. For the constant-exposure series, the available data sets labelled 64-, 128-, 256-, 512- and 1024-projection are used. For the reduced-exposure series the 1024-projection data set is downsampled by repeatedly halving the number of projections while keeping every other one, thereby preserving the equiangular distribution.

B. Determining a ground truth image and its sparsity

The SophiaBeads data set is designed with fixed total exposure ranging from few high-exposure projections to many low-exposure projections. No high-quality data set (many high-exposure projections) is provided for the construction of a ground truth. However, each data set is recorded at slightly offset angular positions and we obtain a ground truth by pooling all projections for each of S1 and S2 and reconstruct using 30 iterations of the Conjugate Gradient Least Squares (CGLS) algorithm, followed by median filtering with a 5×5 filter to reduce noise. The resulting S1 and S2 ground truths are shown in full and close-up in Fig. 1.

To determine gradient sparsity of the ground truth images we count only nonzero gradient magnitude values greater than a threshold chosen empirically to preserve only bead edges and not noise. Thresholded gradient magnitude images are shown in Fig. 1. The S1 ground truth has 54543 nonzero values in its gradient, corresponding to a sparsity level (relative to the total number of pixels) of $54543/1564^2 = 2.2\%$. The same numbers for S2 are 123870 and 5.1%. This quantifies the intuition that S1 is more gradient-sparse than S2, though exact numbers may vary depending on thresholds chosen.

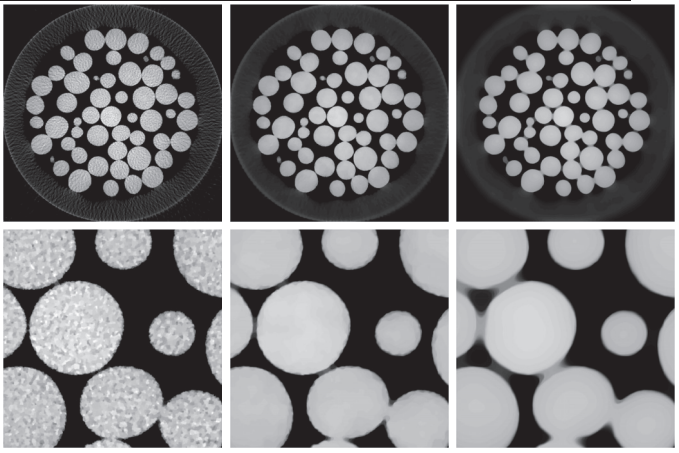

Fig. 2. TV-regularized reconstructions using regularization parameters 10^{-3}, 10^{-2} and 10^{-1} (left to right). Full 1564×1564 images (top row) and 350×350 region of interest around the center (bottom row).

III. Reconstruction problem and algorithm

A. Total variation optimization problem

We denote the log-transformed projection data by b, the 2D fan-beam system matrix by A, an image such as a reconstruction by u, in particular a TV-regularized solution by u_{TV}, and the number of projections by N_θ. To determine a TV-regularized reconstruction (which can be seen as the maximum a posteriori estimate in a Bayesian formulation) of the discrete imaging model $Au = b$ we solve the optimization problem

$$u_{\mathrm{TV}} = \arg\min_u \ \frac{1}{2N_\theta}\|Au - b\|_2^2 + \alpha T_\tau(u), \quad u \geq 0, \qquad (1)$$

where we employ a standard Huber-smoothed TV defined as

$$T_\tau(u) = \sum_j \Phi_\tau(\|D_j u\|_2), \qquad \text{where} \qquad (2)$$

$$\Phi_\tau(z) = \begin{cases} |z| - \frac{1}{2}\tau & \text{if } |z| \geq \tau, \\ \frac{1}{2\tau} z^2 & \text{else.} \end{cases} \qquad (3)$$

Here, α is the TV regularization parameter, D_j is a finite difference approximation to the gradient at pixel j and $\|\cdot\|_2$ denotes the vector 2-norm (or Euclidian norm).

Smoothing is used to make the problem solvable by smooth optimization techniques which are generally faster than their non-smooth counterparts. Depending on the choice of smoothing parameter, τ, this might modify the reconstruction; however here we use a sufficiently small value of $\tau = 10^{-5}$ relative to the image values that smoothing effects are negligible.

Non-negativity is enforced as the object's attenuation coefficients are known to be non-negative and in general non-negativity can lead to substantial reconstruction improvement.

The normalization by N_θ helps to compare reconstructions obtained at different N_θ by compensating the magnitude of the first term which is otherwise proportional to N_θ. As a result, a fixed α value yields the same balance between the two terms

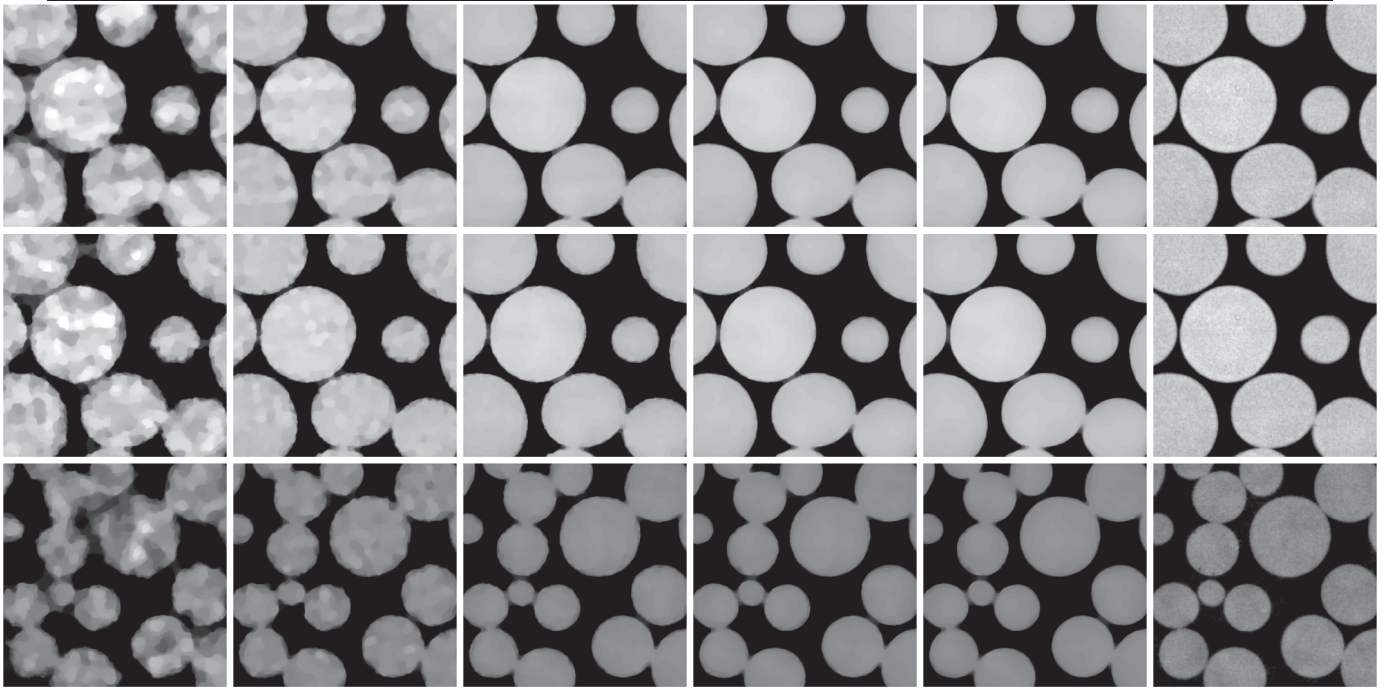

Fig. 3. TV-regularized reconstructions of 64-, 128-, 256-, 512-, 1024-projection data sets and pooled-data ground truths (left to right), showing a 350×350-pixel region of interest. S1 data set of fixed total exposure (top row), S1 and S2 data sets with fixed per-projection exposure (middle and bottom rows).

at different N_θ. This reduces the search for the optimal α to a single initial sweep, the resulting α of which can be reused. In practice we verified this through α sweeps at different N_θ but for brevity have not included results here.

B. High-accuracy optimization algorithm

To solve (1) we used the toolbox TVReg [8], which offers implementations (written in C with MATLAB interface) of accelerated gradient projection methods; specifically we used the provided GPBB (Gradient Projection Barzilai-Borwein) method which among other techniques employ acceleration in form of the Barzilai-Borwein step-size selection. To further accelerate the reconstruction, we employed the ASTRA Tomography Toolbox [9] for GPU-acceleration of the computationally expensive forward and back-projection operators.

We emphasize that our goal here is not necessarily to use the fastest algorithm but one that can reliably solve (1) to high accuracy in reasonable time in order that we indeed assess the quality of the TV-regularized reconstruction and not of an arbitrary early-termination result. TVReg is capable of this through a non-heuristic termination criterion based on the gradient norm magnitude, in contrast to, for example, running a pre-set fixed number of iterations or terminating when a small difference between iterates is encountered.

IV. Results

A. Choosing the regularization parameter

Fig. 2 shows reconstructions for $\alpha = 10^{-3}$, 10^{-2} and 10^{-1} showing the well-known transition from an under-regularized noisy/patchy TV-regularized reconstruction, through to an over-regularized solution where separated beads appear connected due to excessive smoothing. Among a range of values we found $\alpha = 10^{-2}$ to provide the best trade-off and this fixed value was reused in the remaining reconstructions.

B. Assessment of reconstruction image quality

We assess the reconstructions qualitatively through visual inspection. For quantitative assessment we use two error measures with respect to the constructed ground truth u_{GT}: First, the standard relative 2-norm of pixelwise differences: $E_1(u_{\mathrm{TV}}) = \|u_{\mathrm{TV}} - u_{\mathrm{GT}}\|_2 / \|u_{\mathrm{GT}}\|_2$, where $\|\cdot\|_2$ denotes the (Euclidian) 2-norm. The relative 2-norm provides a standardized comparison but is not necessarily the most informative about whether important features have been reliably reconstructed. For the second error measure $E_2(u_{\mathrm{TV}})$, we evaluate the aspect ratio (width:height) of 25 reconstructed beads and report the mean relative error with respect to determined aspect ratios of the ground truth beads. This measure describes how well bead reconstructions reproduce the known bead shapes.

C. Q1: Is it better to collect few high-exposure or many low-exposure projections?

We first address Q1 by determining the TV-regularized reconstruction of the fixed total exposure S1 data set for 64, 128, 256, 512 and 1024 projections. We visually compare a 350×350-pixel region of interest of all reconstructions with the constructed ground truth in the top row of Fig. 3. Visual quality clearly improves with increasing number of projections.

The error measures E_1 and E_2 are plotted in Fig. 4 using a full line. Both error measures agree with visual assessment that

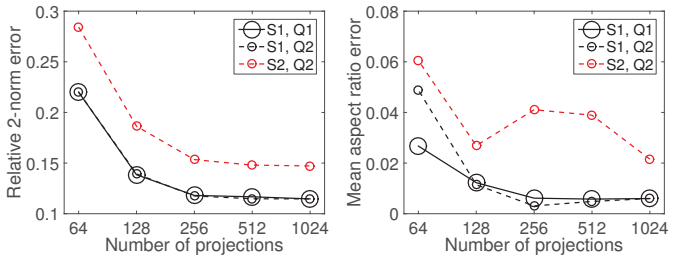

Fig. 4. Relative 2-norm error (left) and mean aspect ratio error (right) for data sets S1 and S2 with fixed total or per-projection exposure, Q1 and Q2.

the 64-projection reconstruction is substantially worse than the others and that error decays with more projections.

D. Q2: What is the dependence on sparsity?

To address Q2 the middle and bottom rows of Fig. 3 show reconstructions for the case of fixed exposure-per-projection for data sets S1 and S2. Corresponding error measures are plotted in Fig. 4 using dashed lines. First, again a clear trend of improved TV-regularized reconstruction quality with increasing number of projections is observed. This is less surprising than in the previous case, since more projections correspond to a higher X-ray exposure. However, for S2 the mean aspect ratio error for 256 and 512 projections is larger than the general trend. We also note that E_1 for S1 in this case almost coincides with the fixed total exposure case.

In case the gradient sparsity does in fact affect the number of projections sufficient for accurate reconstruction, we would expect to see clear differences between S1 and the more gradient-sparse S2 data set. However, visually the S1 and S2 reconstructions show no clear difference in their dependence on the number of projections. The error plots also do not reveal clearly different behavior of S1 and S2 as function of numbers of projections, apart from the previously mentioned E_2 values for S2 at 256 and 512 projections.

V. Discussion and conclusions

In all considered cases the 64-projection reconstructions stand out from the rest as substantially poorer. It seems that artifacts caused by having only 64 projections cannot be effectively removed by TV-regularized reconstruction, no matter whether high- or low-exposure projections are used. This is particularly interesting considering the highly gradient-sparse and round, piece-wise flat regions, for which TV-regularized reconstruction could be expected to excel.

For Q1, we conclude that given a fixed total exposure it appears beneficial to distribute across the highest possible number of projections. Even though each projection is of low quality it appears intuitively sensible to aim for obtaining in a loose sense more independent information about the scanned sample through more projection angles, rather than few high-quality ones. This is however in contrast to the typical message from the sparsity-regularization literature, namely that reconstruction from few projections is possible.

Regarding a possible connection to sparsity in Q2, present results are inconclusive since no clear difference is observed between S1 and S2. However for both S1 and S2 results, there is a large error reduction between 64 and 128 projections. This may hint that there is a number of projections, possibly different for each of S1 and S2, below which TV-regularized reconstruction will not be successful. The SophiaBeads data set only allows subsampling by factors of 2 to preserve equiangular projections. Relevant future work includes the acquisition and analysis of data sets with finer increments of numbers of projections, as well as more sparsity levels.

It should be mentioned that the presented preliminary conclusions may depend on several aspects of the study. For example it is unclear if the pooling approach produces a reliable enough ground truth, and in potential future work, extra care should be taken to acquire ground truth data. Also it is not certain that the error measures used here are the most informative and other options could be considered.

Lastly, regarding how SophiaBeads data sets serve as sparsity-regularization test data, we found TV-regularized reconstruction to work well on the piecewise constant bead images. In that sense, SophiaBeads is quite useful. However for assessing the influence of gradient sparsity we faced shortcomings which we have offered suggestions to address in future work.

Acknowledgments

The work by JSJ was supported by the project "High-Definition Tomography" funded by Advanced Grant No. 291405 from the European Research Council. The work by SBC was supported by the School of Mathematics (UoM), EPSRC CCPi (EP/J010456/1), and BP through the BP International Centre for Advanced Materials (BP-ICAM). Authors would also like to acknowledge the support of Samuel A. McDonald (MXIF) and EU COST action MP1207 (EXTREMA).

References

[1] L. I. Rudin, S. Osher, and E. Fatemi, "Nonlinear total variation based noise removal algorithms," *Physica D*, vol. 60, pp. 259–268, 1992.

[2] J. Bian, J. H. Siewerdsen, X. Han, E. Y. Sidky, J. L. Prince, C. A. Pelizzari, and X. Pan, "Evaluation of sparse-view reconstruction from flat-panel-detector cone-beam CT," *Phys Med Biol*, vol. 55, pp. 6575–6599, 2010.

[3] J. S. Jørgensen and E. Y. Sidky, "How little data is enough? Phase-diagram analysis of sparsity-regularized X-ray computed tomography," *Philos Trans R Soc Lond Ser A*, vol. 373, p. 20140387, 2015.

[4] E. J. Candès, J. Romberg, and T. Tao, "Robust uncertainty principles: Exact signal reconstruction from highly incomplete frequency information," *IEEE Trans Inf Theory*, vol. 52, pp. 489–509, 2006.

[5] S. B. Coban and S. A. McDonald, "SophiaBeads Dataset Project," Tech. Rep., 2015. [Online]. Available: http://dx.doi.org/10.5281/zenodo.16474

[6] S. B. Coban, P. J. Withers, W. R. B. Lionheart, and S. A. McDonald, "When do iterative reconstruction methods become worth the effort?" in *Proc Fully3D*, Newport, RI, USA, 2015.

[7] S. B. Coban, "SophiaBeads Dataset Project Codes," 2015. [Online]. Available: http://dx.doi.org/10.5281/zenodo.16539

[8] T. L. Jensen, J. H. Jørgensen, P. C. Hansen, and S. H. Jensen, "Implementation of an optimal first-order method for strongly convex total variation regularization," *BIT*, vol. 52, pp. 329–356, 2012.

[9] W. van Aarle, W. J. Palenstijn, J. De Beenhouwer, T. Altantzis, S. Bals, K. J. Batenburg, and J. Sijbers, "The ASTRA Toolbox: A platform for advanced algorithm development in electron tomography." *Ultramicroscopy*, vol. 157, pp. 35–47, 2015.

Spatial-frequency-domain study of anticorrelated noise reduction in spectral CT

Mats Persson and Fredrik Grönberg

***Abstract*—In spectral CT, basis material decomposition is commonly used to generate a set of basis images showing the material composition at each point in the field of view. The noise in these images typically contains anticorrelations between the different basis images. Recent studies have demonstrated that reconstruction methods which take the anticorrelations into account give reduced noise in the reconstructed image. In this study we study a denoising problem as a mathematically tractable model for such a reconstruction method, and derive an analytic formula for the resulting image in the spatial frequency-domain. We demonstrate that the method preserves anticorrelations at low and high spatial frequencies but replaces them with positive correlations at intermediate spatial frequencies. This results in less noise and less correlations in the denoised basis images but may also cause artifacts due to cross-talk between basis images. The framework developed here will be useful for analyzing and designing reconstruction algorithms for spectral CT.**

I. Introduction

In spectral computed tomography (CT), a common postprocessing procedure is basis material decomposition, where the registered spectral x-ray transmission data in each measurement is used to estimate the traversed amounts of three different materials. [1] Mathematically, this builds on expressing the linear attenuation coefficient as a linear combination of basis functions $f_1, \ldots, f_M$: $\mu(E) = a_1 f_1(E) + \ldots + a_M f_M(E)$. The basis material decomposition procedure yields the line integrals A_i of the basis coefficients a_i. Subsequently, a_i are obtained from A_i though image reconstruction, either by filtered backprojection (FBP) or an iterative method [2].

The noise in the decomposed projection lines A_i is typically anticorrelated, since the total traversed thickness can be estimated from noisy data more accurately than the proportion of different basis materials along the way, i.e. if one component A_i is estimated to be large, the other ones are likely estimated to be small.

Recent studies have investigated iterative reconstruction algorithms which reconstruct images from projected basis coefficients A_i and demonstrated that the quality of the resulting images can be improved by representing the anticorrelated noise structure in the noise model [3], [4]. However, it is not intuitively easy to see how this improvement varies with properties of the input data or different parameters of the algorithm. The purpose of this work is to elucidate how these algorithms work by studying a mathematically tractable model problem containing the essential features of such a reconstruction algorithm. More specifically, we will address the following questions:

- Can an analytically solvabe model problem model the benefit of such an algorithm?
- Are the resulting basis images less anticorrelated than the original ones?
- Does the decreased noise level come at the cost of bias being introduced in the resulting basis images?

M. Persson and F. Grönberg are with the Department of Physics, KTH Royal Institute of Technology, SE-106 91, Stockholm, Sweden, e-mail: mats.persson@mi.physics.kth.se

II. Theory

For simplicity, we will study a denoising problem instead of a reconstruction problem. In other words, we start with a set of reconstructed basis images with noise that is anticorrelated between the different images. We will then seek the optimal de-noised image using the maximum a posteriori (MAP) method. Let $\boldsymbol{a}$ be a vector containing the basis coefficients of the true, noise-free $N \times N$-pixel basis images in the set: $\boldsymbol{a} = [\boldsymbol{a}_{00}^T, \boldsymbol{a}_{01}^T, \ldots, \boldsymbol{a}_{N-1,N-1}^T]^T$ where $\boldsymbol{a}_{n_1 n_2}$ is the column vector of basis coefficients at pixel (n_1, n_2), indexed from 0 to $N-1$ along each dimension. Thus, $\boldsymbol{a}$ is a column vector with $2N^2$ elements.

In the MAP method, the noise-free image is modelled as an outcome of a random variable. Assume a gaussian prior distribution for $\boldsymbol{a}$ with covariance matrix $\boldsymbol{K}$:

$$p(\boldsymbol{a}) = \frac{1}{(2\pi)^{N^2} |K|^{1/2}} \exp\left(-\frac{1}{2}\boldsymbol{a}^T \boldsymbol{K}^{-1} \boldsymbol{a}\right) \tag{1}$$

and assume a gaussian noise model with covariance matrix $\boldsymbol{C}$ for the measured images $\boldsymbol{a}^m$

$$p(\boldsymbol{a}^{\mathrm{m}}|\boldsymbol{a}) = \frac{1}{(2\pi)^{N^2} |C|^{1/2}} \exp\left(-\frac{1}{2}(\boldsymbol{a}^{\mathrm{m}} - \boldsymbol{a})^T \boldsymbol{C}^{-1} (\boldsymbol{a}^{\mathrm{m}} - \boldsymbol{a})\right) \tag{2}$$

The denoised image $\hat{\boldsymbol{a}}$ is obtained by minimizing the negative log-likelihood with respect to $\boldsymbol{a}$

$$l(\boldsymbol{a}) = \frac{1}{2}\boldsymbol{a}^T \boldsymbol{K}^{-1} \boldsymbol{a} + \frac{1}{2}(\boldsymbol{a}^{\mathrm{m}} - \boldsymbol{a})^T \boldsymbol{C}^{-1} (\boldsymbol{a}^{\mathrm{m}} - \boldsymbol{a}) \tag{3}$$

By applying the discrete Fourier transform separately to each basis image,

$$\tilde{a}_{jk_1k_2} = (\mathcal{F}\boldsymbol{a})_{jk_1k_2} = \frac{1}{N} \sum_{n_1=0}^{N-1} \sum_{n_2=0}^{N-1} a_{jn_1n_2} e^{-2\pi i \frac{k_1 n_1 + k_2 n_2}{N}} \tag{4}$$

Eq. 3 can be written as (omitting an additive constant)

$$l(\tilde{\boldsymbol{a}}) = \frac{1}{2}\tilde{\boldsymbol{a}}^\dagger \left(\tilde{\boldsymbol{K}}^{-1} + \tilde{\boldsymbol{C}}^{-1}\right) \tilde{\boldsymbol{a}} - \tilde{\boldsymbol{a}}^{\mathrm{m}\dagger} \tilde{\boldsymbol{C}}^{-1} \tilde{\boldsymbol{a}} \tag{5}$$

where $\tilde{\boldsymbol{a}} = \mathcal{F}\boldsymbol{a}$, $\tilde{\boldsymbol{a}}^{\mathrm{m}} = \mathcal{F}\boldsymbol{a}^{\mathrm{m}}$, $\tilde{\boldsymbol{C}} = \mathcal{F}\boldsymbol{C}\mathcal{F}^{-1}$ and $\tilde{\boldsymbol{K}} = \mathcal{F}\boldsymbol{K}\mathcal{F}^{-1}$. We now assume that the both the noise and the prior are wide-sense stationary, so that $\tilde{K}_{jk_1k_2j'k_1'k_2'} = 0$ if $k_1 \neq k_1'$ or $k_2 \neq k_2'$ and similar for $\tilde{C}$. This means that $\tilde{\boldsymbol{K}}$ and $\tilde{\boldsymbol{C}}$ are block-diagonal:

$$\tilde{\boldsymbol{K}} = \begin{pmatrix} \tilde{\boldsymbol{K}}_{11} & & & & 0 \\ & \tilde{\boldsymbol{K}}_{12} & & & \\ & & \tilde{\boldsymbol{K}}_{13} & & \\ & & & \ddots & \\ 0 & & & & \tilde{\boldsymbol{K}}_{NN} \end{pmatrix} \tag{6}$$

and similar for $\tilde{\boldsymbol{C}}$. Here, $\tilde{\boldsymbol{K}}_{k_1k_2}$ is the $M \times M$ covariance matrix between the different basis coefficients for one Fourier component. This block-diagonal structure means that (5) can be written as:

$$\begin{aligned} l(\tilde{\boldsymbol{a}}) &= \sum_{k_1k_2} l_{k_1k_2}(\tilde{\boldsymbol{a}}_{k_1k_2}) = \\ &= \sum_{k_1k_2} \frac{1}{2}\tilde{\boldsymbol{a}}_{k_1k_2}^{\dagger}\left(\tilde{\boldsymbol{K}}_{k_1k_2}^{-1} + \tilde{\boldsymbol{C}}_{k_1k_2}^{-1}\right)\tilde{\boldsymbol{a}}_{k_1k_2} - \tilde{\boldsymbol{a}}_{k_1k_2}^{\mathrm{m}\dagger}\tilde{\boldsymbol{C}}_{k_1k_2}^{-1}\tilde{\boldsymbol{a}}_{k_1k_2} \end{aligned} \tag{7}$$

where $\tilde{\boldsymbol{a}}_{k_1k_2}$ is the column vector of basis coefficients at Fourier component (k_1, k_2). The conjugate-symmetry $\tilde{A}_{jk_1k_2} = \tilde{A}^*_{j(-k_1)(-k_2)}$ (indices are defined $\bmod N$) means that the $(-k_1, -k_2)$ and (k_1, k_2) terms must be minimized together:

$$\begin{aligned} \hat{\tilde{\boldsymbol{a}}}_{k_1k_2} &= \operatorname*{argmin}_{\tilde{\boldsymbol{a}}_{k_1k_2}} l_{(-k_1)(-k_2)}(\tilde{\boldsymbol{a}}_{(-k_1)(-k_2)}) + l_{k_1k_2}(\tilde{\boldsymbol{a}}_{k_1k_2}) = \\ &= 2\,\mathrm{Re}\left[\frac{1}{2}\tilde{\boldsymbol{a}}_{k_1k_2}^{\dagger}\left(\tilde{\boldsymbol{K}}_{k_1k_2}^{-1} + \tilde{\boldsymbol{C}}_{k_1k_2}^{-1}\right)\tilde{\boldsymbol{a}}_{k_1k_2} - \right. \\ &\left. -\tilde{\boldsymbol{a}}_{k_1k_2}^{\mathrm{m}\dagger}\tilde{\boldsymbol{C}}_{k_1k_2}^{-1}\tilde{\boldsymbol{a}}_{k_1k_2}\right] \end{aligned} \tag{8}$$

with the solution

$$\hat{\tilde{\boldsymbol{a}}}_{k_1k_2} = \left(\tilde{\boldsymbol{K}}_{k_1k_2}^{-1} + \tilde{\boldsymbol{C}}_{k_1k_2}^{-1}\right)^{-1}\tilde{\boldsymbol{C}}_{k_1k_2}^{-1}\tilde{\boldsymbol{a}}_{k_1k_2}^{\mathrm{m}} \tag{9}$$

The denoising method can therefore be applied by Fourier transforming the basis images, applying Eq. 9 to each Fourier component and inverse Fourier transforming.

In this study we will use a prior probability distribution given by

$$\left(K^{-1}\right)_{jn_1n_2j'n_1'n_2'} = k_j\delta_{jj'}\cdot\begin{cases} 1 & \text{if } |n_1 - n_1'| = 1,\ n_2 = n_2' \\ 1 & \text{if } |n_2 - n_2'| = 1,\ n_1 = n_1' \\ 0 & \text{otherwise} \end{cases} \tag{10}$$

where k_j is a constant determining the penalty strength for each basis image and $\delta_{jj'}$ is the Kronecker delta. This means that variations between horizontally and vertically neighboring pixels are penalized with the square of the difference. The penalty terms for the different basis images are independent. Eq. 10 gives

$$\begin{aligned} &\left(\tilde{K}^{-1}\right)_{jk_1k_2j'k_1'k_2'} = \\ &= 8k_j\delta_{jj'}\delta_{k_1k_1'}\delta_{k_2k_2'}\left(2 - \cos\frac{2\pi k_1}{N} - \cos\frac{2\pi k_2}{N}\right) \end{aligned} \tag{11}$$

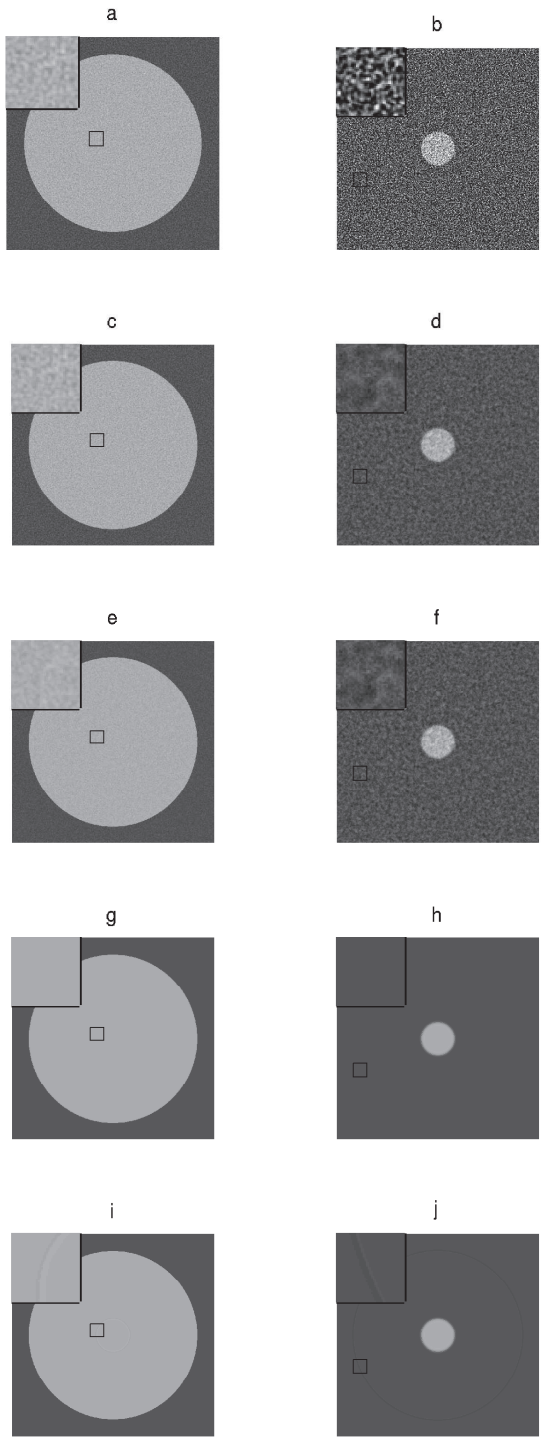

Fig. 1. (a-b) Original noisy basis images: (c)-(d) basis images denoised with the uncorrelated noise model. (e)-(f) basis images denoised with the correlated noise model. (g)-(h) noiseless versions of the images in (c)-(d), i.e. images resulting from the application of the denoising algorithm to noiseless images. (i)-(j) noiseless versions of the images in (e)-(f) The images in the left column are soft tissue images and the images in the right column are iodine images. The insert in the upper left corner of each image shows a magnified view of a region of interest where there is a sharp transition in the other basis image. As seen in (i)-(j) artifacts appear at these locations due to cross-talk between the basis images, and are absent in the noiseless images processed with the uncorrelated noise model (g)-(h).

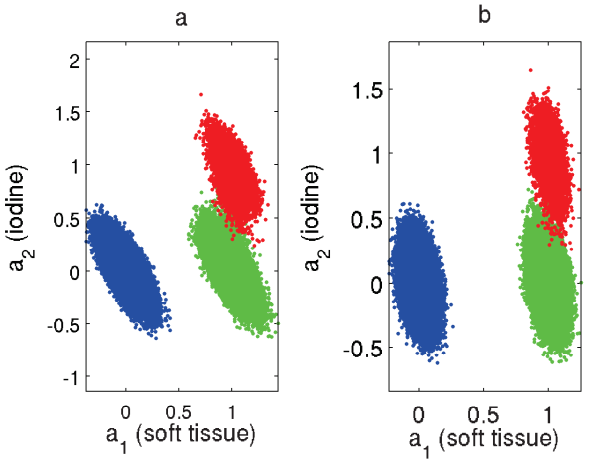

Fig. 2. Scatter plots of $\boldsymbol{a}$ in denoised images with uncorrelated (a) and correlated (b) noise model. Different regions in the image have different colors. Blue: air. Green: soft tissue. Red: iodine insert

III. Methods

To demonstrate the denoising method derived in Sec. I we study a simple phantom consisting of a cylinder of soft tissue, 250 mm in diameter, with an insert, 50 mm in diameter, of 5 mg/ml iodinated contrast agent in its center. Two basis functions are used: the attenuation coefficients of soft tissue and 5 mg/ml iodine, such that $(a_1, a_2) = (1, 0)$ in the phantom outside the insert and $(a_1, a_2) = (1, 1)$ in the insert. Anticorrelated noise was added to these images, with a covariance matrix given by $\tilde{\boldsymbol{C}}_{k_1 k_2} = C \cdot \left(\begin{smallmatrix} 0.011 & -0.059 \\ -0.059 & 0.41 \end{smallmatrix}\right) \cdot (1 + \cos(2\pi k_r/N))^2 \frac{k_r}{N} \mathrm{sinc}^4 \frac{k_r}{N}$ where $k_r = \sqrt{k_1^2 + k_2^2}$ and the constant C is chosen such that the pixel-wise covariance in the image is $\left(\begin{smallmatrix} 0.011 & -0.059 \\ -0.059 & 0.41 \end{smallmatrix}\right)$. This gives the image a noise-power spectrum (NPS) resembling a CT image reconstructed with a Hann window function using linear interpolation [5]. The noise covariance matrix used here was chosen as similar to the noise covariance matrix in the central parts of the decomposed basis images resulting from a simulation of spectral imaging of the studied phantom with an ideal 8-energy bin photon counting detector and 180 projection angles, with $1.0 \cdot 10^6$ photons incident on the object for each detector element and projection angle.

The images were denoised by applying Eq. 9 to their Fourier transforms, with $\tilde{\boldsymbol{K}}$ given by (10) and $k_1 = k_2 = 1$. In addition to using the correct noise covariance matrix $\tilde{C}_{k_1 k_2}$ we also made a denoising using an uncorrelated noise model for comparison, where the off-diagonal entries of $\tilde{C}_{k_1 k_2}$ were set to 0 for each (k_1, k_2). In addition, both the correlated and the uncorrelated denoising methods were applied to the noise-free original images, as a way of calculating the expectation value of the resulting image.

IV. Results

The original noisy images and the denoised images are shown in Fig. 1. Scatter plots of the denoised image pixel values are shown in Fig. 2. The noise standard deviations in the original images are $\sigma_{a_1} = 0.11$, $\sigma_{a_2} = 0.64$ and the corresponding values in the denoised images are $\sigma_{a_1} = 0.091$, $\sigma_{a_2} = 0.14$ for the uncorrelated noise model and $\sigma_{a_1} = 0.054$, $\sigma_{a_2} = 0.14$ for the correlated noise model. The NPS along the positive k_1 axis of each basis image is plotted in Fig. 3. The real and imaginary parts of the correlation coefficient $\mathrm{Re}\left(\mathrm{Cov}(a_1, a_2)/\sqrt{(\mathrm{V}(a_1)\mathrm{V}(a_2))}\right)$ (measuring the in-phase and out-of-phase signal correlations, respectively) are plotted as functions of spatial frequency along the positive k_1 axis in Fig. 4.

V. Discussion

As can be seen in Fig. 1, the image noise is reduced by the denoising, at the expense of spatial resolution. The standard deviation is reduced by 14% for the soft tissue image and 78% for the iodine image with the uncorrelated model and by 49% the soft tissue image and 78% for the iodine image with the correlated model. The correlated model gives 40% and 1% lower noise than the uncorrelated model, for soft tissue and iodine, respectively. For the soft tissue image, this corresponds to dose reduction of 66% with preserved image noise level. The scatter plots in Fig. 2 show that the point clouds for the respective materials are centered at the nominal (a_1, a_2) values for each tissue and that the correlated noise model gives less anticorrelations in the resulting image compared to the uncorrelated noise model. Introducing correlations in the noise model evidently causes the resulting point clouds to become more parallel to the coordinate axes, which reduces the variance along the basis where they are most narrow, i.e. the soft tissue basis.

Fig. 3 shows that the noise power spectra of the original basis images are peaked at intermediate spatial frequencies. The denoising algorithm suppresses those frequencies while preserving the low spatial frequencies. The noise in the iodine basis image is suppressed more than the noise in the soft tissue basis image, since the original noise level is higher in the iodine basis image while the strength of the prior probability distribution, controlled by k_j, is equal in both bases. As seen in Fig. 4, the original image and the image denoised with the uncorrelated model both exhibit strong negative correlations between the two basis coefficients at all spatial frequencies. The image denoised with the correlated model exhibit a strong negative correlation at low and high frequencies and near zero correlation at intermediate frequencies. Evidently, the denoising algorithm has suppressed the noise and removed the anticorrelations at the intermediate spatial frequencies where the original NPS is concentrated.

Careful inspection of noise-free basis images denoised using the correlated noise model (Fig. 1(i-j)) shows that there are weak artifacts in the soft tissue image at the border of the insert and in the iodine image at the border of the phantom. These are due to cross-talk between the different basis images and are absent in the images denoised using the uncorrelated model (Fig. 1(g-h)). This shows that the using the correlated noise model when denoising is associated with a drawback, namely that the resulting basis images may contain artifacts where there is a border in the other basis image. In this case, however, the artifacts are only faintly visible above the noise in Fig. 1(e) and not visible at all in 1(f).

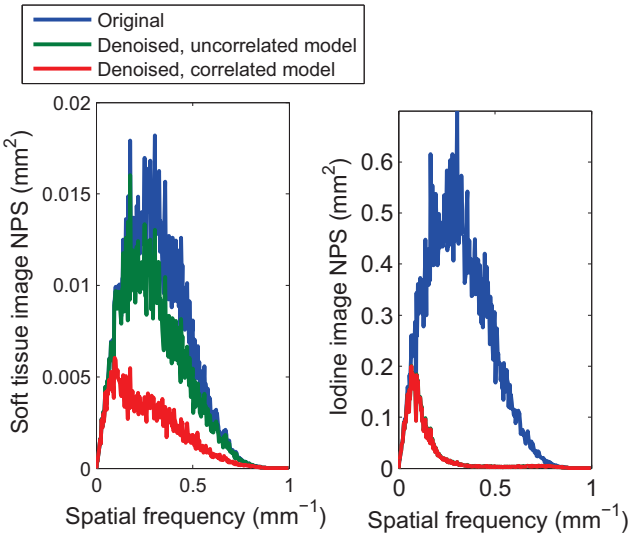

Fig. 3. (Noise power spectrum (NPS) of the original and denoised basis images for soft tissue (left panel) and iodine (right panel). (Right) Real part of the correlation coefficient between $\tilde{a}_1$ and $\tilde{a}_2$, as a function of spatial frequency, plotted along the positive k_1 axis. In the right panel, the NPS for the original image coincides with the one for the image denoised with the uncorrelated model.

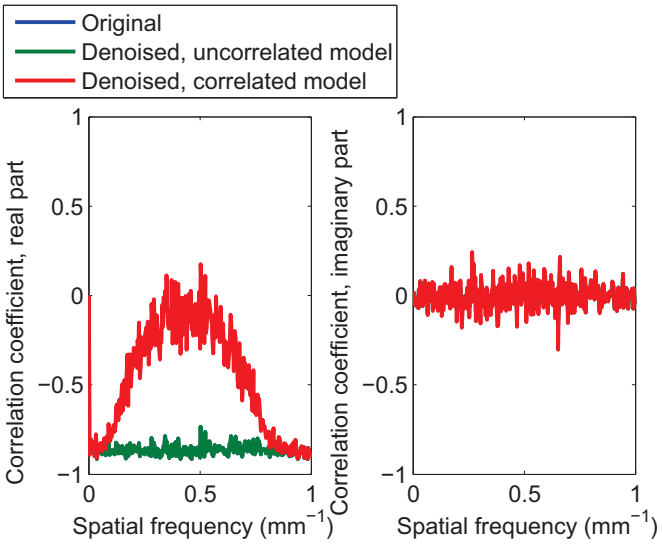

Fig. 4. (Real (left) and imaginary (right) parts of the complex correlation coefficient between $\tilde{a}_1$ and $\tilde{a}_2$, as a function of spatial frequency, plotted along the positive k_1 axis. In the left panel the curve for the uncorrelated curve coincides with the curve for the original model. In the right panel, all three curves coincide.

This suggests an interpretation of the effect of including the noise anticorrelations in the model: it causes the algorithm to remove the anticorrelations at intermediate spatial frequencies in order to lower noise while preserving them at low spatial frequencies. In this way, cross-talk between the basis images, which can cause artifacts, is confined to intermediate spatial frequencies and therefore does not give bias in measurements over large areas in the image. High spatial frequencies are preserved by the algorithm, since the original image NPS used in this study tends to zero at the Nyquist frequency and no denoising is needed.

One limitation of our study is that we assumed that the noise is wide-sense stationary, which is not true in real CT images. However, the noise can still be assumed to be locally wide-sense stationary in a region of the image without sharp transitions. A second limitation is that our regularization term is quadratic, whereas nonquadratic penalty terms such as the Huber penalty [6] are commonly employed, in order to preserve edges in the image. However, most penalty functions are approximately quadratic for small deviations between adjacent pixels. Therefore, the proposed method should be able to approximate a more sophisticated denoising algorithm in slowly-varying image regions, aiding analysis and design of denoising or reconstruction schemes.

VI. Conclusion

We have studied an analytically solvable model for a denoising algorithm for anticorrelated noise in CT and demonstrated that including the anticorrelations in the noise level leads to a reduced noise level and less anticorrelations in the resulting image. This is accomplished by leaving low spatial frequencies unchanged while removing anticorrelations at intermediate spatial frequencies. This introduces bias in the basis images, but since this bias is confined to intermediate spatial frequences, it gives rise to artifacts only at sharp transitions in the image. These insights will be important for guiding the future development of reconstruction algorithms for spectral CT.

Acknowledgment

This study was funded by the Erling-persson Family Foundation (Familjen Erling-Perssons stiftelse). The authors have financial interests in Prismatic Sensors AB.

References

[1] R. E. Alvarez and A. Macovski, "Energy-selective reconstructions in x-ray computerised tomography," *Phys. Med. Biol.*, vol. 21, no. 5, pp. 733–744, Sept. 1976.

[2] C. Schirra, E. Roessl, T. Koehler, B. Brendel, A. Thran, D. Pan, M. Anastasio, and R. Proksa, "Statistical reconstruction of material decomposed data in spectral CT," *Medical Imaging, IEEE Transactions on*, vol. 32, no. 7, pp. 1249–1257, July 2013.

[3] A. Sawatzky, Q. Xu, C. Schirra, and M. Anastasio, "Proximal ADMM for multi-channel image reconstruction in spectral x-ray CT," *Medical Imaging, IEEE Transactions on*, vol. 33, no. 8, pp. 1657–1668, Aug 2014.

[4] K. M. Brown, S. Zabić, and G. Shechter, "Impact of spectral separation in dual-energy CT with anti-correlated statistical reconstruction," *Presented at The thirteenth International Meeting on Fully Three-Dimensional Image Reconstruction in Radiology and Nuclear Medicine, Newport, RI,USA*, 2015.

[5] M. F. Kijewski and P. F. Judy, "The noise power spectrum of CT images," *Phys. Med. and Biol.*, vol. 32, no. 5, p. 565, 1987.

[6] J. A. Fessler, "Grouped coordinate descent algorithms for robust edge-preserving image restoration," *Proc. SPIE*, vol. 3170, pp. 184–194, 1997.

Investigating Pixel Size and Resolution in Optimization-Based CT Image Reconstruction

Sean D. Rose, Emil Y. Sidky, Adrian A. Sanchez, and Xiaochuan Pan

***Abstract*—In this work we propose a simple method for investigating the behavior of reconstructions as a function of pixel size and regularization parameter in optimization-based image reconstruction. The method utilizes numerically converged reconstructions from noiseless data generated by sampling the X-ray transform of a functionally defined phantom or by forward projecting a high-resolution sampling of a simulation phantom. We use this method to investigate the resolution properties of a family of optimization problems whose solutions can be expressed as linear transforms of the data. As pixel size is decreased, system matrix conditioning deteriorates leading to distorted reconstructions. Our results indicate that by choosing a large enough pixel size to avoid this issue, one may be sacrificing resolution unnecessarily. Simple regularization techniques can allow for reconstruction at smaller pixel sizes, decreasing sensitivity of the reconstruction to pixel size and enabling resolution of finer structures.**

I. Introduction

In optimization-based image reconstruction, a continuous object is discretized via expression as a linear combination of elements from some finite-sized expansion set. Most commonly, a set of non-overlapping square pixels is used for this purpose, though other expansion sets, such as Kaiser-Bessel functions, Gaussian blobs, and natural pixels have also been investigated [1]. No matter the choice of expansion set, the process of discretization introduces an inconsistency between projections generated from the discrete representation of the continuous object and the measured projection data. This can potentially lead to artifacts in optimization-based reconstructions.

Confining our attention to the pixel expansion set, the conditioning of the system matrix modeling the X-ray transmission process is dependent on the number of pixels used to represent the measured object. As more pixels are used, the object can be better represented within the expansion set and the inconsistency between projections of a discrete representation of the object and the measured projections can be decreased. Concurrently, the conditioning of the system matrix modeling the X-ray transmission process deteriorates. This leads to a tradeoff between conditioning and representation inherent to all optimization-based image reconstruction methods. The choice of pixel size and regularization strength govern this tradeoff and can have a significant impact on the quality of the reconstructed image [2].

Here we present a simple simulation method for investigating the impact of pixel size and regularization strength in optimization-based reconstruction. The primary motivation behind the method is to facilitate the investigation and development of reconstruction algorithms, and it is therefore purposely constructed to be simplistic and efficient. We apply the method to a family of Tikhonov regularized least squares reconstruction problems and focus on the task of resolving bar-patterns in a simulated Catphan phantom.

This work was supported in part by NIH R01 Grants Nos. CA158446, CA182264, and EB018102. The contents of this article are solely the responsibility of the authors and do not necessarily represent the official NIH views

S. Rose, E. Y. Sidky, A. A. Sanchez and X. Pan are with the University of Chicago, Dept. of Radiology MC-2026, 5841 S. Maryland Avenue, Chicago IL, 60637.

II. Methods

A. Proposed Method

The proposed method involves generating data using a functionally defined simulation phantom. The Radon transform of the simulation phantom is sampled to create sinogram data. This data is then used to perform optimization-based image reconstruction onto image grids with various pixel sizes utilizing optimization problems of varying regularization strength. The reconstructions and the simulation phantom are then sampled onto a high-resolution grid — a grid with pixel size much smaller than the detector bin size — and compared via an image quality metric. In this case we use the image root-mean square error (RMSE), but we note that any number of metrics could be employed. RMSE curves are plotted as a function of pixel size at each considered regularization strength and used to determine an optimal set of parameters. Reconstruction algorithms are run to numerical convergence to eliminate the dependence of the reconstructions on algorithm parameters (e.g. step size, number of iterations, etc.). Note that since the data is generated via sampling of the Radon transform and reconstruction is performed with a discrete-to-discrete forward model, the inverse crime is not committed in this methodology. Note also that if an analytic expression of the Radon transform of the object in question does not exist, a line-intersection based forward projection of a high-resolution discretization of the phantom can also be used to generate the data.

B. Problem and Algorithm

The family of Tikhonov regularized least squares optimization problems we investigate have the form

$$\underset{x}{\operatorname{argmin}} \frac{1}{2}\|Ax-b\|_2^2 + \frac{1}{2}(\lambda\|A\|_2\|x\|_2)^2$$

where $x \in \Re^n$ denotes an estimate of the object in the pixel expansion set, $b \in \Re^m$ denotes the measured sinogram, $A \in \Re^{m\times n}$ denotes a discretized forward model of the X-ray transmission measurement, $\lambda \in \Re$ is a regularization parameter, and $\|\cdot\|_2$ denotes the ℓ_2 norm. When the argument of $\|\cdot\|_2$ is a matrix it returns the maximum singular value of the operator.

The optimization problem is solved to numerical precision in our simulations using the conjugate-gradient least squares (CGLS) algorithm [3]. Numerical convergence is verified by ensuring that three criteria are satisfied. First, we require the normalized ℓ_2 norm of the gradient of the objective function to

be on the order of machine precision

$$\frac{\|A^T(Ax-b)+(\lambda\|A\|_2)^2\,x\|_2}{\|A^Tb\|_2}\sim\epsilon_m$$

Second, we require the objective function to have plateaued as a function of iteration. Third, we require the image RMSE — determined on a high-resolution grid as described above — to have plateaued as a function of iteration. The second and third requirements are assessed subjectively via plots of the respective quantities as a function of iteration on a log-log scale. All optimization-based reconstructions in this study were run to numerical convergence as defined by these criteria or run for $10,000$ iterations. The only reconstructions for which the criteria were not satisfied were unregularized reconstructions at relative pixel sizes of 1.00, 0.67, and 0.50, corresponding to the worst conditioned optimization problems considered. Even so, the second and third criteria were satisfied for these reconstructions.

C. System Geometry and Phantom

We consider a 2D fan beam breast CT system configuration employing a circular source trajectory of radius 100cm with 512 projections taken at equiangular spacing over an angular range of 2π. The system uses a flat-panel detector of length 25cm with 512 detector bins of equal size and a source to detector distance of 150cm. A simulated slice of the Catphan phantom, shown in Figure 1, was used to generate projection data via sampling of the analytic expression for its Radon transform. The background and bars were taken to have attenuation coefficients of 0.244 and 1.26cm^{-1}, respectively, representative of water and aluminum. Two ROIs of the phantom are also shown containing bar patterns spaced 0.33, 0.36, 0.38, and 0.42mm apart. For reference, the detector bin width is 0.48mm, which when divided by the system magnification factor of 1.5, yields a projected bin width of 0.33mm. Note that the RMSE is evaluated over the entire phantom, not just over one of the displayed ROIs.

D. Data model and discrete forward projector

All reconstructions performed in this study employed a ray-driven line-intersection forward projection implementation, often referred to as Siddon's method [4]. This method was chosen because in the limit of small pixel size, it approaches the Radon transform. It is therefore "matched" to the model by which the data was generated. To investigate how the behavior of optimization-based reconstructions would differ were this not the case, data was also generated by sampling the phantom on a 4096×4096 grid and using a discrete-to-discrete forward projection operation designed to model the finite widths of the source and detector. This method generated data by averaging the contribution, as determined by Siddon's method, of 5 equally spaced rays across the source and detector. The source was taken to have size 0.4mm.

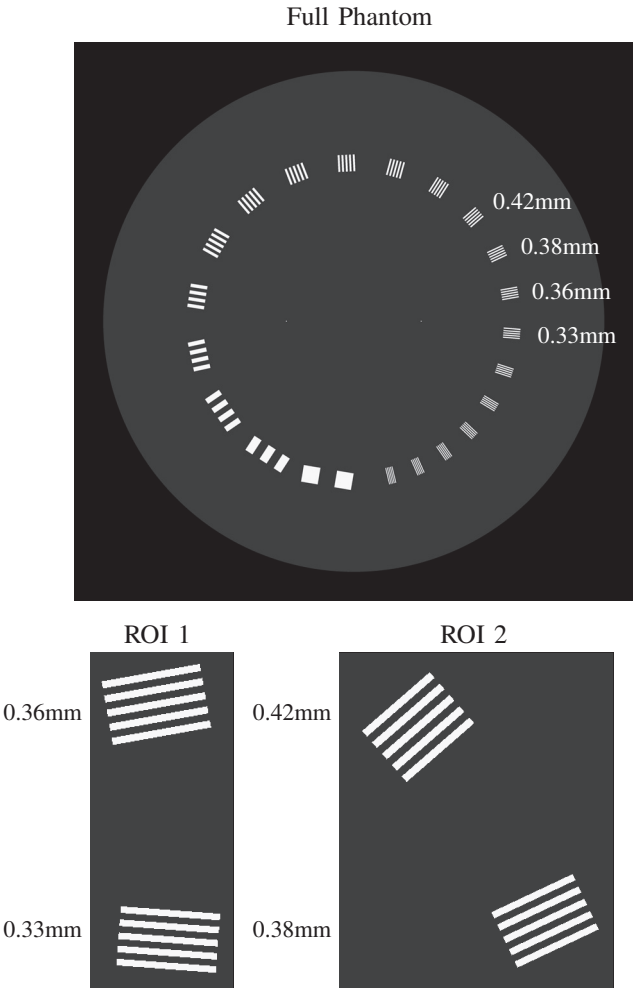

Fig. 1: Full (top) and two ROIs (bottom) of Catphan phantom used for studies. Bar patterns in ROI 1 are separated by 0.33 (bottom pattern) and 0.36mm (top pattern). Patterns in ROI 2 are separated by 0.38 (bottom pattern) and 0.42mm (top pattern). Display window: [0.1, 1.3]

III. Results

RMSE curves were generated by plotting RMSE as a function of relative pixel size, defined as

$$\Delta x_r=\Delta u\frac{r}{d}$$

where Δu is the detector bin size, r is the radius of the source trajectory, and d is the source to detector distance. In Figure 2, we show RMSE curves for reconstructions from the Radon transform data at 5 different values of the Tikhonov parameter λ, and in Figure 3, we show ROIs from the reconstructions containing the 0.33 and 0.36mm bar patterns.

We observe that for small values of λ, deterioration of system matrix conditioning causes an increase in RMSE around relative pixel sizes of 1.00. A subsequent decrease is observed at smaller pixel sizes followed by another slight increase. At relative pixel sizes less than 1.00, the system matrix is not left-invertible, and the unregularized least squares problem ($\lambda=0$) does not have a unique solution. We pick the minimum norm least squares solution by initializing the CGLS algorithm with the zero image [3]. The conditioning of the reconstruction is then controlled by

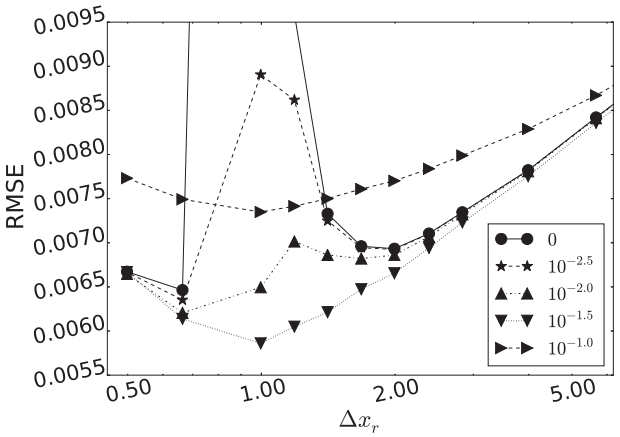

Fig. 2: RMSE as a function of relative pixel size for Tikhonov regularized reconstructions from Radon transform data. Legend indicates value of the regularization parameter λ.

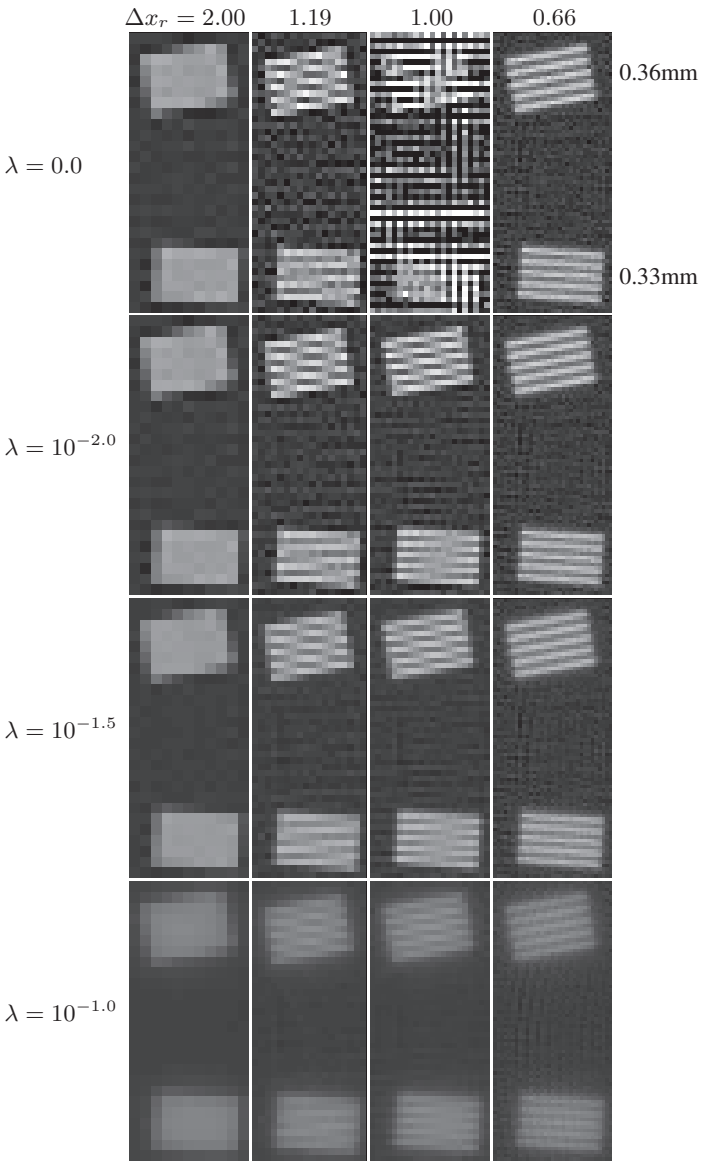

Fig. 3: ROIs containing 0.33 and 0.36mm bar patterns from Tikhonov reconstructions of Radon transform data. Display window: $[0.1, 1.3]$.

the effective condition number, defined as the ratio of the maximum singular value to the minimum nonzero singular value. The effective conditioning of the projection matrix improves at relative pixel sizes just below 1.00, explaining the observed decrease in RMSE.

The unregularized curve has two local minima occurring at relative pixel sizes of 2.00 and 0.66. The presence of a minimum 2.00 suggests that to avoid issues related to poor conditioning and lack of invertibility, one should use a relative pixel size of 2.00 or larger, but as we can see from the RMSE curves and ROI plots, reconstructions at smaller pixel sizes can be obtained and are able to resolve structures which could not possibly be resolved at such large pixel sizes. The minimum at 0.66 suggests that relative pixel sizes below 1.00 may also be used to avoid distortion due to poor conditioning. At these pixel sizes, the system matrix is not left invertible — there are more pixels than measurements — and we will see in the next experiment that using pixel sizes in this regime can lead to artifacts in scenarios in which the forward projection used in reconstruction is not "matched" to the model by which the data was generated. Employing an appropriate strength of regularization — in this case $\lambda = 10^{-1.5}$ — can eliminate the distortion artifacts resulting from poor conditioning entirely.

We see from the RMSE curves that a minimum RMSE of 0.00586 is achieved with the Tikhonov parameter set to $\lambda = 10^{-1.5}$ and a relative pixel size of 1.00. From the ROI plots we observe that the two bar patterns are just barely resolvable with these parameters. At smaller relative pixel sizes, the bars are more clearly resolvable, but from the $\lambda = 10^{-1.5}$ curve, we see the RMSE increases. In the reconstructions, Moire pattern artifacts are visible at relative pixel sizes below 1.00 and provide an explanation for this increase.

In figures 4 and 5 we show RMSE curves and ROIs containing the 0.38 and 0.42mm bar patterns from reconstructions using data generated with the forward projection method modeling source and detector width. We observe that unlike the previous case, the RMSE of the unregularized reconstructions does not significantly decrease at relative pixel sizes less than 1.00 — though not visible in the plot, it does still decrease, but to a lesser extent than in the case of Radon transform data — suggesting that the previously observed decrease cannot be relied upon. In other words, using relative pixel sizes below 1.00 to avoid distortion artifacts due to poor conditioning and improve resolution is not a viable method for unregularized least squares reconstruction. By contrast, distortion artifacts are again eliminated by using an appropriate strength of regularization ($\lambda = 10^{-1.5}$).

The minimum RMSE reconstruction is achieved with relative pixel size 1.19 and Tikhonov parameter $10^{-1.5}$. In this reconstruction the 0.42mm bar pattern is clearly resolvable while the 0.38mm pattern is just barely resolvable. Similar to the case of the Radon transform data, if a relative pixel size of 2.00 or higher were used to avoid conditioning issues, neither of these bar patterns would be resolvable.

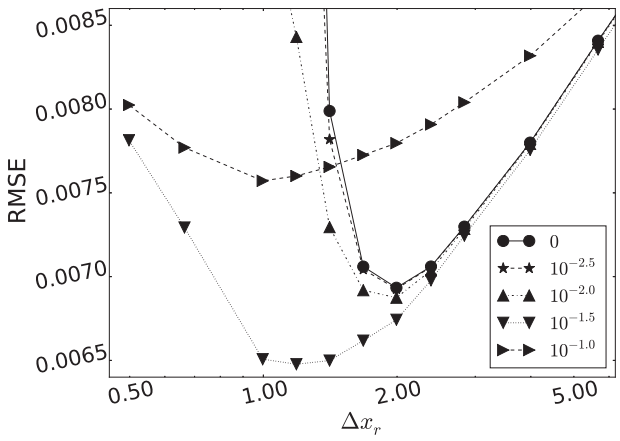

Fig. 4: RMSE as a function of relative pixel size for Tikhonov regularized reconstructions from projection data modeling finite source and detector widths. Legend indicates value of the regularization parameter λ.

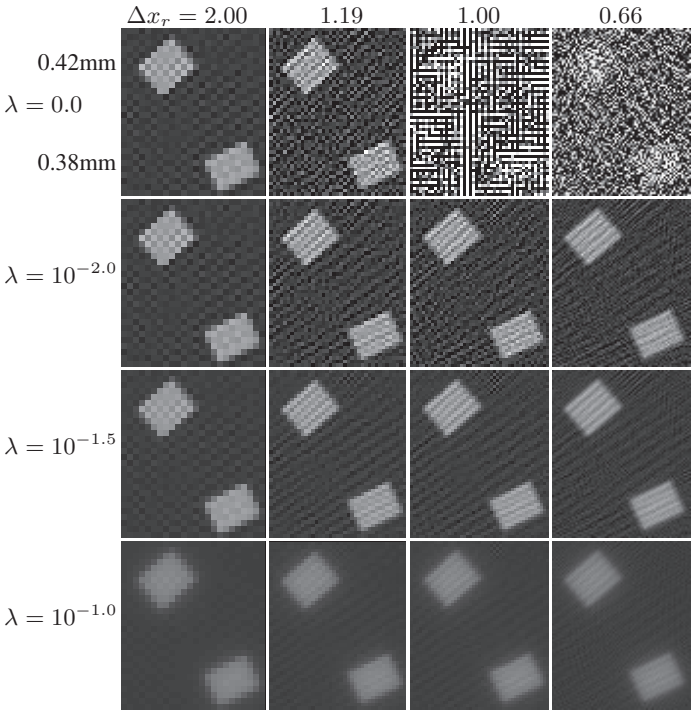

Fig. 5: ROIs containing 0.38 and 0.42mm bar patterns from Tikhonov reconstructions from projection data modeling finite source and detector widths. Display window: $[0.1, 1.3]$

IV. Conclusions

We have proposed and implemented a simple simulation method for investigating the choice of pixel size in optimization-based image reconstruction. Our results indicate that for the system geometry considered a relative pixel size of 2.00 or above must be used to avoid issues related to poor conditioning in unregularized least squares reconstruction. Lower RMSE reconstructions can be achieved by using a simple regularization scheme, in this case Tikhonov regularization, and decreasing the pixel size further. Additionally, the resolution of these lower RMSE reconstructions is better than that of the reconstructions at larger relative pixel sizes, suggesting that by using large enough pixel sizes to avoid conditioning issues one is unnecessarily sacrificing resolution. We demonstrated that this result is not limited to the case of data generated by sampling the Radon transform by demonstrating the same phenomena with data generated using a forward projection scheme modeling finite source and detector widths.

At CT meeting, we will present the results of an investigation into the behavior of reconstructions using distance-driven [5] and Joseph's method [6] forward projection operators in Tikhonov regularized least squares reconstruction schemes. We are also in the process of extending the proposed method to investigating pixel size in optimization-based reconstruction problems with different data-fidelity and regularization terms, such as maximum likelihood based data-fidelity and total variation regularization. Lastly, an investigation of the effect of noise on these results is currently underway and will be presented at the meeting.

References

[1] J. Nuyts, B. De Man, J. A. Fessler, W. Zbijewski, and F. J. Beekman, "Modelling the physics in the iterative reconstruction for transmission computed tomography," *Phys Med Biol*, vol. 58, pp. R63–R69, 2013.

[2] X. Pan, E. Y. Sidky, and M. Vannier, "Why do commercial CT scanners still employ traditional, filtered back-projection for image reconstruction?," *Inverse Problems*, vol. 25, pp. 123009, 2009.

[3] A Bjorck, *Numerical Methods for Least Squares Problems*, SIAM, 1996.

[4] R. L. Siddon, "Fast calculation of the exact radiological path for a three-dimensional CT array," *Med Phys*, vol. 12, pp. 252–5, 1985.

[5] B. De Man and S. Basu, "Distance-driven projection and backprojection in three dimensions," *Phys Med Biol*, vol. 49, pp. 2463–75, 2004.

[6] P. M. Joseph, "An improved algorithm for reprojecting rays through pixel images," *IEEE Trans Med Imaging*, vol. 1, pp. 192–6, 1982.

Dedicated cone-beam breast CT with laterally-shifted CMOS detector

Srinivasan Vedantham, Souleymane Konate, Linxi Shi, Suman Shrestha, Gopal R. Vijayaraghavan and Andrew Karellas

***Abstract*—The availability of complementary metal oxide semiconductor (CMOS) active-pixel detectors with small pixel pitch, low-noise characteristics, and dead-space at the chest-wall similar to mammography present an attractive option for dedicated cone-beam breast CT (CBBCT). However, their field of view is smaller than that used in current clinical CBBCT systems. Hence, the feasibility of laterally-shifted detector geometry was investigated by truncating 17 full cone-beam clinical projection datasets with abnormalities. A weighting scheme was applied to the full set of projections to reduce reconstruction artifacts caused by data redundancy and the convolution of an abrupt truncation boundary, prior to filtered back-projection. Visual analysis did not indicate any discernible artifacts and all lesions were conspicuous. With full-projection CBBCT as the reference, mean (± SD) RMSE (unit of μ, cm^{-1}) for laterally-shifted detector geometry was $4.39x10^{-3}$ (± $1.98x10^{-3}$) across all 17 cases. CBBCT with laterally-shifted detector geometry is feasible and it can provide for imaging with minimal artifacts and with qualitatively and quantitatively similar images as full CBBCT.**

***Index Terms*— Breast, Mammography, Computed Tomography, Breast CT.**

I. Introduction

DEDICATED breast CT can eliminate the tissue superposition problem that can mask or mimic lesions resulting in missed cancers or false-positive exams. Additionally, it does not employ physical compression of the breast. Currently, one dedicated cone-beam breast CT (CBBCT) system has received regulatory approvals in several countries. A recent multi-reader, multi-case (MRMC) reader study employing 18 radiologists interpreting 235 cases with a case mix of 52 negatives, 104 benign findings and 79 cancers reported improved sensitivity and similar specificity with dedicated CBBCT compared to diagnostic mammography [1]. In that study, 93/183 cases (51%) with findings were based on microcalcifications.

Recently, there has been substantial progress in breast CT technology. At our institution, the clinical prototype system that was fabricated (Koning Corp., West Henrietta, NY) to our specific request uses a high power (12 kW), high heat content (1.1 MJ, 1.5 MHU), x-ray tube (M-1581, Varian Medical Systems, Salt Lake City, UT) specifically designed for breast CT. It features a 0.3 mm focal spot that is positioned close to the chest-wall by "flipped" anode-cathode configuration, and is capable of pulsed operation, 70 kV and 250 mA. The combination of small focal spot size and pulsed operation has shown the ability to resolve 0.22 mm $CaCO_3$ spheres at diagnostic dose levels corresponding to 4 mammograms [2]. The system uses a CsI:Tl scintillator coupled amorphous silicon (a-Si) flat-panel detector (PaxScan 4030MCT, Varian Medical Systems, Salt Lake City, UT) with 0.194 mm pixel pitch that was developed for breast CT with reduced dead space at chest-wall of 18.7 mm compared to 34.2 mm of the PaxScan 4030CB detector. The patient support table was redesigned to improve chest-wall coverage [3]. In ongoing studies, the pectoralis muscle was visualized in 49/53 breasts (92.5%) compared to 78.1% with the previous system [4].

Further improvement in chest-wall coverage is possible by using a mammography-format Complementary Metal Oxide Semiconductor (CMOS) active-pixel detector (Dexela 2923, Perkin-Elmer, Santa Clara, CA), which has a specified chest-wall dead-space of 3 mm. This detector has preferable characteristics for CBBCT with an order of magnitude lower noise (165-360 e- [5] compared to 1716-5948 e- [6]) and 0.075 mm pixel pitch that could improve visualization of microcalcifications. Additionally, the detector is capable of 70 frames per second acquisition with 2×2 binning that can reduce scan duration. However, its 29 cm × 23 cm field-of-view (FOV) is smaller than the 40 cm × 30 cm provided by PaxScan 4030MCT. Hence, in this study, the feasibility of the laterally-shifted detector geometry was investigated.

Manuscript submitted on January 24, 2016. This work was supported in part by the National Institutes of Health Grant R01 CA 195512. The contents are solely the responsibility of the authors and to reflect the official views of the National Institutes of Health or the National Cancer Institute.

S. Vedantham is with the Department of Radiology, University of Massachusetts Medical School, Worcester, MA 01655 USA (e-mail: srinivasan.vedantham@umassmed.edu).

S. Konoate was with the Department of Radiology, University of Massachusetts Medical School, Worcester, MA 01655 USA. He is currently at the Harvard T.H. Chan School of Public Health, Boston, MA 02115 USA (email: skonate@hsph.harvard.edu)

L. Shi was with the Department of Radiology, University of Massachusetts Medical School, Worcester, MA 01655 USA. She is currently at the George W. Woodruff School of Mechanical Engineering, Georgia Institute of Technology, Atlanta, GA 30332 USA (email: lshi41@gatech.edu)

Suman Shrestha is with the Department of Radiology, University of Massachusetts Medical School, Worcester, MA 01655 USA (e-mail: suman.shrestha@umassmed.edu).

G. R. Vijayaraghavan is with the Department of Radiology, University of Massachusetts Medical School and UMass Memorial Healthcare, Worcester, MA 01655 USA (e-mail: Gopal.Vijayaraghavan@umassmemorial .org)

A. Karellas is with the Department of Radiology, University of Massachusetts Medical School, Worcester, MA 01655 USA (e-mail: andrew.karellas@umassmed.edu).

II. Methods and Materials

A. Human Subjects

Full cone-beam (CB) projection data from 17 unilateral CBBCT scans of 17 patients with American College of Radiology - Breast Imaging Reporting and Data System (BIRADS®) diagnostic assessment categories of 4 or 5, who participated in an IRB-approved, HIPAA-compliant clinical trial [2, 4, 7] were selected for this study. Subsequent to CBBCT imaging, all study participants underwent biopsy as part of standard care, thus providing histopathology verification. The selected cases correspond to mammographic findings of soft tissue abnormalities (masses) in 8 subjects (4 each of benign and malignant pathology), 8 subjects with microcalcifications of which 4 were pathology-verified to be ductal carcinoma in situ (DCIS), and the remainder were benign, and one subject with both soft tissue abnormality and microcalcifications with malignant pathology.

B. Full CB Projection Dataset Acquisition

Projection datasets were acquired on a clinical prototype system operating at 49 kV, 1.4 mm of Al HVL, 8 ms per projection and 300 projections over 2π. The tube current varied among subjects depending on breast diameter and composition. The mean glandular dose to the breast for the larger cohort was equivalent to 4 mammographic views [2]. It is relevant to note that the system did not employ a bowtie or beam-shaping filter [8], which could result in substantial dose reduction. The detector operated in 2×2 binned mode, resulting in sampling pitch of 0.388 mm.

Schematic of the geometry is shown in Fig. 2. The x-ray source trajectory is assumed to be a circle of radius R and the source to detector distance is represented as D. The three-dimensional (3D) set of object attenuation coefficients to be reconstructed are denoted by $\mu(x)$, where $x \in \mathbb{R}^3$. The attenuation coefficient $\mu(x)$ is assumed to be zero outside a cylinder of constant radius. Cone-beam projections are acquired for each angular position λ on the circular source trajectory with angular spacing of $\Delta\lambda$ (1.2°). The position of the x-ray source is given by $a(\lambda) = \left(R\cos(\lambda), R\sin(\lambda), 0\right)$, where $\lambda \in [0, 2\pi)$. The CB projection data from the x-ray source position $g(\lambda,\theta)$ is defined as:

$$g(\lambda,\theta) = \int_0^\infty \mu\left(a(\lambda) + t\theta\right) dt\,,\ \theta \in S \qquad (1)$$

where, $\theta \in S$, and S is the set of all unit vectors in space. Hereon, the flat-panel detector geometry used to acquire CB projections simultaneously rotates with the x-ray source so that it is always orthogonal to the plane containing the x-ray source position and the y-axis, *i.e.*, the detector is always orthogonal to the unit vector e_v. The rows and columns of the flat-panel detector are respectively parallel to the unit vectors e_u and e_w, respectively, and a point on the detector is given by $P(\lambda,u,w)$. $\hat{I}(\lambda)$ is the point on the detector plane such that the ray emanating from $a(\lambda)$ and passing through AOR is orthogonal to the detector plane. The CB projections appear as a function of the angular position λ and the detector coordinates (u,w), such that $g(\lambda,\theta) = g(\lambda,u,w)$.

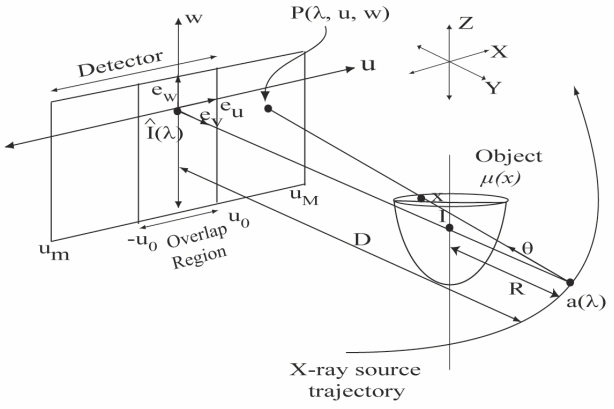

Fig. 1. Schematic of the CB data acquisition geometry using laterally-shifted detector. The three-dimensional (3D) set of object attenuation coefficients to be reconstructed are denoted by $\mu(x)$ and the detector coordinates are denoted as (u,v). Conjugate views provide an overlap region $[-u_0, u_0]$. The drawing is not up to scale.

C. Full CB reconstruction

Geometric calibration data used to reconstruct the breast volume for clinical interpretation was obtained and used in this study. Since the reconstructions provided by the prototype CBBCT system may have been subjected to additional processing, the full CB projection datasets were reconstructed independent of the manufacturer using an implementation of ramp-filtered Feldkamp-Davis-Kress (FDK) algorithm [9]. These full CB reconstructions served as the reference standard for evaluating the laterally-shifted detector geometry.

D. Projection Dataset Preparation

Referring to Fig. 1, it is assumed that the distances R and D are maintained the same as the current system. Then, the CMOS detector needs to be laterally shifted by 5.5 cm to provide the same FOV as the 40 cm of the a-Si detector. This corresponds to a 19% lateral shift of the detector. In this study, we investigated a lateral detector shift of 10.2 cm, which extends the reconstructed FOV by a factor of 1.235. This corresponds to a 35% lateral shift of the detector. This choice was made so that the improved chest-wall coverage due to minimal dead-space can be leveraged to facilitate imaging of the lower axillary lymph nodes. Alternatively, this facilitates increasing D for improved x-ray scatter rejection.

Each acquired full CB projection with the PaxScan detector had a $u \times w$ matrix of 1024×768 pixels of 0.388 mm pitch. For the extended FOV simulated in this study, $(512+110) \times 768$ pixels corresponding to $[u_m, u_0]$ shown in Fig. 1 were retained in each projection. Along the u-coordinate, the overlap region $[-u_0, u_0]$ from complementary views corresponds to 220 pixels.

E. Truncated CB reconstruction

For the laterally-shifted detector geometry and with full 2π acquisition, the lateral truncation issue can be addressed with

filtered back-projection (FBP) methods, such as variants of the FDK algorithm [9]. Cho et al [10] proposed a method where conjugate views are combined and ramp-filtered, followed by weighting and discarding data outside the detector FOV, prior to back-projection using the FDK algorithm. This is referred to as post-weighting FDK. Cho et al. [11] also proposed another alternative method, where the weights are applied to the truncated projections before the ramp-filtering step and is commonly referred to as pre-weighting FDK. Alternative weighting schemes have been proposed in [12-14]. Additionally, back-projection filtration [13], differentiated back-projection [15], and iterative methods [16] have been proposed.

For the laterally-shifted detector geometry, the projections are truncated along the u-coordinate of the detector (Fig. 1). These truncated measurements were corrected as follows: First, a weighting scheme is applied to the full set of projections to reduce reconstruction artifacts caused by data redundancy and the convolution of an abrupt truncation boundary. It is relevant to note that weighting scheme depends only on the u-detector coordinate. For this study, the weighting scheme described in by Cho et al. [11] was utilized:

$$W(u)=\begin{cases}2, & u_m \le u < -u_0 \\ 1+\cos\left(\pi\dfrac{u+u_0}{2u_0}\right), & -u_0 \le u \le u_0 \\ 0, & u_0 < u \le u_M\end{cases} \qquad (2)$$

For every point $x \in \mathbb{R}^3$, using the pre-weighting FDK, the attenuation coefficient $\mu(x)$ can be reconstructed as:

$$\mu(x)=\int_0^{2\pi}\frac{R}{\left\|\left(x-a(\lambda)\right)\bullet e_v\right\|^2}\times \int_{-\infty}^{\infty}W(\xi)\frac{Rg(\lambda,\xi,w)}{\left\|a(\lambda)-P(\lambda,\xi,w)\right\|}h(u-\xi)\,d\xi\,d\lambda \qquad (3)$$

where, $h(t)=\int_{-\infty}^{\infty}|\sigma|\exp(i2\pi\sigma t)\,d\sigma$ and W is the weighting scheme in equation (2). The projection datasets were reconstructed to isotropic voxel size of 0.273 mm to match the full CB reconstruction. The reconstructions were not scaled to Hounsfield units (HU) and hence had units of μ, cm^{-1}.

F. Evaluation

In addition to visual analysis for artifacts, the truncated CB reconstructions were quantitatively evaluated using the root-mean-squared-error (RMSE) metric with the full CB reconstructions as the reference standard. For each clinical case, the effective diameter of the breast (*Deff*) at the chest-wall slice was determined by equating its cross-sectional area to that of a circle. The chest-wall slice is defined as the coronal slice immediately anterior to the pectoralis muscle [4], which was within the imaged FOV for all cases in this study. The effect of breast diameter on RMSE was analyzed.

III. Results

Prior to the study with clinical datasets, algorithm implementation was verified by simulating a homogeneous semi-ellipsoidal breast of 14 cm chest-wall diameter and 10.5 cm chest-wall to nipple length with composition equivalent to 15% fibroglandular weight fraction. Multiple spherical lesions of varying diameters and contrast were included in the breast model. Upon verification of the algorithm implementation, the study with clinical datasets was pursued.

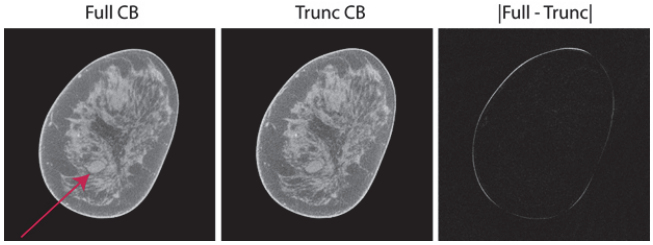

Fig. 2. Matched reconstructed slices (left and middle panels) with soft tissue abnormality (arrow in left panel) that was subsequently pathology-verified to be metastatic adenocarcinoma. The lesion of interest is easily discernible in truncated CB reconstruction (middle panel) and appears visually similar to full-projection CBBCT (left panel). Right panel shows the absolute difference. The reconstructed μ values differ predominantly at the skin-air interface. Image display scales for the reconstructions is $\mu \in [0.15, 0.35]$ cm^{-1} and for the absolute difference image is $\mu \in [0, 0.15]$ cm^{-1}.

A. Visual Analysis

Visual analysis did not show any discernible artifacts. All lesions could be readily visualized with the truncated CB reconstructions. Fig. 2 shows the full CB and truncated CB reconstructions of a slice containing a soft tissue abnormality, which was subsequently pathology-verified as metastatic adenocarcinoma. The absolute difference is also shown and indicates that the difference is predominantly along the skin-air boundary, which is of negligible clinical importance.

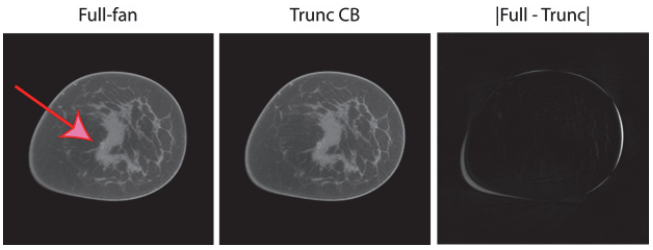

Fig. 3. Matched AvIP of 10 reconstructed slices (left and middle panels) with a microcalcification cluster (arrow in left panel) that was subsequently pathology-verified to be ductal carcinoma in situ. The microcalcification cluster is easily discernible in truncated CB reconstruction (middle panel) and appears visually similar to full-projection CBBCT (left panel). Right panel shows the absolute difference. The reconstructed μ values differ predominantly at the skin-air interface. Image display scales for the reconstructions is $\mu \in [0.15, 0.42]$ cm^{-1} and for the absolute difference image is $\mu \in [0, 0.15]$ cm^{-1}.

In Fig. 3, reconstructions from a study participant who subsequent to CBBCT imaging had a pathology-verified diagnosis of ductal carcinoma in situ (DCIS) are shown. Since microcalcifications are often distributed across multiple slices, scrolling thick-slab along with maximum-intensity projections

(MIPs) are used for evaluating CBBCT images with microcalcifications. The reconstructions in Fig. 3 are the average intensity projections (AvIP) of 10 matched slices, corresponding to a slice thickness of 2.73 mm. The microcalcification cluster (arrow in top panel) is easily discernible on both full CB and truncated CB reconstructions and is better appreciated on soft-copy display. The absolute difference is mostly along the skin-air boundary.

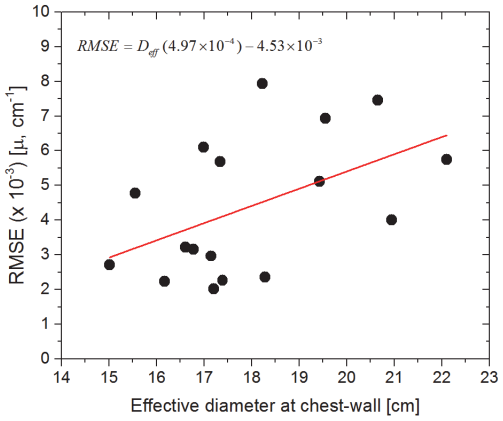

Fig. 4. RMSE as function of the effective diameter of the breast.

B. *Quantitative Analysis*

The mean (± standard deviation, SD) RMSE (unit of μ, cm^{-1}) was 4.39×10^{-3} ($\pm1.98\times10^{-3}$) across all 17 cases and the maximum RMSE was 7.94×10^{-3}. Since the RMSE was determined with the full-CBBCT as the reference standard, the results indicate that the laterally-shifted detector geometry can provide for similar image quality.

Fig. 4 shows the scatter plot of the RMSE as a function of *Deff*. The distribution of *Deff* satisfied the normality assumption ($p=0.344$, Shapiro-Wilk's test). *Deff* was correlated with RMSE ($r=0.494$, $p=0.044$). Linear regression showed that RMSE was marginally dependent on *Deff* with the slope being an order of magnitude lower than the intercept.

IV. Discussion

To our knowledge there have been no prior studies investigating the laterally-shifted detector geometry for CBBCT using clinical datasets. For the chosen lateral detector shift and after scaling for the system magnification (D/R), the region of 6.2 cm diameter centered at the AOR includes data from complementary views, whereas the region outside does not. The median [range] of *Deff* was 17.33 [15.01 – 22.1] cm and corresponds to breasts in the upper quartile [4]. Large breasts were purposely chosen for the study, so that artifacts that occur outside the 6.2 cm diameter region could be visualized. Our study results suggest, given the small differences in μ between the adipose and fibroglandular tissue and even abnormalities, the artifacts, if any, are not discernible. However, where there is a large gradient in μ, such as the skin-air boundary there is deviation between full CB and truncated CB reconstructions. This may have implications for contrast-enhanced CBBCT, and needs to be studied. We simulated the laterally shifted detector geometry by truncating full CB projections. Hence, it does not include the benefit of reduced x-ray scatter due to partial irradiation of the breast [17]. The study does not address the finer sampling and reduced noise of the CMOS detector. Empirical evaluation using such a system setup is being planned and would be addressed in the future.

V. Conclusions

In this study, the feasibility of laterally-shifted detector geometry was investigated in terms of artifacts, visualization of lesions and quantitative evaluation using clinical data from patients that provide for real anatomical backgrounds and lesions. Results from this study show that CBBCT with laterally-shifted detector geometry is feasible and that it can provide for imaging with minimal artifacts and with qualitatively and quantitatively similar images as full CBBCT.

References

[1] E. B. Cole, A. S. Campbell, S. Vedantham, E. D. Pisano, and A. Karellas, "Clinical Performance of Dedicated Breast Computed Tomography in Comparison to Diagnostic Digital Mammography [abstract # SSA01-09]," in *101st Scientific Assembly and Annual Meeting of the Radiological Society of North America (RSNA 2015)*, Chicago, IL, 2015.

[2] S. Vedantham, L. Shi, A. Karellas, A. M. O'Connell, and D. L. Conover, "Personalized estimates of radiation dose from dedicated breast CT in a diagnostic population and comparison with diagnostic mammography," *Phys Med Biol,* vol. 58, pp. 7921-36, Nov 21 2013.

[3] S. Vedantham, A. Karellas, M. M. Emmons, L. J. Moss, S. Hussain, and S. P. Baker, "Dedicated breast CT: geometric design considerations to maximize posterior breast coverage," *Phys Med Biol,* vol. 58, pp. 4099-4118, May 17 2013.

[4] S. Vedantham, L. Shi, A. Karellas, and A. M. O'Connell, "Dedicated breast CT: fibroglandular volume measurements in a diagnostic population," *Med Phys,* vol. 39, pp. 7317-28, Dec 2012.

[5] A. C. Konstantinidis, M. B. Szafraniec, L. Rigon, G. Tromba, D. Dreossi, N. Sodini, P. F. Liaparinos, S. Naday, S. Gunn, A. McArthur, R. D. Speller, and A. Olivo, "X-ray Performance Evaluation of the Dexela CMOS APS X-ray Detector Using Monochromatic Synchrotron Radiation in the Mammographic Energy Range," *IEEE Trans Nucl Sci,* vol. 60, pp. 3969-3980, 2013.

[6] K. Yang, S. Y. Huang, N. J. Packard, and J. M. Boone, "Noise variance analysis using a flat panel x-ray detector: a method for additive noise assessment with application to breast CT applications," *Med Phys,* vol. 37, pp. 3527-37, Jul 2010.

[7] L. Shi, S. Vedantham, A. Karellas, and A. M. O'Connell, "Technical Note: Skin thickness measurements using high-resolution flat-panel cone-beam dedicated breast CT," *Med Phys,* vol. 40, p. 031913, Mar 2013.

[8] S. Vedantham, L. Shi, and A. Karellas, "Dedicated Cone-Beam Breast CT: Design of a 3-D Beam-Shaping Filter," in *57th Annual Meeting of the American Association of Physicists in Medicine (AAPM)*, Anaheim, CA, 2015, pp. 3574-3575.

[9] L. A. Feldkamp, L. C. Davis, and J. W. Kress, "Practical Cone-Beam Algorithm," *J Opt Soc Am A,* vol. 1, pp. 612-619, 1984.

[10] P. S. Cho, R. H. Johnson, and T. W. Griffin, "Cone-beam CT for radiotherapy applications," *Phys Med Biol,* vol. 40, pp. 1863-83, Nov 1995.

[11] P. S. Cho, A. D. Rudd, and R. H. Johnson, "Cone-beam CT from width-truncated projections," *Computerized Medical Imaging and Graphics,* vol. 20, pp. 49-57, Jan-Feb 1996.

A New CT Reconstruction Technique Using Adaptive Deformation Recovery and Intensity Correction (ADRIC)

You Zhang, Jianhua Ma, Jing Wang

Abstract—**Sequential same-patient CT images usually involve deformation-induced and non-deformation-induced voxel intensity variations. We developed a CT reconstruction technique to separate these two voxel intensity variations through an adaptive deformation recovery and intensity correction (ADRIC) algorithm. The ADRIC algorithm applied the 2D-3D deformation technique to a prior high-quality CT volume to recover the deformation field between the prior CT volume and the new, to-be-solved CT volume. Using the deformation-recovered new CT volume, the ADRIC algorithm further corrected the non-deformation voxel intensity variations using an updated algebraic reconstruction technique, which enforced a less stringent total variation smoothing scheme on image difference (ART-dTV). The deformation field and the non-deformation voxel intensity correction were optimized separately and alternately to generate the final CT volume.**

I. Introduction

Frequent CT imaging may increase the risk of secondary cancers, especially for scenarios require repetitive imaging, for instance dynamic myocardial perfusion imaging [1].

To reconstruct high-quality CT images using limited-view projections to reduce the imaging dose, multiple iterative reconstruction techniques [2-7] have been proposed. These techniques, for instance the algebraic reconstruction technique (ART) [2], iteratively optimize the data fidelity through matching the acquired projections with the simulated projections from the reconstructed volumes. In addition, many techniques also use pre-assumed image features like piecewise constancy and intensity gradient sparsity [3-5] to pose additional constraints to further suppress the noise. Total variation (TV) [7], a metric originally proposed for data de-noising, has shown prominent benefits in CT reconstruction. However, the reconstructed CT often suffers from feature changes and detail loss due to over-smoothing, as the piecewise constancy and intensity gradient sparsity assumptions may not hold for complicated anatomical structures.

A new CT reconstruction approach has recently been vigorously investigated [8-10]. Instead of directly reconstructing the CT volume from acquired projections, the new approach estimates it by deforming a previously acquired high-quality CT volume. The image reconstruction thus turns into the optimization of the deformation field to match the acquired projections with the simulated projections from the deformed CT volume [9], which is a 2D-3D deformation process. The successful incorporation of prior CT volume enables accurate image reconstruction with limited-view projections. However, the 2D-3D deformation approach is inherently limited by the fact that the voxel variations between prior and new CT volumes are not necessarily caused by deformation alone. Anatomical and physiological variations between prior and new CT acquisitions, such as tissue calcification, fibrosis/necrosis, and transit of contrast agent in perfusion imaging, can all result in non-deformation-induced voxel intensity variations between the two images. These non-deformation variations cannot be corrected even with the true deformation fields. In contrast, they may adversely affect the deformation field optimization by introducing false signals.

This study developed a new CT reconstruction method to integrate the TV-constrained algebraic reconstruction technique with the 2D-3D deformation technique. The new reconstruction method, named adaptive deformation recovery and intensity correction (ADRIC), was able to recover both the deformation and the non-deformation-induced voxel intensity variations between prior and new CT volumes.

Without losing general applicability, we chose CT myocardial perfusion imaging to evaluate the efficacy of the proposed method. In myocardial perfusion imaging, the spatial misalignments and contrast-agent-induced voxel intensity mismatches between prior and new CT volumes provided a good scenario to examine the efficacy of the ADRIC framework.

II. Materials and Methods

The ADRIC technique is an integration of the 2D-3D deformation technique and the TV-constrained algebraic reconstruction technique (ART):

II.A. 2D-3D deformation technique

For the 2D-3D deformation technique, the new CT volume was deformed from the prior image volume (I_{prior}) using the deformation vector field ($\boldsymbol{DVF}$). The $\boldsymbol{DVF}$ was solved through optimizing the objective function in Eq. 1:

$$\boldsymbol{DVF} = argmin\left[\left\|\boldsymbol{\mathcal{A}} I_{prior}(\boldsymbol{DVF}) - P\right\|_2^2 + \omega * E(\boldsymbol{DVF})\right] \quad (1)$$

$\boldsymbol{\mathcal{A}}$ denotes the projecting matrix that simulates projections from the deformed CT volume. P denotes the acquired on-board projections. $E(*)$ denotes the computation of the deformation energy, which is to regularize and smooth the deformation field [8, 9] for a stable solution. ω denotes the weighting factor that balances the data fidelity constraint and the deformation energy constraint. The 2D-3D deformation generated an intermediate deformation recovered CT volume ($CT^{DR-inter}$) after each optimization.

II.B. TV-constrained ART

You Zhang and Jing Wang are with the Department of Radiation Oncology, UT Southwestern Medical Center at Dallas, Dallas, TX 75390 USA (e-mail: you.zhang@utsouthwestern.edu, jing.wang@utsouthwestern.edu).

Jianhua Ma is with the Department of Biomedical Engineering, Southern Medical University, Guangzhou, Guangdong 510515 China (email: jhma@smu.edu.cn).

ART updated the intermediate deformation recovered CT volume $CT^{DR-inter}$ passed down from 2D-3D deformation by Eq. 2:

$$CT_i^{ART} = CT_i^{DR-inter} + \lambda a_{ij}\left[\frac{p_j - \sum_i a_{ij} CT_i^{DR-inter}}{\sum_i a_{ij}^2}\right] \quad (2)$$

i denotes the CT attenuation coefficient at voxel i. p_j denotes the acquired projection line integral at pixel j. a_{ij} denotes the intersection length of projection line j with CT voxel i for the projection matrix $\boldsymbol{\mathcal{A}}$. λ denotes the relaxation factor.

To further improve the image quality, TV-based smoothing was applied. Traditionally, TV was calculated using the ART-updated CT (CT^{ART} in Eq. 2). However, in this study we took a different approach and calculated TV using the difference image (dCT) between the CT^{ART} and the deformation recovered CT by the composite DVF ($CT^{DR-comp}$):

$$dCT = CT^{ART} - CT^{DR-comp} \quad (3)$$

$CT^{DR-comp}$ was generated by deforming CT_{prior} using the composite DVF ($\boldsymbol{DVF}_{comp}$) accumulated from precedent iterations (Eq. 4):

$$CT^{DR-comp} = CT_{prior}(\boldsymbol{DVF}_{comp}) = CT_{prior}(\boldsymbol{DVF}_{inter-1} \oplus \boldsymbol{DVF}_{inter-2} \ldots \oplus \boldsymbol{DVF}_{inter-k}) \quad (4)$$

$\boldsymbol{DVF}_{inter-x}$ indicates the intermediate $\boldsymbol{DVF}$ solved for each precedent 2D-3D deformation, indexed by x. The k parameter indicates the total number of precedent iterations.

The new TV definition avoided the strong assumption that the whole CT^{ART} was sparse in intensity gradient. Instead, it only assumed the intensity gradient sparsity of dCT. The dCT volume, which was equivalent to the non-deformation-induced voxel intensity variations, was more likely to be sparse in gradient. Thus the new TV definition could potentially reduce the effects of over-smoothing for better reconstruction results. We termed the new approach 'ART-dTV' to differentiate it from the traditional 'ART-TV' approach that regularizes the TV of the whole CT^{ART} directly.

The ART-dTV generated an intermediate intensity corrected CT volume ($CT^{IC-inter}$) after each optimization.

II.C. Framework of the ADRIC technique

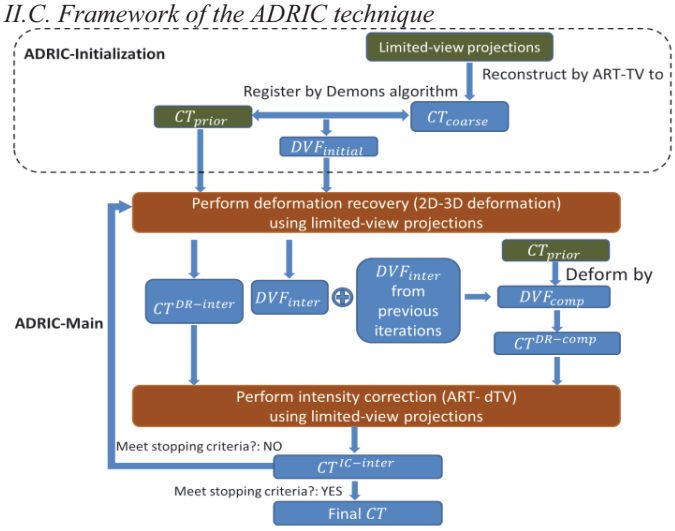

Fig. 1. The framework of the ADRIC technique.

The ADRIC technique can be separated into two stages: the ADRIC-initialization stage and the ADRIC-main stage.

The ADRIC-initialization stage provided an initial DVF ($\boldsymbol{DVF}_{initial}$) to feed into the first implementation of the 2D-3D deformation algorithm. The $\boldsymbol{DVF}_{initial}$ gave the 2D-3D deformation algorithm a good start and prevented it from being trapped at local optima during optimization. To generate $\boldsymbol{DVF}_{initial}$, a coarse CT volume (CT_{coarse}) was first reconstructed from the limited-view projections using the ART-TV algorithm [3]. Then the CT_{coarse} was registered with the prior CT volume CT_{prior} using the Demons registration algorithm [11] to obtain the $\boldsymbol{DVF}_{initial}$.

The implementation procedures of the following ADRIC-main stage were detailed below:

(1). Feed the $\boldsymbol{DVF}_{initial}$, the CT_{prior} (used as I_{prior} in Eq. 1) and the limited-view projections simultaneously into the 2D-3D deformation algorithm. The algorithm will generate the intermediate deformation recovered CT volume $CT^{DR-inter}$ and the corresponding $\boldsymbol{DVF}_{inter}$ according to Eq. 1;

(2). Accumulate the $\boldsymbol{DVF}_{inter}$ with the sequential intermediate DVFs solved in precedent iterations (if any) to the $\boldsymbol{DVF}_{comp}$, and deform CT_{prior} using the $\boldsymbol{DVF}_{comp}$ to $CT^{DR-comp}$ according to Eq. 4;

(3). Feed the limited-view projections, the $CT^{DR-inter}$ and the $CT^{DR-comp}$ simultaneously into the ART-dTV algorithm to generate the intermediate intensity corrected volume $CT^{IC-inter}$ according to Eq. 2 and Eq. 3;

(4). Evaluate the stopping criteria based on data fidelity. If satisfied, exit loop. If not, go to step (5);

(5). Feed the all-zero DVF, the $CT^{IC-inter}$ (used as I_{prior} in Eq. 1) and the limited-view projections simultaneously into the 2D-3D deformation algorithm. Similarly to step (1), the algorithm will generate the intermediate deformation recovered CT volume $CT^{DR-inter}$ and the corresponding $\boldsymbol{DVF}_{inter}$ according to Eq. 1. Then go back to step (2).

By ADRIC, the cumulatively-updated composite DVF and the cumulatively-corrected voxel intensity variations were optimized separately and alternately for the final CT volume. With this adaptive approach, the reconstructed new CT volume could be easily separated into two parts: the deformation recovered CT volume using the final composite DVF (ADRIC deformation recovered CT) and the additional, non-deformation intensity correction based on it (ADRIC intensity correction).

II.D. Simulation using the XCAT phantom and experimental evaluation using the porcine data

We used the digital XCAT phantom [9] to simulate a patient under the CT myocardial perfusion study. Both prior and new CT volumes covering the heart and part of the lung region were simulated. Spatial misalignments were simulated between the prior CT and the new CT, including both respiratory-motion and cardiac-motion induced deformation. Non-deformation voxel intensity variations were also added to the new CT volume to simulate the transit of perfusion contrast agent in the new CT scan.

Limited-view on-board projections were simulated using the new CT volume and spread evenly across a 360° scan angle.

Different numbers of projections were simulated, ranging from 10, 20, 40 to 60, representing different angular sampling sparseness.

In addition to the XCAT study, we used experimentally acquired porcine myocardial perfusion imaging data to further evaluate the efficacy of the ADRIC algorithm. The porcine data were acquired using a 64-slice GE Discovery CT750 HD scanner (GE Healthcare, Waukesha, Wisconsin).

A prior CT volume of the porcine was acquired on the 75% R-R phase of the cardiac cycle through electrocardiography gating. A new CT volume of the 75% R-R phase was later acquired at the same scanner with iodinated contrast agent injected. The difference of acquisition time and the administration of contrast agent introduced both spatial misalignments and non-deformation-induced voxel intensity variations between the prior and new CT volumes.

Similar to the XCAT study, limited-view projections of different angular sampling sparseness levels were simulated using the new CT volume for reconstruction.

II.E. Evaluation

Visual and quantitative comparisons were performed between the reconstructed CT volumes and the 'gold-standard' new CT volumes. For the XCAT study, the 'gold-standard' volume was the simulated new CT volume. For the porcine study, the 'gold-standard' volume was the acquired new CT volume. The root-mean-square error (RMSE) metric was used for quantitative evaluation.

To better evaluate the potential advantage of the ADRIC technique, reconstructions were also performed using the standard 2D-3D deformation technique alone, and the ART-dTV technique alone for comparison.

III. RESULTS

III.A. Simulation using the XCAT phantom

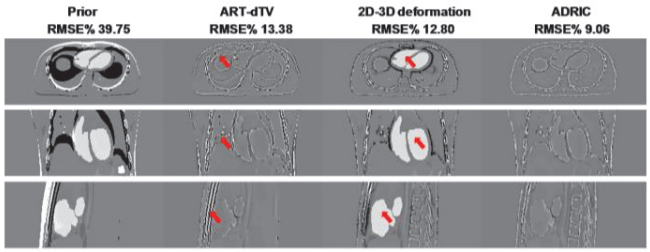

Fig. 2. XCAT study: RMSE values and slice cuts of the difference images between the 'gold-standard' new CT volume and the prior CT/reconstructed CT volumes (by 40 projections). The first column shows the results between the 'gold-standard' new CT volume and the prior CT volume. The other three columns show the results between the 'gold-standard' new CT volume and the CT volumes reconstructed by different techniques. The display window is [-0.015, 0.015].

As shown in Fig. 2, the ART-dTV technique failed to correct multiple remaining intensity mismatches (shown by the arrows in the ART-dTV column). The 2D-3D deformation technique failed to correct non-deformation-induced voxel intensity variations in the cardiac region (shown by the arrows in the 2D-3D deformation column).

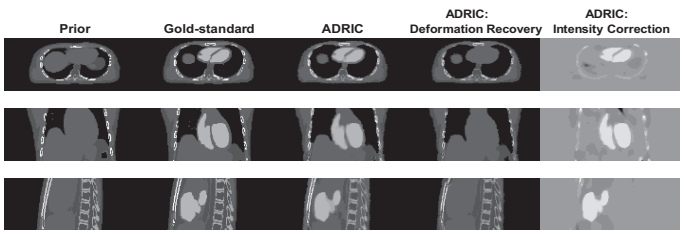

Fig. 3. XCAT study: slice cuts of the prior CT volume, the 'gold-standard' new CT volume, the ADRIC reconstructed CT volume (by 40 projections), the ADRIC deformation recovered CT volume, and the ADRIC intensity correction besides deformation recovery. The display window for the first four columns is [0.03, 0.06]. The display window for the last column is [-0.015, 0.015].

In Fig. 3, the ADRIC reconstructed CT was separated into two components---the ADRIC deformation recovered CT volume (column 4) deformed from the final composite DVF, and the intensity correction (column 5) besides the deformation recovery. The ADRIC deformation recovered CT volume matched the 'gold-standard' CT volume in regions deformed by motion. The ADRIC intensity correction was majorly confined in the cardiac region to correct the non-deformation-induced voxel intensity variations.

Table 1. XCAT study: RMSE values of different reconstruction techniques using different levels of angular sampling sparseness (varied by the number of projections).

No. of projections	Prior	ART-dTV	2D-3D Deformation	ADRIC
10	39.75%	25.45%	18.85%	17.32%
20		19.21%	14.64%	11.90%
40		13.38%	12.80%	9.06%
60		11.04%	12.33%	7.92%

III.B. Experimental evaluation using the porcine data

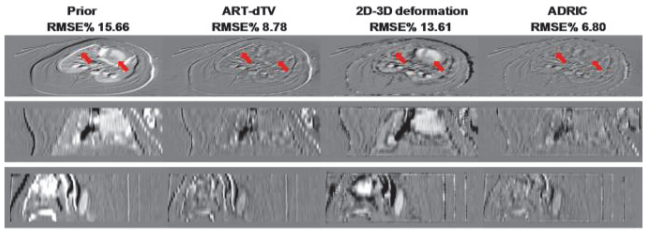

Fig. 4. Porcine study: RMSE values and slice cuts of the difference images between the 'gold-standard' new CT volume and the prior CT/reconstructed CT volumes (by 20 projections).

In Fig. 4, similarly to the XCAT study, the ADRIC technique not only corrected the voxel variations induced from structure deformation (shown by the upper arrows in each subfigure), but corrected the voxel intensity variations induced from the iodinated perfusion contrast agent (shown by the lower arrows in each subfigure).

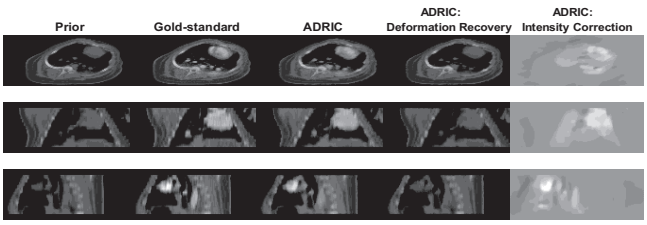

Fig. 5. Porcine study: slice cuts of the prior CT volume, the 'gold-standard' new CT volume, the ADRIC reconstructed CT volume (by 20 projections), the ADRIC deformation recovered CT volume, and the ADRIC intensity correction besides deformation recovery.

Fig. 5 shows the ADRIC deformation recovered CT volume (column 4) and the ADRIC intensity correction (column 5) for the porcine study.

Table 2. Porcine study: RMSE values of different reconstruction techniques with different levels of angular sampling sparseness.

No. of projections	Prior	ART-dTV	2D-3D Deformation	ADRIC
10	15.66%	10.70%	14.91%	8.98%
20		8.78%	13.61%	6.80%
40		7.97%	12.58%	5.82%
60		6.91%	12.14%	5.29%

IV. Discussion

The ADRIC technique developed in this study outperformed both the ART-dTV and the 2D-3D deformation techniques, as evidenced by the XCAT simulation study (Fig. 2, Tables 1) and the experimental porcine study (Fig. 4, Table 2). It successfully recovered the deformation and corrected the non-deformation-induced voxel intensity variations (Fig. 3, Fig. 5). In comparison, the 2D-3D deformation technique could only recover the deformation. The residual non-deformation-induced intensity mismatches were not only un-corrected, but provided false signals that affected the accuracy of the solved DVFs (Fig. 2, Fig. 4). In contrast, the ART-dTV technique viewed all voxel variations as intensity changes and did not explicitly consider the deformation occurred in between. Image features and fine structures were easily smoothed out through large-scale TV regularization. In this study, the ART-dTV technique used dTV instead of the traditional TV to only enforce the sparsity constraint of intensity gradient on the difference image between prior and new CT volumes, to better preserve the image features. However, deformation in between prior and new CT volumes led to complex anatomical variations to make the difference image less sparse in intensity gradient. Thus the ADRIC technique, which performed dTV-constrained intensity correction adapted to the deformation recovered CT volume, provided better reconstruction results than ART-dTV.

The developed ADRIC technique has achieved encouraging results. Nonetheless, future improvements are warranted to further fine-tune the ADRIC technique. Remaining problems with the current technique are the mismatched bony region and the boundary of structures (Fig. 2, Fig. 4). Inaccurate deformation, especially that around the bony region, has been widely observed in different 2D-3D deformation based image reconstruction studies [8, 9]. The discrepancy is potentially introduced by three factors:

1. Deformation energy-based smoothness regularization enforced on the DVFs does not usually apply to structure boundaries, where sliding motion [12] prevails. 2. The image deformation was performed by trilinear interpolation, which has limited accuracy. Interpolation inaccuracy in high gradient regions like bony areas and structure boundaries may result in significant voxel intensity mismatches. 3. The intensity-driven 2D-3D deformation is potentially limited in accuracy, as it fails to consider the biomechanical properties of different tissues.

Improving the accuracy of the 2D-3D deformation algorithm may fundamentally solve the problem, which can be realized through applying patch-based smoothness regularization to better fit the sliding motion, applying a more accurate voxel interpolation model to avoid mismatches in high gradient boundaries, and applying biomechanical models like those based on finite element analysis to obtain a better, more realistic deformation field.

V. Conclusions

An ADRIC technique was developed in this study. Myocardial perfusion imaging scenarios using XCAT simulated phantom data and experimentally acquired porcine data validated the efficacy of the ADRIC technique. Additional patient studies in different clinical scenarios are warranted to further evaluate the ADRIC technique in the future.

Acknowledgment

This work was supported by grants from the American Cancer Society (RSG-13-326-01-CCE), from the US National Institutes of Health (R01 EB020366), and from the Cancer Prevention and Research Institute of Texas (RP130109).

References

[1] A. Rossi, D. Merkus, E. Klotz, N. Mollet, P. J. de Feyter, and G. P. Krestin, "Stress myocardial perfusion: imaging with multidetector CT," *Radiology,* vol. 270, pp. 25-46, Jan 2014.

[2] R. Gordon, R. Bender, and G. T. Herman, "Algebraic reconstruction techniques (ART) for three-dimensional electron microscopy and x-ray photography," *J Theor Biol,* vol. 29, pp. 471-81, Dec 1970.

[3] J. Wang, W. Mao, and T. Solberg, "Scatter correction for cone-beam computed tomography using moving blocker strips: a preliminary study," *Med Phys,* vol. 37, pp. 5792-800, Nov 2010.

[4] E. Y. Sidky and X. Pan, "Image reconstruction in circular cone-beam computed tomography by constrained, total-variation minimization," *Phys Med Biol,* vol. 53, pp. 4777-807, Sep 7 2008.

[5] G. H. Chen, J. Tang, and S. Leng, "Prior Image Constrained Compressed Sensing (PICCS)," *Proc Soc Photo Opt Instrum Eng,* vol. 6856, p. 685618, Mar 3 2008.

[6] J. W. Stayman, H. Dang, Y. Ding, and J. H. Siewerdsen, "PIRPLE: a penalized-likelihood framework for incorporation of prior images in CT reconstruction," *Phys Med Biol,* vol. 58, pp. 7563-82, Nov 7 2013.

[7] X. Jia, Y. Lou, R. Li, W. Y. Song, and S. B. Jiang, "GPU-based fast cone beam CT reconstruction from undersampled and noisy projection data via total variation," *Med Phys,* vol. 37, pp. 1757-60, Apr 2010.

[8] J. Wang and X. Gu, "High-quality four-dimensional cone-beam CT by deforming prior images," *Phys Med Biol,* vol. 58, pp. 231-46, Jan 21 2013.

[9] Y. Zhang, F. F. Yin, W. P. Segars, and L. Ren, "A technique for estimating 4D-CBCT using prior knowledge and limited-angle projections," *Med Phys,* vol. 40, p. 121701, Dec 2013.

[10] Y. Zhang, F. F. Yin, T. Pan, I. Vergalasova, and L. Ren, "Preliminary clinical evaluation of a 4D-CBCT estimation technique using prior information and limited-angle projections," *Radiother Oncol,* vol. 115, pp. 22-9, Apr 2015.

[11] X. Gu, H. Pan, Y. Liang, R. Castillo, D. Yang, D. Choi*, et al.*, "Implementation and evaluation of various demons deformable image registration algorithms on a GPU," *Phys Med Biol,* vol. 55, pp. 207-19, Jan 7 2010.

[12] J. Vandemeulebroucke, O. Bernard, S. Rit, J. Kybic, P. Clarysse, and D. Sarrut, "Automated segmentation of a motion mask to preserve sliding motion in deformable registration of thoracic CT," *Med Phys,* vol. 39, pp. 1006-15, Feb 2012.

Shift-Invariant Projection and Backprojection for Helical CT based on A Self-Consistent Coordinate

Minghao Guo and Hao Gao

***Abstract*—We develop an efficient method to compute projections and backprojections without repeated on-the-fly computations for helical CT. The method utilizes the shift-invariant projections and backprojections based on a self-consistent coordinate with rigorous justification, so that the size of projection and backprojection matrices can be significantly reduced in order to be practically stored on GPU. Numerical results using GPU parallelization suggest that the proposed shift-invariant method has much improved computational efficiency from the conventional on-the-fly method, i.e.,by 3-6 fold acceleration for the projection and 3-16 fold acceleration for the backprojection using standard configuration of helical CT.**

I. Introduction

Helical computed tomography (CT) is perhaps the most popular diagnostic imaging modality. Inspired by compressive sensing [1], [2], Model-Based Image Reconstruction (MBIR) method has revived as an active research field in CT [3], [4] to meet the task-based imaging needs, such as low-dose, limited-angle, sparse-view, and four-dimensional CT scans. Yet, a major drawback of MBIR is its long computational time, for which the projection and backprojection (i.e., the X-ray transform and its adjoint) are often computational dominant.

The efficient computation of projection and backprojection is essential for MBIR to be practically useful. Various algorithms have been developed, such as the Siddon's algorithm [5], the ray-driven method, and the pixel-driven method [6], [7], [8]. Note that the ray-driven method is rarely used for the backprojection and the pixel-driven method is rarely used for the projection since they may introduce artifacts [9], [10]. Recent developments also include fast ray-tracing technique [11], the distance-driven method [10], separable-footprint based method [12], domain-decomposition based parallel algorithms [13], and improved distance-driven method [14].

To accelerate the computation of projection and backprojection, GPU-based parallel algorithms and implementations have been developed, during which the projection and backprojection are computed on-the-fly without saving the matrices due to the storage limitation, particularly for helical CT. As a result, the on-the-fly computation of projection and backprojection requires that the projection and backprojection matrices are repeatedly computed. However, it is possible to alleviate the storage problem using the helical symmetry [15], [16]. Fast backprojection method for analytical image reconstruction was developed by storing numerical weights [15]. A MBIR method was proposed for helical CT using 27-gigabyte stored system matrix from the pixel-driven method [16]. Inspired by their use of rotating coordinates [15], [16], this work aims to further reduce the matrix size that needs to be stored, so that the projection and backprojection can be computed on GPU without the need of repeated computation of matrix elements. Moreover, separate matrices will be used for ray-driven projection and pixel-driven backprojection to avoid the artifacts.

M. Guo and H. Gao are with School of Biomedical Engineering and Department of Mathematics, Shanghai Jiao Tong University, Shanghai 200240, CHINA (e-mail: hao.gao.2012@gmail.com).

II. Methods

A. Self-consistent Coordinate

Let us consider a X-ray source trajectory equally distributed on a helix

$$\{s_\lambda : s_\lambda = (R\cos h\lambda, R\sin h\lambda, l\lambda), \lambda \in S\}, \qquad (1)$$

where R is the radius of the helical trajectory, and S is a set of discrete real numbers specifying the source coordinate per view on the helical trajectory with h and l representing the angular increment and the axial increment per view. without loss of generality, S is assumed to take integer values. Corresponding to s_λ, let the detector plane be D_λ, and V_λ be the field-of-view (FOV) cone generated by s_λ and D_λ. Let L be the axial length of detector, and then the helical pitch can be defined as $l/h \cdot 2\pi/L$.

On the other hand, let $X = \{X_{ijk}, i \le N_x, j \le N_y, k \le N_z\}$ denote the discretized imaging object f with each grid

$$X_{ijk} = \{(x, y, z) : x \in [x_i, x_{i+1}), y \in [y_j, y_{j+1}), z \in [z_k, z_{k+1})\} \qquad (2)$$

where $x_i = i\Delta x + x_0$, $y_j = j\Delta y + y_0$, and $z_k = k\Delta z + z_0$. Moreover, we denote the kth axial slice of X as

$$X_k = \{X_{ijk} : i \le N_x, j \le N_y\}.$$

The discrete image f to be reconstructed is denoted by a column vector

$$f = [f_1, \cdots, f_k, \cdots, f_{N_z}]^T$$

where f_k consists of image voxels on the kth axial slice, i.e.,

$$f_k = [f_{1,1,k}, \cdots, f_{i,j,k}, \cdots, f_{N_x,N_y,k}]^T.$$

Next we define $s = \Delta z/l$ as the ratio between the slice thickness and the axial increment per view for the X-ray source, which is a key parameter for the proposed method. In order for the proposed method to work, s needs to take integer values, which is feasible except very sparse-view scans. Otherwise, we can always slightly tune Δz to have

an integer value for s. Then efficient image reconstruction can be performed by storing shift-invariant projection and backprojection matrix via a self-consistent coordinate (Fig. 1). This will be explained in the next subsection.

Let $\theta = sh$. From bottom to top, each slice of X is rotated from the consecutive slice by θ to be self-consistent with the helical source trajectory, i.e., to form the self-consistent coordinate (Fig. 1). That is, we have the following self-consistent coordinate

$$\hat{r} = (x\cos k\theta + y\sin k\theta, -x\sin k\theta + y\cos k\theta, z), \quad (3)$$

where $z \in [z_k, z_{k+1})$ and r=$(x, y, z) \in R^3$. The grid in the self-consistent coordinate is $\hat{X} = \{\hat{X}_{ijk}\}$ with

$$\hat{X}_{ijk} = \{(\hat{x}, \hat{y}, z) : \hat{x} = x\cos k\theta + y\sin k\theta, \\ \hat{y} = -x\sin k\theta + y\cos k\theta, (x, y, z) \in X_{ijk}\}. \quad (4)$$

On $\hat{X}$, the imaging object is denoted by $\hat{f}$, with the corresponding rotation matrix $\mathbf{R}$, i.e.,

$$\hat{f} = \mathbf{R}f \text{ and } f = \mathbf{R}^{-1}\hat{f} \quad (5)$$

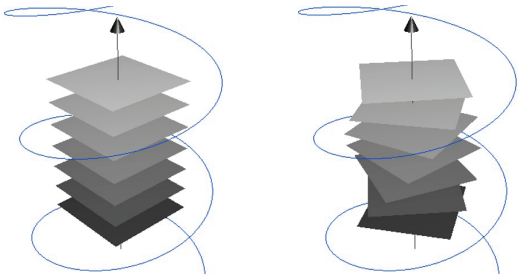

(a) Cartesian coordinate (b) Self-consistent coordinate

Fig. 1. Self-consistent coordinate. For efficient X-ray projection and backprojection, each slice is rotated to be self-consistent with the helical source trajectory, i.e., to form the self-consistent coordinate.

B. Shift-invariant Projection and Backprojection

Let $\mathbf{A}$ and $\mathbf{A}^T$ denote the discretized X-ray projection and backprojection matrix (namely X-ray transform and its adjoint) respectively under the Cartesian coordinate, i.e.,

$$p = \mathbf{A}f \text{ and } f^b = \mathbf{A}^T p \quad (6)$$

where p and f^b are the X-ray projection data and the backprojection image respectively. Here p is a column vector with N_v views and $N_a \cdot N_b$ detector pixels per view

$$p = [p_1, \cdots, p_n, \cdots, p_{N_v}]^T$$

where p_k consists of detector pixels for the nth projection view, i.e.,

$$p_n = [p_{1,1,n}, \cdots, p_{l,m,n}, \cdots, p_{N_a,N_b,n}]^T.$$

For the convenience of discussions, we rewrite $\mathbf{A}$ and $\mathbf{A}^T$ as block matrices, i.e.,

$$\mathbf{A} = \begin{bmatrix} A_{11} & \cdots & A_{1k} & \cdots & A_{1N_z} \\ \cdots & \cdots & \cdots & \cdots & \cdots \\ A_{n1} & \cdots & A_{nk} & \cdots & A_{nN_z} \\ \cdots & \cdots & \cdots & \cdots & \cdots \\ A_{N_v1} & \cdots & A_{N_vk} & \cdots & A_{N_vN_z} \end{bmatrix} \quad (7)$$

and

$$\mathbf{A}^T = \begin{bmatrix} A_{11}^T & \cdots & A_{1n}^T & \cdots & A_{1N_v}^T \\ \cdots & \cdots & \cdots & \cdots & \cdots \\ A_{k1}^T & \cdots & A_{kn}^T & \cdots & A_{kN_v}^T \\ \cdots & \cdots & \cdots & \cdots & \cdots \\ A_{N_z1}^T & \cdots & A_{N_zn}^T & \cdots & A_{N_zN_v}^T \end{bmatrix}, \quad (8)$$

where A_{nk} is a $N_a \cdot N_b$ by $N_x \cdot N_y$ matrix, and A_{kn}^T is a $N_x \cdot N_y$ by $N_a \cdot N_b$ matrix.

Next we consider the discretized X-ray projection matrix $\hat{\mathbf{A}}$ and backprojection $\hat{\mathbf{A}}^T$ under the self-consistent coordinate (Fig. 1),i.e.,

$$p = \hat{\mathbf{A}}\hat{f} \text{ and } \hat{f}^b = \hat{\mathbf{A}}^T p \quad (9)$$

In the following, we will show $\hat{\mathbf{A}}$ is a shift-invariant matrix with

$$[p_{1+is}, \ldots, p_{s+is}]^T = \hat{A}_i[\hat{f}_{L+i}, \ldots, \hat{f}_{U+i}]^T, \quad (10)$$

where

$$\hat{A}_i = \begin{bmatrix} \hat{A}_{1+is,L+i} & \cdots & \hat{A}_{1+is,U+i} \\ \cdots & \cdots & \cdots \\ \hat{A}_{s+is,L+i} & \cdots & \hat{A}_{s+is,U+i} \end{bmatrix}.$$

and

$$\hat{A}_i = \hat{A}_j = \hat{A}. \quad (11)$$

That is we group every s views of projections together with i indexing the projection group. L and U denote the bottom and top axial image slices that overlap the FOV generated by these s source-detector pairs in terms of ray-driven projection. Then we can use the shift-invariant property (10) to efficiently compute the X-ray projections based on a stored sparse matrix $\hat{A}$ of the size $N_a \cdot N_b \cdot s$ and $N_x \cdot N_y \cdot (U - L + 1)$.

Similarly, we will show $\hat{\mathbf{A}}^T$ is also a shift-invariant matrix with

$$\hat{f}_k = \hat{A}_k^T[p_{L'+ks}, \ldots, p_{U'+ks}]^T, \quad (12)$$

where

$$\hat{A}_k^T = [\hat{A}_{k,L'+ks}^T \ldots \hat{A}_{k,U'+ks}^T]$$

and

$$\hat{A}_k^T = \hat{A}_l^T = \hat{A}^T. \quad (13)$$

That is we consider each axial image slice separately indexed by k. Here L' and U' denote the first and last source-detector pairs that have the overlapping FOV with the jth image slice in terms of pixel-driven backprojection. Then we can use the shift-invariant property (12) to efficiently compute the X-ray backprojections based on a stored sparse matrix $\hat{A}^T$ of the size $N_x \cdot N_y$ by $N_a \cdot N_b \cdot (U' - L' + 1)$.

Now we consider an example (Fig 2) to illustrate the shift-invariance of projection and backprojection under the self-consistent coordinate (Fig. 1). Here we consider two consecutive s-groups of projections and two consecutive axial slices for backprojection. Note that a key for shift-invariance is that the angular difference between two consecutive projections differed by s views, i.e., p_n and p_{n+s}, is exactly the same as that between two consecutive axial image slices, i.e., $\hat{f}_k$ and $\hat{f}_{k+1}$, which is equal to $\theta = sh$.

This can be rigorously justified as follows. However, due to the page limitation, the proofs are skipped.

Theorem 1: (*Shift-invariant projection*) Consider an arbitrary detector pixel indexed by (a, b). Let l_1 be the length of the line from s_{λ_1} and detector (a, b) on D_{λ_1}, and l_2 be the length of the line from s_{λ_2} and detector (a, b) on D_{λ_2}. If $\lambda_2 = \lambda_1 + s$,

$$|l_1 \cap \hat{X}_{ijk}| = |l_2 \cap \hat{X}_{i,j,k+1}| \tag{14}$$

where $|.|$ denotes the length.

Theorem 2: (*Shift-invariant backprojection*) For $\hat{r}_1, \hat{r}_2$ in the self-consistent coordinate with $\hat{r}_2 = \hat{r}_1 + (0, 0, \Delta z)$, let l_1 denote the line between s_{λ_1} and $\hat{r}_1$, and l_2 denote the line between s_{λ_2} and $\hat{r}_2$. If $\lambda_2 = \lambda_1 + s$, the intersection point between l_1 and D_{λ_1} is the same as that between l_2 and D_{λ_2}.

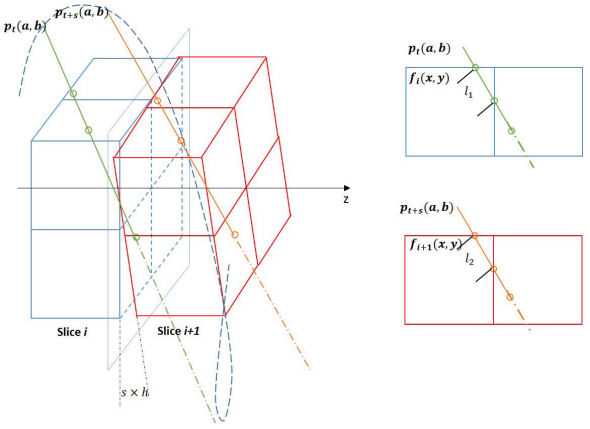

(a) Shift-invariant Projection

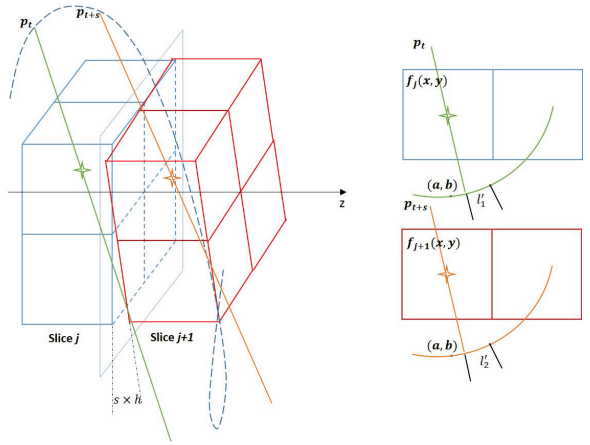

(b) Shift-invariant Backprojection

Fig. 2. Shift-invariant projection and backprojection under the self-consistent coordinate. (a) Shift-invariant projection: the projection matrix element l_1 is the intersection length at $\hat{f}_k(x, y)$ for the projection data $p_n(a, b)$, and the projection matrix element l_2 is the intersection length at $\hat{f}_{k+1}(x, y)$ for the projection data $p_{n+s}(a, b)$; $l_1 = l_2$ since the angular difference between p_n and p_{n+s} is exactly the same as that between $\hat{f}_k$ and $\hat{f}_{k+1}$, i.e., θ. (b) Shift-invariant backprojection: the backprojection matrix element l'_1 is the intersection length at the detector bixel $p_n(a, b)$ through the voxel center $\hat{f}_k(x, y)$, and the backprojection matrix element l'_2 is the intersection length at the detector bixel $p_{n+s}(a, b)$ through the voxel center $\hat{f}_{k+1}(x, y)$; $l'_1 = l'_2$ since the angular difference between p_n and p_{n+s} is exactly the same as that between $\hat{f}_k$ and $\hat{f}_{k+1}$, i.e., θ.

TABLE I
PROJECTION MATRIX SIZES. ROW: VARIOUS PITCHES FROM 0.4 AND 1.2; COLUMN: VARIOUS UNDERSAMPLING RATE FROM 1/16 TO 1; FILE SIZES ARE SHOWN IN GIGABYTES.

	0.4	0.6	0.8	1.0	1.2
1/16	0.24	0.16	0.12	0.10	0.08
1/8	0.50	0.32	0.24	0.20	0.16
1/4	0.98	0.66	0.50	0.40	0.32
1/2	1.98	1.32	0.99	0.78	0.66
1	3.96	2.63	1.98	1.58	1.33

TABLE II
BACK-PROJECTION MATRIX SIZES. ROW: VARIOUS PITCHES FROM 0.4 AND 1.2; COLUMN: VARIOUS UNDERSAMPLING RATE FROM 1/16 TO 1; FILE SIZES ARE SHOWN IN GIGABYTES.

	0.4	0.6	0.8	1.0	1.2
1/16	0.09	0.06	0.04	0.04	0.03
1/8	0.18	0.12	0.09	0.07	0.06
1/4	0.37	0.24	0.18	0.14	0.12
1/2	0.73	0.49	0.37	0.29	0.24
1	1.47	0.98	0.74	0.58	0.49

III. RESULTS

The proposed shift-invariant projection and backprojection and related image reconstruction method were validated using the 3D XCAT phantom. The image size was $512 \times 512 \times 320$. The full scan had 2304 projection views per rotation. The GPU implementation with various pitch sizes from 0.4 to 1.2 and undersampling rate up to $1/16$ were considered to illustrate the improved speed of the proposed method (namely "**M2**") from the conventional method (namely "**M1**"). Here the conventional method **M1** refers to ray-driven projection method and pixel-driven backprojection method using texture interpolation.

A. Matrix Size

The shift-invariant projection and back-projection, i.e., $\hat{A}$ and $\hat{A}^T$, were saved in the Compressed Sparse Row (CSR) format. The projection matrix sizes are summarized in TABLE I. And the maximal matrix size is no more than 4GB, which can be completely stored by a single state-of-art GPU. The backprojection matrix sizes are presented in TABLE II with the maximal size smaller than 1.5GB.

B. Projection

To validate the proposed projection method **M2**, **M2** was performed in comparison with the conventional method **M1** with $pitch = 0.4$ and 1/16 undersampling rate (i.e., 288 projection views per rotation). The projection results with $\times 10$ difference image are displayed in Fig. 3, which suggest the correctness of the proposed projection method. Here the total relative difference is 0.63 %.

To illustrate the efficiency of **M2**, the computational costs are displayed in Fig. 4 with various pitches and undersampling rates, which clearly suggest that **M2** is more efficient than the conventional projection method **M1**. For example, a large portion of computational time (60.24% to 82.27%) can be saved by switching **M1** to **M2**. Moreover, the acceleration rate increases as the pitch increases.

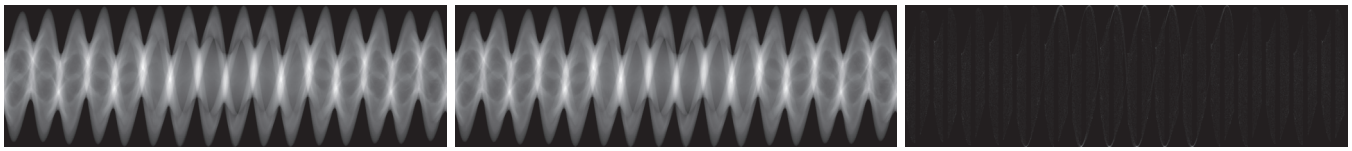

(a) **M1** (b) **M2** (c) Difference ($\times 10$)

Fig. 3. Projection results. The sinogram consisting of central axial slices from projections is presented to demonstrate the correctness of the proposed projection method **M2** in comparison with the conventional projection method **M1**. (a) **M1**; (a) **M2**; (c) difference image ($\times 10$) between **M1** and **M2**.

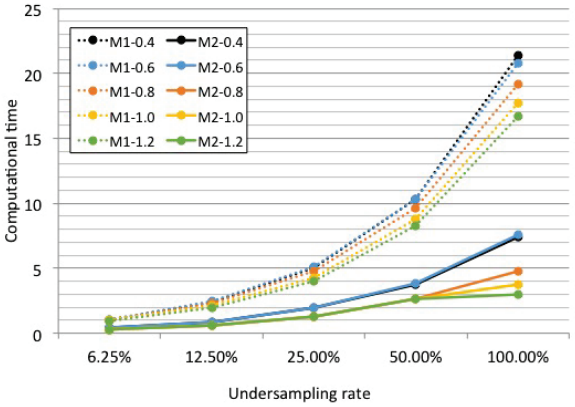

Fig. 4. Computational time for projections. The conventional method **M1** (dotted line) and the proposed method **M2** (solid line) with various pitches (from 0.4 to 1.2) and various underampling rate (from 6.25% to 100.00%).

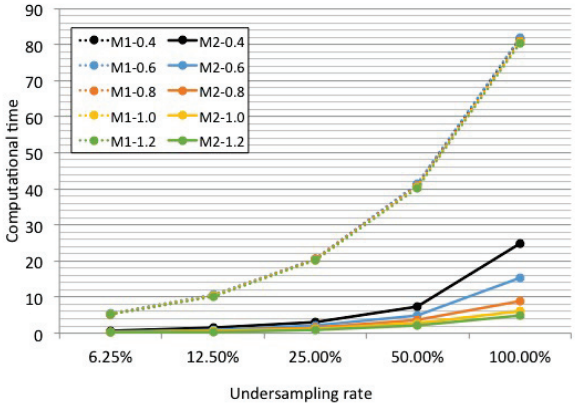

Fig. 6. Computational time for backprojections. The conventional method **M1** (dotted line) and the proposed method **M2** (solid line) with various pitches (from 0.4 to 1.2) and various underampling rate (from 6.25% to 100.00%).

C. Backprojection

To validate the proposed backprojection method **M2**, **M2** was performed in comparison with the conventional method **M1** with $pitch = 0.4$ and 1/16 undersampling rate (i.e., 288 projection views per rotation). The backprojection results with $\times 10$ difference image are displayed in Fig. 5, which suggest the correctness of the proposed backprojection method. Here the total relative difference is 0.20 %.

To illustrate the efficiency of **M2**, the computational costs are displayed in Fig. 6 with various pitches and undersampling rates, which clearly suggest that **M2** is more efficient than the conventional backprojection method **M1**. For example, a large portion of computational time (69.46% to 96.01%) can be saved by switching **M1** to **M2**. Moreover, the acceleration rate increases as the pitch increases or the undersampling rate decreases.

(a) **M1** (b) **M2** (c) Difference ($\times 10$)

Fig. 5. Backprojection results. The central axial backprojection slice is presented to demonstrate the correctness of the proposed method **M2** in comparison with the conventional method **M1**. (a) **M1**; (a) **M2**; (c) difference image ($\times 10$) between **M1** and **M2**.

IV. Conclusion

We have proposed a shift-invariant projection and backprojection method based on a self-consistent coordinate so that the projection and backprojection matrices can be stored instead of being repeatedly computed on-the-fly. Numerical results demonstrate that the proposed method can speed up the projection by 3 to 6 folds and the backprojection by 3 to 16 folds using standard configuration of helical CT.

References

[1] Donoho 2006 *IEEE T Inform Theory* 52(4) 1289-1306
[2] Cands et al 2006 *IEEE T Inform Theory* 52(2) 489-509
[3] Sidky et al 2006 *J Xray Sci Technol* 14 119-139
[4] Chen et al 2008 *Med Phys* 35(2) 660-663
[5] Siddon 1985 *Med Phys* 12(2) 252-255
[6] Herman 1979 *Image Reconstruction from Projections*
[7] Peters 1981 *IEEE T Nucl Sci* 28(4) 3641-3647
[8] Zhuang et al 1994 *IEEE T Nucl Sci* 41(4) 1660-1665
[9] Zeng et al 1993 *IEEE NSS/MIC* 1199-1201
[10] De Man et al 2004 *Phys Med Biol* 49(11) 2463-2475
[11] Zhao et al 2003 *IEEE NSS/MIC* 4 2808-2812
[12] Long et al 2010. *IEEE TMI* 29(11) 1839-1850
[13] Gao 2012 *Med Phys* 39 7110-7120
[14] Miao et al 2013 *J Xray Sci Technol* 22(1) 1-18
[15] Steckmann et al 2009 *Phys Med Biol* 54(12) 3691-3708
[16] Xu et al 2012 *Phys Med Biol* 57(11) 3477-3797

Performance Bounds for Sinogram Decomposition and Potential Benefits of Multi-energy Data

Yaoshen Yuan
Department of Electrical and Computer Engineering
Tufts University
Medford, MA 02155 USA
Email: yaoshen.yuan@tufts.edu

Brian Tracey
Department of Electrical and Computer Engineering
Tufts University
Medford, MA 02155 USA
Email: btracey@eecs.tufts.edu

Eric Miller
Department of Electrical and Computer Engineering
Tufts University
Medford, MA 02155 USA
Email: elmiller@ece.tufts.edu

***Abstract*—X-ray inspection plays an important role in materials identification for airline security. Switched dual-energy (SwDE) systems allow material identification by reconstructing the Compton and photoelectric (PE) coefficients of scanned objects, but dual-energy system performance can be strongly impacted by metal or other highly attenuating materials. Here we study the potential benefits of using multi-energy photon counting detectors to reconstruct the Compton and PE coefficients. Using simulations that employ a modified sinogram decomposition algorithm and reconstructing images after sinogram decomposition, we see that utilizing measurements from a small (< 10) number of bins can noticeably improve performance compared to two bins, in particular when metal is present. In order to understand fundamental performance limits, we carried out theoretical calculations of SNR upper bound based on Cramér Rao lower bound (CRLB) variance estimates. In our parameter study we consider several materials (aluminum and nylon) for objects of varying lengths. The CRLB results show general agreement with our algorithmic reconstructions, confirming that multi-energy measurements appear to be beneficial. Overall, our results suggest that further investigation of multi-energy detectors for airline screening applications is warranted.**

I. Introduction

As terrorism has increasingly threatened aviation security, airport baggage scanning using X-rays or other technologies has become increasingly important. The geometric information provided by CT provides important cues for understanding the bag contents. Materials identification using only the estimated attenuation is possible, but dual- or multi-energy systems can provide additional cues for material identification. Thus, Ying *et al.* proposed a two-step dual-energy CT (DECT) process in which sinogram decomposition is first used to estimate Compton and photoelectric (PE) coefficient sinograms, after which each sinogram is reconstructed [1].

While dual-energy methods can provide valuable new information, the results can be severely corrupted when metal or other highly attenuating objects are present. We seek to understand whether multi-energy CT (MECT) using photon counting detectors can help this problem. As described below, our simulation work shows that a multi-energy extension of [1] shows that a multi-energy method can recover Compton and PE coefficients even in a challenging case where metal artifacts cause a dual-energy method to fail. We find that, even though only two quantities (Compton and PE) are estimated, benefits are seen by including up to 5-10 energy bins.

An important question is whether this improvement reflects differences in the solution methods used, or a fundamental difference in the information available with MECT vs. DECT. Therefore, we calculate theoretical performance bounds using the Cramér Rao lower bound (CRLB), varying the number of energy bins as well as material properties of objects being imaged. This result gives us a theoretical upper limit of SNR that any algorithm can achieve. Therefore, this approach provides a general way to predict the SNR trends. As shown below, the CRLB analysis supports the idea that the multiple energy bins help improve the reconstruction.

In a classic paper, Alvarez and Macovski [2] computed the CRLB for dual-energy sinogram decomposition. They considered the situation where only two individual energy bins are used and the bins have perfect energy resolution. Their work was extended to multi-energy bins by Roessl and Herrmann [3] who modeled both photon-counting detector systems and energy-integrating detector systems, and furthermore account for the imperfect energy resolution of photon-counting systems (modeling overlap between energy bins). We build on this work but assume that only photon counting detectors are used for MECT.

The structure of this paper is as follows. In the next section, we review the CRLB bounds calculation for multi-energy sinogram decomposition. In the Results section, we briefly describe our simulation results (which using a weighted multi-energy decomposition method) and then compare trends from simulations to trends computed using CRLB. Finally, we conclude and suggest directions for future work.

II. Performance Bound Calculation

In this section, the CRLB is used to derive both variance and SNR of A_c and A_p [4][5].Because here we only use photon counting detectors to measure the number of photons falling into each energy bin, no Gaussian noise will be added to our model. Simplifying the results of Roessl and Herrmann [3] to consider only photon counting detectors, the likelihood

function given can be described as the product of Poisson distributions for each bin (Eq.1).

$$P(I_1, I_2, \ldots, I_M | A_c, A_p) = \prod_{i=1}^{M} \frac{\lambda_i^{I_i}}{I_i!} e^{-\lambda_i} \tag{1}$$

where I_i is the photon counts detected at the ith bin and M is the number of bins, A_c and A_p are the values of the Compton and Photoelectric sinogram for a given ray path, and λ_i is the expected number of counts in the ith energy bin. The number of counts is a function of two given estimates A_c and A_p, and is modeled as:

$$\lambda_i(A_c, A_p) = \int S_i(E) e^{-A_c f_{KN}(E) - A_p f_p(E)} dE \tag{2}$$

where $S_i(E)$ is the spectrum for ith bin. We can simulate the spectra for MECT using the model in [3], which models the energy resolution caused by the photon counting detectors, accordingly for imperfect energy resolution (see [3] for details). Then the log-likelihood can be written as

$$L = lnP(I_1, I_2, \ldots, I_M | A_c, A_p) = \sum_{i=1}^{M} [I_i ln\lambda_i - \lambda_i - ln(I_i!)] \tag{3}$$

We assume the parameter vector is $\theta = [Ac, Ap]^T$. The Fisher information matrix with respect to A_c and A_p is

$$I(\theta) = \begin{bmatrix} F_{cc} & F_{cp} \\ F_{pc} & F_{pp} \end{bmatrix} \tag{4}$$

Each element in the matrix is

$$F_{\alpha\beta} = F_{\beta\alpha} = -E\left[\frac{\partial^2 L}{\partial A_\alpha \partial A_\beta}\right] = \sum_{i=1}^{M} \frac{1}{\lambda_i}\left(\frac{\partial \lambda_i}{\partial A_\alpha}\right)\left(\frac{\partial \lambda_i}{\partial A_\beta}\right) \tag{5}$$

where α and β are a notational shorthand and can represent either c and p. Then inverting the Fisher information matrix $I(\theta)$ yields

$$I^{-1}(\theta) = \frac{1}{det(I(\theta))} \begin{bmatrix} F_{pp} & -F_{cp} \\ -F_{pc} & F_{cc} \end{bmatrix} \tag{6}$$

We know that $var(\hat{\theta}_i) \geq \left[\boldsymbol{I}^{-1}(\boldsymbol{\theta})\right]_{ii}$ [4], so CRLBs for A_c and A_p are

$$\begin{aligned} var(\hat{A}_c) = \sigma^2_{A_c} &\geq \frac{1}{det(I(\theta))} F_{pp} = \frac{1}{det(I(\theta))} \sum_{i=1}^{M} \frac{1}{\lambda_i}\left(\frac{\partial \lambda_i}{\partial A_c}\right)^2 \\ var(\hat{A}_p) = \sigma^2_{A_p} &\geq \frac{1}{det(I(\theta))} F_{cc} = \frac{1}{det(I(\theta))} \sum_{i=1}^{M} \frac{1}{\lambda_i}\left(\frac{\partial \lambda_i}{\partial A_p}\right)^2 \end{aligned} \tag{7}$$

The lower bound of variance is shown in Eq.7, so the upper bound of SNR given A_c and A_p is

$$\begin{aligned} SNR_{Ac} &\leq \frac{A_c}{\sigma_{A_c}} \\ SNR_{Ap} &\leq \frac{A_p}{\sigma_{A_p}} \end{aligned} \tag{8}$$

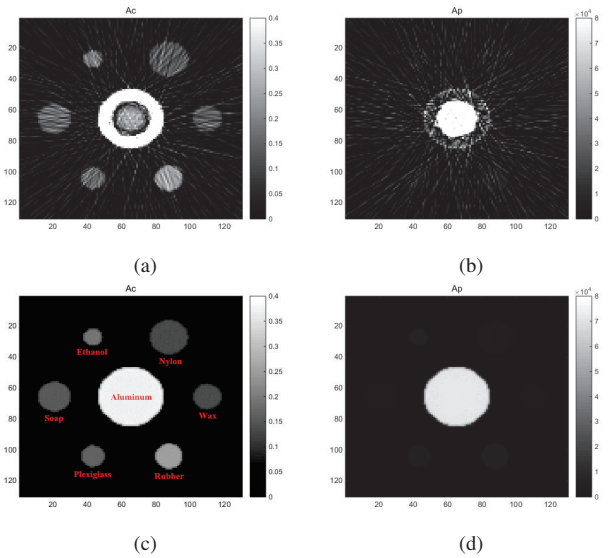

Fig. 1: Simulation for a phantom with high attenuation (aluminum center). First row: reconstructions using SwDE. Second row: reconstruction using MECT with 7 bins. Compton images are in the left column with PE in the right column.

Below we express SNR in decibels. For raypath k, A_c, A_p are given by the line integral through any objects along that raypath of either Compton coefficients or PE coefficients. We can learn from Eq.5 that the SNR upper bound is a function of A_c, A_p and M. In the following sections, we will explore the relationship between these three variables and compare the results to the realistic simulations of different attenuations.

III. Results

To simulate the Compton and PE reconstructions, we construct a phantom with aluminum in the middle, which has a high attenuation (labels in Fig. 1c). We simulated data for a switched dual-energy system (SwDE), in which the object is scanned twice using different spectra (spectrum are taken from [7] and integrating detectors are used (here we do not model additive Gaussian noise for the SwDE detectors, which would degrade SwDE performance). We also simulate performance for the same phantom using a multi-energy (7 bin) approach, by extending the work of Ying *et al.* to the multi-energy case and also weight the data for different bins by the number of counts. The optimization problem solved is:

$$(\theta^k) = \arg\min_{\theta^k} (\boldsymbol{K}(\boldsymbol{\theta^k}) - \boldsymbol{m^k})^T \boldsymbol{\Sigma} (\boldsymbol{K}(\boldsymbol{\theta^k}) - \boldsymbol{m^k}) \tag{9}$$

where θ^k=$\left[A_c^k, A_p^k\right]$ are the estimated quantities for ray k, $\boldsymbol{K}$ is the forward model, $\boldsymbol{K}(\theta^k)$ is the *estimated* M dimensional column vector of log-normalized mean values, and $\boldsymbol{m^k}$ is the data, as a M dimensional column vector of log-normalized measured projections. The weighting term is given by $\boldsymbol{\Sigma}$=diag$\{\boldsymbol{w}\}$ where w is the number of counts. This weighting term is found from a quadratic approximation to likelihood function and was proposed by Bouman for CT

reconstruction [6]. This weighting was found to noticeably improve performance. For both SwDE and MECT, after the data are decomposed into Compton and photoelectric coefficients, filtered backprojection (FBP) method is used to reconstruct the images shown in Fig. 1c.

Fig. 1 shows that the reconstruction using multi-energy bins (7 bins) can noticeably improve the PSNR of both Compton and PE images compared to the SwDE. Artifacts in both Compton and PE images are obviously reduced by using MECT with the proposed weighted multi-energy solution.

Fig. 1 shows results for a single phantom and a single realization. We carried out further simulations for phantoms with high, medium and low attenuation, and averaging across realizations, to study how the number of bins influences image domain results. We computed the PSNR of Compton and PE reconstructions utilizing Eq.9. Here we use a unified peak signal value to calculate the PSNR for all three phantoms, which is the true Compton and PE coefficients of aluminum (0.37 $\text{KeV}^3\text{cm}^{-1}$ and 72440 cm^{-1} respectively). Moreover, the phantom with medium attenuation is the same as Fig. 1c but the aluminum is replaced by cotton and ethanol is replaced by aluminum; the phantom with low attenuation is also Fig. 1c but only aluminum is substituted by cotton. Similar to the calculations of SNR upper bounds, we reconstructed the Compton and PE images using both MECT and SwDE within the range of 2 to 10 energy bins. For each point, we obtain the PSNR by taking the average of 30 calculations. The results are shown in Fig. 2. The circles in the figure represent the PSNR of SwDE. We can notice that the PSNR of high attenuation is obviously lower than the PSNRs of medium and low attenuation. This is close to the result of SNR upper bound, where the SNR upper bound decreases with the increasing length of material. Fig. 2 also shows that the increment of the number of bins can slightly improve the PSNR. For Compton and PE images, the improvement caused by MECT is observable when the bin number is less than 5, but the PSNR becomes flat with continuous increase of bin number, which shows a trend similar to the SNR upper bounds. Furthermore, the improvement is not apparent for the phantom with high attenuation. This is result from the relatively high mean square error (MSE) of the reconstructions with high attenuation since MSE is the denominator of PSNR. Fig. 2 also presents the PSNR obtained by using SwDE. The PSNR of SwDE is much lower than MECT with 2 energy bins. Over 20 dB improvement can be seen for all three phantoms. The result demonstrates a significant benefit of using MECT in reconstructing Compton and PE images in contrast with SwDE.

CRLB RESULTS: As a next simulation step, we used the CRLB calculations described previously to study the SNR upper bounds with respect to the number of bins as well as the length and type of material along a raypath. In the simulation, we calculated the SNR upper bound for 2 bins to 10 bins. For each bin, we used the model of Roessl and Herrmann where realistic energy resolution is considered to obtain the spectrum [3]. We also compare the SNR upper

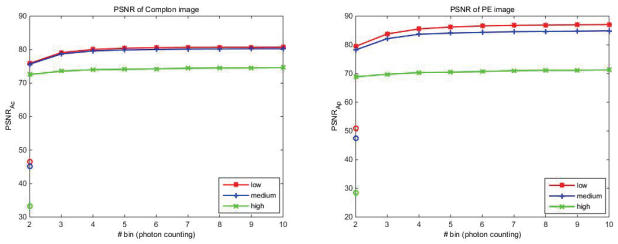

(a) (b)

Fig. 2: Image domain: PSNR (Peak SNR) of both Compton and PE image reconstructed by the weighted method using photon counting detector (weighted MECT), as a function of number of energy bins. The circles in the figure represent the weighted SwDE method. The results demonstrate that the PSNR of weighted SwDE method is much lower than the weighted MECT.

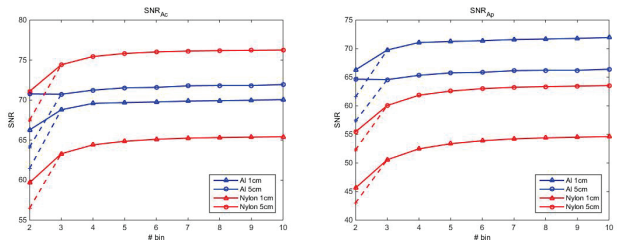

(a) (b)

Fig. 3: Sinogram domain: CRLB-predicted SNR upper bounds for aluminum and nylon. The solid lines indicate the MECT; the dashed lines indicate the SwDE

bound for SwDE using integrating detectors to MECT using photon counting detectors. The asterisks connected by dashed lines in Fig. 3 indicate the SNR upper bounds generated by SwDE. Because the SNR upper bound is a function of the amount of attenuation and the number of energy bins, for each bin number, we simulated different lengths of material. Here we choose 1 cm, 5 cm and 10 cm, which cover a range that reflects how the length influences the SNR upper bound.

In this section, we also study the effects of material attenuation, using aluminum and nylon as examples of high- and low-attenuation materials. The Compton and PE coefficients for aluminum are 0.37 $\text{KeV}^3\text{cm}^{-1}$ and 72440 cm^{-1} respectively. The Compton and PE coefficients for nylon are 0.1325 $\text{KeV}^3\text{cm}^{-1}$ and 2771 cm^{-1} respectively. Thus the SNR upper bounds for these two materials can be used to provide useful information how material attenuation affects the reconstructions.

In work not shown here, we also computed the SNR upper bound for MECT with perfect energy resolution ('ideal MECT'), which means each bin is ideally resolved without energy overlap. The result shows almost no difference in CRLB predictions between the SNR upper bound of MECT using Roessl's model and the upper bound of ideal MECT.

As shown in Fig. 3, for MECT using photon counting

TABLE I: The predicted SNR (in decibels) for upper bounds of 2 bins and 3 bins, modeling ray paths passing through aluminum. While Fig. 3 assumes that all energy bins have equal size in keV, the results shown here were found by a brute force search to find optimal, unequal bin sizes

	Compton		photoelectric	
	2 bins	3 bins	2 bins	3 bins
5 cm	71.03	71.56	64.99	65.78
10 cm	65.71	66.30	55.68	56.64

detector the number of bins has a positive effect on the SNR upper bound when the bin number is small. The SNR upper bound shows little increase as the number of bins increases beyond 5 bins. However, we can observe that the SNR of 2 bins using MECT is higher than the SNR of 3 bins for the case of 5 cm aluminum. While this appears counter-intuitive, it is explained because our calculation assumed that energy band are divided into equal keV ranges, which may not be ideal. If we instead tune to find the optimal separator of energy ranges (instead of splitting the energy range into 2 or 3 equal bins), we can see from Table I that the best SNR upper bound for 3 energy bins is slightly better than the one for 2 energy bins, as expected. This suggests that unequal energy bin spacing may be of some value.

Unlike aluminum, the improvement of nylon is more noticeable as the number of bins increases, but the improvement becomes increasingly small as the number of bins grows beyond 5 bins. As we can see, the SNR upper bound of SwDE, which is indicated by the dashed lines in Fig. 3, is much lower than MECT for both aluminum and nylon. Considering that SwDE employs integrating detectors which generate Gaussian noise (which we are not including in calculations) in addition to Poisson noise [8], the improvement made by MECT in reality may be understated, showing the potential of using MECT for realistic Compton and PE reconstructions.

In addition, the variance of SNR upper bound also depends on the length of material. For both Compton and PE coefficients, when the length is small (1 cm), the upper bound of aluminum is higher than nylon. With the increasing length of materials, the SNR upper bound of aluminum becomes lower than the upper bound of nylon. Our simulation of the SNR upper bound with respect to the length of materials shows that the SNR of aluminum drops much faster than nylon as the length increases, which demonstrates that the SNR of aluminum is more sensitive to the changing length.

IV. Conclusion

In this paper, we presented both simulation results and theoretical performance bounds for dual-energy and multi-energy systems, assuming a sinogram decomposition method is used to decompose data in Compton and photoelectric coefficients. We first reviewed for CRLB computation for multi-energy using photon counting detectors. We then presented both image-domain simulation results and sinogram-domain performance predictions for switched dual-energy and multi-energy systems. The results show that the trend of for simulated performance (PSNR) is similar to the predicted theoretical SNR upper bound. Increasing number of bins can improve the PSNRs of reconstructions regardless of the attenuation of material, though gains become limited as the number of bins increases. In both sets of results, multi-energy performance was better than switched dual-energy, showing the promise of MECT for the Compton and PE reconstructions.

The work shown in this paper is based on a combination of simulated data and performance bound calculation. Our future work will be focused on attempting to demonstrate these gains using experimental data, studying various phantoms. We will study whether or not use of multiple energy bins can improve the reconstructions for the realistic data, and how performance varies with the number of energy bin.

Acknowledgment

This work was in part supported by the U.S. Department of Homeland Security. The views and conclusions contained in this document are those of the authors and should not be interpreted as necessarily representing the official policies, either expressed or implied, of the U.S. Department of Homeland Security.

References

[1] R. Ying, Zhengrong Naidu and C. R. Crawford, "Dual energy computed tomography for explosive detection," *Journal of X-ray Science and Technology*, vol. 14, no. 4, pp. 235–256, 2006.

[2] R. E. Alvarez and A. Macovski, "Energy-selective reconstructions in x-ray computerised tomography," *Physics in medicine and biology*, vol. 21, no. 5, p. 733, 1976.

[3] E. Roessl and C. Herrmann, "Cramér–rao lower bound of basis image noise in multiple-energy x-ray imaging," *Physics in medicine and biology*, vol. 54, no. 5, p. 1307, 2009.

[4] S. M. Kay, "Fundamentals of statistical signal processing, vol. 1: Estimate theory," *Signal Processing. Upper Saddle River, NJ: Prentice Hall*, 1993.

[5] G. Cowan, *Statistical data analysis*. Oxford University Press, 1998.

[6] C. Bouman, K. Sauer *et al.*, "A unified approach to statistical tomography using coordinate descent optimization," *Image Processing, IEEE Transactions on*, vol. 5, no. 3, pp. 480–492, 1996.

[7] O. Semerci, N. Hao, M. E. Kilmer, and E. L. Miller, "Tensor-based formulation and nuclear norm regularization for multienergy computed tomography," *Image Processing, IEEE Transactions on*, vol. 23, no. 4, pp. 1678–1693, 2014.

[8] W. C. Barber, E. Nygard, J. S. Iwanczyk, M. Zhang, E. C. Frey, B. M. Tsui, J. C. Wessel, N. Malakhov, G. Wawrzyniak, N. E. Hartsough *et al.*, "Characterization of a novel photon counting detector for clinical ct: count rate, energy resolution, and noise performance," in *SPIE Medical Imaging*. International Society for Optics and Photonics, 2009, pp. 725 824–725 824.

Noise Model-Based CT Image Denoising by 3D Transform-Domain Collaborative Filtering

Hongyan Liu

***Abstract*—We propose a CT image denoising strategy by combining the block-matching and 3D filtering (BM3D) denoising method with an estimated CT image noise model. The BM3D method, first developed by Foi in 2007, realizes highly effective image denoising through grouping similar image blocks into 3D arrays and applying collaborative filtering on them. However, the BM3D method cannot be directly applied to CT images because of the inhomogeneous noise distribution property of CT images. We therefore modify the original BM3D method by considering local directional noise property during the cube matching step and the hard thresholding step. By applying this modification to the original BM3D method, CT images can be better denoised, and especially the streak artifacts caused by the electronic noise in the CT rawdata can be greatly reduced comparing to the original BM3D results.**

I. Introduction

In the CT field, minimizing the x-ray radiation exposure has always been a major effort for researchers. Meanwhile, reducing the radiation exposure always leads to more severely degraded CT images because of the quantum noise in the low-dose scanned rawdata. Therefore, effective denoising techniques are needed for these low-dose CT images, in order to obtain acceptable images for clinical diagnosis. Denoising can be applied either on the sinogram data for image reconstruction or on the reconstructed images directly, as long as they successfully model the noise property of the sinogram or the images. Currently, denoising methods which successfully model the noise property of CT scans are often applied on the sinogram data [1~2], but fewer methods directly applied on image domain manage to consider the specific noise characteristics of CT images. In this paper, our goal is to develop an effective image denoising method particularly designed for CT images by considering the specific noise distribution property of them.

The BM3D method developed by Foi[3] is an effective nonlocal denoising algorithm. It achieves good noise suppression and spatial resolution preservation at the same time, based on two successive steps: block-matching and collaborative filtering. In the block matching step, an enhanced sparse representation of an image is achieved by grouping similar image blocks to form 3D data arrays. Collaborative filtering is then applied on these 3D arrays to attenuate image noise as well as preserving unique details shared by the 3D arrays. The collaborative filtering approach includes the following four steps: 1) transform 3D groups into sparse group spectra; 2) shrink these spectra by a hard threshold; 3) inverse 3D transform the shrinked spectra; 4) aggregate the block-wise estimates to obtain the final denoised image. A detailed description of the BM3D algorithm can be found in [3].

Manuscript submitted on January 25, 2016.

Hongyan Liu is with Neusoft Medical Systems, Shenyang, 110179, China (e-mail: hannaliu_neusoftct@126.com).

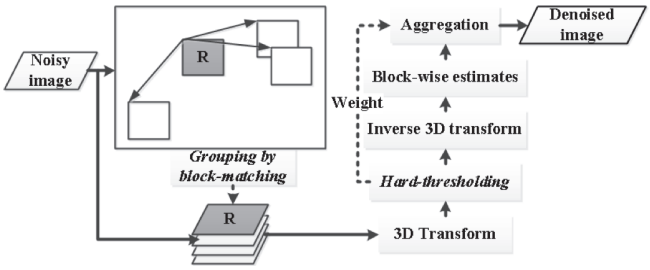

Fig. 1. Flowchart of the BM3D image denoising algorithm. Note that two steps emphasized by italic font are modified in the proposed method for CT images.

In this paper, we propose a modified BM3D algorithm specifically designed for CT image denoising. Directional local noise estimation is obtained by estimating noise characteristics of the low-dose rawdata and analyzing the relationship between noise distribution in rawdata and in reconstructed images. Two steps in BM3D algorithm are then modified by taking consideration of the image noise estimation results, which are emphasized in Fig. 1. Firstly, we modify the block-matching step by considering the directional noise at a certain pixel when computing the similarities between nearby image blocks; Secondly, we modify the hard-thresholding step by adapting the hard threshold to different noise estimation levels at different pixel locations. The conducted experiments with the proposed method show that it can reduce streak artifacts and random noise effectively, as well as preserving acceptable spatial resolution.

II. Proposed Method

A. Modification of "Grouping by Block-Matching" Step

The first modification is on the grouping by block-matching step. We describe briefly the basic process of this step in the original BM3D method at first and then our modifications in the following.

The general idea of grouping by block-matching is to find image blocks which are similar to a reference image block and

then group them together in a 3D array. After all the reference blocks are processed, a sparse representation of the image is obtained which is then used for the collaborative filtering process. During this step, we measure the similarity between the two image blocks by calculating the L2-distance, and blocks are considered similar and grouped only when their similarity with respect to the reference one are smaller than a given threshold.

We denote Z_x an image block of fixed size $N_1 \times N_1$ extracted from a noisy image z, where x is the coordinate of the top-left pixel of the block. Then the similarity between a reference block Z_{xR} and a neighbor block Z_x could be calculated as

$$S(Z_{xR}, Z_x) = \frac{\|Z_{xR} - Z_x\|_2^2}{N_1^2}, \quad (1)$$

where $\|\cdot\|^2$ denotes the L2-norm. Using (1), the result of grouping by block-matching is a set which contains the coordinates of all similar blocks with respect to Z_{xR},

$$S_{xR} = \left\{ x \in X : S(Z_{xR}, Z_x) \le \tau_{xR,x}^{match} \right\}, \quad (2)$$

where $X \subset \mathbb{Z}^2$ denotes the image domain, and the parameter $\tau_{xR,x}^{match}$ is the maximum similarity for the two blocks Z_{xR} and Z_x to be considered similar.

In the basic BM3D method[3], a fixed threshold τ^{match} is given so that $\tau_{xR,x}^{match}=\tau^{match}$ for any given xR and x. However, this general threshold for block grouping is no longer used in our proposed method because of the anisotropic, locally varying noise distribution of CT images. In order to consider the influence of noise during selecting similar image blocks, we define the noise-dependent grouping threshold as

$$\tau_{xR,x}^{match} = \tau^{match} / \sigma_{pixel(xR,x)}^2, \quad (3)$$

where $\sigma_{pixel(xR,x)}^2$ denotes the directional noise variance estimate at the location of xR in the direction along a straight line connecting xR and x. Referring to the noise model built in [4], the directional noise variance $\sigma_{pixel(xR,x)}^2$ of an image pixel xR is proportional to the noise variance of ray projection $p_{j(xR,x)}$, which is an integration of pixel values along a line through pixel xR and x. According to [5] and our discussion above, we can derive the variance of $p_{j(xR,x)}$, as well as the directional pixel variance $\sigma_{pixel(xR,x)}^2$ as

$$\sigma_{pixel(xR,x)}^2 \cong \sigma_{proj(j(xR,x))}^2 \cong \frac{1}{\lambda_j} \exp\left(-p_{j(xR,x)}\right), \quad (4)$$

where λ_j is the estimated photon count of projection j where there is no object present. By redefining the grouping threshold in (3), the directional noise level is considered when deciding whether or not a neighbor block is similar with the reference block. For one certain reference block, neighbor blocks in different directions are given different threshold values based on the noise estimate results. If a ray projection through the center of the reference block goes through a large amount of tissues in one direction, the neighbor blocks in that direction are going to be given a relatively large directional noise variance $\sigma_{pixel(xR,x)}^2$. It means these neighbor blocks are given smaller threshold values, and information in that direction, which usually contains streak artifacts, will be much less preserved in the grouped 3D arrays, and thus be suppressed in the final denoised image after the collaborative filtering process.

B. Modification of "Hard-Thresholding" Step

The hard-thresholding process is conducted on the 3D transform spectrum of the formed 3D grouped array. In the basic BM3D method, this process allows for effective noise attenuation by applying a general hard threshold λ_3D on the transform coefficients. However, this general hard threshold used in the transform domain needs to be adapted to different noise estimation levels at different pixel locations, in order to achieve a good denoising effect for the whole image.

In reference [6], derivation of accurate theoretical noise estimation is provided for 3D FeldKamp images, and the idea of their derivation process can be adapted to images reconstructed by other methods, such as a WFBP reconstruction algorithm described in [7]. Fig. 2(b) shows noise variance estimation of Fig. 2(a), and we could see in the image that areas near the center of the object often have much higher noise level comparing to areas near the edges of the object. Pixel-wise hard threshold is then obtained by a multiplication of the fixed threshold and the pixel-wise noise estimation.

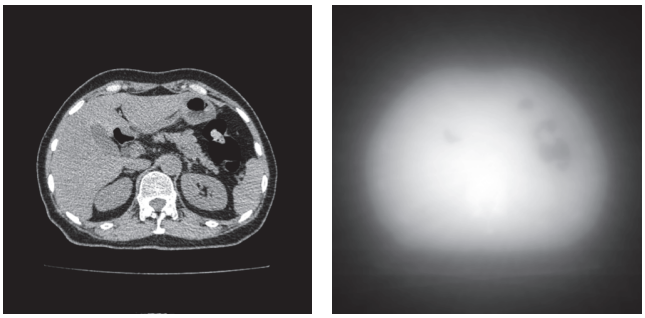

(a) (b)

Fig. 2. An example of noise estimation result. (a). Image reconstructed by weighted-FBP method from a patient scan(display window width 300,window level 1000); (b). Noise variance estimation of (a).

III. Experimental Results

The proposed modified BM3D method was validated by several experimental projection datasets acquired by NeuViz 64 CT Scanner, and we here present only results from one example dataset due to the length limits. For the example dataset, protocol of 120 kVp, 200mA and 0.6 sec/circle was used, and images of 1mm-thick were reconstructed with 3D weighted filtered back-projection. Both the modified BM3D

method and the basic method were applied on the CT images, in order to view the improvements of the proposed method comparing to the original BM3D. We also provide nonlinear sinogram smoothing results[1] for the purpose of comparison.

For our proposed BM3D methods, we skipped the Wiener-Filtering step, and remained only the hard-threshold step for the simplicity of calculation. Results showed that images obtained with or without the Wiener-filtering process show no obvious difference for our modified BM3D method. Parameters for both the proposed and original BM3D method used values from the last column in Table I from [3]. The exceptions included: τ_{match}^{ht} and λ_{3D}, which were modified following the discussion in Section II in our proposed BM3D method, and σ, which we set to 30 for our example data set. For the sinogram smoothing experiment, we select parameter values to reach an approximate 45% noise reduction.

Fig. 3 gave experimental results for two images at different z plane. Both the basic BM3D and our proposed method demonstrated better noise reduction effect comparing to the nonlinear sinogram smoothing method, as well as maintaining a better spatial resolution. By comparing our modified BM3D method with the basic BM3D, it can also be seen from the figure that our modified BM3D suppressed streak artifacts effectively whereas the basic BM3D hardly showed any streak artifact suppression.

IV. Discussion and Conclusion

We develop a modified BM3D algorithm specifically designed for CT image denoising by taking into consideration the anisotropic, inhomogeneous noise property of CT images. The modified BM3D method reduces streak artifacts more effectively comparing to the basic BM3D, and thus demonstrates better performance for CT image denoising.

Several issues should be concerned and studied in our future work. Firstly, more experiments on images of different parts of the body should be conducted, in order to determine whether significant information loss will be caused by the modified BM3D algorithm. Secondly, we should consider developing a modified BM4D[8] algorithm to achieve better x-z plane images.

Acknowledgment

The author would like to express her sincere gratitude to Junlong Han for valuable discussion about the basic BM3D method.

References

[1] T. Li, X. Li, J. Wang, J. Wen, H. Lu, J. Hsieh, and Z. Liang, “Nonlinear sinogram smoothing for low-doseX-ray CT”, *IEEE Transactions on Nuclear Science*, vol. 51,no. 5, pp. 2505-2513, October 2004.

[2] X. Cui，Z. Gui，Q. Zhang，Y. Liu，R. Ma，“The statistical sinogram smoothing via adaptive-weighted total variation regularization for low-dose X-ray CT”，*Optik - International Journal for Light and Electron Optics*, vol.125, no. 18, pp. 5352-5356, September 2014.

[3] K. Dabov, A. Foi, V. Katkovnik, and K. Egiazarian, “Image denoising by sparse 3D transform-domain collaborative filtering,” *IEEE Trans. Image Process.*, vol. 16, no. 8, pp. 2080-2095, August 2007.

[4] H. Bruder, R. Raupach, J. Sunnegårdh, M. Sedlmair, K. Stierstorfer, T. Flohr, “Adaptive iterative reconstruction”, *Proceedings of SPIE-The International Society for Optical Engineering*, vol. 7961, no. 3, pp. 165-177, March 2011.

[5] J.-B. Thibault, C. Bouman, K. Sauer, and J. Hsieh, “A recursive filter for noise reduction in statistical tomographic imaging”, *Proceedings of the SPIE/IS&T Symposium on Computational Imaging IV*, vol. 6065, no. 0X, SanJose, CA, Jan. 16-18 2006.

[6] D. Cai，Y. Xiao，Y. Xing，“Theoretical noise estimation in 3D X-ray cone-beam CT reconstruction”，*IEEE Nuclear Science Symposium Conference Record*, vol. 612, no.3, pp. 3252-3255, October 2010.

[7] J. Christner, K. Stierstorfer, A. Primak, C. Eusemann, T.Flohr, and C. McCollough, “Evaluation of z-axis resolution and image noise for nonconstant velocity spiral CT data reconstructed using a weighted 3D filtered backprojection (WFBP) reconstruction algorithm”, *Medical Physics*, vol.37, no.2, pp. 897-906, February 2010.

[8] M. Maggioni, V. Katkovnik, K. Egiazarian, and A. Foi, “A Nonlocal Transform-Domain Filter for Volumetric Data Denoising and Reconstruction”, *IEEE Trans. Image Process.*, vol. 22, no. 1, pp. 119-133, January 2013.

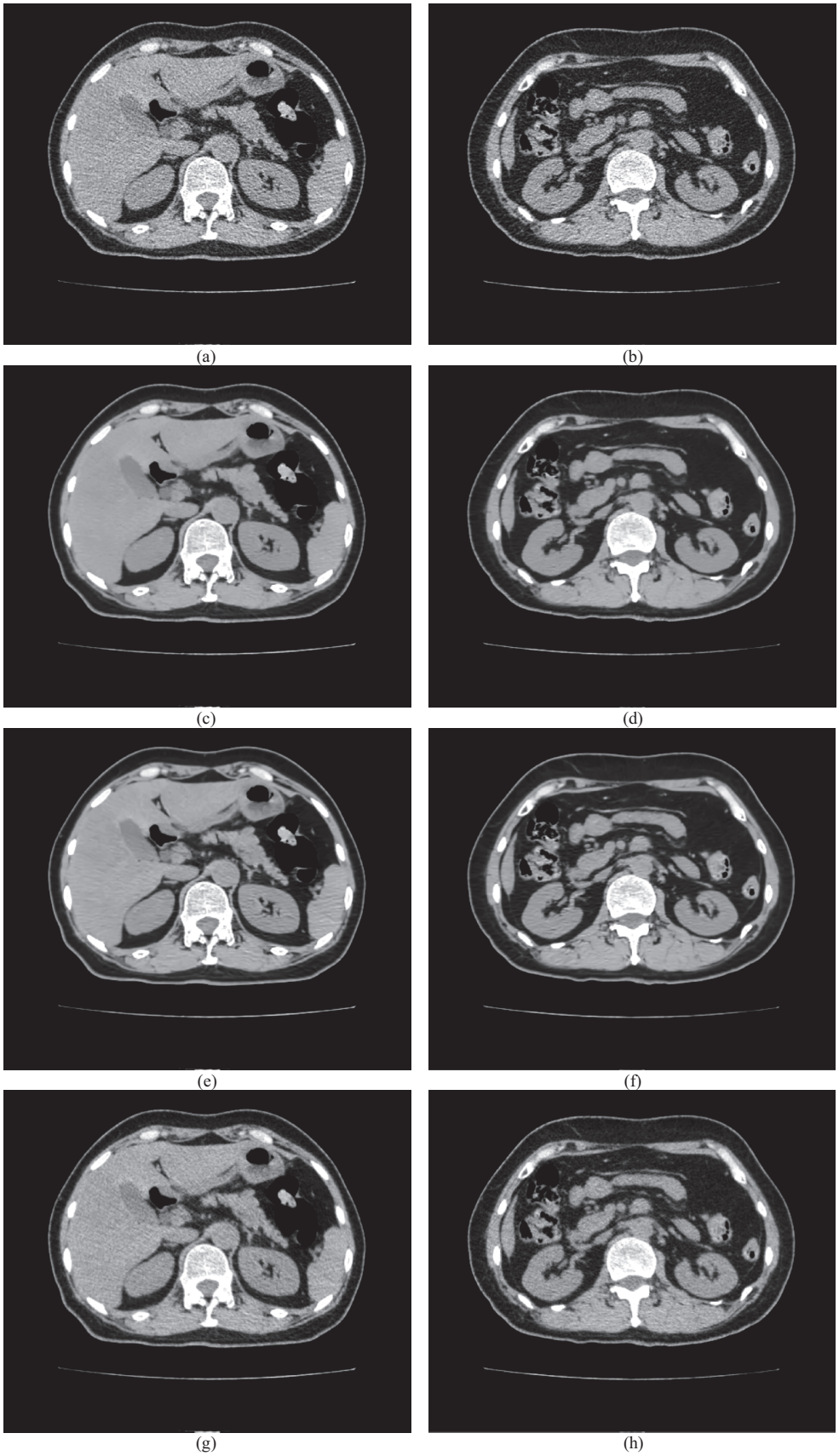

Fig. 3. (a) and (b). Original images reconstructed by weighed FBP; (c) and (d). Images denoised by modified BM3D method; (e) and (f). Images denoised by original BM3D method for comparison; (g) and (h). Images denoised by rawdata smoothing method for comparison.

Material Decomposition for Wide-Cone Dual-Energy CT Using Fast kV Switching

Hewei Gao*, Adam Cohen and Priti Madhav

***Abstract*—In this study, a projection-space material decomposition for wide-cone dual energy CT using volumetric fast kV switching is presented and evaluated in terms of quantitative accuracy and uniformity. A comparison between projection-space and image-space material decomposition is also conducted on virtual monochromatic images, including an assessment of CT number uniformity across 160 mm of detector coverage in Z. Results of two phantoms with multiple contrasts at various dose levels shows that highly quantitative CT spectral imaging can be achieved using volumetric fast kV switching.**

***Index Terms*—Material Decomposition, Dual Energy CT, Fast kV Switching, Wide-Cone CT**

I. Introduction

THANKS to its capability of discriminating materials and making CT quantitative, dual energy computed tomography (CT) imaging has been more and more widely used in clinical diagnosis, as well as industry and security inspections [1]. Volumetric fast kV switching based dual energy spectral imaging on a wide-cone CT system, with detector coverage of 160 mm and more, have many clinical benefits, including the ability of providing material density images for whole organs such as the heart in a single rotation. For the volumetric fast kV switching, a fully physics-based projection-space material decomposition has been developed with an advanced spectral modeling of both X-ray source and detector including the heel effect. For wide cone CT, the heel effect becomes a new challenge due to the fact that X-ray photons at smaller incident angles are attenuated more by the anode target itself than those at larger angles [2].

The main aim of this study is to present the projection-space material decomposition for wide-cone dual energy CT using volumetric fast kV switching and to evaluate its quantitative accuracy and uniformity.

II. Method

The dual energy acquisition with fast kV switching, combined with projection-space material decomposition is currently deployed as Gemstone Spectral Imaging on the GE "Discovery CT750 HD" system and the GE "Revolution HD" products. The principals used here are similar but extended to wide cone coverage.

A. Spectral Modeling for Wide-Cone Dual Energy CT Using Volumetric Fast kV Switching

Taking advantages of the advanced 3D anti-scatter grid along with hardware improvements on X-ray tube, high-voltage generator and low-electronic-noise detector on a 160-mm wide-cone CT system (Revolution CT, GE Healthcare, Waukesha, WI), an advanced spectral modeling and a fully physics-based projection-space material decomposition approach have been developed, where the heel effect on the X-ray tube and the non-uniformity of spectral response on the detector are also modeled, as illustrated in Fig. 1.

All authors are with the GE Healthcare, Waukesha, WI 53188 (E-mail: gaoh@ge.com).

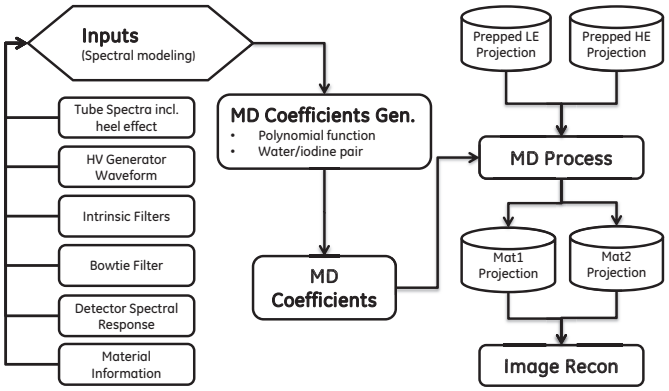

Fig. 1. An illustration of a fully physics-based advanced spectral modeling and project-space material decomposition (MD).

The modeling of low and high kV spectra is fundamental for dual energy CT. For fast kV switching, the tube output spectra for low ($T_l(E)$) and high kV ($T_h(E)$) are controlled by the waveform design in the high voltage generator and may be characterized in the detailed calibration stages [3]. For a wide-cone dual energy CT system, the effective low and high kV spectra ($S_l(E)$ and $S_h(E)$) consist of multiple components,

$$S_l(E) = T_l(E)H_l(E)\exp\left(-\Sigma\mu_i(E)D_i(E)\right)\eta(E),$$
$$S_h(E) = T_h(E)H_h(E)\exp\left(-\Sigma\mu_i(E)D_i(E)\right)\eta(E), \quad (1)$$

where, $H_l(E)$ and $H_h(E)$ represent the heel effect; μ_i and D_i denote the attenuation coefficients and thickness of a given filter in the beam; $\eta(E)$ is the detector energy response. In an ideal case, $\eta(E) = 1 - e^{-\mu_{det}(E)D_{det}}$, with μ_{det} and D_{det} being the attenuation coefficients and thickness of the detector scintillator. In reality, however, it could vary from one detector cell to another.

B. Material Decomposition Approach

A key assumption in dual energy CT imaging is that the attenuation coefficients of any material can be represented by two basis materials (or two basis physical effects) when ignoring k-Edge [4], [5]. For dual energy CT, a pair of

projection data that are acquired under low and high kV can be written as

$$p_l = -\ln\left(\frac{\int S_l(E)e^{-\left(\frac{\mu}{\rho}\right)_1(E)m_1-\left(\frac{\mu}{\rho}\right)_2(E)m_2}dE}{\int S_l(E)dE}\right),$$
$$p_h = -\ln\left(\frac{\int S_h(E)e^{-\left(\frac{\mu}{\rho}\right)_1(E)m_1-\left(\frac{\mu}{\rho}\right)_2(E)m_2}dE}{\int S_h(E)dE}\right). \quad (2)$$

Here, $(\frac{\mu}{\rho})_1(E)$ and $(\frac{\mu}{\rho})_2(E)$ are the mass attenuation coefficients of two basis materials selected; m_1 and m_2 are the corresponding density path lengths.

Once the dual energy low and high spectra $S_l(E)$ and $S_h(E)$ are obtained, it is straightforward to generate m_1 and m_2 from p_l and p_h in projection space using Eq. (2). This process is called material decomposition (MD), which is usually a nonlinear process due to the polychromatic beam used in X-ray CT. It also requires good data alignment between p_l and p_h. In practical applications, the material decomposition may be approximated by polynomial functions [6] such as

$$m_1 = \Sigma\alpha_{ij}p_l^i p_h^j,$$
$$m_2 = \Sigma\beta_{ij}p_l^i p_h^j, \quad (3)$$

with α_{ij} and β_{ij} being the MD coefficients that can be derived using Eq. (2).

Alternatively, materials may be decomposed after reconstruction in image space, which is equivalent to using just the linear teams in Eq. (3). Compared with projection-space MD, Image-space one has advantages of simplicity and no need of data alignment between low kV and high kV but it could easily suffer in beam hardening artifact and MD inaccuracy.

III. Evaluation Conditions

In order to evaluate the performance of MD accuracy and uniformity at various situations, two phantoms filled with multiple levels of iodine contrasts (as shown in Fig. 2)) were scanned using fast kV switching under various dose levels (CTDI ranging from 5.3 mGy to 19.1 mGy):

- Phantom A: liquid iodine-rod phantom (24.5 cm in diameter, custom made) where density of water is known with high confidence. There are 3 tubes symmetrically inserted in the phantom that can be filled with liquid. In our evaluation, we filled water in the tank and three different iodine concentrations (corresponding to about 230, 290 and 330 HU at 120 kV) in the tubes.
- Phantom B: GAMMEX dual-energy phantom (33 cm in diameter, made by Gammex, Inc., Middleton, WI) where densities of iodine contrasts are known with high confidence (5, 10 and 20 mg/cc of iodine rods).

After projection-space MD and conventional image reconstruction, MD accuracy and uniformity are measured on selected contrast locations as regions of interest (ROIs). The values are averaged over central 25-mm thickness along Z and compared with ground truths.

In order to evaluate the MD performance at increased heel effect, phantom A was also scanned at 160 mm collimation using volumetric fast kV switching. The CT number uniformity across Z were measured on the virtual monochromatic images

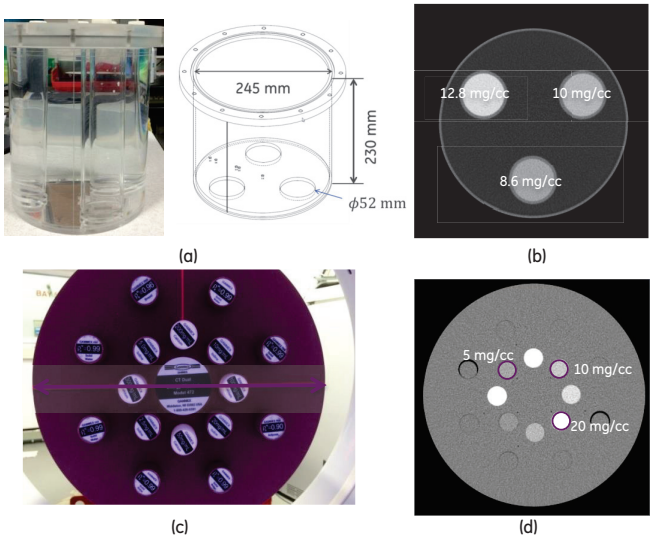

Fig. 2. Two phantoms used in this study. (a) photograph and dimension of phantom A; (b) in-plane CT image of phantom A; (c) photograph and dimension of phantom B; (d) in-plane CT image of phantom B.

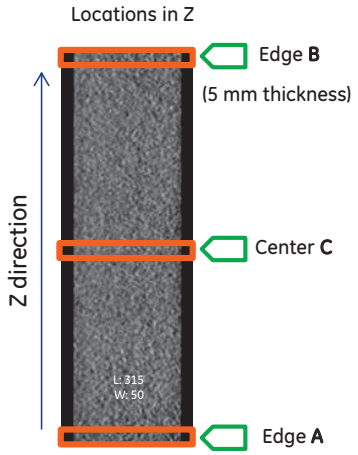

Fig. 3. The three Z-positions selected for evaluation of CT number Uniformity across Z with the increased heel effect. Display window width: 50 HU, level: 315 HU.

generated at 70 keV, for both fully physics-based projection-space MD and pure image-space MD without any advanced post processing.

As the heel effect changes monotonically from one detector side to another, the CT number values of the same dense material , in general, vary monotonically along the Z direction as well. To measure the CT number uniformity quantitatively, three positions in the Z direction ("CENTER" and two "EDGES") are selected , among which the maximum difference are computed and used as our figure of merit, i.e.,

$$\Delta = \max\left(HU_A, HU_B, HU_C\right) - \min\left(HU_A, HU_B, HU_C\right)$$

where HU_A, HU_B and HU_C represent the averaged CT numbers (over 5 mm thickness) in the three Z-positions as shown in Fig. 3. The smaller the Δ value is, the better the CT number uniformity is.

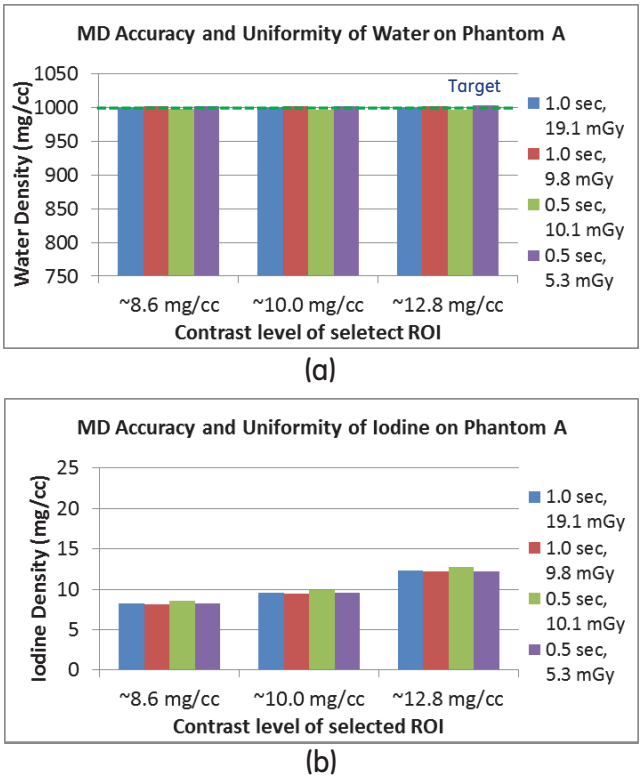

Fig. 4. MD accuracy and uniformity for water density (a) and iodine density (b) of phantom A.

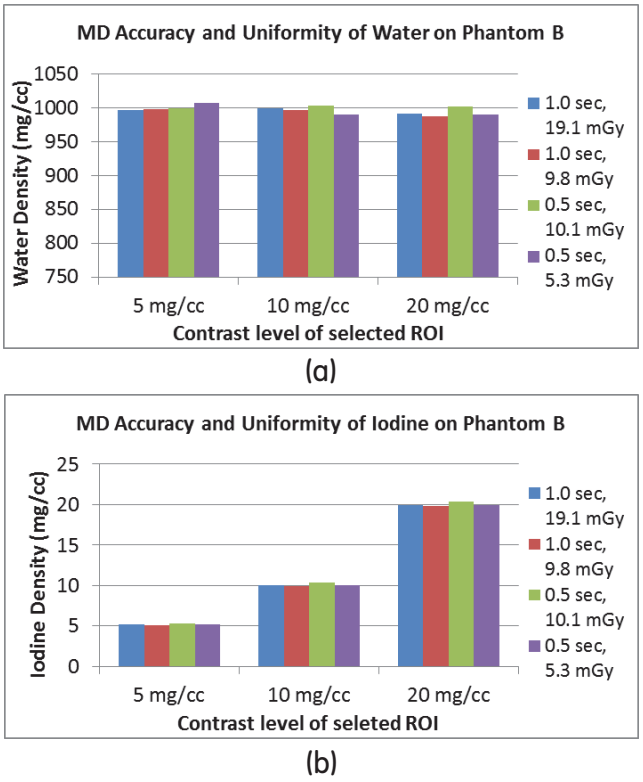

Fig. 5. MD accuracy and uniformity for water density (a) and iodine density (b) of phantom B.

IV. Results

A. In-plane MD Accuracy and Uniformity

For phantom A, the in-plane MD accuracy and uniformity is shown in Fig. 4. Across all the dose and contrast levels, the density accuracy of water is within 1% (10 mg/cc), and the density uniformity of water and iodine are within 1% and 5%, respectively.

For phantom B, the MD accuracy and uniformity is shown in Fig. 5. Across all the dose and contrast levels, the density accuracy of iodine is within 5%, and the density uniformity of water and iodine are within 2% and 5%, respectively.

B. CT Number Uniformity Across Z at Increased Heel Effect

Virtual monochromatic images of phantom A at 70 keV are shown in Fig. 6, with results from both physics-based projection-space MD and pure image-space MD, respectively. Shading artifacts between the iodine rods on the image using image-space MD are observed as expected.

For all the three iodine rods of phantom A on monochromatic image at 70 keV, the averaged CT numbers of selected ROIs in the three Z-positions are listed in Table I. Their corresponding reformatted images are shown in Fig. 7. The maximum CT number change along the Z is less than 5 HU when using the projection-space MD. Similar level of CT number uniformity across Z is also achieved by the image-space MD when one uses slice-dependent MD coefficients. Of course, cupping artifacts in those iodine rods are still observed.

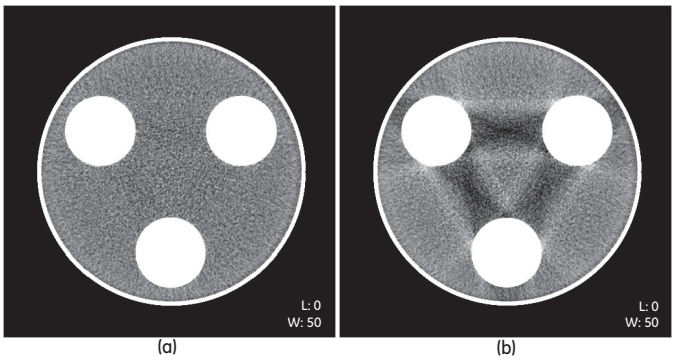

Fig. 6. Virtual monochromatic images at 70 keV. (a) Fully physics-based projection-space MD; (b) pure image-space MD. Display window width: 50 HU, level: 0 HU.

TABLE I
CT numbers (HU) of selected ROIs on monochromatic images in Fig. 7 at three Z-positions shown Fig. 3) .

ROI	Method	HU @Z-Position			Δ
		A	B	C	
1	pMD*	203.5	205.8	205.4	2.3
	iMD$_1$*	201.4	211.8	214.4	13.0
	iMD$_2$*	210.5	210.2	211.8	1.7
2	pMD	236.3	239.5	239.4	3.2
	iMD$_1$	231.5	244.1	247.5	16.0
	iMD$_2$	242.0	242.2	244.6	2.6
3	pMD	309.2	312.7	311.6	3.5
	iMD$_1$	297.6	314.4	318.4	20.8
	iMD$_2$	311.2	311.9	314.7	3.5

* pMD: projection-space MD;
* iMD$_1$: image-space MD with same coefficients for all image slices;
* iMD$_2$: image-space MD with slice-dependent coefficients.

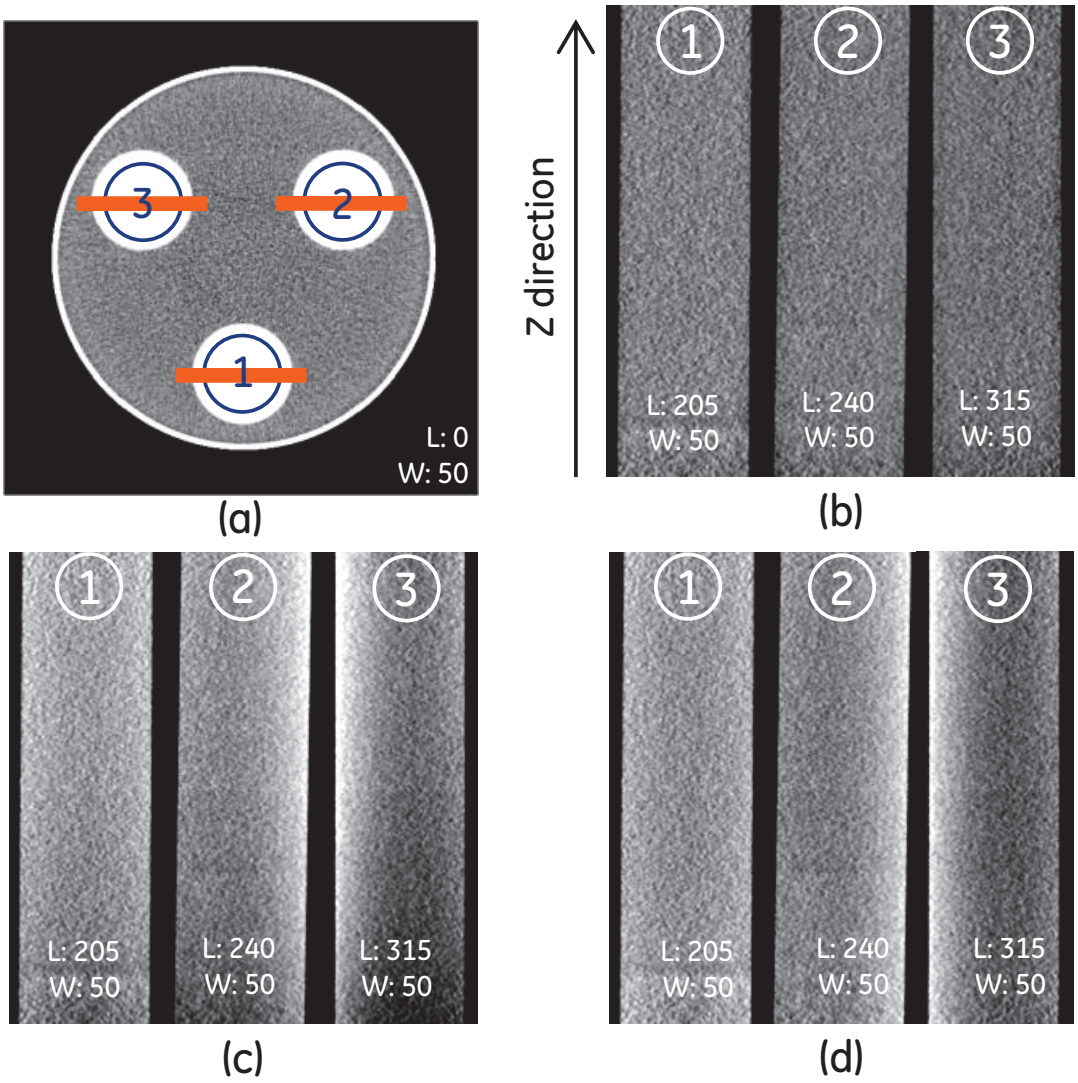

Fig. 7. Reformatted monochromatic images at 70 keV for phantom A. (a) ROIs selected; (b) fully physics-based projection-space MD; (c) image-space MD with one set of MD coefficients for all image slices; (d) image-space MD with coefficients varies to compensate for the heel effect. Display window width: 50 HU, level varies as indicated on the image.

V. Conclusion and Discussion

We presented a fully physics-based projection-space MD for wide-cone dual energy CT using fast kV switching. The phantom study on a wide-cone CT system (up to 160 mm of detector coverage) showed that highly quantitative CT spectral imaging can be achieved with beam hardening free CT images, which are the advantages of physics-based projection-space MD processing.

The increased heel effect can be well compensated in the projection-space MD, leading to less than 5 HU of CT number difference across a 160 mm of detector coverage for iodine levels typical used in clinical applications. A similar level of CT number uniformity across Z may be achieved by using image-space MD as well, despite visible beam hardening artifact.

Acknowledgments

The authors would like to thank CT Physics and Image Quality team at GE Healthcare for support of this study.

References

[1] B. J. Heismann, B. T. Schmidt, and T. Flohr, *Spectral Computed Tomography*. Bellingham WA: SPIE Press, 2012.

[2] H. Gao, A. Cohen, and Y. Imai, "Quantitative uniformity of iodinated contrast across the z-coverage of large cone-angle ct," *The Third International Conference on Image Formation in X-ray Computed Tomography*, pp. 220–223, 2014.

[3] D. Xu, D. A. Langan, X. Wu, J. D. Pack, T. M. Benson, J. E. Tkaczky, and A. M. Schmitz, "Dual energy ct via fast kvp switching spectrum estimation," *Proc. SPIE*, vol. 7258, pp. 72 583T–72 583T–10, 2009.

[4] R. E. Alvarez and A. Macovski, "Energy-selective reconstructions in x-ray computerised tomography," *Physics in Medicine and Biology*, vol. 21, no. 5, p. 733, 1976.

[5] W. A. Kalender, W. H. Perman, J. R. Vetter, and E. Klotz, "Evaluation of a prototype dualenergy computed tomographic apparatus. i. phantom studies," *Medical Physics*, vol. 13, no. 3, pp. 334–339, 1986.

[6] X. Wu, D. A. Langan, D. Xu, T. M. Benson, J. D. Pack, A. M. Schmitz, E. J. Tkaczyk, J. Leverentz, and P. Licato, "Monochromatic ct image representation via fast switching dual kvp," *Proc. SPIE*, vol. 7258, pp. 725 845–725 845–9, 2009.

Optimizing Iterative Image Reconstruction in Digital Breast Tomosynthesis via the Hotelling Observer

Adrian A. Sanchez[1], Emil Y. Sidky[1], Sean D. Rose[1], and Xiaochuan Pan[1,2]

***Abstract*—In this work, we present a method for optimizing linear iterative image reconstruction for signal detection in digital breast tomosynthesis. The figure of merit used for evaluating the reconstruction algorithms is the Hotelling observer efficiency metric, which characterizes the preservation of signal detectability from the data, through the reconstruction algorithm, into the final image. The method is based on prior work optimizing analytic reconstruction [1], and uses information within a small image ROI to characterize algorithm performance. The optimization problem investigated here is a penalized least-squares problem with either a Tikhonov or "roughness" penalty. We consider two detection tasks: detection of a small (roughly 100μm) microcalcification and detection of a 2.5mm low contrast disk. We then compare reconstructed images at a fixed level of Hotelling observer performance for each penalty (roughness or Tikhonov) as well as FBP.**

I. Introduction

Digital breast tomosynthesis (DBT) continues to gain recognition as a valuable approach to obtaining volumetric breast images, avoiding some of the difficulty posed by overlapping tissues in conventional projection mammography [2], [3]. While combining a narrow range of projection angles allows for some depth-dependent attenuation information to be captured, the data acquired is insufficient for true three-dimensional imaging, posing an interesting problem for the development of image reconstruction algorithms tailored to DBT.

To date, most efforts in DBT image reconstruction have used modifications of algorithms developed for x-ray CT. These algorithms have a wide variety of parameters and implementation choices, ranging from pixel size and slice thickness to regularization strength and frequency-dependent filtering. While experience in x-ray CT provides some basic insight into the nature of these algorithms and their respective parameters, there is no guarantee that this experience is sufficient to translate decades of refinement in CT reconstruction algorithms to this still emerging technology. Instead, exhaustive exploration of algorithm implementations and parameter settings is warranted for each algorithm, task, and DBT system design under consideration. An efficiently computed, objective metric of image quality would greatly simplify this task and would help to illuminate basic trends of image quality, providing insight which would be difficult to obtain through manual parameter tuning with a limited number of data sets.

In this work, we develop an efficient implementation of the Hotelling observer (HO) [4] for DBT algorithm design. The HO design we propose is a direct extension of an observer model we have previously proposed for analytic reconstruction algorithms [1], and here we extend its application to iterative reconstruction methods with quadratic objectives. The HO figure of merit, the HO SNR, is computed in the image and projection data domains in order to construct an efficiency metric which can be used for objective algorithm optimization

The HO has been applied to various aspects of DBT by others, including optimization of system acquisition parameters [5], [6], [7], and, similar to the present study, the exploration of image reconstruction's impact on task performance [8], [9]. Unlike most work involving the HO, the method we develop does not apply dimension-reducing channels to the image or observer template. Instead, dimensionality of the covariance matrix is reduced by only considering pixels within a predefined region-of-interest (ROI). Finally, our approach has the benefit of being non-stochastic, meaning that the metric we obtain does not arise from an ensemble of noise realizations. Instead, an analytic quantum noise model is used. This aspect of the model is flexible, however, and our approach can easily be modified to accommodate realization-based noise models, albeit with a resulting statistical uncertainty in the subsequent efficiency metric.

Here, we focus on two versions of penalized least-squares (PLS) reconstruction: PLS with a Tikhonov penalty and PLS with a quadratic "roughness" penalty, which penalizes differences between neighboring pixels. We specifically investigate optimizing the regularization weight parameter for a high- and low-contrast signal detection task, although the method can be applied to any classification task, as will be discussed with regard to future work in Section IV. We then compare the optimized images and performance trends for each iterative algorithm to similar results previously obtained for filtered back-projection.

II. Methods

A. DBT Simulation

We consider a fan-beam acquisition geometry with a configuration meant to mimic the Hologic Selenia Dimensions tomosynthesis system. The source-to-image distance is set to 70cm, and 0.14mm detector pixels are used. The lateral extent of the detector is restricted to 2cm centered on the signal of interest, and the lateral extent of the image ROI used for HO performance estimation is defined by the back-projection of this detector area. There are 15 simulated projections, spaced in 1 deg increments. We include modeling of a 0.4mm focal spot, as well as finite detector element size through 16-fold subsampling on the detector.

[1]The University of Chicago, Department of Radiology, Chicago, IL 60637
[2]The University of Chicago, Department of Radiation and Cellular Oncology, Chicago IL 60637

We consider the line-integration of a continuously defined phantom in order to construct projection data which has already had the negative logarithm applied:

$$\mathbf{g}_i = \int_L f\left(s_i + l\hat{\theta}_i\right) \mathrm{d}l + \mathbf{n}_i, \tag{1}$$

where bold font indicates a vector, $\mathbf{g} \in \mathbb{R}^m$ is the projection data, L is defined as the intersection of the ith ray with the compact support of the object f, s_i denotes the sources position, and $\hat{\theta}_i$ is a unit vector in the direction of the ith ray. The vector $\mathbf{n}$ is an m-dimensional, zero-mean Gaussian random variable, with diagonal covariance. The variance of each element of $\mathbf{n}$ is given by

$$\mathrm{Var}\left\{\mathbf{n}_i\right\} = \frac{1}{\bar{N}_i} + \frac{1}{\bar{N}_0}, \tag{2}$$

where $\bar{N}_0$ is the average number of incident photons for a given ray, and $\bar{N}_i$ is the average number of transmitted photons for the same ray. This model results in the data covariance matrix K_g with elements given by

$$\left(K_g\right)_{i,j} = \begin{cases} \frac{\exp(\bar{\mathbf{g}}_i)+1}{\bar{N}_0} & : i = j \\ 0 & : \text{else} \end{cases}. \tag{3}$$

We have set $\bar{N}_0 = 10^5$ here, but this choice is not critical, since we are more interested in the relative performance of different algorithm settings, rather than absolute task performance. This noise model could be modified to incorporate anatomic noise models based on sample images through the addition of a sample-based covariance matrix to K_g as given above. The subsequent formalism would remain unchanged.

B. Image Reconstruction

PLS-Tikhonov: We begin by describing PLS reconstruction with a Tikhonov penalty. In this case, the final image $f^* \in \mathbb{R}^N$ is obtained as the solution to the optimization problem

$$\mathbf{f}^* = \arg\min_{\mathbf{f}} \|X\mathbf{f} - \mathbf{g}\|_2^2 + \lambda\|\mathbf{f}\|_2^2, \tag{4}$$

where λ is a free parameter controlling the strength of the Tikhonov penalty in the second term. The matrix $X \in \mathbb{R}^{M\times N}$ is a linear projection operator, so that the first term in the optimization problem enforces fidelity of the image to the obtained data. Here, we use a ray-driven model where X computes a sum of weighted line intersection lengths through the pixels of $\mathbf{f}^*$. We note that this problem can be rewritten as

$$\mathbf{f}^* = \arg\min_{\mathbf{f}} \|\tilde{X}\mathbf{f} - \tilde{\mathbf{g}}\|_2^2 \tag{5}$$

where we have defined

$$\tilde{X} = \begin{bmatrix} X \\ \lambda I \end{bmatrix}, \quad \tilde{\mathbf{g}} = \begin{bmatrix} \mathbf{g} \\ 0_{n\times 1} \end{bmatrix}. \tag{6}$$

For a small enough number of pixels, the image $\mathbf{f}^*$ can then be obtained directly through the Moore-Penrose pseudoinverse of $\tilde{X}$:

$$\mathbf{f}^* = \tilde{X}^\dagger\tilde{\mathbf{g}}, \tag{7}$$

where the superscript $\dagger$ denotes the pseudoinverse, and reduces to the conventional left-inverse if a left-inverse of $\tilde{X}$ exists. As mentioned previously, we consider a narrow lateral extent of the detector (roughly 2cm), and also simulate a fan-beam geometry. This is sufficient to allow the pseudoinverse $\tilde{X}^+$ to be computed directly and stored in computer memory. Meanwhile, the image pixel size is matched to the detector pixel size, and slice thickness is set to 8.5 times the image pixel size.

PLS-Roughness: The second algorithm we consider penalizes differences between neighboring pixels by including a discrete gradient operator in the vector magnitude of the penalty term:

$$\mathbf{f}^* = \arg\min_{\mathbf{f}} \|X\mathbf{f} - \mathbf{g}\|_2^2 + \lambda\|\nabla\mathbf{f}\|_2^2, \tag{8}$$

where the discrete gradient operator ∇ is given by

$$\nabla := \begin{bmatrix} \frac{\mathrm{d}_y}{\mathrm{d}_x}\nabla_x \\ \nabla_y \end{bmatrix}, \tag{9}$$

where d_x is the slice thickness and d_y is the image pixel size. The subscripts x and y appended to the operator ∇ denote that forward-differencing is performed in the x and y direction, respectively. Similar to the Tikhonov case, this optimization problem can be solved by computing a pseudoinverse, as in Eqn. 7. Here, the matrix $\tilde{X}$ is given by

$$\tilde{X} = \begin{bmatrix} X \\ \lambda\nabla. \end{bmatrix} \tag{10}$$

C. The Observer Model

As a first step in constructing the Hotelling observer model, we repeat the result from Ref. [4] that the covariance matrix K_y of $\mathbf{y} = A\mathbf{x}$ is given by

$$K_y = AK_xA^T, \tag{11}$$

where A is a matrix, and the superscript T denotes the matrix transpose (or Hermitian conjugate in the case of complex matrix entries). We can therefore relate the image covariance matrix K_f to the data covariance of Eqn. 3 as

$$K_f = \tilde{X}^\dagger K_g \left(\tilde{X}^\dagger\right)^T. \tag{12}$$

One benefit of each of the penalties duscussed above is that they tend to consolidate signal energy into a compact region of the reconstructed image, avoiding the non-physical solutions which would be obtained without regularization when $\tilde{X}$ is poorly conditioned. In order to create an observer model which is sensitive to this property, we apply a decimation operator D to the reconstruction operator $\tilde{X}^\dagger$. This operator selects only the slices whose location coincides to the physical location of the signal in the phantom, discarding other slices. The final covariance matrix in our model is then given by

$$K_{Df} = D\tilde{X}^\dagger K_g \left(\tilde{X}^\dagger\right)^T D^T. \tag{13}$$

The HO's figure of merit, the HO SNR, is then given by $\mathrm{SNR}_f^2 = \left(\mathbf{f}^*\right)^T D^T K_{Df}^\dagger D\mathbf{f}^*$, where $\mathbf{f}^*$ is the reconstruction of the signal to be detected. Finally, the efficiency metric of the HO can be computed as a ratio of SNR_f^2 in the image domain to SNR_g^2 in the data domain, which is given by $\mathrm{SNR}_g^2 = \mathbf{g}^T K_g^{-1}\mathbf{g}$. This ratio cannot exceed 1 and will be equal to 1 only if all of the information in the data relevant to the given task is perfectly preserved through image

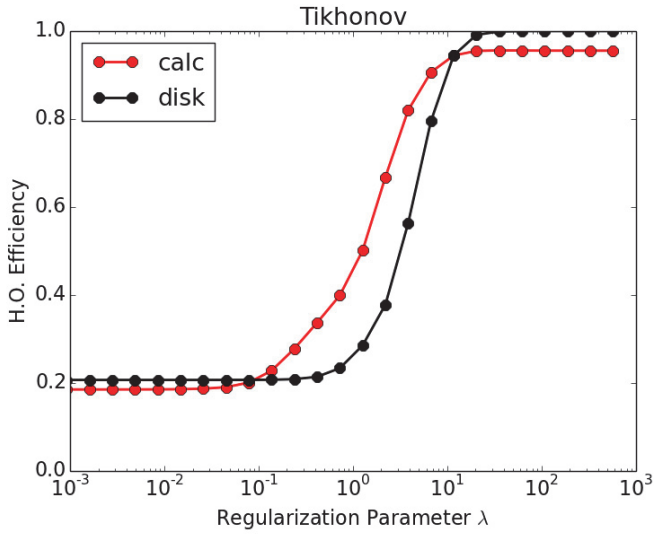

Fig. 1. Hotelling observer efficiency as a function of regularization strength for Tikhonov-regularized PLS. Both the calcification detection and low-contrast disk detection tasks are shown and exhibit similar trends. Interestingly, the plateau seen to the right side of the graph remains level for very large λ, only dropping once numerical issues preclude computation of the pseudoinverse.

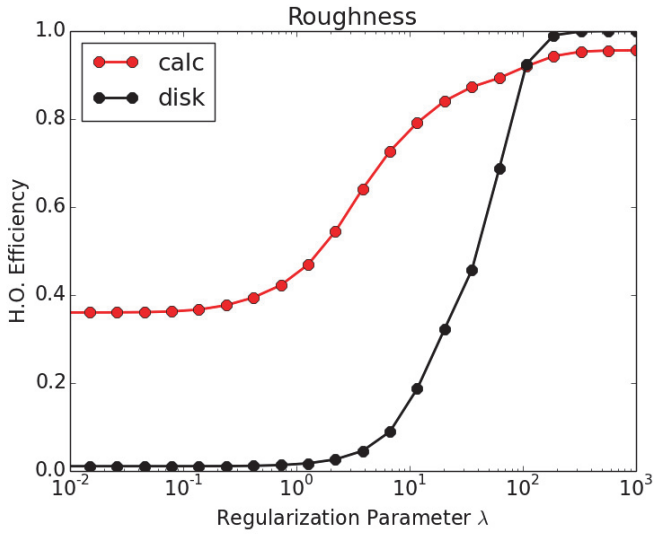

Fig. 2. Similar to Fig 1, but for the roughness penalty.

reconstruction and the decimiation operator which selects the appropriate image slice (or slices for a larger object).

Two tasks are studied here as examples: the detection of a microcalcification, modeled as a Gaussian with full width at half maximum equal to 100μm, and detection of a low-contrast disk. The contrast of the microcalcification is set to the mean attenuation difference between glandular breast tissue and calcium carbonate for an 80kVp x-ray spectrum. The contrast of the low-contrast disk is set to 5% relative to the background.

III. Results

The dependence of HO efficiency on the regularization parameter λ is shown in Figs. 1 and 2 for Tikhonov regularization and roughness, respectively. A similar plot from a previous study is shown for the FBP algorithm for comparison in Fig. 3. In each plot the horizontal axis increases with increasing regularization strength. For the case of FBP, this is quantified via the cutoff frequency for a Hanning filter (relative to the detector Nyquist frequency). Interestingly, the trends for calcification detection are opposite for the iterative algorithms relative to FBP, with increasing regularization monotonically improving detection performance for the iterative methods and degrading performance for FBP.

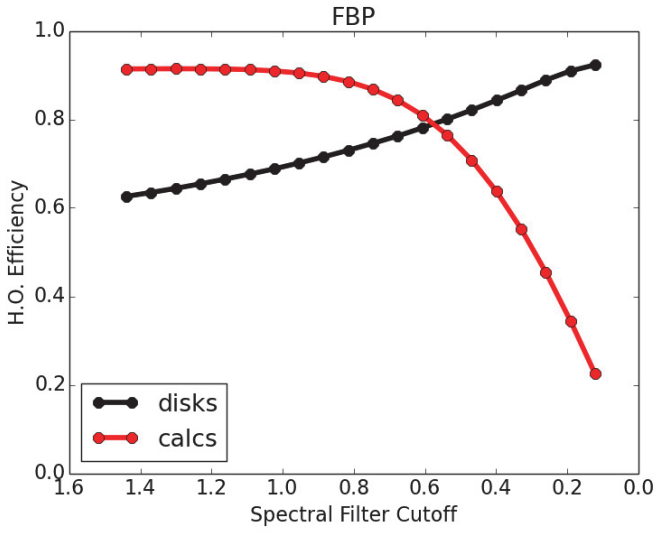

Fig. 3. Hotelling observer efficiency is shown as a function of the Hanning filter cutoff in the FBP algorithm. The cutoff is normalized to the Nyquist frequency of the detector. Note that the horizontal axis is inverted so that regularization increases from left to right, as in the previous figures. However, the trend of HO performance with respect to regularization is reversed for the calcification detection task. The trend is similar to the iterative algorithms for the low-contrast detection task.

Example images at a fixed HO efficiency level of 0.9 are shown for each algorithm for the microcalcification task and low-contrast detection task in Figs 4 and 5, respectively. The image plane is the coronal (cranio-caudal) plane, which leads to nonsquare pixels since the slice thickness is not equal to the in-plane pixel size. One potential application of this methodology is the comparison of algorithms at fixed task performance so that other aspects of algorithm performance (such as resolution or computational efficiency) can be assessed on somewhat equal footing.

IV. Conclusion

We have presented a method for applying task-based assessment via the Hotelling observer to algorithm design in DBT. The method can be applied to conventional analytic algorithms, as demonstrated previously, as well as iterative algorithms with quadratic objectives. Various simplifications have been made here, including a uniform background (known exactly), as well as a simple quantum noise model. In addition to simplifying the metric's implementation, this also facilitates preliminary validation using phantom data, to be presented at the CT Meeting. More sophisticated noise models (such as tissue-mimicking power-law noise) have also been investigated in our work but are omitted here for conciseness. Likewise, more complex tasks, such as discrimination tasks

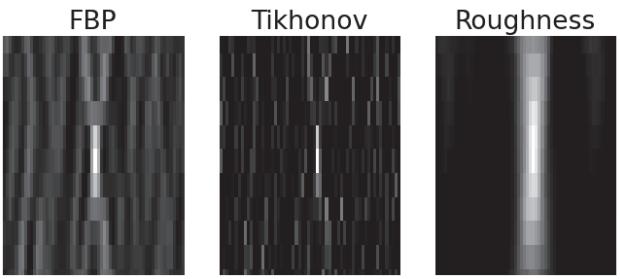

Fig. 4. Shown here are ROIs of reconstructed images (cranio-caudal dimension) of the calcification signal from the same noisy data using different algorithms set at equal levels of HO efficiency. Pixel size, ROI size, and slice thickness are fixed for each algorithm. Note the variety in image texture and resolution despite consistent detection task performance for each algorithm. The display window is [0,$v_{\max}$], where $v_{\max}$ is the maximum pixel value in the image ROI.

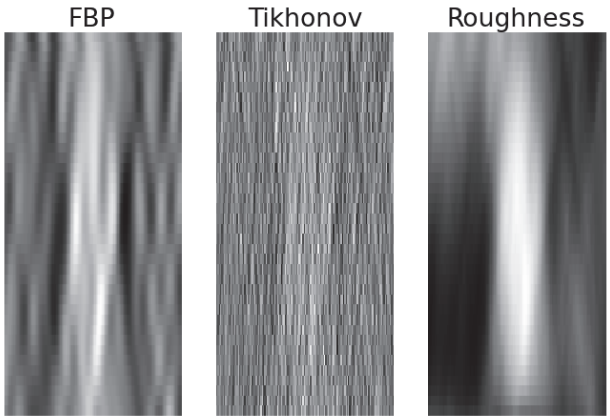

Fig. 5. Similar to Fig. 4 but for the low-contrast disk detection task. The display window is set to include the full range of pixel values present in the image.

which challenge depth resolution are currently under investigation and will be completed by the time of the 2016 CT Meeting.

Acknowledgments

This work was supported in part by NIH R01 Grant Nos. CA120540, CA158446, and EB000225. The contents of this article are solely the responsibility of the authors and do not necessarily represent the official views of the National Institutes of Health.

References

[1] A. A. Snchez, E. Y. Sidky, and X. Pan, "Use of the Hotelling observer to optimize image reconstruction in digital breast tomosynthesis," *Journal of Medical Imaging*, vol. 3, no. 1, pp. 011 008–011 008, 2015. [Online]. Available: http://dx.doi.org/10.1117/1.JMI.3.1.011008

[2] J. T. Dobbins III, "Tomosynthesis imaging: At a translational crossroads," *Medical Physics*, vol. 36, no. 6, pp. 1956–1967, Jun. 2009. [Online]. Available: http://scitation.aip.org/content/aapm/journal/medphys/36/6/10.1118/1.3120285

[3] I. Sechopoulos, "A review of breast tomosynthesis. Part I. The image acquisition process," *Medical physics*, vol. 40, no. 1, p. 014301, 2013. [Online]. Available: http://scitation.aip.org/content/aapm/journal/medphys/40/1/10.1118/1.4770279

[4] H. H. Barrett and K. J. Myers, *Foundations of Image Science*. Hoboken, New Jersey: John Wiley & Sons, Inc., 2004.

[5] A. S. Chawla, E. Samei, R. S. Saunders, J. Y. Lo, and J. A. Baker, "A mathematical model platform for optimizing a multiprojection breast imaging system," *Medical physics*, vol. 35, no. 4, pp. 1337–1345, 2008. [Online]. Available: http://scitation.aip.org/content/aapm/journal/medphys/35/4/10.1118/1.2885367

[6] I. Reiser and R. M. Nishikawa, "Task-based assessment of breast tomosynthesis: Effect of acquisition parameters and quantum noisea)," *Medical physics*, vol. 37, no. 4, pp. 1591–1600, 2010. [Online]. Available: http://scitation.aip.org/content/aapm/journal/medphys/37/4/10.1118/1.3357288

[7] S. Young, P. R. Bakic, K. J. Myers, R. J. Jennings, and S. Park, "A virtual trial framework for quantifying the detectability of masses in breast tomosynthesis projection data," *Medical physics*, vol. 40, no. 5, p. 051914, 2013. [Online]. Available: http://scitation.aip.org/content/aapm/journal/medphys/40/5/10.1118/1.4800501

[8] I. Reiser, B. A. Lau, and R. M. Nishikawa, "Effect of scan angle and reconstruction algorithm on model observer performance in tomosynthesis," in *Digital Mammography*. Springer, 2008, pp. 606–611.

[9] R. Zeng, S. Park, P. Bakic, and K. J. Myers, "Evaluating the sensitivity of the optimization of acquisition geometry to the choice of reconstruction algorithm in digital breast tomosynthesis through a simulation study," *Physics in medicine and biology*, vol. 60, no. 3, p. 1259, 2015. [Online]. Available: http://iopscience.iop.org/0031-9155/60/3/1259

Lattice Sampling Data Acquisition Scheme as an Alternative to Helical Scanning for X-ray Micro-CT

William M. Thompson

***Abstract*—Helical scanning is now beginning to find use in micro-CT for materials science and other applications, due to a desire to increase scanning throughput by increasing the cone angle to make best use out of available x-ray flux. In this situation, the cone beam artifacts from the routinely used circular scan become unacceptable. Whilst the helical trajectory satisfies Tuy's condition and offers theoretically exact reconstruction, it places a hard limit on the allowable pitch that may be used.**

In many micro-CT systems, the acquisition process can essentially be regarded as taking a series of discrete projections; therefore, there is no need for the source to follow a continuous trajectory. We present a technique based on a discrete distribution of source sampling points on a regular lattice, that removes the pitch limit, and may potentially offer higher scanning throughput while maintaining acceptable image quality.

I. Introduction

Cone beam x-ray micro-CT is now a widely-used imaging technique in materials science research [1]. Recently, it is also finding use in analysis of geological samples for oil exploration, where it is necessary to scan long cylindrical cores of rock at high resolution, in order to characterize the porosity. The standard technique for scanning such samples has been to perform multiple circular scans of the object, reconstruct each scan with the FDK algorithm [2] and "stitch" the resulting reconstructed volumes together.

This technique results in prohibitively long acquisition times for routine use, since in order to prevent unacceptable levels of cone beam artifacts in the reconstruction, the cone angle must be kept small, reducing the amount of x-ray flux incident on the detector. In order to speed up the acquisition time to an acceptable level, it is desirable to increase the cone angle; for this reason, use of the helical trajectory paired with exact reconstruction algorithms such as the methods in [3], [4] has been the subject of recent investigation.

Typically, micro-CT systems rotate the object in the path of the x-ray beam to scan with a circular trajectory. To achieve the equivalent of a helical trajectory, an additional object translation is introduced. Although in reality the object is moved, we adopt the standard convention that the source and detector move around the object, which is equivalent by a simple change in coordinate systems. We define the pitch of the helix as the ratio of the absolute translation distance per full source rotation to the detector length of a virtual detector located at the rotation axis.

Whilst the helical trajectory offers the capability of theoretically exact reconstruction, it has the problem that there is a hard limit imposed on the pitch of the helix. If pitch is increased beyond this value, then regions of the reconstruction volume no longer receive the required 180 degree angular range of illumination, introducing severe artifacts. A secondary disadvantage is that the regions of the volume towards the ends of the helical trajectory also do not receive the necessary 180 degrees illumination, which necessitates an over-scan of the trajectory in order to completely cover the region of interest.

The work presented here builds on the author's previous work presented in [5] and [6], extending this in generality to cover the micro-CT geometry. We demonstrate that through the use of a data acquisition scheme where the source points lie on a regular lattice surrounding the object, the disadvantages of the helical trajectory can be mitigated, allowing the pitch to be increased beyond the theoretical limits of the helical trajectory whilst maintaining acceptable image quality. If the time taken to move the system between acquisition points is small compared to the acquisition time of each projection, as is often the case in micro-CT of materials, then this can result in increased overall acquisition speed compared to the helical trajectory.

II. Methods

A. A Discrete Approach

The continuous helical trajectory makes complete sense for medical CT systems, where the source and detector are physically rotated about the object, and the acquisition time for each projection is short. However, in typical micro-CT systems there is no such constraint, and the system can be regarded as fixed during the acquisition of each projection. Therefore, the source can be moved to an arbitrary position for each projection, and we can consider the acquisition process as a set of discrete points.

If we assume that the source-rotation axis and rotation axis-detector distances remain constant during scanning, then the set of all possible source positions is a cylinder surrounding the object. Allowing the set of acquisition points to be chosen freely from the set of all possible positions, then instead of a source trajectory, we now have a pattern of discrete sampling points on the surface of a cylinder. Lattice sampling refers to the case when the sampling points are chosen so as to lie on a regular hexagonal grid, as shown in figure 1. This creates an even distribution of the source points, which, intuitively, should result in more even illumination of the object.

B. Generating an Optimal Lattice

A lattice sampling pattern may be generated from a discretized helical trajectory using a permutation of the possible

Carl Zeiss X-ray Microscopy, Pleasanton, CA 94588, USA. E-mail: william.thompson@zeiss.com

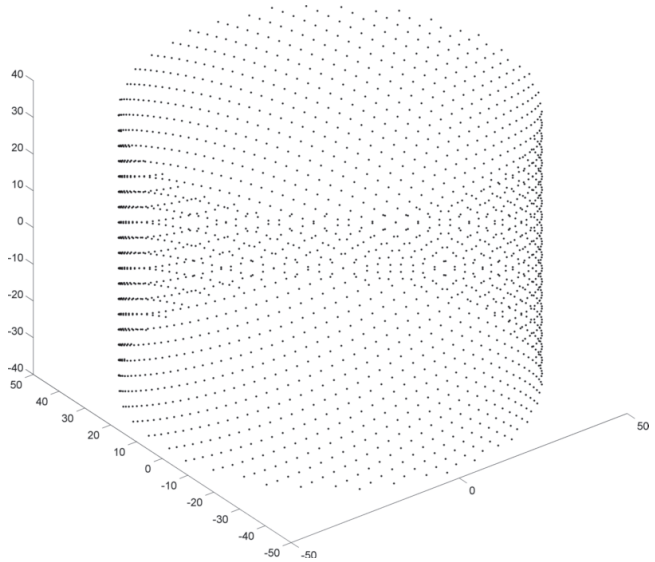

Fig. 1: Lattice sampling pattern (points represent source positions).

z positions for each angle, where the z-axis is defined as the axis of rotation. This results in a sampling pattern where the sets of angular positions and source z positions are the same as for the helical scan, only the order is changed.

In a similar terminology to the helical trajectory, we define each complete set of 360 degree projection angles as a revolution. Then analogous to the pitch of the helical trajectory, we also define the pitch of a lattice sampling pattern as the ratio of the range of z values for each revolution, to the detector length at the rotation axis.

The z coordinate of the i^{th} point on the lattice can be calculated by

$$z_i = \delta_z \Big[\big(k(i-1) \bmod N_A \big) + 1 \Big], \tag{1}$$

where N_A is the number of projection angles per revolution, k is some number coprime to N_A, and δ_z is the distance between consecutive z points. The number k is chosen so as to minimize the standard deviation of the distance of a point on the lattice to its 6 nearest neighbors. Since the lattice is rotationally symmetrical by construction, only one point need be considered, and any point may be chosen. The optimization is a simple empirical process due to the (usually small) finite number of candidate values of k. Note that the discretized helical trajectory can also be viewed as the special case of a lattice for $k = 1$. The optimal value of k depends on the number of projection angles per revolution, the pitch, and the source-rotation axis distance.

Figure 2 shows a flattened out section of the cylinder of possible source positions, with the sampling patterns for an optimized lattice, and the equivalent discretized helical trajectory. Note that the optimized lattice gives a far more even coverage.

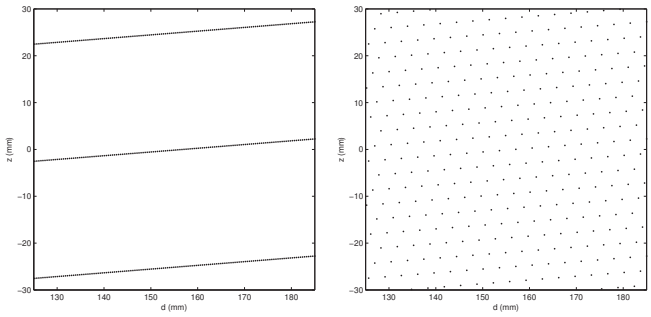

Fig. 2: Sampling patterns for discretized helical trajectory (left) and optimized lattice (right).

C. Reconstruction Algorithms

Due to their independence from any specific scanning geometry, the work so far has focused on iterative methods for reconstruction. Development of a faster analytical reconstruction method is currently under review.

III. Results

Noise-free simulated data were generated for a "multi-sphere" phantom, as shown in the top row of figure 3. Line integrals were calculated analytically using a simple length-of-intersection model, and assuming a mono-energetic spectrum. The phantom is made up of 11 layers of 110 spheres of random radius between 0.1 and 0.3mm, randomly positioned within a cylinder of radius 10mm. A uniform distribution was used for both the spheres' radii and positions. This phantom was chosen since it gives results broadly representative of objects that are often imaged in micro-CT of materials.

Datasets were generated for circle and helical trajectories, and optimized lattice sampling patterns. For the helical and lattice cases, two datasets were generated, the first with pitch 1, and the second with pitch 2. Each dataset consists of 720 projections; in the helical and lattice cases this covers one full revolution. Additionally, for comparison with the pitch 2 reconstructions, a pitch 1 helical dataset was generated with half the angular sampling rate, covering 2 full source revolutions. In each case, the source-rotation axis and rotation axis-detector distances were both equal to 25mm, with a 512×512 detector of size 50×50mm, giving a half-cone angle of approximately 26.5 degrees.

Figure 3 compares central and off-center x-y, and central x-z slices through the reconstructed volumes from the circle and pitch 1 helical and lattice datasets with the ground truth images of the phantom. The off-center x-y slices correspond to the outermost bottom layer of spheres. Figure 4 shows central x-y and x-z slices through the reconstructed volumes from the pitch 2 helical and lattice datasets, and the pitch 1 helical dataset with half angular sampling. In this case it did not make sense to include an off-center x-y slice, since the entire volume is within the fully sampled region of the acquisition scheme.

Reconstructions in each case were performed with 30 iterations of the CGLS algorithm, with forward and back projection

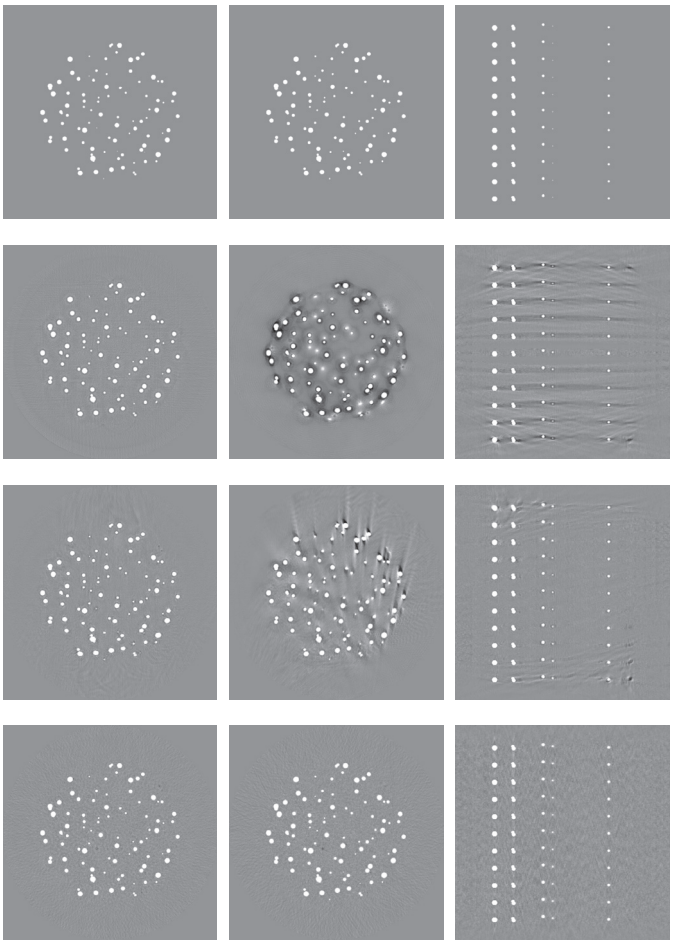

Fig. 3: Reconstructions of the pitch 1 simulated data with common grayscale window of $[-0.2, 0.2]$. Top row: ground truth; second row: circle trajectory; third row: helical trajectory; bottom row: lattice sampling. Left column: central x-y slice; middle column: off-center x-y slice; right column: central x-z slice

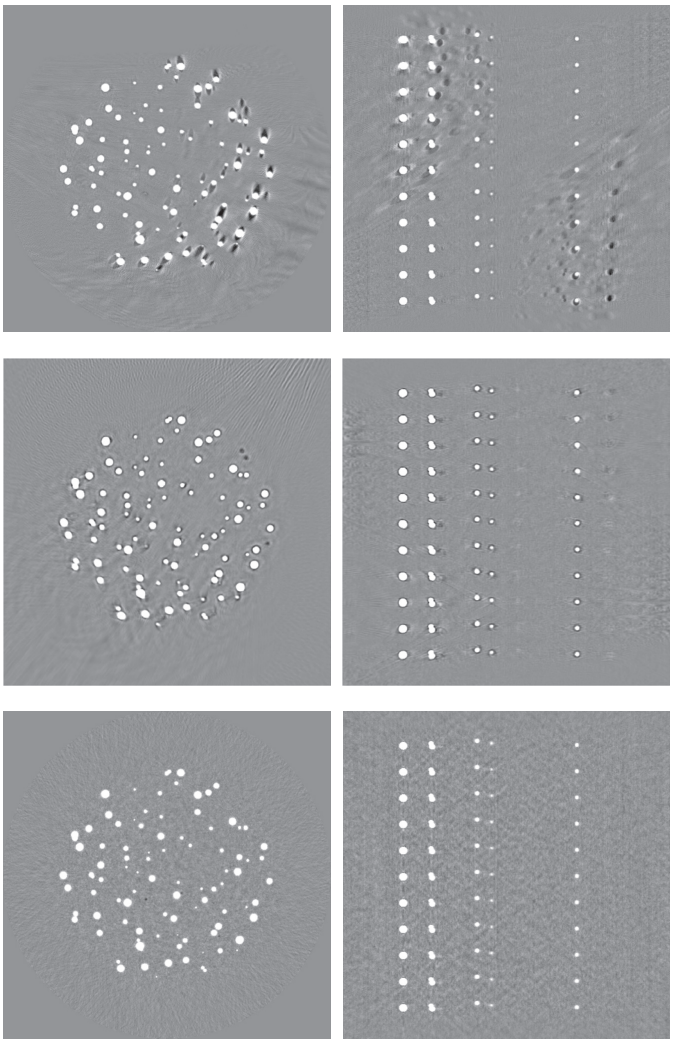

Fig. 4: Reconstructions of the pitch 2 and pitch 1 half angular sampling simulated data with common grayscale window of $[-0.2, 0.2]$. Top row: helical trajectory, pitch 2; middle row: helical trajectory, pitch 1 with half angular sampling; bottom row: lattice sampling, pitch 2. Left column: central x-y slice; right column: central x-z slice.

using the method described in [7]. Reconstructed volumes were of size 512^3 voxels. Figure 5 plots the 2-norm of the image error for particular x-y slices at each iteration in all cases.

IV. Discussion

Central x-y slices of the circle and pitch 1 helical and lattice reconstructions are all of good quality; the low level artifacts are most likely caused by aliasing due to the forward and back projection process used in the iterative algorithm. As expected, the off-center x-y slice of the circle scan reconstruction shows strong cone beam artifacts. The artifacts present in the off-center x-y slice of the helical scan are caused by the fact that this region of the volume is at the end of the helical trajectory, and as such, regions of the slice do not get the necessary range of illumination angles. The off-center x-y slice of the lattice reconstruction shows slightly increased noise and reduced sharpness, again caused by this slice being at the edge of the lattice sampling pattern. The artifacts are far less severe in the lattice case since the illumination angles are still evenly spread out, and only get sparser towards the edges. These observations are backed up by the image errors, which show similar error levels for the central slice in all cases. Significantly lower error is observed in the lattice case for the off-center slice, with a circle scan performing worst, as expected. This demonstrates that for a given length of object or region of interest, the necessary amount of extension of the scan in the z direction is lower for lattice sampling than for the helical trajectory.

The pitch 2 helical reconstructions show severe artifacts, due to the pitch exceeding the theoretical limit. Therefore, certain regions of the volume are not getting the necessary range of illumination angles. The equivalent lattice reconstructions,

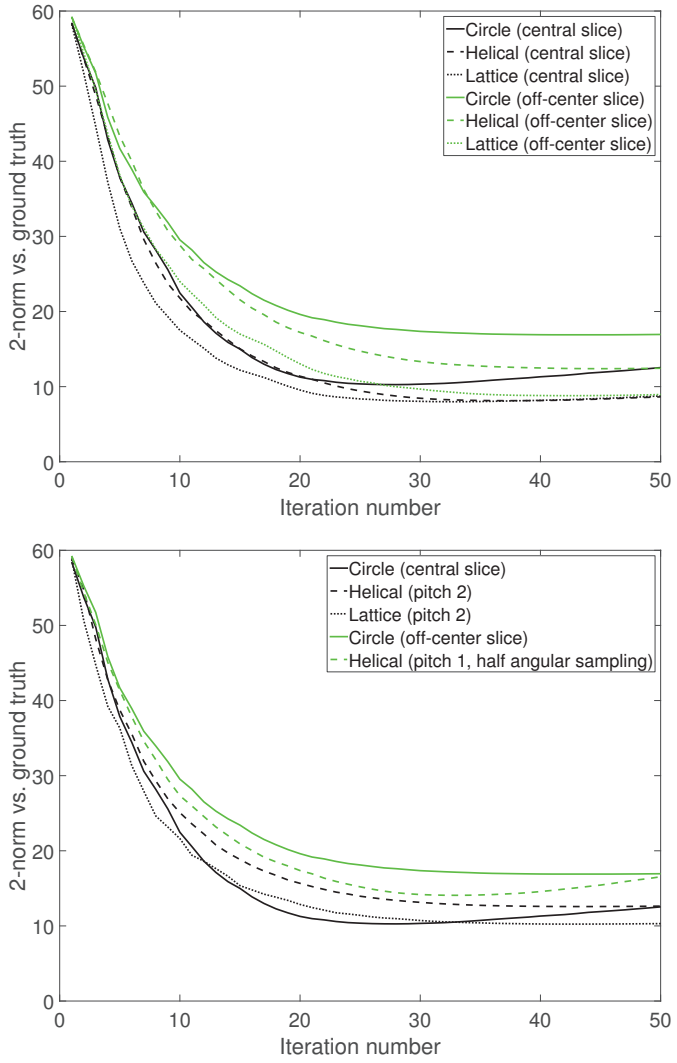

Fig. 5: 2-norm of image errors. Top: experiments with pitch 1; bottom: experiments with pitch 2, and pitch 1 with half angular sampling.

although showing more noise than the pitch 1 case, do not suffer from such artifacts, and are of acceptable quality. Again, these observations are supported by the image errors, showing lower error overall for the lattice case, compared to the helical trajectory.

The purpose of the pitch 2 comparison is to demonstrate that the strict limits on the pitch of the helical trajectory do not apply to lattice sampling; as the lattice pitch is increased, there is a gradual degradation in image quality. Through the use of reconstruction algorithms incorporating TV minimization [8], [9], or statistical methods incorporating edge-preserving regularization [10], it may be possible to mitigate this gradual degradation and extra noise, but it would not be possible to mitigate the severe artifacts caused by increasing the helix pitch beyond its limit. The lattice acquisition scheme may therefore be able to offer increased scanning throughput compared to helical scanning.

Alternatively, with the helical trajectory, in order to cover an increased length of the object with the same number of projections, the pitch can be kept constant, within the theoretical limit, and the angular sampling rate reduced. For this reason, a helical scan covering 2 revolutions at pitch 1, with half the angular sampling rate, was added to the comparisons. Although in this case the severe systematic artifacts are eliminated, there is still a higher overall level of error than with the pitch 2 lattice scan. It is possible that these errors could be reduced by using an exact analytical algorithm, but that was outside the scope of this investigation.

V. Conclusions

By placing source positions on a regular hexagonal lattice on a cylinder surrounding the object, we have demonstrated that the pitch can be increased beyond the theoretical limit for helical scanning, whilst still maintaining acceptable image quality. An equivalent number of x-ray projections may therefore be taken over an increased range in z, offering the potential for increased scanning throughput.

Although this method is clearly not relevant for medical scanners, where source motion is generally continuous, it is well-suited to micro-CT systems where the acquisition time per projection may be long, and there is complete freedom of movement of the system between successive projections. This work demonstrates that in such a system, the helical trajectory may not be the optimal acquisition protocol. Testing of the lattice sampling technique on real experimental samples is currently in progress.

References

[1] E. Maire and P. J. Withers, "Quantitative x-ray tomography," *International Materials Reviews*, vol. 59, no. 1, pp. 1–43, 2014.
[2] L. A. Feldkamp, L. C. Davis, and J. W. Kress, "Practical cone-beam algorithm," *J. Opt. Soc. Am. A*, vol. 1, no. 6, pp. 612–619, Jun 1984.
[3] A. Katsevich, "Analysis of an exact inversion algorithm for spiral cone-beam CT," *Physics in Medicine and Biology*, vol. 47, pp. 2583–2597, 2002.
[4] ——, "Improved exact filtered back-projection algorithm for spiral CT," *Advances in Applied Mathematics*, vol. 32, pp. 681–697, 2004.
[5] W. M. Thompson and W. R. B. Lionheart, "Optimisation of the source firing pattern for real time cone-beam tomography," in *Fully 3D 2011*, 2011, pp. 335–338.
[6] W. M. Thompson, W. R. B. Lionheart, and D. Öberg, "Reduction of periodic artefacts for a switched-source x-ray CT machine by optimsing the source firing pattern," in *Fully 3D 2013*, 2013, pp. 345–348.
[7] W. M. Thompson and W. R. B. Lionheart, "GPU accelerated structure-exploiting matched forward and back projection for algebraic iterative cone beam CT reconstruction," in *The CT Meeting 2014*, 2014, pp. 355–358.
[8] E. Y. Sidky and X. Pan, "Image reconstruction in circular cone-beam computed tomography by constrained, total-variation minimization," *Physics in Medicine and Biology*, vol. 53, no. 17, p. 4777, 2008.
[9] X. Pan, E. Y. Sidky, and M. Vannier, "Why do commercial CT scanners still employ traditional, filtered back-projection for image reconstruction?" *Inverse Problems*, vol. 25, no. 12, p. 123009, 2009.
[10] J. A. Fessler, M. Sonka, and J. M. Fitzpatrick, "Statistical image reconstruction methods for transmission tomography," in *Handbook of Medical Imaging, Medical Image Processing and Analysis*. SPIE, 2000, vol. 2, pp. 1–70.

A software tool for the design and simulation of X-ray acquisition protocols

Álvaro Martínez*, Alba García-Santos*, Inés García, Estefanía Serrano, Javier García, Claudia de Molina, Ramón Polo, Manuel Desco, Mónica Abella

Abstract— The availability of digital X-ray detectors, together with the development of new reconstruction algorithms, open the opportunity to the development of new techniques that provide 3D capabilities to conventional radiology systems. These rely on the acquisition of a limited number of projections with non-standard geometrical configurations. Computer simulations are a valuable tool to explore the possibilities of these techniques before its actual implementation on real systems.

We present a software tool for the design and simulation of X-ray acquisition protocols. It can be used to study the viability of new acquisition protocols on a specific real system or to design the optimal system for a given functionality.

Through a graphical user interface it allows defining flexible projection geometries for any X-ray system configuration. The software provides a preview of the simulated projections and a preliminary reconstruction through GPU-accelerated kernels, as well as the scanned field of view (FOV) and the estimation of the total radiation dose, to allow the evaluation of the protocol in real time.

We show the utility of the software with a preliminary evaluation based on the design of a tomosynthesis protocol and the comparison of the simulated projections with the ones obtained from the real X-ray system.

Index Terms—X-ray, simulation, acquisition protocols, tomography.

I. INTRODUCTION

In the past decades there has been a rapid advance towards the use of digital equipment in radiology. The introduction of digital detectors, together with a more flexible movement of the system, opened the possibility of obtaining 3D information from conventional X-ray systems using flexible geometrical configurations. This allows bringing tomography in situations in which a CT system is not available, such as, for instance, during surgery or ICU.

On the other hand, there is great social concern regarding the radiation dose delivered to the patient. New imaging protocols are aimed at improving image information while reducing the dose to the minimum possible value, according to the ALARA principle ("As Low As Reasonably Achievable").

In this context, computer simulations are a valuable tool to explore the possibilities of new acquisition schemes before implementing them on real systems. Several simulation tools that model X-ray image generation [1]–[4] have been developed in recent years. These are able to simulate the acquisition of 2D images or tomographic studies. However, restrictions generally apply regarding the positioning of the source and the detector, which reduce the ability to simulate new acquisition protocols based on not-standard setups. Furthermore, they do not provide a straightforward method to adapt the positioning of the elements to a real acquisition system.

In this work, we present a tool that makes it possible to design flexible acquisition geometries and protocols adapted to specific system configurations, performing simulations in near real-time thanks to GPU acceleration and providing additional information such as the scanned FOV, the preliminary reconstruction or the dose estimation.

II. METHODS

The purpose of this software tool is to enable the design and simulation of X-ray acquisition protocols. It allows defining flexible projection geometries through a graphical user interface which provides a near real time preview of the acquisition thanks to a fast implementation of a projection kernel. The tool is mainly implemented in MATLAB, with the exception of the projection kernel, which is developed in CUDA to benefit from GPU acceleration techniques.

We define a *protocol* as a set of *positions* defined by the placement and orientation of the X-ray source, patient and detector in the acquisition system. The protocol creation workflow is outlined in Fig. 1.

The first step is to define a set of rules and constraints that affect the placement of the three elements for a given X-ray system (panel 1 of Fig. 2). We refer to this as *system definition*. For instance, a *system definition* may allow moving the source and detector in opposite directions while keeping the FOV centered in the patient's region of interest, replicating a tomosynthesis acquisition.

* These authors contributed equally to this work.

Manuscript submitted March 28th 2016. This work was funded by the projects IDI-20130301, TEC2013-47270-R, IPT- 2012-0401-300000, RTC-2014-3028-1 and the Cardiovascular Research Network (RIC, RD12/0042/0057) from the Spanish Ministerio de Economía y Competitividad (www.mineco.gob.es/).

A. Martínez, A. García-Santos, I. García, C. de Molina, Ramón Polo, M. Desco and M. Abella are with the Biomedical Engineering Department, University of Carlos III, Madrid, Spain and with the Instituto de Investigación Sanitaria Gregorio Marañón (IiSGM), Madrid, Spain (e-mail: mabella@ing.uc3m.es).

M. Desco is also with the Centro de Investigación en Red de Salud Mental (CIBERSAM, CIBER CB07/09/0031), 28007 Madrid, Spain.

E. Serrano and J. García-Blas are with the Computer Architecture and Technology Area, University Carlos III, Madrid Spain.

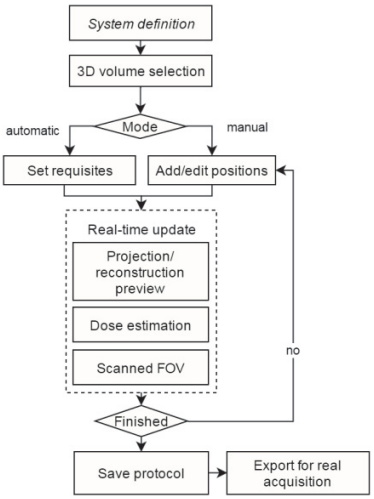

Fig. 1. General workflow followed when creating an acquisition protocol.

After the selection of the 3D volume representing the density map of the patient, the design of the *protocol* is done interactively by adding individual *positions*. The placement of the three elements for each *position* is done through the graphical user interface (GUI) shown in panel 2 of Fig. 2, taking into account the restrictions of the *system definition*. Alternatively, the *positions* can be automatically generated through the definition of final requirements like the size of the scanned FOV, defined as the intersection of all the views, which is shown as a solid polygon.

The preview of the resulting images for each *position* (panel 4 in Fig. 2) is done through a pixel-driven projection kernel. This requires translating the geometry defined in the *real coordinate system*, used for the positioning and angulation of the three elements within the real system, to a second one called the *object coordinate system* (Fig. 3), which is the one used by the projection kernel. We define a *virtual detector* that is placed orthogonally to the line that passes through the source and the origin; the intersection of this line with the *virtual detector*'s plane is denoted as p_{vd}, and corresponds with its center.

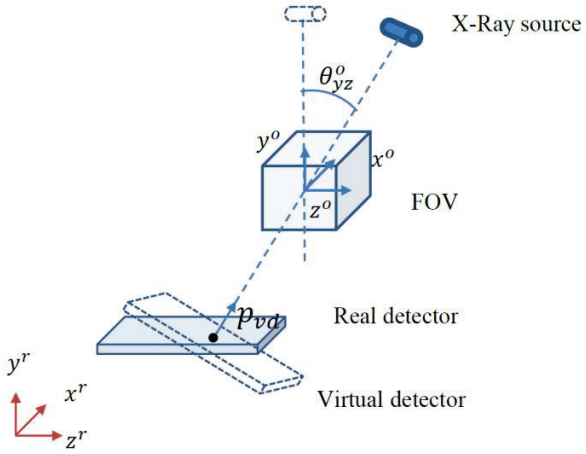

Fig. 3. Visual description of the two coordinate systems used to represent the position of the three elements in the GUI and the projection/backprojection kernels.

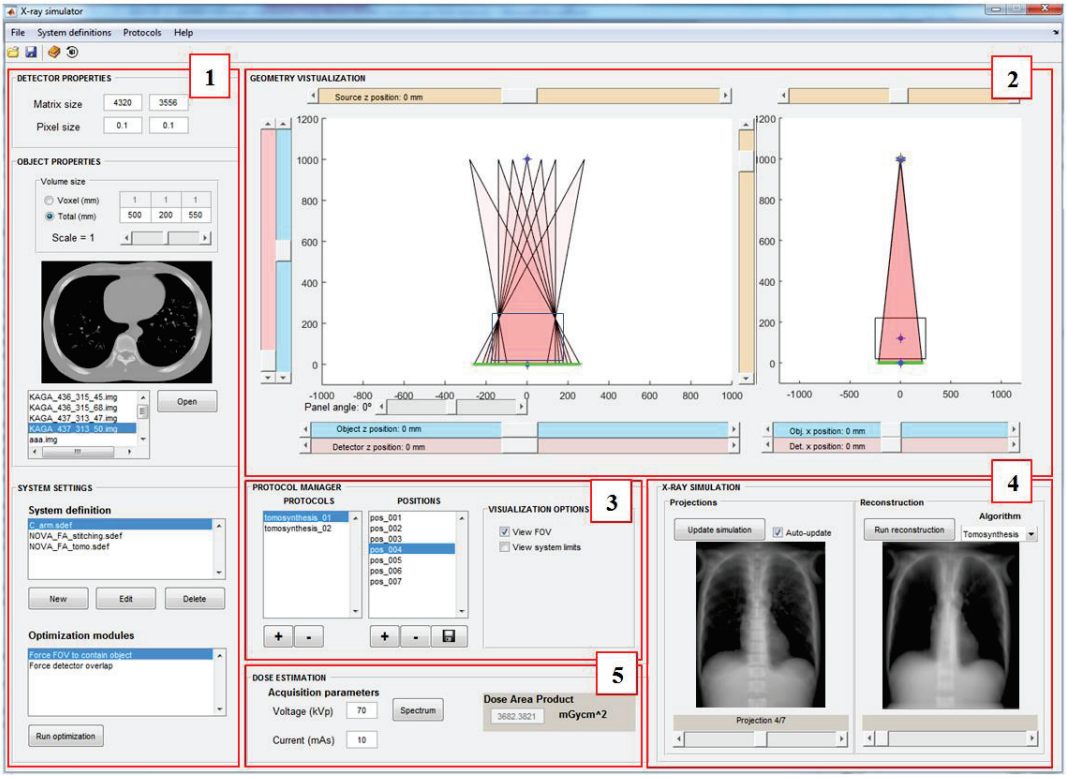

Fig. 2. Graphical user interface of the protocol design tool. The system definition and 3D volume are set in (1), each position is defined in (2) and managed through (3). Simulation is launched and previewed in panel (4). The source spectrum, KV and mAs are set in (5), which also shows the dose estimation.

Any real detector's position in the *object coordinate system* is expressed as a set of linear displacements and angular tilts applied to a *virtual detector* position, as shown in Fig. 4. This optimal virtual detector is located by first calculating the linear displacement (Δ_z in Fig. 4) so that the source-object line passes through the center of the detector, coincident with the p_{vd} point of the virtual detector. The tilting (θ_{yz} in Fig. 4) is then calculated as the angles formed between the real and virtual detectors.

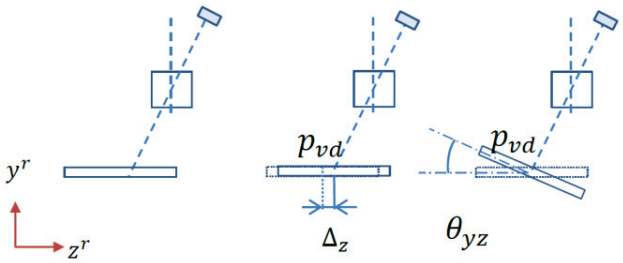

Fig. 4. Calculation of the detector position in the object coordinate system.

The attenuation of the X-rays traversing a material or tissue is modeled by the Beer Lambert Law expressed in Eq. 1,

$$I = \sum_k I_0(\varepsilon_k) \cdot e^{-\sum_i \, mac_i(\varepsilon_k) \int_L \, \rho_i dl} \qquad (1)$$

where $I_0(\varepsilon_k)$ is the energy spectrum, mac_i and ρ_i are respectively the mass attenuation coefficient and density map of material i, and $\int_L \, \rho_i dl$ is the result of the projection kernel. The energy spectrum, as well as the mass attenuation coefficients and density thresholds for each material are provided in text files along with the raw volume data. The $-\log(I)$ projection images are displayed on panel 4 of Fig. 2.

Panel 4 of the GUI additionally displays a preview of the reconstruction, obtained by one of the two currently available methods: an FDK-based kernel implemented in CUDA, and the shift-and-add algorithm for tomosynthesis.

In order to evaluate the tradeoff between image quality and radiation dose, an estimation of the Dose Area Product (DAP) is also performed and showed in the GUI. The DAP used in assessing the radiation risk [5], is calculated for each projection following Eq. 2,

$$DAP(mGycm^2) = n_0 \cdot C \cdot \left(\frac{KV}{80}\right)^{\alpha} \cdot \left(\frac{100}{d}\right)^2 \cdot T \qquad (2)$$

where C corresponds to the used tube current (mAs), d to the focal distance in cm, T to the field size (cm^2), n_0 to the reference beam quantity, and α characterizes beam quantity dependence with Kilo-voltage. The reference beam quantity is previously obtained at 80kV and a source-to-detector distance of 100cm according to Eq. 3,

$$n_0 = \frac{D_{80kV,100cm}(mGy)}{C_0(mAs)} \qquad (3)$$

Once a protocol is designed, its *positions* can be translated into the real system taking into account its own coordinate system and units, included in the *system definition* file.

III. PRELIMINARY VALIDATION

Preliminary evaluation of the tool was done based on the Sedecal NOVA FA digital radiography system shown in Fig. 5, which consists of an automatic ceiling suspension, a mobile elevating table and a tilting vertical wall stand system.

Fig. 5. Picture of the NOVA FA radiography system

We created a *system definition* file representing a tomosynthesis configuration in which the patient is placed on the table and both the X-ray tube and the detector follow a linear trajectory with opposite directions. These are shown in Table 1.

Movement range (mm)	x	y	z
Source	0	*1000*	[-800,800]
Detector	0	0	[-400,400]
Angular range (º)	θ_{xy}	θ_{yz}	θ_{zx}
Source	0	[-30,30]	0
Detector	0	0	0

Table 1. *System definition* for the tomosynthesis protocol. Only relevant parameters are listed. The values in gray are locked, the ones in cursive are common to all positions and the rest can be freely set withing the allowed ranges.

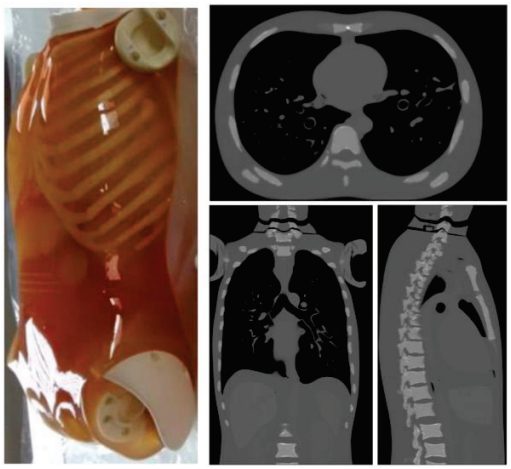

Fig. 6. Picture of the PBU-50 antropomorphic phantom (left) and axial, coronal and sagittal views of the CT volume (right).

The sample is a life-size human thorax phantom (PBU-50 model shown in Fig. 6, manufactured by Kyoto Kagatu), acquired previously with a Toshiba Aquilion/LB (512×512×1645 voxels, 0.931×0.931×0.5 mm voxel size). Axial, coronal and sagittal slices of are also shown in Fig. 6.

We created a tomosynthesis protocol with seven *positions* setting the source-to-detector distance to 1500 mm at the central position, and the appropriate constraints to cover the desired FOV. Fig. 7 shows a diagram of the described acquisition protocol.

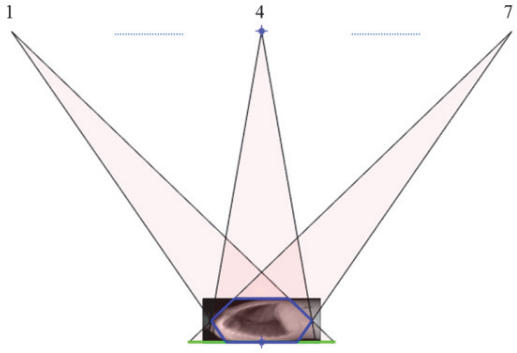

Fig. 7. Diagram representing three of the seven positions of the designed tomosynthesis protocol. The blue polygon outlines the total scanned FOV.

The obtained *positions* were translated into the coordinates of the real system in order to perform the acquisition of the phantom. The images were acquired with a Perkin Elmer XRpad 4336 flat panel detector with a pixel size of 100 µm and a matrix size of 4320×3556 pixels.

The capture of the GUI in Fig. 2 shows the results of both the projection and reconstruction (using the *shift-and-add* algorithm) in panel 4.

Fig. 8 shows three of the seven images resulting from the simulation and the real acquisition.

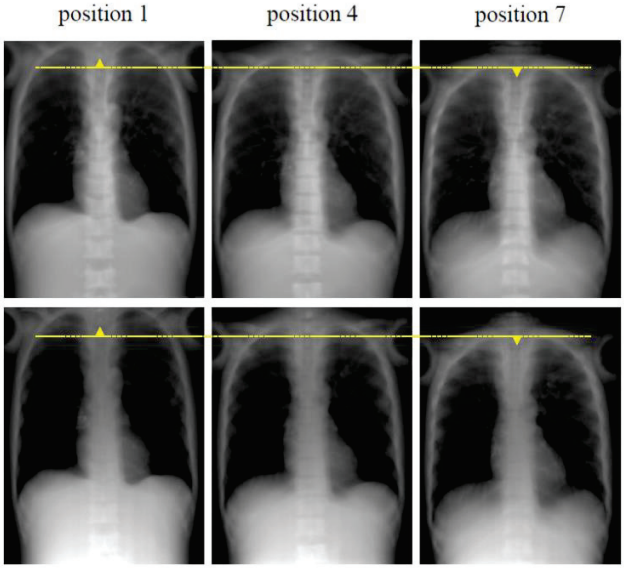

Fig. 8. Comparison between the simulated projections (upper row) and the ones acquired with the real system (bottom row). Only three of the seven positions are shown.

The dotted lines in Fig. 8 highlight the high degree of similarity between the simulated and real data.

IV. DISCUSSION

We have presented a software tool to support the design of X-ray acquisition protocols, that can be used to asess the viability of different acquisition schemes on a real system, as well as to define the optimal system requirements for a specific protocol.

Through a graphical user interface it allows defining sets of flexible projection geometries taking into account the constraints of a given X-ray system configuration. The software provides a near real-time preview of the acquisition and an estimation of the total radiation dose.

The projection kernel takes into account the geometry of the system and the polycromatic nature of the spectra but does not include the scatter estimates.

Preliminary evaluation has been done using the software to design and simulate a tomosynthesis protocol, and to export the *positions* in order to perform a real acquisition. The results showed a high degree of similarity between the simulated and the real data.

The modular approach followed through the design and implementation of this tool allows easy integration of new modules and features. We are currently working on the integration of new reconstruction kernels including other tomosythesis geometries and iterative reconstruction methods for limited angle tomography.

REFERENCES

[1] P. Duvauchelle, N. Freud, and D. Babot, “A computer code to simulate X-ray imaging techniques,” vol. 170, pp. 245–258, 2000.

[2] V. Fanti, R. Marzeddu, G. Massazza, and P. Randaccio, “A simulation tool to support teaching and learning the operation of X-ray imaging systems.,” *Med. Eng. Phys.*, vol. 27, no. 7, pp. 555–559, 2005.

[3] G. Landry, F. deBlois, and F. Verhaegen, “ImaSim, a software tool for basic education of medical x-ray imaging in radiotherapy and radiology,” *Front. Phys.*, vol. 1, no. November, pp. 1–7, 2013.

[4] E. Gallio, O. Rampado, E. Gianaria, S. D. Bianchi, and R. Ropolo, “A GPU Simulation Tool for Training and Optimisation in 2D Digital X-Ray Imaging,” *PLoS One*, vol. 10, no. 11, p. e0141497, 2015.

[5] S. J. Shepard, P. P. Lin, J. M. Boone, D. D. Cody, J. R. Fisher, H. Glasser, J. E. Gray, A. G. Haus, L. V Hefner, R. L. Holmes, F. N. Ranallo, P. L. Rauch, R. P. Rossi, K. J. Strauss, and S. K. Thompson, “Quality Control in Diagnostic Radiology,” Medical Physics Publishing, 2002.

Comparison Weighted Energy Bin *vs.* Weighted Basis Material CT Images

Paurakh L. Rajbhandary and Norbert J. Pelc

Abstract— Spectral imaging systems need to be able to produce "conventional" looking images, and it's been shown that systems with energy discriminating detectors can achieve higher CNR than conventional systems by optimal weighting. Combining measured data in energy bins (EBs) and also combining basis material images have previously been proposed, but there are no studies systematically comparing the two methods. In this paper, we evaluate the two methods for systems with ideal photon counting detectors using CNR and beam hardening (BH) artifact as metrics. For both linear comb-stick spectrum with one delta function per EB and 120-kVp polychromatic simulations, the difference of the optimal CNR between the two methods for the studied phantom is within 1%. For a polychromatic spectrum, beam-hardening artifacts are noticeable in EB weighted images (BH artifact of 3.8% for 8 EB and 6.9% for 2 EB), while weighted basis material images are free of such artifacts.

***Index Terms*— conventional CT images, photon counting detector, optimal CNR.**

I. Introduction

The development of imaging systems with energy discriminating detectors is especially motivated by increased material specificity, but the systems also need to be able to produce "conventional" looking images. Indeed, they ideally should outperform energy integrating detectors in this regard. Schmidt showed that combining energy bin (EB) images (equivalent to post-log combination assuming a linear reconstruction algorithm) offered better CNR and less severe artifact compared to pre-log combination and other methods [1-4]. Combining basis material images produces “equivalent monochromatic” images and depending on the energy, they can have high CNR. In addition, combining basis material images may be more convenient since the data storage may be lower, the system may produce them for other reasons, and the images can be quantitative. While both approaches have been described, there has been no comparison between combined EB images and combined basis material images. We perform the comparative study and show the effects on CNR and BH artifacts for the two methods, both of which can affect image quality and detectability.

P. L. Rajbhandary is a graduate student in Electrical Engineering and N. J. Pelc is professor of Bioengineering and Radiology at Stanford University, California, USA (email: paurakh@stanford.edu).

II. Methods

A. Combining CT images

Schmidt showed that images formed by optimally weighted EB images (Fig. 1a) give superior CNR compared to images formed by pre-log intensity weighting. Optimal weights α in Fig. 1a have been previously established [1]. Effective monochromatic images can be formed using weighted basis material images (Fig. 1b). Basis material images can be formed using a material decomposition estimator [5].

B. CNR Metric

CNR for evaluation is derived using noiseless simulation and analytic derivation of noise. For example, for detectors with five energy bins, the analytic noise map for weighted EB images (Fig. 1a) is derived assuming uncorrelated energy bins as

$$\sigma^2_{\mathrm{Im}} = \alpha[1]^2\,\sigma^2_{\mathrm{Im}[1]} + \alpha[2]^2\,\sigma^2_{\mathrm{Im}[2]} + \cdots + \alpha[5]^2\,\sigma^2_{\mathrm{Im}[5]}, \qquad [1]$$

where $\sigma^2_{\mathrm{Im}[i]}$ is the variance map of i-th energy bin obtained using propagation through reconstruction process.
The analytic noise map for combined basis material images (Fig. 1b) is derived as

$$\sigma^2_{\mathrm{Im}} = \beta[1]^2\,\sigma^2_{\mathrm{Im}[B1]} + \beta[2]^2\,\sigma^2_{\mathrm{Im}[B2]} + 2\beta[1]\beta[2]\sigma_{\mathrm{Im}[B1],\mathrm{Im}[B2]}, \qquad [2]$$

where $\sigma^2_{Im[B1]}$ and $\sigma^2_{Im[B2]}$ are variance maps for basis material images, and $\sigma_{Im[B1],\ Im[B2]}$ is the covariance map between basis material images since these will have significant noise correlation. Variances and covariance of basis material images are obtained using propagation of Cramér-Rao Lower Bound (CRLB) through the reconstruction process. The CRLB gives the lower bound on noise of estimates any unbiased material decomposition algorithm can achieve. Irrespective of material decomposition estimator, the CRLB allows comparison of the best performance of combined basis material images to the combined EB image method.

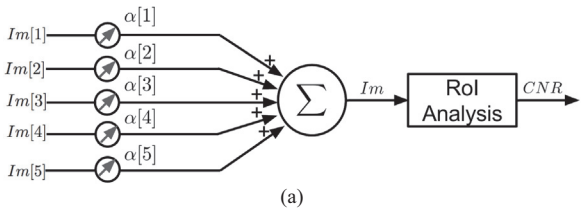

(a)

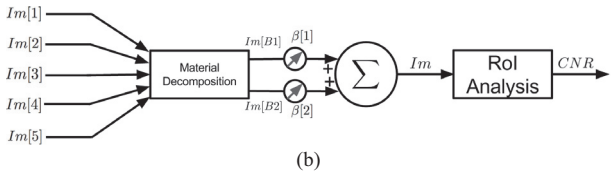

(b)

Fig. 1. (a) Combining EB images and (b) combining material decomposition images to form conventional CT images.

Contrast is calculated as the difference between the average pixel value of a region of interest within the contrast material and local background (water). Since the background pixel values are location dependent (due to BH artifact), selection of the background region can alter the estimated CNR. We therefore obtain local background for contrast estimation from a second phantom simulation with no contrast inserted and using the same ROI as for the contrast insert. This makes CNR estimation robust against beam hardening.

A water cylinder phantom with four pairs of contrast regions – 2 mg/cm^3 iodine, 7.5 mg/cm^3 CaCO3, adipose, and blood – is simulated (Fig. 2a). We also simulated an anthropomorphic head phantom, in which beam hardening artifacts can be caused by bone, to evaluate differences in artifacts between the two methods and see effects on detectability.

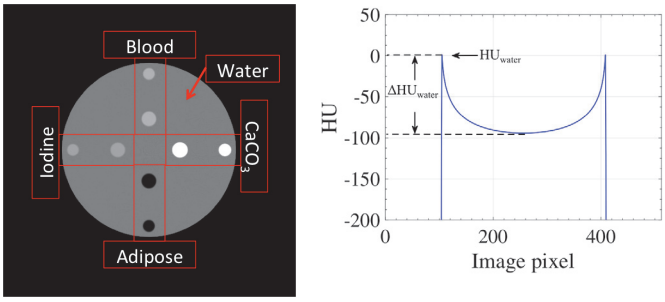

(a) (b)

Fig. 2. (a) Contrast phantom with four contrast material and bone inserts in water cylinder. (b) Line profile along the center of plain water cylinder showing parameters used for the measure of beam hardening artifact.

C. Optimal Weights

Optimal weights β for combining basis materials (Fig. 1b) is calculated with optimization of CNR in the selected contrast region of interest as

$$\beta^* = \underset{\beta}{\operatorname{argmax}}\ \mathrm{CNR}_{MD} = \frac{Im_{contrast} - Im_{background}}{\sigma_{Im,local}} \quad [3]$$

The optimization will yield different values of β based on selected contrast region, and is therefore task-dependent. For example, optimizing iodine contrast versus adipose contrast may yield different β^*. Once an optimal β^* is estimated for a certain task, it is applied to all the pixels in the image.

D. Beam Hardening Metric

BH artifact primarily appears as cupping artifact and streaks between dense objects. When these artifacts are present, they can occlude features. The goal of the study is the compare CNR and BH artifact, both of which in effect can affect detectability.

Beam hardening in images is measured as the percentage-cupping artifact relative to the signal at the edge of the water cylinder (Fig. 2b) as

$$BH = \frac{\Delta HU_{water}}{HU_{water}} \times 100\% \quad [4]$$

BH in the anthropomorphic head image was assessed subjectively.

III. Results

A. Images and Line Profile

Below are the results when the optimal weights α and β are optimized for iodine contrast, but a similar trend is found for other materials. Cupping artifact is visible in polychromatic weighted EB images (Fig. 3a). It is also worth noting that due to cupping, the HU levels of the same contrast material at different radial positions are not consistent in weighted EB images (Fig. 4). For weighted basis material images, there is no cupping artifact, as the material decomposition estimator accounts for non-linear processes such as beam hardening.

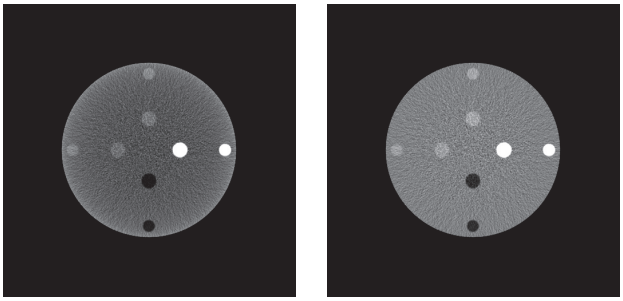

(a) (b)

Fig. 3. CT image with contrast optimized for iodine using (a) EB image weighting and (b) MD image weighting. 2 EB detector with 120 kVp spectrum [- 200 200].

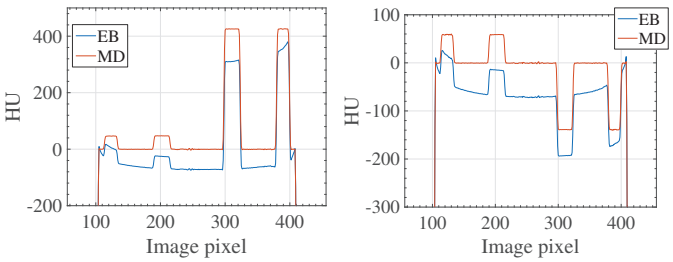

(a) (b)

Fig. 4. (a) Horizontal and (b) vertical line profile of CT images with CNR optimized for iodine. 2 EBs with a 120-kVp spectrum.

B. CNR and BH Artifact

Two sets of simulations were performed – one with a comb-stick spectrum with a single delta-function in each EB and the other with a continuous polychromatic spectrum. With comb-stick spectra, weighted EB and weighted basis images show effectively the same CNR for 2, 5 and 8 EBs (Fig. 5a). Similarly, the CNR is progressively increasing with more EBs. In this case, the material decomposition algorithm is effectively a linear mapping from energy bins to basis materials. Fig. 5b also shows that for comb-stick spectra, as

expected, there is negligible BH artifact for all EBs since the log approximation of line integral is accurate.
In the 120 kVp polychromatic simulation, weighted EB images provide less than 1% better CNR than weighted basis material images (Fig. 5a). The benefit of increasing the number of energy bins is also visible in polychromatic simulation as well. The material decomposition algorithm for polychromatic x-ray is a non-linear process and transforms from N energy bins to two basis materials, correcting for any non-linear process such as beam hardening effect. For EB weighted images, BH is visible and it reduces from 6.9% to 3.8% when increasing the number of EBs from 2 to 8 (Fig. 5b). BH artifact for weighted basis material images is negligible.

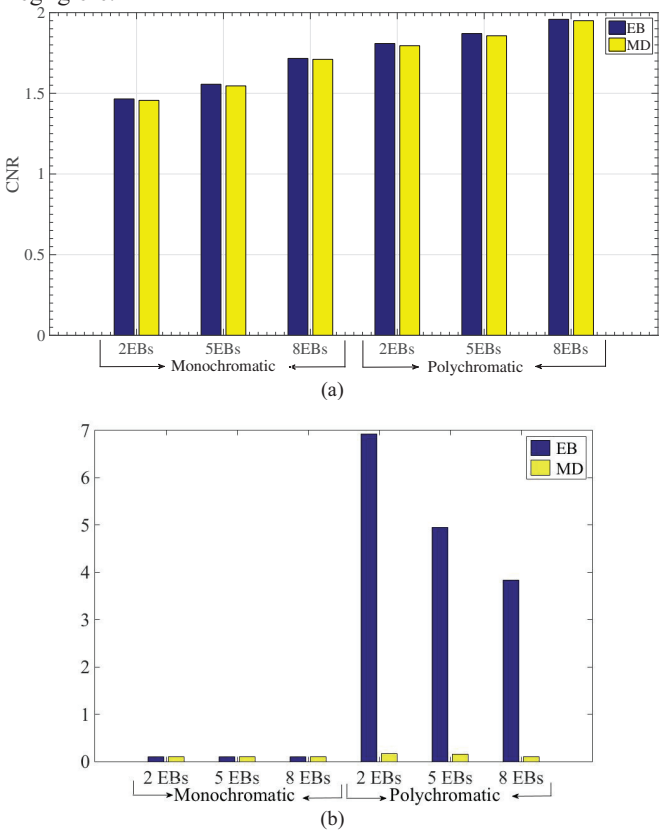

Fig. 5. (a) Iodine CNR for monochromatic, and (b) polychromatic spectrum for different EB detectors.

Fig. 6 shows a comparison of CT images of the anthropomorphic phantom formed by weighted EB and basis material images. In weighted energy bin images (Fig. 6a), BH artifact is visible as dark and bright streaks between and around dense bones. If such artifacts are present over features of interest, this could impact detectability. In weighted basis material images (Fig. 6b), there is no discernable BH artifact. Circular low contrast iodine was inserted in the posterior fossa (shown by the read arrow in Fig. 6). CNR for weighted energy bin and weighted basis material images are 1.0526 ± 0.0004 and 1.0462 ± 0.0005, respectively. Weights were optimized for the inserted low contrast iodine.

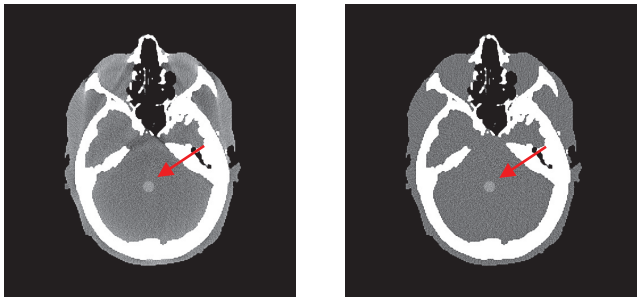

Fig. 6. Simulated brain CT showing (a) beam hardening artifact (red arrows) in CT image formed using EB image weighting, and (b) artifact free image formed using material decomposition weighting. 2 EB detector with weights optimized for iodine are used; display window [-150 150]

IV. Conclusions

Basis material weighted image offers artifact free CT images with CNR that is comparable to weighted energy bin images. The improvement in reduction in BH artifact is more significant at low number of energy bins, as there is more beam hardening with wide energy bin. This shows that given an accurate and noise optimal material decomposition estimator, producing conventional CT images using weighted basis material images will offer similar CNR with no non-linear artifacts. BH effects seen in weighted energy bin images – like cupping artifacts, inconsistent HU of same material at different location, and streaking artifact between dense objects – can affect detectability of subtle features in images. It may be possible to achieve higher CNR by varying the weighting parameter within a single scan from pixel-to-pixel, and will be explored further.

Acknowledgment

The authors would like Taly G. Schimdt and Scott S. Hsieh for valuable discussion to the project. This work was sponsored by Philips Healthcare.

References

[1] T. G. Schmidt, “Optimal “image-based” weighting for energy-resolved CT,” Medical physics, 36(7), 3018-3027 (2009).
[2] R. Alvarez and E. Seppi, “A comparison of noise and dose in conventional and energy selective computed tomography,” Nuclear Science, IEEE Transactions on, 26(2), 2853-2856 (1979).
[3] P. M. Shikhaliev, “Energy-resolved computed tomography: first experimental results. Physics in medicine and biology,” 53(20), 5595 (2008).
[4] J. Giersch, D. Niederlöhner and G. Anton, “The influence of energy weighting on X-ray imaging quality,” Nuclear Instruments and Methods in Physics Research Section A: Accelerators, Spectrometers, Detectors and Associated Equipment, 531(1), 68-74 (2004).
[5] P. L. Rajbhandary, S. S. Hsieh and N. J. Pelc, “Segmented targeted least squares estimator for material decomposition in multi bin pcxds,” Proc. SPIE Medical Imaging, pp. 903319-903319 (2014).
[6] X. Wu, D. A. Langan, D. Xu, T. M. Benson, J. D. Pack, A. M. Schmitz, E. J. Tjacztjm, J. Leverentz and P. Licato, “Monochromatic CT image representation via fast switching dual kVp,” Proc. SPIE Medical Imaging pp. 725845-725845, (2009)

X-ray Tensor Tomography: How much to measure?

Yash Sharma*†, Matthias Wieczorek†, Christoph Jud*, Florian Schaff*, Franz Pfeiffer*‡ and Tobias Lasser†

*Lehrstuhl für Biomedizinische Physik, Physik-Department and Institut für Medizintechnik, Technische Universität München
†Computer Aided Medical Procedures, Technische Universität München
‡Institut für diagnostische und interventionelle Radiologie, Klinikum rechts der Isar, Technische Universität München
Email: y.sharma@tum.de

***Abstract*—X-ray Tensor Tomography (XTT) is a novel imaging modality for reconstructing three-dimensional scattering tensors from dark-field projections obtained in a grating interferometer. However, the method currently suffers from long acquisition times owing to large number of radiographs required for the reconstruction algorithm. In this work, we study the effect of acquisition time on the result of XTT reconstruction. In order to do so, we propose a numerical method for the quantification of sparse acquisition schemes and compare the predicted results to the experimentally obtained results. This work presents a first step for designing sparse acquisition schemes with clinically relevant measuring times for XTT.**

I. Introduction

X-ray imaging using a grating interferometer [1] enables the measurement of absorption, differential phase and dark-field contrast simultaneously. All three modalities provide complimentary information, which is widely used to enhance the capabilities of conventional X-ray CT for both biomedical and material science applications. Absorption contrast is generated by the absorption of X-rays when they pass through the specimen, the shift in the phase of the X-rays is recorded as the phase contrast signal and the dark-field contrast originates from the ultra small scattering of X-rays by sub-micron sized structures. The dark-field signal is measured as a loss of visibility in the grating interferometer and is dependent on the orientation of the scattering structure with respect to the interferometer sensitivity axis [2], [3], [4]. Thus, by varying the relative orientation of a scattering structure with respect to the interferometer, it is possible to deduce information about its orientation from the variations in the dark-field signal.

Two dimensional structure orientations can be recovered from several projections acquired by rotating the sample about the beam propagation direction (i.e. optical axis), this technique is known as X-ray Vector Radiography [5], [6]. Malecki et al. [7] presented an extension of this technique to three dimensions, known as X-ray Tensor Tomography (XTT). In this method, a scattering tensor is reconstructed at every voxel and its smallest half axis represents the main structure orientation [8]. An additional component known as an Eulerian cradle (Figure 1) is added to the grating interferometer, which allows for non-standard acquisition poses that are required to measure all scattering orientations within the sample. This is a promising technique with a number of applications; visualization of the microstructure of fibrous materials and dentinal tubules of human tooth are some examples that have been demonstrated already [7], [8].

XTT is currently limited by large acquisition time owing partly to the large number of measurements and partly to the time required for the movement of several motors. Hence, there is a need to optimize the acquisition geometry for XTT. In order to do so, it is essential to establish a relationship between the acquisition geometry and the expected result. In this work, a methodology to predict the performance of XTT for a given acquisition scheme is presented. The method is used to compare the predicted performance of several acquisition schemes with their actual performance for a phantom consisting of a dense arrangement of carbon fibres.

II. Methods

In this section, we present a numerical method for the comparison of XTT acquisition schemes, known as the Coverage Measure (CM). CM is a measure of the relative

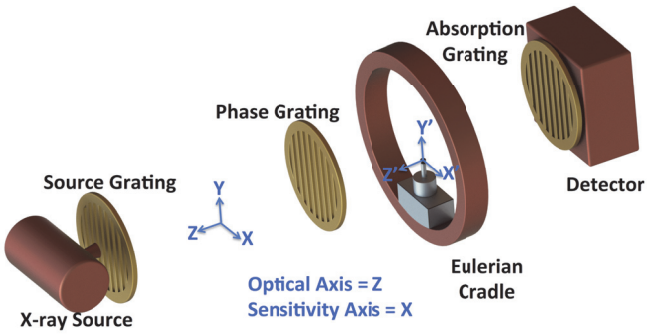

Fig. 1. A schematic of the grating interferometry setup with an Eulerian cradle.

coverage of the unit sphere obtained by a given XTT acquisition scheme. It enables us to predict the performance of sparse acquisition schemes with respect to a standard scheme. In sub-section II-B, we present a method, known as the Performance Measure (PM) for experimentally comparing the results of different acquisition schemes.

A. Coverage Measure

Consider two frames of reference, world frame, denoted by (x, y, z) and sample frame, denoted by (x', y', z') (see Figure 1). We define three rotation angles:

1) ψ- rotation of the sample around y enabled by the rotation of the eulerian cradle around y,
2) θ- rotation of the sample around z', i.e. movement of the sample holder along the circumference of the cradle,
3) ϕ- rotation of the sample around y'.

A tomographic rotation trajectory around y' can be written as a function of ψ and θ:

$$A(\psi, \theta) := \{\alpha := (\psi, \theta, \phi);\ \phi \in [0°, 18°, .., 360°]\} \quad (1)$$

A standard sparse acquisition scheme for absorption CT using 20 equally spaced projection angles can then be written as $A(0, 0)$. In other words, the sample is rotated around the fixed y axis and line integrals of X-ray absorption through the sample along z, also known as the optical axis, are recorded. Let us define $\hat{t}(\alpha)$ as the unit vector along the optical axis for an acquisition pose α. For better visualization, we plot $\pm\hat{t}(\alpha)$ on a unit sphere, assuming that the sample is fixed at the center of the sphere. The points $\pm\hat{t}(\alpha)$ for $A(0, 0)$ are shown in blue in Figure 2(a). Another important variable for XTT is the normalized sensitivity axis, $\hat{s}(\alpha)$. The sensitivity axis of a grating interferometer is the direction in which the phase shift of X-rays is measured. It lies in the plane of the gratings, orthogonal to the grating bars (see Figure 1). We have $\hat{s}(\alpha) = x$ when grating bars are vertical. $\pm\hat{s}(\alpha)$ are plotted in red color on the unit sphere in Figure 2(a), assuming the sample is fixed at the center of the sphere.

In the case of XTT, additional tomographic trajectories are obtained by rotating y' using ψ and θ. The positions of $\pm\hat{t}(\alpha)$ (blue points in Figure 2) are influenced by both ψ and θ. For, $\theta = 0$, $\pm\hat{t}(\alpha)$ lies on one ring at the equator for all values of ψ. Similarly, for $\psi = 0$, $\pm\hat{t}(\alpha)$ lies on one ring at the equator for all values of θ. However, each set of $(\psi \neq 0, \theta \neq 0)$ traces a unique set of two rings above and below the equator as the vectors are symmetric about the origin. Higher values of ψ result in rings being closer to the poles, however, $\psi > 40$ cannot be used in practice as the Eulerian cradle (in our setup) would block the X-ray beam. Red points in Figure 2 show the corresponding positions of $\pm\hat{s}(\alpha)$ on the unit sphere. For $\theta = 0$, $\hat{s}(\alpha)$ lies on a ring at the equator for all values of ψ. For each set of $(\psi, \theta > 0)$, $\pm\hat{s}(\alpha)$ traces two rings above and below the equator.

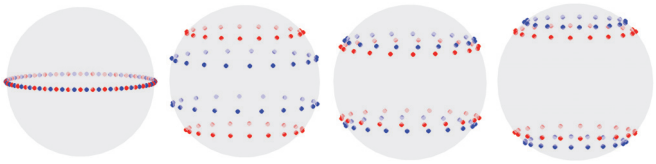

(a) $A(0, 0)$ (b) $A(25, 45)$ (c) $A(50, 45)$ (d) $A(50, 90)$

Fig. 2. Spherical representation of different acquisition schemes $A(\psi, \theta)$. On each sphere, the blue points represent the trajectories of the optical axis ($\pm\hat{t}(\alpha)$) and the red points represent the trajectories of the sensitivity axis ($\pm\hat{s}(\alpha)$).

The visualization of the trajectories of the optical and sensitivity vectors as shown in Figure 2 gives a qualitative understanding of the orientations that are measured with a given acquisition scheme. Below, we present a method for the quantification of such acquisition schemes.

Let Σ and $\mathcal{T}$ be two sets of uniformly distributed points on the unit sphere [9]:

$$\Sigma = \{\sigma_k \in \mathbf{S}^2,\ k = 1, 2, ..., N\} \quad (2)$$

$$\mathcal{T} = \{\tau_k \in \mathbf{S}^2,\ k = 1, 2, ..., N\} \quad (3)$$

where $\mathbf{S}^2$ is the unit sphere and $N = 10000$. The mean vector of Σ is given by:

$$m_\Sigma = \frac{1}{N}\sum_{k=1}^{N} \sigma_k \quad (4)$$

Let X be an acquisition scheme using n different acquisition poses x_i:

$$X := \{x_i := (\psi_i, \theta_i, \phi_i); i = 1, 2, ..., n\} \quad (5)$$

The objective is to define a quantity known as $Coverage(X, k)$ that represents how well the point $\sigma_k \in \Sigma$ is measured by X. The stepwise procedure for calculating $Coverage(X, k)$ is as follows:

1) Define $X_k \subset X$ as the set of poses that sufficiently measure the point $\sigma_k \in \Sigma$:

$$X_k = \{x \in X; \quad w(\sigma_k, x) > T_h\} \quad (6)$$

where $w(\sigma_k, x)$ is a weight factor that determines how well the point σ_k is measured by the acquisition pose x and T_h is an arbitrarily chosen threshold; $T_h = 0.9$ in this case. $w(\sigma_k, x)$ is given by:

$$w(\sigma_k, x) = \left(|\sigma_k \times \hat{t}(x)|\ \langle \sigma_k, \hat{s}(x) \rangle\right)^2 \quad (7)$$

where $|\cdot \times \cdot|$ denotes the magnitude of the cross product and $< \cdot, \cdot >$ denotes the standard scalar product.

2) $\overline{R_k}$ is the mean resulting length of the vectors $\hat{t}(x)$ for all $x \in X_k$:

$$\overline{R_k} = \left\| \frac{1}{|X_k|} \sum_{x \in X_k} \hat{t}(x) \right\| \quad (8)$$

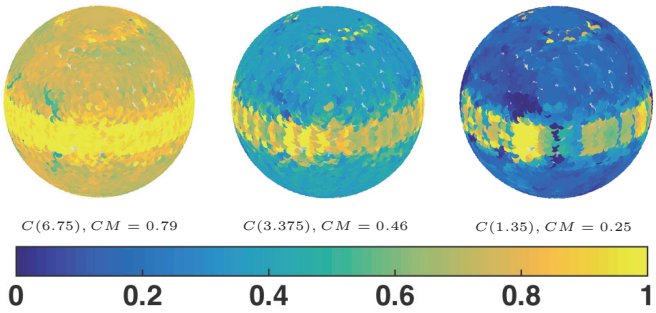

Fig. 3. Coverage Spheres for different acquisition schemes; higher value implies better coverage.

where $|\cdot|$ denotes the number of elements in a set and $\|\cdot\|$ denotes the length of a vector.

3) $\mathcal{T}_k \subset \mathcal{T}$ is the set of points that are measured sufficiently by X_k, assuming that each vector $\hat{t}(x)$ contributes to the measurement of points lying within a cone of opening angle 5° around it:

$$\mathcal{T}_k = \{\tau \in \mathcal{T};\ < \tau, \hat{t}(x) > > cos(2.5°)\ \forall\ x \in X_k\} \tag{9}$$

4) The $Coverage(X,k)$ is then defined as:

$$Coverage(X,k) = 2 \cdot (1 - \overline{R_k}) \cdot \frac{|\mathcal{T}_k|}{N} \tag{10}$$

The quantity $2 \cdot (1 - \overline{R})$ is known as the spherical variance [10] for vectors located on a sphere. A higher value of variance implies that the vectors $\hat{t}(x), x \in X_k$, are distributed widely over the unit sphere and a lower values implies that they are clustered about the mean.

5) Next, $\Gamma(X)$ is defined as:

$$\Gamma(X) = \{\gamma_k := \sigma_k \cdot Coverage(X,k),\ \forall\ \sigma_k \in \Sigma\} \tag{11}$$

and the mean is:

$$m_{\Gamma(X)} = \frac{1}{N} \sum_{k=1}^{N} \gamma_k \tag{12}$$

The normalized vectors $\widehat{m}_{\Gamma(X)}$ plotted on a unit sphere and color coded with their length provide a visual impression of the relative measurement of the different regions of a unit sphere, and is called a Coverage Sphere. Several examples of Coverage Spheres are shown in Figure 3.

6) The angular deviation of the normalized mean vector $\widehat{m}_{\Gamma(X)}$ from the normalized mean vector $\widehat{m}_{\Sigma}$ is a measure of the non-uniformity of the Coverage Sphere. The Coverage Metric, $CM(X)$ is thus defined as:

$$CM(X) = \left\langle \widehat{m}_{\Gamma(X)}, \widehat{m}_{\Sigma} \right\rangle \cdot \frac{1}{N} \sum_{k=1}^{N} Coverage(X,k). \tag{13}$$

B. Performance Measure

In order to correlate the concept of coverage with experimental observations and to study the effect of different acquisition schemes, a phantom made of carbon fibres is studied. The phantom consists of a bunch of carbon fibres in the shape of a knot. This is an interesting sample for XTT as it consists of many different fibre orientations which need to be resolved accurately. XTT measurement is acquired using an acquisition protocol B:

$$\begin{aligned} B = \{b_i := (\psi, \theta, \phi);\ \psi \in [-50, -25, 0, 25, 50], \\ \theta \in [-90, -45, 0, 45], \\ \phi \in [0, 3, 6, .., 180]\} \end{aligned} \tag{14}$$

in a continuous measurement spanning 13.5 hours (ignoring the time required for motor movement), with 8 phase steps and $5s$ exposure per step. The scattering strengths $\zeta_k(r_i)$, for all voxels $r_i, i = 1, 2, .., I$ are simultaneously reconstructed for 13 sampling directions $\epsilon_k, k = 1, 2, ..., 13$. 50 iterations of the block parallel solver outlined in [8] are used. The XTT forward model used for the reconstruction is [7]:

$$d(x) = exp\left(- \int_{\hat{t}(x)} \sum_{k} \left[\zeta_k(r)^2 \cdot w(\epsilon_k, x) \right]\ dr \right) \tag{15}$$

where $d(x)$ denotes the dark-field projection measured at the acquisition pose x and $w(\epsilon_k, x)$ are the weight factors defined in equation (7). After reconstruction, the sampling directions are scaled with the scattering strength at each voxel and mirrored since the scattering tensors should be symmetric. A scattering tensor, $T(r_i) \in \mathbf{R}^{3\times3}$ is then calculated using the 26 scattering vectors. The smallest half axis $\lambda_B(r_i) \in \mathbf{R}^3$ of the scattering tensor represents the main structure orientation in each voxel, obtained using the acquisition scheme B. Figure 4(a) shows streamlines traced using RK4 with the smallest half axes of the ellipsoids; colors represent the orientations of the streamlines. Note that the streamlines do not represent the actual fibres but are an indication of their orientation. $Coverage(B,k)$ is calculated using the method described in section II-A and normalized to 1 for all points on the Coverage Sphere.

XTT reconstruction for the sample is obtained by employing different acquisition schemes (say X) and the resulting vectors $\lambda_X(r_i)$ are compared to $\lambda_B(r_i)$. Two corresponding vectors are considered to be correlated if their intermediate angle is less than 10°. The set of correlated vectors, $Corr(X)$ is thus given by:

$$\begin{aligned} Corr(X) = \{\lambda_X(r_i);\ \langle \lambda_X(r_i), \lambda_B(r_i) \rangle\ < cos(10°), \\ i = 1, 2, .., I\}. \end{aligned} \tag{16}$$

The Performance Metric, $PM(X)$, which determines how well an arbitrary acquisition scheme X performs when compared to B (considered as ground truth) is then given by:

$$PM(X) = \frac{|Corr(X)|}{I} \tag{17}$$

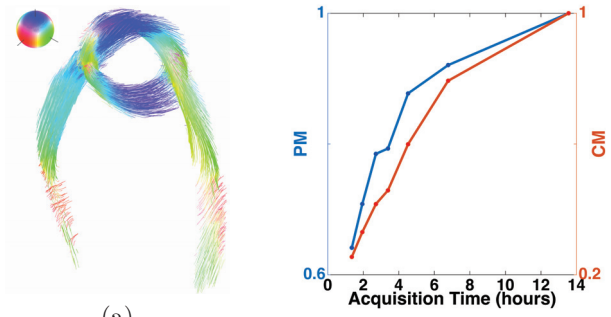

(a) (b)

Fig. 4. (a) Streamline visualization of the orientations of carbon fibres in the phantom (b) Plot of CM vs. acquisition time and PM vs. acquisition time.

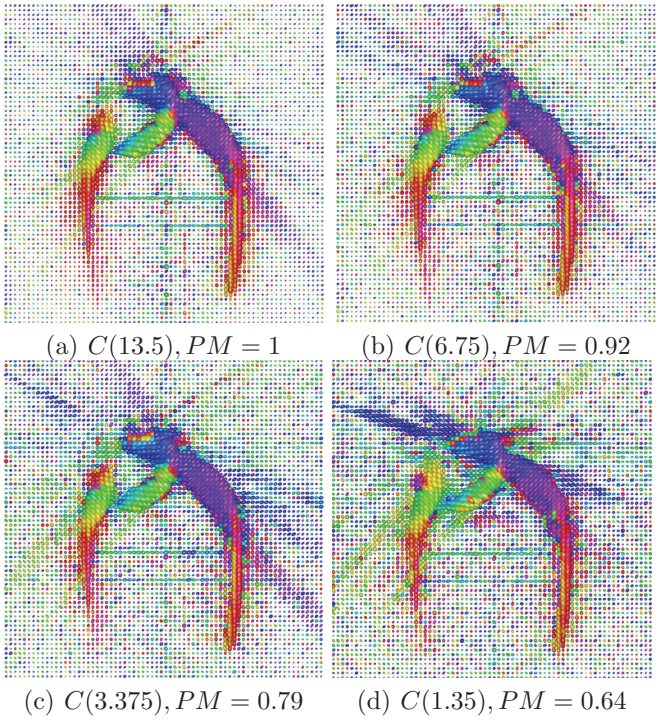

(a) $C(13.5), PM = 1$ (b) $C(6.75), PM = 0.92$

(c) $C(3.375), PM = 0.79$ (d) $C(1.35), PM = 0.64$

Fig. 5. Comparison of the tensors in a single slice obtained using different acquisition schemes.

The Coverage Measure and Performance Measure are now used for studying the effect of acquisition time on the result of XTT reconstruction. Several acquisition schemes, $C(t)$ are defined by downsampling B:

$$C(t) = \{b_{k \cdot \frac{T}{t}}; k = 1, 2, ..., 1220 \cdot t/T\} \qquad (18)$$

where $T = 13.5$ *hours* is the acquisition time for scheme B.

III. Results and Discussion

CM and PM for $C(t)$ are plotted in Figure 4(b) in orange and blue respectively. It can be seen that CM and PM correlate nicely for comparing the acquisition schemes. A single slice of reconstructed tensors for different acquisition schemes is shown in Figure 5. It can be seen that the quality of the result with 6.75 *hours* of measurement is a decent compromise when compared to the one using 13.5 *hours* of measurement. However, there is significant loss in quality when the measuring time is reduced further. The corresponding Coverage Spheres for $C(6.75)$, $C(3.375)$ and $C(1.35)$ are shown in Figure 3.

In conclusion, a method to calculate the relative efficiency of a given XTT acquisition scheme is presented. The method is then used to quantify the effect of reducing the measurement time for an XTT acquisition on the reconstructed result. The results show that the Coverage Measure (CM) is a useful tool for designing sparse XTT acquisition schemes with the aim of achieving clinically relevant measurement times.

Acknowledgment

This work has been supported by BERTI, funded by the European Commission under grant agreement number 605162, and partially funded by the DFG Cluster of Excellence, Munich-Centre for Advanced Photonics (MAP).

References

[1] F. Pfeiffer, T. Weitkamp, O. Bunk, and C. David, "Phase retrieval and differential phase-contrast imaging with low-brilliance X-ray sources," *Nature Physics*, vol. 2, no. 4, pp. 258–261, 2006.

[2] F. L. Bayer, S. Hu, A. Maier, T. Weber, G. Anton, T. Michel, and C. P. Riess, "Reconstruction of scalar and vectorial components in x-ray dark-field tomography," *Proceedings of the National Academy of Sciences*, vol. 111, no. 35, pp. 12 699–12 704, 2014.

[3] F. Bayer, S. Zabler, C. Brendel, G. Pelzer, J. Rieger, A. Ritter, T. Weber, T. Michel, and G. Anton, "Projection angle dependence in grating-based x-ray dark-field imaging of ordered structures," *Opt. Express*, vol. 21, no. 17, pp. 19 922–19 933, Aug 2013.

[4] W. Yashiro, S. Harasse, K. Kawabata, H. Kuwabara, T. Yamazaki, and A. Momose, "Distribution of unresolvable anisotropic microstructures revealed in visibility-contrast images using x-ray Talbot interferometry," *Physical Review B - Condensed Matter and Materials Physics*, vol. 84, no. 9, pp. 1–9, 2011.

[5] F. Schaff, A. Malecki, G. Potdevin, E. Eggl, P. B. Noël, T. Baum, E. G. Garcia, J. S. Bauer, and F. Pfeiffer, "Correlation of X-ray vector radiography to bone micro-architecture." *Scientific reports*, vol. 4, p. 3695, 2014.

[6] T. H. Jensen, M. Bech, O. Bunk, T. Donath, C. David, R. Feidenhans'l, and F. Pfeiffer, "Directional x-ray dark-field imaging," *Physics in Medicine and Biology*, vol. 55, no. 12, p. 3317, 2010.

[7] A. Malecki, G. Potdevin, T. Biernath, E. Eggl, K. Willer, T. Lasser, J. Maisenbacher, J. Gibmeier, A. Wanner, and F. Pfeiffer, "X-ray tensor tomography," *EPL (Europhysics Letters)*, vol. 105, no. 3, p. 38002, 2014.

[8] J. Vogel, F. Schaff, A. Fehringer, C. Jud, M. Wieczorek, F. Pfeiffer, and T. Lasser, "Constrained X-ray tensor tomography reconstruction," *Opt. Express*, vol. 23, no. 12, pp. 15 134–15 151, 2015.

[9] E. W. Weisstein, "Sphere point picking." http://mathworld.wolfram.com/SpherePointPicking.html, accessed December 28, 2015.

[10] K. V. Mardia and P. E. Jupp, *Distributions on Spheres*. John Wiley and Sons, Inc., 2008, pp. 159–192.

Attenuation-Based Reconstruction of Low and High Frequency Components of Detected X-Ray Spectra

Carsten Leinweber, Joscha Maier, Stefan Sawall, Henning Stoschus, Frederic Ballach, Tobias Müller, Michael Hammer, Ralf Christoph, and Marc Kachelrieß

***Abstract*—Several applications in computed tomography (CT) imaging require detailed knowledge about the detected x-ray spectrum. Reconstructing x-ray spectra from transmission data is a promising alternative to experimentally demanding direct measurement techniques. The ill conditioning of this inverse problem is commonly encountered by incorporating prior knowledge of the CT system. However the amount of this prior knowledge has to be carefully selected as it has a strong influence on the resulting spectrum. In this work we present the theoretical framework of a singular value decomposition (SVD) approach which provides detailed x-ray spectra by applying only minimal physical assumptions. The proposed method is tested on simulated data and compared to the expectation-maximization (EM) algorithm widely used in literature.**

***Index Terms*—Detected X-Ray Spectrum, CT, SVD**

I. Introduction

DOSE calculations and artifact reduction techniques require detailed knowledge about the spectral distribution of the x-ray radiation utilized in computed tomography (CT) scanners. Several methods have been developed that aim at assessing the x-ray spectrum experimentally, which can be classified as either direct or indirect. In direct methods the spectrum is measured in a spectroscopic manner which may require additional equipment and dedicated imaging modalities [1], [2]. In contrast data acquisition for indirect methods can generally be performed in standard routine providing not only spectral information about the x-ray source but also about the detector response.

An attractive strategy is to perform transmission measurements of objects of known dimension and material composition and to treat x-ray spectrum reconstruction from this data as an inverse problem. Previously proposed solutions to this problem can again be separated into two categories. In few-parameter modeling methods the spectrum is specified using a functional form with only a small number of free parameters. In an optimization approach these parameters are estimated such that the transmission curve resulting from the model spectrum fits best with the measured transmission data [3]. Bin-by-bin reconstruction methods in contrast attempt to estimate every single bin of a discretized representation of the x-ray spectrum. In these methods the process of x-ray attenuation is formulated as a system of linear equations. Numeric analysis of the corresponding system matrix shows that the problem is ill-conditioned, meaning that small perturbations in the transmission data will lead to large changes in the x-ray spectrum when direct inversion is performed [4]. The thus obtained spectra tend to exhibit negative values and high oscillations not reflecting the physical nature of bremsstrahlung induced radiation. The ill-conditioning of the problem is attributed to the weak dependence of the attenuation coefficient μ to the energy E in the interesting energy range, which can be improved by an appropriate choice of the attenuators [5], [6].

Several procedures have been established that solve the linear system by incorporating *a priori* knowledge or applying regularization techniques. These include expectation-maximimization (EM) [5], iterative perturbation [7], neural networks [8] and singular value decomposition (SVD) [4], [9]. In this work we show how minimal spectral prior information can be used to incorporate high frequency components into spectra estimated with the SVD method resulting in an accurate spectrum with a physically reliable shape.

II. Materials and Methods

A. Measurement model

Under the absence of scatter radiation transmission measurements of polychromatic x-rays can be described by the relation

$$I(d) = \int_0^{E_{\max}} dE\, w(E)\, e^{-\mu(E)\, d}, \tag{1}$$

where $I(d)$ is the intensity of radiation attenuated along the path length d with linear attenuation coefficient $\mu(E)$, relative to the unattenuated radiation. $E_{\max}$ represents the maximum photon energy corresponding to the x-ray tube voltage. The detected spectrum $w(E) = S(E)D(E)$ attributes for both the source spectrum $S(E)$ and the detector response $D(E)$. The principal problem assessed in this work is to reconstruct $w(E)$ with knowledge of $I(d)$, $\mu(E)$ and d.

In order to evaluate the spectrum estimation method described below we generate detected x-ray spectra based on the the model of Tucker *et al.* [10]. We assume a tungsten target for x-ray generation and a CsI:Tl scintillator for detection. Transmission measurements are simulated according to (1) with aluminum (Al) as absorption material and 50 different attenuation length ranging from $0.5\,\mathrm{mm}$ to $200\,\mathrm{mm}$. The

Carsten Leinweber and Joscha Maier: German Cancer Research Center (DKFZ), Im Neuenheimer Feld 280, Heidelberg, Germany and Werth Messtechnik GmbH, Siemensstraße 19, Gießen, Germany

Dr. Stefan Sawall and Prof. Dr. Marc Kachelrieß: German Cancer Research Center (DKFZ), Im Neuenheimer Feld 280, Heidelberg, Germany

Dr. Henning Stoschus, Frederic Ballach, Tobias Müller, Michael Hammer and Dr. Ralf Christoph: Werth Messtechnik GmbH, Siemensstraße 19, Gießen, Germany

Corresponding author: carsten.leinweber@dkfz.de

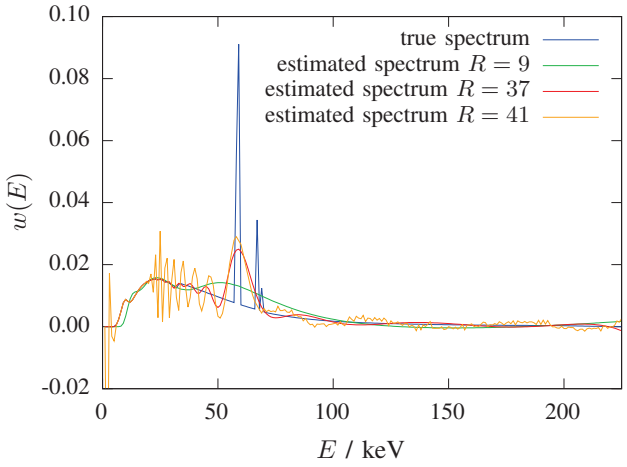

Fig. 1. Comparison between the simulated true spectrum and the spectra $\boldsymbol{w}_\mathrm{R}$ estimated using the truncated singular value decomposition (TSVD). The spectral resolution of the estimated spectrum increases with R. At $R = 41$ the singular value is numerically close to zero resulting in an unstable solution. Hence the estimate exhibits strong oscillations and negative values, which is not in accordance with the physical nature of the problem. The spectral resolution of the stable solution $R = 37$ however is not sufficient to resolve the characteristic lines of the true spectrum.

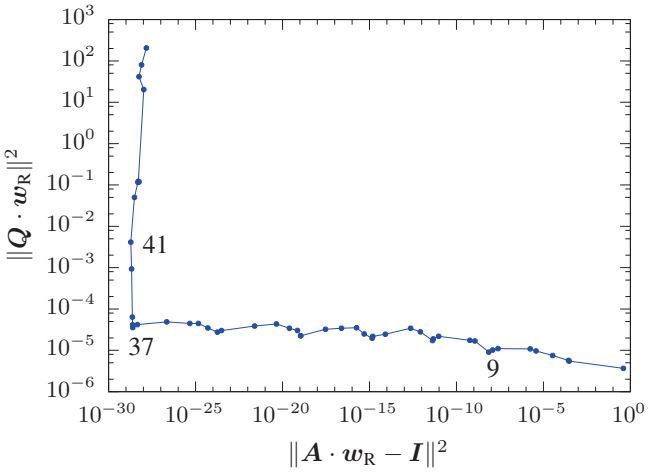

Fig. 2. L-curve criterion. The the L_2-norm of the solution $\|\boldsymbol{Q}\cdot\boldsymbol{w}\|_2^2$ is plotted as function of the residual norm $\|\boldsymbol{A}\cdot\boldsymbol{w}_\mathrm{R} - \boldsymbol{I}\|_2^2$ for different selections of R. The numbers in die graph indicate the R values of the corresponding points. The value closes to the corner of the L-shaped graph provides the solution that optimizes both constrains best. In this case the optimal value is $R = 37$.

attenuation coefficients $\mu(E)$ for Al are taken from Cullen *et al.* [11].

B. Spectrum estimation

As a first step we discretize the detected spectrum into B equally distributed energy bins of width $1\,\mathrm{keV}$. We assume a total number of M measurements with different absorbers and denote the m-th measurement with I_m. The expected attenuation of each measurement can be formulated as

$$A_{mb} = e^{-\mu_{mb}\, d_m},$$

where d_m denotes the absorber thickness and μ_{mb} the corresponding attenuation coefficient at energy bin b. Equation (1) now reads

$$I_m = \sum_b A_{mb}\, w_b.$$

We may estimate the detected spectrum $\boldsymbol{w}$ by minimizing the L_2-norm

$$\chi^2 = \sum_m (\sum_b A_{mb}\, w_b - I_m)^2 = \|\boldsymbol{A}\cdot\boldsymbol{w} - \boldsymbol{I}\|_2^2. \qquad (2)$$

The resulting system of linear equations can be solved using SVD. With help of SVD we decompose the response matrix $\boldsymbol{A}$ into B uncorrelated matrices

$$\boldsymbol{A} = \sum_{b=1}^{B} \boldsymbol{u}_b \cdot s_b \boldsymbol{v}_b^T$$

where $\boldsymbol{u}_b$ are the M-dimensional orthogonal eigenvectors of the $M \times M$ matrix $\boldsymbol{A}\cdot\boldsymbol{A}^T$ and $\boldsymbol{v}_b$ are the B-dimensional orthogonal eigenvectors of the $B \times B$ matrix $\boldsymbol{A}^T\cdot\boldsymbol{A}$. The singular values s_b are the square roots of the eigenvalues of $\boldsymbol{A}\cdot\boldsymbol{A}^T$ or $\boldsymbol{A}^T\cdot\boldsymbol{A}$. According to the principle of SVD the solution to (2) can now be calculated as [12]

$$\boldsymbol{w} = \left(\sum_{b=1}^{B} \boldsymbol{v}_b \cdot \frac{\boldsymbol{u}_b^T}{s_b}\right) \cdot \boldsymbol{I}. \qquad (3)$$

C. Numerical analysis

When the system matrix exhibits full rank or has non-zero singular values (3) exactly solves the linear system $\boldsymbol{A}\cdot\boldsymbol{w} = \boldsymbol{I}$. However the matrix $\boldsymbol{A}$ generally shows singular values which are numerically close to zero. This property is referred to as ill-conditioning and results in numerical instability of the solution. Due to this instability small perturbations in the measurements result in entirely different solutions. Assuming the singular values to appear in descending order

$$1 = s_1 \geq s_2 \geq \ldots \geq s_R > s_{R+1} \approx s_B \approx 0,$$

the numerical instability of the solution can be addressed to the components in (3) with index $b > R$, where R describes the rank of $\boldsymbol{A}$. By only considering the first R singular values in (3) we can calculate an approximate solution $\boldsymbol{w}_\mathrm{R}$ to (2) which is numerically stable. Regularizing $\boldsymbol{w}$ hereby is also referred to as truncated singular value decomposition (TSVD) [13]. With

$$c_b = \frac{\boldsymbol{u}_b^T \cdot \boldsymbol{I}}{s_b}$$

we separate (3)

$$\boldsymbol{w} = \sum_{b=1}^{R} c_b\, \boldsymbol{v}_b + \sum_{b=R+1}^{B} c_b\, \boldsymbol{v}_b = \boldsymbol{w}_\mathrm{R} + \boldsymbol{w}_\mathrm{N},$$

and denote $\boldsymbol{w}_\mathrm{R}$ and $\boldsymbol{w}_\mathrm{N}$ as solution from range and null space respectively. However for the problems discussed here, the singular values typically decrease gradually which makes the determination of the rank of $\boldsymbol{A}$ nontrivial. In Fig. 1 the reconstructed spectra are shown for different selections of R.

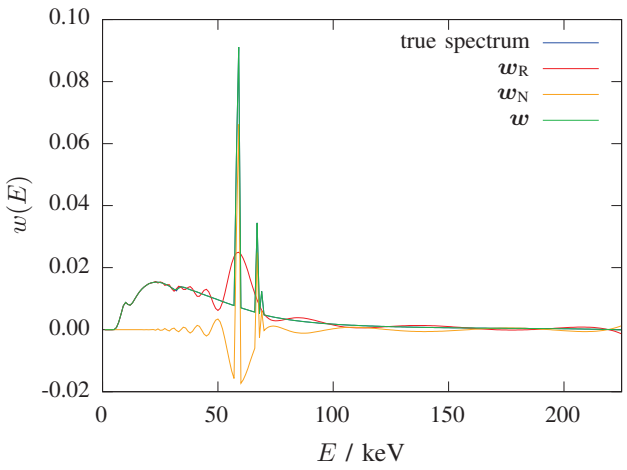

Fig. 3. Spectrum reconstructed with the PTSVD method. The solution from null space $\boldsymbol{w}_\mathrm{N}$ compensates for the low frequencies in the solution $\boldsymbol{w}_\mathrm{R}$ from range. The resulting spectrum $\boldsymbol{w}$ is in good accordance with the simulated true spectrum.

Between the solutions obtained with $R = 37$ and $R = 41$ we observe a significant change in the shape of $\boldsymbol{w}_\mathrm{R}$. This motivates a criterion for choosing the regularization parameter R often referred to as the L-curve criterion [13]. The idea is to find a solution that minimizes both the residual norm $\|\boldsymbol{A} \cdot \boldsymbol{w}_\mathrm{R} - \boldsymbol{I}\|_2^2$ and the L_2-norm of the solution $\|\boldsymbol{Q} \cdot \boldsymbol{w}\|_2^2$ by plotting the latter as function of the former for different R and selecting the value closest to the corner of the thus obtained L-shaped graph. We require maximum flatness of the estimated spectrum by choosing $\boldsymbol{Q}$ as the discretized first derivative:

$$\boldsymbol{Q} = \begin{pmatrix} -1 & 1 & & \\ & \ddots & \ddots & \\ & & \ddots & 1 \\ & & & -1 \end{pmatrix}$$

In Fig. 2 the L-curve for the simulation example is given. The plot reveals that choosing $R > 37$ does not provide a better solution to (2) but leads to a decrease in flatness. Therefore $R = 37$ is the best choice here.

D. Integration of prior knowledge

The regularization method introduced thus far limits the spectral resolution of the estimated spectrum. As shown in Fig. 1 the stable solution $R = 37$ is not capable of reproducing the characteristic lines of the simulated true spectrum. We therefore seek for a method that resolves such spectral details while conserving the accuracy of the TSVD solution.

From $\boldsymbol{A} \cdot \boldsymbol{w}_\mathrm{N} = 0$ follows that we can add any solution from null space to the solution from range without increasing χ^2 in (2) and therefore without loss of accuracy. Let us first assume that we exactly know the contribution of the characteristic peaks which we call $\boldsymbol{w}_\mathrm{C}$ to the total spectrum. We further assume that the difference between the true spectrum and the TSVD solution can be uniquely attributed to high frequencies. We may now choose the $c_b\,\boldsymbol{v}_b$ from null space such that they represent $\boldsymbol{w}_\mathrm{C}$. Minimizing

$$\| \sum_{b=R+1}^{B} c_b\,\boldsymbol{v}_b - \boldsymbol{w}_\mathrm{C} \|_2^2$$

with respect to c_b results in

$$\boldsymbol{w}_\mathrm{N} = \sum_{b=R+1}^{B} (\boldsymbol{v}_b^T \cdot \boldsymbol{w}_\mathrm{C})\,\boldsymbol{v}_b,$$

which can be understood by recalling that $\boldsymbol{v}_b$ are orthogonal eigenvectors. As adding $\boldsymbol{w}_\mathrm{N}$ to $\boldsymbol{w}_\mathrm{R}$ does not alter the spectral information of the solution, the contribution of $\boldsymbol{w}_\mathrm{N}$ must compensate for the difference between the true spectrum and the TSVD solution. In Fig. 3 the results of this method we refer to as prior TSVD (PTSVD) are shown. The reconstructed spectrum $\boldsymbol{w}$ is in good agreement with the simulated true spectrum reproducing the high frequencies of the characteristic peaks as well as the low frequencies of the bremsstrahlung fraction.

In reality however we are not aware of the exact contribution of the characteristic peaks. With knowledge about the target material of the x-ray source though we at least know at which energies we expect high frequency contributions. In the simulation example we use a tungsten target with peak energies E_p at $58.0\,\mathrm{keV}$ and $59.3\,\mathrm{keV}$ for K_α together with $67.2\,\mathrm{keV}$ and $69.1\,\mathrm{keV}$ for K_β [10]. We now treat the assessment of the contribution of these peaks to the characteristic spectrum $\boldsymbol{w}_\mathrm{C}$ as optimization problem using the parameter model

$$\boldsymbol{w}_\mathrm{C}(\boldsymbol{h}) = \sum_{p=1}^{4} h_p\,\boldsymbol{e}_p,$$

where the $\boldsymbol{e}_p$ have a 1 at the entry corresponding to the energy of the p-th peak and zeroes elsewhere and where h_p are the (unknown) peak heights.

Now we define a cost function C that includes physical boundary conditions that are not intrinsically fulfilled by the TSVD method. These are non-negativity of the resulting spectrum $\boldsymbol{w}(\boldsymbol{h}) = \boldsymbol{w}_\mathrm{R} + \boldsymbol{w}_\mathrm{N}(\boldsymbol{h})$ and flatness of the bremsstrahlung spectrum $\boldsymbol{w}(\boldsymbol{h}) - \boldsymbol{w}_\mathrm{C}(\boldsymbol{h})$, which is given by subtracting the characteristic spectrum from the final spectrum. Our cost function thus reads

$$C(\boldsymbol{h}) = \alpha_1 \,\|\boldsymbol{w}(\boldsymbol{h}) \wedge \boldsymbol{0}\|_2^2 + \alpha_2 \,\|\boldsymbol{Q} \cdot (\boldsymbol{w}(\boldsymbol{h}) - \boldsymbol{w}_\mathrm{C}(\boldsymbol{h}))\|_2^2$$

where $\wedge$ is the element-wise minimum operator, i.e. the first term of our cost function penalizes the sum of squares of all negative spectrum entries.

We minimize C with a downhill simplex method. The peak heights h_p are initialized using random start values ranging from 0 to 1. For our investigations we use $\alpha_1 = \alpha_2$.

III. Results

In Fig. 4 a comparison between the results of the PTSVD and the EM method based on the simulated dataset is shown. In order to obtain comparable results we incorporated the same prior information into the EM method as mentioned before for the PTSVD method. The EM algorithm was initialized

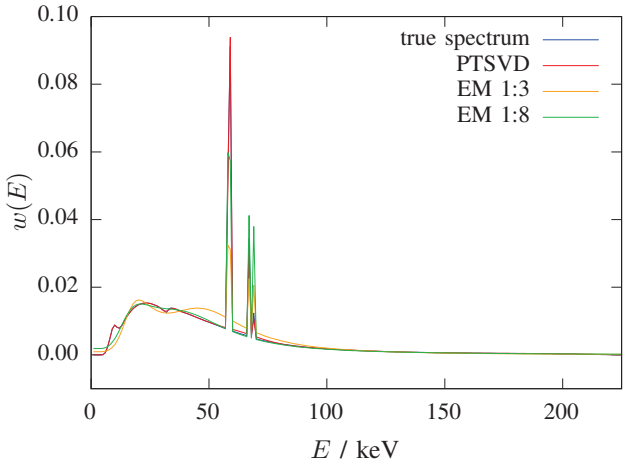

Fig. 4. Comparison between spectra reconstructed with PTSVD and EM. Two results of the EM algorithm are shown for an initial background to peak ratio of 1:3 and 1:8. In both cases 5000 iterations were performed.

TABLE I
COMPARISON BETWEEN PTSVD AND EM

Method	χ^2	d
PTSVD	3.22×10^{-29}	5.52×10^{-05}
EM 1:3	5.57×10^{-07}	4.71×10^{-03}
EM 1:8	6.42×10^{-08}	1.93×10^{-03}

with a constant positive function to fulfill the non-negativity constraint. Characteristic peaks were added to account for K_α and K_β of the tungsten target. The intensity $w(E)$ of each peak was set to a constant value. The ratio between this value and the constant positive function is referred to as initial background to peak ratio. Fig. 4 indicates a strong dependence of the reconstructed spectrum on the initial background to peak ratio. Concerning the squared difference to the true simulated spectrum w_T

$$d = \|w_\mathrm{T} - w\|_2^2.$$

an initial background to peak ratio of 1:8 was manually found to yield the best results. As indicated in Fig. 5 increasing the number of iterations leads to a decrease in χ^2. The quality parameter d however shows a minimum at 5000 iterations and

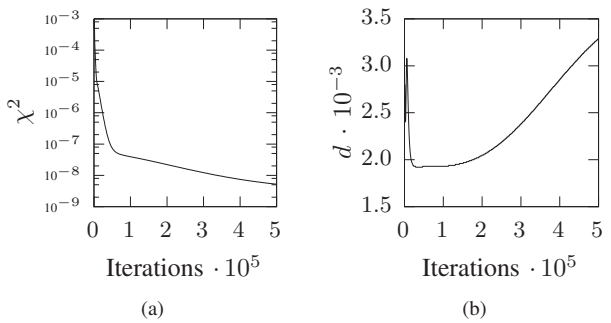

(a) (b)

Fig. 5. Dependence of (a) χ^2 and (b) d of the number of EM iterations. The initial background to peak ratio was set to 1:8.

increases for a higher number of iterations. In table I numbers for χ^2 and d are given for both PTSVD and EM. A comparison between both methods reveals, that PTSVD performs better in reconstructing the true spectrum.

IV. CONCLUSION

We presented a new approach for the reconstruction of detected x-ray spectra by regularizing a TSVD solution with help of minimal prior information. Our method is capable of reproducing high frequency components in the spectrum addressed to characteristic radiation while conserving the accuracy of the TSVD solution. We showed that the proposed approach outperforms the widely used EM algorithm in both accuracy and physical reliability of the resulting spectrum when the same prior knowledge is incorporated in both methods. In future work the influence of perturbations to the implied transmission data like noise on the PTSVD method have to be investigated.

ACKNOWLEDGMENT

The study was supported by the Arbeitsgemeinschaft industrieller Forschungsvereinigungen (AiF) under Grant No. KF2301007NT3. Parts of the x–ray and simulation software were provided by RayConStruct® GmbH, Nürnberg, Germany.

REFERENCES

[1] S. Gallardo, D. Ginestar, G. Verdú, J. Ródenas, V. Puchades, and J. I. Villaescusa, "X-ray spectrum unfolding using a regularized truncated SVD method," *X-Ray Spectrometry*, vol. 35, no. 1, pp. 63–70, 2006.

[2] H. a. Duisterwinkel, J. K. van Abbema, M. J. van Goethem, R. Kawachimaru, L. Paganini, E. R. van der Graaf, and S. Brandenburg, "Spectra of clinical CT scanners using a portable Compton spectrometer." *Medical physics*, vol. 42, no. 4, p. 1884, 2015.

[3] L. Silberstein, "Spectral composition of an X-ray radiation determined from its filtration curve," *The London, Edinburgh, and Dublin Philosophical Magazine and Journal of Science*, vol. 15, no. 98, pp. 375–394, 1933.

[4] S. Tominaga, "A Singular Value Decomposition Approach to X-Ray Spectral Estimation from Attenuation Data," vol. 243, pp. 530–538, 1986.

[5] E. Y. Sidky, L. Yu, X. Pan, Y. Zou, and M. Vannier, "A robust method of x-ray source spectrum estimation from transmission measurements: Demonstrated on computer simulated, scatter-free transmission data," *Journal of applied physics*, vol. 97, no. 12, p. 124701, 2005.

[6] L. Zhang, G. Zhang, Z. Chen, Y. Xing, J. Cheng, and Y. Xiao, "X-ray spectrum estimation from transmission measurements using the expectation maximization method," *2007 IEEE Nuclear Science Symposium Conference Record*, no. 1, pp. 3089–3093, 2007.

[7] "X-ray spectra estimation using attenuation measurements from 25 kVp to 18 MV." *Medical physics*, vol. 26, no. 7, pp. 1269–1278, 1999.

[8] J. M. Boone, "X-ray spectral reconstruction from attenuation data using neural networks," *Medical Physics*, vol. 17, no. 4, p. 647, 1990.

[9] B. Armbruster, R. J. Hamilton, and A. K. Kuehl, "Spectrum reconstruction from dose measurements as a linear inverse problem." *Physics in medicine and biology*, vol. 49, no. 22, pp. 5087–99, 2004.

[10] D. M. Tucker, G. T. Barnes, and D. P. Chakraborty, "Semiempirical model for generating tungsten target x-ray spectra." vol. 18, no. 2, pp. 211–8, 1989.

[11] D. E. Cullen, J. H. Hubbell, and L. Kissel, "Epdl97: the evaluated photon data library," *UCRL-50400*, vol. 6, no. 5, pp. 1–28, 1997.

[12] G. H. Golub and C. Reinsch, "Singular value decomposition and least squares solutions," *Numerische mathematik*, vol. 14, no. 5, pp. 403–420, 1970.

[13] P. C. Hansen, *Rank-deficient and discrete ill-posed problems: numerical aspects of linear inversion*. Siam, 1998, vol. 4.

Spectral response effect-compensated estimator in photon counting CT using low-order Gram polynomials

Okkyun Lee, Steffen Kappler, Christoph Polster, and Katsuyuki Taguchi

***Abstract*—Photon counting detector (PCD)-based computed tomography (CT) exploits the abundant spectral information of the transmitted x-ray spectrum through multiple pulse height analysis to perform the material decomposition. However, it suffers from the spectral response effect (SRE) that distorts the transmitted x-ray spectrum. On the SRE-modeled PCD-CT problem, maximum likelihood (ML) estimator is the conventional method for the compensation of SRE; however, one major drawback of the ML estimator is a heavy computational burden. In this paper, we propose a computationally efficient three-step algorithm to estimate basis sinograms in the PCD-CT based on a hypothesis that energy dependent x-ray transmittance can be modeled by low-order Gram polynomials. Under this hypothesis, original non-linear ML approach can be changed into two-step linearized approach followed by a bias correction step. We validate the proposed method using various simulation studies and show an improved computational efficiency over the conventional ML estimator while accuracy is comparable.**

***Index Terms*—Photon counting, spectral response effect, Gram polynomials, least squares, maximum likelihood**

I. Introduction

Photon counting detector (PCD)-based computed tomography (CT) has recently emerged as a candidate of the spectral CT with the help of advanced detector technology [1]. Multiple comparators in each PCD pixel perform pulse hight analysis (PHA) and provide an abundant spectral information of the transmitted x-ray spectrum; hence, PCD-CT has a great potential in clinical applications such as simultaneous multi-agent imaging and molecular CT with K-edge imaging [1]. However, PCD suffers from pulse pileup effect (PPE) and spectral response effect (SRE) due to the quasi-coincident photons and various interactions (ex. charge sharing and K-escape), respectively. These two effects cannot be resolved simultaneously [1], and it is rather easy to mitigate the PPE than the SRE by reducing x-ray dose level and PCD pixel size. So, we focus on the SRE compensation in this study by reflecting a spectral response function calculated by a Monte Carlo simulation to PCD measurements modeling [2].

On the SRE-compensated PCD-CT problem, the reconstruction can be described as the estimation of basis line-integrals based on the SRE-modeled PCD measurements. Conventional methods are maximum likelihood (ML) and calibration-based estimators. The ML estimator is the well-known method which guarantees an asymptotic optimality and shows promising results in the PCD-CT [3]. However, it requires to solve non-linear optimization problem for each sinogram point and it suffers from the heavy computational time to deal with the entire sinograms. On the other hand, calibration-based approaches such as A-table and polynomial expansion methods [4, 5] are fast but they require additional estimation of noise covariance or polynomial coefficients from empirical calibration process that has no golden standard procedure. Therefore, it is necessary to develop a fast and calibration-free estimator.

In this paper, we propose a computationally efficient three-step algorithm to estimate the basis line-integrals in PCD-CT. For this purpose, we hypothesize that energy dependent x-ray transmittance can be modeled by low-order Gram polynomials [6] when heavy elements are absent. Under this hypothesis, the original non-linear PCD measurements model can be linearized. The first step is then to estimate Gram polynomial coefficients from the linearized PCD model. Next, the basis line-integrals can be estimated by the least squares fitting with the results from the first step and energy dependent basis functions. The final step is a bias correction step to compensate bias factor which comes from the previous linearization procedures. We validate the proposed method using various simulation studies and show that it is more computationally efficient than that of the conventional ML estimator while the accuracy is comparable.

II. Background

The linear attenuation coefficients of human body can be modeled by a linear combination of two energy-dependent basis functions such as photoelectric effect ($\phi_p(E)$) and Compton scattering ($\phi_c(E)$):

$$\mu_a(\mathbf{r}, E) = c_p(\mathbf{r})\phi_p(E) + c_c(\mathbf{r})\phi_c(E), \tag{1}$$

where $c_p(\mathbf{r})$ and $c_c(\mathbf{r})$ are their associated basis coefficients. Line-integral of (1) can then be given by

$$\int \mu_a(\mathbf{r}, E)d\mathbf{r} = v_p\phi_p(E) + v_c\phi_c(E) = \mathbf{\Phi}(E)\mathbf{v}, \tag{2}$$

where $\mathbf{\Phi}(E) = [\phi_p(E), \phi_c(E)]$ denotes the basis functions and $\mathbf{v} = [v_p, v_c]^T$ is the line-integrals of their coefficients. Based on this model, the expected number of photons counted at b-th energy bin can be formulated by

$$\lambda_b(\mathbf{v}) = \int_{E_{min}}^{E_{max}} A_b(E) \exp\left(-\mathbf{\Phi}(E)\mathbf{v}\right) dE, \text{ for } b = 1, 2, \cdots, m, \tag{3}$$

O. Lee and K. Taguchi are with the Department of Radiology and Radiological Science, Johns Hopkins University School of Medicine, Baltimore, MD, 21287 USA e-mail: okkyun2@gmail.com, ktaguchi@jhmi.edu

S. Kappler and Christoph Polster are with the Siemens Healthcare, Forchheim, Germany e-mail: steffen.kappler@siemens.com, christoph.polster.ext@siemens.com

Corresponding author: okkyun2@gmail.com

This research was supported by Siemens grants No. JHU-2012-CT-114-01-Taguchi-40630, No. JHU-2015-CT-1-01-Taguchi-C00218347, and No. JHU-2015-CT-1xx-01-Taguchi-C00219287.

where m is the number of energy bins. $A_b(E)$ consists of the incident x-ray spectrum $S_0(E)$ and the energy bin-dependent function which is calculated by a Monte Carlo simulation to model the SRE [2]. We omit the dependency of PCD pixels for the sake of simplicity and assume that $S_0(E)$ is equivalent to all PCD pixels. Finally, the PCD measurements can be modeled by

$$\mathbf{y} = \boldsymbol{\lambda}(\mathbf{v}) + \boldsymbol{\epsilon}, \tag{4}$$

where $\mathbf{y} \in \mathbb{R}^{m\times 1}$ denotes the measurements vector, $\boldsymbol{\lambda}(\mathbf{v}) \in \mathbb{R}^{m\times 1}$ is its expected number whose b-th element is equivalent to (3), and $\boldsymbol{\epsilon} \in \mathbb{R}^{m\times 1}$ denotes the quantum noise. The PCD-CT problem can then be described as to estimate the line-integrals $\mathbf{v}$ for the entire sinograms and perform either a filtered back-projection (FBP) or an iterative method to get basis images of $c_p(\mathbf{r})$ and $c_c(\mathbf{r})$.

III. Proposed Algorithm

Let us define the energy-dependent x-ray transmittance as follows:

$$X(E) = \exp\left(-\boldsymbol{\Phi}(E)\mathbf{v}\right). \tag{5}$$

When heavy elements are absent, $X(E)$ is a smooth and monotonically increasing function in $E \in [E_{min}, E_{max}]$. We hypothesize that $X(E)$ can be presented by $k-1$ degrees of Gram polynomials as follows:

$$X(E) = \Psi_k(E) + \delta X_k(E) = \sum_{i=0}^{k-1} \theta_i P_i(E) + \delta X_k(E), \tag{6}$$

where $P_i(E)$ is the i-th order Gram polynomial [6], θ_i is the associated coefficient, and $\delta X_k(E)$ is the residual transmittance. After substituting (6) into (3), we can formulate the expected number of photons as follows:

$$\lambda_b(\mathbf{v}) = \sum_{i=0}^{k-1} B_{(b,i)}\theta_i + \eta_{(k,b)}, \text{ for } b = 1, 2, \cdots, m, \tag{7}$$

where $\eta_{(k,b)} = \int_{E_{min}}^{E_{max}} A_b(E)\delta X_k(E)dE$ is the residual factor and

$$B_{(b,i)} = \int_{E_{min}}^{E_{max}} A_b(E)P_i(E)dE. \tag{8}$$

Under the assumption that $\eta_{(k,b)}$ is negligible compared to the quantum noise, the original nonlinear model of the PCD measurements can be linearized as the following matrix equation:

$$\mathbf{y} \triangleq B\boldsymbol{\theta} + \boldsymbol{\epsilon}, \tag{9}$$

where $B \in \mathbb{R}^{m\times k}$ is the sensing matrix whose b-th row and $(i+1)$-th column element is $B_{(b,i)}$, and $\boldsymbol{\theta} \in \mathbb{R}^{k\times 1}$ is the polynomial coefficients vector. Based on this model, we propose a three-step algorithm which will be described in the following sub-sections.

A. Estimation of the Polynomial Coefficients (1^{st} step)

The first step of the proposed algorithm is to estimate the polynomial coefficients $\boldsymbol{\theta}$ in (9) and we propose the following optimization problem:

$$\hat{\boldsymbol{\theta}} = \arg\min_{\boldsymbol{\theta}} ||\mathbf{y} - B\boldsymbol{\theta}||^2 + \lambda||K\boldsymbol{\theta}||^2, \tag{10}$$

where $K \in \mathbb{R}^{k\times k}$ is the contrast matrix to regularize the selected polynomial coefficients. Then, (10) has the solution in a closed form as follows:

$$\hat{\boldsymbol{\theta}} = \left(B^T B + \lambda K^T K\right)^{-1} B^T \mathbf{y}. \tag{11}$$

The estimated x-ray transmittance $\hat{X}(E)$ can then be calculated by

$$\hat{X}(E) = \sum_{i=0}^{k-1} \hat{\theta}_i P_i(E). \tag{12}$$

B. Estimation of the Basis Line-integrals (2^{nd} step)

From the definition of the x-ray transmittance, we can formulate the following least squares fitting problem to estimate the basis line-integrals:

$$\hat{\mathbf{v}} = \arg\min_{\mathbf{v}} \left\| \hat{X}(E) - \exp\left(-\boldsymbol{\Phi}(E)\mathbf{v}\right) \right\|^2. \tag{13}$$

Since it is the non-linear optimization problem, we propose the following linearized least squares fitting by taking a log-operator to each term in the cost function:

$$\hat{\mathbf{v}} = \arg\min_{\mathbf{v}} \left\| \ln\left(\hat{X}(E)\right) + \boldsymbol{\Phi}(E)\mathbf{v} \right\|^2. \tag{14}$$

Note that the values close to zero in $X(E)$ are more likely to occur at the low x-ray energy range so error in those values can be boosted by taking the log-operator. Therefore, we neglect $\hat{X}(E)$ values on $E \in [E_{min}, E_{min} + E_L]$ before taking the log-operator, where E_L is empirically calculated by

$$E_L = 10 \cdot \left(1 - \log_{10}\left(\hat{\theta}_0\right)\right). \tag{15}$$

Since the meaning of the 0-th order polynomial coefficient θ_0 is the average value of the x-ray transmittance, E_L increases as the amount of attenuation increases.

C. Bias Correction (3^{rd} step)

The final step is to compensate a bias in the estimated $\hat{\mathbf{v}}$ caused from the linearized procedures in the previous steps. Since the exact correction is intractable, we apply bias correction tables to correct the bias factor. It is similar with the one in [5], however, we perform it multiple times to improve the accuracy. To generate bias correction tables, we discretize $v_p \in [0, 2]$ and $v_c \in [0, 10]$, and generate a $10,000$ noisy PCD measurements for each combination of (v_p, v_c). After applying the proposed method on these training sets, we can generate bias correction tables of photoelectric effect ($BCT_p^{(1)}$) and Compton scattering ($BCT_c^{(1)}$) by calculating the bias from the estimated results at each combination of (v_p, v_c). Furthermore, the bias corrected training sets can be used again to calculate the remaining bias and then to generate the second bias correction tables $BCT_p^{(2)}$ and $BCT_c^{(2)}$. This process can be repeated to generate subsequent bias correction tables.

D. Practical Implementation

Discrete orthogonal polynomial (DOP) tool box [7, 8] can be used to generate the DOP set which satisfies the nature of Gram polynomials on the discretized domain of $E \in$

$[E_{min}, E_{max}]$. We set E_L as the number of neglecting points by rounding up the value in (15) and limiting it from zero to L_{max} to keep it from having a negative or excessive value. Then, we can group together the estimated x-ray transmittances which have the same E_L value so that these grouped data can be processed at once to estimate the associated basis line-integrals. We provide a pseudo-code implementation of the proposed method to estimate the entire sinograms in Algorithm 1.

Algorithm 1 Pseudo-code Implementation of the Proposed Method.

[1^{st} step]
Estimate the polynomial coefficients using (11).
Calculate the estimated x-ray transmittance using (12).
[2^{nd} step]
Calculate E_L for the entire PCD measurements using (15).
for $\ell = 0, \ldots, L_{\max}$ **do**
  Group together the estimated x-ray transmittances having $E_L = \ell$.
  Neglect the first ℓ points and estimate the basis sinograms using (14).
  Set $\hat{V}_\ell$ as the estimated results.
end for
Set $\hat{V}$ as a combined data of $\hat{V}_\ell$, for $\ell = 0, 1, \cdots, L_{\max}$.
[3^{rd} step]
Set $q = 0$ and $\hat{V}^{(0)} = \hat{V}$.
for $q = 1, \ldots, \text{Iter}_{\max}$ **do**
  $\hat{V}_p^{(q)} = \hat{V}_p^{(q-1)} - BCT_p^{(q)}(\hat{V}^{(q-1)})$
  $\hat{V}_c^{(q)} = \hat{V}_c^{(q-1)} - BCT_c^{(q)}(\hat{V}^{(q-1)})$
  Set $\hat{V}^{(q)}$ as a combined data from $\hat{V}_p^{(q)}$ and $\hat{V}_c^{(q)}$.
end for

We set $L_{\max} = 25$ and $\text{Iter}_{\max} = 3$. We also set $m = k = 4$, as will be explained later, and the contrast matrix as $K = \mathbf{u}\mathbf{u}^T \otimes \mathbf{I}_2$, where $\mathbf{u} = [0, 1]^T$, $\mathbf{I}_2$ is the 2×2 identity matrix, and $\otimes$ is the Kronecker product. λ in (11) is calculated by $\lambda = 0.1 \cdot \lambda_{\max}(B^T B)$, where $\lambda_{\max}(B^T B)$ is the maximum eigen-value of $B^T B$.

IV. Methods

We set $m = 4$ and the associated energy thresholds as $[20, 39, 62, 81]\,\text{keV}$. Total number of incident photons per projection per PCD pixel was given by $275,000$ based on the $0.5\,\text{mm} \times 0.5\,\text{mm}$ pixel size, $500\,\text{mA}$ of currents, and $1\,\text{msec/proj}$ of time duration. To validate the hypothesis, we calculated $\Delta(\eta_k)$ which is given by

$$\Delta(\eta_k) = \frac{1}{m} \sum_{b=1}^{m} \left| \frac{\eta_{(k,b)}}{\lambda_b(\mathbf{v})} \right|,$$

where $\eta_{(k,b)}$ is the residual factor when $\hat{\Psi}_k(E)$ in (6) is the optimal solution of approximating $X(E)$ in the sense of l_2 norm [6]. We define the hypothesis can be considered to be true when $\Delta(\eta_k) \leq 0.02$. We used a simple object consists of water ($0 \sim 36\,\text{cm}$) and bone ($2\,\text{cm}$) to test the tendency of the estimated v_p and v_c, and compared it in terms of bias and standard deviation (SD). We also used the $420\,\text{mm} \times 420\,\text{mm}$ abdominal phantom which is uniformly discretized by 512×512 pixels. We assigned the basis coefficients of photoelectric and Compton scattering to phantom image and performed the $2D$ fan-beam projection for each basis images to generate the ground-truth basis sinograms. The number of PCD pixels per projection view was 1718 and the number of projection views was $1,000$ over 2π. Using these basis sinograms, we generated PCD measurements for each sinogram points with 100 noise realizations. FBP is performed on the estimated basis sinograms and their combined CT images at $E = 55\,\text{keV}$ are compared to the FBP results of the ground-truth basis sinograms. We used Algorithm 1 as the proposed method and Nelder-Mead algorithm [9] as the ML estimator to solve the following problem:

$$\hat{\mathbf{v}} = \arg\min_{\mathbf{v}} \mathcal{L}(\mathbf{v}), \tag{16}$$

where $\mathcal{L}(\mathbf{v})$ is the negative logarithm of the likelihood which is equivalent to

$$\mathcal{L}(\mathbf{v}) = \sum_{b=1}^{m} \left[\lambda_b(\mathbf{v}) - y_b \ln\left(\lambda_b(\mathbf{v})\right) \right]. \tag{17}$$

V. Numerical Results

A. Validation of the Hypothesis

The results of $\Delta(\eta_k)$ for various values of k and objects, which consist of water and bone, are illustrated in Fig. 1. As we can see, $k = 4$ is enough to satisfy $\Delta(\eta_k) \leq 0.02$ in general (the tendency was similar for other thicknesses of bone). The polynomial set $\{P_i(E)\}_{i=0}^{3}$ is illustrated in Fig. 2(a) and the example of the approximation by using it is shown in Fig. 2(b).

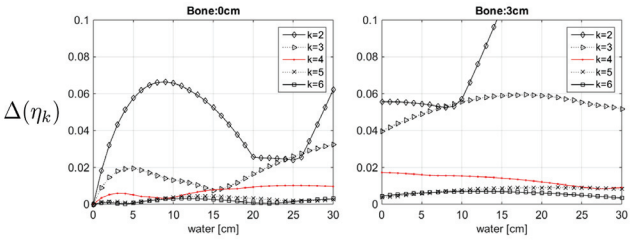

Fig. 1: $\Delta(\eta_k)$ for various k and thicknesses of water and bone.

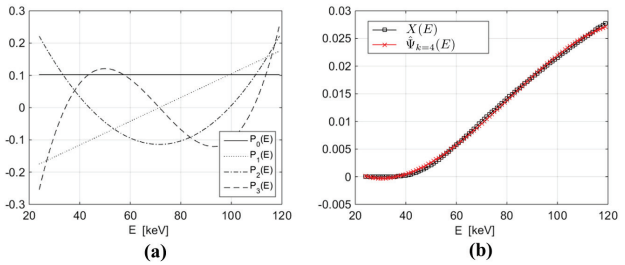

Fig. 2: (a) 0th to 3rd degree of DOPs and (b) the example of the approximation with $16\,\text{cm}$ of water and $3\,\text{cm}$ of bone.

B. Simple Object

The various results of bias and SD for the simple object are illustrated in Fig. 3. The ML estimator shows a strong bias for the photoelectric effect compared to that of the proposed method when water is larger than $30\,\text{cm}$. Both methods meet the Cramer-Rao lower bound (CRLB) except that the SD of the proposed method is slightly larger than CRLB for Compton scattering when water is less than $20\,\text{cm}$. The tendency for different thicknesses of bone was similar (the results are not shown here).

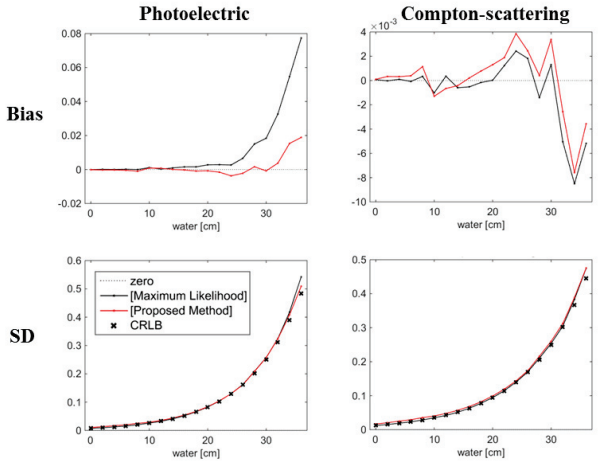

Fig. 3: Various results for the simple object.

C. Abdominal Phantom

The average CT images and their bias and SD images are illustrated in Fig. 4. CT and SD images for both ML estimator and proposed method are qualitatively similar while a certain bias can be observed in the result from the ML estimator, especially around the bone area.

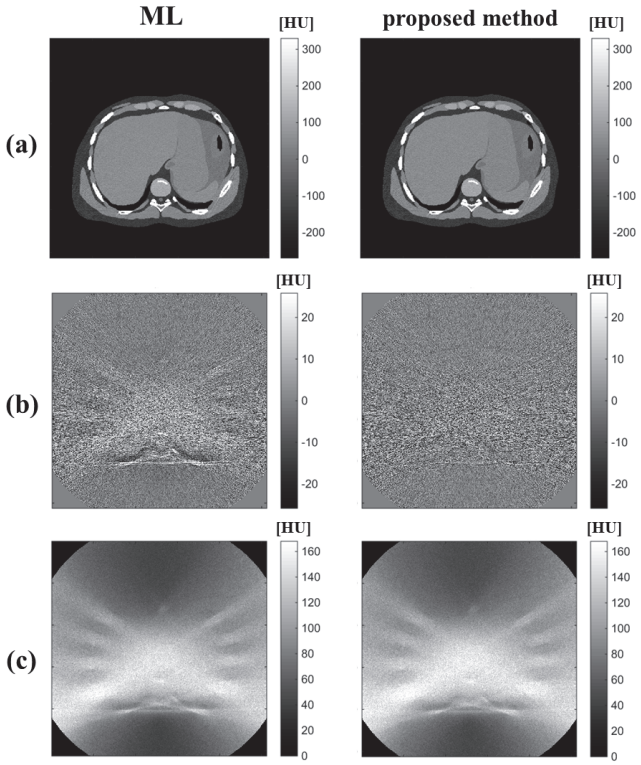

Fig. 4: (a) Average μ_a, (b) bias, and (c) SD images from ML estimator and proposed method.

The average run time for estimating the entire sinograms and the average absolute value of bias and SD calculated in the non-air region are compared in Fig. 5. As we can see, the proposed method is more computationally efficient than ML estimator while the accuracy is comparable.

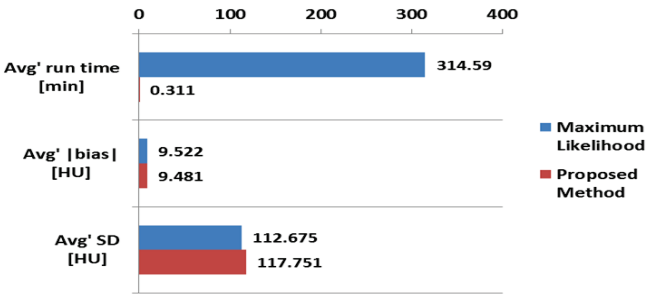

Fig. 5: Comparison of the various quantitative measures.

VI. Conclusion

We developed the computationally efficient algorithm for estimating basis sinograms in the SRE-modeled PCD-CT problem based on the approximation of the x-ray transmittance with low-order Gram polynomials. The algorithm consists of two-step linearized approach and the bias correction step. The proposed algorithm is validated using the various simulation studies and compared with the conventional ML estimator. The results show that the proposed method estimates the entire sinograms in much faster time compared to the ML estimator while the accuracy is comparable.

Acknowledgment

We appreciate the support of Drs. Thomas G. Flohr and Matthew K. Fuld in Siemens Healthcare during the course of the study.

References

[1] K. Taguchi and J. S. Iwanczyk, "Vision 20/20: single photon counting x-ray detectors in medical imaging," *Med. Phys.*, vol. 40, no. 10, pp. 100 901(1–19), October 2013.

[2] J. Cammin, S. Kappler, T. Weidinger, and K. Taguchi, "Photon-counting CT: modeling and compensating of spectral distortion effects," *Proc. of SPIE*, vol. 9412, pp. 941 250(1–6), 2015.

[3] J. P. Schlomka, E. Roessl, R. Dorscheid, S. Dill, G. Martens, T. Istel, C. Bäumer, C. Herrmann, R. Steadman, G. Zeitler, A. Livne, and R. Proksa, "Experimental feasibility of multi-energy photon-counting K-edge imaging in pre-clinical computed tomography," *Phys. Med. Biol.*, vol. 53, pp. 4031–4047, 2008.

[4] L. A. Lehmann, R. E. A. adn A. Macovski, and W. R. Brody, "Generalized image combinations in dual KVP digital radiography," *Med. Phys.*, vol. 8, no. 5, pp. 659–667, September 1981.

[5] R. E. Alvarez, "Estimator for photon counting energy selective x-ray imaging with multibin pulse height analysis," *Med. Phys.*, vol. 38, no. 5, pp. 2324–2334, May 2011.

[6] R. W. Barnard, G. Dahlquist, K. Pearce, L. Reichel, and K. C. Richards, "Gram polynomials and the Kummer function," *Journal of Approximation Theory*, vol. 94, pp. 128–143, 1998.

[7] P. O'Leary and M. Harker, "Discrete polynomial moments and Savitzky-Golay smoothing," *Waset Special Journal*, vol. 72, pp. 439–443, 2010.

[8] M. Harker and P. O'Leary, "Discrete Orthogonal Polynomial Toolobx:DOPBox Version 1.8," *MATLAB Central File Exchange*, 2013, http://www.mathworks.com/matlabcentral/fileexchange/41250-discrete-orthogonal-polynomial-toolbox–dopbox-version-1-8.

[9] J. C. Lagarias, J. A. Reeds, M. H. Wright, and P. E. Wright, "Convergence properties of the Nelder-Mead simplex method in low dimensions," *SIAM J. Optim.*, vol. 9, no. 1, pp. 112–147, 1998.

Texture Enhanced Optimization-Based Image Reconstruction (TxE-OBIR) Algorithm

Huiqiao Xie, Tianye Niu, Huipeng Deng and Xiangyang Tang*

***Abstract*—In order to reduce radiation dose in X-ray computed tomography (CT), the optimization based image reconstruction (OBIR) from sparse projection views has been proposed and investigated. However, the OBIR algorithms usually generate images with quite different texture compared to the widely used reconstruction method (i.e. filtered back-projection – FBP) in clinical practice, which may lead to less confidence while the radiologists/physicians making diagnostic decisions. In this paper, we propose and evaluate a novel and practical texture enhanced OBIR (TxE-OBIR) method, in which a texture image is reconstructed by the FBP algorithm from synthesized projection views of noise and added into the OBIR image. The texture of the TxE-OBIR image is optimized by matching noise magnitude and taking detector cell cross talking effect into account. As confirmed qualitatively by visual inspection and quantitatively by noise power spectrum (NPS) of a water phantom and an anthropomorphic head phantom, the proposed method can produce images with textures that are visually identical to those of the gold standard full view FBP images.**

***Index Terms*—Texture Enhancement, Optimization-Based Image Reconstruction, CT**

I. Introduction

THE X-ray ionizing radiation has become a main concern in the clinical utility of CT scanners. In order to reduce the radiation dose, many approaches, such as bowtie filtration [1], automatic exposure control (AEC) [1, 2] and tube voltage and/or current modulation, have been adopted. In addition, the optimization-based image reconstruction (OBIR) from sparse projection views has been proposed and investigated to further reduce the radiation dose in X-ray CT through acquiring [3, 4]. However, due to the different noise transfer behavior from projections to reconstructed images between the OBIR and FBP algorithms, the OBIR usually generates images with a quite different texture compared to that of the widely used FBP algorithm. Fig. 1 shows the full view FBP and sparse view OBIR images and their noise power spectrum (NPS). Using fewer projection views, the sparse view OBIR can generate an image at the accuracy that is identical to that of the full view FBP and thus reduce radiation dose. However, the sparse view OBIR image has a "flatter" texture, corresponding to the low frequency components (< 0.2 lp/mm) in its NPS.

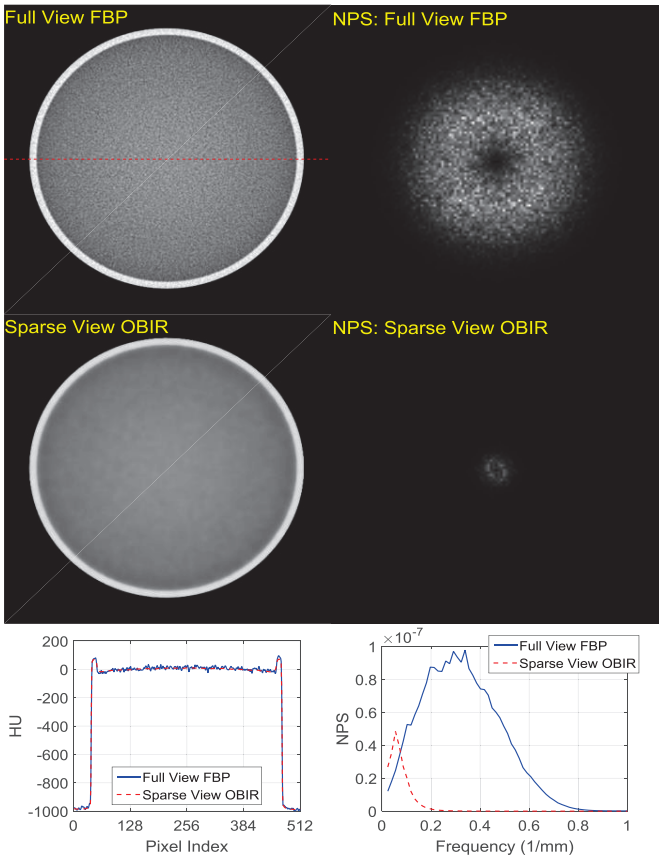

Fig. 1. The image of full view (984) FBP reconstruction of a water phantom and its NPS (top row); The image of 4-time sparser view (246) OBIR of the same water phantom and its NPS (middle row); The profiles of the full view FBP and sparse view OBIR along the center dashed line in the full view FBP image and their radial averaged NPS profile (bottom row). (Display window: $[-100\ 100]$ HU and $[0.0\ 2.0 \times 10^{-7}]$ for images and NPS, respectively.

In this paper, we propose and evaluate a novel and practical texture enhanced OBIR (TxE-OBIR) method, in which, the OBIR is carried out first, followed by adding a texture image that is reconstructed by the FBP algorithm from synthesized full projection views of noise. In synthesizing the projection views of noise, in addition to taking the bowtie and AEC effects are taken into consideration for magnitude equalization, the detector cross talking effect is also taken into account to modulate the NPS of the texture image.

Huiqiao Xie, and Xiangyang Tang are with the Department of Radiology and Imaging Sciences, Emory University School of Medicine, Atlanta, GA 30322, USA.

Tianye Niu is with Sir Run Run Shaw Hospital, Institute of Translational Medicine, Zhejiang University, Hangzhou, China.

Huipeng Deng is with Physics and Algorithm, Sinovision Technologies, Beijing, China.

* corresponding author e-mail: xiangyang.tang@emory.edu

II. Method and Materials

A. The TxE-OBIR Algorithm

Given sparse projection views, the magnitude of noise is acquired at first, which is utilized to synthesize a full set of noise projection views. Then a texture image is reconstructed from the synthesize noise projection views with the FBP algorithm, which is added into the sparse view OBIR image for texture enhancement. This algorithm is referred as texture enhanced optimization-based image reconstruction (TxE-OBIR) and its steps are shown in Fig. 2 as a flow chart.

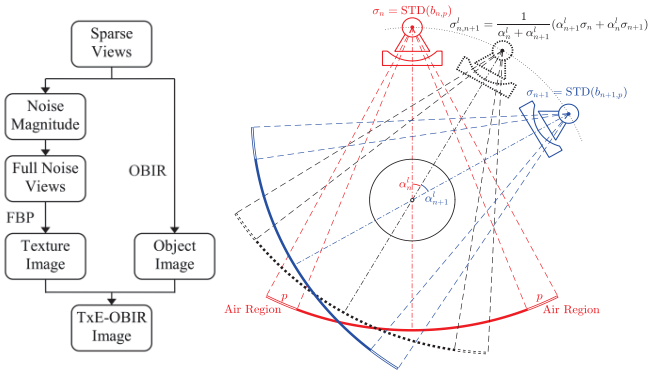

Fig. 2. Flow chart of the texture enhanced optimization-based image reconstruction (TxE-OBIR) method; and illustration of the linear interpolation of noise magnitudes of two adjacent sparse views.

1) Generation of the Texture Image

In general, the X-ray photon noise comes with each detector cell through different views [5]. However, certain dose reduction methods (e.g. AEC [1, 2]), which may jeopardize the noise's statistics, are used in practice. In addition, the X-ray intensity is made relatively uniform across detector cells by beam forming devices (e.g. bowtie filtration [1]), which leads to a virtually constant noise statistics over detector cells [6]. Recognizing these facts, we acquire the magnitude of noise as the standard deviation of the inter-detector cell variance in the regions where no object presents (air region) for each view:

$$\sigma_n = \mathrm{STD}(b_{n,p}) \tag{1}$$

where $b_{n,p}$ stands for the projection data, n is the sparse view index and p is the detector cell index ($p \in$ air region).

Suppose a clinical CT scanner acquire S times projection views in a full scan, the noise magnitude of the lth ($l = 1,2,3,\cdots,S-1$) projection between each pair of adjacent sparse views n and $n+1$ is obtained via linear interpolation as shown in Fig. 2.

Then, the noise projection views are synthesized as

$$\boldsymbol{b}_n^{\mathrm{noise}} = r^{0.5} \cdot \sigma_n \cdot \boldsymbol{x} \tag{2}$$

where $\boldsymbol{x} = N(0,1)$ is a Gaussian random variable with zero mean and unit variance [9] and r is the amplitude modulation factor.

From the synthesized full noise projection views, a texture image can be readily reconstructed with the FBP algorithm and added into the OBIR image for texture enhancement.

2) Optimization-Based Image Reconstruction

In OBIR, the image reconstruction is usually formulated as solving an optimization problem – minimizing the total variation (TV) in an image with constraints in data fidelity and non-negativity [3]:

$$\boldsymbol{f}^* = \arg\min \|\boldsymbol{f}\|_{\mathrm{TV}}, \ \text{s.t.}\ \|\boldsymbol{A}\boldsymbol{f} - \boldsymbol{b}\|_2^2 \le \varepsilon \text{ and } f_j \ge 0 \tag{3}$$

where the column vector $\boldsymbol{b}$ with length $M = N_{\mathrm{d}} \times N_{\mathrm{v}}$ (N_{d} and N_{v} are the number of detector cells and the number of views, respectively) denotes the measured sinogram. $\boldsymbol{f}$ is the cascaded column vector of the image to be reconstructed with length N (the number of image voxels). $\boldsymbol{A}$ is the system matrix with dimension $M \times N$. $\|*\|_{\mathrm{TV}}$ is the TV term which is calculated as in Ref. [4]. $\|*\|_2^2$ represents the l_2 norm, and j, ranging from 1 to N, denotes the index of image voxel.

Note that, the parameter ε constraints the variance of difference between the predicted and raw projections. After beam-hardening and scattering corrections, the noise in projection data should observe Poisson distribution, and thus ε can be estimated from measured projection data [7].

To improve computational efficiency, the optimization problem can be reformatted into [4]

$$\boldsymbol{f}^* = \arg\min \left\{ \|\boldsymbol{f}\|_{\mathrm{TV}} + \frac{1}{t}\left[-\log\left(-\frac{1}{2}\|\boldsymbol{A}\boldsymbol{f} - \boldsymbol{b}\| + \varepsilon \right) \right] \right\}, \ \text{s.t.}\ f_j \ge 0 \tag{4}$$

in which the modified logarithmic term [4] is adopted. This optimization is solved with the GP-BB method [4], and the parameter t is set to 1.0.

B. Modulation of the Texture Image Magnitude

The magnitude modulation factor r in Eq. (2) should be 1.0 if the X-ray intensity in the central detector region corresponding to the object was the same as that in the periphery region corresponding to the air due to the X-ray beam forming devices. However, this situation will not happen in a real CT scan; so, the factor r needs to be adjusted for better texture fitting of the full view scan FBP case.

We calculate the magnitude modulation factor r as

$$r = \overline{\mathrm{NPS}_{0.2}^{\mathrm{water}}} \,/\, \overline{\mathrm{NPS}_{0.2}^{\mathrm{texture}}} \tag{5}$$

where $\overline{\mathrm{NPS}_{0.2}^{\mathrm{water}}}$ is the average of the full view FBP water phantom image NPS that above the threshold of 0.2 times of its maximum, and $\overline{\mathrm{NPS}_{0.2}^{\mathrm{texture}}}$ is the average of the $r = 1.0$ texture image NPS that above the threshold of 0.2 times of its maximum.

C. Detector Cross Talking Effect

The texture image can also be affected by the inter-cell cross talking. By taking this effect into account, we further calculate the noise projection data as

$$b_{n,q}^{\mathrm{noise}} = c \cdot b_{n,q}^{\mathrm{noise}} + \frac{1}{2}(1-c)\left(b_{n,q-1}^{\mathrm{noise}} + b_{n,q+1}^{\mathrm{noise}}\right) \tag{6}$$

where $b_{n,q}^{\mathrm{noise}}$ is the noise projection data generated by Eq. (2); q, ranging from 1 to N_{d}, indexes the detector cell; and parameter c controls the cross talking strength. A smaller c represents higher cross talking between detector cells; and $c = 1.0$ means there is no cross talking.

D. Evaluation

A water phantom and an anthropomorphic head phantom

were used for visual inspection and quantitative performance evaluation of noise power spectrum (NPS) [8, 9]. The water phantom was scanned at 120 kVp, 200 mA and 1.0 s/rot, and the anthropomorphic head phantom was scanned at 120 kVp, 300 mA and 1.0 s/rot. In the scanning, the source to gantry iso distance was 541.0 mm and the gantry iso to detector distance was 408.1 mm. The full view scan acquired 984 projections along the angular range of [0, 2π]. The 4-time sparse projection views (246) were selected in an equal angular step for the OBIR and TxE-OBIR reconstructions.

III. Results

A. NPS and Its Variation over Cross Talking

Fig. 3 shows the normalized NPS of the synthesized texture images over various detector cross talking, in which modulation on the NPS by the detector cross talking is observed. Specifically, the NPS has a lower frequency with a greater cross talking strength, and the modulation effect is more obvious in the frequency range that is greater than 0.3 lp/mm. The texture image has almost the same NPS as that of the full view FBP water phantom image at $c = 0.9$.

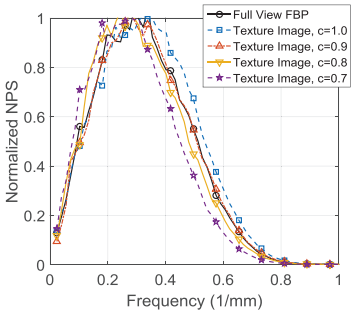

Fig. 3. NPS over various cell cross talking strength ($c = 1.0, 0.9, 0.8$ and 0.7); The NPS of the full view FBP water phantom image is also shown in the figure.

B. Evaluation by Water and Head Phantoms

The full view FBP image, sparse view OBIR image and TxE-OBIR images with different texture enhancement implemented at various noise magnitudes and cross talking of the water phantom and their corresponding NPS are shown in Fig. 4. It is observed that the reconstruction accuracy of OBIR is the same as that of the full view FBP reconstruction. However, the texture in the OBIR is quite different from that of the full view FBP. The major noise power in the OBIR image concentrates at low spatial frequency (< 0.2 lp/ mm), and the noise power in the full view FBP image distributes over the range of 0.0 lp/mm to 0.8 lp/mm.

With the texture enhancement approach, the proposed TxE-OBIR can produce an image with its texture virtually identical to the full view FBP reconstruction. The effect of noise magnitude and detector cross talking on the texture can also been observed in Fig. 4. By matching the amplitude of NPS, the TxE-OBIR can generate an image with the same noise magnitude as that of the full view FBP image. However, the image has a more "crispy" appearance than the full FBP image. By taking the detector cross talking effect into account, the

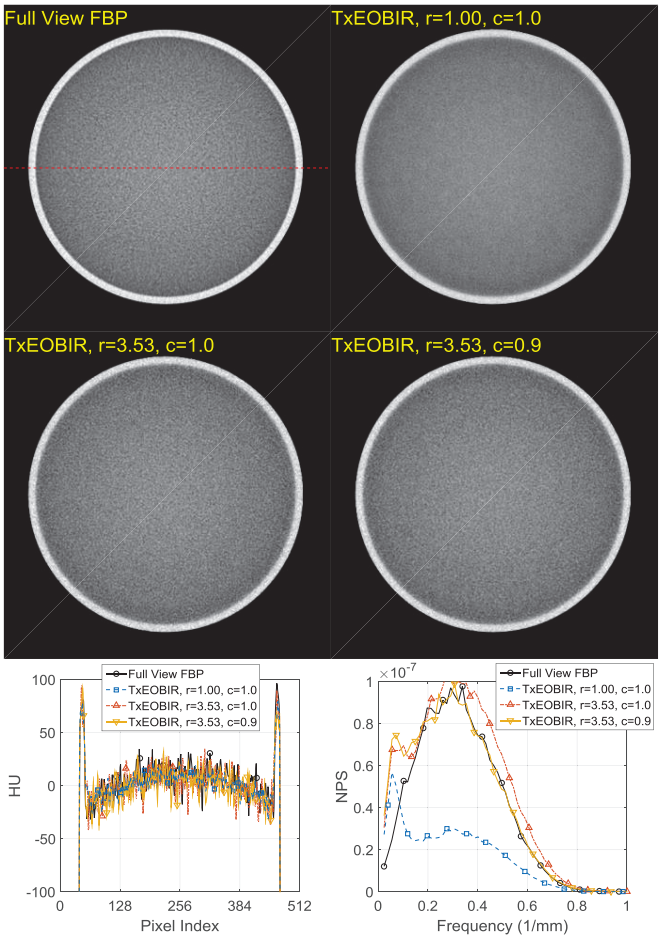

Fig. 4. The full view (984) FBP image and the TxE-OBIR images of original texture magnitude ($r = 1.00$) and matched magnitude ($r = 3.53$) without ($c = 1.0$) and with ($c = 0.9$) detector cell cross talking (top and middle rows); Their profiles along the center dashed line in the full view FBP image and NPS (bottom row). (display window of the images: [−100 100] HU).

"crispy" appearance of the TxE-OBIR image can be "softened" and is identical to the full view FBP image. This visual inspection can be confirmed by comparing the NPS of these images.

The full view FBP image, sparse view FBP image, sparse view OBIR image and the TxE-OBIR images with different texture amplitudes and cross talking strength of the anthropomorphic head phantom are shown in Fig. 5. It is observed that the OBIR algorithm outperforms the FBP algorithm when only sparse projection views are acquired for image reconstruction. Similar to the case of water phantom, by matching the noise magnitude and altering the detector cross talking effect with the parameters that taken from the water phantom scan, the TxE-OBIR can generate an image with texture that is identical to that of the full view FBP image.

IV. Discussions

As can be seen from the image profiles in Fig. 4 and images in Fig. 5, there are capping/cupping and shading artifacts that caused by beam hardening effect. These artifacts can be readily corrected by methods described in other literatures [10, 11].

It is observed that, due to the intrinsic assumption that an

image to be reconstructed is piece-wise continuous and the intrinsic information loss in the acquisition of sparse projection views, the edges and small structures in the images reconstructed by the OBIR and TxE-OBIR from sparse projection views are blurred or lost. Such degradation in the edge and/or fine structure may be partially recovered by *salient views* [12], but a detailed investigation is beyond the scope of this work.

As can be seen from Fig. 1 and Fig. 4, due to the noise suppression ability of the OBIR, images reconstructed by the proposed method has NPS peaks at low frequency ($< 0.1\ \mathrm{lp/mm}$) and is difficult to be eliminated. Fortunately, the human eyes are not sensitive to low frequency noise, especially while the noise texture image is being added into the OBIR image.

It is a practical solution to modulate the noise magnitude and alter the inter-detector cell cross talking while generating the texture image. It should be noted that the beam forming devices cannot guarantee a uniform X-ray intensity and thus noise distribution across detector cells in a real scan. In this paper, we determine the magnitude modulation factor r through water phantom scan. It may be more appropriate way to determine the parameters for texture enhancement by taking the input from radiologists/physicians in practice.

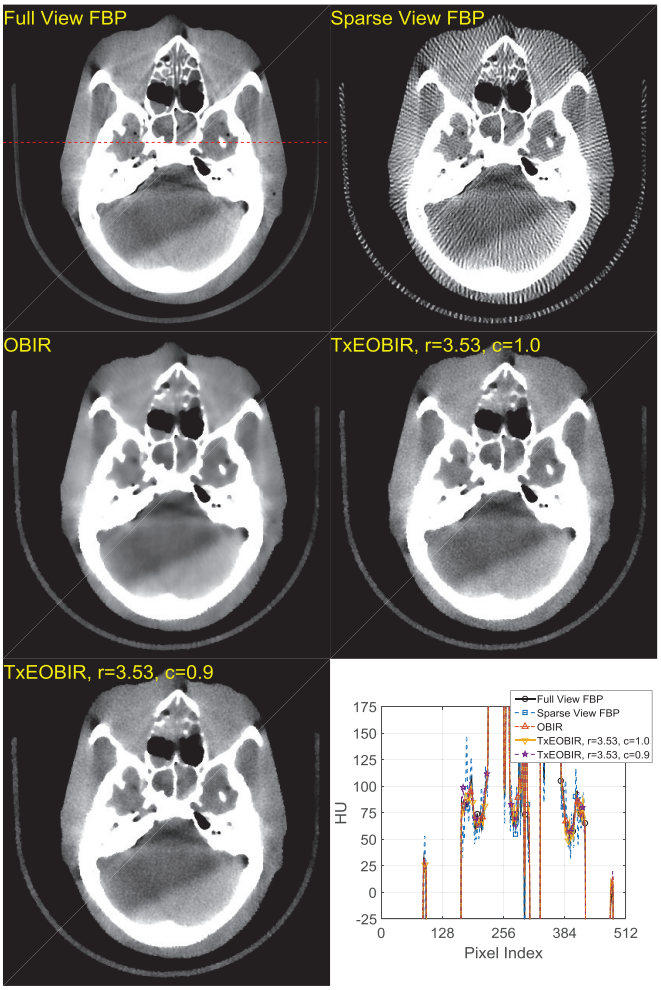

Fig. 5. Images of an anthropomorphic head phantom reconstructed with full view (984) FBP, sparse view (246) FBP, sparse view (246) OBIR, texture enhanced ($r = 3.53$) TxE-OBIR without ($c = 1.0$) and with ($c = 0.9$) detector cell cross talking; the profiles along the dash line in the full view FBP image are also plotted. (display window: $[-25\ 175]$ HU).

V. Conclusions

As confirmed qualitatively by visual inspection and quantitatively by the noise power spectrum (NPS) evaluation using a water phantom and an anthropomorphic head phantom, the proposed method can produce images with textures that are visually identical to those of the gold standard FBP images. The proposed method is a novel and practical solution, and thus is believed to be of clinical relevance in the future.

References

[1] A. Manduca, L. Yu, J. D. Trzasko, N. Khaylova, J. M. Kofler, C. M. McCollough, and J. G. Fletcher, "Projection space denoising with bilateral filtering and CT noise modeling for dose reduction in CT," Medical Physics, vol. 36, no. 11, pp. 4911-4919, 2009.

[2] P. Massoumzadeh, S. Don, C. F. Hildebolt, K. T. Bae, and B. R. Whiting, "Validation of CT dose-reduction simulation," Medical Physics, vol. 36, no. 1, pp. 174-189, 2009.

[3] E. Y. Sidky, C.-M. Kao, and X. Pan, "Accurate image reconstruction from few-views and limited-angle data in divergent-beam CT," Journal of X-Ray Science and Technology, vol. 14, no. 2, pp. 119-139, 01/01/, 2006.

[4] T. Niu, and L. Zhu, "Accelerated barrier optimization compressed sensing (ABOCS) reconstruction for cone-beam CT: Phantom studies," Medical Physics, vol. 39, no. 7, pp. 4588-4598, 2012.

[5] L. Yu, M. Shiung, D. Jondal, and C. H. McCollough, "Development and Validation of a Practical Lower-Dose-Simulation Tool for Optimizing Computed Tomography Scan Protocols," Journal of Computer Assisted Tomography, vol. 36, no. 4, pp. 477-487, 2012.

[6] B. R. Whiting, P. Massoumzadeh, O. A. Earl, J. A. O'Sullivan, D. L. Snyder, and J. F. Williamson, "Properties of preprocessed sinogram data in x-ray computed tomography," Medical Physics, vol. 33, no. 9, pp. 3290-3303, 2006.

[7] K. Yang, S.-Y. Huang, N. J. Packard, and J. M. Boone, "Noise variance analysis using a flat panel x-ray detector: A method for additive noise assessment with application to breast CT applications," Medical Physics, vol. 37, no. 7, pp. 3527-3537, 2010.

[8] K. Faulkner, and B. M. Moores, "Analysis of x-ray computed tomography images using the noise power spectrum and autocorrelation function," Physics in Medicine and Biology, vol. 29, no. 11, pp. 1343, 1984.

[9] M. F. Kijewski, and P. F. Judy, "The noise power spectrum of CT images," Physics in Medicine and Biology, vol. 32, no. 5, pp. 565, 1987.

[10] M. Kachelrieß, K. Sourbelle, and W. A. Kalender, "Empirical cupping correction: A first-order raw data precorrection for cone-beam computed tomography," Medical Physics, vol. 33, no. 5, pp. 1269-1274, 2006.

[11] Y. Kyriakou, E. Meyer, D. Prell, and M. Kachelrieß, "Empirical beam hardening correction (EBHC) for CT," Medical Physics, vol. 37, no. 10, pp. 5179-5187, 2010.

[12] Z. Zheng, and K. Mueller, "Identifying Sets of Favorable Projections for Few-View Low-Dose Cone-Beam CT Scanning," in 11th International Meeting on Fully Three-Dimensional Image Reconstruction in Radiology and Nuclear Medicine, Potsdam, Germany, 2011, pp. 314-317.

Statistical Distributions of Ultra-Low Dose CT Sinograms in the Data Processing Stream

Tzu-Cheng Lee, Ruoqiao Zhang, Adam M. Alessio, Lin Fu, Bruno De Man, Paul E. Kinahan

***Abstract*— Low dose CT imaging is typically constrained to be diagnostic. However, there are applications for even lower-dose CT imaging, including image registration across multi-frame CT images and attenuation correction for PET/CT imaging. We define this as the ultra-low-dose (ULD) CT regime where the exposure level is a factor of 10 lower than current low-dose CT technique levels. In the ULD regime it is possible to use statistically-principled image reconstruction methods that make full use of the raw data (sinogram) information. However, clinical CT scanners have a data processing stream that uses the standard approach of a negative logarithm transformation in as well as pre-log and post-log corrections (most importantly a pre-log non-positivity correction). Our goal is to understand the statistical distribution of ULD CT data through the different data processing steps to understand when analytic or iterative image reconstruction methods may be effective in producing images that are useful for image registration or attenuation correction in PET/CT imaging. We used calibrated simulation studies and the Kolmogorov–Smirnov statistic to evaluate the normality of processed sinogram data. In summary, our results indicate that there are three general regimes: (1) Diagnostic CT, where post-log data are well modeled by normal distribution. (2) Low-dose CT, where normal distribution remains a reasonable approximation and statistically-principled (post-log) methods that assume a normal distribution have an advantage. (3) An ULD regime that is photon-starved and the normal approximation is no longer effective. This leads to fundamental limits in the estimation of ULD CT data when using a standard data processing stream.**

I. Introduction

Concerns with CT dose have led to lower dose scanning protocols, often using statistically-principled (i.e. iterative) image reconstruction methods to suppress the effects of increased quantum noise [1]. These low-dose methods are often developed using the assumption that the projection data after the logarithm transform follow a normal distribution [2]-[4]. However, there are applications for even lower-dose CT imaging, including multi-frame CT image registration and attenuation correction for PET/CT. We have previously shown that several commonly used statistical models are biased in estimating the attenuation coefficients for ultra-low dose CT sinograms [5]. The aim of this study is to determine the statistical distribution due to the data processing steps for ultra-low dose CT sinograms, specifically, we evaluated the impact of the non-positivity correction and the negative log transformation. We would like to determine if the processed data is normally distributed, and if not, we would also like to know that what is its impact on WLS reconstruction algorithms.

Tzu-Cheng Lee, Ruoqiao Zhang, Adam A. Alessio, and Paul E. Kinahan are with the Imaging Research Laboratory, Department of Radiology, University of Washington, Seattle, WA 98195 USA (efrenlee@uw.edu, zhangrq@uw.edu, aalessio@uw.edu, kinahan@uw.edu).

Lin Fu, Bruno De Man are with General Electric Global Research Center, Niskayuna, NY 12309, USA (fulin@ge.com, deman@ge.com)

II. Methods

A. Polyenergetic Cascaded Noise Model

A polyenergetic cascaded noise model was used to simulate the CT signal distribution in this study. The pre-log detector signal, s, was defined as:

$$s = G \cdot \{ \sum_{E=0.5keV}^{120keV} P(C(E)) \cdot W(E) \} + N(0, \sigma) \}$$

where $P()$ is the Poisson function with the mean as the 'detected counts' (C) of each sub-energy E of the spectrum. The weighting term (W) was set to the sub-energy for the integrated photon detector. The gain factor (G) for converting photon counts to detector unit was set at 0.0195 based on our previous studies, and the Gaussian electronic noise (N) was with zero mean and $\sigma = 15$. Energy-dependent absorption, beam-hardening, and scatter were not considered in this study.

B. Acquisition and Non-positivity correction

The x-ray spectra were generated from XPECT tool (ver. 3.5c) and incorporated into CatSim (Computer Assisted Tomography SIMulation, v5.6) system [6], [7]. Each spectrum has 240 sub energies with 0.5 keV in bin size, and the peak energy was set at 120 keV (Fig.1). The NIST [8] tables for linear attenuation coefficients for water were used. Simulated signal distributions of the CT data with were generated for 20,000 realizations each of diagnostic-level (200 mAs), low-dose (10 mAs), and ultra-low dose (0.5 mAs) flux settings for each sub energy. The water thickness varied from 5.0 to 75.0 cm. Non-positive values of the pre-log detector signal were modified with a simple 'flip' correction:

$$F(X) = \begin{cases} X, & X > 0 \\ \varepsilon = 10^{-6}, & X = 0 \\ -X, & X < 0 \end{cases}$$

The post-log Pi value in the attenuation domain was then calculated as $P_i = -\log(F(s)/A)$, where A is the air scan value. For the 2-D 35-cm water phantom simulations, 2000 realizations, each with 224 detectors x 984 projection angles were generated. The images were reconstructed with FBP with default settings in Catsim.

C. *Kolmogorov–Smirnov statistic*

The Kolmogorov–Smirnov (K–S) distance (D_{MAX}) describes a normalized distance (from 0 to 1) between a given sample distribution and a reference distribution [9]. D_{MAX} will be close to zero if the sample data is normally distributed. For a given cumulative distribution function (CDF) of P_i, D_{MAX} is:

$$D_{MAX} = SUP_{P_i}\left|CDF(P_i) - CDF(N(\overline{P_i}, \sigma_{P_i}))\right|$$

where SUP_{Pi} is the supremum of the set of distances, and $N()$ is the normal function. All calculations were performed using Python-3 with the SciPy library (SciPy.Org, ver.0.16.0).

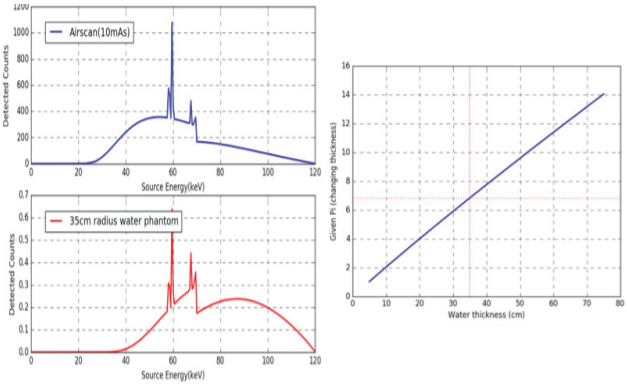

Fig. 1. Left: Simulated x-ray detected counts for the GE Lightspeed CT scanner. Blue: Air scan. Red: Attenuated spectrum with 35cm of water. Right: Attenuation P_i as a function of water phantom thickness.

D. *Statistical distributions at different processing steps*

Fig. 2 shows the distributions for 20K realizations for 35 cm of water. The data in the intensity domain are symmetric with a mean close to the truth. After non-positivity transformation, asymmetry is evident in the low-dose and ultra-low dose regimes. After the log transformation, both the low dose and ultra-low dose settings have skewed distributions, and the latter also display a large bias from the truth. The diagnostic regime data behaves as expected.

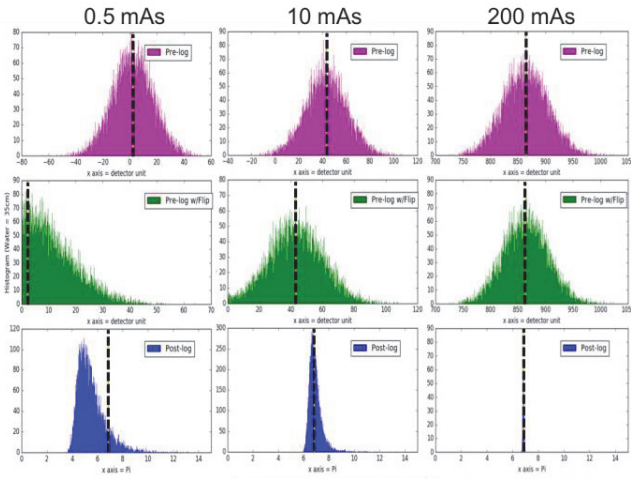

Fig. 2. Histogram of 20,000 realizations of 1D-single detector model with three different flux levels: 0.5, 10, and 200 mAs and three processing stages: ***top*** pre-log raw signal in intensity domain (detector unit), ***middle*** pre-log raw signal with non-positivity correction, and ***bottom*** after taking logarithm with air-scan in attenuation domain (p_i). Ideal values were indicated with vertical line.

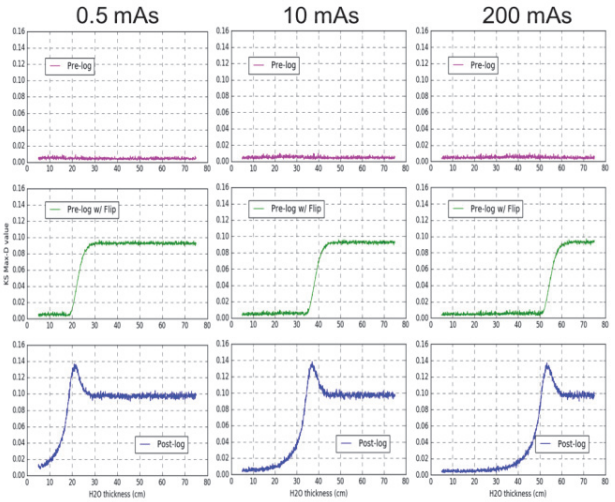

Fig. 3. Kolmogorov–Smirnov distance D_{MAX} as a function of water thickness in the 1D-single detector model (20,000 realizations) with the ultra-low-dose, low-dose, and diagnostic regimes and three processing stages: ***top*** pre-log raw signal in intensity domain (detector unit), ***middle*** pre-log raw signal with "flip" non-positivity correction, and ***bottom*** after taking logarithm with air-scan in attenuation domain (P_i).

E. *K-S distance D_{MAX} at different processing steps*

Figure 3 shows the K-S distance D_{MAX} but now as function of the water attenuation thickness. Distributions without non-positivity correction in the intensity domain are all very close to zero (<0.01) D_{MAX} indicating a normal distribution. With the non-positivity correction, D_{MAX} increases rapidly at approximately 20, 35, and 51 cm of water attenuation for the ultra-low-dose, low-dose, and diagnostic regimes. After the log transformation, the increase in D_{MAX} occurs for thinner layers of water, but with a more gradual transition.

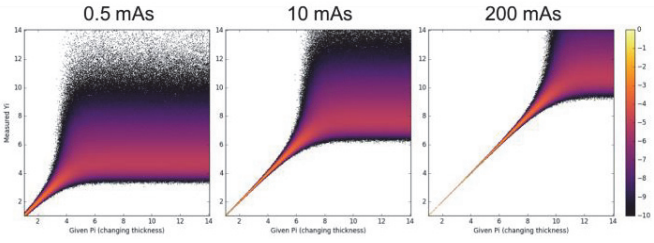

Fig. 4. 2-D Histogram of estimated post-log signal (Y_i) as a function of true attenuation (P_i) for ultra-low-dose, low-dose, and diagnostic regimes. The x-axis is the true attenuation (P_i, a function of the water thickness) and the y-axis is the distribution of estimated attenuation values (Y_i) from 20K realizations. Histogram counts are shown with a log scale for the color table (right).

F. *2-D histogram of signal distribution in attenuation domain*

By combining histograms of estimated Y_i attenuation values for each given true value of P_i, a useful 2-D histogram can be

generated (Fig. 4) [5]. Vertical profiles are PDFs of Y_i for a given true value of P_i

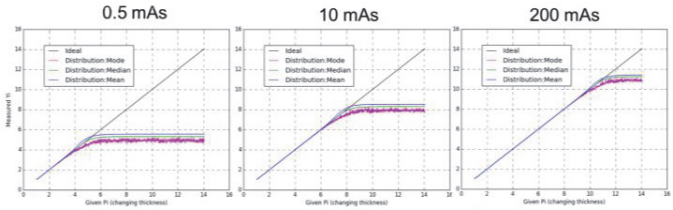

Fig. 5. Bias of the signal distribution in three different flux levels (0.5, 10, and 200 mAs). The vertical line represents the ideal (unbiased) correlation between given P_i and the measured attenuation Y_i. The mean, median, and mode values, are shown.

There are three distinct regions: The first is for low attenuation values and is a linear region where the mean of the distribution is very close to the true value, and where the distribution is normal. The second is a transition region, whose location w.r.t. the attenuation level P_i is dependent on the dose regime and correspond to the rapid increase in D_{MAX} in Fig. 3. Third is a region that is strongly biased (Fig. 5) and with a non-normal distribution (Figs. 3 and 6).

By comparing the ideal given Pi with the measured Y_i of the distributions (*Fig. 5*), one can see the bias starts to show around P_i = 4, 7, and 10 (water thicknesses of 20, 35, and 52 cm). The distribution profiles for the ultra-low dose regime (Fig. 6) reveal that a positive skewness starts to appear between 15.5 and 22.5 cm of the water thickness.

Horizontal profiles in Fig. 4 correspond to likelihood functions (i.e. the relative likelihood of true values of P_i for a given estimated value Y_i). These are shown in Fig. 7. for the ultra-low dose regime, and the ability to find a maximum likelihood disappears at $Y_i = 4.5 \sim 5.8$.

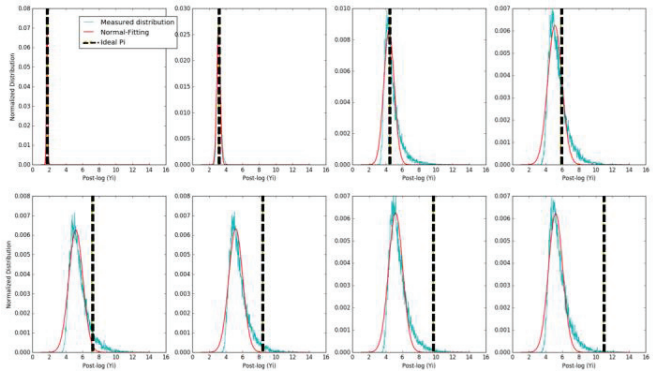

Fig. 6. Distribution profiles of 0.5 mAs flux setting with different water thickness (***Left to right***, ***top to bottom***: 8.5, 15.5, 22.5, 29.5, 36.5, 43.5, 50.5, 57.5cm). (ref Fig. 4 right). The cyan represents the normalized histogram, and the red line shows the normal fitting with the least-squared approach. The black vertical line indicates the ideal P_i value.

G. Catsim simulation of a 35-cm water phantom

To evaluate the results of the 1-D simulations in the context of a 2-D setting where there are a range of attenuation values in a sinogram, we used Catsim to simulate the reconstruction of a 35-cm water phantom at three flux levels. Compared to diagnostic level of setting, the noise effects caused by photon starvation are evident in both low-dose and ultra-low dose settings (Fig. 8). A maximum P_i value for a 35-cm phantom should be at around 6.8. The histogram of the 200 mAs setting shows a narrow peak right on the P_i = 6.8; a broader peak of the histogram in the 10 mAs group deviate slightly to P_i =6.4, whereas for the 0.5 mAs group, an even broader peak deviate heavily down to 4.6.

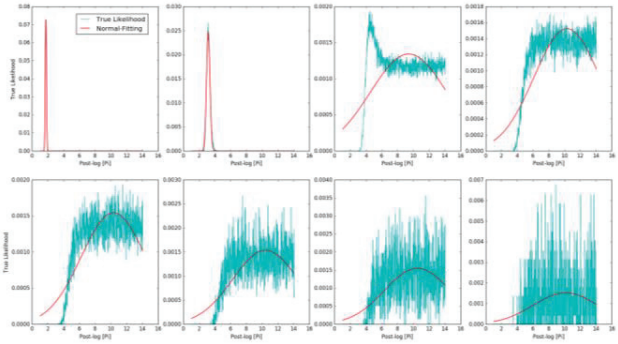

Fig. 7 Likelihood profiles of 0.5 mAs flux for different measured Yi (***Left to right***, ***top to bottom***: Yi = 1.7, 3.1, 4.5, 5.8, 7.1, 8.4, 9.7, 11.0). The cyan line is the possible true values of P_i, (ref Fig. 4 right) and the red line shows a least-squares fit to a normal distribution.

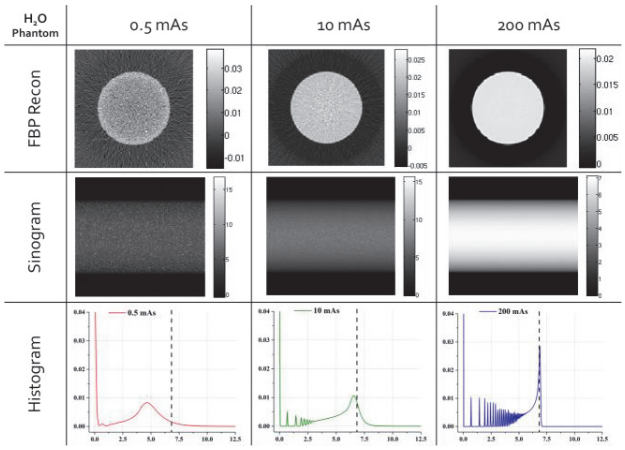

Fig. 8 Catsim simulation of a 35-cm water phantom in three different flux levels (0.5, 10, and 200 mAs). ***top*** the representative FBP reconstructed image (unit: mm^{-1}), ***middle*** post-log sinogram with non-positivity correction, and ***bottom*** the histogram of the sinogram in attenuation domain.

III. Discussion and Conclusions

Through 1-D simulations, we saw that the post-log distribution is skewed but the mode of the distribution is still close to the true attenuation value P_i as the tube flux is lowered from a diagnostic to a low-dose regime. This was true for a wide range of attenuation values. On the other hand, for the ultra-low dose regime, the distribution became wider and markedly skewed, and with substantial bias. We used the Kolmogorov–Smirnov (K-S) distance D_{MAX} to quantify how far the distribution deviated from a normal distribution. In the signal intensity domain, D_{MAX} value was close to zero as a

function of attenuation (i.e. thickness), indicating a normal distribution, until a threshold that depended on the dose regime. Over the next approximately 5 cm of water attenuation, D_{MAX} increased to 1, reaching a plateau where the distribution was dominated by the electronic noise and the non-positivity correction method. After the log conversion, the behavior was more complex, where D_{MAX} increased gradually with attenuation, followed by a rapid increase to a peak value at around the point where the negative values in the intensity domain started to show. Interestingly, the D_{MAX} decreased again and reached a lower plateau. We think this may be due to the balance between the log operation and the lognormal-similar distribution generated by the non-positivity correction, which became more normally-distributed after the log transformation.

Figs. 4-7 demonstrate that there are three distinct regions in the statistical distribution of the post-log sinogram data. For low attenuation values and/or diagnostic regime there is a linear region where the mean of the distribution is very close to the true value, and where the distribution is normal. Beyond a certain attenuation threshold, which depends strongly on dose regime and water thickness, any estimates of the mean, median, or mode are strongly biased (Fig. 5) and the PDF is non-normal (Figs. 3 and 6). In addition, maximum likelihood estimate will fail, as all true attenuation values above the threshold appear to be equally likely (Fig. 7). In between these two regions is a somewhat complex transition region where the Kolmogorov–Smirnov distance D_{MAX} starts to deviate from 0, indicating a non-normal distribution.

The impact of these effects could be seen in the 2-D simulated sinograms. For diagnostic-level of flux, (true maximum of P_i = 6.8), was contained in its linear and symmetric region, and the maximum peak in the histogram is sharp and narrow at 6.8. Whereas for the low-dose setting, Pi 6.8 was at the edge of a biased and skewed distribution. For the ultra-low dose regime, $P_i = 6.8$ is located in the plateau section, and we can see that the peak on the histogram is both broadened and biased.

There are several implications we can draw from this analysis. First is that image reconstruction methods that assume a normal distribution in the post-log sinograms (e.g. WLS methods) may work well in the low-dose regime [4]but the model may be incorrect in the ultra-low-dose regime, leading to no benefit w.r.t. analytic methods [10], [11]. Second is that there is a fundamental limit to estimating the true attenuation value, as past a certain threshold the mean, median, and mode are all heavily biased. In addition there is no defined maximum for the likelihood function[5].

The threshold for this fundamental limit is dependent on the amount of attenuation, the dose regime, the electronic noise, and non-positivity correction method (data not shown). Clearly the threshold can be shifted to some extend by sinogram smoothing methods that suppress non-positive values in the ultra-low-dose domain[12] or sparse sampling and judicious use of iterative image reconstruction methods [13]. However, there is also impact of the increased bias and variance in estimating the weights to be used in a WLS image reconstruction algorithm.

Finally we note that the impact on image reconstruction, either 2-D or 3-D, is not clear due to the range of attenuation values that occur in sinograms and the data redundancy inherent in 3-D CT imaging. Further work is needed to clarify the impact of these fundamental limits in tomography.

ACKNOWLEDGMENTS

Supported in part by NIH grant R01 CA160253.

REFERENCES

[1] J. Nuyts, B. De Man, J. A. Fessler, W. Zbijewski, and F. J. Beekman, “Modelling the physics in the iterative reconstruction for transmission computed tomography.,” *Phys Med Biol*, vol. 58, no. 12, pp. R63–96, Jun. 2013.

[2] T. F. Li, X. Li, J. Wang, J. H. Wen, H. B. Lu, J. Hsieh, and Z. R. Liang, “Nonlinear sinogram smoothing for low-dose X-ray CT,” *Nuclear Science, IEEE Transactions on*, vol. 51, no. 5, pp. 2505–2513, Oct. 2004.

[3] H. Lu, I.-T. Hsiao, X. Li, and Z. Liang, “Noise properties of low-dose CT projections and noise treatment by scale transformations,” *Nuclear Science Symposium Conference Record, 2001 IEEE*, vol. 3, pp. 1662–1666 vol.3, 2001.

[4] J.-B. Thibault, K. D. Sauer, C. A. Bouman, and J. Hsieh, “A three-dimensional statistical approach to improved image quality for multislice helical CT,” *Med Phys*, vol. 34, no. 11, pp. 4526–4544, Nov. 2007.

[5] D. S. Perlmutter, S. M. Kim, P. E. Kinahan, and A. M. Alessio, “Statistical Comparison of Likelihood Models for Low Dose X-ray CT,” presented at the IEEE Nuclear Science Symposium and Medical Imaging Conference, November 10-14, 2014 Seattle WA, 2014.

[6] C. Dodge and M. Flynn, “SU-CC-ValA-05: Advanced Integral Method for the Simulation of Diagnostic X-Ray Spectra,” *Med Phys*, vol. 33, no. 6, p. 1983, 2006.

[7] B. De Man, S. Basu, N. Chandra, B. Dunham, P. Edic, M. Iatrou, S. McOlash, P. Sainath, C. Shaughnessy, B. Tower, and E. Williams, “CatSim: a new computer assisted tomography simulation environment,” *Medical Imaging*, vol. 6510, pp. 65102G–65102G–8, Mar. 2007.

[8] C. T. CHANTLER, “Theoretical Form-Factor, Attenuation and Scattering Tabulation for Z=1-92 From E=1-10 Ev to E=0.4-1.0 Mev,” *Journal of Physical and Chemical Reference Data*, vol. 24, no. 1, pp. 71–591, 1995.

[9] V. W. Berger and Y. Zhou, *Kolmogorov–Smirnov Tests*. Chichester, UK: John Wiley & Sons, Ltd, 2005.

[10] S. M. Kim, A. M. Alessio, D. S. Perlmutter, J.-B. Thibault, B. De Man, and P. E. Kinahan, “Analysis of Statistical Models for Iterative Reconstruction of Extremely Low-Dose CT Data,” presented at the IEEE Nuclear Science Symposium and Medical Imaging Conference, November 10-14, 2014 Seattle WA, 2014.

[11] S. M. Kim, D. S. Perlmutter, A. M. Alessio, J.-B. Thibault, B. De Man, and P. E. Kinahan, “Improved Statistical Models in Iterative CT Reconstruction for PET Attenuation Correction,” presented at the The Third International Meeting on Image Formation in X-Ray Computed Tomography, , June 22-25, 2014. Fort Douglas/Olympic Village, Salt Lake City, Utah, 2014.

[12] T. Xia, A. M. Alessio, B. De Man, R. Manjeshwar, E. Asma, and P. E. Kinahan, “Ultra-low dose CT attenuation correction for PET/CT.,” *Phys Med Biol*, vol. 57, no. 2, pp. 309–328, Jan. 2012.

[13] X. Rui, L. Cheng, Y. Long, L. Fu, A. M. Alessio, E. Asma, P. E. Kinahan, and B. De Man, “Ultra-low dose CT attenuation correction for PET/CT: analysis of sparse view data acquisition and reconstruction algorithms,” *Phys Med Biol*, pp. 7437–7460, Sep. 2015.

Image Quality Comparison of a CBCT Virtual-Isocenter Imaging Trajectory to a Clinical Circular Scan

Andrew M. Davis[1,2], Xiaochuan Pan[1,2], and Charles A. Pelizzari[1]

***Abstract*—Optimization-based reconstruction algorithms have the potential to enable a variety of novel imaging techniques that could improve clinical utility for image-guide radiation therapy (IGRT). One such technique is patient-specific imaging trajectories where the patient's treatment table could be moved to avoid a patient collision with the linac gantry. However, it is important to determine the impact that using such a trajectory has on image quality. In this study, we compare the spatial resolution and the low-contrast resolution of a typical clinical circular scan FDK reconstruction with a MLEM reconstruction from a trajectory where both the linac and treatment table are moving simultaneously. We found that image quality from this new trajectory was comparable to the current clinical standard.**

I. Introduction

In image-guided radiation therapy (IGRT), the most popular treatment modality is the clinical linear accelerator (linac) to which a kV cone-beam computed tomography (CBCT) imaging system is mounted [1], [2], [3]. In clinical practice, the reconstruction workhorse is still the analytic-based FDK algorithm [4], [5]. As such, the formulation of the FDK algorithm necessitates a circular scanning trajectory of the CBCT imaging system. For IGRT with the linac, this is achieved via the rotation of the linac gantry and the mounted CBCT system.

Optimization-based reconstruction methods enable a variety of novel imaging techniques that are difficult, if not impossible, to reconstruct with analytic-based methods [6], [7], [8], [9], [10]. One technique that is possible with optimization-based methods is reconstructing from scanning trajectories for which analytic-based solutions to the inverse problem have not been formulated [11].

With the flexibility in scanning trajectories allowed with optimization-based algorithms, it is conceivable that imaging trajectories could be designed on a patient-specific basis. This would be beneficial for patients who would typically experience a mechanical collision with the linac gantry during treatment. These collisions are particularly common in head and neck, breast, and lung cancer patients [12], [13]. Such a patient would typically have to raise her arms above her head as shown in Figure (1) which puts her arms at risk of collision.

Department of Radiation and Cellular Oncology (1), and the Department of Radiology (2), The University of Chicago, 5841 S. Maryland Avenue, Chicago IL, 60637 Email: amdavis@uchicago.edu

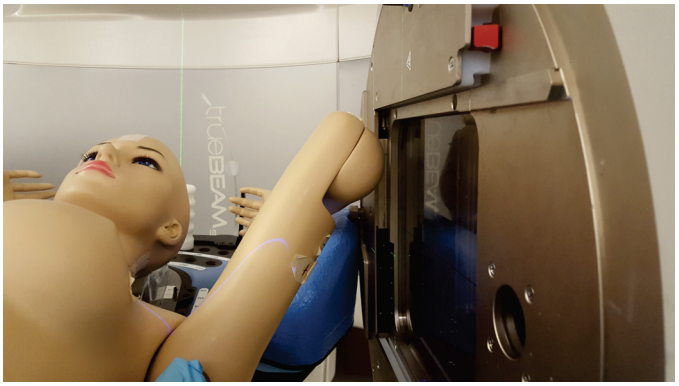

Fig. 1. Typical example of a mechanical collision. The mannequin's raised arms (representing a patient) could collide with the linac head.

If a scanning trajectory could be designed using the treatment table and the linac's mechanical controls to avoid a collision for a given patient, it would both improve patient comfort and reduce costly delays in the clinic. Currently, when a potential collision is detected, the patient must be moved in order for the linac to continue its rotation before the patient can be re-positioned. With optimization-based methods, it is possible to reconstruct from scanning trajectories where both the treatment table and linac are moving simultaneously.

However, in order to justify using a patient-specific imaging trajectory, it is necessary to demonstrate that the image quality from such a scan is not significantly degraded from the current clinical imaging standard. Though linac-mounted system cannot deliver diagnostic-quality images, there are a variety of recommended quality assessment methods for the linac-mounted CBCT system [14]. In this work, we compare some of these metrics for a simple collision-avoiding trajectory with those for the standard clinical circular scan. Most collisions involve the gantry head as shown in Figure (1) rather than the imaging arms. Thus, we have utilized a simple "virtual isocenter" trajectory where the couch translates with gantry rotation, maintaining an increased separation between gantry head and the imaging isocenter within the patient.

II. Methods and Materials

We acquired all of our CBCT scans using Varian's TrueBeam kV imaging system (Varian Medical Systems, Palo Alto, CA). All of the scanning trajectories were implemented with

the TrueBeam 2.0 Developer Mode. This functionality gives researchers control of a variety of scanning parameters that enable scanning configurations that are not available in the clinical mode.

For evaluating image quality metric for the different scanning trajectories, we used our clinic's Catphan 500 (The Phantom Laboratory, Salem, NY). This is a standard quality assessment (QA) phantom for clinical CT devices that provides a series of sections with different objects for calculating image quality metrics. We used the CTP 515 module for evaluating the low-contrast resolution and the CTP 528 module for evaluating spatial resolution.

We placed the center of the low-contrast module at the mechanical isocenter for all of the scans. We then acquired a traditional circular scan as well as the virtual isocenter scan. The virtual isocenter scan provides a trajectory for treating a spot 5 cm below the mechanical isocenter. When the trajectory is acquired, the table moves as the gantry rotates so that this point 5 cm below the mechanical isocenter becomes the effective isocenter of the scan.

For comparison to a clinical standard, we reconstructed the circular scan (679 projection views) using Varian's FDK implementation provided by the iTools reconstruction software. We then reconstructed the circular scan using 100 iterations of the well-understood maximum-likelihood expectation maximization (MLEM) algorithm [15]. We also reconstructed this same scan using two thirds of the projections (452 views) with 100 iterations of the MLEM algorithm. All of the images were reconstructed onto a clinical-resolution voxels of 0.5 mm x 0.5 mm in the transverse slice and 2 mm in the longitudinal direction.

For the virtual isocenter scan, we again used 100 iterations of the MLEM algorithm to reconstruct the 424 projection views. From each projection view acquired from the TrueBeam system, we are able to extract the position information of both the CBCT imaging arms and the table. This information can then be used to correctly account for the position of the phantom's image space in the system matrix of the linearized imaging model we use for formulating the MLEM optimization problem.

To characterize the spatial resolution of the reconstructions, we looked for the smallest line pair gauge that could visually be resolved in the CTP 528 module. To characterize the low-contrast resolution, we calculated the percent contrast of the 1% nominal low-contrast rods in the CTP 515 module. The iTools FDK reconstruction provides an attenuation coefficient mapping to Hounsfield units (HU) whereas the MLEM reconstructions are just a map of the linear attenuation coefficients (μ). The percent contrast is calculated as

$$\frac{\mathrm{HU}_{\mathrm{sig}} - \mathrm{HU}_{\mathrm{back}}}{\mathrm{HU}_{\mathrm{back}} + 1000} \times 100 \tag{1}$$

for the iTools reconstruction, and

$$\frac{\mu_{\mathrm{sig}} - \mu_{\mathrm{back}}}{\mu_{\mathrm{back}}} \times 100 \tag{2}$$

for the MLEM reconstructions.

III. Results

As shown in the top row of Figure (2), all of the reconstructions had approximately the same spatial resolution when looking at the slice from the CTP 528 module. The highest line pair/cm that could be resolved for the FDK was the 7^{th} largest gauge which corresponds to a line spacing of approximately 0.071 cm. For the MLEM reconstructions, the 8^{th} largest gauge is resolved which is a line spacing of approximately 0.063 cm. This is reasonable considering the resolution of the transverse pixels is 0.05 cm x 0.05 cm.

Figure (3) shows a plot of the calculated percent contrast of the five largest supra-slice low-contrast rods that have a nominal 1% contrast for each of the reconstructions. Only the sparse-view circular MLEM reconstruction is plotted as the percent contrast was the same for the full-view reconstruction. The reconstructed slices of this module from the different scans are shown in The bottom row of Figure (2).

IV. Conclusion

In all of the reconstructions of the spatial resolution module shown in the top row of Figure (2), we can see that the 7^{th} largest gauge is visually resolvable. Here, MLEM actually outperforms the clinical FDK reconstruction in that the next smallest gauge is visually resolvable in these reconstructions though it is more difficult with the virtual isocenter reconstruction. This agrees with our previous experience that reconstructions using MLEM generally have better spatial resolution than analytic-based methods.

For the low-contrast resolution shown in Figure (3), we see that the FDK reconstruction and the circular MLEM reconstructions show the same trend in contrast for each of the rods. There is a bias between the two, but this could arise from the fact there are no pre-processing steps performed on the MLEM reconstructions. The iTools FDK has a variety of corrections for effects like beam hardening and ring artifacts that were not used for the MLEM reconstructions.

Figure (3) does show a fixed contrast verses rod diameter for the virtual isocenter trajectory, while reconstructions for the circular trajectory exhibit a characteristic variation with diameter. Given the contrast for the rods is designed to provide the same contrast level for all of the rods at a nominal contrast, one would ideally expect the percent contrast to be the same. In the circular scans, the isocenter is at the center of the phantom. For the virtual isocenter scan, the effective isocenter is actually centered on the 15 mm diameter 1% contrast rod at the bottom of the phantom. Scanning the phantom with a diagnostic CT system would determine if this trend seen in the percent contrast of the circular scans is a physical discrepancy in the 1% contrast rods or an artifact of the reconstruction.

From these results, we found the MLEM reconstructions of the circular scan with full-view and sparse-view data as well as the new virtual isocenter trajectory to be comparable to the current clinical FDK reconstruction from a circular scan. This shows that is indeed possible to reconstruct useful images

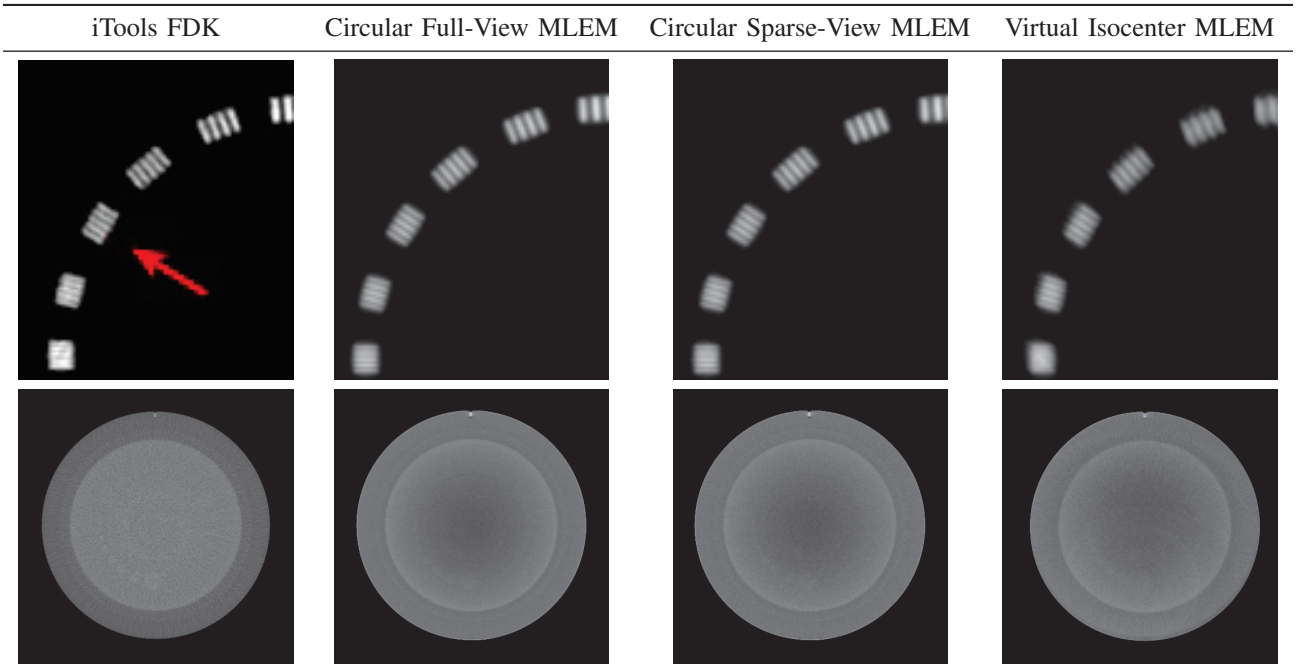

Fig. 2. Images of the two metric modules from the reconstruction studies. The top row shows the region of the module that is visually resolvable in the reconstructed slice. The 7th largest gauge is indicated by the red arrow in the FDK reconstruction which has a display window of [50, 300] HU. The MLEM spatial resolution images have a display window of [0.21, 0.35] cm^{-1}. The second row shows the low-contrast module. The FDK display window is [-160, 230] HU, and the MLEM display window is [0.16, 0.24] cm^{-1}.

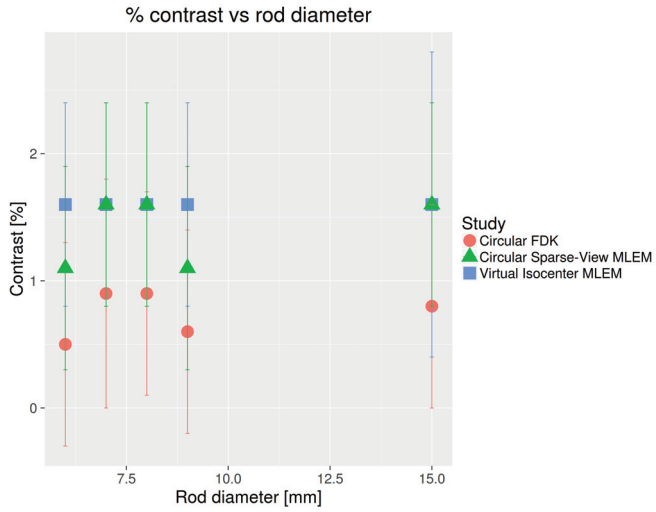

Fig. 3. Plot of percent contrast versus diameter for the nominal 1% contrast rods for each of the reconstructions.

from trajectories where the treatment table and linac gantry are moving simultaneously. As the image quality metrics are comparable to current clinical images, it may be possible to eventually enable collision-avoiding imaging trajectories with optimization-based algorithms. This would provide a real increase in clinical utility in terms of both patient comfort and clinic efficiency.

ACKNOWLEDGMENTS

Funding was provided in part by Varian Medical Systems and NIH Grants R01 CA182264, R01 EB018102, S10 RR021039 and P30 CA14599. The iTools Reconstruction software was provided by Varian iLab, Baden, Switzerland. The contents of this work are solely the responsibility of the authors and do not necessarily represent the official view of any of the supporting organizations.

REFERENCES

[1] M. Rahman, G. J. A. Murad, F. J. Bova, and W. A. Friedman, "LINAC: Past, Present, and Future of Radiosurgery," in *Principles and Practice of Stereotactic Radiosurgery*, L. S. Chin and W. F. Regine, Eds. Springer New York, 2015, pp. 121–134.

[2] D. A. Jaffray, J. H. Siewerdsen, J. W. Wong, and A. A. Martinez, "Flat-panel cone-beam computed tomography for image-guided radiation therapy," *International Journal of Radiation Oncology*Biology*Physics*, vol. 53, no. 5, pp. 1337–1349, Aug. 2002.

[3] D. Létourneau, J. W. Wong, M. Oldham, M. Gulam, L. Watt, D. A. Jaffray, J. H. Siewerdsen, and A. A. Martinez, "Cone-beam-CT guided radiation therapy: technical implementation," *Radiotherapy and Oncology*, vol. 75, no. 3, pp. 279–286, Jun. 2005.

[4] L. A. Feldkamp, L. C. Davis, and J. W. Kress, "Practical cone-beam algorithm," *Journal of the Optical Society of America A*, vol. 1, no. 6, pp. 612–619, Jun. 1984.

[5] X. Pan, E. Y. Sidky, and M. Vannier, "Why do commercial CT scanners still employ traditional, filtered back-projection for image reconstruction?" *Inverse Problems*, vol. 25, no. 12, p. 123009, Dec. 2009.

[6] X. Han, E. Pearson, J. Bian, S. Cho, E. Sidky, C. A. Pelizzari, and X. Pan, "Preliminary investigation of dose allocation in low-dose cone-beam CT," in *2010 IEEE Nuclear Science Symposium Conference Record (NSS/MIC)*, Oct. 2010, pp. 2051–2054.

[7] J. Bian, J. Wang, X. Han, E. Y. Sidky, L. Shao, and X. Pan, "Optimization-based image reconstruction from sparse-view data in offset-detector CBCT," *Physics in Medicine and Biology*, vol. 58, no. 2, p. 205, Jan. 2013.

[8] J. Bian, X. Han, E. Sidky, J. Siewerdsen, and X. Pan, "Investigation of low-contrast tumor detection in algorithm-enabled low-dose CBCT," in *2010 IEEE Nuclear Science Symposium Conference Record (NSS/MIC)*, Oct. 2010, pp. 3479–3482.

[9] X. Han, J. Bian, E. L. Ritman, E. Y. Sidky, and X. Pan, "Optimization-based reconstruction of sparse images from few-view projections," *Physics in Medicine and Biology*, vol. 57, no. 16, p. 5245, Aug. 2012.

[10] J. Bian, J. H. Siewerdsen, X. Han, E. Y. Sidky, J. L. Prince, C. A. Pelizzari, and X. Pan, "Evaluation of sparse-view reconstruction from flat-panel-detector cone-beam CT," *Physics in Medicine and Biology*, vol. 55, no. 22, p. 6575, Nov. 2010.

[11] A. Davis, E. Pearson, X. Pan, and C. Pelizzari, "WE-G-BRF-07: Non-Circular Scanning Trajectories with Varian Developer Mode," *Medical Physics*, vol. 41, no. 6, pp. 523–523, Jun. 2014.

[12] M. F. Tsiakalos, E. Schrebmann, K. Theodorou, and C. Kappas, "Graphical treatment simulation and automated collision detection for conformal and stereotactic radiotherapy treatment planning," *Medical Physics*, vol. 28, no. 7, pp. 1359–1363, Jul. 2001.

[13] L. Padilla, E. A. Pearson, and C. A. Pelizzari, "Collision prediction software for radiotherapy treatments," *Medical Physics*, vol. 42, no. 11, pp. 6448–6456, Nov. 2015.

[14] S. Yoo, G.-Y. Kim, R. Hammoud, E. Elder, T. Pawlicki, H. Guan, T. Fox, G. Luxton, F.-F. Yin, and P. Munro, "A quality assurance program for the on-board imager®," *Medical Physics*, vol. 33, no. 11, pp. 4431–4447, Oct. 2006.

[15] A. P. Dempster, N. M. Laird, and D. B. Rubin, "Maximum Likelihood from Incomplete Data via the EM Algorithm," *Journal of the Royal Statistical Society. Series B (Methodological)*, vol. 39, no. 1, pp. 1–38, Jan. 1977, articleType: research-article / Full publication date: 1977 / Copyright © 1977 Royal Statistical Society.

A Regularized X-ray Tensor Tomography Reconstruction Technique

Saeed Seyyedi*†§, Matthias Wieczorek*, Christoph Jud†, Franz Pfeiffer†‡ and Tobias Lasser*
*Computer Aided Medical Procedures (CAMP), Technische Universität München, Germany
†Chair of Biomedical Physics & Institute of Medical Engineering, Technische Universität München, Germany
‡Department of Radiology, Klinikum rechts der Isar, Technische Universität München, Germany
§s.seyyedi@tum.de

***Abstract*—X-ray Tensor Tomography (XTT) is a novel imaging modality for reconstruction of three-dimensional X-ray scattering tensors from dark-field projections obtained in a grating interferometry setup. In this work we propose a new component-based total variation (TV) regularized conjugate gradient (CG) reconstruction method for XTT data. First results suggest that the proposed method's convergence rate is comparable to different regularization methods, while the resulting reconstructions show less noise and streak artifacts compared to previous, unregularized methods.**

I. Introduction

Conventional X-ray imaging techniques are based on the absorption of X-rays in the examined object. However, X-rays are not only absorbed in the object, but are also refracted and scattered, producing measurable deviations from their original direction, enabling the measurement of new signal components such as phase contrast and dark-field contrast [1].

X-ray Tensor Tomography (XTT) is a novel imaging modality combining three-dimensional X-ray imaging with a Talbot-Lau interferometer, allowing the reconstruction of X-ray scattering tensors revealing the local orientation, anisotropy and average size of microstructures [2], [3].

As shown in the schematic setup of Fig. 1, XTT employs an X-ray grating interferometer including three gratings G_0, G_1 and G_2 between the X-ray source (X) and the detector (D). The sample (S) is freely rotated using three Eulerian angles, while several horizontal steps of the phase grating ($G1$ or $G2$) are used to acquire several images allowing the recovery of three signal components (see Fig. 2), including the dark-field contrast [1] used for XTT.

Malecki *et al.* [3] formulated the first approach of a mathematical forward model for XTT by considering several scattering directions at each point of the sample and proposed a block-based, modified SART-based reconstruction method. Building on this work, Vogel *et al.* [4] introduced an iterative reconstruction scheme for XTT data by generalizing the original approach of Malecki *et al.* to allow the usage of reconstruction methods different from SART. Based on the approach of Vogel *et al.*, we recently proposed a component-based total variation (TV) regularization method for XTT based on the alternating direction method of multipliers (ADMM) [5].

In this paper, we will address the problem of component-based regularized XTT reconstruction again by introducing a more efficient approach to TV regularization for XTT. We will compare the performance and image quality of both methods on experimental data acquired of a sample consisting of wooden sticks.

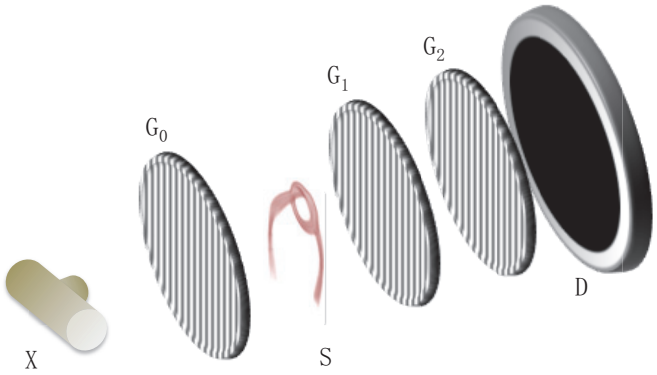

Fig. 1. Schematic of an X-Ray Tensor Tomography setup. It consists of an X-ray source (X), a sample (S), the grating interferometer (G_0,G_1, and G_2) and a detector (D).

II. Methods

For XTT reconstruction we follow the approach introduced by Malecki *et al.* [3] and Vogel *et al.* [4]. To represent the scattering tensors, the aim is to reconstruct scattering coefficients $\zeta_k(x) \in \mathbb{R}$ at each location $x \in \mathbb{R}^3$ corresponding to several pre-selected normalized scattering directions $\hat{\epsilon}_k \in \mathbb{R}^3$, $k = 1, \ldots, K$. A measured dark-field signal $m_j \in \mathbb{R}$, $j = 1, \ldots, J$, can then be modeled as

$$m_j = \exp\left[- \int_{L_j} \sum_{k=1}^{K} \left\langle |\hat{s}_j \times \hat{\epsilon}_k| \zeta_k(\mathrm{x}) \hat{\epsilon}_k, \hat{t}_j \right\rangle^2 \mathrm{d}x \right], \quad (1)$$

where L_j denotes the ray with normalized direction $\hat{s}_j \in \mathbb{R}^3$ corresponding to the j-th measurement, and $\hat{t}_j \in \mathbb{R}^3$ is the normalized interferometer sensitivity direction, orthogonal to the grating lines.

After discretization into I voxels, we rewrite the quantity to be reconstructed, the squared scattering coefficients, as a vector $\eta_k \in \mathbb{R}^I$ (corresponding to the scattering directions

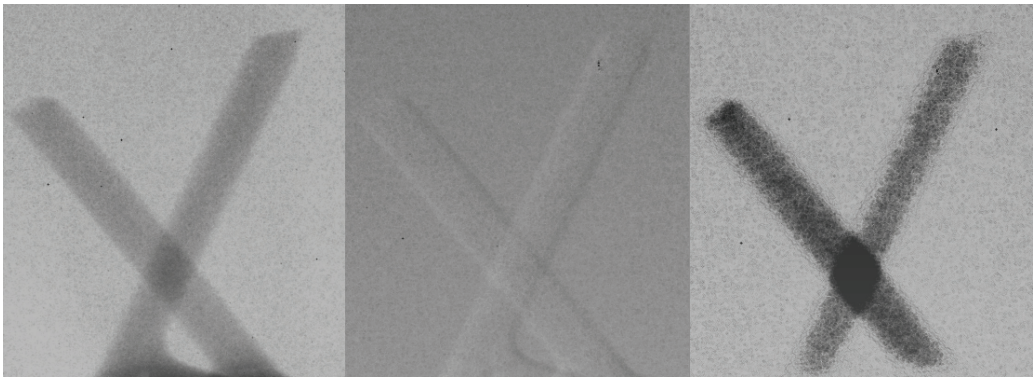

Fig. 2. Example images of the three signals acquired in an X-ray grating interferometry setup, from left to right: absorption, phase contrast and dark-field. The imaged sample consists of two wooden sticks.

$\hat{\epsilon}_k$). The reconstruction problem can now be written as several linear equations

$$-\ln m_j = \sum_{k=1}^{K} v_{kj} \langle a_j^T, \eta_k \rangle, \tag{2}$$

where a_j denotes a single row of the system matrix $A = (a_j) \in \mathbb{R}^{J \times I}$ corresponding to the j-th measurement, and weights $v_{kj} := \left(|\hat{s}_j \times \hat{\epsilon}_k| \langle \hat{\epsilon}_k, \hat{t}_j \rangle\right)^2$, which can be precomputed.

In [4], the linear system is solved using an iterative component-based scheme, where in each "outer" iteration a single step of the conjugate gradient (CG) method is applied to each component η_k separately in parallel, merging the results of the parallel steps at the end of each iteration.

Building on this, we introduced a component-based total variation regularization method in our previous work [5], where we replaced the single CG step with several steps of the ADMM. In order to get useful regularization results [6], several "inner" iterations of ADMM had to be performed for each component η_k,

$$\arg\min_{\eta_k} \left\{ \tfrac{1}{2} \|A\eta_k - m\|_2^2 + \lambda \|z\|_1 \right\} \quad \textit{s.t.} \quad F\eta_k = z, \tag{3}$$

where m denotes the full measurement vector $m = (m_j)$, F denotes the discretized finite differences operator and $\lambda \in \mathbb{R}$ denotes the regularization parameter. In order to keep computational efforts comparable to the previous unregularized approach, the number of "outer" iterations had to be reduced accordingly.

In this work we introduce a new, more efficient approach to incorporate component-based TV regularization into the XTT reconstruction scheme. We keep the iterative component-based scheme of [4], using Q "outer" iterations. However, in addition to the single CG step for each component η_k we add a consecutive step applying TV regularization only to that component η_k, similar to the approach in [7]. In order to apply TV regularization, we use P iterations of ADMM for each component η_k

$$\arg\min_{\eta_k} \left\{ \tfrac{1}{2} \|I\eta_k - \eta_k\|_2^2 + \lambda \|F\eta_k\|_1 \right\}, \tag{4}$$

where I denotes the identity operator. As the ADMM now only operators on the volume, without any projection operations, the computational cost for regularization is now negligible.

The algorithm of the proposed component-based TV regularized CG reconstruction method for XTT is shown in Algorithm 1.

Algorithm 1 TV regularized CG reconstruction for XTT

$\eta_k^0 = 0$ for all $k = 1, \ldots, K$
for outer iteration $q = 1$ to Q **do**
  // pre-compute weighted forward projections
  for scattering directions $k \in \{1, \ldots, K\}$ **do**
    $WFP_k = \text{diag}(v_{kj}) \cdot A \cdot \eta_k^{q-1}$
  end for

  // component-wise reconstruction
  for scattering directions $k \in \{1, .., K\}$ **do**
    // compute right-hand side
    $r = m - \sum_{l \neq k} WFP_l$
    // compute x_k using single CG iteration
    $x_k = \text{CG}(\text{diag}(v_{kj}) \cdot A, \quad r, \quad \eta_k^{q-1})$

    // TV using several ADMM iterations
    for inner iteration $p = 1$ to P **do**
      $x_k = \text{ADMM}(I, \quad x_k, \quad x_k)$
    end for

    // update with relaxation
    $\eta_k^q = (1 - \frac{1}{k})\eta_k^{q-1} + \frac{1}{k} x_k$
  end for
end for

III. Experiments and Results

In order to compare our proposed method (abbreviated as CG+TV) with the original method of Vogel *et al.* [4] (abbreviated as CG) and the previously proposed method of Seyyedi *et al.* [5] (abbreviated as ADMM), we evaluate the results on experimental data acquired of a sample consisting of two wooden sticks. The sample is shown in Fig. 3, it consists

Fig. 3. Photograph of the sample consisting of wooden sticks.

of two wooden sticks attached to a sample holder using hot glue. We use 121 X-ray dark field projections of 320×320 pixels, sparsely sampling the unit sphere. The reconstruction volume was discretized using 320^3 isotropic voxels.

All three methods were implemented within our C++ software framework for linear inverse problems [8]. In order to have comparable computational costs, we selected 54 outer iterations for the original CG method and the proposed CG+TV method (with 5 inner iterations to compute the TV regularization), while we used 6 outer iterations and 9 inner iterations for the ADMM method. Using grid search, we selected the coupling parameter $\rho = 10$ for the ADMM method and $\rho = 100$ for the proposed CG+TV method. The regularization parameter λ was chosen using an adaptive thresholding scheme, such that 99% of the coefficients are zero afterwards.

To study the numerical behavior of the three methods, we computed the normalized residual norms

$$r^{(q)} := \frac{\left\| m - \sum_k diag(v_{kj}) \cdot A \cdot \eta_k^{(q)} \right\|_2}{\|m\|_2}, \tag{5}$$

and also the normalized update

$$\triangle^{(q)} := \frac{\text{mean} \left\| \eta_k^{(q)} - \eta_k^{(q-1)} \right\|_2}{\left\| \eta_k^{(q)} \right\|_2}. \tag{6}$$

Fig. 4 shows a comparison of $r^{(q)}$ and $\triangle^{(q)}$ for the three methods. The CG method shows the smallest residual norm $r^{(q)}$, but oscillating behavior in update $\triangle^{(q)}$, while both the ADMM method and proposed CG+TV method show a larger residual norm and smoother updates.

TABLE I
CNR OF SLICES FROM FIG. 5. REPRESENTATIVE ROI IS MARKED IN RED AND BACKGROUND AS GREEN IN FIG. 5(A).

component	CG	ADMM	CG+TV
$\hat{\epsilon}_1$	2.63×10^5	2.88×10^5	1.32×10^6
$\hat{\epsilon}_8$	2.14×10^5	3.73×10^5	4.84×10^5
$\hat{\epsilon}_9$	4.40×10^5	8.07×10^5	1.04×10^6

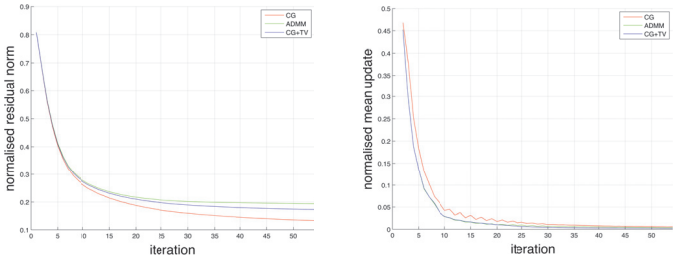

(a) residual norm $r^{(q)}$ (b) update $\triangle^{(q)}$

Fig. 4. Comparison of normalized residual norm $r^{(q)}$ normalized mean update $\triangle^{(q)}$ for the three studied reconstruction methods.

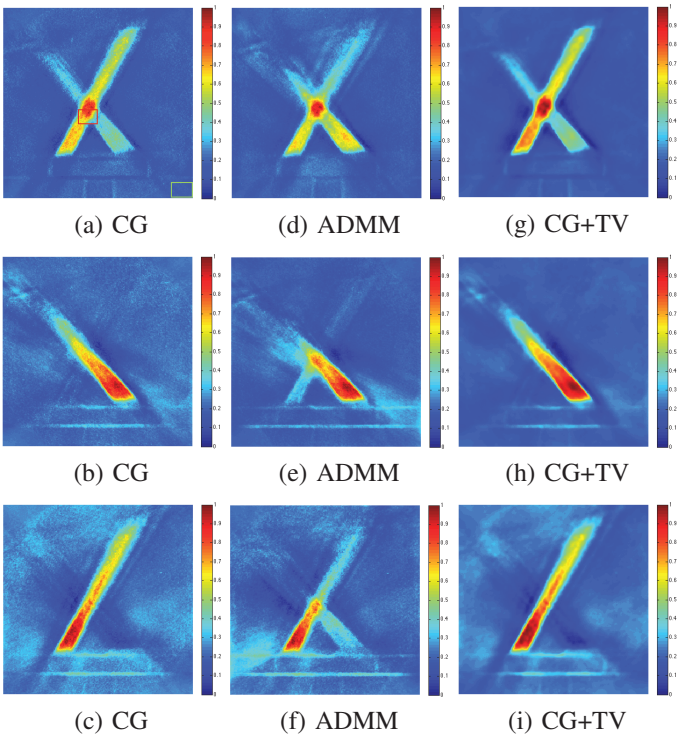

(a) CG (d) ADMM (g) CG+TV

(b) CG (e) ADMM (h) CG+TV

(c) CG (f) ADMM (i) CG+TV

Fig. 5. Center slice of the reconstructed component volumes corresponding to the scattering directions $\hat{\epsilon}_1, \hat{\epsilon}_8$. and $\hat{\epsilon}_9$ for all three methods.

Example reconstructions are shown in Fig. 5 and Fig. 6. In Fig. 5 we show the center slice of reconstructed component volumes η_1 for the scattering direction $\hat{\epsilon}_1 = (1, 0, 0)^T$, η_8 for $\hat{\epsilon}_8 = (0.7, 0.7, 0)^T$ and η_9 for $\hat{\epsilon}_9 = (0.7, -0.7, 1)^T$. On the left hand side, the slices are from the unregularized CG reconstruction, the middle column shows the result of the previous ADMM method, while the right hand side shows the results of the proposed CG+TV method.

We also obtain a quantitative measure for the contrast in the images for the three different methods: we compute the contrast-to-noise ratio (CNR) as,

$$CNR = \frac{|\bar{\eta}_{ROI} - \bar{\eta}_{BG}|}{\sigma_{bg}}, \tag{7}$$

where $\bar{\eta}_{roi}$ and $\bar{\eta}_{bg}$ denote the mean of the scattering signal in

a certain region of interest (ROI) of each component (marked in red in Fig. 5(a)) and background (BG) (marked in green in Fig. 5(a)), respectively. The CNR results are shown in Table I.

Finally, Fig. 6 shows the center slice of the reconstructed tensors using all scattering directions, visualized as ellipsoids with the color encoding the main structure orientation.

IV. Discussion and Conclusion

A comparison of the components in Fig. 5 shows a clear qualitative improvement when using regularization, in particular in terms of suppressed background noise. Compared to our previous ADMM approach, the more efficient proposed CG+TV approach allows for better incorporation of the TV regularization and shows even better noise suppression, while showing less artifacts (see for example Fig. 5(e) vs. (h)). The visualization of the fitted tensors in Fig. 6 also shows a marked improvement, with smoother tensors representing the structure orientations, while the background is less noisy. Quantitatively, the convergence behavior is comparable as seen in Fig. 4, while the CNR is markedly improving, as seen in Table I.

In summary, we have presented a new, efficient component-based TV regularized reconstruction technique for XTT data. First results for our experimental show a marked improved performance both qualitatively and quantitatively when compared to both previous approaches.

Acknowledgments

This work has been supported by BERTI, funded by the European Commission under grant agreement number 605162, and partially funded by the DFG Cluster of Excellence Munich-Centre for Advanced Photonics (MAP). CJ acknowledges the TUM Graduate School for the support of his studies.

References

[1] F. Pfeiffer, M. Bech, O. Bunk, P. Kraft, E. F. Eikenberry, C. Brönnimann, C. Grünzweig, and C. David, "Hard-x-ray dark-field imaging using a grating interferometer," *Nat. mat.*, vol. 7, no. 2, pp. 134–137, 2008.

[2] F. Pfeiffer, T. Weitkamp, O. Bunk, and C. David, "Phase retrieval and differential phase-contrast imaging with low-brilliance x-ray sources," *Nat. phys.*, vol. 2, no. 4, pp. 258–261, 2006.

[3] A. Malecki, G. Potdevin, T. Biernath, E. Eggl, K. Willer, T. Lasser, J. Maisenbacher, J. Gibmeier, A. Wanner, and F. Pfeiffer, "X-ray tensor tomography," *EPL*, vol. 105, no. 3, p. 38002, 2014.

[4] J. Vogel, F. Schaff, A. Fehringer, C. Jud, M. Wieczorek, F. Pfeiffer, and T. Lasser, "Constrained x-ray tensor tomography reconstruction," *Opt. exp.*, vol. 23, no. 12, pp. 15 134–15 151, 2015.

[5] S. Seyyedi, M. Wieczorek, Y. Sharma, F. Schaff, C. Jud, F. Pfeiffer, and T. Lasser, "Component-based TV Rgularization for X-ray Tensor Tomography," in *Biomedical Imaging (ISBI), 2016 IEEE 13th International Symposium on*, April 2016.

[6] S. Boyd, N. Parikh, B. P. E Chu, and J. Eckstein, "Distributed Optimization and Statistical Learning via the Alternating Direction Method of Multipliers," *Found. and Tre. in Mach. Lea.*, vol. 3, no. 1, pp. 1–122, 2011.

[7] E. Y. Sidky and X. Pan, "Image reconstruction in circular cone-beam computed tomography by constrained, total-variation minimization." *Physics in medicine and biology*, vol. 53, no. 17, pp. 4777–4807, Sep. 2008.

[8] M. Wieczorek, J. Vogel, and T. Lasser, "CampRecon - a software framework for linear inverse problems," *TUM Technical Report*, 2014.

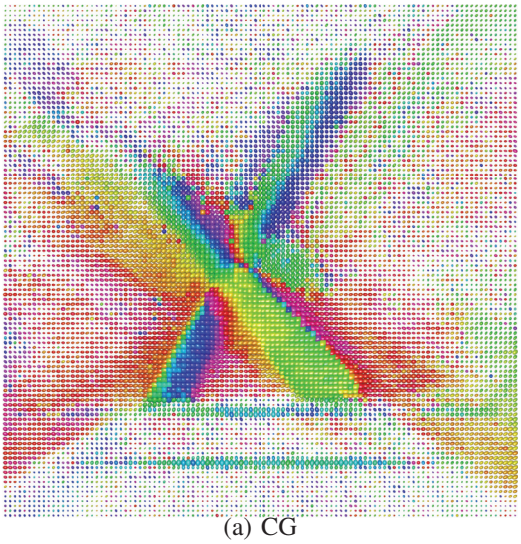

(a) CG

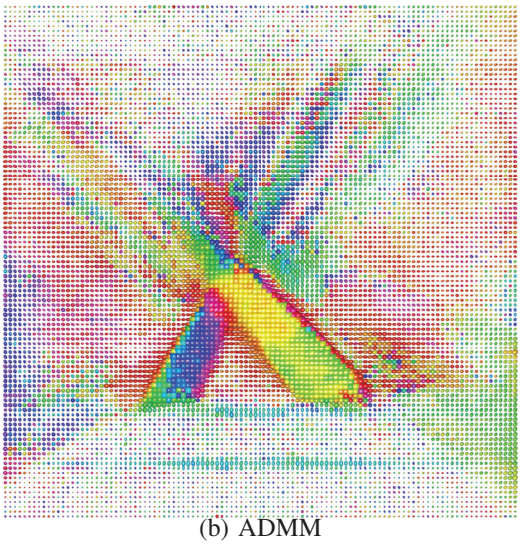

(b) ADMM

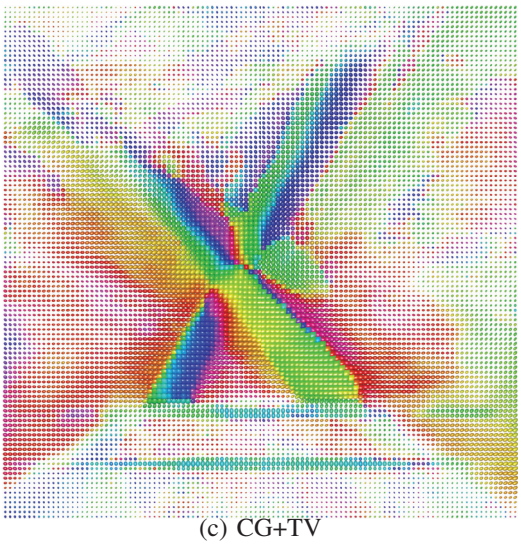

(c) CG+TV

Fig. 6. Tensor visualization of a single slice of the reconstructed volumes for all three methods. Colors represent the structure orientation.

Pre-clinical dark-field CT imaging of small-animal lung disease models

F. Pfeiffer[1], A. Velroyen, A. Yaroshenko, A. Tapfer, S.D. Auweter, K. Hellbach, F.G. Meinel, T. Koehler, M. Bech, P.B. Noël, A.Ö. Yildirim, O. Eickelberg

***Abstract*— Changes in x-ray attenuating tissue caused by lung disorders like emphysema or fibrosis are subtle and thus only resolved by high-resolution computed tomography (CT). The structural reorganization, however, is of strong influence for lung function. Dark-field CT (DFCT), based on small-angle scattering of x-rays, reveals such structural changes even at resolutions finer than the systems resolution and it provides access to their spatial distribution.**

In this contribution we review the recent progress in grating-based in-vivo small-animal imaging, and present several DFCTs of healthy, emphysematous and fibrotic mouse. The tomographies show excellent depiction of the distribution of structural – and thus indirectly functional – changes in lung parenchyma, on single-modality slices in dark field as well as on multi-modal fusion images. Therefore, we anticipate numerous applications of DFCT in diagnostic lung imaging. Finally, we also introduce a scatter-based Hounsfield Unit (sHU) scale to facilitate comparability of scans. In this newly defined sHU scale, the pathophysiological changes by emphysema and fibrosis cause a shift towards lower numbers compared to healthy lung tissue. The presentation is concluded with an outlook to human translation, and discusses the main challenges ahead.

***Index Terms*—phase-contrast imaging, dark-field contrast imaging, lung diseases, COPD, fibrosis, emphysema**

F. Pfeiffer is with the chair for Biomedical Physics, the Institute for Medical Engineering, the Department of Radiology, and the Institute for Advanced Study, Technische Universität München, Munich, Germany (e-mail: franz.pfeiffer@tum.de).

A. Velroyen, and A. Tapfer are with the chair for Biomedical Physics, the Institute for Medical Engineering, Technische Universität München, Munich, Germany.

A. Yaroshenko is with the chair for Biomedical Physics, the Institute for Medical Engineering, Technische Universität München, Munich, Germany and with Philips Medical Systems DMC GmbH, Hamburg, Germany.

S.D. Auweter, K. Hellbach, and F.G. Meinel are with Institute of Clinical Radiology, Ludwig-Maximilians-University Hospital Munich, Germany.

T. Koehler is with Philips GmbH, Innovative Technologies, Research Laboratories, Hamburg and with the Institute for Advanced Study, Technische Universität München, Germany.

P. B. Noël is with Department of Radiology, Technische Universität München, Germany.

M. Bech is with Medical Radiation Physics, Lund University, Lund, Sweden.

A.Ö. Yildirim and O. Eickelberg are with the Comprehensive Pneumology Center, Institute of Lung Biology and Disease, Helmholtz Zentrum München and Ludwig-Maximilians-University Hospital Munich and the German Center for Lung Research (DZL), Munich, Germany

I. Introduction

A. Clinical motivation

In chronic obstructive pulmonary disease (COPD), airflow obstruction and airway inflammation frequently lead to destruction of alveolar architecture with enlargement of distal airspaces, which is referred to as pulmonary emphysema. Conventional chest radiographs have poor to moderate sensitivity particularly in patients with mild to moderate emphysema and cannot be used to reliably assess emphysema severity. Spirometry is commonly used to diagnose COPD/ emphysema but it is highly dependent on the patient's cooperation and effort. Partly due to the limitations of spirometry and conventional imaging techniques, COPD – currently – remains under-diagnosed. Studies have estimated that 60-85% of patients suffering from COPD, mainly those with mild to moderate disease, have not been diagnosed. The substantial morbidity and mortality resulting from this under-diagnosis could be prevented since COPD is a treatable disorder.

For example, if detected early, smoking cessation can substantially slow disease progression and lower mortality. According to the most recent (2012) world health organization (WHO) data, COPD ranks third among all causes of deaths claiming over 3 million lives globally each year (5.6% of all deaths). Further it is the fourth most common cause of disability responsible for over 30 million years lived with disability (YLDs) annually (4.2% of all YLDs). Estimating the cost of COPD to society is difficult, particularly due to under-diagnosis of the disease and the frequency of comorbidities. Nevertheless, it is clear that both direct costs (health care services, medications, treatment) and indirect costs (loss of productivity due to disability or premature death) are substantial. In Europe, COPD has been estimated to affect 5-10% of adults over 40 years of age. This translates to 12-25 million individuals affected by COPD in the European Union.

II. Methodology

A. Overall concept of wave-optical x-ray imaging.

Dark-field (small-angle scatter) image contrast is created through differences in the local scattering power within the sample. Small-angle scattering results from microstructures of a much smaller scale than the spatial resolution of the imaging system. For homogeneous objects that show no or negligible small-angle scattering, the dark-field signal is close to zero, whereas strongly scattering samples yield a significant dark-

field signal. The dark-field signal reveals indirect structural information on the nanometre and micrometre length scale that is inaccessible from the conventional attenuation CT image.

B. Grating-based x-ray dark-field imaging

Figure 2 shows the basic experimental arrangement for grating-based x-ray imaging. It consists of a source grating G0, a phase grating G1, and an analyser grating G2. The source grating (G0), typically placed close to the X-ray tube, is an aperture mask with transmitting slits. It creates an array of periodically repeating line sources and effectively enables the use of relatively large, that is, square-millimetre-sized, x-ray sources, without compromising the coherence requirements of the arrangement formed by G1 and G2. The image contrast itself is formed via the combined effect of the two gratings G1 and G2. The second grating (G1) acts as a phase mask and imprints a periodic phase modulation onto the incoming wave field.

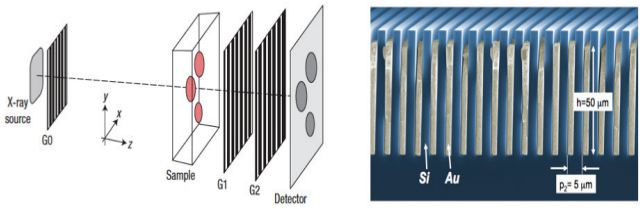

Fig. 2: Basic setup for grating-based x-ray imaging and micrograph of a typical grating structure. (Left) The arrangement for grating-based x-ray imaging (a so-called Talbot-Lau interferometer) consists of a source grating G0, a phase grating G1, and an analyser grating G2. The source grating (G0) is typically placed close to the x-ray tube, whereas G1 and G2 are placed close to the detector, behind the sample. (Right) Scanning electron micrograph of a typical grating structure (here a micro-structured silicon-template with gold fillings) with a period of 5 microns, and a height of 50 microns [for more details, see Pfeiffer et al., Nature Physics, 2008].

Through the Talbot effect, the phase modulation is transformed into an intensity modulation in the plane of G2, forming a linear periodic fringe pattern perpendicular to the optical axis and parallel to the lines of G1 (see Figure 3, left panel). The third grating (G2), with absorbing lines and the same periodicity and orientation as the fringes created by G1, is placed in the detection plane, in front of the detector. When one of the gratings is scanned along the transverse direction, the intensity signal in each pixel in the detector plane oscillates as a function of the grating transverse position (Figure 3, right panel).

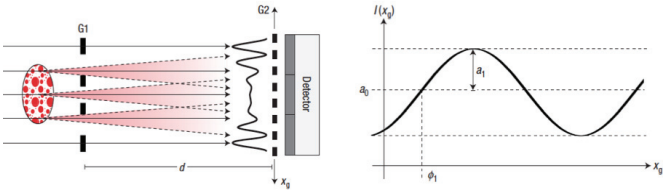

Fig. 3: Contrast generation and data processing in grating-based x-ray imaging. (Left) In order to detect the dark-field (small-angle scattering) signal created by an object, the periodic fringe pattern created by G1 is analysed in the plane of G2. A sample with a significant scattering contribution diffuses the beam and yields a locally reduced fringe visibility. (Right) The signal is obtained by analysing the intensity oscillations in every detector pixel as a function of the grating position G2 [for more details, see Pfeiffer et al., Nature Materials, 2008].

The setup allows obtaining three different image signals (conventional attenuation, phase-contrast, and dark-field contrast) from the object. In order to retrieve these signals, a so-called phase-stepping scan is performed with the interferometer, in which several exposures (typically 3 or 4) are acquired while one grating is stepped sideways in the direction perpendicular to the grating lines. Subsequently Fourier processing of the recorded frames is used to extract the three image signals. A typical result of such a procedure is shown in Figure 4 for a simple test sample.

Fig. 4: Multi-contrast x-ray images of a test sample containing two plastic containers filled with a liquid (water, left, A) and a powder (sugar, right, B). (a) Conventional x-ray attenuation image, (b) differential phase-contrast image, and (c) dark-field image of the same sample [for more details, see Bech et al., Zeitschrift für Med. Physik, 2010].

III. Small-Animal Experiments and Results

A. Small-Animal CT prototype setup

The prototype scanner (see Figure 5) consists of a standard rotating CT gantry with x-ray source, specimen opening, and a flat-panel detector. It comprises additionally a three-grating Talbot-Lau interferometer to extract multi-contrast x-ray projection images. This allows the system to deliver conventional attenuation images, differential phase-contrast images, and dark-field images. In the first step of the development, the compact gantry was built and operated stand-alone in rotating sample mode [11]. In its present configuration, the gantry is now implemented into a typical preclinical CT scanner housing, featuring an animal bed, animal monitoring, gas anaesthesia, and a flat-panel imaging detector.

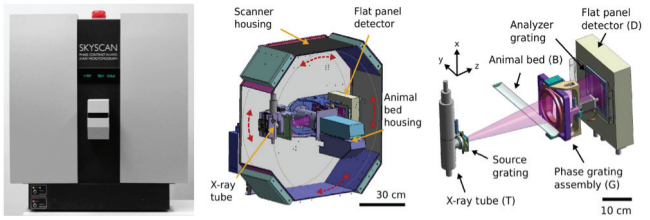

Fig. 5: Small-animal phase- and dark-field CT scanner. (Left) Photograph of the previously developed rotating-gantry CT scanner. (Middle) Schematics of the scanner housing with rotating gantry (gantry movement indicated by red arrows). The gantry is oriented horizontally in the displayed view. The housing dimensions are approximately 95 cm in width, 100 cm in height, and 85 cm in depth. (Right) Grating interferometer implementation, which is contained within the gantry [for more details, see Tapfer et al, PNAS, 2012].

Using the system at hand, we have successfully performed the first in-vivo phase- and dark-field contrast x-ray images of mice (see Figure 6), staying well within the dose limits for small-animal imaging (3.5 mGy in total).

As illustrated, the information gained from each of the three contrast mechanisms is of complementary nature. The conventional x-ray image (Figure 6a) shows very good contrast between bones and soft tissue, mainly due to the increased x-ray attenuation of calcium compared to the lighter soft tissue. The differential phase-contrast image (Figure 6b) enhances details in the soft tissue. In particular the interfaces of air filled regions are clearly shown, such as the trachea (marked by an arrow) or the lungs. Finally, the dark-field image (Figure 6c) enhances features containing sub-pixel-sized microstructures. Particularly the lungs exhibit a strong signal, as their main morphological structures – the alveoli – have a typical size of a few tens of micrometres.

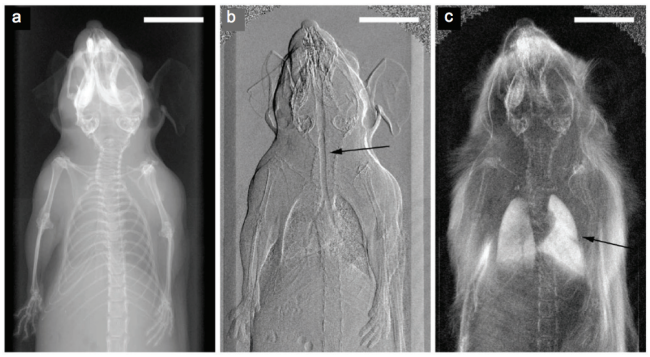

Fig. 6: First in-vivo multi-contrast x-ray images of a mouse. Data processing of the phase-stepping scans (shown in Figure 4) yields three separated and complementary x-ray images. (Left) Conventional x-ray attenuation image. (Middle) Differential phase-contrast image based on x-ray refraction. (Right) Dark-field image based on x-ray small-angle scattering. All three images are intrinsically registered as they are extracted from the same data. Examples of regions of enhanced contrast compared to the attenuation image are marked with arrows, showing the refraction of the trachea (middle) and the small-angle scattering of the lung (right). The total dose for these images was 3.5 mGy [for more details, see Bech et al., Nature Scientific Reports, 2013].

B. Disease screening in small animals

Based on the first successful – and dose-compatible – in vivo proof-of-principle experiments (see above), we have started to exploit the system to assess the full diagnostic potential of the dark-field technology in the area of lung imaging using small-animal (mouse) disease models. One example, showing particularly the potential benefits in diagnosing emphysema (COPD) or fibrosis (in an endpoint study with histological confirmation) is shown in Figure 7 [6][8].

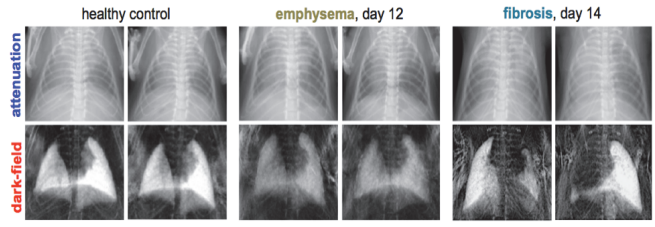

Fig. 7: Conventional in-vivo x-ray transmission (top row) and new x-ray dark-field (bottom row) radiographs of lung disease mouse models. The chosen examples highlight the potential of this new in-vivo medical imaging technology for improving diagnosis, monitoring, and - after potential drug administration - therapeutic response in the case of two important manifestations of chronic pulmonary disease, namely lung emphysema [9][4][6] and lung fibrosis [1]. While difficult (or almost impossible) to assess on the basis of the conventional transmission radiographs, the increased size of alveoli in the lung in the case of lung emphysema results in reduced scattering of x-rays and thus a (homogeneously) lower signal in the x-ray dark-field image, which is clearly detectable (bottom row, centre). In the case of lung fibrosis patches of diseased lung tissue can be clearly identified based on the missing dark-field signal (due to reduced tissue-air interfaces, bottom row, right). All images were recorded with our previously developed small-animal dark-field CT scanner prototype, with a typical total dose of 3-4 mGy for both images.

A further example of a longitudinal study is shown in Figure 8, see [4], which particularly highlights the method's ability to stage emphysema disease progression – and thus therapy monitoring.

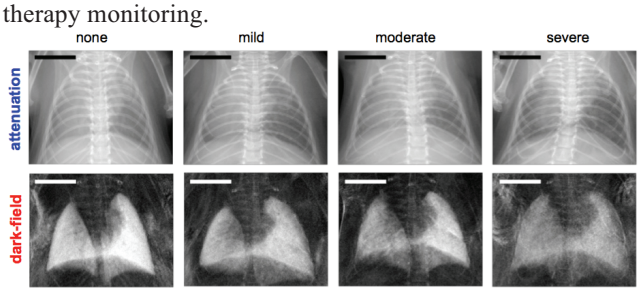

Fig. 8: X-ray transmission and dark-field images of mice in various stages of emphysema severity. Transmission (upper row), and dark-field (lower row) are shown for healthy (left), mildly (middle left), moderately (middle right), and severely (right) emphysematous lungs. The study shows that x-ray dark-field radiography can visualize different stages of emphysema in vivo and demonstrates significantly higher diagnostic accuracy for early stages of emphysema than conventional attenuation-based radiography [for more details, see Hellbach et al., Investigative Radiology, 2015].

C. First in-vivo small-animal dark-field CT images

To further explore the system's capability for performing full in vivo x-ray dark-field CT scans of mice, thoracic tomographic data were acquired of a healthy control mouse, a mouse with pulmonary emphysema, and a mouse with pulmonary fibrosis [3]. The scope of this study was to highlight the feasibility and to demonstrate the potential diagnostic benefit of the novel contrast modality in three-dimensional imaging.

Figure 9 provides an overview of the CT datasets of this study. Comparing the conventional attenuation CT images of the emphysematous mouse (Fig. 9 b, e) with the control (Fig. 9 a, d), only subtle differences towards darker grey values in peripheral lung tissue in the emphysematous case can be observed. The resolution of the imaging system does not allow a direct depiction of the alveolar wall structure. In the corresponding CT slices of the dark-field channel (Fig. 9 g, j for control, h, k for emphysema), the strong difference in signal allows for striking discernibility between control and diseased case. The destruction of alveolar walls and resulting enlargement of air spaces causes significantly reduced small-angle x-ray scattering.

In the case of lung fibrosis (Fig. 9 c, f for attenuation, i, l for dark-field) the replacement of the functional alveolar network by solid scar tissue is clearly apparent in both modalities, since the presented case is at an advanced stage. The dark-field image reveals areas with remaining functional alveolar structure.

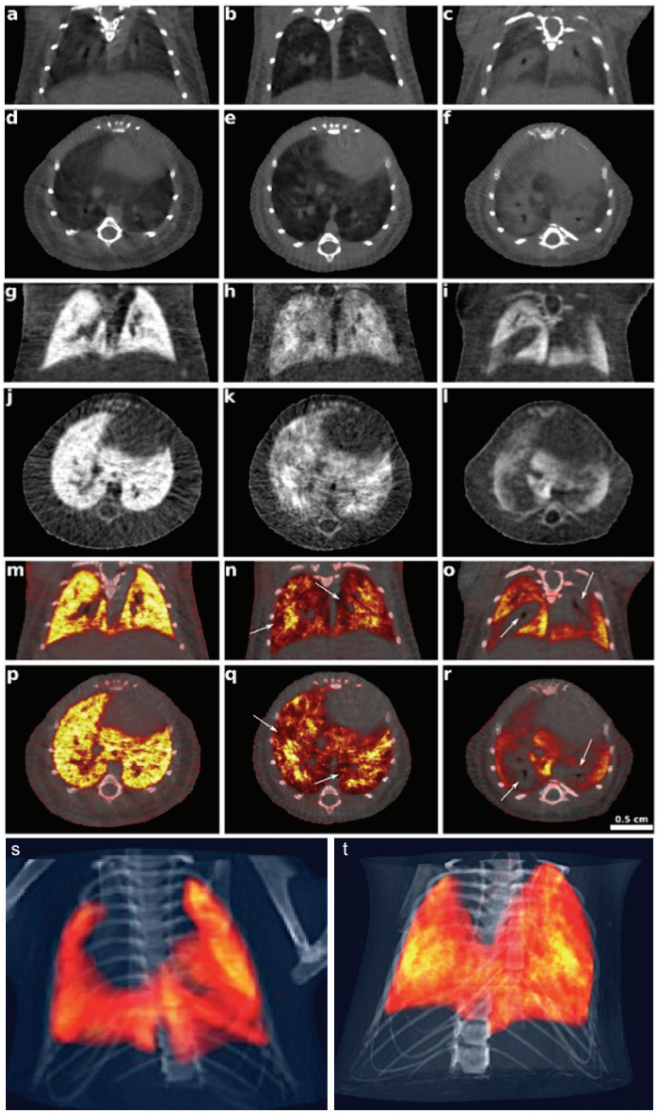

Fig. 9: Attenuation and dark-field CT slices, their fused representation, and volume renderings of lungs of three in vivo mice. Pathophysiological changes are subtle in the attenuation-based, but striking in dark-field images. Grey-value windows for single-modality slices were chosen for best visual appearance, but consistent within the same modality, respectively. (a,d,g,j,m,p,s) Control mouse. (b,e,h,k,n,q) Emphysematous mouse. (c,f,i,l,o,r,t) Fibrotic mouse. (a-c) Coronal slices of attenuation CT. (d-f) Axial slices of attenuation CT. (g-i) Coronal slices of dark-field CT. (j-l) Axial slices of dark-field CT. m-o: Coronal slices of fused CT. (p-r) Axial slices of fused CT. (s,t) Volume renderings of (s) emphysematous and (t) a fibrotic case. The skeletal structure was segmented from attenuation CT, whereas the lung tissue was extracted from dark-field CT and represented by a semi-transparent hot color map [see also https://www.youtube.com/watch?v=WeiADQ0h3B4].

For a better three-dimensional visualization, Fig. 9 s, t provide views of volume renderings of the acquired datasets. Bones were segmented from the attenuation signal, whereas lung tissue was extracted from the dark-field CTs and represented by a semi-transparent hot colour map to enhance inter- and intra-pulmonary structural variations. The 3D views confirm the earlier findings from the 2D slices: The control lung exhibits a strong homogeneous scattering pattern all over its volume, whereas the fibrotic lung lacks scattering areas in the central, peribronchial regions.

IV. Future Translation to Human CT

Based on these first successful pre-clinical, small-animal DFCT application results, the potential translation to human scale can be envisioned. This contribution will focus on the main challenges (grating quality, energy, acquisition strategies) that have to be addressed, before an implementation into a human CT system could be possible.

Translating this modality into a clinical setting has the potential to significantly improve the diagnosis of e.g. COPD, which changes the structure of the lung parenchyma on a micrometre length scale. It even allows monitoring and staging this disease using the additional information on the microstructural changes, which cannot be directly resolved by the imaging system.

References

[1] Yaroshenko, A. et al. Improved in vivo Assessment of Pulmonary Fibrosis in Mice using X-Ray Dark-Field Radiography. *Sci. Rep.* 1–8 (2015).doi:10.1038/srep17492

[2] Einarsdóttir, H. et al. Computer-aided diagnosis of pulmonary diseases using x-ray darkfield radiography. *Phys. Med. Biol.* 9253–9268 (2015).doi:10.1088/0031-9155/60/24/9253

[3] Velroyen, A. et al. Grating-based X-ray Dark-field Computed Tomography of Living Mice. *EBIOM 2*, 1500–1506 (2015).

[4] Hellbach, K. et al. In Vivo Dark-Field Radiography for Early Diagnosis and Staging of Pulmonary Emphysema. *Invest. Radiol.* 50, 430–435 (2015).

[5] Yaroshenko, A. et al. Grating-based X-ray dark-field imaging: a new paradigm in radiography. *Curr. Radiol. Rep. 2*, (2014).

[6] Meinel, F. G. et al. Improved Diagnosis of Pulmonary Emphysema Using In Vivo Dark-Field Radiography. *Invest. Radiol. 49*, (2014).

[7] Meinel, F. G. et al. Diagnosing and Mapping Pulmonary Emphysema on X-Ray Projection Images: Incremental Value of Grating-Based X-Ray Dark-Field Imaging. *PLoS ONE 8*, e59526 (2013).

[8] Yaroshenko, A. et al. Pulmonary Emphysema Diagnosis with a Preclinical Small-Animal X-ray Dark-Field Scatter-Contrast Scanner. *Radiology269(2)*,427-433, (2013).

[9] Schleede, S. et al. Emphysema diagnosis using X-ray dark-field imaging at a laser-driven compact synchrotron light source. *Proceedings of the National Academy of Sciences 109*, 17880–17885 (2012).

[10] Tapfer, A. et al. Experimental results from a preclinical X-ray phase-contrast CT scanner. *Proceedings of the National Academy of Sciences 109*, 15691–15696 (2012).

[11] Tapfer, A. et al. Development of a prototype gantry system for preclinical x-ray phase-contrast computed tomography. *Med. Phys. 38*, 5910 (2011).

Opportunities for phase-based computed tomography in the laboratory

Charlotte Klara Hagen, Anna Zamir, Paul Claude Diemoz, Marco Endrizzi, Fabio Alessio Vittoria, Panagiotis Magshoudlou, Paolo Coan, Alberto Bravin, Paolo De Coppi and Alessandro Olivo

***Abstract*—It has been demonstrated in many instances that phase-based computed tomography (CT) can provide superior contrast-to-noise ratio for weakly attenuating samples than attenuation-based CT. In order to exploit this benefit on a wider scale, phase-based tomography implementations must be compatible with standard x-ray equipment. The edge illumination method, which is based on aperturing a beam and measuring spatial displacements caused by refraction, is an attractive choice for such use due to its low requirements on spatial and temporal coherence. This document provides a brief introduction to the working principle of the edge illumination method and reviews recent advances that lead to increased robustness, faster acquisitions and lower dose delivery. Moreover, it reports on a recent study in which the edge illumination method was applied to samples from the field of tissue engineering, yielding synchrotron-like image quality with exclusively commercially available, laboratory-based x-ray equipment.**

***Index Terms*—computed tomography, phase contrast imaging, x-ray imaging**

I. Introduction

COMPUTED tomography (CT) has come a long way since its invention by Hounsfield and Cormack in the sixties. Regardless of whether it is used for clinical decision making, pre-clinical biomedical research, materials science or homeland security, CT is nowadays an integral part to various aspects of our society. The strength of this three-dimensional imaging modality lies in the wide range of spatial resolution regimes that can be accessed (on the macro-, micro- and even the nano-scale) and the fact that it can be implemented with a variety of x-ray sources (from compact hospital x-ray tubes to large, highly specialized synchrotron facilities) and detectors (from CCD cameras to cutting-edge energy resolving photon counters). Despite this versatility, CT suffers from one limiting issue; since image contrast is based solely on x-ray attenuation (dominated by photoelectric absorption or Compton scattering, depending on the energy used), materials with low atomic number suffer from a low contrast-to-noise ratio (CNR), leading to poor feature detectability. Although higher photon statistics can in principle improve the CNR, this option is often ruled out in practice by tight constraints on dose delivery and acquisition time.

On the other hand, attenuation is not the only physical effect that x-rays undergo when they travel through matter; phase shifts occur at the same time, since the wave velocity is different for different media. A sample's ability to attenuate and shift the phase of an x-ray beam is commonly described by the complex refractive index: $n(k) = 1 - \delta(k) + i\beta(k)$; δ and β drive phase shift and attenuation, respectively, and k is the wave number. For weakly attenuating materials and within the diagnostic energy range, δ can be up to three orders of magnitude larger than β, implying that CNR can be largely improved if phase effects are exploited [1].

Several methods have been developed to use x-ray phase shifts for imaging [2]. When a beam has a sufficient degree of spatial coherence, interference fringes develop as it propagates after exiting the sample, converting phase shifts into measureable intensity variations. This so-called propagation-based phase contrast imaging is however restricted to synchrotrons or micro-focal x-ray sources, due to its stringent coherence requirements. Another way of measuring phase shifts is by exploiting the Talbot effect, which creates an interference pattern (a self-image) at some specific distances downstream of a diffraction grating. Grating interferometry-based phase contrast imaging methods seek to measure this interference pattern as well as any disturbances to it caused by additional refraction introduced by the sample. The Talbot effect intrinsically requires coherence; however,

This work was supported by the UK Engineering and Physical Sciences Research Council (Grant Nos. EP/L001381/1 and EP/I021884/1). PCD and ME are supported by Marie Curie Career Integration Grant Nos. PCIG12-GA-2012-333990 and PCIG12-GA-2012-334056 within the Seventh Framework Programme of the European Union. The authors also acknowledge support by grants from the Medical Research Council, the Royal College of Surgeons of England, the Sparks Children Medical Charity, the British Foreign Office for the UK/USA Stem Cell Collaboration Award and the Mittal Research Fund. PDC is supported by Great Ormond Street Hospital Children's Charity. We would also like to thank the Royal Society/Wolfson Foundation for the tissue engineering laboratory refurbishment grant obtained for the Pediatric Surgery Department at University College London (UCL) Institute of Child Health. Authors thank the European Synchrotron Radiation Facility (Grenoble, France) for having provided beamtime the ID17 staff for their support in image acquisition.

CKH, AZ, PCD, ME, FAV and AO are with with the Department of Medical Physics and Biomedical Engineering, University College London, Malet Place, London WC1E 6BT, United Kingdom.

PM and PDC are with the Institute of Child Health, University College London, 30 Guilford Street, London WC1N 1EH, United Kingdom.

PC is with the Faculty of Medicine, Ludwigs Maximilians University, Marchionistr. 15D, 81377 Grosshadern-Munich, Germany. She is also with the Department of Physics, Ludwigs Maximilians University, Am Coulombwall 1, 85748 Garching, Germany.

AB is with the European Synchrotron Radiation Facility (ESRF), 71 Avenue des Martyrs, 38043 Grenoble, France.

CKH is the corresponding author (e-mail: charlotte.hagen.10@ucl.ac.uk).

implementations with low-coherence x-ray sources are possible by splitting the beam into an array of mutually incoherence but self-coherent sub-sources. Other phase contrast imaging methods also measure x-ray refraction, i.e. the macroscopic manifestation of the phase shift. These methods make use of an analyzer positioned in the beam path behind the sample, which modulates the beam intensity depending on the refraction angle. The analyzer can be a crystal (exploiting the laws of Bragg diffraction) or a single aperture/an array of apertures (exploiting spatial beam displacements resulting from refraction). While demanding less spatial coherence, crystal-based methods still require a temporally coherent beam due to the crystal's narrow-band energy acceptance. In turn, aperture-based methods tolerate low spatial *and* temporal coherence; thus, they can be implemented with conventional x-ray tubes, making them attractive for use in laboratory environments.

This document focusses on the edge illumination method [3,4], a specific aperture-based phase contrast imaging method that was developed initially at the Elettra synchrotron (Trieste, Italy), and more recently in the radiation physics laboratories of University College London (UCL). Following a brief introduction to the working principle of the method, its potential for use in standard laboratory environments is discussed through recent advances on robustness, scan speed and dose delivery. Finally, imaging examples of soft tissue specimens from the field of tissue engineering are presented.

II. The Edge Illumination Method

The edge illumination method converts x-ray refraction into image contrast. This is achieved by illuminating only the edges of a row of pixels with a narrow (typically < 20 μm) laminar beam (collimated by a slit-shaped aperture): a refraction of the beam towards/away from the pixels' active areas causes an increase/decrease in the measured intensity. In order to obtain a two-dimensional image, the sample has to be scanned through the beam. This implementation stems from early developments at the Elettra synchrotron where the flux is sufficiently high to perform fast acquisitions despite the need for sample scanning. When x-ray flux is limited (e.g. with conventional x-ray sources), the edge illumination method is typically implemented in full-field mode [Fig. 1]. In this setup, a mask, i.e. an array of slit-shaped apertures in front of the sample ("pre-sample mask") splits the beam into an array of physically separated beamlets, and a second mask in front of an area detector ("detector mask") creates insensitive areas ("edges") between the pixels. By positioning the pre-sample mask such that each individual beamlet falls partially on a pixel and partially on an absorbing detector mask septum, the edge illumination principle is replicated over the entire field of view (FOV), eliminating the need for sample scanning.

A prototype of such a setup has been built at UCL, based exclusively on commercially available x-ray equipment. The setup features a Rigaku MicroMax 007 HF x-ray tube with rotating molybdenum target (focal spot ≈ 70 μm), a Hamamatsu C9732DK flat panel detector with CMOS read-out (pixel size = 50 μm x 50 μm) and two sets of masks fabricated by electroplating gold strips onto a graphite substrate (Creatv MicroTech Inc., Potomac, MD, USA). The aperture widths of the pre-sample and detector masks are 23 μm and 29 μm, respectively, and their periods are 79 μm and 98 μm.

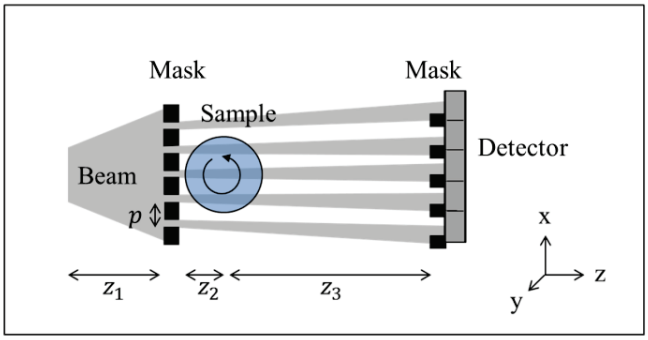

Figure 1. Schematic showing the full-field implementation of the edge illumination method (as seen from top). The distances in the prototype scanner at UCL are z_1=1.6 m, z_2 = 0.05 m and z_3 = 0.35 m.

Intensity variations (contrast) in a single radiograph are typically due to a combination of x-ray attenuation and refraction. The acquisition of a second image frame, after the pre-sample mask is re-positioned such that the beamlets fall onto the opposite sides of the detector mask apertures ("opposite illumination configuration"), and the subsequent processing of these two images according to a dedicated procedure ("phase retrieval") enables the separation of the attenuation and refraction channels [5,6]. If the sample contains scattering structures, each radiograph contains an additional (the so-called "dark field") channel. In that case, the acquisition of a third image frame, with the pre-sample and detector mask apertures fully aligned, is required to separate the attenuation, refraction and dark-field information [7]. In order to acquire a CT dataset, the sample must be rotated and two (or three, for scattering samples) projection images must be acquired at each CT angle. For each transverse sample slice ($y = const.$) this yields sinograms of the following form [8]:

$$S_\beta(x,z;\theta) = -2k\int \beta(x',z')\,dz \quad \text{(attenuation)} \quad (1)$$

$$S_\delta(x,z;\theta) = {}^{\partial}/_{\partial x}\int \delta(x',z')dz \quad \text{(refraction)} \quad (2)$$

$$S_{\sigma^2}(x,z;\theta) = \int \sigma_\Phi^2(x',z')dz \quad \text{(dark-field)} \quad (3)$$

where σ_Φ^2 describes the scattering properties of the sample, $(x',z') = (x\cos\theta - z\sin\theta, x\sin\theta + z\cos\theta)$ are the rotating coordinates of the sample and θ is the rotation angle. These sinograms enable the reconstruction of tomograms of $k\beta$ (attenuation), δ (phase), σ_Φ^2 (dark-field) via standard reconstruction methods, e.g. the filtered back projection (FBP) formula. The derivative in the refraction sinogram imposes the use of an additional integration step or the use of a dedicated filter function in the FBP.

III. Robustness, speed and dose

Since the edge illumination method is compatible with conventional x-ray tubes, it offers potential for a widespread use outside specialized synchrotron radiation facilities. However, the implementation of an imaging setup in non-synchrotron environments such as academic research laboratories or hospitals imposes several stringent requirements: a) the experimental setup should be easy to align and robust towards environmental vibrations, b) acquisitions should be fast, and c) the delivered radiation dose should be low (although the definition of "low" is obviously application dependent). Recently, strategies were developed for the edge illumination method in order to increase its compatibility with these criteria:

a) While the alignment of the pre-sample and detector masks is relatively straight forward and is currently carried out via a semi-automatic procedure [9], manufacturing-related mask imperfections prevent the alignment from being perfect, and therefore a certain, mask-dependent accuracy limit exists which cannot be overcome. Hence, local variations of the illumination level (the fraction of each beamlet falling into the detector mask aperture and therefore onto the pixel active area) across the field-of-view cannot be avoided. However, by applying a "local phase retrieval" procedure [10], this misalignment can be completely accounted for and its negative effect on the retrieved absorption, refraction and dark-field channels eliminated. In fact, the "local" method has been shown to tolerate mask imperfections of up to a few tens of micrometres, which is way above current manufacturing standards.

b) Due to the limited flux of conventional x-ray tubes and the fact that, until now, the separation of attenuation and refraction contrast required two input images, edge illumination CT has suffered from relatively lengthy scan times. To tackle this problem, an alternative phase retrieval method ("reverse projection"), which was first published by Zhu et al. (2010) for grating interferometry [11], has been further developed to make it applicable to EI datasets [12]. Reverse projection retrieval relies on the observation that two images acquired with a rotation offset of 180 degrees between them provide the same information as two acquired in the opposite illumination configurations as described above. This retrieval simplifies the experimental procedure and enables a more efficient (and thus faster) acquisition. In fact, it allows a continuous rotation of the sample while previously this had to be interrupted to reposition the pre-sample mask from one to the opposite illumination configuration at each rotation angle. Keeping the pre-sample mask in a fixed position throughout scans also improves robustness, as it eliminates any potential misalignment caused by repeated motor movements.

c) As a possibility for dose reduction, we have developed a new phase retrieval algorithm that does no longer require two images as input [13]. Instead, it relies only on a single image, and yields the projected thickness of a sample (in a similar manner to the widely used method developed by Paganin *et al.* for propagation-based phase contrast imaging [14]). This retrieval method reduces the number of image frames needed for a CT acquisition/reconstruction and, therefore, the dose and the acquisition time by a factor of 2. Since the method relies on the assumption of a single material sample, it cannot be considered strictly quantitative. However, so far high image quality results were obtained for all biological soft tissue samples that have been investigated.

IV. Application in tissue engineering

Tissue engineering, a sub-discipline of regenerative medicine, aims at the development of replacement organs by combining appropriate scaffolds and cells. An important question is how to produce scaffolds enabling cell adhesion, proliferation and differentiation. There is strong evidence that scaffold microstructure, biomechanical properties and extracellular matrix composition play a crucial role in this. Typically, microstructure and matrix composition are analyzed using histology and electron microscopy. These imaging techniques, however, require destructive sample preparation; hence they are not suitable for a volumetric analysis, longitudinal studies or *in vivo* translation. In a 2013 review paper on imaging modalities used for tissue engineering applications, x-ray phase contrast imaging was identified as a potential method to overcome the current lack of non-destructive, three-dimensional imaging technology that provides detailed scaffold information [15].

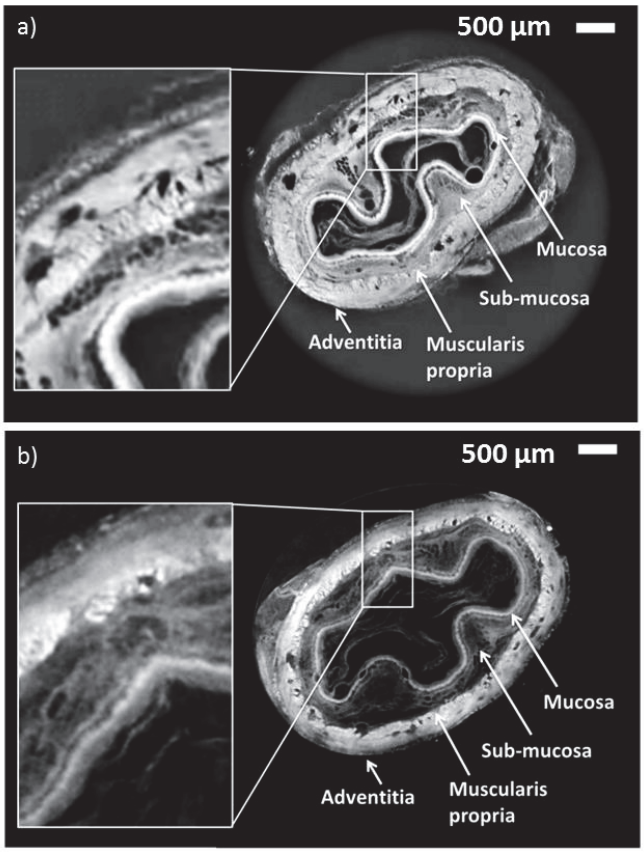

Figure 2. Phase tomograms of a decellularized rabbit esophagus acquired with a) propagation-based phase contrast CT at the ESRF (ID17) and b) the edge illumination method in the

radiation physics laboratories of UCL. Reprinted by permission from Macmillan Publishers Ltd: [Scientific Reports] (16), copyright (2015).

To demonstrate this potential, a range of tissue engineering scaffolds obtained via decellularization of small rodent organs was scanned recently [16], first with propagation-based phase contrast CT at beamline ID17 of the European Synchrotron Radiation Facility (ESRF), and then with the laboratory-based edge illumination setup at UCL. Phase tomograms were reconstructed, showing high image quality for both the propagation-based and the edge illumination data. As an example, Figure 2 shows tomograms of a rabbit esophagus scaffold; in both images, contrast is sufficiently high to identify all native anatomical layers of the esophagus (mucosa, sub-mucosa, muscularis propria, adventitia, as indicated by arrows in the figure), and to assess their structural integrity. The latter is important to judge the performance of the decellularization method used. Most importantly, the fact that an image quality comparable to that of synchrotron-based phase contrast CT was obtained in a standard laboratory using exclusively conventional x-ray equipment indicates that not only does phase contrast CT have the capability to replace histology and SEM for this range of applications, but also that imaging could be performed inside tissue engineering research laboratories, enabling a high-throughput and wide uptake.

V. Summary

Despite many advantages and widespread exploitation, CT imaging is still limited by poor CNR when applied to weakly attenuating samples like biomedical soft tissue. Phase contrast imaging methods can overcome this problem, since the phase exploited by these modalities for contrast generation can be much larger than attenuation effects. The edge illumination method's sensitivity to x-ray refraction is realized through the use of apertures in the beam path. Low demands on spatial and temporal coherence make the method attractive for use outside specialized synchrotron facilities such as research laboratories and hospitals. In order to ensure the method's compatibility with "real life" applications encountered in such environments, strategies for improved robustness, increased acquisition speed and dose reduction have been developed. These advances, together with the recent achievement of synchrotron-like image quality with laboratory equipment for tissue engineering samples, suggest that the edge illumination method provides opportunities for a widespread exploitation of phase-based tomography.

References

[1] A. Bravin, P. Coan and P. Suortti. (2013). X-ray phase-contrast imaging: from pre-clinical applications towards clinics. *Phys. Med. Biol.* 58, R1–R35. doi: 10.1088/0031-9155/58/1/R1

[2] S.W. Wilkins, Y.I. Nesterets, T.E. Gureyev, S.C. Mayo, A. Pogany *et al.* (2014). On the evolution and relative merits of hard x-ray phase-contrast imaging methods. *Philos. Trans. A Math. Phys. Eng. Sci.* 372, 20130021. doi: 10.1098/rsta.2013.0021

[3] A. Olivo, F. Arfelli, G. Cantatore, R. Longo, R.H. Menk *et al.* (2001), "An innovative digital imaging set-up allowing a low-dose approach to phase contrast applications in the medical field", *Med. Phys.* 28, 1610-9. Available: http://www.ncbi.nlm.nih.gov/pubmed/11548930

[4] A. Olivo and R. Speller. (2007) A coded-aperture technique allowing x-ray phase contrast imaging with conventional sources. *Appl. Phys. Lett.* 91, 074106. doi: 10.1063/1.2772193

[5] P.R.T. Munro, C.K. Hagen, M.B. Szafraniec and A. Olivo. (2013). A simplified approach to quantitative coded aperture x-ray phase imaging methods. *Opt. Express* 21, 11187-201. doi: 10.1364/OE.21.011187

[6] P.C. Diemoz, M. Endrizzi, C.E. Zapata, Z.D. Pesic, C. Rau *et al.* (2013). X-ray phase-contrast imaging with nanoradian angular resolution. *Phys. Rev. Lett.* 110, 138105. doi: 10.1103/PhysRevLett. 110.138105

[7] M. Endrizzi, P.C. Diemoz, T.P. Millard, J.L. Jones, R.D. Speller *et al.* (2014). Hard x-ray dark-field imaging with incoherent sample illumination. *Appl. Phys. Lett.* 104, 024106. doi: 10.1063/1.4861855

[8] F.A. Vittoria, M. Endrizzi, P.C. Diemoz, A. Zamir, U.H. Wagner *et al.* (2015). X-ray absorption, phase and dark-field tomography through a beam tracking approach. *Sci. Rep.* 5, 16318. doi: 10.1038/srep16318

[9] T.P. Millard, M. Endrizzi, K. Ignatyev, C.K. Hagen, P.R.T. Munro *et al.* (2013). Method for automatization of the alignment of a laboratory based x-ray phase contrast edge illumination system. *Rev. Sci. Instrum.* 84, 083702. doi: 10.1063/1.4816827

[10] M. Endrizzi, D. Basta and A. Olivo. Laboratory-based x-ray phase-contrast imaging with misaligned optical elements. *Appl. Phys. Lett.* 107, 124103. doi: 10.1063/1.4931778

[11] P. Zhu, K. Zhang, Z. Wang, Y. Liu, Z. Wu *et al.* (2010). Low-dose, simple, and fast grating-based x-ray phase-contrast imaging. *Proc. Natl. Acad. Sci USA* 107, 13576-81. doi: 10.1073/pnas.1003198107

[12] Hagen *et al.*, submitted

[13] P.C. Diemoz, F.A. Vittoria, C.K. Hagen, M. Endrizzi, P. Coan *et al.* (2015). Single-image phase retrieval using an edge illumination x-ray phase-contrast imaging setup. *J. Synchrotron Radiat.* 22, 1072-7. doi: 10.1107/S1600577515008978

[14] D. Paganin, S.C. Mayo, T.E. Gureyev, Miller P.R. and S.W. Wilkins. (2002). Simultaneous phase and amplitude extraction from a single defocused image of a homogeneous object. *J. Microsc.* 206, 33-40. Available: http://www.ncbi.nlm.nih.gov/pubmed/12000561

[15] A.A. Appel, M.A. Anastasio, J.C. Larson and E.M. Brey. (2013). Imaging challenges in biomaterials and tissue engineering. *Biomaterials* 34, 6615-30. doi: 10.1016/j.biomaterials.2013.05.033

[16] C.K. Hagen, P. Maghsoudlou, G. Totonelli, P.C. Diemoz, M. Endrizzi *et al.* (2015). High contrast microstructural visualization of natural acellular matrices by means of phase-based x-ray tomography. *Sci. Rep.* 5, 18156. doi: 10.1038/srep18156

Iterative Reconstruction of Grating-based PCCT Without Phase-Stepping

Maximilian von Teuffenbach, Bernhard Brendel, Andreas Fehringer, Peter B. Noël, Franz Pfeiffer, Thomas Köhler

***Abstract*—Grating-based X-ray phase-contrast computed tomography (PCCT) has been in the focus of a lot of research in recent years. It does not only allow access to information about X-ray attenuation but also about X-ray refraction and small-angle scattering in a sample while still being usable with ordinary polychromatic, incoherent X-ray tubes. The improved functionality over conventional CT comes with the drawback of longer exposure times. This is because standard processing algorithms require not a single image per projection angle but several. Additionally, precise grating movements have to be performed in between, which hinders adaptation of PCCT in a continuously rotating gentry. Here we propose to use an iterative reconstruction algorithm with a forward model based directly on the measured intensities to circumvent the problematic part of projection-based phase retrieval. We show that using this approach successful reconstruction is not only possible with a single stepping position per projection but that, if combined with high frequency moiré fringes, reconstruction is possible without any grating movement at all.**

I. Introduction

SINCE its first clinical use in the 1970s computed tomography (CT) has been developed into a standard imaging technique in medicine and industrial testing. New phase sensitive X-ray imaging techniques offer the possibility to reconstruct not only the spatial distribution of the attenuation coefficient in a sample but also the spatial distribution of the electron density (via sample refraction) and of a small-angle scattering contribution of sub-resolution features in the sample. Using these new imaging modalities phase-contrast computed tomography (PCCT) can offer significantly improved image contrast, especially if the attenuation of the sample is small such as in soft tissue [1].

Grating-based differential phase-contrast (GB-DPC) imaging is one of the most promising X-ray techniques offering phase sensitive information because it can be used with ordinary X-ray sources [2], offers high sensitivity and resolution [1], and has been successfully applied in several studies for biomedical imaging [1]–[8]. It is based on an interferometric self-imaging phenomenon called Talbot effect. An interference pattern is created by introducing the so-called phase grating (G1) into the beam path. This pattern is modulated by the scanned object. A second absorption grating acts as an analyzer grating (G2) to resolve the pattern, which has features below detector pixel size, with a conventional X-ray detector. If used with an incoherent X-ray source, the Talbot interferometer is usually turned into a Talbot-Lau interferometer by introducing another absorption grating (G0) in front of the source to increase spatial coherence [2].

One of the biggest hindrances of wide-spread adaptation of differential phase-contrast tomography is that it requires long acquisition times compared to conventional CT. The main cause for higher acquisition times is the standard procedure of phase stepping. Phase stepping produces transmission, differential phase, and dark-field projections but at least three measurements (interferograms) per projection angle are required. Additionally, precise grating movements have to be performed between the measurements which demands a great deal of stability from the setup and effectively hinders the adaption of PCCT in state-of-the-art continuously rotating CT gentries.

Several methods have been proposed to ease these requirements. Interlaced phase stepping combines rotation and phase stepping in one step but is still limited by speed and stability of the grating movement and suffers from a loss of tangential resolution [3]. Fringe analysis is a method that works with a single shot per angle but loses spatial resolution [4]. The reverse projection method uses complementary information of opposing projections in a 360° scan but only works correctly for weakly refracting objects, does not recover scattering information and, of course, needs a 360° scan [5]. Model-based iterative reconstruction techniques would allow to consider all necessary configurations of the imaging setup, including grating positions, in a forward-model. Several studies using iterative reconstruction techniques have been published but almost all of them utilize transmission, differential phase, and dark-field projections as the basis of their model [6], [9], [10]. As these projections have to be previously processed from the measured interferograms, it means that these techniques can not account for errors introduced during processing and that the interferograms have to be taken in a specific way that allows processing them (a full phase-stepping, opposing projections, etc.) To our knowledge, so far only two studies have based their models on the measured intensities of the interferogram [11], [12]. In [11] an unregularized maximum likelihood model was used and a heuristic method for opti-

M. von Teuffenbach and Andreas Fehringer are with the Chair for Biomedical Physics and the Institute for Medical Engineering, Technische Universität München, Munich, Germany

B. Brendel is with Philips GmbH, Innovative Technologies, Research Laboratories, Hamburg, Germany

P. B. Noël is with the Department of Radiology, Technische Universität München, Munich, Germany

F. Pfeiffer is with the Chair for Biomedical Physics, the Institute for Medical Engineering, and the Institute for Advanced Study, Technische Universität München, Munich, Germany

T. Köhler is with Philips GmbH, Innovative Technologies, Research Laboratories, Hamburg, Germany and with Institute for Advanced Study, Technische Universität München, Munich, Germany

Please send correspondence to Maximilian.Teuffenbach@tum.de

mization was employed that is not guaranteed to converge. Additionally the study was performed on a noise-free numeric phantom and utilized manually constructed starting images containing information about the object. The image acquisition was following the standard phase-stepping procedure.
Intensity-based statistical iterative reconstruction (IBSIR) should give a framework which allows to take all relevant system parameters into account [12], allows to correctly consider measurement noise, and allows any single recorded interferogram to add usable information to the reconstruction. That last point should ease the requirements for the image acquisition process substantially. The goal of this work was to test IBSIR on real measurements using non-standard image acquisition procedures and to test how far that is possible.
First we will formulate the algorithm used in this study by stating the used objective function, forward model, and solver. Then we show that the linear attenuation coefficient μ, electron density δ, and linear scattering coefficient ϵ of a complex biomedical sample can be successfully reconstructed with this method using only a single grating position per projection angle. After that another successful reconstruction is shown where only a single constant grating position is used throught the scan to reconstruct a continuously moved sample.

II. Method

As mentioned in Section I prior to conventional reconstruction in PCCT first a set of three sinograms containing attenuation, differential phase, and dark-field projections has to be obtained via various techniques. The linear attenuation coefficient μ, electron density δ, and a linear scattering coefficient ϵ are then separately reconstructed from one sinogram at a time via filtered back projection (FBP) [1] or iterative reconstruction algorithms [6], [9].
Alternatively, a cost function incorporating a model of the imaging system can be optimized. The cost function contains a data term, calculating the likelihood for the reconstructed images to belong to the measurement, and a regularization term that penalizes deviations of the images from prior knowledge i.e. smoothness of the images. Now the values for μ, δ, and ϵ which minimize the cost function for given measurements I are the best estimate of their distribution in a penalized maximum-likelihood sense.

A. Intensity-based Statistical Iterative Reconstruction

In the following, the index i denotes the measurement for a specific detector element at a specific angular and grating position. For conventional detectors and for high photon counts in photon counting detectors the measured intensities I_i are Gaussian distributed around their expected values $\bar{I}_i$ with variance σ_i^2. The joint negative log-likelihood (without any prefactors) to measure I can be written as

$$L(I|\bar{I}) = \sum_i \frac{1}{\sigma_i^2}(I_i - \bar{I}_i)^2. \tag{1}$$

The forward model for $\bar{I}_i$ is dependent on the distribution of μ, δ, and ϵ and can be written as

$$\bar{I}_i = I_i^0 T_i[1 + V_i^0 D_i \cos(\Phi_i^0 - \Phi_i)] \tag{2}$$

where I^0, V^0, Φ^0 are mean intensity, visibility, and phase position of a blank scan without sample. The transmission T, dark field signal D, and differential phase Φ are defined as

$$T_i = \exp\,[-\int_{l_i} \mu(x)dx], \tag{3}$$

$$D_i = \exp\,[-\int_{l_i} \epsilon(x)dx], \tag{4}$$

$$\Phi_i = \partial_y \int_{l_i} \delta(x)dx, \tag{5}$$

where $\int_{l_i} dx$ is the line integral from detector i to the x-ray source and ∂_y is the partial derivative perpendicular to the grating direction. These can be calculated by a conventional CT projector [13].
For the regularization term a single independent constraint enforcing smoothness can be applied to each of the reconstructed images [12]:

$$R = \sum_{\theta\in\{\mu,\delta,\epsilon\}} \beta_\theta \sum_j \sum_{k\in\mathcal{N}_j} w_{jk}\Psi(\theta_j - \theta_k, \gamma_\theta). \tag{6}$$

The index j runs over all voxels (all three images are defined on the same grid) and k runs over all voxels in the neighborhood $\mathcal{N}_j$ of j. w_{jk} is a distance dependent weight and $\Psi(\cdot)$ is the Huber potential function [14]. Regularization strength β and Huber parameter γ are individually set for all three images such that no details are lost in that image but also significant noise suppression can be observed.
The cost function $C = L + R$ was minimized by iteratively applying a simple steepest descent algorithm separately on one image after the other. That means that the gradient of all voxels in one image was calculated, then a 1D linesearch in gradient direction was performed and the image was updated accordingly. It should be noted that this algorithm is not optimal with respect to execution time at all, but is easy to implement and does not diverge.

B. Data acquisition schemes

To correctly reconstruct μ, δ, and ϵ every part of the sample has to be imaged not only from a sufficient number of angular positions, but also at enough different phase positions to correctly attribute changes in measured intensity to either attenuation, change in phase of the measured X-ray or scattering in the object. Normally this is achieved by phase stepping or scanning of moiré fringes in a specific way, see Section I. We will use two simple methods for data acquisition that can be used with a rotating gentry.

1) Sliding Window: In this variation of the standard phase stepping approach, grating position and angular position of the scanner are changed at the same time. Conventional Fourier processing [7] of these interferograms is possible by interpolating between neighboring views [3] but comes at the

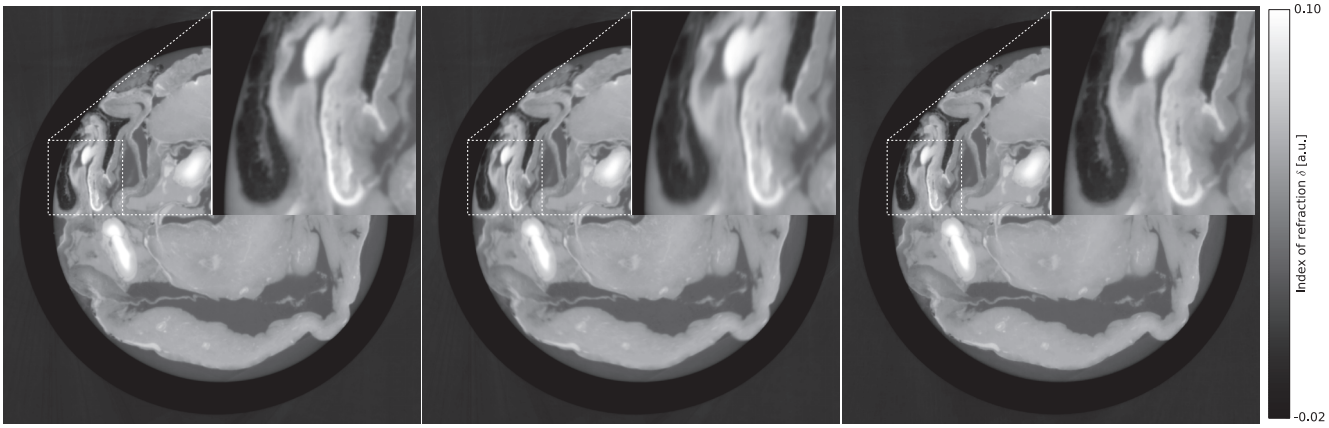

Fig. 1. (a) Reference reconstruction of the refractive index decrement using FBP based on 751 projections each with 5 steps. (b) Reconstruction using sliding-window FBP based 751 projections of 1 step each. (c) Reconstruction of sliding window dataset using intensity-based iterative reconstruction. (b) shows severe blurring in regions far from the center (see zoomed region). (c) shows no blurring in tangential direction and suppresses light streak artifacts outside of the tube seen in (a) and (b). All images are shown on the same window.

cost of blurring in tangential direction. As IBSIR does not require processing of the interferograms, interpolation is not necessary and should lead to reconstructions without tangential blurring.

2) Moiré fringes: Through careful misalignment of G1 and G2 it is possible to create vertically oriented moiré fringes on the detector. If the sample is now rotated, it will move through the fringes, thus allowing measurements of almost every part of the sample at different phase shifts. Only the parts of the sample close to the rotational axis are always situated inside of the same fringe. To circumvent this, we moved the sample by a single pixel after each projection. To stay inside of the detector field of view, this displacement was set to zero every few steps, resulting in a sawtooth-like detector displacement. An equivalent effect can also be achieved, without any mechanical movements, by a technique called focal point shift or electronic beam steering [15].

III. Experimental Results

1) Sliding Window: To demonstrate improvements in resolution for sliding window scans the scan of rat intestines used by [3] was reevaluated. The sample was submerged in a cylindrical container filled with formalin 10 % solution, which was in turn put in a water bath to avoid strong refraction at the container-air interface. Measurements were performed at the ID19 beamline of the European Synchrotron Radiation Facility (ESRF) in Grenoble, France. A monochromatic beam with an energy of 23 keV was produced with a Si(111) double crystal monochromator. The interferometer was located 150 m from the source. It consisted of a phase grating G1 made from silicon and an analyzer grating G2 made from gold on a silicon substrate. G1 had a period of 4.80 µm and a height of 29.5 µm and G2 had a period of 2.4 µm and a height of 50 µm. The inter-grating distance was 481 mm. As detector a scintillator/lens-coupled CCD camera with 2048×2048 pixels and an effective pixel size of 7.5 µm was used. Five interferograms were taken at different grating positions for 751 angular positions evenly spaced over 180 degrees. Each interferogram had an exposure time of 1.5 seconds.
In Fig. 1a, the phase image of the fully sampled dataset was reconstructed for reference using FBP (attenuation and scatter image are omitted as they show very little contrast even for the full dataset). Then the dataset was sampled down to a single interferogram per view, going through the grating positions cyclically. Reconstruction of this dataset using FBP (SW-FBP) is shown in Fig. 1b and using IBSIR is shown in Fig. 1c. IBSIR was initialized with a blurred version of the SW-FBP reconstruction.
The reference scan shows high image quality with clear edges, but slight streak artifacts are visible outside of the sample. SW-FBP reconstruction shows overall image quality comparable to the reference scan, but a slight blurring in tangential direction that increases with the distance to the tomographic axis, see the zoomed region in Fig. 1b. Reconstruction of the reduced dataset with IBSIR shows at least comparable image quality to the reference and does not feature tangential blurring as seen in SW-FBP. Additionally, IBSIR does not show the streak artifacts seen in both FBP and SW-FBP.

2) Moiré fringes: The second method, utilizing vertical moiré fringes was tested on a phantom of five 6 mm rods of PMMA, POM, Nylon, LDPE, and PS, which were submerged in a water bath. The measurement was done using a symmetric Talbot-Lau interferometer with grating distances $\overline{G0G1} = \overline{G1G2} = 85.7$ cm. The three gratings G0, G1, and G2 are all made of gold on a silicon substrate with periods of 5.4 µm. The absorption gratings G0 and G2 have a height of 70 µm and 65 µm respectively. The phase grating G1 is designed to give a phase shift of π at the system design energy of 27 keV. The source is an ENRAF Nonius FR 591 rotating anode X-ray tube with a Molybdenum target operated at 40 kVp and 70 mA. The detector used is a single photon counting PILATUS 100k module with 487×195 pixels and a pixel size of 172×172 µm^2. The effective pixel size is 100×100 µm^2. 3600 interferograms evenly spaced over 360 degrees were each taken with an exposure time of 6 s. After each rotation the

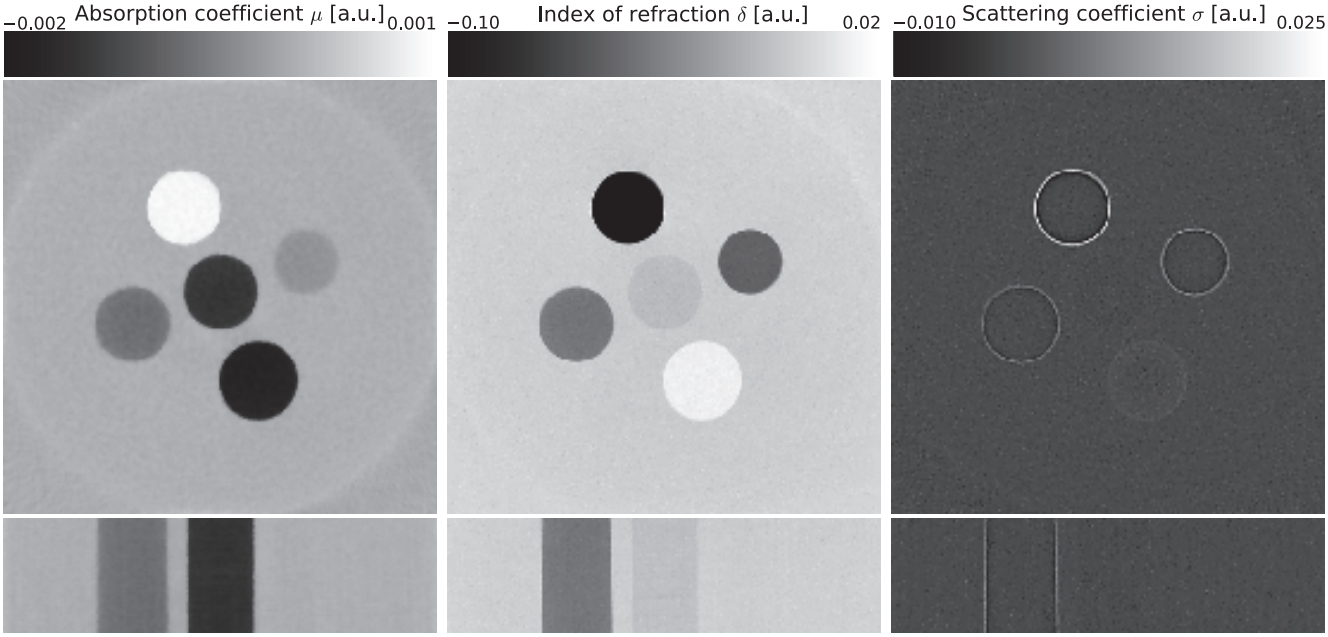

Fig. 2. Axial (upper row) and coronal (lower row) slices of an IBSIR reconstruction using 3600 projections and constant grating positions. All three image modalities of PCCT can be reconstructed without artifacts and with high image contrast.

object was shifted by one pixel and after every 20 shifts the object was returned to its initial position. The moiré fringes had periods of about 8 to 10 pixels. The IBSIR reconstruction was initialized with an zero-valued volume.
In Fig. 2 axial and coronal slices of the reconstructed volume are shown. The images show clear edges and artifact free reconstructions.

IV. Conclusion

In this work we showed that sliding window image acquisition combined with IBSIR allows for substantial dose reduction compared to standard phase-stepping PCCT procedures. The method comes without any loss of resolution or sensitivity, can access attenuation, phase-contrast, and dark-field information separately, and does not require any alterations to usual grating-based setups.
Furthermore, we showed that IBSIR offers a whole new level of freedom in processing and reconstructing grating-based PCCT measurements. It neither requires grating movement nor perfect moiré fringe alignment. This is possible because the proposed method does not require a separate phase-retrieval step prior to reconstruction.
IBSIR seems to be ideally suited to process PCCT measurements with a helically rotating gentry as the method presented in Section III-2 can similarly be used to process measurements with a moving object holder and fringes aligned perpendicular to the movement direction. If future studies of the algorithms behavior for few views, low photon counts, and phase-wrapping are positiv, IBSIR could be a serious step towards the introduction of PCCT to clinical applications.

References

[1] F. Pfeiffer *et al.*, "High-resolution brain tumor visualization using three-dimensional x-ray phase contrast tomography," *Phys. Med. Biol.*, vol. 52, 2007.

[2] F. Pfeiffer *et al.*, "Phase retrieval and differential phase-contrast imaging with low-brilliance X-ray sources," *Nat. Phys.*, vol. 2, 2006.

[3] I. Zanette *et al.*, "Trimodal low-dose X-ray tomography," *Proc. Natl. Acad. Sci.*, vol. 109, 2012.

[4] N. Bevins *et al.*, "Multicontrast x-ray computed tomography imaging using Talbot-Lau interferometry without phase stepping," *Med. Phys.*, vol. 39, 2012.

[5] P. Zhu *et al.*, "Low-dose, simple, and fast grating-based X-ray phase-contrast imaging," *Proc. Natl. Acad. Sci.*, vol. 107, 2010.

[6] T. Gaass *et al.*, "Iterative reconstruction for few-view grating-based phase-contrast CT An in vitro mouse model," *Europhys. Lett.*, vol. 102, 2013.

[7] F. Pfeiffer *et al.*, "Hard-X-ray dark-field imaging using a grating interferometer." *Nat. Mater.*, vol. 7, 2008.

[8] M. Bech *et al.*, "In-vivo dark-field and phase-contrast x-ray imaging." *Sci. Rep.*, vol. 3, 2013.

[9] T. Köhler *et al.*, "Iterative reconstruction for differential phase contrast imaging using spherically symmetric basis functions," *Med. Phys.*, vol. 38, 2011.

[10] D. Hahn *et al.*, "Statistical iterative reconstruction algorithm for X-ray phase-contrast CT," *Sci. Rep.*, vol. 5, 2015.

[11] A. Ritter *et al.*, "Simultaneous maximum-likelihood reconstruction for x-ray grating based phase-contrast tomography avoiding intermediate phase retrieval," *arXiv*, 2013.

[12] B. Brendel *et al.*, "Penalized maximum likelihood reconstruction for x-ray differential phase-contrast tomography," *Med. Phys.*, vol. 43, 2016.

[13] A. Fehringer *et al.*, "A versatile tomographic forward- and back-projection approach on multi-GPUs," *SPIE Med. Imag. 2014: Image Process.*, vol. 9034, 2014.

[14] J. Fessler, *Statistical Image Reconstruction Methods for Transmission Tomography*, 2000.

[15] H. Miao *et al.*, "Motionless phase stepping in X-ray phase contrast imaging with a compact source," *Proc. Natl. Acad. Sci.*, vol. 110, 2013.

Characterization of Tooth Samples with a Talbot-Lau Grating Interferometer µXCT Desktop Device

Christian Gusenbauer, Stefan Hunger, Sascha Senck and Johann Kastner

***Abstract*—An innovative X-ray technology for laboratory studies of polymeric, biologic and medical samples has recently become commercially available by the introduction of a desktop Talbot-Lau grating interferometer µXCT system. Talbot-Lau µXCT increases the imaging capabilities of conventional absorption-based contrast (AC) with differential phase contrast (DPC) and dark-field contrast (DFC). This paper discusses the application of µXCT and Talbot-Lau µXCT in the field of dentistry. We investigated different tooth samples using a desktop Talbot-Lau µXCT and compare the results to high-resolution µXCT of the occlusal surface, dental fillings and root canal. In addition, a suitable image processing routine for data fusion of tooth samples and a custom-made test phantom are presented to optimize data quality.**

***Index Terms*—Talbot-Lau µXCT, grating interferometer, materials characterization, tooth samples**

I. Introduction

IN 2002, the Talbot-Lau effect has been first utilized for X-ray imaging using monochromatic synchrotron radiation [1]. The additional use of a source grating in 2006 has enabled the introduction of this innovative technique to polychromatic and laboratory X-ray sources [2]. Since then the method has evolved concerning grating design, reconstruction techniques, image processing and suitable fields of applications have been identified [3-6]. In-vivo dark-field and phase-contrast X-ray imaging of small animals as well as a setup towards clinical phase-contrast radiography of small joints and mammography have been recently demonstrated by showing their benefits for diagnostics in clinical routine [7]. First clinical demonstrators for radiographic purposes are expected to arrive in near future [8-9].

Submission date is the 25th of January 2016. This work was supported by the K-Project for "non-destructive testing and tomography plus" (ZPT+) and by the COMET program of FFG and the federal government of Upper Austria and Styria and supported by the project "multimodal and in-situ characterization of inhomogeneous materials" (MiCi) and the European Regional Development Fund (EFRE) in the framework of the EU-program IWB2020.

C. Gusenbauer, S. Senck and J. Kastner are with the University of Applied Sciences Upper Austria, Campus Wels, Stelzhamerstraße 23, 4600 Wels, Austria (e-mail: christian.gusenbauer@fh-wels.at, sascha.senck@fh-wels.at, johann.kastner@fh-ooe.at). S. Hunger is with the Johannes Kepler University Linz, Faculty of Medicine, Krankenhausstraße 9, 4021 Linz, Austria (e-mail: stefan.hunger@akh.linz.at).

However, the drawback of existing laboratory grating interferometer µXCT systems is their limited access, user-friendliness, long acquisition times and complexity of operations. With the introduction of the first commercially available desktop Talbot-Lau µXCT system (Bruker SkyScan 1294) for material science applications in the beginning of 2015, this imaging method becomes now accessible to a broader community [10]. This paper focuses on the optimization of dark-field imaging of premolar and molar tooth samples in comparison to absorption contrast µXCT data.

II. Materials and Methods

In this paper one test phantom and two different tooth samples have been studied using the Bruker SkyScan 1294 Talbot-Lau µXCT desktop device. Results are compared to high-resolution and absorption-based laboratory µXCT systems. The test phantom is an inverse step cylinder made of polyoxymethylene (POM), filled with sugar crystals, simulating a porous media due to empty spaces between its particles. This phantom has been used for scan parameter optimizations. The inner diameters of the phantom are ranging from 2 to 12 mm; each step is 2 mm in height. A constant wall thickness of 3 mm ensures equal pre-filtration.

The first tooth sample is an extracted molar tooth from a male adult, root treated with dental fillings (plastic and metallic) inside. The second tooth sample is a premolar tooth of a 13 year old female patient, which had to be extracted during an orthodontic treatment due to shortage of space. The premolar tooth has been prepared ex-vivo with an artificial cavity, followed by the subsequent filling of the cavity with different layers of dental material and curing under laboratory conditions.

A. High-resolution µXCT

The high-resolution µXCT scans (in absorption contrast) have been performed with two different laboratory µXCT devices including (i) a GE Nanotom 180 NF XCT device with a 180 kV high nano-focus X-ray tube and a 2304 x 2304 pixel Hamamatsu flat panel detector allowing a minimal voxel size down to 500 nm and (ii) a RayScan 250 E system with a 225 kV µ-focus X-ray tube from Viscom and a 2048 x 2048 pixel

TABLE I
SCAN PARAMETERS OF USED µXCT DEVICES

Device	Scan parameters	Voxel size	Exposure time
SkyScan (preset 2)	35 kV, Al 0.25 mm	(22.8 µm)³	molar: 512 min, premolar: 2x780 min
SkyScan (preset 5)	50 kV, Cu 0.045 mm	(22.8 µm)³	molar: 616 min, premolar: 2x420 min
RayScan	100 kV, no pre-filter	(12.95 µm)³	premolar: 48 min
Nanotom	100 kV, no pre-filter	(10.5 µm)³	premolar: 62.5 min

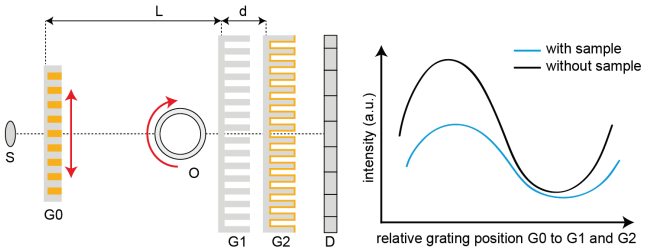

Fig. 1. Sketch of the working principle of a typical Talbot-Lau XCT setup with X-ray source (S), object (O), detector (D), gratings (G0, G1, G2) and distances d and L describing system and interferometer characteristics (left), a phase stepping curve with and without sample (right)

Perkin Elmer flat panel detector, with a minimal voxel size of about 5 µm. The scanning parameters for the Talbot-Lau µXCT and high-resolution µXCTs can be found in **Table I**.

B. Talbot-Lau grating interferometer XCT

The SkyScan 1294 Talbot-Lau grating interferometer XCT setup is consisting of a 60 kV µ-focus X-ray source from PANalytical, a detector from Princeton Instruments with 4000 x 2672 pixels, a source grating G0, acting as an array of line sources, ensuring a sufficient transverse coherence length and a diffractive grating G1, causing phase modulation of the incoming X-rays and resulting in an interference pattern. Since fringe pattern cannot be resolved directly with conventional X-ray detectors, an absorption grating G2 has been placed in front of the detector. Latter two gratings (G1 and G2) are forming up the interferometer. The source grating G0 is used to scan transversely across the repeated intensity pattern, called phase stepping, resulting in a sinusoidal intensity modulation at G2. Rotating the sample stepwise in between the acquisition of the phase stepping curves allows the tomographic operation. A typical Talbot-Lau XCT setup and an exemplary phase stepping curve are shown in **Fig. 1**.

A precise production of gratings with adequate grating properties and a perfect alignment of all three gratings in rotation and tilt are mandatory for proper data extraction. The absorption grating G2 in front of the camera stays statically. The phase grating G1 can be adjusted by rotation and tilting for aligning with respect to G2. The diffractive grating G1 can be moved in direction along the beam for maximum modulation of phase carpet pattern on the surface of grating G2. The source grating G0 can be aligned on its rotational position in correspondence to G1 and G2.

AC is formed due to the absorption mechanism of photons interacting with matter predominantly in form of photoelectric effect and Compton scattering in the low keV range. DPC is related to the index of refraction and image contrast is thus achieved through the local deflection of the X-ray beam. DFC contains the total amount of radiation scattered at small angles, caused by surfaces and interfaces between e.g. material inhomogeneities and matrix. The placement of a sample within optical beam axis will attenuate, refract, and scatter the incoming X-ray and thus perturbing the periodic intensity modulations. A Fourier analysis of the intensity modulations of each detector pixel is used to simultaneously extract co-registered AC, DPC and DFC.

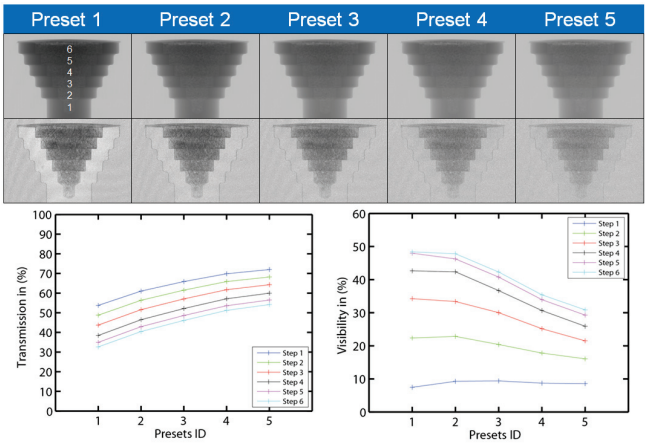

Fig. 2. Top images showing AC and DFC projection images (preset 1-5) of a test phantom, diagrams are showing transmission and visibility values plotted against system presets for the individual steps (step 1: smallest step)

III. EXPERIMENTAL RESULTS

A. Test phantom inverse step cylinder

The thin-walled inverse step cylinder made of POM, filled with sugar crystals, has been used for optimizing the visibility contrast in dark-field imaging. The purpose of this phantom is to vary the energy presets (preset 1 with lowest energy setting, preset 5 with highest energy setting), to match the design energy of the system and to find maximum visibility contrast for varying penetration lengths. It is also of importance to correlate these values to the minimum transmission values, which is necessary for achieving sufficiently high penetration of the material.

Fig. 2 shows projection images of AC and DFC with varying presets as well as diagrams with transmission T and visibility values V. The values for visibility contrast in the case of dark-field images and for the minimum transmission in the case of the absorption images have been calculated for particular region of interests (ROI) in air and within the central part of the individual steps by the following equations:

$$V = \left(1 - \frac{I_{\mathrm{DFC,\,mean,\,ROI}}}{I_{\mathrm{DFC,0,\,ROI}}}\right) \times 100$$

$$T = \left(\frac{I_{\mathrm{AC,mean,ROI}}}{I_{\mathrm{AC,0,ROI}}}\right) \times 100$$

With increasing effective photon energy the material in the AC projection images becomes more transparent, which can

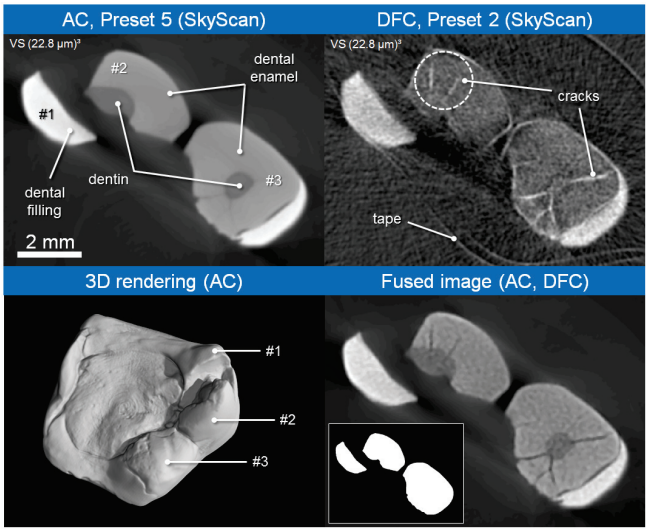

Fig. 3. Top images showing axial AC (SkyScan, preset 5) and DFC (preset 2) XCT slices, bottom images showing a fused image (insert shows binary mask) as well as a 3D rendering (AC, top view of the occlusal surface)

also be seen by an increase in minimum transmission values. In the case of the dark-field signal there is an opposite trend visible for the individual steps by showing a decrease in visibility contrast for higher energy presets, since an increasing transparency of the grating bars (with increasing energy) lowers grating efficiency and visibility contrast. In addition, using higher energy presets the disparity between design energy of the system and the applied spectra is increasing. This is due to the fact that the Talbot distance is directly related to the effective wavelength of the X-rays. The design energy is a setup dependent value characterizing the energy at which maximum visibility is achieved. Furthermore, the average energy behind the object is higher due to beam hardening, leading to an additional disparity and may also shifting the position of maximum visibility.

The results of the individual steps (step1 smallest diameter, step 6 largest diameter) in **Fig. 2** indicate different optimal values for visibility and transmission values for the individual penetration lengths. Depending on the measurement task, most probably more than one set of scanning parameters will lead to optimal data quality.

B. Molar tooth sample

Fig. 3 shows axial slice images through the cusps of the occlusal surface of an adult molar tooth. The molar tooth has been scanned with two different energy presets. Preset 5 (50 kV, 0.045 mm Cu) leads to less pronounced beam hardening artefacts in the case of AC, since additional pre-filtering cuts off low energy photons, whereas preset 2 (35 kV, 0.25 mm Al) yields a slightly stronger dark-field signal respectively higher visibility with less image noise, since this particular energy preset fits better to the design energy and grating efficiency of the Talbot-Lau µXCT system.

Both modalities AC and DFC reveal cracks near the occlusal surface in the dental enamel phase potentially induced by the various treatments (root, dental fillings). Larger cracks are visible both in AC and DFC with significant contrast advantages in the case of DFC, since smaller cracks can only be resolved in the DFC images (indicated by the dashed circle).

A simple image fusion approach has been used to combine suitable information from both image modalities. Therefore, a combination of high-pass filtered AC and DFC images is added to the AC in order to gain a contrast enhancement in AC intensity images:

$$I_{\text{fused}} = I_{\text{AC}} - \text{mask}_{\text{AC}} * I_{\text{DFC, high}} + \text{mask}_{\text{AC}} * I_{\text{AC, high}}$$

The low-pass filtered images are computed by a 2D convolution with a Gaussian function. To obtain the high frequencies of an image, a low-pass filtered version of this image is subtracted. The convolution for the high-pass filtering was realized as a multiplication in frequency domain.

For the fused image, an image mask was generated from AC to mask all regions of the DFC image that are air, leaving only the tooth regions #1, #2 and #3 visible. Summing up all intensities of the AC image and the masked, high-pass filtered AC and DFC (inverted) images, leads to the fusion result shown in the lower right image in **Fig. 3**.

In this fusion method, the physical representation of filling, dental enamel and dentin phases regarding their grey values is preserved and internal structures such as cracks or air gaps are emphasized. Due to the use of a binary mask, no image noise is added in areas of air.

C. Premolar tooth sample

Fig. 4 shows a premolar tooth, which has been scanned with the Talbot-Lau µXCT setup with a dual energy approach (preset 2 and 5). In addition, high-resolution µXCT scans have been used as a reference. The measurement goal for this µXCT task includes the quality assessment of the artificial dental filling. The dental filling has been prepared using the following steps: the creation of the cavity (extracorporeal), conditioning of dental enamel and dentin surfaces by phosphoric acid, followed by the introduction of a layer of wetting material (marked #a in **Fig. 4**). This layer contains pores and higher-dense particles nearly as large as the whole wetting layer. One such particle is the source of a crack within the dentin phase (region indicated by dotted circle in **Fig. 4**). This crack has not been introduced during the preparation of the dental filling, since only two out of three scanning modalities (concerning absorption contrast) are showing the crack in the corresponding slice images. The sample has been first scanned with the RayScan device and there is no crack visible in the AC data. The crack has formed most probably due to the process of sample handling or drying in between the individual scans.

The next step of the dental filling includes a layer wise introduction of a hybrid composite (marked with #b in **Fig. 4**) on top of the wetting layer with several curing steps in between. In this hybrid composite phase, there are different material inhomogeneities like pores, shrinkage holes and cracks clearly visible. One large shrinkage hole is located at the interface between the wetting layer and the hybrid composite layer, from which a small crack is originating. There are some further interface errors visible, which could

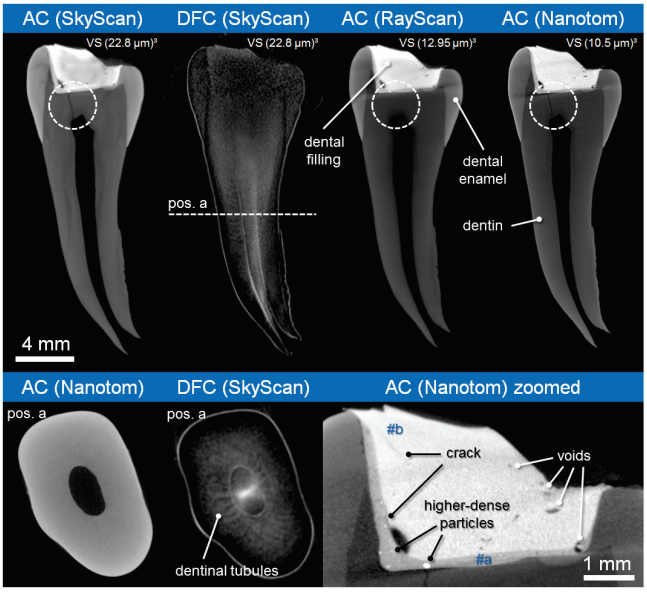

Fig. 4. Top images showing sagittal XCT slices concerning AC (SkyScan, preset 5), DFC (SkyScan, preset 2), AC (RayScan) and AC (Nanotom), bottom images showing a zoomed AC image (Nanotom) of the dental filling as well as axial XCT slices (position a in sagittal view) of root area of AC (Nanotom) and DFC (SkyScan)

reduce the integrity of the dental filling. For the premolar tooth, DFC is not capable of resolving any small crack-like structures or small pores within the dental filling, since the density and penetration lengths hinder contrast formation of defects in the region of the dental filling.

An axial DFC image of the root area of the premolar tooth (bottom image of **Fig. 4**), acquired with a voxel size of (22.8 µm)³, shows morphological information in the sub-voxel region. This dark-field signal is most probably related to dentinal tubules, which are hollow tubes running through the dentin. In the DFC images, there is a preferential direction of these dentinal tubules indicated, since the dark-field signal is direction dependent. In addition, there is also a bright dark-field signal located within the root channel. This bright signal is most probably related to remaining tissue (blood vessels, nerves). AC data (Nanotom), acquired with a voxel size of (10.5 µm)³, is not capable of resolving the dentinal tubules, since these structures are only a few microns in diameter [11]. An additional destructive sample preparation step by reducing the tooth volume near the root area may be required in order to achieve a higher resolution and thus be capable of resolving these dentinal tubules also with AC.

IV. Conclusion

In general, high-resolution µXCT laboratory devices are powerful tools for characterizing biological and medical samples, thus supporting diagnostics in clinical routine. With the introduction of Talbot-Lau µXCT systems new imaging modalities such as dark-field imaging have been introduced to medical applications allowing to resolve e.g. crack-like structures within dental enamel and dentinal tubules within the dentin phase. In addition, DFC is also capable of resolving structures in the sub-voxel region, which can be even smaller than the spatial resolution of comparable high-resolution, absorption-based µXCT systems.

A dual energy approach with the subsequent image fusion of AC with high-pass filtered AC and DFC images allows the characterization of inner structures and defects close to the occlusal surface by emphasizing e.g. cracks due to a strong dark-field signal, while the physical representation of dental filling, dental enamel, and dentin phase regarding their grey values is preserved.

Nevertheless, there are a few drawbacks concerning Talbot-Lau µXCT for materials characterization, since conventional absorption-based µXCT systems usually offer a much faster data acquisition by a factor of 5-10, much higher penetration capabilities and at a certain resolution, AC is also capable of resolving small structures in the range of microns.

Acknowledgment

The authors want to thank Mr. Sasov from Bruker SkyScan for his continuous support and fruitful discussions.

References

[1] A. Momose, S. Kawamoto, I. Koyama, Y. Hamaishi, K. Takai, Y. Suzuki, Demonstration of X-Ray Talbot Interferometry, Japanese Journal of Applied Physics, Vol. 42, pp. 866-868, 2003

[2] F. Pfeiffer, T. Weitkamp, O. Bunk, C. David, Phase retrieval and differential phase-contrast imaging with low-brilliance X-ray sources, Nature Physics, Vol. 2, pp. 258, 2006

[3] S. Rutishauser, M. Bednarzik, I. Zanette, T. Weitkamp, M. Börner, J. Mohr, C. David, Fabrication of two-dimensional hard X-ray diffraction gratings, Microelectronic Engineering, Vol. 101, pp. 12-16, 2013

[4] F. Scholkmann, V. Revol, R. Kaufmann, H. Baronowski, C. Kottler, A new method for fusion, denoising and enhancement of x-ray images retrieved from Talbot–Lau grating interferometry, Physics in Medicine and Biology, Vol 59, page 1425, 2014

[5] N. Bevins, J. Zambelli, K. Li, Z. Qi, G.H. Chen, Multicontrast x-ray computed tomography imaging using Talbot-Lau interferometry without phase stepping, Medical Physics, Vol. 39, No. 424, 2012

[6] C. Gusenbauer, E. Leiss-Holzinger, S. Senck, K. Mathmann, J. Kastner, S. Hunger, W. Birkfellner, Characterization of medical and biological samples with a Talbot-Lau grating interferometer µXCT in comparison to reference methods, Case Studies in Nondestructive Testing and Evaluation, 2016, doi:10.1016/j.csndt.2016.02.001

[7] M. Bech, A. Tapfer, A. Velroyen, A. Yaroshenko, B. Pauwels, J. Hostens, P. Bruyndonckx, A. Sasov, F. Pfeiffer, In-vivo dark-field and phase-contrast x-ray imaging, Scientific Reports, Vol. 3, 2013

[8] M. Stampanoni, Z. Wang, T. Thüring, C. David, E. Rössl, U. van Stevendaal, T. Köhler, M. Trippel, G. Singer, R.A. Kubik-Huch, M.K. Hohl, N. Hauser, Toward clinical differential phase contrast mammography: preliminary evaluations and image processing schemes, 7th Mecial Applications of Synchrotron Radiation Workshop, Shanghai, 2012

[9] A. Momose, W. Yashiro, K. Kido, J. Kiyohara, C. Makifuchi, T. Ito, S. Nagatsuka, C. Honda, D. Noda, T. Hattori, T. Endo, M. Nagashima, J. Tanaka, X-ray phase imaging: from synchrotron to hospital, Philosophical Transactions Royal Society A, 372, 20130023, 2014

[10] S. Senck, C. Gusenbauer, B. Plank, D. Salaberger, J. Kastner, Three-dimensional characterization of polymeric materials using a Talbot-Lau grating interferometer CT, Microscopy and Analysis, Issue 22, pp. 10-12, January/February 2016

[11] R. Schilke, J. A. Lisson, O. Bauß, W. Geurtsena, Comparison of the number and diameter of dentinal tubules in human and bovine dentine by scanning electron microscopic investigation, Archives of Oral Biology, Vol. 45, pp. 355-361, 2000

The Grating-Based Dark-Field Image: Degradation of Quantitative Contrast by System-Specific Sampling Artifacts

Thomas Koenig[1,*], Marcus Zuber[1], Barbara Trimborn[1], Tomas Farago[1], Pascal Meyer[2], Danays Kunka[2], Frederic Albrecht[3], Sascha Kreuer[3], Thomas Volk[3], Michael Fiederle[4] and Tilo Baumbach[1]

[1]Institute for Photon Science and Synchrotron Radiation, Karlsruhe Institute of Technology
76344 Eggenstein-Leopoldshafen, Germany

[2]Institute of Microstructure Technology, Karlsruhe Institute of Technology
76344 Eggenstein-Leopoldshafen, Germany

[3]Department of Anaesthesiology, Intensive Care and Pain Therapy
Saarland University Medical Center & Saarland University Faculty of Medicine,
66421 Homburg (Saar), Germany

[4]Freiburg Materials Research Center, University of Freiburg
Stefan-Meier-Strasse 21, 79104 Freiburg im Breisgau, Germany

[*]thomas.koenig@kit.edu

***Abstract*—The x-ray dark-field contrast accessible via grating interferometry is sensitive to features at length scales well below what is resolvable by a detector system. It is commonly explained as arising from small-angle x-ray scattering (SAXS), and can be implemented both at synchrotron beamlines and with low-brilliance sources such as x-ray tubes. Here, we demonstrate that for tube based setups the underlying process of image formation can be fundamentally different. For detector pixels that comprise multiple grating periods, we show that dark-field images contain a strong artificial and system-specific component not arising from SAXS. Based on experiments carried out with a nanofocus x-ray tube and the example of an excised rat lung, we demonstrate that the dark-field contrast observed for porous media transforms into a differential phase contrast for large geometric magnifications. Using a photon counting detector with an adjustable point spread function, we confirm that a dark-field image can indeed be formed by an intra-pixel differential phase contrast that cannot be resolved as such due to a dephasing between the periodicities of the absorption grating and the Talbot carpet. These findings must not be ignored when measurements are intended to be reproducible across systems.**

I. Introduction

X-ray grating interferometry is a technology that has been under intense investigation [3]. In addition to the well-known absorption images, it also provides the so-called differential phase and dark-field contrasts. While a differential phase image quantifies a specimen's refractive properties, the dark-field image has been introduced as being related to small-angle x-ray scattering (SAXS) [7]. The relation between SAXS and the dark-field contrast has been demonstrated convincingly since, insofar as the properties of a sample engineered to provoke SAXS can be extracted from its dark-field image obtained using synchrotron radiation [8]. A proof of the reverse conclusion, stating that dark-field images are always formed by SAXS, has so far not been brought forward. Quite the contrary, a recent study successfully established a link between sharp edges and the generation of a dark-field signal [12] even if Fresnel propagation can be neglected. Furthermore, local wavefront curvature has been established to generate a dark-field contrast on theoretical grounds [10]. Earlier, also beam hardening [4] and second-order differential phase contrast [11] were identified as sources to the dark-field signal. Hence, there is more to it than conventional SAXS.

II. The Sampling Process

We believe the spatial sampling by the detector is not just one among many influence factors that determine the value of the dark-field contrast, but a major source to it when low-brilliance setups are used. To illustrate our argument, we now shortly revisit the working principle of a grating interferometer. The vast majority of grating interferometric experiments employ a phase grating (G_1) that imprints a periodic phase shift onto an x-ray beam. At certain fractional Talbot distances, this phase shift is turned into an intensity variation, which, in principle, is resolvable by a detector. However, the small periods of the gratings employed make it very challenging to resolve this so-called Talbot carpet. Therefore, an absorption grating (G_2) is usually mounted downstream of the phase grating at such a fractional Talbot distance, matching its period. By scanning either of the gratings, a process called phase stepping, the detector pixels are able to record periodic intensity oscillations even if they cover many grating periods.

Schematically, such a phase stepping process is illustrated in figure 1a, showing an unperturbed Talbot carpet, e. g. obtainable without any object present. For a particular phase stepping position, the Talbot carpet is sampled at a specific

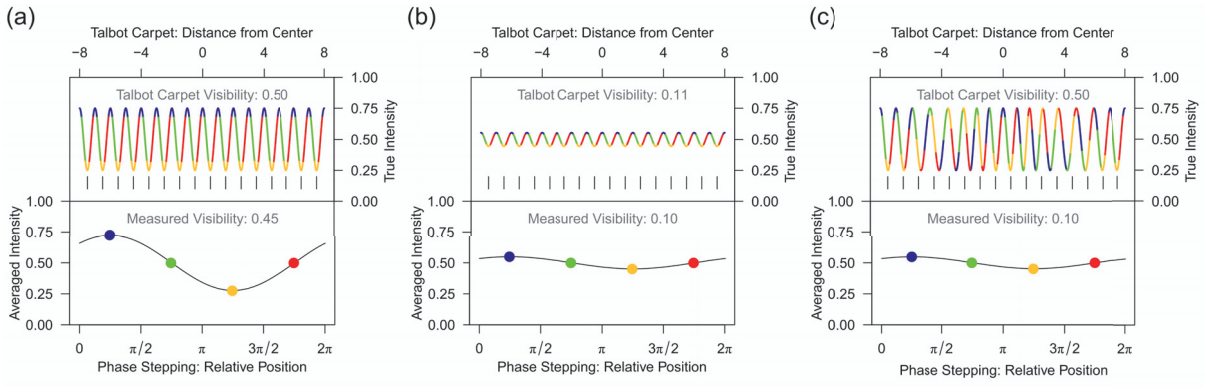

Fig. 1. Schematic illustration of a phase stepping scan for one pixel. Top of each figure: Sinusoidal Talbot carpets (the exact shape does not matter for our argument). The colors refer to the intervals that are seen by the openings of the absorption grating at a particular phase stepping position. The vertical dashes are to guide the eye. Bottom: Phase stepping signals recorded by the corresponding pixel. The colors represent the intensities averaged over the respective regions of the phase stepping scan. The black lines illustrate the periodic function as extracted by a Fourier analysis. (a) No object present; (b) canonical interpretation of the dark-field contrast, as arising from small-angle scattering; (c) pseudo-dark-field contrast caused by a pure phase object.

interval, indicated by the different colors. As the period of the absorption grating is matched to that of the Talbot carpet, the sampling intervals are in phase. The corresponding pixel, which spans many periods of the Talbot carpet, consequently averages over all these intervals, giving rise to a particular sampling point of the phase stepping curve. The grating is then moved to the next position, and so forth. After inserting an object into the beam, the change of the acquired intensity oscillation is used to extract transmission, differential phase and dark-field contrasts, the latter of which is sometimes referred to as normalized visibility.

III. Dark-Field vs. Pseudo-Dark-Field

In figure 1b, we show the example of an idealized ”pure” dark-field object, i.e. with neither absorption nor any phase shifts present. This represents the canonical interpretation of the dark-field signal, and corresponds to a case where SAXS leads to a general reduction in coherence and thus visibility. In other words, the reduction of the measured visibility can be directly linked to the visibility of the Talbot carpet. The measured value deviates from the true one only due to the finite widths of the absorption grating’s apertures.

In stark contrast to this classical case, figure 1c shows a pure phase object without any attenuation of the Talbot carpet’s intensity fluctuations. Yet, refraction by the sample has led to a continuously varying differential phase shift, observable when comparing the positions of the carpet’s minima with the reference markings. If the detector’s pixels used to record the phase stepping curve were just as small as the intervals between these markings, this differential phase shift would be almost perfectly observable. However, if the pixel comprises many carpet periods – 16 in this case – the sampling by means of the absorption grating is no longer in phase with the disturbed periodicity of the Talbot carpet. The resulting *measured* visibility is then equal to the classical dark-field case shown in figure 1b, but the underlying causes are fundamentally different. The case shown in figure 1c is visibility contrast by definition, but it is not a dark-field contrast. We will refer to it as *pseudo-dark-field* since, *after phase-stepping*, it mimics a signal caused by SAXS.

IV. Pseudo-Dark-Field vs. Effective Pixel Size

While it is easy to exchange detectors to vary the pixel size, this usually implies using very different systems. These may come with different scintillators, implying varying absorption efficiencies, photon penetration depths and point spread functions, which introduces systematic errors. A viable option would be to use high resolution synchrotron cameras and then to progressively bin adjacent pixels to form larger areas prior to performing the Fourier analysis. This, however, comes along with a reduction in spatial resolution.

We therefore chose a different approach based on using a spectroscopic, direct-conversion detector. Such detectors mostly feature at least one adjustable energy threshold that is usually employed to obtain spectroscopic resolution [1]. Additionally, a less known property of applying energy thresholds is a change of the detectors effective pixel size. In summary, effects such as charge sharing and characteristic x-rays make a detector pixel become insensitive at its edges and corners, and the effect becomes more and more pronounced the higher an energy threshold is chosen. As a consequence, the sensitive pixel *area* shrinks while the pixel *pitch* remains the same. This manifests as an improvement in the detector’s apparent presampling modulation transfer function $\mathrm{MTF}_{\mathrm{pre}}$ [9, 13]. Modern implementations employing inter-pixel communication are able to eliminate this effect to a large degree [5, 6]. Hence, by using such a detector, it should be possible to measure different dark-field signals when altering the energy threshold and turning inter-pixel communication on and off, provided that our hypothesis is indeed correct.

Changing the energy threshold of course also changes the part of the energy spectrum recorded, and a change of the dark-field signal may then be due to a spectral dependence rather than a varying pixel size. In order to clearly rule this

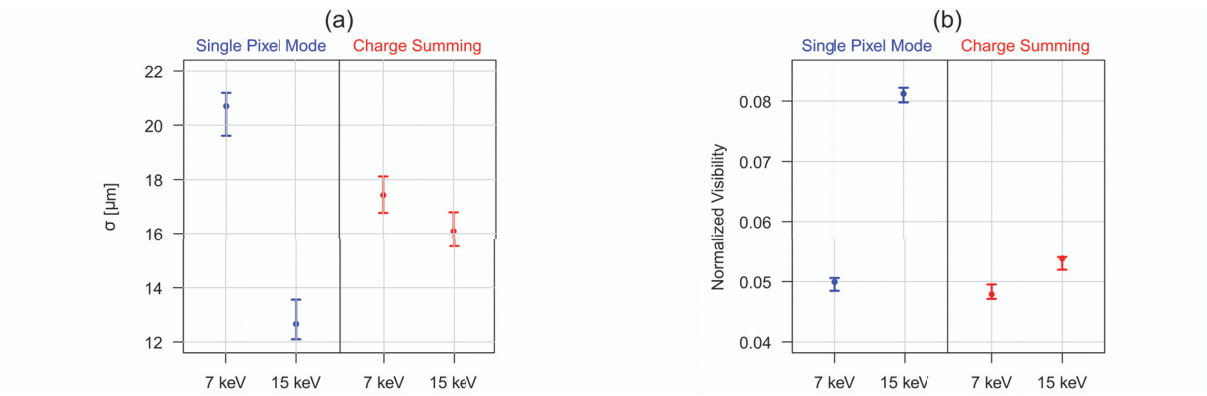

Fig. 2. a) Widths of the apparent point spread functions in terms of the standard deviation σ determined for our spectroscopic x-ray detector. b) Values obtained for the dark-field contrast in a region of interest containing alveolar tissue. Error bars denote 95% confidence intervals.

out, we chose to carry out this experiment at the TopoTomo beamline of the ANKA synchrotron. There, we made use of a monochromatic photon energy of 18 keV and employed a Medipix3RX spectroscopic detector with a 500 μm thick GaAs sensor [5]. It implements inter-pixel communication in its so-called charge summing mode (CSM), which can be turned off to operate the chip in single pixel mode (SPM). Thus, operating this detector in SPM allowed us to vary the effective pixel size by changing the energy threshold, for which we selected 7 and 15 keV. If the two values produce a significantly different dark-field contrast, then there is a strong indication that its value is determined by the pixel size. Repeating this measurement in CSM, where the effective pixel size is almost constant with the energy threshold, allows a cross-check and to rule out possible other systematic errors such as a residual polychromatic component in the intended monochromatic beam. This mode of operation should therefore show only a weak dependence of the dark-field contrast on the energy threshold.

For the following experiments, we used the excised lung of a Sprague Dawley rat. The detector's spatial resolution was determined as described earlier [5]. In figure 2a, we first show the standard deviation σ of the apparent point spread functions that we modelled as Gaussians and that correspond to the four operating points of our detector. In this context, lower values of σ correspond to a smaller effective pixel size. It can be seen very clearly that in SPM we a have strong dependence on the energy threshold, while in CSM we find only a very weak one. Figure 2b quantifies the dark-field contrast as a function of the energy threshold, obtained in a region of interest corresponding to lung tissue. This region generally causes a very pronounced dark-field contrast. If the chip is operated in CSM, i.e. with a less variable effective pixel size, the dark-field contrast remains almost constant. However, turning off this feature shows a substantial reduction of the dark-field contrast, i. e. higher normalized visibilities. Since the photon beam was monochromatic, changing the energy threshold could only alter the effective pixel size. This gives a direct proof of our hypothesis and demonstrates that we are dealing with a pseudo-dark-field contrast that is due to a sampling artifact as illustrated in figure 1c.

V. Pseudo-Dark-Field vs. Geometric Magnification

If indeed the dark-field contrast represents a highly granular intra-pixel differential phase contrast, then we should not be able to acquire a dark-field image at a large geometric magnification. Instead, the corresponding signal should vanish, and only the transmission and differential phase contrasts should remain.

We therefore turn to quantitatively studying this contrast mechanism using an XWT-225 nanofocus x-ray tube (X-RAY WorX, Garbsen, Germany). Figure 3a depicts a patch of a dark-field image aquired at a moderate geometric magnification of 1.9. A pronounced dark-field signal can be found in the lung region, marked by the ellipse. To its right, the heart produces almost no dark-field signal, with the exception of a spot indicated by the arrow. Figure 3b shows the same image region, recorded at a larger geometric magnification of 6.6. Indeed, the dark-field contrast has almost vanished in this geometry.

Figure 3c then illustrates the differential phase contrast at this large magnification. The use of the nanofocus source enables visualizing very fine structures which are particularly found in the lung tissue, again marked by the red circle corresponding to the lung alveoli observed before. The heart shows up as a rather homogeneous region. Comparing this observation with figure 3a, we find a notable correlation between the strong dark-field signal obtained at a low magnification, and the finely structured texture in the differential phase image pertaining to the large geometric magnification. Once again, this confirms that the dark-field contrast is formed by an intra-pixel differential phase contrast under these conditions.

VI. Conclusion

We have presented compelling experimental evidence that, under the conditions we studied, the so-called dark-field contrast does not originate from a SAXS process and does

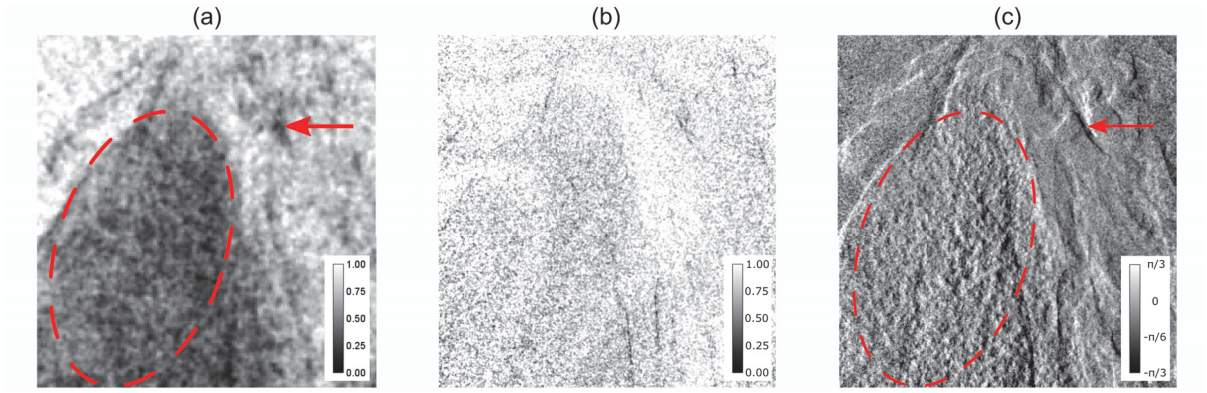

Fig. 3. a & b) Dark-field (i.e. normalized visibility) images shown for two geometric magnifications (M); c) differential phase contrast obtained for the large magnification. The dark-field contrast obtained at low magnification (a) is revealed as a differential phase contrast here.

not show a "dark field" in the sense the term was originally introduced in the field of optical microscopy. Instead, it contains a strong system specific component that is due to sampling conditions and therefore an artifact. If interpreted correctly, the images arising from this might be very useful. However, they are not transferable across systems.

In the past, the normalized visibility, and hence the dark-field contrast were considered a line integral over an object-specific function termed the *linear diffusion coefficient* [2]. Our results clearly show that this is unjustified. The dark-field contrast obtained with typical low-brilliance setups is not quantitative, and neither are tomographic reconstructions.

Medical diagnostics and decision making essentially come down to a classification task, and here very often the precise numerical value of a contrast is of importance. Since the value of this pseudo-dark-field contrast can be changed arbitrarily and substantially by varying the pixel pitch, the focal spot size and the object position, we believe it features only a reduced diagnostic value. Particularly, it opens many possibilities for getting fooled into wrong conclusions by systematic errors.

References

[1] Ballabriga, R., Alozy, J., Campbell, M., Frojdh, E., Heijne, E. H. M., Koenig, T., Llopart, X., Marchal, J., D. Pennicard, Poikela, T., Tlustos, L., Valerio, P., Wong, W. and Zuber, M. [2016]. Review of hybrid pixel detector readout ASICs for spectroscopic X-ray imaging, *J. Inst.* **11**(01): P01007.

[2] Bech, M., Bunk, O., Donath, T., Feidenhans'l, R., David, C. and Pfeiffer, F. [2010]. Quantitative x-ray dark-field computed tomography, *Phys. Med. Biol.* **55**(18): 5529–5539.

[3] Bravin, A., Coan, P. and Suortti, P. [2013]. X-ray phase-contrast imaging: from pre-clinical applications towards clinics, *Phys. Med. Biol.* **58**(1): R1.

[4] Chabior, M., Donath, T., David, C., Bunk, O., Schuster, M., Schroer, C. and Pfeiffer, F. [2011]. Beam hardening effects in grating-based x-ray phase-contrast imaging, *Med. Phys.* **38**(3): 1189–1195.

[5] Hamann, E., Koenig, T., Zuber, M., Cecilia, A., Tyazhev, A., Tolbanov, O., Procz, S., Fauler, A., Baumbach, T. and Fiederle, M. [2015]. Performance of a medipix3rx spectroscopic pixel detector with a high resistivity gallium arsenide sensor, *IEEE Trans. Med. Imag.* **34**(3): 707–715.

[6] Koenig, T., Zuber, M., Hamann, E., Cecilia, A., Ballabriga, R., Campbell, M., Ruat, M., Tlustos, L., Fauler, A., Fiederle, M. and Baumbach, T. [2014]. How spectroscopic x-ray imaging benefits from inter-pixel communication, *Phys. Med. Biol.* **59**(20): 6195.

[7] Pfeiffer, F., Bech, M., Bunk, O., Kraft, P., Eikenberry, E. F., Brönnimann, C., Grünzweig, C. and David, C. [2008]. Hard-X-ray dark-field imaging using a grating interferometer, *Nat. Mater.* **7**(2): 134–137.

[8] Strobl, M. [2014]. General solution for quantitative dark-field contrast imaging with grating interferometers, *Sci. Rep.* **4**.

[9] Tlustos, L., Ballabriga, R., Campbell, M., Heijne, E., Kincade, K., Llopart, X. and Stejskal, P. [2006]. Imaging properties of the Medipix2 system exploiting single and dual energy thresholds, *IEEE Trans. Nucl. Sci.* **53**(1-2): 367–372.

[10] Wolf, J., Sperl, J. I., Schaff, F., Schüttler, M., Yaroshenko, A., Zanette, I., Herzen, J. and Pfeiffer, F. [2015]. Lens-term- and edge-effect in X-ray grating interferometry, *Biomed. Opt. Express* **6**(12): 4812–4824.

[11] Yang, Y. and Tang, X. [2012]. The second-order differential phase contrast and its retrieval for imaging with x-ray Talbot interferometry, *Med. Phys.* **39**(12): 7237–7253.

[12] Yashiro, W. and Momose, A. [2015]. Effects of unresolvable edges in grating-based X-ray differential phase imaging, *Opt. Express* **23**(7): 9233.

[13] Zuber, M., Koenig, T., Hamann, E., Cecilia, A., Fiederle, M. and Baumbach, T. [2014]. Characterization of a 2x3 Timepix assembly with a 500um thick silicon sensor, *J. Inst.* **9**(05): C05037.

Statistically-efficient estimation of Hotelling observer performance with unknown means

Harald Schöndube and Frédéric Noo

***Abstract*—Applying model observer approaches are quickly becoming a method of choice for determining low-contrast detectability in CT imaging. A promising method that allows for a determination of exact confidence intervals on AUC has recently been published by Wunderlich et al. The proposed framework allows for a substantial reduction of noise realizations in case the difference of class means is known exactly. When employing simulated data, this quantity is easily obtained for linear reconstruction algorithms such as FBP. However, for a nonlinear algorithm the situation is more complicated due to the dependence of the reconstruction result from local noise.**

In this work, we propose a method for obtaining the difference of class means in this context. We also present evaluations of our method by performing tests with a bootstrapping approach and by comparing it against a reference method.

I. Introduction

Applying a model observer approach has become widely accepted as gold standard for objectively evaluating image quality in CT. In a simple realization, the receiver operating characteristic curve (ROC) or more directly the area under the ROC curve (AUC) are estimated as a measure of low-contrast detectability (LCD) in a signal-know-exactly / background-known-exactly (SKE/BKE) context. A popular observer is the channelized Hotelling observer (CHO), often applied in combination with Gabor channels [1]. In a recent work from Wunderlich et al. [2] it has been shown that under some relatively broad conditions, exact confidence intervals on AUC in such a setup can be determined directly, i.e., without having to compute the full ROC curve.

When the task at hand is to compare two image reconstruction algorithms A and B with respect to their LCD performance, the actual aim is to estimate the *difference* of the AUC values from the CHO evaluation of the respective data sets. To this end, it is common to estimate - via the Bonferroni inequality - confidence intervals for this difference, namely for $\Delta AUC = AUC_B - AUC_A$ [3]. If for a given choice of algorithms A and B (and potentially their respective dose values), the lower endpoint of the confidence interval for ΔAUC exceeds a margin for non-inferiority ($\Delta AUC_L > -\delta$, with $\delta > 0$), the two methods can be regarded as showing an equivalent LCD performance. Common parameter choices are using $\delta = 0.05$ and requiring a 95% confidence interval on ΔAUC [3], [4], [5].

However, getting the estimates for confidence intervals on AUC small enough for both algorithms A and B to fulfill these requirements may require a lot of images: as to our experience, the number of independent noise realizations necessary can easily reach an order of several thousands. Even when employing simulated data, creating all this data can be a daunting task. Finding ways for lowering the requirements on the amount of data while keeping the confidence intervals small is therefore an attractive goal. In the framework of Wunderlich et al. as discussed above [2] one approach is to apply to the estimation process the knowledge of the *difference of means* $\Delta\mu$ (i.e., the difference of signal and background, which are presumed to be both known exactly) [6], [7]. In our experience, this approach can lower the amount of required noise realizations by about a factor of five without loss of statistical accuracy.

HS is with Siemens Healthcare GmbH, Siemensstr. 1, 91301 Forchheim, Germany. FN is with University of Utah, Department of Radiology, 729 Arapeen Drive, Salt Lake City, UT 84108.
Contact: harald.schoendube@siemens.com

II. Determination of difference of class means

To apply the framework as suggested in [6] it is necessary to determine $\Delta\mu$ separately for each reconstruction algorithm and potentially dose level. In case of a linear reconstruction algorithm such as FBP this is an easy task when dealing with simulated data: we can just reconstruct images from the noise-free CT data and subtract the resulting images from each other. In case of a non-linear algorithm (such as practically all commercially available iterative reconstruction algorithms), however, the situation is less trivial. Due to the dependence of reconstruction parameters on CT data noise, a simple reconstruction from noise-free data will not yield the correct result. The same holds for averaging several reconstructions from high-dose CT data. We have thus developed and tested another approach to estimate $\Delta\mu$ when working with simulated data, which we present in this work.

With simulated data it is computationally most effective to first generate noise-free CT data and then add noise in a second step. The added noise should account both for the (Poisson-distributed) photon noise as well as for the Gaussian electronics (detector readout) noise. Further details for such procedures can be found, e.g., in [8] and [9]. For our purposes, we can exploit this setup in the following way: Start with the noise-free CT data sets from both signal and background. Then, in the noise insertion procedure, add identical noise realizations to both data sets. Apply the reconstruction algorithm at hand and subtract the reconstructed images from each other, yielding a noiseless estimate of $\Delta\mu$ at the dose level corresponding to the inserted CT noise. However, even though being noise-free, the resulting $\Delta\mu$ will still depend somewhat on the actual noise realization (mostly in terms of the shape of the reconstructed contour of the lesion). Thus, we repeated the process 100 times for each dose level and then averaged the 100 resulting realizations of $\Delta\mu$ to obtain an estimate whose

TABLE I
SIZE AND CONTRAST OF THE LESIONS IN THE CCT189 PHANTOM.

Lesion	size	contrast
Lesion 1	3 mm	14 HU
Lesion 2	5 mm	7 HU
Lesion 3	7 mm	5 HU
Lesion 4	10 mm	3 HU

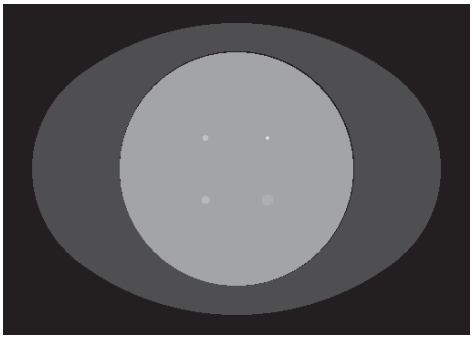

Fig. 1. Noiseless CT image of the CCT 189 phantom with additional annulus as used in our experiments.

dependence on the underlying CT data noise realizations can be neglected. In the following, we will refer to the images used for determining $\Delta\mu$ as training images or training data, whereas the images which are actually used as a base for the AUC evaluation as testing images or testing data

Note that our procedure for obtaining the $\Delta\mu$ estimates assumes the difference in attenuation between the signal and background CT data sets to be negligible in terms of influence on the noise level in the CT signal. However, in typical LCD study situations both the size and contrast of the lesions are small compared to size and attenuation level of the phantom, and thus this assumption can be justified [6].

III. EVALUATION OF OUR APPROACH

To test our approach, we have applied it to simulated CT data of the PhantomLabs CCT189 phantom (also known as the MITA Body phantom). The Phantom consists of a PMMA cylinder of $20\,\mathrm{cm}$ diameter with four cylindrical contrast rods of $40\,\mathrm{mm}$ length each inserted. The contrast rods are placed in parallel and at the same radial distance from the center of the phantom. Each of them has a different diameter and contrast relative to the phantoms body; see table I for an overview of the respective specifications and figure 1 for an image of the phantom. To make the situation somewhat more challenging, we have added an elliptical annulus to the (cylindrical) phantom.

As a first approach we compared the AUC values resulting from our method to a reference which does not require knowledge of $\Delta\mu$. We have chosen the approach of [2] as reference method, as it allows to determine confidence intervals on AUC as well. Due to the lack of a-priori information, the reference method requires a much larger number of repeated experiments to arrive at a similar statistical variability (and hence size of confidence intervals) as it was the case with our approach. For our evaluation, we used 1750 noise realizations for the signal CT datasets and 1750 independent realizations for the background; whereas only 350 noise realizations each were necessary to arrive at the same statistical variability using our proposed approach. Thus, in the end we employed a total of 3900 noise realizations in the former approach, compared with 800 (2×750 testing data sets + 100 training data sets) for our proposed method. We selected various dose (i.e., CT noise) levels and applied an iterative reconstruction (IR) algorithm. As further reference, we also performed the same comparison between using and not using the $\Delta\mu$ for estimating the AUC confidence intervals for a linear FBP algorithm, albeit at a higher dose level.

Figure 2 shows the resulting point estimates and the respective 95% confidence intervals for AUC estimated with each method for all four lesion locations of the CCT189 phantom from images reconstructed with IR and FBP, respectively. Both methods are in good agreement. Furthermore, there is no striking difference between the results for FBP and for IR. This point is significant insofar as it suggests that our approach of estimating $\Delta\mu$ in the non-linear case performs similarly as the established method of reconstructing images from noise-free data in the linear case.

For comparison, figure 3 shows the same evaluation, but this time using for both our proposed and the reference methods *the same number of noise realizations* (namely 350 each for signal and background). The larger span of the confidence intervals as obtained from the reference method with a smaller number of noise realizations is clearly recognizable. One may furthermore notice that there is a difference of the AUC point estimates in this case, which can be readily explained by recognizing that point estimates as obtained from the reference method are positively biased [2] (note, however, that the CIs are exact with both methods).

As a further means to assess the uncertainty induced to our results by variability of the $\Delta\mu$ estimates we performed a bootstrapping analysis of the estimated IR AUC values when varying the input images of the $\Delta\mu$ determination procedure. Our primary goal was to assess the AUC uncertainty caused by variability of the training images relative to the inherent uncertainty caused by statistical variability of the testing data. To this end, we performed a bootstrapping experiment with two nested loops. One loop was generating random sets from the 100 training images; the other one was looping over the 350 noise realizations of the signal and background testing data. To be able to easily separate the influence of training and testing bootstrapping our goal was to generate both AUC estimates varying with testing for a given (fixed) training bootstrap set as well as estimates varying with training for a given testing bootstrap set. Therefore, in this experiment the bootstrap samples of the two loops were defined independently from each other; i.e., for each run of the outer loop the bootstrap sampling of the inner loop was repeated in an identical manner. We performed this test over 800 runs of the outer loop with 800 runs of the inner loop each. From there we computed the variances over the training sets for the testing set being held fixed and the variances over the testing sets for the training set being held fixed. The result showed a far smaller variability of the resulting AUC in dependence of

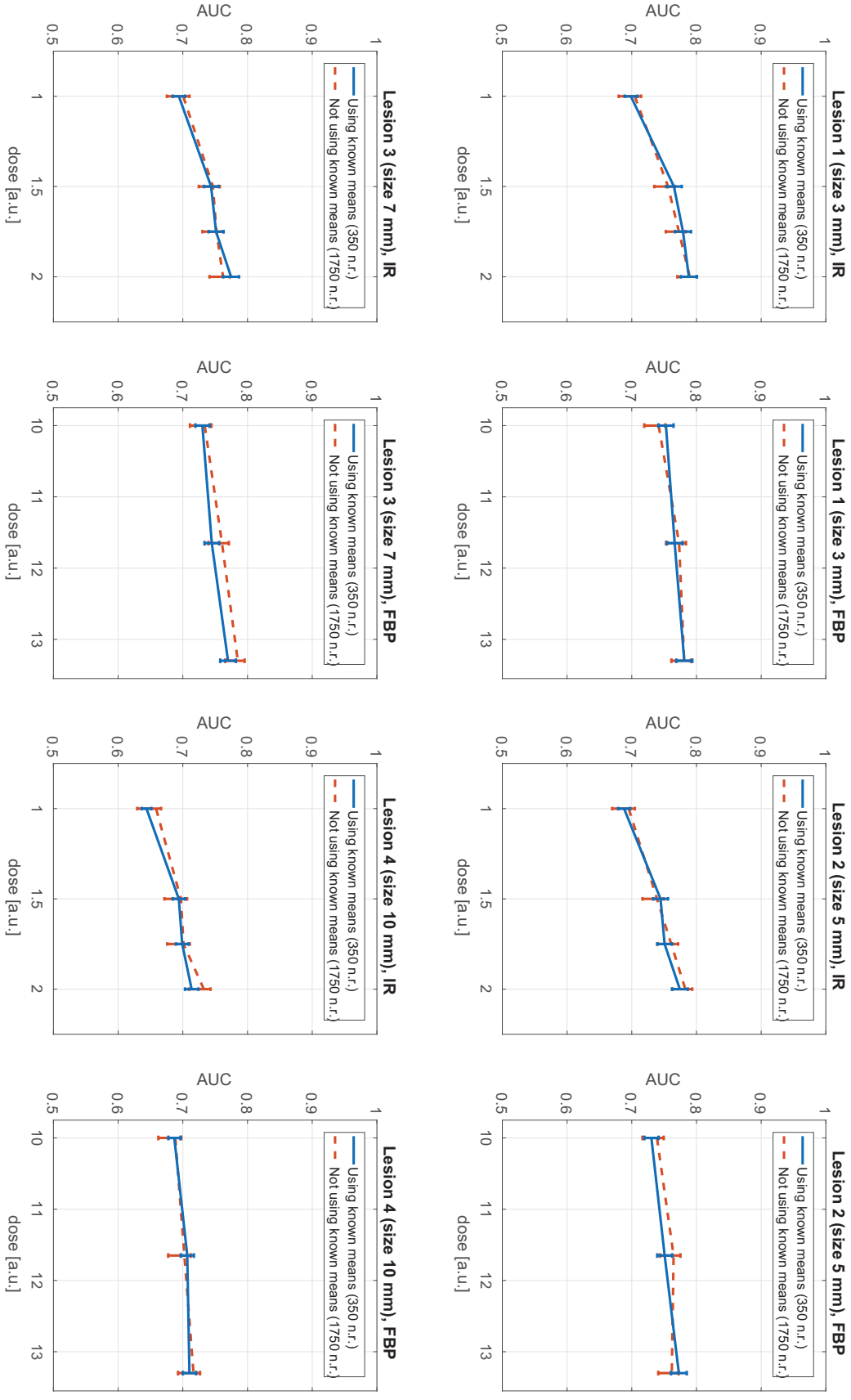

Fig. 2. AUC point estimates and confidence intervals obtained (from 350 x 2 noise realizations) with the method according to [6] using our strategy to estimate $\Delta\mu$ compared to corresponding results (from 1750 x 2 noise realizations) from method [2] (not using knowledge of $\Delta\mu$). (Best appreciated in PDF version, which uses color plots.)

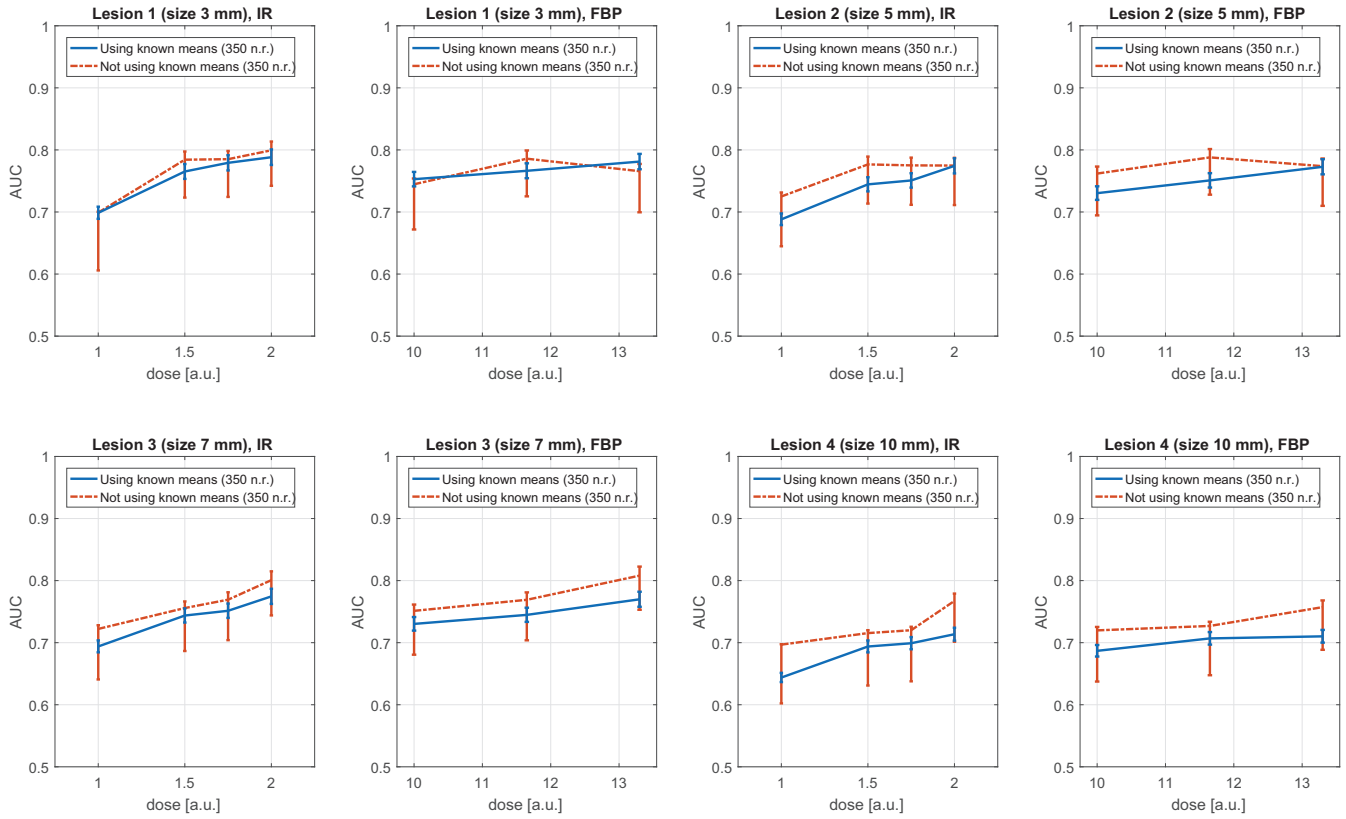

Fig. 3. AUC point estimates and confidence intervals as in figure 2 using the same number of 350 x 2 noise realizations for both methods. (Best appreciated in PDF version, which uses color plots.)

variation in the training images than in dependence of testing set variations. In terms of numbers, the estimated variance over the training sets differed from the one over the testing sets by at least a factor of 30.

IV. Conclusion

As our evaluations show, our proposed method appears to be a viable approach to determine the difference of class means $\Delta\mu$ when using non-linear CT image reconstruction. Used in the context of estimating confidence intervals on AUC as proposed by Wunderlich et al. [2], [6] this knowledge allows for a substantial reduction of the number of repeated experiments while maintaining statistical variability. We have furthermore performed an evaluation of our method against non-parametric estimates on confidence intervals on AUC in a bootstrapping context.

An open question is how our method could be extended to be used on CT data measured on a real system. One possible approach would be to still determine the estimates for $\Delta\mu$ based on simulated data. Due to the properties of the method as proposed in [6] the confidence intervals on AUC could then be estimated using these estimates along with only "background data" (i.e., data of the uniform phantom with no lesions inserted) required to be obtained from the CT system.

References

[1] Harrison H Barrett and Kyle J Myers. *Foundations of image science*. Wiley, 2003.

[2] A. Wunderlich, F. Noo, B.D. Gallas, and M.E. Heilbrun. Exact confidence intervals for channelized hotelling observer performance in image quality studies. *Medical Imaging, IEEE Transactions on*, 34(2):453–464, Feb 2015.

[3] Adam Wunderlich. IQmodelo: Statistical software for task-based image quality assessment with model observers. http://didsr.github.io/IQmodelo/.

[4] Ajit H. Goenka, Brian R. Herts, Nancy A. Obuchowski, Andrew N. Primak, Frank Dong, Wadih Karim, and Mark E. Baker. Effect of reduced radiation exposure and iterative reconstruction on detection of low-contrast low-attenuation lesions in an anthropomorphic liver phantom: An 18-reader study. *Radiology*, 272(1):154–163, 2014. PMID: 24620913.

[5] Jingyan Xu, Matthew K Fuld, George S K Fung, and Benjamin M W Tsui. Task-based image quality evaluation of iterative reconstruction methods for low dose ct using computer simulations. *Physics in Medicine and Biology*, 60(7):2881, 2015.

[6] A. Wunderlich and F. Noo. New theoretical results on channelized hotelling observer performance estimation with known difference of class means. *Nuclear Science, IEEE Transactions on*, 60(1):182–193, Feb 2013.

[7] Adam Wunderlich and Frédéric Noo. Estimation of channelized hotelling observer performance with known class means or known difference of class means. *Medical Imaging, IEEE Transactions on*, 28(8):1198–1207, 2009.

[8] Stanislav Žabić, Qiu Wang, Thomas Morton, and Kevin M Brown. A low dose simulation tool for CT systems with energy integrating detectors. *Medical physics*, 40(3):031102, 2013.

[9] Lifeng Yu, Maria Shiung, Dayna Jondal, and Cynthia H McCollough. Development and validation of a practical lower-dose-simulation tool for optimizing computed tomography scan protocols. *Journal of computer assisted tomography*, 36(4):477–487, 2012.

Scatter Correction for C-Arm CT Using Primary Modulation

Bastian Bier, Kerstin Müller, Martin Berger, Jang-Hwan Choi, Ludwig Ritschl, Marc Kachelrieß, Rebecca Fahrig and Andreas Maier

***Abstract*—Cone-beam computed tomography (CBCT) suffers from a large amount of scatter, resulting in severe scatter artifacts in the reconstructions. Recently, a novel scatter correction approach was introduced using a primary modulator, which is inserted between the X-ray source and the object. The method showed promising results, but was tested on a table-top X-ray system only. In our work, this method is transferred to a clinical C-arm CBCT. Extensions are added to compensate for scanner motion and tube current modulation. We show that scatter correction using primary modulation is possible on a clinical CBCT: scatter artifacts in the reconstructions were able to be removed with the newly extended method. Compared to a slit scan, our approach showed superior results with an improvement of the contrast-to-noise ratio.**

***Index Terms*—C-Arm CBCT, Primary Modulator, Reconstruction, Scatter Correction.**

I. Introduction

SCATTERED radiation is a major problem in CBCT, resulting from the large irradiated volume and the large area covered by the detector of such systems. The amount of scatter measured on the detector often exceeds the measured primary radiation, causing a high scatter-to-primary ratio (SPR) [1]. This has a severe impact on the reconstructions' image quality, where the scatter induces cupping and shadow artifacts as well as contrast loss [2].

Therefore, scatter correction methods are essential in order to remove these artifacts. Existing methods can be divided into hardware-based scatter rejection methods and software-based scatter correction methods [2]. Approaches among the first category are the antiscatter grid (ASG) [3], air gaps [4] and collimation. They are similar in that the geometry and the hardware of the X-ray system are manipulated to reduce measured scatter. Software-based techniques are either based on measurements [5], statistics or deterministic [6]. Hardware and software-based approaches are often combined in order to achieve a clinically satisfying image quality.

Another scatter correction method uses a primary modulator, which is inserted in between the X-ray source and the object. The modulator consists of semitransparent blocks alternating with transparent ones. This pattern modulates the primary radiation and leaves the scattered radiation untouched,

B. Bier, M. Berger and A. Maier are with the Department of Computer Science, Pattern Recognition Lab, Friedrich-Alexander-University Erlangen-Nuremberg, Germany.

K. Müller, J. Choi, L. Ritschl and R. Fahrig are with the Department of Radiology, Stanford University, Stanford, CA, USA. L. Ritschl and R. Fahrig are now with Siemens Healthcare GmbH, Forchheim, Germany.

M. Kachelrieß is with the Medical Physics in Radiology, German Cancer Research Center (DKFZ), Heidelberg, Germany.

Corresponding author: bastian.bier@fau.de

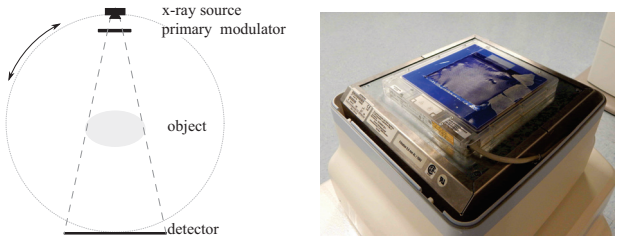

(a) Imaging geometry of the C-arm system with a primary modulator.

(b) Primary modulator mounted on top of the X-ray source.

Fig. 1: Imaging geometry with a primary modulator.

which facilitates scatter estimation either in the frequency domain [7], [8] or the in the spatial domain [9]. The latter method was published recently and is called *improved Primary Modulator Scatter Correction (iPMSE)*. The iPMSE method showed promising results, but was tested on table-top X-ray systems only, where the imaging geometry and the X-ray spectrum is constant for all projections.

In this work, the iPMSE algorithm is extended and transferred to a clinical C-arm CBCT. The imaging geometry of our experimental setup is shown in Figure 1a. The X-ray source and the detector rotate around the object with the modulator mounted on top of the source, as can be seen in Figure 1b. The wobble of the C-arm during rotation as well as the tube current modulation of the system affect the projected modulator pattern. A solution to these problems is proposed by approximating the amplitude and the position of the modulator pattern. In the following, we call this extended algorithm *C-arm iPMSE*.

II. Materials and Methods

A. Theory

1) The iPMSE algorithm: The iPMSE algorithm requires two projection images, as can be seen in Figure 2. The first image is a projection of the primary modulator only, hereafter referred to as reference modulator pattern $\boldsymbol{M}$. The second image is a projection of the object and the primary modulator $\boldsymbol{c}_m$. The algorithm estimates the scatter image $\boldsymbol{c}_s$ with a gradient-based optimization function [9]. From that, the scatter-corrected projection $\boldsymbol{c}_p$ is obtained:

$$\boldsymbol{c}_p = \boldsymbol{M}^{-1} \cdot (\boldsymbol{c}_m - \boldsymbol{c}_s). \tag{1}$$

In $\boldsymbol{M}^{-1}$, each element is the inverse of the value in $\boldsymbol{M}$. Equation 1 shows that $\boldsymbol{M}^{-1}$ must have the same amplitude

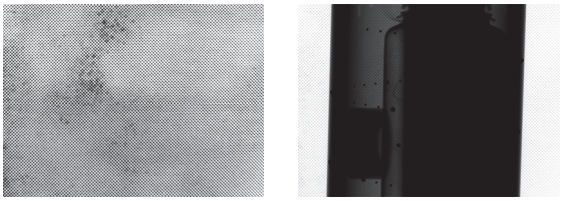

(a) Projection of the modulator $\boldsymbol{M}$.

(b) Projection of the modulator and the object $\boldsymbol{c}_m$.

Fig. 2: Projections required for the iPMSE algorithm.

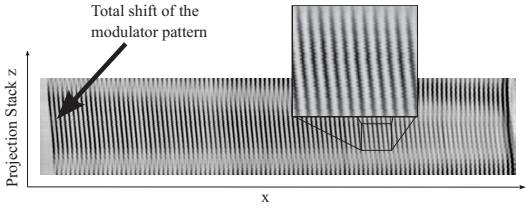

Fig. 3: The reordered projection stack of a modulator acquisition shows two motion effects: a total shift and small deviation in the pattern in adjacent projections.

and position as the modulator pattern in projection $\boldsymbol{c}_m$, otherwise residual modulator patterns persist in the corrected projection image and the scatter estimate may be incorrect.

2) Motion of the Projected Modulator Pattern: In rotations over 200°, the C-arm wobbles and deforms, causing a different position of the projected modulator pattern for each angle. The low-frequent deformation between the X-ray source and the detector is due to the effect of the gravity on the rotating C-arm and results in a total shift of around 15 pixels in the projected modulator pattern. This is indicated by the arrow in the reordered modulator projection stack, shown in Figure 3. The high-frequent wobble of the C-arm causes a sub-pixel shift in the pattern in adjacent projections. This effect is visible in the zoomed-in part in Figure 3, where this motion results in jagged lines.

3) Amplitude Change in the Projected Modulator Pattern: Clinical C-arm systems have a tube current modulation system, which adjusts the exposure parameters (tube voltage, exposure time and tube current) during the acquisition [10]. The changing tube voltage results in a varying modulation amplitude due to the energy-dependent attenuation of the modulator material for different X-ray source intensities as well as in a changing amount of emitted photons, which has to be corrected for.

B. Scatter Correction Workflow: C-arm iPMSE

Figure 4 shows the workflow of the new C-arm iPMSE method. The open-source software framework CONRAD [11] is used for the processing and reconstruction of the projection images. The acquired raw images are preprocessed [12] to obtain the projections in the intensity domain, where the scatter estimation takes place.

1) Establishment of a Modulator Database: The database contains reference projections of the modulator pattern acquired at various tube voltages and angles. Each projection is averaged to reduce noise. This is accomplished by acquiring three, 3D, rotational modulator acquisitions for each tube voltage. For each of the 248 angles, the corresponding projections of the acquisition as well as their direct neighbors are averaged. We acquired projections at 70 kVp, 90 kVp, 110 kVp and 120 kVp for the database. The reference modulator pattern M is then created from these projections.

2) Approximation of the Modulator Amplitude with Linear Interpolation: For each projection c_m, a reference modulator pattern is created, which has the same amplitude as the modulator in the projection c_m itself. This is achieved through a linear interpolation of two modulator patterns in the database, which are acquired at the same angle as projection c_m and at voltages next to projection c_m. This results in an approximation for M with a similar amplitude as the modulator pattern in the projection c_m.

3) Block Matching Registration: The reference modulator pattern M is aligned to the pattern in the projection c_m in a block matching registration step. The algorithm divides the reference projection image into sub blocks of 15 pixels. For each block, a translation, which optimizes the correlation coefficient, is calculated. The sub-pixel accuracy is set to 0.1 pixels and the search radius to 1.5 pixels. All translations are sorted according to their correlation coefficient, and the median translation of the translations corresponding to the highest 10 % is computed. This translation is applied to the reference modulation pattern. The difficulty in the registration is that the modulator pattern is hardly visible in projection c_m. The block matching registration shows robust results, since it uses the information from the entire projection and applies the translation with the best correlation matches. The search radius is restricted to a small area, because the initial estimate for M is already close the correct position, having been created from projections acquired at the same angle.

4) iPMSE: After the amplitude approximation and the registration step, the standard iPMSE algorithm as described in [9] is applied. A part of an iPMSE-corrected projection without and with the proposed extensions is shown in Figure 5a and Figure 5b, respectively. A residual modulator pattern is clearly visible in Figure 5a and is even more apparent in the difference image shown in Figure 5c. This pattern disappears with the new extended method.

C. Postprocessing

The negative logarithm is applied to the scatter-corrected images to obtain projections in the line-integral domain, followed by a noise suppression as suggested by Zhu et al. in [1]. This is essential since noise increases in scatter-corrected projection images [7], [1]. Without a suitable noise suppression, the benefits of the scatter correction can be lost due to the high increase of the noise level. Subsequently, a truncation correction, the standard FDK reconstruction algorithm with the Shepp-Logan kernel, and a ring artifact correction are applied [6].

III. Experiments and Results

All acquisitions were conducted with the Siemens zeego C-arm system (Siemens Healthcare GmbH, Forchheim, Germany). The focal spot size was set to 0.3 mm to reduce the

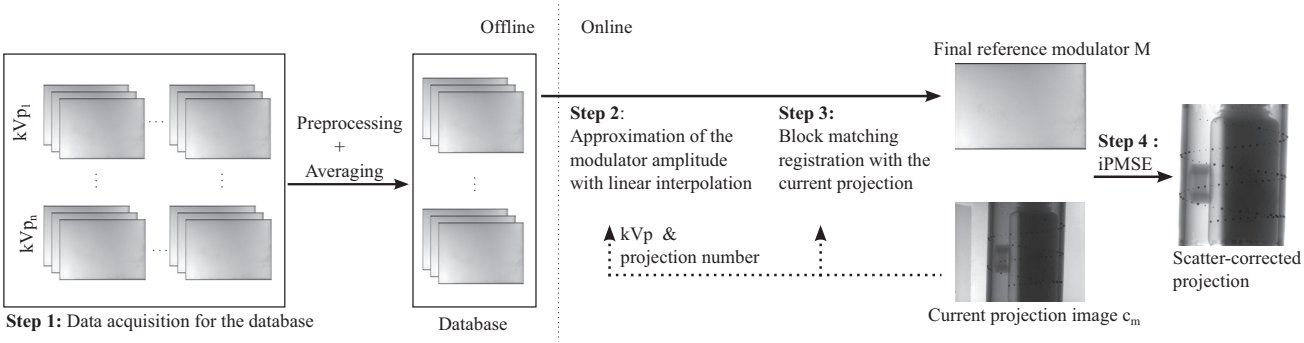

Fig. 4: Workflow of the proposed C-arm iPMSE method. Step1: Establishment of a modulator database. Step 2: Approximation of the modulator amplitude. Step 3: Block matching registration. Step 4: iPMSE algorithm.

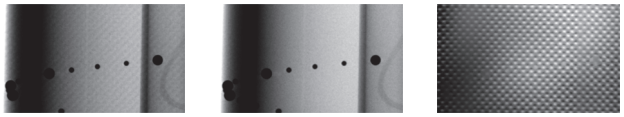

(a) iPMSE-corrected. (b) C-arm iPMSE-corrected. (c) Difference image.

Fig. 5: Parts of iPMSE-corrected projections without and with the added extensions. Residual modulator pattern is removed with the C-arm iPMSE algorithm.

(a) Phantom for Experiment 1. (b) Phantom for Experiment 2.

Fig. 6: Electron density phantom used for the experiments.

penumbra effect. 248 projections with a size of 1240×960 pixels were acquired during one rotation covering 200°. The material of the modulator was erbium, its thickness 0.0252 mm and the block size 0.457 mm (as in [9]). The transmission of the semitransparent blocks at 120 kVp was approximately 80% [13].

Two experiments with different objectives were performed. In both, the Electron Density Phantom (EDP) was scanned (CIRS, Norfolk, VA, USA). The phantom for Experiment 1 is shown in Figure 6a. Two torso shaped objects were placed next to the EDP in order to cause a large amount of scatter and attenuation. The phantom for Experiment 2 is shown in Figure 6a. Only the inner part of the EDP was scanned with an additional water bottle and the plugs from the EDP were placed next to the phantom. Due to its elliptical shape, the tube voltage varied in between 90 and 120 kVp in contrast to the constant tube voltage of 125 kVp in Experiment 1. Further, Experiment 1 was conducted with and without an ASG whereas Experiment 2 was only with ASG.

Figure 7 shows the center slices of the corrected and non-corrected reconstructions of the aforementioned experiments. The first two rows show the results of Experiment 1 with and without the ASG. The last row shows the results of Experiment 2. The first reconstruction in each row is without a scatter correction. All scatter artifacts are present: shadow and cupping artifacts as well as contrast loss. The second column shows reconstructions of a slit scan where the z-collimator aperture, i.e. the field of view (FOV) in z-direction, was minimal in order to reduce the irradiated volume. This has been shown to reduce the amount of scatter and thus should yield better results. Regardless, the scatter artifacts persisted in these reconstructions, although the cupping artifact was slightly suppressed. The last column shows reconstructions using the newly C-arm iPMSE method. Scatter artifacts were successfully removed. A small cupping artifact was visible at the border region of the FOV, which may have also resulted from object truncation. In Figure 8c, line profiles of reconstructions from Experiment 1 and 2 are shown. In the line profiles of the non-corrected and the slit scan reconstruction, the cupping artifact is given by increasing values towards the boundary of the FOV. This artifact disappeared, however, upon using the new method. Further, we computed the contrast-to-noise ratio (CNR) in the reconstructions for nine region-of-interests (ROI) shown in Figure 8a and Figure 8b. Table I shows that the averaged CNR improves in the scatter-corrected reconstructions towards the scatter-distorted and the slit scan reconstructions. In regions with dense material, slight streak artifacts were introduced in the scatter-corrected reconstructions.

TABLE I: Average CNR of the ROIs shown in Figure 8.

	Exp. 1 no ASG	Exp. 1 with ASG	Exp. 2
No Correction	2.39	2.61	2.32
Slit Scan	3.24	2.92	6.51
C-arm iPMSE	**5.98**	**6.01**	**8.62**

IV. Discussion

Incorporating the iPMSE method into a clinical C-arm CT showed promising results. Our new method was able to remove most of the scatter artifacts and could substantially improve the image quality compared to a slit scan. In particular, the disappearance of the cupping and the shadow artifact improved the image quality clearly. Currently, streaking artifacts appear in

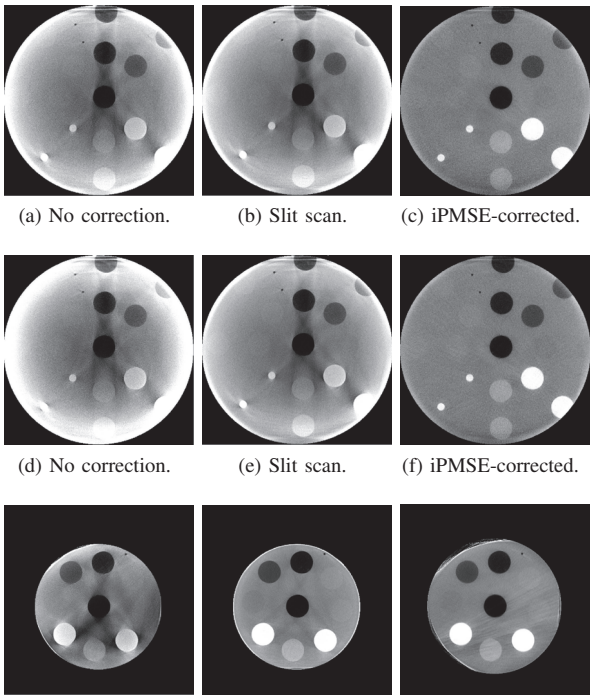

(a) No correction. (b) Slit scan. (c) iPMSE-corrected.

(d) No correction. (e) Slit scan. (f) iPMSE-corrected.

(g) No correction. (h) Slit scan. (i) iPMSE-corrected.

Fig. 7: Reconstruction images. First row: Experiment 1 with ASG. Second Row: Experiment 1 without ASG. Third row: Experiment 2 with ASG. Window level [-1000HU, 1000 HU].

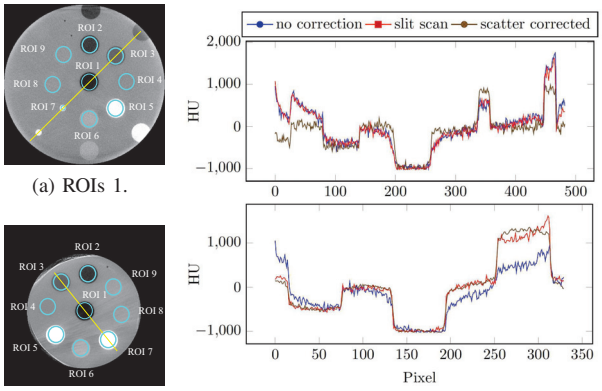

(a) ROIs 1. (b) ROIs 2. (c) Line profiles.

Fig. 8: ROIs and line profiles of the reconstructions. Top: Experiment 1 with ASG. Bottom: Experiment 2 with ASG.

regions of dense material. This is due to the photon starvation effect, which is amplified by the scatter correction when the estimated scatter signal is subtracted from these regions. Further, the combination of the C-arm iPMSE method with the ASG were investigated in Experiment 1, but its use proved to have little effect on the reconstruction results. The slit scan with our clinical scanner proved insufficient as a reference since the narrowest slit of around 20 mm in the isocenter is too wide. Also, overall evaluation is affected by the noise suppression, which is subsequent to the scatter correction. To date, such experiments have been performed with phantom data only. In future studies, we endeavor to acquire real clinical data to further examine the performance of our method, since a lack of a scatter estimate for reference purposes complicated any quantitative evaluation of said method. Further, the occurring streak artifacts have to be investigated in more detail.

V. Conclusion

The present work has proposed a novel scatter correction approach for a clinical C-arm CBCT by extending an existing method using a primary modulator. The challenges behind C-arm motion and tube current modulation were overcome with establishing a modulator database, approximating the amplitudes and a final registration step. We have shown that scatter correction using a primary modulator is possible on a C-arm system, whereby scatter artifacts were able to be removed from the reconstructions.

Acknowledgment

The authors are grateful for the financial support from the NIH Shared Instrument Grant S10 RR026714 supporting the zeego@StanfordLab, the German Research Foundation (DFG), as part of the Research Training Group 1773 “Heterogeneous Image Systems” and DAAD.

References

[1] L. Zhu, J. Wang, and L. Xing, “Noise suppression in scatter correction for cone-beam CT.” *Medical physics*, vol. 36, no. 2009, pp. 741–752, 2009.

[2] E.-P. Rührnschopf and K. Klingenbeck, “A general framework and review of scatter correction methods in x-ray cone-beam computerized tomography. Part 1: Scatter compensation approaches,” *Medical physics*, vol. 38, no. 7, pp. 4296–4311, 2011.

[3] J. H. Siewerdsen, D. J. Moseley, B. Bakhtiar, S. Richard, and D. A. Jaffray, “The influence of antiscatter grids on soft-tissue detectability in cone-beam computed tomography with flat-panel detectors.” *Medical physics*, vol. 31, no. 12, pp. 3506–3520, 2004.

[4] J. A. Sorenson and J. Floch, “Scatter rejection by air gaps: an empirical model,” *Medical Physics*, vol. 12, no. 3, pp. 308–316, 1985.

[5] J. H. Siewerdsen, M. J. Daly, B. Bakhtiar, D. J. Moseley, S. Richard, H. Keller, and D. A. Jaffray, “A simple, direct method for x-ray scatter estimation and correction in digital radiography and cone-beam CT,” *Medical Physics*, vol. 33, no. 1, pp. 187–196, 2006.

[6] M. Zellerhoff, B. Scholz, E.-P. Ruehrnschopf, and T. Brunner, “Low contrast 3D-reconstruction from C-arm data,” *SPIE Medical Imaging*, vol. 5745, pp. 646–655, 2005.

[7] L. Zhu, N. R. Benett, and R. Fahrig, “Scatter correction method for x-ray CT using primary modulation: Theory and preliminary,” *Medical Imaging IEEE*, vol. 37, no. 2, pp. 934–946, 2006.

[8] J. S Maltz, W.-E. Blanz, D. Hristov, and A. Bani-Hashemi, “Cone beam X-ray scatter removal via image frequency modulation and filtering.” *Engineering in Medicine and Biology Society, 2005. IEEE-EMBS 2005*, vol. 2, pp. 1854–1857, 2005.

[9] L. Ritschl, R. Fahrig, M. Knaup, J. Maier, and M. Kachelrieß, “Robust primary modulation-based scatter estimation for cone-beam CT.” *Medical physics*, vol. 42, no. 1, p. 469, 2015.

[10] R. Fahrig, R. Dixon, T. Payne, R. L. Morin, A. Ganguly, and N. Strobel, “Dose and image quality for a cone-beam C-arm CT system.” *Medical physics*, vol. 33, no. 12, pp. 4541–4550, 2006.

[11] A. Maier, H. G. Hofmann, M. Berger, P. Fischer, C. Schwemmer, H. Wu, K. Müller, J. Hornegger, J.-H. Choi, C. Riess, A. Keil, and R. Fahrig, “CONRAD - A software framework for cone-beam imaging in radiology,” *Medical Physics*, vol. 40, no. 11, p. 111914, 2013.

[12] C. Schmidgunst, D. Ritter, and E. Lang, “Calibration model of a dual gain flat panel detector for 2D and 3D x-ray imaging.” *Medical physics*, vol. 34, no. 9, pp. 3649–3664, 2007.

[13] H. Gao, L. Zhu, and R. Fahrig, “Modulator design for x-ray scatter correction using primary modulation: material selection.” *Medical physics*, vol. 37, no. 8, pp. 4029–37, 2010.

Pixel Size Tradeoffs for CdTe Spectral Photon Counting Detectors

Scott S. Hsieh, and Norbert J. Pelc

Abstract—**Energy discriminating photon counting detectors, which measure the energy of individual photons incident on the detector, are promising components for next-generation CT scanners. The most common substrate material in research prototypes today is CdTe or CdZnTe (CZT), popular for its high atomic number and absorption. However, these detectors face tradeoffs. Smaller pixels are desirable to enable fast counting rates and minimize count rate loss. However, smaller pixels also increase the deleterious effects of charge sharing. We explore these tradeoffs and compare different pixel sizes against an ideal photon counting detector that does not suffer from charge sharing.**

Index Terms—**photon counting detectors, spectral CT, count rate loss, CdTe detectors**

I. Introduction

SPECTRAL CT is attractive for its ability to distinguish between materials that appear isointense in single energy CT scans. While the concept of dual energy was described by Hounsfield and investigated shortly after the debut of CT [1], dual energy was neglected for several decades until technical innovations allowed for the simultaneous acquisition at multiple energies. A number of clinical applications have now emerged [2], such as the classification of kidney stones [3].

Current approaches to dual energy involve tradeoffs. Dual source CT can achieve good spectral separation using a tin filter, but suffers from cross-scatter. Rapid kVp switching sources provide more modest spectral separation, although a K-edge filter could mitigate this effect at the expense of flux [4]. Dual layer detectors have limited spectral separation but provide spectral information on all scans and protocols. It should be noted that instead of converging on a single best method for dual energy imaging, the commercial vendors have developed a plethora of approaches, each with their own strengths and weaknesses.

In this context, photon counting detectors (PCDs) have emerged as a technology that could provide all of the benefits of spectral imaging with fewer side effects. Most PCDs use a semiconductor substrate that converts incident x-ray photons into electrons and holes. These charges are collected and packets of charge are processed as individual pulses [5]. In addition, the height of these pulses can be used to infer the energy of the incident photon. PCDs could replace conventional, energy-integrating detectors and have the potential to offer much better noise performance.

However, PCDs suffer from a number of technical limitations. The temporal resolution of PCDs implies a limited count rate. For PCDs that do not provide energy discrimination by pulse height analysis, this leads to count rate loss and a reduction in quantum efficiency [6]. For energy discriminating PCDs, multiple low energy photons arriving in close spatial and temporal proximity could be misinterpreted as a single higher energy photon. Also, the charges from an incident x-ray may be spread over multiple pixels. This phenomenon, known as charge sharing, degrade the accuracy of the pulse height analysis process, causing a single photon to appear as multiple lower energy events. Mechanisms for charge sharing compensation via interpixel communication do exist [7] but these methods are still developing and suffer from reduced effective count rate. For these reasons, current PCDs may not be able to outperform other dual energy technologies at present. [8].

The most common semiconductor substrates for PCDs for CT are CdTe or CdZnTe (CZT). Other substrates such as silicon have also been studied [9], but are not the focus of this work. The introduction of zinc changes the electrical properties of the semiconductor but has a minimal effect on its x-ray properties. In this work, we concentrate primarily on x-ray physics and hence will refer to both as simply “CdTe” detectors. These materials feature a high atomic number and hence attenuation, enabling the fabrication of PCDs of modest thickness. Cd and Te both have a high fluorescence yield. Characteristic photons will commonly be reemitted from the CdTe substrate and may travel hundreds of microns, possibly into to a neighboring pixel, where they contribute to charge sharing or may exit the sensor.

A simple design choice to combat the damaging effects of charge sharing is to increase the pixel size. This reduces the prevalence of charge sharing, as only photons which arrive within a small distance (perhaps 200 μm) of another pixel are susceptible to charge sharing. However, the trend of PCDs has been to make the pixels smaller, not larger. The rationale for smaller pixels is to combat pulse pileup and the associated count rate loss. By reducing the size of each pixel while keeping the count rate of each pixel constant, the effective count rate of the PCD as a whole improves. At very high

This work was supported by Philips Healthcare.

Scott S. Hsieh and Norbert J. Pelc are with the Department of Radiology at Stanford University, Stanford, CA 94305 USA. (e-mail: sshsieh@stanford.edu)

incident count rates, several times larger than the characteristic count rate, the detector may paralyze or produce information that is essentially useless. One school of thought is to regard this as missing information and use data substitution techniques. Another possibility is to control the incident x-ray flux to avoid this outcome [10-12]. Traditionally, the count rate requirements of CT were viewed as being overwhelmingly high, and the use of PCDs in clinical work was seen as being very difficult [13]. However, in recent years new PCDs have emerged with smaller pixels and much faster count rates [14].

Given these tradeoffs, the purpose of this work is to determine an optimal pixel size for a CdTe detector.

II. METHODS

We use two types of Monte Carlo simulations to estimate the performance of PCDs with different pixel sizes. First, we use simulations to calculate the energy response function of the detector substrate. Second, we use another set of simulations to assess the performance of the detector under pileup.

A. Energy response

The energy response of the CdTe detector was calculated using GEANT4 [15] to simulate the transport of x-ray photons of different energy through the semiconductor. The transport of electrical charges within CdTe was performed using a simplified analytic model. We assumed that the charges would be distributed in a sphere of radius 60 microns, and then assumed that any charges in the territory of a pixel would automatically be detected in that pixel. This spherical model is a simplification of more complex electrical processes, such as attraction towards the source or drain due to the bias voltage as well as Coulomb repulsion between charges or random diffusion. The sphere radius is a function of the drift time and other factors [5], and we expect that newer detectors may allow less time for diffusion which would reduce charge sharing effects [16]. We neglected recombination, charge trapping, and other such effects. Besides charge migration from diffusion or repulsion, charges can appear to neighboring pixels because of K-escape. The distance of travel of the characteristic photons in CdTe can be in the hundreds of microns.

We simulated photons at 5 keV steps. For each pixel size and energy, 4000 photons were used to estimate the energy response function of the detector. For each photon, we sampled the energy recorded in the incident pixel, as well as the energy recorded in neighboring pixels. Gaussian noise with standard deviation of 5 keV was added to all data to simulate electronic noise.

As a comparison, we also included cases where the energy response is ideal and no charge sharing is present.

B. Detector simulation

We assumed a 120 kVp spectrum was incident on an object consisting of 1 cm of cortical bone and a variable thickness of water. The brilliance of the spectrum was 700 million photons per second per square millimeter, or approximately 300 mA for a typical source-to-detector distance. Photons propagate through the object, being attenuated according to its interaction probabilities. Photons scattering from the object are eliminated and subsequently ignored. Photons which reach the detector create a pulse whose height depends on the energy deposited in the pixel.

We developed a simple model for the detector response. We assumed the pulse shape is a simple (unipolar) triangle, with a total width of 200 ns (full width at half max of 100 ns). The height of the triangle is directly proportional to the energy deposited within the pixel. Multiple photons arriving in close proximity will trigger triangles that overlap and sum on top of each other. Whenever the signal crosses a predefined threshold, the counter for that bin is incremented.

This detector cannot be characterized as a classic paralyzable detector with a simple dead time. Instead, the detector paralyzes when its signal consistently rises above the highest threshold. However, it is reasonable to consider the duration of the triangle response (200 ns) to be analogous to the dead time, and hence we consider the characteristic count rate of this system to be the inverse of the dead time, or 5 Mcps (million counts per second) per pixel. This counting speed is typical of photon counting detectors of the previous generation [5], but newer detectors are become available which can count much faster [17].

We calculate the variance of the material estimate for a single detector pixel only. Besides counts arising from the pixel being illuminated, false counts also appear which originate from neighboring pixels as a result of charge sharing. These counts are also included in the simulation. However, we do not study the effects of noise correlations in this work. Correlations due to charge sharing may impart frequency dependent DQE penalties.

We assumed the detector used energy binning thresholds of 30 keV, 45 keV, 65 keV, 85 keV, 105 keV and 125 keV. These thresholds were not optimized. Since the maximum photon energy was 120 keV in these simulations, the 125 kVp threshold functioned as a pileup trigger [18].

C. Variance calculation

Converting the counts recorded in each bin into spectral information, such as equivalent thicknesses of basis materials, requires an estimator. One example estimator is the maximum likelihood estimator, which is slow but has good bias and variance properties. A fast, efficient, and accurate estimator in the presence of non-idealities such as pileup has yet to be demonstrated. Therefore, in this work we calculate the Cramer-Rao Lower Bound (CRLB) of the variance for the measured spectral data. This allows us to compare the performance of different PCD architecture without needing an estimator.

Following Reference [19], we calculate the CRLB by assuming that the counts in each bin can be modeled with a

multivariate Gaussian. We use multiple realizations to estimate the mean and covariance matrix of the counts in each bin. The CRLB of the variance can then be calculated from this data.

III. Results

A. Energy response

Figure 1 shows an example energy response function. The pixel where the x-ray photon is directed (denoted in the figure as the primary pixel) collects much, but not all, of the charge. A clear K-escape peak is seen, where approximately 25 keV of energy escapes the pixel in the form of a characteristic x-ray and arrives in an adjacent pixel or exits the detector entirely. We also show the energy response for the illumination of all eight neighboring pixels. This describes the stray or false counts detected in a pixel due to charge sharing from neighboring pixels.

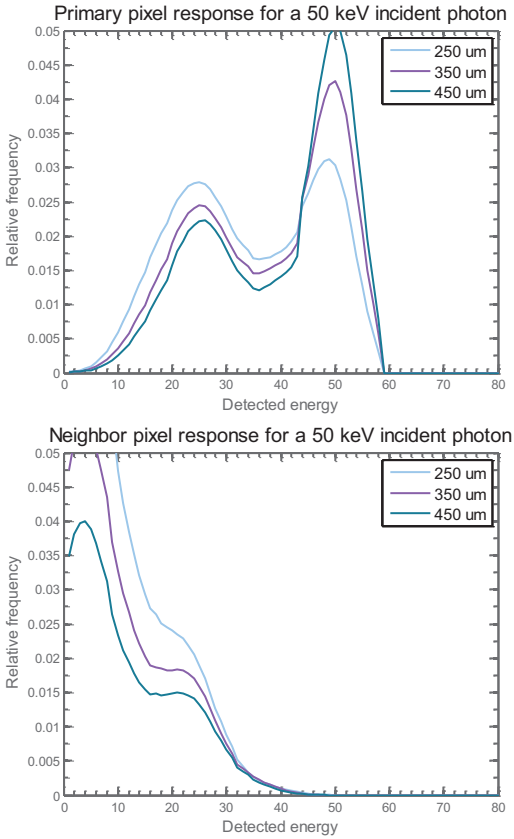

Fig. 1. Energy response for an incident 50 keV photon. We show both the energy response for the (top) primary pixel, that is, the pixel being irradiated, and (bottom) neighboring pixels, which receive energy as a consequence of charge sharing.

B. CRLB comparison

Figure 2 shows the behavior of the variance of a spectral task, the estimation of water material thickness after estimating and canceling out the bone material thickness. As seen in the top plot of Figure 2, as the object becomes thicker and fewer photons arrive at the detector, the variance increases. This is the same behavior expected of Poisson statistics in energy integrating detectors. However, as the object becomes thin, the rate of photons arriving can exceed the characteristic count rate of the detector, and count rate loss ensues. This causes the curve to bend upwards, creating a variance penalty. The 100 um pixel size with ideal energy response counts sufficiently fast that this effect is hardly visible.

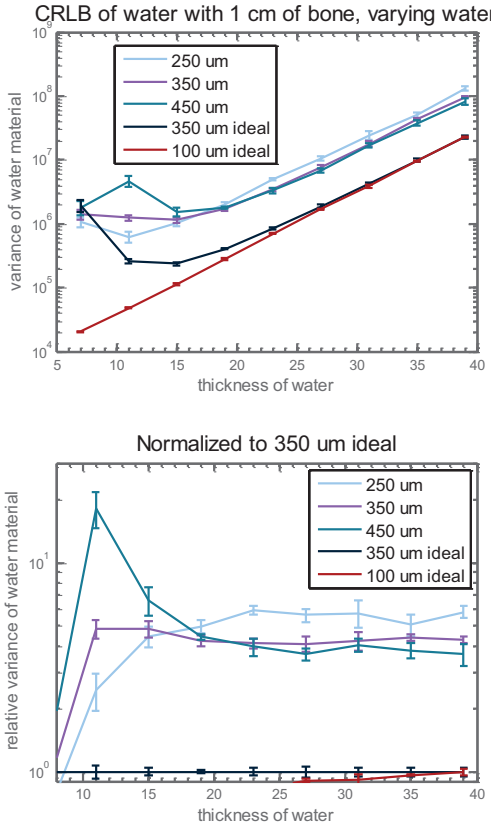

Fig. 2. Variance in the measurement of water (bone cancelled) thickness for a fixed technique as a function of object thickness. "Ideal" detectors have ideal energy response but still suffer from pile-up. (Top) Variance over a large range of object sizes. (Middle) The same data, but normalized by the 350 um pixel size with ideal energy response. Error bars shown pertain to the CRLB estimation but not to errors arising from uncertainty of the energy response functions. As this is a semilog plot, plotting standard deviation instead of variance would yield the same curve shapes but a relabeling of the y-axis.

Compared to the ideal detector with a small (100 um) pixel size, the increase in variance for the detectors simulated here arise from two sources: pileup (or count rate loss) and charge sharing. The 350 um pixel with ideal energy response shows a hypothetical detector with pileup but without charge sharing. Its variance is about four times less than the other realistic detectors considered which have non-ideal energy response. Among the designs with non-ideal energy response, the larger pixel sizes perform moderately better than the smaller pixel sizes except with thin objects, when pileup becomes the limiting factor. However, with thin objects such as pediatric patients, the mA should be reduced to decrease radiation dose.

IV. Conclusions

PCDs are a promising detector choice in future CT systems, but suffer from several non-idealities, including count rate loss and charge sharing. By altering the detector pixel size, we can reduce one of these effects at the expense of increasing the other. Historically, the mandate has been to reduce count rate loss by using very small pixels. However, at this current time, using larger pixels such as 350 to 450 μm offers a modest performance improvement in material separation tasks. This trend reverses for smaller objects, when pileup is the dominating factor. However, when scanning large objects, ray paths with little attenuation do exist but may not be the dominant contributors to image noise. Even though a penalty may be present in rays with short tissue path-lengths, this penalty could be outweighed by the improvement in the long path-lengths, which have much higher noise. It has long been known that improving noise in the photon-starved regions is more important for image quality than adding photons were they are already abundant. We do not take into consideration the resolution differences between these pixel sizes; however, any of the pixel pitches investigated here would be a substantial improvement over the resolution of existing energy-integrating detectors, and at the time of this writing, the resolution of the system would be in any case limited by the focal spot.

The conclusions reached here will change with improving technology. Faster pulse shaping will tilt the balance in favor of larger pixels; reduction of charge sharing from smaller drift times will do the reverse. However, charge sharing from K-escape will be difficult to avoid. An anti-scatter grid could limit the flux along pixel boundaries, reducing charge sharing. Nonetheless, the potential for improvement in photon counting detectors is large. In the present simulations, the disparity between perfect energy response and the simulated energy response was always a variance penalty of at least three. Charge sharing compensation mechanisms could be used to diminish this gap, but may place greater pressure on the electronics and complexity and would diminish the effective count rate capability.

References

[1] R. E. Alvarez and A. Macovski, "Energy-selective reconstructions in x-ray computerised tomography," *Phys. Med. Biol.,* vol. 21, pp. 733, 1976.

[2] T. Johnson, C. Fink, S. O. Schönberg and M. F. Reiser, *Dual Energy CT in Clinical Practice.* Springer Science & Business Media, 2011.

[3] A. N. Primak, J. G. Fletcher, T. J. Vrtiska, O. P. Dzyubak, J. C. Lieske, M. E. Jackson, J. C. Williams and C. H. McCollough, "Noninvasive differentiation of uric acid versus non–uric acid kidney stones using dual-energy CT," *Acad. Radiol.,* vol. 14, pp. 1441-1447, 2007.

[4] Y. Yao, A. S. Wang and N. J. Pelc, "Efficacy of fixed filtration for rapid kVp-switching dual energy x-ray systems," *Med. Phys.,* vol. 41, pp. 031914, 2014.

[5] K. Taguchi and J. S. Iwanczyk, "Vision 20/20: Single photon counting x-ray detectors in medical imaging," *Med. Phys.,* vol. 40, pp. 100901, 2013.

[6] G. F. Knoll, *Radiation Detection and Measurement.* Wiley, 2010.

[7] T. Koenig, E. Hamann, S. Procz, R. Ballabriga, A. Cecilia, M. Zuber, X. Llopart, M. Campbell, A. Fauler and T. Baumbach, "Charge summing in spectroscopic x-ray detectors with high-Z sensors," 2013.

[8] S. Faby, S. Kuchenbecker, S. Sawall, D. Simons, H. Schlemmer, M. Lell and M. Kachelrieß, "Performance of today's dual energy CT and future multi energy CT in virtual non-contrast imaging and in iodine quantification: A simulation study," *Med. Phys.,* vol. 42, pp. 4349-4366, 2015.

[9] H. Bornefalk and M. Danielsson, "Photon-counting spectral computed tomography using silicon strip detectors: a feasibility study," *Phys. Med. Biol.,* vol. 55, pp. 1999, 2010.

[10] S. S. Hsieh and N. J. Pelc, "A dynamic attenuator improves spectral imaging with energy-discriminating, photon counting detectors," *Medical Imaging, IEEE Transactions on,* vol. 34, pp. 729-739, 2015.

[11] S. S. Hsieh and N. J. Pelc, "The piecewise-linear dynamic attenuator reduces the impact of count rate loss with photon-counting detectors," *Phys. Med. Biol.,* vol. 59, pp. 2829, 2014.

[12] E. Roessl and R. Proksa, "Dynamic beam-shaper for high flux photon-counting computed tomography," in *Workshop on Medical Applications of Spectroscopic X-Ray Detectors,* Geneva, Switzerland, .

[13] K. Taguchi, S. Srivastava, H. Kudo and W. C. Barber, "Enabling photon counting clinical x-ray CT," in *Nuclear Science Symposium Conference Record (NSS/MIC), 2009 IEEE,* 2009, pp. 3581-3585.

[14] S. Kappler, T. Hannemann, E. Kraft, B. Kreisler, D. Niederloehner, K. Stierstorfer and T. Flohr, "First results from a hybrid prototype CT scanner for exploring benefits of quantum-counting in clinical CT," in *SPIE Medical Imaging,* 2012, pp. 83130X-83130X-11.

[15] S. Agostinelli, J. Allison, K. Amako, J. Apostolakis, H. Araujo, P. Arce, M. Asai, D. Axen, S. Banerjee and G. Barrand, "Geant4-a simulation toolkit," *Nuclear Instruments and Methods in Physics Research-Section A Only,* vol. 506, pp. 250-303, 2003.

[16] I. Blevis, H. Daerr, M. Rokni, C. Hermann, T. Istel, A. Livne, G. Martens, F. Peyrin, D. Rubin, M. Sigovan, R. Steadman, A. Thran, B. Brendel, R. Levinson, A. Altman, O. Zarchin, L. Boussel, P. Douek and E. Roessl, "Spectroscopy in computed tomography using pixelated photon counting detectors," in *Workshop on Medical Applications of Spectroscopic X-Ray Detectors,* Geneva, Switzerland, 2015.

[17] Z. Yu, S. Leng, S. Jorgensen, Z. Li, R. Gutjahr, B. Chen, X. Duan, A. Halaweish, L. Yu and E. Ritman, "Initial results from a prototype whole-body photon-counting computed tomography system," in *SPIE Medical Imaging,* 2015, pp. 94120W-94120W-7.

[18] S. Kappler, S. Hölzer, E. Kraft, K. Stierstorfer and T. Flohr, "Quantum-counting CT in the regime of count-rate paralysis: Introduction of the pile-up trigger method," in *SPIE Medical Imaging,* 2011, pp. 79610T-79610T-11.

[19] A. S. Wang, D. Harrison, V. Lobastov and J. E. Tkaczyk, "Pulse pileup statistics for energy discriminating photon counting x-ray detectors," *Med. Phys.,* vol. 38, pp. 4265, 2011.

Shading correction assisted iterative conebeam CT reconstruction

Pengwei Wu, Tingyu Mao, Shutao Gong, Jing Wang, Ke Sheng, Yaoqin Xie, Tianye Niu*

***Abstract*—Recent advances in total variation (TV) technology enable accurate CT image reconstruction from highly undersampled and noisy projection measurements. Standard iterative reconstruction algorithms, which work well in conventional CT imaging, fail to perform as expected in cone beam CT (CBCT) application. The major reason is that non-ideal physics issues, including scatter contamination and beam hardening, are more severe in CBCT images and result in large area of shading artifacts. The ideal mathematical assumptions (e.g., piecewise constant property of the reconstructed image) of TV are thus destroyed. To overcome this obstacle, we incorporate shading correction scheme into iterative reconstruction and propose an accurate, fast and stable iterative reconstruction method referred to as shading correction assisted iterative reconstruction (SCAIR). In the proposed method, we modify the TV regularization term by adding a shading correction image to the reconstructed image to compensate for the shading artifacts while maintaining the data fidelity term intact. The new scheme satisfies the piecewise constant mathematical assumption using TV regularization and achieves simultaneous reconstruction and shading correction. To minimize the proposed objective, in each iteration, we update the compensation image using segmentation and low-pass filtering techniques. When compensation image is updated, the objective function is minimized using gradient projection with an adaptive Barzilai–Borwein method to find the optimal solution. The proposed method is evaluated using CBCT projections of the Catphan©600 phantom and a pelvis patient. Compared with conventional iterative reconstruction, the proposed method reduces the overall CT number error from over 200 HU to be less than 30 HU and increases the spatial uniformity by a factor of 1.6 using the same number of projections in the reconstruction. The overall iteration number is decreased by around 40% and the low-contrast objects are faithfully retained after the proposed reconstruction. The proposed SCAIR method is thus practical and attractive as a general solution to CBCT iterative reconstruction.**

***Index Terms*—Iterative Reconstruction, Shading Correction, Conebeam CT.**

P. Wu, T. Mao, S. Gong, J. Wang and T. Niu were supported by the Zhejiang Provincial Natural Science Foundation of China (Grant No. LR16F010001), National High-tech R&D Program for Young Scientists by the Ministry of Science and Technology of China (863 Program, 2015AA020917).

P. Wu, T. Mao, S. Gong, J. Wang and T Niu are with Sir Run Run Shaw Hospital, Zhejiang University School of Medicine; Institute of Translational Medicine, Zhejiang University, Hangzhou, Zhejiang, 310016, People's Republic of China.

P. Wu and T. Mao are also with Department of Electrical Engineering, Zhejiang University School of Engineering, Hangzhou, Zhejiang, 310016, People's Republic of China.

K. Sheng is with Department of Radiation Oncology, University of California, Los Angeles, Los Angeles, CA, USA.

Y. Xie is with Institute of Biomedical and Health Engineering, Shenzhen Institutes of Advanced Technology, Chinese Academy of Sciences, Shenzhen, Guangdong 518055, People's Republic of China.

* Any correspondence should be addressed via email to T. Niu (e-mail: tyniu@zju.edu.cn).

I. Introduction

Recent advances in cone-beam CT (CBCT) enable its tremendous applications in image guided radiation therapy, including treatment setup, calculation of dose distribution and tumor delineation for adaptive radiation therapy. In these applications, high ionizing exposure of CBCT from repeated scans in the fractionated treatment process is the major concern for patient healthcare. To decrease the excessive exposure, low-dose CT protocols are applied in clinic including fewer projection data acquisition and/or lower x-ray tube current. Traditional analytical algorithm is unlikely to reconstruct accurate images using low-dose protocols due to the increased view-aliasing artifacts and statistical noise. As a result, iterative algorithms are proposed to reconstruct faithful CT images since iterative methods readily incorporate the physical constraints and image features into the reconstruction [1]–[3]. Standard low-dose CT reconstruction methods usually model the CT imaging process as the data fidelity term regularized by mathematical assumptions on the image property. For example, total variation (TV) is defined as the L1 norm of the spatial gradient image and enforces the reconstructed CT image to be piecewise constant. CBCT system applies the large-area flat-panel detector to acquire the volumetric image projections in the scan. Non-ideal physics issues, including scatter contamination and beam hardening are more severe in CBCT data acquisition than those in conventional CT scanner and result in severe shading artifacts. The standard low-dose reconstruction algorithms, which work well in conventional CT imaging, fail to perform as expected in CBCT imaging since the ideal mathematical assumptions (e.g., piecewise constant property) in the formulation cannot be satisfied.

To improve CBCT image quality, many algorithms are proposed to correct for the shading artifacts in CBCT image as an independent step, and numerous publications are found in the literature. These methods can be categorized as specific and general correction schemes. Specific correction methods perform correction for artifacts generated from one single physical factor including scatter contamination, beam hardening or photo starvation effects. General correction methods treat the low-frequency shading artifacts as if they come from the same error source. They extract the error mask in either the image or projection domain using image processing technique [4].

Independent operation of shading correction fails to incorporate the correlation of mathematical assumption and physics property in iterative reconstruction process. The reconstruction is thus slow and vulnerable to the non-ideal physics fluctuations. Some researchers include the image processing technique into the iterative process and propose the joint iterative processing

scheme. For example, Niu et al propose to include the statistical noise suppression into the iterative dual-energy material decomposition utilizing the noise correlation properties in the decomposition [5]. These joint schemes outperform their independent counterparts due to the full utilization of the information in the imaging process.

In this work, we incorporate shading correction into the iterative CBCT reconstruction and propose an accurate, fast and stable reconstruction method referred to as the shading correction assisted iterative reconstruction (SCAIR) method. This new strategy performs a fast and stable iterative reconstruction while simultaneously eliminating shading artifacts effectively. We progressively perform shading correction in each iteration by estimating a compensation image which accounts for the shading artifacts in the image. The mathematical assumption (e.g., piecewise constant property) on the regularization term is thus better satisfied. The proposed method is evaluated in the Catphan©600 phantom and a pelvis patient studies. The proposed method does not rely on prior knowledge of the object, and is attractive and practical for clinical applications.

II. Method

A. SCAIR Framework Formulation

To reduce the view-aliasing artifacts from limited data measurements, total variation (TV) is applied as the regularization term to pick up the CT image whose intensity distribution follows the piecewise constant property while the data fidelity is best satisfied. A standard TV regularized iterative reconstruction is written as following:

$$\overrightarrow{f^*} = \underset{\vec{f}}{\arg\min} \left[\left\| M\vec{f} - b \right\|_2^2 + \lambda \left\| \vec{f} \right\|_{TV} \right], \quad (1)$$

where the vector b with a length of N_d (i.e., the number of detector voxels) represents the line integral measurements, M is the system projection matrix modeling the forward projection operation, $\vec{f}$ is the vectorized CBCT image to be reconstructed with a length of N_i (i.e., number of image voxels). $*$ indicates the solution. $\|\blacksquare\|_2$ calculates the L2 norm and $\|\blacksquare\|_{TV}$ is the TV term defined as the L1 norm of the spatial gradient image.

In CBCT reconstruction, the piecewise constant property is usually deteriorated by the severe shading artifacts. The mathematical optimization process is thus slow and unstable due to the inconsistent aims of data fidelity and TV regularization term. To overcome this problem, we construct a compensation image to account for the severe shading artifacts. The optimization formula is rewritten as:

$$\left(\overrightarrow{f^*}, \overrightarrow{f^{*comp}}\right) = \underset{\vec{f}, \overrightarrow{f}}{\arg\min} \left[\left\| M\vec{f} - b \right\|_2^2 + \lambda \left\| \vec{f} + \overrightarrow{f^{comp}} \right\|_{TV} \right], \quad (2)$$

The modified term $\vec{f} + \overrightarrow{f^{comp}}$ takes into account the shading compensation image and approaches to the piecewise constant property required by the TV regularization. The inconsistency between the minimization of TV and the maintenance of data fidelity is greatly suppressed.

B. Updating Scheme

Eq. (2) is solved using a sequential scheme since two variables are included. In each iteration, we update the compensation image $\overrightarrow{f^{comp}}$ based on the assumption that CT number distribution of one tissue component is relatively uniform. The objective function is then minimized using gradient method to find the optimal reconstructed image $\vec{f}$ under the condition that the compensation image is fixed.

B. I. Compensation Image

In CBCT imaging, data acquisition errors destroy the uniformity of the area composed of the same tissue. To enforce the image uniformity, an ideal template image is generated using image segmentation technique and each structure in the template is filled with the CT number of that specific tissue. Low-pass filtration is applied to the difference image between the ideal template and original CBCT image to extract the low-frequency shading compensation image. The compensation image thus mainly corrects for the shading artifacts while maintaining the anatomical structures in the CBCT image. This progress can be illustrated with the following equation:

$$\overrightarrow{f_n^{comp}} = LF\left(SF\left(\overrightarrow{f_{n-1}} + t \cdot \overrightarrow{f_{n-1}^{comp}}\right) - \overrightarrow{f_{n-1}}\right), \quad (3)$$

where the subscript n indicates the current iteration while $n-1$ indicates the previous one, SF is the segmentation and intensity filling operator and t is a scaling factor no more than one to achieve a stable compensation. LF indicates the low-pass SG filtration operation. Segmentation is performed using thresholding and region-based level-set algorithms [4].

An accurate segmentation is not trivial due to the severe shading artifacts. The scaling factor t is applied to prevent the reconstructed image from biased towards an inaccurate template image. t is linearly increased from 0 to 1 in our implementation and is shown as following:

$$t = \begin{cases} \frac{1}{N_s} n, & if\ n \le N_s \\ 1, & if\ n > N_s \end{cases}, \quad (4)$$

where n is the iteration number, and N_s is the number of iterations after which t is fixed as 1 when the optimization is stable. A template image is produced by filling the standard CT number of one tissue into the segmented area.

B. I. Minimization of objective function

When the compensation image is updated and fixed, the optimization objective function of Eq. (2) is rewritten as:

$$\overrightarrow{f^*} = \underset{\vec{f}}{\arg\min} \left[\left\| M\vec{f} - b \right\|_2^2 + \lambda \left\| \vec{f} + \overrightarrow{f^{comp}} \right\|_{TV} \right], \quad (5)$$

In this work, Eq. (5) is solved using gradient projection (GP) method with adaptive BB step size selection scheme as proposed in our previous work [3].

The GP algorithm finds the optimal decreasing direction by projecting the negative gradient of objective onto the feasible set. The updating scheme of this algorithm is shown in the following:

$$\overrightarrow{f_{n+1}} = \max\left(\overrightarrow{f_n} - \alpha_n \overrightarrow{p_n}, 0\right), \quad (6)$$

, where α_n is the step size of the n^{th} iteration. The projected gradient is denoted as $\overrightarrow{p_n}$ which is calculated in Eq. (7):

$$\overrightarrow{p_n}(l) = \begin{cases} \overrightarrow{g_n}(l), & if\ \overrightarrow{g_n}(l) \le 0, or\ \overrightarrow{f_n}(l) > 0 \\ 0, & otherwise \end{cases}, \quad (7)$$

, where l is the voxel index, $\vec{g}$ is the gradient of objective function.

Major steps in our algorithm include the calculation of the gradient of the objective function ($\vec{g}$) and the step size (α) in each iteration. Gradient of the objective function (Eq. (5)) is derived as shown in Eq. (8):

$$\vec{g} = \nabla \left\| \vec{f} + \overrightarrow{f^{comp}} \right\|_{TV} + M^T\left(M\vec{f} - b\right), \quad (8)$$

where T is the transpose operator and ∇ is the gradient operator. An effective adaptive Barzilai-Borwein (BB) method is applied to analytically estimate the step size in each iteration. Being different from the conventional gradient calculation using the gradient of current iteration, BB method estimates the step size based on both the previous and current gradients using a scalar approximation to the secant equations. Calculation details can be found in our previous work [3].

C. Implementation details

Shading artifacts are severe in the CBCT image of large volume (e.g. the pelvis image) and tissue segmentation is difficult or even impossible. An initial compensation image to guarantee a reliable segmentation is preferred to start the iteration. In this work, pelvis patient data using a half-fan bowtie filter presents severe shaded ring artifact around the periphery of the image. The artifact is caused by the scatter signal from modulated primary beam and thus appears as a unique ring pattern in image domain. Due to the correlation between the bowtie modulator and the ring pattern, we extract the artifacts using the modulated air-scan data as if acquired from a flat-field exposure penetrating the bowtie modulator. Details of the algorithm is included in our recent publication [4]. The extracted ring pattern shading artifacts are then used as the initial compensation image in Eq. (3).

To decrease the computation burden, we perform the image segmentation after several iterations instead of in each iteration. The rationale of this operation lies in the fact that reconstruction is a slow and stable process. The difference between reconstructed images from adjacent iterations is relatively small to bring about segmentation improvement.

The stopping criteria used in our proposed method is the cosine of the data fidelity and regularization gradient angles as proposed in Prof. Pan's work [2].

D. Evaluation

The proposed method is evaluated using CBCT projections acquired from the Catphan©600 phantom and a pelvis patient. The CT number error is calculated using the square root of the mean square error (RMSE). To demonstrate that our method has maintained the piecewise constant property of the CBCT image, the spatial uniformity is used as a quality metric, as defined in Eq. (9).

$$\mathrm{SU} = \frac{\max(\mathrm{hist}(I_{tissue}))}{num(I_{tissue})}, \tag{9}$$

, where I_{tissue} is the segmented tissue of the same material and num(■) calculates the number of voxels in the segmented area. SU is unity in an ideal piecewise constant CT image.

III. Result

A. Catphan©600 phantom study

Figure 1 shows the CBCT images reconstructed using full projection data (655 projections) and analytical algorithm without (Figure 1(a)) and with (Figure 1(b)) shading correction, sparse projection data (92 projections) using conventional iterative reconstruction (Figure 1(c)) and the proposed SCAIR method (Figure 1(d)). Iterative algorithm successfully reconstructs accurate CBCT images from sparse projections without loss of image quality. Severe low-frequency cupping artifacts observed in Figure 1(c) is greatly suppressed by the proposed method as shown in Figure 1(d). After SCAIR reconstruction, the overall image quality of Figure 1(d) is comparable to that in the reference image in Figure 1(b). For quantitative evaluation, six ROIs indicated by black rectangles in the reference image (Figure 1(b)) are selected to calculate the RMSE of CT number. SU is calculated as an indicator for the evaluation of global uniformity of these CBCT images. Comparing CBCT image reconstructed using SCAIR method with the one using the conventional iterative reconstruction, the CT number error is reduced from 225 HU to 6 HU and SU is substantially increased from 49.7% to 64.9%.

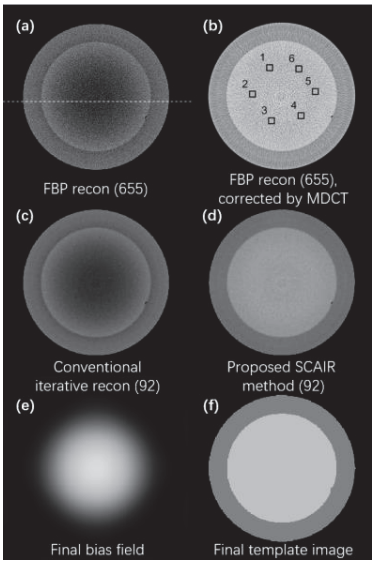

Figure 1. CBCT images of the Catphan©600 phantom: (a) reconstructed using standard FBP algorithm and 655 projections, (b) after MDCT based shading correction using 655 projections (reference image), (c) reconstructed using conventional iterative method and 92 projections (no shading compensation), and (d) reconstructed using the proposed SCAIR method with 92 projections. The final template and compensation image (n=160) are shown in (f) and (e), respectively. Display window: [-250 250] HU.

B. Pelvis Patient study

Figure 2 shows the CBCT images using analytical reconstruction with 655 projections (Figure 2(a)), using analytical reconstruction with 162 projections (Figure 2(b)), using conventional iterative reconstruction with 162 projections (Figure 2(c)) and using the proposed SCAIR method with 162 projections (Figure 2(d)). Using sparse projections, conventional iterative reconstruction suppresses the streaking artifacts due to view aliasing in the images from analytical reconstruction. The proposed SCAIR method (Figure 2(d)) successfully removes the shading artifacts in the CT images using conventional iterative reconstruction (Figure 2(c)). Using the proposed SCAIR method, the CT number error is decreased from 221 HU to 24 HU, the average contrast is increased from 60 to 79 HU and the SU is increased from 33% to 55%.

C. Convergence Behavior and Parameter Sensitivity

The overall iteration number using the proposed SCAIR method is reduced by 40% as compared with that using the conventional iterative scheme. The major reason is that we incorporate the compensation image into the regularization term of the objective function to approach the piecewise constant property which is preferred by the TV regularization

while maintaining data fidelity with shading contamination intact. Therefore, the minimization of TV and data fidelity is consistent and the strength of mathematical optimization is fully utilized.

To demonstrate the convergence performance, the stopping criteria (cos_α) at each iteration is plotted in Figure 4(a). The stopping criteria of the proposed SCAIR method converges faster and more stable than that of the conventional iterative reconstruction method. For example, around iteration number 80, stopping criteria of SCAIR method reaches -0.85 and almost stays there with a little vibration. The stopping criteria of the conventional method is still around -0.5 and vibrates dramatically.

TV term is plotted in Figure 4(b). Since the shading artifacts are suppressed, the overall TV of the CT image using the SCAIR method is smaller than that of the conventionally reconstructed image. The oscillation of the TV is also less intensive using our proposed method than that using conventional reconstruction.

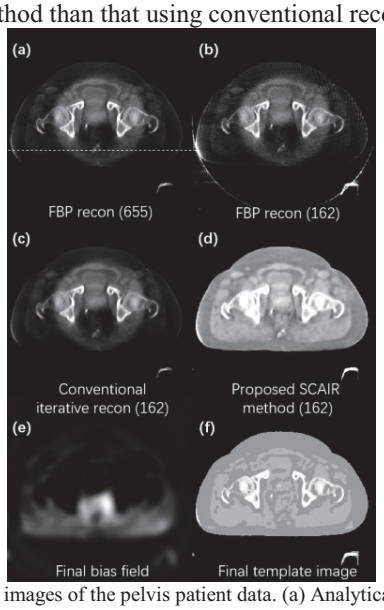

Figure 2. CBCT images of the pelvis patient data. (a) Analytical reconstruction using 655 projections, (b) analytical reconstruction using 162 projections, (c) conventional iterative reconstruction using 162 projections, (d) the proposed SCAIR method using 162 projections, (e) the final compensation image, and (f) the final template image. Display window: [-250 250] HU.

Our proposed SCAIR method introduces a new parameter compared with conventional iterative reconstruction method. That is, the span size of SG filter which is illustrated in Eq. (3). To analyze the sensitivity, we plot the span size of SG filter (in pixels) with respect to the CT number error (RMSE) of the final reconstructed image, as is shown in Figure 3. This figure indicates that our result is not very sensitive to parameter selection.

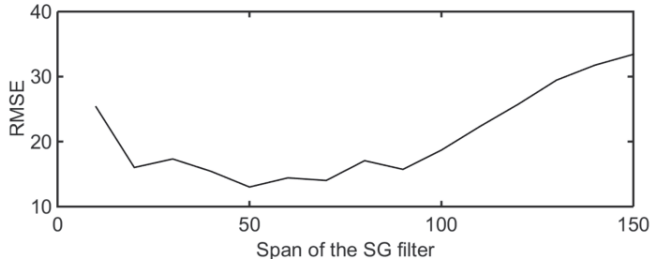

Figure 3. CT number error (RMSE) of the final reconstructed image vs. span size of the SG filter (in pixels).

IV. Conclusion

An effective shading correction assisted iterative reconstruction (SCAIR) method is proposed. Being different from existing algorithm, our reconstruction method incorporates the compensation image into the optimization framework, and achieves an accurate, stable and efficient optimization progress as compared with the conventional iterative method. The proposed method is evaluated on a Catphan©600 phantom and a pelvis patient. Compared with images from traditional iterative reconstruction algorithm, our method achieves less shading artifacts (<3%), less number of iteration (<40%) and higher spatial uniformity (>60%). Therefore, the proposed correction method is practical and attractive as a general solution to clinical applications.

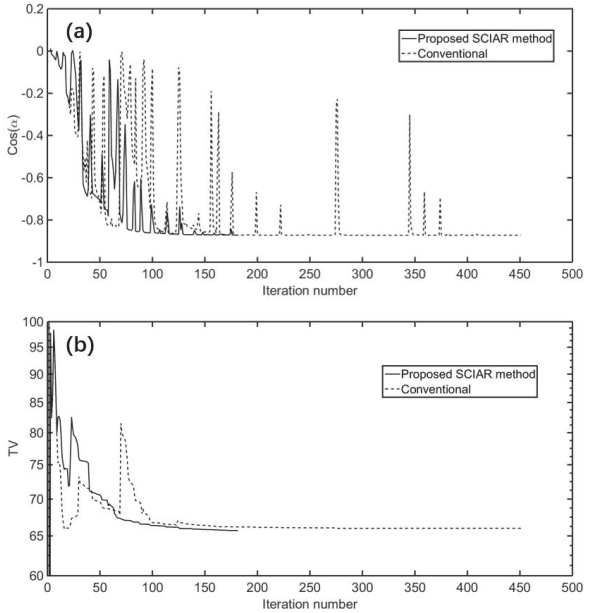

Figure 4. (a) Stopping criteria, (b) TV and (c) objective function with respect to the iteration number for the proposed SCAIR and the conventional iterative reconstruction method. Y axis in (b) and (c) is in logarithmic format.

V. References

[1] G.-H. Chen, J. Tang, and S. Leng, "Prior image constrained compressed sensing (PICCS): a method to accurately reconstruct dynamic CT images from highly undersampled projection data sets," *Med. Phys.*, vol. 35, no. 2, pp. 660–663, 2008.

[2] E. Y. Sidky and X. Pan, "Image reconstruction in circular cone-beam computed tomography by constrained, total-variation minimization," *Phys. Med. Biol.*, vol. 53, no. 17, pp. 4777–4807, Sep. 2008.

[3] T. Niu and L. Zhu, "Accelerated barrier optimization compressed sensing (ABOCS) reconstruction for cone-beam CT: Phantom studies," *Med. Phys.*, vol. 39, no. 7, p. 4588, 2012.

[4] P. Wu, X. Sun, H. Hu, T. Mao, W. Zhao, K. Sheng, A. A. Cheung, and T. Niu, "Iterative CT shading correction with no prior information," *Phys. Med. Biol.*, vol. 60, no. 21, pp. 8437–8455, Nov. 2015.

[5] T. Niu, X. Dong, M. Petrongolo, and L. Zhu, "Iterative image-domain decomposition for dual-energy CT," *Med. Phys.*, vol. 41, no. 4, p. 041901, Apr. 2014.

Denoising-Based Accelerated Statistical Iterative Reconstruction for X-ray CT

Sathish Ramani, Xin Wang, Lin Fu, and Michael Lexa
GE Global Research, Niskayuna, NY 12309, USA

***Abstract*—Model-based image reconstruction (MBIR) is attractive for X-ray CT as it can provide improved image-quality over filtered backprojection (FBP). MBIR entails minimizing a cost criterion involving a data-fidelity term and an image-prior term. Recent advances in MBIR have focussed on using patch-based (e.g., non-local means—NLM and dictionary learning—DL) image-priors that are capable of providing better quality than pixel-difference-based priors. In this work, we propose an MBIR-framework with general-denoising-based image-priors where we minimize a data-fidelity term subject to constraints that force the reconstructed image to be "close" to (several) denoised versions of itself. We treat denoising as a black-box operation, so the proposed framework can handle arbitrary denoisers thus subsuming some of the existing advanced-MBIR methods (e.g., NLM- and DL-based MBIR). We derive iterative reconstruction algorithms for the proposed framework and show how to accommodate momentum-techniques for accelerating reconstruction. Using simulated and real CT datasets, we present numerical results demonstrating the efficacy of one of the proposed algorithms.**

Keywords*—X-ray CT, model-based image reconstruction, image denoising, non-local means, dictionary learning.

I. Introduction

Model-based image reconstruction (MBIR) can provide better image-quality than filtered backprojection (FBP), especially for low-dose and sparse-view scans in X-ray CT [1], [2]. In MBIR, the reconstructed image is usually obtained by *minimizing* a cost function that is a sum of a *statistical data-fidelity* term and one or more *image-prior* terms [1], [2]. Edge-preserving pixel-differences-based image-priors [1], [2], [3] are popular, while recent advances include the use of patch-based image-priors such as non-local means (NLM) [4] and dictionary learning (DL) [5]. These advanced image-priors are capable of providing better image-quality than pixel-based ones [4], [5]. In any case, the above minimization entails the use of (non-linear) iterative algorithms [1], [2] that can be computationally expensive. Recently, Kim *et al.* [3] demonstrated that ordered subsets (OS) [6] and momentum-techniques (MOM) [7], [8] can be used for acceleration of simple gradient-descent (GD) type methods for MBIR with pixel-difference-based priors.

This work is supported by Department of Homeland Security, Science and Technology Directorate, Explosives Division, BAA 13-05, Contract # HSHQDC-14-C-B0048. The authors thank Walter Garms, Morpho Detection Inc., for providing real CT datasets, Dr. D. -J. Kroon, University of Twente, The Netherlands, for providing Matlab code for Non-Local Means denoising, and Dr. Bruno De Man, GE Global Research, Niskayuna, NY, USA, for helpful discussions.

Inspired by [4], [5], we consider a general-denoising-based MBIR-framework where we minimize a statistically weighted least-squares (WLS) data-fidelity criterion subject to constraints that force the reconstructed image to be "close" to (several) denoised versions of itself. We treat denoising as a (non-linear) black-box operation, so the proposed framework accommodates a variety of (non-linear) denoisers thus subsuming existing NLM- and DL-based MBIR methods [4], [5].

Due to the black-box assumption, the proposed constrained optimization is complicated. So we *approximate* each denoiser by its corresponding denoised-estimate at any given iteration: such a strategy is similar to the one-step late [4] and alternating minimization [5] approaches. This approximation together with the separable-quadratic-surrogate (SQS) scheme [6] simplifies optimization leading to a denoising-based SQS (DSQS) algorithm that (approximately) solves the original constrained problem. We also derive a variant of DSQS, called gradient-descent-denoising (GDD) that is similar in spirit to iterative shrinkage/thresholding (IST) [9]. Both DSQS and GDD can accommodate arbitrary denoisers. Similar to [3], we also combine OS [6] and MOM methods [7], [8] with DSQS and GDD for algorithmic acceleration and derive DSQS-OS-MOM and GDD-OS-MOM algorithms. For conciseness, we demonstrate the working of GDD-OS-MOM in this paper via numerical experiments with simulated and real CT scanner datasets.

II. Proposed MBIR Framework

We consider the following optimization problem

$$\hat{\boldsymbol{x}} \stackrel{\text{def}}{=} \arg\min_{\boldsymbol{x}\in\boldsymbol{\Omega}} \frac{1}{2}\|\boldsymbol{y}-\boldsymbol{A}\boldsymbol{x}\|^2_{\boldsymbol{W}} \text{ s.t. } \|\boldsymbol{x}-\boldsymbol{f}^{(l)}_{\boldsymbol{\theta}_l}(\boldsymbol{x})\|^2_2 \leq \varepsilon_l^2, \quad (1)$$

$l = 1,\ldots,L$, where $\varepsilon_l \geq 0$, $\hat{\boldsymbol{x}} \in \mathbb{R}^n$ is the reconstructed result, $\boldsymbol{\Omega}$ is a constraint set (e.g., non-negativity constraint), $\boldsymbol{A} : \mathbb{R}^n \to \mathbb{R}^m$ is the CT system matrix, $\boldsymbol{W}$ is a diagonal matrix with statistical weights, $\boldsymbol{y} \in \mathbb{R}^m$ is the measured data, and $\boldsymbol{f}^{(l)}_{\boldsymbol{\theta}_l} : \mathbb{R}^n \to \mathbb{R}^n$, $l = 1,\ldots,L$ are vector-functions representing L different (non-linear) denoisers with respective denoising-parameter-vectors $\{\boldsymbol{\theta}_l\}_{l=1}^L$.

This formulation encourages the reconstructed image to be nearly consistent with the measured data $\boldsymbol{y}$ while being "close" to denoised versions of itself, as prescribed by the denoisers $\{\boldsymbol{f}^{(l)}_{\boldsymbol{\theta}_l}\}_{l=1}^L$. We treat $\{\boldsymbol{f}^{(l)}_{\boldsymbol{\theta}_l}\}_{l=1}^L$ as black-boxes, i.e., we do not require knowledge of the functional form of $\{\boldsymbol{f}^{(l)}_{\boldsymbol{\theta}_l}\}_{l=1}^L$. This provides flexibility in using a variety of denoisers that reduce both noise (at a voxel-level) and also other CT-related

artifacts (e.g., streaks). We assume that $\{\boldsymbol{f}_{\boldsymbol{\theta}_l}^{(l)}\}_{l=1}^{L}$ are *proper* and *monotone* [10, Defs. 1-2], i.e., $\{\boldsymbol{f}_{\boldsymbol{\theta}_l}^{(l)}\}_{l=1}^{L}$ decrease noise (and artifacts) such that the root mean-squared error of the denoised-estimates decrease monotonically with noise (and artifact) level.

III. Denoising-Based SQS

Due to the black-box nature (and associated non-linearity) of the denoisers $\{\boldsymbol{f}_{\boldsymbol{\theta}_l}^{(l)}\}_{l=1}^{L}$, (1) is a complicated optimization problem to solve that invariably requires iterative treatment. As a first simplification step, we approximate $\boldsymbol{f}_{\boldsymbol{\theta}_l}^{(l)}(\boldsymbol{x})$ with a corresponding denoised estimate, i.e., at a given iteration i with an image-update $\boldsymbol{x}^{(i)}$, we set

$$\boldsymbol{f}_{\boldsymbol{\theta}_l}^{(l)}(\boldsymbol{x}) \approx \boldsymbol{d}_l^{(i)} \stackrel{\text{def}}{=} \boldsymbol{f}_{\boldsymbol{\theta}_l}^{(l)}(\boldsymbol{x}^{(i)}),\ l = 1, \ldots, L. \tag{2}$$

Using (2), we end up with the following sequence of iterations:

$$\boldsymbol{x}^{(i+1)} \stackrel{\text{def}}{=} \arg\min_{\boldsymbol{x}\in\boldsymbol{\Omega}} \frac{1}{2}\|\boldsymbol{y} - \boldsymbol{A}\boldsymbol{x}\|_{\boldsymbol{W}}^2 \text{ s.t. } \|\boldsymbol{x} - \boldsymbol{d}_l^{(i)}\|_2^2 \leq \varepsilon_l^2, \tag{3}$$

$l = 1, \ldots, L$. The iteration in (3) is similar to one-step late [4] and alternating minimization [5] approaches. The accuracy of (2) depends on how well $\{\boldsymbol{f}_{\boldsymbol{\theta}_l}^{(l)}\}_{l=1}^{L}$ remove noise and artifacts, while driving the reconstruction close to the true solution in (1). This in turn depends on proper choice of the denoisers' parameter-vectors $\{\boldsymbol{\theta}_l\}_{l=1}^{L}$.

While (3) is a quadratic problem with an analytic solution, such a solution is hard to implement in practice due to the large sizes of $\boldsymbol{y}$ and $\boldsymbol{x}$. So we resort to the separable-quadratic-surrogate (SQS) approach [6] that majorizes the data-fidelity term in (3) leading to

$$\begin{aligned}\boldsymbol{x}^{(i+1)} \stackrel{\text{def}}{=}\ & \arg\min_{\boldsymbol{x}\in\boldsymbol{\Omega}} \boldsymbol{x}'\boldsymbol{A}'\boldsymbol{W}(\boldsymbol{A}\boldsymbol{x}^{(i)} - \boldsymbol{y}) + \frac{1}{2}\|\boldsymbol{x} - \boldsymbol{x}^{(i)}\|_{\boldsymbol{D}}^2 \\ & \text{s.t. } \|\boldsymbol{x} - \boldsymbol{d}_l^{(i)}\|_2^2 \leq \varepsilon_l^2, l = 1, \ldots, L,\end{aligned} \tag{4}$$

where $\boldsymbol{D} \stackrel{\text{def}}{=} \text{diag}\{\boldsymbol{A}'\boldsymbol{W}\boldsymbol{A}\boldsymbol{1}_n\}$ is a diagonal matrix that satisfies $\boldsymbol{D} \succeq \boldsymbol{A}'\boldsymbol{W}\boldsymbol{A}$ [6] and $\boldsymbol{1}_n$ is $n \times 1$ vector of ones. Due to $\boldsymbol{D}$, (4) can be easily solved and implemented in practice leading to the following algorithm.

Algorithm 1: **Denoising-based SQS (DSQS)**

1) Initial estimate: $\boldsymbol{x}^{(0)}$; $\boldsymbol{d}_l^{(0)} = \boldsymbol{f}_{\boldsymbol{\theta}_l}^{(l)}(\boldsymbol{x}^{(0)})$, $l = 1, \ldots, L$.
2) Repeat Steps 3-5 for $i = 0, 1, \ldots$
3) Gradient-descent-type update:
$$\boldsymbol{u}^{(i)} \stackrel{\text{def}}{=} \boldsymbol{x}^{(i)} - \boldsymbol{D}^{-1}\boldsymbol{A}'\boldsymbol{W}(\boldsymbol{A}\boldsymbol{x}^{(i)} - \boldsymbol{y}). \tag{5}$$
4) Image-update:
$$\boldsymbol{x}^{(i+1)} = \mathcal{P}_{\boldsymbol{\Omega}}\left\{\begin{array}{l}(\boldsymbol{I}_n + \beta\boldsymbol{D}^{-1})^{-1}\boldsymbol{u}^{(i)} + \\ (\boldsymbol{D} + \beta\boldsymbol{I}_n)^{-1}\sum_{l=1}^{L}\lambda_l(\varepsilon_l)\,\boldsymbol{d}_l^{(i)}\end{array}\right\}, \tag{6}$$
where $\boldsymbol{I}_n$ is the identity matrix of size n, $\mathcal{P}_{\boldsymbol{\Omega}}$ denotes orthogonal projection onto $\boldsymbol{\Omega}$, $\beta \stackrel{\text{def}}{=} \sum_{l=1}^{L}\lambda_l(\varepsilon_l)$, $\{\lambda_l(\varepsilon_l) \geq 0\}_{l=1}^{L}$ are Lagrange multipliers such that $\lambda_l(\varepsilon_l) \to \infty$ as $\varepsilon_l \to 0$, $l = 1, \ldots, L$.
5) Denoised-updates: $\boldsymbol{d}_l^{(i+1)} = \boldsymbol{f}_{\boldsymbol{\theta}_l}^{(l)}(\boldsymbol{x}^{(i+1)})$, $l = 1, \ldots, L$.

In practice, it is usually simpler to directly specify meaningful values for λ_l rather than derive them for given $\{\varepsilon_l\}_{l=1}^{L}$. For $L = 1$, the above algorithm is similar to the ones in [4], [5], with (ignoring the index l) $f_{\boldsymbol{\theta}} \equiv$ NLM or DL, respectively.

IV. Gradient-Descent-Denoising (GDD)

In the case of a single denoiser ($L = 1$, ignoring the index l), instead of evaluating $\boldsymbol{f}_{\boldsymbol{\theta}}$ at $\boldsymbol{x}^{(i)}$ in (2), evaluating it at $\boldsymbol{u}^{(i)}$ (5) and setting $\lambda \to \infty$ in (6), we obtain a simple iterative gradient-descent-denoising (GDD) algorithm.

Algorithm 2: **Gradient-descent-denoising (GDD)**

1) Initial estimate: $\boldsymbol{x}^{(0)}$.
2) $\boldsymbol{x}^{(i+1)} = \mathcal{P}_{\boldsymbol{\Omega}}\left\{\boldsymbol{f}_{\boldsymbol{\theta}}\left(\boldsymbol{x}^{(i)} - \boldsymbol{D}^{-1}\boldsymbol{A}'\boldsymbol{W}[\boldsymbol{A}\boldsymbol{x}^{(i)} - \boldsymbol{y}]\right)\right\}$, $i = 0, 1, 2, \ldots$

GDD is similar in form to IST algorithms in image-processing literature [9], but can accommodate a variety of denoisers $\boldsymbol{f}_{\boldsymbol{\theta}}$. Both DSQS and GDD need a proper selection of $\boldsymbol{\theta}$, but unlike DSQS, GDD does not require selection of λ.

V. Acceleration

Similar to Kim *et al.* [3], we combine OS [6] and MOM [7], [11] methods for acceleration of DSQS and GDD above. Specifically, we use the MOM-version in [11, Alg. FGM2] that is simpler than [7, Eq. (3.11)] to obtain the following OS-MOM-version of DSQS. In the sequel, we omit writing ε_l in $\lambda_l(\varepsilon_l)$. Let S denote the total number of subsets and $\boldsymbol{A}_s$, $\boldsymbol{W}_s$ and $\boldsymbol{y}_s$ correspond to the sth subset.

Algorithm 3: **DSQS with OS-MOM (DSQS-OS-MOM)**

1) Initial estimate: $\boldsymbol{x}^{(0)}$; Set $\boldsymbol{a}^{(0)} = \boldsymbol{z}^{(0)} = \boldsymbol{x}^{(0)}$; $t^{(0)} = 1$; $\boldsymbol{d}_l^{(0)} = \boldsymbol{f}_{\boldsymbol{\theta}_l}^{(l)}(\boldsymbol{x}^{(0)})$, $l = 1, \ldots, L$.
2) Repeat Steps 3-10 for $i = 0, 1, \ldots$
3) For each i repeat Steps 4-10 for $s = 0, \ldots, S-1$.
4) $j \stackrel{\text{def}}{=} i + s/S$; $\quad k \stackrel{\text{def}}{=} j + 1/S$.
5) $\boldsymbol{g}^{(j)} \stackrel{\text{def}}{=} S\,\boldsymbol{A}_s'\boldsymbol{W}_s(\boldsymbol{A}_s\boldsymbol{a}^{(j)} - \boldsymbol{y}_s) + \sum_{l=1}^{L}\lambda_l(\boldsymbol{x}^{(j)} - \boldsymbol{d}^{(j)})$.
6) $\boldsymbol{x}^{(k)} = \mathcal{P}_{\boldsymbol{\Omega}}\left\{\boldsymbol{x}^{(j)} - (\boldsymbol{D} + \beta\boldsymbol{I}_n)^{-1}\boldsymbol{g}^{(j)}\right\}$.
7) $\boldsymbol{z}^{(k)} = \mathcal{P}_{\boldsymbol{\Omega}}\left\{\boldsymbol{z}^{(j)} - t^{(j)}(\boldsymbol{D} + \beta\boldsymbol{I}_n)^{-1}\boldsymbol{g}^{(j)}\right\}$.
8) $t^{(k)} = (1 + \sqrt{1 + 4[t^{(j)}]^2})/2$.
9) $\boldsymbol{a}^{(k)} = (t^{(k)} - 1)/t^{(k)}\boldsymbol{x}^{(k)} + \boldsymbol{z}^{(k)}/t^{(k)}$.
10) $\boldsymbol{d}_l^{(k)} = \boldsymbol{f}_{\boldsymbol{\theta}_l}^{(l)}(\boldsymbol{a}^{(k)})$, $l = 1, \ldots, L$.

The above version of DSQS-OS-MOM requires only one gradient evaluation of the data-fidelity term (inside $\boldsymbol{g}^{(\cdot)}$) and one evaluation of all denoisers per subset iteration. Given $\boldsymbol{g}^{(\cdot)}$ and the denoised-estimates $\boldsymbol{d}_l^{(\cdot)}$, the updates of $\boldsymbol{x}^{(\cdot)}$ and the auxiliary variable $\boldsymbol{z}^{(\cdot)}$ are computationally trivial. For GDD in Sec. IV, we arrive at the following GDD-OS-MOM algorithm based on [8, Alg. 1].

Algorithm 4: **GDD with OS-MOM (GDD-OS-MOM)**

1) Initial estimate: $\boldsymbol{x}^{(0)}$; Set $\boldsymbol{a}^{(0)} = \boldsymbol{z}^{(0)} = \boldsymbol{x}^{(0)}$; $t^{(0)} = 1$.
2) Repeat Steps 3-9 for $i = 0, 1, \ldots$
3) For each i repeat Steps 4-9 for $s = 0, \ldots, S-1$.
4) $j \overset{\text{def}}{=} i + s/S; \quad k \overset{\text{def}}{=} j + 1/S.$
5) $\boldsymbol{g}^{(j)} \overset{\text{def}}{=} S\, \boldsymbol{A}_s' \boldsymbol{W}_s (\boldsymbol{A}_s \boldsymbol{a}^{(j)} - \boldsymbol{y}_s).$
6) $\boldsymbol{x}^{(k)} = \mathcal{P}_{\boldsymbol{\Omega}} \left\{ \boldsymbol{f}_{\boldsymbol{\theta}} \left(\boldsymbol{x}^{(j)} - \boldsymbol{D}^{-1} \boldsymbol{g}^{(j)} \right) \right\}.$
7) $\boldsymbol{z}^{(k)} = \mathcal{P}_{\boldsymbol{\Omega}} \left\{ \boldsymbol{f}_{\boldsymbol{\theta}} \left(\boldsymbol{z}^{(j)} - t^{(j)} \boldsymbol{D}^{-1} \boldsymbol{g}^{(j)} \right) \right\}.$
8) $t^{(k)} = (1 + \sqrt{1 + 4[t^{(j)}]^2})/2.$
9) $\boldsymbol{a}^{(k)} = (t^{(k)} - 1)/t^{(k)} \boldsymbol{x}^{(k)} + \boldsymbol{z}^{(k)}/t^{(k)}.$

GDD-OS-MOM also requires only one gradient evaluation, $\boldsymbol{g}^{(\cdot)}$, of the data-fidelity term, but unlike DSQS-OS-MOM, GDD-OS-MOM needs two evaluations of the denoiser $\boldsymbol{f}_{\boldsymbol{\theta}}$.

VI. Practical Implementation

If the denoisers are computation-intensive (e.g., NLM or DL), obtaining $\boldsymbol{d}_l^{(\cdot)}$ in Step 11 of DSQS-OS-MOM or $\boldsymbol{x}^{(\cdot)}$ and $\boldsymbol{z}^{(\cdot)}$ in Steps 7-8 of GDD-OS-MOM for every subset can increase compute time. To mitigate this, we can use the following approximation-strategy:

(a) in DSQS-OS-MOM, computation-intensive denoisers (e.g., NLM, DL) can update corresponding $\boldsymbol{d}^{(k)}$ when k is an integer (i.e., every outer i-iteration), while simple denoisers (e.g., wavelet-thresholding) can still update corresponding $\boldsymbol{d}^{(k)}\ \forall\ k$,

(b) in GDD-OS-MOM, we can use a simple denoiser $\boldsymbol{f}_{\boldsymbol{\theta}_1}^{(1)}$ (e.g., wavelet-thresholding) $\forall\ k$ (every subset iteration), and update $\boldsymbol{a}^{(k)} \leftarrow \boldsymbol{f}_{\boldsymbol{\theta}_2}^{(2)}(\boldsymbol{a}^{(k)})$ after Step 9 using a computation-intensive denoiser $\boldsymbol{f}_{\boldsymbol{\theta}_2}^{(2)}$ whenever k is an integer (every outer i iteration).

These strategies ensure that $\boldsymbol{x}^{(k)}$ and $\boldsymbol{z}^{(k)}$ in both DSQS-OS-MOM and GDD-OS-MOM still use a contribution from simple-denoisers at every k, thus improving image-quality at every subset iteration.

Combining OS with MOM can lead to an unstable behavior of DSQS-OS-MOM and GDD-OS-MOM similar to that reported in [3]. One can adapt the relaxation strategies in [3, Sec. V-B] or dynamically adjust the number of subsets with iterations to circumvent this problem. Here, we use the simpler strategy of resetting $t^{(\cdot)} \leftarrow 1$ and $\boldsymbol{z}^{(\cdot)} \leftarrow \boldsymbol{x}^{(\cdot)}$ whenever $t^{(\cdot)} > t_{\text{thresh}}$.

VII. Experimental Results

For conciseness, we present results only for GDD-based algorithms. We implemented GDD (Algorithm 2), GDD-OS (GDD with OS only), GDD-MOM (GDD with MOM only), and GDD-OS-MOM (Algorithm 4) in Matlab. We set $t_{\text{thresh}} = 30$ for OS-MOM-resetting discussed in Sec. VI. We used FBP reconstruction as $\boldsymbol{x}^{(0)}$ and ran our experiments on a computer with 6-core Intel Xeon X5650 2.67 GHz processor and 24 GB RAM.

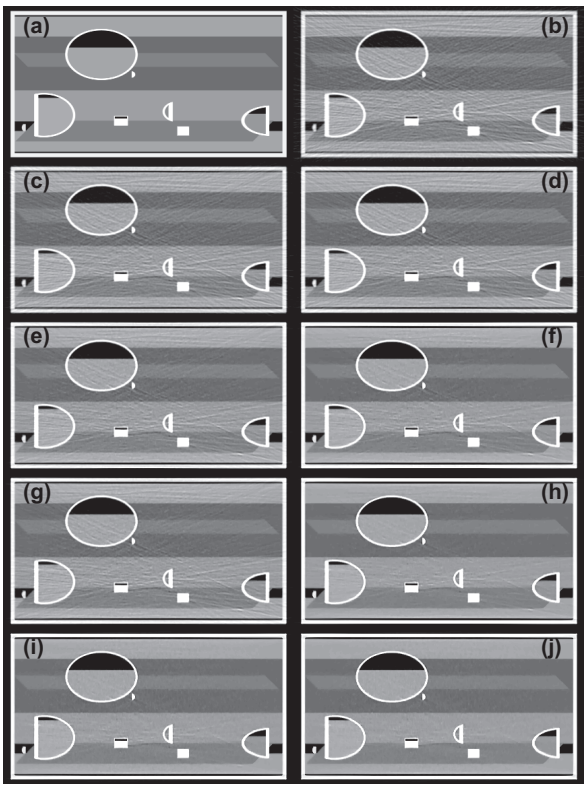

Fig. 1: Mid-slice of the reconstructed volumes on $[0,\ 0.03]$ mm^{-1} display-window from experiment with CatSim data. GDD-based algorithms were run for a total of 600 and 1200 seconds. Corresponding iteration numbers are indicated. (a) Noise-free ground-truth at 90 keV; (b) FBP; (c-d) GDD after 44 and 88 iterations; (e-f) GDD-OS after 15 and 30 iterations; (g-h) GDD-MOM after 39 and 78 iterations; (i-j) GDD-OS-MOM after 10 and 20 iterations.

A. CatSim Data

First, we compare GDD, GDD-OS, GDD-MOM, and GDD-OS-MOM by running them for a fixed CPU-run-time and rank image-quality of the respective results. Using CatSim [12], we simulated axial noisy data (910 columns $\times$ 16 rows $\times$ 900 views) corresponding to a $45 \times 21 \times 50$ cm^3 analytic phantom (containing different materials) at 90 keV (monochromatic source) and 100 mA tube-current. We used 14 subsets for the OS-based methods and set $\boldsymbol{f}_{\boldsymbol{\theta}_1}^{1} \equiv$ soft-thresholding of the coefficients of one level of the 2D Haar frame applied on the axial, sagittal and coronal slices as the denoiser (with fixed threshold-strength $\boldsymbol{\theta}_1$) and reconstructed image-volumes (of size $512 \times 512 \times 26$) using each GDD-version above.

Reconstruction results in Fig. 1 indicate that GDD-OS-MOM is able to reduce noise and streaks earlier than any of its other variations. For instance, GDD-OS-MOM at 600 seconds (Fig. 1i) has lesser streaks compared to GDD, GDD-OS and GDD-MOM at 1200 seconds (Figs. 1d, 1f, 1h, respectively). These results are indicative of the acceleration provided by combining OS-MOM with GDD.

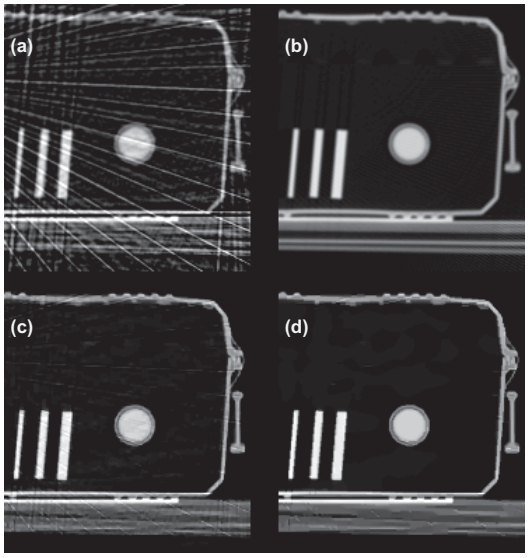

Fig. 2: Reconstruction results on $[0,\, 0.025]$ mm^{-1} display-window for real CT scanner data. Only a part of the field-of-view is shown. (a) FBP result from $10\times$ downsampled-views; (b) FBP result from all views; (c) GDD-OS-MOM with Haar-denoiser (20 iterations; 68 seconds); (d) GDD-OS-MOM with Haar- and NLM-denoisers (20 iterations; 498 seconds).

B. Real Scanner Data

Here, we compare two versions of GDD-OS-MOM: one that uses only the Haar-denoiser above and another that uses both Haar- and NLM-denoisers (using the strategy in Sec. VI). For this, we considered a 2D dataset obtained using a Morpho Detection Inc. CTX 5500 scanner and reconstructed images (of size 512×512) from a retrospectively reduced set of views ($10\times$ reduction) by running 20 iterations (with 8 subset-iterations each) of GDD-OS-MOM with Haar-denoiser and GDD-OS-MOM with Haar- and NLM-denoisers. We used the Matlab implementation of NLM provided by Kroon [13].

Fig. 2 compares reconstruction results for this experiment. Both versions of GDD-OS-MOM (Figs. 2c-2d) provide improvement over FBP obtained from reduced set of views (Fig. 2a). The GDD-OS-MOM images are not only comparable to, but also provide a slight resolution boost (e.g., around the circular region and along the boundary of the box) over FBP from the full set of acquired views (Fig. 2b). Although GDD-OS-MOM with Haar- and NLM-denoisers (Fig. 2d) takes more algorithm-run time, it provides a further reduction in streaks compared to GDD-OS-MOM with only Haar-denoiser (Fig. 2c) indicating the potential of NLM [4].

VIII. Discussion

In this paper, we proposed an MBIR-framework that subsumes existing NLM- and DL-based MBIR approaches [4], [5] for X-ray CT reconstruction by using general-denoising-based image-priors. We derived two iterative algorithms (DSQS in Sec. III and GDD in Sec. IV) that (approximately) solve the proposed denoised-based MBIR problem in (1). We also presented schemes for accelerating DSQS and GDD by combining them with ordered subsets (OS) and momentum (MOM) techniques [3] leading to DSQS-OS-MOM and GDD-OS-MOM versions. The proposed algorithms can handle arbitrary denoisers and are thus attractive for low-dose and sparse-view reconstructions, which can benefit from sophisticated denoisers. Using numerical experiments, we demonstrated the working of GDD-OS-MOM with Haar-frame- and NLM-based denoisers.

We are currently investigating the (empirical) convergence behaviors of DSQS and GDD in terms of solving (1) or arriving at a fixed-point solution. We are also focusing on making their OS-MOM versions *stable* (e.g., by means of relaxation [3] or by using a conservative MOM-step-size parameter $t^{(\cdot)}$) for obtaining practically viable reconstruction quality. Acceleration of the proposed methods using optimal gradients [11] and combining them with message-passing-type schemes [10] are also interesting directions for future research.

References

[1] J. A. Fessler, "Statistical image reconstruction methods for transmission tomography," in *Handbook of Medical Imaging, Vol. 2*, J. M. Fritzpatrick and M. Sonka, Eds. Bellingham: SPIE Press, 2000, ch. 1, pp. 1–70.

[2] J. B. Thibault, K. D. Sauer, C. A. Bouman, and J. Hsieh, "A three-dimensional statistical approach to improved image quality for multislice helical ct," *Med. Phys.*, vol. 34, no. 11, pp. 4526–44, Nov. 2007.

[3] D. Kim, S. Ramani, and J. A. Fessler, "Combining ordered subsets and momentum for accelerated X-ray CT image reconstruction," *IEEE Trans. Med. Imag.*, vol. 34, no. 1, pp. 167–78, 2015.

[4] H. Zhang, J. Ma, J. Wang, Y. Liu, H. Lu, and Z. Liang, "Statistical image reconstruction for low-dose CT using nonlocal means-based regularization," *Comput. Med. Imag. Graph.*, vol. 38, no. 6, pp. 423–35, 2014.

[5] Q. Xu, H. Yu, X. Mou, L. Zhang, J. Hsieh, and G. Wang, "Low-dose X-ray CT reconstruction via dictionary learning," *IEEE Trans. Med. Imag.*, vol. 31, no. 9, pp. 1682–97, Sept. 2012.

[6] H. Erdogan and J. A. Fessler, "Ordered subsets algorithms for transmission tomography," *Phys. Med. Biol.*, vol. 44, no. 11, pp. 2835–51, 1999.

[7] Y. Nesterov, "Smooth minimization of nonsmooth functions," *Math. Prog.*, vol. 103, pp. 127–52, 2005.

[8] P. Tseng, "On accelerated proximal gradient methods for convex-concave optimization," *[Online] Available: http://pages.cs.wisc.edu/~brecht/cs726docs/Tseng.APG.pdf*, 2008.

[9] M. A. T. Figueiredo and R. D. Nowak, "An EM algorithm for wavelet-based image restoration," *IEEE Trans. Img. Proc.*, vol. 12, no. 8, pp. 906–16, Aug. 2003.

[10] C. A. Metzler, A. Maleki, and R. G. Baraniuk, "From denoising to compressed sensing," *arXiv:1406.4175, http://arxiv.org/abs/1406.4175*, 2014.

[11] D. Kim and J. A. Fessler, "Optimized first-order methods for smooth convex minimization," *Math. Prog.*, pp. 1–27, 2015.

[12] B. De Man, S. Basu, N. Chandra, B. Dunham, P. Edic, M. Iatrou, S. McOlash, P. Sainath, C. Shaughnessy, B. Tower, and E. Williams, "CatSim: a new computer assisted tomography simulation environment," in *Proc. SPIE 6510, Medical Imaging 2007: Physics of Medical Imaging*, J. Hsieh and M. J. Flynn, Eds., Mar. 2007, p. 65102G.

[13] D. J. Kroon, "Fast non-local 1D, 2D color, and 3D," *Matlab Central: http://www.mathworks.com/matlabcentral/fileexchange/27395-fast-non-local-means-1d-2d-color-and-3d/content/NLMF.m*, 28 Apr. 2010.

Modeling Mixed Poisson-Gaussian Noise in Statistical Image Reconstruction for X-Ray CT

Qiaoqiao Ding, Yong Long, Xiaoqun Zhang and Jeffrey A. Fessler

***Abstract*—Statistical image reconstruction (SIR) methods for X-ray CT improve the ability to produce high-quality and accurate images, while greatly reducing patient exposure to radiation. The challenge with further dose reduction to an ultra-low level by lowering the X-ray tube current is photon starvation and electronic noise starts to dominate. This introduces negative or zero values into the raw data and consequently causes artifacts in the reconstructed CT images with current SIR methods based on log data. At ultra-low photon counts, the CT detector signal deviates significantly from Poisson or shifted Poisson statistics for the pre-log data and from Gaussian statistics for post-log data. This paper proposes a novel SIR method called MPG (mixed Poisson-Gaussian). It models the raw noisy measurements using a mixed Poisson-Gaussian distribution that accounts for the electronic noise. The MPG method is able to directly use the negative and zero values in the raw data without any pre-processing. We adopt the reweighted least square method to develop a tractable likelihood function that can be easily incorporated into SIR reconstruction framework. To minimize the MPG cost function containing the likelihood function and an edge-preserving regularization term, we use an Alternating Direction Method of Multipliers (ADMM) that divides the o-riginal optimization problem into several sub-problems that are easier to solve. Our results on 3D simulated cone-beam data set indicate that the proposed MPG method reduces noise in the reconstructed images comparing with the conventional FBP and statistical penalized weighted least-square (PWLS) method for ultra-low dose CT (ULDCT) imaging.**

I. Introduction

X-Ray Computed Tomography (CT) provides high-resolution images of anatomical structures for diagnosis and management of human diseases and disorders. For example, CT has had a tremendous impact on cancer. Studies have suggested that current CT usage may be responsible for 1.5%-2% of all cancers in the U.S. [1]. Significantly lowering radiation dosages from CT has become a growing concern both in the public and professional societies. Ultra-low dose CT (ULDCT) scans that still provide suitable image quality could shift CT scans further to the benefit side and open up numerous entirely new clinical applications.

CT image reconstruction method improvements that could realistically and significantly reduce patient radiation exposure while maintaining high image quality is an important area of research to achieve low dose CT imaging. Statistical image reconstruction (SIR) methods [2] improve the ability to produce high-quality and accurate images, while greatly reducing patient exposure to radiation. The challenge with further dose reduction to an ultra-low level by reducing the number of projection views is the aliasing artifacts due to under-sampled sinograms when the number of views is too small [3]. An alternative approach is to lower the X-ray tube current, but this causes photon starvation and electronic noise starts to denominate [4]. This approach introduces negative or zero values into the raw data and consequently causes artifacts in the reconstructed CT images with current data processing methods [5] based on log sinogram data.

The measurement statistical models in most SIR methods assume standard or shifted Poisson statistics for the pre-log data or Gaussian distributions for the post-log data. At ultra-low photon counts, the CT measurements deviate significantly from Poisson or Gaussian statistics. For ULDCT imaging the logarithm simply cannot be used because the raw data have negative or zero values due to the electronic noise in the data acquisition systems (DAS). In [6], the authors substituted the non-positive measurements with a small positive value. Poisson distribution models the number of events which should be non-negative. The shifted Poisson model adds a positive value associated with the variance of electronic noise to the raw data, but the shifted raw data may still be negative or zero for ULDCT imaging. Compound Poisson (CP) distribution [7], [8] that accounts for the polyenergetic X-rays and Poisson light statistics in the scintillator of energy-integrating detector has the potential to accurately model the measurement statistics in ULDCT imaging. However, CP model has a complicated likelihood that impedes direct use in SIR methods and electronic readout noise leads to a distribution that is even more complicated than a CP model.

This paper proposes a new SIR method with a data-fit term associated with the mixed Poisson-Gaussian (MPG) distribution model for CT measurements [9], [10] and the edge-preserving hyperbola regularization. The proposed MPG method is able to directly process negative or zero valued raw data that contain (some, albeit limited) information about the scanned object. We solve the MPG optimation problem using Alternating Direction Method of Multipliers (ADMM, also known as split Bregman method [11]) and its unconstrained subproblems using Conjugate Gradient (CG), Broyden-Fletcher-Goldfarb-Shanno (BFGS).

This paper is organized as follows. Section II mathematically formulates the MPG method for X-ray CT reconstruction as a Penalized-Likelihood (PL) cost function and solves it

Q. Ding (e-mail: dingqiaoqiao@sjtu.edu.cn) and X. Zhang (e-mail: xqzhang@sjtu.edu.cn) are with School of Mathematical Sciences and Institute of Natural Sciences, Shanghai Jiao Tong University. 800, Dongchuan Road, Shanghai, China, 200240

Y. Long (e-mail: yong.long@sjtu.edu.cn) is with the University of Michigan- Shanghai Jiao Tong University Joint Institute, Shanghai Jiao Tong University, 800 Dongchuan Road, Shanghai, China, 200240

J. A. Fessler (e-mail: fessler@umich.edu) is with the Department of Electrical Engineering and Computer Science, University of Michigan, Ann Arbor, MI 48109.

using ADMM. Section III presents numerical experiments and results. Finally, we draw our conclusions in Section IV.

II. Methods

A. Measurement Model

Let y_i denote the number of X-ray photons incident on detector for the ith ray where $i = 1, \cdots, N_d$, and N_d is the number of rays. For a monoenergetic source, we model the number of X-ray photons as :

$$\bar{y}_i = \bar{y}_i(\boldsymbol{x}) \triangleq I_i \exp(-[\boldsymbol{A}\boldsymbol{x}]_i) + r_i \tag{1}$$

where $\boldsymbol{x}$ denotes the attenuation map, and its jth element x_j is the average linear attenuation coefficient in the jth voxel for $j = 1, \cdots, N_p$, where N_p denotes the number of voxels. $\boldsymbol{A}$ is the $N_d \times N_p$ system matrix with entries a_{ij}, and $[\boldsymbol{A}\boldsymbol{x}]_i = \sum_{j=1}^{N_p} a_{ij} x_j$ denotes the line integral of the attenuation map $\boldsymbol{x}$ along the ith X-ray. We treat each I_i and r_i as known nonnegative quantities, where r_i is ensemble mean of background signals such as Compton, scatter and dark current, and I_i is the incident X-ray intensity incorporating X-ray source illumination and the detector gain. Although the measurement model in (1) ignores beam-hardening effects [12], [13], polyenergetic measurement models that account for the source spectrum and energy-dependent attenuation will be employed in our future work.

For the case of normal clinical exposures, the X-ray CT measurements z_i are often modeled as the sum of a Poisson distribution representing photon-counting statistics (1) and an independent Gaussian distribution representing additive electronic noise:

$$z_i = k y_i + y_e \tag{2}$$

where $y_i \sim \text{Poisson}(\bar{y}_i(\boldsymbol{x}))$ and $y_e \sim \text{N}(0, \sigma^2)$, k is a scalar factor modeling the conversion gain from X-ray photons to electrons and σ denotes the standard deviation of electronic noise.

B. Penalized Weighted Least Square for Poisson-Gaussian Mixed Noise

We adopt the reweighted least square method [10] to develop a tractable likelihood function for the mixed Poisson-Gaussian measurement statistical model. Given $\bar{y}_i$, Assuming y_i and y_e are independent, we have

$$\text{E}[z_i] = k\text{E}[y_i] = k\bar{y}_i$$

and

$$\text{Var}[z_i] = k^2\text{Var}[y_i] + \text{Var}[y_e] = k^2\bar{y}_i + \sigma^2$$

We approximate z_i with normal distribution, i.e., $z_i \sim N(k\bar{y}_i, k^2\bar{y}_i + \sigma^2)$, i.e., the Probability Density Function (PDF) of z_i is

$$P(z_i; \boldsymbol{x}) = \frac{1}{\sqrt{2\pi(k^2\bar{y}_i(\boldsymbol{x}) + \sigma^2)}} e^{-\frac{(z_i - k\bar{y}_i(\boldsymbol{x}))^2}{2(k^2\bar{y}_i(\boldsymbol{x}) + \sigma^2)}} \tag{3}$$

The corresponding approximate negative log-likelihood for independent measurements z_i has the form

$$\bar{L}(\boldsymbol{x}) = -\sum_{i=1}^{N_d} \log(P(z_i; \boldsymbol{x})) \equiv \frac{1}{2}\|\boldsymbol{z} - k\bar{\boldsymbol{y}}(\boldsymbol{x})\|^2_{\boldsymbol{W}(\boldsymbol{x})} + \frac{1}{2}\langle \log(k^2\bar{\boldsymbol{y}}(\boldsymbol{x}) + \boldsymbol{\sigma}^2), \boldsymbol{1}\rangle, \tag{4}$$

where $\equiv$ means "equal to within irrelevant constants independent of $\boldsymbol{x}$", the diagonal weight matrix $\boldsymbol{W}(\boldsymbol{x})$ is

$$\boldsymbol{W}(\boldsymbol{x}) = \text{diag}\left\{\frac{1}{k^2\bar{y}_i(\boldsymbol{x}) + \sigma^2}\right\}, \tag{5}$$

$\boldsymbol{z} \in \mathbb{R}^{N_d}$ and $\bar{\boldsymbol{y}}(\boldsymbol{x}) \in \mathbb{R}^{N_d}$ have elements of z_i and $\bar{y}_i(\boldsymbol{x})$ respectively, $\boldsymbol{\sigma}^2 \in \mathbb{R}^{N_d}$ and $\boldsymbol{1} \in \mathbb{R}^{N_d}$have every element equal to σ^2 and 1 respectively, and $\langle \cdot, \cdot \rangle$ is inner product. $\log(\cdot)$ is pointwise operation. We estimate the attenuation map $\boldsymbol{x}$ from the noisy measurements $\boldsymbol{z}$ by minimizing a Penalized-Likelihood (PL) cost function as follows:

$$\hat{\boldsymbol{x}} = \arg\min_{\boldsymbol{x}} \Psi(\boldsymbol{x}) \tag{6}$$

$$\Psi(\boldsymbol{x}) \triangleq \bar{L}(\boldsymbol{x}) + R(\boldsymbol{x}). \tag{7}$$

The regularization term $R(\boldsymbol{x})$ is

$$R(\boldsymbol{x}) = \lambda \sum_{i=1}^{N_r} \beta_r \psi_r([\boldsymbol{C}\boldsymbol{x}]_r), \tag{8}$$

where the regularization parameter λ controls the noise and resolution tradeoff, β_r is the spatial weighting, $\psi_r(\cdot)$ is a potential function, $\boldsymbol{C} \triangleq \{C_{rj}\} \in \mathbb{R}^{N_r \times N_p}$is a sparsifying matrix finite-differencing matrix and $[\boldsymbol{C}\boldsymbol{x}]_r = \sum_{j=1}^{N_p} C_{rj} x_j$. We focus on edge-preserving hyperbola regularization, i.e, $\psi_r(t) = \delta^2(\sqrt{(\frac{t}{\delta})^2 + 1} - 1)$. The regularization term $R(x)$ can be written as $R(x) = \lambda\delta^2(\sqrt{(\frac{\boldsymbol{C}\boldsymbol{x}}{\delta})^2 + 1} - 1)$.

C. Optimization Method

1) Equivalent Optimization Model: Because (6) is hard to solve directly, we introduce auxiliary variables $\boldsymbol{u} \in \mathbb{R}^{N_d}, \boldsymbol{v} \in \mathbb{R}^{N_r}$. Then, we rewrite our problem as the following equivalent constrained problem:

$$\arg\min_{\boldsymbol{x},\boldsymbol{u},\boldsymbol{v}} \frac{1}{2}\left\|\frac{\boldsymbol{z} - kIe^{-\boldsymbol{u}}}{\sqrt{k^2Ie^{-\boldsymbol{u}} + \boldsymbol{\sigma}^2}}\right\|_2^2 + \frac{1}{2}\langle \log(k^2Ie^{-\boldsymbol{u}} + \boldsymbol{\sigma}^2), \boldsymbol{1}\rangle + \lambda\delta^2\left(\sqrt{(\frac{\boldsymbol{v}}{\delta})^2 + 1} - 1\right) \quad \text{s.t.} \quad \boldsymbol{u} = \boldsymbol{A}\boldsymbol{x}, \boldsymbol{v} = \boldsymbol{C}\boldsymbol{x}. \tag{9}$$

In this paper, $e^{(\cdot)}, \log(\cdot), \sqrt{\cdot}$ and division are all pointwise operation. We rewrite (9) as

$$\arg\min_{\boldsymbol{x},\boldsymbol{s}} f(\boldsymbol{s}) \quad \text{s.t.} \quad \boldsymbol{s} := \boldsymbol{P}\boldsymbol{x} \tag{10}$$

where $\boldsymbol{s} \triangleq (\boldsymbol{u}, \boldsymbol{v})^T$, $\boldsymbol{P} \triangleq (\boldsymbol{A}, \boldsymbol{C})^T$.

2) Alternating Direction Method of Multipliers: To solve the optimzation problem in (10), we use Alternating Direction Method of Multipliers (ADMM). Given $\boldsymbol{x}^{(0)}, \boldsymbol{s}^{(0)}$ and $\boldsymbol{b}^{(0)}$ ADMM updates the sequence $(\boldsymbol{x}^{(j)}, \boldsymbol{s}^{(j)}, \boldsymbol{b}^{(j)})$ by

$$\boldsymbol{x}^{(j+1)} = \arg\min_{\boldsymbol{x}} \langle \boldsymbol{b}^{(j)}, \boldsymbol{P}\boldsymbol{x} - \boldsymbol{s}^{j} \rangle + \frac{\mu}{2} \|\boldsymbol{P}\boldsymbol{x} - \boldsymbol{s}^{j}\|_2^2, \quad (11)$$

$$\boldsymbol{s}^{(j+1)} = \arg\min_{\boldsymbol{s}} f(\boldsymbol{s}) + \langle \boldsymbol{b}^{(j)}, \boldsymbol{P}\boldsymbol{x}^{(j+1)} - \boldsymbol{s} \rangle + \frac{\mu}{2} \|\boldsymbol{P}\boldsymbol{x}^{(j+1)} - \boldsymbol{s}\|_2^2, \quad (12)$$

$$\boldsymbol{b}^{(j+1)} = \boldsymbol{b}^{(j)} + \mu(\boldsymbol{P}\boldsymbol{x}^{(j+1)} - \boldsymbol{s}^{(j+1)}). \quad (13)$$

where $\mu > 0$ is the penalty parameter and $\boldsymbol{b} = (\boldsymbol{b}_1, \boldsymbol{b}_2)^T$, $\boldsymbol{b}_1 \in \mathbb{R}^{N_d}, \boldsymbol{b}_2 \in \mathbb{R}^{N_r}$ have the same size as $\boldsymbol{A}\boldsymbol{x}, \boldsymbol{C}\boldsymbol{x}$ respectively. Note that we can also select a vector $\boldsymbol{\mu} = (\mu_1, \mu_2)$ for the two quadratic penalty constraints.

3) Algorithm: Firstly, we solve (11) to obtain $\boldsymbol{x}^{(j+1)}$. Since (11) is quadratic and differentiable on $\boldsymbol{x}$, so we solve it analytically, i.e.,

$$\boldsymbol{x}^{(j+1)*} = \boldsymbol{G}^{-1}\left[\mu_1 \boldsymbol{A}^\top(\boldsymbol{u}^{(j)} - \boldsymbol{b}_1^{(j)}) + \mu_2 \boldsymbol{C}^\top(\boldsymbol{v}^{(j)} - \boldsymbol{b}_2^{(j)})\right] \quad (14)$$

where $\boldsymbol{x}^{(j+1)*}$ represents the exact solution and $\boldsymbol{G} = \mu_1 \boldsymbol{A}^\top \boldsymbol{A} + \mu_2 \boldsymbol{C}^\top \boldsymbol{C}$ is nonsingular because because $A^\top A$ and $C^\top C$ have disjoint null space [14]. Although (14) is an exact analytical solution, it is impractical to store and invert it exactly due to its huge size for CT reconstruction. This step (14) can be solved by CG method and we obtain an approximate update $\boldsymbol{x}^{(j+1)}$.

Due to the structure of $f(\boldsymbol{s})$ and $\boldsymbol{P}$, (12) can be solved separately for $\boldsymbol{u}, \boldsymbol{v}$ as follows:

$$\boldsymbol{u}^{(j+1)} = \arg\min_{\boldsymbol{u}} \frac{1}{2} \left\| \frac{\boldsymbol{z} - kIe^{-\boldsymbol{u}}}{\sqrt{k^2 Ie^{-\boldsymbol{u}} + \boldsymbol{\sigma}^2}} \right\|_2^2 + \frac{1}{2}\langle \log(k^2 Ie^{-\boldsymbol{u}} + \boldsymbol{\sigma}^2), \boldsymbol{1} \rangle + \langle \boldsymbol{b}_1^{(j)}, A\boldsymbol{x}^{(j+1)} - \boldsymbol{u} \rangle + \frac{\mu_1}{2} \|A\boldsymbol{x}^{(j+1)} - \boldsymbol{u}\|_2^2, \quad (15)$$

$$\boldsymbol{v}^{(j+1)} = \arg\min_{\boldsymbol{v}} \lambda\delta^2 \left(\sqrt{(\frac{\boldsymbol{v}}{\delta})^2 + 1} - 1\right) + \langle \boldsymbol{b}_2^{(j)}, \boldsymbol{C}\boldsymbol{x}^{(j+1)} - \boldsymbol{v} \rangle + \frac{\mu_2}{2} \|\boldsymbol{C}\boldsymbol{x}^{(j+1)} - \boldsymbol{v}\|_2^2. \quad (16)$$

We can see that $\boldsymbol{u}, \boldsymbol{v}$ can be solved separately and in parallel. Subproblem (15) is smooth, differentiable nonconvex and separable. We apply BFGS to solve the subproblem (15).

Minimization with respect to $\boldsymbol{v}$ in (16) is the proximal operator of the edge-preserving hyperbola function, and we can update v_j separately. The dual variables is updated straightforwardly as (13). Figure 1 summarizes the optimization algorithm of the proposed MPG method.

1. Select $\boldsymbol{x}^{(0)}$, λ, μ and set $j = 0$
2. Set $\boldsymbol{u}^{(0)} = \boldsymbol{A}\boldsymbol{x}^{(0)}$,$\boldsymbol{v}^{(0)} = \boldsymbol{C}\boldsymbol{x}^{(0)}$ and $\boldsymbol{b}^{(0)} = (\boldsymbol{b}_1^{(0)}, \boldsymbol{b}_2^{(0)}) = 0$

Repeat:

3. Obtain $\boldsymbol{x}^{(j+1)}$ by applying CG iterations to (14)
4. Computer $\boldsymbol{u}^{(j+1)}$ by applying BFGS iterations to (15)
5. Computer $\boldsymbol{v}^{(j+1)}$ by (16)
6. Compute $\boldsymbol{b}_1^{(j+1)}$ and $\boldsymbol{b}_2^{(j+1)}$ using (13)
7. Set $j = j + 1$

Until stop criterion is met.

Fig. 1: ADMM for the proposed MPG reconstruction method

III. Results

In this section, we present numerical results for 3-D cone-beam CT reconstruction using simulated Shepp-logan phantom data. We used filtered back projection (FBP) reconstruction that initialized the proposed MPG method and penalized weighted-least square (PWLS) reconstruction with the edge-preserving hyperbola function [15], and compared performance of these three methods.

We used a $512 \times 512 \times 64$ Shepp-logan phantom and numerically generated a $888 \times 64 \times 984$ noisy sinogram with GE LightSpeed cone-beam geometry corresponding to a monoenergetic source with 10^4 incident photons per ray and no background events, i.e, $r_i = 0, i = 1, \cdots \mathbb{N}_d$. We chose 1000 for the scalar factor k [16] modeling the conversion gain from X-ray photons to electrons in (2) and 330^2 for σ^2 [17], the variance of electronic noise. Some elements of the measurements $\boldsymbol{z}$ are negative due to the small value of $I_i = 10^4$ simulating ULDCT imaging. The proposed MPG method can directly use these data in the reconstruction without any pre-processing. FBP and PWLS are post-log methods that need to take logarithm of the measurements $\boldsymbol{z}$. To obtain line integrals $\boldsymbol{A}\boldsymbol{x}$ for FBP and PWLS reconstruction [18], we substituted the non-positive measurement elements with a small positive value, i.e.,

$$\log\left(\frac{kI_i}{\max(z_i - y_N, \varepsilon)}\right). \quad (17)$$

For the weight in PWLS [18], we also set non-positive measurement elements with a small positive value, i.e.,

$$w_i = \frac{\max(z_i - y_N, \varepsilon)^2}{\max(z_i - y_N, \varepsilon) + \sigma^2}. \quad (18)$$

Here, in (17) and (18), ε is a small positive value and $y_N \sim N(0, \sigma^2)$. The matrix $\boldsymbol{C}$ in (8) was set as the gradient operator along three directions for 3D CT images, the regularization parameter λ was set as 2×10^5 to balance the noise and resolution, and the iteration number was 100 to reconstruct the image. Figure 2 shows the true image and the reconstructions by FBP, PWLS and the proposed MPG method. PWLS method decreases noise and removes artifacts from the FBP initialization as expected, while the proposed MPG method further improves image quality.

IV. Discussion and Conclusion

We proposed a novel SIR method, called MPG (mixed Poisson-Gaussian) for ULDCT imaging. MPG method models the noisy measurements using mixed Poisson-Gaussian distribution which accounts for the electronic noise that dominates when the X-ray dose is at an ultra-low level. We used the

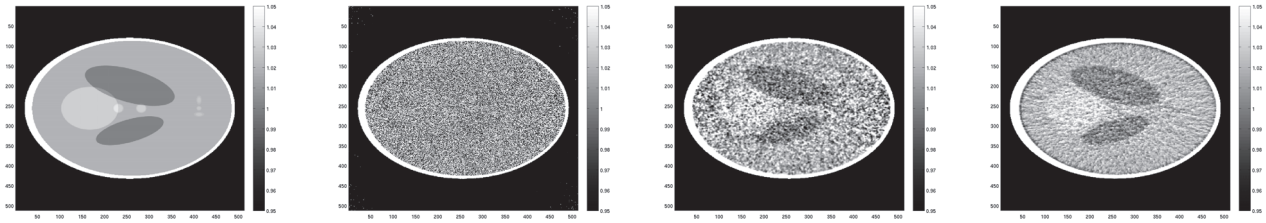

RMS	32.6%	22.3%	15.2%
(a) Ground truth	(b) FBP	(c) PWLS	(d) MPG

Fig. 2: Shepp-Logan phantom reconstructed by FBP, PWLS and the proposed MPG method. (a) Noisefree Shepp-Logan phantom, (b) FBP, (c) PWLS, and (d) Proposed MPG. Images in (b)-(d) have been displayed using the same color scale [as that of (a)]. The second row is the normalized root mean square (RMS) error of the images reconstructed by different method.

reweighted least square method to develop a tractable likelihood function that can be incorporated into SIR reconstruction framework. The proposed MPG method can accommodate edge-preserving hyperbola regularization that preserves edges and can be useful for under-sampled data by reducing the number of views for further dose reduction. We minimize the MPG cost function using ADMM which divides the original optimization problem into several sub-problems that are easier to solve. The proposed MPG method is able to directly use negative and zero values in the raw data without any pre-processing. Preliminary reconstruction results on 3D simulated data set indicate that the proposed MPG method outperforms the conventional FBP and statistical PWLS method.

In future work, we will investigate efficient methods for optimizing subproblem (15) and (16). These two subproblems are a set of 1-D Separable problems that can be solved efficiently by parallel methods. In CT, a nonnegativity constraint is often imposed to model the positivity of the attenuation coefficient that is being reconstructed. We can easily incorporate the nonnegativity constraint in the model (6).

Acknowledgment

This work was finished during a stay of Q. Ding at Germany funded by the China Scholarship Council, whose support is acknowledged. Q. Ding and X. Zhang were partially supported by NSFC (No. 91330102 and GZ1025) and 973 program (No. 2015CB856004). Y. Long was supported in part by SJTU-UM Collaborative Research Program, NSFC (61501292), Shanghai Pujiang Talent Program (15PJ1403900), Returned Overseas Chinese Scholars Program, and SJTU Medicine-Engineering Cross Discipline Program (YG2015QN05).

References

[1] David J Brenner and Eric J Hall, "Computed tomography-an increasing source of radiation exposure," *New England Journal of Medicine*, vol. 357, no. 22, pp. 2277–2284, 2007.

[2] Jean-Baptiste Thibault, Ken D Sauer, Charles A Bouman, and Jiang Hsieh, "A three-dimensional statistical approach to improved image quality for multislice helical CT," *Medical physics*, vol. 34, no. 11, pp. 4526–4544, 2007.

[3] Y Long, L Cheng, X Rui, B De Man, AM Alessio, E Asma, and PE Kinahan, "Analysis of ultra-low dose CT acquisition protocol and reconstruction algorithm combinations for PET attenuation correction," in *Proc. Intl. Mtg. on Fully 3D Image Recon. in Rad. and Nuc. Med*, 2013, pp. 400–3.

[4] Bruce R Whiting, Parinaz Massoumzadeh, Orville A Earl, Joseph A OSullivan, Donald L Snyder, and Jeffrey F Williamson, "Properties of preprocessed sinogram data in X-ray computed tomography," *Medical physics*, vol. 33, no. 9, pp. 3290–3303, 2006.

[5] Johan Nuyts, Bruno De Man, Jeffrey A Fessler, Wojciech Zbijewski, and Freek J Beekman, "Modelling the physics in the iterative reconstruction for transmission computed tomography," *Physics in medicine and biology*, vol. 58, no. 12, pp. R63, 2013.

[6] Jing Wang, Tianfang Li, Hongbing Lu, and Zhengrong Liang, "Penalized weighted least-squares approach to sinogram noise reduction and image reconstruction for low-dose X-ray computed tomography," *Medical Imaging, IEEE Transactions on*, vol. 25, no. 10, pp. 1272–1283, 2006.

[7] Idris A Elbakri and Jeffrey A Fessler, "Efficient and accurate likelihood for iterative image reconstruction in X-ray computed tomography," in *Medical Imaging 2003*. International Society for Optics and Photonics, 2003, pp. 1839–1850.

[8] Patrick J La Rivière, "Monotonic iterative reconstruction algorithms for targeted reconstruction in emission and transmission computed tomography," in *Nuclear Science Symposium Conference Record, 2006. IEEE*. IEEE, 2006, vol. 5, pp. 2924–2928.

[9] Alessandro Foi, Mejdi Trimeche, Vladimir Katkovnik, and Karen Egiazarian, "Practical Poissonian-Gaussian noise modeling and fitting for single-image raw-data," *Image Processing, IEEE Transactions on*, vol. 17, no. 10, pp. 1737–1754, 2008.

[10] Jia Li, Zuowei Shen, Rujie Yin, and Xiaoqun Zhang, "A reweighted L2 method for image restoration with Poisson and mixed Poisson-Gaussian noise," *Inverse Problems and Imaging*, vol. 9, no. 3, 2015.

[11] Tom Goldstein and Stanley Osher, "The split bregman method for L1-regularized problems," *SIAM Journal on Imaging Sciences*, vol. 2, no. 2, pp. 323–343, 2009.

[12] Peter M Joseph and Robin D Spital, "A method for correcting bone induced artifacts in computed tomography scanners.," *Journal of computer assisted tomography*, vol. 2, no. 1, pp. 100–108, 1978.

[13] Idris A Elbakri and Jeffrey A Fessler, "Statistical image reconstruction for polyenergetic X-ray computed tomography," *Medical Imaging, IEEE Transactions on*, vol. 21, no. 2, pp. 89–99, 2002.

[14] Sathish Ramani and Jeffrey A Fessler, "A splitting-based iterative algorithm for accelerated statistical X-ray CT reconstruction," *Medical Imaging, IEEE Transactions on*, vol. 31, no. 3, pp. 677–688, 2012.

[15] Jeffrey A Fessler, "Statistical image reconstruction methods for transmission tomography," *Handbook of medical imaging*, vol. 2, pp. 1–70, 2000.

[16] C.C. Shaw, *Cone Beam Computed Tomography*, Imaging in Medical Diagnosis and Therapy. CRC Press, 2014.

[17] Jingyan Xu and Benjamin MW Tsui, "Electronic noise modeling in statistical iterative reconstruction," *Image Processing, IEEE Transactions on*, vol. 18, no. 6, pp. 1228–1238, 2009.

[18] Adam M. Alessio Paul E. Kinahan Lin Fu, Soo Mee Kim and Bruno De Man, "Comparison between Pre-log and Post-log statistical models in Low-Dose CT iterative reconstruction," *Nuclear Science Symposium and Medical Imaging Conference (NSS/MIC)*, pp. 1–10, 2015.

Auto-tuned Path-based Iterative Reconstruction (aPBIR) for X-ray Computed Tomography

Meng Wu, Andreas Maier, Yan Xia, and Rebecca Fahrig

***Abstract*—Model-based iterative reconstruction (MBIR) techniques have demonstrated many advantages in X-ray CT image reconstruction. The tuning parameter value in MBIR that regulates the strength of the penalty function is critical for achieving good reconstruction results but difficult to choose. The path-based iterative reconstruction (PBIR) method empowered by the path seeking algorithm is capable of efficiently generating a series of MBIR images with different strengths of the penalty function. In this paper, we present an approach to automatically select the tuning parameter value by finding the maximal separation between the noise reduction and the smoothing effects. Simulations shows that the proposed auto-tuned PBIR method produces images that are comparable to the hypothetically "best" MBIR image.**

***Index Terms*—CT, MBIR, Path seeking, PBIR**

I. Introduction

The model-based iterative reconstruction (MBIR) method for 3D computed tomography (CT) has shown potential to improve image quality and reduce radiation dose [1]. The MBIR method is usually formulated in the Bayesian framework as a maximum a posteriori or maximum likelihood problem. However, the prior distribution of the object is unknown, and the maximum likelihood estimator is often ill-posed. A common solution is to add a constraint/regularization to the maximum likelihood model to formulate the penalized maximum likelihood problem. Over last two decades, extensive research has been conducted regarding the most suitable statistical model, penalty function, and acceleration techniques [2]–[4]. Moreover, choosing an appropriate strength of the penalty function, also as known as tuning parameter value, remains as one of the major difficulties of the MBIR method.

In this study, we consider the penalized weighted least-squares (PWLS) algorithm [2]

$$\mu = \underset{\mu \geq 0}{\operatorname{argmin}} \frac{1}{2} \sum_i w_i ([P\mu]_i - l_i)^2 + \beta h(\mu) \tag{1}$$

where P denotes the system matrix for the data acquisition geometry, l_i denotes the logged normalized projection of the ith ray, and w is the least-squares weight to account for the noise level in the X-ray projection data. Function $h(\mu)$ is the penalty function (also known as regularization), μ is the reconstruction image, and β is the tuning parameter that regulates the strength of the penalty function. In this paper, we used the penalized least-squares notation for simplicity

$$\begin{aligned} \text{minimize} \quad & \frac{1}{2}\|A\mu - y\|_2^2 + \beta h(\mu) = g(\mu) + \beta h(\mu) \\ \text{subject to} \quad & \mu \geq 0, \end{aligned} \tag{2}$$

where $A = W^{1/2}P$, $y = W^{1/2}l$, and $g(\mu)$ denotes the least-squares part. W is the diagonal matrix containing w_i. It is well known that the value of the tuning parameter is critical to the reconstruction results [5], [6]. For example, if β is too small, the regularization is not strong enough to suppress noise and artifacts; if β is too big, the image is over blurred and even exhibits patchy behavior. In fact, the values of the tuning parameter (β) produce a series of reconstruction images indexed by β value.

To the best of our knowledge, there is no perfect way to choose the tuning parameter value that would lead to the reconstruction with maximum clinical utility. Instead of focusing on a single optimal tuning parameters, the path-based iteration reconstruction (PBIR) method utilizes path seeking algorithms to efficiently compute the entire reconstruction path that covers all possible tuning parameter values [7], [8]. The PBIR method can provide complete information for a given reconstruction model, but still does not complete the task of finding the optimal tuning parameter. In this paper, we proposed a novel method to automatically select the tuning parameter that maximally separates the denoising and the smoothing effects.

II. Methods

A. Direction-of-gradient path seeking

We first present a path seeking algorithm that uses the direction of one gradient function to constrain the optimization problem thereby encouraging the image to change in the desired direction. For example, if we want to seek the path of increasing strength of the penalty function $h(\mu)$, then we would like to encourage the optimization updates (i.e. gradient descent) to go in the same direction as the $\nabla h(\mu)$. Let us consider adding a linear inequality constraint to the penalized least-squares problem as

$$\begin{aligned} \text{minimize} \quad & g(\mu) + \beta_1 h(\mu) \\ \text{subject to} \quad & \mu \geq 0 \\ & (\mu_j - \hat{\mu}_j) \cdot \nabla_j h(\hat{\mu}) \leq 0 \quad \forall j, \end{aligned} \tag{3}$$

where

$$\hat{\mu} = \underset{\mu \geq 0}{\operatorname{argmin}} \quad g(\mu) + \beta_1 h(\mu). \tag{4}$$

M. Wu, and R. Fahrig are with the Department of Radiology, Stanford University, USA e-mail:mengwu@stanford.edu.

A. Maier and Y. Xia are with Pattern Recognition Lab, Friedrich-Alexander University of Erlangen-Nuremberg, Germany.

TABLE I: Pseudo code for the path seeking algorithm.

Set $\beta = \beta_1$
Reconstruct an image $x = x_{\beta_1}$
For k = 1, 2, 3, ...
1) $s^{(k+1)} = \rho A^T(A\mu^{(k)} - y) + (1-\rho)v^{(k)}$.
2) If recently increase β, use a) otherwise use b).
a) Direction-of-gradient path seeking

$$\mu^{(k+1)} = \text{argmin}\beta h(\mu) + \frac{\rho}{2t}\|\mu - \mu^{(k)} + s^{(k+1)}\|_2^2$$
$$\text{subject to} \quad \mu \geq 0$$
$$(\mu_j - \mu_j^{(k)}) \cdot \nabla_j h(\mu^{(k)}) \leq 0 \quad \forall j$$

b) Standard ADMM step

$$\mu^{(k+1)} = \text{argmin}\beta h(\mu) + \frac{\rho}{2t}\|\mu - \mu^{(k)} + s^{(k+1)}\|_2^2$$
$$\text{subject to} \quad \mu \geq 0$$

3) $v^{(k+1)} = \frac{\rho}{\rho+1}A^T(A\mu^{(k+1)} - y) + \frac{1}{\rho+1}v^{(k)}$
4) If $\|x - x_{\beta_1}\|$ is not increasing, then record x and increase β.
Until $\beta = \beta_2$.

The second linear inequality constraint in Eqn. (3) is inactive because the $\hat{\mu}$ is already optimal for the nonnegative constrained penalized least-squares problem.

If we slightly increase β_1 to β_2 in the direction-of-gradient constrained penalized least-squares problem (3) as

$$\begin{aligned} \text{minimize} \quad & g(\mu) + \beta_2 h(\mu) \\ \text{subject to} \quad & \mu \geq 0 \\ & (\mu_j - \hat{\mu}_j) \cdot \nabla_j h(\hat{\mu}) \leq 0 \quad \forall j \end{aligned} \tag{5}$$

and keep the $\hat{\mu}$ same as in Eqn. (4), the new solution will be suboptimal for the penalized least-squares problem (2) with β_2. But the solution of the problem (3) is still close to the solution of the reconstruction problem because increasing the strength of $h(\mu)$ and the direction-of-gradient constraint have very similar effects. To solve the direction-of-gradient constrained problem (3), we can simply apply a projection onto convex sets (POCS) step [3]. The POCS step will encourage updates of the image that favor minimizing $h(\mu)$, which increases the path seeking efficiency within the optimization framework.

It is not computationally efficient to compute the direction-of-gradient constrained problem (5), which only gives an approximation to the path image at each new β. We can merge the direction-of-gradient step into an efficient optimization solver such as the alternating direction method of multiplier (ADMM) [4]. To adapt the direction-of-gradient optimization, we can add the POCS in the denoising step of the ADMM algorithm. Additional ordinary ADMM steps can be used to improve the accuracy of the path seeking. The direction-of-gradient based path seeking algorithm is summarized in Table I.

For the direction-of-gradient based method, the path seeking is inside the framework of the constrained optimization problem that is more robust to ordered subset errors than the fixed step size update [9]. A suitable number of ordered subsets for the direction-of-gradient path seeking method is between 10 and 20. In order to execute alternatively between the normal and modified ADMM optimization steps, the additional optimization steps need to have the same number of ordered subsets [4], [9].

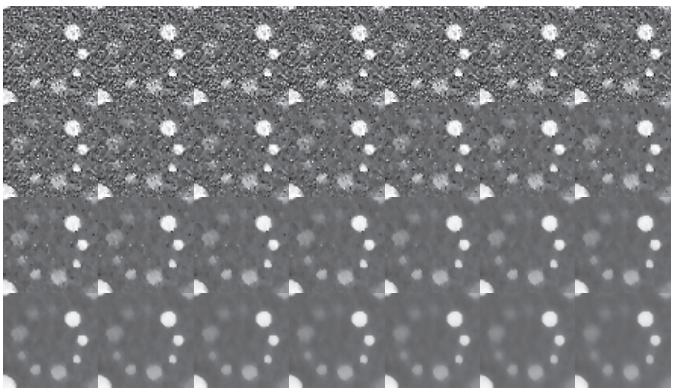

(a) Reconstruction path

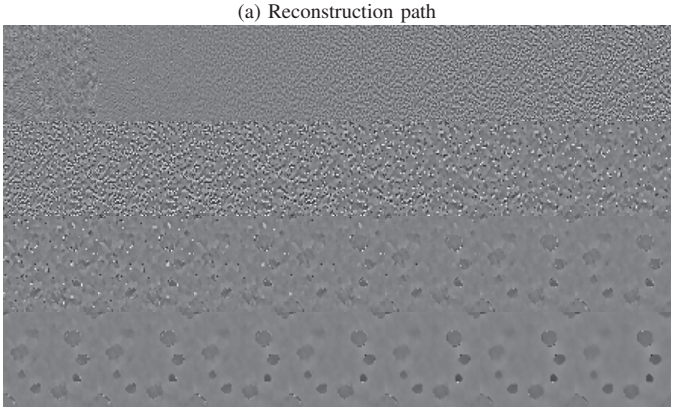

(b) Differences between two consecutive frames

Fig. 1: (a) Twenty eight path images of a 5 cm $\times$ 5 cm region-of-interest in the PWLS reconstruction path. The display window is [-50 150] HU. (b) Difference images between each two consecutive path images. The display window is [-10 10] HU.

B. Automatic tuning

The path seeking algorithm can efficiently compute the reconstruction path, but the task of selecting the optimal tuning parameter value is not completed. Because the entire reconstruction path is already available, one way to choose the appropriate tuning parameter is to apply a numeric metric to those path images and select the frame (or tuning parameter) with the highest score. However, the numeric metric has to be suitable for the clinical task, which is an open research question. In this paper, we present a generic way of selecting the tuning parameter that has maximal separation of noise reduction and smoothing.

Figure 1 (a) shows an example of 28 frames in the MBIR reconstruction path using the path seeking method. The sequence of images changes from noisy to over smoothed. Figure 1 (b) shows the corresponding difference images between each

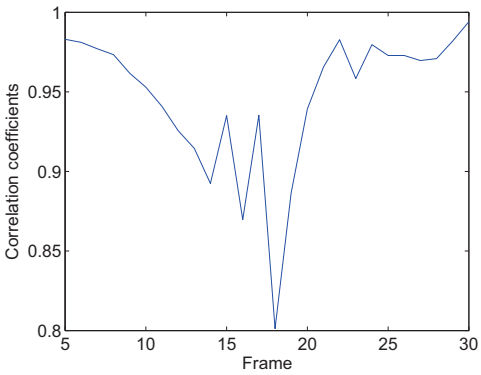

(a)

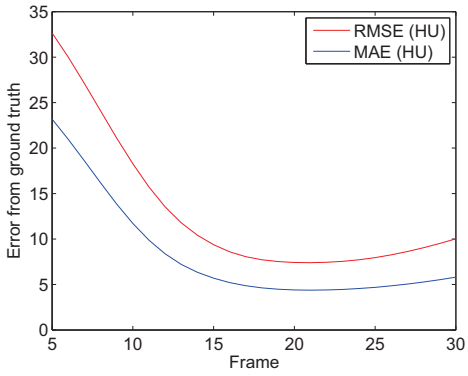

(b)

Fig. 2: (a) Correlation coefficients between two consecutive difference images. (b) RMSE and MAE between each path image and ground truth.

two consecutive path images in Figure 1(a). The effects of changing the penalty function strength are now presented in the difference images. When the tuning parameter is small, increasing the strength of the penalty function mainly reduces the noise in the reconstructions. In the first row of difference images, the changes are uniform throughout the region-of-interest (ROI), and there is no clear structure of the phantom. As the noise level in the reconstructions becomes low (end of the second row), the penalty function starts to influence the shape and value of the soft tissue patterns.

As shown in Figure 1(b), the changes in the first half of the reconstruction path correspond to the noise reduction, and the changes in the second half of the reconstruction path correspond to the smoothing. If we compute the correlation coefficients between each two consecutive difference images, there are high correlations inside the first and second halves as shown in Figure 2(a). At the 18th frame, the correlation coefficient drops because the changes caused by the noise is independent to the structure. Therefore, the corresponding frame implies the maximal separation between the noise reduction and the smoothing effects. Figure 2 (b) shows the root-mean-square-error (RMSE) and the mean-absolute-error (MAE) between each path image and ground truth. The RMSE and MAE both have minimum values around the 18th frame, which validate our assumption. Then, we can apply the same approach to each small regions of the entire image

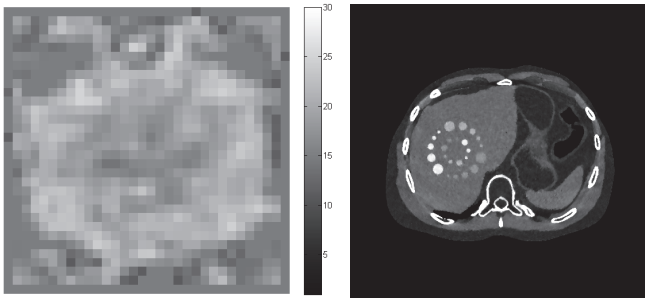

(a) (b)

Fig. 3: (a) Selected ROI frame indices used for optimal tuning parameter selection;. (b) Example of resulting aPBIR image.

to adaptively select optimal tuning parameters (Figure 3). The final auto-tuned PBIR (aPBIR) image is produced by stitching the regions with selected frame from the reconstruction path. In our experiments, we found a region size of 32×32 pixels (2.5 cm×2.5 cm) provides a good trade-off between noise and local structure.

III. Simulations

A typical 64-slice diagnostic CT geometry was used in the simulations. A full circular rotation scan was performed over 360 degrees, containing 984 projections with the size of 888×64 pixels. The reconstructed image size 512×512×30 with in-plane spacing of 0.8×0.8 mm^2, and the slice thickness is 1 mm.

An abdomen XCAT phantom with added soft tissue patterns was used in this work. The phantom spacing of the XCAT phantom is 0.6 mm isotropic. The projection data were simulated in an axial scanning mode using a 120 kVp polychromatic spectrum. Simulated projections of the XCAT phantom were generated assuming an exposure of approximately 100 mAs and 50 mAs.

The simulated projection data are reconstructed using the penalized weighted least-squares (PWLS) method. We used the convex edge-preserving Huber function as the penalty function for image roughness. The transition value from quadratic to linear regions is set to 1, 5, and, 10 Hounsfield units (HU), respectively. The proposed path seeking methods were used to generate path images of the PWLS reconstruction with 30 β values. The range of tuning parameters produces reconstructions ranging from very noisy to over smoothed.

IV. Results

Figure 4 shows aPBIR reconstructions with different the Huber function (different transition values) at two different dose levels. With the automatically tuned parameter, the reconstructions show a good balance between noise reduction and smoothing. There is no visible white noise in the images. The images with the 1 HU Huber function (similar to total variation) exhibit some patchy behavior, and the soft tissue patterns are distorted. When using the 10 HU Huber function, the soft tissue background has more high frequency structures. The shapes of soft tissue contrast patterns in the liver are better preserved by the 10 HU Huber function. There is no

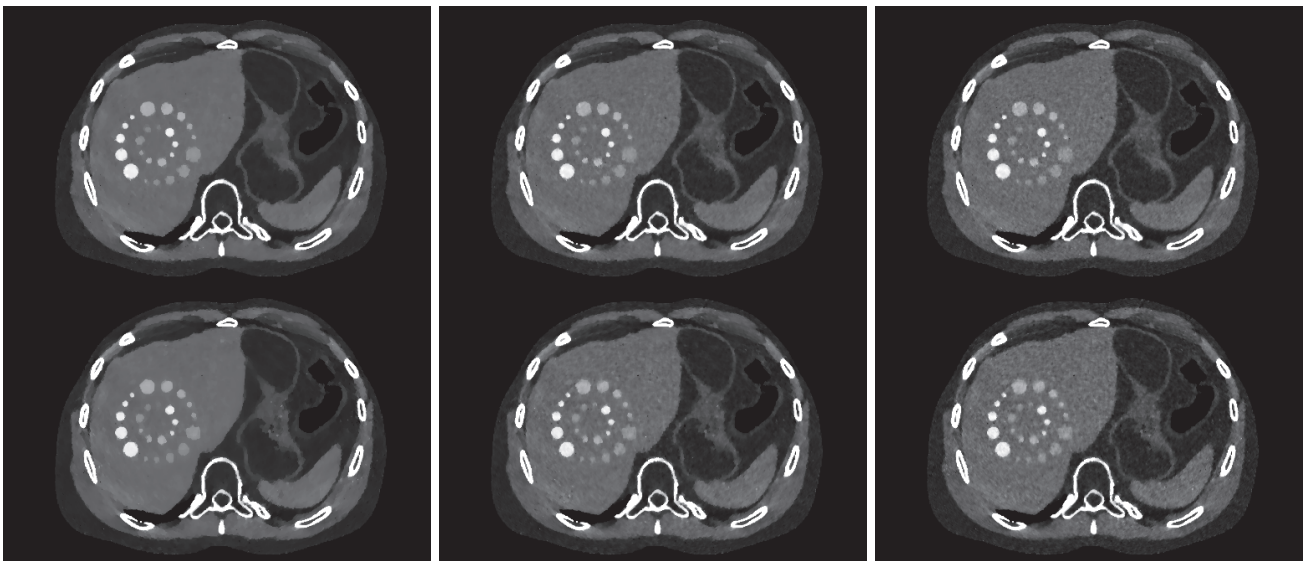

Fig. 4: Reconstruction results of the proposed aPBIR method. The first row uses 100 mAs data, the second row uses 50 mAs data. The columns from left to right correspond to the Huber function with transition values of 1, 5, and, 10 HU, respectively. The display window is [-50 150] HU.

TABLE II: RMSE and MAE measurements of the proposed aPBIR reconstructions in Figure 4 against the ground truth. The measurements for MBIR reconstructions used the image of on the reconstruction with the smallest values.

Dose level (mAs)	100	100	100	50	50	50
Huber parameter (HU)	1	5	10	1	5	10
aPBIR RMSE (HU)	28.2	28.2	28.4	29.0	29.2	29.3
MBIR RMSE (HU)	28.3	28.3	28.4	29.2	29.2	29.4
aPBIR MAE (HU)	8.24	8.59	9.04	8.51	8.93	9.46
MBIR MAE (HU)	8.19	8.41	8.63	8.51	8.79	9.05

obvious visual difference between 100 mAs and 50 mAs reconstructions, although 50 mAs reconstructions have more pepper noise, and the soft tissue patterns are more likely to be distorted.

Table II shows the comparison of RMSE and MAE measurements between the proposed aPBIR method and the ”best” MBIR reconstructions. With the path seeking algorithm, we are able to obtain the reconstruction path of MBIR, and then compute the smallest RMSE and MAE values along the path. Therefore, the error measurements of the MBIR are the smallest values for the given reconstruction model. Note that, those values are unknown in practice because there is not ground truth. The aPBIR images have even slightly smaller RMSE than the ”best” MBIR, because the tuning parameters are adaptively selected for different regions. The MAE measurements for aPBIR method are slightly larger than the ”best” MBIR. Our simulation included beam hardening and partial volume effects, so the error measurements will not go down to zero. In addition, the path seeking algorithm not only permits efficient calculation of reconstructions for monotonically changing tuning parameter, but can also be used to investigate the impact of changing parameters in the penalty function itself.

V. Conclusion

In this paper, we present an approach to automatically select the tuning parameter in iterative reconstruction by finding the maximum separation between noise reduction and smoothing effects. Simulation results show the proposed auto-tuned PBIR produces images that are comparable to the hypothetically ”best” MBIR images. Future work will comprise validation of the algorithm in the clinical datasets. The present paper, however, indicates the feasibility of automatically selecting the tuning parameter using the aPBIR method.

References

[1] J.-B. Thibault, K. D. Sauer, C. A. Bouman, and J. Hsieh, “A three-dimensional statistical approach to improved image quality for multislice helical CT,” *Med. Phys.*, vol. 34, no. 11, p. 4526, 2007.

[2] I. A. Elbakri and J. A. Fessler, “Statistical image reconstruction for polyenergetic X-ray computed tomography,” *IEEE Trans. Med. Imaging*, vol. 21, pp. 89–99, feb 2002.

[3] E. Y. Sidky and X. Pan, “Image reconstruction in circular cone-beam computed tomography by constrained, total-variation minimization.,” *Phys. Med. Biol.*, vol. 53, no. 17, pp. 4777–4807, 2008.

[4] H. Nien and J. A. Fessler, “Fast X-Ray CT Image Reconstruction Using a Linearized Augmented Lagrangian Method With Ordered Subsets,” *IEEE Trans. Med. Imaging*, vol. 34, pp. 388–399, feb 2015.

[5] J. Tang, B. E. Nett, and G.-H. Chen, “Performance comparison between total variation (TV)-based compressed sensing and statistical iterative reconstruction algorithms.,” *Phys. Med. Biol.*, vol. 54, no. 19, pp. 5781–5804, 2009.

[6] A. S. Wang, J. W. Stayman, Y. Otake, G. Kleinszig, S. Vogt, G. L. Gallia, a. J. Khanna, and J. H. Siewerdsen, “Soft-tissue imaging with C-arm cone-beam CT using statistical reconstruction.,” *Phys. Med. Biol.*, vol. 59, no. 4, pp. 1005–1026, 2014.

[7] M. Wu, Q. Yang, A. Maier, and R. Fahrig, “Approximate Path Seeking for Statistical Iterative Reconstruction,” in *Proc. SPIE Med. Imaging*, pp. 9412–46, 2015.

[8] M. Wu, A. Maier, Q. Yang, and R. Fahrig, “Improve Path Seeking Accuracy for Iterative Reconstruction Using the Karush-Kuhn-Tucker Conditions,” in *Intl. Mtg. Fully 3D Image Recon. Rad.*, (New Port, RI), pp. 248 – 251, 2015.

[9] M. Wu, A. Maier, Q. Yang, and R. Fahrig, “Path-based Iterative Reconstruction (PBIR) for X-ray Computed Tomography,” arXiv:1512, pp. 1–10, 2015.

Task-Based Design of Fluence Field Modulation in CT for Model-Based Iterative Reconstruction

Grace J. Gang, Jeffrey H. Siewerdsen, and J. Webster Stayman

***Abstract* — A task-driven imaging framework for prospective fluence field modulation (FFM) is developed in this paper. The design approach uses a system model that includes a parameterized FFM acquisition and model-based iterative reconstruction (MBIR) for image formation. Using prior anatomical knowledge (e.g. from a low-dose 3D scout image), accurate predictions of spatial resolution and noise as a function of FFM are integrated into a task-based objective function. Specifically, detectability index (*d'*), a common metric for task-based image quality assessment, is computed for a specific formulation of the imaging task. To optimize imaging performance in across an image volume, a maximin objective function was adopted to maximize the minimum detectability index for many locations sampled throughout the volume. To reduce the dimensionality, FFM patterns were represented using wavelet bases, the coefficients of which were optimized using the covariance matrix adaptation evolutionary strategy (CMA-ES) algorithm. The optimization was performed for a mid-frequency discrimination task involving a cluster of micro-calcifications in an abdomen phantom. The task-driven design yielded FFM patterns that were significantly different from traditional strategies proposed for FBP reconstruction. In addition to a higher minimum *d'* consistent with the objective function, the task-driven approach also improved *d'* to a greater extent over a larger area of the phantom. Results from this work suggests that FFM strategies suitable for FBP reconstruction need to be reevaluated in the context of MBIR and that a task-driven imaging framework provides a promising approach for such optimization.**

***Index Terms*—Task-based optimization, detectability index, model-based reconstruction, fluence field modulation, CT**

I. Introduction

Computed tomography plays an invaluable role in diagnostic imaging, yet increased usage and public concern about risk associated with ionizing radiation has motivated a large body of research in dose reduction techniques. [1] Among such efforts, there has been increased interest in integrating fluence field modulation (FFM) devices with diagnostic CT. [2]–[4] Compared to automatic exposure control on current scanners, FFM permits much greater freedom in shaping the dose distribution in the patient as well as satisfying more flexible (e.g., spatially-varying or uniform) image quality requirements in the reconstructed image. While previous work has concentrated largely on FFM designs for filtered-backprojection (FBP) reconstruction, this work extends such investigation to model-based iterative reconstruction (MBIR).

It is widely acknowledged that dose reduction techniques must be coupled with image quality needs [5] and that image performance metrics need to be defined based on the imaging task [6]. Towards this end, in this work, we present a task-driven imaging approach to prospectively optimize FFM based on prior specification of the imaging task (e.g., based on disease prevalence, anatomical target, etc.) and the patient anatomy (e.g., from a very low dose 3D scout acquisition). This framework is developed for MBIR using predictors of noise and resolution properties that may be integrated into an expression for task-based detectability. We compare conventional FFM strategies (typically designed based on FBP reconstruction) and the task-driven FFM approach using a penalized-likelihood reconstruction.

This work is supported by NIH grant U01EB018758. G. J. Gang, J. W. Stayman, and J. H. Siewerdsen are with the Department of Biomedical Engineering, Johns Hopkins University, Baltimore, MD 21205 USA (e-mail: {grace.j.gang, web.stayman, jeff.siewerdsen}@jhu.edu).

II. Theoretical Methods

A. Task-Driven Imaging Framework

Task-driven frameworks have previously been used in the context of regularization optimization [7], tube current modulation [8], source-detector trajectory [9]. Figure 1 presents a general task-driven imaging framework. Central to the framework is an optimization loop to identify acquisition parameters (Ω_A) and reconstruction parameters (Ω_R) of interest that maximizes an objective function based on a task-based image quality metric - detectability index (*d'*).

The mathematical form of *d'* is given in Eq.1, corresponding to a non-pre-whitening observer model:

$$d'^2(\Omega_A,\Omega_R) = \frac{\left[\iiint |T(\Omega_A,\Omega_R)\cdot W_{Task}|^2 df_x df_y df_z\right]^2}{\iiint S(\Omega_A,\Omega_R)|T(\Omega_A,\Omega_R)\cdot W_{Task}|^2 df_x df_y df_z} \quad (1)$$

where T and S respectively represents the local modulation transfer function (MTF) and noise power spectrum (NPS) in the reconstructed image and can be predicted by the system model. The MTF and NPS carry dependence on both (Ω_A, Ω_R) and the patient-specific measurements computed from the anatomical model provided by a low-dose 3D scout. In diagnostic imaging, the imaging task can be predefined based on suspected abnormalities and disease prevalence in the anatomical site to be imaged.

In these initial investigations, binary classification tasks were considered, where the task function, W_{Task}, corresponds to the difference between the Fourier transform of two possible outcomes (e.g., one signal vs. another, or signal-present vs. signal absent which simplifies to a detection task).

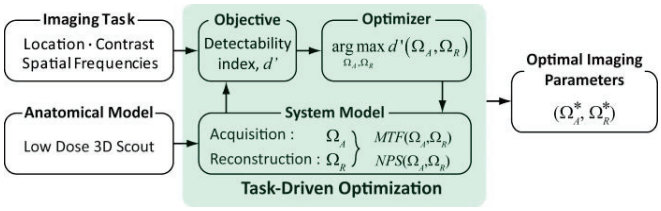

Fig.1. Framework for task-driven imaging.

B. Quadratic Penalized Likelihood Reconstruction

The MBIR method investigated in this work adopts a penalized-likelihood (PL) objective whose solution is given by:

$$\hat{\mu} = \underset{\mu}{\operatorname{argmax}}[\log L(\mu; y) - \beta R(\mu)], \qquad (2)$$

where $L(\mu; y)$ is the likelihood term, $R(\mu)$ is a roughness penalty, and β controls the tradeoff between the two. The measurements, y, are assumed to be independent and Poisson-distributed, with means given by the following forward model:

$$\bar{y} = I_0 e^{-\mathbf{A}\mu} \qquad (3)$$

where I_0 is the number of bare-beam photons per detector pixel and **A** is the forward projection operator. We adopt a traditional quadratic roughness penalty with first-order neighborhood.

C. System Model for Fast Prediction for Noise and Resolution

The noise and resolution predictors for PL reconstruction are based on previous derivations in Refs [10], [11], [12]. Both the spatial resolution and noise are spatially varying in a PL reconstruction. Thus, the MTF, NPS, and *d'* are only meaningful in a local context. [7] A Fourier approximation of the MTF and NPS is given by:

$$T_j \approx \frac{\mathcal{F}\{\mathbf{A}^T D\{\bar{y}(\mu)\}\mathbf{A}e_j\}}{\mathcal{F}\{\mathbf{A}^T D\{\bar{y}(\mu)\}\mathbf{A}e_j + \beta \mathbf{R}e_j\}} \qquad 4(a)$$

$$S_j \approx \frac{\mathcal{F}\{\mathbf{A}^T D\{\bar{y}(\mu)\}\mathbf{A}e_j\}}{\left|\mathcal{F}\{\mathbf{A}^T D\{\bar{y}(\mu)\}\mathbf{A}e_j + \beta \mathbf{R}e_j\}\right|^2} \qquad 4(b)$$

where subscript j denotes voxel location and e_j is the j-th unit vector. The operator $D\{\cdot\}$ converts its vector argument to a diagonal matrix and **R** is the Hessian matrix of the quadratic penalty that is independent of μ or $\bar{y}$.

Since a large number of evaluations of Eq.4 and Eq.1 are required for optimization, several techniques were adopted to speed up computation. First, using **i** to denote projection number, $\mathcal{F}\{\mathbf{A}_\mathbf{i}^T \mathbf{A}_\mathbf{i} e_j\}$ is precomputed and stored for each projection. This expression is scaled by the appropriate $\bar{y}_j$ according to a specific FFM (which determines y) and is summed over all projections to get $\mathcal{F}\{\mathbf{A}^T D\{\bar{y}(\mu)\}\mathbf{A}e_j\}$. Second, $\mathcal{F}\{\mathbf{A}_\mathbf{i}^T \mathbf{A}_\mathbf{i} e_j\}$ was assumed to be independent of voxel location j, i.e., only one set of $\mathcal{F}\{\mathbf{A}_\mathbf{i}^T \mathbf{A}_\mathbf{i} e_j\}$ needs to be stored for *d'* calculation in multiple locations. Such an assumption is reasonable for good angular sampling and voxel locations in the central plane. Lastly, instead of using the full image volume support for e_j, $\mathcal{F}\{\mathbf{A}_\mathbf{i}^T \mathbf{A}_\mathbf{i} e_j\}$ is only computed and stored for a 49×49×49 voxel VOI centered at j. The VOI size is chosen to be bigger than the correlation length between voxels. Since **R** is independent of μ or $\bar{y}$, $\mathcal{F}\{\beta \mathbf{R}e_j\}$ only needs to be precomputed once and stored. These techniques allows fast computation of the MTF, NPS and *d'* – e.g., evaluating *d'* for 50 voxel locations requires 0.06 s.

D. Low Dimensional Parameterization of Fluence Field

An arbitrary fluence field could potentially be specified for each horizontal detector element (denoted as u) and each projection number (denoted as p). Thus, a modulated fluence field pattern is a 2D function on (u, p). To reduce the dimensionality of the optimization, and to enforce smoothness constraints, we parameterize the fluence field (FF) using coefficents for a set of 2D wavelet bases, such that

$$FF(u,p) = \sum_i^n \omega_{\mathrm{ff}}^i \mathrm{B}^i(u,p) \qquad (5)$$

This permits low-dimensional estimation of the coefficient vector, $\vec{\Omega}_{\mathrm{ff}} = [\omega_{\mathrm{ff}}^1, \omega_{\mathrm{ff}}^2, \ldots, \omega_{\mathrm{ff}}^n]^T$. Practical FFM systems are likely to be smoothly-varying in both u and p. That is, x-ray beam profiles are spatially smooth and do not change abruptly from angle to angle. For this reason, the basis functions, $\mathrm{B}^i(\vec{r})$, were chosen to be 2D Gaussian wavelets on (u, p). In addition, projections traversing the same voxel that are 180° apart are assumed to have the same fluence to enforce a symmetric design in 360° rotations. An example set of wavelet functions are illustrated in Fig.2 with coarse sampling along both directions. For the actual optimization, the Gaussians are centered at 17 locations in u and 6 locations in p, giving a total of 17×6=102 coefficients.

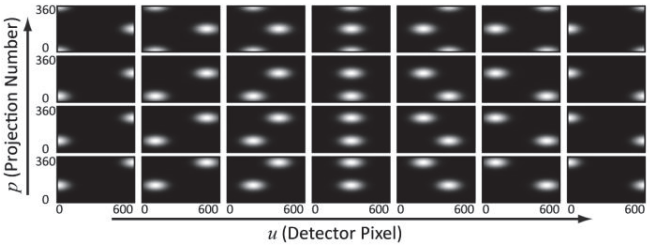

Fig.2. Wavelet bases for low dimensional parameterization of fluence field.

E. Objective Function and Optimizer

To optimize FFM, *d'* values over multiple locations within the reconstruction need to be considered. There are many ways to formulate an objective function, e.g., maximize the mean *d'*, equalizing *d'*, etc. In this work, a maximin objective is used to maximize the minimum *d'*, i.e.:

$$\max_{\vec{\Omega}_{\mathrm{ff}}} \min_{\vec{v}} d'(\vec{v}; \vec{\Omega}_{\mathrm{ff}}) \quad \text{s.t.} \quad \sum_{(u^*,p)} FF(u^*, p) = I_{tot} \qquad (6)$$

where $\vec{v}$ is the coordinate vector for the 3D reconstructed image and represent a set of discrete points within the object over which *d'* is evaluated. By maximizing the minimum *d'*, one guarantees a specific level of detectability in the volume. The optimization is subjected to a total exposure constraint (the sum of the barebeam fluence over all projections and detector locations behind the object, denoted u^*). Due to the non-linear, non-convex nature of the problem, a stochastic and derivative-free optimizer - Covariance Matrix Adaptation Evolution Strategy (CMA-ES) [13] is used to solve this objective.

III. Experimental Methods

A. Phantom and Imaging Task

The CT scan of a cadaver abdomen was used as a digital phantom. The central plane is illustrated in Fig.3(a) with a large number of stimuli shown in Fig.3(b) inserted at locations randomly perturbed around a 11×16 grid. The imaging task is the "detection" of a calcification cluster constructed of three

Gaussian stimuli (width=0.8 mm) evenly distributed along the perimeter of a 4mm diameter circle. Specifically the task is to discriminate the three calcification cluster from a monolithic stimulus – a Gaussian with width equal to 4 mm. We enforce a task definition where all rotational orientations are equally likely (e.g. a symmetric task function). Specifically, the task function is equal to the Hankel transform of the Fourier transform of the stimulus minus the Fourier transform of the larger Gaussian, the result of which is plotted in Fig.3(c).

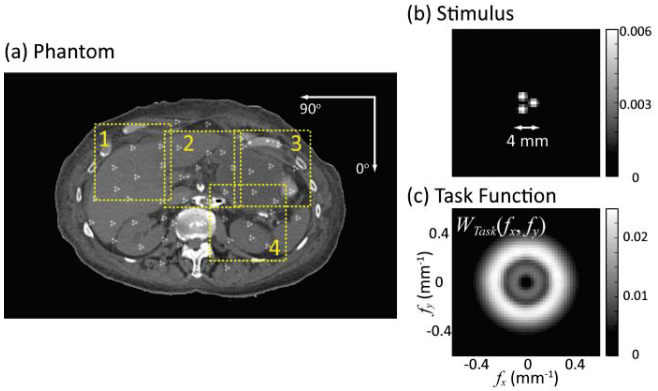

Fig.3. (a) The abdomen phantom is based on a diagnostic CT scan of a cadaver. (b) The stimulus consisting of three narrow Gaussians simulating a cluster of micro-calcifications. (c) The Fourier domain task function corresponding to the discrimination of (b) from a larger Gaussian stimulus. Rotational symmetry is introduced to account for other orientations of the cluster.

B. Image Simulation and Reconstruction

A bare beam fluence of 2.5×10^4 to 4.5×10^4 photons/mm^2 was used to simulate projection images. We considered a system geometry with an 80 cm source-to-axis distance and a 120 cm source-to-detector distance. The detector pixel size was 1.3×1.3 mm and reconstruction voxel size was 0.87×0.87×0.87 mm. A GPU-implemented linear projector was used. Penalized-likelihood reconstruction was performed using 80 iterations of paraboloidal surrogate updates with 20 ordered-subsets in the first 40 iterations and 1 subset in the last 40 to encourage convergence.

C. Comparison with Other Strategies

The task-driven fluence field design was compared with three other strategies. All strategies were subjected to the same total fluence constraint in Eq.6.

(1) Unmodulated: Constant bare-beam fluence with no modulation as a function of either u or p.

(2) Flat fluence on the detector (denoted as "Flat"): Extending the parameterization developed by Gies et al. from tube current modulation to FFM, the fluence field can be expressed as a function of the line integral, l, and a scalar, α, as:

$$FF(u^*,p)=\frac{e^{\alpha l(u^*,p)}}{\sum_p e^{\alpha l(u^*,p)}}I_0^{tot}. \quad (7)$$

When $\alpha=1$, the fluence behind the object incident on the detector becomes flat. This modulation pattern is attractive because the reconstructed image would have isotropic and uniform noise and resolution (hence *d'*) throughout the image.

(3) Extension of the Minimum variance solution in FBP (denoted as "$\alpha=0.5$"): Gies et al. derived that when $\alpha=0.5$, the tube current modulation simplified from Eq.7 by tracing the detector elements corresponding to one voxel location achieves minimum variance in that particular voxel in an FBP reconstruction. Rather than setting a single tube current value per projection angle, we extend this approach to FFM by applying the same strategy to compute a beam shape. The third FFM is calculated from Eq.7 when $\alpha=0.5$.

D. Image Quality Assessment

Detectability index was computed for locations on a 11×16 grid within the phantom (including skin line) and interpolated using radial basis functions to obtain a detectability map, *d'*(*x*, *y*). Reconstructions using FFM from all four strategies were presented for the four ROIs illustrated in Fig.3(a) for visual assessment.

IV. Results

The fluence field for all three strategies are shown in Fig.4. The $\alpha=1.0$ field peaks at projections at 90º and 270º degrees which traverse the lateral direction of the phantom. The $\alpha=0.5$ strategy follows the same trend, but the modulation is smaller. Interestingly, the task-driven fluence field is the opposite of the previous two, with peak fluence around 0º, 180º, and 360º.

This trend can be explained by the local MTF and NPS plots in Fig.5. (Only one location at the center of the image is shown for brevity.) Both the MTF and NPS are anisotropic according to the stastical weighting in each view and applying FFM can, to a certain degree, control the noise-resolution tradeoff with respect to an imaging task. Quadratic PL penalizes noisy data more heavily, resulting in MTF and NPS with almost complementary shapes, i.e., radial directions corresponding to low noise projection data has intrinsically higher resolution and vice versa. The task-driven approach takes advantage of this behavior and further enhances spatial resolution along the f_x direction by increasing fluence in anterior-posterior views, thus boosting signal power [numerator of *d'* in Eq.1]. Although noise is increased along the f_y direction, the intrinsic smoothing of PL alleviates this effect and *d'* is improved overall.

The detectability map, *d'*(*x*, *y*), for the Unmodulated, Flat, $\alpha=0.5$, and Task-Driven strategies are shown in Fig.6 with the minimum *d'* value superimposed. As expected, *d'*(*x*, *y*) for the

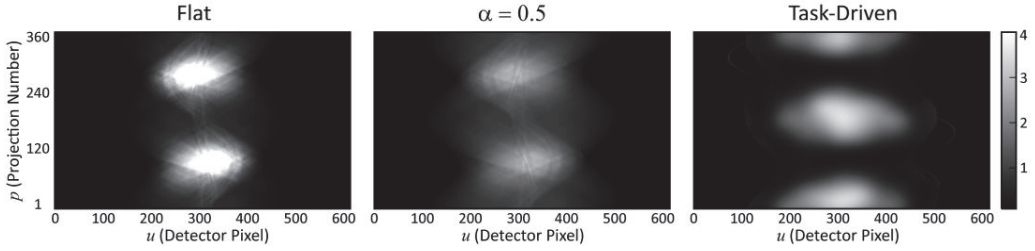

Fig.4. Fluence field modulation patterns for the Flat, $\alpha=0.5$, and Task-Driven strategies.

Unmodulated strategy is the lowest at the center (minimum d'=0.92) and gradually increases towards the edge of the phantom. In comparison, the Flat field results in uniform d' throughout, therefore improving d' at the center but decrease d' at the edge, with a minimum (uniform) d' of 1.25. The $\alpha = 0.5$ field has a d' map that falls between the previous two cases with a minimum d' of 1.06. Relative to the unmodulated case, d' is improved for a larger area over the phantom but to a lesser degree compared to the "Flat" field. The task-driven approach achieved higher minimum d' (=1.36) than other strategies. This is consistent with the maximin objective, according to which the rank order follows Task-driven > Flat > $\alpha = 0.5$ > Unmodulated. The task-driven $d'(x, y)$ is almost uniform within the ribcage where the optimization was performed, suggesting that there is more than one solution that can achieve uniform d'. In addition to a higher minimum d', the task-driven case also achieved a higher d' at every location compared to the Flat field, and improved d' in a large area around the center of the phantom compared to the Unmodulated and $\alpha = 0.5$ strategies.

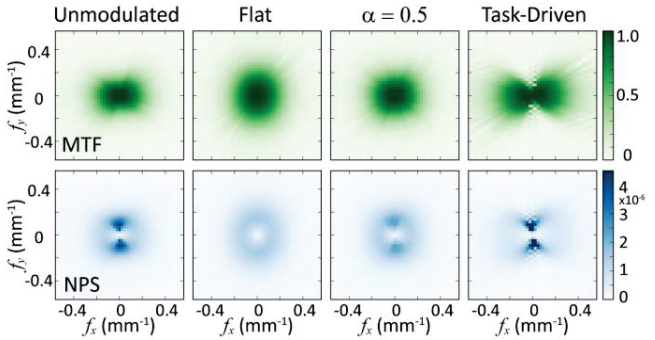

Fig.5. The local MTF (top row) and NPS (bottom row) at the center of the reconstruction for the four FFM strategies.

Trends in d' are generally supported by the reconstructions shown Fig.7 using the four FFM strategies (columns) for the four ROIs (rows) in Fig.3(a). In both the Unmodulated and $\alpha = 0.5$ reconstructions, the imaging task (i.e., distinguish the three separate dots) is visibly easier to perform at the edge of the phantom (left side of ROI 1, upper right corner of ROI 3) than the center (ROIs 2 and 4). The Flat and Task-driven FFM, on the other hand, achieve relative uniform performance across all four ROIs. Comparing across strategies, on the edge of the phantom, the imaging task is the easiest to perform in the unmodulated strategy compared to all others. An example stimulus is marked by the yellow arrow in ROI 1. As one moves towards the right of ROI 1 (i.e., towards the center of the phantom), the Unmodulated reconstruction starts to deteriorate and the task-driven strategy starts showing greater performance as seen by the stimulus indicated by the red arrow. At the center of the phantom (ROIs 2 and 4), the task-driven strategy outperforms the rest, followed closely by the Flat field. Both the unmodulated and $\alpha = 0.5$ strategies fall short in these regions. Example stimuli are indicated in ROIs 2 and 4.

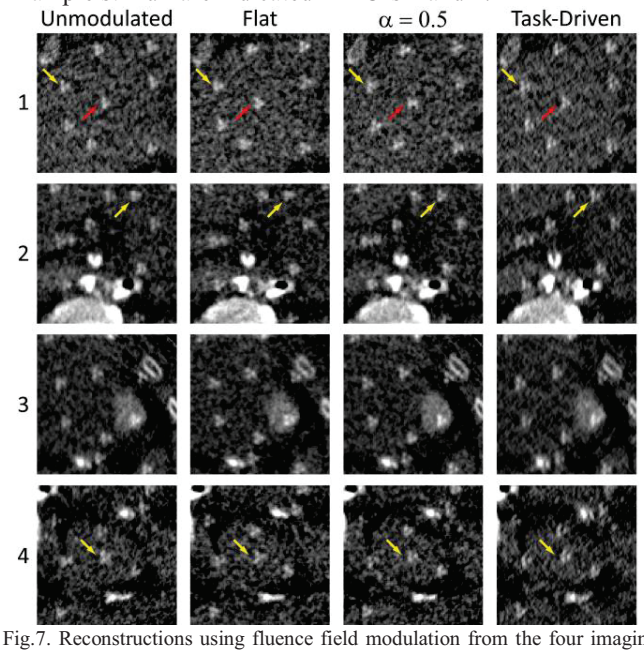

Fig.7. Reconstructions using fluence field modulation from the four imagine strategies (columns) in four ROIs (rows) in the abdomen phantom illustrated in Fig.3(a).

V. DISCUSSION AND CONCLUSIONS

This work presented FFM optimization for MBIR within a task-driven imaging framework. For the mid-frequency task in this investigation, the task-driven approach outperformed conventional strategies originally proposed for FBP reconstruction and yielded unconventional modulation patterns. This suggests that imaging strategies suitable for FBP needs to be reevaluated in the context of MBIR and the task-driven imaging framework provides a promising approach in optimizing imaging performance.

REFERENCES

[1] F. A. Mettler, et al., *Health Phys.*, vol. 95, no. 5, pp. 502–7, Nov. 2008.
[2] S. S. Hsieh and N. J. Pelc, *SPIE Medical Imaging*, 2013, p. 86681Q.
[3] T. P. Szczykutowicz et al., *Phys. Med. Biol.*, vol. 59, no. 5, pp. 1305, 2014.
[4] S. Bartolac, et al., *Med. Phys.*, vol. 38 Suppl 1, p. S2, Jul. 2011.
[5] C. H. McCollough, et al.. *AJR.*, vol. 193, no. 1, pp. 28–39, Jul. 2009.
[6] P. F. Sharp, et al. *Int. Comm. Radiol. Units Meas. (Bethesda, Md)*, 1996.
[7] G. J. Gang, et al., *Med. Phys.*, vol. 41, no. 8, p. 081902, Aug. 2014.
[8] G. J. Gang, et al., *Phys. Med. Biol.*, vol. 60, no.8, p.3129-50, 2015.
[9] Stayman et al., *Proc. Fully 3D*, 2012, pp. 257–260.
[10] J. A. Fessler, *IEEE Trans.*, vol. 5, no. 3, pp. 493–506, Jan. 1996.
[11] Y. Zhang-O'Connor et al., *IEEE Trans.*, vol. 26, no. 3, pp. 335, 2007.
[12] J. W. Stayman et al. *IEEE Trans.*, vol. 23, no. 12, pp. 1543, Dec. 2004.
[13] N. Hansen, et al. *ICGA*, 1995, pp. 57–64.

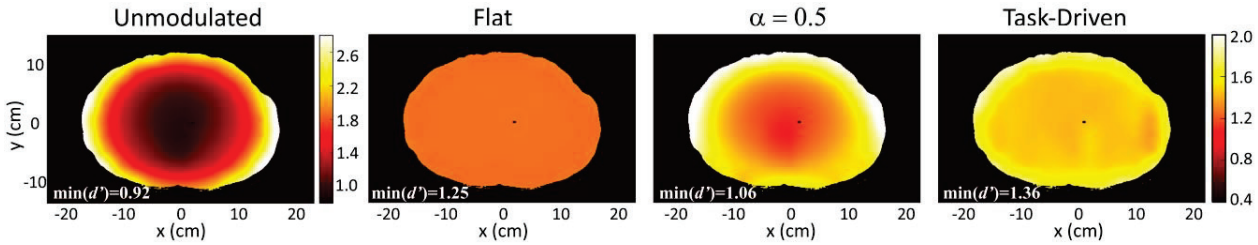

Fig.6. Detectability index maps $d'(x, y)$ for the four FFM strategies,

Computed Laminography System with Various Scanning Configurations for Nondestructive Testing

Miran Park, Ho Kyung Kim, and Seungryong Cho

Abstract— X-ray computed laminography (CL) is widely used in nondestructive testing (NDT) for laterally extended flat objects. In this study, we have developed a benchtop system for computed laminography which can accommodate various scanning trajectories: single-arc, double-arc, oblique, and spherical sinusoidal scanning methods for example. We have particularly investigated oblique vs. spherical sinusoidal scanning in this work in the sparse sampling context to reduce radiation damage to the imaged object. We scanned a RAM card at only 20 views, and reconstructed CL images by using a constrained TV-minimization iterative algorithm. The reconstructed images on the in-planes showed comparable image quality. However, the images along the depth direction showed considerable differences.

I. INTRODUCTION

NONDESTRUCTIVE testing (NDT) including x-ray imaging is becoming more important in modern industry along with high density integration of electronic circuits or with volumetric structuring of micro-components. Classical 2D x-ray inspection would find limited applications in such fields because of the confounding effects of the constituent objects on the projection images, and thus 3D information would be desirable. Computed tomography (CT) indeed is in active use for various industrial NDT. For the laterally extended objects, conventional CT may not be useful because of the poor penetration power of x-rays along the lateral direction. Therefore, accurate tomographic image reconstruction of such object is challenging. X-ray computed laminography (CL) provides high resolution in-plane images with depth images of limited quality for the laterally extended objects [1-3]. CL takes projections only within an accessible range of penetration and produces quasi-3D image information.

Devices in the electronic industry, such as microchips for cell phones, are going through miniaturization and high-density packaging [4]. During inspection, undesirably long x-ray exposure and high radiation dose may lead to damages or failure to the devices [5]. Therefore the reduction of radiation dose is becoming important in x-ray CL for such applications [6]. One way to reduce radiation dose to the object is to limit scanning angle. However, the image quality with limited angle scan was shown to be inferior to the ones with conventional CL that completes a full circular scan [7].

Miran Park and Seungryong Cho are with the Department of Nuclear and Quantum Engineering, Korea Advanced Institute of Science and Technology, Daejeon, South Korea. (e-mail: scho@kaist.ac.kr).

Ho Kyung Kim is with the School of Mechanical Engineering, Pusan National University, Busan, South Korea.

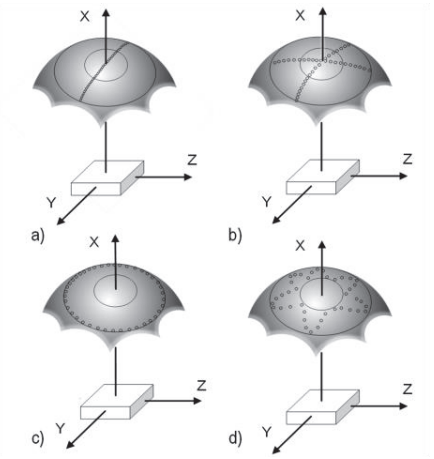

Fig. 1: Four scanning schemes performed using laminography benchtop system : (a) arc (b) double are (c) oblique (d) spherical sinusoidal.

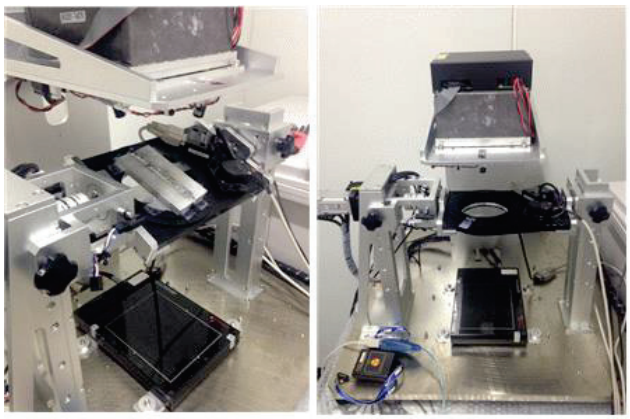

Fig. 2: Laminography benchtop system. This consists of an X-ray source, a tilt motor, a rotation stage, and a detector.

In our previous work [10], we proposed a new scanning scheme namely a spherical-sinusoidal scan for the NDT of radio-sensitive flat objects, and performed a simulation study to compare four scanning configurations: single-arc, double-arc, oblique, and spherical- sinusoidal. The schematic illustrations of the scanning configurations are shown in figure 1. An oblique CT, *i.e.*, a conventional CL configuration, is heavily used for scanning of laterally extended objects in the industrial inspection area. Spherical-sinusoidal scan trajectory is similar to the oblique scan except that the source to the rotation axis distance keeps rocking in a sinusoidal pattern with respect to the source rotation angle. The proposed scanning scheme

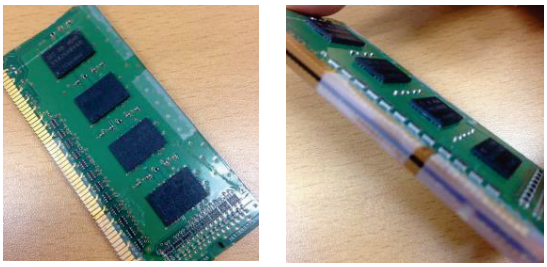

Fig. 3: The scanned object for laminography scanning test. A stacked set of RAM cards was used.

demonstrated its outperformance to the conventional CL scanning schemes in terms of image contrast and accuracy in the context of sparse sampling for low-dose scan.

In this work, we focus on our fabrication of a CL benchtop system which can perform various scan trajectories, especially oblique and spherical sinusoidal scan schemes. We implemented a total-variation minimization algorithm for image reconstruction from only 20 projections. Image quality comparison was made in a qualitative way in this work.

II. Materials and Methods

A. Imaging System and Data collection

The laminography benchtop system consists of an x-ray source, a detector, a tilt motor, and a rotation stage. The rotation stage is held by the tilt motor, and can tilt in a certain angle; the maximum tilt angle in our system is 30 degree. In scanning system, the source and detector are stationary while the object is tilting or rotating in a way that can produce such a scanning geometry in the object-fixed coordinates. The source position always faces normal to the detector surface.

The detector was placed 439 mm away, and has 2352×2944 pixels which binned by a factor of 2 into 1176×1472 in this study. The binned pixel size is $0.99\times0.99\mu m^2$. The x-ray tube voltage and current were set to 70 kVp and 0.3 mA.

In this study, we acquired the data using oblique and spherical sinusoidal scan scheme. For two oblique scans, the tilt angles were set in 30 degree and 20 degree, respectively. For sinusoidal scan, the maximum tilt angle and minimum tilt angle were 30 and 10 respectively, and it had 5 cycles.

A stacked set of random-access memory (RAM) cards was scanned using our system. The object was placed 189 mm away from the x-ray source. The 20 projection-views are all uniformly distributed over the angular range. The step-and-shoot rotation mode was used to acquire projections.

B. Reconstruction Methods

For image reconstruction, CS-inspired adaptive-steepest -descent projection-onto convex-sets (ASD- POCS) algorithm [8][9] was implemented and we will refer that to total- variation (TV) minimization algorithm. In this work, it needs to be noted that TV was not used as a denoising regularization, but was used to seek an optimum image solution among the set of possible images which satisfy the data consistency constraint. To do so the TV minimization algorithm minimizes the l_1 − norm of magnitude of image derivative and finds the solution to the following:

$$\hat{\vec{z}} = argmin\|\vec{z}\|_{TV} \;\; s.t. \;\; [\![M\vec{z} - \vec{p}]\!] < \delta$$

where $\hat{\vec{z}}$ is the solution of the optimization problem constrained by data fidelity. Data fidelity term insures that the difference between calculated projection data $M\vec{z}$ and measured projection data $\vec{p}$ should be less than δ. The value of δ can be found empirically.

The TV minimization algorithm is composed of two steps. First step is projection-onto convex-sets which respects the data fidelity and image pixel positivity condition. The second step is adaptive-steepest-decent operation to find the minimum-TV image. The optimization algorithm that was utilized for minimizing the image TV is gradient decent method. In an attempt to move toward the minimum image TV value, in each TV step gradient decent method calculates the gradient vector by taking the derivative of the image TV.

III. Result

In figure 4 and 5, there are the reconstructed images, which are along the in-plane and depth direction respectively, with oblique and spherical sinusoidal scan using 20 view-projections. Also line profile graphs are shown in figure 6 and 7. The image resolution and contrast are visually comparable in all the in-plane slice images and line profiles with different scanning configuration. It can be also noticed that the images reconstructed from the data at only 20 views by all the scanning schemes are in a good agreement. The solder balls and small components of RAM card have confined structures in figure 4.

The images along the depth direction in figure 5 do not show clear structure of solder balls. Even if the solder balls can be detected, their shapes are elongated and distorted.

However the spherical sinusoidal scan, or our proposed scheme, produced slightly higher contrast of the solder balls. Higher contrast of the image is observed in the line-profile of spherical sinusoidal scan. The graph of figure 6 is the line profile of horizontal red dotted line of figure 5. The background value of spherical sinusoidal is lower than other scan schemes. And the graphs of figure 7 which is the line profile of vertical red dotted line of figure 5 show the spherical sinusoidal scan (black solid line) has higher contrast.

Fig. 4: In-plane slice image through reconstructed image. (from left to right) spherical sinusoidal, oblique tilted with 30 degree, and oblique tilted with 20 degree

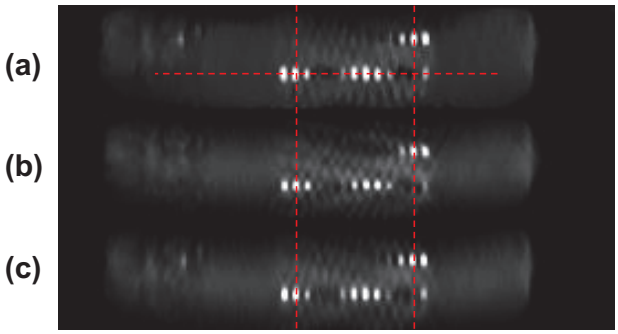

Fig. 5: Depth slice image through reconstructed image. (a) spherical sinusoidal scan (b) oblique scan tilted at 30 degree (c) oblique scan tilted at 20 degree scan

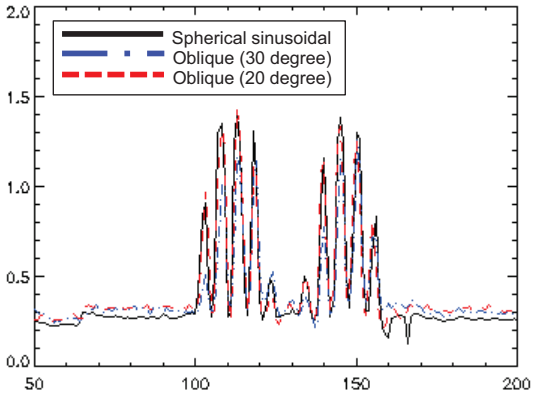

Fig. 6: The line profiles of horizontal red dotted line of figure 5. (a) Spherical sinusoidal scan (b) oblique scan tilted at 30 degree (c) oblique scan tilted at 20 degree scan

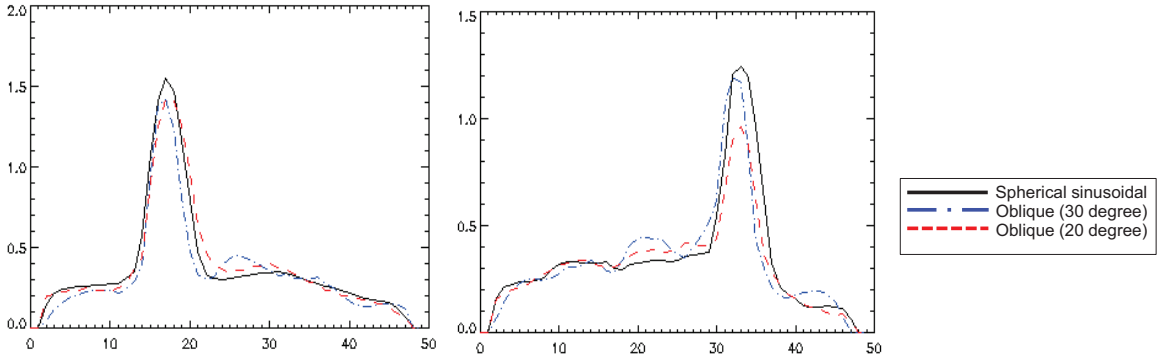

Fig. 7: The line profiles of vertical red dotted line of figure 5 which indicate depth direction. The spherical sinusoidal (black solid line) has higher contrast than other scanning configuration.

IV. Discussion

We focus on the contrast of reconstructed images along depth direction. Overall image qualities are comparable between oblique and spherical sinusoidal scan scheme. As previous simulation study has demonstrated [10], spherical sinusoidal scan is supposed to provides higher data incoherence [11]. Therefore it is considered to provide higher contrast than oblique scans along the object depth direction.

Besides, a certain pattern can be seen in images from oblique scan scheme in figure 5. The streak formed an angle which identical with the tilt angle and those artifacts may interrupt the inspection of objects. However, during data acquisition using spherical sinusoidal scan, the tilt angle of rotation stage is varying in order to change the distance between the source and rotation axis. Repetitive tilt angle adjustments may cause a geometrical error. The effect of system instability will be investigated in our future study using a calibration phantom.

V. Conclusion

In this study, we have developed a benchtop system for computed laminography which can provide various scanning trajectories: the single-arc, the double-arc, the oblique, and the spherical sinusoidal scanning methods. We scanned a RAM card with oblique and spherical sinusoidal scans. The images were reconstructed from only 20 views using constrained TV-minimization algorithm. The reconstructed images along the in-plane direction with different scanning methods showed comparable image quality. However, none of the images along the depth direction indicated defined structures because of incomplete data set. In conclusion, our benchtop system can provide a low-dose computed laminography with various scan trajectories. Moreover, the spherical sinusoidal scan produce higher contrast image than other scans. Further investigations will focus on improving depth resolution of reconstructed images.

Acknowledgment

The authors would like to thank NanoFocus Ray Ltd. for the discussions about system setup. Also the gratitudes are extended to Rizza Pua and Sunhee Wi for their helpful discussions. This work was funded by the National Research Foundation of Korea funded by the Ministry of Science, ICT & Future Planning NRF-2013M2A2A9043476.

References

[1] L. Helfen, F. Xu, H. Suhonen, L. Urbanelli, P. Cloetens, and T. Baumbach, “Nano-laminography for threedimensional high-resolution imaging of flat specimens,” J. Instrum. Vol. 8, no.05, pp. C05006, 2013.

[2] L. Helfen, A. Myagotin, A. Rack, P. Pernot, P. Mikulík, M. Di Michiel, and T. Baumbach, “Synchrotronradiation computed laminography for high-resolution three-dimensional imaging of flat devices,” Phys. Status Solidi, vol. 204, no. 8, pp. 2760–2765, 2007.
[3] M. Yang, G. Wang, and Y. Liu, “New reconstruction method for x-ray testing of multilayer printed circuit board,” Opt. Eng., vol. 49, no. 5, pp. 056501, 2010
[4] D. T. C. Allcock, T. P. Harty, C. J. Ballance, B. C. Keitch, N. M. Linke, D. N. Stacey, and D. M. Lucas, “A microfabricated ion trap with integrated microwave circuitry,” Appl. Phys. Lett., vol. 102, no. 4, pp. 044103, 2013.
[5] D. N. Nguyen, S. M. Guertin, G. M. Swift, and A. H. Johnston, “Radiation effects on advanced flash memories,” IEEE Trans. Nucl. Sci. vol. 46, no. 6, pp. 1744–1750, 1999.
[6] D. Bernard, and R. C. Blish, “Considerations for minimizing radiation doses to components during x-ray inspection,” in Proc. EPTC, 2005, pp 697-704.
[7] F. Xu, L. Helfen, T. Baumbach, and H. Suhonen, “Comparison of image quality in computed laminography and tomography,” Opt. Express, vol. 20, no. 2, pp. 794–806, 2012.
[8] E. Y. Sidky, C.-M. Kao, and X. Pan, “Accurate image reconstruction from few-views and limited-angle data in divergent-beam CT,” J. X-Ray Sci. Tech., vol. 14, pp. 119–139, 2006.
[9] E. Y. Sidky and X. Pan, “Image reconstruction in circular cone-beam computed tomography by constrained, total-variation minimization,” Phys. Med. Biol., vol. 53, no. 17, pp. 4777–4807, 2008.
[10] S. Abbas, M. Park, J. Min, H. K. Kim, and S. Cho, “Sparse-view computed laminography with a spherical sinusoidal scan for nondestructive testing”, Opt. Exp., vol. 22, pp. 17745-17755, 2014
[11] S. Abbas, T. Lee, S. Shin, R. Lee, and S. Cho, “Effects of sparse sampling schemes on image quality in low-dose CT,” Med. Phys. Vol. 40, no. 11, pp. 111915, 2013.

Optimization-based Reconstruction from Megavoltage Cone-beam CT Data in Image Guided Radiation Therapy

Dan Xia, Pascal Paysan, Zheng Zhang, Dieter Seghers, Marcus Brehm, Peter Munro, Andrew M. Davis, Mathias Lehmann, Emil Y. Sidky, Charles Pelizzari, Xiaochuan Pan

***Abstract*—The megavoltage (MV) beam of the linear accelerator (LINAC) for treatment purpose in radiation therapy can also be used to perform cone-beam CT (CBCT) imaging for possibly yielding online information of the tumor under radiation treatment. MV-CT images generally pose relatively low contrast-to-noise ratio (CNR), and most importantly, MV-CT dose to the patient remains a concern. In this work, we investigated optimization-based reconstruction for potentially improving MV-CT-image quality in terms of CNR and for potentially lowering MV-CT imaging dose through the collection of data at views considerably sparser than those in current CT imaging applications. We have carried out the investigation by use of data acquired from a Catphan phantom under various imaging conditions of practical implication. Results of our investigation indicate image-quality improvement in terms of noise reduction and contrast enhancement without sacrificing the spatial resolution compared to the conventional FDK reconstruction, suggesting that it may be possible to obtain images of practical utility in terms of tumor localization and delineation from low-dose MV-CT images reconstructed from sparse-view data by use of optimization-based reconstruction.**

I. Introduction

The on-board kilo-voltage (KV) cone-beam computed tomography (CBCT) imager has been demonstrated to be some utility in image guided radiation therapy (IGRT). Interest exists in exploiting, in addition to on-board KV-CBCT imager, the treatment megavoltage (MV) beam of the linear accelerator (LINAC) to perform CT imaging for possibly yielding online information about the tumor under radiation treatment [1]. The MV-CT imaging approach is attractive because it is easy to implement with minimum hardware modification to the LINAC. MV-CT images generally pose relatively low contrast-to-noise ration (CNR) [2]. Most importantly, with the current scanning configuration, the MV beams at a large number of views may deliver significant amount of radiation dose in addition to the treatment dose, and thus MV-CT dose to the patient remains a concern. In this work, we investigated optimization-based reconstruction for potentially improving MV-CT-image quality in terms of CNR and for potentially lowering MV-CT imaging dose through the collection of data at views considerably sparser than those in current CT imaging applications. We have carried out the investigation using an optimization-based reconstruction method from data acquired in real-data studies with a Catphan phantom under various imaging conditions of practical implication. Specifically, in the study, we have tailored the adaptive-steepest-descent-projection-onto-convex-sets (ASD-POCS) algorithm [3], [4] to reconstruct MV-CT images from data collected. Our previous work has demonstrated that the ASD-POCS algorithm may yield images with reduced noise, improved soft-tissue-contrast, and enhanced spatial resolution from on-board KV CBCT data, as compared to the clinical FDK reconstructions [5]. Results of our investigation indicate image-quality improvement in terms of noise reduction and contrast enhancement without sacrificing the spatial resolution compared to the conventional FDK reconstruction, suggesting that it may be possible to obtain images of practical utility in terms of tumor localization and delineation from low-dose MV-CT images reconstructed from sparse-view data by use of optimization-based reconstruction.

D. Xia, Z. Zhang, A. M. Davis, E. Y. Sidky, and X. Pan are with the Department of Radiology, The University of Chicago, Chicago, IL 60637, USA.

P. Payan, D. Seghers, M. Brehm, P. Munro, and M. Lehmann are with Varian Medical Systems Imaging Laboratory, Tafernstr. 7, CH-5405 Baden-Dattwil, Switzerland.

C. Pelizzari and X. Pan are with the Department of Radiation and Cellular Oncology, The University of Chicago, Chicago, IL 60637, USA.

II. Materials and methods

A. Data acquisition

In this work, we collected data with a Varian TrueBeam system, equipped with an MV flat-panel detector consisting of 1280 x 1280 pixels and a pixel size of 0.336 x 0.336 mm. The MV imager uses a GOS scintillator material. The system was set up to deliver a 6 MV photon beam (6xFFF). The beam generation was manually adapted to deliver a pulse rate matching the MV imager frame rate of 15 fps, leading to a dose per frame of the order of 0.05 MU (monitor units). In this study, a Catphan phantom, which includes two modules for contrast and spatial resolution test, was used to evaluate the MV CBCT imaging. A circular short-scan was conducted and 201 views projections, distributed over an angular range of $\sim$200 degrees, were acquired. The total dose of the scan represented ca. 10 MU.

B. Optimization-based image reconstruction

A discrete-to-discrete linear system is used as the imaging model of the MV-CBCT imager:

$$\mathbf{g} = \mathcal{H}\mathbf{f},$$

where vectors $\mathbf{g}$ and $\mathbf{f}$ denote the discrete data and image, and the system matrix $\mathcal{H}$ describes the cone-beam X-ray transform. The 3D image reconstruction is formulated as a constraint total variation (TV)-minimization program [3],

$$\mathbf{f}^* = \text{argmin}||\mathbf{f}||_{\text{TV}} \qquad \text{s.t.} \qquad D(\mathbf{f}) \leq \epsilon \quad \text{and } \mathbf{f} \geq 0, \quad (1)$$

where $||\mathbf{f}||_{TV}$ denotes the image TV and $D(\mathbf{f})$ is Euclidean data divergence between the measured data $\mathbf{g}$ and model data $\mathcal{H}\mathbf{f}$. Parameter $\epsilon > 0$ is used to control the inconsistency between the measured data and model data. Note that any physical factors that are not modeled into the system matrix $\mathcal{H}$ contribute to the inconsistencies.

The adaptive-steepest-descent-projection-onto-convex-sets (ASD-POCS) algorithm [3] is implemented for numerically achieving the solution specified by the optimization program in Eq. (1). In this study, the size of image voxel is selected to be 0.27 mm, which is close to the size of the detector bin at isocenter. For comparison, the ASD-POCS reconstruction was converted to rectangular-cuboid-shaped voxel of size 1.0 x 1.0 x 2.0, which is used in clinical FDK reconstructions. In an attempt to streamline the reconstruction process, algorithm parameters, such as step sizes of the POCS and TV-minimization steps have been pre-selected for all the data sets, and all reconstructions are terminated after 30 iteration.

III. Results

We have performed image reconstruction by use of the ASD-POCS algorithm from the 201-view data set, and the reconstructed images within one sagittal slice and one transverse slice with several different inserts are displayed in Fig. 1. As a reference, clinical FDK reconstructions are also displayed in the first row of Fig. 1.

Based upon the visual inspection, it can be observed that image distortions in the FDK sagittal slice due to the combination of the cone-beam artifacts and the short-scan is substantially reduced in the ASD-POCS reconstruction. The noise in the ASD-POCS reconstructions in both sagittal and transverse slices is lower significantly than that in the clinical FDK reconstructions. With the reduction of the noise, the fine structures are easy to detect in a relative clean background, as the arrows indicate in the sagittal slice. The boundaries between different objects in ASD-POCS reconstructions appear to be sharper and more clear, which may be potentially useful for accurate tumor localization and delineation.

In attempt to evaluate the performance of ASD-POCS reconstruction for less data, we have also carried out a reconstruction from a 101-view data set, which is extracted from the 201-view data set and uniformly distributed over 200 degrees. The reconstructed images are shown in the third row of Fig. 1. It can be observed that the ASD-POCS reconstruction from the 101-view data set, slightly inferior to the ASD-POCS reconstruction from the 201-view data, appears to be superior to the clinical FDK reconstruction in term of noise reduction and contrast improvement.

In order to quantitatively evaluate the reconstruction contrast, we have calculated the contrast to noise ratio:

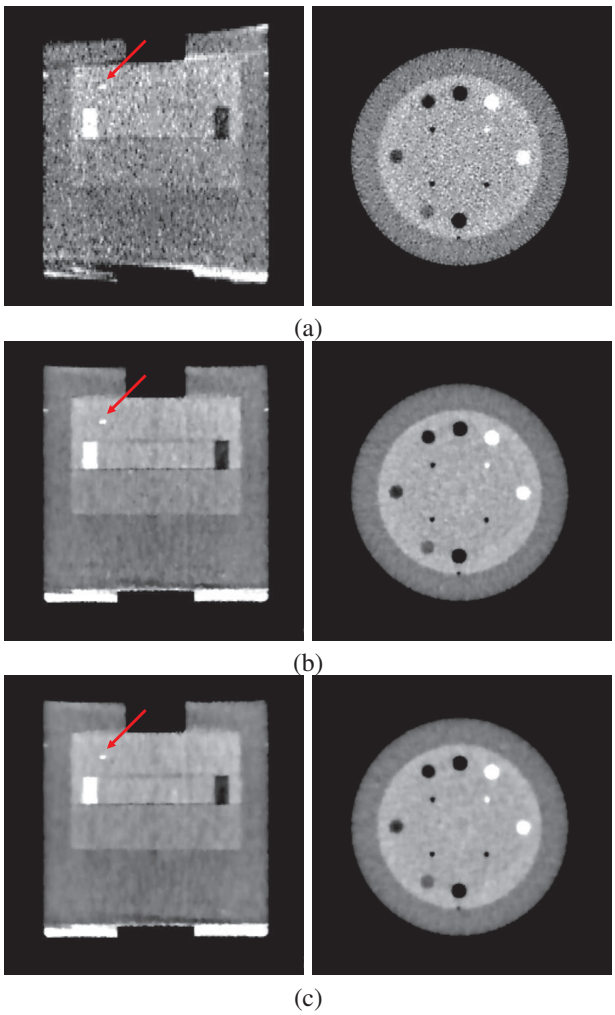

Figure 1. Reconstructed images within a sagittal slice (left column) and a transverse slice (right column) obtained by use of the clinical FDK algorithm (a) and by use of the ASD-POCS algorithm from the 201-view data set (b) and the 101-view data set (c). The display window is [-100, 200] HU.

$$\text{CNR} = \frac{|\bar{\mathbf{f}}_s - \bar{\mathbf{f}}_b|}{\sqrt{\sigma_s^2 + \sigma_b^2}},$$

where $\bar{\mathbf{f}}_s$ and σ_s denote the mean and standard deviation within a region of interest (ROI), and $\bar{\mathbf{f}}_b$ and σ_b denote the mean and standard deviation within a selected background region. We have selected seven (ROIs) containing different inserts and the corresponding background regions, as shown in Fig. 2a. The CNR values obtained from the images reconstructed with the ASD-POCS algorithm from the 201-view and 101-view data sets are shown in Fig. 2b. Again the CNR values obtained from the FDK reconstruction are shown in Fig. 2b as a reference.

The CNR values obtained with ASD-POCS algorithm from both the 201-view and 101-view data sets are in general larger than those obtained with the FDK algorithm, which suggests that ASD-POCS reconstructions are able to preserve the contrast while suppressing noise, yielding a relative high utility for a task of localizing and/or delineating the low-

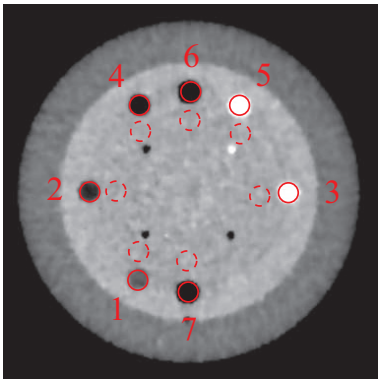

(a)

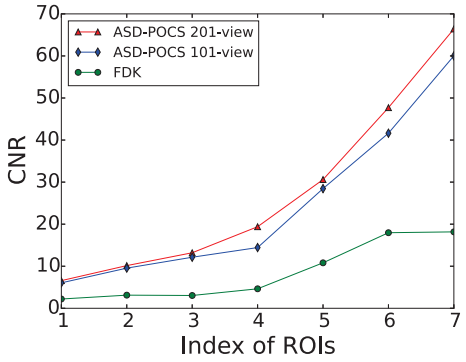

(b)

Figure 2. (a) Selected seven ROIs enclosed by the red solid circles and the corresponding background regions enclosed by the red dash circles. (b) CNR values obtained from the images obtained by use of the clinical FDK algorithm ('○'), the ASD-POCS algorithm from the 201-view data set ('△'), the ASD-POCS algorithm from the 101-view data set ('◇').

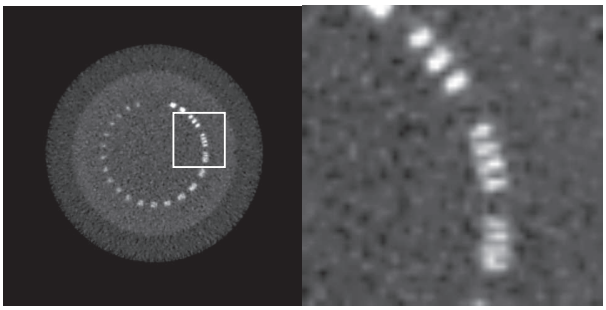

(a)

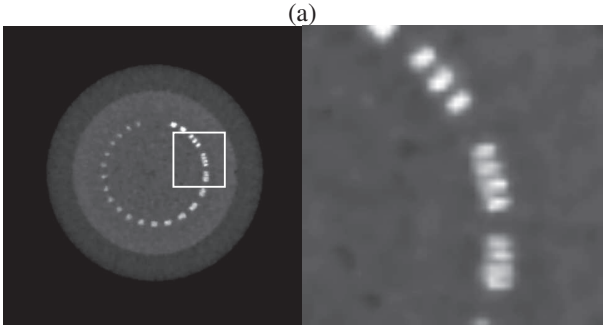

(b)

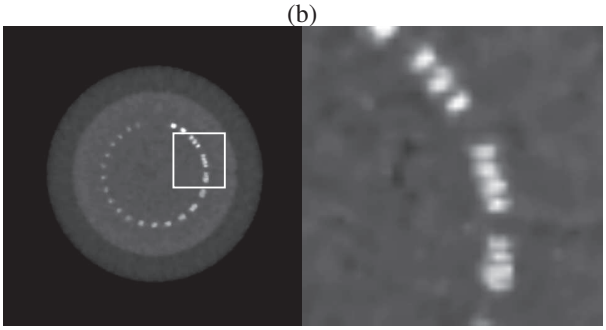

(c)

Figure 3. Full images (left column) and ROI images (right column) with bar patterns obtained by use of the clinical FDK algorithm (a) and by use of the ASD-POCS algorithm from the 201-view data set (b) and the 101-view data set (c). The display window is [-100, 800] HU.

contrast object. Moreover, the CNR values obtained from the 101-view data set is slightly smaller to those obtained from 201-view data set although the mount of data is reduced by half. These quantitative results are consistent with our observation made for the images shown in Fig. 1.

In order to evaluate the performance of the ASD-POCS algorithm for the MV CBCT imaging in terms of spatial resolution, the reconstructions within the transverse slice with bar patterns are displayed in Fig. 3. For the sake of examination of details, ROI images enclosed in the white box of the left column, are displayed in the right column of Fig. 3. It can be observed that the image obtained with ASD-POCS algorithm from the 201-view data set is visually comparable to that obtained with the clinical FDK algorithm in terms of spatial resolution, and the image reconstructed from the 101-view data set is slightly worse.

We also investigated the evolution of reconstruction as a function of the iteration number. We show in Fig. 4 the reconstructed images within a sagittal slice obtained by use of the ASD-POCS algorithm from the 201-view data set at iterations 5, 10, 20, and 30. It can be observed that the reconstruction at early iterations, e.g., iterations 5 and 10, shows the structures with high noise level. Some cone-beam artifacts, such as dark streaks on the top of the phantom, can also be observed in the early iterations. As the iterations progress, the noise is suppressed due to the TV constraint, the boundary becomes clear, and the cone-beam artifacts are reduced, as indicated by the red arrows.

IV. Conclusions

In this work, we have investigated the use of optimization-based reconstruction algorithm, ASD-POCS algorithm, for image reconstructions from MV CBCT data in IGRT. The reconstructions were carried out from the 201-view and the 101-view data sets. The results indicate possible image-quality improvement in terms of noise reduction and contrast enhancement without sacrificing the spatial resolution as compared to the conventional FDK reconstruction. The work may have implication for the development of MV-CBCT imaging of possible practical utility for tumor localization and delineation tasks, enabled by optimization-based reconstruction algorithms tailored to the tasks.

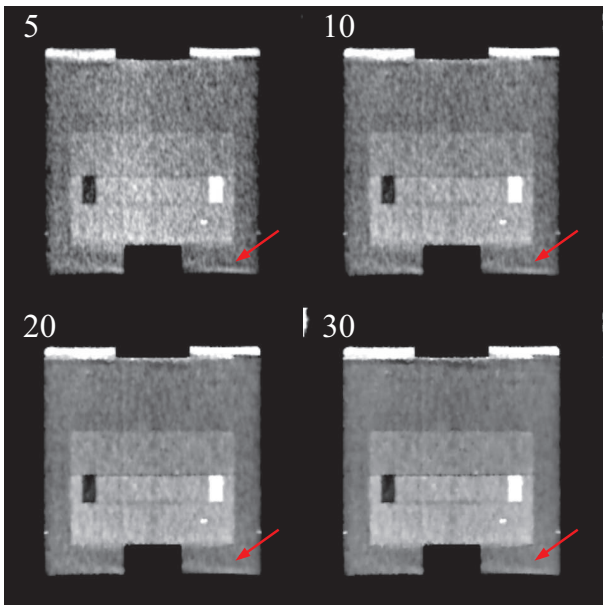

Figure 4. Images within a coronal slice in the reconstruction obtained by use of the ASD-POCS algorithm at different iterations. The iteration number is indicated in each panel. The display window is [-100, 200] HU.

ACKNOWLEDGMENT

This work was supported in part by NIH R01 Grants Nos. CA158446, CA182264, EB018102, and the Varian Research Grant. The contents of this article are solely the responsibility of the authors and do not necessarily represent the official NIH views.

REFERENCES

[1] O. Morin, A. Gillis, J. Chen, M. Aubin, M. K. Bucci, M. R. III, and J. Pouliot, "Megavoltage cone-beam CT: System description and clinical applications," *Med. Dosimetry*, vol. 31, pp. 512–61, 2006.

[2] O. Gayou, D. S. Parda, M. Johnson, and M. Miften, "Patient dose and image quality from mega-voltage cone beam computed tomography imaging," *Med. Phys.*, vol. 34, pp. 499–506, 2007.

[3] E. Y. Sidky and X. Pan, "Image reconstruction in circular cone-beam computed tomography by constrained, total-variation minimization," *Phys. Med. Biol.*, vol. 53, pp. 4777–4807, 2008.

[4] J. Bian, J. H. Siewerdsen, X. Han, E. Y. Sidky, J. L. Prince, C. A. Pelizzari, and X. Pan, "Evaluation of sparse-view reconstruction from flat-panel-detector cone-beam CT," *Phys. Med. Biol.*, vol. 55, pp. 6575–6599, 2010.

[5] X. Han, E. Pearson, C. Pelizzari, H. Al-Hallaq, E. Y. Sidky, J. Bian, and X. Pan, "Algorithm-enabled exploration of image-quality potential of cone-beam CT in image-guided radiation therapy," *Phys. Med. Biol.*, vol. 60, pp. 4601–4633, 2015.

X-Ray Tomography Based on 3D Radon Transform Compatible with Anisotropic Sources

Malte Vassholz[1]*, Benno Koberstein-Schwarz[1], Aike Ruhlandt[1], Martin Krenkel[1], and Tim Salditt[1]
[1]Institut für Röntgenphysik, Georg-August-Universität Göttingen, Friedrich-Hund-Platz 1, Göttingen, Germany

X-ray tomography based on two-dimensional Radon transform is a well-established technique used to map out the three dimensional structure of extended objects in a non-destructive manner. Towards nanoscale resolution with two-dimensional Radon transform based tomography, high brilliance sources are required which are not available in the laboratory. We have recently proposed a new tomography method based on the three-dimensional Radon transform [1] which allows a relaxation of the high brilliance condition within one of the two source dimensions. Here, we review this approach and present additional information on the underlying mathematics. We could show that the so-obtained experimental scheme allows us to record three-dimensional data with isotropic resolution at an anisotropic laboratory source.

I. Introduction

Recently, we have proposed a new x-ray tomography method based on three-dimensional (3D) Radon transform compatible with anisotropic sources [1]. Here we review this work and present additional information on the underlying mathematics along with more details on the experimental implementation.

Computed tomography (CT) with hard x-rays [2]–[6] offers a unique capability to non-destructively map out the 3D structure within the interior of a body or material, owing to a unique penetration power and a quantitatively accountable contrast formation. A persistent challenge for tomography applications with high resolution and/or phase contrast is the required brilliance of the radiation source, impeding applications to be carried out with readily available laboratory sources.

We showed that by suitable generalization of the tomographic measurement geometry as well as the corresponding framework of object reconstruction, some of the present limitations can be lifted. In particular, one can significantly relax the brilliance or source size in one of the two source dimensions. To this end, we replace the conventional framework of the 2D Radon transform (2DRT), which to date is the common basis for analytical x-ray CT, including micro- and nano-CT, with the 3DRT. By proper extension of the data recording scheme, and within controlled geometrical approximations with quantitative error bounds (L. M. Lohse, M. Vassholz, T. Salditt, unpublished), the area integrals required for the 3DRT can be realized experimentally. Thereby, the measurement and reconstruction are made compatible with source properties which can be relaxed along one dimension (the 'low-resolution direction'), while the beam properties along the 'high-resolution direction' determine the resolution and contrast of the entire 3D object reconstruction.

For illustration of the 3DRT measurement and reconstruction, consider the geometry with anisotropic source as sketched in Fig. 1(a). In essence, the 3DRT requires area integrals over a set of parallel planes through the object, and yields one-dimensional (1d) curves $g_{\theta,\phi}(s)$ along the normal of the planes s. Normal vectors $\hat{n}_{\theta,\phi}$ have to be sampled on the unit sphere,

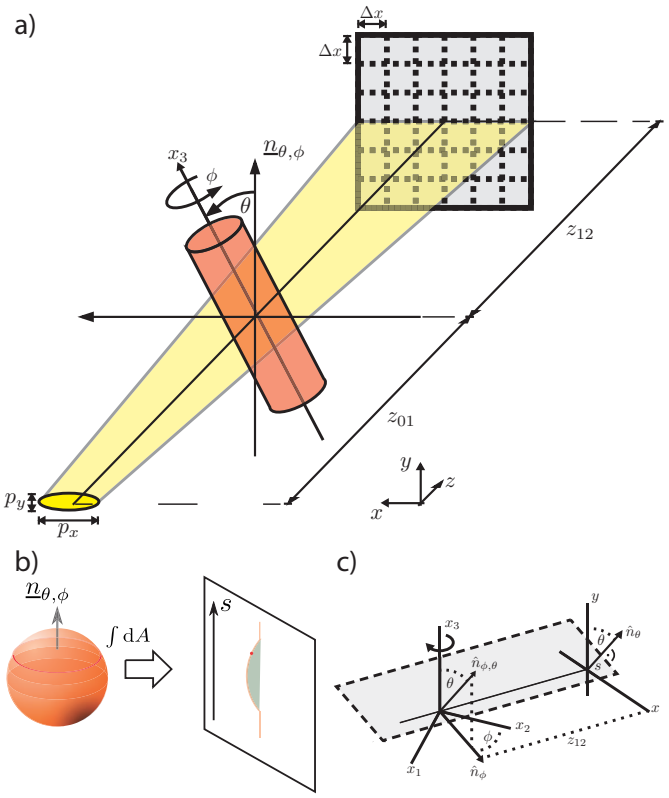

Fig. 1. Schematic of a particular realization of a generalized tomography geometry based on the 3DRT. (a) The tomographic rotation axis is successively tilted by an angle θ with respect to the laboratory y axis, while the object is rotated around this axis by an angle ϕ. Two-dimensional (2D) projection data is acquired and integrated along x, i.e. along the direction suffering from poor resolution and coherence. (b) Illustration of the 1d signal $g_{\theta,\phi}(s)$, corresponding to an integral over parallel planes through the object. (c) Sketch of the coordinate system $\underline{r} = (x_1, x_2, x_3)$ in $\mathbb{R}^3$, to which we will refer as the sample coordinate system. The unit vector $\hat{n}_\phi$ lies in the x_1-x_2 plane. The direction of $\hat{n}_\phi$ is given by the angle ϕ between the x_2-axis and $\hat{n}_\phi$. The unit vector $\hat{n}_{\theta,\phi}$ lies in the x_3-$\hat{n}_\phi$ plane. Its direction is given by the angles ϕ and θ, corresponding to the angles of spherical coordinates. Further, we define a second coordinate system (x, y) rotating with the angle ϕ such that the x-axis is parallel to $\hat{n}_\phi$ and the y-axis stays parallel to the x_3-axis. To this coordinate system we will refer as detector coordinate system.

*mvassho@gwdg.de

as described by the 3DRT operating on the object function $f(\underline{r}),\ \underline{r} \in \mathbb{R}^3$

$$g_{\theta,\phi}(s) = (\mathcal{R}f)(\hat{n}_{\theta,\phi}, s) := \int_{\mathbb{R}^3} \mathrm{d}^3x f(\underline{r})\delta(\underline{r}\cdot\hat{n}_{\theta,\phi} - s), \quad (1)$$

where $\mathcal{R}$ denotes the operator of the Radon transform. Hence, the 3DRT is based on integrals over planes rather than integrals over lines, as the 2DRT. A simple approach how to obtain an area integral $g_{\theta,\phi}(s)$ from a projection image is to integrate the measured 2D image along the low-resolution direction of the source.

II. Data acquisition

To obtain 3DRT data from x-ray projections, the 3DRT is synthesized by two consecutive 2D Radon transforms. In this section we will refer to the coordinate system as defined in Fig. 1(c). As in conventional 2DRT-based tomography, the first 2DRT is performed by the x-ray projection of the sample $f(\underline{r})$ for different angles ϕ, yielding a set of projections $\bar{f}_\phi(x, y)$. A consecutive 2DRT of the x-ray projections $\bar{f}_\phi$ for a set of angles θ results in the 3DRT $\hat{f}_{\theta,\phi}(s)$. Formally, the 2DRT of the x-ray projection $\bar{f}_\phi$ is given by

$$\begin{aligned}
&(\mathcal{R}_{2\mathrm{D}}\bar{f}_\phi)(s,\theta)\\
&= \int_{\mathbb{R}} \mathrm{d}x \int_{\mathbb{R}} \mathrm{d}y\ \bar{f}_\phi(x,y)\,\delta(s - x\sin\theta - y\cos\theta)\\
&= \int_{\mathbb{R}} \mathrm{d}x_1 \int_{\mathbb{R}} \mathrm{d}x_2 \int_{\mathbb{R}} \mathrm{d}x \int_{\mathbb{R}} \mathrm{d}y\ f(x_1,x_2,y)\\
&\quad \cdot \delta(x - x_1\sin\phi - x_2\cos\phi)\cdot\delta(s - x\sin\theta - y\cos\theta).
\end{aligned}$$

By rearrangement of the integrals, the latter equation yields the 3DRT $\hat{f}(s,\phi,\theta)$ of $f(\underline{r})$:

$$\begin{aligned}
&(\mathcal{R}_{2\mathrm{D}}\bar{f}_\phi)(s,\theta)\\
&= \int_{\mathbb{R}} \mathrm{d}x_1 \int_{\mathbb{R}} \mathrm{d}x_2 \int_{\mathbb{R}} \mathrm{d}y\ f(x_1,x_2,y)\\
&\quad \cdot \int_{\mathbb{R}} \mathrm{d}x\ \delta(x - x_1\sin\phi - x_3\cos\phi)\\
&\quad \cdot \delta(s - x\sin\theta - y\cos\theta)\\
&= \int_{\mathbb{R}} \mathrm{d}x_1 \int_{\mathbb{R}} \mathrm{d}x_2 \int_{\mathbb{R}} \mathrm{d}y\ f(x_1,x_2,y)\\
&\quad \cdot \delta(s - (x_1\sin\phi + x_3\cos\phi)\sin\theta - y\cos\theta)\\
&= \hat{f}(s,\phi,\theta).
\end{aligned}$$

Thus the 3DRT of a sample can be experimentally obtained by the x-ray projection of the sample and a consecutive 2DRT in the detection plane. A similar derivation was used by A. V. Bronnikov to derive a phase reconstruction scheme for 2DRT-based tomography [7], [8], and in electron tomography for angular refinement [9].

The acquisition scheme for 3DRT data from x-ray experiments is sketched in Fig. 2. In order to make the tomography scheme robust to anisotropic imaging conditions, the sample is rotated by θ (cf. Fig. 1(a)) and the consecutive 2DRT in the detection plane is only performed within a small intervall $\Delta\theta$ of angles around the high resolution direction, as depicted in Fig. 4(a).

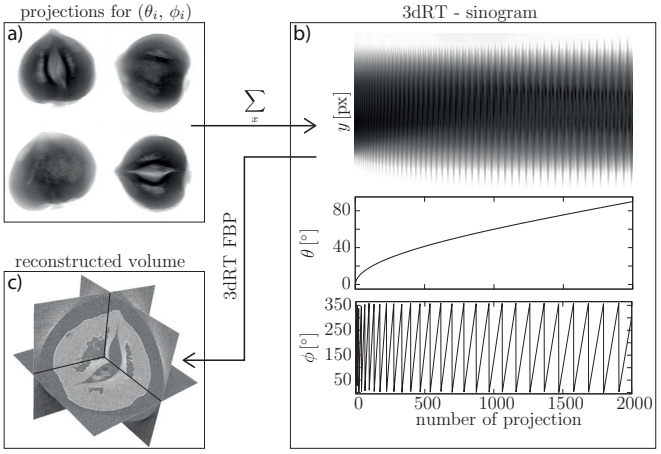

Fig. 2. From data acquisition to the reconstructed volume: a set of x-ray projections is acquired for a discrete set of angles $\{(\theta_i, \phi_i)\}$. The acquired intensity distributions are flat-field corrected and logarithmized, yielding a set of projected absorption images (a). Each of this absorption distribution is summed along the low-resolution direction of the imaging system, x in this case, yielding the discrete 3DRT of the absorption. (b) shows the sinogram equivalent for 3DRT data with the spatial coordinate y along the vertical and the projection index i along the horizontal. The corresponding angles θ_i and ϕ_i are shown below the sinogram. (c) by 3DRT filtered back projection, the sample volume is reconstructed.

III. Reconstruction scheme

For the reconstruction of the 3DRT data the filtered back projection (FBP) is used. In 3D the FBP is formally described by

$$f(\underline{r}) = -\frac{1}{2}(2\pi)^{-2}\left(\mathcal{R}^{\#}_{3\mathrm{D}}\partial_s^2(\mathcal{R}_{3\mathrm{D}}f)\right)(\underline{r}), \quad (2)$$

where $\mathcal{R}_{3\mathrm{D}}$ denotes the 3DRT and $\mathcal{R}^{\#}_{3\mathrm{D}}$ the 3D back projection operator [10]. Thus, the reconstruction scheme consists of the following steps: (1) filter the 3DRT data by its second derivative and (2) back project the filtered signal in 3D. The back projection in 3D is implemented by two consecutive 2D back projections, analogously to the data acquisition. The reconstruction scheme is sketched in Fig. 3 for discrete data.

IV. Experimental data

To test the compatibillity of the method with anisotropic source conditions, we chose a setup based on a sealed tube (DX-Mo10x1-P, GE-Seifert, Germany) with Molybdenum target and a pixelated detector with 55 µm pixel size (Timepix Hexa H05-W0154, X-ray Imaging Europe, Germany), positioned at a distance of $z_{01} + z_{12} = 253.7\,\mathrm{cm}$ from the source. The x-ray beam of the sealed tube with a source spot size of $1\,\mathrm{mm} \times 1\,\mathrm{mm}$ was further confined by slits with an opening of $5\,\mathrm{mm} \times 0.1\,\mathrm{mm}$ (h×v) to emulate an anisotropic source spot. A peeled hazelnut was chosen as object, positioned at $z_{01} = 173\,\mathrm{cm}$ behind the source, fitting to a field of view of 450×450 detector pixels. The data set consists of 8001 x-ray projections for different pairs of (θ, ϕ), chosen to evenly sample the unit sphere [11]. Fig. 4(a, b) show 2D projections of the hazelnut for $\theta = 90°$ (a) and $\theta = 0°$ (b), while keeping ϕ constant. In (a) the side walls of the nut, and in (b) the top and bottom walls are imaged with sharp edges, corresponding to

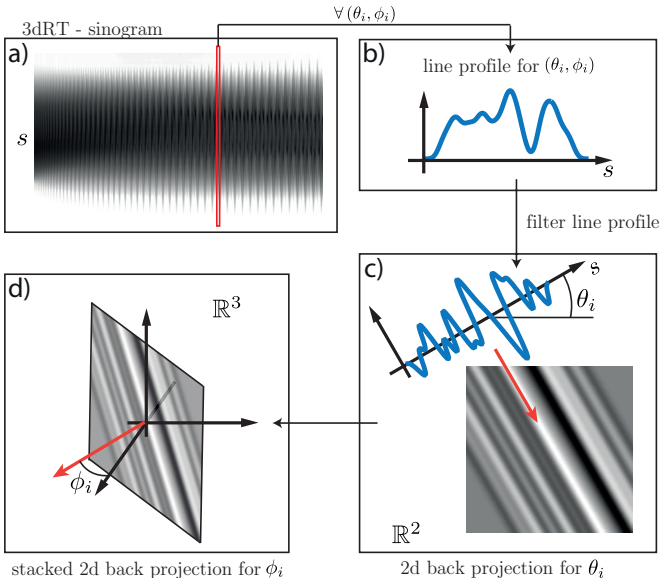

Fig. 3. Filtered back projection for 3DRT data: Starting from the sinogram (a), each line profile (b) is filtered and afterwards back projected in a 2D plane for the corresponding angle θ_i (c). In a last step, the so-obtained 2D image is back projected in 3D space using a stacked 2D back projection for the angle ϕ_i (d). By superposition of the back projections of each line profile, the volume is reconstructed.

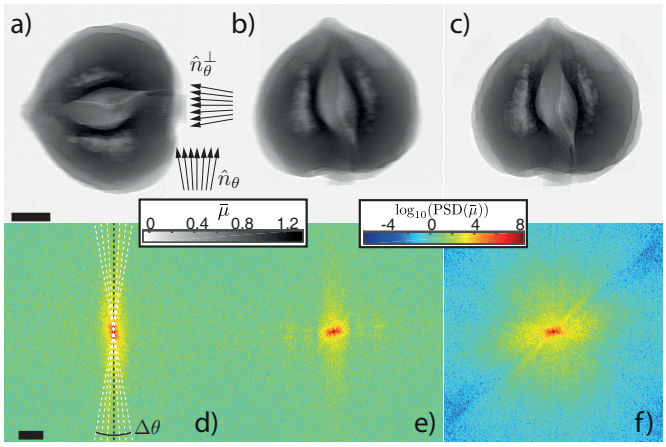

Fig. 4. Experiment: isotropic 'filling' of the 3D Fourier space by the 3DRT. Projection images of the hazelnut are shown for $\theta = 90°$ (a) and $\theta = 0°$ (b), but constant ϕ. In (a) sharp edges are transferred at the side walls of the hazelnut, corresponding to the high-resolution direction of the source, while the top and the bottom walls are blurred, while (b) shows opposite behavior. Application of the 3DRT-FBP reconstruction on the anisotropically blurred projection images yields isotropic resolution, see the re-projection of the reconstructed volume (c) (for the same ϕ as (a, b)). The PSDs (d-f) corresponding to (a-c) quantify this effect. While in (d, e) the signal extends over a large range in the vertical direction but decays rapidly along the horizontal direction, the signal is isotropically distributed up to high Fourier components in (f). In (a) the vectors $\hat{n}_\theta^\perp$ indicate the direction of projection for the consecutive 2DRT. According to the Fourier slice theorem these projections correspond to the central slices in the Fourier space indicated by the dashed lines in (f). Scale bars: 3 mm in (a-c), 3 mm^{-1} in (d-f). (image reference [1])

the respective high-resolution direction. Correspondingly, (a) shows blurred top and bottom edges, and (b) shows blurred side walls, proving the anisotropic source imaging conditions. A re-projection of the reconstructed volume is shown in (c) for the same angle ϕ as in (a, b). The reconstruction shows

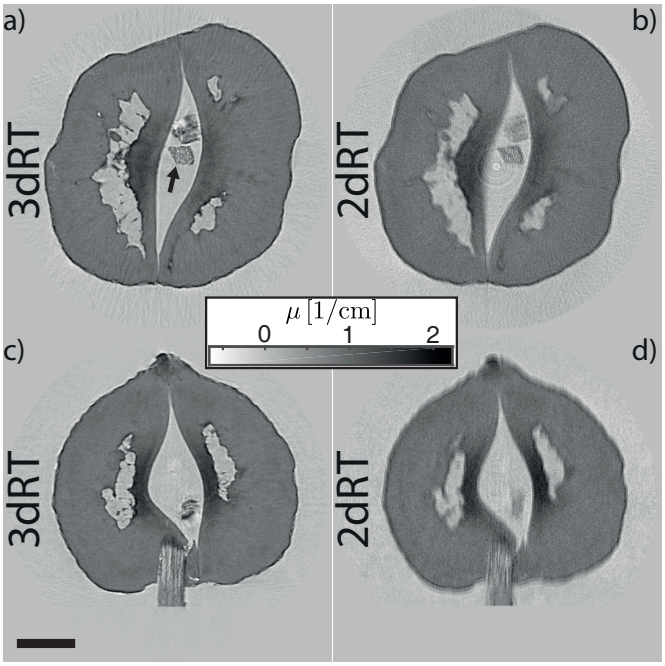

Fig. 5. Slices through an horizontal and a vertical plane of the reconstructed hazelnut volume, shown for the 3DRT-FBP (a, c), and the conventional 2DRT reconstruction (b, d). While the 3DRT is compatible with the source anisotropy, the image quality of the 2DRT reconstruction is severely affected by the anisotropic source. In (a), even the fine details of the wood stick used to mount the hazelnut are well represented (see arrow). Scale bar: 3 mm.

isotropic resolution. The PSDs (d-f) corresponding to the projections (a-c) quantify the isotropic resolution gain. For the 3DRT reconstruction, from each of the 8001 anisotropically blurred projection images, 81 1d data sets were computed by evaluating the 2DRT in a sector of $\pm 10°$ along the high resolution direction, as indicated by the arrows $\hat{n}_\theta$ in Fig. 4(a). Fig. 5 shows orthogonal slices through the reconstructed object for the 3DRT (a, c) and the 2DRT (b, d) reconstruction of the hazelnut. The comparison clearly shows that the 3DRT provides superior image quality with high resolution in all planes.

V. Conclusion

As published in [1], we have shown that the novel data recording and reconstruction scheme presented here can accommodate anisotropic sources, translating the properties of the high-resolution direction (small source size, high partial coherence) isotropically to the full 3d data set. To this end, the object has to be rotated around two axes with a continuous sampling of the unit sphere, which can be obtained in different geometric ways. By geometric means, one can thus escape the flux dilemma for nanoscale tomography at laboratory sources. Apart from spatial resolution, the concept helps to meet a second challenge in analytical x-ray tomography, namely the requirement of sufficiently high spatial coherence to achieve phase contrast.

Finally, we want to mention an entirely different motivation for using 3dRT-based tomography instead of the conventional 2dRT tomography. It can be shown mathematically, that the 3dRT has local properties in the sense that the reconstruction

depends only on the local values s of the Radon transformed object function $(\mathcal{R}f)(s)$ (and its derivatives), significantly facilitating local (ROI) tomography by avoiding the artifacts induced by object components outside the reconstruction volume moving in and out of projections, as commonly observed in 2dRT tomography. While the mathematics of this important difference has been pointed out before [12], it was previously believed that by the nature of the x-ray projection images, only the 2dRT case is experimentally relevant. Here we have shown by a proof-of-concept experiment, that the assumptions and geometrical conditions for area integrals can actually be reached at relevant conditions for analytical x-ray tomography.

ACKNOWLEDGMENT

We thank the German Research Foundation (DFG) through SFB 755/C1 for funding.

REFERENCES

[1] M. Vassholz, B. Koberstein-Schwarz, A. Ruhlandt, M. Krenkel, and T. Salditt *Phys. Rev. Lett.* **116**, 088101 (2016).
[2] A. C. Kak and M. Slaney, *Principles of computerized tomographic imaging* (IEEE, New York, 1988).
[3] T. Buzug, *Computed Tomography : From Photon Statistics to Modern Cone-Beam CT* (Springer-Verlag, Berlin Heidelberg, 2008).
[4] P. Cloetens et al. *PNAS* **103**, 14626 (2006).
[5] F. Pfeiffer, C. Kottler, O. Bunk, and C. David *Phys. Rev. Lett.* **98**, 108105 (2007).
[6] M. Stampanoni, R. Mokso, F. Marone, J. Vila-Comamala, S. Gorelick, P. Trtik, K. Jefimovs, and C. David, *Phys. Rev. B* **81**, 140105 (2010).
[7] A. Bronnikov *J. Opt. Soc. Am. A* **19**, 472 (2002).
[8] A. Bronnikov *Opt. Commun.* **171**, 2394 (1999).
[9] M. Radermacher *Ultramicroscopy* **53.2**, 121-136 (1994).
[10] F. Natterer, *The mathematics of computerized tomography* (SIAM, Philadelphia, 2001).
[11] E. A. Rakhmanov, E. B. Saff, and Y. M. Zhou *Math. Res. Lett.* **1**, 647 (1994).
[12] A. G. Ramm and A. I. Katsevich, *The Radon Transform and Local Tomography* (CRC Press, Boca Raton, 1996), p. 31.

Design and Evaluation of a Parallel and Multi-Platform Cone-Beam X-Ray Simulation Framework

Estefania Serrano*, Javier Garcia Blas*, Ines Garcia†‡,Claudia Molina†‡,Jesus Carretero*, Manuel Desco†‡ and Monica Abella†‡
*Computer Architecture and Technology Area, University Carlos III, Madrid, Spain
Email: esserran@inf.uc3m.es
†Bioengineering and Aerospace Engineering Department, University Carlos III, Madrid, Spain
‡ Instituto de Investigacion Sanitaria Gregorio Marañon, Madrid, Spain

***Abstract*—The development of new flexible X-Ray systems and the exploration of new reconstruction algorithms benefits from the use of computer simulations due to the elimination of the high cost of implementing new acquisition protocols in the actual physical systems. We present a Cone-Beam X-Ray Simulation Framework created with the objective of being flexible and fast, maintaining the compatibility with existing GPUs (CUDA and OpenCL). An optimized execution in different systems is achieved by a modularized implementation by means of a layered architecture and the parallel implementation of the algorithms. We provide a general description of each of the layers, from the algorithm layer at the bottom, with the basic kernels, to the architecture layer at the top, with the different systems configurations that can be executed by the user. We describe the optimizations carry out at each layer in terms of computation and memory management. Finally, we present performance results for different system configurations and hardware platforms.**

***Index Terms*—Backprojection, GPU, parallel processing, projection, simulation, tomography, X-ray**

I. Introduction

THE AVAILABILITY of digital X-Ray detectors and new flexible geometrical configurations open the door to obtain tomographic images in new clinical contexts using new system configurations, different from the standard CT systems. The exploration of new protocols can benefit from computer simulations due to the reduction of the high cost of the study using real systems.

Several simulators accelerated with GPGPUs (General Purpose Graphical Processing Units) have already been presented. IACI CT Simulator [1] and CT Sim [2] are CT simulators targeted to teaching purposes. These examples do not allow flexible geometry configurations and are limited by the type of studies that can be simulated. X-Ray Sim [3] offers similar features as our work, also accelerated by GPU. However, it is based on the projection of digital CAD (Computer Aided Design) models, not on real acquired images, and does not include reconstruction algorithms. Another example is the toolkit ASTRA [4], which provides a solution that can be used to develop advanced reconstruction algorithms, but it is limited to datasets that fit completely in the memory space of a GPU. Furthermore, it lacks of options for standard configurations like helical CT or tomosynthesis.

CUDA and OpenCL programming models have already been used in previous works for the reconstruction of 3D medical imaging. Examples are the works presented in [5] and [6]. In the last one, Siegl et al. studied the usage of OpenCL for high- performance medical image reconstruction by using RabbitCT [7] as a bench-marking platform for CT reconstruction algorithms implemented in OpenCL. They proved that the use of the standard programming model available for different platforms does not penalize the performance excessively, being able to run on different architectures with a loss of around 10

In this work, we present a simulator framework optimized through the use of GPUs, built around different layers. This layer-based architecture permits the fast construction of new X-Ray configurations as well as new flexible reconstruction methods. Another feature is its compatibility with different system setups. We detail the parallelization techniques employed for the framework acceleration and we present an evaluation comparing different system setups over three programming models.

II. Simulation Framework

The Simulation Framework includes several abstraction layers that allow the creation of new configurations based on basic kernels. The general structure of this framework is shown

Manuscript submitted January 25th 2016.

E. Serrano, J. Garcia Blas are with the Computer Architecture and Technology Area, University Carlos III, Madrid Spain. I. Garcia, C. de Molina, M. Desco and M. Abella are with the Biomedical Engineering Department, University of Carlos III, Madrid, Spain and with the Instituto de Investigacion Sanitaria Gregorio Marañon (IiSGM), Madrid, Spain (e-mail: mabella@ing.uc3m.es) M. Desco is also with the Centro de Investigacion en Red de Salud Mental (CIBERSAM, CIBER CB07/09/0031), 28007 Madrid, Spain.

This work was funded by the projects TIN2013-41350-P, IDI-20130301, TEC2013-47270-R, IPT- 2012-0401-300000, RTC-2014-3028-1, the Cardiovascular Research Network (RIC, RD12/0042/0057), and by the EU under the COST Programme Action IC1305 (NESUS).

in Figure 1. We distinguish four main layers, explained in the following subsections.

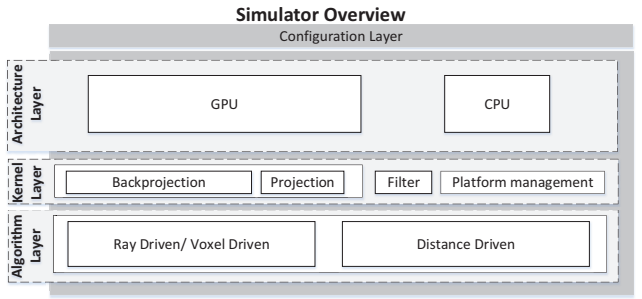

Fig. 1. Overview of the Simulator tool and all its layers.

A. Algorithms layer

This layer contains the minimal execution units, based on the conventional algorithms for data interpolation: ray driven and distance driven for projection and voxel driven and distance driven for backprojection. These algorithms, based on the Cone-Beam geometry (as shown in Figure 2) are the most time consuming parts. For this reason, this layer is were most of the optimizations were made, including the source code parallelization and its implementation in different programming models.

1) Ray Driven and Voxel Driven parallelism: For CUDA and OpenCL implementations, the minimal execution unit that is executed in parallel is the iteration over the v axis. Each of the parallell executions are identified then by the other coordinates: u and z, in the case of the voxel driven algorithm, and s and z in the ray driven algorithm. The parallelism resides in the data independence of each execution, consisting in the voxel or pixel values. This approach has been taken previously in other works for similar applications with good results [8]. The output is stored in the global memory space of the GPU, meanwhile the input data (projections or volume) is stored inside the texture memory of the GPU, which provides automatic interpolation. In the CPU implementation, this interpolation is done using standard 2D and 3D bilinear interpolation equations, implemented inside the algorithms.

2) Distance Driven parallelism: In the case of Distance Driven method, both for Projection and Backprojection operators, the minimal unit of execution is the iteration over the y axis. However, in the distance driven algorithm [9] an additional step is needed, the computation of the boundaries, either on the volume or in the detector. These boundaries are the limits of the voxels and pixels projected in each uz plane. For the computation of these limits, we add four more operations in each iteration. Although independent, these boundaries share the information of the same plane augmenting the locality of the data. However, this boundary computation increases the computational complexity.

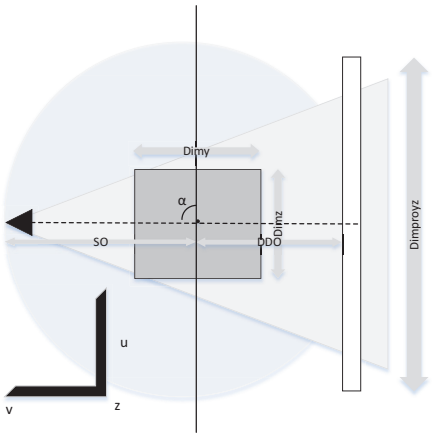

Fig. 2. Basic projection and backprojection configuration. Source, volume, and detector are aligned. Rotation is done around Z axis.

B. Kernel layer

The kernel layer has different modules, which represent the execution core of the simulator, namely the kernels. These kernels will be the main building blocks for the upper layers:

- Backprojection: based on Voxel Driven and Distance Driven interpolation methods. The kernel receives configuration parameters such as source and detector position and object size among others. It implements a basic Cone-Beam backprojector operator.
- Projection: following two approaches: Ray Driven and Distance Driven algorithms. Both based on the computation of the integral of the ray and the interpolation of the contribution to the final pixel.
- Filter: it includes the application of the rampfilter method. To be implemented in GPU, we employed already implemented functions for the Fourier Transform to operate over the Fourier domain on the projections. This is all executed on the GPU with the help of the cuFFT library[1] on CUDA and the clFFT library[2] when employing OpenCL.
- Platform management: it includes several kernels in charge of managing the devices. One of their main functions is memory management. Due to the lack of memory of many of the current GPU devices, it is necessary to include an strategy of partitioning for the simulation of big studies. In our case we have included two levels of partitioning: division of the volume in *chunk*s that are processed separately and division of the projections in *groups*. With the creation of chunks, we avoid the storage of the whole volume in the device memory (or main memory in some cases) and the projections can fit. When partitioning the projections, we avoid the repetition of previous operations over these projections (such as filtering) and at the same time we avoid the memory transfers between host and GPU.

[1]https://developer.nvidia.com/cuFFT
[2]http://clmathlibraries.github.io/clFFT

C. Architecture layer

In this layer, the device architecture is abstracted. Thus, the simulator can run over several platforms including GPU and CPU-only configurations. The objective is the optimization of the algorithms implemented for the different architectures. The three main architectures supported are: x86 CPUs, GPUs, and ARM processors. The programming models that support these architectures are CUDA (for NVidia's GPUs), OpenCL (for GPUs and ARM architectures), and OpenMP (for multi-core CPUs). Through the use of these parallel programming models is possible to increase the performance by parallelizing its execution.

D. Configurations layer

The Configurations layer includes the routines that can be directly executed by the user and implements the different simulation configurations. In this layer, most of the computation consists on the calculation of derived parameters, therefore, it is totally implemented in CPU. This layer is divided in the following parts, as shown in Figure 3:

- Projection and backprojection based on cone-beam: it is the simplest configuration, which directly makes usage of the projection and backprojection kernels without further parameter computation. Thus, there is no need of modification of the standard kernels parameters.
- FDK Reconstruction: it includes the filter kernel execution previous to the basic backprojection kernel.
- Flexible Cone-Beam Projection and Reconstruction with different trajectories. These trajectories are the same as in the basic geometry. In this case, both source and detector can be in any position and orientation. For example, the detector can be tilted or rotated with respect to axis.
- Projection and backprojection based on tomosynthesis: similarly to Wide FOV, it makes use of the projection and backprojection operators. Since for each acquisition it is necessary to modify the kernel parameters, an external loop is required to obtain or process each of the projections. This configuration is available in two forms: 1) the source and detector are moved in opposite directions (Figure 5a); 2) only the source is moved, rotating over the volume with the detector in a fixed position (Figure 5d).
- Wide FOV (Field Of View) acquisition: the main part of this configuration is the projection operator. Depending on the requirements, this increased FOV can be obtained with a displacement of the source and detector along the selected axis (Figure 5c), or with the tilting of the source (Figure 5d).
- Projection and backprojection with helical trajectory: the source and detector are moved through the z axis at the same time that they rotate around the volume (Figure 5e). It makes use of the standard projector and backprojector kernel and includes the simulation of the displacement of the source and detector outside of the algorithm.

TABLE I
DESCRIPTION OF THE STUDIES EMPLOYED IN THE EVALUATION.

Study name	Scapula	DigImouse
Detector pixel Size (mm)	0.14x0.14	0.2992x0.2992
Detector matrix (pixels)	512x512	1024x832
Volume voxel size (mm)	0.087x0.087x0.087	0.1x0.1x0.1
VOI (voxels)	512x512x512	1520x720x832
Number of projections (Cone Beam)	360	360
Number of projections (Tomosynthesis)	11	11
Arc range (degrees)	10	10
Displacement (mm)	125	150

TABLE II
RESULTS IN GIGAUPDATES PER SECOND FOR THE SCAPULA STUDY USING THE DIFFERENT AVAILABLE PROGRAMMING MODELS AND FOR DIFFERENT SYSTEM CONFIGURATIONS.

	Kernel execution			**Overall execution**		
scapula	**CUDA**	**OpenCL**	**CPU**	**CUDA**	**OpenCL**	**CPU**
CB projection	19.184	3.957	0.039	7.844	2.780	0.039
CB backprojection	3.556	3.647	0.019	2.631	2.625	0.019
projection heli	19.122	4.241	0.040	7.795	3.190	0.049
tomo acq	22.249	10.826	0.034	0.128	0.104	0.030
tomo arc	23.070	12.320	0.038	0.105	0.105	0.032

III. EVALUATION

The evaluation was done in a computer with a Windows 10 Operating System. The system's hardware consisted on a Intel Core i5-760 with four cores at 2.8 GHz and 16 GiB of RAM. For the GPU results we used a NVidia 760 GPU, CUDA version 6.5, and OpenCL version 1.2. Regarding CPU evaluation, we used an Intel Core i5-3520 at 3.20 GHz with 16 GiB of RAM.

We used a real acquisition of a cocodrile scapula and a large version of the Digimouse digital phantom which does not fit into commodity GPU memories. The parameters considered for each of the configurations are summarized in Table I. The pitch in the helical acquisition experiment was of 10 mm in the study of the scapula and 25 mm for the mouse study.

The configurations tested were: CB projection, a simple Cone-Beam acquisition with 360 projection with a step angle of 1 degree *CB projection*; cone-beam backprojection with 360 projections with step angle of 1 degree *CB backprojection*; acquisition with helical trajectory over 360 degrees *projection heli*; acquisition using tomosynthesis linear configuration *tomo acq*; acquisition using tomosinthesis arc configuration *tomo arc*. All of them were executed in Ray driven/Voxel driven interpolation mode.

In Tables II and III we show the results for a scapula and a Digimouse studies, respectively. The results are expressed in GigaUpdates per second, measured only with the execution of the kernel (first group of columns) and taking into account the whole execution time of the application including input/output

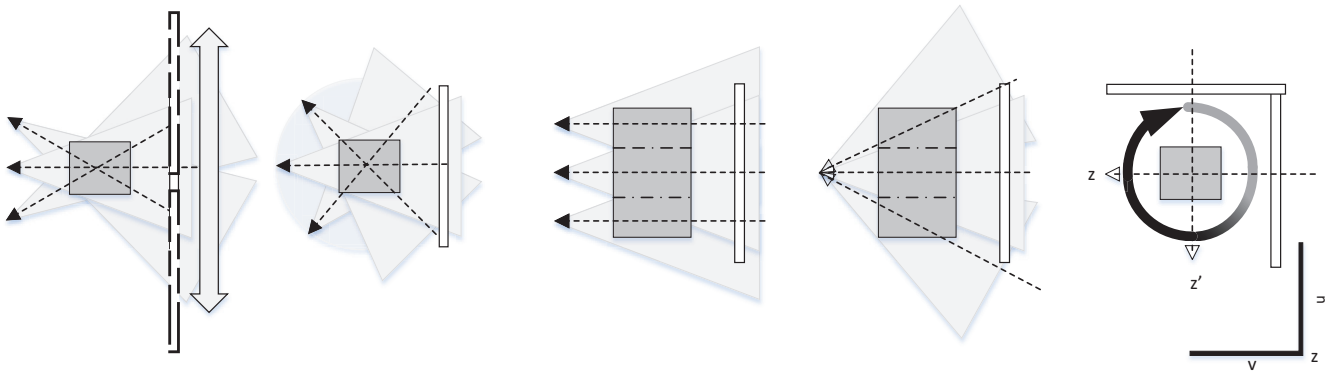

a) Linear Tomosynthesis b) Arc Tomosynthesis c) FOV with displacement d) FOV with Tilting e) Helicoidal geometry

Fig. 3. Graphical representation of the implemented geometries.

TABLE III
RESULTS IN GIGAUPDATES PER SECOND FOR THE DIGIMOUSE STUDY USING THE DIFFERENT AVAILABLE PROGRAMMING MODELS AND FOR DIFFERENT SYSTEM CONFIGURATIONS.

	Kernel execution			Overall execution		
Digimouse	**CUDA**	**OpenCL**	**CPU**	**CUDA**	**OpenCL**	**CPU**
CB projection	1.487	1.942	0.039	1.044	1.096	0.039
CB backprojection	3.191	3.370	0.018	0.920	2.116	0.018
projection heli	1.477	1.931	0.039	1.059	1.114	0.039
tomo acq	4.419	3.982	0.034	0.107	0.110	0.030
tomo arc	0.110	3.682	0.034	0.108	0.110	0.031

operations (second group of columns). In both of them, we obtain the worst performance on the CPU even with the parallelization of the core algorithms using OpenMP. The results for the GPU programming models are very different depending on whether we use OpenCL or CUDA programming models in spite of employing the same acceleration device. For most of the system configurations, OpenCL offers worst results than CUDA when the VOI is small. However, the performance in the Digimouse study is almost the same for both cases. This is due to the better exploitation of the hardware when using CUDA, that is solved when there is enough load to obtain the maximum computational capacity of the card.

IV. DISCUSSION AND CONCLUSION

We have shown a flexible X-Ray simulation framework that is able to simulate different geometries and system configurations, based on the cone-beam geometry. The proposed simulator architecture is layered to facilitate the introduction of future kernels and configurations. Additionally the solution offers compatibility with the majority of hardware platforms (CUDA and OpenCL for GPUs and standard workstations through OpenMP). The simulator easily allows its execution through the command line. These features facilitates its integration with other existing tools. The algorithms implemented are optimized in terms of performance and memory. The obtained results demonstrated that the CUDA programming model performs better for small studies while OpenCL slightly outperforms CUDA for large size studies.

The porting to other interesting parallel architectures such as Intel Xeon Phi would need major changes. This later possibility would imply a bigger transformation due to the programming model. It is important to note that currently Intel Xeon Phi lacks of support for OpenCL 1.2 full profile. This means that there is no support for textures processing and advanced features, preventing the porting of our simulator. As a future work we plan to provide automatic partitioning. This feature will improve the overall performance in case of heterogeneous devices.

REFERENCES

[1] "IACI CT simulator," 2015. [Online]. Available: http://www.iacionline.com/simulators.da
[2] "CT Sim," 2002. [Online]. Available: http://files.b9.com/ctsim/ctsim-manual-latest.pdf
[3] "X-Ray Sim," 2015. [Online]. Available: http://xraysim.sourceforge.net/index.htm
[4] W. J. Palenstijn, K. J. Batenburg, and J. Sijbers, "The ASTRA tomography toolbox," in *13th International Conference on Computational and Mathematical Methods in Science and Engineering, CMMSE*, vol. 2013, 2013.
[5] S. Mukherjeet, N. Moore, J. Brock, and M. Leeser, "CUDA and OpenCL implementations of 3D CT reconstruction for biomedical imaging," in *IEEE Conference on High Performance Extreme Computing (HPEC), 2012*, 2012, pp. 1–6.
[6] C. Siegl, H. Hofmann, B. Keck, M. Prümmer, and J. Hornegger, "OpenCL: a viable solution for high-performance medical image reconstruction?" in *SPIE Medical Imaging*. International Society for Optics and Photonics, 2011, pp. 79 612Q–79 612Q.
[7] C. Rohkohl, B. Keck, H. Hofmann, and J. Hornegger, "Technical Note: RabbitCT - an open platform for benchmarking 3D cone-beam reconstruction algorithms," *Medical Physics*, vol. 36, no. 9, pp. 3940–3944, 2009.
[8] J. G. Blas, M. Abella, F. Isaila, J. Carretero, and M. Desco, "Surfing the optimization space of a multiple-gpu parallel implementation of a x-ray tomography reconstruction algorithm," *Journal of Systems and Software*, vol. 95, pp. 166 – 175, 2014. [Online]. Available: http://www.sciencedirect.com/science/article/pii/S0164121214001034
[9] B. De Man and S. Basu, "Distance-driven projection and backprojection in three dimensions," *Physics in medicine and biology*, vol. 49, no. 11, p. 2463, 2004.

Dual-Rotation C-arm Cone-Beam Computed Tomography to Increase Low-Contrast Resolution

Aymeric Reshef[1,2], Cyril Riddell[2], Yves Trousset[2], Saïd Ladjal[1], and Isabelle Bloch[1]

[1] LTCI, CNRS, Télécom ParisTech, Université Paris-Saclay, 75013, Paris, France
[2] GE Healthcare, Buc, France

***Abstract*—Interventional imaging with C-arm Cone-Beam Computed Tomography (CBCT) lacks low-contrast resolution. The use of bow-tie filters is common in diagnostic Computed Tomography (CT), as they reduce both patient dose and the dynamic range of the signal at the detector. Without a bow-tie filter, a single-rotation acquisition results either in under-exposed areas where the object is thick, or in over-exposed areas where the object is thin. Here, we propose to acquire two rotations in order to compensate for the absence of a bow-tie filter: an un-truncated acquisition at low exposure and a truncated acquisition at higher exposure. We allow the rotations not to be acquired at the exact same positions, and introduce a reconstruction strategy to make full use of our redundant data and reconstruct the full field-of-view. The method is extended to volume-of-interest tomography. Results on a quality assurance phantom show that an angularly finely sampled acquisition of truncated intensity projections increases low-contrast resolution of C-arm CBCT, when combined with a (sub)set of un-truncated, low-intensity projections. Depending on the angular sampling of the un-truncated data, improvement is observed either over the entire field-of-view or over the truncated field-of-view.**

***Index Terms*—C-arm, cone-beam, tomography, iterative reconstruction, low-contrast, bow-tie filter**

I. Introduction

C-arm Cone Beam Computed Tomography (CBCT) plays a growing role in interventional neuroradiology. Intra-arterial injection of iodinated contrast allows the reconstruction of blood vessels with high spatial resolution. On the contrary, imaging soft tissues in the brain is particularly challenging due to design constraints: C-arm systems allow patient imaging at a large range of angulations over three axes of rotations while a lift can vary the distance between the X-ray source and the detector. This flexibility does not allow for efficient scatter rejection with respect to the fixed geometry of diagnostic Computed Tomography (CT) scanners. In addition, CT scanners make use of bow-tie filters to reduce dose to the patient and the dynamic range of the signal at the detector. However, the small number of C-arm CBCT acquisitions that need to be performed per day does not warrant the expensive integration of a bow-tie filter dedicated to brain imaging. Therefore, the dynamic range of the signal that reaches the detector is higher with a C-arm and the low noise level required for low-contrast (LC) detection leads to over-exposure of the periphery of the head, to the extent of saturating the detector. A dual-gain readout prevents saturation [1], [2], yet this mode is not supported by all detectors and does not address over-exposure.

Corresponding author: aymeric.reshef@ge.com. This work was supported by the CIFRE grant No. 873/2014 from the French Association Nationale de la Recherche et de la Technologie (ANRT).

Here, we look at collimation to increase the X-ray intensity for the central densest part of the anatomy. Since the resulting acquisition is truncated, we consider a double acquisition: one rotation without truncation optimized for the thickness of the peripheral anatomy, and one truncated acquisition to increase exposure for the central thickest areas. Previous works using double acquisitions, e.g. [3], [4], [5], [6] targets volume-of-interest (VOI) reconstruction or increased VOI resolution. A standard analytical algorithm, in our context FDK [7], is applied to a synthetized projection set computed from both acquisitions. This implies accurate knowledge of the exposure ratio and either interpolation or identical acquisition geometries. Our approach is intended to be less restrictive. First, we do not assume to know the exposure ratio because truncated data do not contain a reference air measurement of the incoming X-ray beam; second, we do not assume the geometry to be the same for each acquisition. This implies developing a dedicated reconstruction to handle data redundancy, truncation and absence of reference measurement.

The paper is organized as follows. Section II-A briefly describes the acquisition strategy and why standard analytical reconstruction is not applicable when acquisition geometries are different. Section II-B introduces the minimization problem solved by iterative reconstruction. The method is then extended to the case where the truncated field-of-view (FOV) must be reconstructed only. A highly sub-sampled un-truncated data set is used in this case, with the hypothesis that the low-frequencies it contains will be sufficient to correct for the artefacts that degrade volume-of-interest reconstruction from truncated data. Results on the Catphan® phantom LC detection module are presented in Sec. III.

II. Method

A. Acquisition description

Density projections, denoted p, are related to the object f through a linear projection operator R such that $Rf - p = 0$. Ideal system measurements are intensity projections I related to p via the Beer-Lambert law $I = I_0 e^{-p}$, where I_0 is the

intensity of the X-ray beam measured in air. Note that real data are corrupted by noise and scattered radiations.

1) Dual-rotation acquisition: We assume that two sets of intensity projections are available: one set of full FOV projections (indexed by F), and one set of truncated projections (indexed by T). Both sets are acquired with the standard short-scan circular rotation ("spin") available on C-arm systems.

Given a reference air intensity I_0, we define the air measurements of the incoming X-ray beams in both cases as

$$\left\{ \begin{array}{rcl} I_0^{\mathrm{F}} & = & \alpha_{\mathrm{F}} \cdot I_0 \\ I_0^{\mathrm{T}} & = & \alpha_{\mathrm{T}} \cdot I_0 \end{array} \right. , \text{ with } \alpha_{\mathrm{F}} + \alpha_{\mathrm{T}} = 1. \quad (1)$$

Density projections p_n ($n \in \{\mathrm{F}, \mathrm{T}\}$) are obtained from the Beer-Lambert law: $p_n = \log(I_0^n) - \log(I_n)$. If air measurement I_0^n is not available, then p_n is only known up to a constant offset.

2) Dose reduction factor: Assuming that both acquisitions have the same angular sampling and that truncation reduces the exposed detector area by a factor $p < 1$ compared to the un-collimated case, we define the dose reduction factor d as the ratio of $I_0^{\mathrm{F}} + p \cdot I_0^{\mathrm{T}}$ with I_0, yielding

$$d = \frac{I_0}{I_0^{\mathrm{F}} + p \cdot I_0^{\mathrm{T}}} = (\alpha_{\mathrm{F}} + p \cdot \alpha_{\mathrm{T}})^{-1}. \quad (2)$$

B. Reconstruction

1) Analytical reconstruction: If both intensity spins I_{T} and I_{F} were acquired at the very same angular positions ($R_{\mathrm{F}} = R_{\mathrm{T}} = R$), the data could be summed according to

$$p = \left\{ \begin{array}{ll} \alpha_{\mathrm{F}} \cdot p_{\mathrm{F}} + \alpha_{\mathrm{T}} \cdot p_{\mathrm{T}} & \text{in the collimated area,} \\ p_{\mathrm{F}} & \text{elsewhere.} \end{array} \right. \quad (3)$$

Equation (3) is sensitive to offset errors in p_{F} or p_{T}. The Feldkamp-Davis-Kress (FDK) algorithm [7] is a filtered-backprojection type method to reconstruct cone-beam projections from a circular orbit. We denote $f_{\mathrm{FDK}} = R^T D p$ this analytical reconstruction, with D the ramp filter and R^T the transpose of R, that is the backprojection operator.

Ramp filtering is performed in the Fourier space. For acurate reconstruction, the discrete ramp filter is not equal to sampling the continuous Fourier ramp filter, but is computed as the Fourier transform of the finite spatial ramp kernel. This results in a non-zero DC value, which, again, is sensitive to any offset error in p_n.

If acquisition geometries are different, there is no standard solution and for each situation clever re-sampling or extrapolation of the truncated data must be derived. We thus turn to iterative reconstruction as a generic approach that allows multiple geometries and does not require accurate knowledge of the exposures.

2) Minimization criterion: We define two quadratic forms

$$\mathcal{Q}_n(f) = \frac{1}{2}(R_n f - p_n)^T D (R_n f - p_n), \quad n \in \{\mathrm{F}, \mathrm{T}\}$$

that we minimize simultaneously, through:

$$\underset{f}{\operatorname{argmin}} \left\{ \sum_{n \in \{\mathrm{F},\mathrm{T}\}} \alpha_n \mathcal{Q}_n(f) + \chi(f) \right\}, \quad (4)$$

where $\chi(f)$ is a convex regularizing term. If the acquisition geometries of p_{T} and p_{F} were the same, then $R_{\mathrm{T}} = R_{\mathrm{F}} = R$, and Problem (4) would simplify into

$$\underset{f}{\operatorname{argmin}} \left\{ \frac{1}{2}(Rf - p)^T D (Rf - p) + \chi(f) \right\}, \quad (5)$$

with p defined in eq. (3).

3) Iterative algorithm: We adopt a forward-backward splitting scheme [8], yielding a two-step update made of a gradient descent step (iterative FDK) followed by the application of a proximal operator (e.g. filter)

$$\left\{ \begin{array}{rcl} f^{(i+1/2)} & = & f^{(i)} - \tau \sum_n \alpha_n R_n^T D (R_n f^{(i)} - p_n) \\ f^{(i+1)} & = & \mathrm{prox}_{\tau\chi}(f^{(i+1/2)}) \end{array} \right. , \quad (6)$$

where $\tau > 0$ is a constant gradient step and $\mathrm{prox}_{\tau\chi}(f^{(i+1/2)})$ is the proximal operator of scaled function $\tau\chi$ on image $f^{(i+1/2)}$. This scheme was used in [8] with non-linear filtering to correct for cone-beam artifacts.

4) Ramp filtering: For operator D, we discretize the continuous Fourier ramp filter, in order to zeroe the DC component together with all offset errors. Although it introduces a shift in FDK reconstructed images, this shift is removed by the iterative process. The use of the Fourier transform implies data extrapolation. Zero-padding of the signal would introduce strong discontinuities resulting in artifacted reconstructions. Thus, extrapolation is achieved by mirroring the data at each extremity of the signal.

5) Extension to volume-of-interest imaging: If one is only interested in reconstructing the volume of interest defined by the truncated dataset, we need to distinguish between high- and low-frequency artifacts. High-frequency artifacts strongly corrupt the image, but are easily removed for instance by data mirroring as already mentionned. Low-frequency artifacts (small intensity gradient over the FOV, cupping) are less disturbing, but forbid visualizing low contrasts over a uniform background. However, we anticipate that adding a few full-FOV projections will provide sufficient low-frequency information to yield a uniform reconstruction. In this case, we replace weights α_n in eq. (4) by new weights β_n such that

$$\left\{ \begin{array}{rcl} N_{\mathrm{F}} & = & \beta_{\mathrm{F}} \cdot N \\ N_{\mathrm{T}} & = & \beta_{\mathrm{T}} \cdot N \end{array} \right. , \text{ with } \beta_{\mathrm{F}} + \beta_{\mathrm{T}} = 1 \text{ and } \beta_{\mathrm{F}} \ll \beta_{\mathrm{T}}, \quad (7)$$

where N_{F} and N_{T} are the number of projection views in each set, and $N = N_{\mathrm{F}} + N_{\mathrm{T}}$ is the total number of projections.

III. Experiments and Results

A Catphan® phantom LC detection module [9] was acquired on a GE Healthcare IGS-630 biplane system, whose flat-panel detector is 30cm wide. The source-to-detector distance was 1080mm. Each rotation provided 600 intensity projections covering 200°. Three spins were acquired with a vertical FOV height of 5cm, in order to limit scattered radiations, that is not addressed by our method. A full-FOV width was kept for all acquisitions. One spin acquired at 76kVp and 3.4mAs was used as the un-truncated, low-exposure spin. A second spin at 76kVp and 3.4mAs was used

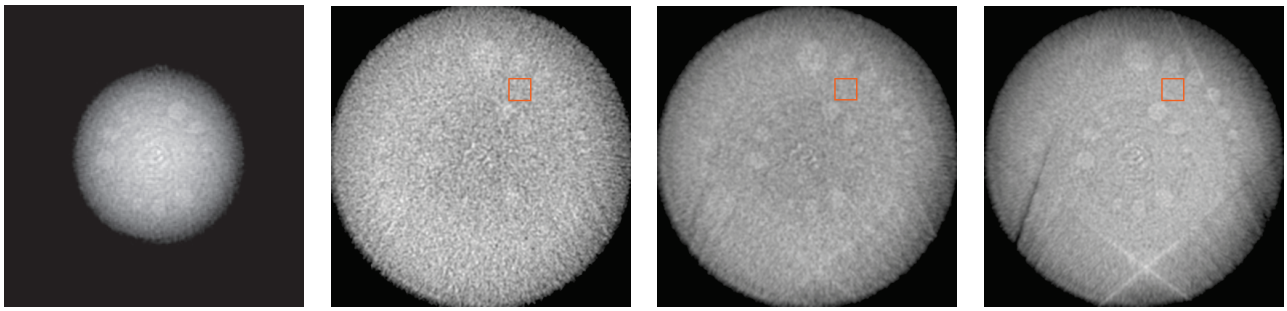

(a) Truncated at 120kVp (b) Un-truncated at 76kVp, $\sigma = 5.6$ (c) $\alpha_{\mathrm{T}} = \alpha_{\mathrm{F}}$, $\sigma = 3.1$ (d) $\alpha_{\mathrm{T}} = 4 \cdot \alpha_{\mathrm{F}}$, $\sigma = 2.7$

Fig. 1: Recontructions of the Catphan® CTP515 module. Standard deviation σ is calculated over the squared region-of-interest. Window level-width: 330-100 in Fig.1a; 570-100 in Fig.1b, 1c and 1d. Isotropic voxel size: 0.78mm.

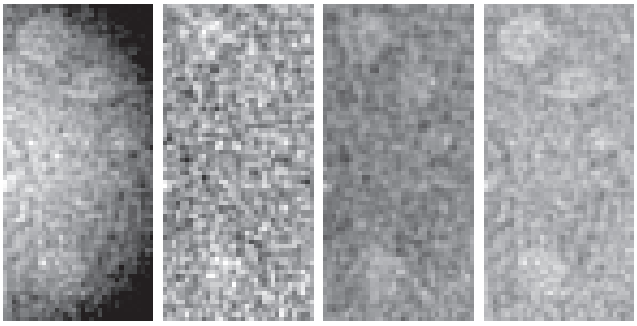

(a) Truncated at 120kVp (b) Un-truncated at 76kVp (c) $\alpha_{\mathrm{T}} = \alpha_{\mathrm{F}}$ (d) $\alpha_{\mathrm{T}} = 4\alpha_{\mathrm{F}}$

Fig. 2: Recontructions of the Catphan® CTP515 module. Detail on central LC inserts from 10 HU (top) to 3 HU (bottom) from Fig.1. Window level-width: 330-100 in Fig.1a; 570-100 in Fig.1b, 1c and 1d. Isotropic voxel size: 0.78mm.

to test the case $\alpha_{\mathrm{T}} = \alpha_{\mathrm{F}}$. In order to test the case $\alpha_{\mathrm{T}} \gg \alpha_{\mathrm{F}}$, we acquired a third spin at a shifted spectrum of 120kVp and 3.4mAs. The dose-area-product (DAP) of a Catphan® acquired at (120kVp, 3.4mAs) was approximately 4 times the DAP of the acquisition at (76kVp, 3.4mAs). We neglected the influence of the X-ray spectrum on the reconstruction problem. Truncation was simulated with $p = \frac{2}{3}$, yielding a dose reduction factor of $d = 1.2$ for $\alpha_{\mathrm{T}} = \alpha_{\mathrm{F}}$ and $d = 1.36$ for $\alpha_{\mathrm{T}} = 4 \cdot \alpha_{\mathrm{F}}$. Contrasts of the Catphan® LC inserts are 10 HU, 5 HU and 3 HU. Their diameters vary from 2mm to 15mm. The diameters of the central (subslice) inserts vary from 3mm to 9mm.

Images are reconstructed by solving eq. (4) using 50 iterations of eq. (6) with $\tau = 0.5$. Because we focus on a quality assurance phantom, the regularization is a simple isotropic linear diffusion filter corresponding to $\chi(f) = \lambda \|\nabla f\|_2^2$. The full width at half maximum (FWHM) is equal to $3.33\sqrt{\lambda}$. Here, the FWHM is set to 1. The reconstruction of p_{F} is our reference image. Reconstructions are visually compared on Fig.1 and Fig.2.

Figure 1a shows the reconstruction from the truncated projections at 120kVp. The central LC inserts are visible, thanks to the high exposure, yet the true uniform background cannot be visualized in a narrow display window due to cupping. Information lying outside the cylinder defined by the truncation is lost. Figure 1b shows the reconstruction from the full-FOV projections only. The image is uniform, but the higher noise decreases LC resolution. Figures 1c and 1d show the reconstructions obtained with the dual acquisition. Images are uniform and contrast resolution is improved due to lower noise. The improvement extends beyond the truncated FOV. Indeed, the backprojection operator redistributes density projections along the entire projection lines. It thus becomes possible to identify small LC inserts of 10 HU and 3 HUH, as shown on Fig.2.

Image standard deviations were computed over a homogeneous region of interest (ROI) overlaid on images from Fig.1. We observe that doubling the exposure at the center of the image (Fig.1c) decreases the standard deviation by 1.8, which is slightly above the expected value, since $\sqrt{2} \approx 1.4$. Multiplying by 5 the exposure at the center of the image (Fig.1d) yields a standard deviation $2.1 \approx \sqrt{5}$ times lower, which is approximately the expected value

Figure 1b shows some oblique streaks that are also present in Fig.1c and Fig.1d. These streaks seem to originate from the bed, which is truncated in all acquisitions. Streak intensities did not prevent LC visualization, but further work is needed to understand how they interact with our method. In particular, kV change seem to induce stronger artifacts as seen on Fig.1d, where the dual-rotation reconstruction involves two energy spectra.

We also tested the reconstruction of a volume of interest using the truncated, high-exposure spin and 18 un-truncated projections uniformly sampled from the un-truncated, low-exposure spin. We replaced weights α_n in eq. (4) by weights β_n defined in eq. (7). Results are shown in Fig.3. Figure 3a is the central part of Fig.1a. It emphasizes the strong non-uniformity when reconstructing from truncated projections only. Figure 3b shows the reconstruction obtained with our

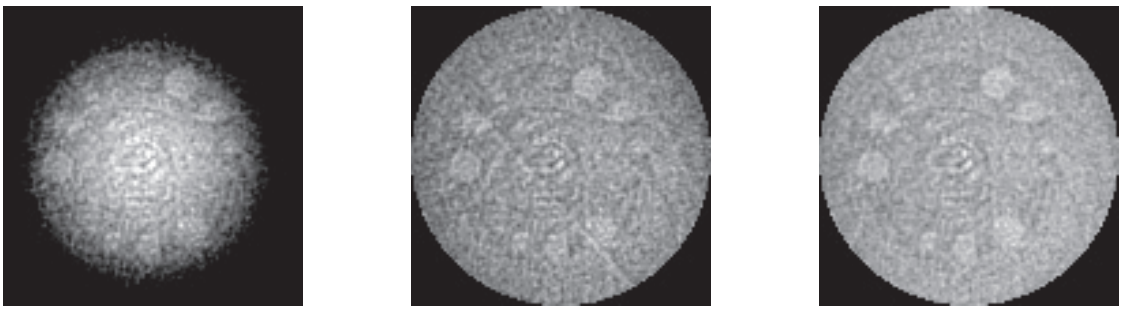

(a) Reconstruction from truncated data only

(b) VOI reconstruction

(c) Ground truth from Fig.1d

Fig. 3: Recontructions of a volume of interest in the Catphan® CTP515 module. Window levels are respectively 585, 345 and 570. Window width is 50. Isotropic voxel size: 0.78mm.

method. It looks similar to Fig.3c, which is the central part of Fig.1d used as our ground truth. This demonstrates that a highly subsampled set of un-truncated projections compensates for truncated data when reconstructing a volume of interest.

IV. Discussion and Conclusion

The dual-rotation acquisition was designed as an alternative to the bow-tie filter. Results on a quality assurance phantom show that an angularly finely sampled acquisition of truncated intensity projections increases LC resolution of C-arm CBCT, when combined with a (sub)set of un-truncated, low-intensity projections. If the un-truncated projections are acquired at a similar angular range, the image is improved over the entire FOV. This case addresses over-exposure of small densities, and shows that dose reduction factors with $p = \frac{2}{3}$ can be achieved without a bow-tie filter. If the un-truncated projections are angularly highly sub-sampled, the image non-uniformity can still be restored over the truncated FOV, given a small change in the weights of the minimization problem. This result confirms that non-uniformity is a low-frequency problem.

The minimization problem we solve includes the ramp filter in the data fidelity quadratic forms. Thus, intensity measurements in air are not needed. This trick may be used in any penalized least-squares problem by replacing the squared norm $\|Rf - p\|_2^2$ by our quadratic form.

This work constitutes a first step towards C-arm CBCT imaging of brain soft-tissue, since focus has been put on imaging a quality assurance phantom with almost no scattered radiations. C-arm CBCT of brain soft tissues faces well-known issues, namely cone-beam artifacts, skull beam-hardening and scatter. It is straightforward to replace the isotropic filter used for the Catphan® with non-linear anisotropic diffusion filters to correct for cone-beam artifacts [8]. Skull beam-hardening should be dealt with using the full-FOV acquisition, that is expected to allow skull segmentation. The biggest challenge remains scatter. We plan to benefit from the truncated acquisition to improve scatter estimation and correction by reading the actual scattered radiations under the collimator blades as suggested in [10].

References

[1] P. G. Roos, R. E. Colbeth, I. Mollov, P. Munro, J. Pavkovich, E. J. Seppi, E. G. Shapiro, C. A. Tognina, G. F. Virshup, J. M. Yu *et al.*, "Multiple-gain-ranging readout method to extend the dynamic range of amorphous silicon flat-panel imagers," in *Medical Imaging 2004*. International Society for Optics and Photonics, 2004, pp. 139–149.

[2] C. Schmidgunst, D. Ritter, and E. Lang, "Calibration model of a dual gain flat panel detector for 2D and 3D x-ray imaging," *Medical Physics*, vol. 34, no. 9, pp. 3649–3664, 2007.

[3] L. Chen, C. C. Shaw, M. C. Altunbas, C.-J. Lai, X. Liu, T. Han, T. Wang, W. T. Yang, and G. J. Whitman, "Feasibility of volume-of-interest (VOI) scanning technique in cone beam breast CT – A preliminary study," *Medical physics*, vol. 35, no. 8, pp. 3482–3490, 2008.

[4] C.-J. Lai, L. Chen, H. Zhang, X. Liu, Y. Zhong, Y. Shen, T. Han, S. Ge, Y. Yi, T. Wang *et al.*, "Reduction in x-ray scatter and radiation dose for volume-of-interest (VOI) cone-beam breast CT A phantom study," *Physics in Medicine and Biology*, vol. 54, no. 21, p. 6691, 2009.

[5] D. Kolditz, Y. Kyriakou, and W. A. Kalender, "Volume-of-interest (voi) imaging in c-arm flat-detector ct for high image quality at reduced dose," *Medical Physics*, vol. 37, no. 6, pp. 2719–2730, 2010.

[6] C. Maaß, M. Knaup, and M. Kachelrieß, "New approaches to region of interest computed tomography," *Medical Physics*, vol. 38, no. 6, pp. 2868–2878, 2011.

[7] L. Feldkamp, L. Davis, and J. Kress, "Practical cone-beam algorithm," *JOSA A*, vol. 1, no. 6, pp. 612–619, 1984.

[8] H. Langet, C. Riddell, A. Reshef, Y. Trousset, A. Tenenhaus, E. Lahalle, G. Fleury, and N. Paragios, "Compressed-sensing-based content-driven hierarchical reconstruction: Theory and application to C-arm cone-beam tomography," *Medical Physics*, vol. 42, no. 9, pp. 5222–5237, 2015.

[9] D. Goodenough, "Catphan 500 and 600 manual," *Greenwich, NY: The Phantom Laboratory*, 2012.

[10] J. Siewerdsen, M. Daly, B. Bakhtiar, D. Moseley, S. Richard, H. Keller, and D. Jaffray, "A simple, direct method for x-ray scatter estimation and correction in digital radiography and cone-beam CT," *Medical Physics*, vol. 33, no. 1, pp. 187–197, 2006.

Two cone-beam consistency conditions for a circular trajectory

Jérôme Lesaint, Rolf Clackdoyle, Simon Rit, Laurent Desbat

***Abstract*—Data consistency conditions are equations that should be satisfied by the projection data if the underlying line integral model perfectly matches the physical reality. In this work, we propose two cone-beam consistency conditions based on previous theoretical works. The source trajectory is circular, with the detector oriented perpendicularly to the plane of the trajectory, as usual. The conditions apply equally well to any planar source trajectory. We introduce two DCC functions that are applied to the cone-beam projections, such that the same constant function value occurs for all projections provided the data are consistent. Evaluations of the functions are easily implemented and any projection whose DCC function value deviates from the constant indicates inconsistency with the rest of the data.**

I. Introduction and related work

Characterization of the range of integral operators involved in Computed Tomography (CT) has been studied for decades, from the classical Helgason-Ludwig data consistency conditions (DCCs) [1], [2] for parallel beam geometry to more recent DCCs in fanbeam geometry [3]–[5]. For the 3D cone-beam (CB) geometry, DCCs have been derived in [6]–[9]. Beyond their theoretical interest, DCCs can be used to detect some systematic effects like patient motion [10], [11] or failing equipment [12], to automatically calibrate CT systems [13] or to correct scatter [14]. In this work, we build upon existing CB theory [15], [16] within a common framework [17]–[19] to develop simple DCCs for the standard circular CB geometry and other planar source trajectories.

II. Notation and theoretical background

We consider a CB-CT system made up of an X-ray source and a flat detector, both undergoing a planar source trajectory (typically, a circle) around the object of interest. The plane containing the trajectory is denoted Π_S. The source location is $\vec{a}_\lambda$ parametrized by the angle $\lambda \in \Lambda$ where $\Lambda \subset \mathbb{R}$ is an interval. Throughout the trajectory, the detector plane Π_λ is perpendicular to Π_S. We let $\vec{u}$ denote one of the two possible unit vectors in the direction of the intersection $\Pi_S \cap \Pi_\lambda$ (for example, the one parallel to the motion of the source). *For each projection*, we define a detector reference frame as follows:

J. Lesaint, R. Clackdoyle and L. Desbat are with the TIMC-IMAG laboratory, CNRS UMR 5525 and Université Grenoble Alpes (e-mail : lesainje@imag.fr and laurent.desbat@imag.fr).

S. Rit is with the CREATIS laboratory, CNRS UMR 5520 and INSERM U1044, Lyon, France (e-mail : simon.rit@creatis.insa-lyon.fr).

This work is partially supported by the Agence Nationale de la Recherche (France), Labex CAMI, number ANR-11-LABX-0004-01 and project "DROITE", number ANR-12-BS01-0018.

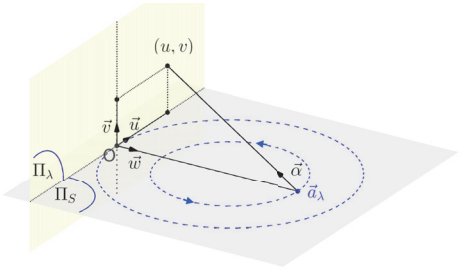

Fig. 1. Description of the geometry and choice of coordinate system. The source $\vec{a}_\lambda$ moves along the circle. And the detector moves accordingly.

the origin is the orthogonal projection of the source onto the detector (the *principal point*). The normal to the detector is $\vec{w}$, pointing in the direction of the source, so that $\vec{a}_\lambda = d\ \vec{w}$ (where d is the distance from the source to the detector). We set $\vec{v}$ so that $(\vec{u}, \vec{v})$ define a reference frame of the detector and $(\vec{u}, \vec{v}, \vec{w})$ is a 3D reference frame. A point on the detector can be written $u\vec{u} + v\vec{v}$. See Fig. 1.

The 3D Radon transform of an attenuation function f is defined by:

$$\mathcal{R}f(\vec{\beta}, s) = \int_{\vec{\beta}^\perp} f(s\vec{\beta} + \vec{y})d\vec{y}$$

with $\vec{\beta} \in \mathbb{S}^2$ ($\mathbb{S}^2$ denotes the unit sphere in $\mathbb{R}^3$) and $s \in \mathbb{R}$. Given a fixed $\vec{\beta} \in \mathbb{S}^2$, we also denote $\mathcal{R}_\beta f$ the 1D-function: $\mathcal{R}_\beta f(s) = \mathcal{R}f(\beta, s)$. The CB projections are defined over the set $\Lambda \times \mathbb{S}^2$ by :

$$g(\lambda, \vec{\alpha}) = \mathcal{D}f(\lambda, \vec{\alpha}) = \int_0^{+\infty} f(\vec{a}_\lambda + t\vec{\alpha})dt \qquad (1)$$

Early CB CT reconstruction methods are based on links between filtering CB data and filtering 3D Radon transform. Following [17] an intermediate function G is defined on the set $\Lambda \times \mathbb{S}^2$ by:

$$G(\lambda, \vec{\beta}) = \int_{\mathbb{S}^2} h(\vec{\alpha} \cdot \vec{\beta})g(\lambda, \vec{\alpha})d\vec{\alpha}, \qquad (2)$$

where the generalized function h is positively homogeneous of degree -2, i.e. $\forall k > 0,\ h(ks) = (1/k^2)h(s)$. In this work, h can be either odd ($\forall x \in \mathbb{R}, h(-x) = -h(x)$) or even ($\forall x \in \mathbb{R}, h(-x) = h(x)$). The relation between the function G and the 3D Radon transform of f is given by:

$$G(\lambda, \vec{\beta}) = s_h \left(h * \mathcal{R}_{\vec{\beta}} f\right)(\vec{a}_\lambda \cdot \vec{\beta}), \qquad (3)$$

where $s_h = 1$ if h is even and -1 if h is odd. A proof of this result can be found in [18]. Note that if the projection data are given by Eq. (1) and if some plane $\Pi(\vec{\beta}, s)$ - defined by its normal direction $\vec{\beta}$ and its signed distance to origin s - contains two source positions $\vec{a}_{\lambda_1}$ and $\vec{a}_{\lambda_2}$ (meaning that $\vec{a}_{\lambda_1} \cdot \vec{\beta} = \vec{a}_{\lambda_2} \cdot \vec{\beta}$), then:

$$G(\lambda_1, \vec{\beta}) = G(\lambda_2, \vec{\beta}). \tag{4}$$

Equation 4 provides a consistency condition.

III. Implementation

In this section, we investigate two practical aspects of the implementation of these DCCs: the evaluation of the function G and the choice of the filter h.

A. Evaluation of the function G

In order to evaluate the function G in practice, we need to express Eq. 2 in terms of detector coordinates. With the (u, v) coordinates of the detector (see Sec. II and Fig. 1), one can write:

$$\vec{\alpha} = \vec{\alpha}(u, v) = \frac{u\vec{u} + v\vec{v} - d\vec{w}}{\sqrt{u^2 + v^2 + d^2}}.$$

This change of variables leads to the following expression:

$$G(\lambda, \vec{\beta}) = s_h \left(h * \mathcal{R}_{\vec{\beta}_D} \tilde{g}_\lambda \right) (\vec{a}_\lambda \cdot \vec{\beta}), \tag{5}$$

where $\tilde{g}$ denotes pre-weighted projections:

$$\tilde{g}_\lambda(u, v) = \tilde{g}(\lambda, u, v) = \frac{d}{\sqrt{u^2 + v^2 + d^2}} g(\lambda, \vec{\alpha}(u, v)).$$

In Eq. 5, $\mathcal{R}\tilde{g}_\lambda$ is the 2D Radon transform at fixed direction $\vec{\beta}_D$ of $\tilde{g}_\lambda$:

$$\mathcal{R}_{\vec{\beta}_D} \tilde{g}_\lambda(s) = \int_{\mathbb{R}} \tilde{g}_\lambda(s\vec{\beta}_D + l\vec{\beta}_D^{\perp}) dl$$

and $\vec{\beta}_D$ denotes the normalized orthogonal projection of $\vec{\beta}$ onto the detector plane Π_λ. As Eq. 5 shows, the evaluation of $G(\lambda, \vec{\beta})$ is three steps : pre-weighting the projection, computation of the 2D Radon transform along lines perpendicular to $\vec{\beta}_D$ and convolution of this 1D function with h at $\vec{a}_\lambda \cdot \vec{\beta}$. While pre-weighting in step 1 is familiar, step 2 may be more involved if $\vec{\beta}_D$ is not aligned with pixel lines and may require complex re-binning and/or backprojection of the data in a virtual detector. The particular choice which is made in this work, makes computations in step 2 considerably easier. This choice is $\vec{\beta} = \vec{v}$. The main result of this work is the following:

Proposition 1. *Let $g = \mathcal{D}f$ for some object function f, with a planar source trajectory $\left\{\vec{a}_\lambda \in \mathbb{R}^3, \lambda \in \Lambda\right\} \subset \Pi_S$; Let h be positively homogeneous of degree -2, odd or even ; the function G defined by:*

$$G(\lambda, \vec{v}) = \int_{\mathbb{S}^2} h(\vec{\alpha} \cdot \vec{v}) g(\lambda, \vec{\alpha}) d\vec{\alpha} \tag{6}$$

is constant (independent of λ).

To better understand this statement, we replace $\vec{\beta}$ with $\vec{v}$ in Eq. 5. For all λ, $\vec{a}_\lambda \cdot \vec{v} = 0$ and $\mathcal{R}_{\vec{\beta}_D} \tilde{g}_\lambda$ is $\mathcal{R}_{\vec{v}} \tilde{g}_\lambda$, the 2D Radon transform of the pre-weighted projection *in the direction* $\vec{u}$ (i.e. along pixel lines) thus depending only on v. Let l_λ be this 1D function defined (in the (u, v) coordinates of the detector) by:

$$l_\lambda(v) = \mathcal{R}_{\vec{v}} \tilde{g}_\lambda(v) = \int \tilde{g}_\lambda(u, v) du, \tag{7}$$

Plugging (7) into (5), Eq. (6) now reads:

$$G(\lambda, \vec{v}) = s_h (h * l_\lambda)(0). \tag{8}$$

B. Choice for the function h

The intermediate function G defined in [17] provides with a unifying framework for various early 3D reconstruction formulas such as the ones from Smith [15] and Grangeat [16], [20]. Both approaches correspond to different choices for the function h. Smith's approach is based on the ramp filter:

$$h_R(s) = \int_{\mathbb{R}} |\sigma| e^{2i\pi\sigma s} ds.$$

Grangeat's approach is based on the derivative filter:

$$h_D(s) = \int_{\mathbb{R}} 2i\pi\sigma e^{2i\pi\sigma s} d\sigma.$$

It is easily verified that both h_R and h_D are positively homogeneous of degree -2 and that they are even and odd respectively.

The choice of h will impact the implementation of Eq. (8). In the case $h = h_D$, Eq. (8) reduces to: $-l'_\lambda(0)$, the derivative of l_λ taken at $v = 0$. The function l will only need to be evaluated in a neighbourhood of $v = 0$ in order to estimate this derivative. In the case $h = h_R$, Eq. (8) remains a standard convolution and the function l_λ will have to be evaluated for all possible v (i.e. on all detector lines). h_D is a local filter whereas h_R is global.

IV. Experiments and results

The following experiments aim to demonstrate that the consistency condition claimed in Proposition 1 can detect unwanted systematic effect in the data. Moreover, the ability to choose between two filters provides flexibility in the task under study.

A. Material and methods

We used a standard Shepp-Logan phantom for the simulations, as described in [21]. Projections were computed using the *Reconstruction ToolKit* [22]. The trajectory of the source was a circle with radius 100. 72 projections were computed over a full angular range of 360 degrees ($\lambda \in [0, 2\pi)$). The source-to-detector distance was 200. The exterior ellipsoid of the phantom has axis semi-lengths of $(55.2, 73.6, 72)$. Each projection has 1024×1024 pixels. And the cone angle was $104°$ in both directions. The extremely large cone-angle was intentional, to emphasize the divergent ray effects because the function $l_\lambda(v)$ is the same for all projections in the parallel case and the consistency conditions are then trivial. The detector is assumed to be perfectly aligned so that pixel lines are aligned with the u-coordinate. Hence, no interpolation was necessary to evaluate the function l_λ as described above.

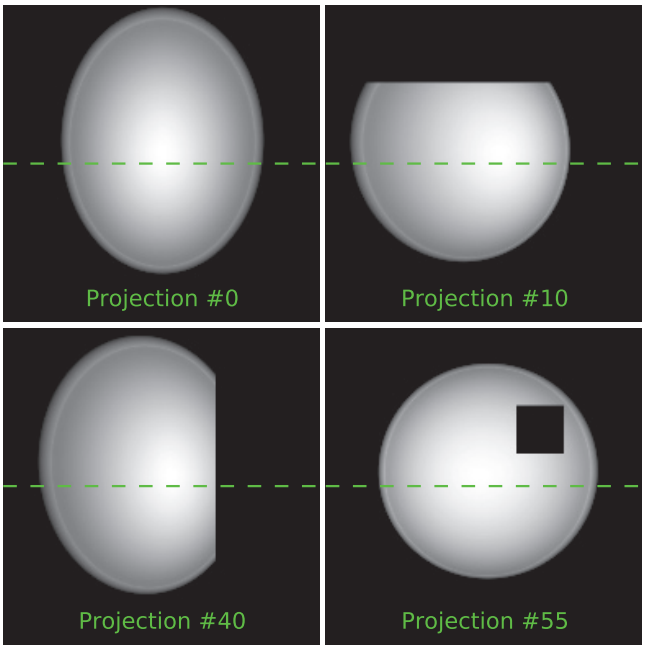

Fig. 2. Scenario 1 : projection truncations. Among the 72 projections, three were truncated as indicated. The dotted line indicates the line $v = 0$. Truncation of proj. #10 (*top right*) is away from the line. Truncation of proj. #40 (*bottom left*) impacts the line. Truncation of proj. #55 (*bottom right*) *is closer to the line. See text for analysis.*)

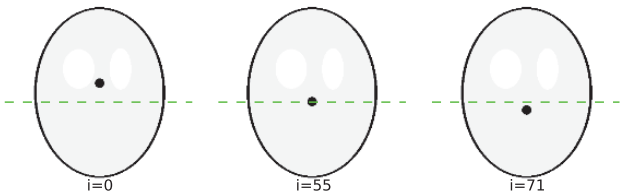

Fig. 3. Scenario 2 : organ motion. The phantom is kept fixed from projections #1 to #20. From projection #21 to the end, one of the ellipsoids is moving. The motion is linear, perpendicular to the line $v = 0$ (dotted line). The moving ellipsoid is a ball of radius 4 and has density 1.0. It intersects the central line in the range of projections #47 to #65.

The derivative filter was implemented with a central difference approximation. The ramp filter was implemented as described in [21]. We also applied a smoothing filter in the v-direction, to account for numerical instabilities. The filter has a support of length 11 pixels. It is applied after the ramp (or derivative) filter.

In the sequel, G_D and G_R denote the function G with the corresponding h_D and h_R respectively. In our first experiment, we study the behaviour of G_R and G_D with respect to truncations. In three projections (#10, 40 and 55), part of the projection is set to zero. Truncation of projection #40 is symmetric around the line $v = 0$ in the detector and simulates a large patient. Truncation of projection #10 is a trans-axial truncation (see Fig. 2). Projection #55 simulates a defect on the detector or an occlusion.

In the second experiment, we simulated an organ motion by moving an ellipsoid along a linear trajectory that crosses the line $v = 0$. The ellipsoid keeps a fixed position during the first 20 projections, then undergoes its motion till the end of acquisition cycle (see Fig. 3).

For each experiment, we compute and plot the function G_D and G_R. And as Proposition 1 states, if the data are consistent, we expect a constant plot.

B. Results

Figure 4 shows the results.

1) Truncation: The use of the ramp filter allows for the detection of any truncation, wherever this truncation occurs whereas only the lateral truncation is detected by the derivative filter (see Fig. 4, *left*). Because the ramp filter has an infinite support, it will detect truncation anywhere in the data (see Fig. 4, *bottom left*). On the other hand, the derivative filter is local and will only detect truncation in the neighbourhood of the line $v = 0$ (see Fig. 4, *top left*). It should be noticed that truncation in projection #10 was detected by the ramp filter because the inconsistency was ”massive”. It would not be able to detect a lighter modification that was far from the central line. The reason being that the lower response of the DCC would be indistinguishable from the background numerical instability.

2) Motion: For the motion experiment, we observed similar behaviour. The derivative filter detected the motion only when the object crossed the line $v = 0$ (see Fig. 4, *top right*). On the other hand, with the ramp filter (see Fig. 4, *bottom right*), the function G_R deviated from its (approximately) constant value long before the object crossed the line $v = 0$. This, again, reflected the global nature of the ramp filter, which makes the DCC able to detect almost any consistency, almost anywhere in the data.

V. Discussion

In this paper, we have revisited existing theoretical results from the DCC perspective. The necessary consistency conditions we derived are easy to implement, comprehensive in the sense that they scan all the data at once and valid under reasonable assumptions on the acquisition geometry. First numerical experiments demonstrate the potential to use the DCC for the detection of data inconsistencies, e.g. truncation, motion. The interesting point in the above experiments is the complementary role that the two filters h_R and h_D can play in the detection of systematic effects directly from the projection data. The ramp filter is able to detect any inconsistency anywhere in a projection. The ramp filter is global. On the other hand, the derivative filter only detects inconsistencies in the neighbourhood of the central plane. The derivative filter is local. As an example, the derivative filter does not detect truncation not affecting the central plane. Depending on the problem under study, this may be an advantage or a disadvantage (consider the case where motion in the central plane needs to be identified while truncation away from this plane occurs). We also noticed the limits of both filters: one

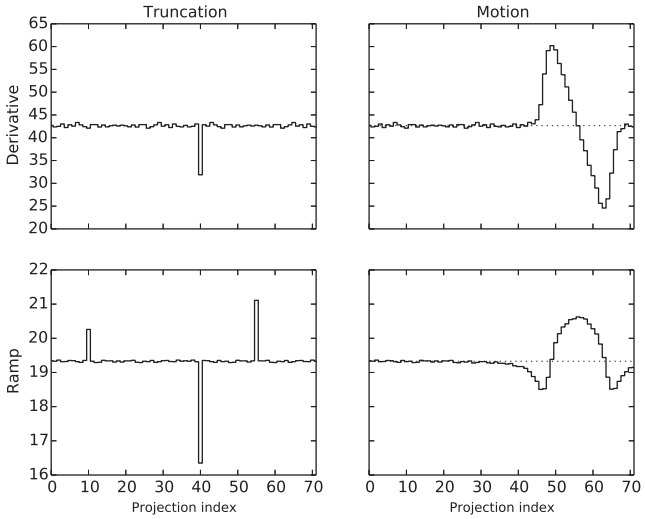

Fig. 4. Numerical simulations : plot of the function G_D (*top*) and G_R (*bottom*) with respect to projection number in the case of truncation (*left*) or motion (*right*). The x-axis is the projection index. The dotted line on the right-hand column is the mean value of the function with no inconsistency.

of them is the numerical instability that prevents detection of low-level inconsistencies far from the central line. The use of a smoothing filter to reduce this noise comes with the attenuation of respective specificities of the two functions.

We emphasize the fact that the DCC with the ramp filter is a truly CB DCC: all the data in each projection are involved in the evaluation of the DCC function. On the other hand, the derivative version is equivalent to a 2D fanbeam DCC: only the data on the intersection of the projection plane with the central plane are used.

Finally, note that we could have considered different $\vec{\beta}$ (not in the $\vec{v}$ direction) in order for the derivative version to access other parts of the projection data. In this case however, the DCC would only be able to compare the projections pairwise (only two cone-beam projections at a time), because for $\vec{\beta}$ different from $\vec{v}$, the plane orthogonal to $\vec{\beta}$ will intersect the source trajectory in at most two points. Whereas, with the specific choice we made for $\vec{\beta}$, all the projections can be checked at once.

REFERENCES

[1] D. Ludwig, "The radon transform on euclidean space," *Communications on Pure and Applied Mathematics*, vol. 19, no. 1, pp. 49–81, 1966. [Online]. Available: http://dx.doi.org/10.1002/cpa.3160190105

[2] S. Helgason, *The Radon transform*, ser. Progress in mathematics. Boston, Basel, Berlin: Birkhuser, 1999. [Online]. Available: http://opac.inria.fr/record=b1095821

[3] R. Clackdoyle, "Necessary and sufficient consistency conditions for fanbeam projections along a line," *Nuclear Science, IEEE Transactions on*, vol. 60, no. 3, pp. 1560–1569, 2013.

[4] R. Clackdoyle and L. Desbat, "Data consistency conditions for truncated fanbeam and parallel projections," *Medical Physics*, vol. 42, no. 2, pp. 831–845, 2015. [Online]. Available: http://scitation.aip.org/content/aapm/journal/medphys/42/2/10.1118/1.4905161

[5] H. Yu, G. Wang, J. Yang, J. D. Pack, M. Jiang, and B. De Man, "Data consistency condition for truncated projections in fan-beam geometry," *Journal of X-ray science and technology*, vol. 23, no. 5, pp. 627–638, 2015.

[6] F. John, "The ultrahyperbolic differential equation with four independent variables," *Duke Math. J.*, vol. 4, no. 2, pp. 300–322, 06 1938. [Online]. Available: http://dx.doi.org/10.1215/S0012-7094-38-00423-5

[7] S. K. Patch, "Consistency conditions upon 3d ct data and the wave equation," *Physics in Medicine and Biology*, vol. 47, no. 15, p. 2637, 2002. [Online]. Available: http://stacks.iop.org/0031-9155/47/i=15/a=306

[8] M. S. Levine, E. Y. Sidky, and X. Pan, "Consistency conditions for cone-beam ct data acquired with a straight-line source trajectory," *Tsinghua science and technology*, vol. 15, no. 1, pp. 56–61, Feb. 2010. [Online]. Available: http://www.ncbi.nlm.nih.gov/pmc/articles/PMC2886312/

[9] R. Clackdoyle and L. Desbat, "Full data consistency conditions for cone-beam projections with sources on a plane," *Physics in Medicine and Biology*, vol. 58, no. 23, p. 8437, 2013. [Online]. Available: http://stacks.iop.org/0031-9155/58/i=23/a=8437

[10] W. Wein and A. Ladikos, "Towards general motion recovery in cone-beam computed tomography," in *Proceedings of The 12th International Meeting on Fully Three-Dimensional Image Reconstruction in Radiology and Nuclear Medicine*, 2013, pp. 54–57.

[11] R. Frysch and G. Rose, "Rigid motion compensation in interventional c-arm ct using consistency measure on projection data." in *Proceedings of the 18th International Conference on Medical Image Computing and Computer Assisted Interventions*, 2015.

[12] S. Patch, "Moment conditions indirectly improve image quality," *Contemporary Mathematics*, vol. 278, pp. 193–206, 2001.

[13] N. Maass, F. Dennerlein, A. Aichert, and A. Maier, "Geometrical jitter correction in computed tomography," in *Proceedings of the third international conference on image formation in x-ray computed tomography*, F. Noo, Ed., 2014, pp. 338–342.

[14] C. Kim, M. Park, Y. Sung, J. Lee, J. Choi, and S. Cho, "Data consistency-driven scatter kernel optimization for x-ray cone-beam ct," *Physics in Medicine and Biology*, vol. 60, no. 15, p. 5971, 2015. [Online]. Available: http://stacks.iop.org/0031-9155/60/i=15/a=5971

[15] B. Smith, "Image reconstruction from cone-beam projections: Necessary and sufficient conditions and reconstruction methods," *Medical Imaging, IEEE Transactions on*, vol. 4, no. 1, pp. 14–25, March 1985.

[16] P. Grangeat, "Mathematical framework of cone beam 3d reconstruction via the first derivative of the radon transform," in *Mathematical Methods in Tomography*, ser. Lecture Notes in Mathematics, G. Herman, A. Louis, and F. Natterer, Eds. Springer Berlin Heidelberg, 1991, vol. 1497, pp. 66–97. [Online]. Available: http://dx.doi.org/10.1007/BFb0084509

[17] R. Clackdoyle and M. Defrise, "Overview of reconstruction algorithms for exact cone-beam tomography," *Proc. SPIE*, vol. 2299, pp. 230–241, 1994. [Online]. Available: http://dx.doi.org/10.1117/12.179253

[18] R. Clack and M. Defrise, "Cone-beam reconstruction by the use of radon transform intermediate functions," *J. Opt. Soc. Am. A*, vol. 11, no. 2, pp. 580–585, Feb 1994. [Online]. Available: http://josaa.osa.org/abstract.cfm?URI=josaa-11-2-580

[19] F. Noo, "Méthodes numériques directes de reconstruction d'images tridimensionnelles à partir de projections coniques." Ph.D. dissertation, Université de Liège, 1998.

[20] P. Grangeat, "Analyse d'un systeme d'imagerie 3d par reconstruction a partir de radiographies x en geometrie conique," Ph.D. dissertation, 1987, thse de doctorat dirige par GARDERET, PHILIPPE Sciences appliques ENST 1987. [Online]. Available: http://www.theses.fr/1987ENST0011

[21] A. Kak and M. Slaney, *Principles of Computerized Tomographic Imaging*. Society for Industrial and Applied Mathematics, 2001. [Online]. Available: http://epubs.siam.org/doi/abs/10.1137/1.9780898719277

[22] S. Rit, M. V. Oliva, S. Brousmiche, R. Labarbe, D. Sarrut, and G. C. Sharp, "The reconstruction toolkit (rtk), an open-source cone-beam ct reconstruction toolkit based on the insight toolkit (itk)," *Journal of Physics: Conference Series*, vol. 489, no. 1, p. 012079, 2014. [Online]. Available: http://stacks.iop.org/1742-6596/489/i=1/a=012079

Intra-operative 3D micro-coil imaging using subsampled tomographic acquisition patterns on a biplane C-arm system

Charlotte Delmas[1,2], Cyril Riddell[1], Yves Trousset[1], Erwan Kerrien[2,3], Marie-Odile Berger[2,3], René Anxionnat[4] and Serge Bracard[4]

***Abstract*—The restriction of CBCT to micro-coil imaging allows for integrating key a priori knowledge that a coil is a high-density spatially sparse curvilinear structure. In this paper, we investigate acquisition patterns specifically designed for biplane systems allowing a faster workflow and reduced dose. Each pattern is a subsampling of a standard tomographic acquisition reconstructed with an ℓ_1-constrained algorithm to promote sparsity together with diffusion filters that promote the curvilinear nature of the coil. Three tensor-based 3D diffusion filters are investigated. Quantitative and qualitative results are provided for one coil and four patients datasets. They show how the reconstruction performs according to the selected acquisition pattern (uniform versus non-uniform subsampling), the quantity of missing information and the selected diffusion filter. We observed a systematically better recovery of the coil in reconstructions obtained using a uniform subsampling pattern but at the cost of being systematically noisier than those obtained with a non-uniform subsampling pattern. Diffusion filtering significantly reduced this structural noise.**

I. Introduction

Endovascular aneurysm coiling is a minimally invasive procedure most commonly used for treating balloon-shaped cerebral aneurysms. A micro-coil (or coil) is a pre-shaped platinum wire that is guided through a catheter inside the aneurysm and that winds as it exits the catheter. Several coils are usually placed one after the other to embolize the aneurysm, thus preventing blood from pressuring the diseased vessel wall and starting an hemorrhage. Real-time guidance and control are obtained using fluoroscopic images acquired with an X-ray biplane C-arm system (Fig.1). Proper positioning of the coils means that no coil loop should enter the parent artery. However, some anatomical configurations of aneurysms require moving the C-arm in positions that are not available due to mechanical restrictions. In such cases, Cone-Beam Computed Tomography (CBCT) provides a 3D depiction of the coil. In the standard CBCT workflow, the X-ray source of the frontal plane of the C-arm rotates over a 200° circular arc (called spin). The lateral plane must be parked prior to the acquisition and repositioned after so that performing CBCT is time-consuming. It is also expensive in terms of X-ray dose to the patient with respect to fluoroscopy. Our purpose is thus to investigate angularly subsampled rotational acquisition patterns that are appropriate for intra-operative 3D coil imaging by taking advantage of the knowledge that the object of interest is a coil.

Authors are with : 1/ GE Healthcare, Buc, France, 2/ Loria, Vandœuvre-lès-Nancy, France, 3/ Inria, Vandœuvre-lès-Nancy, France, 4/ Centre de Neuroradiologie du CHU de Nancy, France. Corresponding author: cyril.riddell@ge.com. This work was supported by the CIFRE grant No. 2012/1280 from the French Association Nationale de la Recherche et de la Technologie (ANRT).

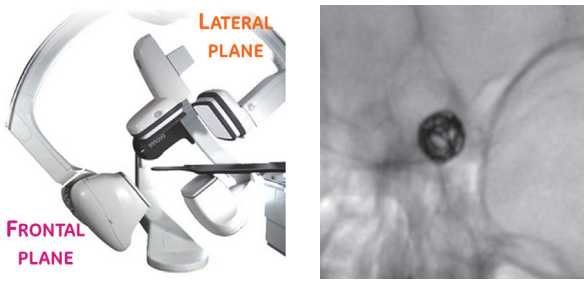

(a) (b)

Fig. 1. (a) GE Healthcare IGS 630 biplane acquisition system. (b) X-ray projection of a single intra-cranial micro-coil

II. Methods

The restriction of CBCT to coil imaging allows for integrating key a priori knowledge of the object of interest: it is a high-density spatially sparse curvilinear structure. Recently developed compressed-sensing-based CBCT reconstruction algorithms have shown promise for reconstructing sparse objects [1]. In our context, we consider a reconstruction algorithm constraining the ℓ_1-norm of the image to promote sparsity together with diffusion filters to also promote curvilinear structures. We here discuss several subsampling schemes of the standard CBCT acquisition designed such that the lateral plane needs not be parked and compare uniform versus non-uniform subsampling.

A. Subsampling patterns

Fig.2 illustrates the three angularly subsampled acquisition patterns that are investigated. Pattern P_0 corresponds to the case where the lateral plane is left in place but not used. The frontal plane angular coverage is thus restricted. It is a limited-aperture tomographic acquisition. Within the aperture limits, the angular sampling is uniform and equal to that of a standard

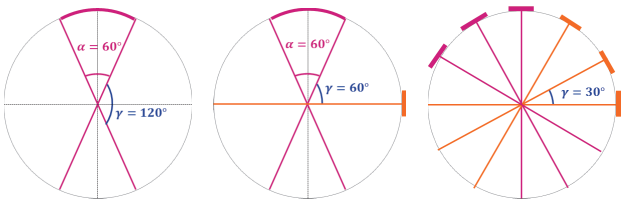

Fig. 2. Acquisition patterns: (a) P_0 is a limited-aperture rotation (aperture angle $\alpha = 60°$), (b) P_1 adds one extra-projection to P_0, (c) P_2 is a uniform subsampling of a full spin acquisition (angular step is $\gamma = 30°$).

CBCT acquisition. For a maximum aperture of $60°$, a gap of $120°$ is not sampled. Pattern P_1 augments pattern P_0 with a single projection acquired with the lateral plane in a direction orthogonal to the central projection of P_0, so that gaps between projections never exceed $60°$. Pattern P_2 corresponds to the case where both planes would rotate simultaneouly, thus allowing for a complete tomographic coverage with uniform subsampling. The largest angular step that was tested was $30°$ amounting to acquiring 6 projections only. In terms of mechanical design, pattern P_2 implies the strongest requirements on the lateral plane: that it can rotate synchronously with and in the same repeatable way as the frontal plane, despite its rather different design. Pattern P_1 only requires reaching a single position precisely and repeatably. Pattern P_0 alleviates any constraint on the lateral plane.

B. Sparse iterative reconstruction through ℓ_1 minimization

Previous works have shown the possibility to handle subsampling using ℓ_1-constrained reconstructions, one in particular in the context of C-arm CBCT imaging of an iodined-injected sparse vessel tree over a non-sparse background [1]. C-arm CBCT imaging of coils falls into the same category. Following [1], we take a hierarchical approach where structures of higher intensity are reconstructed first. It is based on solving the following N penalized reconstruction problems indexed by n:

$$f^{(n)} = \underset{f\geq 0}{\operatorname{argmin}} \frac{1}{2}(Rf-p)^t D(Rf-p) + \lambda^{(n)}||f||_1 \qquad (1)$$

where R is a matrix that models the acquisition pattern, D is the matrix of ramp filtering, p is the vector of the projections acquired with the pattern, f is the vector containing the reconstructed volume and $\lambda^{(n)}$ is a positive scalar that defines the level of sparsity of the solution by acting as an intensity threshold. Vector $f^{(n)}$ is thus an approximation of the solution whose sparsity is proportional to $\lambda^{(n)}$. Since the coil sparsity is not known, N problems (called stages) is defined a priori with N intensity thresholds $\lambda^{(n)} \in [\lambda_{\min}, \lambda_{\max}]$ such that $\lambda^{(n)} \geq \lambda^{(n+1)}$ and $\lambda_{\min} > 0$. At each stage, $f^{(n)}$ is computed as the solution of (1) initialized by $f^{(n-1)}$ using proximal splitting, that is the following 2-step iterative algorithm:

$$\begin{cases} f^{(i+\frac{1}{2})} &= f^{(i)} - \tau R^t D(Rf^{(i)} - p) \\ f^{(i+1)} &= \operatorname{argmin}_{f\geq 0} ||f - f^{(i+\frac{1}{2})})||^2 + \lambda^{(n)}||f||_1 \end{cases} \qquad (2)$$

To get matrix R to model each pattern we must consider the weighting of each projection. It is a single scaling factor when the sampling is uniform. When it is not, as in pattern P_1, it is intuitive that the projection from the lateral plane contains unique information. Indeed, we found necessary to give this extra-projection a weight equal to the sum of the weights of all other projections to get the best results.

C. Structural prior through diffusion filtering

Promoting curvilinear structures is introduced as a filtering operator W modifying (2) into the following 3-step algorithm:

$$\begin{cases} f^{(i+\frac{1}{3})} &= f^{(i)} - \tau R^t D(Rf^{(i)} - p) \\ f^{(i+\frac{2}{3})} &= W(f^{(i+\frac{1}{3})}) \\ f^{(i+1)} &= \operatorname{argmin}_{f\geq 0} ||f - f^{(i+\frac{2}{3})})||^2 + \lambda^{(n)}||f||_1 \end{cases} \qquad (3)$$

Operator W is a diffusion filter such that the filtered image $f^{(i+\frac{2}{3})}$ is solution of the diffusion equation :

$$\begin{cases} \partial_t f &= \nabla^t(T(f).\nabla f) \\ f(t=0) &= f^{(i+\frac{1}{3})} \end{cases} \qquad (4)$$

where ∇ denotes the gradient operator and T is a 3×3 matrix designed to locally modulate the strength and direction of the filtering according to the underlying structures in image f. Three designs of T are investigated :

- $T_{\text{CED}} = U_\theta \text{diag}(\lambda_{\text{CED}}, \alpha, \alpha) U_{-\theta}$ where U_θ is a rotation matrix such that the filtering has diffusivity λ_{CED} along direction θ. This corresponds to Weickert's Coherent-Enhancing Diffusion where U_θ and λ_{CED} are computed as described in [2]. We have $\alpha << 1$, that is no filtering in directions orthogonal to θ, and $\lambda_{\text{CED}} \in [\alpha, 1]$. We expect close to full filtering ($\lambda_{\text{CED}} \to 1$) when the underlying structure is curvilinear and close to no filtering ($\lambda_{\text{CED}} \to \alpha$) otherwise.
- $T_{\text{NLD}} = (1 - \lambda_{\text{CED}})\text{diag}(1,1,1)$ is an isotropic non-linear diffusion tensor based on λ_{CED} only which is expected to smooth out non-curvilinear structures while leaving curvilinear structures unchanged.
- $T_{\text{NLAD}} = U_\theta \text{diag}(\lambda_{\text{CED}}, 1-\lambda_{\text{CED}}, 1-\lambda_{\text{CED}}) U_{-\theta}$ is an anistropic non-linear diffusion tensor combining the two above designs such that curvilinear structures are enhanced and non-curvilinear structures are smoothed out.

III. Experiments

We present results on one coil in air and four clinical data sets obtained right after the first coil was deployed within the aneurysm sack. All five data sets were acquired with the same GE Healthcare IGS 630 biplane C-arm system, following a standard workflow of CBCT spin acquisition (pixel pitch 0.4mm, rotation speed $40°$/s, 150 projections total). The acquisition patterns were derived by extracting the projections from

the full spin. Subsets of projections $P_0(\alpha, \theta)$ were generated following pattern P_0 for eleven values of the aperture angle α from 30° to 60° in steps of 3° and four values of the start angle θ of the rotation from 0° to −30° in steps of 10°. For each subset $P_0(\alpha, \theta)$, a corresponding subset $P_1(\alpha, \theta)$ following pattern P_1 was obtained by adding an orthogonal projection as described in Sec. II-A. Subsets $P_2(\gamma)$ were generated following pattern P_2 for increasing angular steps γ, starting from the ground truth (GT) of 150 projections ($\gamma = 1.5°$) down to as low as 6 projections ($\gamma = 30°$). Fig.2 shows configuration $P_1(60°, 0°)$ and $P_2(30°)$. All ℓ_1-constrained reconstructions, including ground-truth reconstructions of full spins, were performed with the same parameters: $N = 30$, $f^{(0)} = 0$, $\lambda_{\max} = 0.9 \times \max(f^{(1/2)})$ where $f^{(1/2)}$ is a least-square approximation of f, $\lambda_{\min} = 3000$ to separate the coil from other intense anatomical structure (eg. bones). Since we are interested in recovering the shape of the coil (ie its loops), reconstructions were evaluated quantitatively in terms of support only. Let $f^{(01)}$ denote the binarized version of the soft-background thresholded volume $f^{(N)}$. The false negative (FN) rate is defined as the proportion of non-zero voxels of the ground-truth reconstruction of the coil ("true voxels") that are missing in $f^{(01)}$ with respect to the total number of true voxels. The false positive (FP) rate is defined as the proportion of non-zero voxels appearing in $f^{(01)}$ that are not true voxels with respect to the total number of true voxels. The FN (resp. FP) rate best value is 0%. The max value for the FN rate is 100% but can exceed 100% for the FP rate. For settings $P_1(60°, 0°)$ and $P_2(30°)$, reconstructions were also performed using the diffusion filters of Sec. II-C. We compared using algorithm (3) at all stages of the hierarchical approach to using algorithm (2) from stages 1 to $N - 1$ and algorithm (3) at the last stage N. This latter approach is faster because it uses diffusion essentially as a post-processing step. Filtering impact was quantified as the (signed) percentage of improvement in FN (resp. FP) rates with respect to no filtering defined by : $100 \times (\text{FN}_{\text{Filter}} - \text{FN}_{\text{NoFilter}})/\text{FN}_{\text{NoFilter}}$ (resp. $100 \times (\text{FP}_{\text{Filter}} - \text{FP}_{\text{NoFilter}})/\text{FP}_{\text{NoFilter}}$).

IV. Results

Fig.3 shows a scatter plot of the FN and FP rates of each setting $P_1(\alpha, 0°)$ and $P_2(\gamma)$ (one dot per reconstruction). The plots compare patterns P_1 (blue symbols, one symbol per aperture angle α) and P_2 (red symbols, one symbol per angular step γ) for the clinical data combining all 4 patients. We observe very different plot trends between patterns P_1 and P_2. Pattern P_1 curves have a vertical trend, with the FN rate decreasing as the aperture increases with little increase of the FP rate except for patient 4. The same trend was found for pattern P_0 (not shown on plot), with higher FN rates than pattern P_1. With pattern P_2, the FN rate was always lower than with pattern P_1 while the subsampling implied increased FP rate. The two plots of Fig.4 show the influence of the starting angle θ for pattern P_1 for the ex-vivo coil (Fig.4a) and patient 2 (Fig.4b) data. The best starting angle for the ex-vivo coil ($\theta = -30°$) is the worst for the patient case, for which

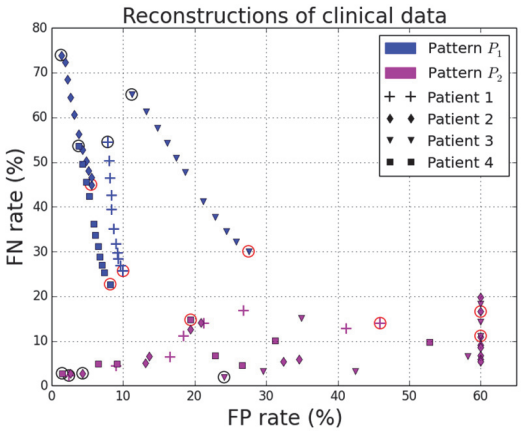

Fig. 3. FN rates against FP rates (clipped to 60%) comparing P_1 and P_2. Black circles : $P_1(30°, 0°)$, $P_2(3°)$. Red circles : $P_1(60°, 0°)$, $P_2(30°)$.

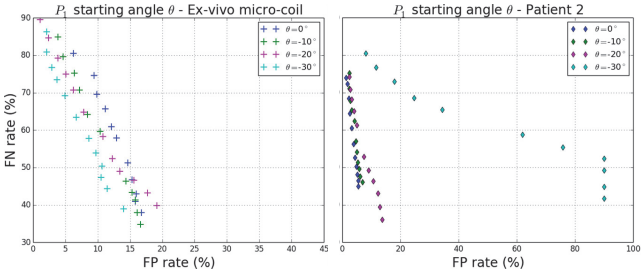

(a) (b)

Fig. 4. Plots of FN rates against FP rates (4b clipped to 90%) showing the impact of the starting angle θ for pattern P_1.

more variability is observed, possibly due to the presence of more intense background structures. Overall, systematically lower FN rates are obtained with pattern P_2 showing a better recovery of the coil in reconstructions than those obtained with pattern P_1, but at the cost of higher FP rates yielding visually noisier reconstructions. Visual inspection of the coil reconstructions as MIP rendering images for patient 1 and patient 2 are provided. A comparison of the ground truth (GT) reconstruction with reconstructions obtained with each pattern of Fig.2 and using algorithm (2) at all stages of the hierarchical approach is provided on Fig.5. Visual quality of the reconstruction is ranked lowest for P_0 (Fig.5b) and highest for P_2 (Fig.5d). Result for P_1 (Fig.5c) shows that using one extra-projection orthogonal to the center orientation of P_0 significantly improves the quality of the reconstruction. The GT reconstruction for patient 2 shows a peripheral loop of the coil (see arrow) on Fig.6a. This key clinical information is not entirely recovered with P_1 whatever the starting angle θ (Fig.6b,6c,6e,6f). It is clearly recovered using $P_2(30°)$ (Fig.6d) ie with 6 projections only. Quantitative results where 3D diffusion filtering of settings $P_1(60°, 0°)$ and $P_2(30°)$. TABLE I reports the percentage of improvement for FN and FP rates averaged over all four clinical data sets. Overall, multi-directional diffusion tensors T_{NLAD} and T_{NLD} had more

impact than T_{CED}. Using diffusion as a post-processing (algorithm (3) at stage N only) generally resulted in better FN and FP rates than using diffusion at all stages of the hierarchical approach. Diffusion filtering with T_{NLAD} reduced the structural noise induced by angular subsampling (decreased FP rates) and recovered some of the missing information (decreased FN rates). It is most significant with pattern P_2 where there is more structural noise than with pattern P_1. Fig.7 shows reconstructions obtained using diffusion at all stages of the hierarchical approach for patient 1 with setting $P_2(30^\circ)$. Coherence enhancing diffusion filter (T_{CED} tensor) resulted in visually smoother coil structures (Fig.7a) with some remaining structural noise. The alternative isotropic tensor T_{NLD} resulted in visually less noisy reconstructions (Fig.7b) while tensor T_{NLAD} appears to produce a good combination of the other two filters (Fig.7c).

V. Discussion and Conclusion

In this paper we evaluated three subsampled rotational acquisition patterns for intra-operative 3D coil imaging that are specifically designed for biplane C-arm systems. Sparse approximation through ℓ_1-constrained reconstruction was used to generate 3D images of the coil in presence of missing projection data. Results obtained for one coil in air and four patient datasets showed how a sparse approximation performs according to both the selected acquisition pattern and the quantity of missing information (angular aperture or angular step) in terms of support recovery and visual inspection. Analysis of false negative and true positive rates clearly distinguished the limited aperture patterns P_0 and P_1 from the uniformly subsampled pattern P_2. Pattern P_0 was deemed insufficient in all cases, and pattern P_2 was ranked best. In between, pattern P_1 showed a non-negligible variability depending on the start angle of the acquisition. This confirms that there exists a preferred direction in which a coil should be imaged, as described in a different context by Varga [3], in order to avoid unfavorable background superimposition. Indeed, we found in one instance that a clinically important information was not recovered with pattern P_1 whatever the starting angle. Pattern P_2 was able to recover this information with as few as 6 projections. We also investigated using 3D diffusion filtering as part of the reconstruction process to promote curvilinear structures. Three different diffusion tensor designs were considered to locally modulate the strength and direction of the filtering. All three filters improved the reconstructions either by promoting curvilinear structure and/or smoothing out structural noise.

References

[1] H. Langet, C. Riddell, A. Reshef, Y. Trousset, A. Tenenhaus, E. Lahalle, G. Fleury, and N. Paragios, "Compressed-sensing-based content-driven hierarchical reconstruction: Theory and application to c-arm cone-beam tomography," *Medical Physics*, vol. 42, no. 9, pp. 5222–5237, 2015.

[2] J. Weickert, *Anisotropic diffusion in image processing*, vol. 1.

[3] L. Varga, P. Balázs, and A. Nagy, "Projection selection dependency in binary tomography." *Acta Cybern.*, vol. 20, no. 1, pp. 167–187, 2011.

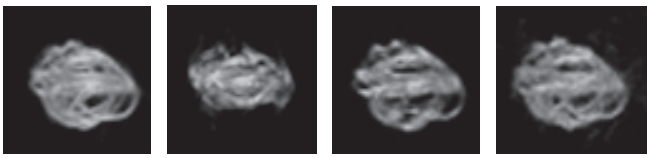

(a) (b) (c) (d)

Fig. 5. Patient 1. MIP rendering of reconstructions without diffusion filtering: (a) GT, (b) P_0 $(60^\circ, 0^\circ)$, (c) P_1 $(60^\circ, 0^\circ)$, (d) P_2 (30°).

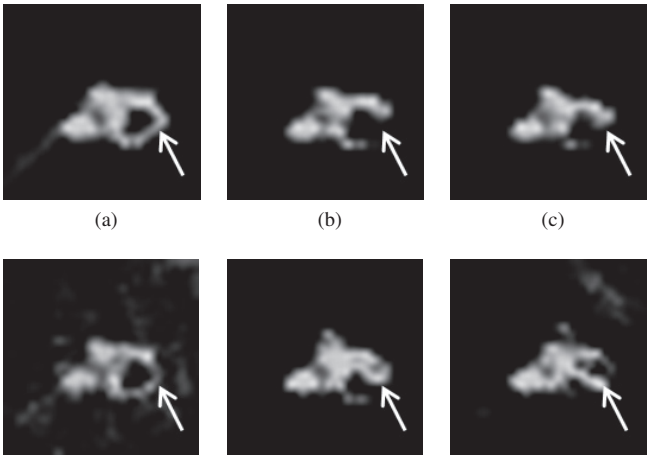

(a) (b) (c)

(d) (e) (f)

Fig. 6. Patient 2. MIP rendering of reconstructions without diffusion filtering: (a) GT, (d) P_2 (30°), (b) P_1 $(60^\circ, 0^\circ)$, (c) P_1 $(60^\circ, -10^\circ)$, (e) P_1 $(60^\circ, -20^\circ)$, (f) P_1 $(60^\circ, -30^\circ)$. White arrow points at a coil loop.

TABLE I
Comparing % improvement of FN and FP rates using diffusion filtering at all stages or last stage only for acquisition patterns $P_1(60^\circ, 0^\circ)$ and $P_2(30^\circ)$

Diffusion tensor T	P_1, all		P_1, last		P_2, all		P_2, last	
	FN	FP	FN	FP	FN	FP	FN	FP
CED	-1	$+3$	-2	-2	$+4$	-11	-4	-14
NLD	-7	$+5$	-6	-8	-22	-27	-24	-28
NLAD	-4	$+2$	-8	-11	-19	-31	-27	-29

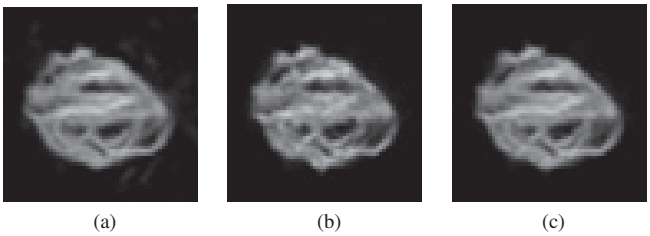

(a) (b) (c)

Fig. 7. Patient 1. MIP rendering of reconstructions with diffusion filtering at all stages and pattern P_2 (30°): (a) CED, (b) NLAD

Reduction of Cone Angle Effect in Cardiac Motion Correction Based on Partial Angle Reconstructed Images in CT

Seungeon Kim, Yongjin Chang, and Jong Beom Ra

***Abstract*—High quality cardiac X-ray CT imaging is important in the diagnosis of various heart diseases. Since the heart is continuously beating during X-ray CT scanning, however, motion artifacts are included in a reconstructed image which may lead misdiagnosis. Recently, we proposed a cardiac motion estimation (ME) and motion compensation (MC) algorithm based on partial angle reconstructed (PAR) images, and showed using a digital phantom and a physical phantom that the algorithm can noticeably improve the image quality by reducing motion artifacts. Since the cone angle effect on 3D PAR images was not considered in the previous study, however, the estimated motion may be less accurate in recent high-end systems having a large detector cone angle. In response, we propose a space-invariant filter, which is designed by analyzing the frequency characteristics of PAR image, so as to remove the cone angle effect in the ME process. Via simulations, it is shown that the proposed filter improves the accuracy of motion estimation and consequently the quality of motion-compensated images.**

***Index Terms*—Cardiac X-ray CT, partial angle reconstruction, motion artifacts, motion estimation and compensation, cone beam CT.**

I. Introduction

Cardiac X-ray CT imaging has become a promising noninvasive tool for early detection of cardiac disease as the gantry rotation speed becomes faster. However, it is still challenging to obtain an artifact-free cardiac image, because the rotation speed is not fast enough compared with cardiac motion. Thereby, many vendors try to reduce motion artifacts by developing an advanced X-ray CT system with faster rotation speed. However, it leads high hardware complexity and consequent cost increase. In response, many software approaches have been proposed to improve the image quality by estimating the cardiac motion and compensating it without hardware modification [1-6].

Recently, we proposed a cardiac ME/MC algorithm based on PAR images [6]. Since a PAR image is reconstructed by using a sinogram with a scan range of β which is much smaller than a short scan range of $\pi+\alpha$, it has high temporal resolution. Our previous algorithm can thereby estimate motion accurately and reduce motion artifacts considerably in the experiments using the digital XCAT phantom and a physical dynamic cardiac phantom. Since the algorithm estimates cardiac motion without considering the cone angle effect on 3D PAR images, however, the estimated motion may be less accurate for an X-ray CT system having a large cone angle.

Seungeon Kim, Yongjin Chang, and Jong Beom Ra are with the School of Electrical Engineering, KAIST, Daejeon 34141, Republic of Korea (e-mail: sekim@issserver.kaist.ac.kr; yjjang@issserver.kaist.ac.kr; jbra@kaist.ac.kr)

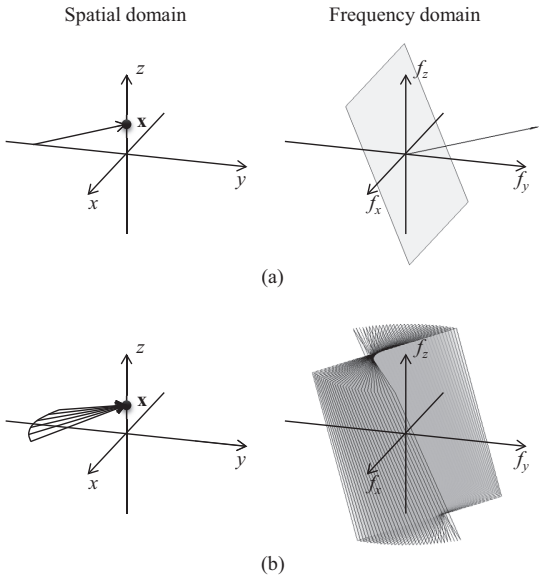

Fig. 1. Local shift-variant Fourier model for (a) a single view and (b) multiple views within a scan range of β.

In this paper, we propose filtering PAR images prior to ME to improve the performance of the previous PAR image-based ME/MC algorithm. Via the proposed filtering, we can remove the cone angle data inconsistency between two PAR images for ME.

This paper is organized as follows. In section II, brief reviews on our previous algorithm and the description on the proposed prefiltering scheme are given. In section III, experimental results are provided, and conclusions are given in section IV.

II. Proposed Method

Our previous algorithm estimates the cardiac motion based on PAR images and incorporates it into image reconstruction for motion compensation [6]. In the algorithm, to estimate the motion, an acquired cone beam sinogram is converted into cone-parallel geometry via a rebinning process. Subsequently, two PAR images are reconstructed at the two phases separated $\mp$ 90° from a target phase, respectively, with a scan range of β.

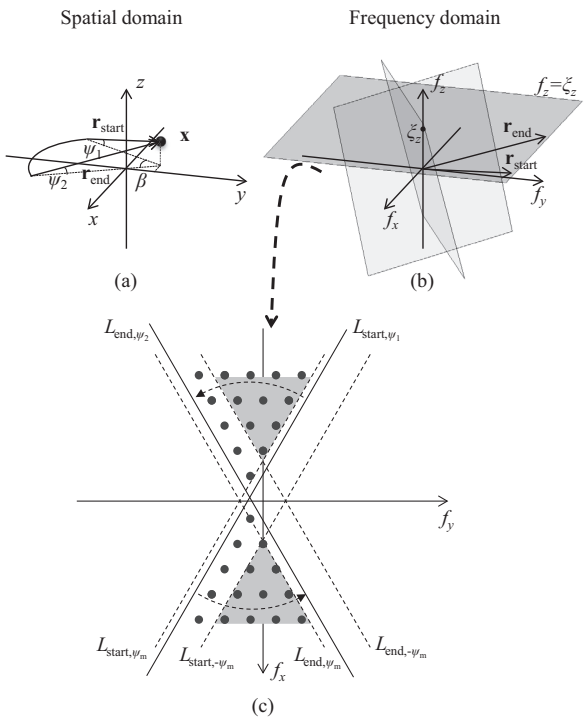

Fig. 2. Illustration of a frequency band filled by the cone-parallel sinogram with an angular range of β, at an arbitrary point **x**.

For the sake of convenience, we consider that the two conjugate PAR images correspond to the phases of 0° and 180°, respectively. To reduce the shading artifacts due to the limited view angle, we apply band-pass filtering to those PAR images, and estimate MVF via non-rigid registration between them. Using the estimated MVF from two conjugate PAR images, we can determine MVFs from the target phase to any arbitrary phases, based on the linear motion assumption. We can then perform motion-compensated reconstruction using the MVFs [7].

As the cone angle increases, however, the inconsistency between conjugate PAR images arises, and consequently the motion estimation may become inaccurate depending on the location. In order to eliminate the image inconsistency, we analyze the frequency characteristics of a PAR image based on a local shift-variant Fourier model [8, 9]. According to this model, at an arbitrary point **x**, the projection for one view contributes to the frequency information on the plane in the frequency domain, whose normal vector equals to a direction vector of the ray passing through **x,** as shown in Fig. 1(a). By extending this model to a continuous scan trajectory, we can determine the frequency band for an arbitrary point **x** in a PAR image at phase 0°, as shown in Fig. 1(b). Similarly, we can also determine the frequency band at the same point **x** in the PAR image at phase 180°. We can easily note that the frequency bands of two PAR images are not the same but have an overlap. Based on this observation, we may eliminate the image inconsistency by using only the common frequency band for each point. Since the common frequency band changes according to the reconstructed point, spatially variant processing is required, which leads to high computational complexity.

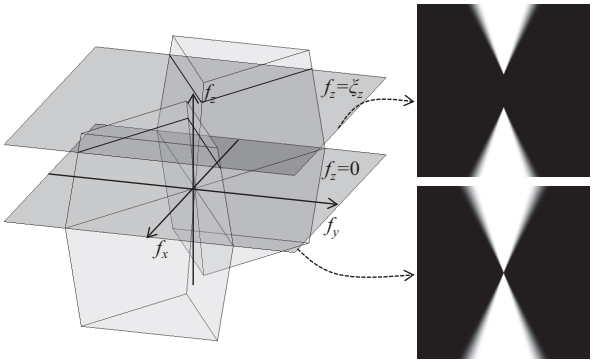

Fig. 3. Proposed space-invariant filter in the frequency domain, to obtain the filtered conjugate PAR images including only the common frequency band information.

In order to solve this problem, we propose to use a shift-invariant filter, which extracts only the common frequency band for any pair of corresponding points between conjugate PAR images. Figure 2 demonstrates the frequency band where the information is filled by the cone-parallel sinogram with an angular view range of β, for an arbitrary point **x** in the PAR image of phase 0°. Here, L_{start,ψ_1} and L_{end,ψ_2} denote the crossing lines between plane $f_{xy}|_{f_z = \xi_z}$ and the frequency planes where the information is provided by ray projections at the start and end views, $\mathbf{r}_{\text{start}}$ and $\mathbf{r}_{\text{end}}$, respectively. For a continuous source trajectory, the frequency band for **x** can be determined as the dotted area in Fig. 2(c), by sweeping a line from L_{start,ψ_1} to L_{end,ψ_2}. Note here that the bounding lines, L_{start,ψ_1} and L_{end,ψ_2}, vary according to the position of **x**. Since the position of reconstruction point **x** is bounded by the detector cone angle range, $-\psi_m$ and ψ_m, the small gray shaded frequency band in Fig 2(c) is only covered for any arbitrary **x**. Similarly, we can note that the same frequency band is covered for any arbitrary point in the PAR image at phase 180°. Based on this observation, we design a shift-invariant filter for PAR images so as to extract the information only in the common frequency band. Note that to prevent unwanted ringing artifacts, a smooth transition is imposed on the filter, as shown in Fig. 3. Applying the proposed space-invariant filter to the conjugate PAR images, we can eliminate the cone angle data inconsistency. We can thereby estimate more accurate motion for compensation.

III. Results

In order to illustrate the effect of cone angle in conjugate PAR images, we adopt two simple numerical phantoms, NP1 and NP2, as shown in Fig. 4. The left NP1 consists of a large static sphere and a small moving sphere, and the right NP2 has an additional large static sphere at the bottom compared with NP1 so that it can cause the cone angle data inconsistency that disturbs ME.

Figure 5 shows the simulation results for the numerical phantoms. In Fig. 5(a), since the object movement can be clearly observed in the difference image even without proposed filtering, the object motion is estimated and compensated well.

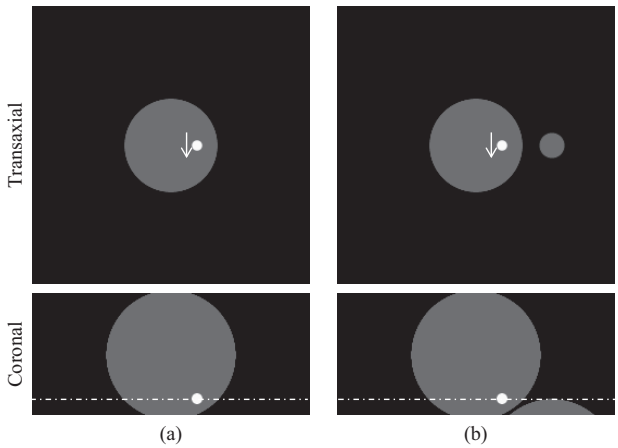

Fig. 4. Two numerical phantoms with a small moving object, which appears as white circles: (a) NP1 and (b) NP2.

If a large static object locates near a moving object, however, the object movement may not be visible in the difference image, as shown in Fig. 5(b), due to the significant difference that is caused by the cone angle data inconsistency. Thereby, the estimated motion becomes erroneous, and motion artifacts still exist in the motion-compensated image. On the other hand, if the proposed prefiltering is applied, the cone angle data inconsistency is removed in conjugate PAR images, as shown in Fig. 5(c), so that the estimated motion becomes more accurate. Consequently, the motion-compensated image quality is also improved as shown in the figure.

We also adopt the digital XCAT phantom [10] to evaluate the proposed algorithm, and Fig. 6 shows the simulation results. It is noted in Fig. 6(a) that the cone angle data inconsistency appears at the boundary between the lung and an organ (indicated by an arrow in the coronal image) and disturbs accurate ME. On the other hand, in Fig. 6(b), we can note that the cone angle data inconsistency is successfully eliminated by using the proposed prefiltering. Thereby, the motion-compensated image quality is considerably improved.

IV. Conclusion

We propose a preprocessing method to improve the performance of the PAR image-based cardiac ME/MC algorithm in X-ray CT. The proposed method attempts to remove the image inconsistency between conjugate PAR images by using only the common frequency band of two PAR images. The method can thereby estimate the motion more accurately even with the scanner having a large detector cone angle. Since the proposed method is based on shift-invariant filtering, it is computationally efficient and easy to implement. Via a phantom simulation study, it is found that the proposed method can estimate accurate motion so that the motion-compensated image quality can be improved.

Acknowledgement

The authors would like to thank Samsung Electronics for providing the financial support.

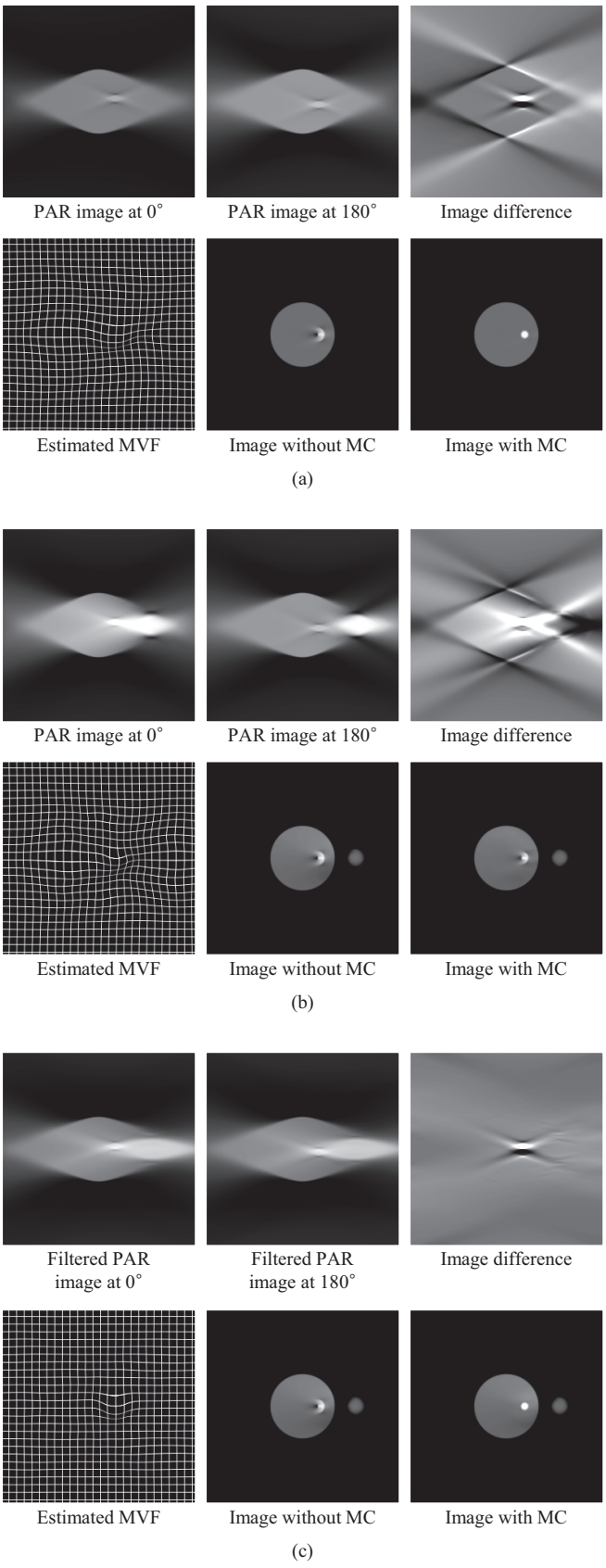

Fig. 5. Simulation results obtained from two numerical phantoms: (a) NP1 without preprocessing, and (b) NP2 without and (c) with proposed prefiltering.

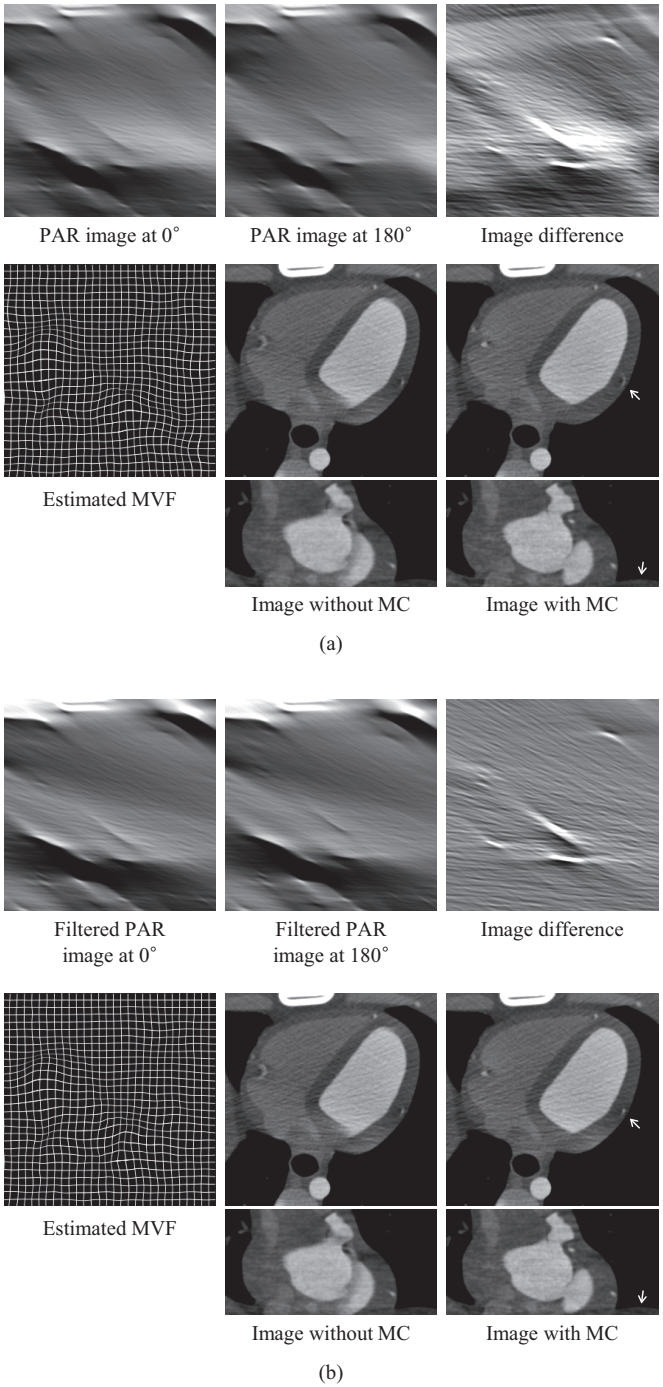

Fig. 6. Simulation results obtained from the digital XCAT phantom (a) without and (b) with proposed prefiltering.

REFERENCES

[1] A. A. Isola, M. Grass, and W. J. Niessen, "Fully automatic nonrigid registration-based local motion estimation for motion-corrected iterative cardiac CT reconstruction," *Med. Phys*. vol. 37, no. 3, pp. 1093–1109, Mar. 2010.

[2] R. Bhagalia, J. D. Pack, J. V. Miller, and M. Iatrou, "Nonrigid registration based coronary artery motion correction for cardiac computed tomography," *Med. Phys*. vol. 39, no. 7, pp. 4245–4254, Jul. 2012.

[3] Q. Tang, J. Cammin, S. Srivastava, and K. Taguchi, "A fully four-dimensional, iterative motion estimation and compensation method for cardiac CT," *Med. Phys*. vol. 39, no. 7, pp. 4291–4305, Jul. 2012.

[4] C. Rohkohl, H. Bruder, K. Stierstorfer, and T. Flohr, "Improving best-phase image quality in cardiac CT by motion correction with MAM optimization," *Med. Phys*. vol. 40, no. 3, pp. 031901, Mar. 2013.

[5] Q. Tang, J. Cammin, and K. Taguchi, "Four-dimensional projection-based motion estimation and compensation for cardiac x-ray computed tomography," in *Proc. Intl. Mtg. on Fully 3D Image Recon. in Rad. and Nuc. Med.*, Lake Tahoe, CA, 2013, pp. 46–49.

[6] S. Kim, Y. Chang, and J. B. Ra, "Cardiac motion correction based on partial angle reconstructed images in x-ray CT," *Med. Phys*., vol. 42, no. 5, pp. 2560-2571, May 2015.

[7] D. Schafer, J. Borgert, V. Rasche, and M. Grass, "Motion-compensated and gated cone beam filtered back-projection for 3-D rotational x-ray angiography," *IEEE Trans. Med. Imaging*, vol. 25, no. 7, pp. 898–906, 2006.

[8] S. Bartolac, R. Clackdoyle, F. Noo, J. Siewerdsen, D. Moseley, and D. Jaffray, "A local shift-variant Fourier model and experimental validation of circular cone-beam computed tomography artifacts," *Med. Phys*., vol. 36, no. 2, pp. 500-512, Feb. 2009.

[9] J. D. Pack, Z. Yin, K. Zeng, and B. E. Nett, "Mitigating cone-beam artifacts in short-scan CT imaging for large cone-angle scans," in *Proc. Intl. Mtg. on Fully 3D Image Recon. in Rad. and Nuc. Med.*, Lake Tahoe, CA, 2013, pp 300-303.

[10] W. P. Segars, G. Sturgeon, S. Mendonca, J. Grimes, and B. M. W. Tsui, "4D XCAT phantom for multimodality imaging research," *Med. Phys*. vol. 37, no. 9, pp. 4902–4915, Sep. 2010.

PRISM: A new software tool for simulating realistic CT data with CAD model based objects

T. Funk, D. Badali, S. Hsieh, T.G. Schmidt

***Abstract*—We are developing PRISM, the Particle/Ray Interaction Simulation Manager, as a simulation platform for x-ray or CT imaging in security applications. PRISM is designed to be customizable and extensible and leverages existing tools such as GEANT4 for Monte Carlo simulation of photon trajectories or scatter, and TASMIP for the definition of the incident spectrum. Ray tracing can be used for accelerated calculation of the distribution of transmitted photons. Objects can be loaded from CAD models, enabling the modeling of complex objects. The detector module includes effects such as noise, crosstalk, gain, and lag. We use PRISM to simulate the CT scan of a suitcase and present the effects of the detector model and the reconstructed CT images.**

***Index Terms*—Computed Tomography, Detector Model, Monte Carlo, Projection Data, Simulation**

I. Introduction

There is increasing desire to use simulations in the design of new X-ray systems for security applications and for characterizing the threat detection performance of existing systems and algorithms. Simulations can potentially overcome current challenges caused by limited access to raw experimental data. To realize these potential benefits, simulations must model objects with realistic complexity. Also, simulations must correctly model system effects such as focal spot blur, detector response, beam hardening and scatter, so that the appearance of threat and non-threat features is realistically depicted in the resulting images.

We are developing a simulation tool capable of generating realistic computed tomography projection data. The goal of this project is not to reinvent the wheel, but rather to provide a platform that combines well validated software tools such as GEANT4[1] and TASMIP[2] for easy use. The platform also allows the import of standard Computer Aided Design (CAD) models, which will enable the modeling of realistic and complex collections of objects.

Fig 1 shows the workflow of the PRISM software. The simulation parameters are configured using a GUI interface, in which the source, detector, trajectory, and object are defined and passed to the simulation engine (GEANT4).

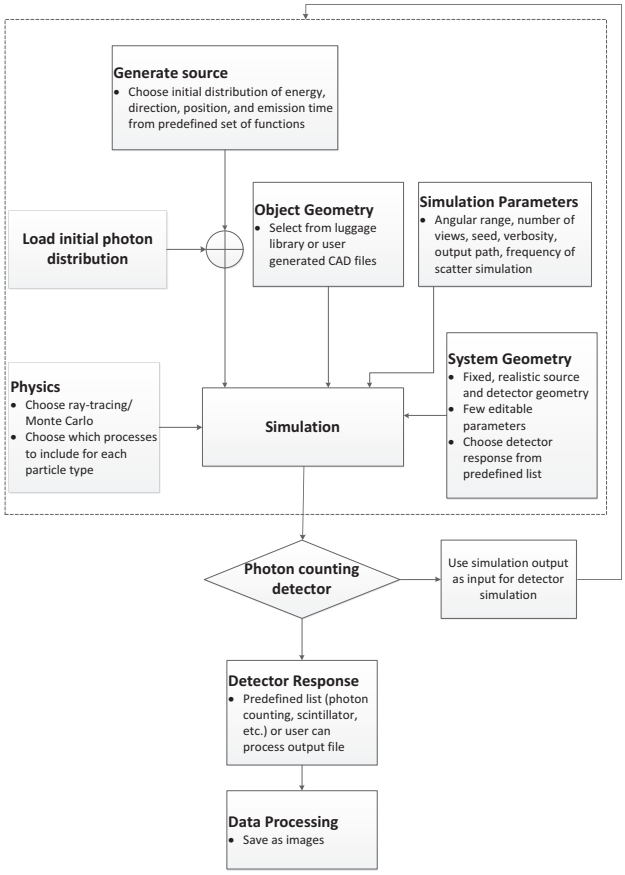

Fig. 1. Workflow of the PRISM software

A typical bottleneck in realistic simulations is time and our aim is to alleviate this by employing various computational strategies such as graphics card computing and multi-core implementations. Monte Carlo simulation of photon transport through the object offers the most realistic distribution of x-ray photons, but full Monte Carlo simulations are quite costly. Ray tracing methods are much faster but cannot simulate scatter accurately. Therefore, we combine ray tracing and Monte Carlo by using Monte Carlo simulations to estimate the scatter distribution, and ray tracing method to produce realistic transmission images, complete with effects such as beam

This work was supported in part by the U.S. Department of Homeland Security under Contract D15PC00024. We also would like to acknowledge invaluable contributions from Augustus Lowell, Brian Wilfley, and Paul Kahn.

Tobias Funk is with Triple Ring Technologies, 39655 Eureka Dr, Newark CA 94560. (tfunk@tripleringtech.com)

Daniel Badali is with Triple Ring Technologies, 39655 Eureka Dr, Newark CA 94560. (dbadali@tripleringtech.com)

Scott Hsieh is with Triple Ring Technologies, 39655 Eureka Dr, Newark CA 94560. (shsieh@tripleringtech.com)

Taly Schmidt is with Marquette University, PO Box 1881, Milwaukee WI, 53201 (tal.gilat-schmidt@marquette.edu)

hardening and focal spot blur. However, PRISM is designed to be modular so that the simulation can be tailored to the user's needs. For imaging based on back scatter, for example, PRISM can be run entirely in Monte Carlo mode.

Hence, we propose to estimate the primary signal using ray tracing and the scatter signal from a subset of projection data. The estimated scatter signal is then denoised, interpolated, and combined with the ray tracing output. Fig. 2 shows a flow chart of the proposed workflow.

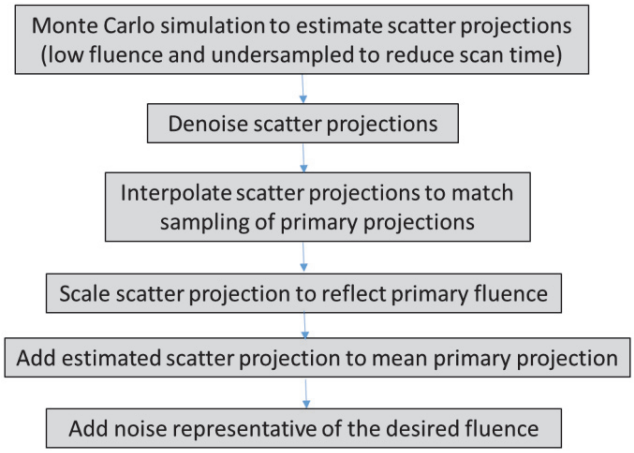

Fig. 2 Scatter variance reduction workflow.

Several types of x-ray detectors are presently available for commercial use. These include (1) amorphous silicon flat-panel detectors, (2) CMOS detectors, (3) scintillator-photodiode detectors, (4) xenon gas detectors, (5) CCD detectors and (6) direct conversion, photon counting detectors. PRISM has a flexible detector module to convert detected x-ray photons into detector images, taking into account various detector imperfections which are included as postprocessing steps. The type of postprocessing is tuned to the detector type. Most effects are parameterized and the strength of each effect can be tuned for easy adaption to realistic detector responses.

The detector module is responsible for the injection of noise. Quantum noise is added to each energy bin, and energy-dependent quantum efficiency and gain factors are also included. For example, an ideal photon counting detector weights all photons equally, but other detectors with finite stopping power will fail to detect all photons and would integrate the total deposited energy[3], [4]. Gaussian electronic noise from the detector readout is also added. Crosstalk is included. Detector lag, which is typically more prominent in amorphous silicon detectors, is modeled as a decaying exponential residual[5]. Veiling glare is also included as an exponential falloff[6].

II. Suitcase Simulation

We have assembled a packed suitcase model using common items (shown in Fig. 3). We also included a handgun with all metal parts converted to plastic, demonstrating the utility of such simulations.

For the example simulations, the source-to-detector distance was 100 cm and the center of rotation was 70 cm from the source. We simulated a 140 kVp X-ray source with a TASMIP spectrum. The detector was 95 cm by 95 cm with 512 x 512 pixels and a pixel pitch of 1.86 mm. We assumed a CMOS detector with a CsI scintillator screen of 3 mm thickness. A circular trajectory was assumed and we simulated 512 projections over 360 degrees.

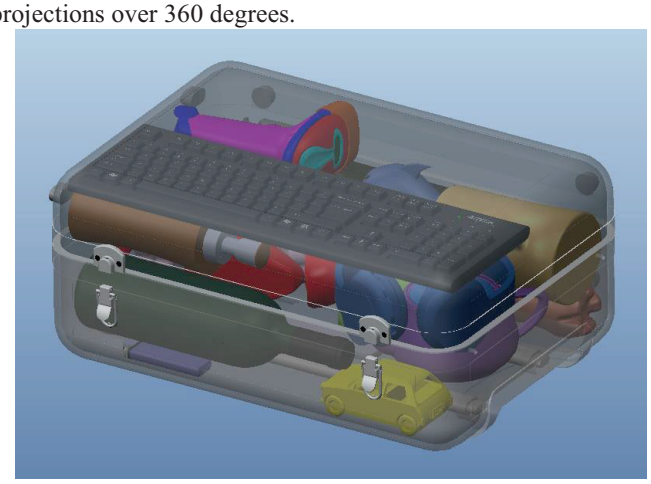

Fig. 3. Rendering of the CAD model of the suitcase.

We used our in house reconstruction engine AccuRabbit[1] to reconstruct the simulated projection data. We used 512^3 voxels with a voxel size of 1 mm.

III. Results

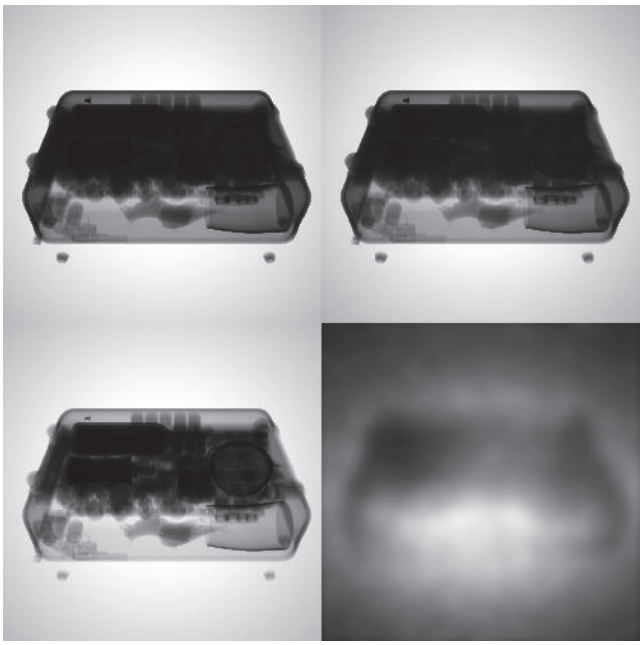

Fig. 4. Projection images (top, left) ray tracing using a monochromatic beam, (top, right) ray tracing using a polychromatic beam, (bottom, left) ray tracing using a polychromatic beam with scatter and focal spot blur added, (bottom, right) smoothed scatter response from Monte Carlo simulation.

[1] AccuRabbit was recently added to the benchmarking website RabbitCT (https://www5.cs.fau.de/research/projects/rabbitct/show_algorithm/?aid=32) and is the most accurate and one of the fastest GPU algorithm listed.

Fig. 4 shows one projection with different post processing applied after the ray tracing step. We compare a monochromatic scan at 180keV and a polychromatic scan at 140kVp. In addition, we show how scatter and focal spot blur degrades the projection images.

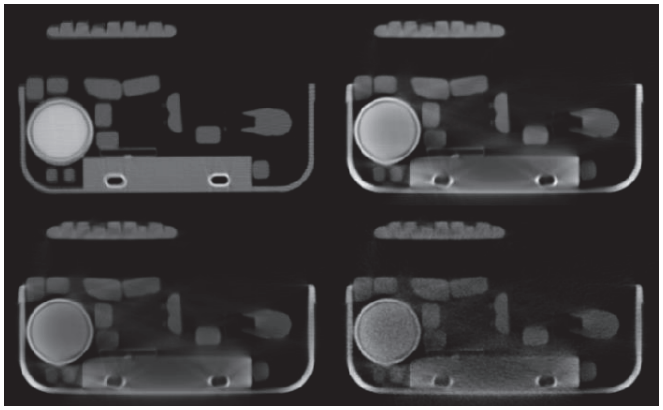

Fig. 5. Cross-section through the reconstructed volume using simulated projection data. (top, left) ray tracing using a monochromatic beam, (top, right) ray tracing using a polychromatic beam, (bottom, left) ray tracing using a polychromatic beam with scatter and focal spot blur added, (bottom, right) same data as on the left with realistic levels of Poisson noise added.

Fig. 6. Cross section through the reconstructed volume using simulated projection data with scatter and focal spot blur with different levels of detector noise (top, left) Poisson noise only, (top, right) added electronic noise and QDE, (bottom, left) added veiling glare (bottom, right) added cross talk.

Fig 5 and Fig 6 show reconstructions of projection data with different levels of physics and detector effects. In particular, Fig 5 shows the appearance of beam hardening artifacts when a polychromatic spectrum is used instead of the monochromatic spectrum. Further artifacts are introduced through the addition of scatter and Poisson noise. We also simulated the effects of detector imperfections such as QDE and electronic noise, vailing glare, and cross talk. The resulting reconstructions are shown in Fig 6. Artifacts due to detector imperfections are subtle but it is very clear that they cannot be ignored in a realistic simulation.

IV. Conclusions

PRISM is being developed as an easy-to-use X-ray simulation platform for security applications. The results demonstrate the ability of PRISM to model realistic detector effects, such as veiling glare and electronic noise. The CAD interface enables the simulation of complex objects, such as the suitcase model presented in this work. Future work is planned to further validate the PRISM tool and to develop a library of luggage models.

References

[1] S. Agostinelli, J. Allison, K. Amako, J. Apostolakis, H. Araujo, P. Arce, M. Asai, D. Axen, and EtAl, “G4--a simulation toolkit,” *Nucl. Instruments Methods Phys. Res. Sect. A Accel. Spectrometers, Detect. Assoc. Equip.*, vol. 506, no. 3, pp. 250–303, 2003.

[2] J. M. Boone and J. A. Seibert, “An accurate method for computer-generating tungsten anode x-ray spectra from 30 to 140 k{V},” *Med. Phys.*, vol. 24, no. 11, pp. 1661–1670, 1997.

[3] W. Zhao, G. Ristic, and J. A. Rowlands, “X-ray imaging performance of structured cesium iodide scintillators,” *Med. Phys.*, vol. 31, no. 9, p. 2594, Aug. 2004.

[4] R. K. Swank, “Absorption and noise in x-ray phosphors,” *J. Appl. Phys.*, vol. 44, no. 9, p. 4199, Oct. 1973.

[5] J. Starman, J. Star-Lack, G. Virshup, E. Shapiro, and R. Fahrig, “A nonlinear lag correction algorithm for a-Si flat-panel x-ray detectors.,” *Med. Phys.*, vol. 39, no. 10, pp. 6035–47, Oct. 2012.

[6] J. A. Seibert, “Characterization of the veiling glare PSF in x-ray image intensified fluoroscopy,” *Med. Phys.*, vol. 11, no. 2, p. 172, Mar. 1984.

A reformulation of the x-ray transmission image reconstruction problem for more accurate modeling of the polychromatic and spatial resolution effects

Lucretiu M. Popescu*

***Abstract*— We present a reformulation of the x-ray transmission tomography problem resulting from taking second order approximations of the integrals of the exponential attenuation term over projection spatial resolution kernel and energy spectrum. The results lead to an algebraic formulation of the transmission tomography problem involving the cross-correlations of image elements' projections, consequence of projection beam finite size and image elements arrangement pattern, as well as the polychromatic nature of the x-ray source. Using a general model for x-ray transmission tomography we derive multiplicative iterative reconstruction schemes for the cases of Gaussian and Poisson noise, and unify the solutions into a single form. The implementations of the new formulations are discussed.**

I. INTRODUCTION

The recent transition from analytic to iterative reconstruction algorithms in x-ray transmission computed tomography (CT) represents a shift from integral geometry view of the image reconstruction problem to algebraic formulations, that are increasingly derived from physical and statistical considerations. The iterative algorithms allow for incorporation of more accurate models of physics and geometry of data acquisition directly into the reconstruction model [1], rather than as data preprocessing steps, with expected positive impact on image definition and noise propagation. The experience of a previous such transition that has taken place in nuclear medicine (PET, SPECT) for about the past two decades, has confirmed such expectations. However, in the case of CT, some anecdotal reports, as well as a fairly recent study [2], have pointed out that the increase in measured image quality can be attributed more to the use of regularization terms, rather than the accurate modeling of x-ray projection beams. Here we show that the solution to the problem of integrating the x-ray attenuation factor over the spatial resolution kernel, as well as the energy spectrum, requires consideration of the image elements projections cross-correlations, leading to an algebraic formulation different from the standard form.

II. X-RAY TRANSMISSION TOMOGRAPHY MODEL

A. The projection data model

For a given x-ray transmission projection data point g_j, the expected detector signal value is given by

$$g_j = I_j \varepsilon_j \int_{\mathcal{E}} \mathrm{d}E \phi_j(E) \xi_j(E) \int_{\mathcal{D}_j} \mathrm{d}\mathbf{y} w_j(\mathbf{y}) \mathrm{e}^{-\sum_i h_i(\mathbf{y}) \mu_i(E)} + b_j \,, \tag{1}$$

where

I_j the expected number of source photons emitted at data point position j.

$\phi_j(E)$ the energy spectrum of the source photons for data point j; $\mathcal{E}$ is the energy domain, $\int_{\mathcal{E}} \phi_j(E) \mathrm{d}E = 1$.

ε_j the average detector efficiency (probability of detection) for photons providing signal in data point j integrated over the energy spectrum ϕ_j.

$\xi_j(E)$ is the average contribution of a photon of energy E to the signal collected in data point j; normalized so that $\int_{\mathcal{E}} \phi_j(E) \xi_j(E) \mathrm{d}E = 1$.

$\mathbf{y}$ is a projection ray (a point in the projection space);

$w_j(\mathbf{y})$ is the spatial resolution kernel, the probability a photon incident along ray $\mathbf{y}$ produces a signal in j; $\mathcal{D}_j$ is the projection domain support of $w_j(\mathbf{y})$, $\int_{\mathcal{D}_j} w_j(\mathbf{y}) \mathrm{d}\mathbf{y} = 1$.

$h_i(\mathbf{y})$ is the distance the ray $\mathbf{y}$ crosses the image element i.

$\mu_i(E)$ is the energy dependent attenuation coefficient of image element i; more about it in section II B.

b_j background signal (scattered photons, ...) at position j.

In (1) the index j can stand for one particular spatial projection as in the case of standard CT, or a combination of spatial projection and source setting as in the case of dual (or multiple) energy CT, or for a spatial projection and detector energy window combination, as in the case of photon-counting energy-resolving detectors, as well as the case of dual layer detectors. The factors $\phi_j(E)$ and $\xi_j(E)$ can be modified accordingly, with $\xi_j(E)$ depending also on the count rate. The system response function is factorized in energy and spatial components $w_j(\mathbf{y}) \xi_j(E)$, which is well justified if $w_j(\mathbf{y})$ is mainly due the acquisition geometry (e.g. the gantry rotation). A more general version of (1) can be written if we take $\xi_j(\mathbf{y}, E)$. Here we will use the factorized version, however, variations of the results derived below can also be obtained for the nonfactorized version of detector response.

When no object is present we have

$$g_{j0} = I_j \varepsilon_j \tag{2}$$

which usually is the value used in practice, however some adjustments may be necessary due to the detector nonlinear response with the incident photon flux.

B. Object attenuation representation

The energy dependent attenuation coefficient $\mu_i(E)$ can expressed as a linear superposition of several components

$$\mu_i(E) = \sum_{l=1}^{L} f_{il} \mu_l(E) \,. \tag{3}$$

If a standard data acquisition is used (a single energy source and energy integrating detector) most often there is little ability to distinguish between multiple components, in which case a single component that provides a good representation of the average attenuation may be used. For spectral CT, two components with low and high atomic number, respectively, can be used. The components can also be chosen by splitting into photoelectric and Compton interaction parts, the dominant photon attenuation

*Office of Science and Engineering Laboratories, Center for Devices and Radiological Health, Food and Drug Administration, E-mail: lucretiu.popescu@fda.hhs.gov.

mechanisms in the CT operating energy range [3, 4]. In particular situations, more components could be used if additional constraints are imposed.

We introduce the following collective notations: $\underline{\hat{g}} \equiv \{\hat{g}_j\}$ the ensemble of data collected, and $\underline{f} \equiv \{f_{il}\}$ the ensemble of all image component coefficients. The former are the data, and the latter are the unknowns to be determined.

With this representation the sensitivity of data model to image values is

$$-\frac{\partial g_j(\underline{f})}{\partial f_{il}} = I_j \varepsilon_j \int_{\mathcal{E}} \mathrm{d}E \phi_j(E) \xi_j(E) \mu_{il}(E) \times \int_{\mathcal{D}_j} \mathrm{d}\mathbf{y} w_j(\mathbf{y}) h_i(\mathbf{y}) \mathrm{e}^{-\sum_i h_i(\mathbf{y}) \mu_i(E)} . \quad (4)$$

III. IMAGE RECONSTRUCTION ALGORITHM

The expressions for $g_j(\underline{f})$ and $\left(-\frac{\partial g_j(\underline{f})}{\partial f_{il}}\right)$ can be introduced into the iterative update equation below

$$f_{il}^{(m+1)} = f_{il}^{(m)} \left[\frac{1}{\sum\limits_{j \in \mathcal{S}_m} \frac{1}{\eta_j} \left(-\frac{\partial g_j}{\partial f_{il}}\right)} \sum_{j \in \mathcal{S}_m} \frac{1}{\eta_j} \left(-\frac{\partial g_j}{\partial f_{il}}\right) \left(\frac{\hat{g}_j}{g_j(\underline{f}^{(m)})}\right)^{\alpha} \right]^{-\lambda}, \quad (5)$$

where $\hat{g}_j$ is a measured projection data point, and S_m is a subset of data points j used for the m-th update. Equation (5) represents a formal unification of two multiplicative update expressions. The first, obtained for $\alpha = 2$, corresponds to the least-squares solution considering independent Gaussian noise $\sigma^2_{\hat{g}_j} = \eta_j g_j$, where η_j is the detector element Fano factor. The second, obtained for $\alpha = 1$, is obtained for photon counting detectors, $\eta_j = 1$, in conditions of Poisson noise, and corresponds to a maximum likelihood expectation maximization (ML-EM) scheme. The second exponent, $\lambda > 0$, is a relaxation parameter applied in keeping with the multiplicative nature of the algorithm. This form was previously presented in [5]. Generalizations considering noise correlations between nearby detector elements can be obtained as in [6].

IV. CALCULATION OF PROJECTION g_j AND $\frac{\partial g_j}{\partial f_{il}}$

A. Integration over the spatial resolution kernel

In (1) the attenuation exponential appears as the integrated of two integrals, one over the spatial resolution kernel, the other over the energy spectrum and detector energy response function. Integrating over the energy can be done by summing over the discretized energy spectrum points as proposed in [7, 8]. The same strategy can be applied to the integration over the spatial resolution kernel by subsampling the spatial resolution range and projecting each line individually. However, the precise projection of each line is the time consuming bottleneck of image reconstruction algorithms, with great effort usually expended to simplify and speed it up [9], so this approach leads to multiple times increase in computation time. Even if this alternative becomes more approachable with the availability of massive parallel computation resources, it obscures the insight into the nature of the problem that a more analytic approach could reveal.

To investigate the problem of the attenuation exponential integration we will use the relation

$$\left\langle \mathrm{e}^{-X} \right\rangle = \mathrm{e}^{-\langle X \rangle + \frac{1}{2}\mathrm{var}(X)} \quad (6)$$

where $\langle f(X) \rangle = \int p(X) f(X) \mathrm{d}X$, with $p(X)$ a probability density. The equation is exact for Gaussians, and a good approximation for other distributions provided the variance is not too large or the distribution not too skewed.

In order to simplify the notations we define

$$\langle X \rangle = \int_{\mathcal{D}_j} w_j(\mathbf{y}) X(\mathbf{y}) \mathrm{d}\mathbf{y} . \quad (7)$$

With this the integral over the spatial resolution domain then can be approximated as

$$\left\langle \mathrm{e}^{-\sum_i h_i(\mathbf{y}) \mu_i(E)} \right\rangle \approx \mathrm{e}^{-\left\langle \sum_i h_i(\mathbf{y}) \mu_i(E) \right\rangle + \frac{1}{2}\mathrm{var}\left(\sum_i h_i(\mathbf{y}) \mu_i(E)\right)} \quad (8)$$

With the notations

$$\langle h_{ij} \rangle = \langle h_i(\mathbf{y}) \rangle , \quad (9a)$$

$$\mathrm{cov}(h_{ij}, h_{i'j}) = \langle h_i(\mathbf{y}) h_{i'}(\mathbf{y}) \rangle - \langle h_{ij} \rangle \langle h_{i'j} \rangle , \quad (9b)$$

the mean and variance in (8) are

$$\left\langle \sum_i h_i(\mathbf{y}) \mu_i(E) \right\rangle = \sum_i \langle h_{ij} \rangle \mu_i(E) \quad (10a)$$

$$\mathrm{var}\left(\sum_i h_i(\mathbf{y}) \mu_i(E) \right) = \sum_{i,i'} \mathrm{cov}(h_{ij}, h_{i'j}) \mu_i(E) \mu_{i'}(E) \quad (10b)$$

From (8) and (3) the transmission projection model (1) becomes

$$g_j(\underline{f}) = I_j \varepsilon_j \int_{\mathcal{E}} \mathrm{d}E \phi_j(E) \xi_j(E) \exp\left[-\sum_i \langle h_{ij} \rangle \sum_l f_{il} \mu_l(E) + \frac{1}{2} \sum_{i,i'} \mathrm{cov}(h_{ij}, h_{i'j}) \sum_{l,l'} f_{il} f_{i'l'} \mu_l(E) \mu_{l'}(E) \right] , \quad (11a)$$

and the sensitivity with f_{il} is

$$-\frac{\partial g_j(\underline{f})}{\partial f_{il}} = I_j \varepsilon_j \int_{\mathcal{E}} \mathrm{d}E \phi_j(E) \xi_j(E) \left[\langle h_{ij} \rangle \mu_l(E) - \sum_{i'} \mathrm{cov}(h_{ij}, h_{i'j'}) \sum_{l'} f_{i'l'} \mu_l(E) \mu_{l'}(E) \right] \times \exp\left[-\sum_i \langle h_{ij} \rangle \sum_l f_{il} \mu_l(E) + \frac{1}{2} \sum_{i,i'} \mathrm{cov}(h_{ij}, h_{i'j}) \sum_{l,l'} f_{il} f_{i'l'} \mu_l(E) \mu_{l'}(E) \right] . \quad (11b)$$

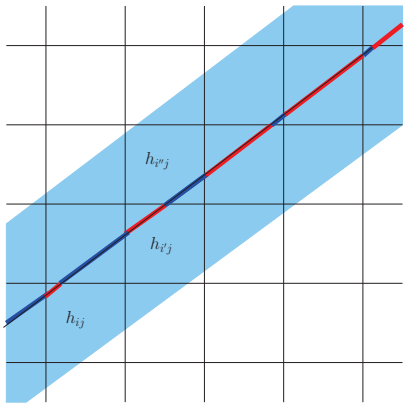

FIG. 1: Schematic representation of a projection beam as it passes through image elements represented as pixels. If two pixels are situated along the projection path so that most rays passing through each of them are simultaneously passing through both of them, and with lengths of similar proportions, (high/high, small/small), then the projections are positively correlated, as is the case with h_{ij} and $h_{i'j}$ in the picture above. If the pixels are positioned relative to the projection beam so that most of the rays are not passing simultaneously through them, or when passing the length have dissimilar values (high/small, small/high), then the projections are negatively correlated, as is the case with h_{ij} and $h_{i''j}$ in the picture above.

For a better understanding of the meaning of cross-correlation of image element projection pairs, $\mathrm{cov}(h_{ij}, h_{i'j})$, see the example in FIG. 1. The interference between the projection path and the image elements arrangement pattern leads to positively and negatively cross-correlated pairs of image elements projections, as function of their relative positions along the path. When using only thin projection lines these correlation terms are neglected leading to artifacts, especially along tangents to the edges of higher attenuating objects [10].

B. Integrating over the energy spectrum

Applying (6) directly over the whole energy spectrum may not work because of the large departure from a bell-shaped distribution of the projection values with energy, therefore we take a decomposition of the spectrum $\phi_j(E)$ in a few more narrow components

$$\phi_j(E) = \sum_k a_{jk}\phi_{jk}(E) \tag{12}$$

with $\int_{\mathcal{E}} \phi_{jk}(E)\mathrm{d}E = 1$, and $\sum_k a_{jk} = 1$. We can write

$$g_j(\underline{f}) = \sum_k I_{jk}\varepsilon_{jk} \int_{\mathcal{D}_j} \mathrm{d}\mathbf{y} w_j(\mathbf{y}) \int_{\mathcal{E}} \mathrm{d}E \phi_{jk}(E)\xi_{jk}(E) \times \mathrm{e}^{-\sum_i h_i(\mathbf{y}) \sum_l f_{il}\mu_l(E)} + b_j \,, \tag{13}$$

with $I_{jk} = I_j a_{jk}$, $\varepsilon_{jk} = \varepsilon_j \int_{\mathcal{E}} \phi_{jk}(E)\xi_j(E)\mathrm{d}E$, and $\xi_{jk}(E)$ being $\xi_j(E)$ renormalized so that $\int_{\mathcal{E}} \phi_{jk}(E)\xi_{jk}(E)\mathrm{d}E = 1$.

For the integral over the energy we introduce the notation

$$\langle Y \rangle_{E,k} = \int_{\mathcal{E}} \phi_{jk}(E)\xi_{jk}(E)Y(E)\mathrm{d}E \,. \tag{14}$$

In order to avoid ambiguities, when necessary, we will use subscripts to distinguish between averaging operators: E, k or just k for integration over energy, and $\mathbf{y}$ for the integration over the spatial resolution kernels. But we will drop them when confusion is not likely in order to avoid cluttering. With this notation equation (13) can be rewritten as

$$g_j(\underline{f}) = \left\langle \sum_k I_{jk}\varepsilon_{jk} \left\langle \mathrm{e}^{-\sum_i h_i(\mathbf{y}) \sum_l f_{il}\mu_l(E)} \right\rangle_{E,k} \right\rangle_{\mathbf{y}} + b_j \,. \tag{15}$$

From (6) we have

$$\left\langle \mathrm{e}^{-\sum_i h_i(\mathbf{y}) \sum_l f_{il}\mu_l(E)} \right\rangle_k = \mathrm{e}^{-\sum_l T_l(\mathbf{y})\langle\mu_l\rangle_k + \frac{1}{2}\sum_{l,l'} T_l(\mathbf{y})T_{l'}(\mathbf{y})\mathrm{cov}(\mu_l,\mu_{l'})_k} \,, \tag{16}$$

where $T_l(\mathbf{y}) = \sum_i h_i(\mathbf{y}) f_{il}$. With (16) in (15) we obtain

$$g_j(\underline{f}) = \sum_k I_{jk}\varepsilon_{jk} \int_{\mathcal{D}_j} \mathrm{d}\mathbf{y} w_j(\mathbf{y}) \exp\left(-\sum_l T_l \langle\mu_l\rangle_k + \frac{1}{2}\sum_{l,l'} T_l(\mathbf{y})T_{l'}(\mathbf{y})\mathrm{cov}(\mu_l,\mu_{l'})_k \right) \tag{17a}$$

$$-\frac{\partial g_j(\underline{f})}{\partial f_{il}} = \sum_k I_{jk}\varepsilon_{jk} \int_{\mathcal{D}_j} \mathrm{d}\mathbf{y} w_j(\mathbf{y}) h_i(\mathbf{y}) \left(\langle\mu_l\rangle_k - \sum_{l'} T_{l'}(\mathbf{y})\mathrm{cov}(\mu_l,\mu_{l'})_k \right) \exp\left(-\sum_l T_l \langle\mu_l\rangle_k + \frac{1}{2}\sum_{l,l'} T_l(\mathbf{y})T_{l'}(\mathbf{y})\mathrm{cov}(\mu_l,\mu_{l'})_k \right) \tag{17b}$$

V. DISCUSSION

For a better understanding of the results, it is helpful to make a comparison to the algebraic formulation of the standard computed tomography problem, which best corresponds to the emission tomography case. In TABLE I we show the projection equations for emission tomography and transmission tomography in the thin line approximation, and integrating over the resolution kernel, respectively. For simplicity here we have taken the monochromatic x-ray transmission case. In the thin line approximation, the logarithmic form of transmission tomography and the standard (emission) tomography form are algebraically equivalent. However, when considering the finite beam size we see a departure, the transmission tomography form requiring the

TABLE I: Comparison of the algebraic formulae for emission tomography, and monochromatic transmission tomography in the approximation of thin projection line and the finite spatial resolution case, respectively.

Projection	Ideal thin line	Finite resolution
Standard (emission) tomography	$g^{\mathsf{e}}(\mathbf{y}) = \sum_i h_i(\mathbf{y}) f_i$	$g^{\mathsf{e}}_j = \int_{\mathcal{D}_j} w_j(\mathbf{y}) g^{\mathsf{e}}(\mathbf{y}) \mathrm{d}\mathbf{y} = \sum_i \left[\int_{\mathcal{D}_j} w_j(\mathbf{y}) h_i(\mathbf{y}) \mathrm{d}\mathbf{y} \right] f_i = \sum_i \langle h_{ij} \rangle f_i$
Transmission tomography	$g^{\mathsf{t}}(\mathbf{y}) = g_0(\mathbf{y}) \mathrm{e}^{-\sum_i h_i(\mathbf{y}) f_i}$	$g^{\mathsf{t}}_j = g_{0j} \mathrm{e}^{-\sum_i \langle h_{ij} \rangle f_i + \frac{1}{2} \sum_{i,i'} \mathrm{cov}(h_{ij}, h_{i'j}) f_i f_{i'}}$
Transmission tomography (log)	$g^{\mathsf{tl}}(\mathbf{y}) = \ln \frac{g_0(\mathbf{y})}{g^{\mathsf{t}}(\mathbf{y})} = \sum_i h_i(\mathbf{y}) f_i$	$g^{\mathsf{tl}}_j = \ln \frac{g_{0j}}{g^{\mathsf{t}}_j} = \sum_i \langle h_{ij} \rangle f_i - \frac{1}{2} \sum_{i,i'} \mathrm{cov}(h_{ij}, h_{i'j}) f_i f_{i'}$

inclusion of the image elements projections cross-correlations, $f_i f_{i'} \mathrm{cov}(h_{ij}, h_{i'j})$, as a higher order approximation, while the standard tomography form preserves its linear character, taking only the averages of the projection elements $\langle h_{ij} \rangle$. It should be noted, that is the latter form that is presented as model-based in some transmission iterative reconstruction algorithms, not the higher order approximation form.

Concerning the practical implementation, the spatial correlations $\mathrm{cov}(h_{ij}, h_{i'j})$ can be computed more easily if the image is represented with spherically symmetric basis functions (blobs), because the projection values are not dependent on incident angles. Only the distances from the blobs to the projection line and how far apart the pair of blobs are from each other are necessary, resulting in only three dimensions being required for a blob projection cross-correlations look-up table. By substantially changing a previous ray tracing algorithm through blobs [11] we have implemented a ray tracing algorithm that retrieves the necessary parameters for the blob projections cross-correlation calculation. However, the full calculation introduces a new loop with the number of operations of order $\mathcal{O}(N^2)$, where N is the length in image elements of a projection line. This makes the algorithm uncompetitive to the alternative of directly ray-racing multiple lines in order to adequately sample the spatial resolution kernel and the image elements projections, however it can be used for analysis of the finite beam size effects.

The second part, integration over the energy spectrum, presented in section IV B, leads to equations that can be directly implemented and used in update equation (5). This is a more convenient alternative to the discrete integration by fine sampling and summation over the energy spectrum and detector response function. The tests carried using a single component, so far, show practically equivalent results, with an increase in speed.

VI. CONCLUSIONS

The differences between transmission and emission tomography go beyond the need to take the logarithm of the data and account for the resulting changes in noise propagation. The projection beam finite size results in image element projections cross-correlation effects, that depend on their overlapping pattern along the projection beam. The second-order approximate equations derived here allow for an analytic investigation of the interference between image element size and representation form (voxel, blob, spline, etc) and the projection beam size and shape. It may also provide new means to investigate and mitigate the streak artifacts produced by high attenuation objects (metal artifacts). The results of the integral over the energy spectrum offer a practical solution to the problem of polychromatic x-ray tracing that can be directly used in the iterative update equations presented, and applicable for standard or spectral CT.

[1] J. Nuyts, B. De Man, J. A. Fessler, W. Zbijewski, and F. J. Beekman, "Modelling the physics in the iterative reconstruction for transmission computed tomography," *Phys. Med. Biol.*, vol. 58, pp. R63–R96, 2013.

[2] C. Hofmann, M. Knaup, and M. Kachelriess, "Effects of ray-modeling: simulation study," in *Proc. 2nd Intl. Mtg. on image formation in X-ray CT*, pp. 17–20, 2012.

[3] R. E. Alvarez and A. Macovski, "Energy-selective reconstructions in x-ray computerized tomography," *Phys. Med. Biol.*, vol. 21, no. 5, pp. 733–744, 1976.

[4] B. De Man, J. Nuyts, P. Dupont, G. Marchal, and P. Suetens, "An iterative maximum-likelihood polychromatic algorithm for CT," *IEEE Trans. Med. Imag.*, vol. 20, no. 10, pp. 999–1008, 2001.

[5] L. M. Popescu and K. J. Myers, "CT image assessment by low contrast signal detectability evaluation with unknown signal location," *Med. Phys.*, vol. 40, no. 11, pp. 111908–10, 2013.

[6] S. Tilley II, J. H. Siewerdsen, and J. W. Stayman, "Model-based iterative reconstruction for flat-panel cone-beam CT with focal spot blur, detector blur, and correlated noise," *Phys. Med. Biol.*, vol. 61, no. 1, p. 296, 2016.

[7] I. A. Elbakri and J. A. Fessler, "Statistical image reconstruction for polyenergetic x-ray computed tomography," *IEEE Trans. Med. Imag.*, vol. 21, no. 2, pp. 89–99, 2002.

[8] J. A. O'Sullivan and J. Benac, "Alternating minimization algorithms for transmission tomography," *IEEE Trans. Med. Imag.*, vol. 26, no. 3, pp. 283–297, 2007.

[9] B. De Man and S. Basu, "Distance-driven projection and backprojection in three dimensions," *Phys. Med. Biol.*, vol. 49, no. 11, p. 2463, 2004.

[10] P. M. Joseph and R. D. Spital, "The exponential edge-gradient effect in x-ray computed tomography," *Phys. Med. Biol.*, vol. 26, no. 3, pp. 473–487, 1981.

[11] L. M. Popescu and R. M. Lewitt, "Ray tracing through a grid of blobs," in *IEEE Nucl. Sci. Symp. Conf. Rec.*, vol. 6, pp. 3983 – 3986, 16-22 Oct 2004.

X-ray Computed Tomography of Flame Structure in Porous Media Burners

Meng Wu, Jared Dunnmon, Yan Xia, Waldo Hinshaw, Norbert Pelc, Andreas Maier, Rebecca Fahrig, and Matthias Ihme

***Abstract*—X-ray Computed Tomography (CT) measurements are applied to combustion systems to obtain non-invasive three-dimensional temperature field measurements at high spatial resolution. X-ray attenuation measurements are obtained using a multi-zone silicon carbide Porous Media Burner (PMB) combusting a radiodense Kr-O_2-CH_4 mixture. A special beam hardening correction is designed to reduce the nonlinearity of the reconstructed krypton attenuation signal resuling from beam hardening by the burner wall. A statistical reconstruction algorithm is investigated to yield the noise reduction in the reconstruction domain. The ideal gas law is then used to estimate the temperature field using reconstructed krypton attenuation. The results demonstrated the potential of CT in obtaining quantitative, spatially resolved temperature field data within optically inaccessible porous media combustion environments.**

***Index Terms*—X-ray Computed Tomography, combustion, beam hardening correction, statistical reconstruction.**

I. Introduction

Porous Media Burners (PMBs) facilitate combustion of a gas mixture within the voids of a solid matrix, which results in combustion properties substantially different than those of a free flame. Stabilization of the flame inside the porous material leads to lower emissions, enhanced combustion stability at lean conditions, and increased burning rates [1]. Due to these characteristics, PMBs show promise as a more efficient, robust, and environmentally friendly alternative to a wide variety of conventional combustion systems. Potential applications for PMBs include surface heaters, domestic heating units, gas turbines, reformers, and afterburners in solid oxide fuel cells [2]. Traditional techniques for PMB combustion measurements are often based on pointwise diagnostics such as thermocouples and exhaust gas probes, which do not yield high-resolution volumetric visualization of internal flame structure or three-dimensional field data. Thus, we investigate the use of X-ray CT technology as an alternative experimental diagnostic that enables research into the detailed physical, chemical, and thermodynamic processes taking place within PMBs.

X-ray CT methods are increasingly being applied to fluid mechanics problems that involve optically inaccessible flow environments. Even in gas-phase phenomena, X-ray CT can be used to create 3-D quantitative datasets describing the mole fraction of krypton, a radiodense tracer gas, at energies characteristic of clinical and research scanners [3]. To increase the contrast of krypton gas, low X-ray energies (45-60 kVp) have been successfully used for imaging. However, as a result of the relatively high attenuation of the solid burner structure and the uncertain path length through the porous media, the transmitted X-ray spectra are altered; this affects the mass attenuation of the krypton in a complex fashion. This nonlinearity may cause inaccurate krypton attenuation measurements in reconstructed CT images. However, since most beam hardening correction algorithms are meant to obtain correct attenuation coefficients of primary attenuators in a scanned object (e.g. water and bone in medical applications), these algorithms are not necessarily well-suited for application to combustion systems where variations in gas-phase attenuation are of interest.

Although krypton has a high atomic number, the density of krypton gas is much lower than water and adipose. Thus, the krypton attenuation measured by CT reconstruction suffers severely from quantum noise. While one may acquire multiple scans and use averaging to improve the Signal-to-Noise Ratio (SNR), it is desirable to minimize the amount of time over which the data must be averaged to ensure steady-state measurements. In this work, we demonstrate that application of statistical reconstruction techniques that have performed well in medical contexts to reconstruction of attenuation data within gas-phase combustion. The application of these techniques show promise in SNR enhancement via noise reduction.

II. Porous Media Burner

The PMB investigated in this work is illustrated in Fig. 1(a). It is placed on the tabletop X-ray radiography system shown in Fig. 1(b). The burner casing consisted of a quartz tube of 0.41 cm thickness, 5.59 cm inner diameter, and 17.78 cm length. The burner matrix consistes of three adjacently placed Silicon Carbide (SiC) disks of 2.54 cm in height and 5.08 cm in diameter. A fine-pore 100 Pores-Per-Inch (PPI) disk was placed furthest upstream for use as a flashback arrestor and flow homogenizer, followed by a 65 PPI disk for flame quenching and a 3 PPI disk that functions as the combustion zone. SiC-disks were held in place via a compression fit using a ceramic fiber insulation lining, visible in Fig. 1(a).

III. Methods

A. Relation between attenuation and temperature

X-ray CT allows reconstruction of the attenuation coefficients, μ, in three spatial dimensions from a set of projections taken over a large number of angles [4]. The attenuation

M. Wu, W. Hinshaw, N. Pelc, and R. Fahrig are in the Department of Radiology, Stanford University, USA e-mail:mengwu@stanford.edu.

J. Dunnmon, and M. Ihme are in the Department of Mechanical Engineering, Stanford University, USA.

Y. Xia and A. Maier are with the Pattern Recognition Lab, Friedrich-Alexander University of Erlangen-Nuremberg, Germany.

This work is supported by the Leading Edge Aeronautic Research for Nasa (LERARN) project with award No. NNX15AE42A.

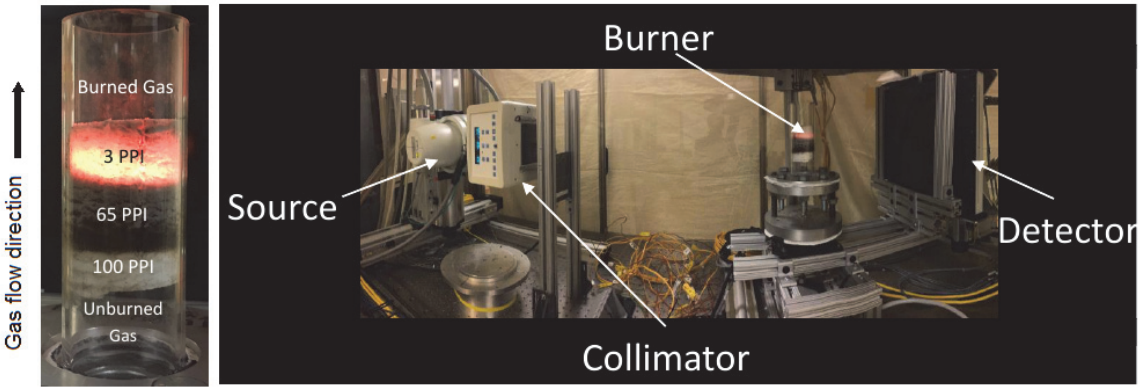

(a) Burner (b) Full Setup

Fig. 1: Experimental setup.

coefficient may be expressed as the following combination of the mass attenuation coefficient m and the density ρ of a known material,

$$\mu(\xi) = m(\xi)\rho, \tag{1}$$

where m is a nonlinear function of the photon energy (ξ) that varies with material composition. Writing Eq. (1) for a mixture of gases and introducing the partial density ρ_j gives [3],

$$\mu(\xi) = \sum_{j=1}^{N} m_j(\xi)\rho_j = \frac{P}{R_u T}\sum_{j=1}^{N} m_j(\xi)X_j W_j, \tag{2}$$

taking W_j as the molar mass of species j, R_u as the universal gas constant, and X_j as the mole fraction. In the case of a radiodense tracer gas such as krypton combined with low-attenuation gases, one may treat Eq. (2) as the combination of attenuation from the tracer and from the solid burner. In this case, one may extend Eq. (2) to yield the following simple expression for gas temperature in terms of known and measured quantities [3],

$$T = \frac{PW_{Kr}X_{Kr}m_{Kr}}{R_u \Delta\mu}, \tag{3}$$

where $\Delta\mu = \mu_M - \mu_B$, μ_B is the attenuation measured in a background scan (with only non-attenuating species in the burner), μ_M is the attenuation of the burner containing a krypton-augmented gas mixture at the effective X-ray energy, and m_{Kr} is the mass attenuation coefficient of krypton at the effective energy. Because light gases such as combustion products and ambient air attenuate negligibly at these energies, the μ_B-value is a good measurement of the appropriate signal to be subtracted to isolate the attenuation resulting from the radiodense tracer [3]. In the current work, we have used projection-based subtraction to compute $\Delta\mu$, which simplifies averaging over multiple scans while requiring only a single application of the beam hardening correction to the final projection set.

B. Beam-hardening correction

As mentioned above, the goal of the beam hardening correction presented here is different from that in most medical CT-applications. To obtain an accurate krypton attenuation image for transformation to an implied temperature signal, it is necessary to compensate for nonlinear effects of varying path length within the quartz tube and SiC porous reticulated foam that make up the body of the burner. Since subtraction is performed in the projection domain, we may apply the same correction to the background and mixture scan sets before subtraction. Note that the effect of the beam hardening correction for the quartz tube will cancel out in the subtraction process. We propose to use a two-step beam hardening correction with prior reconstruction to accurately model the effects of the two materials.

The subtracted polychromatic line-integrals of the background scan and mixture scan are:

$$\begin{aligned}\Delta y =& y_M - y_B \\ =& \log\left(\int I_0(\xi)e^{-\mu_{SiO_2}(\xi)l_{SiO_2}-\mu_{SiC}(\xi)l_{SiC}}\mathrm{d}\xi\right) \\ &- \log\left(\int I_0(\xi)e^{-\mu_{Kr}(\xi)l_{Kr}-\mu_{SiO_2}(\xi)l_{SiO_2}-\mu_{SiC}(\xi)l_{SiC}}\mathrm{d}\xi\right)\end{aligned} \tag{4}$$

where $\mu_i(\xi)$ are the attenuation coefficients of three materials, quartz, SiC, and krypton; l_i, are the path lengths, and $I(\xi)$ denotes the spectrum of the X-ray beam. The desired beam hardening gain correction for krypton is,

$$\alpha(l_{SiO_2}, l_{SiC}) = \frac{\Delta y}{\mu_{Kr} l_{Kr}}, \tag{5}$$

which is a function of path lengths in both the quartz tube and porous media. We have ignored the effect of krypton because of its very low attenuation relative to the solid, and the path length of the quartz tube can be easily calculated from a prior reconstruction. However, the path length within the porous media is hard to quantify explicitly because of its complex internal structure. We therefore simplify the process of computing the gain correction as a polynomial function of l_{SiO_2} and total line integral that includes both materials,

$$\begin{aligned}\alpha(l_{SiO_2}, l_{SiC}) &\approx \alpha(l_{SiO_2}, y) \\ &= \beta_0 + \beta_1 y + \beta_2 y^2 + \beta_3 l_{SiO_2} + \beta_4 y \cdot l_{SiO_2}.\end{aligned} \tag{6}$$

The β-coefficients can be computed with a linear fitting using known X-ray spectrum information. An example of calculated polynomial coefficient values for a 60 kVp spectrum with an

TABLE I: An example of calculated values for polynomial coefficients of the beam hardening correction for 60 kVp spectrum.

β_0	β_1	β_2	β_3	β_4
0.9528	0.1130	-0.0085	-0.0114	0.0016

effective energy of 44.8 keV is shown in Table I. For larger total line integral values, we increase the gain α to compensate for the beam hardening effect. Further, longer quartz-tube path lengths will decrease the correction gain because SiO_2 has a relatively small photoelectric effect compared to SiC. The line integral difference $\Delta y_{\text{corr}} = \alpha \cdot \Delta y$ that has been corrected for beam hardening is used during the reconstruction process.

C. Statistical reconstruction

Attenuation measurements for the krypton tracer within the reconstruction suffer from low signal–this is particularly true when the flame temperature is high. Because CT noise remains at the same level as it would in medical applications, this variation may substantially alter computed krypton attenuation in common FDK reconstructions [5]. Statistical iterative reconstruction techniques based on accurate physical noise modeling and geometric system description, on the other hand, have demonstrated significant image quality improvement over conventional methods [6]. In this study, we therefore consider the penalized weighted least-squares (PWLS) algorithm for X-ray CT reconstruction as an alternative to analytic methods. In PWLS, the attenuation field is reconstructed as,

$$\mu = \underset{0\le\mu\le\mu_{\max}}{\operatorname{argmin}} \sum_{i=1}^{I} w_i([\mathbf{A}\mu]_i - \Delta\bar{y}_i)^2 + \beta \mathrm{R}(\mu), \qquad (7)$$

where $\mathbf{A}$ denotes the system matrix for the data acquisition geometry, Δy denotes the subtracted projection with beam hardening correction, and w contains the least-squares weights. We selected the total variation as the penalty function $\mathbf{R}$:

$$\mathrm{R}(\mu) = \sum_{j=1}^{J} \sum_{k\in N_j} |\mu_j - \mu_k|, \qquad (8)$$

where N_j denotes the indices of the neighbors of voxel j. Total variation minimization has been known to perform well in terms of both noise reduction and edge preservation. Because the quartz tube and porous media will appear as zeros in the reconstruction of subtracted projections (assuming perfect registration), we reduced the weights of the penalty function at voxels describing the solid-gas boundary by half.

IV. Experiments

All experiments were performed using the PMB shown in Fig. 1(a) on the tabletop X-ray radiography system (see Fig. 1(b)). The configuration of the PMB is detailed in Section II. The tabletop system includes a fluoroscopic X-ray source and a flat panel detector with pixel spacing of 0.336 mm. As shown in Fig. 1(b), the burner is placed between the source-collimator assembly (left) and detector (right) on a precision rotating table to acquire 1200 projections over 360 degrees.

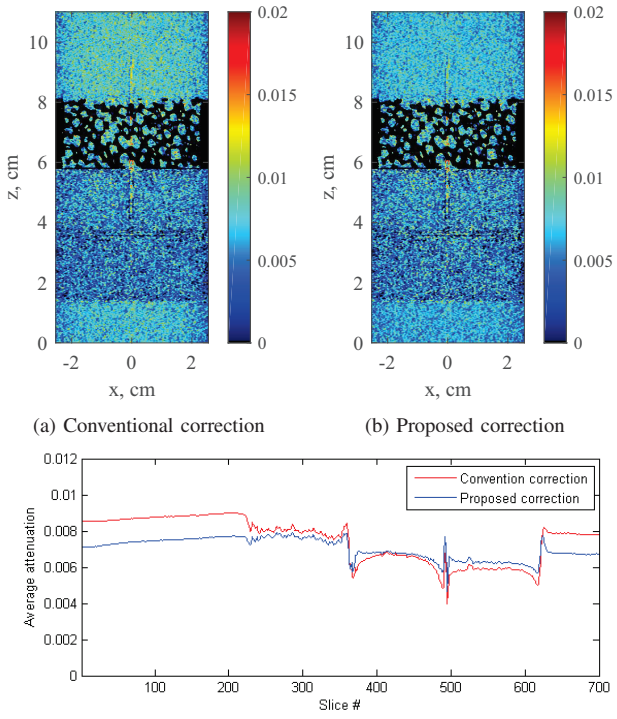

(a) Conventional correction (b) Proposed correction

(c) Average voxel attenuation

Fig. 2: Beam hardening correction results using non-reacting scan data with cold-flow krypton concentration of 35.58% (solid mask in black).

The source-to-isocenter distance was 1061.2 mm, and source-to-detector distance was measured at 1477.9 mm. Tomographic acquisitions were conducted with a 60 kVp and 50 mA X-ray beam to optimize SNR. The 3-D reconstruction volume has a size of 384×384×700 pixels with 0.2 mm isotropic spacing.

V. Results

A. Beam hardening correction

Figure 2(a) and (b) show FDK [5] reconstructions of a tube filled with 36% krypton gas using the dual-material polynomial beam hardening correction [7] and our proposed approach. With our proposed beam hardening correction, the krypton attenuation is more uniform than with the traditional method. For instance, the differences between the gas region and porous media region are smaller than using the conventional correction—this can be observed in Fig. 2(c), which shows the cross-sectionally average attenuation coefficient of the gas voxels at different slices. With our proposed beam hardening correction approach, the reconstruction has the same krypton density inside and outside the 3 PPI porous media, while with the conventional approach this is not the case.

B. Statistical reconstruction

Reconstruction results of a PMB burning a mixture containing 82.5% krypton using both FDK and PWLS are shown in Fig. 3. We used the ADMM accelerated separable quadratic surrogate method with 30 iterations to achieve the solution of the PWLS problem for every fixed β value [8]. Even though

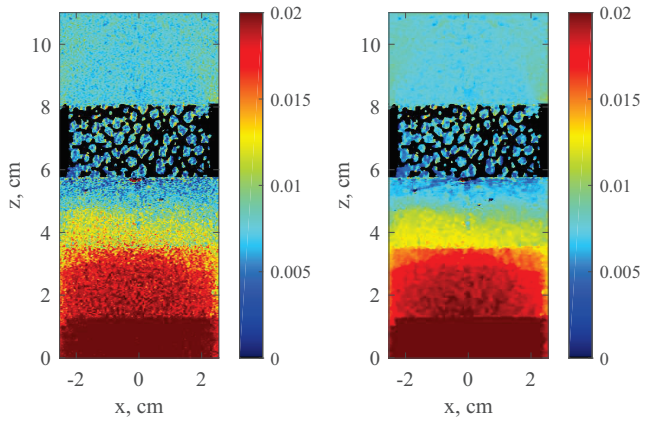

(a) FDK (b) PWLS

Fig. 3: FDK (left) vs. PWLS (right) reconstruction results using burn scan data with the krypton concentration of 82.4% (solid mask in black).

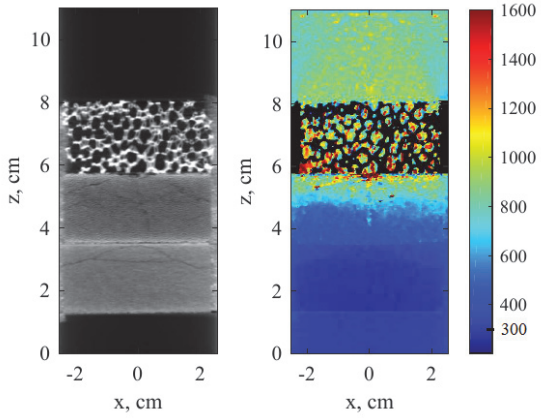

(a) Solid structure (b) Implied temperature

Fig. 4: (Left) Reconstruction result of air scan (i.e., without subtraction) to show the solid porous media structure and (right) implied temperature distribution computed from the reconstruction of PWLS (solid mask in black).

a Hamming window is applied on the ramp filtering of the FDK method to suppress high frequency components, it can be observed that the noise level is fairly high throughout the image. In contrast, the noise in the reconstruction results from the PWLS-algorithm using TV penalty function ($\beta = 4$) is substantially reduced. The interface between the different porous media sections is also more clearly visible in the PWLS result.

Finally, measured standard deviation of a homogeneous region from one reconstructed slice was substantially lower for PWLS (6.1×10^{-4}) than for FDK (2×10^{-3}), indicating that local variations present in the FDK reconstruction has been reduced by over 50 % by the PWLS technique.

C. Temperature analysis

At this point, we can use Eq. (3) to estimate an implied temperature field from the attenuation data of Fig. 3. Specifically, we estimate the temperature field by observing that the product μT is constant for constant P and X_{Kr}; this implies that temperature at a given point is simply $T = \mu_o T_o / \mu$, with inlet temperature T_o known and the attenuation values μ and μ_o obtained from the reconstruction. Note that while the 3 PPI porous media structure can be easily identified and segmented in the CT reconstruction, the 65 PPI and 100 PPI porous media is below the resolution of the CT system. We treat voxels in the 3 PPI section as the separate SiC and gas, and voxels in the 65 PPI and 100 PPI as the mixture of SiC and gas. Thus, the volume fraction of the SiC in the mixture voxels needed to be properly accounted for before converting to temperature.

Because the attenuation is in the denominator of Eq. (3), noise in this field will cause an inordinate amount of variability in the implied temperature field. Thus, reduction in krypton attenuation noise resultant from PWLS results in a substantially smoother temperature field, as shown in Fig. 4. Such results show promise in allowing for reliable extraction of 3-D flame structure and temperature fields from the PMB interior. In these images, for instance, the flame (indicated by regions of high temperature) is settled near the interface between the 3 PPI and 65 PPI regions. Substantial internal structure can be observed throughout, while heat recirculation within the solid matrix is also well visualized.

VI. Conclusion

In this paper, we have demonstrated the application of X-ray CT to combustion systems to obtain non-invasive 3D temperature field measurements. With the particularly designed experimental setup, the implied gas-phase temperature information can be derived from the 3-D reconstructed attenuation data. Further reconstruction methods are undertaken to improve the image quality, including the newly proposed beam hardening correction for reducing nonlinearity of Krypton attenuation as well as the adoption of the statistical reconstruction algorithm for suppressing the noise. From final 3D implied temperature measurements, several key internal physical phenomena, such as heat recirculation and spatial inhomogeneities within the reaction zone, can be observed.

References

[1] D. Trimis and F. Durst, "Combustion in a porous medium-advances and applications," *Combust. Sci. Technol.*, vol. 121, no. 1-6, pp. 153–168, 1996.

[2] M. A. Mujeebu, M. Z. Abdullah, M. A. Bakar, A. Mohamad, R. Muhad, and M. Abdullah, "Combustion in porous media and its applications–a comprehensive survey," *J. Environ. Manage.*, vol. 90, no. 8, pp. 2287–2312, 2009.

[3] J. Dunnmon, S. Sobhani, T. W. Kim, A. Kovscek, and M. Ihme, "Characterization of scalar mixing in dense gaseous jets using X-ray computed tomography," *Exp. Fluids*, vol. 56, p. 193, 2015.

[4] J. Hsieh, *Computed Tomography, Second Edition*. 1000 20th Street, Bellingham, WA 98227-0010 USA: SPIE, Oct. 2009.

[5] L. Feldkamp, L. Davis, and J. Kress, "Practical cone-beam algorithm," *J. Opt. Soc. Am. A*, vol. 1, no. 6, pp. 612–619, 1984.

[6] J.-B. Thibault, K. D. Sauer, C. A. Bouman, and J. Hsieh, "A three-dimensional statistical approach to improved image quality for multislice helical CT," *Med. Phys.*, vol. 34, no. 11, p. 4526, 2007.

[7] J. Hsieh, R. C. Molthen, C. a. Dawson, and R. H. Johnson, "An iterative approach to the beam hardening correction in cone beam CT.," *Med. Phys.*, vol. 27, pp. 23–9, Jan. 2000.

[8] H. Nien and J. A. Fessler, "Fast X-ray CT image reconstruction using the linearized augmented Lagrangian method with ordered subsets," *arXiv Prepr. arXiv1402.4381*, p. 21, Feb. 2014.

Three-Dimensional Two Material Based Beam Hardening Correction for Iterative Reconstruction

Ilmar Hein, Zhou Yu, and Satoru Nakanishi

***Abstract*—A three-dimensional, two material pre-processing beam hardening correction method for x-ray computed tomography is described (BHC3D2M) for implementation in iterative reconstruction (IR). Beam hardening correction (BHC) can be implemented as part of IR; however, the computational cost of adding BHC to IR iterative loops is high. For that reason, a preprocessing method of beam hardening correction for IR is desirable. In this metod, a seed image volume is first reconstructed, which is segmented into bone and water images. Bone and water pathlengths are determined by forward projection. The pathlengths are used as indexes to a lookup table, which is used to correct the projection data. One limitation of earlier beam hardening methods is that water is corrected in preprocessing, and bone in post-processing. The methods to estimate the bone pathlengths were fan beam, thus limiting the accuracy of the bone correction. The forward projection used here is three dimensional, producing a more accurate correction.**

***Index Terms*—x-Ray, CT, Computed Tomography, Beam Hardening Correction**

I. Introduction

Most CT reconstruction algorithms operate under the assumption that the x-ray source is monochromatic. In reality the x-ray source is polychromatic and the x-ray beam is comprised of photons covering a range of different energies. The attenuation of x-rays through tissue is energy dependent. Higher energy photons are attenuated less than lower energy photons, thus the x-rays reaching the detector are "harder" than those that left the source. The primary contributors to beam hardening are soft tissue and bone. If not accounted for, artifacts due to soft tissue beam hardening include cupping, where the image is darker at the center than the edges. Bone beam hardening artifacts consist of dark streaks or bands between high density bone structures, such as temporal bones in the skull. Typical methods of beam hardening correction include two-pass methods, where soft tissue is modelled as water and water beam hardening correction is performed as a preprocessing step. Images are reconstructed and bone beam hardening correction is implemented as a post-processing step [1][2]. In the post-processing step, the image is segmented into water and bone images, and the water and bone pathlengths estimated. One disadvantage of these methods is that pathlength estimation assumes a 2D geometry. Iterative BHC (not reconstruction) methods for beam hardening correction also exist [3][4].

When the CT reconstruction algorithm is an iterative one, BHC can be made part of the iterative process. However, iterative reconstruction is already computationally very intensive, and adding BHC to the reconstruction algorithm will only increase the computational demand.

The BHC3D2M method described here is purely a preprocessing method, which segments images into water and bone and calculates 3D pathlengths via forward projection[5][6][7]. Once the pathlengths are known, a lookup table is used to correct the projection data. BHC3D2M has been tested with phantom, patient head, and patient cardiac data..

II. Correction Algorithm

Fig. 1 shows the block diagram for the 3DBHC2M. The input projection data sinogram PD_{In} is uncorrected. A segmentation image volume is reconstructed, which is segmented into bone and water images. These images are forward projected to calculate the bone and water pathlengths. The pathlengths are inputs to a correction table, which corrects the input sinogram.

Abstract submission to the 4th International Conference on Image Formation in X-Ray Computed Tomography 2016, Bamberg, Germany.

I. Hein, Toshiba Medical Research Institute, USA, Vernon Hills, IL (ihein@tmriusa.com).

Z. Yu, Toshiba Medical Research Institute, USA, Vernon Hills, IL (ihein@tmriusa.com).

S. Nakanishi, Toshiba Medical Systems Corporation, Japan (satoru.nakanishi@toshiba.co.jp).

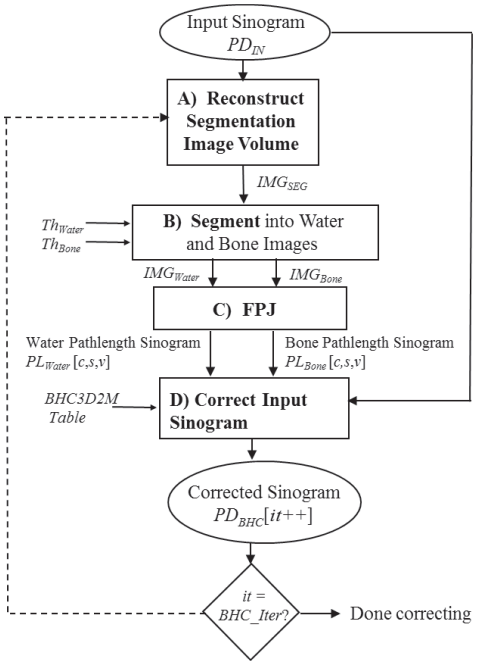

Fig. 1: BHC3D2M Sinogram Correction

A. Reconstruct Segmentation Image Volume

The bone and water pathlengths are calculated by forward projection through water and bone segmented versions of the input volume. Thus, the accuracy of the water and bone pathlength calculations depends on the input volume voxel size. The smaller the input voxel size, the finer the pathlength resolution and the better the correction. Ideally, FOV_{SEG} should be as small as possible and $Matrix_{SEG}$ as large as possible; where FOV_{SEG} is the reconstruction field of view diameter and $Matrix_{SEG}$ is segmentation image matrix size.

The smallest possible FOV_{SEG} is determined by the detector fan angle, since FOV_{SEG} must cover the entire detector. Investigations have shown that $Matrix_{SEG}$ = 512 is fine enough to produce an accurate correction.

B. Segmentation into Water and Bone Images

The segmentation is fractional model based, which assumes that the image consists of water, bone, and water bone mixture. Two parameters, Th_W and Th_B for water and bone, define the segmentation. This illustrated in Fig. 2.

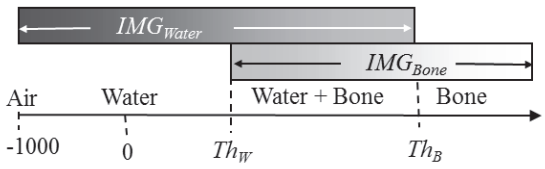

Fig. 2: Segmentation

The model assumes that HU values less than Th_W are pure water, that values are above Th_B are pure bone, and values in between are a water + bone mixture. In the water + bone region, it is assumed that the linear attenuation coefficient μ can be separated into water and bone components f_w and f_b :

$$\mu_{SEG} = f_B[\mu_{SEG}] \cdot \mu_B + f_w[\mu_{SEG}] \cdot \mu_W$$

or in terms of image,

$$IMG'_{SEG} = f'_B[IMG'_{IN}] \cdot \mu_B + f'_w[IMG'_{IN}] \cdot \mu_W$$

where

$$IMG'_{SEG} = IMG'_{SEG} + 1000.$$

The relation ship between μ and the input image IMG'_{SEG} is given by:

$$\mu_{IN} = \mu_W \cdot \frac{(IMG'_{SEG} - 1000)}{1000} - \mu_W$$

The segmented water and bone images are normalized, and are given by

$$IMG_{Bone} = \frac{IMG'_{SEG} \cdot f'_B[IMG'_{SEG}]}{HU_B + 1000}$$

$$IMG_{Water} = \frac{IMG'_{SEG} \cdot f'_W[IMG'_{SEG}]}{1000}$$

where

$$f'_B[IMG'_{SEG}] = f_B\left[\frac{IMG'_{SEG} - 1000}{1000} - \mu_W\right]$$

$$f'_W[IMG'_{SEG}] = 1.0 - f'_B[IMG'_{SEG}]$$

and HU_B is the HU value of bone at effective monochromatic energy.

Water and bone fractional curves are shown in Fig. 3. They are based on the Elbakri & Fessler displacement model [11], using a sine function to model the model.

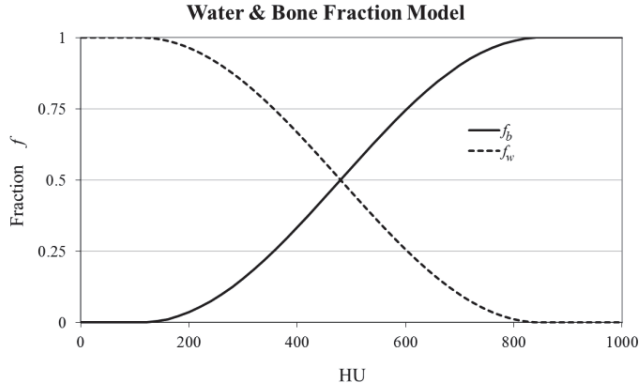

Fig. 3: Water and bone fractional model curves, calculated using sine function (below) with Th_W = 110 and Th_B = 850.

Calculation of f_b and f_w are given by:

$$f_B[HU] = \begin{cases} 0.0 & HU < Th_W \\ \dfrac{1+\sin\left(SinW \cdot (HU - Th_W) - \dfrac{\pi}{2}\right)}{2} & Th_W \le HU \le Th_B \\ 1.0 & HU > Th_B \end{cases}$$

$$f_W[HU] = 1.0 - f_W[HU]$$

where

$SinW = \pi / (Th_B - Th_W)$

C. Forward Projection

Various forward projection algorithms exist in the literature[8][9][10]. For this application, a ray-tracing based forward projection is implemented. The ray is sampled at an evenly spaced positions along the ray, and a 3D interpolation of the voxels surrounding the sampling position are used as the contribution of that sampling point to the ray. Two forward projections are performed, one for IMG_{Water} and the other for IMG_{Water}. The outputs of the forward projections are the pathlength sinograms $PL_{Water}[c,s,v]$ and $PL_{Bone}[c, s,v]$.

D. Correct Input Sinogram

The pathlength sinograms, along with bilinear interpolation, are used to correct the input sinogram by

$$PD_{BHC}[c,s,v] = PD_{IN}[c,s,v] + BHC3D2M\left[PL_{Water}[c,s,v], PL_{Bone}[c,s,v]\right]$$

III. BHC3D2M Table Generation

The table is a four dimensional table, where the correction term is calculated for the all the possible bone and water pathlengths l_b, l_w for each channel and segment *c, s*. For each [*c*, *s*, l_b, l_w] entry, the monochromatic and polychromatic counts *MonoCnt* and *PolyCnt* are determined and the correction term calculated. *MonoCnt and PolyCnt* are calculated from the water and bone pathlengths and linear attenuation coefficients μ_b and μ_b. The monochromatic and polychromatic counts are given by Beer's law:

$$MonoCnt = I_o \cdot e^{-l_B \mu_b[mono] - l_W \mu_w[mono]}$$

$$PolyCnt = \sum_{keV=1}^{kVp} I_o[keV] \cdot e^{-l_B \mu_b[keV] - l_W \mu_w[keV]}$$

Where the I_os are the post-wedge counts. Projection data is logged, so the correction term is the difference between the logged polychromatic and monochromatic counts.

$$BHC3D2M[c, s, l_b, l_w] = \text{Log}(Po) - \text{Log}(PolyCnt) - \text{Log}(MonoCnt)$$

where

$$P_o = \sum_{keV=1}^{kVp} I_o[keV] \cdot$$

In practice, table values are calculated on the fly rather than stored as a table.

IV. Results

BHC2D2N was tested with both phantom and patient data. Data was collected with a Toshiba Aquilion One 320 slice scanner.

A. Cranial Test Phantom

A QRM cranial CT phantom, manufactured by QRM GmBH, Moehrendorf, Germany, was used for quantitative testing. It consists of skull and temporal bone protrusions which produce bone beam hardening artifacts similar to those found in the skull. Fig. 4 shows IR reconstructions with and without BHC3D2M correction. Without correction (image A), significant blooming appears around the skull edge, and a dark band is present between the temporal bone. With BHC3D2M correction the blooming and dark band disappear, and the HU value is consistent.

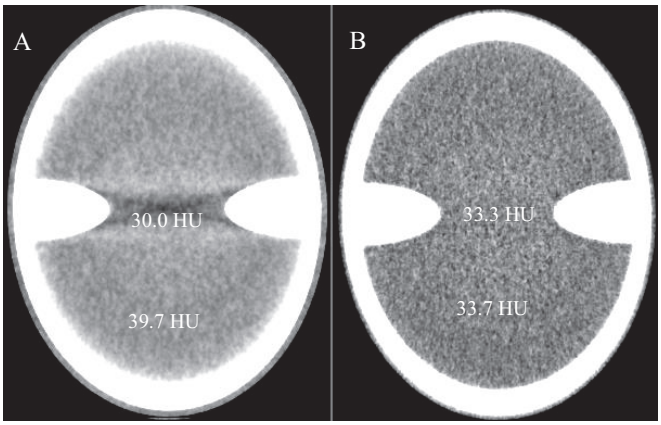

Fig. 4: A) No BHC3DM; B) BHC3D2M. WL=30/WW=80.

B. Clinical Cranial

Figs. 5A shows the cranial IR CT reconstruction without bone beam hardening correction. Various brightening and darkening artifacts are seen in the image, and structure at the top of posterial cranial fossa is not distinct. Fig. 5B shows the same reconstruction with BHC3D2M beam hardening correction. The blooming around the skull is gone, the image is uniform.

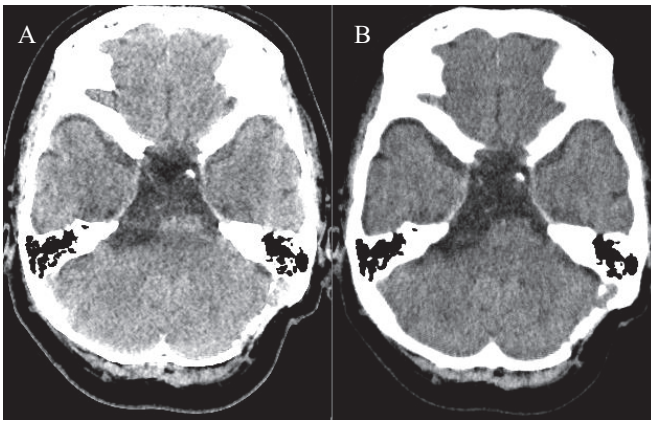

Fig. 5: A) No BHC3DM. B) BHC3D2M Correction. WL= 25/WW=100.

C. Clinical Cardiac

Beam hardening artifacts in cardiac images with iodine-based contrast agents typically show up as a darkening between the left ventricle and descending aorta, as shown in Fig. 6A. Fig. 6B shows the same data when corrected with BHC3D2M. In this case the table used for correction was a water-iodine (Iopromide) based table instead of a water-bone table. With BHC3D2M, the cardiac beam hardening artifacts are eliminated.

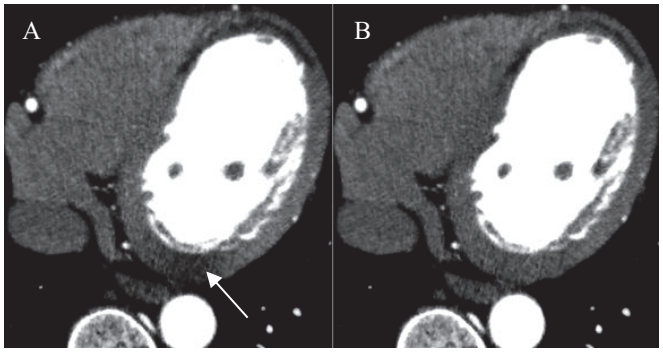

Fig. 6: A) No BHC3D2M. B) BHC3D2M with water-Iopromide table. Arrow indicates beam hardening artifact. WL=125/WW=300

REFERENCES

[1] G. Herman and S. Trivedi, ”A comparative study of two post-reconstruction beam hardening correction methods,” *IEEE Trans. Med. Imaging* 2,128-135 (1985).

[2] P. M. Joseph and R. D. Spital, ”A method for correcting bone induced artifacts in computed tomography scanners,” *J. Comput. Assist. Tomogr*. 2, pp. 100-109 (1978).

[3] G. Van Gompel, K. Van Slambrouck, M. Defrise, K. Batenburg, J. de Mey, J. Sijbers, and J. Nuyts, ”Iterative correction of beam hardening artifacts in CT,” *Med. Phys*. 38, pp. S36-S4 (2011).

[4] J. Hsieh, R. C. Molthen, C. A. Dawson and R. H. Johnson, “An iterative approach to the beam hardening correction in cone beam CT”, *Med. Phys*. 27, 23 (2000).

[5] P. Joseph and C. Ruth, "A Method for Simultaneous Correction of Spectrum Hardening Artifacts in CT Images Containing both Bone and Iodine,” *Med Phys*, **24**, 1629 (1997)

[6] M. Kachelrieß and W. Kalender, “Improving PET/CT Attenuation Correction with Iterative CT Beam Hardening Correction”, *2005 IEEE Nuclear Science Symposium Conference Record*, 1905-1909.

[7] Y. Kyriakou, E. Meyer, D. Prell, and M. Kachelrieß, “Empirical beam hardening correction (EBHC) for CT,” *Med Phys* **37**, 5179 (2010).

[8] B. De Man and S. Basu, “Distance-driven projection and backprojection in three dimensions”, *Phys. Med. Biol* **49**, 2463-2475 (2004)

[9] I. Hein and A. Zamyatin, “System optics in both backprojection and forward projection for model-based iterative reconstruction,” *Proc. SPIE 2013*.

[10] R. Siddon, “Fast calculation of the exact radiological path length for a three-dimensional CT array” *Med. Phys*. **12**, 252–255 (1985).

[11] I. A. Elbakri & J. A. Fessler, "Segmentation-free statistical image reconstruction for polyenergetic x-ray computed tomography with experimental validation," *Phys. Med. Biol*. **48** 2453 (2003).

Studying Performance of A Penalized Maximum Likelihood Method for PET Reconstruction on Nvidia GPU and Intel Xeon Phi Coprocessor

Wei Xu, *Member, IEEE* and Dake Feng

***Abstract*—Penalized Maximum Likelihood (PML) is a Bayesian-based tomographic reconstruction algorithm broadly used for positron emission tomography (PET). Due to its iterative nature and computation complexity, although it outperforms theoretical approaches when dealing with noise, the computational performance is extremely slow without hardware acceleration. Fortunately, there are many accelerator choices nowadays including Nvidia's Kepler GPUs and Intel Xeon Phi coprocessors associated with more programming friendly toolkits and APIs. In this paper, we studied and compared the acceleration performances of a chosen PML approach on CPU, GPU and Phi hardware. A detailed comparison of kernel implementations was discussed. In addition, we also considered a range of criteria including budget plan, implementation difficulty, and data scale.**

***Index Terms*—Tomography reconstruction, PET, acceleration, GPU, Intel Xeon Phi coprocessor, performance analysis.**

I. Introduction

THREE dimensional tomographic image reconstruction – a popular approach to reveal the cross-sectional information of the object is widely utilized in scientific areas including Physics, chemistry, biology and medicine. Its performance has considerable impact on their corresponding industrial applications such as energy material development, drug design, genetic analysis and clinical diagnosis. For its application in transmission X-ray microscopy and electron microscopy, the main challenge is that the images acquired for reconstruction are often degraded – they are taken within a limited angle, from an unstable position, or with reduced dosage. For emission tomography such as PET, since the photon counts in the detector are much less than the transmission tomography, the results are even noisier. Therefore, model-based/statistical approaches are more favorable for such tomographic reconstructions by adding object constraints/priors to the cost function, such as non-negativity, piecewise smoothness, motion models and so on. The reconstruction process iteratively improves the estimate that finally converges to a numerically optimized solution.

This work was supported by the U.S. Department of Energy STTR Phase I Grant# DE-SC0013305.

W. Xu is with Brookhaven National Laboratory, Upton, NY 11973 USA (e-mail: xuw@bnl.gov).

D. Feng is with Peri LLC, Kings Park, NY 11754 USA (e-mail: d.feng@perillc.com).

Unfortunately, for large-scale reconstruction problems, these methods are highly computation demanding. With the development of modern acceleration hardware, we now have many high performance computing (HPC) choices such as supercomputers, Graphics Processing Units (GPUs) and the Many Integrated Core (MIC) coprocessors, together with more friendly programming toolkits and interfaces. Among them, there are some economic HPC architectures including GPUs and coprocessors. Their costs are modest from several hundred to a couple of thousand dollars, while their performances can improve up to a few orders of magnitude compared with traditional CPU-based architecture. However, to parallelize the computation, it still requires the help of high performance computing experts especially to tune up the implementation and optimize its performance.

In this work, we study the acceleration performance on both Nvidia GPU and Intel Xeon Phi coprocessor (mentioned as Phi in following sections) for a PET reconstruction method. The purpose is not to provide the most advanced acceleration techniques for this specific reconstruction algorithm. Instead, we pick the straightforward acceleration implementations as first attempt to parallelize a program in order to quantify the effort, cost and improvement on both platforms. We hope to use our work as a showcase of parallelizing a statistical iterative reconstruction (SIR) method on HPC platforms in consideration of a range of criteria including budget, implementation difficulty and data scale.

The remainder of this paper is as follows. In section II, we introduce the PML method and explain the implementation details on GPU and coprocessor. Section III presents the performance analysis results, followed by conclusions in section IV.

II. Methodology

A. PML

For PET, there are many penalized maximum likelihood methods such as one-step-late (OSL) [1] algorithm, iterative coordinate descent (ICD) [2] algorithm, maximum a posteriori method with surrogate functions [3][4], and ordered-subset-based approaches [5][6]. We selected an approach that follows De Pierro's surrogate functions [3][4] for the log likelihood function but has a closed form expression [7]. This approach is currently used by Tomopy [8] – a Python

based open source tomography package developed for utilization by synchrotron science.

As stated in [7], the PML estimate x is the nonnegative minimizer of $\Phi(x) = -L(x) + \beta\Lambda(x)$, where $L(x)$ is the log likelihood function, $\Lambda(x)$ is the penalty function, and β is the penalty parameter. The authors further constructed de-coupled surrogate functions for Λ and L. Eventually, the closed form solution for jth value of $\boldsymbol{x}$ in the $(n+1)$th iteration is achieved as

$$x_j^{(n+1)} = \frac{-G_j^{(n)} + \sqrt{G_j^{(n)2} - 8E_j^{(n)}F_j^{(n)}}}{4F_j^{(n)}} \quad (1)$$

Where

$$E_j^{(n)} = -\sum_{i=1}^{I} d_i \frac{P_{ij}x_j^{(n)}}{[P\boldsymbol{x}^{(n)} + \boldsymbol{\rho}]_i} \quad (2)$$

$$F_j^{(n)} = 2\beta \sum_{k \in N_j} w_{jk}\gamma(x_j^{(n)} - x_k^{(n)})m_{jk}^{(n)} \quad (3)$$

$$G_j^{(n)} = \sum_{i=1}^{I} P_{ij} - 4\beta \sum_{k \in N_j} w_{jk}\gamma(x_j^{(n)} - x_k^{(n)})m_{jk}^{(n)} \quad (4)$$

Among them, P is the probability matrix, d_i is the number of photon pairs recorded by the i th detector pair, $\boldsymbol{\rho}$ is the accidental coincidence rate, w is the nonnegative weights, N_j is the neighborhood of j, γ is the chosen surrogate function, and $m_{jk}^{(n)}$ is the average of $x_j^{(n)}$ and $x_k^{(n)}$. Please refer to [7] for more details. The benefits of this approach are 1) its simplicity to implement, 2) guaranteed non-negative estimates and monotonic decrease of objective function with increasing iterations, and 3) sufficient choices of surrogate functions.

Since in synchrotron science most experiments can be treated as parallel beam, the corresponding implementation can be developed as the reconstruction for a stack of 2D slices. The pseudocode is shown in Fig. 1. The total number of lines in C is about 840.

```
void PML()
{
  for each iteration n:
    for each slice s:
      for each projection p:
        for each detector pixel d:
          Calculate the intersection points,
            compute distances between them as P;
          Forward project;
          Compute E^(n);
      Compute F^(n) and G^(n);
      Update x^(n+1);
}
```

Fig. 1. Pseudocode for the selected PML approach.

B. Phi implementation

For acceleration on Intel Xeon Phi, we implement parallelism through cilk [9] and develop only offload mode with simple pragma directives. Besides, the implementation was developed in Intel parallel studio that automatically evaluates the best strategies to parallelize code. Afterwards, only simple replacement from standard keywords to parallel keywords is required, while all other algorithm code remain totally unchanged. The vectorization of computing is automatically optimized by Intel compiler by default. In specific, for the PML method, after automatic evaluation, the computation for each slice is parallelized by replacing regular for-loop with *cilk_for*. Additional pragma offload statements are used to set up the offload mode and coprocessor memory space allocation, data transfer and deletion are also added. This acceleration porting from original C code on CPU is extremely light-weighted. The total modification is only about 10 lines of code, with majority of program remain unchanged. For a more advanced parallelization implementation, vectorization by using 512 bit vector instruction set can further improve the performance as reported in [10]. However, it will also require more effort rewriting the program. In this paper, we aim at discussing the first attempted strategy towards parallelism.

C. GPU implementation

When porting to Nvidia GPU, we used CUDA for acceleration. The major difference from Xeon Phi implementation is that we instead serialize the computation of each slice but for every slice we parallelize the computation internally: there are three major steps for parallelization – to compute $E^{(n)}$ based on acquired sinogram, to compute $F^{(n)}$ and $G^{(n)}$, and to update $x^{(n+1)}$. This design is based on the difference of core numbers of each board (2688 on GPU vs. 57 on Phi). To implement, all major steps are rewritten as CUDA kernels and caller functions. Besides, CUDA initialization, memory allocation and transfer (adopted only global memory for simplicity), and CUDA cleanup including memory deallocation are necessary. After this direct migration, the new implementation has about 2100 lines.

III. Performance Analysis

Our experiments are tested on Nvidia Tesla K20X GPU that has 2688 cores, 6GB global memory, 1.31Tflops Peak double precision floating point performance and 3.95Tflops Peak single precision floating point performance [11], and Intel Xeon Phi coprocessor 31S1P that has speed of 1.1 GHZ, 8 GB memory and 57 cores [12]. In the following section, we first evaluate the overall acceleration performances on all hardware platforms, then discuss other criteria including platform porting difficulty and budget plan. All implementations are open source and available online in Github [13][14].

A. Overall performance

Our test data are 3D Shepp Logan with two profiles: 1) small set: 64^3 volume resolution with 100 projections of size 64×91, and 2) large set: 128^3 volume resolution with 200 projections of

TABLE I
Performance (in seconds) on various hardware platforms

Hardware	Small	Large
CPU	7.95	125.79
Phi	1.22	13.36
GPU	0.71	6.43

3D Shepp Logan was used for testing with two data scales. Small profile dataset has 100 projections of size 64×91 with a 64^3 volume resolution, and the large profile has 200 projections of size 128×182 with a 128^3 volume resolution.

size 128×182. All computation stops when convergence is reached. As shown in Table 1, we tested the time performance on CPU, Phi and GPU for both data sets. Compared to CPU, the parallelism on Phi introduced speedup of 6.52 for small profile and 9.42 for large profile while on GPU the speedup is 11.20 for small profile and 19.56 for large profile. Therefore, when the data size is large enough, Phi brings speedup close to one order of magnitude, while GPU brings additional 2 times speedup.

B. *Programming difficulty and budget plan*

As mentioned in last section, Phi implementation added up only 10 lines of code, which is about additional 1.1% effort based on C implementation but gives a speedup of ~10 times faster. For GPU, the CUDA implementation has about 2100 lines of code, where useful original C code only takes up 34% of lines. In another words, the GPU implementation added up 200% new code to enable execution on GPU and gives a speedup of ~20 times faster.

To consider the cost in terms of money, a GPU K20X board costs $2000 as the best deal on market, while a Phi 31S1P board costs $200. Additional cooling devices may be required within $30. Therefore, the ratio of Phi is ~20 $/speedup, while the ratios of GPU is ~100 $/speedup.

We sum up all the related criteria in Fig. 2.

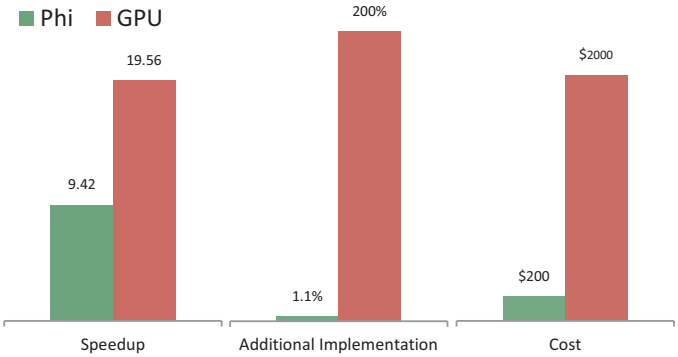

Fig. 2 Performance analysis between Phi and GPU: speedup, additional implementation (in %) and cost (in $).

IV. Conclusion

In this paper, we compared and evaluated as a case study of the HPC performance of a regularized penalty maximum likelihood reconstruction approach for PET on an Nvidia GPU and an Intel Xeon Phi coprocessor. We intended to choose the most intuitive acceleration implementations on Phi and GPU in order to provide a fair comparison about programming difficulty. As a result, we found out that Xeon Phi was almost costless to implement while CUDA implementation required additional twice the effort with an existing CPU implementation. Besides, although GPU version doubles the speedup than Phi, it costs about 10 times of Phi. This observation is also consistent with experiments in other domains.

For both platforms, there are strategies to further improve the performance. For GPU, the usage of texture memory with hardware interpolation, pitched memory write, and the usage of CUDA libraries and toolkits for example Thrust [15] to ease memory management and take advantage of existing hardware accelerated functions. For Phi, as aforementioned, the utilization of vector instruction set can bring additional improvement. As future work, we are summarizing the roadmap to gradually optimize a statistical iterative reconstruction (SIR) method for both GPU and Xeon Phi. We hope the adopted strategies can be generic for use in other SIR algorithms.

References

[1] P. J. Green, "Bayesian reconstructions from emission tomography data using a modified EM algorithm," IEEE Trans. Med. Imag., vol. 9, pp. 84–93, Mar. 1990.
[2] M. S. Bazaraa, H. D. Sherali, and C. M. Shetty, Nonlinear Programming: Theory and Algorithms, 2nd ed. New York:Wiley, 1993, pp. 283–287.
[3] A. R. De Pierro, "On the relation between the ISRA and the EM algorithm for positron emission tomography," IEEE Trans. Med. Imag., vol. 12, pp. 328–333, June 1993.
[4] A. R. De Pierro, "A modified expectation maximization algorithm for penalized likelihood estimation in emission tomography," IEEE Trans. Med. Imag., vol. 14, pp. 132–137, Mar. 1995.
[5] H. M. Hudson and R. S. Larkin, "Accelerated image reconstruction using ordered subsets of projection data," IEEE Trans. Med. Imag., vol. 13, pp. 601–609, Dec. 1994.
[6] S. Ahn and J. A. Fessler, "Globally convergent image reconstruction for emission tomography using relaxed ordered subsets algorithms," IEEE Trans. Med. Imag., vol. 22, pp. 613–626, May 2003.
[7] J-H Chang, J M.M. Anderson, and J. R. Votaw, "Regularized Image Reconstruction Algorithms for Positron Emission Tomography," IEEE Trans. Med. Imag., vol. 23(9), pp. 1165- 1175, Sept 2004.
[8] Gürsoy D, De Carlo F, Xiao X, and Jacobsen C. Tomopy: A framework for the analysis of synchrotron tomographic data. Journal of Synchrotron Radiation, 21(5):1188–1193, 2014.
[9] https://www.cilkplus.org/
[10] Matthias Baer and Marc Kachelrieß, "High Performance Parallel Beam and Perspective Cone–Beam Backprojection for CT Image Reconstruction on Pre–Production Intel Xeon Phi," In proc. Fully3D, pp. 233-236, 2013.
[11] "Tesla Kepler Family Product Overview". Nvidia datasheet. October 2013.
[12] http://ark.intel.com/products/79539/Intel-Xeon-Phi-Coprocessor-31S1P-8GB-1_100-GHz-57-core
[13] https://github.com/PeriLLC/tomopy_peri_0.1.
[14] http://tomopy.readthedocs.org/en/latest/index.html#
[15] N. Bell and J. Hoberock, "Thrust: A Productivity-Oriented Library for CUDA," in GPU Computing Gems, Jade Edition, W.-M. W. Hwu, Ed. Morgan-Kaufmann, 2011.

W. Xu (M'2015) received the B.S. and M.S. degree in Computer Science from Zhejiang University, Hangzhou, China in 2004 and 2006. She received the Ph.D. degree in Computer Science at Stony Brook University in 2012.

From 2013 to 2014, she was an Advanced Applications Engineer in Brookhaven National Laboratory. Since 2015, she has been an Assistant Scientist in Computational Science Initiative in Brookhaven National Laboratory and a visiting Research Assistant Professor in Computer Science Department of Stony Brook University. Her research interests include tomography, high performance computing, big data analysis, (information) visualization and visual analytics.

Dr. Xu was/is PI and Co-PI of a few Department of Energy (DOE) grants and has been reviewers or committee member for many top conferences and journals in the field of medical

imaging and visualization. In 2014, she was selected as a women@energy showcase representing female scientists of STEM fields.

D. Feng received the B.S and M.S. degree in Precision Instrument at Tsinghua University, Beijing, China in 1999 and 2001. He received the Ph.D. degree in Mechanical Engineer at Stony Brook University in 2014.

From 2001 to 2006, he was CTO and co-founder of two startup companies in China. Since 2006, he has been senior engineer and product manager of a startup company in U.S.A. In 2014, he co-founded Peri, LLC and becomes CTO since then. His cross-discipline research interests include parallel computing in image processing and visualization, high-speed machine vision, and Microelectromechanical systems design.

Dr. Feng has published over twelve conference papers. He has four U. S. patents pending. His company won Department of Energy (DOE) STTR Phase I grant in 2015. He is especially skilled at cutting-edge hardware and software development. In 2006 IEEEXtreme Programming Challenge organized by IEEE, the team he led ranked No.2 among 47 international college student teams.

Modeling Shift-Variant X-Ray Focal Spot Blur for High-Resolution Flat-Panel Cone-Beam CT

Steven Tilley II, Wojciech Zbijewski, Jeffrey H. Siewerdsen, J. Webster Stayman
Department of Biomedical Engineering, Johns Hopkins University, Baltimore, MD. Email: web.stayman@jhu.edu

***Abstract*—Flat-panel cone-beam CT (CBCT) has been applied clinically in a number of high-resolution applications. Increasing geometric magnification can potentially improve resolution, but also increases blur due to an extended x-ray focal-spot. We present a shift-variant focal-spot blur model and incorporate it into a model-based iterative-reconstruction algorithm. We apply this algorithm to simulation and CBCT test-bench data. In a trabecular bone simulation study, we find traditional reconstruction approaches without a blur model exhibit shift-variant resolution properties that depend greatly on the acquisition protocol (e.g. short vs. full scans) and the anode angles of the rays used to reconstruct a particular region. For physical CBCT experiments focal spot blur was characterized and a spatial resolution phantom was scanned and reconstructed. In both experiments image quality using the shift-variant model was significantly improved over approaches that modeled no blur or only a shift-invariant blur, suggesting a potential means to overcome traditional CBCT spatial resolution and system design limitations.**

I. Introduction

Flat-panel cone-beam CT (CBCT) is a promising modality for high-resolution applications, such as quantitative trabecular bone analysis in extremities imaging and microcalcification detection in mammography. Current application-specific imaging systems are often unable to resolve all trabeculae or microcalcifications, which can be on the order of 100μm. A high-magnification geometry has the potential to improve resolution, but projections suffer from increased blur due to the extended focal spot. Model-based iterative reconstruction (MBIR) methods have previously demonstrated improved image quality through the use of sophisticated system and noise models. Proper modeling of the x-ray focal spot, and incorporation of this model into a MBIR method, can mitigate the effects of focal spot blur in high-resolution high-magnification reconstructions.

Previously, we have developed a reconstruction method that models detector blur, focal spot blur, and spatial noise correlations using a staged approach (deblurring and other preprocessing followed by reconstruction).[1] Shift-invariant blur models were assumed in order to simplify deblurring. However, such assumptions are not valid at large fan angles, where the angulation of the anode results in a position-dependent apparent focal-spot shape. Moreover, this effect is more pronounced in high-magnification systems due to a larger focal-spot blur. Properly modeling shift-variant focal-spot blur is critical to generating high-resolution images in these systems. Previous work by La Rivière to model shift-variant focal-spot blur addressed deblurring data for multidetector CT systems with the anode-cathode axis of the x-ray source oriented axially.[2]

In this work, we characterize focal spot blur along the anode-cathode axis in a CBCT system where this axis is perpendicular to the axis of rotation (a common orientation in CBCT systems). We use a non-linear objective function that includes shift-variant blur in the forward model (e.g. no deblurring in preprocessing) to reconstruct high-resolution objects in simulation and test-bench studies.

This work was supported by NIH grants R21EB014964, R01EB018896, and an academic-industry partnership with Varian Medical Systems (Palo Alto, CA). The authors would also like to thank Matthew Jacobson for his assistance in developing the reconstruction algorithm.

II. Methods

A. Forward Model and Objective Function

We use the general forward model:

$$y \sim \mathcal{N}(\mathbf{B}\exp(-\mathbf{A}\mu), \mathbf{K}_Y) \tag{1}$$

with measurement vector, y, and object attenuation values, μ. The linear operator $\mathbf{B}$ contains focal spot blur and gain terms (e.g. photons per pixel), $\mathbf{A}$ is the forward projector, and $\mathbf{K}_Y$ is the measurement covariance matrix. The corresponding penalized-likelihood objective function is:

$$\hat{\mu} = \arg\min ||y - \mathbf{B}\exp(-\mathbf{A}\mu)||^2_{\mathbf{K}_Y^{-1}} + \beta R(\mu) \tag{2}$$

where R is a penalty function and β is the penalty strength.

Equation (2) was minimized using a separable paraboloid surrogates approach, similar to that of Erdoğan et al.[3], [4] but with an added separability step in the $\mathbf{B}\exp(-\mathbf{A}\mu)$ term. The resulting baseline algorithm is:

$a = \mathbf{B}^T\mathbf{K}_Y^{-1}\mathbf{B}1$, $\gamma = \mathbf{A}1$, $b = \mathbf{B}\mathbf{K}_Y^{-1}y$
for $n = 1 : N$ **do**
  $l^{(n)} = \mathbf{A}\mu^{(n)}$
  $d^{(n)} = -b - \mathbf{D}\{a\}\exp(-l^{(n)}) + \mathbf{B}^T\mathbf{K}_Y^{-1}\mathbf{B}\exp(-l^{(n)})$
  $h_j^{(n)}(l_j) \triangleq 0.5a_j\exp(-2l_j) + \exp(-l_j)d_j^{(n)}$
  $c_j^{(n)} =$ optimum curvature of $h_j^{(n)}$ from [3]
  $L^{(n)} = \mathbf{A}^T(-\mathbf{D}\{a\}\exp(-2l^{(n)}) - \mathbf{D}\{d_n\}\exp(-l^{(n)}))$
  $c_\mu^{(n)} = \mathbf{A}^T\mathbf{D}\{\gamma\}c^{(n)}$
  $\mu^{(n+1)} = \left[\mu^{(n)} + \frac{-L^{(n)} - \beta\nabla R|_{\mu^{(n)}}}{c_\mu^{(n)} + \beta\nabla^2 R|_{\mu^{(n)}}}\right]_+$
end for

We further extend the algorithm using Nesterov's acceleration method. All reconstructions used 20 ordered subsets.[4] The regularization gradient and curvature were computed using standard surrogate techniques.[4]

B. Shift-Variant Blur Model

We model the shift-variant focal spot blur along directions parallel to the detector. The model approximates a depth-independent blur. (See § IV for a discussion of depth-dependent effects.) Therefore, the blur model can be included in the $\mathbf{B}$ term in (1). To estimate a continuous source-blur model for discrete inputs and outputs, we use nearest neighbor interpolation to create a continous approximation of the input image, apply a convolution operation, then discretize the signal using a rectangular kernel with the dimensions of a pixel and sampling at pixel centers. The full operation is:

$$g[k,l] = \int_{x,y}\int_{\xi,\eta}\sum_{i,j} f[i,j]\,\mathrm{rect}(\frac{\xi - iT_x}{T_x}, \frac{\eta - jT_y}{T_y})T_xT_y$$
$$h(x,y;\xi,\eta)\,\mathrm{rect}(\frac{x - lT_x}{T_x}, \frac{y - kT_y}{T_y})\,d\xi\,d\eta\,dx\,dy \tag{3}$$

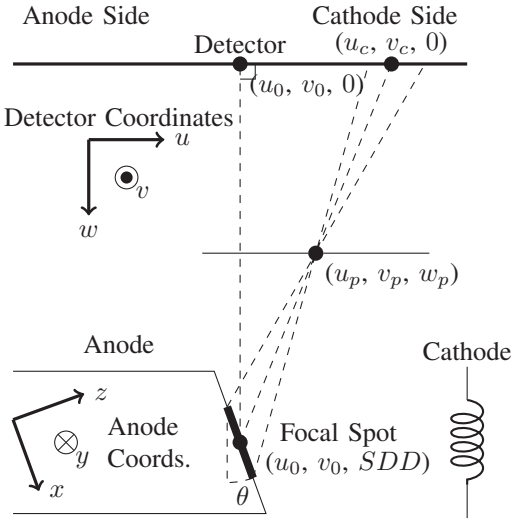

Fig. 1. Geometry used to calculate the focal spot blur impulse response. The focal spot is represented by the bold line on the side of the anode. All coordinates are in detector coordinates. The origin of the anode coordinate system is at (u_0, v_0, SDD).

where f and g are the input and output images, T_x and T_y are the pixel widths along the corresponding directions and $h(\cdot, \cdot; \xi, \eta)$ is the impulse response of a point source at ξ, η. Equation (3) can be approximated by discretizing variables and assuming h is constant over small displacements. We sample x and ξ at intervals of T_x/s and y and η at intervals of T_y/s, where s is an odd integer. Applying these approximations and simplifying leads to:

$$g[k,l] \approx \sum_{j,i,a,b} f[i,j]|1-a||1-b| \; h\left((a+l)T_x, (b+k)T_y; iT_x, jT_y\right) T_x T_y / s^2 \quad (4)$$

where a and b range from $-(s-1)/s$ to $(s-1)/s$ in increments of $1/s$. The transpose operation (e.g. for $\mathbf{B}^T$) requires switching the indices for f and g, and summing over k, l instead of i, j.

The impulse response (h) centered at a given point (u_c, v_c) is assumed to be a binary function, with values either equal to 0 or $k = \text{area}(h(\cdot, \cdot; u_c, v_c))^{-1}$. To determine the value of $h(u, v; u_c, v_c)$, the point (u, v) is backprojected through a pinhole onto the anode. A two dimensional cross section of the geometry is illustrated in Figure 1. The pinhole is placed a distance w_p from the detector and along the line connecting (u_c, v_c) with the center of the focal spot. If the backprojected point is in the rectangular focal spot, $h(u, v; u_c, v_c) = k$, otherwise $h(u, v; u_c, v_c) = 0$. The area of h was found by forward projecting the corners of the focal spot through the pinhole, and applying Bretschneider's formula to the resulting points.[5]

C. Simulation Study

Data were generated from the digital extremities phantom in Figure 2. Line integrals were generated from a high-resolution truth image (3300×2300 image of 30μm voxels) projected onto a one-dimensional detector with 8192 pixels and a 48.5μm pixel pitch. A high-magnification geometry was used, with a source-detector distance of 1200mm, a source-axis distance of 250mm, and an angular spacing of 0.5°. These line integrals were downsampled by a factor of 4 to give a pixel pitch of 194μm. Measurements were generated from the downsampled line integrals (l) according to:

$$y_{\text{noiseless}} = \mathbf{B}_s I_0 \exp(-l) \quad (5)$$

$$y = y_{\text{noiseless}} + \mathcal{N}(0, \mathbf{D}\{y_{\text{noiseless}}\}) + \mathcal{N}(0, \mathbf{D}\{\sigma_{ro}^2\}) \quad (6)$$

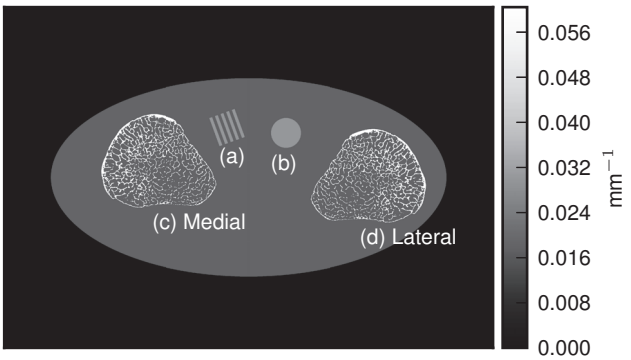

Fig. 2. Digital extremeties phantom with medial (c) and lateral (d) bones, line pairs (a), and a uniform disc (b).

where I_0 is 10^4 photons per pixel, $\mathbf{B}_s$ is the focal spot blur operator (we assume there is no detector blur), and the readout-noise standard deviation (σ_{ro}) is 3.32 photons. The focal spot was modeled as a 5mm×0.8mm rectangle on a 14° anode with the anode-cathode axis parallel to the detector row. The sampling factor (s) was equal to 41. (Note that $\mathbf{B}_s I_0$ is equivalent to $\mathbf{B}$ in (1).) Data were generated using two short scans (short-1 and short-2) spaced 180 degrees apart, and a full scan. The short-1 scan placed the medial bone (Figure 2c) predominately on the anode side, and the lateral bone (2d) predominately on the cathode side. The reverse is true for the short-2 scan.

Data from each scan were reconstructed using the algorithm presented above with three models for focal-spot blur: identity (no blur), shift-invariant blur, and shift-variant blur. The sampling factor (s) used in reconstructions was 11. Data were reconstructed into a 1650×1150 volume of 60μm voxels using a Huber penalty ($\delta = 10^{-4}$). The covariance matrix was modeled as $\mathbf{D}\{y + \sigma_{ro}^2\}$.

The accuracy of trabeculae segmentation in the medial and lateral bones was used as a measure of image quality. The truth segmentation for each bone was found by downsampling the high-resolution phantom to match the reconstruction volume dimensions and thresholding at the average attenuation of bone and fat. Data were reconstructed at several penalty strengths and thresholded at regularly spaced values between the attenuation values of fat and bone. Accuracy was quantified as the mutual overlap between the thresholded truth, t, and the thresholded reconstruction, r:[6]

$$\text{mutual overlap}(t, r) = 2(\sum tr)(\sum (t + r))^{-1} \quad (7)$$

D. Bench Characterization

To apply the approach to physical data, we characterized the focal spot blur on a CBCT test bench consisting of a Rad-94 x-ray tube (Varian, Salt Lake City UT), a PaxScan 4343CB flat-panel detector (Varian, Palo Alto CA), and a SDD of 108 cm. In this work we focus on two-dimensional reconstructions, and therefore only measure one dimensional MTFs along the u axis. MTFs were measured using a tungsten edge[1][7] placed at isocenter (40cm from the source) and translated in the $\pm u$ directions. The detector MTF was measured by placing the edge at the detector. We assume the detector MTF is shift-invariant and fit it to the following model:[8]

$$|MTF_d(f_u)| = \left| \frac{\text{sinc}(f_u T_x)}{1 + H f_u^2} \right| \quad (8)$$

where f_u is the spatial frequency in mm^{-1} and H is a blur parameter. The focal spot MTF at each position u_p was modeled as a rect function with an apparent length $L(u_p)$,

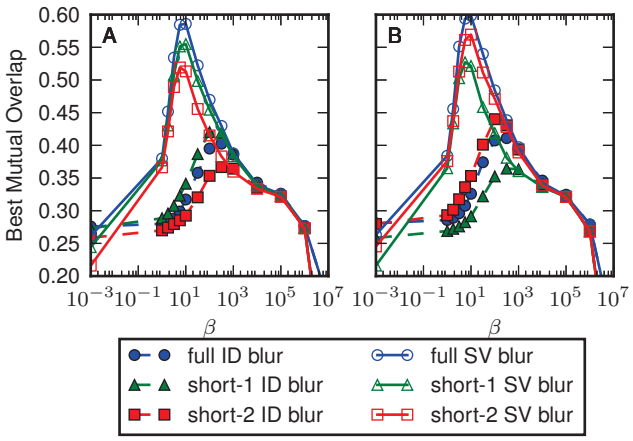

Fig. 3. Best mutual overlap versus β. A) Medial and B) Lateral bone.

resulting in the combined MTF:

$$|MTF_{sd}|(f_u; u_p) = |\text{sinc}(f_u L(u_p)) MTF_d(f_u)| \quad (9)$$

Theoretical apparent blur lengths from anode angle (θ) and focal spot length (L) were fit to the measured lengths to yield estimates for θ and L.

E. Resolution Phantom Study

A cylindrical resolution phantom (CatPhan CTP528 High Resolution Module, Phantom Laboratory, Salem, NY) with variable frequency line pairs was scanned on the CBCT test bench. The source-detector and source-axis distances were 108 cm and 40 cm respectively. A full scan of 720 projections was collected at 80 kVp and 0.504 mAs per projection. Data were reconstructed using the identity and shift-variant blur models, as well as three shift-invariant blur models. The three shift-invariant blurs modeled were the blur at the center of the detector (as in the simulation study) and the blur at either edge of the detector. The presented MBIR algorithm was used with 800 iterations to ensure a nearly converged solution. The reconstruction volume was 170mm×170mm with 100μm voxels. The blur model used the focal spot length and anode angle from § II-D and a subset parameter (s) of 5. We assume that detector blur is negligible and do not model it in the reconstruction algorithm.

III. Results

A. Simulation Study

The best mutual overlap values (over all threshold values) for each (β) are shown in Figure 3. Results are shown for reconstructions with an identity (ID) blur model and the shift-variant (SV) blur model. Each line represents a blur model and scan type combination, and each point represents a reconstruction. A higher best mutual overlap indicates that a segmentation based on that reconstruction is closer to the truth segmentation, and the reconstruction is therefore more accurate. All methods that used the SV model were more accurate than those that used the ID model, which is evident by comparing the maximum of each line. With the ID model, the best quality segmentation of the medial bone is achieved with data from the short-1 scan, which placed the medial bone projections primarily on the high-resolution (anode) side of the detector. The lowest quality was the short-2 scan, which placed the projections primarily on the low-resolution (cathode) side. The full scan reconstructions with the ID model rank between the reconstructions from the two short scans. Neglecting to model blur is equivalent to assuming that classically redundant projections in the full scan (i.e. those with the same integration path but reversed direction) contain the same information, despite the fact that they are subject to different degrees of blurring, which results in a reconstruction whose image quality is a compromise between that of the two short scan reconstructions. Predictably, the lateral bone reconstructions are best when using the short-2 scan and worst when using the short-1 scan, in which the lateral bone projection data was on the high- and low-resolution sides of the detector, respectively.

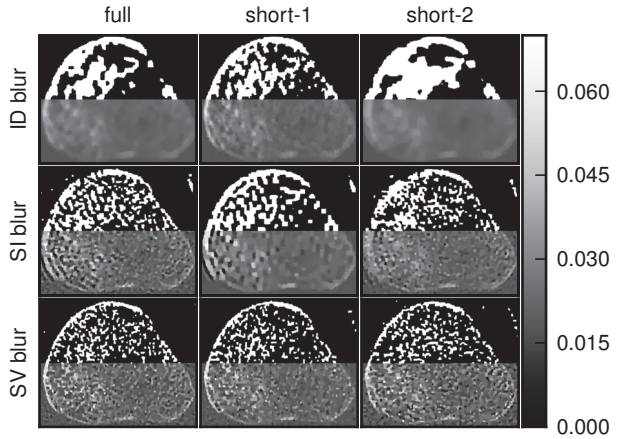

Fig. 4. Reconstructions of the medial bone with the highest mutual overlap over all thresholds and β's. The top half of each reconstruction is thresholded.

When using the SV model, the full scan provides the best reconstruction of both bones, followed by the short-1 scan and then the short-2 scan in the case of the medial bone, and the short-2 scan and then the short-1 scan for the lateral bone. The better image quality of the full scan images over the corresponding high-resolution short-scan reconstructions can be attributed to the additional (low-resolution) data. The SV model can use this additional information to improve the reconstruction without losing details provided by the high-resolution data. In effect, rather than averaging the redundant data, the low-frequency data is used to reduce noise while the high-frequency data maintains spatial resolution. The corresponding low-resolution scan for each bone (short-2 for the medial bone and short-1 for the lateral bone) results in the lowest quality reconstructions due to the increased difficulty in deblurring the data.

Figure 4 shows the medial-bone reconstructions (bottom of each image) and segmentations (top of each image) corresponding to the best possible mutual overlap (optimal threshold and β values) with each scan type and blur model combination. All SV reconstructions depict more trabecular structure than the shift-invariant (SI) or ID models. The difference in image quality among ID reconstructions is readily apparent in these images, with the short-1 scan resulting in the most trabecular detail. Finally, the SI images depict more detail than the ID model but less detail than the SV reconstructions. However, the SI model results in a ringing artifact, particularly evident on the lower left aspect of the medial bone in the full scan reconstruction. This is likely due to blur/model mismatch (the SI model is accurate at the center of the detector but less accurate at the edges).

B. Focal Spot Measurement

The detector MTF and the combined focal-spot and detector MTFs at different positions are shown in Figure 5. The magnification in this system was about 2.7, so that the focal-spot blur dominates over the detector blur. Each combined focal-spot and detector MTF is labeled by the distance of

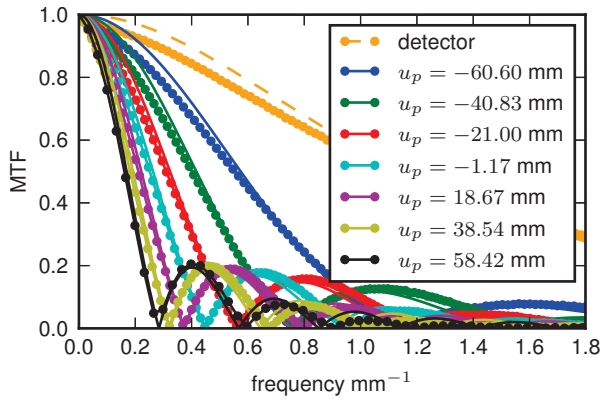

Fig. 5. MTFs and fits for the detector and the detector+source blur at different displacements from the center of rotation.

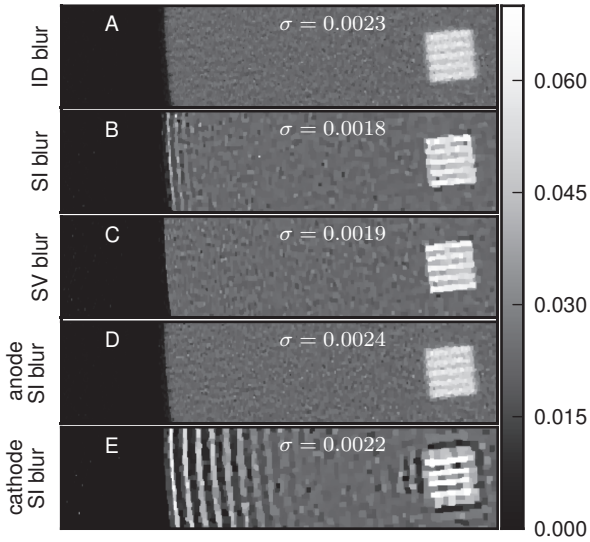

Fig. 6. Physical CBCT reconstructions. Each subfigure shows a portion of the phantom from the edge to one of the line pairs. Each reconstruction has approximately the same noise level (indicated in each subplot in units of mm^{-1} and denoted by σ).

the tungsten edge from the central ray. At positive positions, the edge is on the cathode side, and at negative positions the edge is on the anode side. There is a dramatic difference in MTFs at different positions due to the angulation of the anode. Fits for each MTF are also shown. These fits give the apparent length of the focal spot at each position, which was used to estimate the actual length of the focal spot and the angle of the anode. The focal spot length was found to be 5.23mm and the anode angle was 14.3°.

C. Bench Study

Figure 6 shows the same region-of-interest of five reconstructions, each of which used a different blur model. The three SI blur models are the apparent focal spot size at the center, anode side, and cathode side of the detector. The reconstructions have approximately the same amount of noise (estimated by computing standard deviation in a flat region at the center of the phantom). The line pairs in the SV (6c) and center SI (6b) reconstructions are much sharper than those in the ID reconstruction (6a). That the SI reconstruction line-pairs are roughly as sharp as those of the SV reconstruction suggests that at this distance from isocenter (approximately 4.75cm) the SI approximation is fairly accurate. However, at the edge of the phantom (approximately 7.5cm from isocenter), this assumption breaks down, and the resulting mismatch between the model and the actual blur results in a "ringing" artifact. The anode-side SI blur model (6d) underestimates the blur over most of the detector, reducing ringing compared to the center SI blur model but also reducing the sharpness of the line pairs. The cathode-side SI blur model (6e) overestimates the blur over much of the detector, increasing the ringing artifact.

IV. Discussion

The image quality difference in identity blur model reconstructions from the two different short scans illustrates the importance of considering shift-variance in high-resolution, high-magnification systems. The poor image quality and/or ringing artifact in the reconstructions with a shift-invariant blur model demonstrate that this model is a poor approximation for large objects (relative to the field of view), and that a full shift-variant model is more appropriate. These results also suggest a means to improve local resolution properties when advanced blur models are not available: if the location of a high resolution target in the object is known *a priori,* then that object can be placed such that the high resolution target favors the anode side of the detector during a short scan.

This work suggests x-ray tube orientation is an important factor in system design. Blur shift-variance, and therefore reconstruction resolution, will depend on whether the anode-cathode axis is oriented parallel or perpendicular to the axis of rotation. Models such as the one presented may alter the trade-off associated with tube orientation, allowing for more flexibility in system design. Future studies will analyze three-dimensional reconstructions in order to properly characterize resolution/image quality both in-plane and axially. While we have demonstrated the utility of a depth-independent source blur model, future work will consider depth-dependent source blur effects. In the presented bench study, we estimate that apparent focal spot size approximately doubled over the length of the object along the source-detector direction. By comparison, the measured apparent focal-spot lengths approximately quadrupled over the length the object along the direction parallel to the detector. Thus, depth-dependent shift-variance is a large effect, but not as large as shift-variance due to anode angulation.

We have provided a method to improve image quality with an advanced shift-variant blur model, and used this model to reconstruct high-resolution trabecular details in a simulation study and fine line-pair patterns on a CBCT test bench. This technique could help overcome spatial resolution limits in high-magnification systems, improving current systems and allowing new systems to be designed with higher magnifications for high-resolution applications.

References

[1] S. Tilley II *et al.*, "Model-based iterative reconstruction for flat-panel cone-beam CT with focal spot blur, detector blur, and correlated noise," *Physics in Medicine and Biology*, vol. 61, no. 1, 2016.

[2] P. J. La Rivière *et al.*, "Correction for resolution nonuniformities caused by anode angulation in computed tomography," *IEEE transactions on medical imaging*, vol. 27, no. 9, 2008.

[3] H. Erdoğan *et al.*, "Monotonic algorithms for transmission tomography." *IEEE transactions on medical imaging*, vol. 18, no. 9, Sep. 1999.

[4] ——, "Ordered subsets algorithms for transmission tomography," *Physics in medicine and biology*, vol. 2835, 1999.

[5] E. W. Weisstein, "Bretschneider's Formula," http://mathworld.wolfram.com/BretschneidersFormula.html.

[6] M. Sonka *et al.*, "Chapter 6: Segmentation 1," in *ISE Image Processing, Analysis and Machine Vision*, student ed edition ed. Nelson Engineering, Apr. 2007.

[7] E. Samei *et al.*, "A method for measuring the presampled MTF of digital radiographic systems using an edge test device," *Medical Physics*, vol. 25, no. 1, 1998.

[8] J. H. Siewerdsen *et al.*, "Signal, noise power spectrum, and detective quantum efficiency of indirect-detection flat-panel imagers for diagnostic radiology," *Medical Physics*, vol. 25, no. 5, May 1998.

Lossy Compression of Projection Data from Photon Counting Detectors

Picha Shunhavanich and Norbert J. Pelc

***Abstract*—**

Photon counting x-ray detectors (PCXDs) are being considered for adoption in clinical settings due to their advantages of improved tissue characterization, reduced noise, and lower dose. The benefit of having multiple energy bins data in turn put a burden on the bandwidth of slip ring and data storage subsystems, through which the projection data samples must be transmitted in real-time. The problem is further amplified with PCXDs' increased number of detector channels. This leads to a bandwidth bottleneck problem. In this work, we propose a lossy compression method for raw CT projection data from PCXDs, which includes a step of quantizing prediction residuals prior to encoding. From our modeled prediction error distribution, the quantization level is chosen such that the percentage of variance due to quantization error vs quantum noise variance is equals to 1 or 2 %. Huffman code and Golomb encoder are applied. Using three simulated phantoms, compression ratio of 3.1:1 with 1.15% RMSE to std. of quantum noise and compression ratio of 3.4:1 with 2.85% RMSE to std. of quantum noise are achieved for the 1 and 2 percent quantization error variance, respectively. From the initial simulation results, the proposed algorithm shows good control over compression and image quality of reconstructed image.

***Index Terms*—CT raw projection data, lossy compression, photon counting detector.**

I. Introduction

CT projection data are acquired in the rotating gantry of CT systems and must be transferred through the slip ring in real-time. They are also commonly stored in redundant arrays of independent disks (RAID) prior to image reconstruction [1]. With photon counting x-ray detectors (PCXDs), the bottleneck problem in bandwidth of the slip ring and RAIDs is certain to result since the amount of projection data is multiplied by the number of energy bins obtained. In addition, PCXDs tend to have more and smaller detector channels so as to increase the count rate, which stresses the problem even further. Therefore, compression of the projection data samples prior to data transmission through slip ring is of interest. Compression of raw projection data from conventional CT detectors was reported [2-5]. We have previously investigated lossless compression for PCXD data, incorporating the redundancies available in the multiple energy bins [6], and found that the achieved compression ratio is limited by the quantum noise in the data. In this paper, we propose a lossy compression for PCXD data that obtains compression beyond this restriction.

Unlike lossless compression, lossy compression allows the decompressed data to not be exactly the same as the original data. Nevertheless, lossy compression in medical imaging can maintain diagnostic accuracy [7, 8].

Our compression method is divided into two parts: prediction (estimating the data value) and encoding (reducing the bit representation of the prediction residual before data transfer). This paper focuses on the encoding part, which has an extra step to quantize the prediction error prior to encoding.

II. Prediction

The detail of our prediction can be found in our previous work [6]. Its summary is as follows.

Our prediction of x_i, a projection data sample in energy bin i, is the weighted average of the values that are physically close to it: the projection data samples in the adjacent view and detector cells (a, b, c, and d), and an approximation of x_i calculated from other energy bins ($\tilde{x}_i$).

$$x_{i,predict} = w_i^{(1)}a + w_i^{(2)}b + w_i^{(3)}c + w_i^{(4)}d + w_i^{(5)}\tilde{x}_i \quad (1)$$

where $x_{i,predict}$ is the prediction of x_i and $w_i^{(j)}$'s are the weights for energy bin i.

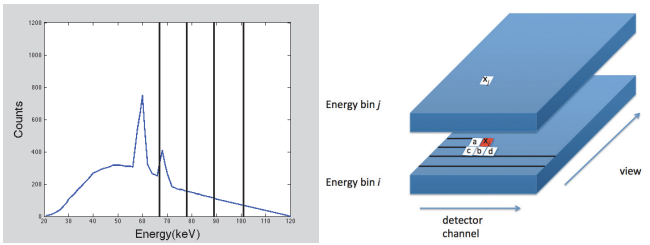

Fig. 1. The x-ray spectrum and partitioning for 5 energy bins indicated by vertical bars (left) and the schematic diagram for projection data samples (right).

$\tilde{x}_i$ is calculated by assuming object composed of two basis materials, water and calcium, with thicknesses computed from the projection data in energy bin 1 and 3.

$$\begin{bmatrix} d^{water} \\ d^{Ca} \end{bmatrix} = \begin{bmatrix} \mu_{eff,1}^{water} & \mu_{eff,1}^{Ca} \\ \mu_{eff,3}^{water} & \mu_{eff,3}^{Ca} \end{bmatrix}^{-1} \begin{bmatrix} log\left(\frac{I_{o,1}}{x_1}\right) \\ log\left(\frac{I_{o,3}}{x_3}\right) \end{bmatrix} \quad (2)$$

$$\tilde{x}_i = I_{o,i}e^{-\mu_{eff,i}^{water}d^{water}-\mu_{eff,i}^{Ca}d^{Ca}}$$

This work was supported in part by the National Institutes of Health under Grant R21EB01557401 and U01EB017140 and in part by Anandamahidol Foundation.

P. Shunhavanich is with Bioengineering and Radiology Departments, Stanford University, Stanford, CA 94305 USA (email: picha@stanford.edu)

N. J. Pelc is with Bioengineering and Radiology Departments, Stanford University, Stanford, CA 94305 USA (email: pelc@stanford.edu)

where d^{water} and d^{Ca} are the water and Ca thicknesses. $\mu_{eff,i}^{water}$ and $\mu_{eff,i}^{Ca}$ are the effective attenuation coefficients of the two basis materials in energy bin i, and $I_{0,i}$ is incident intensity of energy bin i.

The optimal weights for (1) are assumed to be about the same for all objects and are computed from a least squares fit to data in a training CT projection data database. These weights are thus fixed and known prior to the scan and can be different in different parts of the sinogram. We applied our proposed three-component context in this analysis.

III. Quantization

A. Uniform Quantization

A uniform quantization is applied to the prediction error (or residual) to reduce the number of possible values to a smaller set. The range of prediction errors is divided into n inner intervals of the same length L, resulting in quantization boundaries $(-(n/2)L, \cdots, -2L, -L, 0, L, 2L, \cdots, (n/2)L)$ if n is even and $(-(n/2)L, \cdots, -3L/2, -L/2, L/2, 3L/2, \cdots, (n/2)L)$ if n is odd. A quantized value is the midpoint of the interval that a residual occupies, except for when the residual falls outside of the outer boundaries $-(n/2)L$ or $(n/2)L$, in which it is quantized to $-(n/2)L + L/2$ or $(n/2)L - L/2$, respectively.

The number of quantization levels is chosen to be suitable for each sinogram pixel location depending on the level of quantum noise. In other words, we would allow more quantization error (difference between the actual and quantized values) if the quantum noise of that sample is large. We also limit the probability of quantization error due to each outer quantization interval to 0.01% by setting the outer boundary accordingly. In particular, the quantization level is selected such that

$$\frac{Var(Q)}{Var(X)} = c\,\% \qquad (3)$$

$$\Pr\left(R \le -\frac{n}{2}L\right) = \Pr\left(R \ge \frac{n}{2}L\right) = 0.01\%$$

$$L \ge 2$$

where Q is a quantization error, X is a detected number of photons, R is a prediction residual, and c is a constant (e.g. 1 or 2).

If the above conditions cannot be satisfied, the residual will not be quantized (i.e., full accuracy is retained).

Since the accuracy of context determination is important, the projection data inside patient area of energy bin 5 is transmitted without quantization, and we use energy bin 5 to calculate the context for all energy bins. Moreover, pixels along object boundary with high signal variation could have large quantization errors, causing the build-up of errors in subsequent pixels. Thus, the projection samples at 4 detector channels along phantom boundary are not quantized in this analysis.

B. Model of Prediction Error

The distribution of prediction error is assumed to be Gaussian with zero mean and standard deviation that is a linear function of standard deviation of the quantum noise. The coefficients of this linear function are specific to each context and are pre-computed from a least-square fit of standard deviation of prediction residual to standard deviation of quantum noise in training CT data in database.

The standard deviation of quantum noise is obtained from the square root of the average values of projection data samples near the coordinate of the projection data sample in consideration, x_i (e.g. 10 x 11 samples indicated in the yellow region of Fig. 2).

In the quantization process of a projection data sample, the compressor first acquires the standard deviation of quantum noise. Then, the standard deviation of prediction residual is calculated, and the modeled probability distribution of prediction error at that projection sample is obtained. This distribution is subsequently used to determine the quantization boundaries. Finally, the prediction error is quantized with the computed quantization boundaries.

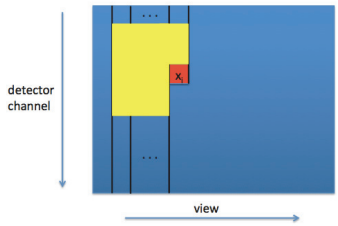

Fig. 2. The schematic diagrom of projection data indicating samples included in averaging to find variance of quantum noise in yellow

IV. Encoder

The following encoders were used to encode the prediction errors. If constraint (3) holds, Huffman coding is applied to the quantized prediction error. If not, Golomb code is employed for the non-quantized prediction error.

A. Huffman code

Huffman code is a type of optimal prefix code. It represents values that occur more frequently with fewer bits, thus reducing the average number of bits needed. In our case, the Huffman table is calculated from the distribution of quantized residuals from our model, which is also known at the decompressor side and does not need to be transmitted.

B. Golomb code

It is commonly accepted that the residuals from a deterministic predictor in continuous-tone images follow a zero-centered two-sided geometric distribution [9]. Since Golomb codes are optimal for one-sided geometric distributions of nonnegative integers [10], we map our prediction residuals to nonnegative integers and encode them with a Golomb coder. The encoding process is done by dividing a nonnegative integer y into an upper part (⌊y/k⌋) and lower part (y mod k), where k is a positive integer parameter. The transmitted data is the upper and lower parts in unary and binary representations, respectively. In our implementation, the parameter k is context-dependent and is adaptively updated.

V. Evaluation Methods

In this work, we assume simple fan-beam geometry, resulting in a 2D projection data for each energy bin. The x-ray spectrum and partitioning of energy bins are displayed in Fig. 1 (left).

The projection data used in the performance evaluation of our proposed lossy compression was obtained by analytical forward projection of three simulated phantoms: a cylindrical low contrast water phantom (with inserts of either dilute iodine, dilute calcium carbonate, dense water, or adipose), a cylindrical water phantom with 8 inserts of bone with different density, and a head phantom [11].

The projection data is lossy compressed, and the image is reconstructed from the decompressed projection data. This image is then compared to the image reconstructed with the original projection data.

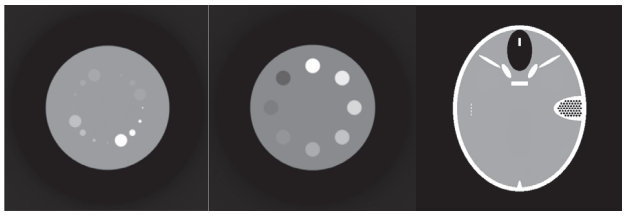

Fig. 3. The tested simulated phantoms: a cylindrical low contrast water phantom with insert of different materials (left), a cylindrical water phantom with 8 inserts of bone with different density (middle), and a head phantom (right) [11].

VI. Results

The error images, or the differences between the reconstructed images from lossy and original projections are shown in Fig. 4 and 5. Streaks are observed in regions with larger quantization errors, which tend to result from larger prediction errors (e.g. in areas with higher projection sample value variation). The uniform region seen in the error images is the zero-error region where prediction residuals are not quantized due to low detected counts in the center area of phantoms (the proposed quantization constraint is not met). The relatively higher errors at the boundary of the uniform zero-error region are caused by larger quantization errors in some transitions between non-quantized and quantized sinogram pixels.

Compared to percent quantization error variance c=1%, c=2% gives worse image quality with more streaks and 2.03 HU higher average root mean squared error (RMSE) due to quantization, but achieve 0.27:1 increase in average compression ratio. Nevertheless, both cases significantly improve the compression ratio (3.15:1 and 3.42:1) from a typical 2:1 lossless compression ratio, while degrading the reconstructed image quality with relatively low ratio of RMSE to the standard deviation of quantum noise (1.15% and 2.85%). This ratio shows that even though the error could be quite high, it comes from the fact that the quantum noise variance is high as well. The average RMSE is 1.32 HU for c=1% and 3.35 HU for c=2%. While the former has -7 HU minimum error and 7 HU maximum error, the latter has -16 HU mimum error and 18 HU maximum error.

With this initial results, the value of percent quantization error variance c between 1 and 2% could be preferred, considering the trade-off between compression ratio and quantization error.

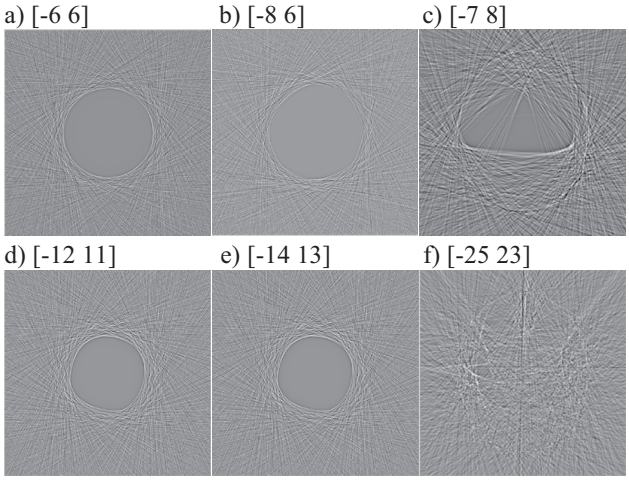

Fig. 4. Difference image between the reconstructed images from lossy and original projection data for energy bin 1 when percent quantization error variance c=1% (top row) and 2% (bottom row). The result of low-contrast (left), 8-insert (middle), and head phantoms (right) are displayed with minimum and maximum values as indicated in HU in the square bracket.

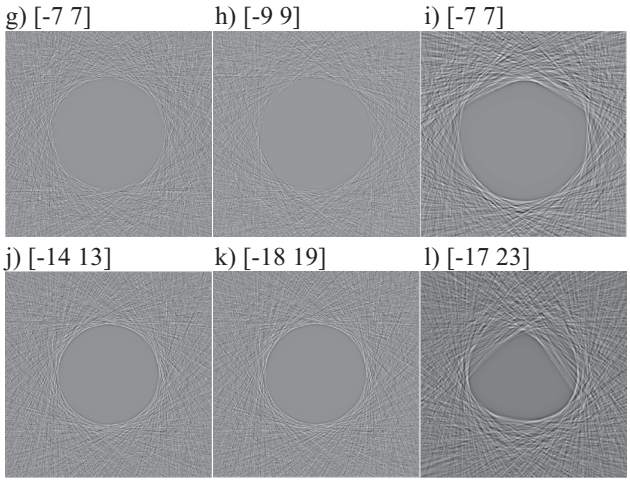

Fig. 5. Difference image between the reconstructed images from lossy and original projection data for energy bin 4 when percent quantization error variance c=1% (top row) and 2% (bottom row). The result of low-contrast (left), 8-insert (middle), and head phantoms (right) are displayed with minimum and maximum values as indicated in HU in the square bracket.

TABLE I
Performance Comparison

Phantom		c=1%[a]	c=2%[a]
Low-contrast	Compression ratio[b]	3.22	3.48
	RMSE[c] (HU)	1.22	3.00
	Mimimum error (HU)	-6	-13
	Maximum error (HU)	6	13
	Ratio of RMSE to Std. of quantum noise[d]	1.02%	2.38%
8-insert	Compression ratio[b]	3.27	3.53
	RMSE[c] (HU)	1.34	3.24
	Mimimum error (HU)	-8	-17
	Maximum error (HU)	8	16

	Ratio of RMSE to Std. of quantum noise[d]	0.62%	1.39%
Head	Compression ratio[b]	2.96	3.26
	RMSE[c] (HU)	1.39	3.81
	Mimimum error (HU)	-7	-19
	Maximum error (HU)	8	24
	Ratio of RMSE to Std. of quantum noise[d]	1.80%	4.78%
Average	Compression ratio[b]	3.15	3.42
	RMSE[c] (HU)	1.32	3.35
	Mimimum error (HU)	-7	-16
	Maximum error (HU)	7	18
	Ratio of RMSE to Std. of quantum noise[d]	1.15%	2.85%

[a]c is a parameter in quantization level constraint (3), the percent variance of quantization error to quantum noise variance.

[b]The number of bits of maximum data samples, 14 bits, was used in computing the compression ratio, while the number of bits representing an uncompressed projection data is assumed to be 15.

[c]The root mean square error (RMSE) due to quantization, or the standard deviation in the error image, is calculated from the region inside phantom boundary of the difference between reconstructed images from lossy and original projection data. The calculated standard deviation is averaged over energy bin 1 to 4 (since data in object boundary of energy bin 5 is not quantized) and shown in HU.

[d]The ratio of RMSE due to quantization (or standard deviation in error image) to standard deviation of quantum noise is averaged over energy bin 1 to 4 since data in object boundary of energy bin 5 is not quantized.

VII. Conclusions

From the simulation results, the proposed lossy compression shows an improvement in reducing number of bits needed to represent the projection data from PCXDs. Unlike lossless compression, the achieved compression ratio is not limited by quantum noise variance. However, a careful evaluation of lost information in reconstructed image is needed to ensure the diagnostic quality of the data.

References

[1] A. W. Wegener and Y. Ling, "Adaptive compression of computed tomography projection data," Dec. 14 2010, US Patent 7,852,977.

[2] A. Wegener, N. Chandra, Y. Ling, R. Senzig, and R. Herfkens, "Real-time compression of raw computed tomography data: technology, architecture, and benefits," in *SPIE Medical Imaging*. International Society for Optics and Photonics, 2009, pp. 72 582H–72 582H.

[3] K. T. Bae and B. R. Whiting, "CT data storage reduction by means of compressing projection data instead of images: Feasibility study 1," *Radiology*, vol. 219, no. 3, pp. 850–855, 2001.

[4] K. T. Bae and B. R. Whiting, "Method and apparatus for compressing computed tomography raw projection data," Feb. 5 2008, US Patent 7,327,866.

[5] S. S. Young, B. R. Whiting, and D. H. Foos, "Statisically lossless image compression for CR and DR," in *Medical Imaging'99*. International Society for Optics and Photonics, 1999, pp. 406–419.

[6] P. Shunhavanich and N. J. Pelc, "Lossless Compression of Projection Data from Photon Counting Detectors," in *SPIE Medical Imaging*. International Society for Optics and Photonics, 2016.

[7] D. A. Koff and H. Shulman, "An overview of digital compression of medical images: Can we use lossy image compression in radiology?" *Canadian Association of Radiologists Journal*, vol. 57, no. 4, pp. 211–7, 10 2006.

[8] D. Koff, P. Bak, P. Brownrigg, D. Hosseinzadeh, A. Khademi, A. Kiss, L. Lepanto, T. Michalak, H. Shulman, and A. Volkening, "Pan-canadian evaluation of irreversible compression ratios (lossy compression) for development of national guidelines," *Journal of digital imaging*, vol. 22, no. 6, pp. 569–578, 2009.

[9] A. N. Netravali and J. O. Limb, "Picture coding: A review," *Proceedings of the IEEE*, vol. 68, no. 3, pp. 366–406, 1980.

[10] R. G. Gallager and D. C. Van Voorhis, "Optimal source codes for geometrically distributed integer alphabets (corresp.)," *Information Theory, IEEE Transactions on*, vol. 21, no. 2, pp. 228–230, 1975.

[11] Z. Yu, F. Noo, F. Dennerlein, A. Wunderlich, G. Lauritsch, and J. Hornegger, "Simulation tools for two-dimensional experiments in x-ray computed tomography using the FORBILD head phantom," *Physics in medicine and biology*, vol. 57, no. 13, p. N237, 2012.

Simultaneous Gain Parameter Estimation in Model-Based Cone-Beam CT Image Reconstruction

Zhiqian Chang, Ken Sauer
Department of Electrical Engineering
University of Notre Dame
Notre Dame, IN 46556
Email: zchang1@nd.edu, sauer@nd.edu

Debashish Pal, Somesh Srivastava and Jean-Baptiste Thibault
GE Healthcare
Waukesha, WI 53188
Email: Debashish.Pal@ge.com

Charles Bouman
School of Electrical and Computer Engineering, Purdue University
West Lafayette, IN 47907
Email: bouman@purdue.edu

***Abstract*—Model-based, iterative image estimation methods demand accurate modeling of instruments. Inaccuracies in measurements, particularly when correlated in space and/or time, result in reduced diagnostic quality due to local biases in reconstructions. We present a method of estimating gain parameters in X-ray CT systems simultaneously with reconstruction of 3D imagery. It is applied in this paper to cone-beam data, compensating for unmodeled biases in detectors at edges of modules.**

I. Introduction

Model-based methods of reconstruction have proven an important tool for improving image quality in X-ray CT systems [1], [2], [3]. Iterative solution of associated optimization problems, however, may be more sensitive to errors in models than conventional, single-pass, backprojection techniques. Previously, we have corrected for partial blockage of reference-normalization sensors [4] by estimating a relatively small number of detector gain parameters simultaneously with reconstruction. Each of these parameters scales photon count data at detectors and becomes an additive factor in a detector row after transformation by the $\log()$ operator. Modeling of this "DC" offset in projection data allows compensation for inconsistent photon count scaling among various projection angles and removal of low-frequency shading in iterative estimates. Somewhat similarly, parameters in polynomial beam-hardening correction may be estimated simultaneously [5], [6].

A major trend in CT scanners has been toward wider detectors, allowing capture of the whole heart in a single beat with uniform IV contrast, and other applications in which the cone-beam aspect becomes important. Large detector arrays may be composed of many rectangular sub-arrays, with the geometry of their arrangement precluding a perfectly uniform angular spacing of detectors, and necessitating some variation in the relative positions of boundary detectors in adjacent sub-arrays, shown in Fig. 1. This geometry is to have focally-aligned sub-arrays to reduce distortions and other generic detection challenges. However, the boundary detectors may have slightly different responses from those in the center of a block, and if this response is not accurately modeled, systematic local bias may arise.

Image slices at the boundaries of a wide-cone scan, particularly a full rotation at a single bed position (e.g. slice locations marked by A, B and C in Fig. 1), are sampled spatially quite differently from those near the center. With boundary image slices incompletely sampled and the estimation problem underdetermined, problematic artifacts may arise from any systematic errors in data. Fig. 2b presents an example of cone-beam artifacts using native geometry iterative reconstruction (IR) methods. An analytical reconstruction specifically designed to address sampling inconsistencies in the cone-beam geometry is shown for reference, and remains absent of cone-beam artifacts. While some of this systematic bias in IR can be reduced by the simultaneous DC estimation process, the artifact can not be entirely compensated by the approach. In this paper, we augment the offset estimation process with a second set of parameters representing signal-dependent gain in the projection domain.

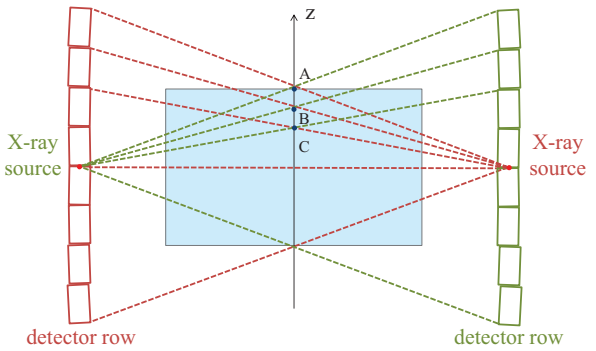

Fig. 1: Cone-beam axial acquisition trajectories at two opposite view angles. Reconstruction volume is indicated by the blue box. (The sketch is for illustration and not to scale.)

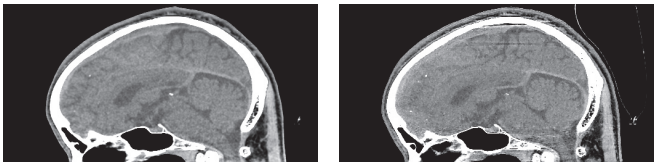

(a) (b)

Fig. 2: Cone-beam reconstructions using FBP (a) and statistical IR approach (b). Display window width 200 HU.

II. Description of Method

A quadratic model of the log-likelihood in CT for image x, projection data y and vector of DC correction parameters d may be written as

$$\ln p(y|x,d) \approx -\frac{1}{2}(y+d-Ax)^T W(y+d-Ax)+c(y), \quad (1)$$

where A represents forward projection in native geometry, W is a diagonal weighting matrix with entries proportional to received radiation strength, and $c(y)$ is independent of the parameter vectors x and d. For wider cone-beam CT, we find that DC compensation cannot fully capture the inconsistencies between y and Ax of the rows at detector module boundaries. According to Beer-Lambert law, projections are estimated by

$$y_j = -\log\left(\frac{\lambda_j}{\gamma_j \lambda_{0,j}}\right) = -\log\left(\frac{\lambda_j}{\lambda_{0,j}}\right) + \log\gamma_j, \quad (2)$$

where λ_j and $\lambda_{0,j}$ are measured and incident photon counts at projection ray j respectively. The scaling factor γ_j is considered fluctuating around value 1 in z-dimension (i.e., along table moving direction), which can be fixed with a DC correction. However, should there be any mis-estimation in λ_j due to detector efficiency or scatter level differences at detector module boundaries, systematic error may exist in some measurements. The amount of mismatch is here modeled as proportional to the integral density of the projection rays. Since the discrepancies are generally observed to be a very small fraction of the line integrals, we use a simple linear model to approximate the mismatch. The log-likelihood function can then be written as

$$\ln p(y|x,g,d) \approx -\frac{1}{2}\sum_{j=1}^{M} w_j(g_j y_j + d_j - A_{j*}x)^2 + c(y). \quad (3)$$

The correction factors g_j and d_j will be constant along some variables, and may be non-zero only for selected subsets of detector indices. We define the entries of g as

$$g_j := 1+\alpha_r, \quad j \in \Omega_r, \quad (4)$$

where Ω_r is a non-overlapping sub-collection of data indices ($j = 1,2,...,M$), divided by physical detector row indices. Similarly, the elements of vector d are defined as

$$d_j := \beta_{v,r}, \quad j \in \Omega_{v,r} \quad (5)$$

where $\Omega_{v,r}$ is a non-overlapping sub-collection of data indices divided by view and row indices.

We pursue a maximum *a posteriori* probability (MAP) reconstruction for image x with an *a priori* model $U(x)$, and maximum likelihood (ML) estimate for gain parameters α and β. Rewriting (3) in vector format, the objective function is formed as

$$\Phi(x,G,d) = \frac{1}{2}(Gy+d-Ax)^T W(Gy+d-Ax)+U(x), \quad (6)$$

where the diagonal matrix $G = \text{diag}\{g_j\}$. To perform ML estimation of the parameters α and β at a given image x, we carry on the computation using Newton's method for convex optimization, and the update equations are as follows,

$$\beta_{v,r}^{(n)} = \beta_{v,r}^{(n-1)} - \frac{\sum_{j\in\Omega_{v,r}} w_j(g_j^{(n-1)}y_j + d_j^{(n-1)} - A_{j*}x^{(n-1)})}{\sum_{j\in\Omega_{v,r}} w_j} \quad (7)$$

$$\alpha_r^{(n)} = \alpha_r^{(n-1)} - \frac{\sum_{j\in\Omega_r} w_j y_j(g_j^{(n-1)}y_j + d_j^{(n)} - A_{j*}x^{(n-1)})}{\sum_{j\in\Omega_r} w_j y_j^2}. \quad (8)$$

To avoid introducing the row-dependent biases from preprocessed data y to image domain, the DC and gain corrections as described in (7) and (8) are applied ahead of the image update in each iteration. Algorithm 1 shows a pseudocode of the implementation for a total iteration number of N. This simultaneous sinogram correction is a generic technique that in theory should work well with any gradient-based IR methods [7], [8], [9].

Algorithm 1 Simultaneous sinogram correction for model-based cone-beam CT reconstruction

Require: preprocessed projection estimation y, statistical weights W and initial reconstruction image $x^{(0)}$.
1: compute forward projection of initial condition $Ax^{(0)}$
2: **for** n = 1 to N **do**
3: update DC vector $\beta^{(n)}$ using (7)
4: update gain vector $\alpha^{(n)}$ using (8)
5: update image: $x^{(n)} \leftarrow \arg\min_x \Phi(x^{(n-1)}, G^{(n)}, d^{(n)})$
6: update forward projection $Ax^{(n)}$
7: **end for**

III. Results

We apply the proposed method to axial cone-beam CT scan data acquired on a Revolution CT scanner (GE Healthcare, Waukesha, WI). A water phantom is tested for uniformity check, without significant gradients along z; and a clinical head scan is used for demonstration of the technique in a challenging case where sampling non-uniformity is more difficult to address given the gradient changes in patient's anatomy. All data is composed of 984 views per rotation, 1.0 sec/rotation and 160 mm collimation. Subsequent model-based IR (MBIR) results are reconstructed with the q-GGMRF as *a priori* image model using a gradient based IR algorithm that simultaneously updates all the voxels [7], [8]. All images are reconstructed at thickness of 0.625 mm.

A. Image Quality

The first experiment is done on an isotropic 20 cm water phantom, scanned at 120 kV and 680 mA. The standard MBIR (without DC and gain correction) method tends to create shadings in some axial images of locations marked by A, B and C in Fig. 1, corresponding to detector module edges, shown in Fig. 3b. The shadings are usually centered in the scan field of view, and they create ripple-like effect in z-direction, which forms strip artifacts in reformatted coronal or sagittal images, as in Fig. 4b. FBP does not show similar artifacts, because

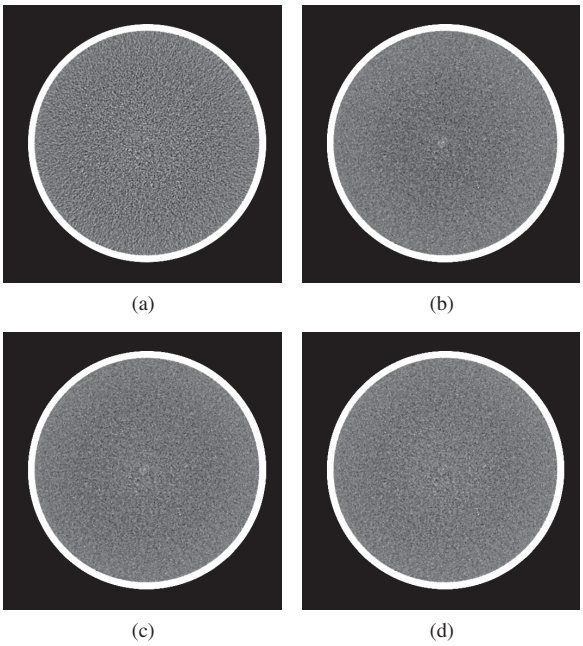

Fig. 3: Cone-beam reconstruction of water phantom at slice location B. (a): FBP; (b): standard MBIR; (c): MBIR with DC correction; (d): MBIR with DC and gain correction. Display window width 100 HU.

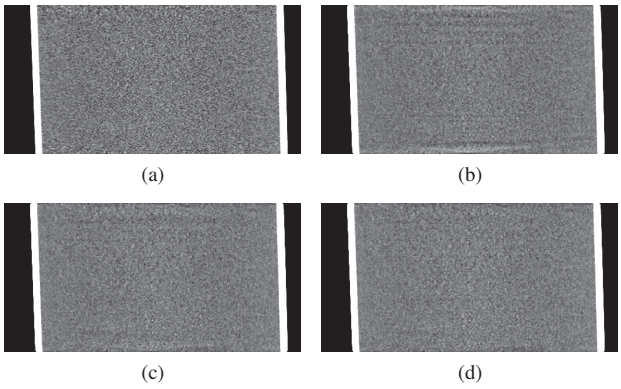

Fig. 4: Cone-beam reconstruction water phantom in coronal view. (a): FBP; (b): standard MBIR; (c): MBIR with DC correction; (d): MBIR with DC and gain correction. Display window width 100 HU.

cone-beam analytical reconstruction methods generally use some rebinning and filtering techniques as pretreatments, and such row-dependent biases may not be reflected in image space. For native-geometry-based IR techniques, reconstruction is very sensitive to systematic errors in projection data and some compensation may be required. In Figs. 3c and 4c, only DC correction in (7) is applied to iterative estimation while α is set to 0. Artifact reduction is evident, but residual errors persist. With gain correction included, images in Figs. 3d and 4d have successfully eliminated artifacts introduced by the under-sampling associated with wide-cone geometry. At 100 HU display window width, the water phantom is, appropriately, much more uniform.

We also applied the algorithm 1 on a clinical head dataset, scanned at 140 kV and 270 mA. Similar to the improvement

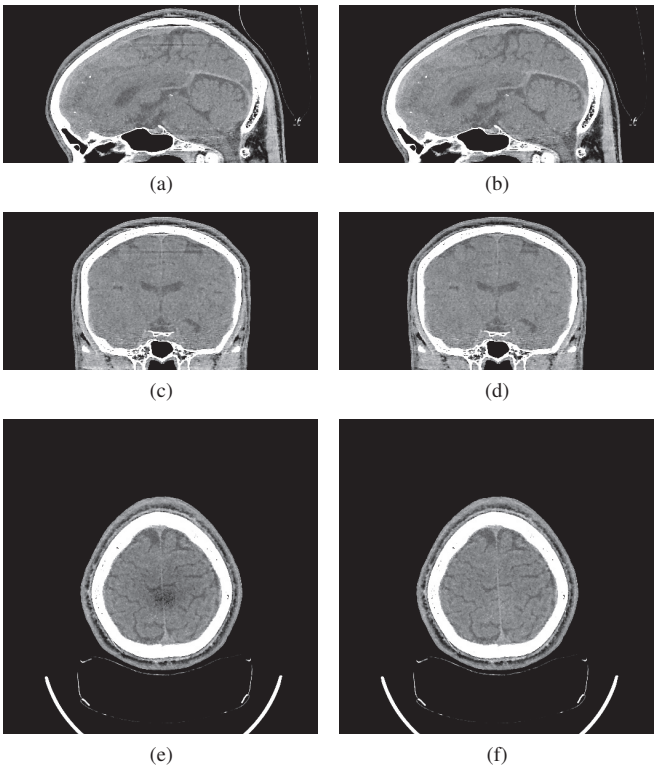

Fig. 5: Clinical cone-beam head reconstruction. (a), (c), (e): standard MBIR in sagittal, coronal and axial views; (b), (d), (f): MBIR with DC and gain correction in sagittal, coronal and axial views. Slice location C from Fig. 1 is chosen for axial images. Display window width 200 HU.

seen in the water phantom, the horizontal streaking artifacts in the sagittal and coronal images, which correspond to shadings in trans-axial plane, are successfully removed. The usual advantages of the IR method have been maintained: compared to FBP, MBIR has lower noise levels and finer details.

B. Convergence Discussion

The DC and gain parameters α and β are simultaneously estimated within iterative loop, and their convergence behaviors are critical to the robustness of the algorithm. As shown in Figs. 6 and 7, the convergence speeds are relatively fast due to convexity of the quadratic penalty. Here we choose one of the "problematic" slice locations, marked C in Fig. 1, and compare its offset parameters against adjacent rows. The DC components in Fig. 6 consistently move to one direction, suggesting there are some DC mismatches in the data but nothing particular is about the specific row r_C. The conclusion is also supported by DC profile plot in Fig. 8. However, the gain profile plots in Figs. 7 and 9 indicate systematic estimation errors in the projection data y at detector module edges, which would lead to the cone-beam artifacts using native geometry IR methods if not well compensated.

C. Computational Cost

The DC and gain offset estimation described in Algorithm 1 is highly parallelizable, and the computation is very efficient

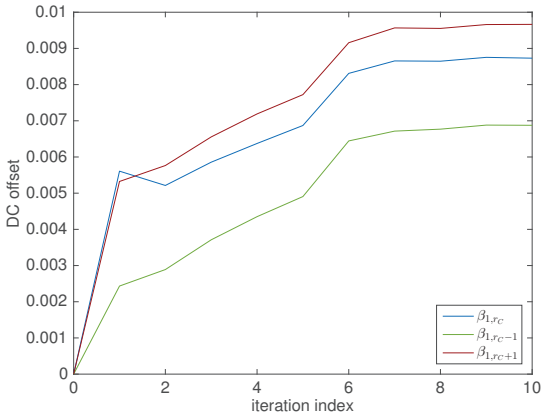

Fig. 6: Clinical head scan DC components $\beta_{v,r}$ estimation plots for view 1 and row indices of r_C, $r_C - 1$ and $r_C + 1$ (in the scale of integral density).

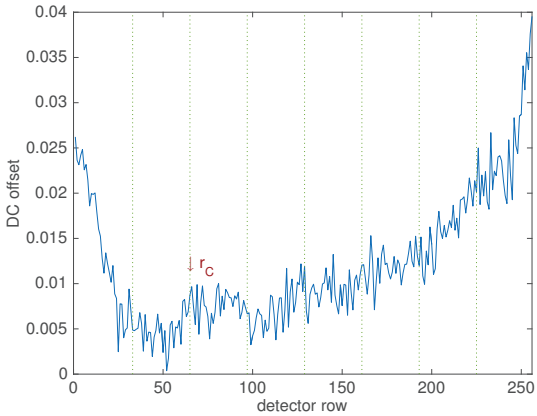

Fig. 8: Clinical head scan converged DC parameter profile $\beta_{v,*}$ for view 1 (in the scale of integral density, dotted lines mark detector module boundaries).

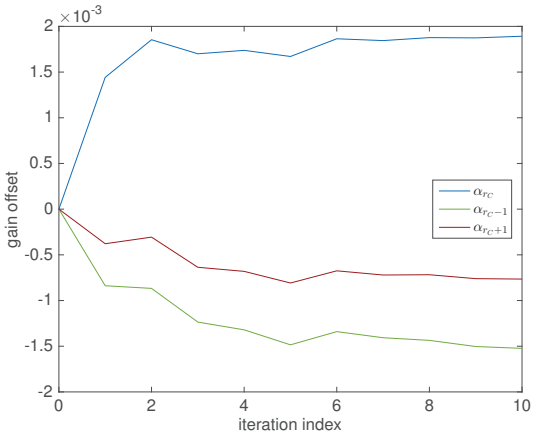

Fig. 7: Clinical head scan gain components α_r estimation plots for row indices of r_C, $r_C - 1$ and $r_C + 1$.

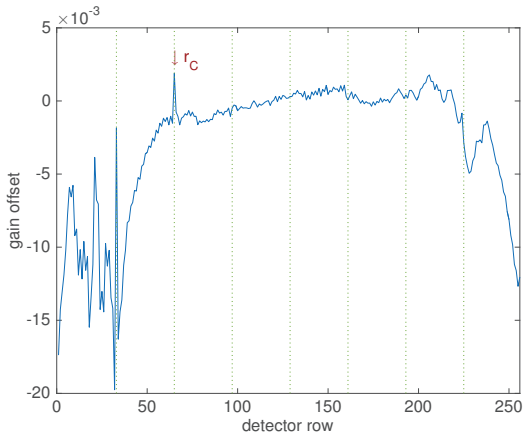

Fig. 9: Clinical head scan converged gain parameter profile α (dotted lines mark detector module boundaries).

since it only involves addition and multiplication operations. In real time tests, the extra cost of simultaneous parameter estimation is negligible compared to overall computational time of IR algorithm.

IV. Conclusion

Our approach to simultaneously correct row-dependent sinogram mis-estimation in iterative reconstruction framework yields relatively robust control of cone-beam related artifacts in the 3D volume. This improvement could extend the merit of IR methods in native geometry reconstruction to wider cone settings. Our subsequent work with these innovations will include robustness testing on various clinical applications and more extensive convergence and image quality studies.

Acknowledgment

This work has been supported by GE Healthcare.

References

[1] D. Politte, S. Yan, J. O'Sullivan, D. Snyder, and B. Whiting, "Implementation of alternating minimization algorithms for fully 3D CT imaging," in *Proc. of SPIE/IS&T Symp. Computat. Imag. II*, San Jose, CA, Jan. 17-18 2005, pp. 362–373.

[2] A. Ziegler, T. Köhler, and R. Proksa, "Noise and resolution in images reconstructed with FBP and OSC algorithms for CT," *Medical Physics*, vol. 34, no. 2, pp. 585–598, February 2007.

[3] J.-B. Thibault, K. Sauer, C. Bouman, and J. Hsieh, "A three-dimensional statistical approach to improved image quality for multi-slice helical CT," *Medical Physics*, vol. 34, no. 11, pp. 4526–4544, November 2007.

[4] J.-B. Thibault, Zhou Yu, K. Sauer, C.A. Bouman, and J. Hsieh, "Correction of gain fluctuations in iterative tomographic image reconstruction," in *Proc. of 9th International Meeting on Fully Three-Dimensional Image Reconstruction in Radiology and Nuclear Medicine*, Lindau, Germany, July 9-13 2007.

[5] Y. Kyriakou, E. Meyer, D. Prell, and M. Kachelriess, "Empirical beam hardening correction (EBHC) for CT," *Medical Physics*, vol. 37, no. 10, pp. 5179–5187, 2010.

[6] P. Jin, C. Bouman, and K. Sauer, "A model-based image reconstruction algorithm with simultaneous beam hardening correction for x-ray CT," *IEEE Trans. on Comput.*, vol. 1, no. 3, September 2015.

[7] Z. Yu, J.-B. Thibault, C. Bouman, K. Sauer, and J. Hsieh, "Fast model-based X-ray CT reconstruction using spatially nonhomogeneous ICD optimization," *IEEE Trans. on Image Processing*, vol. vol. 20, no. 1, pp. 161–175, January 2011.

[8] L. Fu, Z. Yu, J.-B. Thibault, B. De Man, M. G. McGaffin, and J. A. Fessler, "Space-variant channelized preconditioner design for 3d iterative ct reconstruction," in *Proc. Intl. Mtg. on Fully 3D Image Recon. in Rad. and Nuc. Med*, 2013, pp. 205–208.

[9] D. Kim and J. A. Fessler, "Optimized momentum steps for accelerating X-ray ct ordered subsets image reconstruction," *Proc. 3rd Intl. Mtg. on image formation in X-ray CT*, pp. 103–106, 2014.

Simple method for beam-hardening correction based on a 2D linearization function

Cristóbal Martínez, Claudia de Molina, Manuel Desco, and Monica Abella

***Abstract*— CT images are often affected by beam-hardening artifacts due to the polychromatic nature of the spectra. These artifacts appear in the image as cupping in homogeneous parts and streaks among dense parts in heterogeneous objects.**

We propose a new correction method based on the complete calibration of the beam hardening effect by means of a very simple phantom, extending the idea of the commonly used linearization method. The calibration, completely based on experimental measurements, does not require any prior knowledge about spectra or tuning correction parameters.

Preliminary evaluation done using simulations of a real size human head phantom showed better artifact compensation than the equivalent method proposed by Joseph and Spital.

***Index Terms*—Beam-hardening, CT, artifacts, cupping, streaks, polychromatic.**

I. Introduction

THE relationship between the intensity of the beam incident and transmitted through a material can be given by the Beer-Lambert Law, following the expression:

$$I = I_0 \exp\left(-\int_{path} \mu dl\right) \rightarrow Ln\frac{I_0}{I} = \int_{path} \mu dl = \mu L \qquad (1)$$

where I_0 is the incident intensity, μ the attenuation coefficient, *path* the trajectory followed by the ray, and L is the total length traversed. From this equation, the attenuation image (log of the beam attenuation) is directly proportional to the traversed thickness.

However, due to the polychromatic nature of the spectra and the integration property of the detectors used in most CT scanners, equation (1) has to be rewritten as:

$$I = \int I_0(\varepsilon) \exp\left(-\int_{path} \mu(\varepsilon) dl\right) d\varepsilon \qquad (2)$$

Now, both the attenuation coefficient and the transmitted intensity depend on the energy (ε), therefore the attenuation image is not proportional to the material thickness anymore.

Manuscript submitted April 1st 2016. This work was funded by the projects IDI-20130301, TEC2013-47270-R, IPT- 2012-0401-300000, RTC-2014-3028-1 and the Cardiovascular Research Network (RIC, RD12/0042/0057) from the Spanish Ministerio de Economía y Competitividad (www.mineco.gob.es/).

All authors are with the Biomedical Engineering Department, University of Carlos III, Madrid, Spain and with the Instituto de Investigación Sanitaria Gregorio Marañón (IiSGM), Madrid, Spain (e-mail: mabella@ing.uc3m.es) M. Desco is also with the Centro de Investigación en Red de Salud Mental (CIBERSAM, CIBER CB07/09/0031), 28007 Madrid, Spain.

This effect results mainly in two artifacts in reconstructed images: cupping in homogeneous regions and streaks among dense objects (like bone) [1]. These artifacts can be compensated by dual energy acquisition [2], which requires high dose, or including the polychromatic nature of the spectrum in an iterative reconstruction method, which implies high computational burden.

Several algorithms have been proposed in the literature to compensate for these artifacts when using single KV acquisitions and analytical reconstruction. Most simple approximations consider the patient as an homogeneous material, correcting only the cupping artifact with the linearization method [3, 4], which is insufficient to correct dark streaks. Nalcioglu et al. estimates the bone and soft tissue amount from the uncorrected image, in order to calculate correction terms, but the knowledge of the spectrum is necessary [5].

The method described by Joseph et al [6] compensates the streak artifacts after a previous reconstruction and a bone segmentation that is forward projected. This method substitutes the need of the knowledge of the spectra for two parameters that affect the streaks reduction and the bone quantification recovery [7]. The calculation of these parameters can be cumbersome due to their dependency with the source parameters and the sample used. To solve it, Kyriakou et al [8] propose an iterative algorithm to calculate these parameters automatically and [9] goes a step further avoiding also the bone segmentation step, through the combination of the original image and a transformed image by a histogram spreading. These two methods are based on the iterative optimization of a cost function, which can imply high computational burden.

In this work, it is presented a new method for beam hardening correction based on a complete and empirical calibration extending the idea of the water linearization to a 2D function. Using a very simple phantom in a calibration step, we obtain a look-up table (LUT) with the correction factors corresponding to each traversed bone thickness value. Then, for a given study, the corrected reconstruction is obtained by: (1) bone segmentation in a preliminary FDK reconstruction, (2) traversed bone calculation at each pixel by the bone projection, (3) correction of each pixel in the projections using the corresponding linearization function, and (4) reconstruction of the corrected projections. We evaluate the method using simulated data of a real-size human head phantom, the PBU60 model manufactured by Kyoto Kagatu.

II. Materials and Methods

A. Calibration

In the calibration phase we obtain the 2D beam-hardening function (F_{BH}) assuming only two different materials in the volume, bone and soft tissue:

$$F_{BH}(t_w, t_b) = \ln\left[\frac{I_0(\varepsilon)}{\int I_0(\varepsilon)\cdot e^{-\int_{path}\sum_i \mu_i(\varepsilon)dl}d\varepsilon}\right] \quad (3)$$

where t_w and t_b are the line integrals of water and bone respectively given by:

$$t_i = \int_{path} \rho_i \cdot dl; \quad \mu_i(\varepsilon) = mac(\varepsilon) * t_i \quad (4)$$

where $mac(\varepsilon)$ and ρ_i are the mass attenuation coefficient the density of tissue i and *path* is the trajectory followed by the ray.

In order to obtain the empirical $F_{BH}(t_w, t_b)$, it is necessary to measure different combinations of traversed thicknesses of soft tissue and bone. To this end, we use the simple calibration phantom shown in Fig 1, which consists of two semicylinders made of PMMA and aluminum, which present similar attenuation properties to soft tissue and bone respectively.

To generate the matrix of the traversed thicknesses for each material (t_w and t_b): (1) soft tissue and bone are segmented by thresholding of a previous reconstruction preformed with Mangose, an FDK-based algorithm [10], (2) soft tissue and bone masks are forward projected (Fig 1).

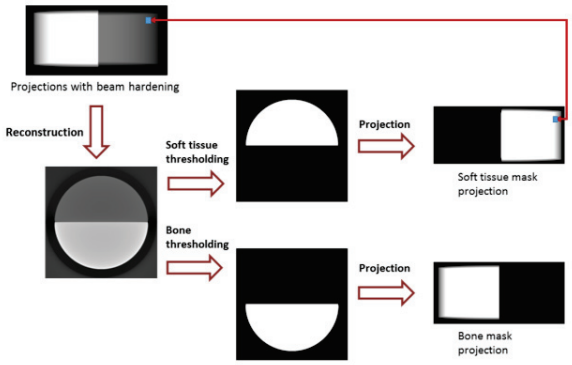

Fig 1. Calibration process.

The F_{BH} function is built by the correspondence of the traversed bone and soft tissue corresponding with each projection value. Due to phantom geometry, we do not sample the whole support of F_{BH} function. In order to estimate the missing values (Fig 2, left), we use the following strategy:

1. 1D curves corresponding to no bone traversed axis and no soft-tissue traversed axis are fitted with:
$$F_{BH}(t_w, 0) = b * {t_w}_0{}^c; \quad F_{BH}(0, t_B) = b * {t_B}_0{}^c \quad (5)$$
where b and c are free parameters to adjust the curve.
2. The 1D curves paralell to the $t_B$axis (for each amount of soft tissue traveresed) are fitted with:
$$F_{BH}(t_w, t_{Bi}) = a + b * {t_B}^c \quad (6)$$
where a is thickness of traversed water (Fig 2, right).
3. The 1D curves paralell to the t_w axis (for each amount of bone traveresed) are fitted with:
$$F_{BH}(t_{wi}, t_B) = a + b * {t_w}^c \quad (7)$$
where a is thickness of traversed bone.

The complete surface is shown in Fig 3, left.

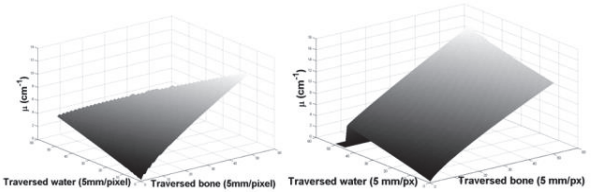

Fig 2. Original beam-hardening function without fitting (left). First fitting in water traversed direction applied to beam hardening function (right).

The ideal 2D function corresponding to the monochromatic case is determined by the tangent plane to the F_{BH} function. To this end, we obtain the tangent to the 1D curves corresponding to the no bone traversed axis and no soft-tissue traversed axis (approximated with the mean value of the 4% of the total points). The monochromatic plane is then determined by the equation:

$$P(x, y) = A \times x + B \times y \quad (8)$$

where A and B are the tangents corresponding to soft tissue and bone curves respectively.

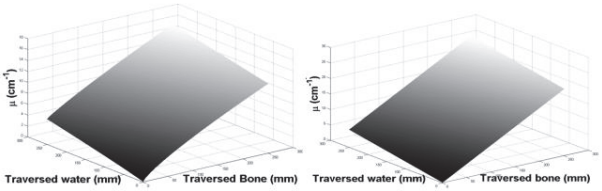

Fig 3. Obtained beam-hardening surface (left) and ideal (monochromatic) function (right).

The correction is based on the substitution of the real surface values for the monochromatic function values which have the same bone and soft tissue traversed, the relating function has the following expression:

$$T(t_w, t_b) = a + b * t_w + c * t_b + d * t_w^2 + \\ + e * t_b^2 + f * t_w t_b \quad (9)$$

However, T function is not injective,so it is not possible to obtain the correction value for each given bone/soft-tissue thicknesses pair, we create one linearization function for each thickness of bone traversed ($bone_i$), which follows the expression:

$$T_{bone_i} = a \times {p_i}^2 + b \times p_i + c \quad (10)$$

The result of the calibration process is a look-up table (LUT) that provides the linearization function for each thickness of traversed bone.

B. Correction

The beam hardening correction process is sketched in Fig 4. First, the bone is segmented on a preliminary reconstruction and projected to obtain the total traversed bone thickness for each pixel in the projection data. This information is used to address the LUT and obtain the linearization function corresponding to that thickness of traversed bone. Finally, the pixel is corrected applying that linearization function.

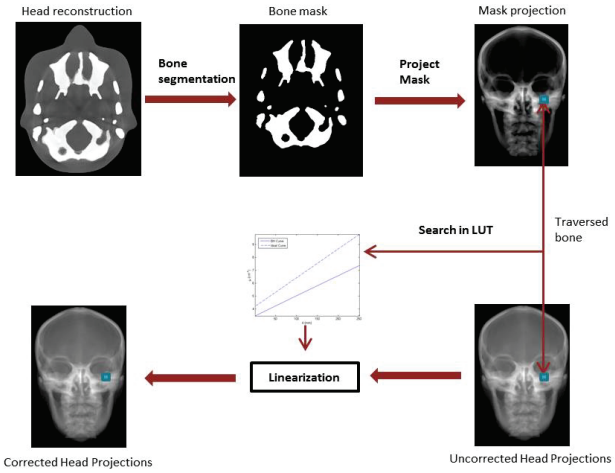

Fig 4. Workflow of the process to obtain the corrected projections.

C. Assessment of performance

Evaluation was done on simulated data based on a CT of a real-size human head phantom (PBU-50 model, manufactured by Kyoto Kagatu) shown in Fig 5, adapted to have three different attenuation coefficients: soft tissue, hard bone and marrow (densities 0.8, 1.92, 1.6 gr/cm^3, respectively). The CT volume was 512×512×500 pixels, with 0.5 mm isotropic voxel.

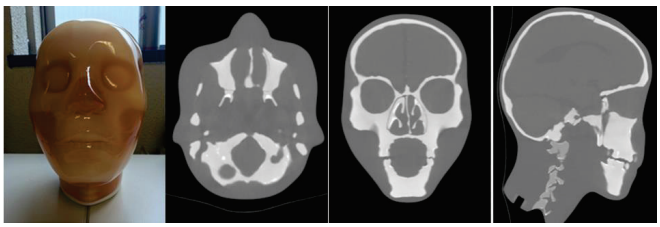

Fig 5. Phantom front view (top-left), axial (top-right). coronal (bottom-left). and sagittal CT slices (bottom-right).

Simulations were generated with a simulator implemented in GPU [11], based on a cone-beam system with a distance source object and object detector source equal to *104 cm* and *57 cm* respectively. We used a spectrum similar to those used in the clinic: polyenergetic 100 kVp spectrum, with 0.2 cm aluminum filtration, and the detector was modeled as a simple photon counting system with a pixel size equal to *0.774 mm*.

Fig 6 shows an axial slice of the head obtained with a monochromatic and polychromatic spectra showing beam hardening effect (streaks).

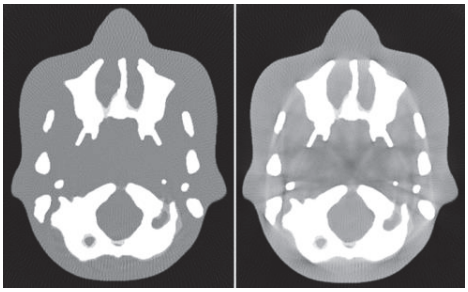

Fig 6. Axial slice of the phantom reconstruction of the monochromatic (left) and polychromatic simulations (right).

The proposed correction scheme was compared with the results obtained with the Joseph and Spital method.

In order to obtain differents regions to measure the imrpovement, volume has been separated in five different regions. Mean Squared Error (MSE) was obtained for bone and soft tissue and the percentage of improvement with respect to the polychromatic reconstruction was obtained as:

$$P_{Improvement} = \frac{MSE_{polycromatic} - MSE_{corrected}}{MSE_{polycromatic}} \quad (8)$$

We also obtained three different profiles in the two slices of the head, each one with different bone structures, these profiles can be seen on the Fig 7.

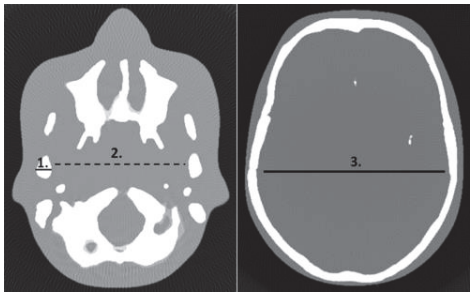

Fig 7. Axial slices 1 (left) and 2 (right) used for assessment. Line 1 shows the beam hardening effect, line 2 the bone value and line 3 cupping effect.

III. Results

Fig 8 shows the polychromatic data corrected with both proposed method (left) and Joseph-Spital method (right), showing a better streak compensation with the proposed method.

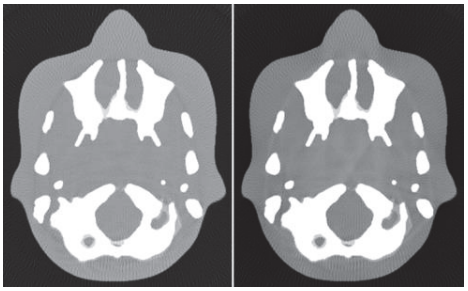

Fig 8. Polychromatic phantom reconstruction with the proposed method (left) and with the JS method (right).

Table I shows an improvement in all regions when using the proposed method. Results for the JS method are not consistent for bone through the different slices. The lower improvement

in soft tissue error in slice 1, characterized by more bone, is due to the streak artifacts still present after the correction

TABLE I. Improvement percentage

Study	P_I(JS)	P_I(PL)
Soft Tissue Slice 1	89.97 %	98.15 %
Bone Slice 1	98.87 %	99.87 %
Soft Tissue Slice 2	92.19 %	98.87 %
Bone Slice 2	92.40 %	99.77 %
Whole soft tissue	90.39 %	97.13 %
Whole bone	96.14 %	99.76 %

As it can be seen on top panel of Fig 9, the cupping is corrected with both methods. However, the JS method underestimates the value of bone and the streaks are not totally corrected in slice 1. These can be seen on the middle and bottom panel of the Fig 9, corresponding to the profile 1 and 2 respectively.

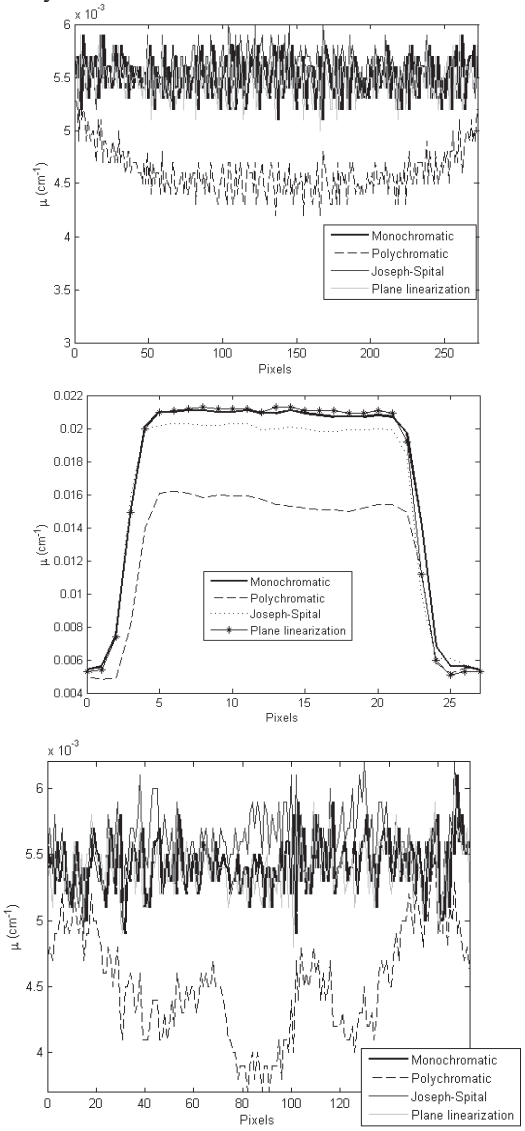

Fig 9. Profiles 1, showing the cupping artifact in slice 2 (top),2, showing the effects of the streaks in slice 1 (middle) and 3, showing the bone recovery in slice 1 (bottom).

IV. Discussion

We have proposed a new method to correct the beam-hardening artifacts in CT. The method is based on the complete characterization of the beam hardening effect by means of a very simple calibration phantom, extending the idea of the commonly used water linearization method.

A preliminary evaluation based on simulations showed that the proposed method outperforms the Joseph-Spital method both visually and analytically in terms of artifact reduction (9% percent on soft tissue and 7% on bone). The proposed method avoids the need of tuning parameters determining which is usually calculated heuristically. Furthermore, since the correction in JS method is based on the projection of bone, optimal parameters are different depending on bone structure and the reconstructed volume.

Our method gives an optimal correction for every study independently of the sample structure or the reconstructed volume. Since it is based on empirical measurements, we expect to correct also the artifacts derived from scattering.

References

[1] J. F. Barrett and N. Keat, "Artifacts in CT: Recognition and Avoidance," *RadioGraphics,* vol. 24, pp. 1679-1691, 2004.

[2] P. Sukovic and N. H. Clinthorne, "Design of an experimental system for dual energy X-ray CT," *IEEE Nucl Sci Symp,* vol. 2, pp. 1021-1022, 1999.

[3] R. A. Brooks and G. D. Chiro, "Beam hardening in x-ray reconstruction tomography," *Phys. Med. Biol.,* vol. 21, pp. 390-8, 1976.

[4] P. K. Kijewski and B. E. Bjärngard, "Correction for beam hardening in computed tomography," *Med Phys,* vol. 5, pp. 209-214, 1978.

[5] O. Nalcioglu and R. Y. Lou, "Post-reconstruction Method for Beam Hardening in Computerised Tomography," *Phys. Med. Biol.,* vol. 24, pp. 330-40, 1979.

[6] P. M. Joseph and R. D. Spital, "A method for correcting bone induced artifacts in computed tomography scanners," *J. Comp. Assisted Tomo.,* vol. 2, pp. 100-8, 1978.

[7] C. de Molina*, et al.*, "Complete scheme for beam hardening correction in small animal computed tomography," *IEEE Nuclear Science Symposium and Medical Imaging Conference (NSS/MIC),* pp. 3835-3838, 2012.

[8] Y. Kyriakou*, et al.*, "Empirical beam hardening correction (EBHC) for CT," *Med Phys,* vol. 37, pp. 5179-5187, 2010.

[9] S. Schüller*, et al.*, "Segmentation-free empirical beam hardening correction for CT," *Med Phys,* vol. 42, pp. 794-803, 2015.

[10] M. Abella*, et al.*, "Software Architecture for Multi-Bed FDK-based Reconstruction in X-ray CT Scanners," *Comput Methods Programs Biomed,* vol. 107, pp. 218-32, 2012.

[11] E. Serrano*, et al.*, "Design and Evaluation of a Parallel and Multi-Platform Cone-Beam X-Ray Simulation Framework," *CT meeting proc.,* vol. (in press), 2016.

Towards Material Decomposition on Large Field-of-View Flat Panel Photon-Counting Detectors — First *in-vivo* Results

Kerstin Müller, Moiz Ahmad, Martin Spahn, Jang-Hwan Choi,
Silke Reitz, Niko Köster, Yanye Lu, Rebecca Fahrig, and Andreas Maier

***Abstract*—Dual-energy CT imaging allows to separate materials and tissue based on their attenuation behavior using two different X-ray spectra. Various techniques exist to acquire X-ray and CT images with two different energies. One approach utilizes a specific detector technology to discriminate the photons in the emitted X-ray spectrum by their energy instead of integrating the energy as in current applied detector technology. Photon-counting detectors (PCDs) offer several advantages compared to traditional energy integrating detectors such as improved detective quantum efficiency (DQE). However, due to manufacturing challenges, PCDs are still part of on-going research and not applicable in a clinical scanner, yet. In this paper, a first step towards *in-vivo* material decomposition for iodinated contrast agent from background tissue in a porcine study using a large field-of-view photon-counting detector is presented. First preliminary results are encouraging to further exploit material decomposition methods using the presented photon-counting detector. However, major challenges remain with the current technology that need to be investigated and addressed in future work.**

***Keywords*—C-arm Angiography, Photon-Counting Energy-Resolving Detectors, Material Decomposition, Image Formation**

I. Introduction

Photon-counting detectors (PCD) offer significant advantages to current energy-integrating flat panel detectors (FDs) such as improved detective quantum efficiency (DQE) and photon energy resolution [1], [2], [3]. In particular the ability to differentiate material properties dependent on photon energies has attracted significant attention as it allows material decomposition with a single scan, as data with both energies is acquired simultaneously. This enables 2-D projection-based decomposition of materials [4], [5], [6]. The acquisition of a high energy (HE) and total energy (TE) image at the same time point with a PCD, assuming 2 energy bins, solves the problem of degraded image quality due to motion artifacts. For example for a 2D digital subtraction angiography (DSA), where the mask and the fill images are acquired at different time points, severe motion artifacts can occur as visible in Fig. 1. Modern C-arm systems allow to select the mask image and also provide motion correction algorithms. However, these cannot eliminate severe motion between mask and fill images.

K. Müller, M. Ahmad are with the Radiological Sciences Lab, Department of Radiology, Stanford University, Stanford, CA, USA. E-mail: kmuell@stanford.edu. M. Spahn, S. Reitz, and N. Köster are with Siemens Healthcare GmbH, Forchheim, Germany. J.-H. Choi and Rebecca Fahrig were with the Radiological Sciences Lab, Stanford University, Stanford, CA, USA. R. Fahrig is now with Siemens Healthcare GmbH, Forchheim, Germany. Y. Lu and A. Maier are with the Pattern Recognition Lab, Department of Computer Science, Friedrich-Alexander-Universität Erlangen-Nürnberg.

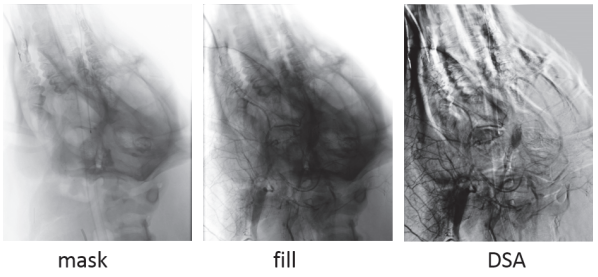

Fig. 1. Prominent motion artifact in DSA image may occur because mask and fill image were acquired at different time points.

Current photon-counting detector technology still poses significant challenges. Amongst other problems, an excess of detected photons results in pulse pile-up and the detected count rates are energy dependent and spatially varying [2], [3]. So called homogenization approaches to compensate those effects exist which result in significant improvements of the acquired image stacks [7], [8]. Assuming a PCD with two energy bins, a total energy (TE), high energy (HE), and low energy (LE) image stack is acquired. The most benefit of the homogenization techniques exists for the TE image. Results for the individual energy bins (HE, LE), however may be inferior (cf. Fig. 2). As pulse pile-up favors lower count rates, detectors typically can only account for smaller pixel sizes and the X-ray tube needs to be set to low exposure rates. As a result, the acquired 2-D images have a noisy appearance and material separation is not possible on the raw 2-D images.

All the previously mentioned challenges make it difficult to advance from simulated phantom PCD experiments towards integration into a clinical system. In this paper, a first attempt towards projection-based material decomposition with a large field-of-view photon-counting detector in an *in-vivo* porcine study is presented. A non-linear denoising technique is applied to the generated 2-D (LE, HE) image stacks to perform a simple linear material decomposition. To the best of our knowledge, this is the first study on *in-vivo* material decomposition using a large field-of-view PCD.

II. Materials and Methods

A. Photon-Counting Detector (PCD) Imaging

A large field-of-view dual-energy photon-counting detector (XCD) for its application in interventional radiology was ”piggy-back” mounted to the flat panel detector (FD) of an

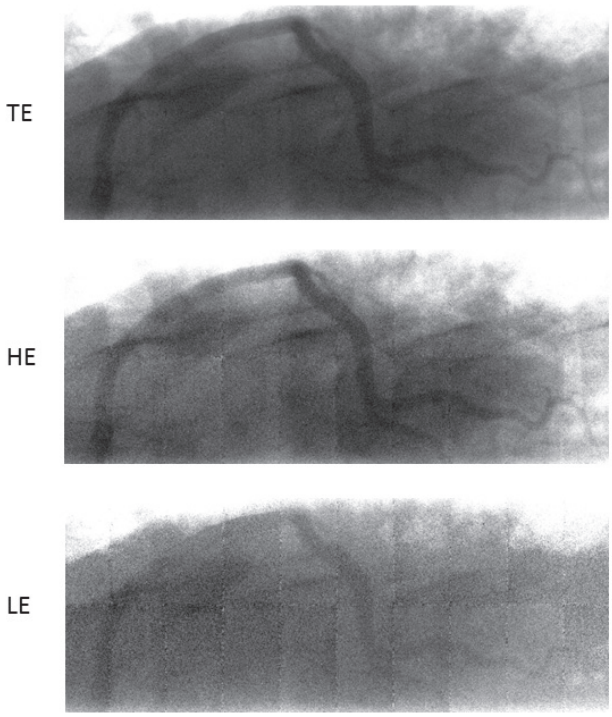

Fig. 2. Homogenization algorithms improve spatially varying detection behavior, but detector module artifacts are still present in the HE and LE processed images.

Artis zeego system (Siemens Healthcare GmbH, Forchheim, Germany). The detector is a customized OEM product manufactured by XCounter AB (Danderyd, Sweden). The detector features a 1 mm cadmium telluride (CdTe) layer to convert absorbed X-ray energy to an electrical signal. The detector covers an active area of 30×5 cm^2 made up of several individual modules, each having a size of 1.25×2.5 cm^2. Overall the 2D image matrix is 3072×512 pixel with an isotropic pixel resolution of 100μm. The exposure integration range is from 100μs-5s. The XCD features two energy bins per pixel with an adjustable threshold with a counter depth of 12 bit. The adjustable thresholds are only mean values and can vary between different pixel modules. The two bins allow synchronous acquisition of a total energy (TE) and a high energy (HE) image can be performed. The detector also features a charge sharing correction feature to restore the energy that may spread over several neighboring pixel due to fluorescence or charge dispersion and to count the event only once. The detector design is similar to the small PCD presented in Ullberg et al. [1]. The readout of the XCD is performed over a gigabit ethernet connection and the generated 2D images are visualized and stored on an external workstation. The same pre-processing and conditioning as described in Ahmad et al. was applied to the TE and HE image stacks [9].

B. TE-guided Bilateral Filtering

As previously mentioned, the 2D HE and LE image stacks suffer from severe pixel noise compared to the TE image stack (cf. Fig. 2). In order to improve image quality and to reduce noise, a non-linear joint bilateral filtering (JBF) technique is applied [10], [11], [12]. The approach exploits the improved image quality of the TE image $I_{\mathrm{TE}}(\boldsymbol{x})$ to filter the respective (HE, LE) image under guidance at position $\boldsymbol{x}$. The bilateral filtered image $I'_b(\boldsymbol{x})$ from the non-filtered image $I_b(\boldsymbol{x})$, where $b \in \{\mathrm{HE}, \mathrm{LE}\}$ can be computed by

$$I'_b(\boldsymbol{x}) = \frac{1}{c(\boldsymbol{x})} \sum_{\boldsymbol{u}} g_s(\boldsymbol{x},\boldsymbol{u}) g_I(\boldsymbol{x},\boldsymbol{u}) I_b(\boldsymbol{x}), \quad (1)$$

$$c(\boldsymbol{x}) = \sum_{\boldsymbol{u}} g_s(\boldsymbol{x},\boldsymbol{u}) g_I(\boldsymbol{x},\boldsymbol{u}), \quad (2)$$

$$g_s(\boldsymbol{x},\boldsymbol{u}) = e^{-\frac{||\boldsymbol{x}-\boldsymbol{u}||_2^2}{2\sigma_s}} \quad (3)$$

$$g_I(\boldsymbol{x},\boldsymbol{u}) = e^{-\frac{(I_{\mathrm{TE}}(\boldsymbol{x})-I_{\mathrm{TE}}(\boldsymbol{u}))^2}{2\sigma_I}} \quad (4)$$

Here, σ_s denotes the spatial standard deviation and σ_I denotes intensity standard deviation used for the joint bilateral filter.

C. Material Decomposition

Due to the non-linearity of the photon count rate and since the material decomposition is spatially quite variant, we chose a simple linear model for material separation and assume that this model is valid in a small patch of the image. In order to compute a soft tissue suppressed image that only shows contrast agent, we analyzed a small area Ω_{ST} containing only soft tissue to compute regression coefficients m and t solving the least-square problem:

$$\arg\min_{m,t} = \sum_{\boldsymbol{x}\in\Omega_{\mathrm{ST}}} ||\ln(I'_{\mathrm{HE}}(\boldsymbol{x})) - (m \cdot \ln(I'_{\mathrm{LE}}(\boldsymbol{x})) + t)||_2^2. \quad (5)$$

The contrast projection $I_{\mathrm{C}}(\boldsymbol{x})$ showing only iodinated contrast agent can be computed by

$$I_{\mathrm{C}}(\boldsymbol{x}) = \ln(I'_{\mathrm{HE}}(\boldsymbol{x})) - (m \cdot \ln(I'_{\mathrm{LE}}(\boldsymbol{x})) + t). \quad (6)$$

D. Evaluation

1) Digital Subtraction Angiography (DSA): The PCD generated iodine images $I'_{\mathrm{HE}}(\boldsymbol{x})$ were compared to DSA-like data. DSA is a popular method in angiographic imaging for visualization of iodine-based contrasted vessels. For DSA-imaging, the reference frame $I'_{b,\mathrm{ref}}(\boldsymbol{x})$, without contrast injection is acquired and subtracted to get only the contrast-filled projection $I_{\mathrm{b,DSA}}(\boldsymbol{x})$:

$$I_{\mathrm{b,DSA}}(\boldsymbol{x}) = I'_b(\boldsymbol{x}) - I'_{b,\mathrm{ref}}(\boldsymbol{x}). \quad (7)$$

This procedure can be performed for both energy bins b (HE, LE).

2) Contrast-to-Noise Ratio (CNR): In order to quantitatively evaluate the contrast within vessel structure to background, the contrast-to-noise ratio (CNR) was computed.

III. Experiments

Stanford Universitys Administrative Panel on Laboratory Animal Care approved the protocol for this *in-vivo* animal study. Arterial femoral access was established using percutaneous puncture for hemodynamic monitoring, administration of medications, and the injection of contrast agent. For the 2D scan a 20 mL of 100% iodinated contrast agent (Omnipaque 350 mg/mL, GE Healthcare, Princeton, NJ) was administered over a pigtail catheter placed in the aortic root. The contrast was delivered with a rate of 8 mL/s using a power injector (Medtron, Saarbrücken, Germany). The 2D acquisition was performed with requesting 81 kV, 10 ms and 800 mA from the X-ray tube and the thresholds of the XCD were set to 8 keV for the lower and 39 keV for the higher energy bin.

IV. Results

In the following section, the results of the TE-Guided filtering and the material decomposition are presented in comparison to conventional DSA-imaging. All algorithms were realized using the CONRAD software package [13].

A. TE-guided Bilateral Filtering

In a first experiment, we explored whether TE-guided JBF filtering reduces noise, improves image quality and still allows to identify tissue clusters in a HE/LE channel scatter plot. A 1×1 cm^2 patch of the image showing a contrasted vessel and soft tissue background was selected for the scatter plot. Fig. 3 shows the LE versus HE scatter plot for a small region of interest containing an iodinated contrasted vessel and water-like background tissue. It can be seen that without smoothing, no materials can be differentiated. Only after extensive smoothing, material clusters for separation of different materials form even though spatial resolution is drastically reduced. As shown in Fig. 4, with TE-guided bilateral filtering similar tissue clusters as seen with strong spatial smoothing appear, but preserving the spatial resolution. Spatial smoothing with $\sigma_s = 5$ and a TE-guided filtering with $\sigma_s = 5$ and $\sigma_I = 10$ were compared. Visual comparison before and after filtering of the LE channel which contains the most noise also confirms the effectiveness of the TE-guided filtering, while Gaussian smoothing enables the same differentiation and degrades severely the spatial resolution (cf. Fig. 5).

B. Material Decomposition

Subsequently, we explored different methods to emphasize the contrast filled right coronary vessel tree. As a first attempt we investigated only a single detector tile as a first proof of concept due to the large differences in energy count behavior between the different detector modules. Fig. 6 displays the results of the different methods. DSA of the HE channel shows the contrast filled vessel with a CNR of 1.66. Using the TE-guided filter improves the CNR to 2.46. On the LE channel, the contrast is barely visible at a CNR of 0.64. There is only high contrast at the top of the vessel, while contrast is significantly reduced in most parts. TE-guided filtering also improves contrast to a CNR of 1.32. The material decomposition image also shows sub-optimal contrast compared to the denoised HE channel. But the material decomposed image does not suffer from any motion artifact. Its CNR is also higher than the HE

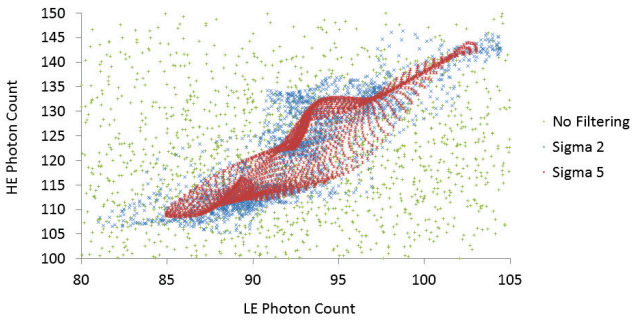

Fig. 3. Scatter plot for LE and HE photon counts. Identification of underlying material or tissue in the non-filtered 2D HE and LE stack is not possible, due to the excessive noise and spatially variant energy discrimination. Extensive spatial filtering (2D-Gaussian filter) allows to form clusters for water and iodine while decreasing spatial resolution.

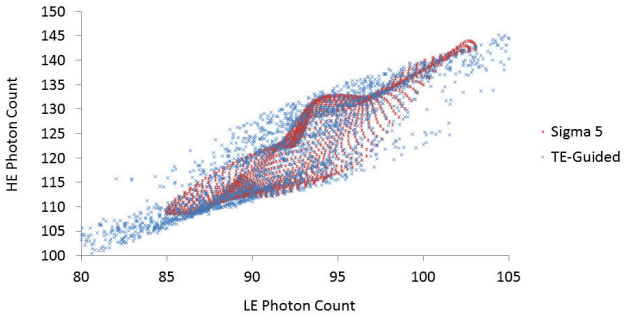

Fig. 4. TE-guided filtering improves the ability to identify material and tissue clusters in the 2D TE raw data, comparable to Gaussian filtering using a strong spatial sigma.

raw image with 2.00 as noise is greatly reduced. The non-uniformity of the energy counts across the single tile causes the top part of the image and the bottom left to loose contrast. Note that the water calibration was performed in the left center of the tile which delivers the best signal-to-noise characteristics in the image.

V. Discussion and Conclusion

In this proof-of-concept study the goal was to investigate the first attempts towards material decomposition using *in-vivo* data acquired with a large field-of-view photon-counting detector. As a first feasibility test a simple and local method for material separation was chosen due to the detectors spatial variations. After pre-processing of the TE image stacks using homogenization methods, the spatially variant energy resolution and noise still pose the biggest challenges. TE-guided filtering reduces noise drastically while preserving spatial information. This results in increased CNR rates in DSA images for HE and LE. However, DSA has the large disadvantage that motion artifacts are introduced. Material decomposition techniques are not effected, as the image is computed from simultaneously acquired TE and HE image stacks. The current detector shows significant differences in energy sensitivity and energy resolution abroad detector modules. In particular at the tile borders neighboring pixels may have significantly different

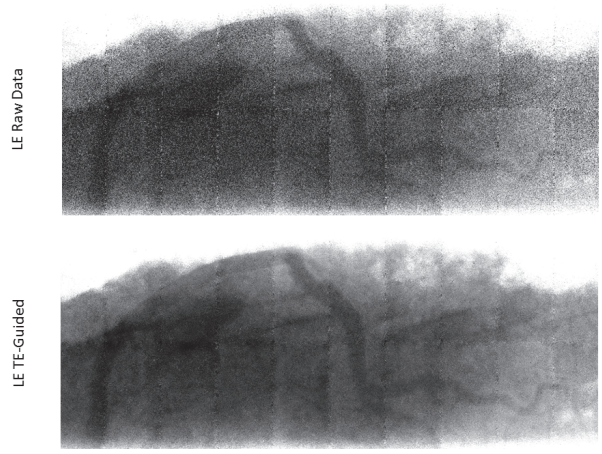

Fig. 5. LE channel before and after TE-guided filtering: The filtering reduces noise significantly and preserves the edges of the contrast filled vessel. Note that also the impression of the patches between the detector elements is reduced as these are less apparent in the TE images.

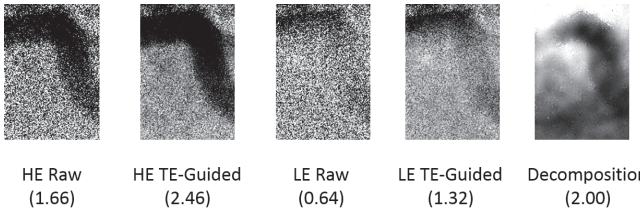

Fig. 6. Patches of the different techniques to extract iodinated contrasted vessel from background and respective CNR.

properties in terms of spectral separation. To alleviate this, we investigated only a single tile for material decomposition. Still, the CNR of the decomposed image is only slightly better than the DSA of the LE projection of the same patch. It should be mentioned that the trimming of the detector is not sufficient and will be addressed in future work. Overall, we believe that further investigations using more sophisticated methods found in literature [14], [15], [16], [17] will help to improve material decomposition that will finally enable applications as single shot DSA.

Disclaimer: The concepts and information presented in this paper are based on research and are not commercially available.

Acknowledgment

The authors gratefully acknowledge funding support from the NIH Shared Instrument Grant S10 RR026714 supporting the zeego@StanfordLab, and Siemens Healthcare GmbH Advanced Therapies. Special thanks also goes to Yamil Saenz for his help with the in-vivo pig experiment.

References

[1] C. Ullberg, M. Urech, N. Weber, A. Engman, A. Redz, and F. Henckel, "Measurements of a Dual-Energy Fast Photon Counting CdTe Detector with Integrated Charge Sharing Correction," *Proceedings of SPIE Medical Imaging*, vol. 8668, pp. 86 680P–86 680P–8, 2013.

[2] K. Taguchi and J. Iwanczyk, "Vision 20/20: Single photon counting x-ray detectors in medical imaging," *Medical Physics*, vol. 40, no. 10, p. 100901, 2013.

[3] C. H. McCollough, S. Leng, L. Yu, and J. Fletcher, "Dual-and Multi-Energy CT: Principles, Technical Approaches, and Clinical Applications," *Radiology*, vol. 276, no. 3, pp. 637–653, 2015.

[4] D. Niederlöhner, F. Nachtrab, T. Michel, and G. Anton, "Using the Medipix2 Detector for Photon Counting Computed Tomography," in *IEEE Nuclear Science Symposium Conference Record*, vol. 4, Fajardo, Puerto Rico, 2005, pp. 2327–2331.

[5] N. Maaß, S. Sawall, M. Knaup, and M. Kachelrieß, "Dose minimization for material-selective CT with energy-selective detectors," in *IEEE Nuclear Science Symposium and Medical Imaging Conference (NSS/MIC)*, Valencia, Spain, 2011, pp. 4447–4452.

[6] Y. Lu, J. Geret, M. Unberath, M. Manhart, Q. Ren, R. Fahrig, J. Hornegger, and A. Maier, "Projection-based Material Decomposition by Machine Learning using Image-based Features for Computed Tomography," in *The 13th International Meeting on Fully Three-Dimensional Image Reconstruction in Radiology and Nuclear Medicine*, Newport, RI, USA, 2015, pp. 448–451.

[7] J. Jakubek, "Data processing and image reconstruction methods for pixel detectors," *Nuclear Instruments and Methods in Physics Research Section A: Accelerators, Spectrometers, Detectors and Associated Equipment*, vol. 576, no. 1, pp. 223–234, 2007.

[8] D. Vavrik, T. Holy, J. Jakubek, S. Pospisil, Z. Vykydal, and J. Dammer, "Direct thickness calibration: way to radiographic study of soft tissues," in *Astroparticle, Particle and Space Physics, Detectors and Medical Physics Applications*, vol. 1. World Scientific, 2006, pp. 773–778.

[9] M. Ahmad, R. Fahrig, M. Spahn, J.-H. Choi, N. Köster, S. Reitz, W. Hinshaw, L. Pung, T. Moore, A. Maier, and K. Müller, "First in-vivo Experiments with a Large field-of-view Flat Panel Photon-Counting Detector," in *Proceedings of the Fourth CT Meeting*, Bamberg, Germany, 2016, p. submitted.

[10] G. Petschnigg, R. Szeliski, M. Agrawala, M. Cohen, H. Hoppe, and K. Toyama, "Digital photography with flash and no-flash image pairs," *ACM Transactions on Graphics*, vol. 23, no. 3, p. 664, 2004.

[11] L. Yanye, M. Michael, O. Taubmann, T. Zobel, Q. Yang, J.-H. Choi, M. Wu, A. Doerfler, R. Fahrig, Q. Ren, J. Hornegger, and A. Maier, "Projection-Based Denoising Method for Photon-Counting Energy-Resolving Detectors," in *Bildverarbeitung für die Medizin 2015*, Lübeck, 2015, pp. 137–142.

[12] M. Manhart, R. Fahrig, J. Hornegger, A. Dörfler, and A. Maier, "Guided Noise Reduction for Spectral CT with Energy-Selective Photon Counting Detectors," in *Proceedings of the Third CT Meeting*, Salt Lake City, UT, USA, 2014, pp. 91–94.

[13] A. Maier, H. G. Hofmann, M. Berger, P. Fischer, C. Schwemmer, H. Wu, K. Müller, J. Hornegger, J.-H. Choi, C. Riess *et al.*, "CONRAD – A software framework for cone-beam imaging in radiology," *Medical Physics*, vol. 40, no. 11, p. 111914, 2013.

[14] E. Meyer, R. Raupach, M. Lell, B. Schmidt, and M. Kachelrieß, "Frequency split metal artifact reduction (FSMAR) in computed tomography," *Medical Physics*, vol. 39, no. 4, pp. 1904–1916, 2012.

[15] S. Faby, S. Kuchenbecker, S. Sawall, D. Simons, H.-P. Schlemmer, M. Lell, and M. Kachelrieß, "Performance of today's dual energy CT and future multi energy CT in virtual non-contrast imaging and in iodine quantification: A simulation study," *Medical Physics*, vol. 42, no. 7, pp. 4349–4366, 2015.

[16] C. Maaß, M. Baer, and M. Kachelrieß, "Image-based dual energy CT using optimized precorrection functions: A practical new approach of material decomposition in image domain," *Medical Physics*, vol. 36, no. 8, pp. 3818–3829, 2009.

[17] M. Petrongolo, X. Dong, and L. Zhu, "A general framework of noise suppression in material decomposition for dual-energy CT," *Medical Physics*, vol. 42, no. 8, pp. 4848–4862, 2015.

Tensor Framelet based iterative image reconstruction algorithm for low-dose multislice helical CT

Haewon Nam
Yonsei Institute of Convergence Technology
Yonsei University
Incheon, Republic of Korea 406-804
Email: haewonn@yonsei.ac.kr

Minghao Guo
School of Biomedical Eng. and
Department of Mathematics
Shanghai Jiao Tong University
Shanghai 200240, China

Hao Gao
School of Biomedical Eng.
and Department of Mathematics
Shanghai Jiao Tong University
Shanghai 200240, China
Email: hao.gao.2012@gmail.com

***Abstract*—This work is to investigate the feasibility of improving the imaging quality for low-dose multislice helical computed tomography (CT) via iterative reconstruction with tensor framelet (TF) regularization. We develop the TF-based iterative image reconstruction algorithm for multislice helical CT. The imaging model takes the flying focal spot into account, and the GPU computing is adopted for efficiently implementing a fast parallel algorithm of X-ray forward and backward projections. The image regularization for noise and artifact reduction is enforced by TF, as a high-order generalization of isotropic total variation regularization. The solution algorithm for image reconstruction is based on the alternating direction method of multipliers or the so-called split Bregman method. The proposed method was validated using the experimental data from a Siemens SOMATOM Definition 64-slice helical CT scanner, in comparison with FDK and the Katsevich algorithm. To test the algorithm performance with low-dose data, an ACR phantom was scanned and the data was equally undersampled with various factors. The proposed method was robust for the low-dose data with 25% undersampling factor. An effective iterative image reconstruction algorithm has been proposed for low-dose multislice helical CT with improved image quality from FDK and the Katsevich algorithm.**

I. Introduction

X-ray computed tomography (CT) has been one of the most widely used medical imaging techniques since Hounsfield invented the first commercial medical X-ray machine in 1972 [1]. The Helical CT was first invented by I. Mori [2] in the late 1980s and was developed by W. Kalender [3] in the 1990s. The number of detector rows has been increased to achieve larger volume coverage with a reduced scan time and improved z-resolution.

Helical CT reconstruction algorithms can be categorized into two groups: Analytic reconstruction and iterative algorithm, and analytic reconstruction can be sub-divided into exact and approximate reconstruction methods. The Feldkamp-Davis-Kress algorithm (FDK) is a well-known approximate analytic reconstruction algorithm [4] and it can be generalized for helical scan trajectories [5], [6]. However, FDK generates helical artifacts due to data insufficiency. A conventional filtered backprojection (FBP) algorithm can be implemented with data interpolation [7] to soften helical artifacts, but this may generate another type of artifact caused by data approximation. In 2002, Katsevich introduced an exact FBP-type reconstruction algorithm based on the PI-line and Tam-Danielsson window [8], and details for the numerical implementation of the Katsevich algorithm are given in [9], [10]. An alternative derivation of the Katsevich algorithm is provided by Chen [11]. Meanwhile, another exact method of backprojection-filtration (BPF) has been developed by Zou and Pan [12], and these ideas have inspired several subsequent exact reconstruction methods [13], [14], [15].

In this article, we propose an iterative reconstruction algorithm to improve multi-slice helical CT based on tensor framelet (TF) [16], [17] regularization. The method belongs to a sparsity-regularized model-based iterative reconstruction, which is inspired by compressive sensing [18]. This paper is organized as follows: Section II provides the method details, including the minimization problem, TF regularization, and optimization algorithm for iterative multislice helical CT image reconstruction. Section III presents the validation of the proposed method for low-dose multislice helical CT in comparison with FDK and the Katsevich algorithm, with sparse-view data. Section IV summarizes this work.

II. Methods

A. Minimization Problem

The mathematical formulation of an iterative CT reconstruction can be expressed by a least-square minimization problem as

$$\mathbf{x} = \arg\min_{\mathbf{x}} \frac{1}{2}\|\mathbf{A}\mathbf{x}-\mathbf{y}\|_2^2 + \lambda R(\mathbf{x}), \tag{1}$$

where $\mathbf{x}$ is the three-dimensional image to be reconstructed with given projection data $\mathbf{y}$ and the projection matrix $\mathbf{A}$. The first term indicates the data fidelity in the L^2-norm. The second term consists of $R(\mathbf{x})$ as a regularization function with regularization parameter λ. For example, the TV norm is a popular regularization choice for sparsity-based CT image reconstruction [19], [20].

In this paper, we solve equation (1) with the given data $\mathbf{y}$ from the multislice helical CT system. The projection matrix $\mathbf{A}$ contains the helical geometry with the flying focal spot [21].

For the forward projection $\mathbf{A}$ and its adjoint $\mathbf{A}^T$, parallelized algorithms with an infinitely narrow beam are used with GPU implementation [22].

B. Tensor Framelet Regularization

Consider a 3D image $\mathbf{x}$ as a tensor,

$$\mathbf{x} = \{x_{ijk}, i \le N_x,\ j \le N_y,\ k \le N_z\}$$

where x_{ijk} is the (i,j,k)-th voxel in three-dimensional image space, N_x, N_y, and N_z are the number of voxels in the x, y and $z-$axis respectively. We define $\mathbf{x}_x$, $\mathbf{x}_y$, and $\mathbf{x}_z$ as 1D unfolded matrices of $\mathbf{x}$ along the x, y, and $z-$axes, respectively. The TF transform is constructed using the standard $1D$ framelet transform [23], e.g., the 1D piecewise linear tight frame with the following refinement masks.

$$\omega_0 = \frac{1}{4}[1\ 2\ 1],\ \omega_1 = \frac{\sqrt{2}}{4}[1\ 0\ -1],\ \omega_2 = \frac{1}{4}[-1\ 2\ -1].$$

The operator ω_0 is an averaging operator, and the two other operators ω_1 and ω_2 are the first and second differential operators, respectively. Note that ω_0 smoothes the image, while ω_1 and ω_2 enhance the edges. Define

$$\mathbf{M}_j\mathbf{x} = \frac{1}{\sqrt{3}}\begin{bmatrix} \omega_j * \mathbf{x}_x \\ \omega_j * \mathbf{x}_y \\ \omega_j * \mathbf{x}_z \end{bmatrix}, \forall j = 0,1,2,$$

where $*$ denotes the convolution operator. The TF regularization function $\mathbf{W}$ and its adjoint $\mathbf{W}^T$ are respectively defined as below.

$$\mathbf{W}\mathbf{x} = [\mathbf{M}_0\mathbf{x},\ \mathbf{M}_1\mathbf{x},\ \mathbf{M}_2\mathbf{x}]^T, \tag{2}$$

and

$$\mathbf{W}^T\mathbf{y} = \mathbf{M}_0^T(\mathbf{M}_0\mathbf{x}) + \mathbf{M}_1^T(\mathbf{M}_1\mathbf{x}) + \mathbf{M}_2^T(\mathbf{M}_2\mathbf{x}),\ \texttt{for } \mathbf{y} = \mathbf{W}\mathbf{x}. \tag{3}$$

The TF norm is defined as $\lambda\|\mathbf{W}\mathbf{x}\|_1 = \lambda_0\|\mathbf{M}_0\mathbf{x}\|_1 + \lambda_1\|\mathbf{M}_1\mathbf{x}\|_1 + \lambda_2\|\mathbf{M}_2\mathbf{x}\|_1$, where $\|\mathbf{M}_j\mathbf{x}\|_1 = \sqrt{|\omega_j * \mathbf{x}_x|^2 + |\omega_j * \mathbf{x}_y|^2 + |\omega_j * \mathbf{x}_z|^2}$, for all $j = 0, 1,$ and 2. TF transform $\mathbf{W}$ is left invertible and $\mathbf{W}^T\mathbf{W} = I$, by the simple calculation [16]. If $\lambda_0 = 0, \lambda_1 \neq 0$, and $\lambda_2 = 0$, $\|\mathbf{W}\mathbf{x}\|_1$ corresponds to the isotropic TV norm of $\mathbf{x}$. In other words, TF regularization is a high-order generalization of TV.

With the TF regularization, equation (1) becomes

$$\mathbf{x} = \arg\min_{\mathbf{x}} \frac{1}{2}\|\mathbf{A}\mathbf{x} - \mathbf{y}\|_2^2 + \lambda\|\mathbf{W}\mathbf{x}\|_1. \tag{4}$$

The TF regularization term is defined as the isotropic shrinkage TF norm [16]:

$$\lambda\|\mathbf{W}\mathbf{x}\|_1 = \sum_{l=1}^{L}\sum_{j=1}^{2}\lambda_{l,j}\|\mathbf{M}_j^l\mathbf{x}^l\|_1 + \lambda_{L,0}\|\mathbf{x}^L\|_1. \tag{5}$$

C. Optimization Algorithm

The TF regularization (5) is the summation of L1-norm. To solve the non-differentiable L_1 minimization problem (4), we choose the alternating direction method of multipliers (ADMM) [24] or the so-called Split Bregman method [25]. In general it is difficult to solve the L1-regularized minimization problem because it has non-differentiable L1 term. The basic idea of ADMM is to split L1 and L2 components by introducing auxiliary variables and split into three decoupled steps. Becuase of decoupling, we can efficiently solve it from its optimal condition by the conjugate gradient method. Note that TF is more computationally efficient than TV due to $\mathbf{W}^T\mathbf{W} = I$.

D. Quantitative Metrics

To evaluate the performance of the proposed algorithm quantitatively in comparison to FDK and the Katsevich algorithm, four different quantitative metrics are selected.

1) Image Similarity - Universal Quality Index (UQI): The Universal Quality Index (UQI) [26] was measured to evaluate the similarity between the reconstructed and true images. We considered the image from the scanner to be the true image. Given the ROI within the reconstructed and true images, the associative mean of the image μ , the variance and covariance of μ with the true image $\mu_{\texttt{true}}$ over the ROI are denoted as $\bar{\mu}$, σ^2, and $\texttt{Cov}(\mu, \mu_{\texttt{true}})$, respectively. The definition of UQI is

$$\texttt{UQI} = \frac{4\ \texttt{Cov}(\mu, \mu_{\texttt{true}})}{\sigma^2 + \sigma_{\texttt{true}}^2}\frac{\bar{\mu}\cdot\bar{\mu}_{\texttt{true}}}{\bar{\mu}^2 + \bar{\mu}_{\texttt{true}}^2}.$$

The UQI measures the intensity similarity between two images, and its value ranges $[0,1]$. A UQI value close to 1 indicates a better level of similarity between the reconstructed and true images.

2) Image Noise - SNR and CNR: To evaluate the quantitative noise level of the reconstructed images, we chose two different metrics, SNR and CNR. The definitions are as follows.

$$\texttt{SNR} = \frac{\bar{\mu}_{\texttt{ROI}}}{\sigma_{\texttt{ROI}}}$$

$$\texttt{CNR} = \frac{|\bar{\mu}_{\texttt{ROI}} - \bar{\mu}_{\texttt{ROI}_{\texttt{air}}}|}{\sqrt{\sigma_{\texttt{ROI}}^2 + \sigma_{\texttt{ROI}_{\texttt{air}}}^2}}$$

where $\sigma_{\texttt{ROI}}$ and $\sigma_{\texttt{ROI}_{\texttt{air}}}$ refer to the standard deviations and $\bar{\mu}_{\texttt{ROI}}$ and $\bar{\mu}_{\texttt{ROI}_{\texttt{air}}}$ refer to the mean pixel value in a ROI inside and the background of the phantom, respectively.

3) Image Resolution - MTF: To evaluate the resolution of the reconstructed images, MTF is calculated based on [26], [27]. An Edge Spread Function (ESF) was obtained along the profile of the red line on Figure 1. The Line Spread Function (LSF) was achieved by differentiating the ESFm and the MTF was obtained from the Fourier transformation of the LSF. Normalization was performed as MTF(0)=1.

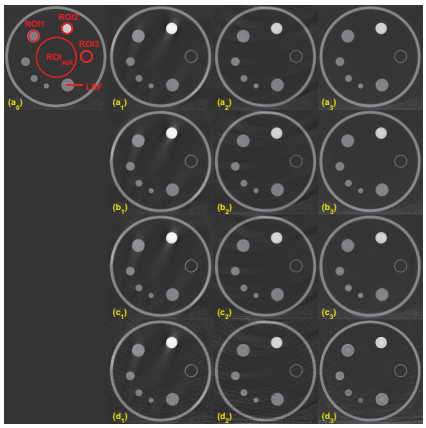

Fig. 1. Reconstucted images with various sampling step sizes. The image on (a_0) shows the three ROIs, and the red line is set for the computation of LSF for MTF. $\mathrm{ROI}_{\mathtt{AIR}}$, ROI of air, is defined to compute the CNR for ROI1-ROI3.

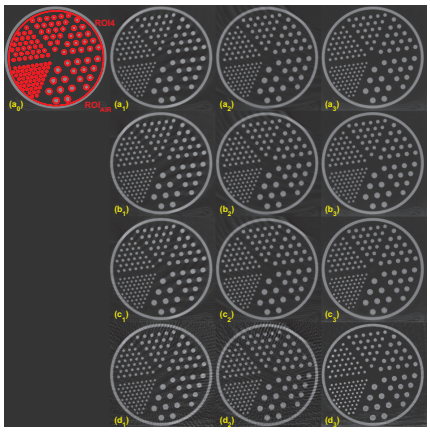

Fig. 2. Reconstucted images with various sampling step sizes. The image on (a_0) shows ROI4 and $\mathrm{ROI}_{\mathtt{AIR}}$.

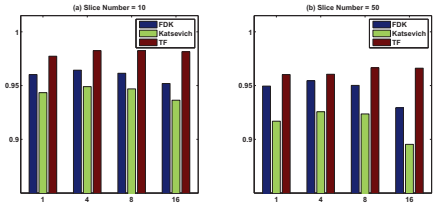

Fig. 3. Image similarity measure: UQI results for various sampling step size. (a): UQI bar plot for the 10-th slice. (b): UQI bar plot for the 50th slice.

III. Result

A. Data Acquisition

The multislice helical CT reconstruction quality was evaluated using the American College of Radiology (ACR) CT accreditation phantom (Data Spectrum Corporation. Model: ECT/DLX/P). Siemens SOMATOM Definition 64-slice helical CT scanner was used to generate the helical CT projection data. Details of the scan parameters were as follows: 100 kV voltage with 165 effective mAs, $\mathrm{CTDI}_{\mathtt{vol}}$ 6.51 mGy, and DLP 130.8 mGy-cm. There was a 3.05 *s* scan time, 0.5 *s* gantry rotation time, and $64 * 0.6$ mm collimation with z-flying focal spot. The helical pitch is set to be $p = 1$, with 2304 projections per rotation. Image volume resolution is: 2 *mm* slice thickness and 0.9766×0.9766 mm^2 axial resolution. The whole image volume has $512 \times 512 \times 88$ voxels. A 21.6 cm inside diameter cylindrical ACR phantom is used.

B. Evaluations with sparse-view data

To evaluate with sparse-view performance, we fixed the dose level at 100kV. Images were reconstructed at four different sampling steps, 1, 4, 8, and 16. The full view data has 2304 views per 360^o. Sampling step 4 was achieved by taking 576 data uniformly per 360^o. Similarly, sampling steps 8 and 16 were achieved with 288 and 144 views per 360^o, respectively. The results of the reconstruction images with different view-angles are shown in Figures 1 and 2. The images (a_0) and (b_0) are from the scanner on both figures. From the top to the bottom rows, images are reconstructed CT images by sampling steps 1, 4, 8, and 16. Each column shows images from a different reconstruction algorithm. From left to right, each column consists of images by scanner, FDK, Katsevich and the TF algorithm. As shown in the first row, reconstruction images at sampling step 1 are streak-free for all reconstruction algorithms. However, streaks appeared on the images with FDK and Katsevich for sparse-view data. The TF algorithm was the least influenced by sparsity. The last column of the Figures 1 and 2 showed that visually the TF reconstruction outperformed the other reconstruction methods. On Figure 1 (a_0) and Figure 2 (a_0), ROI's are defined as in the previous section.

For the evaluation of similarity between the reconstructed image and the scanner image, we computed the UQI for each slices 10 and 50. The ROI for the UQI is set as the whole phantom area on a given slice. Figure 3 shows the result of UQI with various sampling step sizes. Both plots (a) and (b) show that the TF algorithm achieved the highest value, which means that the image reconstructed using the TF algorithm was the most similar to the scanner image.

For the quantitative evaluation of the noise level of the reconstructed images, we computed the SNR and CNR on ROIs 14. Figure 4 shows the SNR and CNR results. The first row consists of the SNR results for ROI1-ROI4. The second row is the result of the CNR of ROI1-ROI4. Both SNR and CNR indices have a similar pattern. The TF algorithm achieved the highest SNR and CNR except for a few points in ROI2 and ROI4. For the quantitative evaluation of the image resolution, MTF is computed as described in subsection II-D3. The LSF is computed with the ROI indicated in Figure 1 (a_0). The TF algorithm achieved the highest MTF, especially when the fewest sample generated the highest MTF difference among other reconstructed methods.

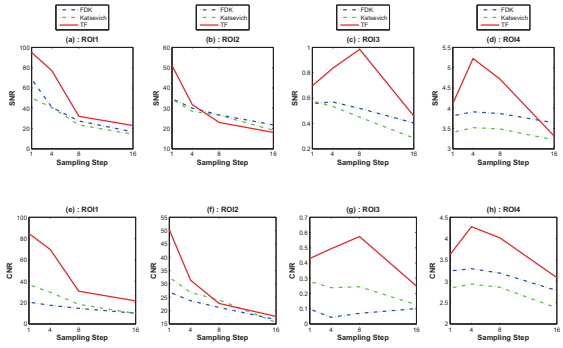

Fig. 4. Image noise measures: SNR and CNR results for the various sampling step sizes. First row: SNR result, second row: CNR results.

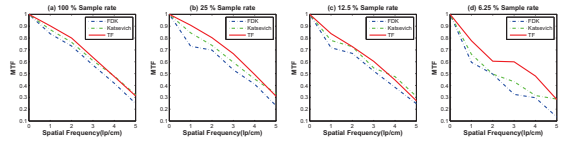

Fig. 5. Image resolution measure: Results of MTF curves with different reconstruction algorithms over various sampling levels.

IV. Conclusions

To summarize, we have successfully developed a GPU-based TF iterative image reconstruction algorithm for low-dose multislice helical CT, and have shown that the TF method provided improved image quality over the FDK and the Katsevich algorithms when dealing with sparse-view data, using UQI, SNR, CNR, and MTF measurements as evaluation metrics.

Acknowledgments

H. Nam was supported by the Basic Science Research program through NRF(#2015R1C1A2A01054731) of Korea funded by the ministry of Education Science and Technology. M. Guo and H. Gao were partially supported by the NSFC (#11405105), the 973 program (#2015CB856000), and the Shanghai Pujiang Talent Program (#14PJ1404500).

References

[1] G. Hounsfield, 1972, “A method of apparatus for examination of a body by radiation such as x-ray or gamma radiation”, US. Patent No. 1283925.

[2] I. Mori, 1986, “Computerized tomographic apparatus utilizing a radiation source”, US Patent No. 4630202.

[3] W. A. Kalender, W. Seissler, E. Klotz, P. Vock, 1990, “Spiral volumetric CT with single-breathhold technique, continuous transport, and continuous scanner rotation”, *Radiology*, 176(1), 181-183.

[4] Feldkamp, L. A., Davis, L. C., and Kress, J. W. 1984, “ Practical cone-beam algorithm”, *JOSA A*, 1(6), 612-619.

[5] Wang, G., Lin, T. H., Cheng, P. C., and Shinozaki, D. M. 1993, “A general cone-beam reconstruction algorithm”, *Medical Imaging*, IEEE Transactions on, 12(3), 486-496.

[6] I. Hein, K. Taguchi, M. Silver, M. Kazarna, and I. Mori, 2003, ”Feldkamp-based cone-beam reconstruction for gantry-tilted helical multislice CT”, *Med. Phys.*, 12, 3233-3242.

[7] K. Taguchi and H. Aradate, 1998, ”Algorithm for image reconstruction in multi-slice helical CT”, *Med. Phys.*, 25, 550-561.

[8] A. Katsevich, 2002, ”Theoretically exact filtered backprojection-type inversion algorithm for spiral CT”, *SIAM J. Appl. Math*, 62, 2012-2026.

[9] F. Noo, J. Pack, and D. Heuscher, 2003, ”Exact helical reconstruction using native cone-beam geometries”, *Phys. Med. Biol.*, 48, 3787-3818.

[10] H. Yu, and G. Wang, 2004, ”Studies on implementation of the Katsevich algorithm for spiral cone-beam CT”, *J. X-Ray Sci. Technol*, 12, 97-116.

[11] Chen, G. H. 2003, “An alternative derivation of Katsevichs cone-beam reconstruction formula”, *Medical physics*, 30(12), 3217-3226.

[12] Y. Zou and X. Pan, 2004, “Exact image reconstruction on Pi-linew from minimum data in helical cone-beam CT”, *Phys. Med. Biol.*, 49, 941-959.

[13] Zou, Y., and Pan, X. 2004, “Image reconstruction on PI-lines by use of filtered backprojection in helical cone-beam CT”, *Physics in medicine and biology*, 49(12), 2717.

[14] Ye, Y., and Wang, G. 2005, “Filtered backprojection formula for exact image reconstruction from cone-beam data along a general scanning curve”, *Medical Physics*, 32(1), 42-48.

[15] Ye, Y., Zhao, S., Yu, H., and Wang, G. 2005, “A general exact reconstruction for cone-beam CT via backprojection-filtration”, *Medical Imaging, IEEE Transactions on*, 24(9), 1190-1198.

[16] H. Gao, T. Li, Y. Lin, L. Xing, 2012, ”4D cone beam CT via spatiotemporal tensor framelet”, *Med. Phys. Letter*, 39, 6943-6946.

[17] H. Gao, X. S. Qi, Y. Gao, and D. A. Low, 2013, “Megavoltage CT imaging quality improvement on TomoTherapy via tensor framelet”, *Med. Phys.*, 40(8), 081919.

[18] Donoho, D. L. 2006, “Compressed sensing”, *Information Theory, IEEE Transactions on*, 52(4), 1289-1306.

[19] Sidky, E. Y., Kao, C. M., and Pan, X. 2006, “Accurate image reconstruction from few-views and limited-angle data in divergent-beam CT”, *Journal of X-Ray Science and Technology*, 14, 119-139.

[20] Chen, G. H., Tang, J., and Leng, S. 2008, “Prior image constrained compressed sensing (PICCS): a method to accurately reconstruct dynamic CT images from highly undersampled projection data sets”, *Medical physics*, 35(2), 660-663.

[21] Flohr, T. G., Stierstorfer, K., Ulzheimer, S., Bruder, H., Primak, A. N., and McCollough, C. H. 2005, 11Image reconstruction and image quality evaluation for a 64-slice CT scanner with z-flying focal spot”, *Med. phys.*, 32(8), 2536-2547.

[22] H. Gao, 2012, ”Fast parallel algorithms for the x-ray transform and its adjoint”, *Med. Phys.*, 39(11), 7110-7120.

[23] Dong, B., and Shen, Z. 2010, “MRA based wavelet frames and applications”, IAS Lecture Notes Series, Summer Program on The Mathematics of Image Processing, Park City Mathematics Institute, 19.

[24] Boyd, S., Parikh, N., Chu, E., Peleato, B., and Eckstein, J. (2011), “Distributed optimization and statistical learning via the alternating direction method of multipliers”, Foundations and Trends in Machine Learning, 3(1), 1-122.

[25] T. Goldstein, and S. Osher, 2009, “The Split Bregman method for L1-regularized problems”, *SIAM J. Imaging Sci.*, 2, 323-373.

[26] Y. Gao, Z. Bian, J. Huang, Y. Zhang, S. Niu, Q. Feng, W. Chen, Z. Liang, and J. Ma, 2014, “Low-dose X-ray computed tomography image reconstruction with a combined low-mAs and sparse-view protocol”, *Optics Express*, 22(12), 15190-15210.

[27] P. F. Judy, 1976, “The line spread function and modulation transfer function of a computed tomographic scanner”, *Med. Phys.*, 3(4), 233-236.

Impact of Image Constraints and Object Structures on Optimization-Based Reconstruction

Zheng Zhang, Dan Xia, Xiao Han, Emil Y. Sidky, Charles Pelizzari, and Xiaochuan Pan

***Abstract*—Image constraints play an important role in the design of optimization-based reconstruction in cone-beam computed tomography (CBCT). In this work, we investigate the impact of image constraints on optimization-based reconstructions, including constraints on image-total-variation (TV), image-ℓ_2 norm, and image-ℓ_1 norm. Furthermore, the impact is likely to be dependent upon other factors such as the anatomies of the objects to be reconstructed. Therefore, we also investigate how the impact varies for objects with distinctively different anatomies. We consider convex optimization programs with the aforementioned image constraints. In an attempt to minimize the effect of the potential algorithm variability on the investigation, we utilize the same primal-dual algorithm to solve all of the convex optimization programs considered. As expected, results show that different image constraints can impact considerably differently image reconstructions for objects with distinct anatomies.**

I. Introduction

Image constraints play an important role in the design of optimization-based reconstruction in cone-beam computed tomography (CBCT). Among numerous image constraints, image-total-variation (TV), image-ℓ_2 norm, and image-ℓ_1 norm are used widely as image constraints in the design of optimization programs. It is of theoretical as well as practical interest to investigate how image constraints impact optimization-based reconstructions. In this work, we investigate specifically the impact of constraints on image-total-variation (TV), image-ℓ_2 norm, and image-ℓ_1 norm on their respective reconstructions. Furthermore, the impact is likely to be dependent upon other factors such as the anatomies of the objects to be reconstructed. Therefore, we also investigate how the impact varies for objects with distinctively different anatomies.

We form, without loss of generality, three optimization programs consisting of a data fidelity term, which is the L2 norm of the discrepancy between measured data and the image model, and one of the three aforementioned image constraints. Therefore, the programs are convex, and image reconstructions are accomplished through solving the programs. In an attempt to minimize the effect of the potential algorithm variability on the investigation, we utilize the same primal-dual algorithm developed by Chambolle and Pock (CP) [1] to solve all of the convex optimization programs considered. The CP algorithm has been shown to be capable of handling effectively system matrix of large size of practical CT interest [2].

In an effort to investigate the impact of the image constraints on reconstructions of objects with distinct anatomies, we have performed reconstructions for a digital-subtraction-angiography (DSA) image and a Rando-phantom image. As expected, results show that different image constraints can impact considerably differently image reconstructions for objects with distinct anatomies.

Z. Zhang, D. Xia, Xiao Han, and E. Y. Sidky are with the Department of Radiology, the University of Chicago.

C. Pelizzari is with the Department of Radiation & Cellular Oncology, the University of Chicago.

X. Pan is with Departments of Radiology and Radiation & Cellular Oncology, the University of Chicago.

II. Materials and Methods

A. CBCT Imaging Systems and Data Acquisition

In this work, we collect data from two objects with different levels of sparsity by using two cone-beam CT (CBCT) scanners.

a) Rando-Phantom Study: We first investigate reconstructions from data of a Rando phantom collected with an onboard CBCT imager in a radiation therapy system. The CBCT imager consists of a flat-panel detector composing of 1024×768 bins of size 0.388×0.388 mm^2. The distances from the source to the rotation axis, and to the flat-detector surface, are 100 cm and 150 cm, respectively. The data were collected at 353 projections, uniformly distributed over a short-scan angular range of 196 degrees.

b) DSA-Data Study: For demonstration purpose, we also reconstruct images a set of existing DSA data collected with a clinical C-arm CBCT system. The detector of the C-arm CBCT system composes of 1024×1024 bins of size 0.194×0.194 mm^2, and the source-to-rotation-axis distance is about 70 cm, and the source-to-detector distance is about 110 cm. The DSA data set contains 108 projections acquired over an angular range of approximately 200 degrees.

B. Optimization-Based Reconstruction

In the optimization-based reconstruction considered, the model data $\mathbf{g}_0$ and image $\mathbf{f}$ are vectors with M pixels and N voxels, respectively, and they are related through a discrete-to-discrete (D-D) linear model, i.e.,

$$\mathbf{g}_0 = \mathcal{H}\mathbf{f}. \tag{1}$$

$\mathcal{H}$ denotes the system matrix of size $M \times N$.

In an optimization-based reconstruction, the optimization program specifies a set of feasible solutions (i.e., the images,) which may be obtained by use of algorithms to solve the optimization program. In this work, let $D_{\ell_2}(\mathbf{f}) = ||\mathbf{g} - \mathcal{H}\mathbf{f}||_2^2$ denote the data-ℓ_2 norm, where $\mathbf{g}$ indicate the measured data; and we consider optimization programs in which the data-ℓ_2 norm is minimized under different image constraints, respectively. Specifically, the programs considered include

a) Program D_{ℓ_2}-$||\mathbf{f}||_{TV}$: image-TV-constrained data-ℓ_2 minimization

$$\mathbf{f}^* = \underset{\mathbf{f}}{\operatorname{argmin}} D_{\ell_2}(\mathbf{f}) \;\; \text{s.t.} \;\; ||\mathbf{f}||_{TV} \leq t_1 \;\; \text{and} \;\; f_j \geq 0, \quad (2)$$

where $||\mathbf{f}||_{TV} = ||\,|\nabla \mathbf{f}|\,||_1$ denotes the image TV, ∇ a matrix representing a finite differencing approximating to the image gradient, and $t_1 \geq 0$ a pre-selected image-TV-constraint parameter.

b) Program D_{ℓ_2}-$||\mathbf{f}||_{\ell_2}$: image-ℓ_2-constrained data-ℓ_2 minimization

$$\mathbf{f}^* = \underset{\mathbf{f}}{\operatorname{argmin}} D_{\ell_2}(\mathbf{f}) \;\; \text{s.t.} \;\; ||\mathbf{f}||_{\ell_2} \leq l_2 \;\; \text{and} \;\; f_j \geq 0, \quad (3)$$

where $||\mathbf{f}||_{\ell_2} = \sum_{j=1}^{N} f_j^2$ denotes the image-ℓ_2-constraint, and l_2 a pre-selected image-ℓ_2-constraint parameter.

c) Program D_{ℓ_2}-$||\mathbf{f}||_{\ell_1}$: image-ℓ_1-constrained data-ℓ_2 minimization

$$\mathbf{f}^* = \underset{\mathbf{f}}{\operatorname{argmin}} D_{\ell_2}(\mathbf{f}) \;\; \text{s.t.} \;\; ||\mathbf{f}||_{\ell_1} \leq l_1 \;\; \text{and} \;\; f_j \geq 0, \quad (4)$$

where $||\mathbf{f}||_{\ell_1} = \sum_{j=1}^{N} |f_j|$ denotes the image-ℓ_1-constraint, and l_1 a pre-selected image-ℓ_1-constraint parameter.

The optimization programs described above are convex, and they can thus be solved with numerous algorithms, including the CP algorithms. In this work, we apply the CP algorithm to reconstructing images through solving the programs.

C. Reconstruction Parameter Selection

In a practical reconstruction, numerous parameters can impact the final reconstruction. Program parameters are needed for specifying the optimization program; algorithm parameters are used for determining the convergence path; and and convergence parameters are considered for designing practical convergence conditions.

Program parameters: Image-voxel size, system matrix $\mathcal{H}$, and image-constraint parameters t_1, l_2, or l_1 are key to specifying the programs, among the numerous program parameters necessary for specifying the programs. The selection of program parameters can significantly affect the properties of reconstructions. In this work, we employ a ray-driven projection model to calculate elements of the system matrix $\mathcal{H}$. In the Rando-phantom DSA-data studies, we reconstruct images with isotropic voxels of sizes 0.488 mm and 0.247 mm, respectively. Parameters t_1, l_2, and l_1 are selected based largely on visual evaluation. Due to the limited space, we show reconstructions obtained only with one value of t_1, l_2, or l_1 used in optimization program in Eqs. 2-4, respectively, and will report reconstructions obtained with additional program parameters at the conference.

Algorithm parameters: Algorithmic parameters in the CP algorithm affects the convergence path and rate. Due to the limited space, we will discuss the algorithm parameters in the conference.

Convergence parameters: Convergence parameters are used to check whether the final reconstruction satisfies the convergence conditions of the designed optimization program. In this work, the convergence conditions considered include the estimated D_{ℓ_2}, conditional primal-dual gap [2], and estimated image-TV, or image-ℓ_2 and image-ℓ_1. Details will be reported in the conference.

III. Results

a) Rando-Phantom Study: We first perform image reconstructions from Rando-phantom data and show the results in Fig. 1. It can be observed that the reconstruction with an image-TV constraint in the left panel of of Fig. 1 shows suppressed noise in the background and sharper bony structures. While the reconstruction with the image-ℓ_2 constraint appears to be similar to the image-TV reconstruction, it contains a considerably noisy background and bony structures with somewhat degraded the spatial resolution. On the other hand, reconstruction with image-ℓ_1 constraint, shown in the right panel, possesses noisy, sprinkled-salt texture. This is likely duo to the fact that the structure of the Rando-phantom image is substantially non-sparse, because it is well-known that image-ℓ_1 constraint promotes solutions with sparse structures. For cases considered, image constraints appear to impact reconstruction textures significantly when the object is non-sparse.

b) DSA-Data Study: Using the CP algorithm, we also reconstructed images from the DSA data, and show the results in Fig. 2. Images in the top row are displayed with a window [0.0, 0.5] cm^{-1} for showing the background detail, whereas images in the bottom row are shown by using a window [0.1, 0.5] cm^{-1} for visualizing the blood vessels only. We observe that reconstructions obtained by use of image-TV, image-ℓ_2, and image-ℓ_1 constraints show visual differences much less significant than those in reconstructions of the Rando-phantom images, which have much less sparser anatomies than the DSA images. The image reconstructed with image-TV constraint seems to have cleaner background than the other two. However, as shown in the bottom row, when the background noise is thresholded out, reconstructions with all three image constraints become comparable to each other with vessels well illustrated.

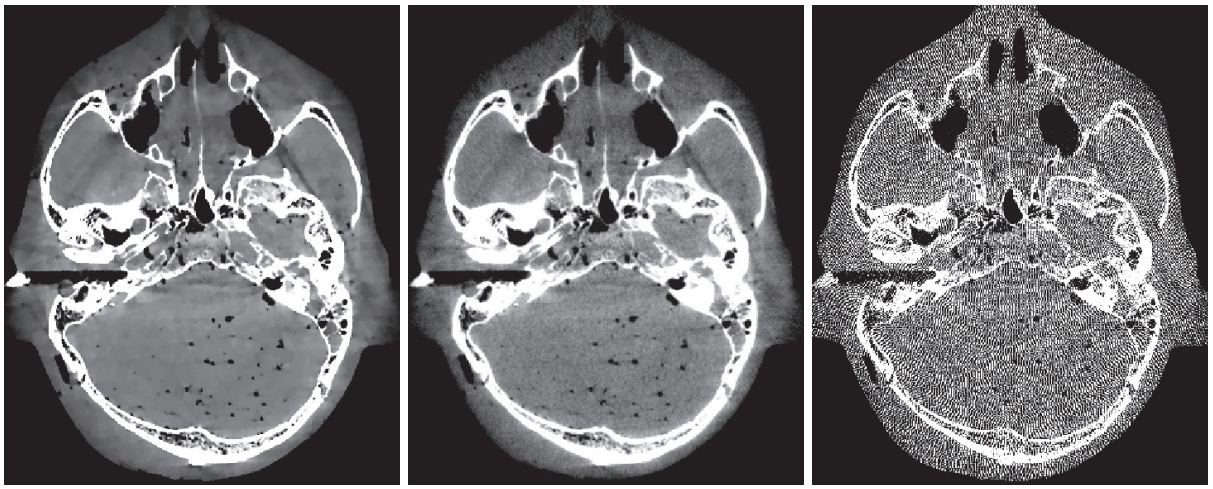

D_{ℓ_2}-$||\mathbf{f}||_{TV}$ D_{ℓ_2}-$||\mathbf{f}||_{\ell_2}$ D_{ℓ_2}-$||\mathbf{f}||_{\ell_1}$

Figure 1. A transverse slice in the Rando image reconstructed by use of the CP algorithm solving optimization programs D_{ℓ_2}-$||\mathbf{f}||_{TV}$, D_{ℓ_2}-$||\mathbf{f}||_{\ell_2}$, and D_{ℓ_2}-$||\mathbf{f}||_{\ell_1}$. Display windows: [0.2, 0.35] cm^{-1}.

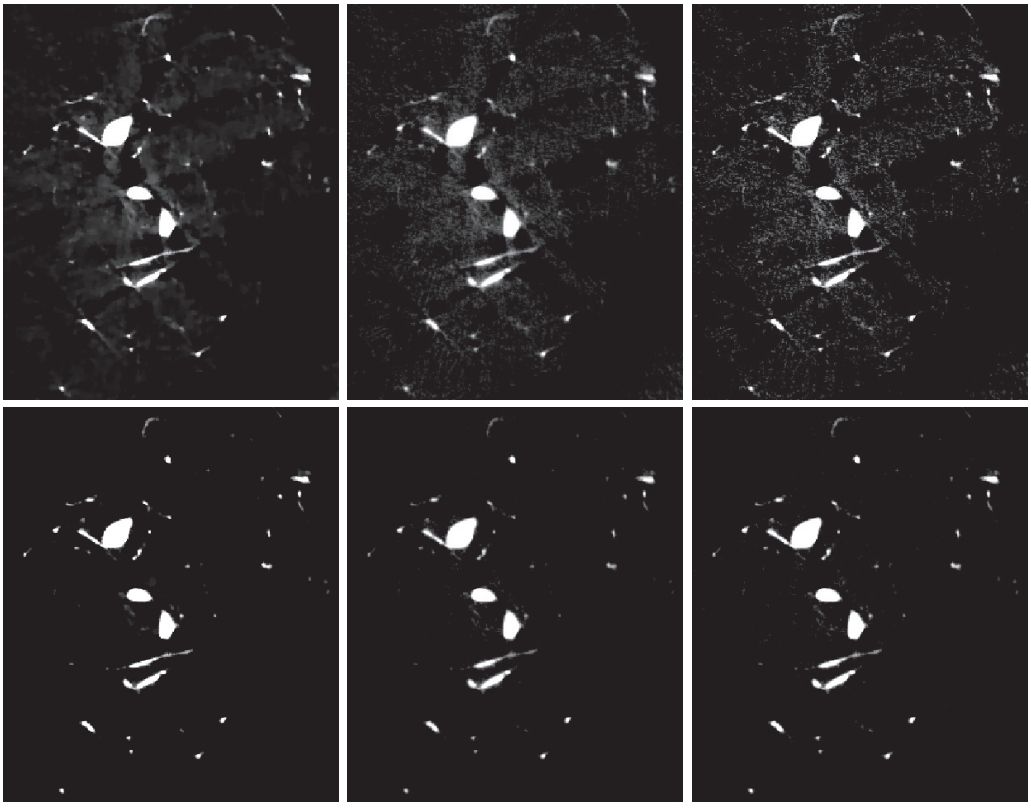

D_{ℓ_2}-$||\mathbf{f}||_{TV}$ D_{ℓ_2}-$||\mathbf{f}||_{\ell_2}$ D_{ℓ_2}-$||\mathbf{f}||_{\ell_1}$

Figure 2. A transverse slice in the DSA image reconstructed by use of the CP algorithm solving optimization programs D_{ℓ_2}-$||\mathbf{f}||_{TV}$, D_{ℓ_2}-$||\mathbf{f}||_{\ell_2}$, and D_{ℓ_2}-$||\mathbf{f}||_{\ell_1}$. Display windows: [0.0, 0.5] cm^{-1} (top row) and [0.1, 0.5] cm^{-1} (bottom row).

IV. Discussions

In this work, we have investigated optimization-based problems with different designs of image constraints, and studied how the image constraints may impact the reconstruction for objects with different levels of sparsity. We employ a primal-dual algorithm, which has been proved mathematically to solve many convex optimization programs, especially for those under consideration in this abstract. Visual inspection of study results reveals that, reconstructions based upon D_{ℓ_2}-$||\mathbf{f}||_{TV}$ show suppressed noise/artifacts and enhanced resolution, for both sparse and non-sparse objects; while reconstructions based upon D_{ℓ_2}-$||\mathbf{f}||_{\ell_1}$ seem to be able to reconstruct images with reasonable visual quality only when the object is sparse. Conversely, reconstructions based upon D_{ℓ_2}-$||\mathbf{f}||_{\ell_2}$ appear to be comparable to that obtained with D_{ℓ_2}-$||\mathbf{f}||_{TV}$, but with higher noise level and degraded spatial resolution.

The study suggests that different image constraints in optimization-based reconstructions may yield images with distinct properties for the same object. Moreover, impact of image constraints on reconstructions may vary for objects with different anatomies. It is worth noting that, the behavior of the optimization-based reconstruction may also depend on other factors, such as program parameter selection and data condition.

V. Acknowledgments

This work was supported in part by NIH R01 Grant Nos. CA158446, CA182264, and EB018102. The contents of this article are solely the responsibility of the authors and do not necessarily represent the official views of the National Institutes of Health.

References

[1] A. Chambolle and T. Pock, "A first-order primal-dual algorithm for convex problems with applications to imaging," *J. Math. Imag. Vis.*, vol. 40, pp. 1 – 26, 2011.

[2] E. Y. Sidky, J. H. Jørgensen, and X. Pan, "Convex optimization problem prototyping for image reconstruction in computed tomography with the Chambolle–Pock algorithm," *Phys. Med. Biol.*, vol. 57, no. 10, p. 3065, 2012.

Study of the possibilities of Surface-Constrained Compressed Sensing (SCCS) Method for Limited-View Tomography in CBCT systems

Claudia de Molina, Juan FPJ Abascal, Manuel Desco, Mónica Abella

Abstract— **Limited view tomography has many potential applications in Cone Beam Computed Tomography systems (CBCT) such as in dental imaging or surgical scenarios where the detector-source pair movements are limited, in dynamic studies to accelerate the acquisition, or simply to reduce the dose. Traditionally, this problem has been approached as a TV reconstruction problem but some recent works suggest that the use of prior information highly improves the image quality and removes the artifacts due to the lack of data.**

We present a study of the possibilities of limited-view acquisition using a new Surface-Constrained Compressed Sensing (SCCS) method for CBCT based on the Split Bregman algorithm. It takes advantage of the surface information of the sample as an imposed constraint to help in the recovery of the contour of the sample and in the definition of the other edges and details.

The SCCS method presents low computational time through GPU-accelerated kernels and high flexibility as it allows reconstructing non-standard limited-view geometries. Besides, being based on the Split Bregman algorithm, SCCS presents low memory requirements, easy incorporation of additional regularization terms, and the independence of the regularization parameters from the acquisition protocol.

We generated simulated data from real acquisitions of two different small animal studies considering different span angles and number of projections. Results show the improvement of the image quality in terms of detail definition and contour recovering when using the SCCS method compared with the FDK and TV-based reconstruction methods for CBCT scenarios.

Index Terms— **CT, limited-view tomography, surface, envelope, constraint**

I. Introduction

The limited-view reconstruction with analytics approaches results in images with severe artifacts: streaks, lack of definition of the edges and object distortion. The reconstruction problem of such incomplete data sets implies severely ill-posed inverse problems hindering the application of analytic FDK-like methods. For this reason, it is advisable to use iterative methods that include prior information such as sample-based priors or structural priors in order to compensate the lack of data in most of the directions. Prior image constrained compressed sensing (PICCS) has been widely applied and explored in Cone Beam Computed Tomography (CBCT) but the direct extrapolation to the limited-view tomography is not so obvious due to the lack of a good prior image.

In some recent works the limited-angle problem has been solved using Total Variation (TV) regularization [1-4]. The TV problem can be efficiently solved with the Split Bregman formulation, which has been shown to be optimum for solving constrained problems with L1 regularization terms [5-8]. In a previous work [9], we presented a preliminary study of the use of limited view acquisition possibilities showing acceptable results in the center of the sample but the contour of the sample was not well recovered due to the lack of the perpendicular data to the edges. To compensate that limitation, shape-information based methods have been previously used in a few works from different fields such as Fluorescence Molecular Tomography [10], Electron tomography [11], Multimodal Image Reconstruction [12], or object-based reconstruction [13]. In [14] a shape mask is first reconstructed and then applied to obtain optical tomographic images with a large limited span. However, its use for limited angle CBCT solving the TV minimization problem has not been explored and optimized.

In this work we present a study of the limited view acquisition possibilities offered using a new surface-constrained compressed sensing (SCCS) method for CBCT. The proposed method includes prior information of the envelope of the object under study as an imposed constraint using the Split Bregman formulation [5]. This approach can be applicable to any CBCT system such as preclinical CT to speed up the acquisition in dynamic studies; 3D dental imaging, mammography systems or the new generation of cone-beam C-arms (such as Ziehm Vision2 Vario 3D) where the span angle is often limited.

We evaluate the surface-constrained method with simulated cone-beam data generated from two different small animal

Manuscript submitted January 25th 2016.

Claudia de Molina, Juan FPJ Abascal, Manuel Desco and Mónica Abella are with the Biomedical Engineering Department, University of Carlos III, Madrid, Spain and with the Instituto de Investigación Sanitaria Gregorio Marañón (IiSGM), Madrid, Spain (e-mail: mabella@ing.uc3m.es)

M. Desco is also with the Centro de Investigación en Red de Salud Mental (CIBERSAM, CIBER CB07/09/0031), 28007 Madrid, Spain.

This work was funded by the projects IDI-20130301, TEC2013-47270-R, IPT- 2012-0401-300000, RTC-2014-3028-1 and the Cardiovascular Research Network (RIC, RD12/0042/0057) from the Spanish Ministerio de Economía y Competitividad (www.mineco.gob.es/).

studies (head and abdomen) considering different scenarios where the span angle and the number of projections are limited.

II. MATERIALS AND METHODS

A. Reconstruction algorithm

The reconstruction problem used in the previous work [9] follows the idea of the isotropic Total Variation (TV) minimization:

$$\min\|\nabla(u)\|_1 \text{ s.t. } \|Au-f\|_2{}^2 < \sigma^2$$
$$\|\nabla(u)\|_1 = \sqrt{(\nabla_x u)^2 + \left(\nabla_y u\right)^2} \quad (1)$$

where u is the reconstructed image, $\nabla_x u$ and $\nabla_y u$ are the gradients of u along the x and y directions, A is the system matrix, f is the acquisition data and σ^2 is the data noise. Following the TV minimization, we propose a new surface-constrained compressed sensing (SCCS) method based on the minimization of the total variation subject to a support constraint, which contains the surface a-priori information and the data penalty function formulated as:

$$\min\|\nabla(u)\|_1 \text{ s.t. } u \in \Omega, \|Au-f\|_2{}^2 < \sigma^2 \quad (2)$$

where Ω is the subspace that corresponds with the support of the sample.

Using the Split Bregman formulation [5], L1-constrained optimization problems can be efficiently solved by converting equation (2) into a sequence of unconstrained problems:

$$\left(u^{k+1}, dx^{k+1}, dy^{k+1}, v^{k+1}\right) = \min\|(dx, dy)\|_1 + \frac{\mu}{2}\left\|Au - f^k\right\|_2^2 + \frac{\lambda}{2}\left\|dx - \nabla_x u - {b_x}^k\right\|_2^2 + \frac{\lambda}{2}\left\|dy - \nabla_y u - {b_y}^k\right\|_2^2 + \phi(v \in \Omega) + \frac{\gamma}{2}\left\|v - u - {b_v}^k\right\|_2^2 \quad (3)$$

$$f^{k+1} = f^k + f - Au^{k+1} \quad (4)$$

$${b_x}^{k+1} = {d_x}^k + \nabla_x u^{k+1} - {d_x}^{k+1} \quad (5)$$

$${b_y}^{k+1} = {d_y}^k + \nabla_y u^{k+1} - {d_y}^{k+1} \quad (6)$$

$${b_v}^{k+1} = {b_v}^k + u^{k+1} - v^{k+1} \quad (7)$$

where μ, λ and γ are regularization parameters. The equation (3) leads to several sub-problems: one that contains only L2 norm terms and the rest (with the L1 terms) that are solved using analytical formulas. Equations (4-7) are the Bregman iterations that impose constraints for data, total variation and support, respectively.

The SCCS method is partially implemented in Matlab and it makes use of GPU-accelerated kernels. Thanks to its flexibility design, it is possible to reconstruct non-standard limited-view cone beam geometries considering the exact position of source-detector pair.

For our experiments we compared the proposed SCCS method defined in (3), (4) and (5) with TV method (without surface prior) and FDK reconstruction, which is the conventional method used in cone-beam scanners. For TV and SCCS we used μ=2, λ=1, γ= 10^{-2} and α=10^{-4} (for details about how to select these parameters we refer to [5-7]).

B. System under study and simulated data

The experiments are based on a small animal μCBCT system by Sedecal available at our laboratory [15] with the geometry described in Fig. 1. Limited-view data were simulated from the two real small animal studies shown in Figure 2. The complete data set were 360 projections of 520x520 pixels (0.2 mm pixel size). These data were reconstructed with an FDK-based method [16] obtaining a volume of 520x520x570 pixels (pixel size: 0.125 mm).

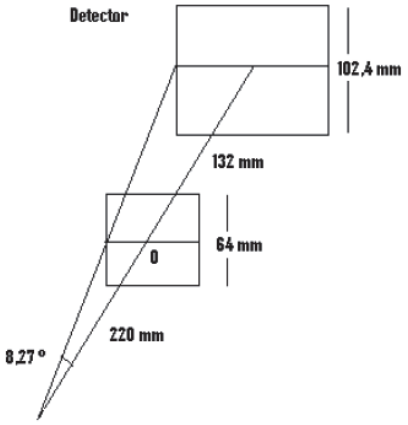

Fig. 1. Geometry of the micro CBCT system under study

Different limited-view acquisitions were simulated using a multiple-GPU parallel implementation of a voxel-driven projector.

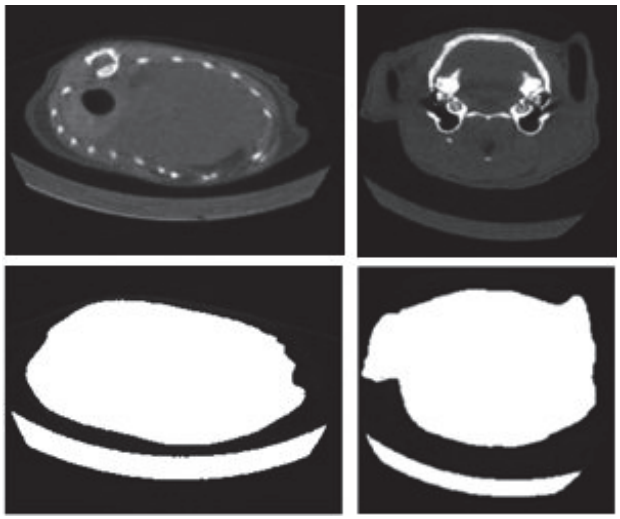

Fig. 2. Top: Axial slice of abdomen study of 520x520 pixels (left) and head study of 520x520 pixels (right). Bottom: support masks extracted from the top studies by basic morphological operations

Three different limited view acquisition protocols were performed in order to present the benefits of using the shape constraint in different limited view cases (Fig. 3): (a) span angle of 90 degrees, (b) a more complicated scenario where non-consecutive and symmetric projections are acquired,

specifically, two sets separated by 90 degrees with a span angle of 45 degrees for each group, (c) same span angle but with data generated from the views where most of the edges are perpendicular to the rays direction.

All of those data sets were reconstructed using the FDK, the TV algorithm and the proposed SCCS method in order to perform a preliminary qualitative comparison.

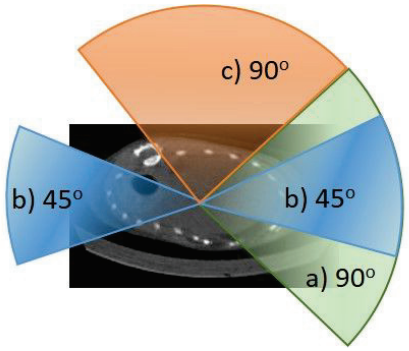

Fig. 3. Scheme that represents the angle spans used for each experiment.

C. *Results*

Left column of Fig. 4 shows the abdomen for the span angle of 90 degrees (case a)) with the FDK, TV and SCCS methods. With the surface-constrained method the contour of the study is well recovered and the definition of the details inside is enhanced compared with the standard TV method. Both TV and SCCS reduce the streak artifacts in a similar way but the contour and the details inside are better recovered with the SCCS method.

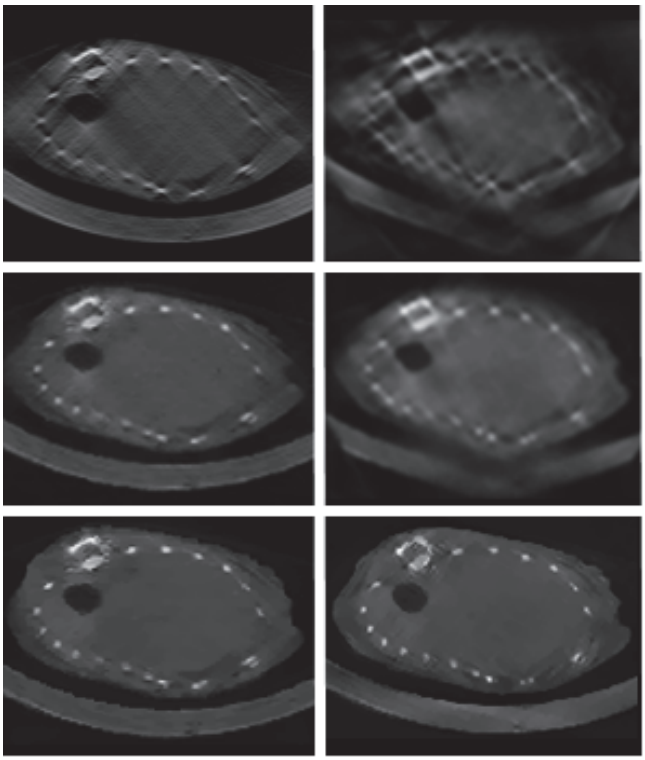

Fig. 4. From top to bottom: FDK, TV and SCCS reconstructions of the abdomen study for a span angle of 90 (left column) and a span angle of 90º divided into two different groups, {30º -75º} and {120º -165º} (right column).

Right column of Fig. 4 shows the results for the abdomen study for the limited-view acquisition protocol where the data set is separated by 90 degrees in two groups (case b). With the TV method the streaks are reduced but with the SCCS method the streaks are completely removed and the shape and edges definition is highly improved compared to the FDK and TV reconstructions.

Fig. 5 shows the results for the most complicated scenario (case c) where the simulated data is perpendicular to most of the edges. In this case, the image quality is highly enhanced in terms of the definition of the bone details, the shape and the streaks reduction.

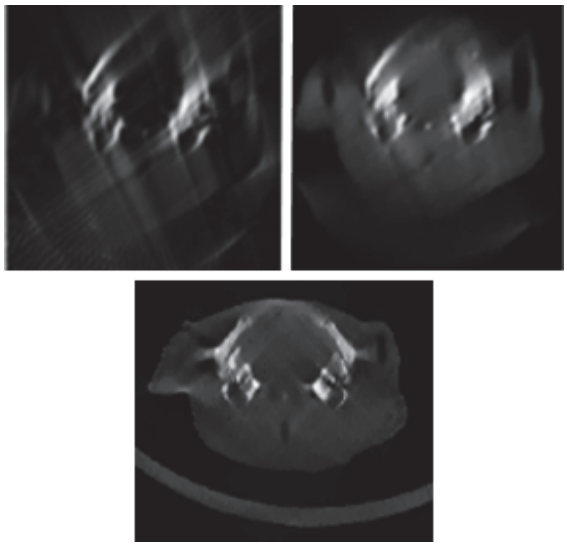

Fig. 5. Central slice of the head study reconstructed with FDK (top-left), TV (top-right) and SCCS (bottom) for same angular span (90º) with a uniform sampling of 1 but centered in the top view.

III. DISCUSSION AND CONCLUSIONS

We have presented a preliminary study of the possibilities of limited–view acquisition using a new surface constrained iterative method for CBCT with two different small animal studies. Results show an image enhancement when using the SCCS proposed method compared with the FDK and the TV reconstruction in terms of details and contour definition.

For a span of 90 degrees, the results for the simplest study (abdomen) show a better definition of the details and the edges. In situations in which it is not possible to acquire consecutive projections, for example in the case of a surgery where the patient monitoring equipment may block the rotation of the C-arm, two non-consecutive sets of projections may result in good quality reconstructed images when using the surface constrained SCCS method, not possible with the regular TV and FDK. Finally, for the last scenario where the collected data is perpendicular to most of the edges in the head study, the contour and the edge definition are highly enhanced when using the SCCS method compared with the results of FDK and TV methods.

The enhancement is obtained by using the surface of the sample as a prior, which can be obtained easily with a portable 3D scanner. Results presented in this work were obtained assuming that the sample surface is perfectly known. The effect of possible errors in the estimation of the surface as well

as the real implementation will be studied in future work. However, we expect that as long as the estimated surface is larger than real one (overestimated support), the support will guided the reconstruction method proving enhanced results.

REFERENCES

[1] J. Velikina, S. Leng, G-H. Chen, "Limited view angle tomographic image reconstruction via total variation minimization", Proc. SPIE 6510, Medical Imaging 2007: Physics of Medical Imaging, 651020

[2] X. Duan, L. Zhang, Y. Xing, Z. Chen, J. Cheng, "Few-view projection reconstruction with an iterative reconstruction-reprojection", IEEE Transactions on Nuclear Science, 56 (3): 1377-1382, 2009

[3] E. Y. Sidky, C-M. Kao, X. Pan, "Accurate image reconstruction from few-views and limited-angle data in divergent-beam CT", Medical Physics, 25(7): 1772–1782, 2009

[4] V Kolehmainen, S Siltanen,SJarvenp J P Kaipio1 , P Koistinen , M Lassas , J Pirttila¨ and E Somersalo. Statistical inversion for medical x-ray tomography with few radiographs: II. Application to dental radiology, Phys. Med. Biol. 48 (2003) 1465–1490

[5] T Goldstein, S. Osher, "The Split Bregman Method for L1-Regularized Problems", SIAM Journal on Imaging Science, 2009

[6] JFP-J Abascal, Judit Chamorro-Servent, Juan Aguirre, Simon Arridge, Teresa Correia, Jorge Ripoll, Juan José Vaquero, Manuel Desco, Fluorescence diffuse optical tomography using the split Bregman method, Medical Physics 2011, 38 (11) 6275-6284

[7] J F P J Abascal, M Abella, A Sisniega, J J Vaquero, and M Desco. Investigation of different sparsity transforms for the PICCS algorithm in small-animal respiratory gated CT. PLOS ONE 10(4): e0120140, 2015. DOI: 10.1371/journal.pone.0120140

[8] Vandeghinste, Bert, Bart Goossens, Jan De Beenhouwer, Aleksandra Pizurica, Wilfried Philips, Stefaan Vandenberghe, and Steven Staelens. 2011. "Split-Bregman-based Sparse-view CT Reconstruction." InFully 3D 2011 Proceedings, 431–434.

[9] C de Molina, J F P J Abascal, J Pascau, M Desco, M Abella. Evaluation of the Possibilities of Limited Angle Reconstruction for the use of Digital Radiography System as a Tomograph. IEEE Nuclear Science Symposium and Medical Imaging Conference (2014 NSS/MIC), 2014.

[10] Daifa Wang, Jin He, Huiting Qiao, Xiaolei Song, Yubo Fan, Deyu Li, High-Performance Fluorescence Molecular Tomography through Shape-Based Reconstruction Using Spherical Harmonics Parameterization, Plos One, April 14, 2014

[11] Gopinath A1, Xu G, Ress D, Öktem O, Subramaniam S, Bajaj C. Shape-based regularization of electron tomographic reconstruction. IEEE Trans Med Imaging. 2012 Dec;31(12):2241-52.

[12] Daniil Kazantsev , William R. B. Lionheart, Philip J. Withers, Peter D. L ee, Multimodal Image Reconstruction Using Supplementary Structural Information in Total Variation Regularization, Sensing and Imaging, 2014.

[13] G. Gaullier, ; Lab. Regional des Ponts et Chaussees, ERA 27 LCPC, Strasbourg, France ; Charbonnier, P. ; Heitz, F. Introducing shape priors in object-based tomographic reconstruction, 2009 16th IEEE International Conference on Image processing (ICIP)

[14] W. Krauze, P. Makowski, M. Kujawińska, Total Variation Iterative Constraint algorithm for limited-angle tomographic reconstruction of non-piecewise constant structures, Proc. SPIE 9526, Modeling Aspects in Optical Metrology 2015

[15] J. J. Vaquero, et al., "Assessment of a New High-Performance Small-Animal X-ray Tomograph," *IEEE Trans. Nucl. Sci.,* vol. 55, pp. 898-905, 2008.

[16] Abella, M., J.J. Vaquero, A. Sisniega, J. Pascau, A. Udías, V. García, I. Vidal, and M. Desco, Software Architecture for Multi-Bed FDK-based Reconstruction in Xray CT Scanners. Computer methods and programs in biomedicine, 2011. (in press). 685618.

Acquisition and reconstruction of optimal trajectories for cone-beam x-ray CT

Andrew Kingston, Glenn Myers, Shane Latham,
Thomas Heyang Li and Adrian Sheppard
Department of Applied Mathematics
Research School of Physics and Engineering
The Australian National University
Email: andrew.kingston@anu.edu.au

Trond Varslot
FEI Trondheim
Stiklestadveien 1 N-7041
Norway
Email: trond.varslot@fei.com

***Abstract*—We present a new, inherently discrete type of trajectory for cone-beam CT in which the goal is to improve quality and efficiency by sampling the space of possible source locations in the most uniform manner possible. Such trajectories are optimal in the sense of producing projection sets with the highest level of mutually independent data, and in being as isotropic as possible when considering viewing angles from within the object. Critically for applications, the trajectories also allow for fast iterative reconstruction, accelerated by shift-invariant filtering applied to the reconstruction volume. The new approach provides high acquisition efficiency and reduced artifacts while bring the flexibility of iterative reconstruction to very large datasets. A combination of the new trajectory with fast iterative reconstruction is demonstrated on very large datasets of greater than 30 billion reconstructed voxels.**

I. Introduction

In many forms of cone beam tomography it is desirable to work at a high cone angle to maximise the flux emerging from the point source. While low cone-angle tomography can be performed via approximations such as the Feldkamp-Davis-Kress method for circular scanning [1], the circle trajectory is fundamentally incomplete and does not provide sufficient information for reconstruction from high cone-angle data. Performing high cone-angle reconstructions demands a scanning trajectory that involves motion of the source in two dimensions relative to the scanned object, commonly achieved by allowing object translation perpendicular to the plane of rotation. Such scanning trajectories are considered complete if they satisfy Tuy's sufficiency criterion [2], which states in essence that a trajectory is complete if all planes which cut the object also intersect the scanning trajectory.

One important class of trajectories that satisfy Tuy's condition are helical trajectories, for which a theoretically exact reconstruction formula of the filtered backprojection (FBP) type was found by Katsevich in 2001 [3]. The Katsevich formula was utilised in an X-ray micro-tomography instrument developed at the Australian National University that incorporated helical scanning with very high cone-angles [4]. Numerous issues needed to be overcome to produce high-quality images from that instrument, and work at this facility also highlighted certain fundamental shortcomings of the helical trajectory [5]. One shortcoming is that, for a helical trajectory, the average magnification experienced by each voxel is not constant, leading to blurry regions in the reconstructed object and nonuniform levels of noise. This is a consequence of the fact that at any given moment the parts of the object that are closer to the sample are subject to a much higher geometric magnification than those parts that are further away. At the cone angle of 60° in standard use at the abovementioned facility, the maximum difference in magnification is a factor of three. This issue was ameliorated through the use of a 'double' helix trajectory [6]. Other issues with helical scanning trajectories include: low detector utilisation, since at high cone angles more than half of the detector falls outside the Tam-Danielsson window [7], [8] and is therefore redundant data that needs to be masked away [6], and a high sensitivity to geometric misalignment of the apparatus, with slight misalignment and trajectory errors manifesting as "streak" artifacts. [9]

These problems are largely a consequence of the fact that a helical scanning trajectory is anisotropic, i.e. highly nonuniform when viewed from the perspective of a point within the object [6]. The double-helix trajectory improves symmetry and thus reduces anisotropy, and other more isotropic trajectories include lower-pitch helices such as the 3PI trajectory [10]. Both methods lengthen the required scanning path and therefore increase the number of projections that must be acquired to produce artifact-free reconstruction through FBP.

Tuy's sufficiency condition only makes sense by considering scanning trajectories as lines in which the sampling density along the line is high enough to satisfy the Nyquist sampling condition - i.e. the angular spacing between adjacent source points is comparable to the angular spacing between adjacent detector pixels. Theoretically exact reconstruction schemes (e.g. of the FBP type) require such dense sampling along the acquisition path, but iterative reconstruction methods liberate us from this constraint. Iterative reconstruction offers great possibilities for artifact reduction and for new imaging modalities [11], particularly the incorporation of a-priori information about the object [12], [13]. To date, iterative reconstruction methods have been aimed primarily at allowing tolerable reconstruction quality from noisy or sparse data as is obtained from PET, SPECT or electron tomography [14]. In these situations, it is necessary to use extremely robust but slowly

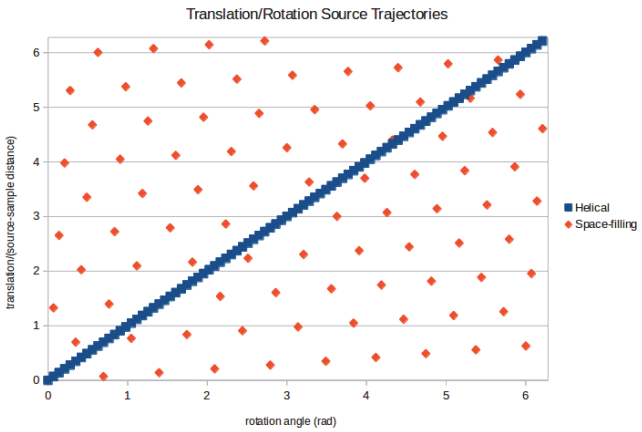

Fig. 1. The depiction of a traditional helical x-ray source trajectory [blue] compared with a space-filling trajectory [red] in the space of possible source locations for a (z, θ) scanning apparatus.

converging reonstruction algorithms such as the Simultaneous Iterative Reconstruction Technique (SIRT). The focus of the current work is the production of detailed, high quality images from very large industrial- and micro-CT data sets, which demands a more computationally efficient iterative reconstruction scheme. In this context, speed of convergence can be prioritised over robustness. Recent increases in affordable compute power, particularly through the use of graphical processing units (GPUs) that may contain over 10,000 processor cores, are making iterative reconstruction practical in many contexts [14], [15], although, to our knowledge, there has been no application to full-scale multi-Gigavoxel images up to this time.

II. Space Filling Scanning Trajectories

This work considers scanning pathways not as a continuous line but as a set of distinct points placed in the space through which the source point can move. For the common instrument configuration where the sample can be translated parallel to the axis of rotation, the space of possible source points is the surface of a cylinder that we parameterise by (z, θ) or $(z, r\theta)$, where z is the position parallel to the rotation axis, θ is the rotation angle and r is the focus-object distance.

Within this framework it is natural to consider trajectories that uniformly fill this two-dimensional space, i.e. trajectories for which the source points are distributed in a uniform manner throughout the space. We call this type of trajectory a space filling trajectory (SFT); there are numerous practical ways to achieve this type of trajectory; one example is shown in figure 1. In this case the basic path is still helical, although with a much reduced pitch and increased spacing compared to the helical trajectory shown in blue in figure 1. To maximise coverage of the source point plane, source points are arranged to form an approximately hexagonal tesselation of the plane.

Such a trajectory has several inherent advantages over finely-sampled linear paths. Firstly, due to the increased spacing between adjacent viewing angles, and since no large areas of source space are unpopulated, SFT yields data with a larger amount of mutually independent information about the sample. In terms of ray paths, SFT projection data is maximally independent given the constraints of the imaging apparatus. Space-filling is optimal in the absence of information about the object, in contrast to the method of Stayman and Siewerdsen [16] that aims to optimise the trajectory for a particular object.

From this property it is reasonable to expect reconstructions with lower levels of noise and geometric artifacts for a given acquisition time. Secondly, the trajectory is maximally isotropic when viewed from a point within the object, so that the directions of the rays passing through each point are as uniformly distributed on the unit sphere as is possible.

The isotropic nature of the rays passing through each object point means that an unfiltered backprojection of projection data results, to a good approximation, in uniform blurring of each object point by comparison with the true object [17]. This property is critical for the rapid iterative reconstruction method described in the following section.

III. Accelerated Iterative Reconstruction

As mentioned above, one advantageous property of SFT is that unfiltered backprojection produces data that is uniformly blurred, quite distinct from other trajectories where the blurring is directional and location dependent. SFT thus allows for shift-invariant spatial filtering after backprojection, such as a deconvolution kernel applied in Fourier space. This naturally allows for reconstruction methods of the backprojection-filtering (BPF) type, where the filtering step is applied in the object volume space, following backprojection. In 1980, Colsher [17] analysed the case of idealised positron emission tomography (PET) data and proposed an exact reconstruction algorithm of the BPF type with a new type of shift-invariant spatial filtering. SFT data is similar to PET, except that SFT contains a discrete set of source positions rather than the quasi-continuum of PET. Due to the large spacing along the acquisition pathway, iterative methods are required to reconstruct SFT projection data. Therefore we incorporate post-backprojection filtering into iterative reconstruction method to accelerate convergence, and use a simpler, faster spatial filtering than the Colsher filter. Multi-grid BPF (MG-BPF) iterative schemes are ideal in this context; indeed, a multi-grid scheme with spatial filtering was proposed by Press in 2006 for inversion of the discrete Radon transform [18]. Our method closely follows the full multigrid method described in Press [18], with the Radon and inverse Radon transform replacd by cone-beam projection and backprojection, and with high-pass filtering based on Fourier deconvolution. The algorithm begins with a low-resolution approximation that can be obtained from coarsened projection data with little computational expense, using a standard iterative method. This initial guess is then refined at progressively higher resolutions by repeated applications of BPF. Unlike many iterative reconstruction techniques, in MG-BPF the corrections applied at higher resolutions simply add information at higher spatial frequencies; figure 2 shows how an image is refined at higher resolution. The nature of

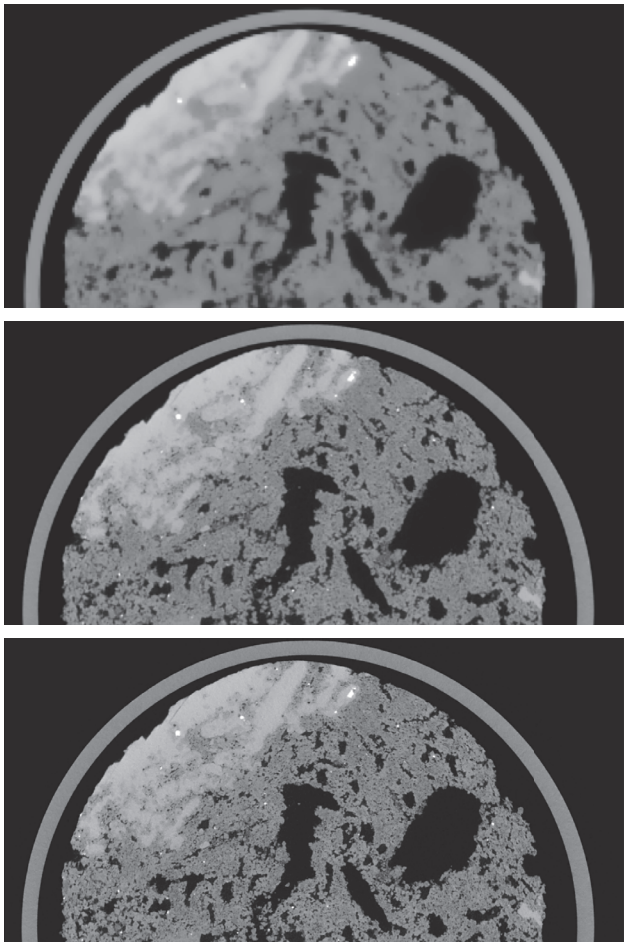

Fig. 2. A cropped slice through the reconstructed image of a rock sample showing the progressive refinement during MG-BPF reconstruction. Top: coarse image at one-quarter resolution; middle: half resolution; bottom: full resolution.

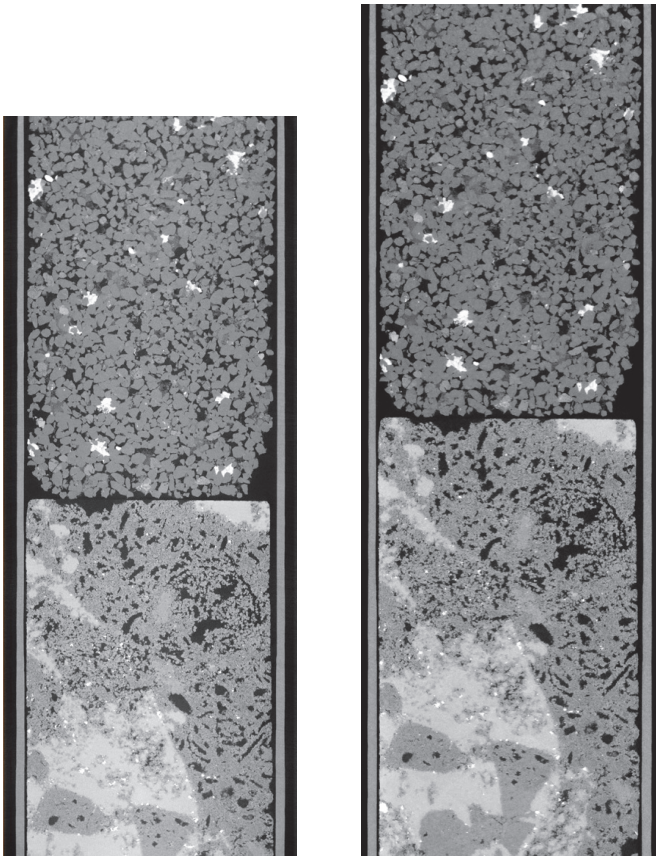

Fig. 3. The central vertical slice of reconstructed data of the combined 5mm sandstone-limestone sample showing the application of an iterative reconstruction method on a dataset of unprecendented size. Left: Helical scannning, reconstructed by FBP; Right: SFT, reconstructed by two iterations of MG-BPF. The images contain, respectively, 2640x2640x5000 and 2640x2640x6000 voxels at a voxel size of 2.0 μm.

the spatial filtering means that it is possible to configure the filtering applied at each resolution so that the total filtering applied over all resolutions closely approximates the total required deconvolution. Finally, the entire detector provides usable data and each detector pixel contributes a relatively uniform level of information to the reconstruction.

IV. Results

We present the results of preliminary data acquisition and reconstruction. The sample is 5 mm in diameter and comprises Berea sandstone and Edwards limestone joined together in an aluminium tube. A double helix and a space filling trajectory dataset were both acquired using a detector containing 3072x3072 pixels, then reconstructed using helical FBP and MG-BPF respectively. For both trajectories the acquisition time was 5 hours, however the double-helix trajectory comprised four times more projection data: 300 GB vs. 75 GB. Data was reconstructed at 2640x2640x5000 and 2640x2640x6000 voxels at a voxel size of 2.0 μm. Results of the reconstruction are shown in figures 3 and 4. The SFT reconstruction is larger since it includes some slightly degraded data in the overscan regions at the top and bottom.

For computational speed, projection and backprojection operations were implemented for GPUs in CUDA. The reconstruction hardware consisted of a small cluster of four 'super' workstations, each with two 12-core Intel Xeon processors, 512 GB of RAM and three NVIDIA Titan X GPUs (1 GHz clock, 12 GB RAM and 3072 cores). Reasonable convergence was achieved after just two iterations at the finest resolution. Since lower resolutions impose a negligible computational expense, overall computation time is roughly four times longer than an FBP method. Total reconstruction time for MG-BPF was 13 hours, showing that the method is computationally expensive but feasible. To our knowledge, this represents a significant advance in efficiency and scale compared to existing iterative reconstruction algorithms.

V. Conclusion

We have introduced scanning trajectories that are inherently discrete and which sample the space of the possible viewing angles in the most uniform manner possible. Such trajectories

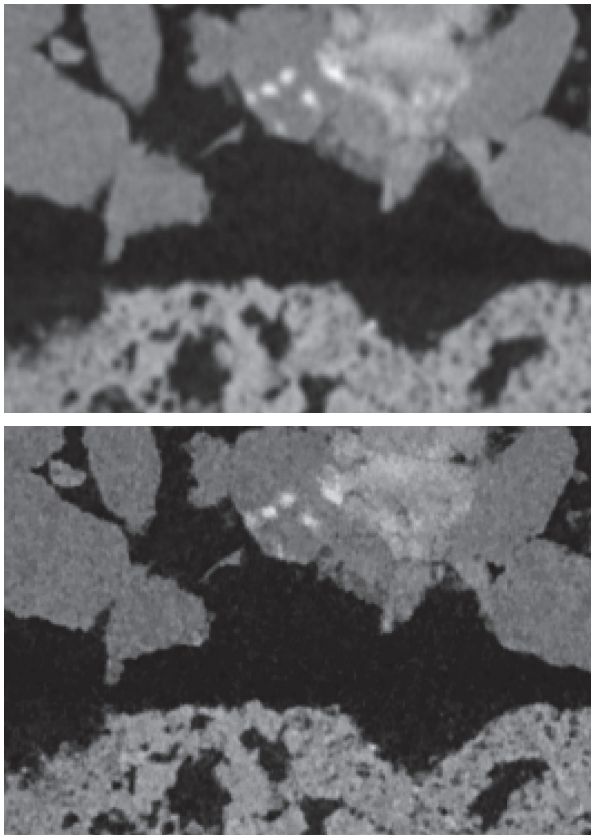

Fig. 4. A close-up of a small region of reconstructed data from figure 3 containing both sandstone and carbonate. Top: Helical scannning, reconstructed by FBP; Bottom: SFT, reconstructed by two iterations of MG-BPF. The MG-BPF method yields sharper, slightly noisier data.

should yield improved data acquisition efficiency, and produce data that can be reconstructed efficiently via multi-grid backprojection-filtering type methods, allowing iterative reconstruction of extremely large datasets for the first time. High quality reconstructions are obtained for very large datasets for which the reconstructed volume contains tens of Gigavoxels. This approach lays a foundation for the wider application of iterative reconstruction techniques to improve acquisition efficiency and image quality.

Acknowledgment

The authors acknowledge the financial support of the Australian Research Council through Linkage Project LP150101040 and Future Fellowship FT100100470, and the use of supercomputer time provided by Australia's National Computational Infrastructure (NCI).

References

[1] L. A. Feldkamp, L. C. Davis, and J. W. Kress, "Practical cone-beam algorithm," *J. Opt. Soc. Am. A*, vol. 1, pp. 612–619, 1984.

[2] H. K. Tuy, "An inverse formula for cone-beam reconstruction," *SIAM J Appl. Math.*, vol. 43, pp. 546–552, 1983.

[3] A. Katsevich, "Theoretically exact filtered backprojection-type inversion algorithm for spiral CT," *SIAM Journal on Applied Mathematics*, pp. 2012–2026, 2002.

[4] T. Varslot, A. Kingston, G. Myers, and A. Sheppard, "High-resolution helical cone-beam micro-CT with theoretically-exact reconstruction from experimental data," *Medical Physics*, vol. 38, no. 10, pp. 5459–5476, Sep. 2011. [Online]. Available: http://scitation.aip.org/content/aapm/journal/medphys/38/10/10.1118/1.3633900

[5] A. Sheppard, S. Latham, J. Middleton, A. Kingston, G. Myers, T. Varslot, A. Fogden, T. Sawkins, R. Cruikshank, M. Saadatfar, N. Francois, C. Arns, and T. Senden, "Techniques in helical scanning, dynamic imaging and image segmentation for improved quantitative analysis with X-ray micro-CT," *Nuclear Instruments and Methods in Physics Research Section B: Beam Interactions with Materials and Atoms*, vol. 324, pp. 49–56, Apr. 2014. [Online]. Available: http://www.sciencedirect.com/science/article/pii/S0168583X14000457

[6] T. Varslot, A. Kingston, G. Myers, and A. Sheppard, "Considerations for high-magnification high-cone-angle helical micro-CT," vol. 8506, 2012, pp. 850 614–850 614–10. [Online]. Available: http://dx.doi.org/10.1117/12.929304

[7] K. C. Tam, S. Samarasekera, and F. Sauer, "Exact cone beam CT with a spiral scan," *Physics in Medicine and Biology*, vol. 43, no. 4, p. 1015, 1998. [Online]. Available: http://stacks.iop.org/0031-9155/43/i=4/a=028

[8] P.-E. Danielsson, P. Edholm, J. Eriksson, and M. Magnusson, "Towards exact reconstruction for helical cone-beam scanning of long objects. A new detector arrangement and a new completeness condition," in *Proc. 1997 Meeting on Fully 3D Image Reconstruction in Radiology and Nuclear Medicine (Pittsburgh)(DW Townsend and PE Kinahan, eds.)*, 1997, pp. 141–144.

[9] T. Khler, R. Proksa, C. Bontus, M. Grass, and J. Timmer, "Artifact analysis of approximate helical cone-beam CT reconstruction algorithms," *Medical Physics*, vol. 29, no. 1, pp. 51–64, Jan. 2002. [Online]. Available: http://scitation.aip.org/content/aapm/journal/medphys/29/1/10.1118/1.1413518

[10] A. Katsevich, "3pi algorithms for helical computer tomography," *Advances in Applied Mathematics*, vol. 36, no. 3, pp. 213–250, Mar. 2006. [Online]. Available: http://www.sciencedirect.com/science/article/pii/S0196885806000029

[11] J. Nuyts, B. De Man, J. A. Fessler, W. Zbijewski, and F. J. Beekman, "Modelling the physics in the iterative reconstruction for transmission computed tomography," *Physics in medicine and biology*, vol. 58, no. 12, p. R63, 2013. [Online]. Available: http://iopscience.iop.org/0031-9155/58/12/R63

[12] G. R. Myers, A. M. Kingston, T. K. Varslot, M. L. Turner, and A. P. Sheppard, "Dynamic tomography with a priori information," *Applied Optics*, vol. 50, no. 20, pp. 3685–3690, Jul. 2011. [Online]. Available: http://ao.osa.org/abstract.cfm?URI=ao-50-20-3685

[13] K. J. Batenburg, S. Bals, J. Sijbers, C. Kbel, P. A. Midgley, J. C. Hernandez, U. Kaiser, E. R. Encina, E. A. Coronado, and G. Van Tendeloo, "3d imaging of nanomaterials by discrete tomography," *Ultramicroscopy*, vol. 109, no. 6, pp. 730–740, May 2009. [Online]. Available: http://www.sciencedirect.com/science/article/pii/S0304399109000114

[14] B. Goris, W. Van den Broek, K. J. Batenburg, H. Heidari Mezerji, and S. Bals, "Electron tomography based on a total variation minimization reconstruction technique," *Ultramicroscopy*, vol. 113, pp. 120–130, Feb. 2012. [Online]. Available: http://www.sciencedirect.com/science/article/pii/S0304399111002658

[15] S. Van Aert, K. J. Batenburg, M. D. Rossell, R. Erni, and G. Van Tendeloo, "Three-dimensional atomic imaging of crystalline nanoparticles," *Nature*, vol. 470, no. 7334, pp. 374–377, Feb. 2011. [Online]. Available: http://www.nature.com/nature/journal/v470/n7334/abs/nature09741.html

[16] J. W. Stayman and J. H. Siewerdsen, "Task-based trajectories in iteratively reconstructed interventional cone-beam CT," in *The 12th International Meeting on Fully Three-Dimensional Image Reconstruction in Radiology and Nuclear Medicine*, 2013, pp. 257–260. [Online]. Available: http://istar.jhu.edu/pdf/Stayman_Fully3D2013_TaskBasedTrajectories.pdf

[17] J. G. Colsher, "Fully three-dimensional positron emission tomography," *Physics in Medicine and Biology*, vol. 25, no. 1, pp. 103–115, Jan. 1980.

[18] W. H. Press, "Discrete Radon transform has an exact, fast inverse and generalizes to operations other than sums along lines," *Proceedings of the National Academy of Sciences*, vol. 103, no. 51, pp. 19 249–19 254, Dec. 2006. [Online]. Available: http://www.pnas.org/content/103/51/19249

Spectral Breast CT by Single Photon Counting

William C. Barber, Huanjun Ding, Jan C. Wessel, Nail Malakhov, Gregor Wawrzyniak, Jan S. Iwanczyk, Eirik Næss-Ulseth, and Sabee Molloi

***Abstract*—The application of single photon counting x-ray imaging arrays to breast computed tomography (CT) imaging can potentially improve image quality, reduce dose, and allow new methods using spectral information. We are developing spectral breast CT based on the development of stacked curved one dimensional (1D) arrays of edge illuminated silicon (Si) strip detectors. The Si strip detectors directly convert X-ray energy into charge collected and readout with low noise mixed signal application specific integrated circuits. The Si wafer is edge illuminated to provide a large detective quantum efficiency (DQE) within the dynamic range required for breast CT. The Si strips are oriented towards the X-ray focal spot to avoid depth of interaction (DOI) errors. For clinical in vivo use, a breast CT imaging system based on photon counting detectors must show efficacy justifying the disruptive replacement of existing methods. This can be done by showing improved image quality and or new applications while maintaining or reducing patient dose. For this application the photon counting detectors require high intrinsic spatial resolution, high dynamic range, and a high linear output count rate (OCR). To take full advantage of spectral methods, the detectors require low noise performance with good energy resolution across both the dynamic and OCR range of the application. The detectors presented here produce 5 lp/mm^2 spatial resolution, 80% DQE at 65 kVp, and a linear OCR up to 40 million cps/mm^2. The energy resolution is maintained at ~ 2 keV full width at half maximum (FWHM) across the dynamic and OCR range. The imaging methods presented here use a stack of 1D curved arrays to scan the breast helically in a pendant geometry with collimator based scatter rejection. Phantom breast CT imaging studies with simulated micro-calcification (μCa) and mass lesions demonstrate improved results compared to mammography and cone beam CT using energy integrating detectors. The system is expected to offer superior image quality to detect μCa at a clinically relevant dose level while improving lesion detection by energy weighted reconstruction using four energy bins.**

***Index Terms*—Engineering in medicine and biology, biomedical engineering, biomedical imaging, medical diagnostic imaging, cancer, X-ray tomography, phantoms, semiconductor materials, silicon, ionizing radiation sensors, X-ray detectors, application specific integrated circuits, mixed analog digital integrated circuits.**

Manuscript received January 25, 2016. This work was supported in part by the National Cancer Institute (NCI) of the National Institutes of Health (NIH) under Grant R44 CA177093 and in part by the Research Council of Norway under grant BIA 235489/O30.

W. C. Barber and J. C. Wessel are with DxRay Inc., Northridge, CA 91324 USA and Interon A.S., Asker, Norway.

H. Ding and S. Molloi are with the Dept. of Radiological Sciences, University of California Irvine, Irvine, CA 92697 USA.

N. Malakhov, G. Wawrrzyniak, and E. Næss-Ulseth is with Interon A.S., Asker, Norway.

J. S. Iwanczyk is with DxRay Inc., Northridge, CA 91324 USA.

I. Introduction

BREAST cancer is one of the most frequently diagnosed cancers among US women.[i] Its early and reliable detection remains a challenge using current imaging techniques. So far mammography is the only breast screening modality that has been shown to reduce breast cancer mortality.[ii] Recently digital mammography (DM) systems with increased dynamic range using pixellated flat panel detectors are replacing film screen systems due to contrast resolution advantages among women who are pre- or peri-mentopausal and/or have dense breast tissue[iii]. Contrast enhanced DM is being developed using iodine. Yet despite DM's impressive advantages in detection performance, imaging time, and cost-effectiveness, intense debate has addressed its limitations.[iv] As a two-dimensional (2D) projection technique, the main challenge for mammography is the superimposition of the breast anatomy, which results in reduced contrast resolution. Overlap of the normal breast parenchyma may obscure tumor identification, which is exacerbated when dense breasts are imaged.[v] As a result, mammography's sensitivity in detecting lesions has been considered questionable, especially for specific patient groups.[vi] It is estimated that mammography screenings miss as many as 50% of breast cancers.[vii] In addition, mammography's positive predictive value remains as low as 0.20,[viii] which contributes to the large number of false positive findings in biopsies recommended after mammography. Such limitations have increased the interest in developing three-dimensional (3D) breast imaging techniques, which can eliminate the anatomical noise induced by overlapping of the breast tissue, and thereby improve the sensitivity and specificity in lesion detection, especially for dense breasts.

In an effort to improve breast cancer detection a number of alternatives have been developed to replace mammography including magnetic resonance imaging (MRI)[ix] , molecular breast imaging (MBI)[x], breast ultrasound (US), breast optical metabolic imaging (OMI)[xi], digital breast tomosynthesis (DBT) with limited information in depth[xii], and dedicated breast computed tomography (BCT)[xiii]. BCT based on flat panel detectors scans in the coronal plane around the breast in its pendant geometry.[xiv] This technique has been reported to have improved sensitivity due to its ability to provide 3D information about breast tissues. System parameters, including optimized spectra and gantry geometry, have been extensively investigated by several research groups.[xv,xvi,xvii] An initial clinical study suggests that cone beam BCT provides

significantly better visualization of soft tissue lesions than mammography.[xviii] A recent study has also shown that BCT has significantly lower anatomical noise than mammography and breast tomosynthesis, providing the ultimate solution to minimize the anatomical noise induced by overlap of the breast tissue.[xix]

Despite the substantial advances and demonstrated promise of BCT, several challenges remain with respect to its clinical implementation. A major barrier is the limited ability to detect μCas, due to the intrinsic spatial resolution of the detector and insufficient noise suppression at the clinically relevant dose level. In a clinical study, results suggest that standard mammography outperformed cone beam BCT in visualizing μCas.[xx] A recent study reported μCa detection of 150 μm at a dose level of 11 mGy using a flat panel detector with reduced pixel pitch of 75 μm.[xxi] A reduction in detector pixel pitch results in a quadratic decrease in the measured signal in each pixel and when imaging at a low dose level for screening the measured signal must compete with the electronic noise from the flat panel detectors, and the image quality will be substantially compromised due to the low contrast-to-noise ratio (CNR). Another challenge for cone beam BCT systems is the presence of scatter radiation, which substantially reduces contrast resolution. Scatter is a critical issue that impacts image quality in cone beam CT. Scatter rejection grids are impractical in a cone beam geometry and even if realized would create poor dose efficiency by blocking active area of the detector.

II. Methods

These two limitations, namely the electronic noise and scatter, are eliminated in the development of a low dose spectral breast CT system based on photon counting detectors (PCDs) in a multi-slit, multi-slice geometry. With PCDs the electronic noise can be effectively eliminated, regardless of detector pixel pitch and dose. The scatter is eliminated by using a multi-slit, multi-slice geometry. Both edge illuminated PCDs (Philips/Sectra MicroDose™ recently with two energy windows) and line energy integrating detectors (Adani Mammoscan™) are used in a scanning slit geometry for mammography and have been shown to eliminate 97% of the scatter. Scatter is much more of a problem in BCT which is performed on the uncompressed breast as compared to mammography where the breast is compressed to reduce scatter. Thus the low dose spectral BCT system developed here brings the advantages of scatter elimination to BCT. Additionally, the PCDs developed here have excellent energy resolution (2 keV across the entire dynamic range) and a very high output count rate (OCR) allowing us to lower dose by optimal energy weighting while simultaneously increasing tissue specific contrast and quantifying iodine concentration. Unlike conventional flat panel detectors which measure the integrated electrical charge (total current) induced by radiation (photocurrent) and the detector's bias (dark current), energy resolved photon counting detectors count individual x-rays and bin them according to their energies. It has previously been shown that the CNR of BCT can be improved by 30% to 90% using a PCD with optimal energy-weighting,[xxii] resulting in at least 40% decrease in patient dose.[xxiii]

A. Development of PCDs for BCT

The main challenge in applying PCDs in CT is the high photon flux required in clinical imaging. For spectral CT it is also a challenge to maintain good energy resolution at high flux. Achieving the required OCR while maintaining energy resolution requires very low noise preamplifiers operating at very fast peaking times which are connected to pixels with good charge collection over short length scales. We achieve this for BCT using custom designed application specific integrated circuits (ASICs) wire bonded directly to contact strips on a fully depleted Si junction wafer and supported by a common printed circuit board (PCB) substrate used in an tilted edge illumination geometry. The edge illumination provides rapid charge collection across the narrow junction independent of energy within the dynamic range of BCT. The direct wire bonding introduces little stray capacitance to the inputs of the preamplifier and can be accomplished on short length scales. The fast peaking time of the preamplifier eliminates the dark current's contribution to the electronic noise allowing room temperature operation of Si as an x-ray detector. The edge illumination can also provide sufficient DQE when using the relatively low-Z Si as a direct converter. Although mammography is performed with typical tube voltage settings ranged between 25 and 35 kVp, which is sufficient to transit the compressed breast, we are using 65 kVp to perform CT on uncompressed breasts. All of this combines together to produce good energy resolution across the entire dynamic range at high OCR and DQE for BCT in an all solid-state low-cost design using standard Si wafer processing, PCB manufacturing, and wire bonding.

Figure 1 shows a schematic of the side view of a single Si strip module edge illuminated at a 3º angle providing a 1 cm DOI in the incident direction. We have simulated the DQE of a direct conversion Si detector at various x-ray tube voltages from a tungsten anode with 2.2 mm Al filtration. Studies suggested that the soft tissue lesion CNR can be enhanced with a tube voltage in range of 40 to 70 kVp[xxiv,xxv,xxvi]. The 1 cm thick attenuation length of the 3° edge illuminated Si detectors used in our system is expected to have a DQE of 80% at 65 kVp. The ASICs are mounted on the PCB substrate and fit within the active area of the sensor and a slit collimator

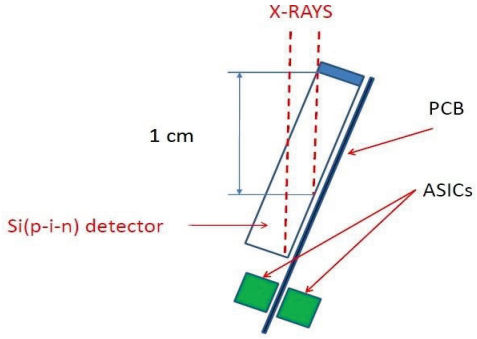

Figure 1. Schematic of a side view along the edge of the edge illuminated detector.

with an opening between 100 μm and 500 μm can be used to adjust the slice thickness. A substrate PCB with tiled modules in an arc with the strips pointed to the x-ray focal spot is used to scale to the required FOV with no DOI errors. A gap between each module such that the same board when stacked and shifted by one module width will overlap the dead space produced by the guard rings on the lateral sides of each module. The substrate PCBs could contain any number of Si strip modules in principle and are symmetric so that identical PCBs can be stacked. This geometry avoids absorption underneath the guard ring in the incident direction, overlaps dead space under the lateral guard rings, avoids DOI errors, provides sufficient DQE for BCT, and eliminates all of the out of plane scatter all at once.

The output count rate (OCR) as a function of input count rate has been measured by setting one threshold just above the electronic noise floor and recording all the counts with energy above the threshold setting as a function of time. A 50 watt X-ray tube (CMX005, Source 1 X-Ray, Campell, CA) was set to 50 kVp and the tube current was increased from 1 μA to 600 μA with a thick 0.1 mm wide slit collimator 1 cm above the detector. This collimator geometry creates a 1D row of 100 μm by 100 μm pixels. A 0.5 mm thick Cu filter was used with a source to detector distance of roughly 20 cm.

The energy resolution was measured by using characteristic X-ray peak of Ag at 22keVwhich produced by^{109}Cd source decays. A dose of 9.229 μCiof ^{109}Cd sourceplaced on a thick 0.5 mm wide slit brass collimator 1 cm above the detector. This collimator geometry creates a 1D row of 100 μm by 500 μm pixels with a 100 μm pitch along the long axis. The counts above a single threshold set to 100 keV are recorded during a fixed frame time and then the threshold's setting is lowered by 0.25 keV and the exposure is repeated covering a range from 100 keV to 0 keV. The function of the number of counts above the threshold setting is digitally differentiated by a forward-backwards method to a pole of order 5 to generate the spectrum. The photopeak at 22 keV fitted to a Gaussian function whose full width at half maximum (FWHM) is used to determine the energy resolution.

B. BCT Imaging with PCDs

Experimental images were acquired on a bench-top BCT system using a Si strip PCD shown in **Figure 2**. A tungsten anode x-ray tube with a focal spot size of 0.8 mm (XRB101, Spellman, Hauppauge, NY) was used as the x-ray source. A high precision direct drive rotary motor (Kollmorgen Goldline DDR D062M, Danaher Motion, Wood Dale, IL) offered the rotational mechanism, and the phantoms were placed on top of a platform, which was positioned over the motor. Two slit collimators, fore and aft with respect to the phantom, were used to provide fan beam geometry to minimize scatter. Lead and brass were used for the fore and aft collimator, respectively. The slice thickness (0.46 mm) was determined by the 0.5 mm width of the aft collimator and magnification. A minimum magnification setup, approximately 1.1, was used to overcome the limitations from the relatively large x-ray tube focal spot size.

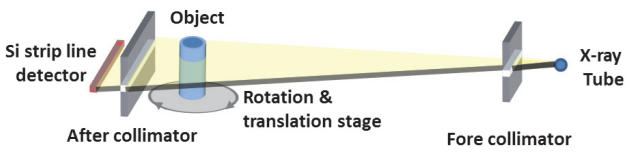

Figure 2. Schematic diagram of the bench-top photon counting breast CT system.

The x-ray tube voltage was set to 65 kVp and a 2.7 mm aluminum (Al) filter was used yielding a half value layer (HVL) of 2.18 mm Al, suggesting dose efficiency and feasibility for a dedicated breast CT.[15, 27] The electronic noise was eliminated without any loss of signal by setting the lowest threshold above the noise floor, 4 keV. The rotation speed of the motor was approximately 0.976 RPM for 360°, resulting in 1229 frames per scan at 20 frames per second. The images were acquired at five different dose levels corresponding to an ESAK of 0.6, 1.2, 3, 6, and 8 mGy per CT scan. The exposure level was determined by matching the noise level in the reconstructed image with respect to the 14 cm phantom image with simulated MGD range. Different dose levels were adjusted by changing the tube current. A calibrated ionization chamber (20×6-0.6, Radcal, Monrovia, CA) was used to measure the dose level to the phantom in air kerma (mGy). The middle of the charge-collection volume of the ion chamber was positioned at the same level with the center of fore collimator aperture. The radiation field size was larger than the active volume of the ion chamber at the isocenter. The sensitivity variation across the pixels was compensated by implementing a flat-field correction technique, which used open flood field images. The images were reconstructed by using a filtered back projection (FBP) algorithm with a ramp filter and the voxel size of 23 × 23 × 23 μm^3. Two hundred fifty μCa images (5 sizes of μCas × 5 doses × 10 images for each setting) were combined with 250 control images without μCa to ultimately form 500 images for an observer study.

III. RESULTS

Figure 3 shows the output count rate as a function of tube current which is proportional to the input count rate, for a typical 100 μm pixel of the Si strip detector. The output is linear to 40Mcps/mm^2 and saturates just below 100Mcps/mm^2.

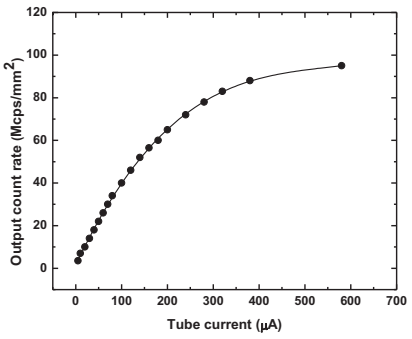

Figure 3. Graph of the output count rate as a function of X-ray tube current.

Figure 4 shows a ^{109}Cd spectrum as a function of energy for a 100 μm pixel of the Si strip detector. The FWHM energy resolution is approximately 1.7 keV or 8.5 % at 22 keV.

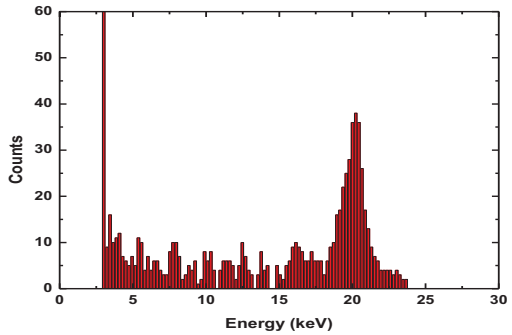

Figure 4. Schematic of a side view along the edge of the edge illuminated detector.

IV. Conclusion

We investigated the detectability of μCas with a photon counting BCT system using Si strip photon counting detectors. The simulation and experimental results both showed reduced detectability for the μCas smaller than 140 μm with an ESAK of 3 mGy. The results of an observer study for the average-sized breast phantom with the proposed system showed an average AUC of the μCas larger than 120 μm were greater than 0.89 ± 0.07 at a MGD of 3 mGy. The proposed photon counting BCT system based on a Si strip detector is expected to offer superior image quality to detect μCas with a dose level equivalent to standard two-view mammography.

REFERENCES

[i] A. Jemal, R. Siegel, J. Q. Xu and E. Ward, "Cancer Statistics, 2010," Ca-Cancer J Clin **60**, 277-300 (2010).

[ii] S. Feig, "Comparison of Costs and Benefits of Breast Cancer Screening with Mammography, Ultrasonography, and MRI," Obstet Gyn Clin N Am **38**, 179-+ (2011).

[iii] M. Sala, M. Comas, F. Macia, J. Martinez, M. Casamitjana and X. Castells, "Implementation of Digital Mammography in a Population-based Breast Cancer Screening Program: Effect of Screening Round on Recall Rate and Cancer Detection," Radiology **252**, 31-39 (2009).

[iv] J. S. Drukteinis, B. P. Mooney, C. I. Flowers and R. A. Gatenby, "Beyond Mammography: New Frontiers in Breast Cancer Screening," The American Journal of Medicine **126**, 472-479 (2013).

[v] V. P. Jackson, R. E. Hendrick, S. A. Feig and D. B. Kopans, "Imaging of the Radiographically Dense Breast," Radiology **188**, 297-301 (1993).

[vi] C. K. Kuhl, S. Schrading, C. C. Leutner, N. Morakkabati-Spitz, E. Wardelmann, R. Fimmers, W. Kuhn and H. H. Schild, "Mammography, breast ultrasound, and magnetic resonance imaging for surveillance of women at high familial risk for breast cancer," J Clin Oncol **23**, 8469-8476 (2005).

[vii] C. K. Kuhl, S. Schrading, C. C. Leutner, N. Morakkabati-Spitz, E. Wardelmann, R. Fimmers, W. Kuhn and H. H. Schild, "Mammography, breast ultrasound, and magnetic resonance imaging for surveillance of women at high familial risk for breast cancer," J Clin Oncol **23**, 8469-8476 (2005).

[viii] D. B. Kopans, "The Positive Predictive Value of Mammography," American Journal of Roentgenology **158**, 521-526 (1992).

[ix] T. H. Helbich, "Contrast-enhanced magnetic resonance imaging of the breast," Eur J Radiol **34**, 208-219 (2000).

[x] B. B. Koolen, T. S. Aukema, A. J. G. Martinez, W. V. Vogel, L. C. Ontanaya, M. V. Peeters, C. J. J. Vroonland, E. J. Rutgers, J. M. Benlloch Baviera and R. A. V. Olmos, "First Clinical Experience with a Dedicated PET for Hanging Breast Molecular Imaging," Eur J Cancer **48**, S67-S67 (2012).

[xi] A. Poellinger, "Near-infrared imaging of breast cancer using optical contrast agents," J Biophotonics **5**, 815-826 (2012).

[xii] S. Richard and E. Samei, "Quantitative breast tomosynthesis: From detectability to estimability," Med. Phys. **37**, 6157-6165 (2010).

[xiii] S. J. Glick, "Breast CT," Annu. Rev. Biomed. Eng. **9**, 501-526 (2007).

[xiv] M. P. Tornai and R. L. McKinley, "A high-performance SPECT-CT system for dedicated molecular breast imaging," Journal of Nuclear Medicine **52**, 673-674 (2011).

[xv] W. T. Yang, C. C. Shaw, L. Chen, C. Altunbas, T. Wang, C. J. Lai, K. Cheenu, S. J. Tu, X. Liu and G. J. Whitman, "Cone beam breast CT - a feasibility study with surgical mastectomy specimens.," Breast Cancer Research and Treatment **94**, S210-S210 (2005).

[xvi] W. A. Kalender, M. Beister, J. M. Boone, D. Kolditz, S. V. Vollmar and M. C. C. Weigel, "High-resolution spiral CT of the breast at very low dose: concept and feasibility considerations," Eur Radiol **22**, 1-8 (2012).

[xvii] P. Russo, G. Mettivier, A. Lauria and M. C. Montesi, "X-ray Cone-Beam Breast Computed Tomography: Phantom Studies," Ieee Transactions on Nuclear Science **57**, 160-172 (2010).

[xviii] K. K. Lindfors, J. M. Boone, T. R. Nelson, K. Yang, A. L. C. Kwan and D. F. Miller, "Dedicated breast CT: Initial clinical experience," Radiology **246**, 725-733 (2008).

[xix] L. Chen, C. K. Abbey, A. Nosrateih, K. K. Lindfors and J. M. Boone, "Anatomical complexity in breast parenchyma and its implications for optimal breast imaging strategies," Med. Phys. **39**, 1435-1441 (2012).

[xx] K. K. Lindfors, J. M. Boone, T. R. Nelson, K. Yang, A. L. C. Kwan and D. F. Miller, "Dedicated breast CT: Initial clinical experience," Radiology **246**, 725-733 (2008).

[xxi] Y. T. Shen, Y. C. Zhong, C. J. Lai, T. P. Wang and C. C. Shaw, "Cone beam breast CT with a high pitch (75 mu m), thick (500 mu m) scintillator CMOS flat panel detector: Visibility of simulated microcalcifications," Med. Phys. **40**, 101915 (2013).

[xxii] J. Giersch, D. Niederlohner and G. Anton, "The influence of energy weighting on X-ray imaging quality," Nuclear Instruments & Methods in Physics Research Section a-Accelerators Spectrometers Detectors and Associated Equipment **531**, 68-74 (2004).

[xxiii] H. Q. Le, J. L. Ducote and S. Molloi, "Radiation dose reduction using a CdZnTe-based computed tomography system: Comparison to flat-panel detectors," Med. Phys. **37**, 1225-1236 (2010).

[xxiv] B. Chen and R. Ning, "Cone-beam volume CT breast imaging: Feasibility study," Med. Phys. **29**, 755-770 (2002).

[xxv] S. J. Glick, S. Thacker, X. Gong and B. Liu, "Evaluating the impact of X-ray spectral shape on image quality in flat-panel CT breast imaging," Med Phys **34**, 5-24 (2007).

[xxvi] M. Weigel, S. V. Vollmar and W. A. Kalender, "Spectral optimization for dedicated breast CT," Med. Phys. **38**, 114-124 (2011).

Multi-scale Circular Conebeam Interior Tomography using Bedrosian Identity: Verification with Real Data

Yo Seob Han[1], Minji Lee[1], John Paul Ward[2], Michael Unser[3], Seungryoung Cho[4] and Jong Chul Ye[1,*]

***Abstract*—Circular trajectory is quite often used in conebeam CT (CBCT) such as C-arm CT, dental CT and so on. However, if the cone angle is wide, the FDK algorithm suffers from conebeam artifacts. Moreover, it exhibits severe truncation artifacts if the detector is truncated in transverse-ways. To mitigate these artifacts, we propose a reconstruction method that consists of two steps: multi-scale interior tomography using 1D TV in both horizontal and vertical virtual chord lines, which is followed by spectral blending in Fourier domain. For spectral blending, we develop a Fourier domain analysis technique to identify the missing frequency regions and design a bow tie window for weighting. Experimental results with a real head phantom confirm that the proposed method significantly improves the reconstruction quality and reduces the computational time significantly.**

***Index Terms*—Conebeam artifact, Interior tomography, Bedrosian theorem, Multiscale decomposition, Spectral Blending.**

I. Introduction

CIRCULAR CBCT trajectory has been widely used in practice since the trajectory can be easily implemented in hardware compared to other geometries such as helical [1] or saddle [2] trajectories. In the circular trajectory, the FDK algorithm is the de facto standard, but it suffers from the conebeam artifacts as the cone angle increases. These artifacts become more severe when only part of detector is used for imaging the region-of-interior (ROI) to reduce the radiation dose.

Specifically, interior tomography approaches reduce the x-ray dose by preventing x-ray illumination outside of the ROI. However, due to the detector truncation, the conventional filtered back projection type algorithm cannot be used. To address this problem, the authors in [3] showed that if the object is essentially piecewise constant, then ROI can be solved uniquely and stably via the total variation (TV) minimization. However, this methods requires 2D or 3D total variation minimization and iterative applications of forward and backward projections, which is computationally very expensive.

[1]Bio Imaging & Signal Processing Lab., Dept. of Bio and Brain Engineering, Korea Advanced Institute of Science & Technology (KAIST), 291 Daehak-ro, Yuseong-gu, Daejon, Korea. (minjilee@kaist.ac.kr, hanyoseob@kaist.ac.kr, jong.ye@kaist.ac.kr).

[2]Department of Mathematics, University of Central Florida, Orlando, FL 32815. (john.ward@ucf.edu).

[3]Biomedical Imaging Group, École Polytechnique Fédérale de Lausanne (EPFL), CH-1015, Lausanne, Switzerland. (michael.unser@epfl.ch).

[4]Medical Imaging & Radiotherapeutic Lab., Dept. of Bio and Brain Engineering, Korea Advanced Institute of Science & Technology (KAIST), 291 Daehak-ro, Yuseong-gu, Daejon, Korea. (scho@kaist.ac.kr).

In interior tomography problems from circular trajectory, two types of artifacts reside: one from truncated detectors and the other from missing frequency regions. To address the first artifact, our group recently proposed the multi-scale interior tomography algorithm using 1D TV [4]. Then, to reduce the second type artifacts, we also extended the Fourier blending idea proposed for half-scan FBP algorithm [5] to our multi-scale interior tomography approach, and provided a novel Fourier domain two-way weighting scheme [4]. Unlike the original Fourier blending idea in [5], our method is based on rigorous analysis of Fourier components. The resulting algorithm is computationally so efficient that it can be easily used in a clinical environment.

The main goal of this paper is, therefore, to demostrate the effectiveness of this algorithm using real data. For this, we first review the recent theory of multi-scale circular conebeam interior tomography using Bedrosian identity and spectal blending [4] and provide experimental results using real data.

II. Thoery

A. Conebeam artifact problem

1) Fourier analysis of DBP on virtual chord lines: In the 3-D CBCT problem, let the variables $\boldsymbol{\theta}$ denote a vector on the unit sphere $\mathbb{S}^2 \in \mathbb{R}^3$. Then, the x-ray transform is formally define as

$$D_f(\mathbf{a}, \boldsymbol{\theta}) = \int_0^\infty f(\mathbf{a} + t\boldsymbol{\theta}) dt \ , \tag{1}$$

where f corresponds to the linear attenuation coefficients and $\boldsymbol{\theta} \in \mathbb{S}^2$ denotes the x-ray photon propagation direction and $\mathbf{a} \in \mathbb{R}^3$ refers the x-ray source location in a actual source trajectory $\mathbf{a}(\lambda), \lambda \in [\lambda_{\min}, \lambda_{\max}]$.

For the given source trajectory $\mathbf{a}(\lambda)$, we now define the *differentiated backprojection (DBP)*:

$$g(\mathbf{x}) \ = \ \int_{\lambda^-}^{\lambda^+} d\lambda \frac{1}{\|\mathbf{x} - \mathbf{a}(\lambda)\|} \frac{\partial}{\partial \nu} \ D_f \left(\mathbf{a}(\nu), \boldsymbol{\theta}\right)\big|_{\nu=\lambda} \tag{2}$$

where $[\lambda^-, \lambda^+] \subset [\lambda_{\min}, \lambda_{\max}]$ denotes the appropriate intervals from the source segments between $\lambda_{\min}$ and $\lambda_{\max}$, and $1/\|\mathbf{x} - \mathbf{a}(\lambda)\|$ denotes the distance weighting. The chord line on the DBP data can be representated as a Hilbert transform relationship [1], [6], [7]. Unfortunately, in CBCT, the Hilbert transform relationship is established only on the actual chord line. As our novel contribution, we generalized the Hilbert transform relationship from the actual chord line to a virtual chord line [4].

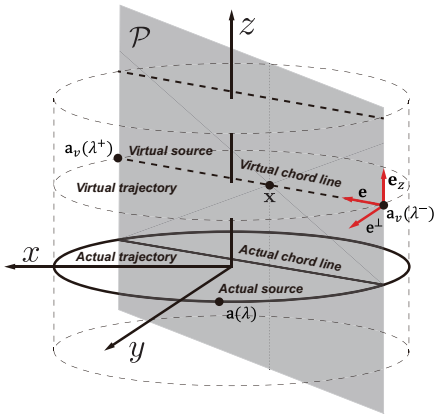

Fig. 1. Source trajectories and virtual chord lines. The dark circle is an actual trajectory and the dark line is an actual chord line. The set of gray-dot circle are virtual trajectory and the dark-dot line is a virtual chord line.

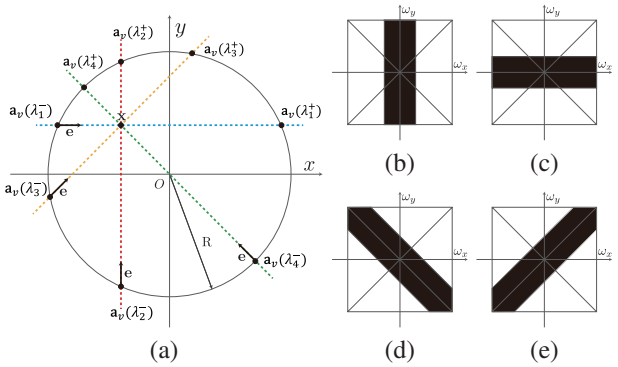

Fig. 2. The missing frequency region. (a) The top view of a point $\mathbf{x} = (x, y, z)$ and an source trajectory. The blue line indicates the horizontal directional virtual chord line between $\mathbf{a}_v(\lambda_1^-)$ and $\mathbf{a}_v(\lambda_1^+)$ and the red line denotes the vertical directional virtual chord lines between $\mathbf{a}_v(\lambda_2^-)$ and $\mathbf{a}_v(\lambda_2^+)$. (b)(c) The missing frequency region for horizontal and vertical directions, respectively. (d) (e) The missing frequency region for the diagonal directional virtual chord lines that correspond to the yellow and green lines, respectively.

The virtual coordinate system can be explained by three unit vectors which are the z-axis $\mathbf{e}_z$, the chord line direction (i.e., filtering direction) $\mathbf{e}$, and their perpendicular axis $\mathbf{e}^\perp$. Using the coordinate system, a new coordinate (x', y', z) is representated from a primary Cartesian coordinate such that

$$\mathbf{x} = x'\mathbf{e} + y'\mathbf{e}^\perp + z\mathbf{e}_z \ . \tag{3}$$

At the new coordinate, the corresponding spatial frequency is defined by $(w_{x'}, w_{y'}, w_z)$. Then, we have the following gerenalized Hilbert transform relationship.

Theorem II.1. [4] Let the source trajectory $\mathbf{a}(\lambda), \lambda \in [\lambda^-, \lambda^+]$ have no discontinuities. Suppose, furthermore, position $\mathbf{x}$ is on the viritual chord line that connects the two virtual source positions $\mathbf{a}_v(\lambda^-)$ and $\mathbf{a}_v(\lambda^+)$, and has the coordinate values (x', y', z) on the virtual chord line coordinate system (3). Then, the differentiated backprojection data in (2) can be represented as

$$g(\mathbf{x}) = \frac{1}{2\pi}\int_{-\infty}^{\infty} d\omega_{x'}\ \hat{\phi}(\omega_{x'}, y', z) j\,\mathrm{sgn}(\omega_{x'}) e^{j\omega_{x'}x'} \tag{4}$$

where

$$\hat{\phi}(\omega_{x'}, y', z) := \frac{1}{(2\pi)^2}\int d\omega_{x'} \int_{\omega_z \in \{(\omega_{x'}, \omega_{y'}, \omega_z) \notin \mathcal{N}(z)\}} d\omega_z \\ \hat{f}(\omega_{x'}, \omega_{y'}, \omega_z) e^{j(y'\omega_{y'} + z\omega_z)} \ ,$$

and the missing frequency set $\mathcal{N}(z)$ on z is given by

$$\mathcal{N}(z) = \left\{ (\omega_{x'}, \omega_{y'}, \omega_z) \mid -A \le \frac{\omega_{x'}}{z\omega_z} \le B \right\}, \tag{5}$$

where

$$A = \frac{1}{x' + \sqrt{R^2 - (y')^2}},\ B = \frac{1}{\sqrt{R^2 - (y')^2} - x'}.$$

which trivially becomes an empty set when $z = 0$.

2) Missing frequency regions: Thanks to Theorem II.1, we can identify the missing frequency region. Fig. 2 shows various missing frequency regions depends on the filtering direction. If all of the chord lines head for the horizontal direction (blue line at Fig. 2(a)), then the missing frequency region for a given z can be written as

$$\left\{ (\omega_x, \omega_y, \omega_z) \mid -\frac{z\omega_z}{x + \sqrt{R^2 - y^2}} \le \omega_x \le \frac{z\omega_z}{\sqrt{R^2 - y^2} - x} \right\}$$

, where $z\omega_z \le 0$; on the contrary, for the vertical direction (red line at Fig. 2(b)), the missing frequency region can be explained such that

$$\left\{ (\omega_x, \omega_y, \omega_z) \mid -\frac{z\omega_z}{y + \sqrt{R^2 - x^2}} \le \omega_y \le \frac{z\omega_z}{\sqrt{R^2 - x^2} - y} \right\}$$

.

The missing frequency region is illustrated in Fig. 2(b)(c) for $x \ll z, y \ll z$, respectively. In addition, Fig. 2(d)(e) represents the missing frequency regions related to the diagonal filtering directions.

B. Multi-scale Interior Tomography using Bedrosian Identity

In interior tomography problems, an available DBP data on a virtual chord line is truncated within FOV $x_\pi \in (e1, e2)$. Accordingly, when Hilbert transform is applied to the truncated data, we can expect truncation artifacts since there exists a null space:

$$\mathcal{H}h_{\mathcal{N}}(x_\pi) \ = \ 0, \quad \text{where} \quad x_\pi \in (e1, e2). \tag{6}$$

Here

$$h_{\mathcal{N}}(x_\pi) \ = \ \frac{1}{\pi}\int_{\mathbb{R}\setminus(e1,e2)} dx'_\pi\ \frac{\psi_\pi(x'_\pi)}{x'_\pi - x_\pi}, \tag{7}$$

for some function $\psi_\pi(x)$. Thus, we are interested in imposing 1D TV to correct any data $h_{\mathcal{N}}(x_\pi)$ belong to the null space.

By decomposing interior tomgoraphy problems based on the 1D TV formulations, the computational cost is much lower than it is for high-dimensional TV [3], [8], [9]. Moreover, we can significantly reduce the computational complexity based on the Bedrosian identity of Hilbert transform.

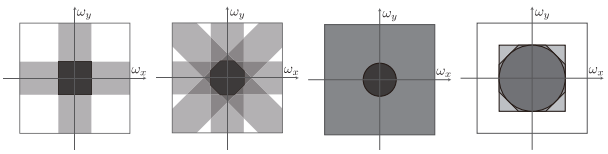

Fig. 3. The common missing frequency region according to the filtering directions. (a), (b), and (c) indicate the missing frequency region according to the number of missing frequency regions with different filtering directions. The dark region denotes a common missing frequency region, respectively. (d) Overlapped illustration of the common missing frequency regions.

Theorem II.2. (see [10]) *Let $w, f \in L_2(\mathbb{R})$ be low-pass and high-pass signals such that the Fourier transform of $w(x)$ vanishes for $|\omega| > \omega_0$, with $\omega_0 > 0$, and the Fourier transform of $f(x)$ vanishes for $|\omega| < \omega_0$. Then, we have*

$$\mathcal{H}\{w(x)f(x)\} = w(x)\mathcal{H}\{f(x)\} \ . \tag{8}$$

Accordingly, the interior tomography problem is formulated as

$$\min_{f_L} \|f_L\|_{TV(\mathrm{L};E)} \quad \text{subject to} \quad g = \mathcal{H}(f_L + f_H) \ . \tag{9}$$

where f_L and f_H denote the low and high freqeuncy component of a object f, respectively. By solving Eq. (9), the low freqeuncy component $f_L(x)$ is reconstructed under TV constraint. Moreover, it is possible to reconstruct low-resolution image in the down-sampled domain, so the computational bunden is significantly reduced. From the reconstruncted signal $f_L(x)$, the residual signal $g_H(x)$ is extracted by substracting $\mathcal{H}f_L(x)$ from $g(x)$. If $g_H(x)$ does not overlap with the spectral band-width of the truncation window, then Theorem II.2 is satisfied, so, $f_H(x)$ is directly calculated by

$$f_H(x) = \frac{-\mathcal{H}\{w(x)g_H(x)\}}{w(x)}, \quad x \in E. \tag{10}$$

The multiscale decomposition method is summarized in Fig. 4.

C. Conebeam artifact reduction using spectral blending

However, the recovered signal is not the exact solution due to the missing frequency regions. Indeed, the best signal we can expect is that the signals with missing frequency components as shown in Fig. 2. Therefore, to minimize the cone beam artifacts that are recovered from the interior tomography algorithm, we need spectral blending that optimally combines the interior tomography reconstruction in multiple filtering directions so that the resulting missing frequency components can be reduced to those of Fig. 3. Moreover, based

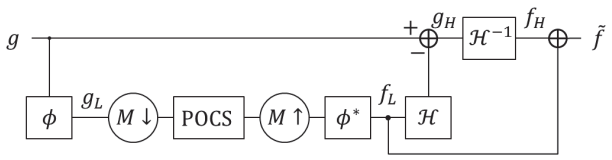

Fig. 4. Flowchart of the proposed multiscale reconstruction approach for interior tomography problem.

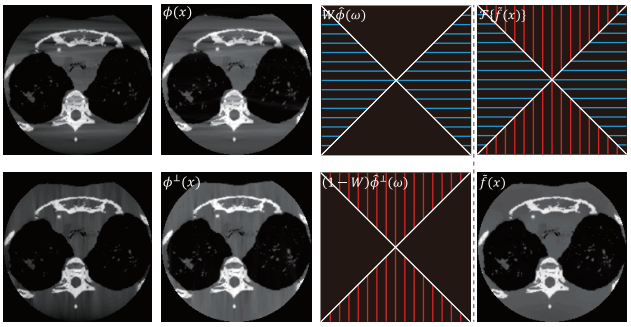

Fig. 5. ROI tomography reconstruction results using (a) BPF, (b) the proposed multiscale reconstruction method along horizontal ($\phi(x)$) and vertical ($\phi^{\perp}(x)$) filter directions, and (c) their the spectral blending results from the two filtering directions.

on Fig. 3, the size of the missing frequency regions from two orthogonal filtering directions is still comparable to that of multiple filtering directions. Since additional filtering direction requires additional applications of iterative interior topography algorithm, the computational complexity increases; so this paper just utilities the two filtering directions along x- and y- axis and apply the optimal spectral blending.

More specifically, as shown in the Fig. 3, it is possible to minimize the missing frequency region by blending appropriate frequency components of the reconstruction from the two orthogonal filtering directions. The shape of missing frequency region is described as Fig. 2(b) owing to the horizontal filtering direction, then it can be minimized by applying the row-wise bow tie window like Fig. 5(c) blue window. On the contrary, the shape is described as Fig. 2(c) owing to the vertical filtering direction, then it can be also minimized by applying the column-wise bow tie window like Fig. 5(c) red window. Finally, by blending both the weighted spectrums, the missing frequency region can be minimized in the 2D Fourier domain in each slice. Therefore, we apply 2D Fourier transform for each z-slice and use the spectral blending, which significantly reduces the computational burden. The concept of spectral blending simply is illustrated in Fig. 5. The multiscale decomposition interior tomography algorithm is used for both horizontal and vertical directions, respectively. Then, using spectral weighting with a bow-tie window, they are blended into one image.

III. Results

The reconstruction domain resolution of the real head phantom was $512 \times 512 \times 512$ voxles with voxel size $0.589 \times 0.589 \times 0.684$ mm^3, and the phantom size is $(-150, 150) \times (-150, 150) \times (-175, 175)$ mm^3. The resolution of the detector is 1024×250 array matrix with detector pitch of 0.4×0.4 mm^2 and the number of views is 720. The distance from source to rotation axis is 1700 mm, and the distance from source to detector is 2250 mm. The radius of FOV was about 36 mm. Since a transverse-ways offset is applied as 5.0 pitch, when the projection data was acquired, the ROI of the reconstructed head phantom is biased toward the right-bottom side.

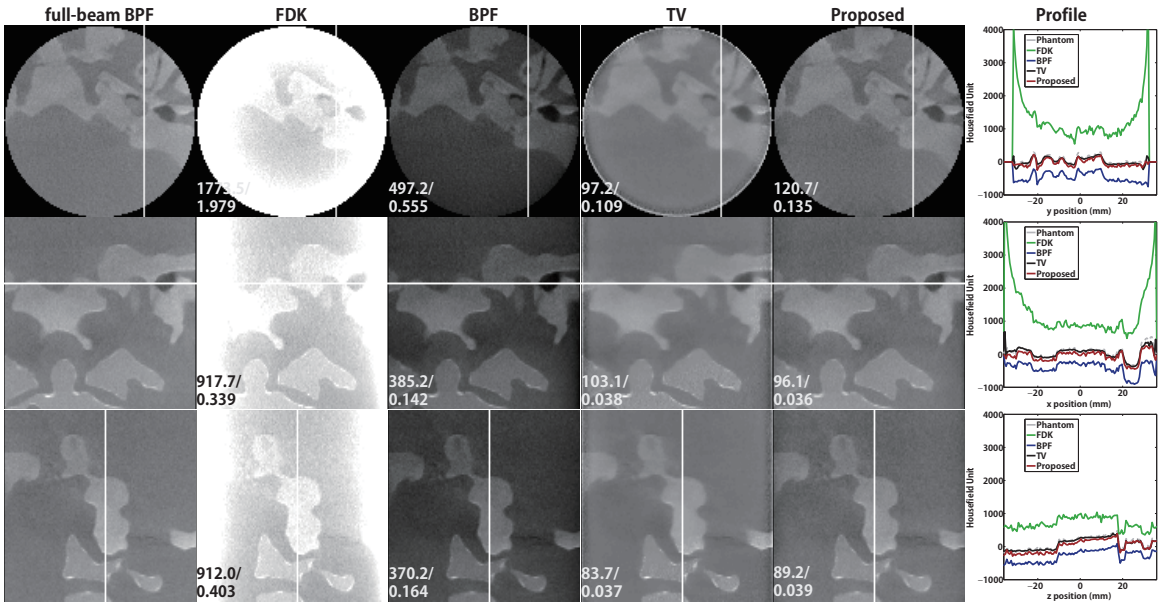

Fig. 6. The reconstruction results of real head phantom. From top to bottom, the each row denotes the cross section for the transection at $z = -11.3$ mm (*i.e.* off-mid-plane), the coronal at $y = -3.8$ mm, and the sagittal at $x = -0.9$ mm. The profiles corresponds to the CT numbers along the white lines of the reconstructed results. The profiles of full-beam BPF, FDK, BPF, TV and proposed method are represented by gray-dot, green, blue, and red, respectively.

In Fig. 6, reconstruction results for a real head phantom are shown in the region $(-36, 36) \times (-36, 36) \times (-36, 36)$ mm^3. Although the proposed method is truncated as about 70%, the results in Fig. 6 are very similar to that of the full-beam result. Unlike the TV reconstruction, the noise textures could be recovered by the proposed method, and confirmed that the algorithm does not result in unnatural smoothing. This is because TV is only applied at the low frequency reconstruction, and the high frequency reconstruction is done an using analytic formula.

When the computation time is compared between the proposed and conventional iterative (TV) method, a performance of reconstruction is 2.2 slice/sec for the proposed method, however, in the conventional case, the performance is 0.0667 slice/sec. This shows that the proposed method is 34.3 times accelerated over the conventional.

IV. Conclusion

In this paper, we provided a novel analysis of the missing frequency region using Fourier domain analysis, which is distinct from the Radon domain approach in [5]. Based on the analysis, an optimal spectral blending scheme that weights the reconstruction from two orthogonal filtering directions was proposed. We further demonstrated that the DBP data from the circular cone beam data has a similar Hilbert transform relationship on virtual chord lines, but the content is different owing to the missing frequency regions. Accordingly, our algorithm consisted of two step reconstruction procedure: first, the multiscale decomposition interior tomography algorithm using 1D TV penalty on the virtual chord lines, which is followed by spectral blending of a two reconstructions from horizontal and vertical filtering directions. The proposed method provided the reconstruction result with significantly reduced conebeam and missing frequency artifacts. Furthermore, all the processing were done in 1D virtual chord lines, which significantly reduces the computational complexity.

This work was supported by Korea Science and Engineering Foundation by Grant NRF- 2014R1A2A1A11052491.

References

[1] Y. Zou and X. Pan, "Exact image reconstruction on PI-lines from minimum data in helical cone-beam CT," *Physics in Medicine and Biology*, vol. 49, no. 6, pp. 941, 2004.

[2] Haiquan Yang, Meihua Li, Kazuhito Koizumi, and Hiroyuki Kudo, "Exact cone beam reconstruction for a saddle trajectory," *Physics in Medicine and Biology*, vol. 51, no. 5, pp. 1157–1172, 2006.

[3] Hengyong Yu and Ge Wang, "Compressed sensing based interior tomography," *Physics in Medicine and Biology*, vol. 54, no. 9, pp. 2791–2805, 2009.

[4] Minji Lee, Yoseob Han, John Paul Ward, Michael Unser, and Jong Chul Ye, "Interior tomography using 1d generalized total variation. part ii: Multiscale implementation," *SIAM Journal on Imaging Sciences*, vol. 8, no. 4, pp. 2452–2486, 2015.

[5] JD Pack, Z Yin, K Zeng, and BE Nett, "Mitigating cone-beam artifacts in short-scan CT imaging for large cone-angle scans," *Fully 3D Image Reconstruction in Radiology and Nuclear Medicine*, pp. 307–310, 2013.

[6] Jed D Pack and Frédéric Noo, "Cone-beam reconstruction using 1D filtering along the projection of M-lines," *Inverse Problems*, vol. 21, no. 3, pp. 1105–1120, 2005.

[7] Y. Zou and X. Pan, "Image reconstruction on PI-lines by use of filtered backprojection in helical cone-beam CT," *Physics in Medicine and Biology*, vol. 49, no. 12, pp. 2717, 2004.

[8] J. Yang, H. Yu, M. Jiang, and G. Wang, "High-order total variation minimization for interior tomography," *Inverse Problems*, vol. 26, no. 3, pp. 035013, 2010.

[9] Weimin Han, Hengyong Yu, and Ge Wang, "A general total variation minimization theorem for compressed sensing based interior tomography," *Journal of Biomedical Imaging*, vol. 2009, pp. 21, 2009.

[10] Frederick W King, *Hilbert transforms*, vol. 2, Cambridge University Press Cambridge, UK, 2009.

Efficient Area-Based Ray Integration Using Summed Area Tables and Regression Models

Sungsoo Ha, Heyi Li, and Klaus Mueller

***Abstract*—The increasing popularity of iterative reconstruction algorithms has raised the attention onto how to build more accurate, realistic CT system models. In our work, we model the CT projectors based on volume integrals. The higher computational complexity in computing the exact volume integration is hidden by memory-efficient, fast, and accurate look-up tables. For further reductions we also derive a simple linear regression model from the table. We demonstrate our ideas with data obtained with a fan-beam flat-detector CT system. We observe speed-ups of up to 30% while keeping a higher or at least similar image quality than existing advanced CT system models.**

***Index Terms*—CT system matrix, forward projection, line integral model, area-based model, volume integral model**

I. Introduction

With the increasing popularity of iterative reconstruction algorithms in the field of CT medical imaging, modeling a realistic CT system in software is becoming more crucial than ever. The CT system model can be represented by a huge matrix, **W**, whose columns correspond to the voxels subject to reconstruction (an N×1 vector) and the rows are the projections (or line integrals, an M×1 vector) that are measured by CT scanner. Then, each element, w_{ij}, of the matrix indicates the contribution of a voxel j to a detector cell i, so called weight coefficient. This gives rise to the linear algebra equation:

$$\mathbf{W} \cdot \mathbf{X} = \mathbf{P}$$

where **X** is the unknown image and **P** are the observed projection data. The process of calculating the line integrals is known as the forward projection and its reverse model, generally defined as the transpose of the forward projection, is known as back projection. As the size of the CT system matrix is enormous, the coefficients are usually computed on-the-fly during forward- and back projection.

The most intuitive and simplest way to compute the coefficient, w_{ij}, would be the line integral. It computes the intersection length between the *j*-th voxel and the *i*-th ray [1][2]. Here, a ray is depicted by a zero width line that connects the X-ray (point) source and the center of the detector cell for the ray-driven approach (or the center of a voxel for the voxel-driven approach). This kind of CT system modeling has low computational complexity but it can suffer from under-sampling and aliasing [3].

The other approach, which is much closer to a real CT system and which overcomes the sampling problems is the volume integration based approach. In this model, a single ray can be depicted by a 3D polygon (or 2D polygon for fan-beam) that connects the X-ray source with a detector cell. However, computing the intersected volume is not a trivial task and incurs high computational complexity. This precludes its use in iterative reconstruction routines where many intersections need to be computed.

Two well reported approaches exist which approximate the intersection volume. The first approach is the distance-driven (DD) method [3] that computes the coefficient as the row or slab intersection length combined with the overlap coefficient. The overlap coefficient is computed based on the length or area of overlap between a voxel and a detector cell when they are mapped onto each other as seen by the source. The other approach is the separable footprint (SF) method [4] which approximates the voxel footprints as 2D separable functions. This approximation not only greatly simplifies the computation of the coefficient but has also been shown to be more accurate than the DD methods, while keeping similar computational cost.

Recently, Ha et al. [5] introduced a method that computes the intersection volume exactly, and they also proposed three strategies that can approximate the volume at good accuracy. The approximate approaches aimed to make the volume integration process suitable for GPU-acceleration [6][7], using their massively parallel architecture to overcome the high computational cost of the exact ray-voxel intersection.

In this paper, we chose to go a different route with better computational efficiency while maintaining high accuracy. Here we were inspired by an established technique in computer graphics and texture mapping, called summed-area tables [8]. Our proposed method precomputes sampled intersection volumes and stores them in a summed area table such that unknown samples can be mapped into the table and be calculated using simple bilinear interpolation.

Our second approach derives a simple linear regression model from the table. While this method reduces accuracy, it is significantly faster. However, interestingly we can show that the reduced accuracy tends to occur in rays less frequently encountered and therefore reconstruction quality does not seem to suffer. We tested both methods with fan-beam X-ray flat-detector CT data and observed a computational cost reduction of up to 30% with a loss in image quality.

The remainder of our paper is organized as follows. Section II discusses details, Section III presents results. Finally, Section IV presents conclusions.

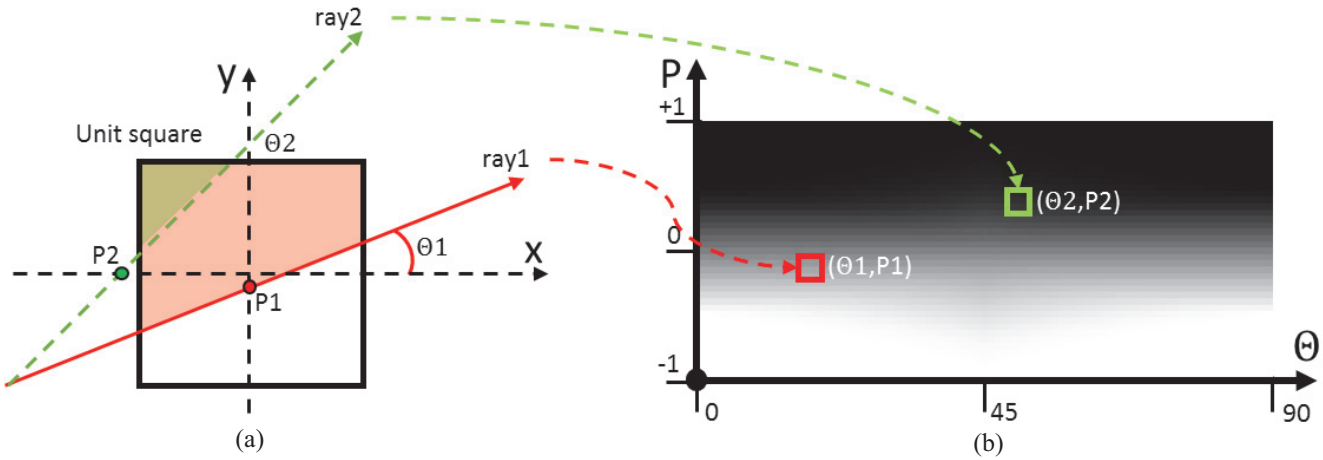

Figure 1. One side area look-up table. (a) Schematic view to compute intersection area between fan-beam and a unit pixel and (b) look-up table constructed with 1 degree and 0.05 mm step size resolution (99% accuracy).

II. Methodology

A. One-side Area Look Up Table (LUT)

We define a ray as a zero-width line that connects the X-ray point source to a point on a detector. Then, one side area is the area between a ray and unit square in one side either left or right. We parameterize the area by the ray incident angle, θ, which is measured from the x-axis to the ray, and an intersection point, P. The point is computed as an intersection point with the y-axis if the angle is less than or equal to 45 degrees. Otherwise it is computed with the x-axis to always have a single intersection point. The one-side area Look-Up Table (LUT) is a table that contains all possible one-side areas ranging from 0 to 360 degrees and -1 to 1 for the ray incident angle and intersection point, respectively. Then, given two parameters, θ and P, one side area is fetched from the LUT using bi-linear interpolation. The intersection area between a pixel and a fan-beam modeled by two rays can be efficiently computed by fetching two one side areas from the LUT and subtract one from the other. Figure 1 shows the schematic view of this with an example usages of the LUT.

Due to symmetry given the square area of a voxel, we only need to store from 0 to 90 degrees. We use step sizes of 1 degree and 0.05 mm to construct the LUT. The size of the LUT is, thus, 41×91 which takes up only about 15 K Bytes, which is trivial amount memory for most of modern computer. The accuracy of the LUT is measured by comparing it with analytical solutions of 1,000 random pairs of the two input parameters, θ and P. We find an accuracy of roughly 99% with a maximum error of 0.004.

B. One-side Area Regression Model

Figure 2 shows curves of the one side area LUT along the P-Area axis. Note that each curve corresponds to a column vector of the LUT constructed in previous section. We observe that all curves vary within the range of the curves extracted at 0 and 45 degrees. Approximation can be obtained by abstracting the curves with a piece-wise non-linear regression model. Here, we take a simple piece-wise linear regression model that can cause at most 0.1207 error (about 12% with 45° ray incident angle and $\pm$ 0.5 mm) to take advantage of low computational complexity as follows.

$$Area = \begin{cases} -P + 0.5 & , -0.5 < P < 0.5 \\ 0 & P \le -0.5 \\ 1 & P \ge 0.5 \end{cases}$$

We analyze the effect of the error by simulating a realistic set of forward projections over 360 degrees spaced by 1 degree. Note that in the area-based approach the forward and back projection are symmetric operators and so we only examine one. We draw an *error map* by computing the errors our regression model can make. In the LUT matrix view, we subtract the first column vector (0° ray incident angle) by the others. Then we measure the occurrence of each element in the LUT during projections, yielding a *frequency map*. This map represents how often each element is used during projections in a given CT system. The total number of fetches will be (# projections) × (# pixels) × (# detector cells affected by each pixel) × (at most 4 LUT elements for bilinear interpolation). The *average error* that can occur during projections is estimated by multiplying the error map and the frequency map. The total expected error is then computed by summing all values in the average error map. Figure 3 shows the three maps computed with the fan-beam flat-detector CT system and the average error is 1.0891 %.

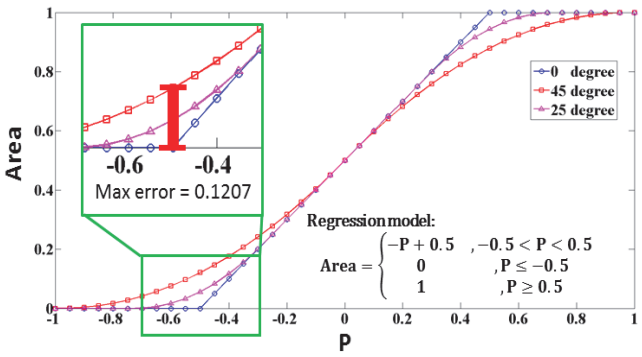

Figure 2. One side area piece-wise linear regression model

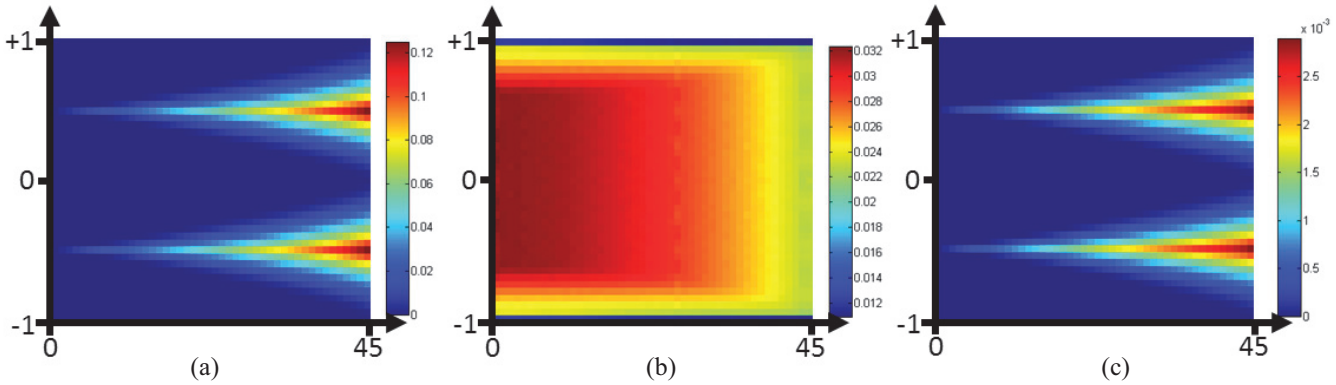

Figure 3. One side area piece-wise linear regression model. (a) error map, (b) frequency map and (c) average error map.

III. Results

We tested the two proposed CT system models with a fan-beam flat-detector X-ray CT system with a detector size of 1024 cells spaced by 0.384 mm. The source to detector distance is 1147.7 mm and the source to rotation center distance is 647.7 mm. The fan-angle is about 19.4 degrees. For the forward/back projection analysis, we used a 512×512 Shepp-Logan phantom data with 0.415 × 0.415 mm^2 pixel size. All experiments use 360 views uniformly distributed over 360 degrees and the forward/back projection operators are implemented using the pixel driven method. Note that all implementations are accelerated by an NVIDIA Tesla K40c.

A. Forward projection

In area-based CT system models, forward- and back-projection operators are symmetric. We measure the accuracy of our regression model for forward projection by comparing it with the LUT-based approach. We define the normalized root mean square error (NRMS) as

$$e(\phi) = \frac{1}{N}\sum_{i}^{N} \left\| F_{\phi}^{LUT}(i) - F_{\phi}^{REG}(i) \right\|_2$$

where $F_{\phi}(i)$ returns normalized forward projected value at a detector cell i at a projection angle, ϕ, such that

$$F_{\phi}(i) = \frac{\sum_{j=1}^{M} f(j) \cdot w_{ij}}{\sum_{j=1}^{M} w_{ij}}.$$

Here, $f(j)$ is a j-th pixel value, and N and M represent the number of detector cells and pixels. The w_{ij} is the contribution of a pixel j to a detector cell i that computes either by look-up table or regression model and superscript, *LUT* and *REG*, used to indicate them, respectively. Figure 4 shows the NRMS measurement over 360 views. As the same pattern is repeated every 90 degrees, we only show 0° to 90° projection angles. As the projection angle increases, there are more chances that a ray can have the incident angles, θ, around 45°, and it reaches the maximum occurrence around 30° and 64° projection angles as the combination effect with fan-angles (19.4°). At this time the error is about 0.002106 (about 2% error). After the peak point, the error goes down as the occurrence reduction of erroneous ray incident angles.

B. Within iterative CT reconstruction

The proposed methods were plugged into a simultaneous algebraic reconstruction technique (SART) framework that updates each projection at a time.

$$f_j^{k+1} = f_j^k + \lambda \cdot \frac{\sum_i \left[\frac{p_i - \sum_{i=1}^{N} w_{ij} \cdot f_j^k}{\sum_{i=1}^{N} w_{ij}} \right] w_{ij}}{\sum_i w_{ij}}$$

where f_j^k is reconstructed j-th pixel at k-th iteration and p_i is i-th projection data. The constant factor, λ, is update step size. Using the SART, we measure the performance in terms of time and reconstruction quality. We used Shepp-Logan phantom

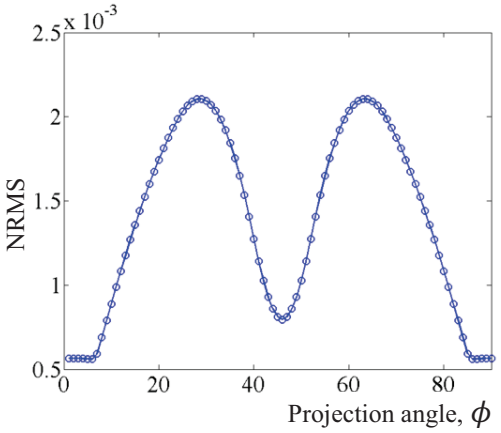

Figure 4. NRMS error comparison between look-up table and regression model approach as forward projectors.

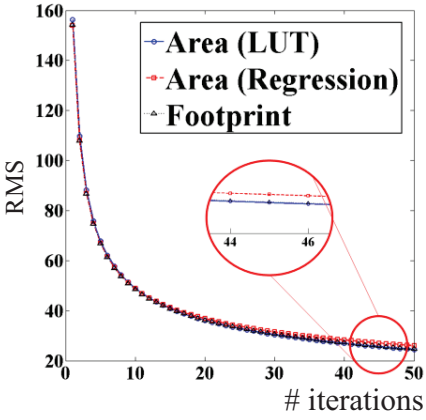

Figure 5. Convergence comparisons among three different projectors, LUT-, Regression model- and Footprint-based.

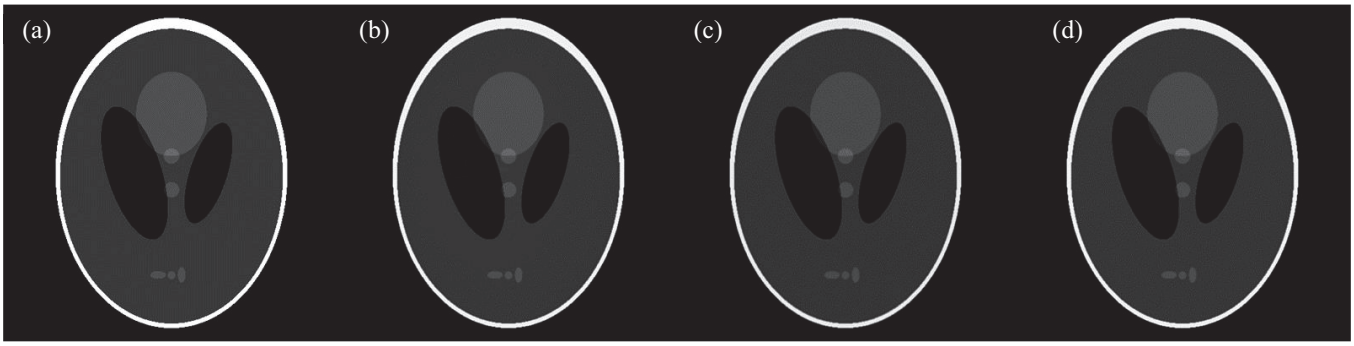

Figure 6. Visual comparisons. (a) Shepp-Logan phantom, (b) Footprint, (c) LUT and (d) Regression

data for this, and the projection data were simulated using the LUT based approach as it has about 99% of accuracy to compute the intersection area compared to an analytical solution. Finally, we compared our methods with the state-of-the-art footprint-based approach [4]. In the following, the experimental results were obtained by running 200 iterations with 0.01 update step size.

Convergence: We measure the convergence rate among three different projection methods. Two are the proposed ones and the other is the separable footprint. To maintain fairness among different approaches, we define the root mean square (RMS) errors as follows:

$$RMS = \sum_{i=1}^{M} \left\| \hat{f}(i) - f_{sart}^{norm} \right\|_2$$

where $\hat{f}$ is the reference phantom data we used to generate projection data and f_{sart}^{norm} is reconstructed image normalized by the maximum value. Figure 5 shows the result. All methods have similar convergence rate and converge to similar solution. (at 45 iterations, 25.58, 25.72 and 27.05 for LUT, Regression and Footprint, respectively).

Visual Assessment: Figure 6 presents visual comparisons of reconstructed images after 200 iterations. As all methods are converged to a similar solution, the visual look is also similar to each other.

Time Performance: The SART consists of 4 kernels, Forward Projection (FP), Correct, Back Projection (BP) and Update. We measure the running time of each kernel. There are 360 projections and we run it 200 times. The average time is presented in Table 1. In our implementation, both projection operators were implemented based on the pixel-driven method. As the result, BP is faster than FP in all methods because it does not require atomic operations; while it is necessary for the FP to avoid race condition. For the FP, with LUT, we can achieve 10% of speed-up due to the reduced computational complexity and Regression can improve the time performance another 15%.as it does not require memory fetching operations for the LUT. For similar reasons, in the BP, the proposed methods are faster by about 15% and 30% for LUT and Regression, respectively.

TABLE I. TIME PERFORMANCE COMPARISON [MILLISECOND]

	FP	Correct	BP	Update
Footprint	0.215		0.170	
LUT	0.192	0.025	0.147	0.05
Regression	0.161		0.121	

IV. CONCLUSION

We described and studied two area-based methods to construct a more realistic and accurate CT system model. We find that both methods can outperform the separable footprint method in terms of time complexity without a loss in reconstruction image quality. In future work we would like to investigate this finding further in the context of cone-beam and helical CT.

ACKNOWLEDGMENT

This research was supported by the MSIP (Ministry of Science, ICT and Future Planning), Korea, under the "ICT Consilience Creative Program" (IITP-2015-R0346-15-1007) supervised by the IITP (Institute for Information & communications Technology Promotion). We also thank Medtronic, Inc. for their continued support.

REFERENCES

[1] R.L. Siddon, "Fast calculation of the exact radiological path for a three-dimensional CT array," Med. Phys. 12(2):252-255, 1985.
[2] P,M. Joseph, "An improved algorithm for reprojecting rays through pixel images." IEEE Trans Med Imaging 1(3):192-196, 1983.
[3] B. De Man and S. Basu, "Distance-driven projection and backprojection in three dimensions," Phys. Med. Biol. 49(11), 2463-2475, 2004.
[4] Y. Long, J. A. Fessler, and J. M. Balter, "3D forward and back-projection for x-ray CT using separable footprints," IEEE Trans. Med. Imaging 29(11), 1839-1850, 2010.
[5] S. Ha, A. Kumar, and K. Mueller, "A Study of Volume Integration Models for Iterative Cone-Beam Computed Tomography," Fully3D Image Reconstruction in Radiology and Nuclear Medicine, June 2015.
[6] F. Xu, K. Mueller, "Accelerating popular tomographic reconstruction algorithms on commodity PC graphics hardware," IEEE Trans. on Nuclear Science, 52(3):654-663, 2005
[7] F. Xu, K. Mueller, "Real-Time 3D Computed Tomographic Reconstruction Using Commodity Graphics Hardware," Physics in Medicine and Biology, 52:3405-3419, 2007.
[8] C. Franklin, "Summed-area tables for texture mapping," ACM SIGGRAPH computer graphics 18(3), 207-212, 1984

Analytical Statistical Reconstruction Algorithm with the Direct Use of Projections Performed in Fan-beam Scanners

Robert Cierniak

***Abstract*—The main aim of the paper presented here is strictly concerned with the originally formulated 3D reconstruction algorithm for spiral cone-beam x-ray tomography. The approach proposed here is based on a fully analytical formulation of the reconstruction problem. The method can be classed as a statistical reconstruction method, which significantly improves the quality of the subsequently reconstructed images, so allowing a decrease in the x-ray dose absorbed by a patient during examination. The analytical roots of the algorithm proposed here permit a decrease in the complexity of the reconstruction problem in comparison with algebraic approaches. In this paper, I proved that this statistical approach, originally formulated for parallel beam geometry, can be adapted for fan-beam geometry of scanner, with the direct use of projections, and consequently for helical cone-beam scanners. Computer simulations have shown that the reconstruction algorithm presented here outperforms conventional analytical methods with regard to the image quality obtained.**

I. Introduction

Currently, the most significant challenge in the field of medical computer tomography is the development of image reconstruction algorithms from projections which would enable the reduction of the impact of measurement noise on the quality of tomography images. This kind of approach is intended to improve high resolution image quality and, in consequence, reduce the dose of X-ray radiation while at the same time preserving an appropriate level of quality in the tomography images. The concept has found its application in the form of statistical reconstruction algorithms. One of the most interesting from the scietific and practical point of view, an approach, called MBIR (Model-Based Iterative Reconstruction), is presented in publications like [1], where a probabilistic model of the measurement signals is described analytically. The objective in these solutions was devised according to an algebraic scheme for formulating the reconstruction problem [2]. An algebraic scheme has been selected in this case for one very obvious reason - the measurement noise can be modelled relatively easily, because each measurement is considered separately. Nevertheless, as is well known, such a scheme adds significant calculative complexity to the problem. The time for image reconstruction becomes unacceptable from the practical point of view. For instance, if the image resolution is assumed to be I $\times$ I pixels, the complexity of the algebraic problem is of the level of I $\times$ I $\times$ $number\_of\_measurements$ $\times$ $number\_of\_cross-sections$ (in 3D tomography); a multiple of I to the power of four in total.

Corresponding author: Robert Cierniak, Institute of Computational Intelligence, Czestochowa University of Technology, Armii Krajowej 36, 42-200 Czestochowa, Poland, e-mail: cierniak@kik.pcz.czest.pl

The difficulties mentioned above connected with the use of an algebraic methodology can be limited by using an analytical strategy of reconstructed image processing. In previous papers I have shown how to formulate the analytical reconstruction problem consistent with the ML methodology for parallel scanner geometry [5]. This strategy has been used for fan-beams [3], and finally for the spiral cone-beam scanner [6]. However, an approach to the reformulation of the reconstruction problem from parallel to real scanner geometries, called rebinning, was applied there. The rebinning approach in the 3D spiral version involves a nutating slice CT image reconstruction method described in the literature by its abbreviation ASSR (Advanced Single Slice Rebinning) [7]. Much more popular 3D reconstruction methods, which are implemented in practice, are FDK (Feldkamp)-type algorithms that the use projections obtained from spiral cone-beam scanners directly (see e.g. [8]). In this paper, we present a mathematical derivation of a method for the direct (i.e. without rebinning) adaptation of fan-beam projections to the statistical analytical reconstruction algorithm originally formulated by me. This solution is directly applicable to 3D spiral cone-beam scanner geometry.

II. Adaptation of the 2D Analytical Approximate Reconstruction Problem to Fan-beam Projections

The 2D analytical approximate reconstruction problem was originally formulated for a parallel scanner geometry [3], as follows:

$$\mu_{\min} = \arg\min_{\mu} \left(\frac{n_0}{2} \sum_{i=1}^{\mathrm{I}} \sum_{j=1}^{\mathrm{J}} \cdot \right.$$
$$\left. \cdot \left(\sum_{\bar{i}} \sum_{\bar{j}} \mu\left(x_{\bar{i}}, y_{\bar{j}}\right) \cdot h_{\Delta i, \Delta j} - \tilde{\mu}\left(x_i, y_j\right) \right)^2 \right), \quad (1)$$

where coefficients $h_{\Delta i, \Delta j}$ are

$$h_{\Delta i, \Delta j} = \Delta_\alpha \sum_{\psi=0}^{\Psi-1} int\left(\Delta i \cos\psi\Delta_\alpha + \Delta j \sin\psi\Delta_\alpha\right), \quad (2)$$

and $\tilde{\mu}\left(i,j\right)$ is an image obtained by way of a back-projection operation; $int\left(\Delta s\right)$ is an interpolation function used in the

back-projection operation; every projection is carried out after a rotation by Δ_α.

This concept can also form the starting point for the design of a 3D reconstruction algorithm for spiral cone-beam scanner geometry. One of the principal reconstruction methods devised for the cone-beam spiral scanner is the generalized FDK algorithm. The FDK algorithm is a development of a conventional fan-beam reconstruction approach with direct use of measurements performed in a fan-beam scanner (see e.g. [4]). In the traditional FDK approach, the fan-beam projections are filtered in two dimensions and then back-projected in three dimensions. This methodology is adapted to our original iterative model-based reconstruction concept.

Taking into consideration the definition of the two-dimensional inverse Fourier transform, and the frequential form of the relation between the original image of a cross-section of an examined object represented by function $\mu(x,y)$ and the image obtained after the back-projection operation $\tilde{\mu}(x,y)$, we obtain:

$$\tilde{\mu}(x,y) = \int_{-\infty}^{\infty}\int_{-\infty}^{\infty} \frac{1}{|f|} M(f_1,f_2)\, e^{j2\pi(f_1 x + f_2 y)} df_1 df_2, \quad (3)$$

which, after converting to polar coordinates and using the projection slice theorem (taking into account a full revolution of the projection system), takes the form:

$$\tilde{\mu}(x,y) = \frac{1}{2}\int_{-\pi}^{\pi}\int_{-\infty}^{\infty} \bar{P}(f,\alpha^p)\, e^{j2\pi f(x\cos\alpha^p + y\sin\alpha^p)} df d\alpha^p. \quad (4)$$

Then, after transferring the projections into the spatial domain, we have the formula:

$$\tilde{\mu}(x,y) = \frac{1}{2}\int_{-\pi}^{\pi}\int_{-\infty}^{\infty} \int_{-\infty}^{\infty} \bar{p}^p(s,\alpha^p)\, e^{j2\pi f(x\cos\alpha^p + y\sin\alpha^p)} \cdot e^{-j2\pi f s} ds df d\alpha^p. \quad (5)$$

Arranging the right hand side of the above formula and changing the order of integration, we get:

$$\tilde{\mu}(x,y) = \frac{1}{2}\int_{-\infty}^{\infty}\int_{-\infty}^{\infty}\int_{-\pi}^{\pi} \bar{p}^p(s,\alpha^p)\, e^{j2\pi f(x\cos\alpha^p + y\sin\alpha^p - s)} d\alpha^p ds df. \quad (6)$$

Next, after converting the attenuation function into polar coordinates, we obtain:

$$\tilde{\mu}(r\cos\phi, r\sin\phi) = \frac{1}{2}\int_{-\infty}^{\infty}\int_{-\infty}^{\infty}\int_{-\pi}^{\pi} \bar{p}^p(s,\alpha^p)\, e^{j2\pi f[r\cos(\alpha^p-\phi)-s]} d\alpha^p ds df. \quad (7)$$

Note here that the substitution $x\cos\alpha^p + y\sin\alpha^p = r\cos(\alpha^p - \phi)$ refers to the point (r,ϕ), to which the reconstruction process applies, and the variable s specifies the location on the screen.

Of course, we should also take into account the application of the interpolation function used during the back-projection operation, which should be placed appropriately (a frequency representation of this function) in the formula above to finally obtain:

$$\breve{\mu}(x,y) = \frac{1}{2}\int_{-\infty}^{\infty}\int_{-\infty}^{\infty}\int_{-\pi}^{\pi} INT(f)\, p^p(s,\alpha^p)\, e^{j2\pi f[r\cos(\alpha^p-\phi)-s]} d\alpha^p ds df. \quad (8)$$

After suitable transformation we obtain a relationship, which is fundamental for the fan-beam image reconstruction method:

$$\breve{\mu}(x,y) = \frac{\mathrm{R}_f}{2}\int_{-\infty}^{\infty}\int_{-\beta_m}^{\beta_m}\int_{-\beta}^{2\pi-\beta} INT(f)\, p^f(\beta,\alpha^f)\cos\beta\, e^{j2\pi f \dot{u}\sin(\dot{\beta}-\beta)} d\alpha^f d\beta df, \quad (9)$$

and further

$$\breve{\mu}(x,y) = \frac{\mathrm{R}_f}{2}\int_{0}^{2\pi}\int_{-\beta_m}^{\beta_m} p^f(\beta,\alpha^f) \cos\beta \int_{-\infty}^{\infty} INT(f)\, e^{j2\pi f \dot{u}\sin(\dot{\beta}-\beta)} df d\beta d\alpha^f. \quad (10)$$

Unfortunately, there is a serious drawback associated with the use of the fan-beam reconstruction method formulated like this. It stems from the dependence of equation (10) on the parameter $\dot{u}$, which poses certain practical problems when carrying out the calculations during the reconstruction process. Instead of a simple formula for the convolution kernel, it now becomes necessary to determine a different form of the kernel for every point of the object's cross-section. This is because $\dot{u}$ represents the distance of the point (r,ϕ) from the radiation source. Therefore, by changing the angle α^f, we also change $\dot{u}$. The appropriate adjustment is based on a term in equation (10), which is reproduced here in a suitably amended form:

$$int(s) = \int_{-\infty}^{\infty} INT(f)\, e^{j2\pi f \dot{u}\sin(\dot{\beta}-\beta)} df. \quad (11)$$

In this equation, the integration is carried out with respect to the frequency f. The next step will be to make a substitution for f, using the following expression:

$$f^f = \frac{f\cdot\dot{u}\cdot\sin\beta}{\mathrm{R}_f\cdot\beta}. \quad (12)$$

If at the same time we change the limits of integration, the convolving function will be modified to:

$$int^f(\beta) = \frac{\mathrm{R}_f \cdot \beta}{\dot{u} \cdot \sin\beta} \int_{-\infty}^{\infty} INT\left(\frac{f^f \cdot f_0}{f_0^f}\right) e^{j2\pi f^f \mathrm{R}_f \beta} df^f, \tag{13}$$

where

$$f_0^f = \frac{f_0 \cdot \dot{u} \cdot \sin\beta}{\mathrm{R}_f \cdot \beta}. \tag{14}$$

Unfortunately, even here we encounter problems caused by the dependence of the cut-off frequency f_0^f on the parameter $\dot{u}$. On the other hand, if we were to establish a constant value for f_0^f it would mean that the reconstruction process for the point (r, ϕ) would have a different resolution (determined by the value of the cut-off frequency f_0) for every angle α^f. However, if we put aside the assumption of uniform resolution for the resulting reconstructed image, then, by manipulating the values $\dot{u}$ and f_0, the varying value of f_0^f can be fixed as:

$$f_0^f = \mathrm{f}_0^f = \frac{1}{\mathrm{R}_f \cdot \Delta_\beta}. \tag{15}$$

Let us assume that we apply a linear interpolation function in formula (9), i.e. the following form of this function:

$$int_L(s) = \begin{cases} \frac{1}{\Delta_s}\left(1 - \frac{|s|}{\Delta_s}\right) & \text{for} \quad |s| \le \Delta_s \\ 0 & \text{for} \quad |s| \ge \Delta_s \end{cases}. \tag{16}$$

The frequency form of the interpolation function shown in equation (16) is given by this formula:

$$INT_L(f) = \frac{\sin^2(\pi f \Delta_s)}{(\pi f \Delta_s)^2}. \tag{17}$$

Taking into account in the formula (13) the proposed interpolation function given by (17), we obtain the following relation:

$$int_L^f(\beta) = \frac{\mathrm{R}_f \cdot \beta}{\dot{u} \cdot \sin\beta} \frac{1}{\Delta_s'} \int_{-\infty}^{\infty} \Delta_s' \frac{\sin^2(\pi f \Delta_s')}{(\pi f \Delta_s')^2} e^{j2\pi f \mathrm{R}_f \beta} df, \tag{18}$$

where

$$\Delta_s' = \frac{f_0}{f_0^f}. \tag{19}$$

It is easy to show that it gives

$$int_L^f(\beta) = \frac{\mathrm{R}_f \cdot \beta}{\dot{u} \cdot \sin\beta} \begin{cases} \frac{1}{\Delta_s'}\left(1 - \frac{\mathrm{R}_f|\beta|}{\Delta_s'}\right) & \text{for} \quad |\beta| \le \Delta_s' \\ 0 & \text{for} \quad |\beta| \ge \Delta_s' \end{cases}, \tag{20}$$

and next, bearing in mind relations (15) and (19), it leads immediately to:

$$int_L^f(\beta) = \frac{\beta}{\dot{u} \cdot \sin\beta} \begin{cases} \frac{\Delta_s}{\Delta_\beta}\left(1 - \frac{\Delta_s|\beta|}{\Delta_\beta}\right) & \text{for} \quad |\beta| \le \frac{\Delta_\beta}{\Delta_s} \\ 0 & \text{for} \quad |\beta| \ge \frac{\Delta_\beta}{\Delta_s} \end{cases}. \tag{21}$$

Finally, if we assume that $\Delta_s = 1$, it gives

$$int_L^f(\beta) = \frac{\beta}{\dot{u} \cdot \sin\beta} int_L(\beta), \tag{22}$$

where

$$int_L(\beta) = \begin{cases} \frac{1}{\Delta_\beta}\left(1 - \frac{|\beta|}{\Delta_\beta}\right) & \text{for} \quad |\beta| \le \Delta_\beta \\ 0 & \text{for} \quad |\beta| \ge \Delta_\beta \end{cases}. \tag{23}$$

In consequence, returning to the formula (10), we obtain

$$\breve{\mu}(x,y) = \frac{1}{2} \int_0^{2\pi} \int_{-\beta_m}^{\beta_m} p^f\left(\beta, \alpha^f\right) \frac{\mathrm{R}_f \cos\beta}{2\dot{u}} \frac{\Delta\beta}{\sin\Delta\beta} int_L(\Delta\beta)\, d\beta d\alpha^f. \tag{24}$$

Fortunately, we can linearize relation (25) by considering expressions inside the integration, namely $\frac{\Delta\beta}{\sin\Delta\beta}$.

In the case of linear interpolation I use only line of integrals from the neighborhood of a given pixel (x, y), then $\Delta\beta \le \Delta_\beta$, and $\sin\Delta\beta \approxeq \Delta\beta$. Additionally, it is possible to omit the term $\frac{\mathrm{R}_f \cos\beta}{2\dot{u}}$ taking into account the fact that each projection value $p^f\left(\beta, \alpha^f\right)$ has its equivalent $p^f\left(-\beta, \alpha^f + \pi + 2\beta\right)$, as shown in Figure 1.

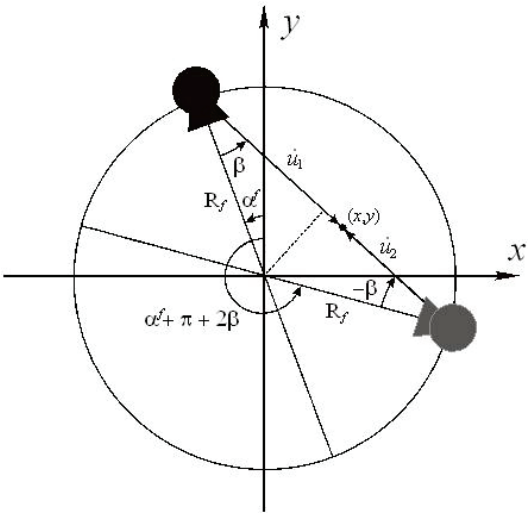

Fig. 1. Selecting complementary projection values

Because of this we can notice that the sum of this pair of projections is proportional to $\frac{\dot{u}_1+\dot{u}_2}{4\dot{u}_1} + \frac{\dot{u}_1+\dot{u}_2}{4\dot{u}_2} = \frac{(\dot{u}_1+\dot{u}_2)^2}{4\dot{u}_1\dot{u}_2}$. This means that for $\dot{u}_1 \approxeq \dot{u}_2$ this factor is equal to 1, and finally, we can write

$$\breve{\mu}(x,y) \approxeq \frac{1}{2} \int_0^{2\pi} \int_{-\beta_m}^{\beta_m} p^f\left(\beta, \alpha^f\right) int_L(\Delta\beta)\, d\beta d\alpha^f, \tag{25}$$

which is consistent with a form of the formula of the back-projection operation for parallel beams. Therefore, formula (25) can be used directly to obtain a reference image for the analytical statistical iterative reconstruction algorithm which was originally formulated for parallel beam scanner geometry.

III. Experimental results

In my experiments, I have used projections obtained from a C-arm scanner. Paremeters: $SDD = 1025$mm (Source-to-Detector Distance); $\mathrm{R}_f = 825\mathrm{mm}$ (SOD (Source-to-AOR Distance)); number of views per rotation $\Psi = 538$; number of pixels in detector panel 756; detector side 307.2mm. During the simulations, the size of the processed image was fixed at $\mathrm{I} \times \mathrm{J} = 512 \times 512$ pixels. The coefficients $h_{\Delta i,\Delta j}$ were precomputed before we started the reconstruction process and these coefficients were fixed for the subsequent processing. I started the actual reconstruction procedure and perform the back-projection operation to get a blurred image of the x-ray attenuation distribution in a given cross-section of the investigated object. The image obtained in this way was then subjected to a process of reconstruction (optimization) using an iterative statistically-tailored procedure. The starting point of this procedure we can choosen as a result of using any standard reconstruction method, for example a reconstruction FBP algorithm. It is worth noting that our reconstruction procedure was performed without any regularization regarding the objective function described by (1).

View of the reconstructed images after 70000 iterations are presented (Table 2(a).b. For comparison, the image reconstructed by a standard FBP reconstruction method (Table 2(b).b) is also presented.

IV. Conclusion

I have shown in this paper fully feasible statistical reconstruction algorithm for fan-beam projections. It is proved that this statistical approach, originally formulated for parallel beam geometry, can be adapted for fan-beam geometry of scanner, with the direct use of projections. In consequence, merely after a few additional transformations, this algorithm can be used for helical cone-beam scanners. Simulations have been performed, which prove that our reconstruction method is very fast (thanks to the use of FFT algorithms) and gives satisfactory results with suppressed noise, without introducing any additional regularization term.

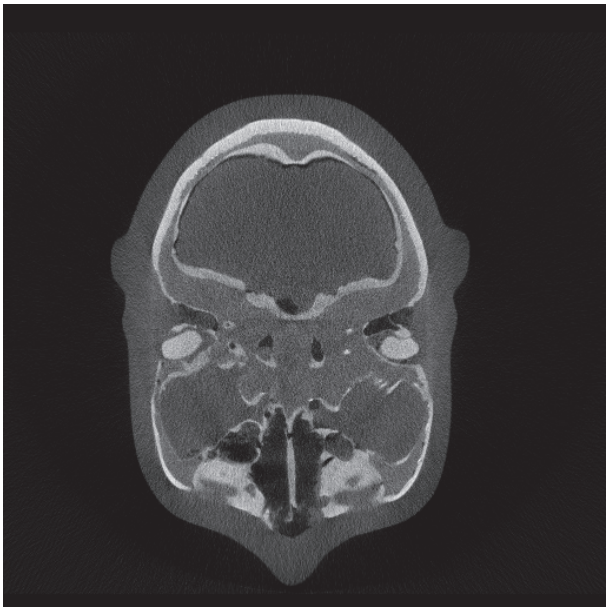

(a)

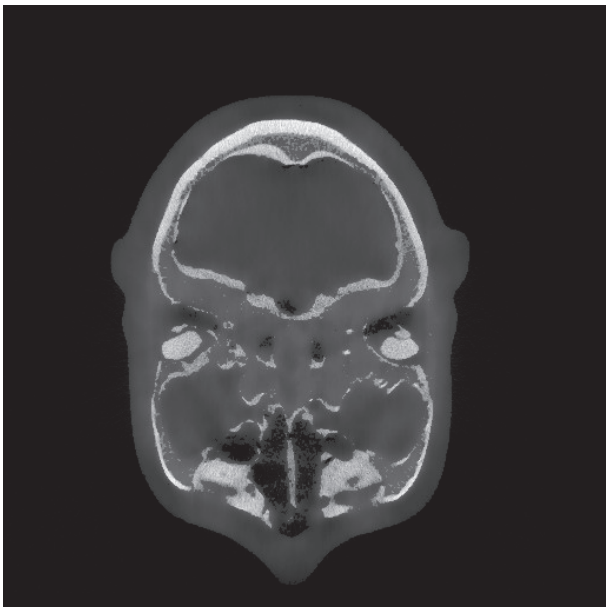

(b)

Fig. 2. View of the images reconstructed image using the standard FBP with Shepp-Logan kernel (a); reconstructed image using the method described in this paper after 30000 iterations (b)

References

[1] Bouman, C., Sauer, K.: A unified approach to statistical tomography using coordinate descent optimization. IEEE Tran. Image Processing 5, 480–492, 1996.

[2] J. -B Thibault, K. D. Sauer, C. A. Bouman, J. Hsieh, *A three-dimensional statistical approach to improved image quality for multislice helical CT*, Medical Physics, vol. 34, No. 11, pp. 4526–4544, 2007.

[3] Cierniak, R.: An analytical iterative statistical algorithm for image reconstruction from projections. Applied Mathematics and Computer Science 24, 7–17, 2014.

[4] Lewitt, R.M.: Reconstruction algorithms: transform methods, Proc IEEE, vol. 71, No. 3, 390–408, 1983.

[5] R. Cierniak, *New neural network algorithm for image reconstruction from fan-beam projections*, Neurocomputing, vol. 72, pp. 3238–3244, 2009.

[6] Cierniak, R.: A three-dimensional neural network based approach to the image reconstruction from projections problem. In: Rutkowski, L., Tadeusiewicz, R., Zadeh, L.A., urada, J. (eds.) LNCS, vol. 6113, pp. 505–514. Springer, Heidelberg, 2010.

[7] Kachelrieß, M., Schaller, S., Kalender, W.A.: Advanced single-slice rebinning in cone-beam spiral CT. Medical Physics 27, 754–773, 2000.

[8] Cierniak, R., Knas, M.: *An analytical statistical approach to the 3D reconstruction problem*, in Proc. of the 12th International Meeting on Fully Three-Dimensional Image Reconstruction in Radiology and Nuclear Medicine, pp. 521–524, July 2013.

Dual-band projection alignment applied in X-ray microscopy

Sebastian Allner, Andreas Fehringer, Jonathan Schock, Franz Pfeiffer, and Peter B. Noël

***Abstract*—In many cases one tomographic X-ray investigation does not suffice to answer a specific question. Therefore, multi-modal (e. g. dual-energy CT) imaging can be used to obtain all necessary information about the sample. One frequent problem arising from multiple datasets is that they have to be registered in order to analyze the volumes appropriately. Usually, a volume registration is performed which has several disadvantages. Here, we propose an alternative method to align the volumes intrinsically in the tomographic reconstruction process. We enforce the tomographic consistency of a dual-energy scan by performing a combined reconstruction and align the projections according to their projection estimate. We show that this combined alignment approach intrinsically registers a dual-energy scan and does not degrade the separate reconstructions.**

I. Introduction

In the last years, multi-modal (e. g. dual-energy CT) imaging has gained a lot of interest because it offers more information about the sample than a simple CT scan. But even if the two scans are performed subsequently in one device alignment imperfections can occur. This is even worse if the datasets were acquired on different devices with different detectors, pixel sizes, and various other differences in the setups. An additional source of error would be a sample drift within one of the scans. This corrupts one scan completely and usually the measurement has to be performed again. To still obtain a consistent reconstruction there are several alignment approaches to improve the alignment of one dataset. A rather simple approach is the center-of-mass alignment [1] which is based on a common center of mass in all projections. This algorithm neglects beamhardening and does not work for samples moving partly out of the beam for some projections, and is therefore hardly viable for most tomographic scans and scan geometries. Another frequently used method is to register opposing images [2] ($\phi, \phi + 180°$) which also does not work for half-scan measurements or geometries with large opening angles. In addition, it neglects that also the opposing projection might suffer from misalignment. Both of these techniques hardly work for a single tomographic scan. Other alignments based on the redundancy of the measured data [3] may also just work for a single tomographic scan, as the correlation e.g. for a dual-energy scan do not match well enough. A different approach is based on enforcing the intrinsic consistency of a tomographic scan [4] (referenced as tomoconsitency) which relies on calculating a projection estimate from the currently assumed scan geometry with the given projections. Subsequently, the projections are matched onto these projection estimates.

Sebastian Allner, Andreas Fehringer, Jonathan Schock, Franz Pfeiffer, and Peter B. Noël are with the Department of Physics and Institute of Medical Engineering, Technische Universität München, Garching, Germany.

Franz Pfeiffer, and Peter B. Noël are with Department of Radiology, Klinikum rechts der Isar, Technische Universität München, Munich, Germany.

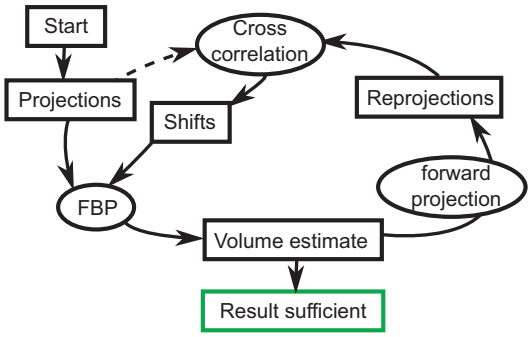

Figure 1. Scheme of iterative tomoconsistency alignment.

In this work we applied tomoconsistency to a dual-energy scan of a stone drilling core and performed the projection alignment based on a combined reconstruction of both energies. We show that the combined alignment does not corrupt the reconstructed images of each energy but intrinsically registers both volumes with respect to each other. Additionally, we display the improved alignment with difference images of both energies to show the FBP mismatch and plot 2-D histograms of the dual-energy scan to support our findings.

II. Materials and Methods

A. Tomoconsistency alignment

The alignment method of tomoconsistency [4] is based on calculating a reconstruction estimate from all projections with their initial (mis-)alignment. The projection estimates indicate how the original projections should be aligned as the reconstruction is more consistent than the projections itself, because the low-frequency components of many adjacent projections are similar according to the Fourier slice theorem [5]. Therefore, the original projections are matched onto the reprojections for which the low-frequency features are most crucial. This matching is done by cross-correlating the measured and simulated projections. The overall quality of the alignment is improved.

Figure 1 displays the iterative alignment scheme. From the volume estimate reconstructed with filtered backprojection, reprojections are simulated with the corresponding geometry. The shifts of the projections with respect to the projection estimates are recovered by cross-correlation and fed into the the FBP of next iteration. This is done until the resulting image is sufficiently aligned.

B. Correlation analysis

We used a cross-correlation of projections and reprojections for determining projection shifts. The position of the maximum of the cross-correlation is interpreted as projection shift to improve the initial reconstruction because the images appear most similar with this shift. To ensure a robust alignment the background should be flat. Also the impact of the very outer parts of the projection should not have a large influence as they contain the most artifacts. Therefore, the matching is performed with the projection line integrals, combined with a mask focusing on the interior.

C. Scale equalization

Due to the energy dependence of the attenuation coefficients the total scale of high and low-energy FBP are not comparable. In order to perform a combined alignment with the same impact of both measurements, their scales have to match. Therefore, the line integral projections of one of the scans are scaled. For our application, a linear scaling factor suffices. The factor is extracted by performing two separate FBP reconstructions and divide one of them through the other. The outcome is then plotted into a histogram from which the highest peak corresponds to the scaling factor. To avoid numerical instabilities and a large influence of noise, a region inside the sample is chosen for the procedure.

D. Scanning parameters

The dual-energy scan of the stone drilling core was performed with a ZEISS Versa XRM and both energies were acquired in direct succession. For both scans 1600 angles were equidistantly acquired over a total range of $360°$. The exposure times were $30\,\mathrm{s}$ for the low, and $3\,\mathrm{s}$ for the high energy. The acceleration voltage was set to $60\,\mathrm{kVp}$ and $160\,\mathrm{kVp}$, respectively. The scans were performed in direct succession to show the case of best possible pre-alignment.

III. Results

In order to perform the combined alignment via tomoconsistency we calculate the FBP necessary for the projection estimate from both projection sets into one volume. Therefore, the reconstructed image is afflicted by the projections and misalignment of both low, and high energy measurements. As the quantitative values of both separate reconstructions are on a different scale because of the changing attenuation coefficient with different energies they should be normalized to guarantee an equal impact of both energies on the alignment. The key feature of the combined alignment is, that the projections of both energies are reconstructed within one FBP volume. With a projector using projection matrices [6] the projections of both scans are just appended and projected with their respective geometry information. Therefore, the FBP is a mixture of the attenuation values of both energies and influenced by all projection shifts. For this application the projections look similar enough that the shift recovery is not influenced by differences in attenuation values of both energies. For the alignment of this dual-energy dataset, 3 iterations of tomoconsistency were performed with decreasing blurring of the reconstructed volume to enable a smooth shift recovery.

Figure 2 shows the FBP reconstruction without additional alignment, with tomoconsistency alignment of one separate scan and the result of the reconstruction after combined alignment. These images look very much alike. Therefore, the alignment for the low energy measurement alone is good. Separately considered, the reconstructions for the high-energy (no figure) also show no degradation. The misaligment of the dual-energy scan can be seen in figure 3.

The difference images of low and high energy reveal a total volume mismatch as all features in the unaligned and separately aligned FBP show a margin to the left and right. Therefore, a sample movement between the two separate scans must have happened. The difference of reconstructions after combined alignment do not show these margins. Therefore, the volumes are registered with respect to each other.

One application of dual-energy CT is extracting material information of a sample from the energy dependent attenuation coefficients of the reconstruction. This can be accomplished by counting the pixels with a certain attenuation in both energy bands and plotting the information in a two-dimensional histogram. This method fails, if the reconstructed volumes are not registered with respect to each other.

Figure 4 shows the two-dimensional histograms of the attenuation coefficients of low and high-energy FBP. The background in the left and central images is created by image pixels directly on the misalignment margin. They exhibit a specific attenuation in one image band and a (not material-specific) value in the other FBP, depending on the adjacent material. For the combined alignment, this background disappears as the volumes are registered with respect to each other.

IV. Conclusion

We showed that the combined tomoconsistency alignment of a dual-energy scan registers the reconstructed volumes. This is accomplished by performing a combined FBP of both energies into one volume and matching the projections on the projection estimates emerging from this FBP. Therefore, the following individual reconstructions of each energy with the respective alignment information from combined tomoconsistency alignment are intrinsically registered with respect to each other. In this work, we realigned a dual-energy scan of a stone drilling core where both energies were

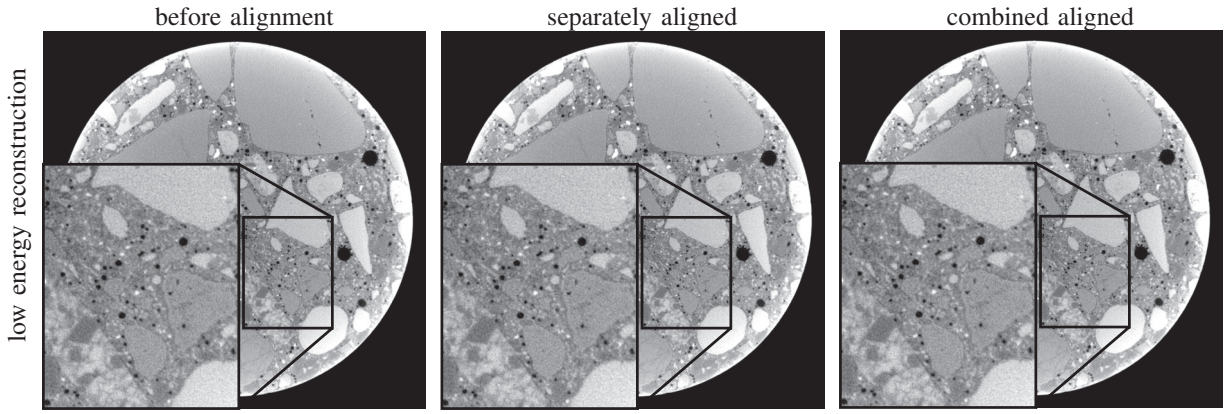

Figure 2. FBP reconstructions from the low-energy dataset. The left image shows the FBP without alignment. The sharp image impression suggests that there is no mis-alignment present in the low energy dataset. The central reconstruction is aligned with tomoconsistency by itself, and the right image shows the FBP aligned aligned with the help of both datasets. The two post-aligned FBP appear very similar, which indicates that tomoconsistency does not degrade the well-aligned image.

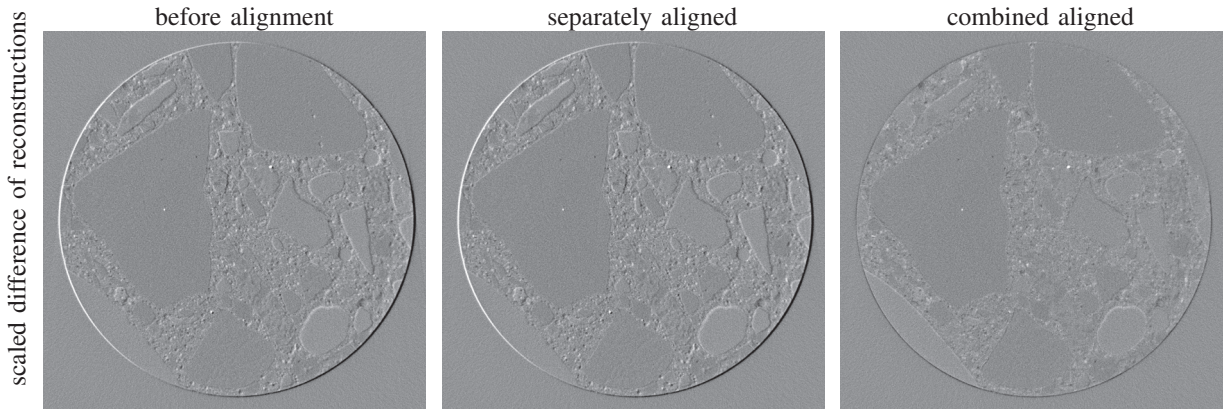

Figure 3. Difference of FBP reconstructions from low and high-energy scan. The projections were multiplied by an equalization factor to be on the same scale. The features appearing in the images are due to misalignment or polychromatic characteristics of the materials in the sample. As before, the left image was reconstructed without additional alignment, for the middle one both images were aligned separately, and right FBP was aligned in a combined manner.

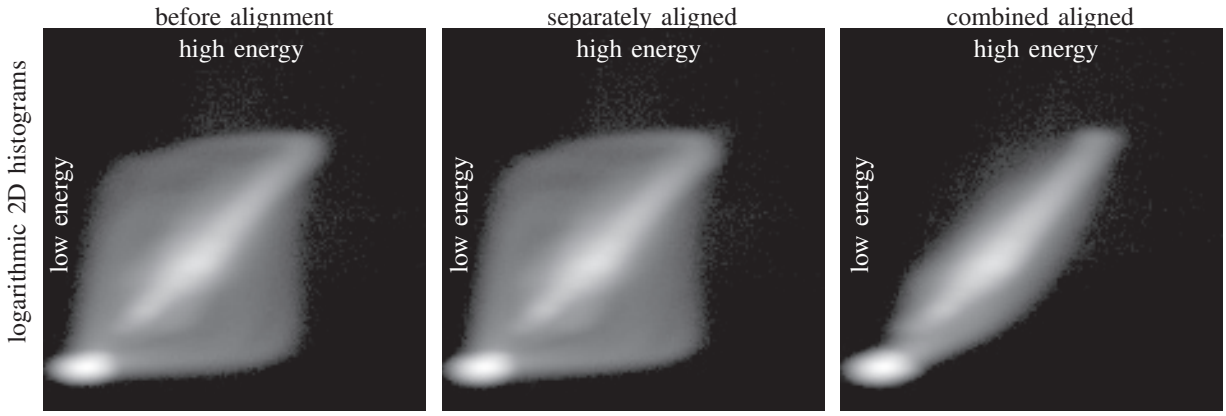

Figure 4. Two-dimensional histograms of the dual-energy scan. On the x-axis the attenuation values of the high energy are plotted against the low-energy attenuation on the y-axis. The histograms are displayed with a logarithmic scale to improve the visualization of the background originating from misalignment.

measured in direct succession. Nevertheless, this alignment is not limited to scans from one device and can in principle also register scans from different devices with e. g. different detectors.

The improved alignment allows to perform further image analysis like for example material segmentation or multi-band filtering.

REFERENCES

[1] M. Guizar-Sicairos, A. Diaz, M. Holler, M. S. Lucas, A. Menzel, R. A. Wepf, and O. Bunk, "Phase tomography from x-ray coherent diffractive imaging projections," *Optics express*, vol. 19, no. 22, pp. 21 345–21 357, 2011.

[2] T. Donath, F. Beckmann, and A. Schreyer, "Automated determination of the center of rotation in tomography data," *JOSA A*, vol. 23, no. 5, pp. 1048–1057, 2006.

[3] A. Aichert, N. Maass, Y. Deuerling-Zheng, M. Berger, M. Manhart, J. Hornegger, A. K. Maier, and A. Doerfler, "Redundancies in x-ray images due to the epipolar geometry for transmission imaging," in *Proceedings of the third international conference on image formation in x-ray computed tomography, F. Noo, Ed*, 2014, pp. 333–337.

[4] M. Guizar-Sicairos, J. J. Boon, K. Mader, A. Diaz, A. Menzel, and O. Bunk, "Quantitative interior x-ray nanotomography by a hybrid imaging technique," *Optica*, vol. 2, no. 3, pp. 259–266, 2015.

[5] T. M. Buzug, *Computed tomography: from photon statistics to modern cone-beam CT*. Springer Science & Business Media, 2008.

[6] A. Fehringer, T. Lasser, I. Zanette, P. B. Noël, and F. Pfeiffer, "A versatile tomographic forward-and back-projection approach on multi-gpus," in *SPIE Medical Imaging*. International Society for Optics and Photonics, 2014, pp. 90 344F–90 344F.

Motion compensated reconstruction for 3D head motion

Seokhwan Jang, Seungeon Kim, Mina Kim, and Jong Beom Ra

***Abstract*—In X-ray CT imaging, a basic assumption is that an imaging object has no motion. However, a patient who has a mental or behavior disease cannot hold his/her head still during the scan, and thereby severe motion artifacts occur in the reconstructed image. In order to reduce the artifacts due to the 3D rigid motion of the patient's head, we propose a FDK-based motion compensated reconstruction algorithm. The algorithm is based on the motion parameter estimation by maximizing the quality of motion compensated reconstructed image. We evaluate the validity of the proposed motion estimation and compensation algorithm by using a numerical phantom with motion.**

***Index Terms*—FDK algorithm, X-ray CT, image reconstruction, motion estimation, motion compensation, 3D rigid motion, head imaging**

I. Introduction

X-ray CT is actively utilized for the diagnosis of head injury or organic lesion of the brain. However, unexpected or uncontrolled patient head motion is one of the major problems in CT image based diagnoses. For example, infant patients or even adult patients who have a mental or behavior disease can hardly control their heads. Those head movements during the CT scan cause motion artifacts such as blurring or streaks in the reconstructed images, which lead to false diagnosis or re-scanning.

In order to alleviate the artifacts due to the patient's motion, many approaches have been tried. One of them is based on the improvement on the gantry rotation time of the scanner, which is very expensive. As another approach, J-H Kim et al. recently presented a motion correction method using an optical motion tracking system [1]. It needs, however, an accurate synchronization between the scanner and the external tracking system and thereby increases the system complexity. As the other approach, B. Herbert et al. presented a reconstruction algorithm for motion correction of non-cardiac organs such as skull [2]. In their approach, a rebinning process from the cone-beam geometry to the cone-parallel beam geometry is used, which reduces the temporal accuracy of the projection data. In addition, a rather simple 2D motion model is adopted for describing the motion problem, which is not considered very practical.

S. Jang, S. Kim, M. Kim, and J. B. Ra are with the School of Electric Engineering, Korea Advanced Institute of Science and Technology (KAIST), Daejeon 34141, Korea (e-mail: shjang@issserver.kaist.ac.kr; sekim@issserver.kaist.ac.kr; makim@issserver.kaist.ac.kr; jbra@kaist.ac.kr).

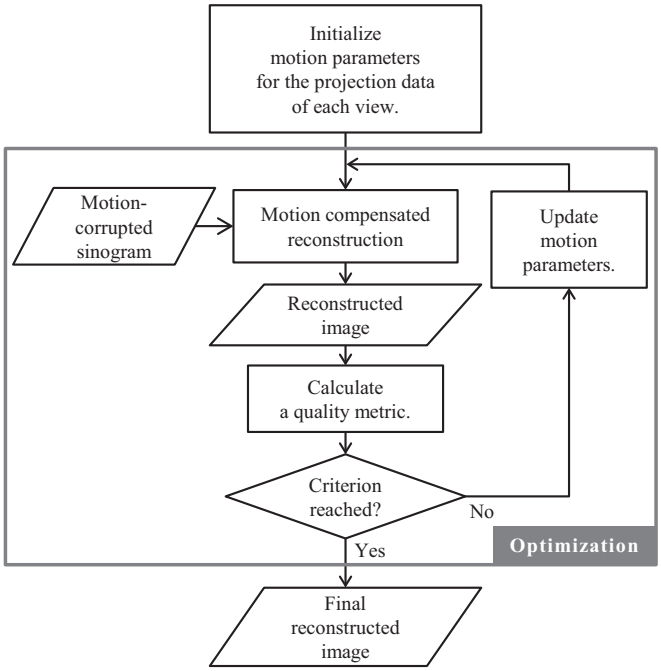

Fig. 1. The proposed ME/MC algorithm for 3D head motion

In this paper, we propose a FDK-based motion compensated (MC) reconstruction algorithm. In the algorithm, the compensation is performed on the basis of accurate 3D rigid motion estimation of an object, which is achieved via the maximization of the quality of the MC reconstructed image. To verify the performance of the algorithm, we simulate realistic patient motion on a numerical phantom and attempt to compensate the motion.

The paper is organized as follows. In Section II, the proposed MC reconstruction algorithm for 3D rigid motion is described. Experimental results are shown in section III. Finally, we conclude the paper in section IV.

II. Method

Figure 1 shows overall structure of the proposed algorithm. In the algorithm, FDK-based MC reconstruction is first performed by using motion corrupted sinogram with initialized motion parameters. We then calculate an image quality metric of the MC image and the motion parameters are updated so as to minimize the quality metric. This procedure is iteratively performed using the updated motion parameters until the updated amount becomes sufficiently small. The finally

reconstructed image is obtained via the MC reconstruction with the converged or the estimated motion parameters.

A. 3D rigid motion model

A pose of a 3D rigid body can be modeled with parameter vector $\boldsymbol{\Theta}$, which consists of three rotations, ψ, θ, and φ along the x, y, and z axes, respectively, and three translations, t_x, t_y, and t_z. The pose of an object is then represented as a transformation matrix of

$$\mathbf{P}_{\boldsymbol{\Theta}} = \left[\mathbf{R}|\mathbf{t}\right]. \tag{1}$$

Here, $\mathbf{R}$ denotes a 3×3 orthonormal rotation matrix and $\mathbf{t}$ denotes a 3×1 translation vector**.** Note that matrix $\mathbf{P}_{\boldsymbol{\Theta}}$ has a size of 3×4 and represents three rotations followed by three translations.

An object motion during the scan can be described by $\boldsymbol{\Theta}$'s at a small number of adjacent control points, by assuming that the whole object motion is continuous and smooth. The object motion can thereby be obtained via B-spline interpolation of $\boldsymbol{\Theta}$'s of the control points distributed along the time axis. For motion compensation in the reconstruction, a moving object for a pre-defined stable source/detector trajectory may be interpreted as a static object with a re-defined source/detector trajectory. The corresponding new trajectory, or the poses of the source and detector, can be determined by using the inverse of the poses of the moving object. Namely,

$$\mathbf{P}_{\boldsymbol{\Theta}}^{-1} = \left[\mathbf{R}^T\middle|-\mathbf{R}^T\mathbf{t}\right]. \tag{2}$$

B. FDK-based motion-compensated reconstruction

We adopt a FDK-based MC reconstruction algorithm to compensate the motion of an imaging object. Since a cone-beam projection data at a certain view is affected by the object motion at that view, in the FDK algorithm, the motion can be compensated view by view by transforming the geometry of source and detector using the estimated motion and applying the filtered backprojection [3].

To apply this motion compensation procedure to the FDK algorithm without degrading the MC image quality, we modify two parts of the FDK algorithm to be suitable for the transformed geometry: pre-weighting factor w_{d} and redundancy weight w_{r}. The FDK-based MC reconstruction procedure can then be written as

$$\begin{aligned}\hat{f}(\mathbf{x};\boldsymbol{\Theta}) = \frac{1}{2}\int_0^{2\pi}\left(\frac{R(\beta;\boldsymbol{\Theta})}{L(\mathbf{x};\boldsymbol{\Theta})}\right)^2 \\ \times\int_{-\infty}^{\infty} w_{\mathrm{r}}(\gamma,\beta)w_{\mathrm{d}}(u',v',\beta;\boldsymbol{\Theta})\,p(u',v',\beta)h(\tilde{u}-u')du'd\beta\end{aligned}, \tag{3}$$

where $p(u,v,\beta)$ is the cone-beam projection data and $h(\cdot)$ denotes the ramp filter.

In Eq. (3), the pre-weighting factor is originally derived from the Jacobian of the 2D parallel to fan beam transformation. For rather than a circular one, radius R from the origin to the source point varies as the view changes. Therefore, the Jacobian can be expressed as

$$|\mathbf{J}| = \left(\frac{R}{\sqrt{R^2+u}} - \frac{u}{R\sqrt{R^2+u}}\frac{\partial R}{\partial\beta}\right). \tag{4}$$

Note here that if $\partial R/\partial\beta$=0, Eq. (4) becomes the same pre-weighting factor as in the fan beam reconstruction of a circular trajectory.

In the proposed algorithm, the pre-weighting factor needs to be extended to 3D. Using Eq. (4), the factor can be derived as

$$\begin{aligned}&w_{\mathrm{d}}(u',v',\beta;\boldsymbol{\Theta}) \\ &= \frac{1}{\sqrt{R(\beta;\boldsymbol{\Theta})^2+u'^2+v'^2}}\left(R(\beta;\boldsymbol{\Theta}) - \frac{u'}{R(\beta;\boldsymbol{\Theta})}\frac{\partial R(\beta;\boldsymbol{\Theta})}{\partial\beta}\right),\end{aligned} \tag{5}$$

where (u',v') represent the coordinates of the virtually transformed detector, as shown in Fig. 2(b). Note also that Eq. (5) becomes the same as the weight in the ordinary FDK if the variation of R is zero.

Meanwhile, the proposed MC reconstruction algorithm adopts an extended Parker weight [4, 5] as the redundancy weight. In the re-defined source/detector geometry to compensate the object motion, we may extend the field-of-view

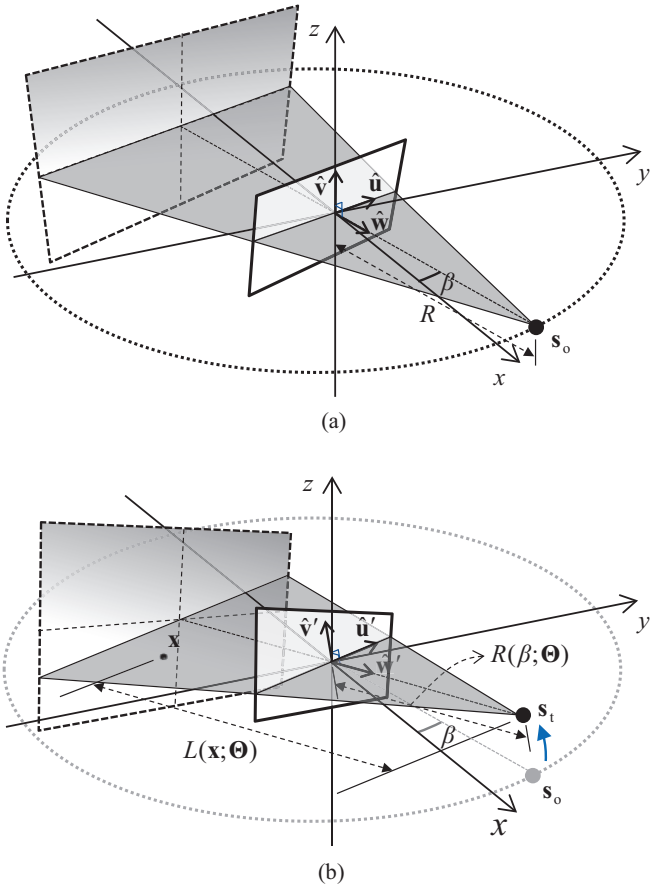

Fig. 2. Illustrations of (a) the ordinary FDK reconstruction algorithm and (b) the proposed FDK-based MC reconstruction algorithm

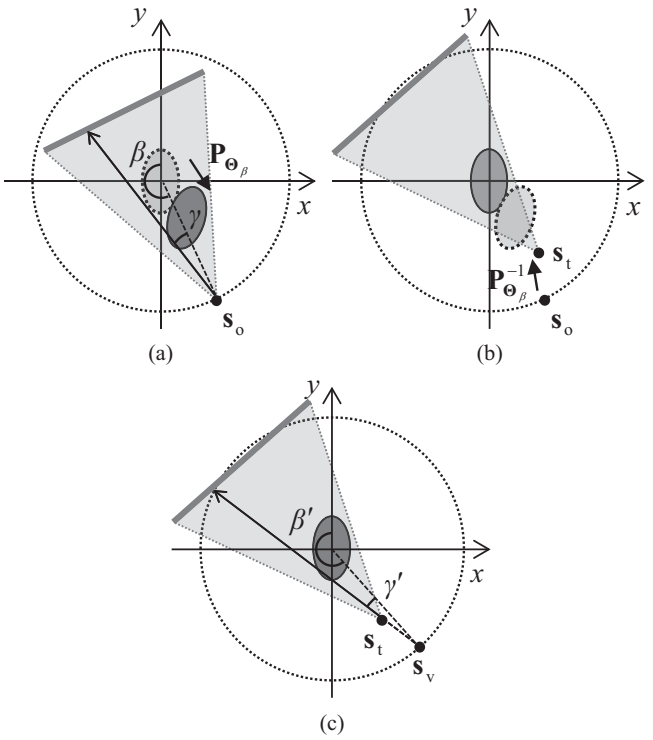

Fig. 3. Re-definement of γ and β for MC reconstruction. (a) Scan trajectory with object motion, (b) object MC and (c) virtual scan trajectory after object MC

of a sinogram using a virtual fan angle. Then, the extended Parker weight on a ray specified by (γ, β) can be written as

$$w_r(\gamma,\beta)=\begin{cases}\sin^2\left(\frac{\pi}{4}\frac{\beta}{\Gamma_m-\gamma}\right), & 0\le\beta\le 2\Gamma_m-2\gamma\\ 1, & 2\Gamma_m-2\gamma\le\beta\le\pi-2\gamma,\\ \sin^2\left(\frac{\pi}{4}\frac{\pi+2\Gamma_m-\beta}{\gamma+\Gamma_m}\right), & \pi-2\gamma\le\beta\le\pi+2\Gamma_m\end{cases} \quad (6)$$

where $2\Gamma_m$ is a virtual fan angle.

Since a pair of source and detector can be out of a circular trajectory in the MC reconstruction, however, the extended Parker weight defined in a circular trajectory cannot be used directly. For example, to compensate the object motion shown in Fig. 3(a), if the pose of a source and detector pair is transformed as shown in Fig. 3(b), (γ, β) should be re-calculated according to the re-defined geometry. We hence assign the position of a virtual source to $\mathbf{s}_v$, as shown in Fig. 3(c), where an extended ray passing the transformed source position, $\mathbf{s}_t$, intersects the circular trajectory. We then obtain new γ and β, or γ' and β', for determining the extended Parker weight in the circular trajectory.

C. Optimization for ME/MC

In the proposed ME/MC algorithm, we utilize the Shannon's entropy of the reconstructed image as the cost function [6, 7]. We thereby try to qualify the artifacts due to object motion, which is to be minimized. The downhill simplex method is adopted for the optimization to estimate the motion parameters and consequently to obtain MC reconstructed images.

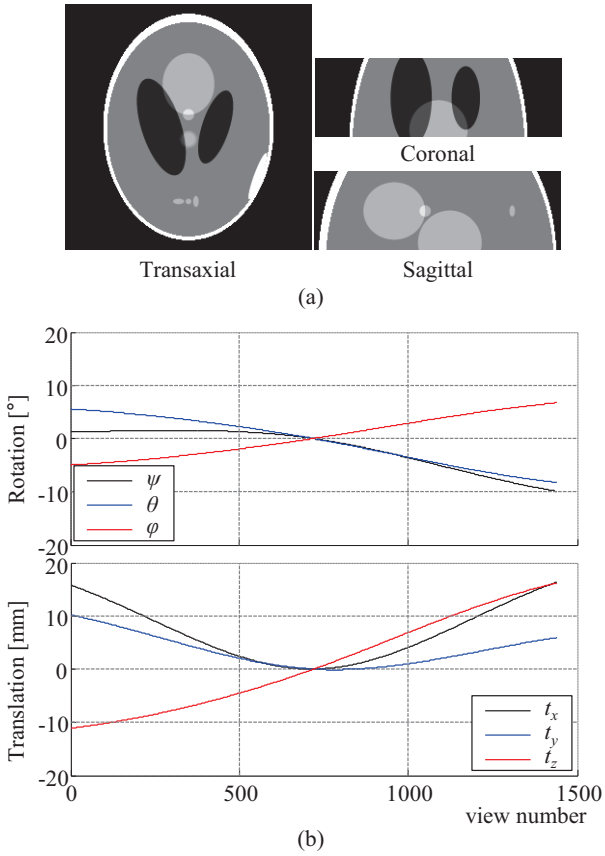

Fig. 4. (a) The 3D Shepp-Logan phantom and (b) the simulated variation of motion parameters during the scan

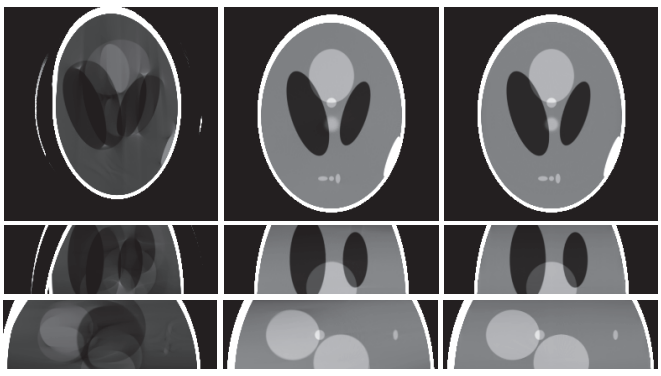

Fig. 5. Reconstructed images using the sinogram of the phantom with motion: (a) the ordinary FDK algorithm and (b) the proposed MC algorithm obtained by using the true motion parameters. (c) FDK reconstructed image using the sinogram of the phantom with no motion, for comparison. (level/window: 1.02/0.05)

III. Experimental Results

A. FDK-based MC reconstruction

To evaluate the proposed MC reconstruction algorithm, we use the projection data obtained from the 3D Shepp-Logan phantom moving with smoothly varying motion parameters

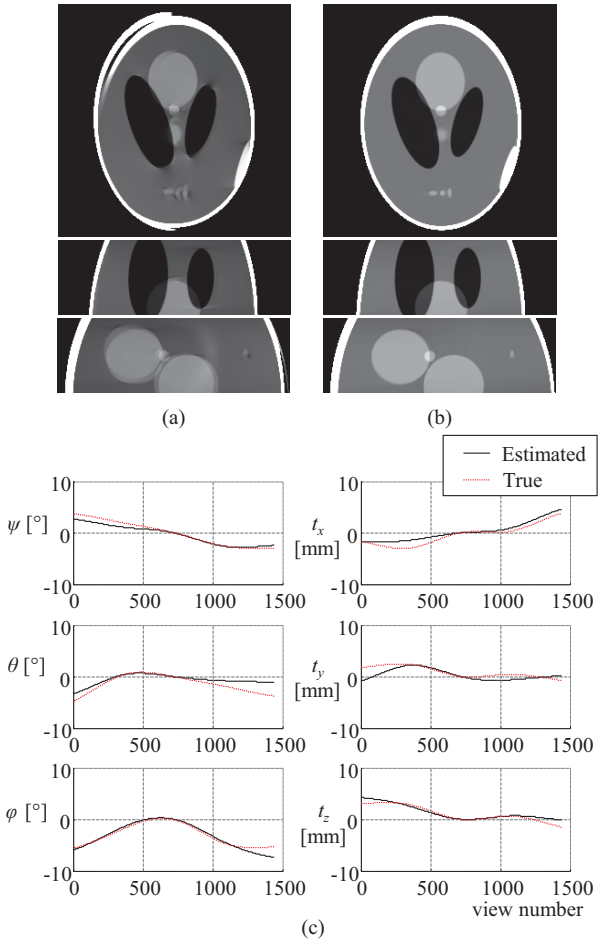

Fig. 6. Reconstructed images (a) before and (b) after ME/MC. (c) Estimated and true motion parameter changes along the time or the view number

during the scan, as shown in Fig. 4. The data are obtained from a hypothetical scanner with 128 channels. The size of reconstructed images is set to 256×256×100 with a voxel size of 0.8×0.8×0.8 mm^3 in this experiment.

Figure 5 (a) shows that the image reconstructed using the ordinary FDK algorithm includes considerable motion artifacts. In contrast, we can note in Figs. 5(b) and (c) that the proposed MC algorithm can produce a well-reconstructed image if the true motion parameters are given.

B. Proposed ME/MC algorithm

To examine the proposed ME/MC algorithm, we adopt a moving phantom with the true motion parameters as in Fig. 6(c). For the estimation of motion parameters, each of them is assumed to have five control points equally distributed in the time axis. Thereby, the parameters of 30 dimensions are estimated. The total number of iterations to estimate the parameters is about 400. The size of reconstructed images is set to 256×256×100 with a voxel size of 0.8×0.8×0.8 mm^3.

Figure 6(a) shows that the reconstructed image obtained using the ordinary FDK algorithm includes considerable motion artifacts. On the other hand, in the MC image obtained using the proposed ME/MC algorithm, the artifacts are noticeably reduced, as shown in Fig. 6(b). In addition, the estimated motion parameters appear similar to the true ones, as shown in Fig. 6(c). As further work, we plan to consider a ME/MC reconstruction problem for larger movements of the object.

IV. Conclusion

In this work, we propose a FDK-based MC reconstruction algorithm for 3D rigid motion, which can be represented using six motion parameters. The trajectory of a pair of source and detector is virtually transformed according to the object motion so that the object can be considered to have no motion in the transformed trajectory. Applying the FDK algorithm along the transformed trajectory with some modifications, we reconstruct a MC object image based on extended Parker weights. Via the simulation using a numerical phantom with movement, we prove the proposed MC reconstruction algorithm can compensate the object motion effectively by estimating the rigid phantom motion.

Acknowledgment

The authors would like to thank Samsung Electronics for providing the financial support.

References

[1] J. H. Kim, J. Nuyts, A. Kyme, Z. Kuncic, and R. Fulton, "A rigid motion correction method for helical computed tomography (CT)," *Physics in medicine and biology*, vol. 60, no. 5, pp. 2047-2073, 2015.

[2] B. Herbert, R. Christopher, K, Stierstorder, K. Michael, and F. Thomas, "Motion correction of skull and breathing motion with motion artefact metric (MAM) optimization," in *Proceeding of the 13th international meeting on fully three-dimensional reconstruction in radiology and nuclear medicine*, pp. 178-181, 2015.

[3] D. Schäfer, J. Borgert, V. Rasche, and M. Grass, "Motion-compensated and gated cone beam filtered back-projection for 3-D rotational X-ray angiography," *Medical Imaging*, *IEEE Transactions on*, vol. 25, no. 7, pp. 898-906, 2006.

[4] M. D. Silver, "A method for including redundant data in computed tomography," *Medical Physics*, vol. 27, no. 4, pp. 773-774, 2000.

[5] K. Taguchi, "Temporal resolution and the evaluation of candidate algorithms for four-dimensional CT," *Medical physics*, vol. 30, no. 4, pp. 640-650, 2003.

[6] C. Rohkohl, H. Bruder, K. Stierstorfer, and T. Flohr, "Improving best-phase image quality in cardiac CT by motion correction with MAM optimization," *Medical physics*, vol. 40, no. 3, 031901, 2013.

[7] Y. Kyriakou, R. M. Lapp, L. Hillebrand, D. Ertel, and W. A. Kalender, "Simultaneous misalignment correction for approximate circular cone-beam computed tomography," *Physics in medicine and biology*, vol. 53, no. 22, pp. 6267, 2008.

A new linearization method for X-ray spectral data

Veronique Rebuffel, Emil Popa, Clarisse Fournier and Loick Verger.

***Abstract*—Spectral detectors open new possibilities in medical applications, both for radiography and tomographic systems. They potentially permit to decrease noise, to improve material differentiation, and to remove artifacts. Beam hardening effect, resulting in artefacts in CT and bias in radiography, is due to poly-chromaticity of tube spectra and to detector response. We illustrate in this paper the non-linearity induced by a spectral detector due to its non-perfect response, even for pure spectrometric detector. We propose an iterative linearization method, using a detector model. Examples are presented using simulation.**

***Index Terms* — Spectral Detector, Linearization, Beam Hardening artifacts, Tomography, Spectral CT.**

I. Introduction

Multi energy counting mode detectors are to become a serious alternative to the standard integrating systems, and should open up new possibilities for medical applications. Compared to typical dual energy applications such as bone-tissue separation, the use of multi-energy detectors should allow to improve the separation of materials with close attenuation properties (such as adipose and soft tissue), to differentiate between more than two materials including K edge materials, and to reach accurate quantification of concentrations (contrast agent, calcification ratio).

Additionally, spectral detectors should help in the correction of beam hardening (BH) artifacts. The removal of BH artifact is a great challenge. It induces the so-called cupping and streaking artifacts in CT, bias in radiographic imaging, and cannot be neglected for quantitative measurements.

When using standard integrating detectors, many beam hardening removal methods have been proposed and some of them are currently used. In the case of a single material object, an experimental material calibration is efficient. Dual material decomposition, whatever the method is used, allows a significant reduction of beam hardening effect at the price of noise increase. Dedicated to CT geometry, a class of methods benefits from a first reconstruction to get information. Others perform a few iterations of alternative steps <reconstruction / correction of projections>. Also, modified algebraic reconstruction algorithms integrate a non-linear projection model. Statistical algorithms directly use a non-linear direct model in the inversion processing [1].

Non-linearity of radiographic data in terms of material thickness is due to the spectral distribution of the tube, coupled with the detector response. Spectral detectors could reduce the corresponding non linearity by taking into account the detector model. If detector imperfections, such as charge sharing and pile-up effects at high photon fluxes, are ignored, the benefit of energy resolved detectors clearly falls down.

Material decomposition techniques have been adapted to these new detectors which provide several energy bins. Generally, they are based either on a polynomial approach [2], or on a maximization of the likelihood function of the measurements [3]. In CT geometry, material decomposition can be applied before or after the reconstruction process, or jointly such as in recently publications. Broadly speaking, these methods reduce beam hardening effects, but often increase noise, and some of them are time consuming.

In this paper we propose a rather simple approach that processes spectral data. Thus it can be applied in radiography, or tomography when using a projection-based approach. A data linearization is performed, and is applicable for any number of energy bins. We first present a typical spectral detector and model it. The response effect on spectral measurement is illustrated. Then the proposed method is detailed. Results are presented on elementary spectra, radiographic and CT images.

II. Materials and Methods

A. Spectral Detector Modelling

Recently emerged semiconductor based X-ray detectors offer new capabilities in counting mode with energy discrimination. Thanks to a direct conversion from photon to collected charges, they are able to count the photons in several energy channels at high count rates. Some of them may even reach hundred channels [4,5].

An accurate model of a semiconductor detector [6] has been developed in our lab to predict the detector response at any energy. This model has been validated with experimental prototypes. Based on a Monte Carlo code, physical interactions of photons and electrons inside the crystal are simulated. Drift transport, diffusion, and charge sharing are taken into account. Finally, electronics modelling provides the final pulse waveforms and noise.

The detector response is calculated over all energies and the

This paper was submitted at CT conference for review on 29th January 2016.
V. Rebuffel is with CEA, Grenoble, F 38000 FRANCE (e-mail: veronique.rebuffel@cea.fr). E. Popa was with CEA, Grenoble, F 38000 FRANCE. (e-mail: author@lamar.colostate.edu). C. Fournier is with CEA, Grenoble, F 38000 FRANCE (e-mail: clarisse.fournier@cea.fr). L. Verger is with CEA, Grenoble, F 38000 FRANCE (e-mail: loick.verger@cea.fr).

result stored in a matrix format (Detector Response Matrix, DRM, generalization of the usually named Detector Response Functions, DRF). Fig. 1 presents the DRM of a detector 3mm thick, 500µm pitch, and the response to an 80keV pulse (one column of the matrix). This detector model was integrated in Sindbad, a software able to produce realistic radiographs of any object in any geometry [7].

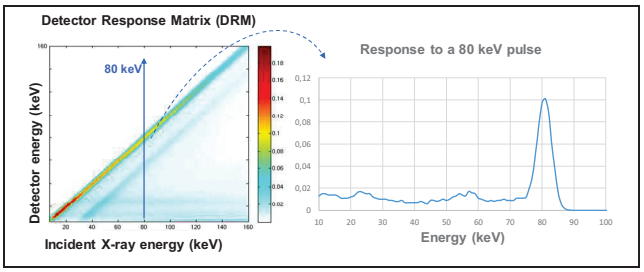

Fig. 1. Detector response matrix for a CdTe detector, 3mm thick, 500 µm pitch. On the right, response to a 80 keV pulse.

B. *Modelling Spectral Measurement*

For an incident spectrum $N_0(E)$ the expected number of transmitted photons at energy E through an object of attenuation $att(E)$ is given by:

$$N(E) = N_0(E)e^{-att(E)} \quad \text{with} \quad att(E) = \int \mu(l,E)dl \tag{1}$$

where the linear attenuation coefficient μ is material specific.

When using the DRM previously introduced, and assuming a linear discrete formalism, the number of photons effectively measured in one energy channel k is:

$$N_k = \sum_{E=1}^{N_E} DRM_{(k,E)} N(E) = \sum_{E=1}^{N_E} DRM_{(k,E)} N_0(E) e^{-att(E)} \tag{2}$$

$DRM_{(k,E)}$ is the contribution of energy E to channel k. For a pure spectroscopic detector with narrow bins – about 1keV width – such as [4], channel k corresponds to an energy E_k and $DRM_{(k,E)}$ is the corresponding element of the DRM matrix.

Most of multi-energy detectors provide larger bins. We note N_C the channel number. The log-measurement (N_C-dimensional vector) is finally defined by:

$$mes = (mes_1, .. mes_k, .. mes_{N_C}), \; mes_k = -\log(N_k / N_{0,k}) \tag{3}$$

Finally, let us introduce the following normalized matrix, called System Weighting Matrix (SWM):

$$\Psi_{(k,E)} = \frac{DRM_{(k,E)} N_0(E)}{\sum_{E'=1}^{N_E} DRM_{(k,E')} N_0(E')} \tag{4}$$

We get:

$$mes_k = -\log\left(\sum_{E=1}^{N_E} \Psi_{(k,E)} e^{-att(E)} \right) \tag{5}$$

Equation (5) shows that measurement non-linearity is due to poly-chromaticity especially for large channels k, but also because of the SWM even for thin channels ("true" spectroscopic detector).

Notice that the pile-up effect is not currently integrated in our formalism: it cannot be modelled in such a linear way. It should be added when considering high level fluxes.

In Fig.2, we illustrate this model by representing the length-normalized attenuation measurement $(1/l)mes_k$ for a homogeneous material of various thicknesses l and N_C=N_E bins. The spectral detector used is the previously presented one. For a perfect spectroscopic detector the result is independent on l:

$$\frac{1}{l} mes_k = \frac{1}{l} \log\left(e^{-\mu(E_k)l}\right) = \mu(E_k) \text{ for any } k \in 1..., N_C$$

The obtained functions clearly depend on l, especially at low energy. The theoretical $\mu_{th}(E)$ is also drawn. Experiments using our spectral detector have validated these measures.

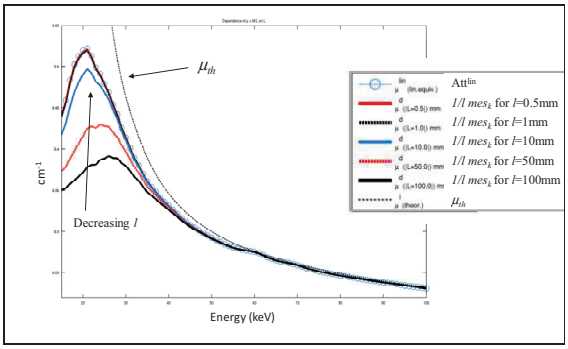

Fig. 2. Length-normalized attenuation measurement for a plastic (POM), thickness varying from 0.5mm to 100 mm, DRM of Fig.1 is used. Theoretical (tabulated) attenuation is drawn. Att^{lin} is explained hereafter (eq (8)).

Finally, we used an object model to reduce the unknown dimension. We can assume ([7]):

$$\mu(E) = \sum_{u=1}^{N_B} a_u f_u(E) \tag{6}$$

Where f_u are the basis functions, typically photoelectric and Compton effects, or two material basis (in that case N_B=2), and a_u the decomposition coefficients that depends on the voxel material only and not on energy (additional functions should be considered when K-edge materials are present). Using the line-integrals $A_u = \int a_u(l)dl$, we get:

$$att(E) = \sum_{u=1}^{N_B} A_u f_u(E) \tag{7}$$

C. *The proposed linearization method*

Let us introduce the "linear" attenuation:

$$att_k^{lin} = \sum_{E=1}^{N_E} \Psi_{(k_k,E)} att(E) \tag{8}$$

which is a first order linear approximation for mes_k. Effectively, a Taylor expansion around the mean value of (5) can be written, for a homogeneous material of thickness l :

$$mes_k = att_k^{lin} - \frac{1}{l} \log\left(1 + \frac{1}{2} \sum_{E=1}^{N_E} \Psi_{(k,E)} \left(att(E) - att_k^{lin} \right)^2 \right)$$

(See APPENDIX).

It can be easily demonstrated that the normalized measurement $(1/l)\,mes_k$ for each k monotonically increases with respect to l, is strictly inferior to att_k^{lin}, and converges to it:

$$\lim_{l\to 0} mes_k = att_k^{lin}$$

Generalization to an inhomogeneous material uses the line-integral of attenuation coefficient. In Fig 2, the linear attenuation curve is superimposed with the one corresponding to 0.5 mm and is the limit of all the curves when l tends to 0.

The main idea of our method is the following: from mes_k, let us recover att_k^{lin}, instead of estimating the theoretical value att_k^{th} (dashed curve), that would correspond to the inversion of equation (5). The linearized value att_k^{lin} allows artifact-free reconstruction, and quantitative estimation of material thicknesses in radiography.

The algorithm combines the previous equations to propose an iterative scheme based on a fixed-point framework. Let us introduce the "deformation" function: $w_k = \dfrac{mes_k}{att_k^{lin}}$

At each iteration we estimate an update of att_k^{lin} via an estimation of deformation function. We use the vectorial notation $\overline{V}$ for any vector $V_k, k = 1,....N_k$.

TABLE 1. Proposed algorithm framework

Initialization: $\overline{att}^{lin(0)} = \overline{mes}$

For each iteration:

- Step 1: computation of the object model (vector $\overline{A}$) by inverting :

$$\overline{att}^{lin} = (\Psi \times \overline{f}) \times \overline{A}$$

- Step 2 : computation of the expected deformation function:

$$\overline{W} = \frac{-\ln\left(\Psi \times e^{-\overline{f}\times\overline{A}}\right)}{\Psi \times \overline{f} \times \overline{A}}$$

- Step 3 : estimation of the linear attenuation:

$$\overline{att}^{lin} = \frac{\overline{mes}}{\overline{W}} \quad (per\ component\ k)$$

The stopping criteria is a threshold on the variation between two iterations or a fixed number of iterations. The algorithm is applied on spectral data vector (one per pixel). The output is the vector att_k^{lin}, of dimension N_C, number of detector channels.

Notice that in step 2, the dimension of the matrix $(\Psi \times \overline{f})$ is (N_C, 2). The inversion can be pre-computed by mean square method if N_C is small (typically 4 or 6). When hundreds of channels are available, such as in [4], then a pre-merging of channels in larger ones is recommended, depending on the noise level. In any cases, step2 (i.e. equation (8)) is linear and its inversion easier and better conditioned than the inversion of equation (5).

III. Results

A. Spectral measurement

Let us consider the previous measurement mes_k for 100mm of POM, acquired with the detector presented in §IIA (1keV width bins), a 140 kV tube spectra. The spectral vector corresponding to one pixel detector is processed by our algorithm. Result after 20 iterations is presented in Fig.4-left. Similar computation in Fig4_right for l=250mm. Noise is represented by its 10% and 90% quantiles. We can notice a slight increase of noise, but in both cases the resulting curve ("corrected") has converged to the "linear" curve in a few iterations.

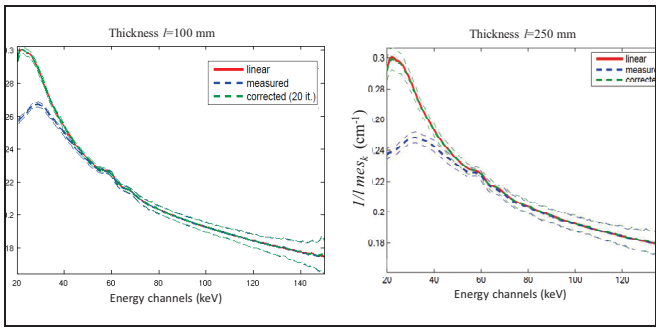

Fig. 4. Measured attenuation (length-normalized) and resulting linear attenuation att_k^{lin} after 20 iterations for two thicknesses: 100 mm (left) and 250 mm (right). Here NC=NE=120 (full spectral detector).

B. Spectral radiography

In this example, we simulated a wedge made of water (20, 60, 120 and 180mm thick steps) with small bone cylinders upon the steps.

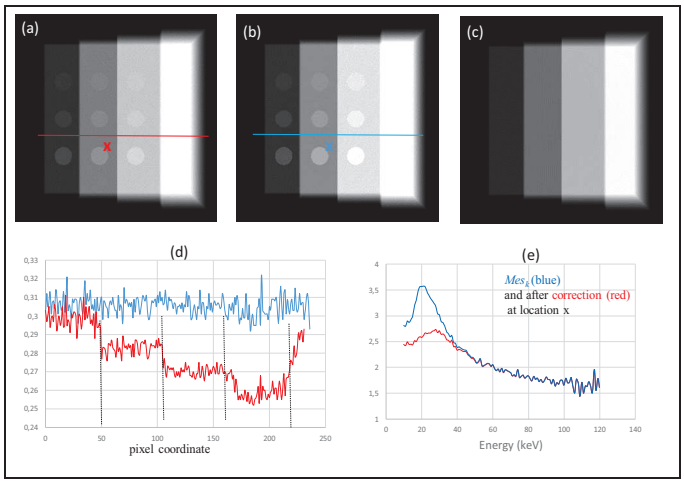

Fig. 5. (a) measured spectral image, (b) after linearization, (c) true thicknesses, (d) profiles on image (a-red) and (b-blue), both normalized by (c). (e) vector along energy axis, before and after linearization, at pixel noted "x" on the image.

In Fig.5, (b) is the result of the linearization of (a). (d) shows profiles on (a) and (b), but after normalization by the true water thickness (c). Non linearity, visible on the measured image (material steps can be distinguished) has disappeared thanks to linearization. (e) curves are similar to Fig.4. ones, at the image location pointed by the "x" mark.

C. *Spectral CT*

Using our simulation software, we simulate a cylinder made of water, diameter 15cm. Scanner geometry is used. Here we used NE=90, NC = 30, NB=2. Standard analytical reconstruction is performed on each energy channels, before and after the linearization. Fig. 6 shows the reconstructed volume for the 30keV channel with and without the proposed linearization. Corresponding profiles are shown on Fig 8, left. The same object with two aluminum inclusions is presented in Fig.7. Here the energy channel is around 40keV. Slight noise was added. Corresponding profiles are shown on Fig 8, right.

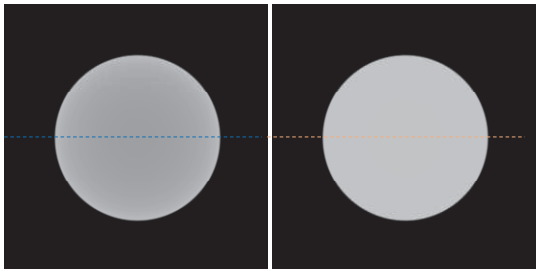

Fig. 6. Reconstruction of 15cm diameter cylinder, without (left) and with (right) linearization. Standard FBP is applied on linearized data. Energy 30keV. Noise free.

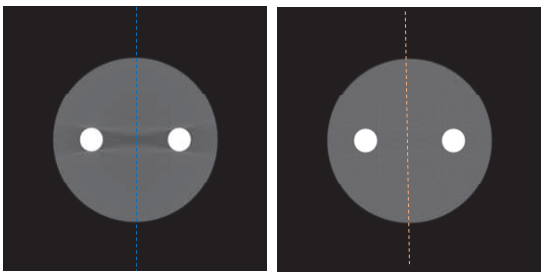

Fig. 7. Reconstruction of 15cm diameter cylinder with aluminum inclusions, without (left) and with (right) linearization. Standard FBP is applied on linearized data. Energy 40 keV.

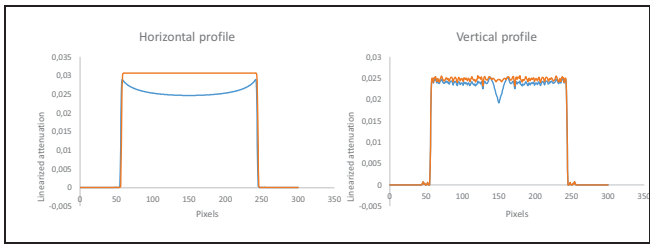

Fig. 8. Horizontal profiles on cylinder of Fig.5 (left) and Vertical ones on cylinder of Fig.6 (right). For both, blue (resp. orange) profile is before (resp. after) linearization.

IV. Discussion and Conclusions

We propose a iterative method to find a linear approximation of non-linear energy-dependent attenuation coefficient with very encouraging results on simulation examples. We do not try to estimate the theoretical attenuation, i.e. the physical value, which would be a complete inversion of the system response. The principle is to estimate a linear value, thus assuring artifact removal. The provided value depends on the system but that can be robustly calibrated because it no more depends on location inside object.

For this work we assume that the flux is sufficiently low to avoid pile-up phenomenon. We also consider collimated geometry to be allowed to neglect scatter radiation.

Additional studies are currently addressed, especially concerning noise behavior, and optimization of the number of energy channels. Future works will concern regularization. Also an integration into a reconstruction algorithm is envisaged. In the current version, it is be usable both in radiography and CT, with any number of energy bins depending on the detector used. Experimental tests will be conducted, with a detector prototype permitting a lot of possible bins configurations.

Appendix

We used the following approximation:

$$\log\left(\sum_i a_i \exp(\beta_i)\right) \approx \sum_i a_i \beta_i + \log\left(1+\sum_i a_i \frac{(\beta_i - \bar{\beta})}{2}\right) \quad \text{with} \quad \bar{\beta} = \sum_i a_i \beta_i$$

References

[1] B. De Man et al. « An iterative Maximum-Mikelihood Polychromatic Algorithm for CT », IEEE TMI, vol. 20, N0. 10, Octobre 2001.

[2] B. Brendel et al. "Empirical, projection-based basis-component decomposition method". Biomedical Optics and Imaging - Proceedings of SPIE. Vol. 7258, 2009.

[3] JP. Schlomka et al. « Experimental feasibility of multi-energy photon-counting K-edge imaging in pre-clinical computed tomography ». Physics in Medicine and Biology 53, no 15 (2008): 4031-4047.

[4] A. Brambilla et al. "CdTe linear pixel X-ray detector with enhanced spectrometric performance for high flux X-ray imaging," IEEE TNS, vol 59, pp 1552-1558, 2012.

[5] A. Brambilla et al. "Fast CdTe and CdZnTe Semiconductor Detector Arrays for Spectroscopic X-Ray Imaging", IEEE TNS, vol. 60, NO.1, Feb 2013

[6] G. Montémont et al. "Simulation and Design of Orthogonal Capacitive Strip CdZnTe Detectors", IEEE TNS, vol. 54, issue 4, pp. 854-859, 2007

[7] V.Rebuffel et al. « New Functionalities of SINDBAD Simulation Software for Spectral X-Ray Imaging Using Counting Detectors with Energy Discrimination ». In Proc. IEEE NSS-MIC, 2550-2554, 2012.

[8] R.E. Alvarez, & A. Macovski. « Energy-selective reconstructions in X-ray computerized tomography ». Physics in Medicine and Biology 21, no 5 (1976): 733-744.

Material-Based Scatter Correction for Computed Tomography

Xue Rui*, Yannan Jin, and Peter M. Edic

***Abstract*— Scatter in computed tomography (CT) measurements can result in bias of the Hounsfield Unit (HU) values in the reconstructed images. This effect cannot be ignored especially with wider collimation configurations and larger patient size. For dual-energy CT, the impact of scatter needs to be studied carefully to avoid bias in the quantitative estimates of the contrast agent concentration. Previous studies for scatter correction were derived from a physics-based model and fitted with measurement data. However, this approach is limited to an object that contains a single, homogenous material. The accuracy degrades in the presence of high-Z (high atomic number) materials like bone or iodine. Our proposed approach accounts for these materials by utilizing the basis material path lengths after material decomposition (MD) of dual-energy projection data. The scatter model we developed is not only dependent on the detected X-ray intensity but also material path lengths acquired from the MD process. This scatter model is more accurate, especially for an object containing high-Z materials. This leads to more quantitative CT numbers (HU values) in the final dual-energy images (density images and monochromatic images).**

Keywords—Computed Tomography, Contrast Imaging, Cardiac Imaging, Dual Energy, Scatter Correction.

I. Introduction

Coronary artery disease (CAD) is the leading cause of morbidity and mortality in the United States, accounting for more than $500 billion in costs annually in the U.S. [1]. Coronary CT angiography (CCTA) is an emerging test that evaluates CAD by direct anatomic visualization of stenoses to identify individuals who may benefit for invasive coronary angiography (ICA) [2]. Nevertheless, previous studies [3] have demonstrated that angiographic methods alone are sometimes deficient in identifying stenoses that cause ischemia. One novel approach to improve the physiologic assessment of CAD is to utilize the dual-energy CT (DECT) and DECT perfusion (DECTP) [4] to augment anatomic CCTA with surrogates of blood volume to provide a physiological measure of ischemia.

Dual-energy CT differentiates and classifies materials by utilizing data acquired using two different energy spectra. The two main categories of dual-energy CT technologies available today are projection-based approaches [5-9] and image-based approaches [10-12]. Projection-based dual-energy CT incorporates energy-dependent models for basis material decomposition (MD) within tissue, and properly removes the beam-hardening effect for both water and high-Z (high atomic number) materials such as bone and contrast agents. However, the performance of cardiac DECT can be further improved to provide quantitative estimates of iodine density in the myocardium using CT perfusion techniques. The basis material images generated as a result of projection-based material decomposition is only the first step towards the quantitative estimation of the distribution of the iodine density in the myocardium – a surrogate for blood volume. The proper correction of other physical effects, especially scatter, also plays an important role.

Scatter correction is crucial for Hounsfield Unit (HU) accuracy and has been intensively studied for many years [13-16]. One solution is a forward-scatter convolution model which estimates the scatter intensity based on the measured data in the projection domain [13]. This fast and efficient approach has utility for clinical CT scanning, but it is based on the assumption that the object comprises a homogeneous material (e.g. water). In cardiac CT, a more accurate model is required to generate quantitative, physiologically-relevant distributions of absolute iodine density within myocardial tissue. The impact of scatter in energy-resolved CT has been studied by Wiegert *et al.,* which is based on Monte Carlo simulation; they report on the bias in material decomposition accuracy [17]. In this study, we propose to utilize the material decomposition results of projection-based dual-energy CT as input for scatter correction and develop a scatter correction model that is adaptive for different materials.

II. Material and Method

The proposed scatter correction algorithm incorporating material information is shown in a flowchart in Figure 1. We selected water and iodine as the basis materials. An initial scatter correction algorithm based on the assumption that the object contains a homogeneous material is used to correct the scatter in the high- and low-energy sinograms, p_h and p_l, respectively. A polynomial-based material decomposition process is performed to obtain the water and iodine sinograms, p_w and p_i respectively, which includes beam-hardening correction. The material-specific information is then input into the proposed scatter model to estimate the scatter intensity in

Xue Rui and Yannan Jin are researchers with the Image Reconstruction Laboratory, GE Global Research, Niskayuna, NY. Peter M. Edic is a Principal Engineer in the CT, X-ray and Functional Imaging Organization at GE Global Research, Niskayuna, NY.

the high- and low-energy sinograms separately. The scatter intensity is then removed from the measurement signal. The corrected high- and low-energy sinograms are again used for more accurate material decomposition and subsequent reconstruction.

The total scatter intensity distribution generated by the object includes all projection rays and can be calculated by convolving the scatter from each projection ray with a smoothing kernel, which incorporates knowledge about the frequency content in the scatter profile. In our analysis, a

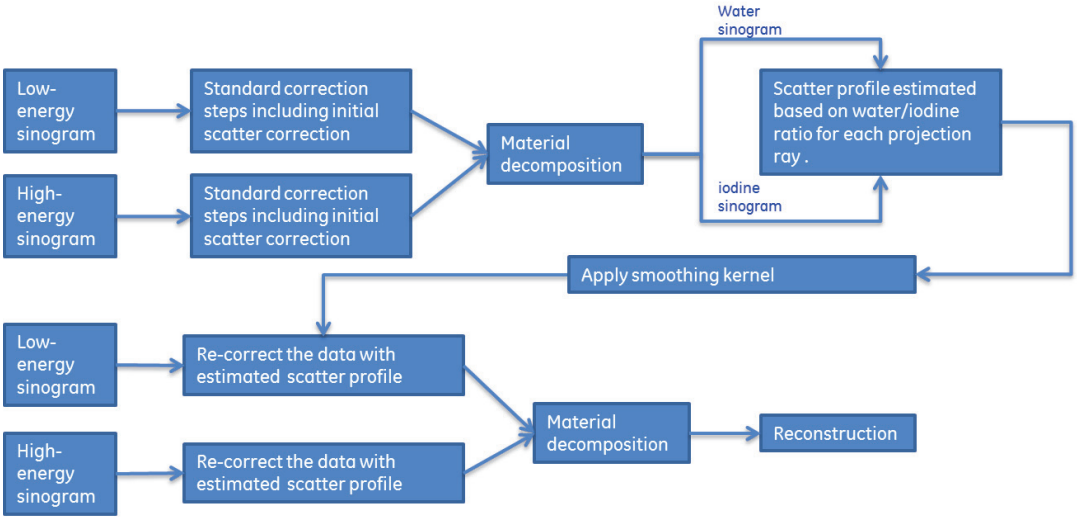

Figure 1. Scatter correction scheme for dual energy CT using material-specific information.

A forward scatter model based on the measured X-ray intensity and the line integral of the linear attenuation coefficeint can be used to estimate the scatter intensity. For a single material, the scatter intensity produced by a pencil beam can be modeled as [13],

$$I_{sc} = KI_t^a \left(-\log\left(\frac{I_t}{I_0}\right)\right)^b$$

where, I_{sc} is the scatter intensity, K is a constant which depends on the scatter cross section and system gain, I_0 is the intensity of the X-rays incident on the detector in the absence of an object, I_t is the measured intensity of the corresponding projection ray with an object present, a and b are the parameters that can be tuned according to measurements to control the power of the intensity and the projection value.

To incorporate the material information into the scatter model, for each projection ray, the line integrals of the density distribution for each basis materials are used, which in our analysis, are the water projection value (p_w) and the iodine projection value (p_i). The ratio of the iodine and water projection values, which reflects the amount of high-Z material in the projection path, is utilized to modulate the power of the intensity and the total projection value contributions to the scatter estimate. Therefore, the scatter intensity can be calculated as,

$$I_{sc} = KI_t^{a_1+a_2\frac{p_i}{p_w}} \left(-\log\left(\frac{I_t}{I_0}\right)\right)^{b_1+b_2\frac{p_i}{p_w}}$$

where, K, a_1, a_2 and b_1, b_2 are the parameters that can be tuned separately according to the measurements from a given CT system for a given imaging application – cardiac CT, in this case.

Gaussian convolution kernel G is used for this purpose.

$$I_s = I_{sc} * G$$

The estimated scatter signal incorporating the material-specific information is used to correct the high- and low-energy sinograms. The material decomposition process is performed to generate the images for each basis material. Monochromatic images can be generated from the improved basis material density estimates for a selected energy.

III. Phantom Measurement

We assessed the impact of scatter on the fidelity of reconstructed HU value. The anthropomorphic phantom selected for this investigation includes a heart model (Gammex Inc., Middleton, WI) inserted into a thorax phantom (QRM-Thorax, QRM GmbH, Germany) which is surrounded by a large patient ring in order to model large patients, increasing the amount of the scatter signal in the measurement data. The heart model comprises regions with differing nominal values of iodine density: (A) myocardium – 5 mg I/mL, (B) perfusion deficit – 2.5 mg I/mL, (C) aorta – 17.5 mg I/mL, and (D) left ventricle – 17.5 mg I/mL.

Phantoms were scanned at GE Global Research on a clinical CT scanner (LightSpeed VCT, GE Healthcare, Waukesha, WI). The dual-energy scan data were acquired in a rotate-rotate acquisition mode: two scans at two different operating voltages of the X-ray tube (80kVp/140kVp) were taken sequentially. The projection data were angularly aligned before applying projection-based material decomposition. To evaluate the impact of the scatter, each phantom was scanned using two different collimation settings: 5 mm and 40 mm. The scatter intensity approximately increases linearly with

increasing collimation. For 40 mm collimation, significant scatter is expected in the measurement. The 5 mm collimation measurement is used as a reference image with minimal amount of scatter. All of the scans were performed at 500 mA with 984 views per rotation. Here we want to make it clear that the phantom we measured is stationary, and there is no cardiac motion in our measurement. Figure 2 shows the heart model with different regional inserts with differing iodine concentration, and the phantom used for data acquisition. The aorta was positioned within the heart model so as to fit within the 10 cm cylindrical open region in the thorax phantom.

Figure 2. Anthropomorphic Phantom Configuration. Phantom configuration includes: heart inserts and a thorax with a large patient ring. The heart model contains regions of interest with various iodine concentrations: (A) myocardium – 5 mg I/mL, (B) perfusion deficit - 2.5 mg I/mL, (C) aorta – 17.5 mg I/mL, and (D) left ventricle – 17.5 mg I/mL.

We selected three regions of interest (ROIs) in the heart model of the phantom which have different iodine concentrations to assess the accuracy of the HU values in the reconstructed monochromatic images. The ROI selection is shown in Figure 3. ROI 1 and 2 are located in the regions with high concentration of iodine contrast agent (17.5 mg I/mL), aorta and left ventricle models, respectively. ROI 3 is allocated at the location of a perfusion deficit with relatively lower iodine concentration (2.5 mg I/mL).

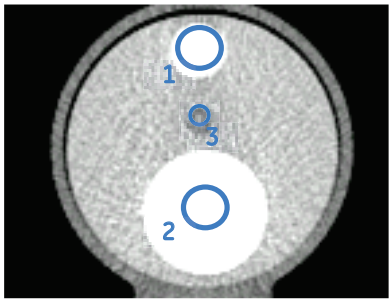

Figure 3. Region-of-interest location within for the heart insert. ROI 1, 2 and 3 correspond to the aorta region, the left ventricle region, and the perfusion deficit, respectively.

IV. Results and Discussion

The scatter correction algorithm was implemented and the model tuned using the data acquired on the clinical CT system. The phantom measurement with 5-mm collimation was used as the reference image with minimal scatter signal. The "ground truth" scatter profile is obtained by taking the difference between the measurement from 40 mm collimation and the 5 mm collimation data. The scatter model is tuned according to the "ground truth" scatter intensity. The parameters used in the results reported in the study are as following:

$$K = 0.013,$$
$$a_1 = 0.96, a_2 = -3.0,$$
$$b_1 = 1.2, b_2 = -3.0.$$

Figure 4 shows the scatter profile estimated by the proposed scatter correction algorithm for low-energy scan at a tube voltage of 80 kVp.

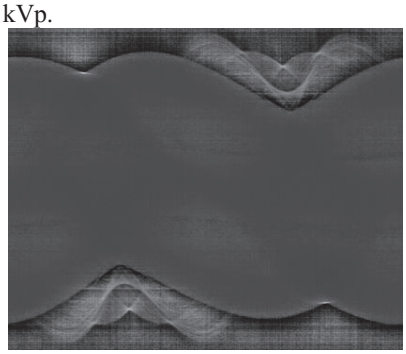

Figure 4. The scatter intensiy estimated by the proposed scatter correction algorithm for low-energy (80 kVp) scan.

Figure 5 shows the central slice of the reconstructed monochromatic images at 70 keV for the data acquired at 40 mm collimation with scatter correction. The reference image for the data acquired at 5-mm collimation is also shown for comparison. No obvious shading artifact is observed for the scatter corrected image.

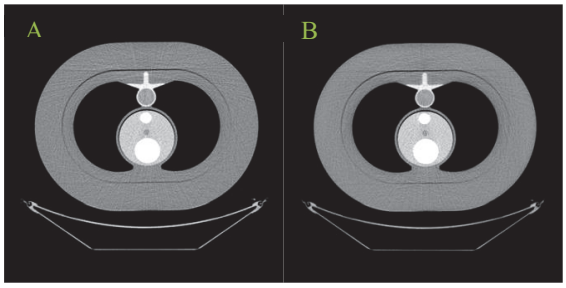

Figure 5. Recontructed monochromatic images at 70 keV. The images show the central slice of the reconstructed image volume with a display [window, level] of [600, 1400] HU. Image A is the scatter-corrected image of the measurement taken with 40-mm collimation. Image B is the reference image of the measurement taken with 5 mm collimation.

We also implemented the scatter correction algorithm reported in [13] for homogenous material. We used the parameters reported in the reference with $a = 0.8$ and $b = 1.2$. The constant $K$was tuned according to our measurement with the value of 0.013. Monochromatic images at 70 keV were generated for (1) uncorrected data, (2) the scatter correction model proposed in [13] for single material, and (3) the proposed scatter correction model. Quantitative ROI measurements on the monochromatic images were recorded and compared to the reference images with 5 mm collimation.

The bias of the quantitative ROI measurements is reported in Figure 6. For ROI regions 1 and 2 with high iodine

concentration, the uncorrected data has significant negative bias due to the scatter. With a single-material scatter correction algorithm, the accuracy of the HU value is improved for these regions. With the proposed scatter correction algorithm, the accuracy of the measurement in the region of high iodine concentration is further improved. There is slightly over-correction for ROI 2. For the deficit region (ROI 3), there is slight improvement of the HU accuracy with the proposed method, mostly because the iodine concentration for this region is the lowest in our heart insert, and the proposed scatter correction algorithm has minimal impact for this region when considering the full 360° acquisition. The accurate modeling of the scatter required more than just the material information.

Figure 6. The bias of the ROI measurement for (1) uncorrected data, (2) the data corrected by a single-material scatter correction algorithm, and (3) the data corrected by the proposed scatter correction algorithm.

V. Conclusion

We developed and implemented a material-specific scatter correction model for dual-energy CT. Previous research efforts for scatter correction were derived from a physics-based model. However, this approach is limited to an object that contains a single, homogenous material. The accuracy degrades in the presence of high-Z materials like bone or iodine. Our approach estimates the scatter profile from projection data, the measured X-ray intensity, as well as the material-specific path lengths. We demonstrated that we can improve the HU accuracy significantly after incorporating the material-specific information in the scatter model, using our heart phantom. To further improve the accuracy of the scatter model, more measurements for better tuning of the algorithm will be performed. More sophisticated scatter models can also be developed to better address the scatter caused by different materials within the X-ray beam. The phantom we measured does not have any cardiac motion; for clinical imaging, simultaneous sampling can be employed where patient and involuntary organ motion is present.

VI. Acknowledgement

Research reported in this publication was supported by the National Heart, Lung, And Blood Institute of the National Institutes of Health under Award Number R01HL111141. The content is solely the responsibility of the authors and does not necessarily represent the official views of the National Institutes of Health.

References

1. Lloyd-Jones, Donald, et al. "Heart disease and stroke statistics—2010 update A report from the American Heart Association." *Circulation* 121.7 (2010): e46-e215.
2. Budoff, Matthew J., et al. "Diagnostic performance of 64-multidetector row coronary computed tomographic angiography for evaluation of coronary artery stenosis in individuals without known coronary artery disease: results from the prospective multicenter ACCURACY (Assessment by Coronary Computed Tomographic Angiography of Individuals Undergoing Invasive Coronary Angiography) trial." *Journal of the American College of Cardiology* 52.21 (2008): 1724-1732.
3. Tonino, Pim AL, et al. "Angiographic versus functional severity of coronary artery stenoses in the FAME study: fractional flow reserve versus angiography in multivessel evaluation." *Journal of the American College of Cardiology* 55.25 (2010): 2816-2821.
4. Truong, Quynh A., et al. "Rationale and design of the dual-energy computed tomography for ischemia determination compared to "gold standard" non-invasive and invasive techniques (DECIDE-Gold): A multicenter international efficacy diagnostic study of rest-stress dual-energy computed tomography angiography with perfusion." *Journal of Nuclear Cardiology* (2014): 1-10.
5. Alvarez, Robert E., and Albert Macovski. "Energy-selective reconstructions in x-ray computerised tomography." *Physics in medicine and biology* 21.5 (1976): 733.
6. Kalender, Willi A., et al. "Evaluation of a prototype dual-energy computed tomographic apparatus. I. Phantom studies." *Medical physics* 13.3 (1986): 334-339.
7. Xu, Dan, et al. "Dual energy CT via fast kVp switching spectrum estimation."*SPIE Medical Imaging*. International Society for Optics and Photonics, 2009.
8. Wu, Xiaoye, et al. "Monochromatic CT image representation via fast switching dual kVp." *SPIE Medical Imaging*. International Society for Optics and Photonics, 2009.
9. Pack, Jed D., et al. "Fast kVp switching CT imaging of a dynamic cardiac phantom." *SPIE Medical Imaging*. International Society for Optics and Photonics, 2009.
10. Flohr, Thomas G., et al. "First performance evaluation of a dual-source CT (DSCT) system." *European radiology* 16.2 (2006): 256-268.
11. Johnson, Thorsten RC, et al. "Material differentiation by dual energy CT: initial experience." *European radiology* 17.6 (2007): 1510-1517.
12. Maaß, Clemens, Matthias Baer, and Marc Kachelrieß. "Image-based dual energy CT using optimized precorrection functions: A practical new approach of material decomposition in image domain." *Medical physics* 36.8 (2009): 3818-3829.
13. Ohnesorge, B., T. Flohr, and K. Klingenbeck-Regn. "Efficient object scatter correction algorithm for third and fourth generation CT scanners." *European radiology* 9.3 (1999): 563-569.
14. Ning, Ruola, Xiangyang Tang, and David Conover. "X-ray scatter correction algorithm for cone beam CT imaging." *Medical physics* 31.5 (2004): 1195-1202.
15. Zhu, Lei, N. Robert Bennett, and Rebecca Fahrig. "Scatter correction method for X-ray CT using primary modulation: Theory and preliminary results." *Medical Imaging, IEEE Transactions on* 25.12 (2006): 1573-1587.
16. Poludniowski, G., et al. "An efficient Monte Carlo-based algorithm for scatter correction in keV cone-beam CT." *Physics in medicine and biology* 54.12 (2009): 3847.
17. Wiegert, Jens, Klaus Jürgen Engel, and Christoph Herrmann. "Impact of scattered radiation on spectral CT." *SPIE Medical Imaging*. International Society for Optics and Photonics, 2009.

Explosive Detection in Aviation Security Using CT: Advanced Reconstruction Algorithms and Publically Available Datasets

Harry E. Martz, Jr., and John Beaty

***Abstract*— CT scanners are deployed world-wide to detect explosives in checked baggage. While similar to single- and dual-energy multi-slice CT scanners used today in medical imaging, some recently developed explosives detection scanners employ multiple sources and detector arrays to eliminate the mechanical rotation of a gantry, provide photon counting detectors for spectral imaging, and produce limited number of views to reduce cost. For each bag scan, the resulting reconstructed images are automatically processed by threat detection algorithms to screen for explosives and other threats. Human operators review the images only when these automated algorithms report the presence of possible threats. The US Department of Homeland Security (DHS) has requirements for future scanners that include dealing with a larger number of threats, higher probability of detection, lower false alarm rates and lower operating costs. One tactic that DHS is pursuing to achieve these requirements is to augment the capabilities of the established security vendors with third-party algorithm developers. A third-party in this context refers to academics, national laboratories, and companies other than the established vendors. DHS is particularly interested in exploring the model that has been used very successfully by the medical imaging industry, in which university researchers develop algorithms that are eventually deployed in commercial medical imaging equipment. The purpose of this presentation is to discuss opportunities for third-parties to develop advanced reconstruction algorithms using publically available databases.**

***Index Terms*— Explosive detection, aviation security, CT, reconstruction algorithms, automated threat detection.**

I. Introduction

THE use of advanced reconstruction technologies may soon enable airports to detect more explosive threats and reduce the costs associated with explosives detection. Explosives detection imaging systems based on computed tomography (CT), a technology that is commonly used in nondestructive evaluation, medical imaging as well as baggage screening, uses algorithmic schemes to produce images of baggage and to apply automated threat detection algorithms to these images to determine if threats are present in baggage.

Harry Martz is the director of the Nondestructive Characterization Institute with the Lawrence Livermore National Laboratory, Livermore, CA (martz2@llnl.gov).

John Beaty is the director of technology development at the ALERT DHS Center of Excellence at Northeastern University, Boston, MA (J.Beaty@neu.edu).

The Department of Homeland Security (DHS) Science and Technology (S&T) [1] Center of Excellence [2] for Awareness and Localization of Explosives-Related Threats (ALERT) [3] at Northeastern University engaged scientists in nondestructive evaluation, security and the medical fields from academia, industry and national laboratories to work with vendors on developing new reconstruction, segmentation and automated target recognition (ATR) algorithms. As a first step, datasets and metrics in the public domain were used. At least one method was assessed as promising and is currently being integrated with a commercial product.

The medical imaging field has used academic research to significantly improve medical imaging equipment. Following this model, the participants at the Advanced Development for Security Applications (ADSA) [4] workshops convened by ALERT showed that third-party party researchers could develop applicable reconstruction algorithms using unclassified data obtained by scanning objects containing benign materials such as saline, rubber and clay on medical CT scanners [5]. Tests based on image and detection metrics were developed to assess reconstruction performance in lieu of taking more expensive and restricted government tests [6].

A sample of the reduction of artifacts in an original (left) and new (right) image is shown in this figure [6].

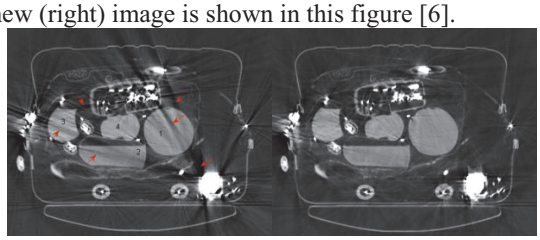

The tests also demonstrate the improved performance because the detection features have been compacted from the original images (left) to the improved images (right) [6].

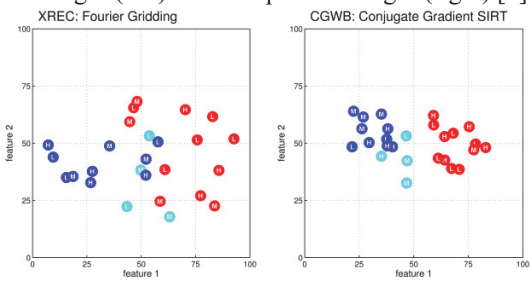

The advanced reconstruction methods may allow for the following: (1) detecting a larger population of threats with lower masses and thinner thicknesses; (2) reducing labor costs

associated with resolving false alarms; and (3) enabling CT to be deployed at the checkpoint and for cargo inspection.

In addition to the researchers who worked on this project, other researchers may use the publically available dataset and metrics to develop improved algorithms by building on the research performed by this project.

II. Acknowledgements

This research was funded by the Science & Technology Directorate of the Department of Homeland Security (DHS). This work was performed under the auspices of the U.S. Department of Energy by Lawrence Livermore National Laboratory under Contract DE-AC52-07NA27344. The work was performed by Northeastern University under Contract 2013-ST-061-ED0001.

References

[1] http://www.dhs.gov/science-and-technology
[2] http://www.dhs.gov/science-and-technology/centers-excellence
[3] http://www.northeastern.edu/alert/
[4] http://www.northeastern.edu/alert/transitioning-technology/adsa/
[5] http://www.northeastern.edu/alert/transitioning-technology/alert-datasets
[6] https://myfiles.neu.edu/groups/ALERT/strategic_studies/ADSA03_final_report.pdf

Whitening transform based noise reduction for spectral CT

Yan Liu and Zhou Yu

***Abstract* – Independent basis material image denoising in spectral computed tomography (CT) has been found insufficient due to strong noise correlations between different bases. To account for the correlations, one common approach is to model an accurate covariance matrix in a cost function and solve the corresponding optimization problem. However, directly solving such a problem often requires an accurate covariance model and could be difficult for parameter optimization. To mitigate these drawbacks, we proposed an alternate solution by using a whitening transform. In the presented method, firstly, the noisy basis images were decorrelated by whitening transform. Then an independent denoising method was applied in the whitening domain for noise reduction. Finally, the denoised basis images were calculated by the inverse whitening transform. Since the whitening transform decorrelates a joint denoising problem into independent denoising problems which can be handled easily, the denoising efficiency is improved. The preliminary results show that the proposed method can yield lower noise images at a fixed bias and resolution level as compared to the conventional independent basis image denoising techniques. Moreover, the results also indicate that denoising parameters selection in whitening basis are more intuitive than in the material basis.**

***Index Terms* – spectral CT, denoising, whitening transform, correlations.**

I. Introduction

Spectral computed tomography has enabled in many clinical applications such as kidney stone classification, renal lesion diagnosis and tumor detection etc. [1] Since spectral CT relies on multiple acquisitions from different energy spectrums, without increasing the overall radiation dose the SNR for each energy spectrum can be reduced Up to now, various image processing and reconstruction methods with noise suppression capability have been investigated to reduce spectral CT noise. As one of the major strategies, restoring the poly-energetic measurements from different energy acquisitions has been explored. For example: E. Roessl and R. Proksa investigated a method to denoise the energy-resolved projection data for improving the SNR [2]. H. Bruder, *et al* proposed a frequency blending technique for both low and high energy image denoising [3]. One drawback of these methods would be the noise levels and noise textures in final basis images or mono-energetic images are not predictable due to the reconstruction and decomposition.

Another major strategy, which could be applied for spectral CT noise reduction, is to apply an image restoration in mono-energetic images. For example, J. Fan, *et al* proposed a mono-energetic image based denoising method to suppress the basis material image noise at two selected keVs [4]. Although this method can reduce the mono-energetic image noise, the drawback of this framework is that the noise of two selected mono-energetic images are correlated. Therefore, this method might not be an optimal solution.

The third strategy for spectral CT noise reduction is to apply restoration or reconstruction techniques in decomposed material basis. Specifically, in the spectral CT, the attenuation coefficient of each pixel can be expressed as a linear combination of different material attenuations, that is:

$$\mu(E,x,y) \approx \sum_{i=1}^{M} \mu_i(E,x,y) c_i(x,y) , \qquad (1)$$

where $\mu_i(E,x,y)$ are the energy dependent attenuation coefficients for *ith* basis materials at indices (x,y), $c_i(x,y)$ denotes the pixel value of different basis images at indices (x,y), M is the number of energies. Unlike the first and second strategies, instead of reducing poly-energetic images or mono-energetic image noise, this strategy suppresses the noise of decomposed basis material images. However, the inverse of Eq. 1, which is also called material decomposition, indicates strong noise correlations between different basis materials images are introduced during the material decomposition procedure. To compensate this correlated noise and improve the image quality, one common strategy is to model an accurate covariance matrix in a cost function and solve optimization problem. For example, many iterative reconstruction methods have been proposed to include the noise covariance model in a cost function [5, 6, 7] and use joint regularizations for image quality control [8]. However, solving such correlated optimization problems often requires time consuming optimization algorithms.

In this paper, to overcome the drawbacks and limitations mentioned above, we proposed a novel spectral CT denoising method by using whitening transform. In our method, the poly-energetic sinograms were firstly decomposed to basis material sinograms and reconstructed by FBP algorithm. Then a whitening transform followed by an independent noise reduction method was applied to the reconstructed basis material images for noise reduction in whitening domain. Finally, the inverse whitening transformation was applied to transform the denoised whitening domain images to basis material images. As compared to other methods mentioned above, two major advantages have been found: 1) the noise reduction in whitening domain is more efficient than in basis material domain; 2) since the whitening transform can decorrelate noise and represents the desired images on orthonormal basis, the denoising parameters selection are more intuitive as compared to the other techniques.

Y. Liu and Z. Yu are with the Toshiba Medical Research Institute USA, Vernon Hills, IL, 60061 USA

The reminder of this paper is organized as follows. Section 2 briefly reviews the general whitening transform concept, covariance estimation and denoising algorithm. Section 3 presents the experimental results. Finally, discussion and conclusion are given in Section 4.

II. Methods

A. Whiting transform

The eigenvalue decomposition of noise covariance matrix Σ_{y_i} can be represented as:

$$\Sigma_{y_i}\Phi = \Phi\Lambda, \tag{2}$$

where matrix Φ is a square matrix, whose i^{th} column is the eigenvector of covariance matrix, Λ is a diagonal matrix whose diagonal elements are the corresponding eigenvalues. The whitening transform matrix can be represented by:

$$W = \Lambda^{-1/2}\Phi^T, \tag{3}$$

Applying the whitening transform W to basis images can decorrelate noise and transform basis images to a new orthonormal basis. Since the noise in whitening domain is independent, it can be reduced seperately.

B. Covariance matrix estimation

According to our previous publication in [8], the noise covariance matrix of basis material sinograms can be accurately calculated. However, the derivation of the noise covariance of basis images would be complicated and relies on reconstruction algorithms. Although it might be possible to estimate an image covariance with known reconstruction technique, the accurate covariance derivation is beyond the scope of this study. In this study, instead of deriving the analytic expressions of the image space covariance matrix, we assume the covariance is shift invariant and can be approximately estimated from local image patches selected from uniform areas. The results indicated this approximation works properly for noise reduction.

C. Denoising algorithm

Since the whitening transform can decorrelate a joint denoising problem into several independent denoising problems and the covariance matrix $\sum_{\hat{f}}^{-1}$ becomes an identity matrix in whitening domain, many denoising filters or algorithms can be used to suppress image noise in whitening domain. For example, we can use spatial filters or frequency filters with low pass capability to suppress high frequency noise. In this study, we use a penalized weighted least squares (PWLS) method for iterative image denoising. The general cost function for PWLS can be represented as:

$$\min \frac{1}{2}(f-\hat{f})^T \sum_{\hat{f}}^{-1}(f-\hat{f}) + \beta R(f) \tag{4}$$

where $\hat{f}$ is the input noisy image, f is the desired noise-free image, $\sum_{\hat{f}}^{-1}$ is the inverse covariance matrix of the noisy image, β is a regularization parameter to control the denoising strength, $R(f)$ denotes the regularizers. In this study, without loss of generality, we use an isotropic quadratic regularization for whitening domain denoising. Finally, the denoised basis material images were calculated by inverse whitening transform.

III. Results

A. Image acquisitions

A dual-energy phantom data was acquired at 80 and 135 kVp. The tube current was set to 400 and 100mAs respectively to match the total dose. The sinogram space material decomposition method [9] followed by filter-back projection reconstruction were applied to generate water and bone basis material images.

B. Visual comparison

The denoised 50keV, 75keV and 135keV mono-energetic zoom-in images are shown in Fig. 1. The conventional independent basis material based denoising results at matched resolution level are also showed for comparison purpose. From the resulting images we can observe that both whitening transform based denoising method and independent basis material based denoising method can reduce image noise at three keV levels. In addition, in 50 keV and 135keV case, the whitening transform results have better image quality in terms of lower noise as compared to the independent basis material denoising results.

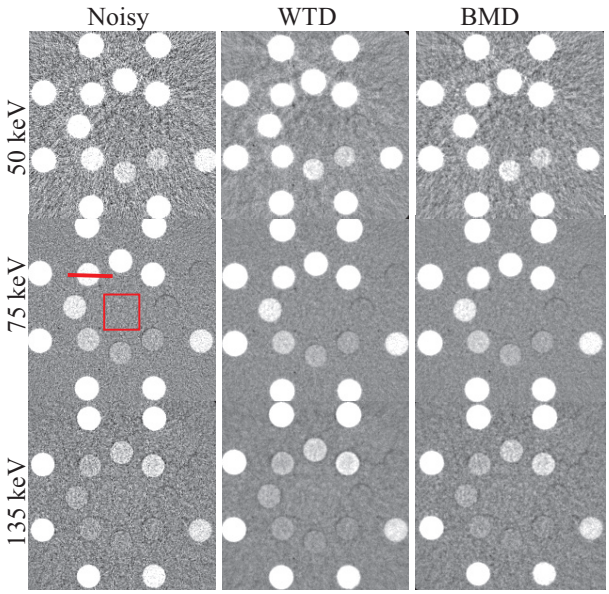

Fig. 1. The visual comparison between the noisy images (left column), whitening transform based denoising (WTD) images (middle column) and independent basis material based denoising (BMD) images (right column).

C. Quantitative comparison

To quantify the image quality improvements as compared to the conventional independent basis material based image denoising method, we calculated the standard deviation of selected ROI (as indicated in Fig. 1) at matched resolution scenario. The profiles go across the same inserts as indicated in Fig. 1 were plotted in Fig.2 to confirm the images resolutions.

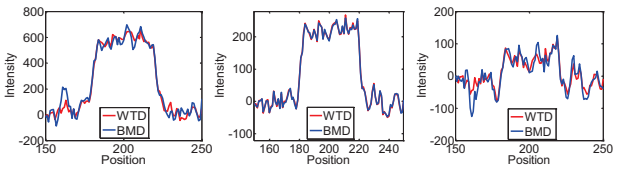

Fig. 2. The profiles of the insert at (a) 50 keV, (b) 75 keV and (c) 135 keV.

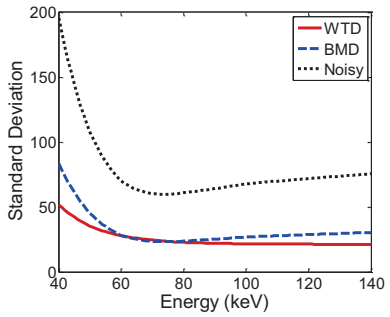

Fig. 3. The standard deviation versus keV curve in the clinically relevant diagnostic energy range (40keV – 140keV).

The standard deviation versus keV curves were ploted in Fig. 3. From the curve we can observe inmatched resolution scenario, the whitening transform denoied image have lower noise as compared to basis material denoised images at higher and lower keV levels.

D. Denoising parameters study

In general, the image noise are monotonically decreased as we increase the regularization strength in conventional CT denoising or reconstruction. However, this assumption might not be true for spectral CT. To validate this hypothesis, we fixed the water basis denoising regularization strength and gradually increased the bone basis denoising regularization strength. Table 1 shows the standard deviation of the selected ROI at 75 keV. From Table 1 we can observe the 75 keV image noise was decreased until β=18 and gradually increased as we continued to increase the regularization strength of bone basis.

Table 1. The STD of mono-energetic image at 75keV at fixed water basis regularization strength

β_{bone}	3	6	18	54	108
75keV STD	65.847	37.896	14.212	25.247	34.320

The non-monotonic noise trend in Table 1 can be explained by Fig.4. In this figure, the noisy basis coefficients at uniform area are plotted by blue dots and the denoised basis coefficients are plotted by red dots, black dash line was drawn along 75keV direction. The image noise at 75keV can be quantified by projecting the dots cloud to the dash line, as shown by the black solid line. From the figure we can observe as we increased the bone basis regularization strength, the denoised coefficients cloud was rotated and compressed along bone direction. The projection length (i.e., black solid line) along 75 keV direction was decreased until reaching the "minimum point" and then increased as we continued to "rotate" the coefficients cloud. Therefore the noise of the mono-energetic image would not be monotonically decreased.

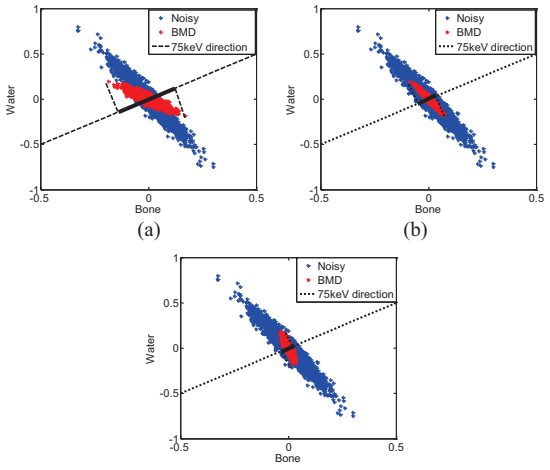

Fig. 4. The basis material coefficients covariance clouds at fixed regularization strength in water basis. The regularization strength in bone basis are (a) $\beta_{bone}=3$; (b) $\beta_{bone}=18$; (c) $\beta_{bone}=108$.

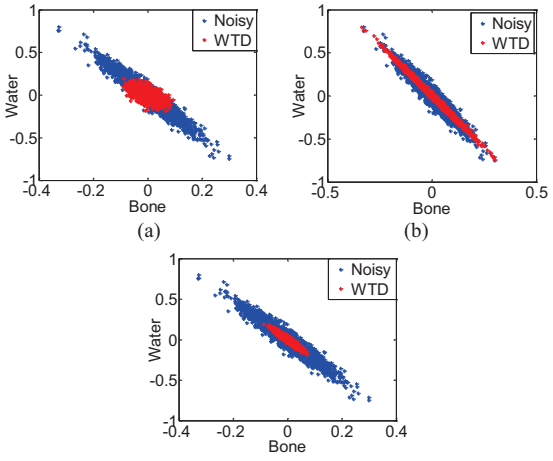

Fig. 5. The basis material coefficients covariance clouds for proposed Whitening transform based denoising algorithm. (a) Denoising along the long axis (one direction of eigenvectors). (b) Denoising along the short axis (another direction of eigevecotrs). (c) Denoising along both directions.

In contrast to the conventional independent basis material image denoising method mentioned above, the proposed whitening transform method can decorrelate the noise covariance and the denoise strength always consistent with the eigenvectors' directions. Figure 5 shows an example for coefficients changes for the proposed whitening transform based denoising. Since the denoising strengths are always consistent with the long and short axis orthogonal directions, the image noise are always monotonically decreased as we increased regularization strength. In addition, the resulting images show better textures as compared to the basis material denoising method.

In addition to the advantage mentioned above, another benefit of suppressing image noise along orthogonal direction is that the noise level of the mono-energetic images are easier to be controlled as compared to other techniques mentioned in the introduction section. By giving different denoising strength to different whitening basis, the trend of noise versus keV curve can be controlled. For example, in figure 6, we

observe the noisy images have higher noise at 40 and 140 keV and lower noise at 70 keV. To maintain the image quality at 70 keV and reduce noise at 40 and 140 keV, strong denoising strength was applied in long axis direction (one of whitening transformation basis which has higher image noise) as shown in Fig. 5 (a). The benefit is that the image noise at 40 and 140 keV can be reduced without affecting the image quality at 70 keV, as shown by the green curve in Fig. 6. If we want to reduce the overall image noise (blue curve in Fig. 6), the noise should be suppressed on all whitening transformation bases as shown in Fig. 5(c). The flatness of the noise versus keV curve can be controlled by giving different denoising strength to different whitening basis, as shown by the red and blue curve in Fig. 6.

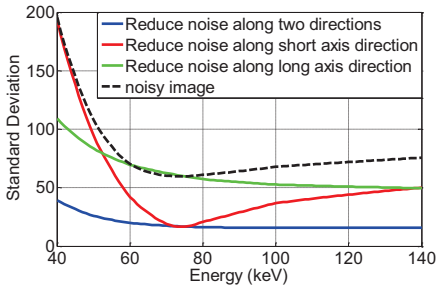

Fig. 6. The standard deviation versus keV curve in the clinically relevant diagnostic energy range (40keV – 140keV).

IV. Discussion and Conclusion

In this paper, we proposed a whitening transform based denoising method for spectral CT. The results show the proposed method can efficiently suppress image noise as compared to the conventional independent basis image denoising technique. In image quality comparison study, we fixed the image resolution and compared the noise level in the clinically relevant diagnostic energy range (40keV – 140keV). We found the proposed method can achieve up to 80% noise reduction. In addition, we demonstrated the regularization parameters at different whitening transform basis can control the minimum noise level (at around 75 keV) and the flatness of the noise versus keV curve. Since many spectral CT clinical applications rely on mono-energetic images for diagnosis, the proposed method can provide consistent mono-energetic image qualities at all keV levels. Our future work will include designing advanced denoising filters such as edge persevering regularizers for whitening transform denoising.

References

[1] M. Karcaaltincaba and A. Aktas, “Dual-energy CT revisited with multidetector CT: review of principles and clinical applications,” *Diagnostic and Interventional Radiology*, 17(3), pp. 181-194, Sep, 2011.

[2] E. Roessl, R. Proksa, “Likelihood-based spectral data projection domain de-noising” Patent US20140005971 A1, 2014.

[3] H. Bruder, E. Klotz, M. Petersilka, R. Raupach and H. Schondube, “Method for Iterative Image Reconstruction for Bi-Modal CT Data”, US9,082,167,B2, 2015.

[4] Y. Liu, Z. Yu, and Y. Zou, “Impact of covariance modeling in dual-energy spectral CT image reconstruction,” *2015 SPIE conference proceeding*, 2015.

[5] R. Zhang, J. B. Thibault, C. Bouman, K. Sauer, and J. Hsieh, “Model-based iterative reconstruction for dual-energy X-ray CT using a joint quadratic likelihood model,” *IEEE Transactions on Medical Imaging*, vol. 31, no. 1, pp. 117-134, Sep, 2013.

[6] Y. Long and J. A. Fessler, "Multi-Material Decomposition Using Statistical Image Reconstruction for Spectral CT," *IEEE Transactions on Medical Imaging*, vol. 33, no. 8, pp. 1614-1626, Aug, 2014.

[7] Y. Liu and Z. Yu, "A joint iterative reconstruction algorithm for dual energy CT using ADMM," *The 13th International Meeting on Fully Three-Dimensional Image Reconstruction in Radiology and Nuclear Medicine*, 2015

[8] K. M. Mrown, S. Zabic and G. Shechter, "Impact of Spectral Separation in Dual-Energy CT with Anti-Correlated Statistical Reconstruction," *The 13th International Meeting on Fully Three-Dimensional Image Reconstruction in Radiology and Nuclear Medicine*, 2015

[9] Y. Zou, and M. D. Silver, “Analysis of fast kV-switching in dual energy CT using a pre-reconstruction decomposition technique,” *Proceeding of SPIE Medical Imaging 2008,* vol. 6913, pp. 691313-691313-12, 2008.

Accelerated Parallel and Distributed Iterative Coordinate Descent (ICD) for X-ray CT

Madison G. McGaffin Jeffrey A. Fessler
Dept. of Electrical Engineering and Computer Science, University of Michigan

***Abstract*—This paper describes a new distributed algorithm for accelerating model-based image reconstruction in X-ray CT using iterated coordinate descent (ICD). The key novel component is a majorizer whose Hessian involves a block-diagonal matrix with triangular blocks (BDTriB). The resulting majorize-minimize algorithm combines aspects of ICD and the distributed block-separable surrogates (DBSS) algorithm for CT reconstruction [1]. Unlike traditional ICD, the proposed algorithm is also amenable to acceleration using Nesterov's momentum [2] and the optimized gradient method (OGM) [3]. A simple preliminary experiment indicates potential for significant acceleration over traditional ICD and promising performance for distributed computing.**

I. Introduction

Model-based image reconstruction (MBIR) in X-ray CT may improve image quality over direct reconstruction methods like filtered backprojection, but long reconstruction times impede widespread clinical use. Accelerating model-based reconstructions involves improving the mathematical structure of the numerical optimization algorithms [3], [4] and exploiting both modern hardware [5], [6] and distributed computing [1], [7]. This paper describes a parallelizable version of ICD.

Consider the following penalized weighted least-squares (PWLS) image reconstruction problem [8]:

$$\widehat{\boldsymbol{x}} = \underset{\boldsymbol{x} \succeq \boldsymbol{0}}{\operatorname{argmin}} \; \Psi(\boldsymbol{x}), \quad \Psi(\boldsymbol{x}) = \mathsf{L}(\boldsymbol{A}\boldsymbol{x}) + \mathsf{R}(\boldsymbol{C}\boldsymbol{x}), \qquad (1)$$

with CT system matrix $\boldsymbol{A} \in \mathbb{R}^{M \times N}$, finite differences matrix $\boldsymbol{C} \in \mathbb{R}^{K \times N}$, and data-fit and regularizer terms L and R:

$$\mathsf{L}(\boldsymbol{p}) = \sum_{i=1}^{M} \frac{w_i}{2}(p_i - y_i)^2, \qquad \mathsf{R}(\boldsymbol{d}) = \sum_{k=1}^{K} \beta_k \psi(d_k), \qquad (2)$$

with nonnegative statistical weights $\{w_i\}$ and regularization parameters $\{\beta_k\}$, where $\{y_i\}$ denotes the measured sinogram (log) data. We assume the convex potential function ψ is smooth with bounded curvature.

Suppose that we have B compute nodes that communicate via some interconnect; *e.g.*, multiple GPUs or processors on a single computer or multiple computers connected by a network. Data communication over this interconnect typically is slower than communication and computation within each node. Accordingly, we solve (1) by finding a majorizer consisting of a sum of B components that we minimize in parallel and then communicate the results to update the image $\boldsymbol{x}$.

Supported in part by NIH grant U01 EB018753 and Intel equipment donations. Email: {mcgaffin | fessler}@umich.edu .

II. Methods

The proposed method combines the distributed block-separable surrogate (DBSS) [1] in a majorize-minimize (MM) framework [9] using a form of ICD for the inner minimizations and momentum for acceleration [2], [3].

A. Distributed block-separable surrogates

We start with a majorizer based on the distributed block-separable surrogate (DBSS) [1]. We partition the image $\boldsymbol{x}$ into B blocks, $\{\boldsymbol{x}_b\}$, *i.e.*, $\boldsymbol{x} = (\boldsymbol{x}_1, \ldots, \boldsymbol{x}_B)$, typically by axial slabs. The corresponding components of the CT system matrix $\boldsymbol{A}$ and the finite differencing matrix $\boldsymbol{C}$ are $\{\boldsymbol{A}_b\}$ and $\{\boldsymbol{C}_b\}$, respectively, where, *e.g.*, $\boldsymbol{A} = [\boldsymbol{A}_1, \ldots, \boldsymbol{A}_B]$ and $\boldsymbol{A}_b$ is the submatrix of $\boldsymbol{A}$ having columns correspond to the pixels in $\boldsymbol{x}_b$. During each outer iteration, each computational node updates one of these sub-images, after which the sub-images are communicated between blocks.

In each outer iteration n, we form a block separable surrogate $\Phi^{(n)}$ as follows:

$$\Phi^{(n)}(\boldsymbol{x}) \triangleq \frac{1}{2}\left\|\boldsymbol{x} - \boldsymbol{x}^{(n)}\right\|_{\boldsymbol{M}}^2 + \left(\boldsymbol{x} - \boldsymbol{x}^{(n)}\right)' \nabla\Psi\left(\boldsymbol{x}^{(n)}\right) + \Psi\left(\boldsymbol{x}^{(n)}\right), \qquad (3)$$

where the iteration-invariant, block-diagonal, $N \times N$ matrix $\boldsymbol{M}$ majorizes the Hessian of the cost function, *i.e.*, $\boldsymbol{M} \succeq \nabla^2\Psi$. This is a tangent majorizer [9], *i.e.*, it satisfies

$$\Phi^{(n)}\left(\boldsymbol{x}^{(n)}\right) = \Psi\left(\boldsymbol{x}^{(n)}\right), \quad \Phi^{(n)}(\boldsymbol{x}) \geq \Psi(\boldsymbol{x}) \qquad \forall \boldsymbol{x} \succeq \boldsymbol{0}. \qquad (4)$$

Therefore, any $\boldsymbol{x}^{(n+1)}$ that descends the surrogate $\Phi^{(n)}$ will also descend the original cost function Ψ. For the MBIR problem (1), this property ensures convergence to $\widehat{\boldsymbol{x}}$ [9].

The DBSS [1] has the block-diagonal Hessian $\boldsymbol{M}_{\text{DBSS}} \triangleq \operatorname{diag}\{\boldsymbol{M}_{\text{DBSS},b}\}$, where

$$\boldsymbol{M}_{\text{DBSS},b} \triangleq \boldsymbol{A}_b' \boldsymbol{\Lambda}_b \boldsymbol{W} \boldsymbol{A}_b + \boldsymbol{C}_b' \boldsymbol{K}_b \boldsymbol{B} \boldsymbol{C}_b,$$
$$\boldsymbol{W} = \operatorname*{diag}_i\{w_i\}, \quad \boldsymbol{B} = \operatorname*{diag}_k\left\{\beta_k \cdot \max_d \psi''(d)\right\}, \qquad (5)$$

where $\boldsymbol{\Lambda}_b$ and $\boldsymbol{K}_b$ are determined by the partition of $\boldsymbol{x}$:

$$\boldsymbol{\Lambda}_b \triangleq \operatorname*{diag}_i\left\{\frac{[\boldsymbol{A}\boldsymbol{1}]_i}{[\boldsymbol{A}_b\boldsymbol{1}]_i}\right\}, \qquad \boldsymbol{K}_b \triangleq \operatorname*{diag}_k\left\{\frac{[|\boldsymbol{C}|\boldsymbol{1}]_k}{[|\boldsymbol{C}_b|\boldsymbol{1}]_k}\right\}, \qquad (6)$$

where $|\boldsymbol{C}|$ denotes the element-wise absolute value of $\boldsymbol{C}$. This majorizer is block-separable, *i.e.*, it decomposes into B independent functions over different groups of pixels $\{\boldsymbol{x}_b\}$:

$$\Phi^{(n)}_{\text{DBSS}}(\boldsymbol{x}) = \sum_{b=1}^{B} \Phi^{(n)}_{\text{DBSS},b}(\boldsymbol{x}_b), \tag{7}$$

The DBSS algorithm descends each block surrogate $\Phi^{(n)}_{\text{DBSS},b}$ using ordered subsets with momentum acceleration (OS-MOM) [1], [3].

B. Distributed iterated coordinate descent

The DBSS algorithm does not *exactly* minimize each block-separable surrogate $\Phi^{(n)}_{\text{DBSS},b}$ because that would require too many inner iterations of OS-MOM to be practical. Although merely descending each surrogate is sufficient to ensure convergence, mere descent precludes using momentum-based techniques to accelerate the outer iterations.

To design a majorizer for which ICD can perform *exact* minimization, we propose to further majorize the block-separable matrix $\boldsymbol{M}_{\text{DBSS}}$ with a block-diagonal matrix having (lower) triangular blocks (BDTriB): $\boldsymbol{D} + \boldsymbol{T}$. We invert each of the triangular blocks of the BDTriB matrix *exactly* simply using back-substitution, *i.e.*, one sweep of ICD. By a proof similar to the one in [3], this design allows us to accelerate the outer iterations using momentum.

For derivation (but not implementation), define the $N \times N$ block diagonal matrix $\boldsymbol{T} = \text{diag}\{\boldsymbol{T}_b\}$ where each block $\boldsymbol{T}_b$ is lower-triangular and defined as follows:

$$[\boldsymbol{T}_b]_{ij} = \begin{cases} [\boldsymbol{A}_b'\boldsymbol{W}\boldsymbol{A}_b + \boldsymbol{C}_b'\boldsymbol{B}\boldsymbol{C}_b]_{ij}, & i \geq j \\ 0, & \text{else.} \end{cases} \tag{8}$$

This definition retains the block structure of $\boldsymbol{M}_{\text{DBSS}}$. We choose the diagonal matrix $\boldsymbol{D}$ such that for all $\boldsymbol{z} \in \mathbb{R}^N$, the following majorization condition holds:

$$\boldsymbol{z}'(\boldsymbol{D} + \boldsymbol{T})\boldsymbol{z} = \boldsymbol{z}'\left(\boldsymbol{D} + \frac{1}{2}(\boldsymbol{T} + \boldsymbol{T}')\right)\boldsymbol{z} \geq \boldsymbol{z}'\boldsymbol{M}_{\text{DBSS}}\boldsymbol{z}. \tag{9}$$

In particular, in each block we design diagonal $\boldsymbol{D}_b$ such that:

$$\boldsymbol{z}_b'\left(\boldsymbol{D}_b + \frac{1}{2}(\boldsymbol{T}_b + \boldsymbol{T}_b')\right)\boldsymbol{z}_b \geq \boldsymbol{z}_b'\boldsymbol{M}_{\text{DBSS},b}\boldsymbol{z}_b. \tag{10}$$

Expanding the definition of $\boldsymbol{T}$ (8), we design $\boldsymbol{D}_b$ such that:

$$\begin{aligned} \boldsymbol{D}_b &\succeq \boldsymbol{M}_{\text{DBSS},b} - \frac{1}{2}(\boldsymbol{T}_b + \boldsymbol{T}_b') \\ &= \boldsymbol{A}_b'\boldsymbol{\Lambda}_b\boldsymbol{W}\boldsymbol{A}_b + \boldsymbol{C}_b'\boldsymbol{K}_b\boldsymbol{B}\boldsymbol{C}_b \qquad (11) \\ &\quad - \frac{1}{2}(\boldsymbol{A}_b'\boldsymbol{W}\boldsymbol{A}_b + \boldsymbol{C}_b'\boldsymbol{B}\boldsymbol{C}_b + \boldsymbol{G}_b) \\ &= \boldsymbol{A}_b'\boldsymbol{W}\left(\boldsymbol{\Lambda}_b - \frac{1}{2}\boldsymbol{I}\right)\boldsymbol{A}_b + \boldsymbol{C}_b'\boldsymbol{B}\left(\boldsymbol{K}_b - \frac{1}{2}\boldsymbol{I}\right)\boldsymbol{C}_b - \frac{1}{2}\boldsymbol{G}_b, \qquad (12) \end{aligned}$$

where $\boldsymbol{G}_b$ contains the diagonal of $\boldsymbol{A}_b'\boldsymbol{W}\boldsymbol{A}_b + \boldsymbol{C}_b'\boldsymbol{B}\boldsymbol{C}_b$. The entries of $\boldsymbol{\Lambda}_b$ and $\boldsymbol{K}_b$ (6) are greater than or equal to unity if nonzero. We majorize the nondiagonal terms in (12) with the following "SQS-like" majorizer [10]:

$$\begin{aligned} \boldsymbol{D}_{\text{SQS},b} \triangleq \text{diag}\Bigg\{ &\left(\boldsymbol{A}_b'\boldsymbol{W}\left(\boldsymbol{\Lambda}_b - \frac{1}{2}\boldsymbol{I}\right)\boldsymbol{A}_b\right. \\ &\left. + |\boldsymbol{C}_b|'\boldsymbol{B}\left(\boldsymbol{K}_b - \frac{1}{2}\boldsymbol{I}\right)|\boldsymbol{C}_b|\right)\boldsymbol{1}\Bigg\}. \end{aligned} \tag{13}$$

Thus, our final diagonal component for the bth block is

$$\boldsymbol{D}_b \triangleq \boldsymbol{D}_{\text{SQS},b} - \frac{1}{2}\boldsymbol{G}_b, \tag{14}$$

which one can verify is nonnegative. Computing this majorizer requires no more time than computing the diagonal majorizer for the SQS-MOM inner step of the DBSS algorithm. In other applications, *e.g.*, phase-contrast CT, the gram matrix $\boldsymbol{A}'\boldsymbol{\Lambda}_b\boldsymbol{A}$ may have negative entries. In these cases, the SQS majorizer (13) may be very loose or difficult to compute, and one can use another technique to find a diagonal majorizer, *e.g.*, the memory-efficient algorithm in [11].

C. Minimizing the new surrogate

The new surrogate for the bth block is

$$\Phi^{(n)}_b(\boldsymbol{x}_b) = \frac{1}{2}\left\|\boldsymbol{x}_b - \boldsymbol{x}_b^{(n)}\right\|^2_{\boldsymbol{D}_b + \boldsymbol{T}_b} + \boldsymbol{x}_b'\nabla_{\boldsymbol{x}_b}\Psi\left(\boldsymbol{x}^{(n)}\right). \tag{15}$$

The matrix $\boldsymbol{D}_b + \boldsymbol{T}_b$ couples the entries of $\boldsymbol{x}_b$ together, but because it is lower triangular, we minimize $\Phi^{(n)}_b$ *exactly* using back substitution with a nonnegativity constraint. That is, we loop though each pixel x_j of $\boldsymbol{x}_b$ in a predetermined order and for each pixel solve the 1D minimization problem

$$\begin{aligned} x_j^{(n+1)} &= \underset{x_j \geq 0}{\text{argmin}} \ \frac{\omega_j}{2}\left(x_j - x_j^{(n)}\right)^2 + x_j g_j, \\ &= \max\left(x_j^{(n)} - \frac{1}{\omega_j}g_j, 0\right), \end{aligned} \tag{16}$$

where

$$\begin{aligned} \omega_j &\triangleq [\boldsymbol{D}]_{jj} + \boldsymbol{a}_j'\boldsymbol{W}\boldsymbol{a}_j + \boldsymbol{c}_j'\boldsymbol{B}\boldsymbol{c}_j, \\ g_j &\triangleq \left[\nabla \text{R}\left(\boldsymbol{x}^{(n)}\right)\right]_j + \boldsymbol{a}_j'\boldsymbol{W}\left(\boldsymbol{r}^{(n)} + \boldsymbol{r}_b\right) \\ &\quad + \boldsymbol{c}_j'\boldsymbol{B}\boldsymbol{C}_b\left(\boldsymbol{x}_b^{(n+)} - \boldsymbol{x}_b^{(n)}\right), \\ \boldsymbol{r}^{(n)} &\triangleq \boldsymbol{A}\boldsymbol{x}^{(n)} - \boldsymbol{y}, \quad \boldsymbol{r}_b \triangleq \boldsymbol{A}_b\left(\boldsymbol{x}_b^{(n+)} - \boldsymbol{x}_b^{(n)}\right), \end{aligned} \tag{17}$$

and $\boldsymbol{a}_j$ and $\boldsymbol{c}_j$ denote the jth columns of $\boldsymbol{A}$ and $\boldsymbol{C}$, respectively. The vector $\boldsymbol{x}_b^{(n+)}$ contains the state of $\boldsymbol{x}_b$ after the all the pixels before the jth pixel have been updated. Updating the jth pixel involves:

- computing the column vectors $\boldsymbol{a}_j$ and $\boldsymbol{c}_j$;
- computing ω_j and g_j, which involves finite differences (for the second term of g_j) and inner products;
- solving the one-pixel update problem (16);
- and finally updating the residual buffer

$$\boldsymbol{r}_b \leftarrow \boldsymbol{r}_b + \boldsymbol{a}_j\left(x_j^{(n+1)} - x_j^{(n)}\right). \tag{18}$$

These are the same steps as ICD [12] applied to (7) with the minor addition of the "relaxation" $[\boldsymbol{D}]_{jj}$ in ω_j.

TABLE I
MOMENTUM-ACCELERATED DISTRIBUTED ICD ALGORITHMS

1) Distribute $\left\{\boldsymbol{x}_b^{(0)}\right\}$ to the B computational nodes, initialize $\boldsymbol{z}^{(0)} = \boldsymbol{x}^{(0)}$. Compute $\boldsymbol{r}^{(0)} = \boldsymbol{A}\boldsymbol{x}^{(0)} - \boldsymbol{y}$ and $\{\boldsymbol{D}_b\}$ (14). Set $t^{(0)} = 1$.
2) Loop outer iteration $n = 1, \ldots, N_{\text{iter}}$:
   a) $t^{(n+1)} = \frac{1}{2}\left(1 + \sqrt{1 + 4\left(t^{(n)}\right)^2}\right)$
   b) In parallel for $b = 1, \ldots, B$:
      i) Minimize block surrogate (15) using ICD to compute $\boldsymbol{x}_b^{(n+1)}$.
      ii) Momentum update:

$$\begin{aligned}
\text{No momentum} &: \boldsymbol{z}_b^{(n+1)} = \boldsymbol{x}_b^{(n+1)}, \\
\text{FGM} &: \boldsymbol{z}_b^{(n+1)} = \boldsymbol{x}_b^{(n+1)} + \tfrac{t^{(n)}-1}{t^{(n+1)}}\left(\boldsymbol{x}_b^{(n+1)} - \boldsymbol{x}_b^{(n)}\right) \\
\text{OGM} &: \boldsymbol{z}_b^{(n+1)} = \boldsymbol{x}_b^{(n+1)} + \tfrac{t^{(n)}-1}{t^{(n+1)}}\left(\boldsymbol{x}_b^{(n+1)} - \boldsymbol{x}_b^{(n)}\right) \\
&\quad + \tfrac{t^{(n)}}{t^{(n+1)}}\left(\boldsymbol{x}_b^{(n+1)} - \boldsymbol{z}_b^{(n)}\right)
\end{aligned}$$

   c) Broadcast node residuals $\{\boldsymbol{r}_b\}$ to compute $\boldsymbol{r}^{(n+1)}$ and edge slices of $\boldsymbol{x}_b^{(n+1)}$.
3) Output: $\boldsymbol{z}^{(N_{\text{iter}})}$.

Between outer iterations, we synchronize the regularizer gradient $\nabla \mathsf{R}\left(\boldsymbol{x}^{(n)}\right)$ and residual $\boldsymbol{r}^{(n)} = \boldsymbol{A}\boldsymbol{x}^{(n)} - \boldsymbol{y}$ between computational nodes. The latter needs no additional projections or backprojections because

$$\boldsymbol{r}^{(n+1)} - \boldsymbol{r}^{(n)} = \sum_{b=1}^{B} \boldsymbol{r}_b, \tag{19}$$

so each node needs only to communicate residual updates $\{\boldsymbol{r}_b\}$ and edge voxels to compute $\nabla_{\boldsymbol{x}_b} \mathsf{R}\left(\boldsymbol{x}^{(n)}\right)$.

D. Momentum-based acceleration

In each outer iteration, the proposed algorithm forms and exactly minimizes a block-separable quadratic surrogate for the original cost function. This places the proposed algorithm in the same category as iterative shrinkage and thresholding (ISTA) and momentum-accelerated SQS algorithms. Thus, the distributed ICD algorithm can be improved with momentum-based acceleration *e.g.*, Nesterov's fast gradient methods (FGM) [2] or the optimized gradient method (OGM) [13]. Table I summarizes these algorithms.

Traditional ICD methods are not in general amenable to momentum-based acceleration [14]. For example, simply running ICD on the block-separable surrogate $\Phi_{\text{DBSS}}^{(n)}$ in (7) is equivalent to the proposed algorithm with each $\boldsymbol{D}_b = \boldsymbol{0}$. Although this basic approach descends the surrogate $\Phi^{(n)}$ and converges, it is incompatible with momentum-based acceleration; applying momentum-based acceleration to this basic combination of DBSS with ICD may cause divergence. The additional under-relaxation provided by $\boldsymbol{D}_b$ (14) allows us to use ICD for exact minimization of a quadratic majorizer, making the algorithm compatible with momentum-based acceleration. This property is the key contribution of this work.

III. PRELIMINARY EXPERIMENT

To illustrate the concept, we simplified the CT reconstruction problem (1) to a one-dimensional 512-"pixel" problem. We formed the system matrix $\boldsymbol{A}$ using a Toeplitz matrix with point spread function $\frac{1}{r^{1/2}}$ so the Gram matrix $\boldsymbol{A}'\boldsymbol{A}$ has response proportional to $\frac{1}{r}$ [15]. The data-fit weights were uniform $w_i = 1$, and regularizer weights β_k were also uniform. We used a quadratic regularizer potential function $\psi(d) = \frac{1}{2}d^2$. This is an extreme simplification of the CT reconstruction problem for a preliminary investigation.

A. Single-node relaxation and acceleration

We compared 6 methods for $B = 1$: conventional **ICD** and ICD with the proposed relaxation (**RICD**), with and without FGM [2] (**(R)ICD+FGM**), or OGM [13] (**(R)ICD+OGM**). In this "one-node" setting, $\boldsymbol{\Lambda} = \boldsymbol{W} = \boldsymbol{I}$ in (6) and (1).

Fig. 2(a) plots the cost function per iteration for all 6 algorithms. Clearly, applying momentum to basic ICD without additional relaxation is infeasible.

The additional relaxation from the diagonal matrices $\{\boldsymbol{D}_b\}$ (14) slows the convergence of RICD compared to ICD. However, because every loop through all the pixels in RICD corresponds to minimizing a quadratic surrogate, we can apply momentum. With momentum acceleration, RICD converges faster than regular ICD. Furthermore RICD+FGM is provably convergent.

B. Distributed accelerated ICD

We also implemented the proposed distributed ICD algorithms on a simulated network of 2, 4 and 8 nodes. As the number of nodes B in the network increases, the block-separable majorizer becomes looser; Fig. 1(d) shows this effect in the increasing entries of the diagonal majorizer $\boldsymbol{D}$.

Fig. 2(b) shows the value of the cost function *vs.* iteration for normal ICD and RICD+OGM for 1, 2, 4, and 8 nodes. The ICD algorithms use the block-separable surrogate [1], and RICD-OGM uses the proposed BDTriB majorizer. As B increases, the larger majorizer values $\{\boldsymbol{D}_b\}$ slow convergence on a per-iteration basis. However the increase of the majorizer values as the number of nodes doubles is less than a factor of 2, so there is opportunity to accelerate the algorithm with distributed computing provided the communication overhead is not too high.

We simulated the time behavior of the distributed algorithms by

$$\Delta t_{\text{iter}} = \begin{cases} 1, & B = 1 \\ \alpha_{\text{overhead}} B + \frac{1}{B}, & B > 1. \end{cases} \tag{20}$$

Each node beyond the first ($B > 1$) adds some overhead due to communication and synchronization, α_{overhead}, but reduces how long it takes to compute the parallelizable workload, $\frac{1}{B}$. In this experiment, we assumed $\alpha_{\text{overhead}} = 0.05$. This is a pessimistic estimate; in other experiments with non-ICD algorithms, we found $\alpha_{\text{overhead}} \approx 0.01$ for multiple GPUs connected to the same computer or $\alpha_{\text{overhead}} \approx 0.03$ for computers connected by Ethernet.

Fig. 2(c) plots the value of the cost function *vs.* estimate time for the distributed (R)ICD algorithms. The distributed ICD algorithms reach peak performance at only two nodes, and is still slower than RICD on one node. The RICD algorithm

(a) Full $N \times N$ Hessian of Ψ (b) DBSS Hessian, $B = 4$ (c) $\boldsymbol{T}$ for Proposed BDTriB (d) Diagonal of Relaxation $\boldsymbol{D}$

Fig. 1. Full Hessian of Ψ, Hessian of block-separable majorizer for $B = 4$, and $\boldsymbol{T}$ and $\boldsymbol{D}$ for BDTriB majorizer for the simplified reconstruction problem in Section III.

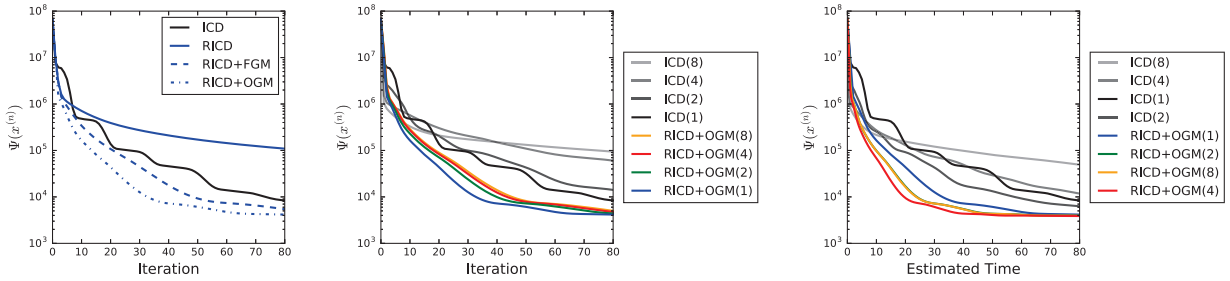

(a) Accelerated ICD (b) Cost Ψ *vs.* Iteration for various B (c) Cost Ψ *vs.* Estimated Time

Fig. 2. Cost function curves for the experiment in Section III.

can exploit further parallelism, and convges most quickly on four nodes; the overhead from the eight-node configuration slows overall convergence. Although this preliminary experiment suggests only modest parallelization is useful, our selection for α_{overhead} is pessimistic and the time-characteristics of a real distributed system are difficult to estimate *a priori*.

IV. Summary

We explored accelerating ICD using momentum and distributed computing. With additional relaxation based on matrix majorization, we can combine ICD [3] with the momentum methods that have been effective in accelerating ordered-subsets methods. A proof-of-concept experiment suggests that this approach can accelerate ICD. The proposed method also shows promising accelerations via distributed computing, by combining momentum-based acceleration with block-separable surrogates [1]. The voxels on the boundary between blocks might converge slower than others; this effect could be mitigated by dithering the block boundaries [1].

The sequential nature of ICD algorithms seems not well matched to computing hardware that becomes increasingly parallel. Nevertheless, the general techniques for accelerating and distributing ICD described here are also relevant to accelerating dual coordinate ascent algorithms for CT, *e.g.*, [5], that are amenable to implementation on modern hardware.

References

[1] D. Kim and J. A. Fessler. Distributed block-separable ordered subsets for helical X-ray CT image reconstruction. In *Proc. Intl. Mtg. on Fully 3D Image Recon. in Rad. and Nuc. Med*, pp. 138–41, 2015.

[2] Y. Nesterov. A method of solving a convex programming problem with convergence rate $O(1/k^2)$. *Soviet Math. Dokl.*, 27(2):372–76, 1983.

[3] D. Kim, S. Ramani, and J. A. Fessler. Combining ordered subsets and momentum for accelerated X-ray CT image reconstruction. *IEEE Trans. Med. Imag.*, 34(1):167–78, January 2015.

[4] H. Nien and J. A. Fessler. Fast X-ray CT image reconstruction using a linearized augmented Lagrangian method with ordered subsets. *IEEE Trans. Med. Imag.*, 34(2):388–99, February 2015.

[5] M. McGaffin and J. A. Fessler. Alternating dual updates algorithm for X-ray CT reconstruction on the GPU. *IEEE Trans. Computational Imaging*, 1(3):186–99, September 2015.

[6] R. Sampson, M. G. McGaffin, T. F. Wenisch, and J. A. Fessler. Investigating multi-threaded SIMD for helical CT reconstruction on a CPU. In *Proc. 4th Intl. Mtg. on image formation in X-ray CT*, 2016.

[7] J. M. Rosen, J. Wu, T. F. Wenisch, and J. A. Fessler. Iterative helical CT reconstruction in the cloud for ten dollars in five minutes. In *Proc. Intl. Mtg. on Fully 3D Image Recon. in Rad. and Nuc. Med*, pp. 241–4, 2013.

[8] J-B. Thibault, K. Sauer, C. Bouman, and J. Hsieh. A three-dimensional statistical approach to improved image quality for multi-slice helical CT. *Med. Phys.*, 34(11):4526–44, November 2007.

[9] M. W. Jacobson and J. A. Fessler. An expanded theoretical treatment of iteration-dependent majorize-minimize algorithms. *IEEE Trans. Im. Proc.*, 16(10):2411–22, October 2007.

[10] H. Erdoğan and J. A. Fessler. Ordered subsets algorithms for transmission tomography. *Phys. Med. Biol.*, 44(11):2835–51, November 1999.

[11] M. G. McGaffin and J. A. Fessler. Algorithmic design of majorizers for large-scale inverse problems, 2015. arxiv 1508.02958.

[12] Z. Yu, J-B. Thibault, C. A. Bouman, K. D. Sauer, and J. Hsieh. Fast model-based X-ray CT reconstruction using spatially non-homogeneous ICD optimization. *IEEE Trans. Im. Proc.*, 20(1):161–75, January 2011.

[13] D. Kim and J. A. Fessler. Optimized first-order methods for smooth convex minimization. *Mathematical Programming*, 2016. To appear.

[14] A. Chambolle and T. Pock. A remark on accelerated block coordinate descent for computing the proximity operators of a sum of convex functions. *SMAI J. of Computational Mathematics*, 1:29–54, 2015.

[15] N. H. Clinthorne, T. S. Pan, P. C. Chiao, W. L. Rogers, and J. A. Stamos. Preconditioning methods for improved convergence rates in iterative reconstructions. *IEEE Trans. Med. Imag.*, 12(1):78–83, March 1993.

X-Ray Dark Field Investigation of Friction Contact Materials in Lamella Drive Couplings

Jens Maisenbacher, Friedrich Prade, Jens Gibmeier, Franz Pfeiffer and Jürgen Mohr

***Abstract*—Friction contact materials play a major role in drive couplings conveying forces from the engine to the gear. Oftentimes cooling agents are used in order to enhance the lifetime of the device. This however comes at the drawback of the oil-based cooling agent infiltrating the pore network of the friction contacts and thereby diminishing the adhesion between friction partners. Therefore it is of paramount importance to characterize the degree of infiltration for various combinations of friction contact materials, cooling agents and runtime non-destructively. For this purpose, computed tomography is a well suited method. However, it inherently suffers from a decrease of the field of view by increasing the image resolution. Using a Talbot-Lau interferometer and dark field contrast it is possible to integrally analyze the porosity in the friction contrast materials on a 100 × 100 mm² area, as is shown in this paper.**

***Index Terms*—dark field, engineering, friction contact materials, lamella drive coupling, X-ray**

I. Introduction

DRIVE couplings are an integral part of most motor vehicles as they serve as connection between engine and gears. While there are several coupling concepts, some require employing a cooling agent in order to enhance the life span of the device. During its operation the pores of the friction contact are repeatedly filled by and washed out of cooling agent, though after sufficient operating time, the cycle comes to an end. The cooling agent now infiltrating the pore network of the friction contact material diminishes the adhesive forces in the drive coupling rendering the device malfunctioning. Consequently, it is necessary to estimate the lifespan of different combinations of friction contact materials and cooling agents.

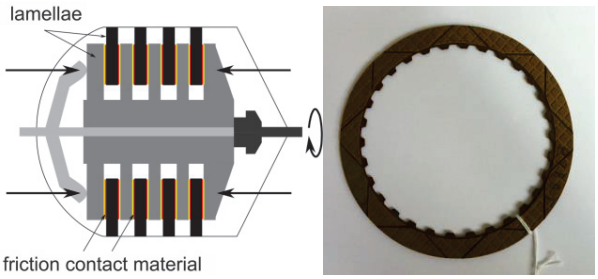

Fig. 1. Schematic of lamella drive coupling (*left side*) and photograph of a single lamella with friction contact material (*right side*).

In order to characterize different material combinations non-destructive testing has to be preferred, as it is necessary to screen several stages of the infiltration process. X-ray computed tomography (CT) seems to be a well suited method. It allows non-destructive testing and hence makes it possible to examine several time steps during the operation of the drive coupling. The downside is its inherent loss of field of view at higher geometrical magnifications. The latter are necessary however to resolve pore sizes in the micrometer regime. Furthermore, for this particular problem, reference measurements are necessary, as the oil-based cooling agent and the also carbon based friction contrast materials cannot be distinguished in absorption CT.

An easier, less time consuming approach is presented in this contribution using grating based X-ray dark field contrast [1, 2]. The principle of grating based dark field measurements using a lab source has also been introduced in [3]. In this paper we would like to demonstrate an application of the method in non-destructive qualitative porosity analysis.

II. Description of the Measurement

Grating based Talbot-Lau interferometers work on the principle of a phase grating introducing an interference pattern through interaction with the X-ray beam. This pattern repeats itself within certain Talbot-distances d_T in beam direction given by

$$d_T = \frac{p_1^2}{8\lambda}. \quad (1)$$

The authors appreciate financial support by the Helmholtz-Society via the Virtual Institute – New X-Ray Analytical Methods in Materials Science (VI-NXMM). The gratings have been fabricated in the framework of the Karlsruhe Nano Micro Facility (KNMF).

J. Maisenbacher and J. Gibmeier are with the Institute for Applied Materials – Material Science and Engineering, Karlsruhe Institute for Technology, Karlsruhe, Baden-Würtemberg 76131 Germany (e-mail: Jens.Maisenbacher@kit.edu).

F. Prade and F. Pfeiffer are with Technical University of Munich, Garching, Bavaria 85748 Germany.

J. Mohr is with the Institute for Microstructure Technology, Karlsruhe Institute for Technology, Karlsruhe, Baden-Würtemberg 76131 Germany.

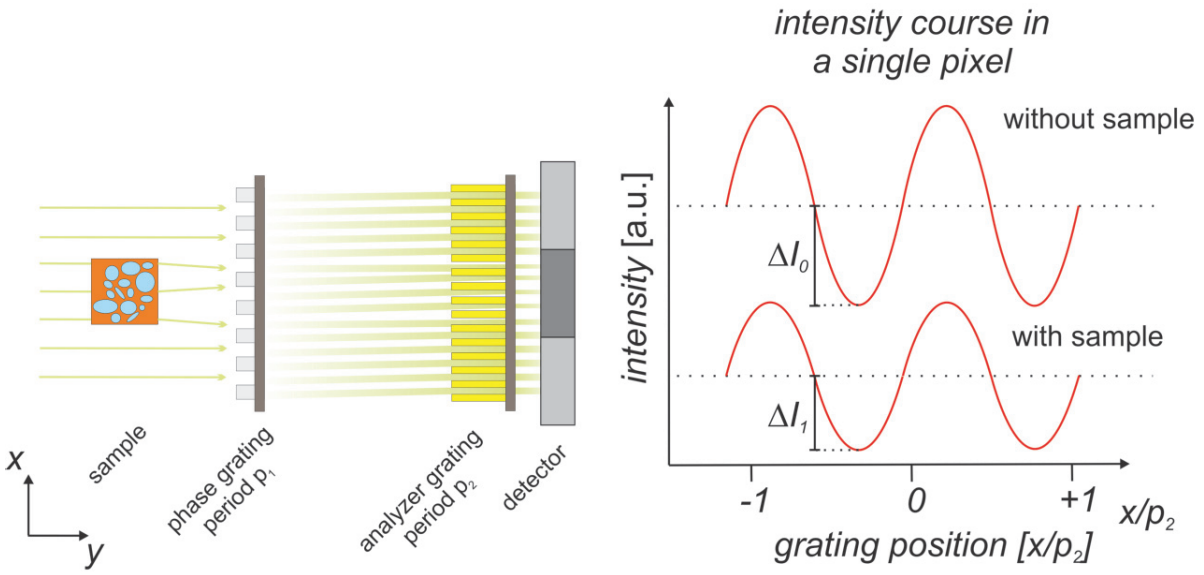

Fig. 2. Schematic of the experimental setup (*left side*) and the obtained intensity course in the highlighted pixel (*right side*). The phase grating introduces an interference pattern which is discriminated against by the analyzer grating. Hence, even small deflections of the pattern can be detected even when the resolution of the detector is not able to resolve the interference pattern itself.

Where, p_1 denotes the period of the phase grating and λ the wavelength. Placing a sample into the beam generally alters the beam propagation. Using a Talbot-Lau interferometer either combination of absorption, phase shift and small angle scattering may be analyzed. This is done by comparing measurements with and without sample and scanning the displacement of the interference pattern compared to the analyzer grating. Therefore either grating is moved in transversal direction for at least one grating period. This ensures that at each pixel the minimum and maximum intensity is detected. The intensity course in one pixel thereby describes in good approximation a cosine function (see Fig. 2). The visibility, which is a measure for the obtainable image quality in phase and dark field contrast, is defined as:

$$V = \frac{I_{\max} - I_{\min}}{I_{\max} + I_{\min}}. \qquad (2)$$

Theoretically an analyzer grating is not necessary if the detector resolution is sufficient to resolve the interference pattern.

For sufficient coherence, experiments on lab sources often require a source grating [3]. This way, several individually coherent, but mutually incoherent virtual sources are created.

A. *Grating based dark field measurements*

The dark field signal thereby corresponds to the decrease of the amplitude compared to the reference measurement. The decrease of the amplitude is caused by small angle scattering in the sample. This causes a mismatch between the interference pattern and the analyzer grating. Hence there is a decrease of the amplitude and the visibility. Furthermore the signal is isotropic, as only deviations perpendicular to the grating lamellae are detected. In turn this allows analyzing anisotropic scattering behavior of samples [4].

B. *Experimental procedure*

The experiments in this contribution were performed at the Institute of Medical Engineering at the Technische Universität Munich. A MXR-160HP/11 X-ray tube (Comet AG) at an acceleration voltage of 90 kV was used at 0.8 kW Power. The radiation was filtered by 3 mm Al before passing the interferometer.

The source grating was positioned 2 cm behind the X-ray

TABLE I
GRATING PARAMETERS

Symbol	Quantity	Value
p_0	Period of the source grating	10 µm
h_0	Height of the source grating	160-170 µm
	Duty cycle of the source grating	0,5
	Material of the source grating	Au
p_1	Period of the phase grating	5 µm
h_1	Height of the phase grating	10 µm
	Duty cycle of the phase grating	0,5
	Material of the phase grating	Ni
p_2	Period of the analyzer grating	10 µm
h_2	Height of the analyzer grating	160-170 µm
	Duty cycle of the analyzer grating	0,5
	Material of the analyzer grating	Au

Grating parameters of the Talbot-Lau interferometer. The gratings were fabricated at the Institute for Microstructure Technology at the Karlsruhe Institute for Technology. The microstructures of the gratings were on Si wafers with a thickness of 500 µm (source grating), 200 µm (phase grating) and 150 µm (analyzer grating).

tube. The distance between source and phase grating l, as well as the distance between phase and analyzer grating d were $l = d = 1.15$ m. The source and analyzer grating consisted of Au lamellae of 160-170 µm height and a period of 10 µm with a duty cycle of 0.5. The microstructures were on Si wafers of 500 µm (source grating) and 150 µm (analyzer grating) thicknesses. The phase grating consisted of lamellae made from Ni at a period of 5 µm and a height of 10 µm. The duty cycle was 0.5 and they were situated on a Si wafer of 200 µm thickness. An overview of the grating parameters is given in table 1. The mean visibility of the setup amounted to 25 % with peak values up to 38 %.

As detector, a Varian PaxScan 2520D with a CsI-scintillator and a pixel size of 127 µm was used. The samples were mounted on an Eulerian cradle at a distance of 0.89 m to the source grating. This resulted in an image magnification of 2.6.

III. Results

The obtained results of the measurements are presented in fig. 3 and fig. 4. For comparison, the signals in absorption contrast (in the upper row) and in dark field contrast (in the lower row) are given. The circular area in the images marks the field of view, which is in this case defined by the area of the analyzer grating. On the right hand side of the circular field of view, the dark field signal appears noisy. This is due to a lower visibility in that area.

The investigated samples are made of paper (b2, d1, d2, and e1), paper with shell limestone (a2) or carbon (a1, b1, b3 and f). In addition, some are grouted (e2, f) and some are otherwise patterned (a2, b2, d1, d2 and e1).

Generally, the results show an enhanced contrast in the patterned friction contact materials in comparison to the absorption measurements. For sample a2 there are also more details visible within one structure of the pattern. This specific detail however is likely to come from damage on the backside of the material.

Sample b1 in fig. 3 and sample e2 in fig. 4 show granular structures in absorption contrast that cannot be seen in dark field contrast.

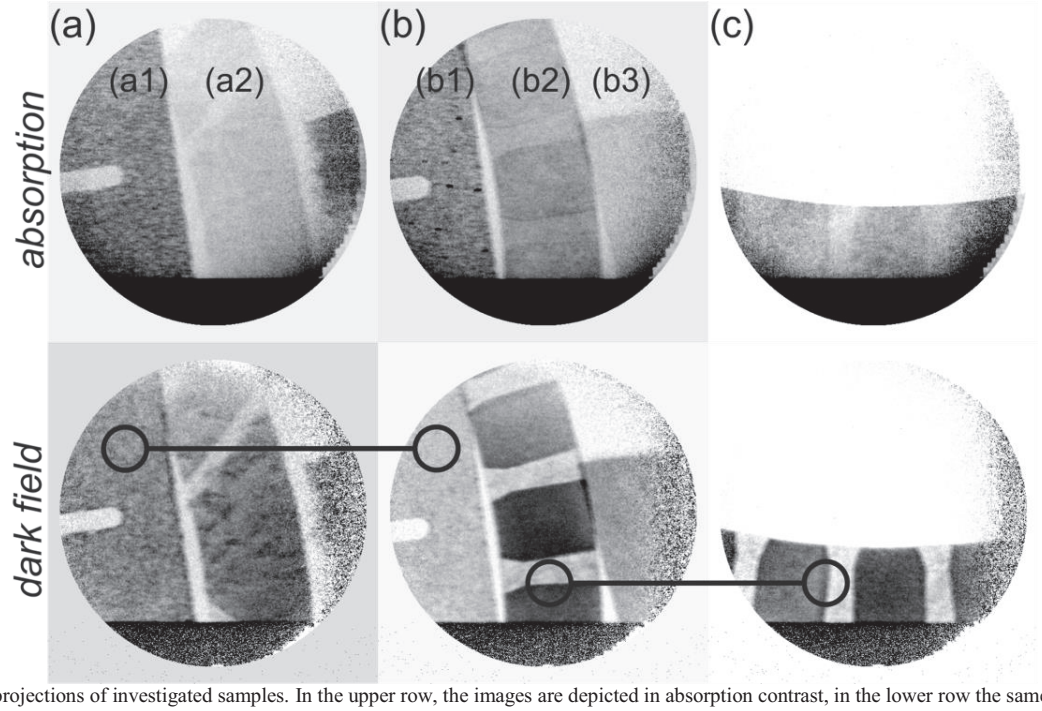

Fig. 3. X-Ray projections of investigated samples. In the upper row, the images are depicted in absorption contrast, in the lower row the same samples respectively are presented in dark field contrast.
(a1): carbon, non-grouted I (a2): paper with shell limestone
(b1): carbon, non-grouted II (b2): paper III (b3): carbon
(c): sample (b2) rotated by 90°
In comparison between dark field and absorption images obvious difference are at hand. While at sample (b1) the contrast is higher in absorption contrast, at the samples (a2) and (b2) more details are recognizable in dark field contrast. In sample (a1) and (b3) there is no significant difference between absorption and dark field contrast.
Furthermore, while (a1) and (b1) only differ in absorption contrast by some black spots in (b1), in dark field contrast the samples are different in their respective grey value. This indicates differences in their respective microstructure. Sample (b3) appears brighter than (a1) and (b1) in absorption, but is darker than (b1) in dark field contrast).
The comparison of the dark field images of (b2) and (c) shows no significant difference concerning their contrast. Since the Talbot-Lau interferometer is only sensitive for scattering perpendicular to the grating lamellae (here in horizontal direction), it can be assumed, that (b2) exhibits a scattering but anisotropic microstructure.

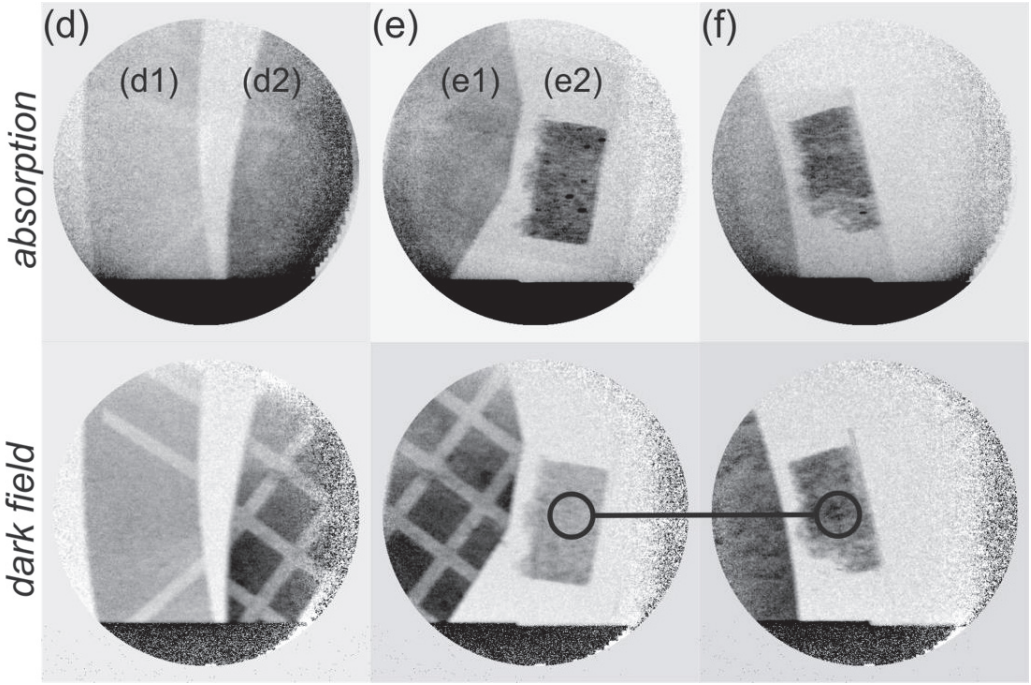

Fig. 4. X-Ray projections of investigated samples. In the upper row, the images are depicted in absorption contrast, in the lower row the same samples respectively are presented in dark field contrast.
(d1): paper I (d2): paper II
(e1) = (d2): paper II (e2): carbon, grouted I
(f): carbon, grouted II
In the same manner as above, there is a gain and a loss with the dark field images concerning the contrast. The samples (d1) and (d2) show more details in dark field contrast, whereas sample (e2) shows less. Sample (f) exhibits approximately identical degree of details.
(d1) and (d2) differ in dark field contrast; however a difference is also visible in absorption. (e2) and (f) on the other hand seem similar in absorption, but clearly differ in dark field contrast.

The samples a1, b3 and f appear with seemingly no change of contrast in the dark field images.

Anisotropic scattering could not be detected in any sample. This was studied by rotating the friction contact materials as it is demonstrated in fig. 3 with sample b2 and c. The same sample was imaged, after a rotation of 90°. However no noticeable change in contrast, except for a bit brighter area (highlighted in fig. 3 c) could be detected.

Comparing samples a1 and b1 they appear to absorb similarly. However in dark field contrast, their contrast is clearly different. This indicates to differences in their microstructure. Different pore sizes could be an explanation as well as particles of different sizes. The same can be observed with samples e2 and f: similar in absorption, but clearly different in their dark field signal.

IV. Conclusion

Generally, a gain in information could be observed when investigating friction contact materials of a lamella drive coupling non-destructively by means of X-ray dark field imaging in contrast supplementary to conventional X-ray absorption contrast CT.

It was shown, that the contrast within one sample could be significantly increased. Furthermore, other materials, that appeared similar in absorption, exhibit different properties in dark field contrast. The reason for this probably lies in a different microstructure i.e. regarding porosity or particles/fibers of different sizes/diameters. This should be clarified fairly easily using microscopy, which requires sectioning of the sample. A rather sophisticated, yet potentially fruitful task would be to try and quantitatively connect a parameter describing the microstructure (mean particle diameter / mean pore size / …) to the dark field contrast signal. In [5 and 6] a method to quantitatively interpret the dark field signal independent of the grating setups are presented, which might be the base for this endeavor.

References

[1] Yashiro, W., Terui, Y., Kawabata, K., & Momose, A. (2010). On the origin of visibility contrast in x-ray Talbot interferometry. *Optics express*, *18*(16), 16890-16901.

[2] Pfeiffer, F., Bech, M., Bunk, O., Kraft, P., Eikenberry, E. F., Brönnimann, C., ... & David, C. (2008). Hard-X-ray dark-field imaging using a grating interferometer. *Nature materials*, *7*(2), 134-137.

[3] Pfeiffer, F., Weitkamp, T., Bunk, O., & David, C. (2006). Phase retrieval and differential phase-contrast imaging with low-brilliance X-ray sources. *Nature physics*, *2*(4), 258-261.

[4] Jensen, T. H., Bech, M., Bunk, O., Donath, T., David, C., Feidenhans, R., & Pfeiffer, F. (2010). Directional x-ray dark-field imaging. *Physics in medicine and biology*, *55*(12), 3317.

[5] Strobl, M. (2013). General solution for quantitative dark-field contrast imaging with grating interferometers. *arXiv preprint arXiv:1312.0473*.

[6] Prade, F., Yaroshenko, A., Herzen, J., & Pfeiffer, F. (2016). Short-range order in mesoscale systems probed by X-ray grating interferometry. *EPL (Europhysics Letters)*, *112*(6), 68002.

Convex Temporal Regularizers in Cardiac C-arm CT

Oliver Taubmann*, Günter Lauritsch†, Gregor Krings‡, Andreas Maier*
*Pattern Recognition Lab, Friedrich-Alexander-University Erlangen-Nuremberg
and Erlangen Graduate School in Advanced Optical Technologies, Germany
†Siemens Healthcare GmbH, Forchheim, Germany
‡University Medical Center Utrecht, Netherlands

E-mail: oliver.taubmann@fau.de

***Abstract*—Dynamic cardiac imaging typically requires the use of gating. In the case of computed tomography (CT), this results in an angular undersampling that renders reconstruction difficult. Prior work has shown that incorporating information from the full scan, i. e. from all cardiac phases, can be beneficial in this regard, for instance by regularization. This paper compares three convex temporal regularizers for 4-D cardiac C-arm CT in both a numerical phantom and clinical patient data. Regularizations based on the nuclear norm, temporal total variation as well as a tight-frame wavelet transform are studied. While all of them improve reconstruction quality notably, the former turns out to be the least effective. The latter two yield comparable results at near-optimal parameterization. However, temporal total variation appears to be more forgiving w. r. t. over-regularization.**

I. Introduction

In electrocardiogram (ECG) gated CT imaging, reconstruction is impeded by missing data due to angular undersampling. Many existing approaches alleviate this problem by directly or indirectly incorporating information from the full acquisition, i. e. from all cardiac phases, when reconstructing an individual phase. For instance, a regular reconstruction from all available data, despite exhibiting motion artifacts, can serve as a prior for regularization [1], or it can be used to identify and remove the object-dependent artifact patterns [2].

In interventional cardiac C-arm CT, motion-compensated reconstruction has been employed to be able to use all projection images by correcting for non-rigid motion—estimated from intermediate reconstructions—during back-projection [3], [4]. For dynamic (4-D) imaging, i. e. reconstruction of multiple phases, it is especially helpful to make use of redundancy observed in the temporal dimension of the reconstructed images [4], [5]. In the context of iterative algebraic reconstruction techniques (ART), this can be achieved conveniently by extending regularization to the temporal domain [6]–[10].

In this work, we investigate the use of temporal regularizers for 4-D reconstruction of the left ventricle using angiographic C-arm devices. In particular, we focus on convex priors as they can readily be incorporated in most optimization methods used in tomographic reconstruction due to their convergence properties. The convergence behavior of three distinct regularizers is analyzed empirically and compared in a numerical phantom. Visual results are also presented for clinical patient data.

II. Materials and Methods

A. Gated Iterative Reconstruction

With a rectangular gating window, a subset of the available projection data is selected for each cardiac phase $t \in \{1, 2, \ldots, N_{\text{phases}}\}$ to be reconstructed. We denote the current solution in image space for each t as $\boldsymbol{I}^t$ and forego iteration indices for the sake of readability. We initialize with zeros, $\boldsymbol{I}^t = \boldsymbol{0}$, and in each iteration perform the following sequence of steps: **(i)** A simultaneous ART (SART) update step, consisting of 8 subiterations, on all $\boldsymbol{I}^t$ based on their respective data determined by ECG gating. In a subiteration, each projection image corresponds to one subset update applied simultaneously with a relaxation factor of 0.8 and subsequent enforcing of non-negativity. **(ii)** A reduction of the spatial total variation (TV) of all $\boldsymbol{I}^t$, applied with a relaxation factor of 0.5. Spatial TV minimization is carried out in analogy to the description in section II-C. **(iii)** One of three temporal regularizers described in the following sections.

A total of 30 iterations is performed. We choose this simple reconstruction scheme to focus on the effect of each temporal regularizer. For spatial regularization, TV is selected exemplarily due to its wide-spread and successful use in compressed sensing reconstruction, but it is not the primary subject of our study.

B. Temporal Rank-Reducing Regularization

The $\boldsymbol{I}^t$ are not independent. In fact, they show the same object in different states with the underlying variation governed by a small number of intrinsic components. Albeit a simplification, the assumption that few linear components may explain most of the dynamics reasonably well can serve as a global measure of consistency along the temporal domain [9]. In terms of linear algebra, this can be expressed as the rank of a matrix, i. e. the number of linearly independent rows or columns it contains. The observed rank is expected to be higher than it should ideally be due to the influence of artifacts and noise which also cause variations in the images. To mitigate this influence in our current image estimates $\boldsymbol{I} = [\boldsymbol{I}^1, \boldsymbol{I}^2, \ldots, \boldsymbol{I}^{N_{\text{phases}}}] \in \mathbb{R}^{N_{\text{voxels}} \times N_{\text{phases}}}$, arranged column-wise in a matrix, we find the solution to the proximal operator,

$$\text{prox}_{\|\|_*, \lambda_{\text{NN}}}(\boldsymbol{I}) = \underset{\boldsymbol{I}'}{\text{argmin}} \frac{1}{2} \|\boldsymbol{I} - \boldsymbol{I}'\|_{\text{F}}^2 + \lambda_{\text{NN}} \|\boldsymbol{I}'\|_*, \quad (1)$$

where $\|\boldsymbol{I}'\|_*$ denotes the nuclear norm, i. e. the sum of the singular values of $\boldsymbol{I}'$, and $\|\cdot\|_\mathrm{F}$ the Frobenius norm used to calculate the squared Euclidean distance of the images. λ_NN controls the strength of the regularization. While using the rank function itself would result in an NP-hard reconstruction problem, the nuclear norm as its best convex approximation over the unit ball of matrices yields a proximal operator with an analytical solution that consists in a soft-thresholding of the singular values [11],

$$\boldsymbol{I} \leftarrow \boldsymbol{U}(\boldsymbol{\Sigma} - \mathbf{1}\cdot\lambda_\mathrm{NN})_+\boldsymbol{V}^\top, \tag{2}$$

where $\boldsymbol{U}\boldsymbol{\Sigma}\boldsymbol{V}^\top$ is the singular value decomposition (SVD) of $\boldsymbol{I}$, $(\cdot)_+$ the element-wise computation of $\max(\cdot, 0)$, and $\mathbf{1}$ the identity matrix the size of $\boldsymbol{\Sigma}$. Regarding memory efficiency, note that with $N_\mathrm{phases} \ll N_\mathrm{voxels}$, the required dimensions of the involved matrices reduce to $N_\mathrm{voxels} \times N_\mathrm{phases}$ for $\boldsymbol{U}$, and $N_\mathrm{phases} \times N_\mathrm{phases}$ for $\boldsymbol{\Sigma}$ and $\boldsymbol{V}^\top$.

C. Temporal Total Variation Regularization

In contrast, temporal total variation (tTV) [6]–[8] is a more local measure of consistency. Similar to the well-known spatial TV approach, it is based on the idealization that medical images are "cartoons" exhibiting large homogeneous regions for, e. g., certain tissue types, separated by sharp edges at organ boundaries. Considering such a model and disregarding the effects of limited resolution, in the case of motion, the gray values of affected voxels should "jump" when an edge is displaced across them, i. e. instantly change the organ they are affiliated with, and stay constant otherwise. More precisely, while traditional TV postulates sparsity in the domain of the spatial image gradient, the sparsifying transform used for tTV is the temporal gradient, estimated by forward differences,

$$\mathcal{D}_t\boldsymbol{I} = [\boldsymbol{I}^2 - \boldsymbol{I}^1, \boldsymbol{I}^3 - \boldsymbol{I}^2, \ldots, \boldsymbol{I}^1 - \boldsymbol{I}^{N_\mathrm{phases}}]. \tag{3}$$

We minimize the tTV norm of the current image estimates by iteratively descending along its negative gradient with respect to the image voxels,

$$-\frac{\partial}{\partial \boldsymbol{I}}\|\boldsymbol{I}\|_\mathrm{tTV} = -\frac{\partial}{\partial \boldsymbol{I}}\|\operatorname{vec}(\mathcal{D}_t\boldsymbol{I})\|_1, \tag{4}$$

using a backtracking line search to find a suitable step length. $\operatorname{vec}(\boldsymbol{I}) = [\boldsymbol{I}^{1\top}, \ldots, \boldsymbol{I}^{N_\mathrm{phases}\top}]^\top$ is a vectorization operator. The non-differentiability of $|x|$ at the origin is avoided by "corner rounding," i. e. its derivative is approximated as $\frac{x}{|x|+\varepsilon}$, with $\varepsilon = 10^{-4}$. After a fixed number of gradient descent iterations is performed (10 in our experiments), the resulting tTV-reduced volumes $\boldsymbol{I}_\mathrm{tTV}$ are used to update the current images, $\boldsymbol{I} \leftarrow \boldsymbol{I} + \lambda_\mathrm{tTV}(\boldsymbol{I}_\mathrm{tTV} - \boldsymbol{I})$, with the relaxation factor λ_tTV controlling the regularizer strength. The convexity of the L^1-norm guarantees that after a convex combination ($0 < \lambda_\mathrm{tTV} < 1$) with $\boldsymbol{I}_\mathrm{tTV}$, $\boldsymbol{I}$ will be smaller in terms of the tTV norm than before [12]. Note that, in analogy to the relationship between the nuclear norm and the rank operator, in a d-dimensional space, L^1 is the convex envelope of the L^0-quasi-norm on $[-1, 1]^d$ [13]. While L^0 is a better measure of sparsity, its use would again render the overall reconstruction problem NP-hard.

D. Temporal Tight-Frame Regularization

Another common choice are sparsifying transforms based on wavelet decompositions, a big advantage of which is their invertibility. Tight frames (TF) are redundant wavelet systems popular in image restoration problems as they provide very sparse representations of piecewise smooth functions [10], [14], [15]. We use the piecewise linear TF basis,

$$\boldsymbol{h}_0 = \frac{1}{4}[1, 2, 1],\ \boldsymbol{h}_1 = \frac{\sqrt{2}}{4}[1, 0, -1],\ \boldsymbol{h}_2 = \frac{1}{4}[-1, 2, -1], \tag{5}$$

where $\boldsymbol{h}_0$ is a low-pass kernel while $\boldsymbol{h}_1$ and $\boldsymbol{h}_2$ correspond to first and second order difference operators, respectively [10]. By component-wise convolution along the temporal dimension t with periodic boundary conditions, denoted by $*_t$, we compute coefficient images $\boldsymbol{C} = \{\boldsymbol{C}_i : \boldsymbol{C}_i = \boldsymbol{h}_i *_t \boldsymbol{I}\}$. If $\boldsymbol{W}$ is the operator performing this decomposition, $\boldsymbol{C} = \boldsymbol{W}\boldsymbol{I}$, its adjoint is $\boldsymbol{W}^T = \boldsymbol{W}^{-1}$, where $\boldsymbol{W}^\top\boldsymbol{C} = \sum_{i=0}^2 \boldsymbol{h}_i \star_t \boldsymbol{C}_i = \boldsymbol{I}$ and $\star_t$ denotes correlation in analogy to $*_t$. Sparsity is enhanced by reducing the summed up high-pass component energies [10], $\|\boldsymbol{C}\|_\mathrm{TF} = \|\operatorname{vec}(\sum_{i=1}^2(\boldsymbol{C}_i)^2)^{\frac{1}{2}}\|_1$, where $(\cdot)^2$ and $(\cdot)^{\frac{1}{2}}$ are to be understood element-wise. To this end, we find,

$$\operatorname{prox}_{\|\|_\mathrm{TF},\lambda_\mathrm{TF}}(\boldsymbol{C}) = \operatorname*{argmin}_{\boldsymbol{C}'} \sum_{i=0}^{2} \frac{1}{2}\|\boldsymbol{C}'_i - \boldsymbol{C}_i\|_\mathrm{F}^2 + \lambda_\mathrm{TF}\|\boldsymbol{C}'\|_\mathrm{TF}, \tag{6}$$

which is used in the update step, $\boldsymbol{I} \leftarrow \boldsymbol{W}^\top \operatorname{prox}_{\|\|_\mathrm{TF},\lambda_\mathrm{TF}}(\boldsymbol{W}\boldsymbol{I})$, and realized by element-wise vector shrinkage [14],

$$\boldsymbol{C}^t_{i,j} \leftarrow \begin{cases} \boldsymbol{C}^t_{i,j} & \text{if } i = 0, \\ \boldsymbol{C}^t_{i,j} \cdot \left(1 - \lambda_\mathrm{TF}\cdot(\sum_{i=1}^2(\boldsymbol{C}_{i,j})^2)^{-\frac{1}{2}}\right)_+ & \text{else,} \end{cases} \tag{7}$$

with $\boldsymbol{C}^t_{i,j}$ the j-th element of coefficient image $\boldsymbol{C}^t_i$ and λ_TF the regularization parameter.

III. Experiments

A. Data

For evaluation, a numerical phantom data set was used [16]. Projection images were generated [17] using a polychromatic spectrum, discretized in energy bins 5 keV wide from 10 keV to 90 keV (peak energy), and a time-current product of 2.5 mAs per X-ray pulse. For bones and bone marrow, material properties match the mass attenuation coefficients found in the NIST X-ray table[1]. Contrasted blood in the left ventricle and aorta was simulated as iodine-based contrast agent (Ultravist-150, Bayer AG, Leverkusen, Germany) mixed with equal parts water. All other structures were modeled with the absorption behavior of water for modified densities. The acquisition protocol is identical to that of the clinical data sets described below. Additionally, a set of projection images with complete angular sampling for the end-diastolic phase (static phantom) was generated to reconstruct a ground truth image using SART with spatial TV regularization (relaxation factor 1.0) as described above. A heart rate of 120 bpm was simulated, resulting in 10 observed heartbeats.

[1] http://physics.nist.gov/PhysRefData/Xcom/html/xcom1.html

A clinical patient data set was acquired with an Artis zee biplane (Siemens Healthcare GmbH, Forchheim, Germany). 133 projection images were captured at approx. 30 Hz with an angular increment of 1.5° during one 5 s long rotation of the C-arm. The isotropic pixel resolution was 0.31 mm/pixel (0.21 in isocenter), the detector size 960×960 pixels. The heart was paced through external stimulation to 140 bpm, resulting in 13 heartbeats. The gating windows cover 12.5 % of the heart cycle each and use all data without overlap, such that $N_{\text{phases}} = 8$. Contrast agent was administered in the left ventricle (42 ml, undiluted) and right atrium (50 ml, 60 % dilution). All images were reconstructed on a grid of 256^3 voxels covering a volume of $(25.6\,\text{cm})^3$.

B. Evaluation

For the phantom study, the root mean square error (RMSE) to the ground truth is calculated over a region of interest (ROI) tightly enclosing the heart to assess convergence. In order to study the sensitivity of the results w. r. t. regularizer strength, a 1-D grid search is conducted for each $\lambda_\diamond$, $\diamond \in \{\text{NN, tTV, TF}\}$, such that we obtain sets of parameter values covering an "interesting" range, i. e. near-optimal as well as under- and over-regularized settings. Visual results are shown for both the phantom and the clinical data set.

IV. Results

Figs. 1 and 3 show reconstructed image slices of the phantom and the clinical data set, respectively, while the plots in Fig. 2 summarize the quantitative results of the phantom study. While both TF and tTV achieve similar RMSE values at the optimum, the "valley" of the TF curve is much more pronounced (Fig. 2), indicating that it is more sensitive to the choice of $\lambda_\diamond$. This is reflected by the strongly regularized result being blurred in the case of TF (Fig. 1f), but not tTV (Fig. 1d). At near-optimal parameterization, both yield visually comparable images (Figs. 1e and 1c). This also holds for the clinical case when using the same $\lambda_\diamond$ (Figs. 3c and 3b). Rank-based regularization does not achieve quite as low RMSE values and introduces a blur even for the optimal parameter value (Figs. 1a and 3a). All tested settings of temporal regularization outperform spatial TV alone ($\lambda_\diamond = 0$ in Fig. 2, Figs. 1h and 3d). Universally, convergence is faster in the first iterations for a higher $\lambda_\diamond$, but then levels out earlier.

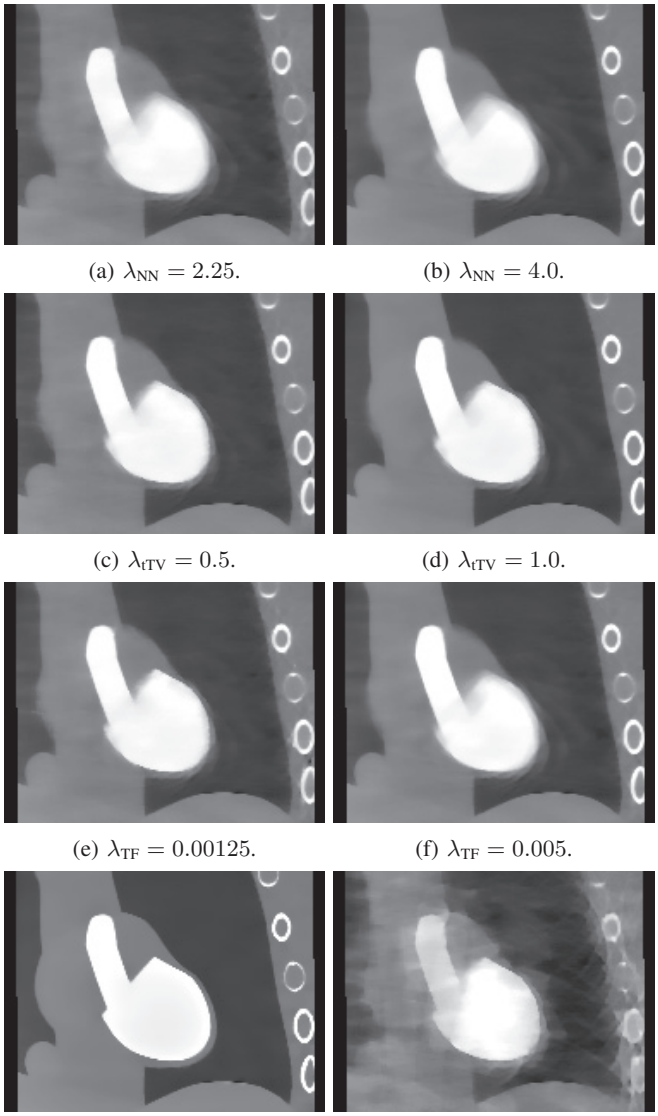

(a) $\lambda_{\text{NN}} = 2.25$. (b) $\lambda_{\text{NN}} = 4.0$.

(c) $\lambda_{\text{tTV}} = 0.5$. (d) $\lambda_{\text{tTV}} = 1.0$.

(e) $\lambda_{\text{TF}} = 0.00125$. (f) $\lambda_{\text{TF}} = 0.005$.

(g) Ground truth reconstruction. (h) No temporal regularization.

Fig. 1: Reconstructed images of the phantom data set in end-diastole. The best results in terms of RMSE achieved for each regularizer are shown on the left (a, c, e), strongly regularized results on the right (b, d, f). Ground truth reconstructed from static data (g) and an image obtained without temporal regularization (h) are shown for comparison. All images are displayed with the same window at $[\text{center}, \text{width}] = [300, 2600]$ HU.

V. Discussion and Conclusion

The difficulty of the reconstruction problem is illustrated well by the poor performance of the variant without temporal regularization; with about 10-13 distinct views available per phase, it features a degree of undersampling that is extremely challenging even in the context of compressed sensing.

Although tTV lacks a simple closed-form solution of its proximal operator, requiring optimization based on, e. g., iterative descent or primal-dual splitting algorithms [13], its comparatively forgiving nature w. r. t. parameterization renders it highly useful. When this property is not critical, TF regularization is a viable alternative due to its straight-forward implementation. It should be noted that TV as a spatial regularizer could put tTV at an advantage due to synergy effects, so it may be worthwhile to test combinations with other spatial regularizers as well. While the results demonstrate that rank-reduction is inferior to the other methods on its own, it could be investigated whether its global approach, which is capable of suppressing local outliers, might complement other regularizers well at early stages of the optimization when used in combination.

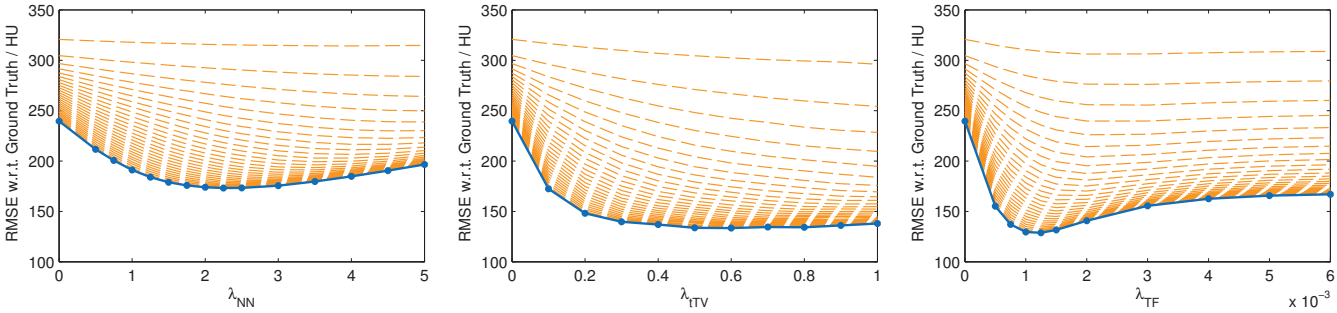

Fig. 2: RMSE for reconstructed images of the phantom data set over a range of parameter values around the optimum for each regularizer. While the solid line is the result after 30 iterations, the dotted lines correspond to previous iterations, visualizing the varying speeds of convergence.

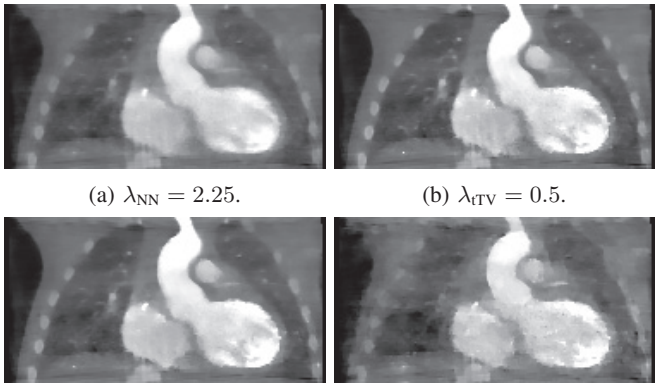

(a) $\lambda_{\mathrm{NN}} = 2.25$. (b) $\lambda_{\mathrm{tTV}} = 0.5$.

(c) $\lambda_{\mathrm{TF}} = 0.00125$. (d) No temporal regularization.

Fig. 3: Reconstructed images of the clinical data set in end-diastole. The best parameterization determined in the phantom study was used for each regularizer (a, b, c). An image obtained without temporal regularization (d) is shown for comparison. All images are displayed with the same window at $[\mathrm{center}, \mathrm{width}] = [630, 3260]$ HU.

Similar results obtained in both the phantom and a clinical case using identical parameterization are reassuring w. r. t. generalizability and applicability, although further experiments are advised for validation. Nonetheless, we can conclude that exploiting redundancy in the temporal domain through regularization is a highly valuable tool for improving image quality of 4-D cardiac C-arm CT.

Disclaimer

The concepts and information presented in this paper are based on research and are not commercially available.

References

[1] G.-H. Chen, J. Tang, and S. Leng, "Prior image constrained compressed sensing (PICCS): a method to accurately reconstruct dynamic CT images from highly undersampled projection data sets," *Med. Phys.*, vol. 35, no. 2, pp. 660–663, 2008.

[2] G. C. Mc Kinnon and R. Bates, "Towards imaging the beating heart usefully with a conventional CT scanner," *IEEE Trans. Biomed. Eng.*, vol. BME-28, no. 2, pp. 123–127, 1981.

[3] K. Müller, A. Maier, C. Schwemmer, G. Lauritsch, S. D. Buck, J.-Y. Wielandts, J. Hornegger, and R. Fahrig, "Image artefact propagation in motion estimation and reconstruction in interventional cardiac C-arm CT," *Phys. Med. Biol.*, vol. 59, no. 12, pp. 3121–3138, 2014.

[4] O. Taubmann, A. Maier, J. Hornegger, G. Lauritsch, and R. Fahrig, "Coping with Real World Data: Artifact Reduction and Denoising for Motion-Compensated Cardiac C-arm CT," *Med. Phys.*, vol. 43, no. 2, pp. 883–893, 2016.

[5] O. Taubmann, G. Lauritsch, A. Maier, R. Fahrig, and J. Hornegger, "Estimate, Compensate, Iterate: Joint Motion Estimation and Compensation in 4-D Cardiac C-arm Computed Tomography," in *MICCAI*, 2015, pp. 579–586.

[6] H. Wu, A. Maier, R. Fahrig, and J. Hornegger, "Spatial-temporal Total Variation Regularization (STTVR) for 4D-CT Reconstruction," in *SPIE Med. Imag.*, 2012, p. 83133J.

[7] C. Mory, V. Auvray, B. Zhang, M. Grass, D. Schäfer, S. Chen, J. Carroll, S. Rit, F. Peyrin, P. Douek, and L. Boussel, "Cardiac C-arm computed tomography using a 3D + time ROI reconstruction method with spatial and temporal regularization," *Med. Phys.*, vol. 41, p. 021903, 2014.

[8] V. Haase, O. Taubmann, Y. Huang, G. Krings, G. Lauritsch, A. Maier, and A. Mertins, "Make the Most of Time: Temporal Extension of the iTV Algorithm for 4-D Cardiac C-Arm CT," in *Bildverarbeitung für die Medizin*, 2016, pp. 170–175.

[9] J.-F. Cai, X. Jia, H. Gao, S. B. Jiang, Z. Shen, and H. Zhao, "Cine cone beam CT reconstruction using low-rank matrix factorization: algorithm and a proof-of-principle study," *IEEE Trans. Med. Imag.*, vol. 33, no. 8, pp. 1581–1591, 2014.

[10] J.-F. Cai, B. Dong, S. Osher, and Z. Shen, "Image restorations: total variation, wavelet frames and beyond," *J. Am. Math. Soc.*, vol. 25, pp. 1033–1089, 2012.

[11] K.-C. Toh and S. Yun, "An accelerated proximal gradient algorithm for nuclear norm regularized linear least squares problems," *Pac. J. Optim.*, vol. 6, no. 3, pp. 615–640, 2010.

[12] L. Ritschl, F. Bergner, C. Fleischmann, and M. Kachelrieß, "Improved total variation-based CT image reconstruction applied to clinical data," *Phys. Med. Biol.*, vol. 56, no. 6, p. 1545, 2011.

[13] S. Boyd and L. Vandenberghe, *Convex Optimization*. Cambridge University Press, 2004.

[14] X. Jia, B. Dong, Y. Lou, and S. B. Jiang, "GPU-based iterative cone-beam CT reconstruction using tight frame regularization," *Phys. Med. Biol.*, vol. 56, no. 13, p. 3787, 2011.

[15] M. Manhart, A. Fieselmann, and Y. Deuerling-Zheng, "Evaluation of a Tight Frame Reconstruction Algorithm for Perfusion C-arm CT Using a Realistic Dynamic Brain Phantom," in *CT Meeting*, 2012, pp. 123–126.

[16] W. P. Segars, G. Sturgeon, S. Mendonca, J. Grimes, and B. M. W. Tsui, "4D XCAT phantom for multimodality imaging research," *Med. Phys.*, vol. 37, pp. 4902–4915, 2010.

[17] A. Maier, H. Hofmann, C. Schwemmer, J. Hornegger, A. Keil, and R. Fahrig, "Fast Simulation of X-ray Projections of Spline-based Surfaces using an Append Buffer," *Phys. Med. Biol.*, vol. 57, no. 19, pp. 6193–6210, 2012.

Motion Estimation Using a Penalized Image Sharpness Criterion for Resolution Recovery in Extremities Cone-Beam CT

Alejandro Sisniega, J. Webster Stayman, Qian Cao, John Yorkston, Jeffrey H. Siewerdsen, Wojciech Zbijewski

***Abstract*— Recent advances in imaging hardware, such as the development of CMOS x-ray detectors, have the potential to enhance spatial resolution of cone-beam CT (CBCT) systems to a level consistent with quantitative imaging of bone microarchitecture (~100 μm detail size). This capability would be of particular value in dedicated extremities CBCT. The accuracy in such applications will be diminished by subtle, sub-mm patient motion that cannot be managed with immobilization.**

We propose an image-based motion compensation method for high-resolution extremities CBCT that requires no fiducials or external trackers. The algorithm allows for the compensation to be applied only within a Region of Interest (RoI), so that the motion can be assumed to be locally rigid. Motion estimation is achieved by optimizing a cost-function that contains an autofocus term that favors sharp images and a penalty term that penalizes non-smooth motion. The non-convex optimization problem is solved using the CMA-ES algorithm. Following evaluation of several image sharpness metrics for application in extremities motion estimation, the variance of image gradient was chosen as the autofocus term. The effects of other parameters of the objective function (e.g. regularization strength) were evaluated in simulation studies of a hand phantom with synthetic motion patterns of variable amplitude (0.25-10 mm). Small motion amplitudes benefited from strong regularization, whereas weaker regularization was preferred for large motions.

Excellent motion compensation was obtained in the simulated data. After compensation, the structural similarity index (SSIM) computed against a static reference volume was > 0.95 for motions up to 1 mm and >0.8 for larger motions. An 80% increase in SSIM compared to uncompensated image was found for the largest motion (10 mm). Real data of a wrist phantom acquired on a CMOS testbench with 0.5 – 10 mm amplitude object motion confirmed improved visualization of the trabeculae and increased SSIM after motion compensation. The method was applied to motion contaminated patient data from the dedicated extremities CBCT, yielding visible reduction of motion artifacts.

The proposed image-based motion compensation provides robust correction of RoI motion in extremities imaging by using a simple, locally rigid motion model coupled with a penalized image sharpness criterion.

***Index Terms*—High-resolution CBCT, motion compensation, extremities imaging, autofocus.**

I. Introduction

Quantitative metrics of bone microarchitecture have been extensively studied in pre-clinical micro-CT imaging and found to provide a sensitive biomarker with potential applications in early detection and staging of osteoarthritis and osteoporosis [1]. Clinical implementation of such metrics is challenged by the relatively small size of the pertinent bone features (e.g. ~100 μm for trabeculae). Encouraging initial results in in-vivo assessment of bone microarchitecture were obtained with dedicated Flat-Panel Detector (FPD) extremities CBCT (Fig. 1A) owing to the high spatial resolution of FPDs [2]. Further improvements in spatial resolution are necessary to establish extremities CBCT as a platform for clinical evaluation of bone morphology. This will involve improvement in hardware, in particular implementation of a CMOS detector, and algorithmic developments, including compensation of patient motion.

The CMOS technology offers smaller pixel size, higher readout speed, and reduced electronic noise compared to FPDs. Fig. 1B shows an experimental testbench emulating the extremities CBCT system and equipped with a CMOS detector with 100 μm pixel pitch. Point Spread Function measurements showed >20% improvement in FWHM with CMOS-based CBCT compared to the current FPD-based CBCT (194 μm pixel pitch).

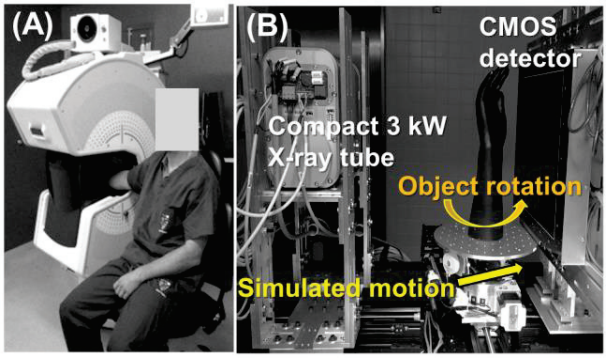

Figure 1. (A) FPD-based extremities CBCT. The system will be upgraded to a CMOS detector to enhance spatial resolution and enable in-vivo quantitative imaging of bone microarchitecture. In addition to the improved hardware, compensation of small, involuntary patient motion will be essential for achieving the required spatial resolution. (B) Experimental testbench implementing the CMOS detector in the geometric configuration of the extremities CBCT. An additional horizontal translation stage is included to enable simulated sample motion.

The application of a CMOS detector is a significant step toward reliable visualization of bone detail. However, even slight, sub-mm patient motion will challenge the accuracy of quantitative assessment of bone microarchitecture. For such small motions, patient immobilization (typically adequate for current applications of extremities CBCT) is not sufficient, and robust motion compensation will be necessary.

This work was supported by NIH Grant R01- EB018896.

A. Sisniega, J. W. Stayman, Q. Cao, J. H. Siewerdsen and W. Zbijewski are with the Department of Biomedical Engineering, Johns Hopkins University, Baltimore, MD, USA.

J. Yorkston is with Carestream Health, Rochester, NY, USA.

Email: wzbijewski@jhu.edu

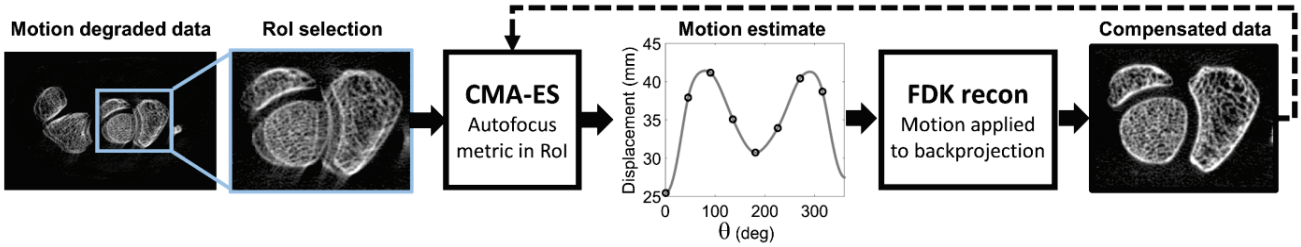

Figure 2. Workflow of the motion compensation. The compensation is applied locally to a RoI where the motion can be assumed rigid. The motion trajectory is represented using a b-spline model and estimated by CMA-ES optimization of a non-convex cost function that maximizes image sharpness.

We propose a motion compensation strategy for extremities CBCT based on the "autofocus" concept, in which the motion trajectory is estimated by maximizing a metric of image sharpness. Variations of autofocus techniques have been previously employed for misalignment compensation in CBCT [3, 4] and in the context of motion compensation for cardiac CT [5] and head CBCT [6]. Compared to approaches based on fiducial markers [7, 8] or external trackers [9], the proposed method does not require changes in the imaging workflow. Moreover, since the autofocus approach is purely image-based, the motion compensation can be restricted to a specific region of interest (RoI) (in contrast to algorithms relying on 3D-2D registration [10]). In application to bone microarchitecture, the RoIs will often consist predominately of bone voxels. This supports the assumption that the local motion is rigid, greatly simplifying the motion estimation compared to the complex and deformable motion of the whole extremity.

We introduce a new form of the autofocus objective that employs a novel regularization term penalizing large object displacements, and uses a spline-based model of rigid motion. The performance of a variety of image sharpness metrics in extremity motion estimation is investigated. The proposed autofocus objective is non-convex and exhibits local minima. A statistical optimization method is thus applied for motion estimation (compared to the more common choice of a simplex algorithm) and a restart strategy is introduced to homogenize performance across a wide range of motion amplitudes. The method is evaluated with simulated and experimental data. Application to patient data from current clinical CBCT prototype is presented.

II. Motion Compensation Framework

A flowchart of the algorithm is shown in Fig 2. An initial, motion-contaminated reconstruction is obtained and the RoI to be compensated is selected. It is assumed that the motion of the RoI is rigid, even if the extremity as a whole undergoes a more complex transformation. The motion trajectory T consists of a 6 DoF rigid transformation of the RoI at each projection angle θ. Each DoF is represented as a cubic b-spline (B):

$$T(\theta, j) = \sum_{i=0}^{N} c_{ij} B(\theta - \theta_i) \qquad (1)$$

where j enumerates the DoF (j = 1,…,6) and N is the number of spline knots. The motion trajectory of the RoI is estimated by finding the b-spline coefficients c_{ij} through maximization of the following objective function:

$$\hat{T} = \arg\min_T S(T, \mu) - \beta R(T) \qquad (2)$$

where μ is the reconstructed RoI, and $S(T,\mu)$ is an image sharpness metric. In each iteration, S is computed on a volume obtained from a reconstruction for which the current motion estimate T was applied during the backprojection. $R(T)$ is a penalty (regularization) term encouraging smooth motion trajectories, and β is a scalar penalty strength. The regularization penalizes the first order difference of the positions of the RoI in subsequent projections:

$$R(T) = \sum_{k=1}^{8} \sum_{q=2}^{N_\theta} \sqrt{(x_{k,q}(T) - x_{k,q-1}(T))^2 + (y_{k,q}(T) - y_{k,q-1}(T))^2 + (z_{k,q}(T) - z_{k,q-1}(T))^2} \qquad (3)$$

where x_{kq}, y_{kq}, and z_{kq} are the coordinates of the k-th corner of the RoI in projection q.

The optimization in Eq. 2 is not convex and exhibits multiple minima that challenge conventional gradient-based methods. Instead, the minimization was performed with the Covariance Matrix Adaptation Evolution Strategy (CMA-ES) [10]. At each iteration, a population of 20 RoI volumes was generated in parallel for a set of candidate motion trajectories using a GPU implementation of Feldkamp (FDK) reconstruction. Failure to converge or residual motion after a fixed number of iterations was handled by restart of the CMA-ES iterations with increased size of the solution space to be explored (σ) [11].

Several image sharpness metrics have been proposed for autofocus compensation of motion and geometric misalignment. In the latter context, entropy and gradient based metrics were shown to be the most appropriate [12]. Here, four metrics were evaluated for the task of extremity motion correction: (i) image variance, previously used in microscopy autofocus applications [13], and given by $Var(T,\mu) = -\sum_j (\mu_j - \bar{\mu})^2$, where $\bar{\mu}$ is the average attenuation value in the volume; (ii) Entropy $E(T,\mu) = \sum_l h_l(\mu) \cdot \log h_l(\mu)$, where h_l is an intensity histogram with 256 bins; (ii) the (negative) squared spatial gradient [3] $G(T,\mu) = -\sum_j \nabla_x(\mu_j)^2 + \nabla_y(\mu_j)^2 + \nabla_z(\mu_j)^2$; and (iv) the (negative) gradient variance $V(T,\mu) = -Var\left(\sqrt{\nabla_x(\mu_j)^2 + \nabla_y(\mu_j)^2 + \nabla_z(\mu_j)^2}\right)$.

The performance of the metrics was evaluated in a population of motion-contaminated bone images obtained by simulating 3000 random motion trajectories over a 0-50 mm range of average motion amplitudes (where the average amplitude is equivalent to mean displacement in each motion trajectory).

III. Experimental Evaluation

The evaluation used data acquired on a CMOS-based x-ray testbench (Fig. 1B). The system geometry emulated the extremities CBCT prototype. The CMOS detector was a Dalsa

Xineos 3030 (Eindhoven, NL) with a pixel size of 0.1 mm and 600 μm-thick CsI columnar scintillator. A 3kW, small focal spot (0.3 FS), rotating anode x-ray source (IMD RTM 37, Italy) was operated at 90 kV (+0.2 mm Cu), and 0.12 mAs per projection; 720 projections were acquired over 360°. The bench included a linear translation stage that was synchronized with the rotation stage to simulate patient motion. Reconstruction voxel size was 0.075 mm for image evaluation and 0.5 mm for motion estimation; FDK algorithm with Hann apodization and cutoff at the Nyquist frequency was used.

A simulation study was performed to explore the performance of motion compensation as a function of number of spline knots N and regularization strength β. A cadaveric wrist was imaged on the testbench and reconstructed to obtain a static image. Motion contaminated projections were simulated by applying a projection-wise rigid transformation to the volume followed by a forward projection. Simulated motion trajectories involved translations in the transaxial (x-y) plane with amplitudes ranging from 0.25 mm to 10.0 mm. Each translation was performed as linear motion that began at 90° gantry rotation and finished at 150° gantry rotation. Motion was modelled with spline interpolation with 360 control points to obtain smooth trajectories. Motion compensation involved a maximum of 4000 iterations of CMA-ES applied to a 200x200x20 voxels RoI including 3 carpal bones (see Fig. 5). The optimization was considered converged for changes in the cost function smaller than 10^{-4}. A restart with 4-fold increase in σ was performed for cases for which convergence was not achieved. Maximum runtime was ~30 min if convergence was not reached earlier.

Experimental evaluation involved an anthropomorphic hand phantom acquired on the testbench with motion implemented as a lateral translation of the linear stage with a slope of 1 mm per degree of rotation. A static volume (no motion) and scans with 0.5, 1.0 and 10 mm amplitude motions were acquired

The performance of motion compensation in the simulation and experimental studies was quantified using the structural similarity index (SSIM), with the static image as reference [14]:

$$SSIM = \frac{(2\bar{\mu}_{ref}\bar{\mu}_{MC} + c_1)(2\sigma_{ref-MC} + c_2)}{(\bar{\mu}_{ref}^2 + \bar{\mu}_{MC}^2 + c_1)(\sigma_{ref}^2 + \sigma_{MC}^2 + c_2)} \quad (4)$$

where $\bar{\mu}_j$ is the average attenuation and σ_j is the variance of the attenuation values in image j. The index *ref* denotes the reference static image, *MC* denotes the motion compensated image, and $\sigma_{ref\text{-}MC}$ is the covariance between the two images. The regularization terms c_1 (= 10^{-4}) and c_2 (= $3\text{x}10^{-4}$) stabilize the measurement in regions of very low attenuation. The method was also applied to a motion contaminated patient knee scan obtained on the current generation FPD-based extremities CBCT.

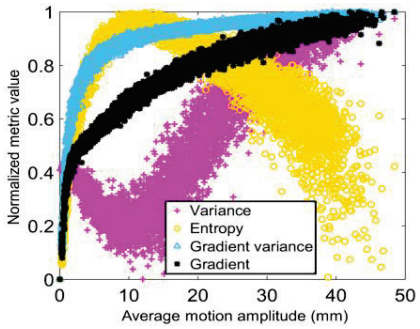

Figure 3. Normalized autofocus sharpness metrics as a function of average motion amplitude for an ensemble of fifty random realizations of motion. Gradient based metrics showed a lower number of local minima and monotonic increase with motion.

IV. Results

The normalized value of the various image sharpness metrics is shown as a function of average motion amplitude in Fig. 3 (the metrics were normalized by subtracting their minimum value and dividing by maximum value so that 0 represents a perfectly focused image).An ideal sharpness metric for motion estimation should monotonically decrease towards a global minimum corresponding to a static image. At a fixed motion amplitude, narrower dispersion of the metric is preferred, as it indicates weaker local minima (the metric is consistent across motions with the same average displacement but different trajectories). Image variance is not monotonic, showing a strong local minimum at ~10 mm amplitude. Entropy is monotonically increasing for motion amplitudes of up to 10 mm, but decreases with increasing motion at larger amplitudes. This reflects the fact that images with significant motion blur are relatively uniform and thus exhibit small entropy. While successful motion compensation has been shown with entropy-based metrics [4], this particular objective may thus not be well suited for large motions. Both gradient-based metrics are monotonically increasing throughout the investigated range of motions. Gradient variance exhibits lower dispersion and was chosen for the studies presented here.

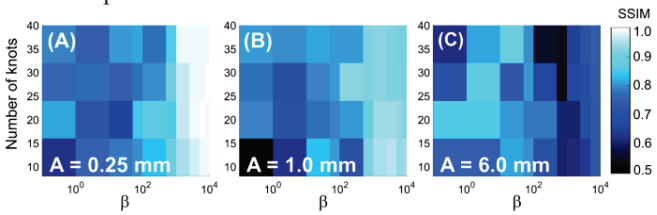

Figure 4. SSIM as a function of number of knots in the b-spline motion model (N) and regularization strength (β) for small (A), moderate (B) and large (C) motions.

Fig. 4 shows the performance of motion compensation as a function of regularization strength β and number of knots in the motion model N. Only CMA-ES runs with no restart were included in this investigation. Strong regularization is preferred for small motion amplitudes, achieving almost perfect correspondence with the reference image (SSIM > 0.9). As motion amplitude increases, the value of β yielding maximum SSIM decreases. Optimal β for 6 mm motion is 10^2-10^3x smaller than that for sub-mm motion. This is likely because large β encourages solutions that smooth out the large motions. The trend in the number of knots is weaker, with a combination of a low number of knots and small β yielding sub-optimal performance, which may involve solutions with oscillatory b-spline motion patterns. For the 6 mm motion, combination of a large number of knots with moderate β (~10^3) resulted in slow convergence (not reached within the 4000 CMA-ES iterations), indicating the need for a restart. Fig. 5 shows a selection of image results from the simulation study in Fig 4. Motion-compensated images corresponding to parameters of the objective function yielding maximum SSIM are compared to uncompensated reconstructions and the reference static volume for 0.5 mm and 10 mm motion. Significant reduction in motion-induced artifacts and recovery of trabecular detail are achieved for both small and large motions. The plot of maximum SSIM (obtained at "optimal" values of β and N) as a function of motion amplitude shows almost perfect structure recovery (SSIM > 0.95) for

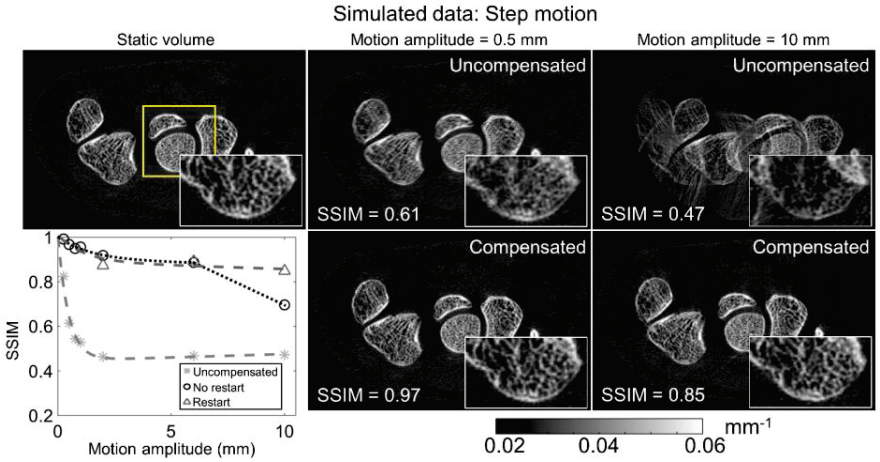

Figure 5. Motion compensation in simulated data for small (0.5 mm) and large (10 mm) motion amplitudes using optimization parameters yielding best SSIM for a given motion amplitude. The performance of the method improves for smaller motion amplitudes, but recovery of the trabecular structure and significant reduction of artifacts is apparent in both cases. This is quantified by the plot of SSIM (computed against the reference static volume) as a function of motion amplitude. Compensation using CMA-ES without restart (circles) is compared to that with restart (triangles), showing the benefits of restart for cases with large motion amplitudes (>5 mm). The square in the static image marks the RoI used for motion estimation.

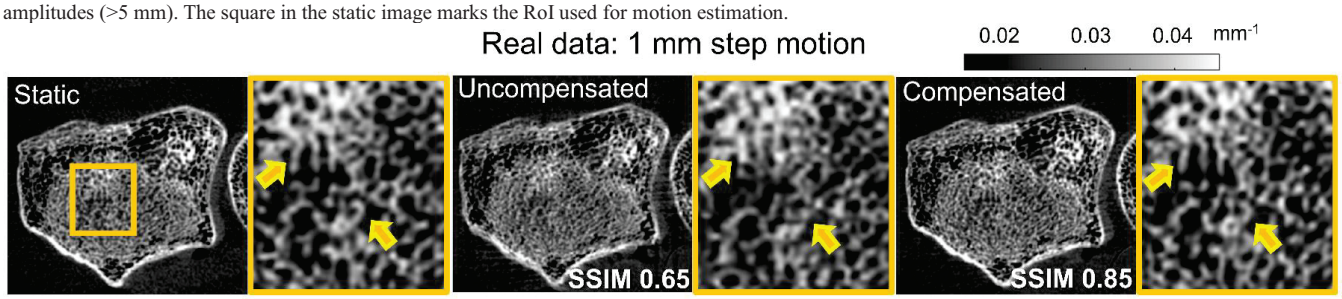

Figure 6. Motion compensation in experimental testbench data with step motion generated by a linear translation of the volume during the acquisition. Motion-induced artifacts (double contours) are reduced and details of the trabecular architecture are recovered after compensation (arrows).

motions <= 1 mm and significant improvement compared to no compensation for larger motions (~2x increase in SSIM). For motions > 5 mm, CMA-ES restart is essential for optimal results.

Fig. 6 shows the results of benchtop experiments. Even for the relatively small 1 mm motion, significant deterioration in the visualization of the trabeculae is found (arrows). Motion compensation successfully recovers the trabecular structure, with 30% improvement in SSIM, confirming the simulation results.

Fig. 7 shows the application of the compensation algorithm to patient data from FPD-based extremities CBCT with artifacts due to insufficient immobilization. The scan was processed using the proposed method using a 9x9x1.2 cm RoI centered at the femoral head. Significant reduction of motion artifacts is apparent. This indicates that the motion found in an RoI can in some cases be applied outside of the RoI to yield partial correction of the artifacts throughout the volume.

VI. Conclusion

A purely image-based motion compensation framework for high resolution CBCT extremities imaging was presented and evaluated. The performance of the method as a function of the autofocus metric, regularization strength and motion model was investigated. The algorithm recovered trabecular structure and suppressed motion artifacts across a broad range of motion amplitudes. In particular, almost perfect correction was achieved for sub-mm motions representative of small, involuntary patient drift that cannot be controlled with immobilization.

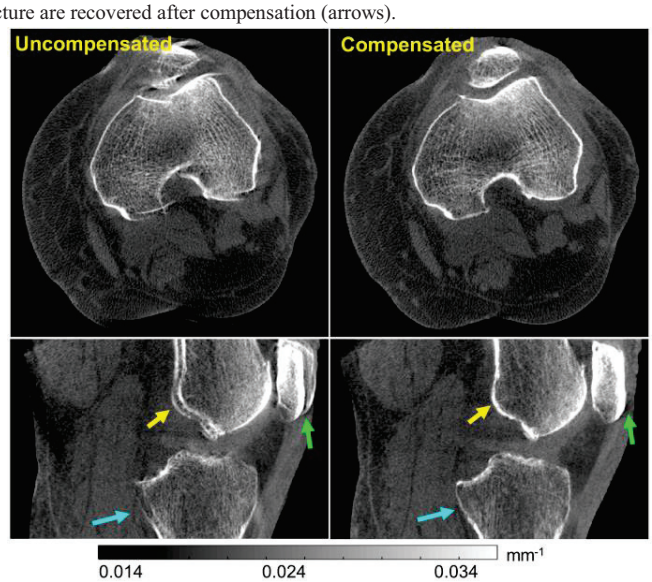

Figure 7. Motion compensation in patient data.

References

[1] H. Weinans, et al., *Bone* 51(2), pp. 190–6, 2012.
[2] A. Muhit, et al. *Proc. SPIE Medical Imaging* vol. 8672, 867203, 2013.
[3] A. Kingston, et al. *Med. Phys.*, vol. 38, no. 9, pp. 4934, 2011.
[4] Y. Kyriakou, et al. *Phys. Med. Biol.*, vol. 53, no. 22, pp. 6267, 2008.
[5] A. Katsevich, et al. *SIAM J. Imaging Sci.*, vol. 4, no. 1, pp. 200, 2011.
[6] J. Wicklein, et al., *Proc. SPIE Medical Imaging* vol. 8668, 86681S, 2013.
[7] J.-H. Choi, et al., *Med. Phys.*, vol. 41, no. 6, pp. 061902, 2014.
[8] M. W. Jacobson and J. W. Stayman, *IEEE Nucl. Sci. Symp. Conf. Rec.*, pp. 5240, 2008.
[9] J.-H. Kim, et al., *Phys. Med. Biol.*, vol. 60, no. 5, pp. 2047–2073, 2015.
[10] M. Unberath, et al., *Proc. SPIE Medical Imaging* vol. 9413, pp. 94130D, 2015.
[11] N. Hansen and S. Kern, *Proc. 8th Int. Conf. Parallel Probl. Solving from Nat. - PPSN VIII*, vol. 3242/2004, pp. 282–291, 2004.
[12] J. Wicklein, et al., *Med. Phys.*, vol. 39, no. 8, pp. 4918–31, 2012.
[13] J. M. Mateos, et al., *Cytometry Part A*, vol. 81A, pp. 213-221, 2012.
[14] Z. Wang, et al., *IEEE Trans. Image Process.*, vol. 13, no. 4, pp. 600–612, 2004.

Optimization of the Geometry and Speed of a Moving Blocker System for Cone-beam Computed Tomography Scatter Correction

Xi Chen, Luo Ouyang, Hao Yan, Xun Jia, Bin Li, Qingwen Lyu, You Zhang, and Jing Wang

Abstract— **A moving blocker based strategy has shown promising results for scatter correction in cone-beam computed tomography (CBCT). Different parameters of the system design affect its performance in scatter estimation and image reconstruction accuracy. In this work, we evaluate the performance in scatter estimation and image reconstruction accuracy under various combinations of width and separation of the lead strips at different moving speeds by Monte Carlo simulation. The scatter estimation error varied from 0.8% to 5.8% when the combinations of width and separation of the lead strips ranging from 5 pixels to 100 pixels at the detector plane. CT number error in the reconstructed CBCT images can be reduced to 24 HU, if we use strip width 10 pixels and gap width 30 pixels at a blocker moving speed over 15 pixels per projection. The moving blocker system can achieve accurate reconstruction if we use the optimized parameters.**

I. Introduction

In recent years, cone-beam computed tomography (CBCT) mounted on the gantry of the linear accelerator has become an instrumental part of volumetric image guidance in radiation therapy [1]. However, due to the broad beam geometry utilized in such systems, the presence of scatter contamination within the projection data will lead to reduction of image quality by introducing image artifacts, reducing contrast, and limiting CT number accuracy, especially for sites requiring large field of view (FOV).

Various strategies have been proposed for estimating the scatter signal in projection images including analytical calculation, Monte Carlo (MC) simulation and beam blocker-blocker-based techniques. In our previous study [2-3], we proposed a scatter correction strategy based on a moving blocker system and demonstrated its effectiveness. Scatter was estimated by interpolating values in un-blocked regions from the scatter signal in blocker regions. Instead of the missing primary signal of the blocked region through interpolation, only the primary signal in the unblocked regions was used to reconstruct the CBCT image. This method can simultaneously estimate scatter signal and reconstruct the complete volume within the FOV from a single scanning. method is not limited to full-fan scan geometry and small size of FOV.

In this work, we systematically investigate how variations in the design and speed of moving blocker affect imaging performance. We evaluate the performance in scatter estimation and image reconstruction accuracy under various combinations of width and separation of the lead strips at different moving speed. The present investigation involves MC simulations of projection images of a pelvis phantom using CBCT geometry at clinically realistic radiation doses.

II. Materials and Methods

A. Monte Carlo simulation

Fig. 1 illustrates the design of lead strips and the geometric setup of the moving blocker for CBCT imaging. The blocker consists of equally spaced lead strips which are 3.2 mm in thickness. For our study, various combinations of strip width and gap were investigated. The lead strips of the blocker are aligned perpendicular to the gantry rotation axis z and moves back and forth along the rotation axis z, as indicated in Fig. 1(c).

The MC simulation toolkit utilized in this study is gDRR[4]. The accuracy of photon transport in this package has been previously demonstrated by comparing simulation results with those from EGSnrc, as well as indirectly by comparing computed radiation dose with measurements [5]. The spectrum used in our study is 125kVp and the number of photons is 5.0e+9. Phantom was generated based on a pelvis patients CT dataset. The scan geometry is illustrated in Fig.1 (c). Projections were down sampled by a factor of 2 to yield a size 512×512 with pixel size 0.8 mm ×0.8 mm. The MC simulated data used in this study were projection data with lead strips of

This work was supported in part by the Cancer Prevention and Research Institute of Texas (RP130109), the American Cancer Society (RSG-13-326-01-CCE), US National Health Institute (R01 EB020366) and the National Natural Science Foundation of China (61401349).

Xi Chen is with the Department of Radiation Oncology, UT Southwestern Medical Center, Dallas, TX 75235, USA, also with the Institute of Image Processing and Pattern Recognition, Xi'an Jiaotong University, Xi'an, Shaanxi 710049 China, and also with the Beijing Center for Mathematics and Information Interdisciplinary Sciences, Beijing 10048 China. (e-mail: Xi2.Chen@UTSouthwestern.edu).

Luo Ouyang, Hao Yan, Xun Jia, You Zhang and Jing Wang are with the Department of Radiation Oncology, UT Southwestern Medical Center, Dallas, TX 75235, USA. (e-mail: Luo.Ouyang@UTSouthwestern.edu, yhhere @126.com , Xun.Jia@UTSouthwestern.edu, You.Zhang@UTSouthwestern. edu, Jing.Wang@UTSouthwestern.edu).

Bin Li and Qingwen Lyu is with School of Biomedical Engineering, Southern Medical University, Guangzhou 510515, China. (e-mail: libin371@smu.edu.cn, gzbeer@smu.edu.cn).

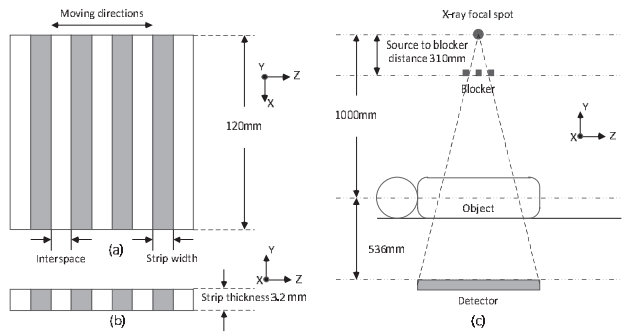

Fig. 1. Illustration of the blocker and its location in an on-board imaging system. (a) Anterior view of the blocker. (b) Cross section view of the blocker. (c) A blocker is inserted between the X-ray source and the imaging object and it moves back and forth along the gantry rotation axis z during CBCT acquisition.

width and the gap varying from 0.8 to 16 mm, corresponding to 4 mm (5 pixels) to 80 mm (100 pixels) where they were projected onto the detector panel plane.

B. Residual interpolation technique

For one projection image, the scatter signal detected in the blocked region was used to estimate the scatter component of the unblocked region using cubic B-Spline interpolation [6]. In order to study the penumbra effects of the strips, ray-tracing technique was employed. Using different blockers, the regions (2~4 pixels wide) adjacent to the edges of the strip were excluded from the scatter estimation to avoid penumbra effects. For the unblocked region, the estimated scatter signal S_{es} was compared to the scatter signal S_{mc} simulated by MC. The residual error is S_{mc} - S_{es}. The relative error $R(u,v,\theta)$ of log-transformed projection signals introduced by scatter estimation is:

$$R(u,v,\theta)=\frac{\log\left(\frac{I_{mc0}}{P_{mc}(u,v,\theta)+S_{mc}(u,v,\theta)-S_{es}(u,v,\theta)}\right)}{\log\left(\frac{I_{mc0}}{P_{mc}(u,v,\theta)}\right)},\quad (u,v)\in unblocked\ region, \tag{1}$$

where u, v denote the coordinates of the detector and θ denotes the gantry angle, I_{mc0} is the incident x-ray intensity and P_{mc} is the primary signal generated by MC simulation. The errors in unblocked region were interpolated to blocked regions to obtain the error map of scatter simulation within a projection.

In order to improve the efficiency of MC simulation, projection data was simulated at sparse angles and then interpolated to other projection angles. From Xu et al's study[7], when the simulated projection number becomes larger than 15, further increasing this parameter value does not help reduce the error significantly anymore. In this study, we chose projection number 36 to obtain projections of sufficient accuracy. The 36 projections were distributed evenly over a 360^0 arc. The 36 relative error map $R(u,v,\theta)$ (θ=0^0,10^0,…350^0) were interpolated by angles to get 660 error maps. Since the photon numbers were limited in MC simulation, the primary logarithm-transformed projection data (i.e., line integral) were simulated analytically. A total of 660 views acquired over a 360^0 arc at a frame rate of 5.5 frames/s. The MDCT of the pelvis phantom were considered as noise-free.

After the noise-free line integrals $p(u,v,\theta)$ are calculated, the noisy primary signal $I'(u,v,\theta)$ is generated according to the following noise model:

$$I'(u,v,\theta)=Possion\left(I_0 exp\left(-p(u,v,\theta)\right)\right)+Normal(0,\sigma_e^2), \tag{2}$$

where I_0 is the incident x-ray intensity and σ_e^2 is the electronic noise variance. And then, the log-transformed projection measurements after scatter correction can be expressed as:

$$\tilde{I}(u,v,\theta)=\log\left(\frac{I_0}{I'(u,v,\theta)}\right)\times R(u,v,\theta). \tag{3}$$

C. Iterative image reconstruction based on total variation

In this study, a total variation (TV) based algebraic iterative reconstruction (ART) algorithm is adopted to reconstruct the CBCT image from the partially blocked projection data. The algorithm is formulated as a constraint optimization (CO) model under the framework of compressed sensing. Constraint optimization incorporates the data fidelity and image constrains, such as the regularity measure TV in this work.

D. Performance evaluation metrics: RMSE

To quantitatively evaluate the accuracy of the scatter estimation, we first computed the relative root mean squared error of scatter (rRMSE) in unblocked regions of detector by comparing the interpolated scatter to the Monte Carlo simulated scatter:

$$rRMSE(\theta)=\sqrt{\frac{\sum\sum_{(u,v)\in unblocked\ region}\left(\frac{(S_{es}(u,v,\theta)-S_{mc}(u,v,\theta))}{S_{mc}(u,v,\theta)}\right)^2}{N}}, \tag{4}$$

where N is the number of pixels in unblocked region.

Qualitative and quantitative comparisons were performed on the CBCT reconstruction after scatter correction. The reconstructed images were generated with a size of 256×256 ×140 voxels, where the voxel size is 2.0274 mm × 2.0274 mm ×2.0274 mm. All of the reconstructed images were converted Hounsfield unit (HU) and compared qualitatively and quantitatively. We used root mean square error (RMSE) of CT number $CT_{bs}(x,y,z)$of the reconstructed images of partially blocked projections with scatter correction, as compared to the CT number $CT_{ub}(x,y,z)$ of the image reconstructed from unblocked projections, the RMSE was calculated as:

$$RMSE=\sqrt{\frac{\sum_{z=21}^{120}\sum_{(x,y)\in ROI(z)}\left(CT_{bs}(x,y,z)-CT_{ub}(x,y,z)\right)}{M}}, \tag{5}$$

where 100 slices were used for calculation and we selected the pelvis area as the ROI for each slice, M is the number of voxels for calculation.

III. RESULTS

A. Scatter estimate error

Fig.2 shows the Monte Carlo simulation results on scatter estimation error of three angles, when different blockers were applied between the X-ray source and imaging object. The scatter estimation error in unblocked regions of detector was quantified by rRMSE described in Eq.(4). Both the lead strips width and the gap varying from 0.8 to 16 mm, corresponding to 4 mm (5 pixels) to 80 mm (100 pixels) where they were projected onto the detector panel plane. The scatter estimation error varied from 0.8% to 5.8% with simulated combinations

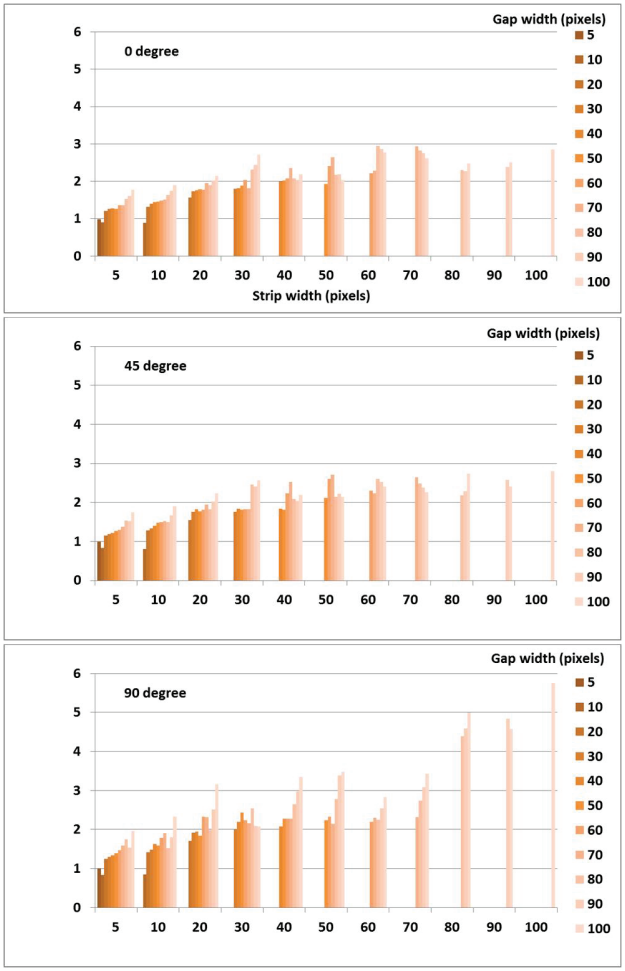

Fig. 2. Scatter estimation error in the unblocked regions of detector plane, as both strip width and gap width varied from 5 pixels to 100 pixels (as projected on the detector plane).

of lead strip width and gap width. As seen from Fig. 2, scatter estimation error increases as the gap width increases and the strip width increases.

B. Reconstruction Results

Fig. 3 shows one axial slice of the reconstruction images of the pelvis phantom at a blocker moving speed of 20 pixels per projection. Fig. 3(a) is showing CBCT reconstructed from partially unblocked projections as a 10 pixel-blocked-10 pixel-gap (B10G10) moving blocker was applied; the reconstruction result is terrible (RMSE=201.9). The central part of the slice is missing. The reason is that the gap is too narrow (G10). Some voxels in the object cannot be reconstructed successfully at specific speed because of insufficient measurement data. Fig. 3(b) is the CBCT reconstructed from a B10G30 moving blocker produced projection data, the result is good (RMSE=23.6); Fig. 3(c) is from a B20G40 moving blocker and Fig. 3(d) is from a B20G60 moving blocker, their results are acceptable (RMSE=32.2, 32.8). It can be observed that the CBCT image reconstructed from projections acquired with a narrower-strip-wider-gap blocker has fewer artifacts. Wider gap can bring more information for reconstruction, but it

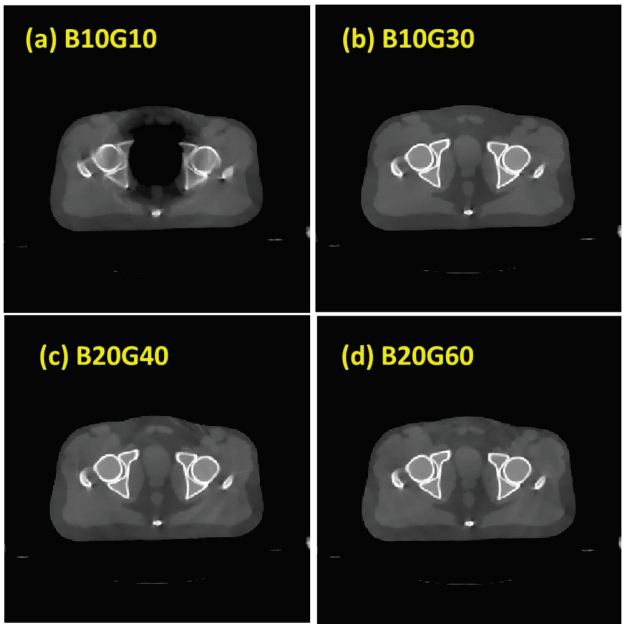

Fig. 3 One axial slice of the pelvis CBCT images from projections with varied blocker designs, blocker moving speed is 20 pixels per projection. Display widow [-500, 1000] HU.

also caused accuracy decrease in scatter estimation. As can been seen in Fig3 (c) and (d), strip width is the same and gap width is different, but the reconstructed results are almost the same. There should be a compromise between strip width and gap width.

Fig. 4 shows one axial slice of the reconstruction images of the pelvis phantom of a B20G40 blocker at various moving speed. If the moving speed is too slow (eg. 1 pixel per projection), the reconstruction result is bad (RMSE=48.7). If the speed is increased to 5 pixels per projection, the reconstructed result is better (RMSE=36.6). When the speed is above 10 pixels per projection, the RMSE will decrease to around 33; when the speed is above 20 pixels per projection, the RMSE will decrease to 32 and come to stable.

Fig.5 shows the CT number error RMSE in the CBCT images reconstructed from partially unblocked projection datasets. The partially unblocked projections were generated by simulating the blocker motion at various speeds (from 1 pixel per projection to 30 pixels per projection) during CBCT acquisition. Since scatter estimation error increases as the gap increases and the strip width increases, and considering making a 0.8 mm width lead strip (corresponding 5 pixels blocked region width) is impractical, in these datasets, we only investigated the scenario where the strip width is 10 pixels and 20 pixels, and the gap width varies from 5 pixels to 60 pixels. As can be seen in Fig.5, for strip width 10 pixels, the RMSE is almost below 40 except two scenarios which are gap width 10 pixels at the speed of 20 pixels per projection (RMSE= 201.9) and gap width 20 pixels at speed of 30 pixels per projection (RMSE= 164.7). For strip width 20 pixels, the RMSE is almost below 70 except the scenario that gap width is 10 pixels at speed of 15 pixels per projection (RMSE= 88.1) and at speed of 30 pixels per projection (RMSE= 436.8). So we should choose gap width bigger than 20 pixels and moving speed over 15 pixels per projection to perform our scatter correction method.

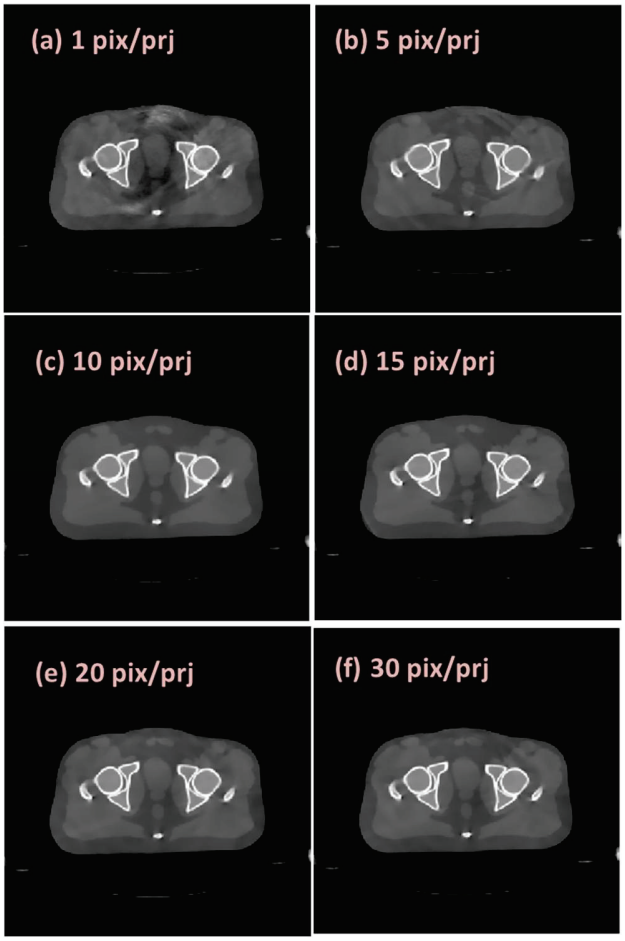

Fig. 4 One axial slice of the pelvis CBCT images from projections with varied moving speed, blocker design is strip width 20 pixels and gap width 40 pixels. Display widow [-500, 1000] HU.

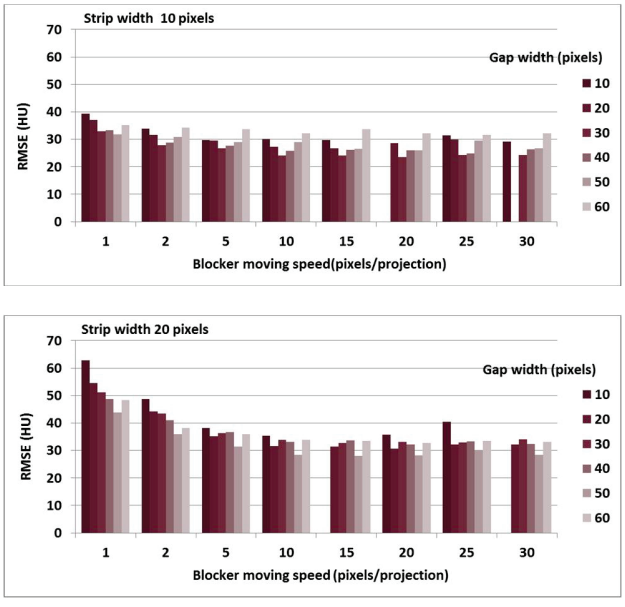

Fig. 5. CBCT image reconstruction error when different moving blockers were applied. Simulations of the blocker lead strip width is 10 pixels and 20 pixels, the gap width is from 5 pixels to 60 pixels, and the blocker moving speed is from 1 pixel per projection to 30 pixels per projection. (For obvious showing, we did not show the scenarios where RMSE is above 70).

IV. Discussion and Conclusion

In this work, we optimized the geometry and speed of a moving blocker system for CBCT scatter correction. Scatter signal was simulated by Monte Carlo calculation with various combinations of width and separation of the lead strips, ranging from 5 pixels to 100 pixels at the detector plane. The scatter estimation error varies from 0.8% to 5.8% and increases as the gap width increases and the strip width increases. In our simulation study, we considered the penumbra effects introduced by lead strip thickness and blocker moving. For different blocker moving speed, the number of pixels affected is different. The total penumbra in one strip shadow is 4 pixels, 6 pixels and 8 pixels for moving speed below 10 pixels, 10-20 pixels and 20-30 pixels per projection, respectively.

In this study, we found that if the gap is too narrow (G10 and G20), there will be a possibility of reconstruction failure at some moving speeds. This is because a certain region of projections may be blocked throughout the whole acquirement procedure. And then, reconstruction failures occurred in certain area of the image due to the lack of information. The missing area might be recovered by more advanced reconstruction algorithm with prior information. But at present, we should use gap width bigger than 20 pixels avoiding the reconstruction failure. On the other hand, In order to guarantee the accuracy of scatter estimation, the strip width should not be wider than 20 pixels. Also, we should consider the feasibility in practice, so we did not investigate the scenario of strip width of 5 pixels. In this work, we just investigated CBCT reconstruction with scatter correction in the condition of strip width of 10 pixels and 20 pixels. The results show that the gap width should be large enough to achieve acceptable reconstruction accuracy. As can be seen in Fig.5, if the strip width is 10 pixels and gap width is 30 pixels, we can get an optimal result. The moving speed does not have a very strong effect on reconstruction result if it is not too slow. If the moving speed is over 15 pixels per projection, the reconstruction results will change no more than 2 HU.

References

[1] D.A. Jaffray, J.H. Siewerdsen, J.W. Wong, and A.A. Martinez, “Flat-panel cone-beam computed tomography for image-guided radiation therapy,” *Int. J. Radiation Oncology Biol. Phys.*, Vol.53, pp.1337-1349, 2002.

[2] J. Wang, W. Mao, and T. Solberg, “Scatter correction for cone-beam computed tomography using moving blocker strips: a preliminary study,” *Med. Phys*., Vol.37, pp.5792-5800, 2010.

[3] L. Ouyang, K. Song, and J. Wang, “A moving blocker system for cone-beam computed tomography scatter correction,” *Med. Phys*., Vol.40, pp.071903, 2013.

[4] X. Jia, H. Yan, L. Cerviño, M. Folkerts, and S.B. Jiang, “A GPU tool for efficient, accurate, and realistic simulation of cone beam CT projections,” *Med. Phys*., Vol.39, pp.7368-7378, 2012.

[5] D. Montanari, E. Scolari, C. Silvestri, Y.J. Graves, H. Yan, L. Cervino, R. Rice, S.B. Jiang, and X. Jia, "Comprehensive evaluations of cone-beam CT dose in image-guided radiation therapy via GPU-based Monte Carlo simulations," Phys. Med. Biol., Vol.59, pp.1239-1253, 2014.

[6] J. Siewerdsen, M. Daly, B. Bakhtiar, D. Moseley, S. Richard, H. Keller, and D. Jaffray, "A simple, direct method for x-ray scatter estimation and correction in digital radiography and cone-beam CT," *Med. Phys*., Vol.33, pp.187-197, 2006.

[7] Y. Xu, T. Bai, H. Yan, L. Ouyang, A. Pompos, J. Wang, L. Zhou, S.B. Jiang, and X. Jia, "A practical cone-beam CT scatter correction method with optimized Monte Carlo simulations for image-guided radiation therapy," Phys. Med. Biol., Vol.60, pp.3567-3587 ,2015,.

Task-Based Regularization Design for Detection of Intracranial Hemorrhage in Cone-Beam CT

H. Dang, J. W. Stayman, J. Xu, A. Sisniega, W. Zbijewski, X. Wang, D. H. Foos, N. Aygun, V. E. Koliatsos, and J. H. Siewerdsen

***Abstract*—Prompt and reliable detection of acute intracranial hemorrhage (ICH) is critical to treatment of a number of neurological disorders. Cone-beam CT (CBCT) systems are potentially suitable for detecting ICH (contrast 40-80 HU, size down to 1 mm) at the point of care but face major challenges in image quality requirements. Statistical reconstruction demonstrates improved noise-resolution tradeoffs in CBCT head imaging, but its capability in improving image quality with respect to the task of ICH detection remains to be fully investigated. Moreover, statistical reconstruction typically exhibits nonuniform spatial resolution and noise characteristics, leading to spatially varying detectability of ICH for a conventional penalty. In this work, we propose a spatially varying penalty design that maximizes detectability of ICH at each location throughout the image. We leverage theoretical analysis of spatial resolution and noise for a penalized weighted least-squares (PWLS) estimator, and employ a task-based imaging performance descriptor in terms of detectability index using a nonprewhitening observer model. Performance prediction was validated using a 3D anthropomorphic head phantom. The proposed penalty achieved superior detectability throughout the head and improved detectability in regions adjacent to the skull base by ~10% compared to a conventional uniform penalty. PWLS reconstruction with the proposed penalty demonstrated excellent visualization of simulated ICH in different regions of the head and provides further support for development of dedicated CBCT head scanning at the point-of-care in the neuro ICU and OR.**

I. Introduction

Intracranial hemorrhage (ICH) is associated with a variety of neurological disorders, including hemorrhagic stroke and traumatic brain injury [1]. Non-contrast-enhanced multi-detector CT (MDCT) is the current front-line modality for diagnosis of acute ICH with high sensitivity but is commonly only available in a dedicated radiology suite or emergency department. Compared to MDCT, cone-beam CT (CBCT) systems typically have smaller footprint, greater portability, and lower cost, and therefore are potentially more suitable for diagnosis of acute ICH at the point of care (e.g., neurological ICU, urgent care, ambulance, and sports and military theatres). However, current CBCT systems face major challenges in image quality required for detecting ICH (blood-to-brain contrast 40-80 HU, size down to 1 mm) [1].

Recent research aims to develop high-quality CBCT for detection of ICH using mobile C-arms or a dedicated head CBCT system designed specifically to provide optimal performance in ICH detection [2]. A high-fidelity artifact correction framework has also been proposed and demonstrates major reduction in artifacts in CBCT of the head, including scatter, beam hardening, and detector lag and glare [3]. Moreover, a statistical reconstruction method has been proposed to compute statistical weights that account for noise in the measurements following artifact corrections, demonstrating improved noise-resolution tradeoffs in CBCT of ICH compared to conventional filtered backprojection [4].

This work was supported by the U.S. NIH R01-CA-112163 and academic-industry partnership with Carestream Health (Rochester, NY).

The authors are with Johns Hopkins University, Baltimore, MD 21205 USA (corresponding author is J. H. Siewerdsen, jeff.siewerdsen@jhu.edu).

This work addresses two important questions with respect to high-quality CBCT of ICH. First, statistical reconstruction tends to produce nonuniform spatial resolution and noise in the image. For example, Figure 1 shows an image reconstructed using penalized weighted least-squares (PWLS) as in [4], and the conspicuity of the same ICH lesion in various locations of the head is seen to depend strongly on the local spatial resolution and noise characteristics. Various methods have been developed to address this problem by designing a spatially varying penalty that encourages uniform spatial resolution or noise. For example, Fessler *et al.* designed a penalty that includes a spatially varying certainty term to encourage a uniform point spread function (PSF), providing uniform spatial resolution throughout the image [5]. A second important consideration is that imaging performance should be defined with respect to a specific task [6]. In the case of ICH detection, the task is to discriminate a low-contrast, mid-frequency lesion from a relatively uniform background. One way in which statistical reconstruction can be leveraged to maximize performance is to design a penalty that maximizes detectability index (d') [7] for a particular task. However, due to nonuniform spatial resolution and noise, a penalty designed to maximize detectability at one location may not necessarily maximize detectability at another. The two considerations described above are therefore intimately connected, and one may design a spatially varying penalty (analogous to the one in [5]) to maximize detectability.

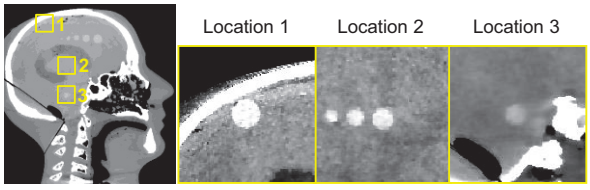

Figure 1: Illustration of nonuniform spatial resolution and noise in a 3D image reconstructed by PWLS. The anthropomorphic head phantom containing simulated ICH was scanned on a FPD-CBCT test-bench at 24 mGy. Grayscale window: [-10, 110] HU.

In this work, we propose a spatially varying penalty that optimizes detectability for ICH detection at all locations through a CBCT image of the head. Previous related work by Qi *et al.* optimized directional weights in a penalty to improve detectability for breast lesion detection at an unknown location in 3D PET [8]. Gang *et al.* optimized a parameter that weights the regularization term in 2D CT to maximize detectability at an unknown location for a few generic detection tasks [9]. This work builds on the method in [9] but differs in two aspects. First, this work introduces a comprehensive and general framework to design a spatially varying penalty for maximal detectability. Second, we extend the design from 2D CT in [9] to 3D CBCT and focus on designing a penalty for a specific task in head imaging. We first validate prediction of spatial resolution and noise characteristics at various locations in 3D, and we then define a 3D detectability index that provides an objective function in penalty design. The performance of the proposed penalty is evaluated on a 3D anthropomorphic head phantom in comparison to a conventional penalty.

II. METHODS

A. Penalized Weighted Least-Squares Reconstruction

We choose a PWLS reconstruction method previously developed for CBCT head imaging [4], whose forward model assumes mono-energetic x-rays and independent measurements as:

$$\bar{y} = \mathbf{D}\{g\}\exp(-\mathbf{A}\mu) \tag{1}$$

where $\bar{y}$ denotes the mean measurements, μ is the image estimate, $\mathbf{A}$ is the linear projection operator (and $\mathbf{A}^T$ is the linear backprojection operator), g are the measurement-dependent gains, and $\mathbf{D}$ is an operator that converts a vector into a diagonal matrix.

The PWLS objective can be written as:

$$\begin{aligned} \hat{\mu} &= \arg\min_{\mu} \frac{1}{2}\|\mathbf{A}\mu - l\|_{\mathbf{W}}^2 + \beta R(\mu) \\ R(\mu) &= \frac{1}{2}\sum_j \sum_{k\in N_j} w_{jk}\psi(\mu_j - \mu_k) \end{aligned} \tag{2}$$

where l denotes line integrals derived from the measurements y, and $\mathbf{W}$ is a diagonal weighting matrix. The statistical weights in $\mathbf{W}$ are computed to account for noise in the measurements and noise following artifact corrections (if such corrections are present in the data processing) [4]. The regularization term in Eq. (2) penalizes differences between every voxel μ_j and its neighboring voxel μ_k by a penalty function ψ along with directional weights w_{jk}, and is weighted by a scalar regularization parameter β. We refer to this penalty below as the "conventional penalty".

To design a penalty that maximizes detectability, one can modify the regularization parameter, directional weights, and/or penalty function. In this work, we focus on designing a spatially varying β map while keeping the directional weights (w_{jk}=1 for first-order neighbors) and penalty function (quadratic function) the same throughout the image. Optimization of the directional weights and penalty function for maximal detectability are subjects of future work. The proposed spatially varying penalty can be written as:

$$\begin{aligned} \hat{\mu} &= \arg\min_{\mu} \frac{1}{2}\|\mathbf{A}\mu - l\|_{\mathbf{W}}^2 + R'(\mu) \\ R'(\mu) &= \frac{1}{2}\sum_j \beta_j \sum_{k\in N_j} w_{jk}\psi(\mu_j - \mu_k) \end{aligned} \tag{3}$$

where R' denotes the new regularization term.

As a point of reference, we consider another form of spatially varying penalty derived by Fessler *et al.* [5] that encourages uniform spatial resolution (referred to below as the "uniform resolution penalty") and can be written as:

$$R(\mu) = \frac{1}{2}\sum_j \sum_{k\in N_j} \kappa_j \kappa_k w_{jk}\psi(\mu_j - \mu_k), \quad \kappa_j = \sqrt{\sum_i a_{ij}^2 \mathbf{W}_i \Big/ \sum_i a_{ij}^2} \tag{4}$$

where κ_j represents the certainty of all rays that intersect the j^{th} voxel and a_{ij} denotes the $(i, j)^{th}$ element of matrix $\mathbf{A}$.

B. Task-Based Performance Prediction

Previous work [5] shows that if the spatially varying term is spatially smooth, its effects on image quality are essentially local. Thus, while β will be spatially dependent in the resulting penalty, in the design stage, we assume β values at other voxels are the same as the β value at the voxel of interest (i.e., assumes a conventional penalty). One can then derive analytical expressions of the local PSF and local covariance for the PWLS estimator in Eq. (2) using a first-order Taylor expansion and the Implicit Function Theorem as in [5]:

$$\left[PSF(\hat{\mu})\right]_j = \left[\mathbf{F}(\bar{\mu}) + \beta\mathbf{R}\right]^{-1}\mathbf{F}(\mu^{true})e_j \tag{5}$$

$$\left[Cov(\hat{\mu})\right]_j = \left[\mathbf{F}(\bar{\mu}) + \beta\mathbf{R}\right]^{-1}\mathbf{F}(\mu^{true})\left[\mathbf{F}(\bar{\mu}) + \beta\mathbf{R}\right]^{-1}e_j \tag{6}$$

where $\mathbf{F}$ is the Fisher information matrix defined as $\mathbf{F}(\mu) = \mathbf{A}^T\mathbf{D}[\bar{y}(\mu)]\mathbf{A}$, $\mathbf{R}$ is the Hessian of $R(\mu)$ in the PWLS objective (and is not dependent on the input image when a quadratic penalty function is used), e_j is a unit vector specifying location in the image (with unity j^{th} element and zero elsewhere). In real data when μ^{true} (truth image) and $\bar{\mu}$ (PWLS reconstruction of noiseless data) are not available, a "plug-in" method [5] can be used.

Since the local PSF and covariance are evaluated in a relatively uniform region (brain), the matrix of local PSF and covariance can be approximated as circulant in a small region-of-interest (ROI). Their discrete Fourier transform are then the local modulation transfer function (MTF) and noise-power spectrum (NPS) within the ROI:

$$MTF(f)_j = |H(f)|/H(0), \text{ where } H(f) = FT\left\{\left[PSF(\hat{\mu})\right]_j\right\} \tag{7}$$

$$NPS(f)_j = \left|FT\left\{\left[Cov(\hat{\mu})\right]_j\right\}\right| \tag{8}$$

With predictions of local MTF and NPS, one may predict the task-based performance of the PWLS estimator in terms of detectability index d' [7], which relates metrics of MTF and NPS to a spatial-frequency-dependent task function and an observer model. Many observer models can be formulated - in this work, the nonprewhitening (NPW) matched filter observer model. This model does not bias the results according to the characteristics of the observer and has demonstrated reasonable agreement with human observer performance for simple tasks in tomosynthesis and CBCT [10]. The detectability index with a NPW observer model can be written as:

$$d'^2 = \frac{\left[\iiint \left(MTF_j \cdot W_{Task}\right)^2 df_x df_y df_z\right]^2}{\iiint NPS_j \left(MTF_j \cdot W_{Task}\right)^2 df_x df_y df_z} \tag{9}$$

The task function W_{Task} in this work is defined as the difference of two Gaussian functions, representing a low-contrast, mid-frequency task such as ICH detection expressed as follows:

$$W_{\text{Task}} = C\left[\exp\left(-|\mathbf{f}|^2/2\sigma_1^2\right) - \exp\left(-|\mathbf{f}|^2/2\sigma_2^2\right)\right] \tag{10}$$

where C is the blood-to-brain contrast (0.011 mm^{-1}), σ_1 = 0.35 mm^{-1}, and σ_2 = 0.25 mm^{-1} corresponding to discrimination of a characteristic feature length of ~2 mm, approximated using the average of four standard deviations of each Gaussian function in the spatial domain.

C. Proposed Regularization Design Framework

While the design goal is to maximize d' at every location in the image, one may start with maximizing d' at one location. The optimization problem can be written as:

$$\hat{\beta}_j = \underset{\beta_j}{\text{argmax}}\, d'^2(\beta_j) \tag{11}$$

While directly solving Eq. (11) might be possible, we choose a simple scheme in this work to maximize d' by evaluating d' for different β values with regular spacing and choosing the β that yields the maximum d'.

Repeating the optimization at every voxel is computationally impractical for 3D CBCT. We accelerate the design process in two steps. First, we exploit the observation that the optimal β is slowly varying between neighboring voxels and therefore perform the optimization on a 25×25×25 downsampled grid (internal to the cranium) and then interpolate β at intermediate voxels using radial basis functions. Second, since the local PSF reduces toward zero at

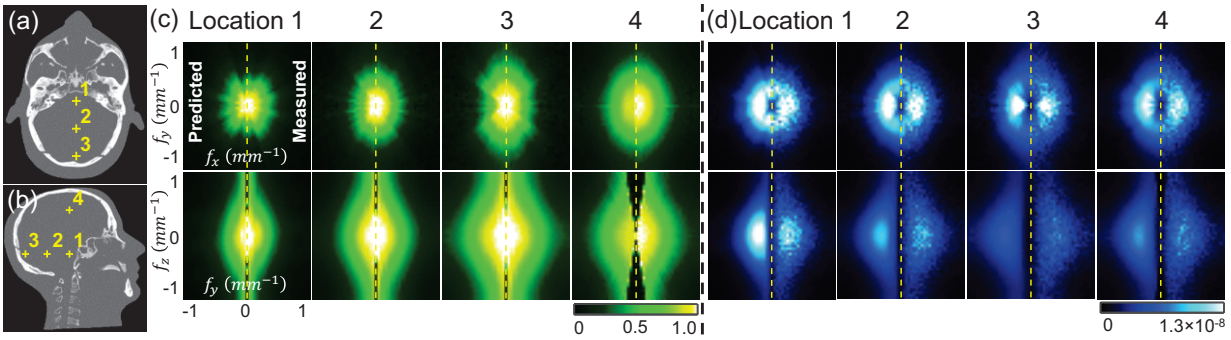

Figure 2: Validation of 3D MTF and NPS prediction. (a-b) 3D head phantom used in this work. Grayscale window: [0, 0.04] mm^{-1}. (c-d) Predicted and measured 3D local MTF (c) and NPS (d) at location 1-4 denoted in Fig. 2. In each plot, the left half is prediction from Eq. (5-8), and the right half is measurements from PWLS reconstructions. Units are scalar for the 3D MTF and $[(mm^{-1})^2(mm)^3]$ for the 3D NPS.

voxels sufficiently far from the impulse, one may divide the grid into K subgrids, and in each k^{th} subgrid place N_k unity impulses in the input e_k and predict for N_k locations simultaneously. The prediction accuracy is not affected provided that the impulses are far apart. This applies to the prediction of the local covariance as well. The combination of the downsampled grid and simultaneous prediction reduced the number of calculations needed from the number of voxels (e.g., ~512^3 in 3D CBCT) to the number of subgrids. In this work, we placed impulses at 50 voxels apart, which divided the grid into 2^3=8 subgrids. A pseudocode outline of the design framework is shown in Algorithm 1.

Algorithm 1: Spatially varying penalty design for maximum d'

Input precomputed **R**
for each subgrid k = 1 to K
  Construct e_k with N_k unity elements (uniform spacing)
  Use Eq. (5-6) to predict local PSF and covariance for N_k locations simultaneously
    for each voxel j on the k^{th} subgrid
      Use Eq. (7-9) to compute MTF, NPS, and d' at different β
      Estimate β that maximizes d'
    end for
end for
for each voxel not on the grid
  Interpolate β based on the optimal β on the grid
end for
return a β map

III. Experimental Results

We evaluated the proposed penalty in simulation studies using the 3D digital head phantom shown in Fig. 2(a-b). The digital phantom was created by performing a CT scan of a realistic physical head phantom at high dose and setting all soft tissues (including the brain) to a constant value (40 HU). The resulting phantom preserves realistic bone attenuation and exhibits no noise or artifact in soft tissue. A system geometry previously identified for a dedicated CBCT head scanner [2] was used, with a 100 cm source-to-detector distance, 55 cm source-to-axis distance, and 0.556 × 0.556 mm^2 detector pixel sizes. Projections (N = 720) without noise and with Poisson noise were simulated over 360° using 2×10^5 photons per detector pixel. Images were reconstructed with 390×485×498 voxels and 0.5×0.5×0.5 mm^3 voxel sizes. Artifact corrections were not considered in this work.

We first validated the prediction of 3D local MTF and NPS, including locations throughout the brain and adjacent to the cranium. Figure 2(c-d) shows the 3D local MTF and NPS at four locations denoted in Fig. 2 with a nominal β value for this dataset ($10^{6.4}$). In each plot, the left side shows the prediction from Eq. (5-8), and the right side shows the measurements from PWLS reconstructions. For prediction, we used 100 iterations of the conjugate gradient (CG) algorithm in Eq. (5) for complete convergence of the local PSF, and we applied the CG algorithm twice in Eq. (6) to achieve convergence in the local covariance. For measurements, the local PSF was measured by subtracting two PWLS reconstructions with and without an impulse (no noise added), and local covariance was measured from a large ensemble (n = 100) of PWLS reconstructions with different noise realizations following the method in [9]. 100 iterations of separable quadratic surrogate updates [11] were performed to achieve a nearly converged PWLS image. A ROI size of 21×21×21 voxels was large enough to cover the main extent of the local PSF and covariance and was therefore used in DFT operations. For both MTF and NPS, good overall agreement can be seen between prediction and measurements at all four locations in both x-y plane and z direction. The spatial dependence of MTF and NPS can also be seen. For example, the MTF broadens and is less isotropic near the periphery, whereas the NPS is reduced at certain frequencies according to the magnitude of line integrals from location 1 to 4.

To design a β that maximizes d' at one location, we predicted the local MTF and NPS at different β values and computed d' as a function of β. Figure 3(a) shows the 3D task function from Eq. (10). Figure 3(b) shows a calculation of d' as a function of β at the four locations in Fig. 2. At each location, the function $d'(\beta)$ exhibited a concave shape and a clear optimum, suggesting the possibility of directly solving for β - for example, using gradient-based optimization. For each location, the d' reduced at lower β (dominated by high NPS) and higher β (dominated by over-smoothing). The optimal β is also seen to vary over an order of magnitude, suggesting the design of a spatially varying penalty. It is worth mentioning that we observed a lower level of agreement between prediction and measurement in the limit of very low β (~$10^{5.0}$), which is attributed to the high conditioning number of the matrices to be inverted in Eq. (5-6) and could potentially be solved by preconditioning. However, such disagreement is

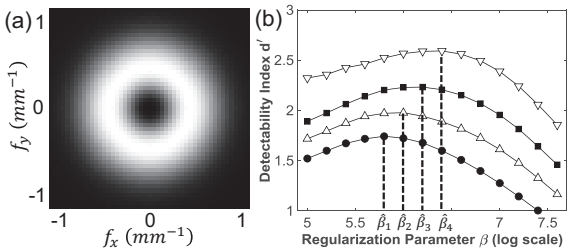

Figure 3: (1) A 3D task function for ICH detection. Grayscale window: [0, 3.3×10⁻⁴] mm^{-1} (b) Detectability index computed as a function of regularization parameter β at 4 locations denoted in Fig. 2. The optimal β were at $\hat{\beta}_j$ ($j = \{1,2,3,4\}$).

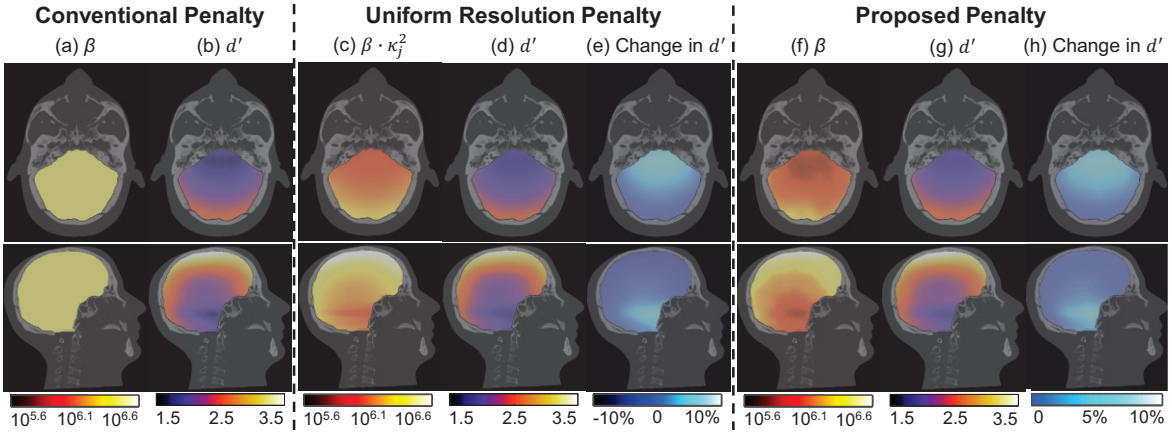

Figure 4: Maps of penalty strength and detectability in ICH detection. (a-b) Scalar β and resulting d' distribution for the conventional PWLS penalty. (c-e) For the uniform resolution penalty: (c) product of certainty (κ_j^2) and a scalar β, (d) the resulting d' distribution, and (e) relative change in d' compared to the conventional penalty (f-h) For the proposed d'-optimization penalty: (f) the β map, (g) the resulting d' distribution, and (h) relative change in d' from the "best" conventional penalty.

not believed to affect the results, since those β values are much smaller than the range of interest about the optimal β value.

Figure 4 shows the results for the proposed penalty in comparison to the (spatially uniform) conventional penalty and the (spatially varying) uniform resolution penalty. For the conventional penalty, a scalar β value of $10^{6.4}$ was chosen to achieve the highest mean d' in the head. For the uniform resolution penalty (shown simply as a point of reference as another form of spatially varying penalty), regularization was such as to encourage uniform PSF width of 0.95 mm (FWHM averaged over all radial directions). Fig. 4(f) shows the β map resulting for the proposed d' optimization penalty, which is seen to follow a similar overall trend as the uniform resolution penalty: penalty strength is lower in regions of high attenuation near the interior skull base and is higher at the periphery near the cranium. Fig. 4 (b), (d), and (g) show the d' map from each penalty, each exhibiting strong spatial variation in d' with highest value near the periphery and reduced performance in the interior of the cranial vault. Fig. 4 (e) and (h) show the change in d' (relative to the conventional penalty) achieved by the two spatially varying penalties. Compared to the conventional penalty, the uniform resolution penalty provides a 10% increase in d' in the interior of the brain near the skull base but a slight (5%) reduction in d' at the periphery adjacent to the cranium. This is somewhat expected, since the uniform resolution penalty was designed to achieve uniform spatial resolution (and not maximum detectability). Figure 4(h) shows that the proposed penalty improves d' up to ~10% and preserves the highest d' (i.e., does not reduce d') in comparison to the best conventional penalty.

PWLS image reconstructions corresponding to each type of penalty are shown in Fig. 5. Three simulated 3D spherical ICH lesions of 2 mm diameter and 50 HU contrast were added to regions in the deep interior of the brain near the skull base and at the periphery adjacent to the cranium. The best conventional penalty exhibited good visualization of ICH adjacent to the cranium but yielded an over-smoothed image in the deep interior near the skull base. The uniform resolution penalty improved conspicuity of the lesion (particularly near the skull base) and achieved a more uniform appearance of spatial resolution in the image compared to the conventional penalty. The proposed d'-optimization penalty yielded improved visualization of ICH in both regions, particularly in the deep interior region near the skull base.

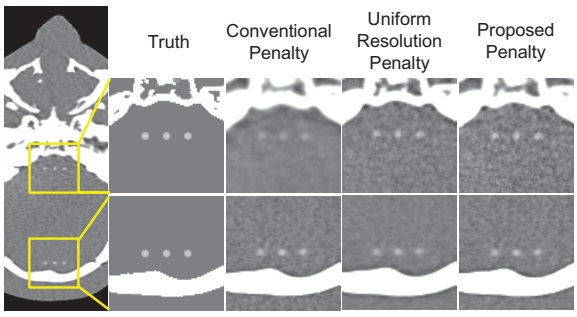

Figure 5: Image reconstruction of a 3D spherical ICH lesion of 2 mm diameter and 50 HU contrast. Grayscale: [-50, 130] HU.

IV. Conclusion

Image reconstruction in a manner that specifically incorporates a formulation of the imaging task and optimizes penalty design with respect to local, task-based imaging performance presents a promising approach for "task-driven image reconstruction." For high-quality CBCT imaging of the head, this paper shows that the spatially varying penalty strength could be reliably predicted with respect to an ICH detection task, providing optimal detectability at each location throughout the 3D image. The proposed penalty demonstrated improved or equivalent visualization of ICH in PWLS images compared to a conventional penalty and supports the application of CBCT for ICH detection at the point of care in the ICU and/or operating theater.

References

[1] Parizel, *et al.* "Intracranial hemorrhage: principles of CT and MRI interpretation," *Eur. Radiol.* (2001)
[2] Xu, *et al.* "Design and characterization of a dedicated cone-beam CT scanner for detection of acute intracranial hemorrhage," *Proc. SPIE* (2016)
[3] Sisniega, *et al.* "High-fidelity artifact correction for cone-beam CT imaging of the brain," *Phys. Med. Biol.* (2015)
[4] Dang, *et al.* "Statistical reconstruction for cone-beam CT with a post-artifact-correction noise model: application to high-quality head imaging," *Phys. Med. Biol.* (2015)
[5] Fessler, *et al.* "Spatial resolution properties of penalized-likelihood image reconstruction: space-invariant tomographs," *IEEE Image Proc.* (1996)
[6] Wagner, *et al.* "An assortment of image quality indexes for radiographic film-screen combinations---can they be resolved?" *Proc. SPIE* (1972)
[7] ICRU Report 54, "Medical Imaging-The Assessment of Image Quality"
[8] Yang, *et al.* "Regularization design in penalized maximum-likelihood image reconstruction for lesion detection in 3D PET," *Phys. Med. Biol.* (2014)
[9] Gang, *et al.* "Task-based detectability in CT reconstruction by filtered backprojection and penalized likelihood estimation," *Med. Phys.* (2014)
[10] Gang, *et al.* "Analysis of Fourier-domain task-based detectability index in tomosynthesis and cone-beam CT in relation to human observer performance," *Med. Phys.* (2011)
[11] Erdoğan, *et al.* "Ordered subsets algorithms for transmission tomography," *Phys. Med. Biol.* (1999)

A Biomechanical Modeling Guided CBCT Reconstruction Technique (Bio-recon)

You Zhang, Joubin Nasehi Tehrani, Jing Wang

***Abstract*—2D-3D deformation has emerged as a new CBCT reconstruction technique through deforming a prior high-quality CT/CBCT image to the new on-board CBCT image, guided by limited-view projections. The accuracy of this intensity-based technique, however, is often limited in low-contrast image regions with subtle intensity differences. The solved deformation vector fields (DVFs) may also be biomechanically unrealistic. To address these problems, this study developed a biomechanical modeling guided CBCT reconstruction technique (Bio-recon), through combining the 2D-3D deformation with finite element analysis based biomechanical modeling of anatomical structures. The reconstruction accuracy of the Bio-recon technique was compared to that of the 2D-3D deformation technique using eleven lung cancer patients, both in the image domain and in the DVF domain through clinician tracked lung landmarks.**

I. Introduction

CBCT imaging has nowadays become the routine clinical practice for image-guided radiation therapy. However, frequent imaging for daily treatments introduces additional radiation dose to patients, increasing the risk of secondary cancers. In addition, the CBCT image quality is often impaired by increased scatter with less accurate Hounsfield units. Recently, a new CBCT reconstruction approach has been investigated, which reconstructs the new on-board CBCT through deforming a previously acquired high-quality CT/CBCT image [1-4]. The deformation of the 3D image is guided by the acquired 2D on-board projections (2D-3D deformation). With the high-quality image as prior information, the imaging dose can be substantially reduced by acquiring much fewer projections for reconstruction. The deformation approach also passes along the accurate Hounsfield units from the high-quality prior image to the reconstructed CBCT image, enabling more accurate dose calculation for radiation therapy [5].

Currently the available 2D-3D deformation techniques are purely intensity-based, aiming to match the intensity maps between the acquired on-board projections and the simulated projections from the deformed CBCT images. This approach usually works well for high-contrast regions. However, its accuracy is often limited in low-contrast regions with subtle intensity differences. In addition, the solved deformation fields may not be biomechanically realistic, as the deformation fails to consider the elastic properties of anatomical structures. To address these problems, in this study we developed a biomechanical modeling guided CBCT reconstruction technique (Bio-recon), which combined the 2D-3D deformation technique with finite element analysis based biomechanical modeling (FEM) [6-11] of anatomical structures. The reconstruction accuracy of the Bio-recon technique was evaluated using eleven lung patients and compared to that of the 2D-3D deformation technique.

You Zhang, Joubin Nasehi Tehrani and Jing Wang are with the Department of Radiation Oncology, UT Southwestern Medical Center at Dallas, Dallas, TX 75390 USA (e-mail: you.zhang@utsouthwestern.edu, Joubin.Nasehitehrani@utsouthwestern.edu, jing.wang@utsouthwestern.edu).

II. Materials and Methods

In general, Bio-recon extracted the deformation fields generated by 2D-3D deformation at high-contrast structure boundaries as the boundary condition, and used this boundary condition to drive finite element analysis to optimize the deformation fields within the structure boundaries. The optimized deformation fields were then fed back into the 2D-3D deformation as a new starting point for further optimization, which formed an iterative loop. Details of the 2D-3D deformation technique, the biomechanical modeling of lungs, and the whole work-flow of Bio-recon were introduced below:

II.A. Inverse-consistent 2D-3D deformation technique

In common practices, the deformation fields were defined on the new CBCT image voxel grids and pointed back to the prior image. However, since the biomechanical modeling of structures was based on the prior image and the boundary condition was defined on the prior image, the inverse deformation fields defined on prior image voxel grids were also needed. To address this problem, in this study inverse-consistent [12] 2D-3D deformation was performed, which could be formulated as an optimization problem shown in Eq. 1 and Eq. 2:

$$\begin{aligned}\boldsymbol{DVF} = \\ argmin\Big\{\big\|\boldsymbol{\mathcal{A}}Def\big(I_{prior},\ \boldsymbol{DVF}\big) - P\big\|_2^2 + \\ \big\|\boldsymbol{\mathcal{A}_{inverse}}Def\big\{Def\big(I_{prior},\ \boldsymbol{DVF}\big),\ \boldsymbol{DVF_{inverse}}\big\} - P_{inverse}\big\|_2^2 + \\ \omega * E(\boldsymbol{DVF}) + \omega * E(\boldsymbol{DVF_{inverse}})\Big\}\end{aligned} \quad (1)$$

$$\boldsymbol{DVF_{inverse}} = -\boldsymbol{DVF} \quad (2)$$

$\boldsymbol{DVF}$ denotes the deformation vector field defined on the new CBCT image voxel grids. $\boldsymbol{DVF_{inverse}}$ denotes the inverse deformation vector field defined on the prior image voxel grids, of which the sign of values was opposite to that of $\boldsymbol{DVF}$ (Eq. 2). I_{prior} denotes the high-quality prior image. $Def(*)$ denotes the deformation operation. $\boldsymbol{\mathcal{A}}$ denotes the projection matrix of the on-board projections P corresponding to the new CBCT image. $\boldsymbol{\mathcal{A}_{inverse}}$ denotes the projection matrix of the simulated projections $P_{inverse}$ corresponding to the prior image. $E(*)$ computes the deformation energy [1], which is to regularize the smoothness of both $\boldsymbol{DVF}$ and $\boldsymbol{DVF_{inverse}}$. ω denotes the weighting factor balancing the data fidelity term and the

deformation energy term. The symmetric terms in Eq. 1 were enforced to optimize the inverse-consistency of ***DVF***, such that Eq. 2 will be able to hold.

II.B. Biomechanical modeling of the lung

In this study the lung was modelled as an uncoupled hyper-elastic Mooney-Rivlin material, of which the accuracy was validated in previous publications [11, 13]. The uncoupled Mooney-Rivlin material can be described as:

$$SE = c_1(\tilde{I}_1 - 3) + c_2(\tilde{I}_2 - 3) + 0.5K(lnJ)^2 \quad (3)$$

SE denotes the strain-energy. $\tilde{I}_1$ and $\tilde{I}_2$ denote the first and second invariants of the deviatoric right Cauchy-Green deformation tensor. c_1 and c_2 denote the corresponding material parameters for $\tilde{I}_1$ and $\tilde{I}_2$. K denotes the bulk modulus and J denotes the determinant of the deformation gradient tensor. In this study, we chose $c_1 = c_2 = 0.135\ kPa$ and $K = 27$ as the material parameters [6, 8, 11].

The lung biomechanical modeling can be described in three steps:

1. Perform lung segmentations. The lungs were segmented using the ITK-SNAP software [14]. By ITK-SNAP, an intensity threshold was first applied on the prior image to select the region of interest (ROI). An automatic segmentation based on the level-set method was subsequently performed within the ROI. The automatic segmentations were manually fine-tuned as the last step to correct the residual errors.

2. Based on the lung segmentation, tetrahedral meshes were built using the Iso2Mesh package [15]. In detail, first a coarse 3D tetrahedral mesh was generated using Tetgen [16]. Then the mesh surface was extracted from the coarse mesh and underwent automatic check and repair. Laplacian smoothing was further applied to smooth the mesh surface. Based on the repaired and smoothed mesh surface, a new high-quality volumetric tetrahedral mesh was re-generated by Tetgen for FEM.

3. The boundary condition was defined as the deformation fields of the tetrahedral nodes on the mesh surface, which were extracted from the inverse deformation fields solved by 2D-3D deformation. The biomechanical lung DVF was then derived through combining the uncoupled Mooney-Rivlin hyper-elastic material modeling, the tetrahedral mesh and the extracted boundary condition. In this study, the FEBio package [17] was used to perform the final finite element analysis to solve the lung biomechanical DVF.

Note that the lung biomechanical DVF was defined on the nodes of the tetrahedral mesh. To convert the DVF defined on nodes to the DVF defined on the prior image voxel grids, the barycentric coordinates [18] of each prior image voxel were computed to find its corresponding tetrahedral element. Then the DVF of each voxel was calculated by weighting the DVFs of the four tetrahedral element nodes using the barycentric coordinates.

The whole work-flow of the Bio-recon technique was shown in Figure 1.

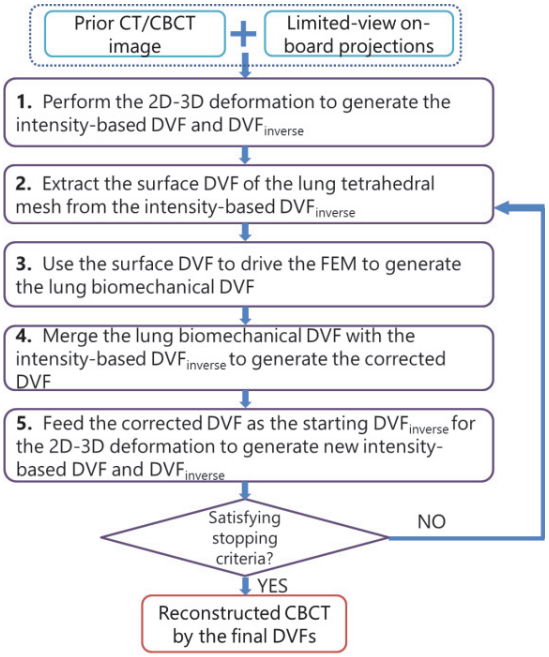

Fig. 1: Flow-chart of the Bio-recon technique.

II.C. Patient study and evaluation

Eleven patients were used to evaluate the efficacy of the Bio-recon technique, each with a 4D-CT set [8]. For each patient, ~80 anatomical landmarks were manually identified by a clinician for lung vascular and bronchial bifurcations, on both the end-expiration (EE) and end-inspiration (EI) 4D-CT phase images to track the lung motion. In total 872 landmarks were tracked for the eleven patients. For each patient, the 4D-CT EE phase was used as the prior CT image. The EI phase was used as the new image to simulate on-board projections for CBCT reconstruction. Different numbers of projections spreading across a full 360° scan angle were simulated, ranging from 5, 10 to 20, to represent different angular sampling sparseness.

The reconstructed CBCT volumes were compared with the 'ground-truth' 4D-CT EI volumes to evaluate the reconstruction accuracy via the root mean squared error (RMSE) metric. The solved DVFs by the Bio-recon technique, representing the deformation between the EE and EI phases, were also compared to the tracked landmark motion for accuracy evaluation.

For comprehensive evaluation, the reconstruction accuracy of the Bio-recon technique was also compared to that of the inverse-consistent 2D-3D deformation technique. Compared to Bio-recon, the 2D-3D deformation technique fed the DVF solved from the previous iteration directly into the next iteration as a new starting point, without performing the FEM-based biomechanical correction shown as steps 2-4 in the flow-chart of Fig. 1.

III. RESULTS

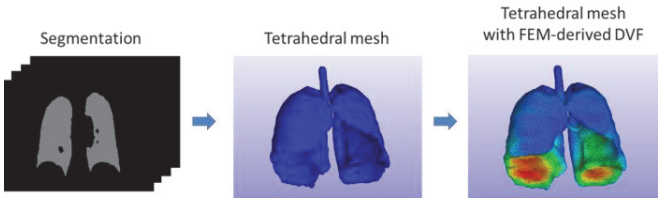

Fig. 2: Work-flow of the lung biomechanical modeling.

As shown in Fig. 2, the tetrahedral mesh was generated from the lung segmentation. And the FEM DVF was derived based on the uncoupled Mooney-Rivlin hyper-elastic material model and the boundary conditions extracted from 2D-3D deformation-generated DVFs. The FEM DVF was color-coded with hotter regions indicating larger deformations.

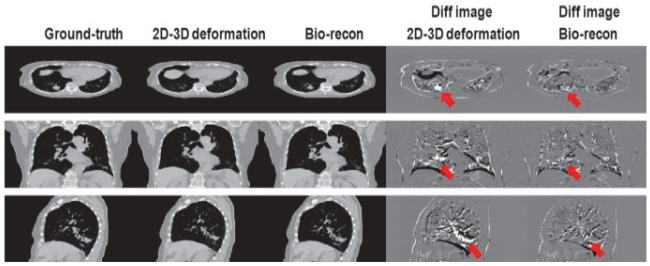

Fig. 3: Slice cuts of the 'ground-truth' 4D-CT EI image, the reconstructed CBCT image by the 2D-3D deformation technique, the reconstructed CBCT image by the Bio-recon technique, and the corresponding difference images between the 'ground-truth' and the reconstructed images. 10 projections were used for reconstruction.

Fig. 3 compares the reconstruction accuracy between the 2D-3D deformation technique and the Bio-recon technique using difference images. As can be clearly seen, Bio-recon has substantially reduced the mismatches inside the lung.

Table 1: RMSE results between the reconstructed images and the 'ground-truth' 4D-CT EI phase images for each patient, based on different angular sampling sparseness (by different numbers of projections) and different reconstruction methods. 'Original' RMSE shows the RMSE between the prior image (4D-CT EE phase) and the 'ground-truth' new image (4D-CT EI phase).

Patients	Original RMSE	RMSE after CBCT Reconstruction					
		2D-3D Deformation: 5 proj	Bio-recon: 5 proj	2D-3D Deformation: 10 proj	Bio-recon: 10 proj	2D-3D Deformation: 20 proj	Bio-recon: 20 proj
P01	15.32%	11.15%	11.19%	10.31%	9.62%	9.19%	8.60%
P02	18.89%	13.60%	13.97%	13.55%	12.01%	10.07%	10.10%
P03	14.11%	10.67%	9.55%	10.20%	8.52%	8.22%	7.76%
P04	19.49%	15.87%	12.77%	14.06%	10.45%	9.46%	8.92%
P05	20.07%	13.81%	13.69%	11.31%	11.11%	9.51%	9.25%
P06	13.18%	9.21%	8.97%	8.63%	8.07%	7.14%	7.17%
P07	18.24%	13.41%	11.23%	10.17%	9.17%	8.70%	7.89%
P08	23.15%	16.06%	14.40%	15.59%	11.50%	9.95%	9.46%
P09	18.52%	11.65%	11.62%	10.39%	10.50%	9.35%	9.51%
P10	20.90%	17.02%	14.63%	15.76%	12.22%	12.06%	9.99%
P11	19.64%	13.03%	12.94%	12.45%	11.07%	10.01%	9.34%
Average ± S.D.	**18.32 ± 2.86%**	**13.23 ± 2.32%**	**12.27 ± 1.83%**	**12.04 ± 2.29%**	**10.39 ± 1.32%**	**9.42 ± 1.18%**	**8.91 ± 0.91%**

Table 2: (Average ± S.D.) Residual errors of DVF tracked landmark motion between the prior image and the reconstructed image for each patient, based on different angular sampling sparseness (by different numbers of projections) and different reconstruction methods. 'Landmark motion' shows the (average ± S.D.) motion amplitude of landmarks manually tracked between the prior image (4D-CT EE phase) and the 'ground-truth' new image (4D-CT EI phase).

Patients	Landmark Motion (mm)	Residual errors after CBCT reconstruction (mm)					
		2D-3D Deformation: 5 proj	Bio-recon: 5 proj	2D-3D Deformation: 10 proj	Bio-recon: 10 proj	2D-3D Deformation: 20 proj	Bio-recon: 20 proj
P01	6.4 ± 3.1	5.5 ± 2.1	3.6 ± 1.9	5.5 ± 2.1	2.9 ± 1.6	5.4 ± 2.1	2.7 ± 1.4
P02	6.2 ± 6.9	5.3 ± 5.6	3.9 ± 4.1	5.7 ± 6.1	3.4 ± 3.4	4.8 ± 5.1	3.0 ± 2.7
P03	6.8 ± 3.8	5.6 ± 3.3	3.0 ± 1.9	5.9 ± 3.5	2.7 ± 1.6	4.8 ± 3.1	2.7 ± 1.5
P04	6.3 ± 4.8	5.8 ± 4.3	3.7 ± 3.0	5.7 ± 4.2	3.2 ± 2.7	4.6 ± 3.2	2.9 ± 2.4
P05	5.4 ± 2.7	4.6 ± 2.4	3.3 ± 1.9	4.3 ± 2.3	3.0 ± 1.7	3.7 ± 2.3	2.6 ± 1.5
P06	6.2 ± 2.2	4.7 ± 1.4	2.8 ± 1.4	5.2 ± 1.6	2.8 ± 1.4	3.9 ± 1.6	2.7 ± 1.5
P07	4.3 ± 3.2	4.0 ± 2.6	2.8 ± 1.7	3.6 ± 2.4	2.8 ± 1.8	3.5 ± 2.4	2.8 ± 2.0
P08	6.1 ± 5.1	5.4 ± 4.3	3.4 ± 2.3	5.4 ± 4.4	3.0 ± 2.0	4.1 ± 3.6	2.8 ± 1.9
P09	4.3 ± 2.6	3.4 ± 2.1	2.0 ± 1.4	3.2 ± 2.1	1.9 ± 1.3	2.8 ± 2.0	1.7 ± 1.2
P10	8.3 ± 6.4	7.8 ± 5.8	4.9 ± 4.2	7.6 ± 5.6	4.2 ± 3.4	6.8 ± 4.9	3.7 ± 3.0
P11	10.8 ± 7.8	8.1 ± 5.3	5.1 ± 3.8	8.6 ± 5.8	4.5 ± 3.2	7.8 ± 5.3	3.8 ± 2.7
Average ± S.D.	**6.5 ± 5.1**	**5.5 ± 4.1**	**3.5 ± 2.9**	**5.6 ± 4.3**	**3.1 ± 2.4**	**4.8 ± 3.8**	**2.9 ± 2.1**

Table 1 and Table 2 show the RMSE values and the residual errors of DVF tracked landmark motion, respectively. The Bio-recon technique offered better accuracy as compared to the 2D-3D deformation technique, especially in Table 2.

IV. DISCUSSION

Bio-recon has achieved substantial improvement as compared to the 2D-3D deformation technique, especially on the DVF accuracy. The results suggested that incorporating organ biomechanical modeling into reconstruction helped to achieve more realistic DVFs based on the material elastic properties, which could be viewed as additional constraints that helped the DVF optimization. Since FEM derived the biomechanical DVFs through considering each tetrahedral element in the organ mesh, it also helped to correct the erroneous DVFs in the low-contrast regions not well deformed by the intensity-based 2D-3D deformation technique. The corrected low-contrast regions in turn helped to improve the DVFs in the high-contrast regions through the iterative approach of Bio-recon, which generated better deformed images in both low-contrast and high-contrast regions as compared to the 2D-3D deformation technique (Fig. 3).

Another interesting observation is that using 20 projections for reconstruction, the superiority of the Bio-recon technique over the 2D-3D deformation technique on the RMSE values became less prominent (Table 1). However, the Bio-recon technique still enjoyed much better DVF accuracy as compared to the 2D-3D deformation technique (Table 2). It suggested that good RMSE values did not necessarily indicate high-quality deformation and reconstruction. The DVFs could be unrealistic, even with a high RMSE value, which would lead to substantial

errors if the solved DVFs were used for motion tracking or treatment dose accumulation in radiation therapy.

Constant elasticity parameters were used in this study for all the patients. Previous studies suggested that the elastic parameters were usually patient-specific, depending on the age, the disease type and the disease location [8]. Biomechanical modeling based on patient-specific elasticity parameters may further improve the reconstruction accuracy, which will be investigated in the future.

Currently the lung was modeled as an isotropic, homogeneous organ with the same elasticity parameters. In reality, the biomechanical parameters of the lung can vary between different lung lobes and between the lung and the tumor. The elasticity parameters are also different between the parenchyma, the lung vessels, and the lung bronchial trees. Though previous studies have validated the accuracy and efficacy of modeling the lung as a whole homogeneous organ [6, 8], further studies are warranted to investigate the potential benefits of exploring the lung heterogeneity [10] to further improve the reconstruction accuracy. In addition, biomechanical modeling of other structures, including the spine, the ribs and the chest wall, may also help to further improve the reconstruction accuracy.

In this study, the accuracy of the developed Bio-recon technique was evaluated using eleven lung cancer patients. The Bio-recon technique is also promising for the liver CBCT reconstruction, of which the accuracy usually suffers from low soft-tissue contrasts inside the liver. Application of this technique to improve the reconstruction quality of liver CBCT is currently in progress.

V. Conclusion

The Bio-recon technique substantially improved both the reconstructed image quality and the DVF accuracy, showing the benefit of incorporating material biomechanical properties into DVF optimization and image reconstruction.

Acknowledgment

This work was supported by grants from the American Cancer Society (RSG-13-326-01-CCE), from the US National Institutes of Health (R01 EB020366), and from the Cancer Prevention and Research Institute of Texas (RP130109). The contents of this article are solely the responsibility of the authors and do not necessarily represent the official views of the funding agencies.

REFERENCES

[1] Y. Zhang, F. F. Yin, W. P. Segars, and L. Ren, "A technique for estimating 4D-CBCT using prior knowledge and limited-angle projections," *Med Phys,* vol. 40, p. 121701, Dec 2013.

[2] Y. Zhang, F. F. Yin, T. Pan, I. Vergalasova, and L. Ren, "Preliminary clinical evaluation of a 4D-CBCT estimation technique using prior information and limited-angle projections," *Radiother Oncol,* Mar 25 2015.

[3] J. Wang and X. Gu, "High-quality four-dimensional cone-beam CT by deforming prior images," *Phys Med Biol,* vol. 58, pp. 231-46, Jan 21 2013.

[4] J. Wang and X. Gu, "Simultaneous Motion Estimation and Image Reconstruction (SMEIR) for 4D Cone-Beam CT," *Medical Physics,* vol. 40, Jun 2013.

[5] Y. Zhang, F. F. Yin, and L. Ren, "Dosimetric verification of lung cancer treatment using the CBCTs estimated from limited-angle on-board projections," *Med Phys,* vol. 42, pp. 4783-95, Aug 2015.

[6] K. K. Brock, M. B. Sharpe, L. A. Dawson, S. M. Kim, and D. A. Jaffray, "Accuracy of finite element model-based multi-organ deformable image registration," *Med Phys,* vol. 32, pp. 1647-59, Jun 2005.

[7] A. Al-Mayah, J. Moseley, and K. K. Brock, "Contact surface and material nonlinearity modeling of human lungs," *Phys Med Biol,* vol. 53, pp. 305-17, Jan 7 2008.

[8] R. Werner, J. Ehrhardt, R. Schmidt, and H. Handels, "Patient-specific finite element modeling of respiratory lung motion using 4D CT image data," *Med Phys,* vol. 36, pp. 1500-11, May 2009.

[9] H. Zhong, J. Kim, H. Li, T. Nurushev, B. Movsas, and I. J. Chetty, "A finite element method to correct deformable image registration errors in low-contrast regions," *Phys Med Biol,* vol. 57, pp. 3499-515, Jun 7 2012.

[10] M. Li, E. Castillo, X. L. Zheng, H. Y. Luo, R. Castillo, Y. Wu*, et al.*, "Modeling lung deformation: a combined deformable image registration method with spatially varying Young's modulus estimates," *Med Phys,* vol. 40, p. 081902, Aug 2013.

[11] J. N. Tehrani, Y. Yang, R. Werner, W. Lu, D. Low, X. Guo*, et al.*, "Sensitivity of tumor motion simulation accuracy to lung biomechanical modeling approaches and parameters," *Phys Med Biol,* vol. 60, pp. 8833-49, Nov 21 2015.

[12] D. Yang, H. Li, D. A. Low, J. O. Deasy, and I. El Naqa, "A fast inverse consistent deformable image registration method based on symmetric optical flow computation," *Phys Med Biol,* vol. 53, pp. 6143-65, Nov 7 2008.

[13] A. D. Freed, J. Carson, D. Einstein, and R. E. Jacob, "Viscoelastic model for lung parenchyma for multi-scale modeling of respiratory system phase II: Dodecahedral micro-model," *Pacific Northwest National Laboratory (Battelle),* 2012.

[14] P. A. Yushkevich, J. Piven, H. C. Hazlett, R. G. Smith, S. Ho, J. C. Gee*, et al.*, "User-guided 3D active contour segmentation of anatomical structures: significantly improved efficiency and reliability," *Neuroimage,* vol. 31, pp. 1116-28, Jul 1 2006.

[15] Q. Q. Fang and D. A. Boas, "Tetrahedral Mesh Generation from Volumetric Binary and Gray-Scale Images," *2009 Ieee International Symposium on Biomedical Imaging: From Nano to Macro, Vols 1 and 2,* pp. 1142-1145, 2009.

[16] H. Si, "TetGen, a Delaunay-Based Quality Tetrahedral Mesh Generator," *Acm Transactions on Mathematical Software,* vol. 41, Jan 2015.

[17] S. A. Maas, B. J. Ellis, G. A. Ateshian, and J. A. Weiss, "FEBio: finite elements for biomechanics," *J Biomech Eng,* vol. 134, p. 011005, Jan 2012.

[18] Z. Zhong, X. Gu, W. Mao, and J. Wang, "4D cone-beam CT reconstruction using multi-organ meshes for sliding motion modeling," *Physics in medicine and biology,* vol. 61, p. 996, 2016.

Motion Evoked Artifact Deconvolution

Brian E. Nett[1], Jang Hwan Cho [2], and Jed D. Pack [3]
[1] GE Healthcare, 3000 N. Grandview Blvd., W-1180, Waukesha WI , USA
[2] Endra, Inc, 3600 Green Ct #350, Ann Arbor, MI , USA
[3] GE Global Research Center, One Research Circle, Niskayuna, NY USA,

I. Introduction

In computed tomography (CT) reconstruction the image function to be reconstructed, $f(x, y, z)$, is generally assumed to be stationary during the acquisition. When this assumption is violated motion artifacts become apparent in the reconstructed images due to the inconsistency between projections as the image function is really a function of time as well, $f(x, y, z, t)$. Motion compensation techniques have been developed which make an estimate of the time dependent changes and account for these changes in the reconstruction. Several such approaches have been developed in the literature. One specific implementation of a motion estimation and correction algorithm is the SnapShot Freeze (SSF) algorithm from GE Healthcare [1]. The SSF algorithm uses three reconstructed image volumes as input: identifies the coronary arteries, estimates the motion in the coronary arteries and compensates for the motion near the coronary arteries. In this work we present a straightforward method which may be used in conjuction with a vessel specific motion estimation and compensation approach. The aim of this algorithm is to reduce the residual motion artifacts adjacent to the cardiac chambers. These artifacts are caused by the fact that the chambers (e.g. the left ventricle (LV)) may deform rapidly during the acquisition. Since the contrast in the LV is much greater than the surrounding myocardium these inconsistencies can lead to false hyper-attenuation and hypo-attenuation in the myocardium. The technique proposed here aims to mitigate these errors by correcting for the change in the contrast enhanced region throughout the scan. This method is termed Motion Evoked Artifact Deconvolution (MEAD), as this approach is analogous to a deconvolution operation. In the case of cardiac imaging MEAD may be applied in combination with targeted motion estimation and compensation processing such that the images will have been corrected in both the vessels and the myocardium. MEAD is also computationally inexpensive compared with fully iterative techniques aimed at solving the same problem.

II. Methods

A. Algorithm Description

This algorithm has been developed in a general manner and may apply to a variety of areas where motion artifacts exist. Since the primary motivation of this work is for cardiac imaging we use cardiac specific terminology below. However, one may directly substitute the contrast filled myocardium with any other image feature that generates artifacts in the neighboring tissue due to significant differences in attenuation values. The primary goal of this algorithm in this specific context is to correct for the areas of false hyper-attenuation and hypo-attenuation in the myocardium which are caused by changes in the contrast throughout the acquisition time window. In this section we provide a description of the algorithm. We first begin by defining several variables that will be used throughout the description. For simplicity the dependent variables are suppressed.

- $_{\Phi_N}$ - the phase corresponding to a given set of data, (i.e. the center phase) of that data
- N - integer number, corresponds to the prescribed phase, where $(2 \cdot N - 1)$ total phases are used
- y - projection data
- y_{meas} - measured projection data, assumed to be pre-processed
- f - image data
- F - Fourier transform of the image data
- R - Radon transform, more generally the forward x-ray projection operator
- R^{-1} - inverse Radon transform, more generally CT reconstruction such as FBP (Filtered-BackProjection) type, FBPD (Filtering the BackProjection of Differentiated data) type or iterative reconstruction.
- FFT - Fast Fourier Transform
- $IFFT$ - Inverse Fast Fourier Transform
- HT - Hard Thresholding operation
- LP - Low Pass filter
- ^{con} - contains only high contrast material such as iodinated contrast and bone
- ^{residual} - the difference between the reconstruction incorporating changing contrast and the reconstruction of the contrast at one phase
- ^{mead} - the final output image, (Motion Evoked Artifact Deconvolution)

The general flow for the algorithm is depicted in Figures 1 and Figure 2. The assumption is that some contribution to artifacts in the myocardium is caused due to inconsistencies caused by the change of shape of the highly attenuating chamber, which is directly adjacent to the myocardium. These are the artifacts which this algorithm aims to address, and artifacts such as beam hardening are outside the current scope. This algorithm can be viewed simply as two steps: Step 1- create a forward model to reproduce the artifacts due to motion

of the chamber (Figure 1), Step 2- subtract the motion evoked artifacts from the initial image (Figure 2). This process is analogous to a deconvolution of the artifacts caused by the motion of the contrast filled chamber.

We begin by explaining Step 1, where the forward model of the motion artifacts is created. Here the term forward model should not be confused with the forward projection operator; rather, the forward motion model is the generation of an image which simulates the motion artifacts. Starting from the measured projection data multiple images are reconstructed at different phases, assume here $(2 \cdot N - 1)$ total phases are used, where the image f_{Φ_N} corresponds to the prescribed image. After images are reconstructed at multiple phases a hard thresholding operation is applied to the images such that the only non-zero contributions in the image are above a given HU (Hounsfield Unit) threshold. Thus after the thresholding only bone, injected contrast and foriegn material such as implanted metal will have non-zero values. A possible varation not demonstrated here would be to use multiple thresholding levels such that the values below a certain threshold would also be included. For the purpose of this description the abreviation $(^{con})$ will be used here as in this case the thresholding is performed with the aim of identifying the areas of high contrast $(^{con})$ relative to tissue and motion of these objects can induce artifacts. A forward projection operation in the native coordinates then may be used to estimate the projection through the reconstruction at each phase. These projections may then be combined using a smooth feathering weight for the contributions from the basis images. Finally the image may be reconstructed using a standard image reconstruction algorithm such as the Parker weighted FBP [2] (Figures 1). This image, $f^{con}_{\Phi_1:\Phi_{(2\cdot N-1)}}$, will contain the motion artifacts (hyper/hypo myocardial values) caused by inconsistencies in the high contrast object throughout the scan. Given the known relationship between projections and Fourier space we can also formulate this method in frequency space. For parallel-beam tomography the Fourier Slice Theorem provides a direct link between projection space and Fourier space. In the case of cardiac imaging using third generation geometry the mapping will not be exact as the Fourier Slice Theorem assumes that parallel projections are used in the acquisition. The difference lies in the fact that there is a slight time shift between the true parallel projection and the rebinned fan-beam projection. However, since this is a fraction of the time of the scan we do not believe this approximation will limit to the performance of this technique. Since the Fourier transform is significantly faster the forward projection in Figure 1 can be replaced with FFT, the view angle based smooth weighting of the projections is replaced with smoothing varying angular masks that are multiplied by the FFT (where the angular masks applied to neighboring basis images sum to unity), and the FBP reconstruction is replaced with the $IFFT$.

After obtaining the forward motion model, $f^{con}_{\Phi_1:\Phi_{(2\cdot N-1)}}$, we turn to Step 2 where we subtract the motion evoked artifacts from the original image. First the difference is taken between the forward motion model and the high contrast only image

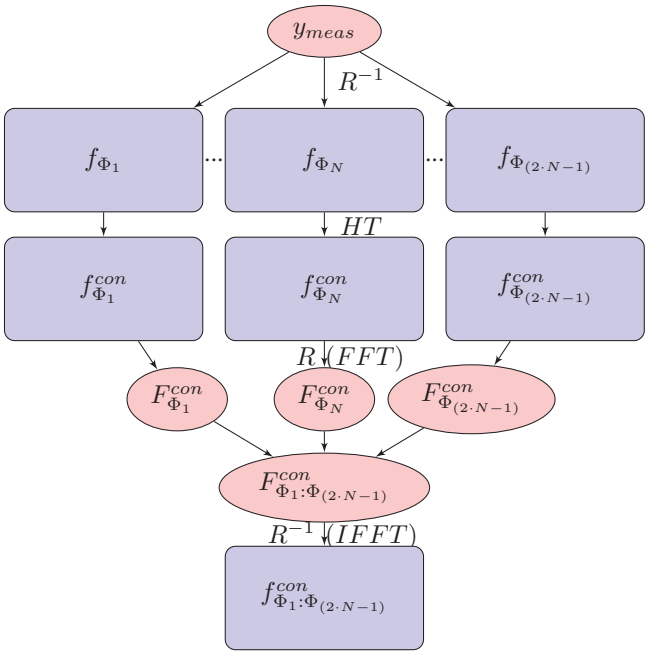

Fig. 1. Schematic diagram of the MEAD algorithm operating in $Fourier$ space, where the description of each step is given in the main text.

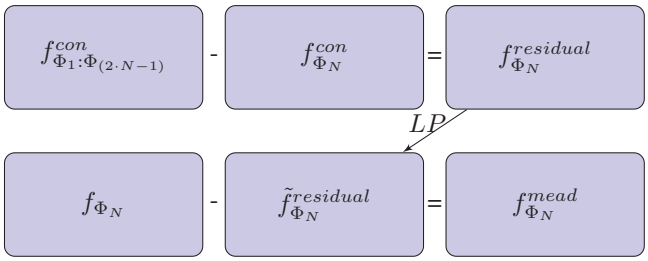

Fig. 2. The schematic operation to calculate the residual artifact image $f^{residual}_{\Phi_N}$ and subtract a filtered version of it from the original image f_{Φ_N}.

corresponding to the prescribed phase. This result is referred to here as $f^{residual}_{\Phi_N}$ and represents the artifacts evoked from high contrast objects. In the case that N is much less than the number of acquired views a low pass filter is applied to the residual to ensure that high frequency artifacts are not propagated to the final image. This choice is re-enforced by the knowledge that these motion evoked artifacts are low in frequency for clinically realistic motion of the high contrast object.

This concludes the general description of the MEAD algorithm. An additional step which is taken for the cardiac data is to define a map in image space where SSF is performed. The SSF map has smooth transitions between the regions where SSF is applied and where no SSF corrections were made. This mask is used such that the correction image, $\tilde{f}^{residual}_{\Phi_N}$, is set to zero within the region where SSF has been applied. In this manner the MEAD algorithm will not make any contribution to the reconstruction of the coronary arteries.

This behavior is desired as the SSF algorithm provides superior vessel correction as a true motion estimation and compensation algorithm is required for the coronary vessels.

Note, also that this algorithm may be applied in an iterative manner where the MEAD algorithm is applied to each of the input phases, and then the MEAD algorithm is applied again using the output from the first round of MEAD processing.

B. Input Datasets

The initial evaluation of the algorithm is performed on numerical phantoms and clinical scan data. The numerical phantom was generated from the XCAT anatomical and motion mode [3] and the forward projections were generated with Catsim[4]. The sample data presented here corresponds to a heart rate of 55bpm. Clinical data was taken from a Lightspeed VCT scanner with a gantry rotation period of 350ms. The heart rate for the patient data presented here was in the range of 78-80 bpm during the acquisition. The reconstructions for the clinical data were centered on 75% RR. The simulation data was performed with axial acquisitions with a gantry rotation period of 280ms and the first clinical data were from retrospectively gated helical scans. In Figure 3 we demonstrate each of the intermediate steps needed to generate the forward motion model for a given slice in a clinical data set (Step 1). After the forward motion model is computed it may be used in order to subtract the motion evoked artifacts (Step 2). For this same clinical case this procedure is demonstrated in Figure 4. The results were not found to be highly dependent on the threshold value used and a value of 200HU was used for results presented here.

III. Results

Numerical phantom results are shown in Figure 5 and Figure 6. The images in Figure 5 correspond to an active phase in the motion cycle (50% RR). The upper row are the images before and after the MEAD processing and the lower row are a subtraction from a reference image of the static XCAT phantom. Since the phase is not exactly matched the subtraction differences at the chamber boundaries are expected, and one should focus on the myocardium region in the subtraction images.

Several slices were chosen in uniform steps of 3.125mm in a clinical data set in order to demonstrate the effect of the MEAD processing on the reconstructed images. The first set of images (Figure 7) was generated in slices where the opacified chamber displayed significant motion. In addition to the comparison of axial slices which are in the identical location, we have included reformatted images from the AW (Advantage Workstation) where other planes through the volumes are displayed. These planes are oriented along the short axis (Figure 8) of the heart rather than along the planes relative to the scanner.

Finally, a demonstration of the possibility to perform multiple iterations of MEAD processing is presented. In this case MEAD was called for each of the input phases, thus MEAD was performed three times (i.e. the number of phases used) for

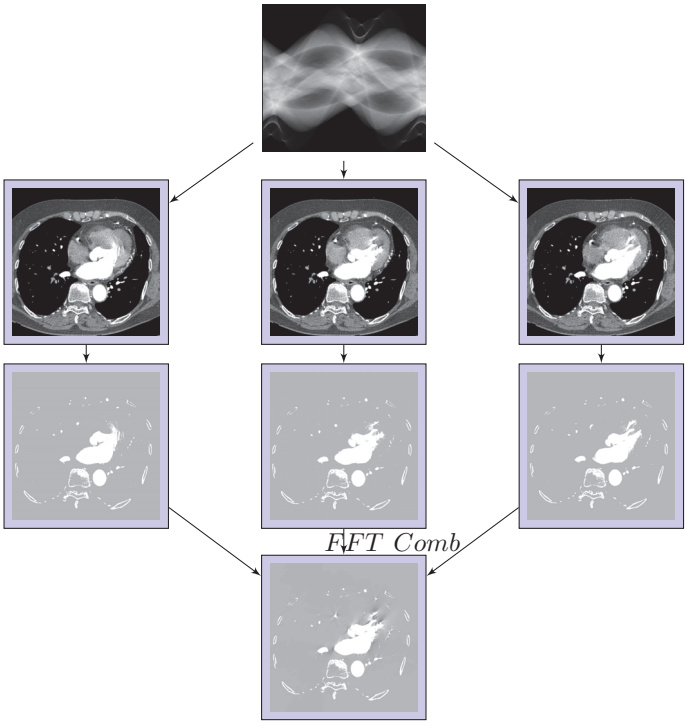

Fig. 3. The results of a slice from a clinical case processed with Step 1 of the MEAD algorithm, where the forward model of the motion artifacts is generated. Note, that the format for this diagram matches that of Figure 1 where the notation was introduced.

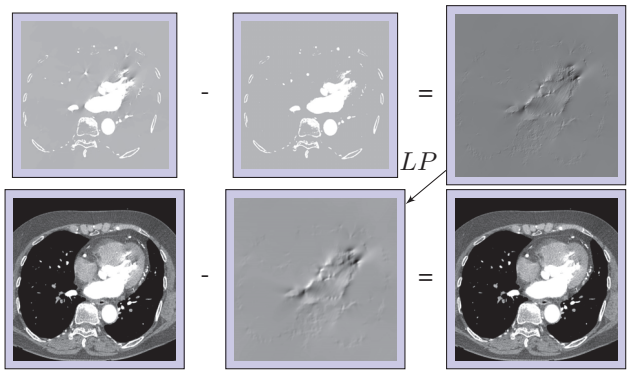

Fig. 4. The results of a slice from a clinical case processed with Step 2 of the MEAD algorithm, where the residual from the forward model of the motion artifacts is subtracted from the original. Note, that the format for this diagram matches that of Figure 2.

iteration 1 and one time for the second iteration. The results demonstrate that significant improvement is possible for the second iteration of MEAD processing (Figure 9).

IV. Conclusions

An adjunct method was presented for vessel specific motion estimation and compensation algorithms, which aims to reproduce motion artifacts in the myocardium and subtract these

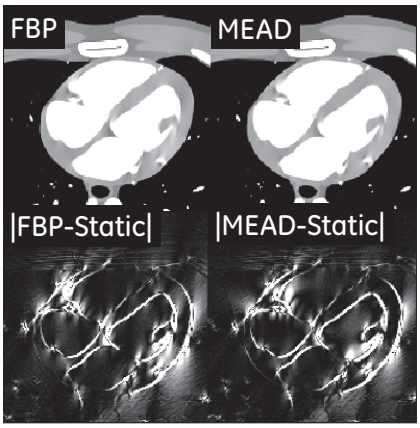

Fig. 5. Example images from the active motion phase of the XCAT phantom data before and after MEAD (upper row) [-200 200] HU, and the subraction from a static reference image (lower row) [0 50]HU.

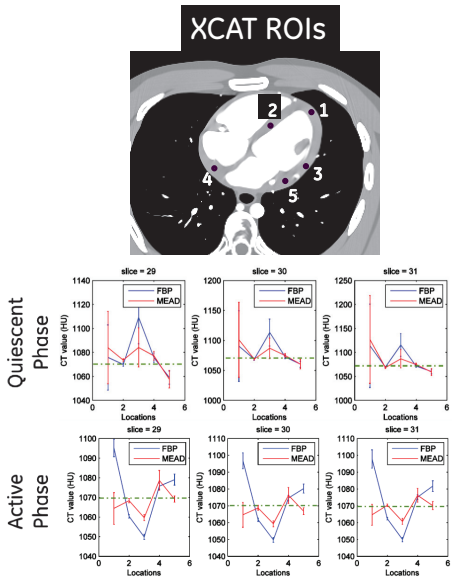

Fig. 6. Measurement results of the regions of interest (ROIs) in the myocardium for FBP and MEAD where the ROI locations are shown (upper panel) and the values in the ROIs are plotted relative to the reference value for the stationary phantom. The error bars correspond to the std deviation within each ROI.

artifacts from the initial reconstruction. Results were presented on phantom and clinical datasets.

References

[1] B. Nett, J. Pack, and D. Okerlund, "Task based assessment of a motion compensation algorithm via simulation of a moving stenotic vessel," *SPIE Medical Imaging.*, 2013.

[2] D. L. Parker, "Optimal short-scan convolution reconstruction for fan beam CT," *Med. Phys.*, vol. 9, pp. 254–257, 1982.

[3] W. Segars, M. Mahesh, T. Beck, E. Frey, and B. Tsui, "Realistic CT simulation using the 4D XCAT phantom," *Med. Phys.*, 2008.

[4] B. DeMan, S. Basu, N. Chandra, B. Dunham, P. Edic, M. Iatrou, S. McOlash, P. Sainath, C. Shaughnessy, B. Tower, and E. Williams, "CatSim: a new computer assisted tomography simulation environment," *SPIE Medical Imaging*, vol. 6510, p. 65102G, 2007.

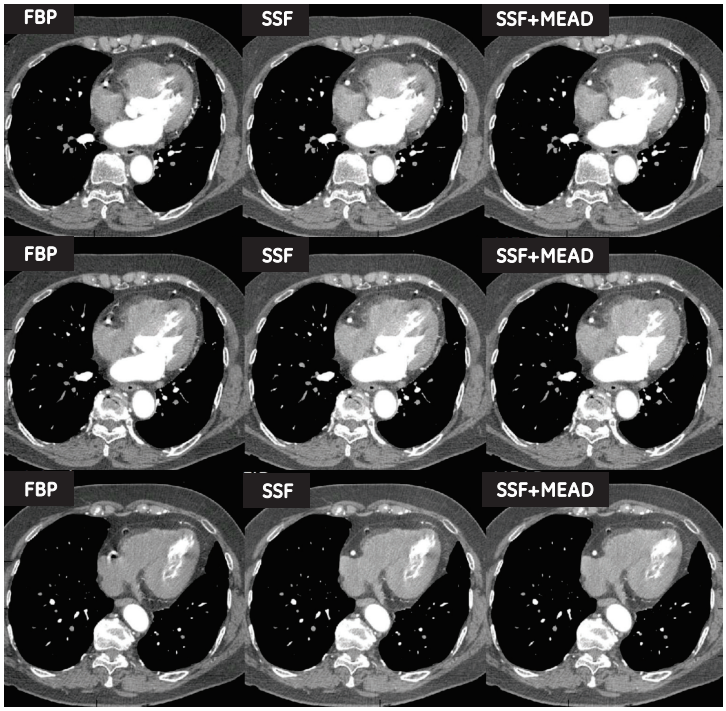

Fig. 7. Reconstruction results comparing the original image, the vessel corrected SSF image and the SSF+MEAD correction image (HR=78-80 bpm). [-300 300]HU

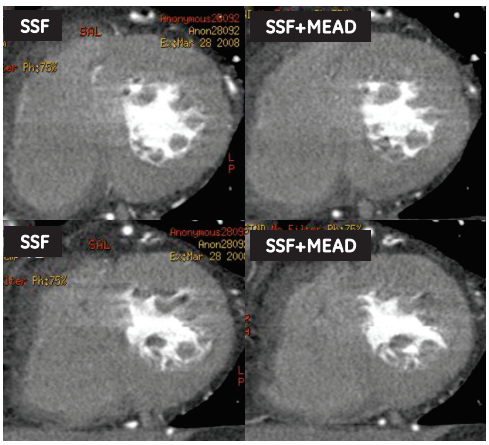

Fig. 8. Short axis reformats taken from a 3D workstation of approximately the same slices comparing SSF and SSF+ MEAD corrections. [-300 300]HU

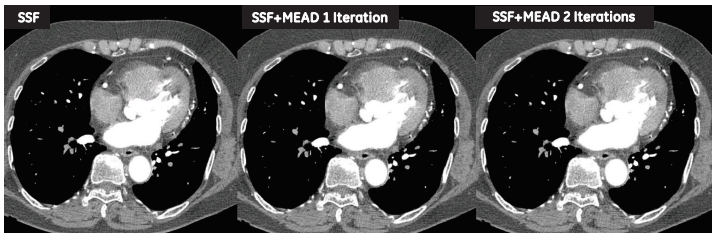

Fig. 9. Reconstruction results demonstrating the feasability of multiple iterations of MEAD processing. [-300 300]HU

Truncation Artifact Reduction by Exploiting Data Derivative and Image-TV Constraints in C-arm CBCT

Dan Xia, David A. Langan, Stephen B. Solomon, Hao Lai,
Zheng Zhang, Buxin Chen, Emil Y. Sidky, and Xiaochuan Pan

***Abstract*—The C-arm imager is used increasingly as a cone-beam computed tomography (CBCT) scanner in surgical and interventional procedures to provide information about the disease or tumor useful in guidance of its treatment. Analytic algorithms such as the FDK algorithm are employed currently for image reconstruction in C-arm CBCT imaging. However, analytic algorithm reconstructions often suffer from artifacts as a result of the presence of truncation, metal/high-contrast objects, and other data degrading factors. Evidence exists suggesting that optimization-based iterative algorithms may be more flexible in dealing with the data degrading factors than analytic algorithms. In this work, we have investigated optimization-based reconstruction from animal data collected with a clinical C-arm CBCT scanner. In the reconstruction, we use a derivative data fidelity term along with an image-total-variation (TV) constraint for dealing effectively with data truncation. The results of the study suggest that the optimization-based reconstruction with a data-derivative fidelity term may yield images with reduced truncation artifacts and enhanced low-contrast anatomy as compared to the clinical FDK reconstruction.**

Figure 1. Picture of GE Innova 4100 Angiographic Imaging System used in this work to acquire C-arm CBCT data.

I. Introduction

C-arm cone-beam computed tomography (CBCT) has been shown to be of value in image-guidance interventional/surgical procedures. For example, it has been used increasingly frequently in the treatment and management of liver diseases by yielding 3D spatial information of the diseases and and their feeding arteries, thus aiding in treatment planning and assisting interventional radiologists to navigate a catheter to the disease sites for embolization procedures [1]. In current clinical C-arm CBCT, analytic algorithms such as the FDK or its variants are used for image reconstruction from data are collected. The analytic algorithms require projection data with densely sampled views, and they are susceptible to data degrading factors such as data truncation, metal/high-contrast, and cone-beam artifacts.

In recent years, there exists an increased level of interest in optimization-based reconstructions, as evidence suggests that they may be more flexible in dealing with the data degrading factors, and in accommodating non-circular scanning configurations of practical interest, than analytic algorithms [2], [3]. In this work, we investigate optimization-based reconstruction from animal data collected with a clinical C-arm CBCT scanner. In the reconstruction, the image is designed by an optimization program in which a derivative data fidelity term is added, along with an image-total-variation (TV) constraint, for dealing effectively with data truncation. We apply a primal-dual algorithm developed by Chambolle and Pock (referred as to CP algorithm) to reconstruct the image by solving the optimization problem [4]. Data containing truncation were collected from a swine by use of the C-arm CBCT system. The results of the study suggest that the optimization-based reconstruction with a data-derivative fidelity term may yield images with reduced truncation artifacts and enhanced low-contrast anatomy as compared to the clinical FDK reconstruction.

D. Xia, Z. Zhang, B. Chen, E. Y. Sidky, and X. Pan are with the Department of Radiology, The University of Chicago, Chicago, IL 60637, USA.

D. A. Langan and H. Lai are with GE Global Research Center, Niskayuna, NY 12309, USA.

S. B. Solomon is with Memorial Sloan Kettering Cancer Center, New York, NY 10065, USA.

II. Materials and methods

A. Data acquisition

A C-arm system (GE Healthcare, Innova 4100 Angiographic Imaging System) as shown in Fig. 1 was used to acquire the C-arm CBCT data. This system consists of an X-ray source and a flat-panel detector, mounted onto the opposing ends of the C-arm. The distances from X-ray source to the rotation center and to the detector are 720 mm and 1165 mm, respectively. A swine was scanned at Memorial Sloan Kettering Cancer Center with clinical protocols, 148-view projection data over an angular range of 200 degrees were acquired. Since the field of view (FOV) of this C-arm CT system can not cover the

whole transverse section of the scanned swine, the projection data was truncated. Since the trajectory of the X-ray source mounted on a C-arm gantry is in general not an ideal circular trajectory due to mechanical flexion and other factors, a geometric projection matrix representing the mapping between detector and image spaces [5] was incorporated into the image reconstructions to account for the realistic scanning geometry, .

B. Optimization-based image reconstruction

1) Optimization-based reconstruction program: A process of a C-arm CBCT imaging can be modeled by a linear discrete-to-discrete model,

$$\mathbf{g} = \mathcal{H}\mathbf{f}, \tag{1}$$

where vectors $\mathbf{g}$ and $\mathbf{f}$ denote the discrete model data and image, and system matrix $\mathcal{H}$ describes cone-beam X-ray transform. For the practical C-arm imaging, the actual C-arm scanning geometry is taken into account by incorporating the geometric projection matrix into the system matrix $\mathcal{H}$. the constrained optimization problem can be mathematically described as: [6]

$$\mathbf{f}^* = \underset{\mathbf{f}}{\operatorname{argmin}} D_W(\mathbf{g_m}, \mathcal{H}\mathbf{f}) \quad \text{s.t.} \quad ||\mathbf{f}||_{TV} \leq \gamma \quad \text{and} \quad f_i \geq 0, \tag{2}$$

where $||\mathbf{f}||_{TV}$ denotes the image total variation (TV), which is ℓ_1-norm of the gradient magnitude image, parameter $\gamma > 0$ is used to control the TV of the reconstructed image, the weighted ℓ_2-norm data fidelity, defined as

$$D_{\mathrm{w}}(\mathbf{g_m}, \mathcal{H}\mathbf{f}) \quad = \|\mathcal{F}_c(\mathcal{H}\mathbf{f} - \mathbf{g_m})\|_2^2 \quad , \tag{3}$$

$\mathcal{F}_c = (1-c)\mathcal{D}_u + c\mathcal{I}$, $\mathcal{I}$ is the identity matrix, and $\mathcal{D}_u$ depicts an antisymmetric matrix representing a finite differencing along the u-direction. When parameter $c = 1$, D_w becomes the regular data-ℓ_2 norm given by

$$D_{\ell_2}(\mathbf{g_m}, \mathcal{H}\mathbf{f}) = \|(\mathcal{H}\mathbf{f} - \mathbf{g_m})\|_2^2 . \tag{4}$$

Parameter c controls the contributions of D_{ℓ_2} and $\mathcal{D}_u$ to the optimization program. In this work, the operator $\mathcal{D}_u$ represents a convolution with a 3 point kernel $[-1, 0, 1]$. Since the operator $\mathcal{D}_u$ de-emphasizes the low-frequency components of the data, it may lower the sensitivity of the reconstruction to low-frequency data artifacts due to the data truncation. On the other hand, the second term, $c\mathcal{I}$ in $\mathcal{F}_c$ is introduced to compensate for the potential loss of the reconstruction gray level due to $\mathcal{D}_u$. It can be observed that parameters γ and c play important roles in determination of the reconstruction properties and the selection of these parameters, in general, depends on the practical clinical tasks. Details about the selection of parameters will be presented in the conference.

2) Reconstruction algorithms: The primal-dual algorithm developed by Chambolle and Pock [7], [6] can be used to solve convex optimization problems, including that in Eq. (2), for image reconstruction in CT. In this work, we have tailored the CP algorithm to reconstructing images from truncated C-arm CBCT data. The details about the tailoring and implementation of the algorithm will be presented at conference.

3) practical convergence conditions: The convergent conditions for the CP algorithm include (a) the TV value and D_w approach their respective constraint parameter values selected, and (b) the conditional primal-dual (cPD) gap becomes zero. However, these conditions cannot be achieved in practical reconstructions because it would take infinite number of iterations without a computer precision constraint. Therefore, in this work we adopted practical convergence conditions which will be discussed in detail at the conference.

III. Results

Using the CP algorithm to solve the optimization program defined in Eqs. (2) and (3), we have performed image reconstructions from the swine data acquired with the C-arm CBCT system. Images were reconstructed on a 3D array of 600 x 800 x 660 of cubic voxels of size 0.464 mm. It is important to select appropriate program parameters c and γ for given data, and we will report at the conference how the parameters can be determined in a study. In the work, c and γ are chosen to be 0.05 and 12000. With the practical convergence conditions defined, we obtained the convergent reconstructions and display them, along with the FDK reconstructions, in Fig. 1. In an attempt to demonstrate the effect of the data-derivative fidelity term in the optimization program on the reduction of data truncation, we have also conducted image reconstruction by solving the optimization problem in Eq. (2) with c=1.0, i.e., without the data-derivative fidelity term.

For a reference, we display in Fig. 2a FDK reconstructions within a set of coronal, sagittal, and transverse slices of the swine. It can be observed that the reconstructions suffer from severe streak artifacts caused by data truncation and other physical factors. In Fig. 2b, we display the convergent reconstructions obtained by solving the optimization program without the data-derivative fidelity term, i.e., c=1.0. While the streak artifacts due to data truncation and other physical factors are reduced in the reconstructions, some high and low intensive (i.e., cupping) artifacts appear in the peripheral regions (or around the FOV edge) in the reconstructions due to the lack of correction for transverse truncations. On the other hand, with the data-derivative fidelity term (i.e., c=0.05), the optimization-based reconstructions shown in Fig. 2c minimize effectively both types of artifacts observed in Figs. 2a and 2b. As such, low-contrast soft-tissues may be distinguished better than other reconstructions.

IV. Conclusions

In this work, we have investigated optimization-based reconstruction from truncated swine data collected with a clinical C-arm CBCT scanner. In the study, the image is specified by an optimization program in which a derivative data fidelity term is added, along with an image-total-variation (TV) constraint, for dealing effectively with data truncation; and the CP algorithm was tailored to reconstruct the image by solving the optimization problem. Visual inspection of the reconstruction results reveals that, with the appropriately designed optimization program and algorithm, images can be obtained with quality improved, in terms of streak artifact reduction and low contrast

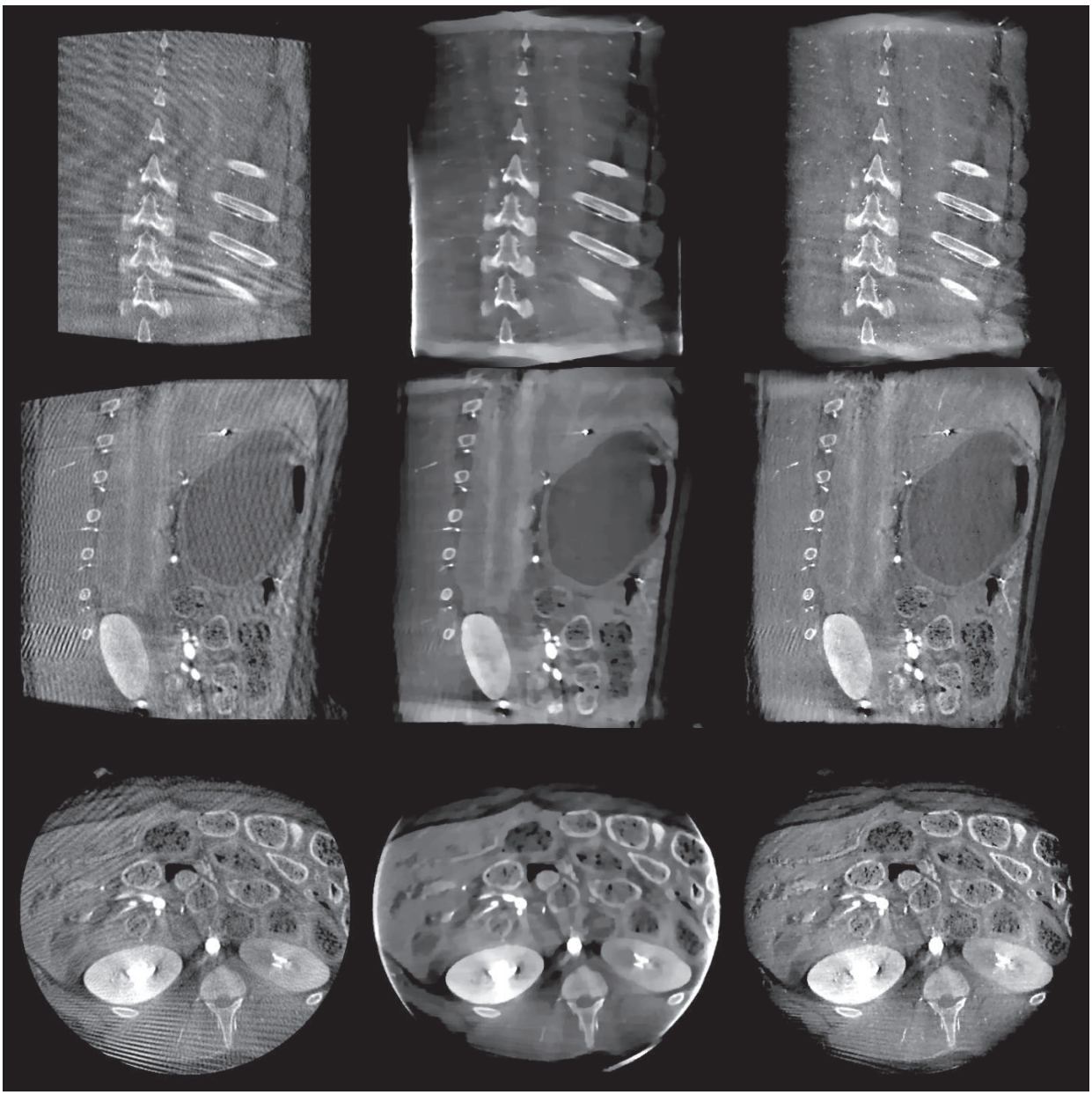

(a) (b) (c)

Figure 2. Reconstructed images of the swine within a set of coronal (row 1), sagittal (row 2), and transverse (row 3) slices obtained by use of the FDK algorithm (a) and the CP algorithm with c=1.0 (b) and c=0.05 (c), respectively. The display window is [0.12, 0.28] cm^{-1}.

enhancement, on those of the clinical FDK reconstruction. The study may bear implications for an enhanced practical utility of C-arm CBCT imaging in surgical and interventional procedures.

ACKNOWLEDGMENT

This work was supported in part by NIH R01 Grants Nos. CA158446, CA182264, and EB018102. The contents of this article are solely the responsibility of the authors and do not necessarily represent the official NIH views.

REFERENCES

[1] V. Tacher, A. Radaelli, M. Lin, and J.-F. Geschwind, "How i do it: cone-beam CT during transarterial chemoembolization for liver cancer," *Radiol.*, vol. 274, pp. 320–334, 2015.

[2] S. Singh, M. K. Kalra, J. Hsieh, P. E. Licato, S. Do, H. H. Pien, and M. A. Blake, "Abdominal CT: Comparison of adaptive statistical iterative and filtered back projection reconstruction techniques 1," *Radiol.*, vol. 257, pp. 373–383, 2010.

[3] X. Han, E. Pearson, C. Pelizzari, H. Al-Hallaq, E. Y. Sidky, J. Bian, and X. Pan, "Algorithm-enabled exploration of image-quality potential of cone-beam CT in image-guided radiation therapy," *Phys. Med. Biol.*, vol. 60, pp. 4601–4633, 2015.

[4] E. Y. Sidky, D. N. Kraemer, E. G. Roth, C. Ullberg, I. S. Reiser, and X. Pan, "analysis of iterative region-of-interest image reconstruction for x-ray computed tomography," *J. Med. Imaging*, vol. 1, p. 031007, 2014.

[5] B. E. Claus, "Geometry calibration phantom design for 3D imaging," *in Medical Imaging, Proc. SPIE*, vol. 6142, pp. 61 422E–61 422E, 2006.
[6] E. Y. Sidky, J. H. Jørgensen, and X. Pan, "Convex optimization problem prototyping for image reconstruction in computed tomography with the Chambolle-Pock algorithm," *Phys. Med. Biol.*, vol. 57, pp. 3065–3091, 2012, PMCID:PMC3370658.
[7] A. Chambolle and T. Pock, "A first-order primal-dual algorithm for convex problems with applications to imaging," *J. Math. Imag. Vis.*, vol. 40, pp. 120–145, 2011.

Reduction of beam hardening artifacts on real C-Arm CT data using statistical polyenergetic image reconstruction

Richard Bismark, Robert Frysch, Georg Rose

Institute for Telematics and Medical Engineering, University of Magdeburg, Germany

***Abstract*—This work aims for an implementation of a three dimensional polyenergetic statistical reconstruction (PSR) technique by A. Elbakri and J. A. Fessler [1] which can be used for real x-ray computed tomography data from setups like C-Arm CT. Prior knowledge of the x-ray spectrum and the material composition of the object is generally necessary, whereas a pre-segmentation of the object into different materials is not. The well-known beam hardening artifacts inside the reconstructed volume (cupping, streaks and shadows) should not occur since the algorithm applies a physical model of the x-ray propagation through the reconstruction volume. We assume that the object consists of a known number of materials. Furthermore, we assume one voxel can only contain an overlap of at most two materials, depending on its density value. The measurements are performed on a pig cadaver head with a C-Arm CT system. In case of a metal presence inside the object, we achieved an increase in image quality with a reduction of beam hardening artifacts. We compared the PSR with a filtered-back projection and a monoenergetic iterative reconstruction with a preprocessed water correction for beam hardening. Additionally, we investigated the impact of the detector response function in the reconstruction. The results are promising for clinical imaging with metal implants or needles.**

***Index Terms*—Beam hardening, C-Arm CT, Cone beam CT, EM Algorithm, Flat panel detector, Metal artifacts, Polychromatic statistical iterative CT-Reconstruction**

I. INTRODUCTION

X-ray computed tomography imaging is a widely used technique, especially as diagnostic method in clinical daily routine. The most common reconstruction method is the filtered-back projection (FPB). The FBP image suffers from well-known beam hardening artifacts due to the nonlinear absorption process which is not taken into account in the reconstruction method. Another disadvantage of the FBP is its need for certain scanning geometries such as circle trajectories. Statistical methods can include arbitrary scanning trajectories, prior knowledge like object constrains and variance properties.

The higher the energy of the photons, the lower the attenuation. This causes an increase in mean energy of a polyenergetic x-ray beam. Thus, the x-ray radiation gets "harder" while propagating through an object. As a consequence, the effective attenuation coefficient of the medium decreases with the penetration depth which is the main reason for the cupping artifact. Beam hardening effects become even more important at the edges between different material types and can lead to streak and shadow artifacts in the reconstructed image.

Common methods to reduce beam hardening artifacts are based either on preprocessing of the measured data, like a water correction [2], [3] or a post image processing of the reconstructed image.

Another approach is based on dual energy CT. Two different measurements of the same object with two different x-ray spectra deliver two different energy dependend reconstructions. This fact enables the splitting of the attenuation coefficients into contributions of the Compton effect and the photoelectric effect. The main drawback is the need for two x-ray spectra which results in increased patient dose and measurement effort.

Theoretical background

Our proposed method is based on the iterative polyenergetic statistical reconstruction (PSR) algorithm by Elbakri et al [1], [4]. This method uses a physical model of the absorption process and incorporates it into an expectation maximization approach. Therefore, the statistical character of the radiation is incorporated for means of noise reduction. That combines the properties of statistical weightings with the polyenergetic characteristic of the measured intensities.

The algorithm monotonically decreases a penalized likelihood cost function using quadratic surrogates and Huber penalty regularization. With $[\dots]_+$ denoting the

non-negativity constraint, the update step of voxel j is written as

$$\rho_j \rightarrow \left[\rho_j - \frac{M\hat{N}_j + \beta \frac{\partial S}{\partial \rho_j}}{d_j + \beta \frac{\partial^2 S}{\partial \rho_j^2}} \right]_+ . \quad (1)$$

Here, $\beta \frac{\partial S}{\partial \rho_j}$ and $\beta \frac{\partial^2 S}{\partial \rho_j^2}$ are terms of a regularization (smoothness constraints) with an appropriate penalty potential $S(\rho)$ regarding only each ρ_j voxel's nearest neighbors. M is a scalar which is proportional to the size of a used subset ξ of projections to update the density ρ_j in a voxel j.

$$d_j \coloneqq \sum_k m_k^2 \left(E_{\text{eff}}\right) \sum_i a_{ij} \gamma_i Y_i \quad (2)$$

Equation 2 basically represents an iteration independent back projection of the measured intensity Y_i which can be calculated once as a preprocessing step. $\gamma_i = \sum_j a_{ij}$ denotes the path length through the object. The effective energy of the x-ray beam with an energy spectrum $X(E)$ is given by the centroid

$$E_{\text{eff}} = \frac{\int E \cdot X\left(E\right) dE}{\int X\left(E\right) dE}. \quad (3)$$

$\hat{N}_j$ contains a forward projection $\bar{Y}_i$ of the current volume ρ_j which is compared with the measured intensities Y_i and backprojected afterwards. The projection model for the ith ray is the energy-dependent Lambert–Beer law:

$$\bar{Y}_i = \int dE\, I_i\left(E\right) \exp\left\{ -\sum_k m_k\left(E\right) s_i^k(\rho) \right\}. \quad (4)$$

Thereby, $s_i^k(\rho) \coloneqq \sum_j a_{ij}^k \rho_j$ is a classical forward projection of voxels consisting of material k. $I_i\left(E\right)$ is a blank scan containing the information of the initial x-ray spectrum and the detector response. $m_k\left(E\right)$ is the known energy dependence [5] of the kth material and $a_{ij}^k = a_{ij} f_j^k$ are the geometry factors combined with the information which material the voxel consists of. Elbakri et al [4] used the following choice:

$$f_j^k = \begin{cases} 1 & \text{voxel } j \text{ belongs to the } k\text{th material} \\ 0 & \text{else} \end{cases}. \quad (5)$$

$\hat{N}_j$ can be written as

$$\hat{N}_j = \sum_{i \in \xi} \sum_k a_{ij}^k \left(1 - \frac{Y_i}{\bar{Y}_i}\right) \frac{\partial \bar{Y}_i}{\partial s_i^k}. \quad (6)$$

This type of polyenergetic reconstruction method needs a presegmentation of the reconstructed volume. In a follow up, the authors expanded the method with a "Displacement Model" [4] which allows material mixtures in voxels.

II. METHODS

We implemented a polychromatic ray-based forward projector and a voxel-based TT-footprint backward projector [6], [7] on GPU hardware with OpenCL programming language. The spectrum is divided into 40 energy bins. Moreover, we assumed the object to consist of water, bone and one specific material like a known metal compound. Depending on its density, the fraction $f_j^k = f^k\left(\rho_j\right)$ of the materials in the jth voxel is approximated continuously by cubic splines for material compositions. Thus, the material is just identified by its density. Regarding the energy-dependent attenuation, a natural choice of material components is water (similar to tissue), bone and a known metal or metal compound.

To reach faster convergence we applied an ordered subsets technique with two projections (circa perpendicular) per update. In contrast to Elbakri et al., $\bar{Y}_i$ and its gradient are calculated on-the-fly from the forward projection s_i^k, instead of interpolating precalculated values. This means, the gradient is computed explicitly by derivating (4).

We estimated the x-ray spectrum $X\left(E\right)$ by Monte Carlo simulations [8], taking into account the 12° opening angle and Cu, Al prefiltering of the incident x-rays. Furthermore, we used preprocessed projection data which were normalized and processed only with a scatter correction routine. Note that this means in particular that no water correction has been applied. We incorporated a detector response function $D\left(E\right)$ into the forward projection (4) to model the measurement characteristics more accurate.

$$I\left(E\right) = X\left(E\right) \cdot D\left(E\right) \quad (7)$$

The C-Arm system uses a CsI scintillator-based detector. Responses of NaI(Tl), CsI(Tl) and CsI(Na) detectors above 20keV behave qualitatively similar [9]. Since the used energy bins lie in the interval from 20 to 100 keV, we used the response functions of Roberts et al [10].

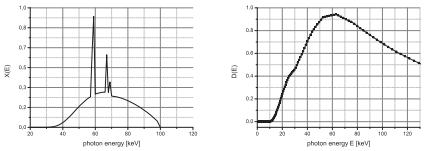

Figure 1: The used x-ray spectrum in arbitrary units [8] (left) and the detector response function [10] in arbitrary units which is used for the PSR algorithm (right).

III. RESULTS

The following reconstructed volumes are iterated 100 times over all projections covering 200° of a circular short scan.

To achieve a result with properties similar to a clinical application, we penetrated a head of a pig cadaver with a needle consisting of nitinol (TiNi). The head was scanned with an angular sampling of 248 over 200° and a detector with 616×480 pixel and a resolution of $0.616\,\text{mm} \times 0.616\,\text{mm}$. The tube voltage was set to 100 kV. We reconstructed the object on a $256 \times 256 \times 256$ grid with an isotropic voxel size of $1 \times 1 \times 1\,\text{mm}^3$. For the regularization penalty we used a Huber loss function.

The monochromatic statistical reconstruction (MSR) is basically the same routine as the implemented PSR, but treats all voxels as water. The MSR routine is initialized with a monoenergetic x-ray spectrum $X(E) = \delta(E - E_0)$. Additionally, we applied water corrected projections which are also used for the FBP reconstruction. Thus, the MSR algorithm is a statistical but monoenergetic iterative reconstruction. That makes the comparison more reliable and illustrates the consistency of the physical model of the implementation, since the results are similar to the FBP.

We compared reconstructed volumes of different reconstruction methods in one specific axial slice. The standard FBP image in figure 2a has stronger shadow artifacts than the iterative MSR in figure 2b. Both display a similar representation of the needle. The PSR in figure 2c has less shadow artifacts and a sharper needle reconstruction. The difference image in figure 2d shows the compensation of the shadow artifacts and the difference of the determined density of the needle.

Using a constant detector response or an arbitrary linear function, we state a decrease in image quality (see figure 2e,2f) compared with 2c where the response function by Roberts et al [10] was used. Figure 2b shows the slice which is similar to the FBP.

The needle has a diameter of 2 mm. This is roughly equivalent to the measured size of the needle diameter in the PSR volume of about 3 voxels (see figure 4). We can state that, only the PSR can achieve a sharp and more accurate shaped needle.

A similar measurement was done with a 5 euro cent coin which mainly consists of Steel ($\sim 94\%$). The estimated thickness and the diameter of the reconstructed coin are equal to the true vaules of a 5 euro cent coin with respect tolerance induced by the voxel size. The shadow artifacts in figure 3 caused by the coin are much stronger then the TiNi-needle induced shadows, since the gray values and the corresponding density are practically zero.

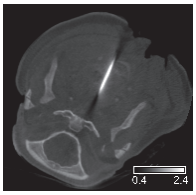

(a) An obtained slice of the FBP reconstruction of the C-Arm CT.

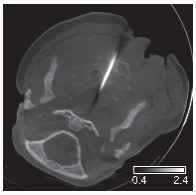

(b) Treating all voxels like water, use of watercorrected projections and initialize with a monoenergetic x-ray spectrum (MSR) results in a reconstruction similar to the FBP.

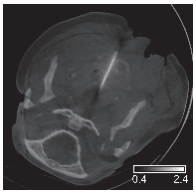

(c) The result of the implemented PSR algorithm shows a thinner reconstruction of the needle.

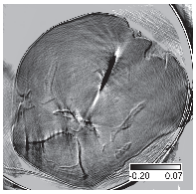

(d) The difference image of 2b and 2c shows the compensation of the streak artefacts.

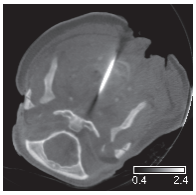

(e) PSR with a linear detector response function $D(E)$.

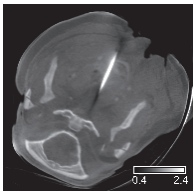

(f) PSR with a constant detector response function $D(E)$.

Figure 2: Comparison of slices of reconstructed volumes of the pig head based on different algorithms.

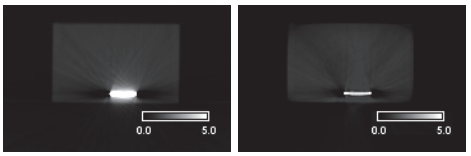

Figure 3: FBP and PSR of the 5 euro cent coin.

IV. DISCUSSION

The comparison between the FBP and the PSR shows that the dark regions caused by metal arti-

facts are reduced and the structure of the surrounding volume is clearer. However, some less darker regions remain probably caused by scatter effects as previously observed by Elbakri and Fessler [4]. If we initialize the reconstruction routine with a monochromatic spectrum and treat all voxels as water, we observe beam hardening artifacts similar to the FBP, as shown in the comparision of figure 2a and figure 2b. The comparison of MSR and PSR is more reliable since both reconstruction methods are statistical and iterative algorithms.

To investigate the remaining shadow artifacts, a proper scattering simulation needs to be done. We plan to implement such a scattering into simulated projection data and compare the resulting reconstruction with scatter-free simulations.

Another remaining issue is the quantification of the density values of the reconstructed bones and the needle. The reconstructed needle has a density of $1.7\,\mathrm{gcm}^{-3}$ but nitinol has a density of $6.45\,\mathrm{gcm}^{-3}$ and the bones are in the order of $1.20 \ldots 1.45\,\mathrm{gcm}^{-3}$ instead of $1.92\,\mathrm{gcm}^{-3}$.

It is observable that the non-linear detector response of Roberts et al [10] can suppress the shadow artifacts with the highest success. Hence, we can suppose that a poor assumption about the detector response can cause artifacts such as the non-linear beam hardening itself. The detector response is particularly important in this regions since the non-linearity occurs for high energies (i.e. above 60 keV).

Better results may be accomplished if more information about the measuring process is used. For example, it is known that the product of time and current of the x-ray tube adapts during the scan depending on the absorption of the object. This product is linearly proportional to the count of emitted x-ray photons (for constant tube voltage) and may be considered in future work.

Another approximation made is stating $I\,(E)$ in (7) to be independent of the detector pixel. A detailed measurement of the incoming spectrum for each detector pixel could help to achieve better results and could be a proof for the used x-ray spectrum, which is estimated via Monte Carlo simulations. Using spectra of Spek Calc [8] without copper filtration leads to similarly poor results as e.g. the usage of another response function in figure 2e and figure 2f.

Conclusion

We present a cone-beam CT implementation of the PSR routine of I. Elbakri and J. A. Fessler [4] for the angiographic C-arm device, showing a clear image quality improvement. Beam hardening artifacts can be reduced while the surrounding tissue is less blurred. The overall image quality is enhanced, so that the algorithm can make clinical diagnosis more reliable. It seems that the response function $D(E)$ of the detector system plays a key role and its properties need to be known sufficiently.

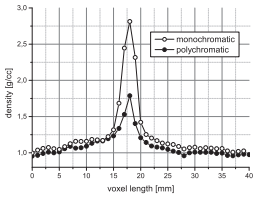

Figure 4: Contrast profile of figure 2b and figure 2c.

ACKNOWLEDGMENTS

The work of this paper is partly funded by the German Ministry of Education and Research (BMBF) within the Forschungscampus *STIMULATE* under grant number '03FO16101A'.

References

[1] I. Elbakri and J. Fessler, "Statistical image reconstruction for polyenergetic x-ray computed tomography," *Medical Imaging, IEEE Transactions on* **21**, pp. 89–99, Feb 2002.

[2] O. Nalcioglu and R. Y. Lou, "Post-reconstruction method for beam hardening in computerised tomography," *Physics in Medicine and Biology* **24**(2), p. 330, 1979.

[3] P. M. Joseph and R. D. Spital, "A Method for Correcting Bone Induced Artifacts in Computed Tomography Scanners," *Journal of Computer Assisted Tomography* **2**, pp. 100–108, 1978.

[4] I. A. Elbakri and J. A. Fessler, "Segmentation-free statistical image reconstruction for polyenergetic x-ray computed tomography with experimental validation," *Physics in Medicine and Biology* **48**(15), p. 2453, 2003.

[5] J. H. Hubbell and S. M. Seltzer, "Tables of x-ray mass attenuation coefficients and mass energy-absorption coefficients from 1 kev to 20 mev for elements z = 1 to 92 and 48 additional substances of dosimetric interest," 1989, 1990, 1996.

[6] Y. Long, J. A. Fessler, and J. M. Balter, "3d forward and back-projection for x-ray ct using separable footprints," *IEEE Trans. Med. Imaging* **29**(11), pp. 1839–1850, 2010.

[7] R. Frysch, T. Pfeiffer, S. Bannasch, S. Serowy, S. Gugel, M. Skalej, and G. Rose, "C-arm perfusion imaging with a fast penalized maximum-likelihood approach," 2014.

[8] G. Poludniowski, G. Landry, F. DeBlois, P. M. Evans, and F. Verhaegen, "Spekcalc : a program to calculate photon spectra from tungsten anode x-ray tubes," *Physics in Medicine and Biology* **54**(19), p. N433, 2009.

[9] D. Aitken, B. Beron, G. Yenicay, and H. Zulliger, "The fluorescent response of nai(tl), csi(tl), csi(na) and caf2(eu) to x-rays and low energy gamma rays," *Nuclear Science, IEEE Transactions on* **14**, pp. 468–477, Feb 1967.

[10] D. Roberts, V. Hansen, A. Niven, M. Thompson, J. Seco, and P. Evans, "A low z linac and flat panel imager: comparison with the conventional imaging approach," *PHYSICS IN MEDICINE AND BIOLOGY* **53**, pp. 6305 – 6319, November 2008. Copyright 2008 Institute of Physics. This is the author's accepted manuscript.

A Spectral Geometrical Model for Compton Scatter Tomography Based on the SSS Approximation

Ivan G. Kazantsev
Institute of Computational Mathematics
and Mathematical Geophysics
Novosibirsk, Russia
Email: kazantsev.ivan6@gmail.com

Ulrik L. Olsen, Henning F. Poulsen
Department of Physics
Technical University of Denmark
Lyngby, Denmark
Emails: ullu@dtu.dk, hfpo@fysik.dtu.dk

Per C. Hansen
COMPUTE Department
Technical University of Denmark
Lyngby, Denmark
Email: pcha@dtu.dk

***Abstract*—The forward model of single scatter in the Positron Emission Tomography for a detector system possessing an excellent spectral resolution under idealized geometrical assumptions is investigated. This model has the form of integral equations describing a flux of photons emanating from the same annihilation event and undergoing a single scattering at a certain angle. The equations for single scatter calculation are derived using the Single Scatter Simulation approximation. We show that the three-dimensional slice-by-slice filtered backprojection algorithm is applicable for scatter data inversion provided some assumptions on the attenuation map are justified.**

I. Introduction

The Compton scatter phenomenon is inherent of such tomographic imaging modalities as the X-ray transmission Computed Tomography (CT) [1], the Single Photon Emission Tomography (SPECT) [2] and the Positron Emission Tomography (PET) [3]. Many authors succesfully apply transmission CT algoritms for the Compton scatter imaging systems both with the external and the internal sources of radiation. It has been shown that SPECT can be considered as Compounded Conical Radon Transform [4], and PET as a perturbation of the X-ray transform [5]. In this paper we focus on the analytical aspects of deriving an idealized forward model of the Compton single scatter in the PET.

Idealized models of image formation in tomography are useful instruments for exploring the potentials and limits of reconstructive ability of data acquired in an imaging modality of interest. Usually having the form of an integral transform or differential equation, the idealized model is expected to answer the principal questions: whether the available noiseless data are sufficient to restore an object under investigation, to what extent the objects frequencies are recoverable, etc. In the case when an explicit inversion formula is not available, a discrete version of the idealized forward operator can be combined with algebraic iterative methods to answer these questions.

As compared to idealized models, there is comprehensive Monte Carlo (MC) statistical simulation in much more wide use. The MC modeling is able to take into account every technical detail of photon transport and detection phenomena and therefore there is a demand for computer resources. The MC statistical simulation (as well as physical phantom studies) are the 'gold standard' for verification of scatter modelling. Reference [3] states: "Nevertheless, the complexity and computing requirements of Monte Carlo simulation led to the development of analytical simulation tools based on simplifying approximations to improve speed of operation". Those analytical simulation tools are known as Single Scatter Simulation (SSS) and they have been proven to be fast and efficient in modeling the main scatter features together with discreteness of detectors and many other factors [6]. While the SSS model estimates a scatter flux detected within finite detector elements for a range of energies, the idealized model provides a sample value of a scatter for a given energy and detected at a given point of detector. That is, in the idealized model the detector system has an excellent energy resolution and the size of each detector element approaches zero. It is assumed that detectors count all incoming single scattered photons of a certain energy, or equivalently, the photons scattered once under a certain angle.

II. Methods

The integral model of PET using primary photons [5] operates with internal sources of isotope activity $f(x,y,z)$ within a functionalizing medical object described by the known linear attenuation map $\mu(x,y,z)$ and a pair of detectors A and B:

$$P^{AB} = \exp\left[-\int_A^B \mu(x',y',z')dl'\right]\int_A^B f(x,y,z)dl, \qquad (1)$$

where dl, dl' are the elements of integration along AB. Equation (1) factorizes integrals over the activity f and the attenuation μ, thus reducing the problem to a classical X-ray CT provided that the data P^{AB} undergoes attenuation correction. Then the data can be treated as integrals of f along the lines of response, which are thought to be trajectories of propagation of primary (unscattered) photons with energy $E = 511$ keV. The support of the attenuation map μ is a domain $D(\mu)$, and the support of the activity function f is a domain $D(f) \subset D(\mu)$ of unknown structure. The PET problem consists in reconstruction of the activity f and its support $D(f)$ exploiting data P^{AB}, recorded by a multitude of detectors (A,B) positioned around the object. A physical feature of PET is basically a huge amount of photon pairs (u,v), collinearly traveling in opposite directions from the annihilation point C, where positron resulting from isotope

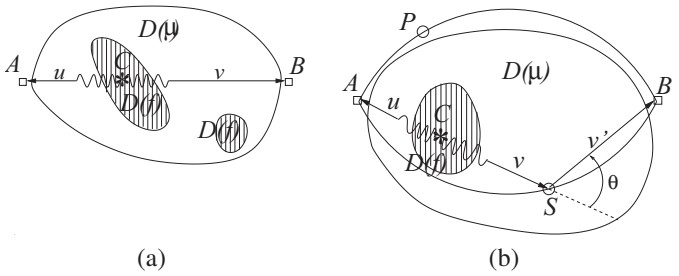

Fig. 1. (a) Primary photons (u, v) of energy $E = 511$ keV, originating from annihilation point $C \in D(f)$. (b) Single Compton scatter happens in point $S \in D(\mu)$, v' is a photon v with energy E', scattering with angle θ. The P is geometrically potential point for scatter with angle θ, however it is out of domain μ ($P \notin D(\mu)$, $\mu(P) = 0$), therefore does not contribute to the B.

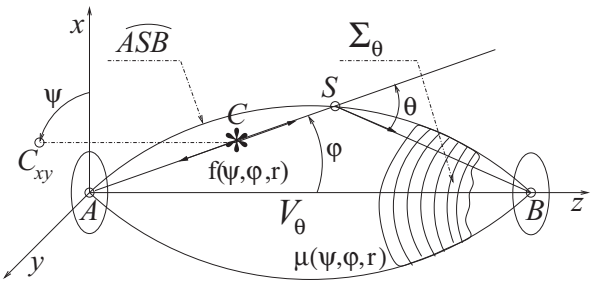

Fig. 2. A 3D geometric model of single scattering. Circular detectors are centered at the points A and B; S is a scattering point with the polar coordinates $(\psi, \varphi, |AS|)$ and the scatter angle θ; C_{xy} is a projection of C onto the plane xAy; C is an annihilation event. The surface Σ_θ is a loci of points S of scatter under the angle θ and the spherical coordinates $(\psi, \varphi, |AS|)$, $\angle ABS = \theta - \varphi$.

decay meets some of free electons of the media μ (Figure 1 (a)). In addition to primary photons, there are the ones v' with energies $E' < E$ that undergo the Compton scatter (Figure 1 (b)), and the energies are connected to the scattering angle θ by the Compton relation: $E' = E/(2 - \cos\theta)$.

A. Single Scatter Simulation Approximation

The Single Scatter Simulation (SSS) technique [6] estimates the expected single scatter coincidence rate in the detector pair (A, B) as an integral over the total scatter volume $V = D(\mu)$:

$$S_V^{AB} = \iiint_V dV \frac{\sigma_{AS}\sigma_{BS}}{4\pi|AS|^2|BS|^2} \frac{\mu}{\sigma_C}\frac{\partial\sigma_C}{\partial\Omega}(\epsilon_A I^A + \epsilon_B I^B), \tag{2}$$

where

$$I^A = e^{-(\int_A^S \mu dl + \int_S^B \mu' dl)} \int_A^S f dl,\ I^B = e^{-(\int_A^S \mu' dl + \int_S^B \mu dl)} \int_S^B f dl. \tag{3}$$

Here, σ_{AS} and σ_{BS} are geometrical cross-sections of the detectors A and B, f is the emitter activity, $\mu = \mu(E, S)$ is the linear attenuation coefficient depending on the photon energy E and the scatter point S, $\epsilon_A = \epsilon_{AS}\epsilon'_{BS}$ and $\epsilon_B = \epsilon'_{AS}\epsilon_{BS}$ are related to the detection efficiency for the detectors A and B, $\frac{\partial\sigma_C}{\partial\Omega}$ is the differential cross-section. Primed and unprimed quantities are evaluated at the scattered and unscattered photon's energy, respectively.

Equation (2) is symmetric in terms of A and B so that primary photons are recorded both at A and B. We try to modify formula (2) within idealized assumptions on excellent energy resolution of pointwise detectors. Therefore a one-sided version of (2) is investigated, where only one detector A is tuned to counting the primary photons. In this case, we can set $I^B = 0$ in (3). Let us denote, omitting other dependencies,

$$Q_{f,\mu}(x, y, z) \equiv \frac{\mu}{\sigma_C}\frac{\partial\sigma_C}{\partial\Omega}\epsilon_A e^{-(\int_A^S \mu dl + \int_S^B \mu' dl)} \int_A^S f dl, \tag{4}$$

where (x, y, z) are Cartesian coordinates of the scatter point S. Thus, we transform equation (2) to the more compact form

$$S_V^{AB} = \iiint_V dV \left(\frac{\sigma_{AS}\sigma_{BS}}{4\pi|AS|^2|BS|^2}\right) Q_{f,\mu}(x, y, z). \tag{5}$$

This equation is a starting point for derivation both of total and sample Compton scatters at a certain angle.

B. Geometrical Model of the Compton Single Scatter

The SSS approximation is sufficiently generic to deal with the scatter volume V (or, equivalently, an integration domain, or a support of the attenuation map μ) of an arbitrary shape. However, for the purposes of this research, a precise boundary of the V (and the limits in volume integral (5)) should be explicitly specified as well as a system of coordinates needs to be chosen. The following basic geometrical observations are useful in analytical single scatter modeling.

Let us assume that the detectors A and B are small disks of radius $\delta \ll 1$. It is easily seen (Figure 2) that all the scatter points S (with some scattering energy E', or scattering angle θ) are located on an equi-scatter surface (denoted as Σ_θ) of the football-shape rotation body (denoted as V_θ) generated by the arcs $\widehat{ASB}$ with the detectors A and B fixed. The arcs are parts of the circles with diameter $d = |AB|/\sin\theta$.

Let us assume that the detector B records the photons scattered under the scattering angles θ such that $\theta \le T$, for some thresholding angle $T \le \pi/2$. We find it useful to exploit the spherical coordinates (ψ, φ, r) with the origin at the point A for describing the total scatter volume V_T and the equiscatter surface Σ_θ:

$$\begin{aligned} V_T &= \{(\psi, \varphi, r)|\, \psi \in [0, 2\pi), \phi \in [0, T], r \in [0, |AS|],\} \\ \Sigma_\theta &= \{(\psi, \varphi, r)|\, \psi \in [0, 2\pi), \phi \in [0, \theta], r = |AS|\}. \end{aligned} \tag{6}$$

Let us recall the Law of Sines for $\triangle ABS$

$$|AS|/\sin(\theta - \varphi) = |BS|/\sin(\varphi) = d. \tag{7}$$

It can be shown that

$$|AS| = |AB|\frac{\sin(\theta - \varphi)}{\sin\theta},\ |BS| = |AB|\frac{\sin\varphi}{\sin\theta}. \tag{8}$$

The term $\int_A^S f dl$ is of multiple use in the scatter calculations. For any scatter point S, it is expressed as follows

$$\int_A^S f dl = \int_0^{|AS|} f(\psi,\varphi,r)dr = \int_0^{|AB|\frac{\sin(\theta-\varphi)}{\sin\theta}} f(\psi,\varphi,r)dr. \quad (9)$$

The idealized model for the total scatter (parameterized by the threshold T and denoted as S_T^{AB}) will be developed using the SSS integral (5) calculated at points within the small detectors A and B, and then averaged over (A,B) disks area as follows

$$S_T^{AB} = \lim_{\delta\to 0}\frac{1}{(\pi\frac{\delta^2}{4})^2}\int_A dA\int_B dB\iiint_{V_T} dV_T \times\left(\frac{\sigma_{AS}\sigma_{BS}}{4\pi|AS|^2|BS|^2}\right)Q_{f,\mu}(x,y,z). \quad (10)$$

The geometrical cross-sections of A and B incident to the rays AS and SB are respectively

$$\sigma_{AS}\approx(\pi\delta^2/4)\cos\varphi,\ \sigma_{BS}\approx(\pi\delta^2/4)\cos(\theta-\varphi). \quad (11)$$

Substituting (11) into (10), we estimate the total single scatter in the following form

$$S_T^{AB} = \iiint_{V_T} dV_T\left(\frac{\cos\varphi\cos(\theta-\varphi)}{4\pi|AS|^2|BS|^2}\right)Q_{f,\mu}(x,y,z). \quad (12)$$

We change the rectangular variables (x,y,z) in (12) for other (spherical-like) curvilinear coordinates (ψ,φ,θ), where ψ,φ are the spherical coordinates and $\theta\in[0,T]$ is the scattering angle (while the distance $|AB|$ is fixed), as follows

$$\begin{aligned} x &= X(\psi,\varphi,\theta) = |AS|\sin\varphi\cos\psi,\\ y &= Y(\psi,\varphi,\theta) = |AS|\sin\varphi\sin\psi,\\ z &= Z(\psi,\varphi,\theta) = |AS|\cos\varphi. \end{aligned} \quad (13)$$

For changing variables in (12), we calculate the elementary volume

$$dV_T = dxdydz = |J|d\psi d\varphi d\theta, \quad (14)$$

where J is the Jacobian matrix

$$J = \begin{bmatrix} \partial X/\partial\psi & \partial X/\partial\varphi & \partial X/\partial\theta\\ \partial Y/\partial\psi & \partial Y/\partial\varphi & \partial Y/\partial\theta\\ \partial Z/\partial\psi & \partial Z/\partial\varphi & \partial Z/\partial\theta \end{bmatrix} \quad (15)$$

and $|J|$ is its determinant. Due to (8), we have

$$|J| = \frac{|AB|^3\sin^2(\varphi)\sin^2(\theta-\varphi)}{\sin^4(\theta)} = \frac{|AS|^2|SB|^2}{|AB|}, \quad (16)$$

and (12) becomes

$$\begin{aligned} S_T^{AB} &= \iiint_{V_T} d\psi d\varphi d\theta\,|J|\,\frac{\cos\varphi\cos(\theta-\varphi)}{4\pi|AS|^2|BS|^2}\,Q_{f,\mu}(\psi,\varphi,\theta)\\ &= \int_0^{2\pi}d\psi\int_0^T d\theta\int_0^\theta d\varphi\,\frac{\cos\varphi\cos(\theta-\varphi)}{4\pi|AB|}\,Q_{f,\mu}(\psi,\varphi,\theta). \end{aligned} \quad (17)$$

Finally, we derive the total scatter equation under further idealized assumptions $\epsilon_A\equiv 1$ in the following integral form:

$$S_T^{AB} = \int_0^T d\theta\int_0^\theta d\varphi\frac{\cos\varphi\cos(\varphi-\theta)}{4\pi|AB|}\int_0^{2\pi}d\psi\,\frac{\mu(\psi,\varphi,|AS|)}{\sigma_C} \times\frac{\partial\sigma_C}{\partial\Omega}\,e^{-\left(\int_A^S\mu dl+\int_S^B\mu' dl\right)}\int_0^{|AS|} f(\psi,\varphi,r)dr. \quad (18)$$

Let us represent equation (18) in the form

$$S_T^{AB} = \int_0^T \xi_\theta^{AB}d\theta, \quad (19)$$

where the integrand

$$\xi_\theta^{AB} = \int_0^\theta d\varphi\frac{\cos\varphi\cos(\varphi-\theta)}{4\pi|AB|}\int_0^{2\pi}d\psi\frac{\mu(\psi,\varphi,|AS|)}{\sigma_C} \times\frac{\partial\sigma_C}{\partial\Omega}\,e^{-\left(\int_A^S\mu dl+\int_S^B\mu' dl\right)}\int_0^{|AS|} f(\psi,\varphi,r)dr \quad (20)$$

is a sample value of the scatter. Here θ and E' are fixed, therefore the factor $\frac{1}{\sigma_C}\frac{d\sigma_C}{d\Omega}$ in (20) is a scalar and for brevity can be omitted without loss of generality .

C. Slice-by-slice Convolution Blurring Model

An essential simplification can be achieved assuming $\mu = const$. Then equation (20) can be written down in the cylindrical coordinates (ψ,ρ,z) after some algebra as follows

$$\xi_\theta^{AB} = \frac{\mu}{4\pi|AB|}\int_0^{|AB|}dz\int_0^{R_\theta(z)}d\rho\frac{z(z\cos\theta+\rho\sin\theta)}{\rho(z^2+\rho^2)^{3/2}} \times e^{-\frac{|AB|\mu}{\sqrt{z^2+\rho^2}}(z+\rho\tan(\theta/2))}\int_0^{2\pi}d\psi f(\psi,\rho,z), \quad (21)$$

where radius of the circular section of V_θ with the coordinate z is

$$R_\theta(z) = \frac{\sqrt{a^2-(z-a)^2\sin^2\theta}-a\cos\theta}{\sin\theta},\ a\equiv\frac{|AB|}{2}. \quad (22)$$

Multiplying equation (21) by $1\equiv\rho/\rho$ and denoting the kernel

$$h_\theta(\rho,z)\equiv\frac{\mu}{4\pi|AB|}\frac{z(z\cos\theta+\rho\sin\theta)}{\rho^2(z^2+\rho^2)^{3/2}}e^{-\frac{|AB|\mu(z+\rho\tan(\theta/2))}{\sqrt{z^2+\rho^2}}}, \quad (23)$$

we can reduce (21) to

$$\xi_\theta^{AB} = \int_0^{|AB|}dz\int_0^{2\pi}d\psi\int_0^{R_\theta(z)}h_\theta(\rho,z)f(\psi,\rho,z)\rho d\rho. \quad (24)$$

It follows from this representation that the inner double integral $\int_0^{2\pi}d\psi\int_0^{R_\theta(z)}h_\theta(\rho,z)f(\psi,\rho,z)\rho d\rho$ in (24) is a value of the convolution of the function f section by the plane parallel

to xOy with the coordinate z, and the radially symmetric kernel $h_\theta(\rho, z)$ with a circular support of radius $R_\theta(z)$. The outer integral $\int_0^{|AB|} dz$ represents the X-ray transform of the slice-by-slice blurred version of the activity function f along the lines parallel to the direction z. This slice-by-slice distance-dependent blurring model of the projection formation is known in Transmission Electron Microscopy and it is proven to be invertible [7] provided full data are available. The reconstruction technique derived was named as the Defocus-gradient Corrected Backprojection (DGCBP) algorithm. Thus, we have reduced the simplified Compton scatter model to the already developed reconstruction algorithm. This algorithm was numerically tested [7] by simulating different types of noise based on the principles proposed by Baxter et al. [8]. Theoretical study of the noise propagation properties of the scatter forward transform (20) is a subject of the future research.

Let us introduce the Fourier transform pairs: $F(k_1, k_2, k_3) = \mathcal{F}_3\{f(x, y, z)\}$, $H_\theta(k_1, k_2, z) = \mathcal{F}_2\{h_\theta(\rho, z)\}$, and $P_\theta^{\alpha,\beta} = \mathcal{F}_2\{\xi_\theta^{\alpha,\beta}\}$. Here $\xi_\theta^{\alpha,\beta}$ is a scatter projection in the direction specified by the unit vector parameterized by the spherical angles $(\alpha, \beta) \in \mathbb{S}^2$. The scatter projection $\xi_\theta^{\alpha,\beta}$ is a collection of the scatter forward transform (20) samples ξ_θ^{AB}, where the points A and B belong to the lines that constitute a bundle of parallell lines in the direction (α, β). The DGCBP algorithm consists of the following steps.

Step 1. Deconvolution of the projection $P_\theta^{\alpha,\beta}$ with the Tikhonov regularized inverse filter and stacking the results along z for all directions $(\alpha, \beta) \in \mathbb{S}^2$:

$$b_\theta^{\alpha,\beta}(x, y, z) = \mathcal{F}_2^{-1}\Big\{\frac{P_\theta^{\alpha,\beta}(k_1, k_2)\, H_\theta(k_1, k_2, z)}{H_\theta(k_1, k_2, z)^2 + \lambda(k_1^2 + k_2^2)}\Big\}. \quad (25)$$

Step 2. Generation of the integral image $c_\theta(x, y, z)$ as summation of the backprojections $b_\theta^{\alpha,\beta}$ over all the projection directions $(\alpha, \beta) \in \mathbb{S}^2$:

$$c_\theta(x, y, z) = \iint_{\mathbb{S}^2} b_\theta^{\alpha,\beta}(x, y, z) \partial\alpha\partial\beta. \quad (26)$$

Step 3. Ramp-filtering in the Fourier domain of the integral image $C_\theta(k_1, k_2, k_3) = \mathcal{F}_3\{c_\theta(x, y, z)\}$:

$$F(k_1, k_2, k_3) \approx C_\theta(k_1, k_2, k_3) \times \sqrt{k_1^2 + k_2^2 + k_3^2}. \quad (27)$$

III. Simulation study

The numerical experiments were performed using a numerical test phantom of 256^3 size. It consists of 7 and 11 spheres serving as a support of the activity function $f \equiv 1$ immersed into a larger sphere filled with water with the linear attenuation coefficient $\mu = 0.096cm^{-1}$ (Figure 3 (a)). Images of three central sections are shown in Figure 3 (b) of the test object (the upper row), and of the reconstruction (the bottom row) from $1,000$ scatter projections randomly oriented over $\mathbb{S}^2$. Projections of 256×256 size each beeing numerically generated with a scattering angle $\theta = 30^\circ$ using formula (20). The regularization parameter $\lambda = 0.01$ of the Tikhonov filter is used in the DGCBP algorithm, Step 1, equation (25).

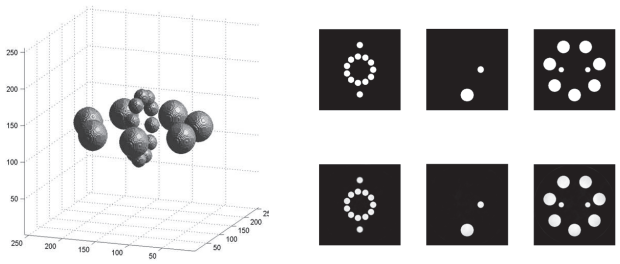

(a) (b)

Fig. 3. (a) The 3D view of a test object with 7 and 11 spheres of the unit activity immersed into the imaginable sphere filled with water and digitized into an image of 256^3 size. (b) Images of three central sections of the test object (the upper row), and the DGCBP reconstruction (the bottom row) from $1,000$ randomly chosen scatter projections.

IV. Conclusion

The closely related integral transforms (18) and (20) describing the total and sample single scatter projection formation have been derived from the classical SSS approximation (2). The single scatter image formation includes integration of the emitter activity f over a bundle of compound cones with a common vertex at the point A. Those cone integrals are weighted by the linear attenuation μ and some geometrical factors. We can conclude therefore that the integral transforms obtained belong to the family of the Compounded Conical Radon Transforms [4]. With some improvements in the detector energy resolution, the energy-selected PET could be a source of the new opportunities.

Acknowledgments

We thank Drs. Robert Lewitt and Samuel Matej for fruitful discussions. This work was partially supported during the stay of the first author with the Department of Physics of the Technical University of Denmark.

References

[1] S. Norton, "Compton scattering tomography", *Journal of Applied Physics*, vol. 76, no. 4, pp. 2007–2015, 15 August 1994.
[2] G. Rigaud, M. K. Nguyen and A. K. Louis, "Modeling and simulation results on a new Compton scattering tomography modality," *Simulation Modeling: Practice and Theory*, vol.33, pp. 28–44, April 2013.
[3] H. Zaidi, "Scatter modelling and correction strategies in fully 3-D PET," *Nuclear Medicine Communications*, vol. 22, pp. 1181–1184, 2001.
[4] M. K. Nguyen, T. T. Truong, C. Driol and H. Zaidi, "On a Novel Approach to Compton Scattered Emission Imaging," *IEEE Trans. Nucl. Sci.*, vol. 56, no. 3, pp. 1430–1437, June 2009,
[5] Th. Koesters, "Derivation and Analysis of Scatter Correction Algorithms for Quantitative Positron Emission Tomography", Disseration Thesis, Muenster University, 2010.
[6] C. C. Watson, "New, faster, image-based scatter correction for 3D PET," *IEEE Trans. Nucl. Sci.*, vol. 47, pp. 1587–1594, 2000.
[7] I. G. Kazantsev, J. Klukowska, G. T. Herman, and L. Cernetic, "Fully three-dimensional defocus-gradient corrected backprojection in cryo-electron microscopy", *Ultramicroscopy*, vol. 110, pp. 1128–1142, 2010.
[8] W. T. Baxter, R. A. Grassucci, H. Gao, and J. Frank, "Determination of signal–to–noise ratios and spectral SNRs in cryo–EM low–dose imaging of molecules", *Journal of Structural Biology*, vol. 166, pp. 126–132, 2009.

A robust method for calculation of proton stopping power ratio using dual energy CT

Vicki T. Taasti*[1], Jørgen B. B. Petersen[1], Jesper Thygesen[2], Ludvig P. Muren[1], Cai Grau[1] and David C. Hansen[1]

***Abstract*—Treatment planning for proton therapy is based on estimation of the proton stopping power ratio (SPR) which is used for range determination. In this study we propose a new parametrization of SPR for dual energy CT (DECT). The parametrization is compared to two other DECT methods for estimation of SPR. Further, the robustness of the parametrization towards tissue variations and towards noise is investigated. It is found that the root-mean-square error of this new SPR parametrization is lower than for the other SPR estimation methods we have compared to, and the new SPR parametrization is also more robust against elemental weight fraction changes of human tissues and against CT noise.**

***Keywords*— CT noise, dual energy CT, proton stopping power ratio, proton therapy, robustness.**

I. Introduction

TREATMENT planning with protons relies on correct and robust calculation of stopping power ratio (SPR) relative to water, since SPR is used for calculating the range of protons in human tissue. The main advantage of proton therapy is the well-defined range of protons. However, currently the largest source of range uncertainty is the SPR estimation which therefore gives the main contribution to the employed range and treatment margins in treatment planning of proton therapy [1]. As large treatment margins will diminish the advantage of proton therapy, it is thus desirable to be able to reduce the SPR uncertainty and thereby the margins.

The current state-of-art method for estimating SPR for proton therapy planning is the so-called "stoichiometric method" proposed by Schneider *et al*. in 1996 [2]. This method is based on conventional single energy CT. A piecewise linear fit based on a list of reference human tissues is used to determine the estimated SPR from the CT numbers (measured in Hounsfield Unit, HU) in the CT image.

* Vicki Trier Taasti: victaa@rm.dk
[1] Aarhus University Hospital, Department of Oncology, Aarhus, Denmark.
[2] Aarhus University Hospital, Department of Clinical Engineering and Department of Radiology, Aarhus, Denmark.

SPR can be estimated using an approximation of the Bethe formula, see [2]:

$$\mathrm{SPR}^{\mathrm{teo}} = \rho_e \frac{\ln(2m_e c^2) - \ln\left(\frac{\beta^2}{1-\beta^2}\right) - \beta^2 - \ln(I)}{\ln(2m_e c^2) - \ln\left(\frac{\beta^2}{1-\beta^2}\right) - \beta^2 - \ln(I_{\mathrm{w}})}. \quad (1)$$

Here ρ_e is the electron density of the target material relative to water, m_e is the mass of the electron and β is the velocity of the proton projectile relative to the speed of light, c. I and I_{w} are the mean excitation energies of the target material and water, respectively. For a given initial kinetic energy of the projectile, the two unknowns in eq. (1) are ρ_e and $\ln(I)$.

It has been shown that SPR can be estimated more accurately using dual energy CT (DECT) than with the stoichiometric method [1,3]. A number of calibration methods for estimating SPR from DECT images have been developed [1,3-6]. These methods all estimate ρ_e and $\ln(I)$ separately, and from these values the estimate for SPR is calculated from eq. (1). Further, the DECT methods presented so far do not estimate $\ln(I)$ directly, but rather they estimate the effective atomic number, Z_{eff}, for the target material, which can be seen as a weighted average of the atomic numbers for the constituent elements [1,3,5-6]. Z_{eff} is then used to estimate $\ln(I)$ from a fitted expression based on a list of reference human tissues [3]. The most recent DECT method was presented by Han *et al*. [4]. Here, $\ln(I)$ was estimated directly from the measured CT numbers in the low and high energy CT.

In this study we propose a new parametrization method for estimating SPR based directly on the CT numbers in the two DECT images, avoiding a prior estimation of ρ_e and $\ln(I)$, and thereby obviating the need for a Z_{eff} estimation. This new SPR parametrization is thus a one-step process in contrast to the other mentioned DECT methods, which are two- or three-step processes. Therefore in the new SPR parametrization there is only one source of deviations, where in the other methods each step in the estimation process introduces an additional source of deviations for the final SPR estimate.

In this study we also investigate the robustness of the new SPR parametrization with respect to changes in density and elemental composition of human tissues and with respect to noise in the CT images.

II. Method and Material

We propose to estimate the SPR from DECT using a parametrization of the reduced CT numbers:

$$u_j = \frac{\mathcal{H}_j}{1000} + 1\,, \tag{2}$$

where j represents either the low (j=L) or the high (j=H) energy CT spectrum, and $\mathcal{H}$ is the CT number. Our proposed SPR parametrization has two different expressions depending on the tissue type it is used for. We have divided the tissues into two categories, soft tissues and bone tissues, based on their CT numbers in the low energy CT spectrum, $\mathcal{H}_L$ (we have chosen the CT number in the low energy image since this gives the largest separation between the soft and bone tissues, whereby the probability of a wrong assignment is minimized). Tissues with $\mathcal{H}_L \leq 200$ HU are assigned to the soft tissue group and tissues with $\mathcal{H}_L > 200$ HU are assigned to the bone tissue group. With this tissue separation, we propose a SPR parametrization of the following form,

$$\mathrm{SPR}^{\mathrm{soft}} = (1+x_1)u_H - x_1u_L + x_2u_L^2 + x_3u_H^2 + x_4(u_L^3 + u_H^3) \tag{3a}$$

$$\mathrm{SPR}^{\mathrm{bone}} = (1+x_1)u_H - x_1u_L + x_2\frac{u_L}{u_H} + x_3(u_L^2 - u_H^2) + x_4(u_L^3 + u_H^3) \tag{3b}$$

To find the two set of parameters, x_i, in eq. (3) we used the list of 34 reference human tissues with known density and elemental weight fractions given in table 1 in [3]. From the density and elemental weight fractions of the reference human tissues their theoretical SPR was calculated by eq. (1).

To calculate $u_{L/H}$ for the reference tissues, the method described by Landry *et al*. [7] was used,

$$u_j^{\mathrm{cal}} = \frac{\rho\sum_i \frac{w_i}{A_i}\left(Z_i + k_{1,j}\cdot Z_i^{2.86} + k_{2,j}\cdot Z_i^{4.62}\right)}{\rho_{\mathrm{w}}\sum_{i,\mathrm{w}} \frac{w_i}{A_i}\left(Z_i + k_{1,j}\cdot Z_i^{2.86} + k_{2,j}\cdot Z_i^{4.62}\right)}. \tag{4}$$

Here Z_i, A_i and w_i are the atomic number, the atomic weight and the elemental weight fraction of the i'te element in the compound, respectively. ρ is the mass density of the compound and the subscript "w" in the denominator refers to water. The superscript "cal" (an abbreviation for "calculated") is used to indicate that these reduced CT numbers are not measured.

The two parameters k_1 and k_2 characterize the CT energy spectrum and they are determined by making calibration CT scans of materials with known elemental composition. For the calibration CT scans we used a Gammex 467 electron density calibration phantom (Gammex, Middleton, WI) with thirteen different insert materials of tissue equivalent electron density. The phantom was CT scanned with a Dual Source CT scanner (SOMATOM Definition Flash, Siemens Healthcare, Forchheim, Germany). Image acquisition was carried out in dual energy mode, with a tube voltage pair of 80/140Sn kVp (Sn: 0.4 mm extra tin prefiltration) and a CT dose index of $\mathrm{CTDI_{vol}} = 20.6$ mGy.

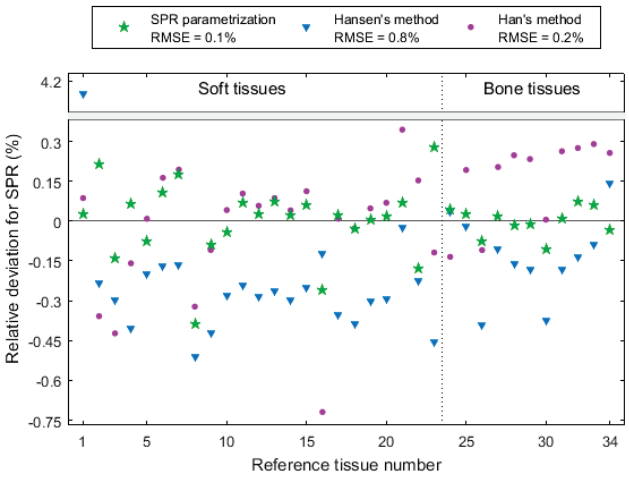

Fig. 1. Plot of the relative deviations for SPR for each standard reference tissue used in the fitting procedures for the three SPR estimation methods. Soft tissues are plotted to the left of the vertical line and bone tissues to the right.

The two parameters, $k_{1,j}$ and $k_{2,j}$, were then found by minimizing the difference of eq. (2) and (4) for the insert materials.

We have compared our results for the SPR parametrization to two other DECT, one three-step method and one two-step method. For the three-step method we chose the method presented by Hansen *et al*. [1], and for the two-step method we chose the method presented by Han *et al.* [4]. The latter is a two-material decomposition method, where each tissue is assumed to be decomposable into either water and polystyrene (soft tissues) or water and a 23% aqueous solution of $CaCl_2$ (bone tissues). We made a slight change to this method since we used a separation point of $\xi = u_H/u_L = 0.97$ instead of $\xi = 1$ as suggested in [4], i.e. tissues with $\xi \geq 0.97$ were assigned to the soft tissue group and tissues with $\xi < 0.97$ were assigned to the bone tissue group.

A. Test of robustness towards tissue variations

To test the robustness of the parametrization we changed the reference tissues and calculated their new SPR estimates based on the fit performed for the standard reference tissues. We used the same scheme for making changes to the reference tissues as applied by Yang *et al*. [3], i.e. we made the assumption that the density and the elemental weight fractions could be altered independently. So we either rescaled the density or changed the elemental weight fractions in the reference tissue. For both types of changes we made variations in the range $\alpha \in [-5\%, 5\%]$.

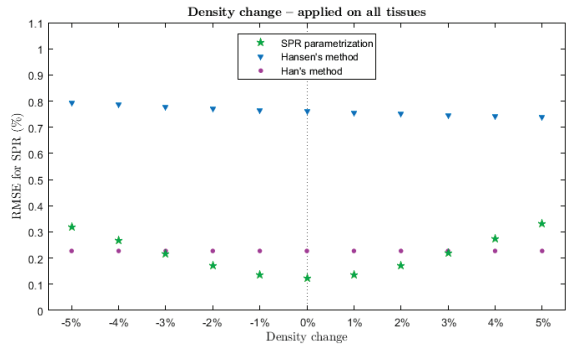

(a)

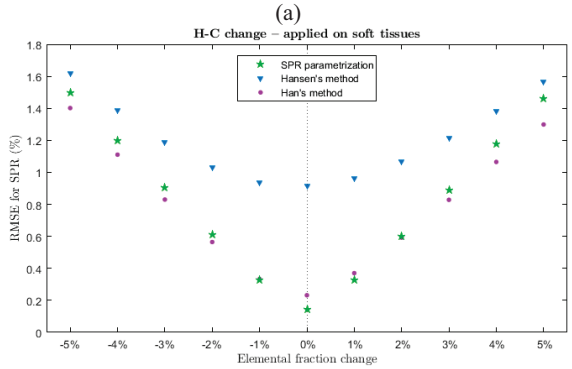

(b)

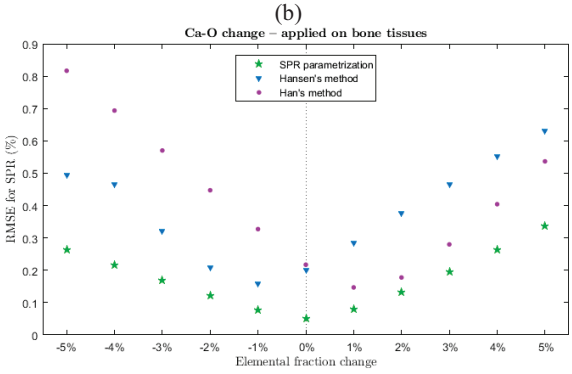

(c)

Fig. 2. Root-mean-square errors for each step of change in the tissue variations. (a) Changing the density. (b) Changing the elemental weight fraction of hydrogen and carbon in soft tissues. (c) Changing the elemental weight fraction of calcium and oxygen in bone tissues.

For density changes, we did a rescaling, so the new density was given as $\rho' = \rho \cdot (1 + \alpha/100\%)$. The density changes were applied on all 34 reference tissues.

When changing the elemental composition, the elemental weight fractions of two elements was changed together to ensure the sum of the elemental weight fractions was always equal to one. This way the elemental weight fraction changes were performed by: $w_a' = w_a + \alpha$ and $w_b' = w_b - \alpha$, where $w_{a,b}$ are the two elemental weight fractions to be changed. We only changed the major elemental components in the tissues, which are oxygen and carbon for all the tissues, together with hydrogen for soft tissues and calcium for bone tissues.

For each change, the theoretical SPRs for the reference tissues were recalculated and new SPR estimates were made.

B. Test of robustness towards noise in the CT images

CT images are always influenced by noise. CT numbers for homogenous material will therefore not be constant over all pixels covering the material. To investigate the impact of CT noise on the SPR estimates from the new SPR parametrization we added noise to the calculated CT numbers for the reference human tissues. The noise values were sampled from a normal distribution with a mean of zero and a standard deviation corresponding to the standard deviations for the CT numbers for the Gammex inserts. Since the DECT images of the Gammex phantom were acquired at clinical dose values (21 mGy) the noise level was clinically realistic.

We calculated the water equivalent range error which the noise would result in over 10 cm of the reference tissues. We assumed a pixel size of 1 mm, giving 100 pixels through the 10 cm. A new random noise value was added in each pixel and the SPR estimates for each pixel were calculated. The water equivalent range error was then calculated as

$$\Delta R_{\mathrm{w}} = 1\ \mathrm{mm} \sum_{i=1}^{100} \mathrm{SPR}_i - 10\ \mathrm{cm} \cdot \mathrm{SPR}^{\mathrm{teo}} \ . \qquad (5)$$

We reran this calculation 10,000 times and used the mean value for ΔR_{w} as our estimate of the water equivalent range error over 10 cm of a reference tissue.

When applying noise, the SPR estimates for Hansen's method and for Han's method could get complex, therefore we had to make minor changes to these methods to avoid this problem.

III. Results

Applying the new SPR parametrization on the standard reference tissues gave a root-mean-square error (RMSE) of 0.12%, compared to a RMSE of 0.76% for Hansen's method and 0.23% for Han's method. In fig. 1 it is seen that the main improvement is in bone tissues, where the RMSE for the SPR parametrization was 0.05%, compared to 0.20% and 0.22% for Hansen's method and for Han's method, respectively.

A. Test of robustness towards tissue variations

In fig. 2 the results for three out of the six tissue variations are shown. Changing the density, the RMSE increased using the SPR parametrization, but the RMSE did not change for the two other methods, as is seen in fig. 2(a).

For changes to the elemental weight fractions of hydrogen and carbon (fig. 2(b)) the RMSE increased faster

TABLE I
ROOT-MEAN-SQUARE (RMS) AND MAXIMUM (MAX.) FOR THE MEAN OF THE 10,000 CALCULATIONS OF THE WATER EQUIVALENT RANGE ERRORS THROUGH 10 CM OF A REFERENCE HUMAN TISSUE, WHEN APPLYING NOISE TO THE CALCULATED CT NUMBERS. THE RESULTS ARE GIVEN IN MM. IN PARENTHESES THE RMS AND THE MAX. OF THE STANDARD DEVIATION (STD.) OVER THE 10,000 CALCULATIONS ARE STATED, THESE RESULTS ARE ALSO GIVEN IN MM.

Method	RMS (STD.)	Max. (STD.)
SPR parametrization	0.16 (0.59)	0.40 (1.71)
Hansen's method	1.12 (0.63)	2.13 (0.79)
Han's method	0.71 (0.54)	1.09 (0.61)

for the SPR parametrization than for the other methods, but as the RMSE of the standard tissues was lowest for the SPR parametrization, the RMSEs for the non-standard tissues were comparable to the other methods. The results for the H-O change were similar.

The RMSEs for the change in the calcium and oxygen content were significantly lower for the SPR parametrization than for the two other methods, as is seen in fig. 2(c). Similar results were obtained for the change of Ca and C. For changes of the carbon and oxygen content none of the methods gave any RMSE increases.

B. Test of robustness towards noise in the CT images

The root-mean-square (RMS) and the maximum for the water equivalent range errors for the 34 reference human tissues are listed in table I. From the table it is seen that the SPR parametrization resulted in the lowest errors. These errors were the mean of the errors calculated in the 10,000 calculations. The standard deviations for the errors over the 10,000 calculation were nearly the same for all three methods and for all tissues. Lung tissue had a relatively high standard deviation using the SPR parametrization. However, the mean error plus one standard deviation was still lower than the mean error for lung tissue using Hansen's method.

IV. DISCUSSION

The proposed parametrization for SPR has a lower RMSE than the two other DECT methods for SPR estimation. The RMSEs for the SPR estimates for the standard reference tissues are, however, not clinically realistic since they were calculated for the tissues which the methods were fitted for and further the CT numbers were noise-free. The RMSEs found here are therefore lower bounds. But as the three methods were tested under the same conditions the SPR parametrization can still be assumed to perform the best.

The new SPR parametrization is also more robust against variations in the elemental composition of human tissues as can be seen from fig. 2. For density changes the SPR parametrization is though less stable than the two other methods, but still the density must change by 4% before the RMSE for the SPR parametrization is no longer the lowest. Such high density change might not be clinically realistic. Therefore the SPR parametrization can be seen as robust towards tissue variations. This will lead to an increased robustness of the SPR calculation for proton therapy planning.

The main advantage of the SPR parametrization is nevertheless the increased robustness towards noise in the CT images. Applying noise to the calculated CT numbers the SPR parametrization gave the lowest errors for the water equivalent ranges through 10 cm of tissue.

Lowering the deviations for the SPR is an important step towards obtaining the full potential of proton therapy. Today range uncertainty margins are usually set around 3.5% of the range + 1 mm [8]. For deep seated tumors, this will result in substantial uncertainty margins and large volumes of normal tissue will be irradiated to high doses. If the range uncertainty can be reduced, smaller treatment margins can be applied in proton treatment planning, and when less normal tissue is being exposed to high doses the risk of side effects will be reduced. Using the SPR parametrization can bring us one step closer to achieving this goal.

REFERENCES

[1] D. C. Hansen, J. Seco, T. S. Sørensen, J. B. B. Petersen, J. E. Wildberger, F. Verhaegen and G. Landry, "A simulation study on proton computed tomography (CT) stopping power accuracy using dual energy CT scans as benchmark", *Acta Oncologica* **54**, 1638–1642 (2015).

[2] U. Schneider, E. Pedroni and A. Lomax, "The calibration of CT Hounsfield units for radiotherapy treatment planning", *Phys. Med. Biol.* **41**, 111-124 (1996).

[3] M. Yang, G. Virshup, J. Clayton, X. R. Zhu, R. Mohan and L. Dong, "Theoretical variance analysis of single- and dual-energy computed tomography methods for calculating proton stopping power ratios of biological tissues", *Phys. Med. Biol.* **55**, 1343-1362 (2010).

[4] D. Han, J. V. Siebers, and J. F. Williamson, "A linear, 790 separable two-parameter model for dual energy ct imag- 791 ing of proton stopping power computation," Phys. Med. 792 Biol. 43, 600–612 (2016).

[5] N. Hünemohr, B. Krauss, C. Tremmel, B. Ackermann, O. Jäkel and S. Greilich, "Experimental verification of ion stopping power prediction from dual energy CT data in tissue surrogates", *Phys. Med. Biol.* **59**, 83-96 (2014).

[6] A. E. Bourque, J. F. Carrier and H. Bouchard, "A stoichiometric calibration method for dual energy computed tomography", *Phys. Med. Biol.* **59**, 2059-2088 (2014).

[7] G. Landry, J. Seco, M. Gaudreualt, F. Verhaegen, "Deriving effective atomic numbers from DECT based on a parametrization of the ratio of high and low linear attenuation coefficients", *Phys. Med. Biol.* **58**, 6851-6866 (2013).

[8] H. Paganetti, "Range uncertainties in proton therapy and the role of monte carlo simulations", *Phys. Med. Biol.* **57**, R99-R117 (2012).

Dual-energy CT spectra optimization for proton treatment planning

Gloria Vilches-Freixas, Jean Michel Létang, Nicolas Ducros and Simon Rit

***Abstract*—The purpose of this study was to determine the optimal dual-energy spectra for the treatment planning of proton therapy. We have evaluated the effect of various voltages and tin filtration combinations on the relative electron density (RED) map accuracy and precision. The RED is directly related to the stopping-power (SP) map and thus to the accuracy of the proton range estimation. An acquisition setup representing a medium-size body irradiation was evaluated. For all spectra combinations, virtual CT projections of the Gammex 467 tissue characterization phantom were simulated with realistic energy-integrating detector response model. Two situations were simulated: an ideal case without noise (infinite dose) and a realistic situation with a Poisson noise corresponding to a 20 mGy central dose. To derive the RED maps from dual-energy imaging, the projection-based basis material decomposition method proposed by Alvarez and Macovski (1976) was implemented. It was observed that the energy separation between the incident spectra had little influence on the RED accuracy but a strong influence on the precision. Different optimal ranges of low and high energy tube voltages and additional tin thicknesses that maximize the overall accuracy and the precision of RED maps were found. However, when studying each phantom material separately, a large variability of the optimal spectra was observed. An emphasis on the materials present in the anatomical region of interest must be made during the optimization process of the dual-energy spectra.**

I. Introduction

Dual energy computed tomography (DECT) imaging consists in recording two sets of acquisitions of an object at different X-ray voltages. By combining these images, either in the projection domain (prior to image reconstruction) or in the image domain (after image reconstruction), one can characterize the patient tissues. Relative electron density (RED) and effective atomic number (Z_{eff}) are quantities commonly used for material segmentation in radiotherapy applications that can be estimated from DECT. In the proton therapy context, the range of protons in patients is determined from the stopping power ratio (SPR) of tissues relative to water along the beam path. SPR can be derived from RED and Z_{eff} maps and the Bethe-Bloch equation [1], or by establishing a polyline curve (RED, SPR/RED) through calibration [2]. There are different commercial strategies to perform DECT such as dual-source, fast kV-switching and dual-layer scanners. For all techniques, the choice of the low energy (LE) and the high energy (HE) spectra influences the imaging output. The performance of dual-energy imaging is commonly evaluated in terms of contrast-to-noise ratio (CNR) or signal-to-noise ratio (SNR). In this work, we focus on finding an optimal combination of voltages and source filtration to maximize the figure of merit specific to proton therapy dose calculations: the accuracy and the precision of the extracted RED maps.

Université de Lyon, CREATIS, CNRS UMR5220, Inserm U1206, INSA-Lyon, Université Lyon 1, Centre Léon Bérard, Lyon, France (e-mail: simon.rit@creatis.insa-lyon.fr).

II. Materials and Methods

A. Phantom

The 33-cm diameter Gammex RMI 467 (Gammex, Middleton, WI) tissue characterization phantom was used to represent a medium-size body. Sixteen inserts mimicking human tissue attenuation properties positioned as described in Figure 1 with mass densities ranging from 0.3 to 1.82 g/cm^3 and known chemical compositions were considered. The index-to-material mapping and the reference RED values are provided in Figure 1. For each insert, the electron density relative to water was estimated by:

$$RED_m = \frac{\rho_m \sum_i \omega_i \left(\frac{Z}{A}\right)_i}{\rho_{\mathrm{W}} \left(\frac{Z}{A}\right)_{\mathrm{W}}} \quad (1)$$

where the index m refers to the insert material and the label W to water. ρ is the mass density, ω_i is the fraction by weight of the i^{th} element and Z/A is the ratio of number of electrons per molecular weight.

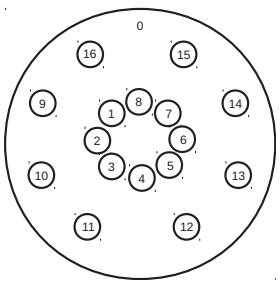

ID	Materials	RED
0	Water	1.000
1	CB2-50% $CaCO_3$	1.470
2	BR12 Breast	0.957
3	SB3 Cortical Bone	1.693
4, 15	AP6 Adipose	0.922
5, 14	LV1 Liver	1.069
6	BRN-SR2 Brain	1.046
7, 12	Water Solid	0.990
8, 9	LN300 Lungs	0.292
10	LN450 Lungs	0.438
11	CB2-30% $CaCO_3$	1.285
13	IB3 Inner Bone	1.092
16	B200 Bone Mineral	1.102

Fig. 1: Left: Gammex 467 phantom. Right: Insert ID, material name and reference RED values.

B. X-ray spectra

SpekCalc [3] was used to generate the X-ray spectra from 60 kV to 140 kV with 2 kV steps, 10° anode angle, 2.5 mm Al (required minimum filtration according to the NCRPM [4]) and 1000 mm air filtration. Each spectrum was filtered with tin (Sn) thicknesses [5] ranging from 0 to 2.5 mm at 0.1 mm

increments. For the LE acquisitions, the tube voltage was varied from 60 kV to 90 kV, whereas for the HE acquisitions it was varied from 80 kV to 140 kV. No tin filtration was considered for the LE acquisitions, only the 2.5 mm Al inherent filtration to maximize the energy gap.

C. Image simulation

Combining voltages and tin thicknesses, a total of 12896 sets of CT projection data were simulated with and without noise. Virtual CT acquisitions of the Imaging Ring (IR) X-ray system (MedPhoton, Salzburg, Austria) were carried out by means of deterministic simulations in Gate [6] with realistic energy-integrating detector response model. Scatter-free fan-beam of 807 pixels of 1 mm acquired with 360 projections were considered. The source-to-center distance was 626 mm and the source-to-detector distance was 1026 mm. For the realistic scenario, realistic Poisson noise was applied to the projections to deliver a central dose of 10 mGy with each voltage and filtration combination, and thus a total central dose of 20 mGy with the dual-energy acquisition. In a previous work [7], we observed that the dose balance between energy levels was not critical for material decomposition with dual-energy imaging. For this reason, the same dose at the center was considered for the low and the high energy acquisitions.

1) Detector response: The detector response was generated using Monte Carlo simulations. The flat panel detector of the IR was modeled in Gate as a stack of layers of different material according to the manufacturer's description. The response of the detector was obtained by measuring the energy deposit in the scintillator layer with monoenergetic pencil beams of energies ranging from 1 to 140 keV [8]. The energy-dependent detector response used in this study is shown in Figure 2 .

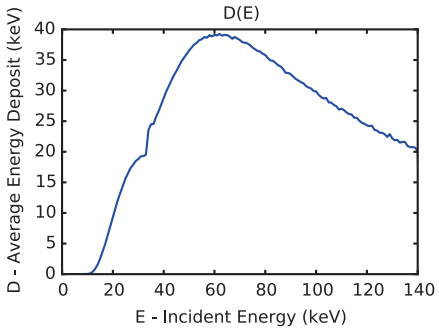

Fig. 2: Energy-dependent detector response.

2) Dose - Number of photons: For each imaging setup the number of primaries per simulation, N_{prim}, required to deliver a central dose, D_c, of 10 mGy was determined analytically assuming an homogeneous water medium:

$$N_{prim} = \frac{D_c \; A_{beam}}{\int_E S(E) \; e^{-\mu_{\mathrm{W}}(E) \; R} \; \left(\frac{\mu_{en}(E)}{\rho}\right)_{\mathrm{W}} \; E \; \mathrm{d}E} \tag{2}$$

where A_{beam} is the area covered by the beam at the isocenter, S is the energy-dependent incident spectrum, $(\mu_{en}/\rho)_{\mathrm{W}}$ and μ_{W} are the energy-dependent mass energy absorption coefficient and the linear attenuation coefficient of water taken from the NIST database [9], and R is the radius of the phantom.

3) Energy gap: For each X-ray spectra pair the incident energy gap, ΔE, was calculated as the separation between the average energies of the incident spectra:

$$\Delta E = \int_0^{E_2} S(E) \; E \; \mathrm{d}E - \int_0^{E_1} S(E) \; E \; \mathrm{d}E \tag{3}$$

where E_1 and E_2 are the maximum energies of the LE and the HE spectra, respectively.

D. Decomposition method

The two-material decomposition method proposed by Alvarez and Macovski (1976) [10] was implemented in the projection domain. The key idea is that the attenuation coefficient of the scanned object, $\mu(\boldsymbol{x}, E)$, can be expressed as a linear combination of two energy-dependent basis functions of two materials with energy-independent coefficients. Water (W) and compact bone (B) were chosen as basis materials. Their respective energy-dependent mass attenuation coefficients, (μ/ρ), were the basis functions and their mass densities, ρ, the coefficients:

$$\mu(\boldsymbol{x}, E) = \rho_{\mathrm{W}}(\boldsymbol{x}) \; \left(\frac{\mu}{\rho}\right)_{\mathrm{W}}(E) + \rho_{\mathrm{B}}(\boldsymbol{x}) \; \left(\frac{\mu}{\rho}\right)_{\mathrm{B}}(E) \tag{4}$$

Two sinograms of the same object are available in DECT by performing an acquisition with LE and HE spectra. A system of two equations can then be determined for each projection angle:

$$I_{\mathrm{LE}}(\rho_{\mathrm{W}}, \rho_{\mathrm{B}}) = \int_E S_{\mathrm{LE}}(E) \; D(E) \exp\left(-\int_L \mu(\boldsymbol{x}_l) \; \mathrm{d}l\right) \mathrm{d}E \tag{5}$$

$$I_{\mathrm{HE}}(\rho_{\mathrm{W}}, \rho_{\mathrm{B}}) = \int_E S_{\mathrm{HE}}(E) \; D(E) \exp\left(-\int_L \mu(\boldsymbol{x}_l) \; \mathrm{d}l\right) \mathrm{d}E \tag{6}$$

where L is the line-segment between the source and a detector pixel, I_{LE} and I_{HE} are the measured intensities, S_{LE} and S_{HE} are the weights of the polychromatic photon spectra, and $D(E)$ the detector response. Instead of solving this system numerically, the unknowns can be obtained by direct approximation with a power series of the logarithm of I_{LE} and I_{HE} [11] through a calibration procedure. A fourth degree polynomial with twelve terms was used to solve this system of equations. Image reconstructions of water and compact bone mass densities were performed using filtered backprojection on a 380×380×1 grid with 1×1×1 mm^3 voxels size, i.e., in the central slice only. On a pixel-by-pixel basis, the RED image was derived from the total mass density image ρ and Equation 1:

$$\rho(\boldsymbol{x}) = \rho_{\mathrm{W}}(\boldsymbol{x}) + \rho_{\mathrm{B}}(\boldsymbol{x}) \tag{7}$$

$$\left(\frac{Z}{A}\right) = \frac{\rho_{\mathrm{W}}}{\rho} \; \left(\frac{Z}{A}\right)_{\mathrm{W}} + \frac{\rho_{\mathrm{B}}}{\rho} \; \left(\frac{Z}{A}\right)_{\mathrm{B}} \tag{8}$$

E. Figures of merit

For each (LE, HE, mm Sn) tuple, the estimated RED image was compared to the ground-truth values. The relative accuracy and precision were calculated in a region-of-interest (ROI) of 3/4 the size of the insert. The absolute accuracy and the precision of the RED averaged over all inserts were also computed. First, the reconstructed RED images without noise were used to determine the optimal voltages and filtration that maximizes the overall accuracy. Then, the RED images acquired in a realistic imaging setup, in the presence of noise, were investigated. Finally, the optimal energy spectra for a representative tissue of each insert group was studied separately.

III. Results and Discussion

For both the ideal and the realistic situations, a relative electron density image per (LE, HE, mm Sn) tuple was obtained after decomposition and reconstruction. In total, 12896 tuples were investigated. The reconstructed RED images were compared to the ground-truth values and, for each image, the following quantities were extracted: accuracy and precision averaged over the sixteen phantom inserts, and accuracy and precision for each phantom insert separately. From among these data, a tuple of values that maximizes the overall accuracy was selected: (78 kV LE, 94 kV HE, 0.1 mm Sn). From this point, a sensitivity analysis of the accuracy and the precision as a function of the low voltage, the high voltage and the additional filtration was done. Orthogonal slices for both the ideal scenario and the noisy situation are shown in Figure 3. The last row of Figure 3, which corresponds to the overall precision of the realistic situation, shows that the worst precision is achieved at those ranges where the accuracy is maximized.

For the realistic scenario, the overall accuracy and precision were plotted against the incident energy gap, as shown in Figure 4. The overall accuracy was not strongly dependent on the spectra separation, whereas the overall precision asymptotically approached a 4.7% level with increasing energy gap. This level of precision was achieved from an energy gap of 60 keV. A zero precision was expected for the simulations without noise. Nevertheless, due to the voxelized phantom geometry with a sub-optimal resolution, interpolation errors of the 3D reconstruction process affected the overall precision. A constant value of 2.6% was estimated for all RED images without noise which is included in the noisy simulations of Figure 3 and 4.

The SPR map estimated from the RED image would then be used to compute the proton range in the patient. Even though the presence of noise in the SPR image is a concern, the noise is likely to be averaged along the voxels of the beam path and, thus, the final impact on the proton range should not be dramatic. On the other hand, accuracy errors will add up along the beam path and the error in the range will be more significant. For this reason, maximizing the accuracy seems more appropriate. Moreover, the 20 mGy central dose value considered in this study is very low and, increasing the imaging dose would improve the precision.

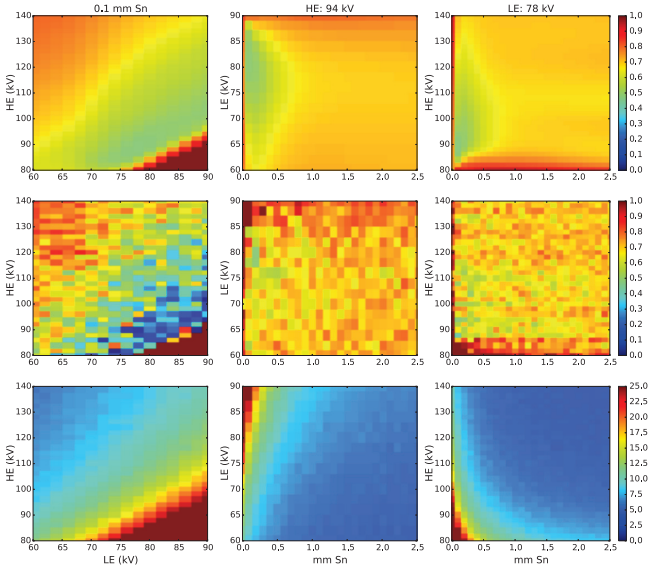

Fig. 3: Overall RED accuracy and precision as a function of the LE, HE and tin filtration. From top to bottom: overall accuracy for the ideal situation (no noise), overall accuracy (middle) and overall precision (bottom) for the realistic acquisition. From left to right: LE-HE plot at 0.1 mm Sn, LE-mm Sn plot at HE: 94 kV, HE-mm Sn plot at LE: 78 kV. Colorbars indicate the percentage error and the relative uncertainty for the accuracy and the precision, respectively.

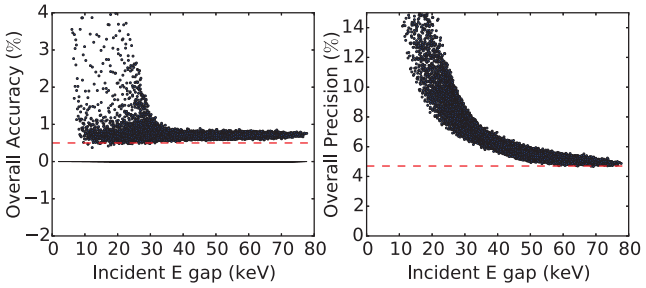

Fig. 4: Overall RED accuracy and precision as a function of the incident energy gap for the realistic acquisition scenario. Dashed red lines indicate the 0.5% accuracy level (left) and the 4.7% precision level (right).

Another approach to reduce image noise is to make use of regularized reconstruction algorithms instead of filtered backprojection for image reconstruction.

The accuracy and the precision of each phantom insert relative to the (78 kV LE, 94 kV HE, 0.1 mm Sn) tuple are shown in Figure 5. Low density tissues (lungs LN300 and LN450) show the worst precision. In terms of accuracy, all inserts fall within the $\pm 1\%$ error range.

Then, we studied whether the optimal spectra determined in terms of the overall accuracy corresponded to the optimal spectra for each insert group. One representative insert per tissue group was selected: LN450(10) for the low (RED$<$0.5), AP6(15) for the medium (0.5$<$RED$<$1.2) and CB2-50(1) for the high (RED$>$1.2) density. From the (78 kV LE, 94 kV HE,

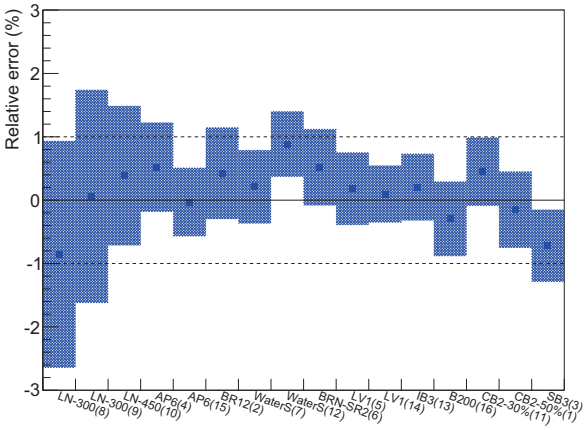

Fig. 5: RED accuracy and precision results for each insert of the Gammex 467 phantom (78 kV, 94 kV, 0.1 mm Sn) for the 20 mGy acquisition.

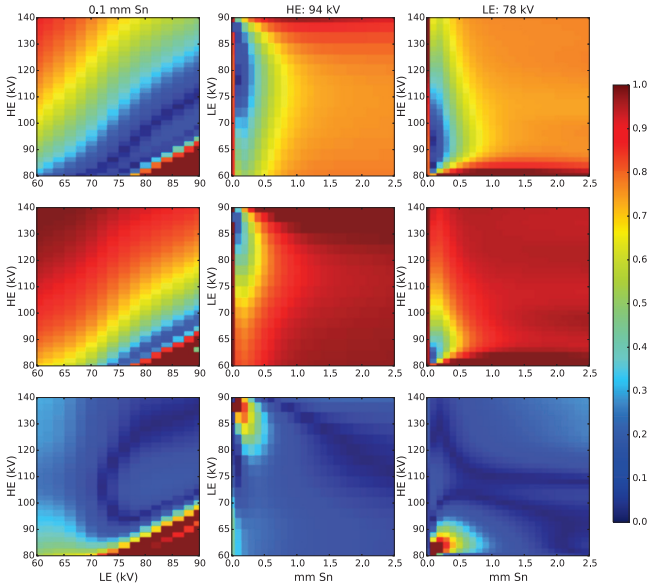

Fig. 6: From top to bottom, RED accuracy results as a function of the LE, HE and tin filtration for the insert: LN450, AP6 and CB2-50. From left to right: LE-HE plot at 0.1 mm Sn, LE-mm Sn plot at HE: 94 kV, HE-mm Sn plot at LE: 78 kV. The colorbar indicates the percentage error for the accuracy. Data corresponding to the ideal situation, without noise.

0.1 mm Sn) point, orthogonal slices were plot to study the dependence of the inserts accuracy with the low voltage, the high voltage and the additional filtration. Due to the limited space, only those plots relative to the ideal situation are shown in Figure 6. However, these plots mask the increased presence of noise in the low density inserts. Low and medium density inserts are more sensitive to the energy spectra than high density inserts. The optimal spectra selected by means of the overall accuracy seems adequate for low and medium density inserts. According to these plots, for high density tissues it is preferable to have high LE, medium HE and high filtration.

IV. Conclusion

An extensive study of the impact of the dual-energy spectra on the relative electron density accuracy and precision was done. An ideal situation without noise and a realistic acquisition with a total dose of 20 mGy were considered. The optimal range of low and high energy tube voltages and additional tin thicknesses in terms of accuracy and precision were not the same. The precision was improved with increasing energy separation between the incident spectra, whereas the accuracy showed little dependence. According to these results, a material selective spectra optimization is advisable when performing dual-energy imaging of different human regions for proton treatment planning. Moreover, it would be interesting to reproduce the same study considering a large-size patient.

Acknowledgment

This work was partially supported by grant ANR-13-IS03-0002-01 (DEXTER project) from the French National Research Agency (ANR). This work was performed within the framework of the LABEX PRIMES (ANR-11-LABX-0063) of Université de Lyon, within the program ”Investissements d’Avenir” (ANR-11-IDEX-0007) operated by the ANR.

References

[1] M. Yang, G. Virshup, J. Clayton, X. R. Zhu, R. Mohan, and L. Dong, “Theoretical variance analysis of single- and dual-energy computed tomography methods for calculating proton stopping power ratios of biological tissues.” *Phys. Med. Biol.*, vol. 55, no. 5, pp. 1343–1362, 2010.

[2] N. Kanematsu, T. Inaniwa, and Y. Koba, “Relationship between electron density and effective densities of body tissues for stopping, scattering, and nuclear interactions of proton and ion beams,” *Med. Phys.*, vol. 39, no. 2, pp. 1016–1020, 2012.

[3] G. Poludniowski, G. Landry, F. DeBlois, P. M. Evans, and F. Verhaegen, “SpekCalc: a program to calculate photon spectra from tungsten anode x-ray tubes.” *Phys. Med. Biol.*, vol. 54, no. 19, pp. N433–N438, 2009.

[4] N. C. on Radiation Protection and M. Measurements. Bethesda, “Medical x-ray, electron beam and gamma-ray protection from energies up to 50 MeV, Report No. 102.”

[5] A. N. Primak, J. C. Ramirez Giraldo, X. Liu, L. Yu, and C. H. McCollough, “Improved dual-energy material discrimination for dual-source CT by means of additional spectral filtration.” *Med. Phys.*, vol. 36, no. 4, pp. 1359–1369, 2009.

[6] S. Jan, G. Santin, D. Strul, S. Staelens, K. Assié, and D. Autret, “GATE: a simulation toolkit for PET and SPECT,” *Phys. Med. Biol.*, vol. 49, pp. 4543–4561, 2004.

[7] G. Vilches-Freixas, J.-M. Letang, K. Presich, P. Steininger, and S. Rit, “Optimal dose balance between energy levels for material decomposition with dual-energy X-ray CT,” in *Radiotherapy and Oncology, Elsevier, Vol.115, pp.S506-S507, Barcelona (Spain)*, 2015.

[8] D. A. Roberts, V. N. Hansen, A. C. Niven, M. G. Thompson, J. Seco, and P. M. Evans, “A low Z linac and flat panel imager: comparison with the conventional imaging approach.” *Phys. Med. Biol.*, vol. 53, no. 22, pp. 6305–6319, 2008.

[9] J. H. Hubbel and S. M. Seltzer, “Tables of X-ray mass attenuation coefficients and mass energy-absorption coefficients. National Institute of Standards and Technology (NIST). Retrieved September 2007.”

[10] R. E. Alvarez and a. Macovski, “Energy-selective reconstructions in X-ray computerized tomography.” *Phys. Med. Biol.*, vol. 21, no. 5, pp. 733–744, 1976.

[11] K.-S. Chuang and H. K. Huang, “Comparison of four dual energy image decomposition methods,” *Phys. Med. Biol.*, vol. 33, no. 4, p. 455, 1988.

Fan-Beam Reconstruction Under Motion and Data Truncation: Comparing Analytic and Iterative Approaches

Jan Hoskovec, Fabien Momey, Rolf Clackdoyle, Laurent Desbat and Simon Rit

***Abstract*—In this paper, we compare analytic and iterative fan-beam reconstruction approaches when the object undergoes some rigid motion during the scan, and in the situation of truncated projections. Based on our recent work presenting an exact analytic reconstruction method for this problem, we are able to predict the field of theoretically reconstructible points for our method. The object motion is handled by using a reference frame attached to the object, which therefore appears static while the source trajectory undergoes a non-circular "virtual" motion. We implemented the iterative reconstruction as the convex minimization of a data-fidelity term under non-negativity constraint and regularization to solve this static problem with virtual source trajectory. We compared the reconstructed field of view for the two methods on 2D fan-beam Shepp-Logan phantom simulations. Our results show that both methods validate the predicted reconstructible zone and correlate well in terms of reconstruction quality. The iterative reconstruction also demonstrates that in certain cases it is possible to recover structures beyond the strict analytic frontier of reconstructibilty.**

***Index Terms*—Tomography, Region-Of-Interest Tomography, Dynamic Tomography.**

I. Introduction

In [1], we reported on a method for performing exact analytic 2D fan-beam reconstruction when the object of interest has undergone a perfectly known rigid translation during the circular scan, also involving data truncation. Rigid object motion transforms the circular source trajectory into a virtual one which can involve data truncation. The method exploits the data redundancy from the 2π source trajectory to extend the field of reconstructible points where Differentiated Back-Projection with Hilbert filtering (DBP-H) [5] can be performed. The algorithm was tested in a proof-of-concept study on Shepp-Logan phantom simulations with several motion cases and detector sizes.

In this paper, we compare the results given by our analytic algorithm with an iterative reconstruction approach, particularly in terms of the predicted field of reconstructible points. Our results from Shepp-Logan phantom simulations show a very good match regarding the almost perfectly reconstructed zone of the phantom, and highlight possibilities for the iterative method to reconstruct beyond the predicted field of view.

II. Materials and Methods

A. Geometry

Our work takes place in the context of 2D fan-beam reconstruction from a circular scan around the object. The geometry is illustrated in Fig.1. Fan-beam projections of a density function $f(\vec{x})$ can be written as:

$$p(\alpha,\beta)=\int_{-\infty}^{\infty} f(\vec{v}_\beta - t\vec{\alpha}_\beta)dt \tag{1}$$

with β the polar angle of the source from the vertical axis and $\vec{v}_\beta = R\vec{\beta} = R(-\sin\beta,\cos\beta)^T$ the source position. The fan angle is denoted α and $\vec{\alpha}_\beta = (-\sin(\alpha+\beta),\cos(\alpha+\beta))^T$ is the direction of the ray emanating from the source. The angular conventions taken here are illustrated Fig. 1.

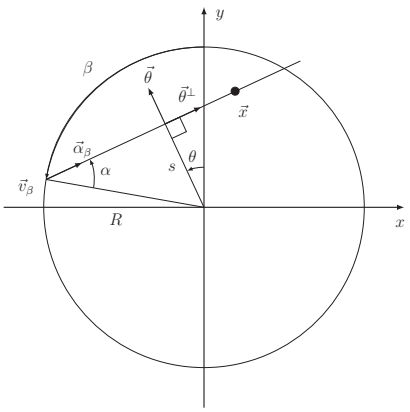

Fig. 1. The fan-beam projection geometry. The source is at $\vec{v}_\beta$ and the trajectory radius is R. A measured ray in the fan-beam geometry is parametrized by (α,β). Also shown are the equivalent parameters (s,θ) expressing the same ray in the parallel projection geometry.

Fan-beam data $p(\alpha,\beta)$ can be related to equivalent parallel-beam projections $\bar{p}(s,\theta)$ via the following change of variables:

$$\theta = \alpha+\beta-\frac{\pi}{2} \tag{2}$$

$$s = R\sin\alpha, \tag{3}$$

therefore

$$p(\alpha,\beta)=\bar{p}(R\sin\alpha,\alpha+\beta-\frac{\pi}{2}). \tag{4}$$

B. DBP-H Formula

We summarize here our analytical reconstruction method, which was presented in [1]. This method belongs to the DBP-H family, sometimes called simply DBP, or BPF, for Backprojection-Filtration. More specifically, the DBP-H algorithm used here is of the "backproject first" approach [9], which begins by performing two backprojections of the unprocessed sinogram data onto the target pixel grid. Then, via a simple sum of partial derivatives of each weighted backprojection, we obtain the same Hilbert image of the object of interest as if we had performed a differentiation along the flat detector before backprojecting.

The general DBP-H reconstruction formula is given by

$$H_\phi f(\vec{x}) = \frac{-1}{2\pi} b_\phi(\vec{x}) = \frac{-1}{2\pi}\int_\phi^{\phi+\pi} \frac{\partial}{\partial s}\bar{p}(s,\theta)\Big|_{s=\vec{x}\cdot\vec{\theta}} \mathrm{d}\theta. \tag{5}$$

This work was supported by the DROITE project (Dynamic ROI tomography, Theory and Experiments), funded by the French ANR (N° ANR-12-BS01-0018).

Jan Hoskovec is with Laboratoire Hubert Curien ; CNRS UMR 5516, Saint-Étienne, France and with CREATIS ; CNRS UMR 5220 ; INSERM U 1044, Lyon, France, and was supported by an Allocation de Recherche from la Région Rhône-Alpes. E-mail: jan.hoskovec@univ-st-etienne.fr

Fabien Momey is with TIMC-IMAG ; CNRS UMR 5525, Grenoble, France

Rolf Clackdoyle was with Laboratoire Hubert Curien, is now with TIMC-IMAG ; CNRS UMR 5525, Grenoble, France

Laurent Desbat is with TIMC-IMAG ; CNRS UMR 5525, Grenoble, France

Simon Rit is with CREATIS ; CNRS UMR 5220 ; INSERM U 1044, Lyon, France

where $H_\phi f$ denotes a 1D Hilbert transform along the vector $\vec{\phi} = (\cos\phi, \sin\phi)^T$. With the "backproject first" approach, we obtain $b_\phi(\vec{x})$ by the following relation (see [1] or [9] for full derivation):

$$b_\phi(\vec{x}) = \frac{\partial}{\partial x}\int_\phi^{\phi+\pi} \bar{p}(\vec{x}\cdot\vec{\theta},\theta)(-\sin\theta)\mathrm{d}\theta + \frac{\partial}{\partial y}\int_\phi^{\phi+\pi} \bar{p}(\vec{x}\cdot\vec{\theta},\theta)(\cos\theta)\mathrm{d}\theta \quad (6)$$

where $\vec{\theta} = (-\sin\theta, \cos\theta)^T$.

1) Handling motion and truncation for DPB-H reconstruction: The "backproject first" DBP-H algorithm is useful in the context of motion-compensated reconstruction, since all motion corrections can be included *before* the sinogram data is processed in any manner. Our algorithm from [1] does just that when it rearranges motion contaminated full-scan fan-beam data into an equivalent, static, parallel-beam geometry.

When the object undergoes a (rigid) translation, the sinogram data may become truncated (when part of the object "leaves" the scanner's field-of-view during the scan). Since a rigid displacement of the object (described by a vector $\vec{d}_\beta$ parametrized by the gantry angle) is equivalent to a deformation of the X-Ray source trajectory by subtracting the same vector from its physical path, static truncation (due to limited detector width) and dynamic truncation (induced by object motion) can be handled as the same problem.

Observing the virtual trajectory $\vec{v}_\beta - \vec{d}_\beta$, we recall that with the DBP-H methods, we can compute a Hilbert image of a point if it is observable from a large enough segment of the (here, virtual) trajectory [5][6][8]. Such a point becomes theoretically reconstructible via (5). We refer to this type of point as a Hilbert point.

Taking advantage of the data redundancy inherent to a full scan, our algorithm can also recover points for which such a segment of the virtual trajectory is not available, but where data from the opposite side of the scan can fill in the gap. See [1] for details.

In practice, to reconstruct the object, we also need to be able to invert the Hilbert transform of the points we obtain. With a small *a priori* about the image support, we can invert Hilbert points using the finite-support Hilbert transform inversion formula from [3] on all line segments of Hilbert points which cross the entire object support. This condition also influences the choice of the angle ϕ.

C. Iterative reconstruction method for truncated projections and a virtual trajectory

Our iterative reconstruction algorithm looks for the static image $\boldsymbol{f}$ which minimizes the least squares criterion - the data-fidelity term - under a non-negativity constraint, with a regularization term:

$$\boldsymbol{f}^+ = \underset{\boldsymbol{f}\geq 0}{\arg\min}\left\{ \left\| \mathbf{R}^\beta \cdot \boldsymbol{f} - \boldsymbol{p}^\beta \right\|_2^2 + \mu\, \mathcal{J}_{\text{prior}}(\boldsymbol{f}) \right\}, \quad (7)$$

where $\boldsymbol{p}^\beta = \{\boldsymbol{p}^{\beta_k} | k = 1 \ldots N_\beta\}$ stands for the set of N_β fan-beam projections, and $\mathbf{R}^\beta$ is the model of fan-beam projections along the virtual (perturbed) source trajectory at the virtual angular positions $\{\beta_k | k = 1 \ldots N_\beta\}$.

The data-fidelity term ensures consistency of the model with the data. A non-negativity constraint is added as the object to be reconstructed is known to have positive values. The term $\mathcal{J}_{\text{prior}}$ accounts for prior information. The constraint and the regularizer are necessary for the reconstruction algorithm to effectively converge to a relevant solution, avoiding artifacts amplifications and noise. The hyperparameter μ controls the tradeoff between data fitting and regularization.

We chose an edge-preserving smoothness regularizer expressed as a relaxed total variation (TV) prior [7]:

$$\mathcal{J}_{\text{prior}}(\boldsymbol{f}) = \sum_i \sqrt{\|\nabla_i \cdot \boldsymbol{f}\|_2^2 + \epsilon^2}\,, \quad (8)$$

with $\epsilon > 0$ the relaxation parameter and ∇_i a finite difference operator approximating the spatial gradient at position i.

The minimization of (7) was carried out by the VMLM algorithm [4], a limited memory quasi-Newton method, for which we have added the handling of the non-negativity constraint.

III. Simulations and reconstructions

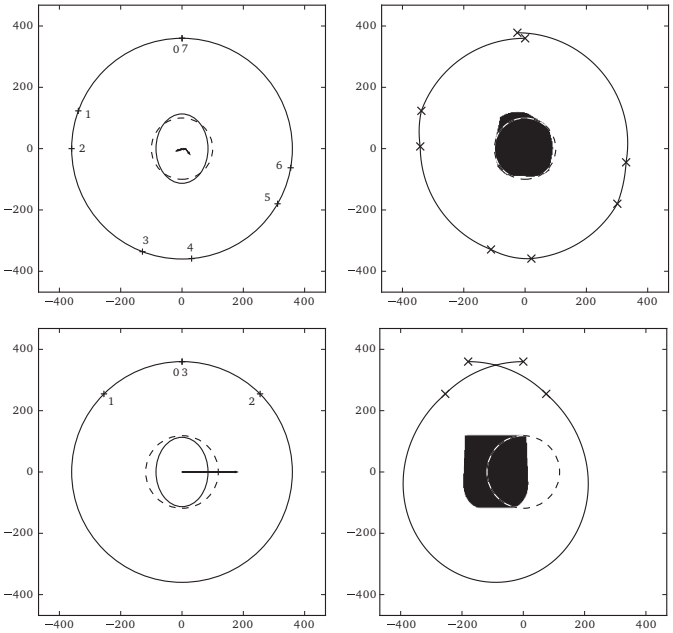

Fig. 2. Top left: Representation of motion 1. Bottom left: Representation of motion 2. Top right and bottom right: virtual trajectory, static FOV and regions of Hilbert points (in black) obtained respectively with the motions 1 and 2.

We simulated the projection data of an off-centered slice of the 3D Shepp-Logan phantom [2] for two cases of rigid motion of the phantom. Each case corresponded to a sequence of constant-velocity translations of the phantom during a circular scan of radius $R = 360$ mm with a flat detector at 480 mm from the source. *Motion 1* consisted of translations that occurred only during scan intervals $\beta \in [70°, 90°] \cup [159°, 185°] \cup [240°, 270°]$, which were respectively translations by vectors $R(-0.05, -0.02)^T, R(0.08, 0.02)^T, R(0.05, -0.04)^T$. *Motion 2* consisted of a single translation, occurring during the scan interval $\beta \in [45°, 315°]$, by the vector $R(0.5, 0)^T$. The rigid motions, as well as the equivalent ("virtual") source trajectories, are illustrated in Fig.2.

In this study the motion was assumed to be perfectly known, so was the corresponding virtual trajectory. For both methods, we reconstructed an image of 510×510 pixels with a sampling rate of 1 mm in both directions.

The analytic method proceeds by first introducing a map of Hilbert points. Its comparison with the *a priori* known phantom support helps to identify convenient Hilbert filtering directions. Once the direction is chosen, the corresponding Hilbert images are generated, and finite Hilbert inversion carried out along Hilbert lines. More details can be found in [1].

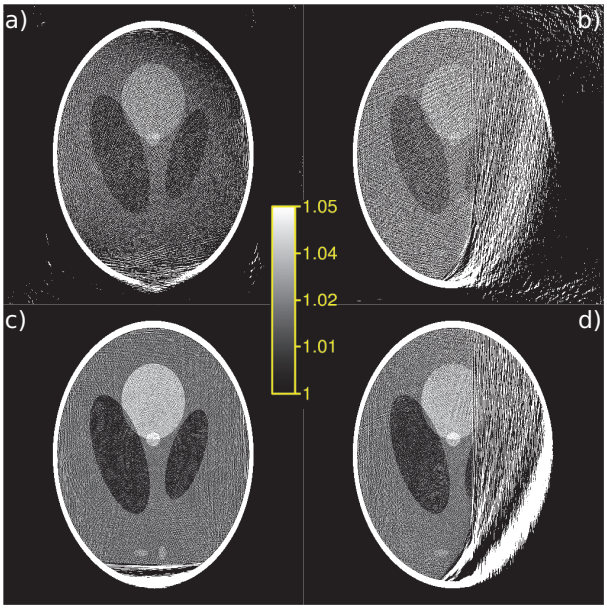

Fig. 3. Reconstructions of simulated cases *motion 1* (first column) and *motion 2* (second column) with the iterative reconstruction method. (a-b) Reconstruction without non-negativity constraint and without regularization. (c-d) Reconstruction with non-negativity constraint and without regularization.

For the iterative reconstruction, the value of ϵ was chosen to be 10^{-3}, *i.e.* $1/10$ of the minimum contrast value of the Shepp-Logan phantom. Therefore structures with contrast larger than this value would be preserved in the image, and smoothed otherwise. The hyperparameter μ was carefully tuned "by hand" until a satisfactory reconstruction quality was reached. A suitable value found was $\mu = 10^3$. The quality of the iterative reconstruction strongly depends on the degree of regularization. In general, a low value of μ or no regularization causes errors due to reprojection model approximations and noise amplification. Therefore, it is essential to regularize the solution, and preliminary results tended to verify this claim, as illustrated in Fig. 3 compared to Fig. 4(f)(g). Furthermore, we observed in our reconstructions a dramatic effect of the non-negativity constraint appeared to drive the algorithm to "put the information in the right zones", see Fig. 3(c)(d) compared to Fig. 3(a)(b).

Fig. 4 shows the reconstructions obtained with both methods. Fig. 5 displays horizontal profiles taken across two different horizontal lines through the phantom.

The analytic reconstructions were accurate in the predicted regions. We recall that the method proposed is mathematically correct for the intersection of the region of Hilbert points with all lines that traverse the (known) support of the object without contracting a non-Hilbert point. For motion 2, a set of Hilbert points not satisfying this condition was easily identified and corresponds to the bright white region of Fig. 4(e). For the reconstructions of motion 1 with horizontal filtering ($\phi = 0$), the profiles in Fig. 5 indicate excellent quantitative reconstruction in the predicted regions (Fig. 4(c)). For reconstructions with an oblique filtering directions (Fig. 4(d)(e)) however, there seemed to be at times a small positive bias related to the difficulties of choosing the right constant for the finite Hilbert inversion, visible as faint light bands along the filtering direction.

For the iterative reconstruction, we immediately note that the effective reconstruction zone stretches beyond the boundary between the theoretically reconstructible and non reconstructible points, even though the error is higher in the zone of uncertainties (*cf.* Fig. 4(h)(i) and Fig. 5). This behavior is probably due to these regions suffering

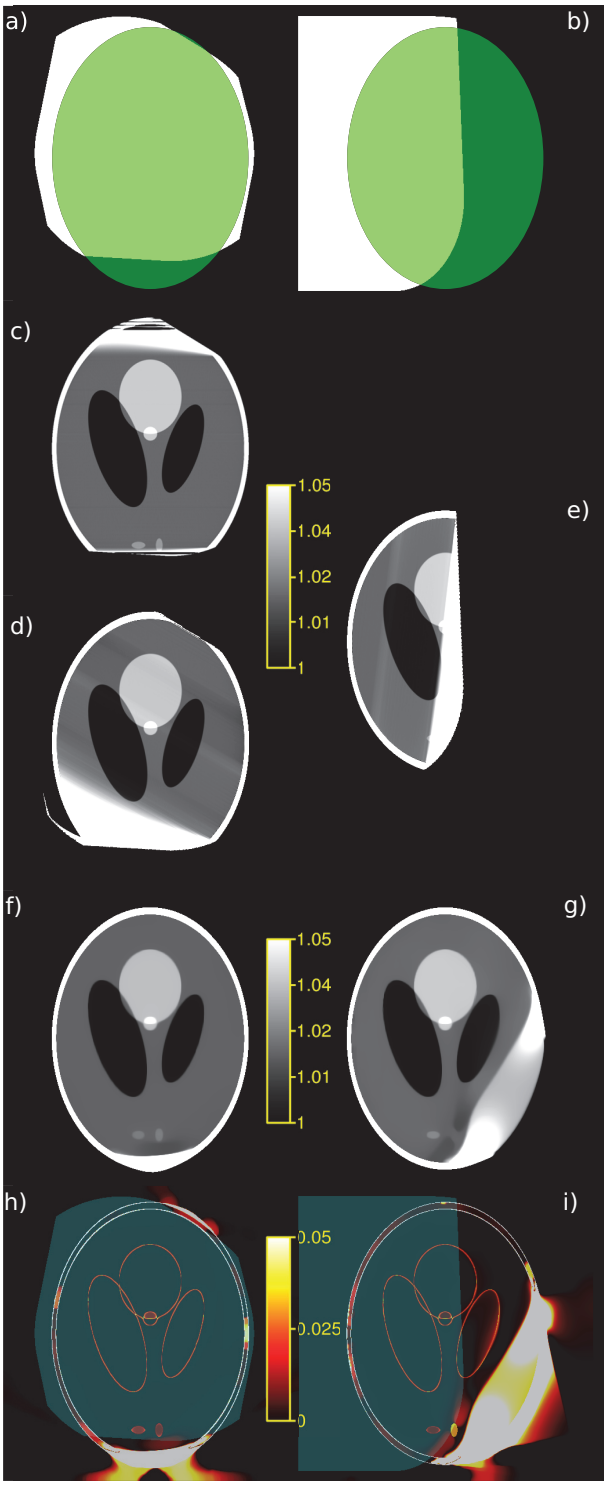

Fig. 4. Reconstructions of simulated cases *motion 1* (first column) and *motion 2* (second column) with both the analytic and iterative reconstructions methods. (a-b) Predicted FOV of reconstructible points. (c-e) Reconstruction with the analytic DBP-H method. (c) and (d) both correspond to motion 1, using different values of ϕ. (f-g) Iterative reconstruction. (h-i) Absolute value of the difference's map between ground truth image and iterative reconstruction, superimposed with the predicted FOV (in cyan).

only small amounts of missing data that prevent an analytic solution. The iterative algorithm was able to recover some structures. We note

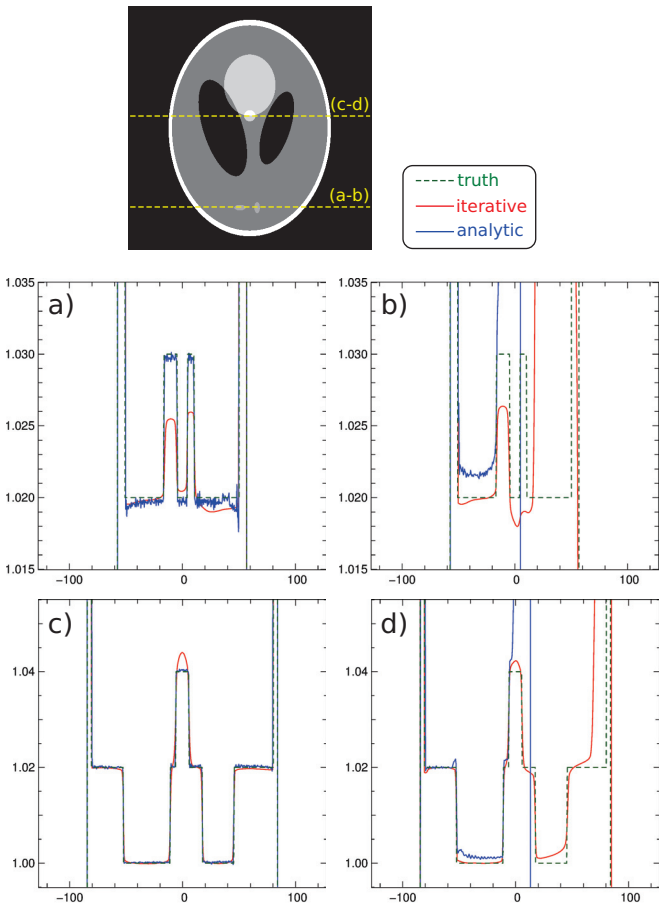

Fig. 5. Profiles taken in the reconstructions of Fig. 4. (a-c) *motion 1*. (b-d) *motion 2*. Note that the vertical scale for (a) and (b) is magnified by nearly 2.5 times compared to the one for (c) and (d).

that the regularization played a strong role here because Fig. 3 showed poor recovery of the iterative algorithm in exactly the "non-Hilbert point" areas of the object. In general, the quality of such extrapolations is strongly object-dependent, and some lines of response can bring more information than others if the structures are oriented in suitable directions. We also notice from the profiles of Fig. 5 that injecting regularization causes some bias in the recovered values of the finer structures even in the areas identified as reconstructible. This can be mitigated by decreasing the value of the hyperparameter μ, but at the cost of increasing the variance of reconstruction errors as seen in Fig. 3. Hence the regularization in our experiments showed the usual trade-off between bias and variance of the solution. However, there is no indication in the "non-reconstructible" region which features are correct and which are incorrect. Although, in Fig. 4(g), the large black ellipsoid on the right is correctly recovered, the small white ellipsoid at the bottom is completely missing.

IV. Discussion and conclusion

The results of our simulations show good coherence of the reconstructible regions predicted by the analytic method and the part of the image where the reconstruction by the iterative method was quantitatively successful. The iterative method, however, manages to recover certain features outside that region in a way which is still readable, although great care must be taken with interpreting such features in the non-reconstructible zone.

Our results also showed that the regularization and non-negativity constraint were essential for the iterative reconstruction to produce a good trade-off between bias and variance.

The analytic method's potential was constrained by the need to have Hilbert points aligned on a segment crossing the object support entirely in order to be able to recover that part of the image. Implementing an iterative one-sided Hilbert transform inversion method alongside the analytic backprojection could lead to a reconstruction method where the whole reconstructible region is recovered.

References

[1] J. Hoskovec, R. Clackdoyle, L. Desbat and S. Rit. *Exact fan-beam reconstruction with arbitrary object translations and truncated projections*. To appear in: IEEE Trans. Nucl. Sci., 2016.

[2] A.C. Kak and M. Slaney. *Principles of Computerized Tomographic Imaging*. Piscataway, NJ, 1988.

[3] S.G. Michlin and A.H. Armstrong. *Integral equations and their applications to certain problems in mechanics, mathematical physics and technology*. London, 1957.

[4] J. Nocedal. *Updating quasi-Newton matrices with limited storage*. Mathematics of computation, vol. 35, no. 151, pp. 773-782, 1980.

[5] F. Noo, R. Clackdoyle, and J.D. Pack. *A two-step Hilbert transform method for 2D image reconstruction*. Phys. Med. Biol., vol. 49, no. 17, p. 3903, 2004.

[6] J.D. Pack, F. Noo, and R. Clackdoyle. *Cone-beam reconstruction using the backprojection of locally filtered projections.* IEEE Trans. Med. Imag., vol. 24, no. 1, pp. 70–85, 2005.

[7] L.I. Rudin, S. Osher and E. Fatemi. *Nonlinear total variation based noise removal algorithms*. Physica D: Nonlinear Phenomena, vol. 60, no. 1, pp. 259-268, 1992.

[8] D. Xia, E. Sidky, L. Yu, Y. Zou, and X. Pan. *Exact ROI image reconstruction with perturbed source trajectories in C-arm CT*. Nuclear Science Symp. Conf. Rec., vol. 4. IEEE, 2005, pp. 4–pp.

[9] G.L. Zeng. *Image reconstruction via the finite Hilbert transform of the derivative of the backprojection*. Med. Phys., vol. 34, no. 7, pp. 2837–2843, 2007.

Author List

L

M

N